

SOLAR CELL ARRAY DESIGN HANDBOOK

Volume I

Jet Propulsion Laboratory
California Institute of Technology
Pasadena, California 91103

(NASA-CR-149364) SOLAR CELL ARRAY DESIGN
HANDBOOK, VOLUME 1 (Jet Propulsion Lab.)
496 p HC A21/MF A01 CSCL 22B

N77-14193

Unclas
G3/18 58973

October 1976

NATIONAL AERONAUTICS AND SPACE ADMINISTRATION

ABSTRACT

The Solar Cell Array Design Handbook is written at a practicing engineering level and provides a comprehensive compilation of explanatory notes, design practices, analytical models, solar cell characteristics, and material properties data of interest to personnel engaged in solar cell array performance specification, hardware design, analysis, fabrication and test.

Twelve handbook chapters discuss the following: historical developments, the environment and its effects, solar cells, solar cell filters and covers, solar cell and other electrical interconnections, blocking and shunt diodes, substrates and deployment mechanisms, material properties, design synthesis and

optimization, design analysis, procurement, production and cost aspects, evaluation and test, orbital performance, and illustrative design examples. A comprehensive index permits rapid locating of desired topics.

The handbook consists of two volumes: Volume I is of an expository nature while Volume II contains detailed design data in an appendix-like fashion. Volume II includes solar cell performance data, applicable unit conversion factors and physical constants, and mechanical, electrical, thermal, optical, magnetic, and outgassing material properties. Extensive references are provided.

Preceding page blank

PURPOSE OF HANDBOOK

This handbook is intended to serve as a working tool for individuals doing creative design of solar cell arrays, including the selection of materials and components. It is intended that the material in the handbook relate to three different levels of design activity. The first of these is at the systems level, where emphasis is on the overall characteristics of the solar cell array and its relationship to the spacecraft system and the intended mission. The second is at the equipment level, where emphasis is on the attainment of a producible design, component and material selection, and analytical performance prediction and optimization. The third level is concerned with design verification, testing, and design review. Thus, the handbook permits the checking of computerized analyses by design reviewers and management to assure that no major computational errors have occurred by accident.

The handbook also describes test methods which are typically being used to verify that requirements have been met.

The handbook is intended to be of maximum use to two levels of engineering personnel. To those not previously engaged in solar cell array design, brief engineering level introductions, historical reviews, and current state-of-the-art description will introduce them to the subject rapidly. Design details and step-by-step procedures, augmented by actual design examples, permit them, then, to develop design criteria, design and analyze an array, and test it. To the design specialist who is knowledgeable about the contents of the handbook, it has the advantage of providing detailed design and reference data collected in one place for easy access.

Preceding page blank

HANDBOOK ORGANIZATION AND CONTENT

Volume I of this handbook was organized to provide especially the novice designer with an understanding of the basic design concepts which permit creative design using new materials and a furthering of the state of the art for new, complex missions in a changing economic environment, in addition to providing the historical perspective and a compilation of the data of the current technology. To enhance the usefulness of the handbook in this respect, the material in Volume I was divided into the following 12 chapters, organized in sequence by chapter to answer the following questions:

1. What is solar cell array design all about?
2. What is the (environmental) problem?
3. Solar Cells
4. Covers
5. Interconnectors
6. Substrates
7. Materials

} What do we have to build with?

8. How do we invent a new design?
9. How will the design perform?
10. How do we transform the design into hardware?
11. How do we test hardware and establish design adequacy?
12. Can you illustrate the design process?

Volume II of this handbook contains detailed design data in an appendix-like format. Included are electrical and mechanical solar cell characteristics and mechanical, electrical, optical, thermal and other material properties. Applicable and frequently used unit conversion factors and physical constants are also included.

Each chapter is subdivided into technological topics and subtopics. The chapter and topic titles are given in the general Tables of Contents at the beginning of each volume. Subtopic titles are given in detailed Tables of Contents at the beginning of each chapter.

AUTHORSHIP AND ACKNOWLEDGEMENTS

This handbook was prepared by the Power Sources Engineering Department of TRW Defense and Space Systems Group, Space Vehicles Division (author and editor, H. S. Rauschenbach), under Contract No. 953913 with the California Institute of Technology, Jet Propulsion Laboratory, Pasadena, California.

Active support in the creation of this document of Ernst Cohn at NASA Headquarters and J. V. Goldsmith and R. H. Josephs at JPL is gratefully acknowledged. Valuable and significant material developed over the years by many authors (referenced in the text) has been included in this handbook with permission graciously given by the following publishers:

American Astronautical Society
American Chemical Society
American Electroplaters Society
American Institute of Aeronautics and Astronautics
American Institute of Chemical Engineers
American Nuclear Society
American Society for Testing and Materials
American Society of Mechanical Engineers

Centre National d'Etudes Spatiales
Chemical Rubber Publishing Company
Deutsche Gesellschaft fur Luft - und Raumfahrt e. V.
Gordon and Breach, Science Publishers, Ltd.
Institute of Electrical and Electronics Engineers, Inc.
Photovoltaic Specialists Conferences
Transactions on Aerospace and Electronic Systems
IECEC Conferences
McGraw-Hill Book Co.
Pergamon Press, Inc.
Southwest Research Institute
The Royal Society (London)
TRW Systems Group
Van Nostrand Reinhold Co.
Verein Deutscher Ingenieure - Verlag GmbH

Also appreciated are the contributions of many in government and industry who graciously contributed their time to the review of draft versions of this handbook. Most of their comments were incorporated in this document while others are planned to be incorporated in future editions.

Comments regarding this document are invited and should be directed to Jet Propulsion Laboratory, California Institute of Technology, Pasadena, California 91103, Attention: Energy Conversion Systems Section.

LEGAL NOTICE

This handbook was prepared under government contract and attempts to document the knowledge, data, and information which may be of current significance to solar cell array design.

It should be recognized that there exists a large number of patents which relate to all aspects of solar cell array design, fabrication, and testing, including solar cells, other materials, processes, components, arrangements, and designs. Some of these patents have been described in this handbook, but many more have not even been referred to. The description in this handbook of any component, process, apparatus, material, design, composition, or any other feature of any article may fall within a claim of an existing patent. It is not the intent of any of the authors, editors, and contributors to this handbook—nor is it the intent of any of the sponsoring or performing organizations involved in the preparation of this handbook—to induce anyone to infringe any existing patent. It is the responsibility of the prospective user of any of the information, material, data, and descriptions in this handbook to determine whether such usage constitutes infringement or noninfringement of any patent or otherwise legally protected or proprietary right.

Specifically, neither the United States, the National Aeronautics and Space Administration, the California Institute of Technology, the Jet Propulsion Laboratory, TRW Defense and Space Systems Group, nor any of the employees of these organizations, nor the preparers, editors, or approvers of this document, nor any other person:

- a) Makes any warranty or representation, expressed or implied, with respect to the accuracy, completeness, or usefulness of the information contained in this document, or that the use of any information, apparatus, method, or process disclosed in this document may not infringe privately owned rights; or
- b) Assumes any liabilities with respect to the use of, or for damages resulting from the use of any information, apparatus, method or process disclosed in this document.
- c) Sanctions, approves or recommends any designs, practices, selections or procedures contained in this document for a specific purpose, use, or project.

VOLUME I

CONTENTS

(Note: Detailed Tables of Contents are given at the beginning of each chapter.)

	Page
1. Evolution of Solar Cell Array Design and Hardware	1-1
1.1 History of Solar Cell Arrays	1.1-1
1.2 History of Solar Cells and Covers	1.2-1
1.3 Evolution of the Design Process	1.3-1
1.4 Design Standardization	1.4-1
2. The Environment and Its Effects	2-1
2.1 The Terrestrial Environment for Space Hardware	2.1-1
2.2 Launch and Flight Dynamics	2.2-1
2.3 The Space Environment	2.3-1
2.4 Solar Radiation in Space	2.4-1
2.5 The Space Radiation Environment	2.5-1
2.6 Orbital Effects	2.6-1
3. Solar Cells	3-1
3.1 Solar Cell Types	3.1-1
3.2 Electrical Characteristics	3.2-1
3.3 Effects of Corpuscular Radiation	3.3-1
3.4 Effects of Cell Thickness	3.4-1
3.5 Effects of Illumination	3.5-1
3.6 Effects of Temperature	3.6-1
3.7 Reverse-Biased Solar Cells	3.7-1
3.8 Mechanical Characteristics	3.8-1
3.9 Contacts	3.9-1
3.10 Optical Characteristics	3.10-1
3.11 Theoretical Solar Cell Models	3.11-1
3.12 Recent Developments and Future Trends	3.12-1
4. Solar Cell Filters and Covers	4-1
4.1 Construction and Terminology	4.1-1
4.2 The Cover/Space Interface	4.2-1
4.3 The Cell/Cover Interface	4.3-1
4.4 Discrete Inorganic Covers	4.4-1
4.5 Integral Inorganic Covers	4.5-1
4.6 Integral Organic Covers	4.6-1
4.7 Conductive Coatings	4.7-1
4.8 Angle-of-Incidence Effects	4.8-1
5. Electrical Interconnections	5-1
5.1 Terminology	5.1-1
5.2 Interconnector Design Examples	5.2-1
5.3 The Solar Cell Interconnector Design Problem	5.3-1
5.4 Wiring and Cabling	5.4-1
5.5 Isolation Diodes	5.5-1
5.6 Connectors and Terminals	5.6-1

Preceding page blank

CONTENTS (Continued)

	Page
6. Substrates and Deployment Mechanisms	6-1
6.1 Solar Cell Arrays - An Overview	6.1-1
6.2 Substrates Designs	6.2-1
6.3 Deployment Mechanisms	6.3-1
6.4 Array Orientation Drive and Power Transfer Mechanisms	6.4-1
7. Material Properties	7-1
7.1 General Characteristics of Some Specific Metals	7.1-1
7.2 General Characteristics of Some Specific Nonmetals	7.2-1
7.3 Mass, Density and Weight	7.3-1
7.4 Centroids, Moments of Inertia and Radii of Gyration	7.4-1
7.5 Elastic Modulus, Poisson's Ratio and Ultimate Strength of Metals	7.5-1
7.6 Elastic Modulus, Poisson's Ratio and Ultimate Strength of Silicon and Glass	7.6-1
7.7 Elastic Modulus, Poisson's Ratio and Ultimate Strength of Other Nonmetals	7.7-1
7.8 Elongation and Reduction in Area	7.8-1
7.9 Electrical Properties of Conductors	7.9-1
7.10 Electrical Properties of Dielectrics	7.10-1
7.11 Thermal Expansion Properties	7.11-1
7.12 Specific Heat and Heat Conductance	7.12-1
7.13 Transmission, Reflection, and Absorption of Light	7.13-1
7.14 Emission and Absorption of Heat	7.14-1
7.15 Magnetic Properties	7.15-1
7.16 Outgassing and Weight Loss	7.16-1
8. Design Synthesis and Optimization	8-1
8.1 Development of Design Requirements and Criteria	8.1-1
8.2 Design Optimization	8.2-1
8.3 Radiation Shielding Design	8.3-1
8.4 Optical Design	8.4-1
8.5 Thermal Design	8.5-1
8.6 Conceptual Array Design	8.6-1
8.7 Electrical Design	8.7-1
8.8 High-Voltage Arrays	8.8-1
8.9 Electrostatic Shielding Design	8.9-1
8.10 Magnetic Design	8.10-1
9. Design Analysis	9-1
9.1 Circuit Analysis	9.1-1
9.2 Practical Solar Cell Models	9.2-1
9.3 Array Circuit Models	9.3-1
9.4 Array Electrical Performance Prediction	9.4-1
9.5 Shadow Analysis	9.5-1
9.6 Thermal Analysis	9.6-1
9.7 Thermomechanical Stress Analysis	9.7-1
9.8 Fatigue and Wearout Analysis	9.8-1
9.9 Reliability Analysis	9.9-1
9.10 Orbital Mechanics	9.10-1
9.11 1-MeV Fluence Analysis	9.11-1
10. Designing for Production and Cost	10-1
10.1 Impact of the Design on Project Costs	10.1-1
10.2 Specifications	10.2-1
10.3 Solar Cell, Cover and Blocking Diode Specifications	10.3-1
10.4 Assembly Processes	10.4-1
10.5 Material and Process Specifications	10.5-1
10.6 Specifying Quality	10.6-1
10.7 Nondestructive Test (NDT) Methods	10.7-1

CONTENTS (Continued)

	Page
11. Evaluation and Test	11-1
11.1 The Test Program	11.1-1
11.2 Electrical Performance Measurements	11.2-1
11.3 Standard Solar Cells	11.3-1
11.4 Spectral Distribution and Response	11.4-1
11.5 Solar Cell Contact Integrity	11.5-1
11.6 Thermophysical Properties	11.6-1
11.7 Corpuscular Irradiation	11.7-1
11.8 Ultraviolet Irradiation	11.8-1
11.9 Combined Environments	11.9-1
11.10 Insulation Resistance and Voltage Breakdown	11.10-1
11.11 Temperature Cycling	11.11-1
11.12 Dark Forward Testing	11.12-1
11.13 Orbital Flight Data	11.13-1
11.14 Significance of Test Data, Uncertainties and Errors	11.14-1
12. Design Example	12-1
12.1 Conceptual Design	12.1-1
12.2 Preliminary Design	12.2-1
12.3 Final Design	12.3-1

CHAPTER 1

EVOLUTION OF SOLAR CELL ARRAY DESIGN AND HARDWARE

CONTENTS

	Page		Page
1.1 History of Solar Cell Arrays	1.1-1	1.3 Evolution of the Design Process	1.3-1
1.1.1 Solar Cell Powered Spacecraft	1.1-1	1.3.1 Design Phases	1.3-1
1.1.2 Deployable Array Development	1.1-2	1.3.2 The Design Organization	1.3-1
1.1.3 Trends and Typical Designs	1.1-4	1.3.3 Design Personnel	1.3-2
1.2 History of Solar Cells and Covers	1.2-1	1.3.4 Uncertainties and Risks	1.3-2
1.2.1 Solar Cell Types	1.2-1	1.3.5 Human Engineering	1.3-2
1.2.2 Solar Cell Development	1.2-1	1.4 Design Standardization	1.4-1
1.2.3 Solar Cell Contacts	1.2-2	References	1. R-1
1.2.4 Solar Cell Covers and Coatings	1.2-3		

TABLES

1.1-1 U.S. Space Launches as of December 31, 1973	1.1-1	1.1-2 Spacecraft Orbiting, Totals as of December 31, 1973	1.1-1
---	-------	---	-------

FIGURES

1.1-1 Solar Cell Output as a Function of Time for Transit 4B and TRAAC	1.1-2	1.1-2 Evolution of Solar Cell Array Configurations	1.1-3
--	-------	--	-------

CHAPTER 1

EVOLUTION OF SOLAR CELL ARRAY DESIGN AND HARDWARE

In a time period of less than two decades, solar cell arrays have grown in size from less than 1 watt to over 10 kW of electrical output in space. New designs on the drawing boards and in the development laboratories are for arrays having a power output ranging from 10 to 100 kW.

In the same time span, the solar cell array design effort has matured from a spirited pioneering effort into a sophisticated, systematized, computer-aided process. While it has not been possible to adequately define or improve, or otherwise influence the creative

design activity, all other aspects of the design process have been formalized and, for good reason, subjected to documentation, control, and verification.

In this chapter a brief, general overview is given of the historical development of solar cell array hardware and the array design process without going into technical detail. The current state of the art of solar cell array technology of interest to array design is discussed in detail in Chapters 2 through 12. Where appropriate, cross-references are given in the text.

1.1 HISTORY OF SOLAR CELL ARRAYS

1.1.1 Solar Cell Powered Spacecraft

The space age arrived on October 4, 1957, when the USSR launched into earth orbit Sputnik 1, a 23-inch aluminum sphere weighing 184 pounds, returning density, temperature, cosmic ray and meteoroid data for 21 days. This satellite, as well as its successor, Sputnik 2, were powered by chemical batteries only. The first solar cell array that successfully operated in space was launched on March 17, 1958, on board Vanguard I, the second U.S. earth satellite. This solar cell array consisted of six solar panels distributed over and mounted to the outer surface of an approximately spherical spacecraft body. Each panel was made of 18 p-on-n solar cells of 2 x 0.5 cm size, having approximately 10 percent energy conversion efficiency at 28°C. This solar array system provided less than 1 watt of power for more than 6 years.

Tables 1.1-1 and 1.1-2 show the total number of spacecraft successfully launched between 1957 and 1973; this group includes 87 percent of all spacecraft launched during this time span. Most of these spacecraft have used solar cell arrays as the primary power source.

Table 1.1-1. U.S. Space Launches as of December 31, 1973 (Ref. 1.1-1)

Year	Successes*	Failures	Total
1957	0	1	1
1958	7	10	17
1959	11	8	19
1960	16	13	29
1961	29	12	41
1962	52	7	59
1963	37	8	45
1964	54	5	59
1965	62	6	68
1966	70	4	74
1967	59	3	62
1968	47	3	50
1969	40	1	41
1970	28	1	29
1971	29	4	33
1972	30	0	30
1973	23	2	25

*Payload(s) injected into orbit.

- International payloads are included, if launched by U.S. booster.
- Classified U.S. payloads are included.

Table 1.1-2 Spacecraft Orbited, Totals as of December 31, 1973 (Ref. 1.1-1)

Sponsor	Earth Orbit	Lunar Missions	Planetary Impact/Orbit	Solar Orbit	Totals
Australia*	2	--	--	--	2
Canada*	6	--	--	--	6
ESRO*	7	--	--	--	7
France*	11	--	--	--	11
Germany*	3	--	--	--	3
Intelsat*	17	--	--	--	17
Italy*	3	--	--	--	3
Japan	4	--	--	--	4
NATO*	2	--	--	--	2
PROC	2	--	--	--	2
UK*	7	--	--	--	7
USA**	681	29	1	16	727
USSR***	741	21	9	8	779
Totals	1486	50	10	24	1570

*Includes launches from the U.S. boosters of satellites built by sponsors or built jointly under cooperative agreements with the U.S.

**U.S. totals consist of exclusively U.S. sponsored satellites, including unidentified satellites, but not including Atlas-Centaur, Saturn, or Titan III non-functional payloads.

***USSR totals include unidentified Russian spacecraft; these totals do not include earth-parking platforms used for injecting payload spacecraft into other orbits.

Since 1957 solar arrays have grown in size and complexity. The largest U.S. solar array flown was on Skylab 1, launched on May 14, 1973, into near-earth orbit. Skylab carried two separate solar array systems: the Orbital Workshop (OWS) array and the Apollo Telescope Mount (ATM) array. The Orbital Workshop array design consisted of two deployable wings. Each wing consisted of 73,920 n-on-p solar cells of 2 x 4 cm size, providing in excess of 6 kW of electric power in orbit. The OWS array in flight actually consisted of one wing only; during launch a meteoroid/thermal shield tore loose from the OWS, ripping away the second wing.

The ATM array consisted of four deployable wings, carrying a total of 123,120 solar cells of 2 x 2 cm and 41,040 cells of 2 x 6 cm size, and providing in excess of 10 kW of electric power in orbit.

Typical early satellites were approximately spherical. At first as for Vanguard I, relatively small solar cell assemblies were attached to the satellite housing. Soon, however, the entire usable exterior surface of satellite housings was being utilized for the mounting of solar cells to accommodate increasing power requirements. To extend the available solar cell array area, the satellites were fitted with so-called "solar cell paddles." Explorer 6, launched in August of 1959, was the first spacecraft to use paddles. Of the four 51-cm² paddles, one failed to extend fully and lock. The solar cells of the resultant three-paddle array rapidly degraded in the Van Allen belt and all transmission was lost in 2 months.

This failure was followed by a string of successes, and solar cells became a preferred power supply. Then, on July 9, 1962, a high-altitude nuclear explosion, "Starfish," released an estimated 10²⁵ fission electrons that became trapped in the lower region of the Van Allen belt. The resultant damage to solar cell arrays, evident in Figure 1.1-1, rapidly caused a number of spacecraft to cease transmission.

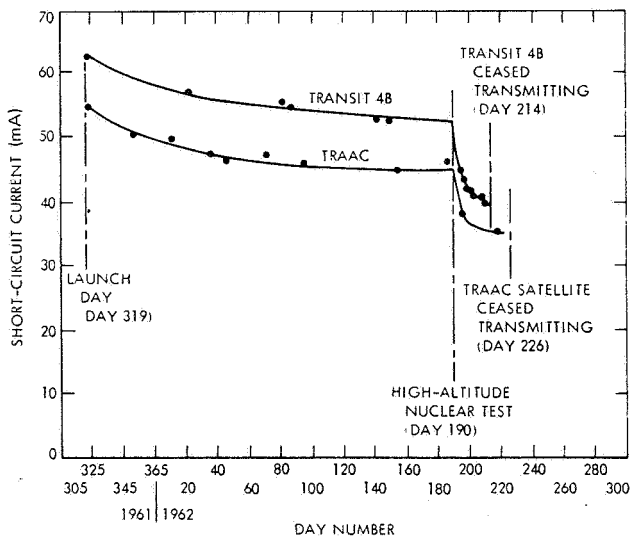


Fig. 1.1-1. Solar Cell Output as a Function of Time for Transit 4B and TRAAC (Ref. 1.1-1)

Radiation damage became a subject of intense interest, and changes were implemented to improve radiation resistance of arrays. These included the n-p solar cell, increased base resistivity, and more careful shielding by coverslides. As power requirements increased, detailed criteria for the array were evolved. Ranger Block II, Mariner 2, Mariner 4, Nimbus 1 (1964), and Pegasus (1965) marked a return to flat-mounted solar cells to accommodate thermal expansion better than the popular rigid-shingling method (see Section 5.2). In flat-mounting, however, only the coverslide and its adhesive shielded each cell. On several spacecraft launched in 1967 and 1968, coverslides slightly smaller than the solar cells were used for ease in construction and because of tolerances necessary in cell and coverslide size. Any adhesive that extruded around the coverslide was carefully cleaned away. As a result, on Intelsat 2-F4, the Applications Technology Satellite (ATS)-1, and the Gravity Gradient Test Satellite (GGTS) about 5 percent of the solar cell

front area was bare or covered only by a thin contact bar. The rapid degradation of those solar cell arrays has been attributed to low energy protons of the outer region of the Van Allen belt entering the bare solar cell surface and damaging the junction (see Sections 3.3.3 and 8.3.6).

Satellite designs soon required more powerful solar cell arrays than could be provided from paddles. Oriented or semioriented solar cell panels provided one answer, while cylindrical, body-mounted solar cell panels for larger diameter launch vehicles provided another. Further increases in power requirements in recent years have led to the development of large, deployable arrays. Designs have included the range from simple deployable rigid solar cell panels to multipanel, multiple-foldout arrays, accordion-style fold-out, and rollout arrays. Figure 1.1-2 illustrates some of the generic configurations.

1.1.2 Deployable Array Development

As the power requirements of satellites increased, the need for larger arrays of solar cells indicated a trend toward deployable arrays. Recognizing this potential need, various companies and government agencies began to develop such arrays several years ago. Some of the fundamental considerations of deployable array designs included:

- Type of solar cell - single crystal silicon or thin film
- Substrate - rigid panel or flexible
- Stowage and deployment - protection of the cells during launch environments and deployment techniques
- Array stiffness - to minimize interaction with the spacecraft control system.

There are several ways to categorize the deployable arrays developed over the last several years: (1) by packaging technique (rollup, flat-pack, wrap-around); (2) by substrate design (rigid panels, flexible membranes); and (3) by deployment technique (folded, rolled, or telescoping booms actuated electrically, mechanically, or pneumatically).

Array Substrates

Most deployable arrays flown to date have used rigid panel substrates. Aluminum honeycomb panels with aluminum or fiberglass/epoxy facesheets were the typical construction, although machined panels have been used and electroformed nickel and aluminum substrates have been investigated.

As one departed from conventional array designs, emphasis was placed on the use of new materials and unconventional designs. More recent rigid or semi-rigid substrate designs of honeycomb panels included the use of graphite/epoxy and Kapton polyimide film facesheets. Other recent substrate designs used cut metal or composite material framing/closeout members. Also under development were graphite/epoxy, fiberglass, and Kapton polyimide film "framed membrane" panels.

For rollup array designs, the substrates have typically been constructed from single layer or laminates of fiberglass/epoxy and Kapton polyimide film. The use of film-type substrates to support glassed silicon cells requires protection during handling and launch environments.

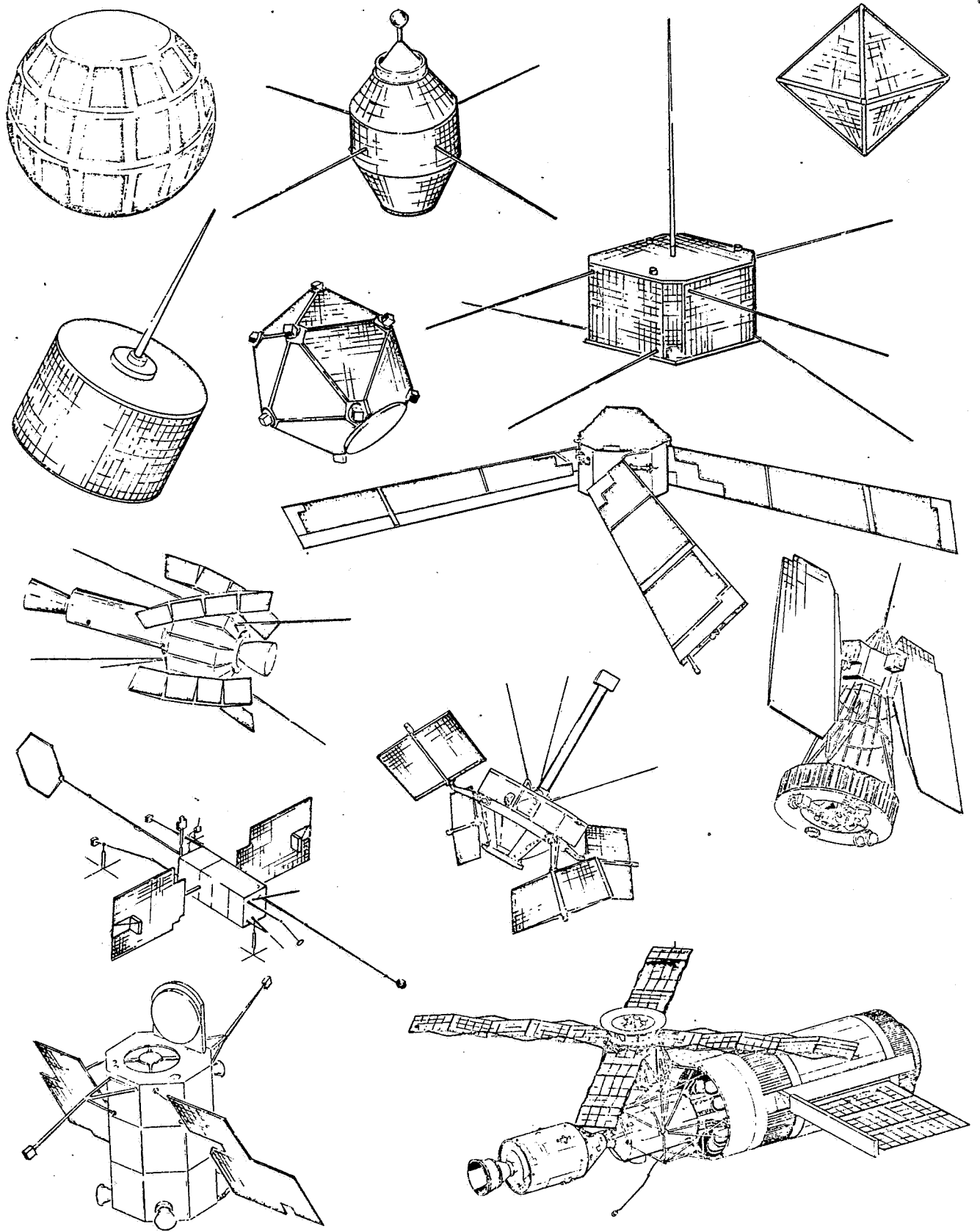


Fig. 1.1-2. Evolution of Solar Cell Array Configurations

Array Stowage and Deployment

Rigid panel substrates for deployable arrays are usually hinged together and folded accordion-style or wrapped around the outside of the satellite. Deployment is accomplished by either torsion springs at the panel hinges or by means of an auxiliary member, such as a folded beam or an extendible boom.

For flexible substrates the two basic concepts are: (1) rollup, where the cell stack (cells, interconnects, power buses, and substrate) is rolled on a cylindrical drum and deployed, using one or more extendible booms, and (2) foldout, where the cell stack is folded and deployed accordion-fashion by one or more extendible booms. Actuation of the extendible boom can be achieved through electrical, mechanical, or pneumatic method.

Strength/Stiffness Considerations

The large-area array designs necessitate careful attention to strength and stiffness requirements. In many respects, such designs are stiffness rather than strength critical. Array stiffness is a major factor during both the launch phase and the orbital phase. During the launch phase the most severe environmental load arises from the launcher release load and from the acoustic field. It has been common practice to structurally design a lightweight array such that its natural frequency is substantially higher than the environmental driving frequency. This has been accomplished, in most cases, by the use of high-modulus materials in a rigid, stiff design configuration, and has resulted in natural frequencies above 30 Hz. However, this has also resulted in a relatively heavy design.

Recently, less stiff, lightweight solar cell array designs have been developed having natural frequencies as low as 10 Hz yet being able to successfully endure such launch environments without incurring unnecessary weight penalties.

During the orbital phase, deployed array stiffness is a major factor in the interaction of the relatively flexible array with the spacecraft attitude control system. The control system must be designed to accommodate the low natural frequencies of the deployed large array. Typical values for arrays in the multikilowatt sizes range from 0.03 to 1 Hz. Specific dynamic array design criteria for each spacecraft must be separately defined, together with the design criteria for the attitude control system characteristics. Typically, the deployment boom is the greatest determinant of array stiffness. Hence, stiffer booms require the use of high modulus materials, the use of larger diameter booms, and/or the use of truss-type extendible elements.

1.1.3 Trends and Typical Designs

The increased power requirements on recent satellites clearly indicate the need for larger area solar cell arrays. Hence, there are continuous efforts to develop more efficient (specific power, specific weight) deployable solar cell arrays through the use of new materials, new design configurations, and higher efficiency solar cells.

United States contractors and NASA centers have developed both rollup and foldout concepts. Fairchild Hiller, General Electric, and Ryan (under JPL contracts) and Hughes Aircraft (under Air Force contracts) have pursued the rollup approach with various arrangements of extendible booms. The Boeing Company developed a foldout array under JPL funding using beryllium-framed panels of pretensioned fiberglass tape as a substrate. TRW Systems has recently developed a Kapton polyimide film facesheet/aluminum honeycomb substrate foldout design (flat-pack or wraparound). Lockheed, under NASA sponsorship, has developed several large-area foldout array concepts, including the Space Station array.

Foreign industry and space agencies have also been very active in the development of array designs and technology. In Germany, Messerschmitt-Bölkow-Blohm has developed graphite/epoxy facesheet/honeycomb core substrate flat-pack designs. Engins MATRA, France, has developed fiberglass/epoxy facesheet/honeycomb core substrate flat-pack designs. In England, the Royal Aircraft Establishment is developing a perforated Kapton polyimide film membrane flat-pack design. The Canadian Communication Research Centre is developing a Kapton/fiberglass laminate membrane flat-pack design.

For gross satellite configuration studies, the power-to-weight ratio, or specific power, is the significant parameter. Typically, the specific power is a function of array size, array type, orbit altitude, mission duration, and solar cell type. With present technology for multikilowatt arrays, specific power from 15 to 44 W/kg (7 to 20 W/lb) can be achieved. Projections as high as 110 W/kg (50 W/lb) have been reported using improved solar cells, newer materials and advanced design configurations. Generally, the smaller the array, the greater the structural penalty which degrades specific power. For arrays smaller than 1 kW, flexible substrate (rollup) arrays offer no advantage and a deployable array using rigid panels is preferred.

Additional details on solar cell array substrate and deployment mechanism designs are provided in Chapter 6.

1.2 HISTORY OF SOLAR CELLS AND COVERS

Solar cells are semiconductor devices which convert solar energy utilizing the photovoltaic effect. Photovoltaic energy conversion is based on a quantum-mechanical process by which incident photons free charge carriers from their otherwise bound conditions within a semiconductor. In a solar cell, a p-n junction collects the freed charge carriers and forces them through an externally connected electric load.

Solar cell covers are transparent plates that shield the solar cells from excessive damage by space environments and otherwise enhance the power output capability of the solar cells.

1.2.1 Solar Cell Types

Many types of different solar cells have been developed, but only two types have achieved prominence. Foremost is the single-crystal silicon cell which presently has a typical maximum energy conversion efficiency of 10 to 14 percent at 25°C under air-mass-zero sunlight conditions. The corresponding electrical output is about 15 to 20 mW/cm² at approximately 0.45 volt. To date, these silicon solar cells have been manufactured almost exclusively for space programs and have cumulatively amounted to 50 to 70 kW of electric output.

The second type of solar cell is the thin-film cadmium-sulfide cell, or more correctly, the Cu₂S-CdS cell. To date, thin-film cells with about 10 kW cumulative electric output have been fabricated. Cells were found to be highly unstable and sensitive to humidity—problems which have precluded their use for space application. However, these difficulties have theoretically been solved. The CdS cell is amenable to very low cost mass production techniques.

While the thin-film cells (cadmium sulfide, cadmium telluride, indium phosphide) appear to offer advantages of low cost, good radiation resistance and handleability, their low efficiency and lack of stability under thermal cycling imply that the single crystal silicon cell will remain the basic building block of solar arrays for quite some time. Several U. S. and European groups are again actively doing development in CdS cells, claiming to be close to the solution of the stability problem (Ref. 1.2-1).

1.2.2 Solar Cell Development

After considerable theoretical and experimental work, started in the 1930's and carried on with great vigor during the 1940's, the Bell Telephone Laboratories produced the first practical solar cell in 1954. This cell is of the planar single crystal silicon type and was the forerunner of today's solar cell. Significant technological advances which permitted the development of such solar cells were breakthroughs in purifying the silicon material, growing crystals by the Czochralski method (late 1940's and early 1950's), and forming p-n junctions by high-temperature vapor diffusion in 1954 by Fuller and Ditzenberger (Ref. 1.2-2).

The early solar cells were of circular shape (approximately 3 cm in diameter) determined mainly by the grown crystal diameter. These cells were of the p-on-n, wraparound contact type and had relatively low conversion efficiencies (up to 6 percent), mainly due to high internal resistance (in the order of 5 to 10 ohms) and excessive material defects. The theoretical maximum efficiencies calculated at that time ranged from about 18 to 22 percent for a solar intensity of 1 kW/m² of AM1 spectrum* (see Section 3.2.6).

It is interesting to note that in the United States the original material used for solar cells was n-type silicon, while in the USSR it was p-type material. P-type silicon was used by the Russians (1956) for two reasons: (1) to scientifically contrast the U. S. work, and (2) p-type material was cheaper in the USSR than n-type. It was found later that cells made from p-type silicon were more resistant to corpuscular radiation as found in space than cells made from n-type material. Thus, after discovery of the Van Allen radiation belts, U. S. solar cell production switched over to diffusion of n-layers into p-type silicon after 1960 (Ref. 1.2-2).

While the Bell Telephone solar cell was initially considered for terrestrial use only, the success of solar cells in space began in 1958 when rectangular 0.5 x 2 cm cells (still p-on-n) were selected for the Vanguard satellite. Later cell sizes were increased to 1 x 2 cm, 2 x 4 cm, and larger. Contact grid lines over the active cell area were utilized to reduce cell internal resistance to between 0.1 and 1 ohm; silicon monoxide antireflective coatings and improved processes increased peak cell conversion efficiencies to just below 13 percent at AM0 conditions (by 1960) with the mean at around 10 to 11 percent (Ref. 1.2-2).

Between 1961 and 1971 no major progress in silicon solar cell technology was reported. Emphasis was placed on achieving radiation resistance and weight and cost reductions. A large number of avenues to improve cell efficiency or reduce cost were attempted and abandoned. Foremost among those efforts were the developments of the dendritic cell and the lithium-doped cell, both utilizing single-crystal silicon.

Dendritic solar cells are fabricated from silicon sheet which has been produced by dendritic growth,

* AM1—"Air-Mass One." Indicates the modification of the space, or "Air-Mass Zero" (AM0) solar spectral intensity distribution by the filtering effect of one layer of earth atmosphere of minimum average thickness; i. e., perpendicular to the mean earth surface (see also Section 2.4.2).

rather than by cutting and slicing of large, cylindrical crystals for conventional silicon cells. In the dendritic growth technique two coplanar dendrites from a single crystal seed are introduced into the molten silicon. As these seeds are pulled from the melt, a silicon web freezes between them, resulting in a continuous length of silicon ribbon having the proper finished solar cell dimension in its cross section. Major difficulties were encountered with temperature control (better than $\pm 0.02^\circ\text{C}$ at approximately 1420°C is required) to achieve uniform dendritic growth. Solar cell energy conversion efficiency of such cells has been nearly as high as that obtained during the same time period from conventional cells (Ref. 1.2-3).

The development of lithium-doped, single-crystal silicon cells was initiated in the early 1960's and continued through 1974 to improve the resistance of solar cells to corpuscular radiation. It had been discovered that the controlled introduction of small quantities of elemental lithium would anneal radiation-induced defect centers in the silicon lattice; thereby, in orbits where radiation levels were high, solar cell electrical output would degrade less. Lithium-annealing of radiation damage was indeed achieved in cells produced in pilot-line quantities.

Lithium doping was found to be most effective in annealing the cell's electrical degradation that was caused by protons and neutrons. For annealing to occur, solar cells manufactured from oxygen-rich silicon required to operate at temperatures of at least 50°C while those manufactured from float-zone processed silicon required at least 30°C . It was also found that the lithium concentration and doping profile had to be adjusted for a specific end-of-life charged-particle fluence for lithium-doped silicon solar cells to realize a net gain in power output over conventional silicon solar cells; the annealing rate (i. e., the rate of recovery of the electrical output after irradiation) was not found to be a reliable indicator of cell quality (Refs. 1.2-4 and 1.2-5).

In 1972 Dr. Lindmayer of COMSAT Laboratories announced the first step in solar cell efficiency improvement in 10 years. Efficiency was increased for space application cells by about 30 percent over state-of-the-art space cells. This improvement was achieved by critically examining and revising existing theories, increasing the cell blue response, decreasing the internal cell resistance to about 0.05 ohm, and improving the charge carrier collection process within the cell. The resultant, so-called "violet" cell, maintained its superior performance after electron bombardment with integrated fluences beyond 10^{16} 1-MeV e/cm² (Ref. 1.2-6).

Another noteworthy development announced in 1972 was the Vertical Multijunction (VMJ) solar cell device, which has since been fabricated in pilot-line quantities. An experimental array has been assembled from these cells and tested. The VMJ device took its name from its construction: many alternate layers of n- and p-type silicon form a multilayer stack similar to a "layer cake." By turning the "layer cake" on its side, the layers stand vertical, and sunlight impinges from above, on the "sides" of the "layers," so to speak. Each junction separates the charge carriers, and the junction voltages add up algebraically. A pair of ohmic contacts, one on each end of the stack, permit extraction of power. By its nature, the device produces high voltage at low current and has inherently a relatively low internal resistance. This makes the VMJ device at least conceptually very attractive for solar concentrator and,

perhaps, high power density applications. While some theoretical work has accompanied the experimental development to permit some degree of VMJ design optimization, the current key factor which restricts exploitation of this concept is the absence of any reasonable fabrication technology (Ref. 1.2-7).

Another type of vertical multijunction solar cell, announced in 1973, is constructed from a single piece of silicon into which narrow, vertical-wall grooves are etched. After diffusion and final processing, the vertical junctions are electrically connected in parallel rather than series (Ref. 1.2-8).

Between 1972 and 1975 a variety of single-crystal silicon solar cells were developed and marketed under a variety of names. Just prior to 1972, "blue-shifted," "ultra-blue," "violet," and "drift field" cells had appeared. Now, "high-efficiency," "super-blue," "black," "enhanced," "augmented," "hybrid," "intermediate," and other types made their debut. During late 1974 and early 1975 two of these types were being manufactured in production quantities by Heliotek. One type, designated as an "intermediate" cell, showed approximately 10 percent higher output than conventional cells, while the other type, designated the "high efficiency" cell, showed approximately 20 percent higher output than conventional cells (see Section 3.12 for detailed data). This output gain was achieved by careful optimization of the solar cell design and construction, introduction of an electric field into the base region to improve minority carrier collection, a shallow diffused junction with enhanced blue sensitivity, an optimized contact grid line system, and an improved Ta₂O₅ antireflective coating. Glassed cell performance is further enhanced by use of a selected coverslide adhesive (Dow Corning 93-500) and a coverslide ultraviolet rejection filter having a lower cut-on wavelength (0.35 μm) than used for conventional cells (0.41 to 0.435 μm) (Refs. 1.2-9 and 1.2-10).

1.2.3 Solar Cell Contacts

Solar cell contacts are metallizations on the solar cell p- and n-type silicon semiconductor surfaces which permit making of low resistance electrical connections to the cell, typically by soldering or welding thin wires or metallic ribbons to the cell contacts.

The general problem with metallic contacts on semiconductor surfaces is that the metal/semiconductor interface tends to form a junction with a typical barrier voltage of its own which subtracts from the cell's photo voltage. The required technique is to make this interface "ohmic," i. e., free of nonlinear electrical behavior. The technique has not always been performed flawlessly, neither in the early solar cell days, nor today. The payoff from low resistance ohmic contacts is improved cell efficiency.

During the 1950's the predominant contact application technique was electroless nickel plating of unmasked portions of the otherwise finished silicon solar cell wafer immersion of the plated cells in soldering flux and liquid solder baths.

The advent of the n-on-p solar cells also brought along a new contacting technique: a vacuum-deposited thin layer (a few hundred angstroms) of titanium, followed by a similarly deposited, much thicker layer (1 to 2 μm) of silver. These layers were then sintered at about 600°C to improve contact adhesion to the silicon and reduce contact resistance. Usually, the sintered cells were then solder-dipped.

The titanium-silver contact system was later found to be sensitive to humidity by noting that completely finished solar panels in uncontrolled, long-term storage had suffered unexplained power losses. Analysis revealed that the inherently corrosive titanium-silver couple had reacted with water vapor from the atmosphere, causing the formation of an oxide interface layer between the titanium and the silver. This layer increased the cell series resistance and, therefore, lowered the cell conversion efficiency. Workers at AEG-Telefunken quickly found a solution by adding palladium between the two contact metals during the evaporation process, thereby electrochemically passivating this contact system, with a slight economic penalty. Such passivated cells are being fabricated now in increasing quantities for space use.

Many other contact systems of interest have been developed, but have not been used on as large a scale as the electroless nickel and titanium-silver contact systems described above. Except for evaporated and sintered aluminum contacts, all other systems used in the U.S. or in Europe use less economically attractive schemes, and provide only marginally superior contact adhesion and electrical conductivity over the titanium-silver system. The humidity resistance of the titanium-silver system with either palladium passivation or protection by solder is more than adequate for space use, except that solder may impose an undesirable weight penalty.

The original circular Bell Telephone cell had wrap-around contacts; that is, both the n- and p-contacts are on the same solar cell side, namely on the back side. By 1958 space applications forced cell shapes to be rectangular or square for enhanced packing density, and cell internal resistance forced the contacts to be placed on each of the respective cell sides; i. e., the n-contact on the cell n-side, the p-contact on the p-side. By 1964 wraparound contacts had reappeared, but this time for the purpose of utilizing more active cell area for energy conversion for the rectangular and square cells. However, neither increased cell efficiency nor enhanced power output materialized from wraparound contact cells, because internal losses seemed to increase at the same rate at which the active cell area was increased.

Solar cell contacts and cell interconnectors used on space arrays are subject to solar-eclipse induced thermal cycling. This thermal cycling can cause severe mechanical stresses in both the solar cell interconnectors and solder or weld joints, and can cause fatigue failures. In the past, space missions were rather short (typically less than 2 years); however, real problems are being encountered as design goals for spacecraft life approach 10 years.

Additional discussions of solar cell contacts and related topics can be found in the following sections of this handbook:

- Contact Corrosion - Section 2.1.6
- Contact Descriptions - Section 3.9
- Temperature Cycling Effects - Section 5.2.2
- Interconnector-related Effects - Sections 5.2 and 5.3

1.2.4 Solar Cell Covers and Coatings

Since the beginning of solar cell use in space, it has been recognized that in practical applications solar cells must be used in conjunction with other optical elements. Initially, solar cell filters were employed for temperature control only. But by 1960 it was generally recognized that transparent covers were also required to protect the solar cells from charged particle irradiation found in space above a 400-km altitude. Since 1960 solar cell array designers, therefore, considered both thermal control and shielding from corpuscular radiation. A third consideration, also investigated since the late 1950's, has been micrometeoroid erosion of unfiltered solar cell surfaces and, later in this period, of both the solar cell covers and their filters.

Some success was achieved in the late 1950's with silicon oxides, SiO_x , applied by special methods directly to the solar cells. These direct coatings promised to offer some advantages over glass covers with respect to decreased weight and costs. Although the emittance was not quite as high as with glass, the improvement over the uncovered cell was quite significant. Higher values of emittance could be obtained with thicker oxide films but only at the expense of impaired adhesion and transparency of the coating.

For the direct coatings to be effective, the reflectivity, and therefore the absorption constant and the index of refraction of the deposited coating, had to be low. This implied that the coating had to be thick relative to the wavelength under consideration. However, thick vacuum-deposited coatings were difficult to achieve. Absorption, due to accumulated impurities in the region where high transmission was required, and mechanical instabilities (like blistering and cracking) provided severe limitations.

For this reason the economically less desirable method of mounting a separate coverslide to the silicon solar cell had to be chosen. Glass provides excellent emissivity for low temperature radiation and has high transmission for solar radiation. In addition, glass covers give better protection against corpuscular and ultraviolet radiation and micrometeorites than direct coatings can give.

The two types of covers most frequently used between 1960 and 1974 were fused silica and microsheet. Fused silica was used in a thickness ranging from 75 μm (0.003 inch) to 1.5 mm (0.060 inch) with the three most common thicknesses being 150, 300, and 500 μm . Microsheet was used only in a 150- μm thickness.

To effect efficient heat transfer from the cells to space, the glass covers had to be cemented directly to the cells. This created a new problem: all cements darkened under the strong ultraviolet radiation present in space and reduced the solar illumination incident on the cells. To reduce adhesive darkening, ultraviolet reflecting coatings were developed to keep the damaging ultraviolet radiation away from the cement.

The protection of the coverglass adhesive was obtained through the incorporation of ultraviolet-reflective coatings initially having cut-on wavelengths of 450 μm . (The cut-on wavelength is defined as that wavelength where the transmittance has reached its 50 percent value.) The good results obtained with

these covers and filters, together with more radiation tolerant silicone adhesives which became available, led to a gradual lowering of the cut-on wavelength to first 430 and then 400 μm . Recent developments of more and more blue sensitive solar cells pushed the cut-on wavelength to even lower values. Present "super blue" or "violet" sensitive cells require approximately a 350- μm cut-on wavelength to fully realize their improved energy conversion capability.

To optimize the solar cell cover and filter design and at the same time protect the ultraviolet reflective coating from possible degradation by low energy, heavy particles in space, the ultraviolet reflective coating was placed inside the solar cell/cover stack, while the outside surface of the cover was coated with an antireflective coating. This outer antireflective cover coating, vacuum-deposited magnesium fluoride (MgF_2), reduced reflection losses on the first surface from approximately 4 percent to approximately 2 percent.

Inside the cell/cover stack, provisions were required to match the optical impedance of the cover to those of the cover adhesive and the silicon. Choice of a transparent silicone adhesive, instead of the originally used epoxy, and application of a silicon monoxide (SiO) coating to the silicon accomplished these objectives. The silicon monoxide antireflective coating on the solar cell was used since the early 1960's and throughout 1975. With this coating, cell output degraded in glassing by approximately 2 to 5 percent due to mismatches of the indices of refraction between cover glass, the adhesive, and the silicon monoxide. Work was started in Europe in the late 1960's to reduce such glassing losses by better matching of the indices of refraction. Solar cell antireflective coatings using TiO_x , Ta_2O_5 , and others indeed improved glassed cell performance. Considerable development effort was required, however, before a repeatable process and optimized electrical performance was obtained. Since late 1974, the Heliotek high-efficiency production cells use a Ta_2O_5 coating.

1.3 EVOLUTION OF THE DESIGN PROCESS

The process of engineering design, in general, can be described in many ways. In the least formal sense it is the movement from the general to the specific, from disorder to order, and from thought to matter. In the most formal sense it consists of the identification of a set of design requirements and constraints followed by the steps of synthesis, analysis, selection, fabrication, test, and evaluation. On the one hand the design process is logical and mathematical, while on the other it is intuitive and defies description. The process is affected by the kind of product it is applied to, by the organizational environment under which it is applied, by time and fiscal constraints, and—perhaps most important—by the skills, experience, and personalities of the personnel responsible for its execution.

The design process for solar cell arrays is essentially identical to the general design process, with perhaps one major exception being the relatively large number of design constraints imposed on the array design. Perhaps more than any other component on a modern spacecraft or satellite, the solar cell array has a very noticeable design impact on almost any other subsystem or system on board. This impact is never unilateral; it imposes a multitude of design constraints on the array which are frequently in mutual conflict with each other and with the desires of a straightforward array design. A major part of the array designer's job is to participate in tradeoff studies and "work the interfaces" so that not only an adequate array design results, but also that design penalties on other subsystems are minimized. It can be said, therefore, that the successful solar cell array designer, from the overall satellite systems point of view, is also a master in technical compromise.

1.3.1 Design Phases

The design process begins with the conceptual design phase during which the general nature of the spacecraft and an associated solar cell array are conceived which might satisfy the general mission requirements. The typical result of this phase may be the selection of either a body-mounted solar array or a deployable two-axis stabilized, flat array having an approximate specified area. If it is to be a deployable array, then some thought should be given to the packaging and deployment scheme. The design process then continues into the synthesis phase in which solar cells, covers, substrates, and other parts and materials are selected; solar cell layouts are prepared; and the functional designs for substrates and stowage, and deployment mechanisms are evolved that would permit both building of "breadboards" and physical and computer simulation of hardware. The design process then proceeds to the analysis phase during which calculations are made to predict the solar cell array performance for certain postulated environmental conditions. During the evaluation and test phase, experiments are conducted and the analytical and experimental results are compared with the requirements.

Depending upon the outcome of this comparison, the design is recycled, often many times, through synthesis, analysis, and evaluation until the desired results are obtained. This design reiteration almost always includes some form of design optimization which may range in scope from a simple design improvement to a true maximization of a payoff function, such as maximum power output per unit weight. More often than not, design optimization consists of performing "tradeoff" studies which lead either to the optimization of the overall satellite system with respect to some definite criteria, or to a balance between various design objectives. As a consequence of system optimization, the array designer should not find himself surprised when a well optimized satellite system leads to highly nonoptimized solar cell array design.

The end product of the final design phase is a set of plans, drawings, specifications, and procedures according to which the design will be transformed into hardware.

Even though the division of the design process into the various design phases may be of great significance within a given project organization, it has no significance in the context of the technical content of this handbook other than leading to an increasingly detailed and finalized design status.

1.3.2 The Design Organization

Solar cell arrays are being designed within the framework of the aerospace industry. The major difference between design activities in the aerospace industry and in the commercial industry is that in the former relatively few but technically highly complex and costly systems are being developed, while in the latter emphasis is on high-volume production of relatively low-cost items. Aerospace systems must be designed to perform reliably from the outset since there is usually no opportunity for recall and repair.

To meet this challenge, management science has evolved organizational structures which make possible the design and development of complex systems. The line and staff organization of most commercial businesses have been superseded by an overlay or matrix structure which combines vertical administrative and budgetary control (a Project Office) with horizontal access to functional departments or groups responsible for the actual design and development of the hardware. A functional group controls all of the skills and facilities necessary to design or produce a particular product. It is analogous to the commercial product design team with the exception that it contains simultaneous design activities — all responsible to a single point of functional management control. Thus, all of the skills, experience, and facilities of the group can be directed to the solution of critical problems as they arise in one project or another.

In most aerospace organizations the functional group is the custodian of design knowledge, techniques, test and performance data, practices and procedures related to the products under its charter. It maintains a historical record of past design activities. It sponsors the development of new concepts, techniques, and processes. It provides trained personnel to assist project and marketing groups in the preparation of conceptual and preliminary designs for proposals and system-level design studies. In the case of the latter, the management of the functional group has the responsibility and authority to approve the designs for which it would be normally responsible.

Within the constraints imposed by a project/functional management structure designed to foster the development of complex systems, the design process for a particular component is fairly predictable. Usually the design concept of the component will not be radically new or different. It will have evolved from earlier proven designs. (When the concept does represent a departure from a previous approach, it will have first been subjected to a form of adversary procedure in which the results of preliminary development activities are presented and defended to program and system engineering management teams charged with dual responsibilities of maintaining customer satisfaction and confidence, and of producing profits for the company.) In the early stages of a program a three-way tug-of-war may exist between the program office, system engineering, and the functional group over design requirements and constraints, and budget and schedule requirements. Within the organizational matrix, however, there is always a management level at which these controversies can be resolved.

1.3.3 Design Personnel

In practice, the solar cell array "designer" is a member of a design team. Furthermore, he is most likely a specialist in a particular field. During the entire array design process, many "designers" will have contributed to the design, each in his own right.

The early conceptual design is frequently done by a "systems specialist" whose main concern is to evolve the overall satellite system concept. The "solar cell array specialist" gets involved no later than during the preliminary design phase. Actually, he is more

of an "array generalist" than a specialist, because he must now consider the many aspects and inter-faces of importance in the design process. Frequently he assumes a technical managing role as a "responsible engineer." Especially during the intermediate and final design phases he is a member of the "design team" which evolves the detailed design. Other members of this design team typically include specialists from the following engineering areas: product (packaging) design, structures, dynamics, electrical design, materials, and processes, quality assurance, testing, manufacturing engineering, thermodynamics, heat transfer, procurement, reliability, and others.

1.3.4 Uncertainties and Risks

Even though solar cell arrays have been successfully designed, fabricated and flown for nearly two decades, there is no design which has been or will be carried forward with full knowledge of all the important facts pertaining to the environment, materials, or processes. For this reason, the designer must be able to cope with uncertainty to the extent that he must attempt to quantize uncertainty and use it as a design parameter. This need for quantization of uncertainty arises from the need to transmit from one engineer to another, from the array designer to the spacecraft designer, from technical personnel to the manager, the risks which are associated with one design approach or another. In this sense, the progression from the conceptual through the final design stages can be viewed as reduction, but not elimination, of uncertainty.

1.3.5 Human Engineering

Finally, the solar cell array design involves human engineering. An important consideration in terms of overall project cost and schedule are those man-hardware interfaces that occur during the fabrication, test, and spacecraft integration phases. Accidental damages to designs that are difficult to fabricate, awkward to handle due to size or flexibility, or difficult to test adequately are frequently not purely accidental. The array design team (array designer, fabrication, and test engineers) must consider these aspects of the overall design early in the design process; otherwise, the ability to turn a design into a tested hardware reality may be severely hampered.

1.4 DESIGN STANDARDIZATION

The benefits of standardized components and subassemblies and assemblies in terms of economy, resource allocation, technical performance and even reliability (through uniformity of product) are all too well known to be debated. Solar cell arrays and their components, being significant cost items in almost any satellite program, have therefore been scrutinized for possible ways of standardization for a long time.

For the past several years, standardization of solar cells, covers, and assemblies has been increasingly pursued. Efforts have been underway at NASA and the USAF, supported heavily by private industry, to tackle this problem. Ironically, the major obstacle to such standardization is of an economic nature and is related to the cost of the launch vehicle. For cost reasons, the lowest performance launch vehicle for a particular mission is selected, forcing close weight and high operating efficiency constraints on the spacecraft/payload design. This, in turn, usually has two effects on the array design:

- Solar cell packing density is optimized
- Solar cell stack and interconnecting circuitry design is tailored for minimum weight and minimum cost.

For example, any degree of overdesign in terms of a cell or cover thicker than absolutely required, or of a higher performance at a higher cost, is thereby virtually ruled out. The economic penalty paid for such an individually optimized array over a non-optimized (i. e., standardized, off-the-shelf) design, however, typically is small relative to the cost for a more powerful launch vehicle. Of course, as technological advances are made both in the space sciences and in the production arena and as space program management philosophies change, the aforementioned relationships between costs and performance are most likely to change. Such change, on one hand, may accelerate the pace of standardization, while on the other hand, it may be accelerated by the process of standardization.

Much of the material in this handbook, especially the sections on design requirements, design criteria, and interface constraints, can be helpful to those engaged in standardization efforts.

REFERENCES (CHAPTER 1)

- 1.1-1 Miscellaneous data from TRW and JPL files.
- 1.2-1 J. Besson et al., "Evaluation of CdS Solar Cells as Future Contenders for Large Electricity Production," Conference Records of the 11th IEEE Photovoltaic Specialists Conference, 1975.
- 1.2-2 P. A. Crossley, G. T. Noel, and M. Wolf, "Review and Evaluation of Past Solar Cell Development Efforts," Final Report, RCA Astro-Electronics Division, Princeton, New Jersey, June 1968.
- 1.2-3 R. G. Seidensticker, "Dendritic Web: A Viable Material for Silicon Solar Cells," Conference Records of the 11th IEEE Photovoltaic Specialists Conference, 1975.
- 1.2-4 P. A. Berman and J. Weingart, "Proceedings of the Third Annual Conference on Effects of Lithium Doping on Silicon Solar Cells," JPL TM 33-467, April 1971.
- 1.2-5 P. A. Berman and R. K. Yasui, "Lithium-Doped Solar Cell Pilot Line Fabrication and Test Programs," JPL TM 33-677, October 1974.
- 1.2-6 J. Lindmayer and J. Allison, "An Improved Silicon Solar Cell - The Violet Cell," Conference Records of the 9th IEEE Photovoltaic Specialists Conference, 1972.
- 1.2-7 B. L. Sater et al., "The Multiple Junction Edge Illuminated Solar Cell," Conference Records of the 10th IEEE Photovoltaic Specialists Conference, 1973.
- 1.2-8 R. K. Smeltzer et al., "Vertical Multijunction Solar Cell Fabrication," Conference Records of the 10th IEEE Photovoltaic Specialists Conference, 1973.
- 1.2-9 E. L. Ralph and J. Scott-Monck, "Development and Space Qualifications of New High-Efficiency Silicon Solar Cells," Records of International Conference, Photovoltaic Power Generation, Hamburg, Germany, September 1974.
- 1.2-10 W. Luft, "Radiation Effects on High Efficiency Silicon Solar Cells," Records of the International Conference, Evaluation of Space Environment on Materials, Toulouse, France, June 1974.

CHAPTER 2
THE ENVIRONMENT AND ITS EFFECTS

CONTENTS

	Page		Page
2.1 The Terrestrial Environment for Space Hardware	2.1-1	2.4 Solar Radiation in Space	2.4-1
2.1.1 The Atmosphere	2.1-1	2.4.1 Temperature in Space	2.4-1
2.1.2 Humidity	2.1-2	2.4.2 The Solar Constant	2.4-2
2.1.3 Ozone	2.1-3	2.4.3 Ultraviolet Solar Radiation	2.4-7
2.1.4 Sand and Dust	2.1-5	2.4.4 Solar Radiation Pressure	2.4-8
2.1.5 Fungus	2.1-5	2.4.5 Albedo	2.4-8
2.1.6 Corrosion	2.1-5	2.5 The Space Radiation Environment	2.5-1
2.1.7 Handling, Transportation and Gravity	2.1-7	2.5.1 Definition of Radiation Terms	2.5-1
2.1.8 Chemical Compatibility	2.1-7	2.5.2 Geomagnetically Trapped Electrons	2.5-3
2.2 Launch and Flight Dynamics	2.2-1	2.5.3 Geomagnetically Trapped Protons	2.5-3
2.2.1 Dynamic Forces During Launch and Space Flight	2.2-1	2.5.4 Solar Flares Protons	2.5-3
2.2.2 Acceleration	2.2-1	2.5.5 Radiation at Synchronous Altitude	2.5-3
2.2.3 Shock (Mechanical)	2.2-2	2.5.6 Interplanetary Radiation	2.5-5
2.2.4 Vibration	2.2-2	2.5.7 Radiation Zones of the Planets	2.5-5
2.2.5 Acoustic Field	2.2-4	2.5.8 Effects of Radiation on Solar Cell Arrays	2.5-5
2.3 The Space Environment	2.3-1	2.5.9 Particulate and Ultraviolet Radiation Combined	2.5-7
2.3.1 The Solar System	2.3-1	2.6 Orbital Effects	2.6-1
2.3.2 The Space Vacuum	2.3-2	2.6.1 Spacecraft Motion in Orbit	2.6-1
2.3.3 The Space Plasma	2.3-3	2.6.2 Solar Eclipses — Power Loss and Temperature Cycling	2.6-1
2.3.4 Meteoroids	2.3-4	2.6.3 Solar Cell Array Orientation	2.6-1
2.3.5 Deposits	2.3-5	References (Chapter 2)	2.R-1
2.3.6 Gravity	2.3-5	NASA Space Vehicle Design Criteria Monographs	2.R-4
2.3.7 Time in Space	2.3-5		
2.3.8 Magnetic Fields	2.3-5		

TABLES

2.1-1 Normal Composition of Clean, Dry Atmospheric Air Near Sea Level	2.1-2	2.3-1 Characteristics of the Solar System	2.3-1
2.1-2 Gas Pressures and Concentration in Space	2.1-2	2.3-2 Characteristics of 10 Notable Asteroids	2.3-2
2.1-3 Elastomers According to Ozone Resistance	2.1-5	2.3-3 Sublimation of Metals in High Vacuum	2.3-2
2.2-1 Typical g-Forces During Launch/Ascent	2.2-1	2.3-4 Coverglass Transmittance Degradation	2.3-4
2.2-2 Typical g-Forces During Reentry	2.2-1	2.3-5 Space Mission Durations	2.3-5
2.2-3 Typical Mechanical Shock Loads	2.2-2	2.4-1 Variation of Solar Intensity with Earth-Sun Distance	2.4-3
2.2-4 Sources and Magnitudes of Typical Vibration Environments	2.2-3	2.4-2 Orbital Constants of the Planets and Solar Intensity at Planetary Distances	2.4-3
2.2-5 Typical Random Vibration Levels During Launch/Ascent	2.2-3	2.4-3 Solar Spectral Irradiance at 1 AU	2.4-4
2.2-6 Typical Sinusoidal Vibration Levels	2.2-3	2.4-4 Solar Spectral Irradiance - Standard Curve, Abridged Version	2.4-6
2.2-7 Typical Acoustic Field Levels During Launch/Ascent	2.2-5	2.4-5 Energy in Various Types of Radiation	2.4-7

2.5-1	Major Solar Flare Proton Events During Twentieth Cycle	2.5-4	2.6-1	Examples of Solar Array Orientation	2.6-4
FIGURES					
2.1-1	Altitude Variations of Density, Temperature and Pressure	2.1-1		0.15-mm Thick Fused Silica Covers and Infinitely Thick Back Shields	2.5-6
2.1-2	Breakdown Voltage Versus Altitude	2.1-2	2.5-3	Multiplication Factors for Damage Equivalent 1-MeV Fluence Shown in Figure 2.5-2 for Four Different Cover Thicknesses for (a) 0-Degree Inclined Orbits and (b) 90-Degree Inclined Orbits	2.5-6
2.1-3	Humidity Degradation of Ti-Ag Contact Solar Cells	2.1-4			
2.1-4	Schematic Diagrams of Solar Cell Contact Interface Layers	2.1-7			
2.3-1	The Basic Solar System	2.3-1	2.5-4	Damage Equivalent 1-MeV Fluence in Circular Earth Orbits due to Trapped Protons for P_{mp} of Silicon Cells Protected by 0.15-mm Thick Fused Silica Covers and Infinitely Thick Back Shields	2.5-7
2.3-2	Magnetic Flux Density of the Geomagnetic Field	2.3-6			
2.4-1	Energy Balance Determines Array Temperature in Space	2.4-1	2.5-5	Multiplication Factors for Damage Equivalent 1-MeV Fluence Shown in Figure 2.5-4 for Four Different Cover Thicknesses for (a) 0-Degree Inclined Orbits and (b) 90-Degree Inclined Orbits	2.5-8
2.4-2	Conventional Mariner Solar-Array Temperature Versus Heliocentric Distance at Normal Incidence	2.4-1			
2.4-3	Solar Spectral Irradiance	2.4-3			
2.4-4	Silicon Solar Cell Short-Circuit Current Output Versus Solar Intensity	2.4-7	2.5-6	Average Absorbed Dose in 0.15-mm Thick Covers in Circular Earth Orbits due to Trapped Electrons	2.5-9
2.4-5	Calculated Maximum Contribution of Earth Albedo Illumination to Solar Cell Output as a Function of Altitude for a Uniform Diffuse Reflecting Earth with Albedo Equal to 0.34	2.4-8	2.5-7	Average Absorbed Dose in 0.15-mm Thick Covers in Circular Earth Orbits due to Trapped Protons	2.5-9
2.5-1	Integral Solar Flare Proton Fluxes for Three Solar Cycles	2.5-4	2.6-1	Maximum Number of Annual Satellite Eclipses in Circular Earth Orbits	2.6-2
2.5-2	Damage Equivalent 1-MeV Fluence in Circular Earth Orbits due to Trapped Electrons for I_{sc} and P_{mp} of Silicon Cells Protected by		2.6-2	Fractional Sun Time of Circular Earth Orbits	2.6-3
			2.6-3	Orbit Period and Eclipse Duration of Circular Earth Orbits	2.6-3

CHAPTER 2

THE ENVIRONMENT AND ITS EFFECTS

The solar cell array environment consists of the atmospheric conditions and mechanical loads imposed during fabrication, assembly, storage, transportation, stowage and launch, and deployment in and exposure to the space environment.

The terrestrial environment of significance to space solar cell arrays is exposure to temperature, humidity, surface contamination, vibration, mechanical shock, and handling in the 1-g gravity field. The significant launch environment consists of vibration, exposure to acoustic fields, pyrotechnic shock, and rapid depressurization. The important space environment is characterized by high vacuum, particulate and electromagnetic radiation (including solar radiation), plasma and meteoroids.

A significant environmental effect, known as "temperature cycling," is caused by the periodic interruption of the array's insolation during solar eclipses.

The data in this chapter are of a general nature and are intended for conceptual design activities only. More detailed data for solar cell array design and analysis are given in Volume II of this handbook. Detailed and precise environmental design criteria are usually prepared by NASA or other agencies for major, specific programs and missions; these criteria should be consulted. Especially helpful are the "NASA Space Vehicle Design Criteria Monographs" (listed after the references in this chapter).

2.1 THE TERRESTRIAL ENVIRONMENT FOR SPACE HARDWARE

A terrestrial environment may have deleterious effects on space-type cell arrays. Uncontrolled atmospheric conditions during assembly and storage may lead to hardware performance deterioration or failure. The flight operation within the extent of the atmosphere of the earth or other planets may impose certain restrictions on the design. The nature of the most significant terrestrial environments and their potential effects on solar cell arrays are discussed in this chapter.

2.1.1 The Atmosphere

The atmosphere is a gaseous envelope that surrounds the earth, extending from sea level to an altitude of several hundred kilometers. The upper limit of the atmospheric gas pressure decreases with increasing distance from the earth until it reaches the so-called interplanetary value of 10^{-11} newton/cm²

near 20,000 km. The variations of temperature and pressure in the atmosphere are illustrated in Figure 2.1-1. The corresponding composition of the atmosphere is shown in Tables 2.1-1 and 2.1-2.

Electrical Arcing

Partial vacuum at high altitudes can cause flash-over between electrical conductors. The breakdown voltage is a function of air density and the spacing of electrodes, being lowest at an altitude of 33.3 km at an atmospheric pressure of $760 \text{ N}\cdot\text{m}^{-2}$ (Figure 2.1-2).

Effect of Pressure/Altitude on Array

During ascent, following launch, the solar cell array is subjected to rapid depressurization. The rate of this depressurization depends upon the rate of ascent and the rate of air leakage from the shroud,

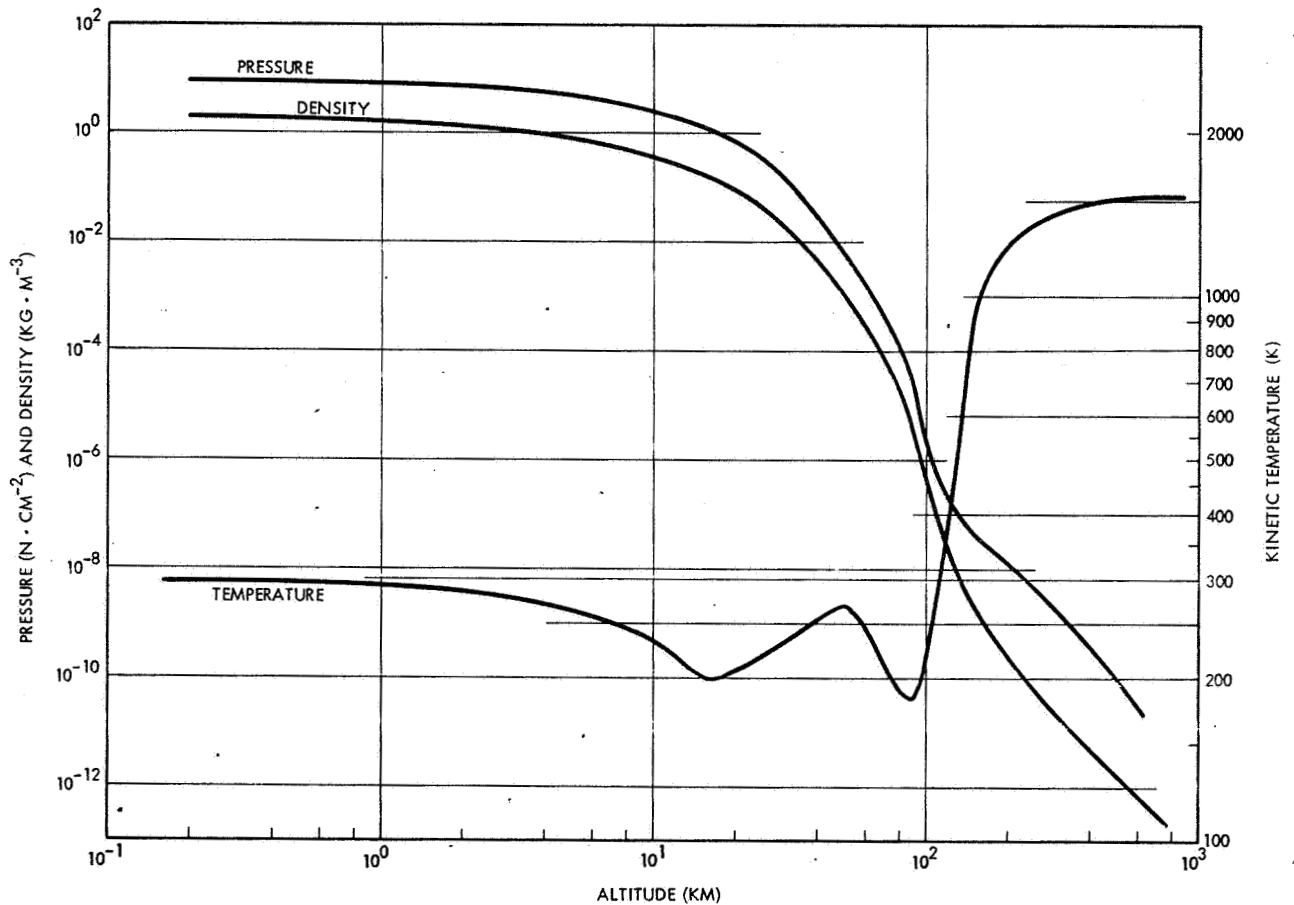


Figure 2.1-1. Altitude Variations of Density, Temperature and Pressure (Ref. 2.1-2)

Table 2.1-1. Normal Composition of Clean, Dry, Atmospheric Air Near Sea Level (Ref. 2.1-1)

Constituent Gas and Formula	Content (percent by volume)
Nitrogen (N ₂)	78.084
Oxygen (O ₂)	20.9476
Argon (Ar)	0.934
Carbon dioxide (CO ₂)	0.0314
Neon (Ne)	0.001818
Helium (He)	0.000524
Krypton (Kr)	0.000114
Xenon (Xe)	0.000087
Hydrogen (H ₂)	0.00005
Methane (CH ₄)	0.0002
Nitrous oxide (N ₂ O)	0.00005
Ozone (O ₃)	Summer: 0 to 0.000007 Winter: 0 to 0.000002
Sulfur dioxide (SO ₂)	0 to 0.0001
Nitrogen dioxide (NO ₂)	0 to 0.000002
Ammonia (NH ₃)	0 to trace
Carbon monoxide (CO)	0 to trace
Iodine (I ₂)	0 to 0.000001

and therefore is highly mission dependent. Typical depressurization rates range from 1 to 10 minutes to reduce the initial ambient pressure to 1 percent or less.

Solar cell array components are generally not sensitive to such depressurization, except for elements containing gas-filled voids. Such elements, like honeycomb substrates, box beams, or foams, must be vented with sufficiently large openings to prevent excessive internal net pressure from damaging these elements. An even more catastrophic result can be expected when a large amount of moisture is trapped inside inadequately vented voids, especially when the satellite protective shroud (nose cone) is ejected early and the array is subjected to high temperatures by aerodynamic and/or solar heating.

2.1.2 Humidity

The moisture content of the atmosphere is commonly expressed by the relative humidity, defined as the ratio of the actual vapor pressure of the water vapor contained in the air to the saturated vapor pressure of water vapor at the same temperature. Air with a constant water vapor content will experience a decrease in relative humidity with a rise in temperature. Another measure of atmospheric moisture content is the dew point. The dew point temperature, which is a function of the absolute quantity of moisture in the air, is the temperature to which the air must be lowered for water vapor to condense. Atmospheric moisture ranges from low relative humidity to precipitation.

Table 2.1-2. Gas Pressures and Concentration in Space

(Adapted from "Chemical Engineering Progress, Symp. Ser." L. D. Jaffe, Vol. 59, No. 40, Copyright 1963 by the American Institute of Chemical Engineers, New York)

Altitude (km)	Pressure (mm Hg)	Temperature (°C)	Concentration (molecules, atoms, or ions/cm ³)	Composition
Sea Level	760	-40 to +40	2.5 x 10 ¹⁹	78% N ₂ , 21% O ₂ , 1% Ar
30	9 to 10	-40	4 x 10 ¹⁷	N ₂ , O ₂ , Ar
230	10 ⁻⁶	10 ³	10 ¹⁶	N ₂ , O, O ₂ , O ⁺
926	10 ⁻⁹	10 ³	10 ⁶	O, He, He ⁺ , O ⁺ , H
7400	10 ⁻¹³	10 ³	10 ³	H ⁺ , H, He ⁺
26,000	<10 ⁻¹²	10 ³ to 10 ⁵	10 ¹ to 10 ²	85% H ⁺ 15% H ⁺⁺

Unit Conversion Factor: Multiply mm Hg by 133.32 to obtain N·m⁻².

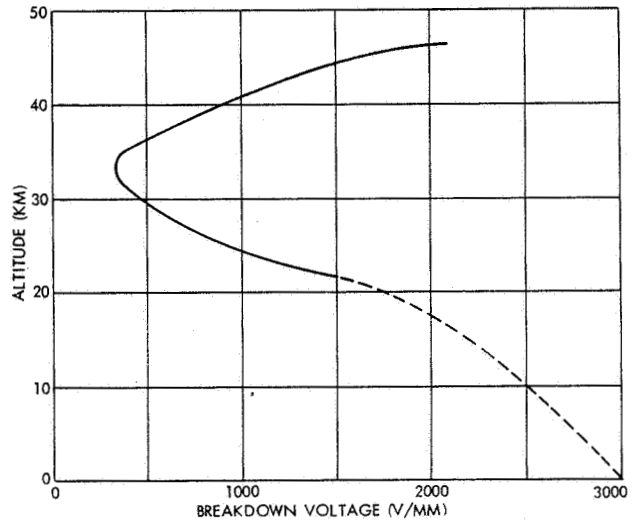


Fig. 2.1-2. Breakdown Voltage Versus Altitude (Ref. 2.1-2)

Relative humidity is measured with hygrometers. Directly recording hygrometers are frequently used in solar array or other spacecraft production areas where humidity control and its documentation is required.

Control of Humidity

The major control of humidity is achieved by modern refrigeration-type air-conditioning processes. In these processes the naturally occurring increase in relative humidity associated with a decrease in air temperature is circumvented by condensing and removing from the air significant quantities of water. Typical relative humidity values in many modern plants lie below 60 percent. Humidity-sensitive solar

cells with unprotected titanium-silver (Ti-Ag) contacts or contact grid lines are typically stored in desiccated bags, together with card-type humidity indicators. If solar cell arrays require long storage periods, they should also be stored in a very low humidity environment.

Effects of Humidity on Solar Cells

The currently available types of solar cells having Ti-Ag contacts should be considered susceptible to degradation in humid environments, especially when conditions of both high humidity (above 60 percent relative humidity) and high temperature (above 40°C) exist. Generally, problems due to exposure to humidity can be encountered during:

- Long-term storage of solar cells or assembled arrays, especially in uncontrolled environments in high-temperature, high-humidity climates.
- Extensive temperature cycling testing of unprotected solar cells in gaseous environments that contain some humidity.

Conditions of high humidity and high temperature cause a corrosion process in the cell contacts, as discussed in Section 2.1.6 (Corrosion). The rate at which the corrosion process proceeds increases with increasing temperature and with increasing amounts of water that can actually penetrate into the interface of the contact metals. Contaminants present in minute quantities in the metallizations may accelerate the corrosion process.

During 1968, a controlled test was performed to study the effect of accelerated humidity testing (Ref. 2.1-3). This test showed that solderless silicon solar cells with Ti-Ag contacts were sensitive to humidity exposure at elevated temperature. This sensitivity led to power loss when operating in the knee region of the current-voltage characteristic. The degradation was small for solderless cells which had not undergone preheating after the Ti-Ag contacts had been formed. Cells preheated to 220°C for 2 minutes or more showed a wide range of degradation depending on several factors, one being the cell manufacturer (Figure 2.1-3).

Glassed solderless cells using Dow Corning XR-6-3489 silicone adhesive showed approximately one-third of the degradation of corresponding bare cells. Solar cells with solder coverage on all contact surfaces exhibited no or insignificant degradation when subjected to the same exposure for which the solderless cells showed deterioration. Storage at normal air-conditioned indoor conditions resulted in minute degradation for solderless cells.

This study, as well as others, showed that the electrical power degradation of solderless solar cells was accompanied or preceded by blistering of the contact layer and peeling of the contacts and grid lines away from the silicon. A number of investigations were then initiated which, to date, have not fully explained the degradation mechanism.

Protection of Solar Cell Contacts from Humidity

The following methods are effective in protecting the Ti-Ag contacts:

- Solder coating of the contacts and the gridlines.

- Protecting the contacts and gridlines with coatings such as when cells are assembled into arrays. Complete contact and gridline area protection is required.

None of these protection methods, however, are fully effective in all possible environmental conditions for the following reasons:

- Solder becomes "porous" during temperature cycling testing, as shown in Section 5.3 (The Solar Cell Interconnector Design Problem).
- Adhesive covering the cell contacts (either to hold the cover to the cell or the cell to the substrate) may contain water (either as a result of curing or by absorption from the air) or may permit slow propagation of water from the atmosphere to the contacts.
- Certain RTV adhesives yield acidic products upon curing that may combine with atmospheric moisture and may aid the solar cell contact corrosion process for a limited period of time after assembly. Some users of such adhesives (see Section 7.2) have observed contact corrosion while others have reported that even solder free contacts were not affected after long-term storage.

A significant breakthrough in the development of humidity-resistant solar cell contacts was the addition of palladium as an interlayer between the titanium and the silver coating. The palladium passivates the inherently corrosive Ti-Ag couple, as described in Section 2.1.6 (Corrosion). In a practical sense, however, palladium passivation may not be 100 percent effective in protecting Ti-Ag contacts from corrosion owing to imperfections in the solar cell manufacturing process.

Effects of Humidity on Adhesives

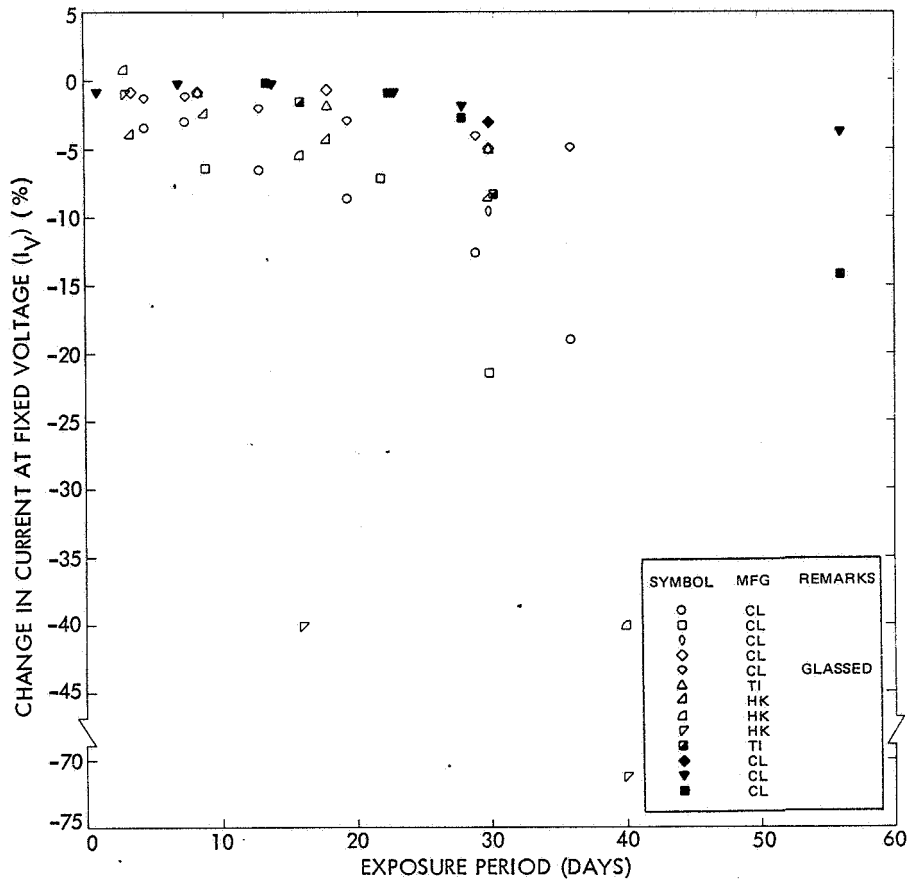
Control of humidity during the assembly process may be required. Certain adhesives will not develop their highest adhesive strength in presence of high humidity, while other adhesives may require a high humidity level for adequate curing. The specific manufacturer's recommendations for each adhesive to be used should be followed carefully.

Effects of Humidity on Structural Components

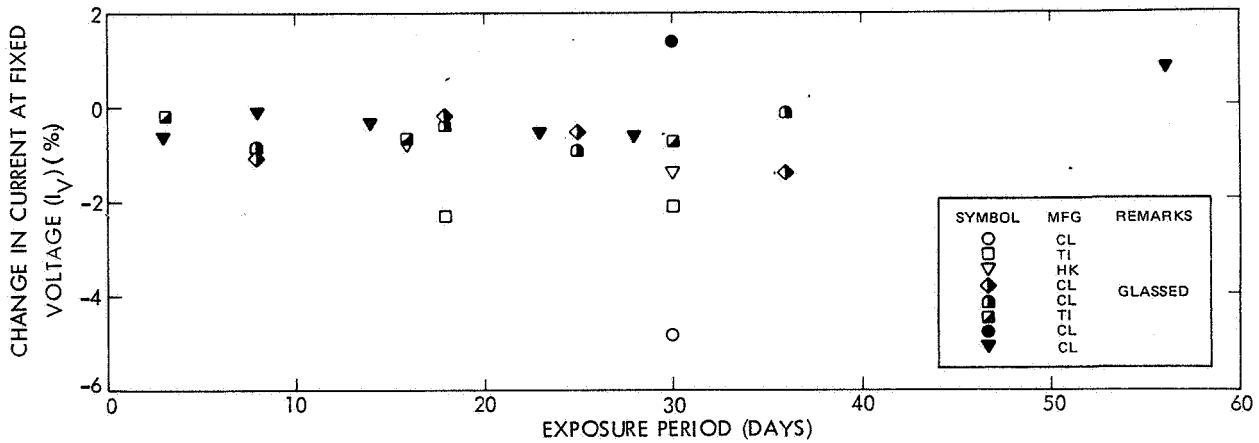
A relatively large quantity of moisture trapped inside voids (such as in honeycomb panels, box beams, or resilient materials) will vaporize during and after the launch phase both due to loss of ambient pressure and due to aerodynamic and solar heating. Structural damage can usually be prevented only by providing adequate vent openings.

2.1.3 Ozone

Ozone occurs naturally in the atmosphere. Ozone (O₃) is produced mainly by a photochemical action of short-wavelength, solar-ultraviolet radiation (below 0.2537 μm) on molecular oxygen (O₂). It is also produced during electrical storms as a consequence of lightning. Man-made ozone occurs mainly in the vicinity of metropolitan areas and is caused by ultraviolet light sources, motor and generator brushes, and photochemical processes which produce smog. The ultraviolet radiation from solar simulators also produces significant amounts of ozone.



(a) CHANGE IN OUTPUT CURRENT AS A FUNCTION OF EXPOSURE TIME FOR SOLAR CELLS WITHOUT SOLDER ON THE GRIDLINES. CELLS EXPOSED TO A TEMPERATURE OF 45°C AND A RELATIVE HUMIDITY OF 90%. OPEN SYMBOLS FOR PREHEATED CELLS AND FILLED SYMBOLS FOR NON-PREHEATED CELLS.



(b) CHANGE IN OUTPUT CURRENT AS A FUNCTION OF EXPOSURE TIME FOR COMPLETELY SOLDER COVERED SOLAR CELLS. CELLS EXPOSED TO A TEMPERATURE OF 45°C AND A RELATIVE HUMIDITY OF 90%. OPEN SYMBOLS FOR PREHEATED CELLS, AND FILLED SYMBOLS FOR NON-PREHEATED CELLS.

Fig. 2.1.3. Humidity Degradation of Ti-Ag Contact Solar Cells (Ref. 2.1.3)

High concentrations of ozone are explosive and toxic. A concentration of 1 part per million (ppm) of ozone is lethal to man. Typical ozone concentrations on the earth's surface range from near zero to normally less than 3 parts per hundred million (pphm) and up to 6 pphm during periods of intense smog. The ozone concentration increases with altitude. Ozone concentrations in solar simulator installations must be prevented by adequate ventilation.

Ozone causes cracking of natural rubber, butadiene-styrene (SBR), butadiene-acrylonitrile (NBR), and some other elastomers under stress. Ozone-cracking resistance of an elastomer part is dependent on exposure time, temperatures, material strains, humidity, and ozone concentration. Polymers classified according to ozone resistance are presented in Table 2.1-3. To increase the resistance to ozone, antiozonants may be added to the materials. An antiozonant is a substance which inhibits cracking due to the action of air containing ozone when the elastomer is subjected to tension strains. The effect of an antiozonant may be lost after exposure to high vacuum at room or elevated temperature.

Table 2.1-3. Elastomers According to Ozone Resistance (Ref. 2.1-4)

Inherently Ozone-Resistant	Ozone Resistant (if properly compounded)	
	Without Antiozonant	With Antiozonant
Acrylons Hypalon Vyram Hycar 4021 LS-53 Kel-F elastomer Poly FBA Silicone Vitron A	Brominated butyl Butyl Neoprene Urethane (Gentane S)	Buna N Carboxylic Buna N Butadiene-styrene (SBR) Vinyl pyridine Natural rubber Synthetic cis 1-4 polyisoprene cis 1-4 polybutadiene Conventional polybutadiene Mercapan modified adducts of polybutadiene Polysulfide Urethane (Adiprene B, C)

From Ref. 2.1-4. Reprinted with permission of the Southwest Research Institute.

Effects of Ozone on Solar Cell Arrays

The effects of ozone on solar cell array materials are generally negligible. However, the use of materials sensitive to ozone should be avoided if either (a) the array or its materials will be stored for extended periods of time in geographic areas where smog is prevalent, (b) the array is to operate at the fringes of the earth's atmosphere, or (c) the array is to be exposed for long periods of time in ambient air to the radiation from a solar simulator.

2.1.4 Sand and Dust

Sand consists of loose, siliceous particles ranging in size from approximately 0.08 to 1.0 mm in diameter. Dust consists of multiple composite particles ranging from 0.1 to 80 μm in diameter. Dust particles may be electrically conductive and are usually soluble in water.

Sand and dust are most severe in low humidity regions. Dust becomes airborne with slight winds and may remain suspended for hours as dust clouds. During wind storms, dust particles penetrate almost any enclosure which is not hermetically sealed.

The effects of sand and dust on equipment and materials include:

- Increased friction between sliding surfaces, causing abrasion, excessive wear, and binding of parts
- Degradation of plastics and elastomers used for dynamic seals
- Clogging of orifices, such as vent ports
- Contamination of lubricants
- Erosion of paints, coatings, glass, plastics, and surface finishes
- Short circuiting of electrical elements

Also, dust may be hygroscopic; its presence on metallic surfaces may aggravate corrosion. A small amount of dust on the solar cell covers has a negligible effect on the sunlight transmission to the solar cells.

2.1.5 Fungus

Fungus is an organism which is encountered primarily in tropical climates and which feeds on organic matter (nutrients) such as wood, paper, cotton, cellulose, paints, plastics, rubber, etc. Even a coating of dust or dirt will support fungi growth. Fungus growth is often accompanied by a high moisture content.

The effects of fungi on solar cell arrays are as follows:

- Properties of polymers change due to plasticizer loss
- Surfaces etch, and coverslide antireflection coating may be destroyed
- Bonded joints delaminate
- Electrical apparatus may short circuit, caused by conductive moist elements of fungi
- Solar cell arrays may suffer degradation of electrical output and mechanical strength.

All solar cell array parts and assemblies should be suitably protected from dirt and humidity.

2.1.6 Corrosion

Corrosion is the deterioration and loss of material due to a chemical reaction between the material and its environment. Corrosion of or in solar cell arrays should be prevented by proper environmental control during the array's terrestrial life. Surface treatment of solar cell arrays to prevent corrosion is usually undesirable because such treatments tend to be unstable in space vacuum and contaminate nearby thermal control surfaces and optical elements.

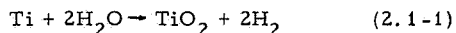
Corrosion of Solar Cell Contacts

The most important corrosion phenomena on solar cell arrays is the potential deterioration of Ti-Ag contacts on silicon solar cells in humid environments [see Section 2.1.2 (Humidity)]. The corrosion mechanism of both Ti-Ag and Pd-passivated Ti-Ag contacts is discussed in the following.

It is now generally believed that during the process of degradation of Ti-Ag contacts on silicon solar cells, the Ti layer is changed from a metallic to a nonmetallic state (Refs. 2.1-5, 2.1-6, and 2.1-7). As a result, the bond between the Ag and the Ti layers is weakened, increasing the contact resistance and decreasing physical contact adhesion. This is consistent with the observation that after peeling off the overlying layer of a degraded contact, a Ti-containing substance remains on the silicon surface, and not much Ti adheres to the silver layer (Refs. 2.1-5 and 2.1-8). As the remaining Ti material is semitransparent, it is not metallic Ti, and is assumed to be some form of titanium oxide. No direct analytical proof of this composition was found.

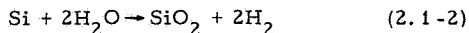
A variety of mechanisms have been proposed to explain the changes observed (Refs. 2.1-5 through 2.1-8). Those elements common to all proposed mechanisms include the absorption and/or condensation of moisture, gases, and/or other impurities from the ambient environment by defects (i. e., pin holes, pores, cracks, etc.) in the Ag layer; generation of hydrogen gas by some reaction at or near the Ti layer; and eventual production of a more or less amorphous and relatively weak TiO₂ layer in place of the original Ti-Ag interface.

The least agreement is on the specific mechanism by which the Ti becomes converted from a metal to an oxide. Bishop (Ref. 2.1-7) proposed that Ti reacts with water to form TiO₂ and hydrogen according to Eq. (2.1-1):



Bishop demonstrated corrosion of metallic Ti by an aqueous solution of one-molar fluoride at pH5, but presents no similar data for water without large halide ion concentrations. Also, no information on reaction rates is given. Calculations are presented showing that the amount of hydrogen that would be needed to form the blisters he observed could be produced by reaction of a layer of Ti 5- μm thick, according to Eq. (2.1-1).

Bishop also described a reaction not mentioned by others, which may be responsible for producing blisters without a simultaneous change at the Ti-Ag interface. This is the reaction of silicon with water according to Eq. (2.1-2):

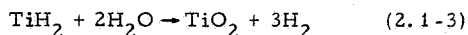


This could occur if the Ti layer were incomplete or porous beneath the known porous Ag layer.

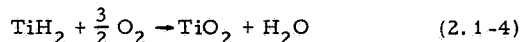
Fischer and Gereth (Ref. 2.1-8) and others suggested that the Ag of the upper layer forms a galvanic couple in the presence of moisture in the pores, wherein the Ti is the anode and the Ag is the cathode. They referred to results reported (Ref. 2.1-9) showing that Ag coupled to Ti in strong acids promotes corrosion of Ti. These authors claimed that this situation also applied in solar cell contacts.

Becker and Pollack (Ref. 2.1-6) have postulated quite a different mechanism for oxidation of Ti. According to these authors, when solar cells are sintered in hydrogen after depositing the contact layers,

the Ti layer is partially converted to TiH₂. Then, when contacted by water, TiH₂ reacts to give TiO₂ and hydrogen according to Eq. (2.1-3):



TiH₂ may also react with oxygen according to Eq. (2.1-4):



Note that in this concept the silver layer has no active role other than as a trap for the required moisture. A similar conclusion was reached in the work reported in Ref. 2.1-5.

Berman and Yasui (Ref. 2.1-10) showed that prolonged exposure of solar cell contacts to 80°C at low relative humidity produced no degrading effects. Hence, the temperature used during most high humidity testing was, by itself, not the cause of the observed effects. On the other hand, water appeared to be an essential ingredient (Ref. 2.1-5).

Fischer and Gereth (Ref. 2.1-8) described the use of a layer of palladium (Pd) between the Ti and Ag layers to inhibit the degradation that occurred with plain Ti-Ag contacts. They reviewed other possible candidates that might make more stable contact systems than Ti-Ag, including Ag alone, aluminum, gold, tantalum, silver, titanium-aluminum, etc. They pointed out the pitfalls of these combinations and indicated the uniqueness of the Ti-Ag combination for this application (except for the sensitivity to moisture).

These authors claimed that a Pd layer may be expected to inhibit the corrosion of the underlying Ti layer because it had been shown by others that a small (0.5 to 2 percent) amount of Pd alloyed with Ti, or a plating of Pd on Ti, passivated the Ti surface in strong acids. It was claimed that this occurred because the "electrochemical exchange potential" of the Ti-Ag couple was shifted from a more negative value (more corrosive) to a less negative value (less corrosive) by the action of the palladium. Data supporting this mechanism was shown for a two-molar HCl solution, but none was offered for a solution that represented what may be expected at a solar cell contact surface. Results of tests of solar cells made with Ti-Pd-Ag contacts (layer thicknesses of 35, 100, and 5000 μm , respectively) at 90°C and 100 percent relative humidity showed no significant degradation in 600 hours. It was not stated whether these test articles had been sintered. Physical and electrical characteristics of the palladium-containing contacts were reported by Fischer and Gereth to be excellent.

Yasui and Berman (Ref. 2.1-11) have reported the results of considerable humidity testing (80°C, 95 percent relative humidity) of a variety of commercially made solar cells having contacts with and without palladium. They showed that the mechanical strength of Ti-Pd-Ag top contacts either remained constant or increased slightly over 720 hours, as did solder-coated Ti-Ag contacts, whereas nonsoldered Ti-Ag contacts decreased in strength by 50 percent. Relative power output (illuminated) after 720 hours of testing was reported as about the same for Ti-Pd-Ag contacts as for Ti-Ag contacts. Much of this loss was due to degradation of the antireflective coating on the test specimens, however, so the effect of the Pd itself was obscured.

Becker and Pollack (Ref. 2.1-6) analyzed the composition of the various layers of Ti-Ag and Ti-Pd-Ag under different conditions. They show that after sintering in hydrogen the composition of the usual Ti-Ag is as shown in Figure 2.1-4a (composition of "interface material" not identified). After extended humidity exposure, the composition was as shown in Figure 2.1-4b, where x and y varied independently from zero upward from sample to sample, and from point to point over a single contact. Thus, a well-defined Ti-containing layer remained after exposure. However, the location of TiO_2 in this layer was localized (spotty), rather than uniform.

The composition of the layers in a Ti-Pd-Ag contact after sintering is shown in Figure 2.1-4c; whereas, after humidity exposure, the composition was as shown in Figure 2.1-4d.

The exact structure of the "amorphous layer" in Figure 2.1-4d was not determined except it was shown to contain Ti and Pd. Significantly, this layer was distributed uniformly over the entire area occupied by the silver layer. The uniformity and physical characteristics of this layer are probably responsible for the increase in bond strength observed for Ti-Pd-Ag contacts during humidity tests. The formation of moisture-resistant intermetallic compounds is probably responsible for the lack of blistering and peeling observed.

In summary, the articles reviewed above show what happens when nonsolder-coated solar cell contacts degrade in humidity tests, and that the inclusion of palladium improves the contact in several ways. However, these references do not clearly show how palladium produces its passivating effect.

2.1.7 Handling, Transportation and Gravity

One of the greatest potentially damaging terrestrial environments is handling. This category includes the accidental dropping of tools onto solar cell arrays; handling of surfaces covered with thermal control paint with oily hands; snagging of clothing on solar cell covers, interconnectors, or standoff terminals; and bumping into arrays with other objects. Other more subtle and sometimes less obvious sources which may damage solar cell arrays may arise from handling stresses imposed, especially on lightweight arrays. Such stresses may arise from the effects of gravity, inadequately designed shipping containers or handling equipment, or from excessive vibration or shock caused by ground or air transportation. Adequate consideration and usually an extra amount of foresight should, therefore, be applied in this area. The array designer will be involved at least by participating in establishing the necessary requirements for control and protection during the entire array fabrication/assembly/test/storage/integration period.

2.1.8 Chemical Compatibility

Problems due to chemical incompatibility arise occasionally during the assembly or use of solar cell arrays. The three most important ones are as follows:

- Certain adhesives (R63-489, for example) will not cure because of the presence of residues of certain cleaning fluids, solvents, or other adhesives.

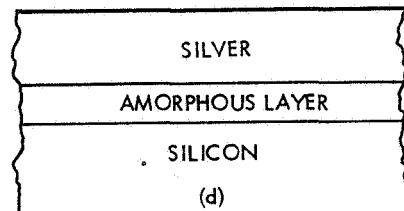
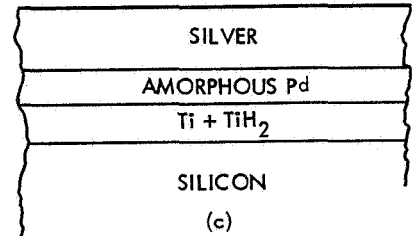
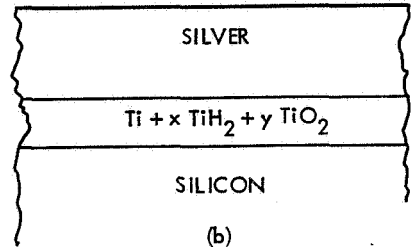
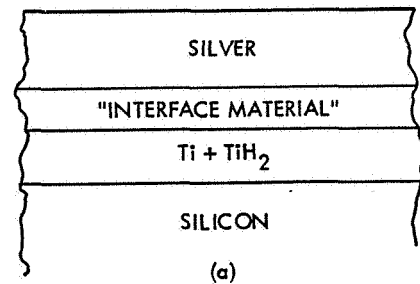


Fig. 2.1-4. Schematic Diagrams of Solar Cell Contact Interface Layers (for explanations see text)

- Soldering or welding operations may be impeded by the presence of residues of certain cleaning fluids or solvents.
- Propellant spillage or exhaust plumes may cause solar cell cover or cover adhesive damage.

The designer should be aware of these phenomena and consider them in his design when specifying assembly processes and establishing rework procedures.

2.2 LAUNCH AND FLIGHT DYNAMICS

The launch and flight of a spacecraft is accompanied by a number of events that can cause significant mechanical stresses on the array:

- Acceleration
- Mechanical Shock
- Vibration
- Acoustic Field

Some or all of these "environments" can combine to lead to some temporary, very high mechanical stress levels. Additionally, even higher stress levels may occur when at the same time the array is at some very low or very high temperature (relative to room temperature).

Vibrational and shock forces are transmitted to the solar cell array by structural members and, as long as it is sufficiently dense, by the surrounding air. The magnitudes and frequency spectra of the forces from their original sources are modified by the transmitting media before they reach the solar cell array (amplitudes may be attenuated or amplified). Inasmuch as the actual forces acting on the array are very dependent upon the choice and the design of a specific launch vehicle, satellite, and structural spacecraft and array system, the data given in this chapter can serve as a general guide only.

2.2.1 Dynamic Forces During Launch and Space Flight

The initial launch phase of a space vehicle is characterized by engine ignition and an intense acoustic field from the rocket engine exhaust which builds up in intensity until the moment of launcher release. The acoustic field is reflected from the ground to the launch vehicle and diminishes as the launch vehicle rises. The acoustical excitation increases again sharply due to aerodynamic disturbances as the vehicle approaches the speed of sound. Once past the speed of sound, aerodynamic excitation diminishes until stage separation when the vehicle is subjected to shock forces resulting from exploding bolts and/or second stage engine ignition.

Vibration and shock are generally negligible during space flight. However, in a mission which requires maneuvering for rendezvous or for transfer between orbits and/or soft landing by throttling, vibration and shock during space flight may be significant. Sources of dynamic forces may arise from the operation of maneuvering or landing engines (startup, shutdown, random pulsing and discrete-frequency thrust variations), touchdown, or rendezvous. It should be noted that even though the solar cell array may not be operating at the time of the earth launch, it is usually electrically biased by an energy storage battery. Therefore, the array must be designed to withstand the adverse effects of acceleration and vibration loads without potentially short-circuiting or discharging the battery.

2.2.2 Acceleration

Acceleration forces are encountered during launch and in orbit when linear or angular velocities are changed. Acceleration forces are also inherent in mechanical shock and vibration.

Acceleration is commonly given in terrestrial g units where 1 g equals 9.8 m/s^2 (32.2 ft/s^2). To obtain the forces on a body in a different gravitational field or under acceleration, the weight under a 1 g acceleration or terrestrial weight is multiplied by the number of g units. Typical acceleration values used in solar cell array design are given in Tables 2.2-1 and 2.2-2.

Table 2.2-1. Typical g-Forces During Launch/Ascent*
(Solar Cell Array Test Levels)

Launch Vehicle	Intensity (g)	Time
Saturn/Apollo Lunar Module	8 to 12	5 minutes in each of three mutually perpendicular axes
Titan III	4.5	420 seconds
Thrust Augmented Delta	5 to 10	5 minutes each axis
Atlas Centaur	1 to 7.3	5 minutes each axis

* Data contained in Tables 2.2-1 and 2.2-3 through 2.2-7 have been taken from various spacecraft project and launch vehicle specifications that are no longer readily available for reference purposes.

Table 2.2-2. Typical g-Forces During Reentry

Planet	Direct Entry at Escape Velocity†			Direct Entry at Orbital Velocity†			Entry by Decay from Satellite Orbit
	$\theta = 5^\circ$	20°	90°	$\theta = 5^\circ$	20°	90°	
Venus	28.6	112	326	14.3	56	163	8.9
Earth	28.3	111	324	14.3	55.5	162	9.5
Mars	1.6	6.3	18.3	0.8	3.2	9.2	9.2

† Where θ is the reentry angle with the horizontal, and decelerations are given in earth g's.

Under high acceleration loads, parts not rigidly mounted will deflect from the 0-g or 1-g position. This deflection may be temporary or permanent, depending upon the softness of the mounting elements. For example, adhesive-mounted solar cell stacks will temporarily move slightly, while blocking diodes that are supported only by their soft leads may bend permanently. Inadequately supported conductors attached to solar cell contacts may pull the cell contacts off the silicon wafer.

To avoid potential problems caused by sustained acceleration, components should be oriented such as to nullify or minimize the effects of acceleration. Also, the avoidance of large moments by mounting parts close to their center of mass, providing adequate stress relief, and fastening wires at short intervals close to the substrate is important.

2.2.3 Shock (Mechanical)

Shock, sometimes referred to as impulse or impact loading, may be defined as a suddenly applied load of short duration. The magnitude of a shock load is usually high but the time duration of the loading is relatively small. The characteristic of a shock load which makes it different from a static load is the time required for the force to rise from zero to a maximum, compared to the natural period of vibration of the structure. If the time of load application is less than one-half the natural period of the structure, it is considered an impact load. If the time of load application is greater than three times the natural period of the structure, it is considered a static load.

The response of a solar cell array under shock conditions has characteristics similar to those of systems under acceleration and vibration. The initial deformation of the structure is large, and then goes to zero as a damped harmonic oscillation. The intensity of the response of a structure to a pulse loading depends upon the natural frequency of the structure and the intensity and duration of the pulse.

In most cases, shock loads need not be considered for solar cell arrays which are located some distance away from the booster interface. If, however, the array attaches to the structure close to the booster interface or close to active deployment/latchup or pyrotechnic elements, shock isolation may be required to prevent solar cell or coverglass cracking.

Sources of shock environment include:

- Transportation and handling
- Pyrotechnic (firing of explosive bolts, cable cutters, restraining mechanisms, etc.)
- Deployment (initial release, latchup)
- Rocket engine ignition
- Rocket engine combustion instability
- Stage separation forces
- Satellite separation forces
- Impact loads due to meteoroid bombardment
- Docking loads
- Landing impact loads.

Typical values used in solar cell array design are given in Table 2.2-3.

2.2.4 Vibration

Vibration may be defined as a cyclically varying displacement of a body from its equilibrium position, or as the cyclically varying deformation of a body from its equilibrium shape. Vibration may be free or forced. Free vibration in an elastic system refers to

a system free of impressed forces but under the action of forces inherent in the system itself. A freely vibrating system will vibrate at one or more of its natural frequencies. Forced vibration refers to a vibrating system under the excitation of an external force, i.e., a forcing function, which may be of a sinusoidal or random frequency nature.

Table 2.2-3. Typical Mechanical Shock Loads*
(Solar Cell Array Test Levels)

Launch Vehicle	Peak Intensity (g)	Time
Saturn/Apollo Lunar Module	15	10 to 12 ms rise time 0 to 2 ms duration Three shocks in each of three mutually perpendicular directions
Titan III	2500 (near booster interface) 480 (away from booster interface)	50 to 10,000 Hz 80 to 10,000 Hz

* See Table 2.2-1 footnote.

In general, the frequency or frequency spectrum of the exciting force is independent of the natural frequency of the system. However, the frequency or frequency spectrum of a force actually driving a component may be severely altered by the elements which connect this component with the exciting force. This is particularly true for fixed solar cell arrays which are mounted via relatively long structural members to the spacecraft/booster interface elements, and for deployable arrays.

When the frequency of the driving force is near the natural frequency of the structure, resonance will occur. When no damping is available in the system and when the driving frequency is equal to the natural frequency, the amplitude of vibration increases until the system becomes nonlinear. Nonlinearity is often associated with permanent damage, such as deformation or bond separation. Avoiding or damping of resonance in the array support and in the array panels is a primary objective of the structural designers. The solar cell array designer, however, provides necessary inputs and interface considerations.

Vibrational exciting forces encountered during transportation, launch, and flight (see Tables 2.2-4 through 2.2-6) are almost always of a random frequency and random amplitude nature. To permit design and test engineers to perform their functions, the natural vibration environment is idealized, and the system response is evaluated in simplified fashion. The response of solar cell arrays is typically expressed in one of three quantities: amplitude, acceleration, and mean-square acceleration density; all of these are functions of frequency. Many other quantities are also used, the differences being either semantic or due to slightly different mathematical definition.

Table 2.2-4. Sources and Magnitudes of Typical Vibration Environments*

Source	Vibration Environment
Jet aircraft	Acoustical vibration due to jet wake and combustion turbulence. Frequency range up to 500 Hz and maximum amplitude approximately 25 μm .
Piston engine aircraft	Engine vibration range up to 60 Hz and maximum amplitude to 0.25 mm. Propeller vibrations range up to 100 Hz with maximum amplitudes to 0.25 mm. Amplitudes of vibration vary with location in aircraft.
Ships	Engine vibration in diesel or reciprocating steam types range up to 15 Hz with maximum amplitudes to 0.5 mm. Most vibrations are amplified. An amplification factor of 3 is usually acceptable.
Trucks	Suspension resonance of 4 Hz with maximum amplitude of 13 cm. Structural resonance above 80 Hz and maximum amplitude of 0.13 mm.
Passenger automobiles	Suspension resonance of 1 Hz and maximum amplitude of 15 cm. Irregular transit vibrations due to road roughness above 20 Hz and maximum amplitude of 50 μm .
Railroad trains	Broad and erratic frequency range. Isolation resonant frequency of 20 Hz has been successful in railroad applications.
Rocket noise generated in exhaust stream	Usually most severe vibration environment in missiles. Results in random high amplitude vibrations during launch in atmosphere. Characterized by a broad spectral distribution coinciding with resonance frequencies of vehicle structure, skin, and equipment.
Space vehicles earth launch	Approximately 10 g's rms, 600 to 1600 Hz. Acoustical noise in field of payload 150 decibels for 60-second duration.
Space vehicles low earth orbit	Vibration range to 1000 Hz and up to 50 g's for 5-minute duration.
Space vehicles lunar orbit	Vibration range above 1000 Hz and up to 50 g's for 10-minute duration.
Lunar launch	Vibration levels up to 15 g's with frequency spectrum greater than 1000 Hz.
Lunar landing	Vibration levels up to 50 g's and frequency range from a few to several thousand Hertz.

* See Table 2.2-1 footnote.

Table 2.2-5. Typical Random Vibration Levels During Launch/Ascent†

(Solar Cell Array Test Levels)

Launch Vehicle	Frequency Range	Intensity
Saturn/Apollo Lunar Module	15 - 100 Hz	0.01 g ² /Hz to 0.06 g ² /Hz
	100 Hz - 1 kHz	0.06 g ² /Hz
	1 kHz - 2 kHz	0.06 g ² /Hz to 0.015 g ² /Hz
Titan III	20 - 800 Hz	0.01 g ² /Hz to 0.4 g ² /Hz
	800 - 1500 Hz	0.4 g ² /Hz
	1.5 - 2.0 kHz	0.4 g ² /Hz to 0.3 g ² /Hz
Atlas/Agena	20 - 150 Hz	0.023 g ² /Hz
	150 - 300 Hz	0.023 g ² /Hz to 0.045 g ² /Hz
	300 - 2000 Hz	0.045 g ² /Hz
Thrust Augmented Delta	20 - 2000 Hz	0.07 g ² /Hz
		11.8 g rms
Scout	20 Hz - 20 kHz	0.07 g ² /Hz 11.8 g rms

† See Table 2.2-1 footnote.

Table 2.2-6. Typical Sinusoidal Vibration Levels‡

(Solar Cell Array Test Levels)

Launch Vehicle	Frequency Range	Intensity
Saturn/Apollo Lunar Module	5 - 10 Hz	0.5 cm double amplitude
	10 - 18 Hz	1.0 g
	18 - 78 Hz	1.0 g increasing to 18 g
	78 - 200 Hz	18 g peak
Atlas Agena	200 Hz - 2 kHz	10 g
	5 - 250 Hz	±2.3 g
	250 - 400 Hz	±3.7 g
Atlas Centaur	400 - 2000 Hz	±7.5 g
	20 - 2000 Hz	21 g rms peak
	100 - 1000 Hz	0.4 g ² /Hz
Thrust Augmented Delta	10 - 50 Hz	±3.8 g
	50 - 500 Hz	±7.5 g
	500 - 2000 Hz	±21.0 g
Scout	10 - 53 Hz	±0.3 m/s constant velocity
	53 - 100 Hz	±10.5 g
	100 - 2000 Hz	±7.5 g

‡ See Table 2.2-1 footnote.

Amplitude-Frequency Spectrum

Usually expressed as "double amplitude," this quantity gives the peak-to-peak deflection (response) of a point on the array relative to the tiedown (excitation) points plotted as a function of frequency. This maximum deflection must be limited by the design process for two reasons:

- To prevent excessive bending of the array substrate with attendant potential structural damage of the substrate, solar cells, cell covers, or interconnectors.
- To prevent the array from touching other spacecraft components or the shroud and damaging itself or these components.

Acceleration-Frequency Spectrum

Usually expressed in g units (1 g is a force of 9.8 N created by the earth's gravitational field on a mass of 1 kg), it is also an "amplitude" type of quantity and is plotted as a function of frequency. Acceleration amplitude is typically measured by accelerometers placed at the excitation point and various response points, especially where large vibrational amplification is expected. Acceleration amplitude is applicable only for the description of sinusoidal vibration, and is especially helpful to identify resonance frequencies. Both the peak and the rms amplitude of acceleration, A , is being used:

$$A_{\text{rms}} = \left\{ \frac{1}{T} \int_0^T [A_{\text{peak}} \sin(\omega t)]^2 dt \right\}^{1/2}$$

where $\omega = 2\pi f$, T is the period, and t is time.

For the special case of purely harmonic motion, this expression reduces to:

$$A_{\text{rms}} = \frac{\pi}{2\sqrt{2}} A_{\text{average}} = \frac{1}{\sqrt{2}} A_{\text{peak}}$$

Mean-Square Acceleration Density Spectrum

Usually expressed in units of g^2/Hz , this quantity is proportional to power density and is used to quantize the severity of random vibration. Random vibration is characterized by independent statistical variations of both amplitude and frequency as time passes. Thus, at each instant of time there exists both a probability distribution for the acceleration amplitude and an associated continuous vibration frequency spectrum. To make this information useful, both the amplitude probability distribution and the frequency spectrum is required not for each instant of time, but rather for a longer time interval, such as for the entire launch phase during which vibration exists. As a most useful quantity, a mean-square spectral density function $W(f)$ has been defined such that

$$\int_0^{\infty} W(f) df = \lim_{T \rightarrow \infty} \frac{1}{T} \int_0^T f^2(t) dt$$

where f is the frequency, T is the period, and t is time.

Minimizing the Effects of Vibration

The effects of vibration may be minimized by the following techniques:

- Providing solar cell array substrate isolation from the spacecraft structure
- Changing the natural frequency of the solar cell array by modifying its shape, mass, or stiffness, or breaking up of larger areas into smaller ones or into modules
- Dissipating energy and limiting amplitude by use of dampers, resilient pads, or additional tiedowns
- Avoiding sharp bends, fillets, notches, and long runs of unbonded (fastened) wire
- Spacing wire spot bonds and interconnector joints at irregular intervals to prevent buildup of large deflections
- Riveting members rather than welding because they provide interface friction and, therefore, damping between members. Cold-driven rivets should not be loaded in tension because of residual stress concentration at the formed head.
- Locking bolts and nuts because they tend to loosen under vibration and shock. Slippage of the joint due to excessive clearance in a bolt hole should be avoided by using close tolerance bolts or dowel pins. Bolts made from materials with low yield strengths, such as 18-8 stainless steel, tend to stretch and loosen under shock loads even though they have a high ultimate strength. The fatigue strength of bolts may be increased by cold working such as rolling of thread, rolling of fillets near head, and shot peening the shank. Typical locking devices include threading of lock wires through holes in the nuts or bolts and then fastening them to the structure, friction nuts with a polymeric insert or distorted holes, and friction bolts with a polymeric insert in the threaded portion. Lockwashers should be used cautiously as locking devices when shock and vibration are present. Bolted structures provide friction damping between members and may be more desirable than a welded structure if damping is required.

2.2.5 Acoustic Field

An intense acoustic field is generated by two mechanisms during launch: first by rocket engine exhaust and its reflection from the ground to the launch vehicle and the shroud that covers the payload, and second by aerodynamic excitation of the shroud itself at high air speeds. The vibrating launch vehicle and shroud also generates an acoustic field inside the volume enclosed by the shroud which, in turn, excites a vibrational response of the solar cell array. Acoustically induced vibration (random frequency distribution) of the solar cell array is especially high for body mounted arrays that are in close proximity to the shroud. Frequently, the acoustically induced vibrations of the array are larger than vibrations transmitted to the array through structural components so that meeting the acoustic field requirements becomes one of the more important design aspects.

Typical failure modes during acoustic testing, however, are similar to those observed during vibration testing and typically occur in the substrate rather than the solar cells or their associated components. The design recommendations made in Section 2.2.4 to minimize the effects of vibration also apply to minimizing the effects of acoustic fields.

The acoustic field intensity is measured with microphones and is expressed in units of "dB sound pressure level." The decibel (dB) scale is a logarithmic ratio of power levels, of the square of force levels, of the square of displacement levels, or of the square of acceleration levels. If F is the measured acoustic field intensity (force per unit area), then the dB level is

$$\text{dB} = 10 \log_{10} (F^2/F_0^2) = 20 \log_{10} (F/F_0)$$

where F_0 is a reference sound pressure level, usually taken as $2 \times 10^{-5} \text{ N/m}^2$ ($0.0002 \text{ dynes/cm}^2$). Typical sound pressure levels are shown in Table 2.2-7 for test and design purposes. The expected flight level is generally 3 dB lower in each one-third octave band.

Table 2.2-7. Typical Acoustic Field Levels During Launch/Ascent*

(Solar Cell Array Qualification Test Levels)**

1/3 Octave - Band Center Frequency (Hz)	1/3 Octave Band Sound Pressure Levels (dB)		
	Atlas Centaur	Titan IIC	Titan IID
5	98		
6.3	102		
8	105		
10	108		
12.5	111		
16	114		
20	117		
25	120		
31.5	122		
40	125		
50	127	124	136
63	129	125.5	138
80	131	127	140.5
100	132	129	142.5
125	133.5	130.5	144
160	134.5	131.5	145
200	135.5	132.5	146
250	136	133.5	147
315	136.5	134	147.5
400	139	134.5	148
500	133.5	134	147.5
630	131	133.5	147
800	129	133	146.5
1,000	127	132	145.5
1,250	125	131	145
1,600	123	129.5	143
2,000	121	128.5	142
2,500	119	126.5	140
3,150	117	125	138.5
4,000	115	123	136.5
5,000	112.5	121.5	135
6,300	110	120	133.5
8,000	108	118	131.5
10,000	106.5		129.5
Overall SPL	146.0	145.0	158.0

*See Table 2.2-1 footnote.

**Reference level $2 \times 10^{-5} \text{ N}\cdot\text{m}^{-2}$.

2.3 THE SPACE ENVIRONMENT

2.3.1 The Solar System

The solar system consists of the sun as a central body (with approximately 99 percent of the total mass), nine planets, their 31 known satellites, tens of thousands of asteroids, and countless numbers of smaller objects which are occasionally observed as comets, meteors, or meteorites. All of these bodies revolve in slightly elliptical orbits about the sun. All of the planetary orbits can be bounded by a thin disk, having a diameter of 80 astronomical units (AU) or 1/800th of a light-year.

The characteristics of the solar system are summarized in Table 2.3-1 and in Figure 2.3-1. The properties of the sun are discussed below; its radiation is treated in Section 2-4. The orbital terminology and the orbits of artificial satellites are described in Section 2.6.

Asteroids

The asteroids (planetoids or minor planets) are small irregular-shaped bodies of widely differing sizes (from 1 to 500 miles) whose solar orbits lie principally between those of Mars and Jupiter, with mean distances from the sun of 2.1 to 3.5 AU. Eight asteroids have perihelia smaller than that of earth, and one (Icarus) penetrates even closer to the sun than Mercury. It is estimated that there are 80,000 asteroids

brighter than the 19th magnitude. Orbital elements are available today for about 2000 of them, as shown in Table 2.3-2.

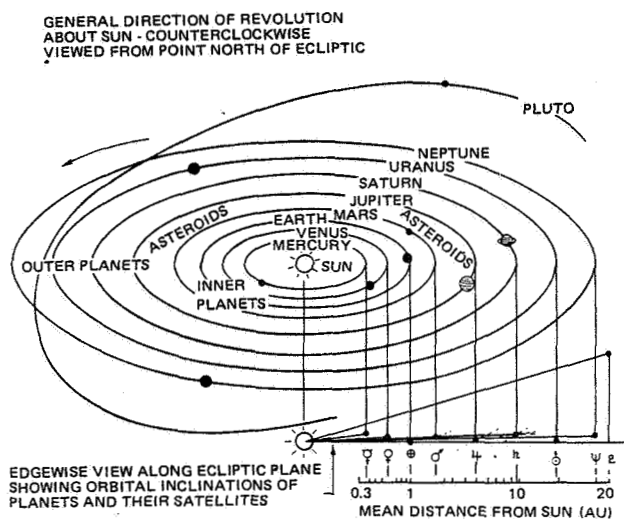


Fig. 2.3-1. The Basic Solar System (Ref. 2.3-1)

Table 2.3-1. Characteristics of the Solar System (adapted from Refs. 2.3-1 and 2.3-2)

(For the values of the solar intensity at the planets see Section 2.4)

Body	Semi-Major Axis to Sun (AU) [*]	Period Earth-Years (Earth = 1)	Mean Diameter (Earth = 1)	Relative Mass (Earth = 1)	Number of Natural Satellites	Equatorial Surface Gravity (Earth = 1)	Surface Temperature (°C)	Albedo	Surface Atmospheric Pressure (in atmospheres)	Atmospheric Composition
Sun	-	-	109.2	3×10^5	-	28	6500	-	-	
Mercury	0.387	0.241	0.379	0.055	0	0.380	400	0.06	<<1	Traces of heavy gases
Venus	0.723		0.956	0.815	0	0.893	430	0.76	16?	93 percent CO ₂ ; possibly N ₂ trace of water vapor
Earth	1.000	1.00	1.00	1.00	1	1.00	15	0.36	1	See Table 2.1-1
Mars	1.524	1.88	0.535	0.108	2	0.377	30 to -120	0.15	0.01	90 to 100 percent CO ₂ remainder unknown, but upper limit for N ₂ is possibly 3 percent
Jupiter	5.203	11.9	11.14	317.9	12	2.54	-140	0.51	>>1	NH ₃ , CH ₄ , H ₂ , He
Saturn	9.539	29.5	9.47	95.1	10	1.06	-170	0.50	?	
Uranus	19.25	84.0	3.69	14.5	5	1.07	-210	0.66	?	
Neptune	30.04	164.8	3.50	17.0	2	1.4	-220	0.62	?	
Pluto	39.64	247.7	1.17	0.87	0	0.7?	-220	0.16	?	Heavy gases?
Earth's Moon	-	0.075	0.272	0.012	0	0.165	-150 to 130	0.07	10 ⁻¹⁷	Traces of very heavy gases

^{*} 1 AU = 92,959,670 miles = 1.4959789×10^{11} m.

(Data from Ref. 2.3-2 used with permission of McGraw-Hill Book Company)

Table 2.3-2. Characteristics of 10 Notable Asteroids (Ref. 2.3-1)

Catalog No. and Name of Asteroid	Period About Sun (years)	Mean Distance to Sun (AU)		Orbital Eccentricity	Orbital Inclination to Ecliptic (deg)
		Perihelion	Aphelion		
1 Ceres	4.60	2.56	2.98	0.076	10.0
2 Pallas	4.61	2.12	3.42	0.234	34.8
3 Juno	4.36	1.98	3.36	0.258	13.0
4 Vesta	3.63	2.15	2.57	0.089	7.1
1566 Icarus	1.12	0.19	1.97	0.827	23.0
Apollo	1.81	0.64	2.33	0.566	6.4
588 Achilles	11.90	4.44	5.98	0.148	10.3
617 Patroclus	11.88	4.47	5.94	0.141	22.1
433 Eros	1.76	1.13	1.78	0.223	10.8
944 Hidalgo	13.95	1.99	9.59	0.656	42.5

Comets

The observable aspect of a comet is the extensive atmosphere (coma, tail) which is developed and irretrievably lost during passage through the inner solar system. The source (an unobserved nucleus, probably a few miles in diameter) forfeits perhaps a thousandth part of itself in each passage. To date, some 550 different comets have been satisfactorily observed. The motion is found to be Keplerian and eccentric, the periods of the closed ellipses being long (thousands of years for about 450 objects) or short (6 or 8 years for fewer than 100 objects). Halley's famous comet is one of a few hybrids between these two classes. In spite of the prevalence of near-parabolic orbits, no fundamentally extrasolar object has yet been recorded.

2.3.2 The Space Vacuum

The vacuum of space consists of a low-density gas mixture, consisting primarily of hydrogen, helium, protons, and alpha particles. The estimated gas pressure in interplanetary space is approximately $10^{-18} \text{ N}\cdot\text{m}^{-2}$ (10^{-16} mm Hg). In interstellar space, pressures lower than $10^{-27} \text{ N}\cdot\text{m}^{-2}$ may be encountered. The best vacuum obtainable in a laboratory ranges from 10^{-12} to $10^{-15} \text{ N}\cdot\text{m}^{-2}$; however, $10^{-12} \text{ N}\cdot\text{m}^{-2}$ is considered practical for the best commercial vacuum systems with $10^{-8} \text{ N}\cdot\text{m}^{-2}$ (10^{-6} mm Hg) being more typical for space chambers. The transition between the atmosphere and space is discussed in Section 2.1.1 (The Atmosphere).

For design purposes the following are recommended (Ref. 2.3-4):

- Gas pressure $10^{-11} \text{ N}\cdot\text{m}^{-2}$
- Density $10^{-23} \text{ g}\cdot\text{cm}^{-3}$
- Kinetic gas temperature $2 \times 10^5 \text{ K}$

Effect of Vacuum on Metals

The high vacuum of outer space will cause volatile materials, plasticizers, and additives to vaporize. Metals which might vaporize at an appreciable rate, if heated in this high-vacuum environment, are magnesium, cadmium, and zinc. These should be avoided for outer-space applications unless they are maintained at a low temperature, utilized in thick sections, or are overcoated with some other material of lesser volatility. Of the above metals, magnesium was utilized on the exterior of the Midas II satellite. The

problems associated with utilizing volatile materials are at least twofold: they are removed by the action of the space vacuum from the devices in which they are intended to be used, and they may condense on the cooler surfaces, possibly causing electrical short-circuiting, change of surface emissivities, or change in optical properties of mirrors and solar cell covers. Sublimation of the base material can be retarded by the use of surface coatings with low-vapor pressures, for example, inorganic coatings such as oxides.

In general, the weight loss rate in vacuum increases directly with increasing vapor pressure of the material. Table 2.3-3 presents a list of several metals and their corresponding sublimation rates for different temperatures.

Table 2.3-3. Sublimation of Metals in High Vacuum (Ref. 2.3-3)

Element	Temperature ($^{\circ}\text{C}$) at Which Given Sublimation Rate Occurs			Melting Point ($^{\circ}\text{C}$)
	0.1 $\mu\text{m}/\text{yr}$	10 $\mu\text{m}/\text{yr}$	1 mm/yr	
Cadmium	38	77	122	320
Zinc	71	127	177	420
Magnesium	110	171	243	650
Silver	480	590	700	960
Aluminum	550	680	810	660
Beryllium	620	700	840	1280
Copper	630	760	900	1080
Gold	660	800	950	1060
Chromium	750	870	1000	1870
Iron	770	900	1050	1540
Nickel	800	940	1090	1450
Titanium	920	1070	1250	1670
Molybdenum	1380	1630	1900	2610
Tantalum	1790	2040	2320	2980
Tungsten	1870	2150	2480	3430

Note: To convert sublimation rate g in gm/cm^2 to cm/s , divide g by density in gm/cm^3 .

The mechanical properties of materials in vacuum are different from those exhibited in air. Some metals tested in vacuum grow stronger, while others become weaker and have altered creep and fatigue properties (Refs. 2.3-5, 2.3-6, and 2.3-7).

The following two surface reactions in air are believed to be the controlling factors in these differences: (a) the surface of the material strengthens and hardens by oxidation or is altered by gas diffused into its interior, or (b) surface cracks form and adsorbed gases tend to wedge the crack. The material will be stronger in either vacuum or in air, depending upon which of these reactions is the controlling factor. Ordinary glass is three times as strong in a vacuum of 10^{-5} mm Hg as it is in air. Surface finishes can, therefore, be expected to control or significantly influence the strength of metals in vacuum (Refs. 2.3-5 and 2.3-7).

Effects of Vacuum on Plastics

The weight loss exhibited by organic polymers in vacuum is usually the result of the evaporation of relatively lower molecular weight fractions, unreacted additives, contaminants, adsorbed (on surfaces) and absorbed (in bulk) gases, moisture, and others. The loss of these additives and contaminants, however, can

change important properties of the polymers. For example, the loss of a plasticizer by evaporation in a vacuum environment will produce a more rigid or brittle part with a corresponding decrease in elongation and increase in tensile and flexure strength. Electrical components, such as capacitors, may change in value if the insulating materials used in their construction lose moisture or other contaminants which are trapped during their manufacture.

The rate of weight loss at a given pressure and temperature varies as a function of time. The initial weight loss is usually high and is due to the loss of adsorbed gases, water, and other contaminants. During this stage, the total weight loss may be as great as 3 percent for some polymers. This relatively high initial weight loss will drop to a very low value when the loss of weight is due primarily to degradation of the basic polymer.

In general, polymers of relatively high molecular weight, such as Teflon, do not evaporate or vaporize in vacuum, but when supplied with sufficient thermal energy they decompose or depolymerize. These polymers have such low vapor pressures that the thermal energy required to cause evaporation exceeds that required to break the chemical bonds of the polymer. Many polymers of engineering importance do not sublime or evaporate in high vacuum environments, and the thermal stability of these polymers should be at least as good in high vacuum as in the earth atmosphere.

The following additional points should be noted:

- Weight loss rate and amount of weight loss are greatest early in the test period when the materials at or near the surface evaporate. These loss factors decrease subsequently to a rate determined principally by diffusion rates through the polymer to the surface.
- Rigid plastics are, in general, preferred over flexible, elastomeric materials.
- Materials with minimum number and quantity of additives and modifiers are preferred.
- Complete cure of the plastics must be obtained by extended time and/or elevated temperature post-curing to ensure the elimination of unreacted, low molecular fractions in the product.
- Those materials exhibiting high loss rates but considered necessary for use on space vehicles because of special desirable properties should be preconditioned in vacuum at elevated temperature to reduce, as much as possible, the potential loss of the material to space.

Lubricants in Space Vacuum

Conventional lubricants are generally not suitable for use in the space vacuum because of their high vapor pressure which results in loss of fluid by evaporation. Even if the rate of evaporation of a fluid lubricant is acceptable, the vapors may condense on cooler surfaces such as lenses, solar cell covers, and thermal control surfaces. Other problems associated with using a lubricant in a vacuum are (a) the absence of oxygen—essential to forming a metallic soap, and

(b) the absence of absorbed water vapor necessary for the lubricating properties of bearing materials, such as graphite.

Lubricants are discussed further in Section 6.4.1.

2.3.3 The Space Plasma

According to Ref. 2.3-8, solar cell arrays, as well as the spacecraft of which they are part, may be subject to electrical charging by the surrounding plasma. This charging is especially significant during magnetic substorm activity.

The usual, or "quiet," magnetospheric structure is such that at synchronous orbit, a satellite is immersed in a so-called "cold" (energy ≤ 1 eV) plasma of moderate density (≤ 10 particles per cm^3), and there are no "hot" (kilovolt) particles. However, at the onset of magnetic substorms, large electric fields develop across the magnetotail, and the electric and magnetic field ($\vec{E} \times \vec{B}$) convection drives a new plasma toward the earth from as far out as the orbit of the moon. As this plasma, having an initial energy of ~ 100 eV, is driven into stronger magnetic fields near earth, it heats considerably due to approximate invariance of the particles' magnetic moment.

Other (poorly understood) electric fields or time-varying magnetic fields near synchronous orbit drive out the cold (1 eV) component, and it is replaced by a hot (10 to 20 keV) plasma. The simultaneous loss of the cold and the appearance of the very hot plasma of density 0.1 to 1 particle per cm^3 can lead to severe electrostatic charging of exposed surfaces of the satellite. Large differential voltages may build up between various surfaces of differing materials, and especially between illuminated and shadowed dielectric surfaces. These voltages may at times exceed the breakdown potentials of the materials involved, thus producing arc discharges. The electromagnetic pulses from such discharges may provide sufficient energy at the proper frequencies to produce false signal pulses into either the receiving antennas or into the cabling between electronics boxes, thus initiating an "anomaly" in the spacecraft command status.

The satellite charging phenomenon just outlined has been observed directly by the low-energy plasma probe experiment aboard ATS-5, as reported in the literature by DeForest (Ref. 2.3-9). The latter experimental observation has shown surface potentials on ATS-5 during satellite eclipse of up to -9 kV.

DeForest noted that during such disturbed periods (in the winter months, at least) the electron fluxes in these injection events could be sufficiently high to charge ATS-5 to between ~ 50 to 300 volts in sunlight, and between -1000 and -9000 volts during eclipses. He ascribed this large difference in the illuminated and eclipsed values of satellite potential to the absence of the photoelectron current during eclipses.

It has been estimated that a cylindrical surface in geosynchronous orbit could charge to a potential of -22 kV relative to the surrounding plasma (-17 kV for a plane surface).

Recently, the observations of charging of the geostationary satellite ATS-5 during substorm injection events in the local morning sector, and correlations made (by Ref. 2.3-8) between substorm activity on ground magnetograms and the incidence of anomalous

events on a DSCS-II satellite and other geostationary satellites when located in the local morning sector lead to the conclusion that some anomalies in electronics subsystems must be either directly or secondarily caused by such satellite charging phenomena as discussed above.

Based on the foregoing considerations it was predicted that a particular DSCS-II anomaly would repeat during eclipse operation. The anomaly, in fact, did occur at the time the first eclipse was experienced.

Recommendations for Satellite Future Design Practices

Based on the models for satellite interaction with unfavorable plasma environments, and on test results, the following preliminary recommendations bearing on future satellite systems are made:

- High intensity, high frequency arc discharge sources should be identified by careful examination of the proposed structures and how they would respond to a high energy electron environment, using charging models as they become available, especially from in-flight data from orbiting, instrumented satellites.
- Adequate shielding design of boxes, cables and connectors must be employed. Twisted-pair and common mode rejection techniques may be required.
- Grounding techniques should be reviewed so that the entire satellite system is well grounded from both low-level signal processing and high-voltage arcing considerations. Single-point grounding techniques may be potentially inappropriate.
- Low impedance grounding of outer metallized layers in thermal blankets or on solar cell array substrates should be provided.
- On nonmetallic solar cell array substrates, all metallic elements, such as aluminum honeycomb core and metallic inserts, should be grounded.
- The surface areas of dielectrics or insulated conductors exposed to bombardment by high energy (substorm-associated or otherwise) electrons should be minimized.
- Consideration should also be given to satellite level electric field and arc-induced tests on future programs to qualify the design, in addition to normal EMC testing. These should also be augmented with material and unit level qualification testing.

2.3.4 Meteoroids

Interplanetary space contains many small particles called meteoroids. When a meteoroid passes through the earth's atmosphere, its luminous, incandescent body is called a "meteor." The remnants of meteoroids found at the earth's surface are termed meteorites.

Meteoroids are classified according to their most likely origin and frequency of occurrence; they may originate either from asteroids or from comets. Cometary meteoroids may occur sporadically or in streams or showers while asteroidal meteoroids occur only sporadically.

Asteroidal meteoroids are relatively dense (with an average of approximately 3.5 g cm^{-3}), stone-like, iron-rich, irregularly shaped particles. Cometary meteoroids are less dense (with an average of 0.5 g cm^{-3}) and frequently possess a dustball or porous structure. Even though most of the cometary meteoroids are less than 1 mm in diameter, their greater frequency and hypervelocity (an average of 20 km/s, and as high as 72 km/s) may cause a threat to spacecraft and solar cell arrays.

The meteoroidal particle mass of most concern to solar cell arrays is estimated to lie between 10^{-6} and 10^{-3} g since particles with mass below 10^{-6} g, in general, do not have sufficient energy to cause significant damage, while particles with mass greater than 10^{-3} g are less frequently encountered.

To assess the potential damage of meteoroids to solar cell arrays, two sets of information are required:

- Meteoroidal particle mass and frequency of occurrence
- Probability of intercepting such particles in a given orbit at a certain date.

The data for the meteoroid environment is given in Refs. 2.3-10 and 2.3-4.

Effects of Meteoroids on Solar Cell Arrays

The damage expected from meteoroid impacts on the solar array is primarily erosion of the cover glass and of the substrate rear surface thermal control coating.

Coverglass erosion would consist first of mechanical abrasion of the antireflective coating (typically magnesium fluoride) and then pitting of the cover itself similar to sandblasting. Heavier particles impacting the solar cell cover at high velocity may cause the covers to crack (Ref. 2.3-11); however, very few such particles, if any, are expected to impact an array in earth orbit.

The degradation of cover slide transmittance, as measured by a change in solar cell short-circuit current, has not been well established. Estimates were made in 1964 by A. Conn based on Refs. 2.3-12, 2.3-13, and 2.3-14, and in 1970 by R. W. Rostron (Ref. 2.3-15). This data is shown in Table 2.3-4. Orbital performance of satellites have not indicated significant damage due to meteoroids.

Table 2.3-4. Coverglass Transmittance Degradation in Earth Orbit Due to Micrometeoroid Damage

Time in Orbit (years)	Relative Transmittance	Source
0	1.00	-
1	0.99	Conn
10	0.98	Conn
10	0.99	Rostron
100	0.97	Conn

2.3.5 Deposits

One source of solar cell array output degradation in space may be contamination of the solar cell array surfaces by engine exhaust plumes and by condensation of outgassing products stemming from exposed nonmetallic materials or from sublimating metals on the spacecraft. This contamination may cause solar cell array output degradation by two different mechanisms: (a) loss of light transmission to the solar cells, and (b) increased solar cell operating temperature. The increase in cell temperature is due to a deterioration in the thermo-optical characteristics of the cell covers and thermal control surfaces on the array back side. Attempts have been made to experimentally measure the impact of exhaust plumes on array power loss, but significant effects (probably in excess of 2 percent) were not found (Refs. 2.3-16 through 2.3-20). Theoretical predictions of the effects of deposits from outgassing materials are more severe, being estimated to reach 10 percent for Skylab (Ref. 2.3-21). Actual flight data of Skylab during 200 days in orbit has shown evidence of such deposits; however, their impact on solar cell array performance was not distinguishable from the small, but measurable, total array degradation due to all environmental effects, including ultraviolet and corpuscular irradiation (Ref. 2.3-22).

2.3.6 Gravity

The gravitational potential, U , of the earth decreases approximately with the square of the distance from the center of the earth, r as follows:

$$U = \frac{GE}{r^2}$$

where $GE = 398601.2 (\pm 0.4) \text{ km}^3 \text{ s}^{-2}$, the geocentric gravitational constant (Ref. 2.3-4). Computations of satellite orbits require detailed considerations of the nonspherical shape and nonhomogeneous mass distribution of the earth.

Effects of Zero Gravity

The effects of zero gravity on solar cell array materials and assemblies are generally beneficial, especially when the array is large and of lightweight construction. However, absolute zero gravity rarely exists on actual solar cell arrays due to a number of disturbing forces which may be caused by any of the following:

- Gravity gradients
- Spacecraft velocity and attitude changes
- Solar cell array reorientation
- Solar radiation pressure
- Spacecraft spinning or tumbling.

Simulation of zero gravity for the testing of larger, deployable lightweight arrays is difficult to achieve but has been done repeatedly and successfully, utilizing so-called "zero-g" fixtures.

Gravity Gradient Torques

Because the gravitational potential in an inverse square law field varies with altitude, the center of gravity of a body will not lie at its mass center. Unless the gravitational force passes through the mass

center, a torque will result. Although this effect generally degrades attitude accuracy, it can provide control capability for a spacecraft which is properly configured.

2.3.7 Time in Space

In the past, typical satellite design lifetimes ranged from several months to 3 years. Recent successful spaceflights have prompted the planning of longer duration missions. Examples are communication satellites and manned earth-orbiting space stations for 10-year durations and unmanned Grand Tour reconnaissance missions to Jupiter, Saturn, Uranus, and Neptune or Pluto, requiring mission durations of 6 to 12 years. Some typical mission durations are shown in Table 2.3-5.

Table 2.3-5. Space Mission Durations

Space Mission	Nominal Duration
Earth orbit, 560 km orbit	90 minutes
Lunar landing, one way	2.5 days
Lunar reconnaissance mission, no landing, no lunar orbit	5 days
Lunar landing, earth-return	1 to 2 weeks
Close solar probe, one way instrumented	4.5 months
Mars landing, one way	9 months
Mars reconnaissance mission, no landing, no Martian orbit	12 months
Venus reconnaissance, planetary orbit and return to earth	1.25 years
Mercury reconnaissance, planetary orbit and return to earth	1.5 years
Mars reconnaissance, planetary orbit and return to earth	2.5 years
Jupiter reconnaissance, planetary orbit and return to earth	3.7 years
Saturn reconnaissance, planetary orbit and return to earth	4.5 years

The effects of time in space are adverse, causing continuing degradation of the array. The probability of failure of the solar cell interconnecting system and/or soldered or welded joints by metal fatigue increases with exposure time, especially with the number of thermal cycles due to solar eclipses. Solar cell cover, and adhesive damage due to the space radiation are cumulative functions of time.

2.3.8 Magnetic Fields

The earth's magnetic field, also called the geomagnetic or terrestrial magnetic field, originates in its center, but is neither coincident with the earth's geographic poles nor symmetrical to the earth's surface. The total strength of geomagnetic field varies from approximately 3×10^{-5} tesla (T) [0.30 to 0.35 gauss (G)] at the equator to approximately 6.5 to 7.0×10^{-5} T (0.65 to 0.70 G) at the magnetic poles. With increasing altitude the field strength falls off approximately with the cube of the distance from the center of the hypothetical earth's magnet (Figure 2.3-2).

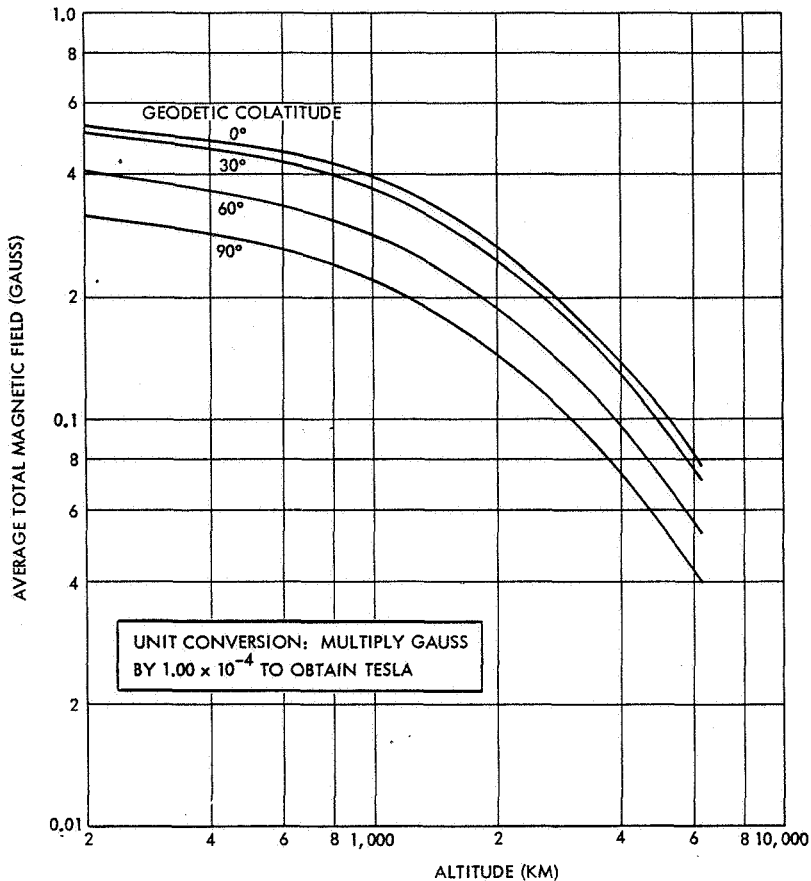


Figure 2.3-2. Magnetic Flux Density of the Geomagnetic Field (Ref. 2.3-4)

The geomagnetic field is disturbed by the solar plasma. The solar plasma also limits the extent of the geomagnetic field in the direction of the sun to approximately 10 earth radii.

The geomagnetic field strength at synchronous altitude is approximately 1.38×10^{-7} T (138 gammas). The magnetic field strength in interplanetary space is due to the solar plasma; its magnitude is about 5×10^{-9} T (5 gammas) at a distance of 1.0 to 1.5 AU from the sun. The interplanetary magnetic field strength temporarily increases by up to two orders of magnitude during periods of increased solar activity.

Effects of Magnetic Fields

Magnetic fields produced by the solar cell array may have an impact on two other subsystems: attitude control and magnetic field experiments.

For a spacecraft in an environmental magnetic field (such as the earth's magnetic field) the presence of residual magnetism or current loops will result in

a torque on the vehicle. Occasionally this phenomenon is purposely used for attitude control (e.g., Tiros, OAO) but most often the effect is undesirable. For this reason, especially on spacecraft carrying large solar cell arrays, the electrical solar cell circuits are laid out such that the current loops produce no net torque.

For missions flying sensitive magnetometers, the entire spacecraft and solar cell array designs may be restricted to the use of nonmagnetic materials (potentially excluding Kovar and Invar for cell interconnector material) and careful circuit layout, so that the magnetic fields induced by the spacecraft or the array have a negligible strength at the magnetometer location.

Magnetic fields produced by electrical current loops can be minimized by laying out the solar cell circuits such that fields from neighboring circuit loops cancel each other. Different degrees of field cancellation can be achieved by different methods as described in Section 8.10 (Magnetic Design).

2.4 SOLAR RADIATION IN SPACE

2.4.1 Temperature in Space

Interplanetary space consists of widely separated gas molecules, so that the concept of temperature environment in space is quite different from the concept of temperature as an environment in the atmosphere. Due to the extremely low density of the interplanetary gas mixture, it is necessary to consider temperature in terms of kinetic theory of gases. Based on this theory, gas temperatures of several thousand degrees have been predicted. However, since these high temperature gas molecules are so widely scattered, they have a negligible effect on the temperature of a solar cell array due to the small amount of heat energy involved. The temperature of a space vehicle, therefore, is determined not by the temperature of the surrounding atmosphere, but rather as a result of radiation from other sources, such as the sun, and re-radiation to the heat sink of space.

The primary external source of thermal energy for a solar cell array traveling within the solar system is direct radiation from the sun. The heat flux intensity varies inversely as the square of the distance from the sun (see Section 2.4.2).

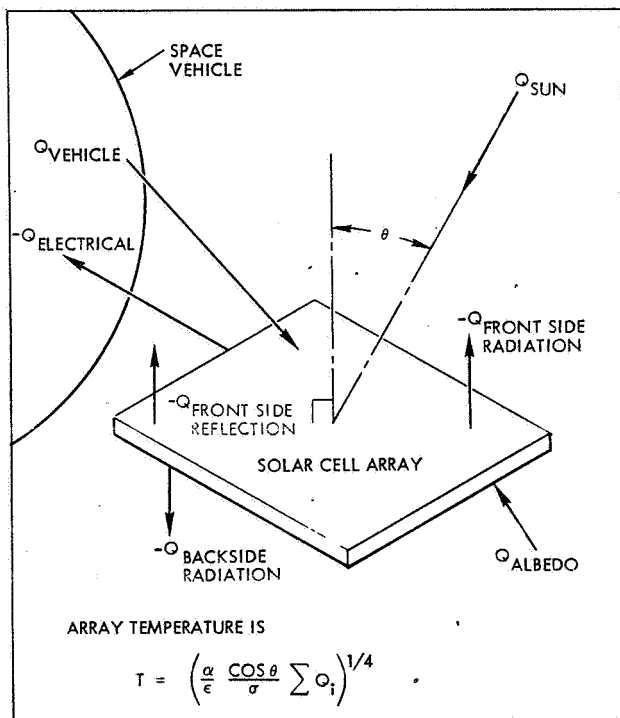


Fig. 2.4-1. Energy Balance Determines Array Temperature in Space

Another, secondary source of heat for bodies in close proximity to a planet is their reflected and emitted energy. The emission and reflectivity of heat energy from a planet depends on its temperature and emissive properties, and on its albedo (reflective properties). The albedo represents the percentage of incident energy reflected by a planet. The average albedo for several solar system bodies is given in Section 2.3.1.

The steady-state temperature of a solar cell array in space can be determined by an energy balance equation, as shown in Figure 2.4-1.

The results of such thermal analysis, described in detail in Section 9.6, are shown in Figure 2.4-2 for a typical flat, oriented array configuration for various solar distances.

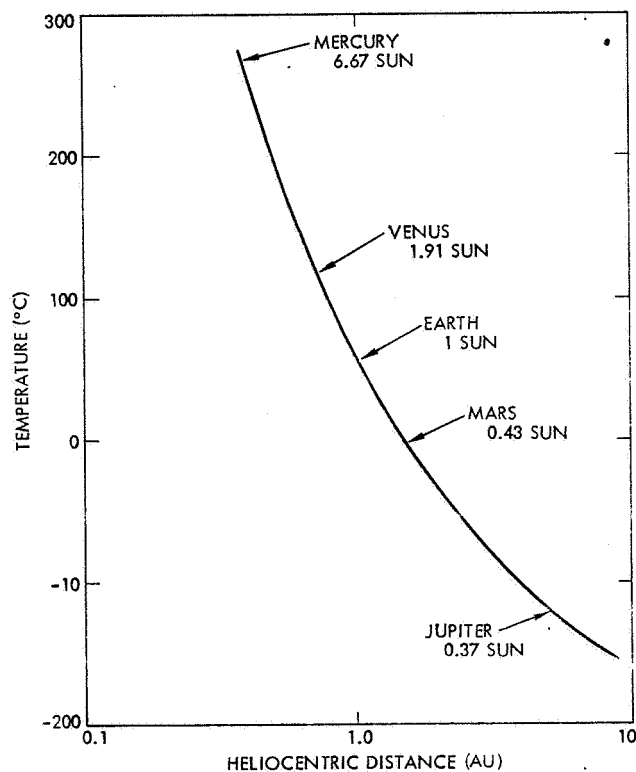


Fig. 2.4-2. Conventional Mariner Solar-Array Temperature Versus Heliocentric Distance at Normal Incidence (Illustrative Example)

Effects of Temperature on Solar Cell Arrays

The two major effects of temperature on solar cell arrays are electrical and mechanical in nature.

• Electrical Effects

The output voltage of silicon solar cells decreases with increasing temperature at a rate of approximately 2 to 2.5 mV per degree Celsius, while the cell output current increases slightly at a rate of generally less than 0.1 percent per degree Celsius (for more precise data see Chapter 3). Near room temperature, the solar cell power output decreases with increasing temperature at a rate of approximately 0.4 to 0.6 percent per degree Celsius. At approximately 300°C the energy conversion efficiency of silicon solar cells becomes zero.

Exposure of silicon solar cells to temperature of up to 400°C in vacuum is generally not harmful unless the cell contacts are covered with solder or another metal that would melt. Molten lead-tin solder on the contacts may dissolve some of the silver contact metallization and thereby weaken the metal-to-silicon bond and possibly increase internal electrical losses. In severe cases, the contact may separate from the cell and cause significant electrical output loss (see Section 9.9). Molten contact metal may also short-circuit the solar cell p-n junction, especially when the solar cells are reverse biased (see Section 3.9).

• Mechanical Effects

Exposure of solar cell arrays to low temperature causes mechanical stresses in the array components. These stresses arise from materials that are in intimate contact with each other but have different coefficients of linear thermal expansion. The material combinations of great interest to array designers are the cover and cell adhesives and solar cell interconnect systems (see Sections 5.3 and 9.7).

Exposure of solar cell arrays to many cycles of alternating high and low temperature causes cyclic stress variations that may lead to fatigue failures. Failure by fatigue typically occurs at stress levels that are considerably lower than those required to cause failure during a single exposure (see Section 9.8).

High temperature causes reduction of the ultimate strength of most materials, but especially of plastics and solder. It also may cause creep, material decomposition, and melting. (Typical solder melting temperatures are around 175°C.)

Low temperature causes severe stresses in assemblies which may cause adhesive bond delamination, and solar cell and cover cracking.

Alternating high and low temperatures cause cyclic stresses which may lead to fatigue failures of adhesive bonds, soldered and welded joints, solar cell interconnectors, diodes, and diode leads.

2.4.2 The Solar Constant

The sun is typical of the most numerous class of stars with spectral designation dG2 and black-body surface temperature of approximately 6000°K (Ref. 2.4-1). The sun emits radiation in the wavelength range between 1×10^{-10} m (X-rays) and 30 m (radio frequency). The peak of the spectrally emitted energy occurs at 0.48 μ m and approximately 77 percent of the emitted energy lies in the band from 0.3 to 1.2 μ m which is of interest to current silicon solar cells. Approximately 1 percent of the energy lies below 0.3 μ m and approximately 22 percent lies above 1.2 μ m. The total energy received from the sun on a unit area perpendicular to the sun's rays at the mean earth-sun distance, termed an astronomical unit (AU = 1.4959789×10^{11} m), is called the solar constant. The solar intensity at solar distances other than 1 AU is typically expressed as a fraction or a multiple of the solar constant.

The Value of the Solar Constant

The value of the solar constant has been revised many times. The most widely used values for solar array work during the period between 1958 and 1972 were 1400 W/m² and 1396 W/m², based on the work done by Johnson (Ref. 2.4-2). Recently, the value of the solar constant was revised to a design value of 1353 W/m² or 1.940 cal cm⁻² min⁻¹ (Ref. 2.4-3). It is taken for a mean earth-sun distance of 1 AU equal to 1.496×10^{13} cm and in the absence of the earth's atmosphere. The estimated error is ± 2.1 mW cm⁻² or ± 0.03 cal cm⁻² min⁻¹. (The calorie is the thermochemical calorie and the milliwatt is 10^{-3} absolute joule per second.)

Effects of Revising the Solar Constant

Revisions in the value of the solar constant may only affect the predicted solar cell array temperature in orbit. There is no effect on the photovoltaic performance of the solar cell on the array, because solar cells are calibrated in near-space against the sun directly without having to know the solar intensity (see Section 11.3). Inasmuch as changes in the measured values of the solar constant do not alter the sun's actual intensity, they also do not alter the solar cell output obtained in space at a given distance from the sun.

Variation of Solar Intensity with Sun Distance

On the basis of the foregoing value adopted for the solar constant, the values shown in Table 2.4-1 were derived by Ref. 2.4-3 to give variation in total solar irradiance* with changes in earth-sun distance during the year. According to this reference, such variation can be determined with greater accuracy than the absolute value of the solar constant.

Table 2.4-2 gives the corresponding solar intensity values for the other planets of the solar system (based on Refs. 2.4-4 and 2.4-5).

*The term "total solar irradiance" refers to total radiant energy received at a given distance, whereas the term "solar constant" describes the same parameter at 1 AU. This handbook has adopted the generally accepted terms "solar illumination" and "solar intensity" instead of "solar irradiance" to minimize potential confusion with radiation effects (i. e., ultraviolet, charged particles, etc.).

Table 2.4-1. Variation of Solar Intensity with Earth-Sun Distance (Ref. 2.4-3)

Date	Solar Intensity* (mW·cm ⁻²)	Relative **
January 3 (perihelion)	139.9	1.0340
February 1	139.3	1.0296
March 1	137.8	1.0185
April 1	135.5	1.0015
May 1	133.2	0.9845
June 1	131.6	0.9727
July 4 (aphelion)	130.9	0.9675
August 1	131.3	0.9704
September 1	132.9	0.9823
October 1	135.0	0.9978
November 1	137.4	1.0155
December 1	139.2	1.0288

*The changes in sun-earth distance for the same date from year to year are such that values may vary by ±0.1 mW cm⁻². For precise comparison, the table of radius vector given in the American Ephemeris (Ref. 2.4-4) should be consulted.

**Relative to 135.3 mW·cm⁻²

Solar Spectral Irradiance

The spectral irradiance of the sun at the distance of 1 AU in the absence of the earth's atmosphere (i. e., at air-mass zero, see below) is given in Table 2.4-3 and Figure 2.4-3. The estimated error in these values is ±5 percent in the wavelength range of 0.3 to 3.0 μm, and greater outside these wavelength limits, according to Ref. 2.4-3. A useful, abridged version of the solar spectral irradiance is given in Table 2.4-4.

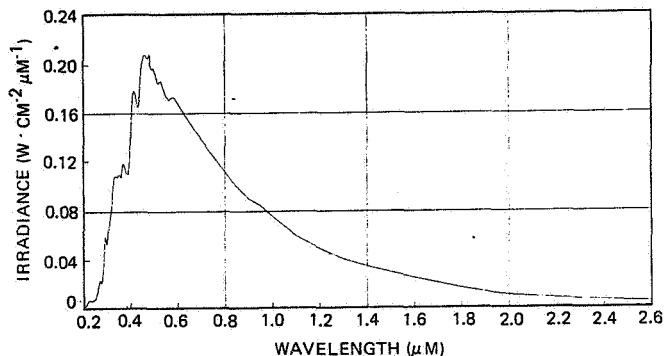


Fig. 2.4-3. Solar Spectral Irradiance (Ref. 2.4-3)

Table 2.4-2. Orbital Constants of the Planets and Solar Intensity at Planetary Distances (Ref. 2.4-3)

Planet	Semimajor Axis of Orbit		Sidereal Period (days)	Eccentricity of Orbit 1971 (ε)	Solar Intensity at Distance of Semimajor Axis*		Ratio of Max to Min Intensity** $\left(\frac{1+\epsilon}{1-\epsilon}\right)^2$
	(AU)	(10 ⁶ km)			Solar Constant	mW·cm ⁻²	
Mercury	0.387 099	57.91	87.9686	0.205 629	6.673 5	902.9	2.303
Venus	0.723 332	108.21	224.700	0.006 787	1.911 3	258.6	1.028
Earth	1.000	149.60	365.257	0.016 721	1.000 0	135.3	1.069
Mars	1.523 69	227.94	686.980	0.093 379	0.430 7	58.28	1.454
Jupiter	5.2028	778.3	4 332.587	0.048 122	0.036 95	4.999	1.212
Saturn	9.540	1427	10 759.20	0.052 919	0.010 99	1.487	1.236
Uranus	19.18	2869	30 685	0.049 363	0.002 718	0.3678	1.218
Neptune	30.07	4498	60 188	0.004 362	0.001 106	0.1496	1.018
Pluto	39.44	5900	90 700	0.252 330	0.000 643	0.0870	2.806

*Solar intensity is $1/R^2$ in units of the solar constant and $135.3/R^2$ in mW·cm⁻² where R is the semimajor axis of the planetary orbit.

**Values of eccentricity change with time; the ratio of solar intensity at perihelion to that at aphelion in the last column is computed on the assumption of constant eccentricity.

Table 2.4-3. Solar Spectral Irradiance at 1 AU (Solar Constant of $135.30 \text{ mW}\cdot\text{cm}^{-2}$) (Ref. 2.4-3)

Wavelength, λ (μm)	Average Irradiance, * P_λ ($\text{W}\cdot\text{cm}^{-2}\mu\text{m}^{-1}$)	Area under curve, 0 to λ , A_λ ($\text{mW}\cdot\text{cm}^{-2}$)	Portion of solar constant with wavelength $<\lambda$, D_λ (%)	Wavelength, λ (μm)	Average Irradiance, * P_λ ($\text{W}\cdot\text{cm}^{-2}\mu\text{m}^{-1}$)	Area under curve, 0 to λ , A_λ ($\text{mW}\cdot\text{cm}^{-2}$)	Portion of solar constant with wavelength $<\lambda$, D_λ (%)
0.120	0.000010	0.00059993	0.00044	0.425	0.1693	16.0439	11.858
0.140	0.000003	0.00073000	0.00054	0.430	0.1639	16.8769	12.474
0.150	0.000007	0.00072000	0.00058	0.435	0.1663	17.7024	13.084
0.160	0.000023	0.00093000	0.00069	0.440	0.1810	18.5707	13.726
0.170	0.000063	0.00135000	0.00101	0.445	0.1922	19.5037	14.445
0.180	0.000125	0.00230000	0.00170	0.450	0.2006	20.4857	15.141
0.190	0.000271	0.00428000	0.00316	0.455	0.2057	21.5014	15.892
0.200	0.00107	0.010985	0.0081	0.460	0.2066	22.5322	16.653
0.210	0.00229	0.027785	0.0205	0.465	0.2048	23.5607	17.414
0.220	0.00575	0.067985	0.0502	0.470	0.2033	24.5809	18.168
0.225	0.00649	0.098585	0.0729	0.475	0.2044	25.6002	18.921
0.230	0.00667	0.131485	0.0972	0.480	0.2074	26.6297	19.682
0.235	0.00593	0.162985	0.1205	0.485	0.1976	27.6422	20.430
0.240	0.00630	0.193560	0.1430	0.490	0.1950	28.6237	21.156
0.245	0.00723	0.227385	0.1681	0.495	0.1960	29.6012	21.878
0.250	0.00704	0.263060	0.1944	0.500	0.1942	30.5767	22.599
0.255	0.0104	0.306660	0.2267	0.505	0.1920	31.5422	23.313
0.260	0.0130	0.365160	0.270	0.510	0.1882	32.4927	24.015
0.265	0.0185	0.443910	0.328	0.515	0.1833	33.4214	24.702
0.270	0.0232	0.548460	0.405	0.520	0.1833	34.3379	25.379
0.275	0.0204	0.657160	0.486	0.525	0.1852	35.2592	26.060
0.280	0.0222	0.763660	0.564	0.530	0.1842	36.1827	26.743
0.285	0.0315	0.897910	0.644	0.535	0.1818	37.0977	27.419
0.290	0.0482	0.09716	0.811	0.540	0.1783	37.9979	28.084
0.295	0.0584	1.36366	1.008	0.545	0.1754	38.8822	28.738
0.300	0.0514	1.63816	1.211	0.550	0.1725	39.7519	29.381
0.305	0.0603	1.91741	1.417	0.555	0.1720	40.6132	30.017
0.310	0.0689	2.24041	1.656	0.560	0.1695	41.4669	30.648
0.315	0.0764	2.60366	1.924	0.565	0.1705	42.3169	31.276
0.320	0.0830	3.00216	2.219	0.570	0.1712	43.1712	31.908
0.325	0.0975	3.45341	2.552	0.575	0.1719	44.0289	32.542
0.330	0.1059	3.96191	2.928	0.580	0.1715	44.8874	33.176
0.335	0.1081	4.49691	3.324	0.585	0.1712	45.7442	33.809
0.340	0.1074	5.03566	3.722	0.590	0.1700	46.5972	34.440
0.345	0.1069	5.57141	4.118	0.595	0.1682	47.4427	35.065
0.350	0.1093	6.11191	4.517	0.600	0.1666	48.2797	35.683
0.355	0.1083	6.65591	4.919	0.605	0.1647	49.1079	36.296
0.360	0.1068	7.19366	5.317	0.610	0.1635	49.9284	36.902
0.365	0.1132	7.74366	5.723	0.620	0.1602	51.5469	38.098
0.370	0.1181	8.32191	6.151	0.630	0.1570	53.1329	39.270
0.375	0.1157	8.90641	6.583				
0.380	0.1120	9.47566	7.003				
0.385	0.1098	10.0302	7.413				
0.390	0.1098	10.5792	7.819				
0.395	0.1189	11.1509	8.242				
0.400	0.1429	11.8054	8.725				
0.405	0.1644	12.5737	9.293				
0.410	0.1751	13.4224	9.920				
0.415	0.1774	14.3037	10.572				
0.420	0.1747	15.1839	11.222				

*Spectral irradiance averaged over small bandwidth centered at λ :

0.3 to 0.75 μm (bandwidth, 0.01 μm)

0.75 to 1.0 μm (bandwidth, 0.05 μm)

1.0 to 5.0 μm (bandwidth, 0.1 μm)

Table 2.4-3. Solar Spectral Irradiance at 1 AU (Solar Constant of $135.30 \text{ mW}\cdot\text{cm}^{-2}$)(Continued)(Ref. 2.4-3)

Wavelength, λ (μm)	Average Irradiance,* P_λ ($\text{W}\cdot\text{cm}^{-2}\mu\text{m}^{-1}$)	Area under curve, 0 to λ , A_λ ($\text{mW}\cdot\text{cm}^{-2}$)	Portion of solar constant with wavelength $<\lambda$, D_λ (%)
0.640	0.1544	54.6899	40.421
0.650	0.1511	56.2174	41.550
0.660	0.1486	57.7159	42.658
0.670	0.1456	59.1869	43.745
0.680	0.1427	60.6284	44.810
0.690	0.1402	62.0429	45.856
0.700	0.1369	63.4284	46.880
0.710	0.1344	64.7849	47.882
0.720	0.1314	66.1139	48.865
0.730	0.1290	67.4159	49.827
0.740	0.1260	68.6909	50.769
0.750	0.1235	69.9384	51.691
0.800	0.1107	75.7934	56.019
0.850	0.0988	81.0309	59.890
0.900	0.0889	85.7234	63.358
0.950	0.0835	90.0334	66.544
1.000	0.0746	93.9859	69.465
1.100	0.0592	100.676	74.409
1.200	0.0484	106.056	78.386
1.300	0.0396	110.456	81.638
1.400	0.0336	114.116	84.343
1.500	0.0287	117.231	86.645
1.600	0.0244	119.886	88.607
1.700	0.0202	122.116	90.256
1.800	0.0159	123.921	91.590
1.900	0.0126	125.346	92.643
2.000	0.0103	126.491	93.489
2.100	0.0090	127.456	94.202
2.200	0.0079	128.301	94.827
2.300	0.0068	129.036	95.370
2.400	0.0064	129.696	95.858
2.500	0.0054	130.286	96.294
2.600	0.0048	130.796	96.671
2.700	0.0043	131.251	97.007
2.800	0.00390	131.661	97.3104
2.900	0.00350	132.031	97.5838
3.000	0.00310	132.361	97.8277
3.100	0.00260	132.646	98.0384
3.200	0.00226	132.889	98.2180
3.300	0.00192	133.098	98.3724
3.400	0.00166	133.277	98.5047
3.500	0.00146	133.433	98.6200
3.600	0.00135	133.573	98.7239
3.700	0.00123	133.702	98.8192
3.800	0.00111	133.819	98.9057
3.900	0.00103	133.926	98.9848
4.000	0.00095	134.025	99.0580
4.100	0.00087	134.116	99.1252
4.200	0.00078	134.199	99.1862
4.300	0.00071	134.273	99.2412

Wavelength, λ (μm)	Average Irradiance,* P_λ ($\text{W}\cdot\text{cm}^{-2}\mu\text{m}^{-1}$)	Area under curve, 0 to λ , A_λ ($\text{mW}\cdot\text{cm}^{-2}$)	Portion of solar constant with wavelength $<\lambda$, D_λ (%)
4.400	0.00065	134.341	99.2915
4.500	0.00059	134.403	99.3373
4.600	0.00053	134.459	99.3787
4.700	0.00048	134.510	99.4160
4.800	0.00045	134.556	99.4504
4.900	0.00041	134.599	99.482195
5.000	0.0003830	134.63906	99.511500
6.000	0.0001750	134.94806	99.717709
7.000	0.0000990	135.05506	99.818965
8.000	0.0000600	135.13456	99.877724
9.000	0.0000380	135.18356	99.913939
10.000	0.0000250	135.21506	99.937221
11.000	0.0000170	135.23606	99.952742
12.000	0.0000120	135.25056	99.963459
13.000	0.0000087	135.26091	99.971109
14.000	0.0000055	135.26801	99.976356
15.000	0.0000049	135.27321	99.980200
16.000	0.0000038	135.27756	99.983415
17.000	0.0000031	135.28101	99.985965
18.000	0.0000024	135.28376	99.987997
19.000	0.0000020	135.28596	99.989623
20.000	0.0000016	135.28776	99.990953
25.000	0.000000610	135.29328	99.995037
30.000	0.000000300	135.29556	99.996718
35.000	0.000000160	135.29671	99.997568
40.000	0.000000094	135.29735	99.998038
50.000	0.000000038	135.29801	99.998525
60.000	0.000000019	135.29829	99.998736
80.000	0.000000007	135.29855	99.998928
100.000	0.000000003	135.29865	99.999002
1000.000	0.000000000	135.30000	100.000000

*Spectral irradiance averaged over small bandwidth centered at λ :

0.3 to 0.75 μm (bandwidth, 0.01 μm)

0.75 to 1.0 μm (bandwidth, 0.05 μm)

1.0 to 5.0 μm (bandwidth, 0.1 μm)

Table 2.4-4. Solar Spectral Irradiance - Standard Curve, Abridged Version (Ref. 2.4-6)

λ = wavelength, μm E_λ = solar spectral irradiance averaged over small bandwidth centered at λ , $\text{W}\cdot\text{m}^{-2}\cdot\mu\text{m}^{-1}$ $D_{0-\lambda}$ = percentage of the solar constant associated with wavelengths shorter than λ , and solar constant = $1353 \text{ W}\cdot\text{m}^{-2}$								
λ	E_λ	$D_{0-\lambda}$	λ	E_λ	$D_{0-\lambda}$	λ	E_λ	$D_{0-\lambda}$
0.115	0.007	1×10^{-4}	0.43	1639	12.47	0.90	891	63.37
0.14	0.03	5×10^{-4}	0.44	1810	13.73	1.00	748	69.49
0.16	0.23	6×10^{-4}	0.45	2006	15.14	1.2	485	78.40
0.18	1.25	1.6×10^{-3}	0.46	2066	16.65	1.4	337	84.33
0.20	10.7	8.1×10^{-3}	0.47	2033	18.17	1.6	245	88.61
0.22	57.5	0.05	0.48	2074	19.68	1.8	159	91.59
0.23	66.7	0.10	0.49	1950	21.15	2.0	103	93.49
0.24	63.0	0.14	0.50	1942	22.60	2.2	79	94.83
0.25	70.9	0.19	0.51	1882	24.01	2.4	62	95.86
0.26	130	0.27	0.52	1833	25.38	2.6	48	96.67
0.27	232	0.41	0.53	1842	26.74	2.8	39	97.31
0.28	222	0.56	0.54	1783	28.08	3.0	31	97.83
0.29	482	0.81	0.55	1725	29.38	3.2	22.6	98.22
0.30	514	1.21	0.56	1695	30.65	3.4	16.6	98.50
0.31	689	1.66	0.57	1712	31.91	3.6	13.5	98.72
0.32	830	2.22	0.58	1715	33.18	3.8	11.1	98.91
0.33	1059	2.93	0.59	1700	34.44	4.0	9.5	99.06
0.34	1074	3.72	0.60	1666	35.68	4.5	5.9	99.34
0.35	1093	4.52	0.62	1602	38.10	5.0	3.8	99.51
0.36	1068	5.32	0.64	1544	40.42	6.0	1.8	99.72
0.37	1181	6.15	0.66	1486	42.66	7.0	1.0	99.82
0.38	1120	7.0	0.68	1427	44.81	8.0	0.59	99.88
0.39	1098	7.82	0.70	1369	46.88	10.0	0.24	99.94
0.40	1429	8.73	0.72	1314	48.86	15.0	4.8×10^{-2}	99.98
0.41	1751	9.92	0.75	1235	51.69	20.0	1.5×10^{-2}	99.99
0.42	1747	11.22	0.80	1109	56.02	50.0	3.9×10^{-4}	100.00

(Reprinted with permission of the American Society for Testing and Materials. Copyright 1974)

Air Mass Zero

The earth's atmosphere is a spectrally selective filter which modifies both the sun's spectral distribution and the sun's intensity, as seen by an observer on or near the earth. The optical path through the atmosphere from the sun to a point on the earth's surface at normal sea level, perpendicular to the local mean earth surface, is said to have penetrated "air mass one" or AM1. Other air mass values indicate the ratio of the optical path length through the atmosphere to the path length through AM1.

In the absence of any atmospheric attenuation or modification of the sun's radiation, the optical air mass is zero, denoted by "AM0."

The atmospheric attenuation due to an air mass is spectrally selective and nonlinear with air mass.

As an example, the direct solar intensity (i. e., without sky radiation) near sea level on a clear day near noon is approximately $100 \text{ mW}/\text{cm}^2$ while in free space (i. e., at AM0) the solar intensity is $135.3 \text{ mW}/\text{cm}^2$. The short-circuit current output of a silicon solar cell at AM0, however, will not be 135.3 percent of its near-sea level output, but only approximately 120 percent. The difference arises from the change in spectral distribution by the atmosphere that is most pronounced between AM0 and AM1, as shown in Figure 2.4-4.

This figure also illustrates that the silicon solar cell's energy conversion efficiency is higher for AM1 spectral conditions than for AM0 conditions. The AM1 spectrum is deficient in the short-wavelength or "blue" region of the spectrum, and, therefore, a relatively greater percentage of the incident total solar energy is in the larger wavelength region of the spectrum where the cell is spectrally more sensitive.

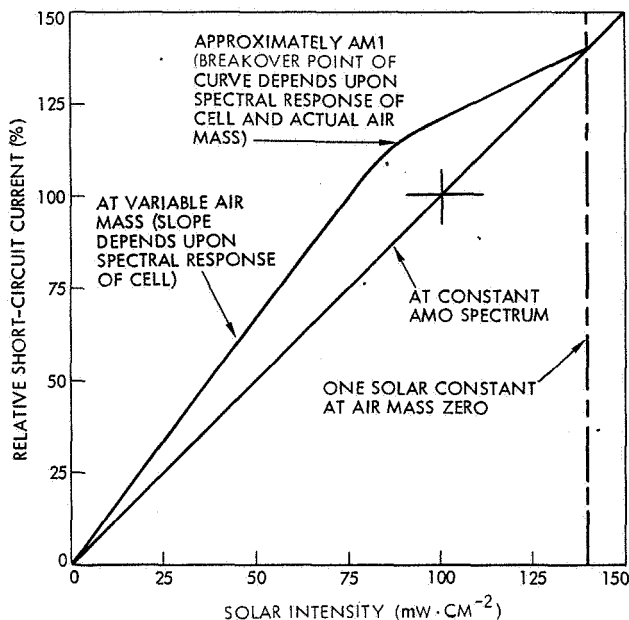


Fig. 2.4-4. Silicon Solar Cell Short-Circuit Current Output Versus Solar Intensity [Collimated sun light perpendicularly incident on solar cell and on Eppley Normal Incidence Pyrheliometer (Ref. 2.4-7)]

2.4.3 Ultraviolet Solar Radiation

Radiation is propagated in small units called photons, each photon containing one quantum of energy. The actual value of the energy in a quantum is given by Planck's equation

$$E = h\nu$$

where

$$\nu = c/\lambda = \text{frequency of the radiation}$$

$$\lambda = \text{wavelength of the radiation}$$

$$c = \text{velocity of light} = 3 \times 10^8 \text{ m} \cdot \text{s}^{-1}$$

$$h = \text{Planck's constant} = 6.6262 \times 10^{-34} \text{ Js}$$

Each absorbed photon or quantum of radiation energy causes one light-absorbing molecule of the absorbing material to be activated. Since there are 6.025×10^{23} (Avogadro's number) molecules contained in a gram-mole, it requires 6.025×10^{23} photons to activate a gram-mole. This unit of radiation is called an einstein.

Since the energy of the quantum is inversely proportional to the wavelength of the radiation, the short wavelength ultraviolet possesses much more energy per quantum than does the visible or infrared. The energy in various types of radiation and their wavelengths are given in Table 2.4-5. Because of the absorption properties of the upper atmosphere (ozone in particular), little energy from wavelengths shorter than $0.3 \mu\text{m}$ (3000 angstroms) reaches the earth. The small fraction of ultraviolet radiation that does penetrate the atmosphere nevertheless accounts for widespread destruction of many materials on the earth.

Table 2.4-5. Energy in Various Types of Radiation

Description	Wavelength (μm)	Frequency (Hz)	Joule per Quantum	Calories per Einstein
X-rays	1×10^{-3}	3×10^{18}	1.96×10^{-15}	2.84×10^8
Far ultraviolet	0.1	3×10^{15}	1.96×10^{-18}	284,500
Ultraviolet	0.2	1.5×10^{15}	9.82×10^{-19}	142,300
Near ultraviolet	0.3	1×10^{15}	6.55×10^{-19}	94,840
Visible (violet)	0.4	7.5×10^{14}	4.91×10^{-19}	71,120
Visible (blue-green)	0.5	6×10^{14}	3.93×10^{-19}	57,000
Visible (orange)	0.6	5×10^{14}	3.27×10^{-19}	47,400
Visible (red)	0.7	4.3×10^{14}	2.81×10^{-19}	40,600
Visible (red)	6.8	3.7×10^{14}	2.42×10^{-19}	35,500
Near infrared	1.0	3×10^{14}	1.96×10^{-19}	28,450
Infrared	10.0	3×10^{13}	1.96×10^{-20}	2,845
Far infrared	100.0	3×10^{12}	1.96×10^{-21}	284

Experimental ultraviolet light and vacuum environmental studies on polymers do not, in most cases, provide data below $0.2 \mu\text{m}$. Information is needed down to $0.01 \mu\text{m}$, with particular attention being given to irradiation effects found with the Lyman alpha line at $0.1216 \mu\text{m}$. The Lyman alpha line is responsible for some of the ionizations and chemical reactions of gaseous atoms and molecules in the ionosphere. It is possible that radiation from this line may also induce similar or related changes in polymers. For this reason, further studies are required. Studies of the influence of Lyman alpha radiation in vacuum on materials are, however, difficult with currently available equipment and techniques.

Effect of Ultraviolet Light on Materials

Since no oxygen is present in outer space, damage to plastics materials from ultraviolet radiation is generally minor. The presence of oxygen is essential for major damage to occur. The following materials have been studied under vacuum conditions while being irradiated with ultraviolet light (0.20 to $0.25 \mu\text{m}$) and were found to exhibit insignificant damage: polyester, epoxy and phenolic laminates, aluminum oxide, and polyethylene. In the presence of oxygen, ultraviolet damage can be reduced by incorporating into the original material an ultraviolet inhibitor. In utilizing these types of inhibitors, a vacuum weight-loss study is necessary on the finished composition to determine whether their effectiveness would be lost by vaporization in outer space.

Specific data on material degradation due to ultraviolet radiation may be found in Chapter 7 (Material Properties) and in Chapter 11 (Evaluation and Test).

Effects of Ultraviolet Radiation on Solar Cells and Covers

Ultraviolet radiation darkens solar cell covers and the coverslide adhesive. This darkening reduces the sunlight transmission to the solar cells. The degree to which such transmission degradation occurs is presently uncertain. Estimates for fused silica coverslides cemented with the best available silicone adhesives to the cells range from 0 to 10 percent. In practically all orbits, ultraviolet irradiation is accompanied by simultaneous irradiation with particles. For this combined radiation effect see Section 2.5.6.

Solar cell and cover degradation due to ultraviolet radiation is related to specific products that may be found in Chapter 4 (Solar Cell Filters and Covers), in Chapter 7 (Material Properties), and in Chapter 11 (Evaluation and Test).

Ultraviolet Radiation Dose

For solar cell array work, the ultraviolet exposure dose is typically expressed in "equivalent sun hours," or "ESH." To be meaningful, such equivalence must always be associated with a wavelength band in which the equivalence was established. For example, a test specimen exposed to an intensity of two ultraviolet suns as measured between 0.2 and 0.3 μm for 100 hours is said to have been exposed to "200 ESH in the 0.2- to 0.3- μm wavelength band."

It should be noted that the accumulated ultraviolet dose on solar cell assemblies is a function of solar distance, illumination angle, and array configuration (approximately $1/\pi$ for cylindrical arrays).

2.4.4 Solar Radiation Pressure

Bombardment of the various surfaces of a vehicle by photons emanating from the sun produces small, but significant, forces. Because the center of pressure is not generally coincident with the center of mass, disturbance torques will result. At altitudes in excess of 9000 km this is often the dominant environmental disturbance. The radiation pressure, $d\vec{F}$, on a differential area, dA , can be represented as

$$d\vec{F} = -V \left\{ (1 + \nu)(\vec{x}_s \cdot \vec{n})^2 \vec{n} + (1 - \nu)(\vec{x}_s \cdot \vec{n}) [\vec{n} \times (\vec{x}_s \times \vec{n})] \right\} dA$$

where

ν = surface reflectivity (unity for complete reflection)

\vec{n} = outward unit vector normal to the surface

\vec{x}_s = unit vector to the sun

V = solar pressure constant

V varies inversely as the square of the distance of the vehicle from the sun, and is approximately $4.5 \times 10^{-6} \text{ N}\cdot\text{m}^{-2}$ ($0.94 \times 10^{-7} \text{ lb}/\text{ft}^2$) in the vicinity of the earth. The resulting differential torque is $d\vec{N} = \vec{r} \times d\vec{F}$ where \vec{r} is the distance of dA from the center of mass; the total torque is obtained by integrating $d\vec{N}$ over all unshaded portions of the vehicle (Ref. 2.4-1).

2.4.5 Albedo

The albedo of a body in space is the ratio of the amount of electromagnetic radiation reflected by the body to the amount incident upon it. The total reflected energy contains components due to reflections from clouds and scattering by the atmosphere. Albedo expressions are generally somewhat imprecise because they depend heavily on local meteorological conditions, and the spectral characteristics of the reflected radiation are often unknown. Albedo values reported in the literature for a planet may represent the average of a series of estimates or measurements, and may represent either the wavelength band encompassing the solar spectrum or only the visible portion of the solar spectrum.

Table 2.3-1 in Section 2.3 contains representative values of albedo for the planets and the earth's moon. Other values of earth albedo are reported in Refs. 2.4-9 through 2.4-14. Ref. 2.4-13 provides additional albedo information for the planets.

The radiation received by a solar cell array from albedo has an effect on its thermal equilibrium temperature and also may affect the light input and, therefore, the power output of the array. Both effects are strong functions of orbit altitude, of the instantaneous geometric relationship between the sun, the earth, and the spacecraft, and of the configuration of the spacecraft and its array. Refs. 2.4-15 through 2.4-19 contain analyses which determine the amount of radiation intercepted by bodies or surfaces in orbit about the earth. Ref. 2.4-9 also contains an analytical treatment of this problem and presents calculated values of radiation incident to spheres, cylinders, hemispheres and flat plates in planetary orbit resulting from either albedo or planetary thermal emission. The results are tabulated in the form of geometrical factors presented as a function of circular orbit altitude and the angular relationships between the sun, earth, and body configurations.

The analyses reported in Refs. 2.4-9 and 2.4-15 through 2.4-19 were performed to assist in the development of predictions of spacecraft temperature and do not address the contribution of albedo to the electrical output of solar cell arrays. However, analysis of low-altitude earth-orbiting spacecraft telemetry data has demonstrated the presence of a variable component in solar array output due to reflected sunlight. Ref. 2.4-20 contains the results of analyses and tests performed to determine the contribution of albedo to solar cell output.

Figure 2.4-5 shows the calculated maximum albedo contribution to solar cell output as a function of altitude. For a solar cell to receive this maximum albedo illumination, the solar cell must be oriented toward the earth at the subsolar point. For this calculation the earth was assumed to be a uniform diffuse reflector with an albedo of 0.34. The spectral characteristics of the reflected light was assumed to be similar to air mass one sunlight in the wavelength region of the solar cell's spectral response. On the dark side of the earth the albedo is zero.

Figure 2.4-5 (and the results of the geometrical analysis referenced above) can be used to develop models of solar cell array performance due to albedo contributions in low-altitude applications. To achieve reasonably accurate results, it is necessary to include expressions in the model which characterize the attitude of the solar array panels with respect to the earth.

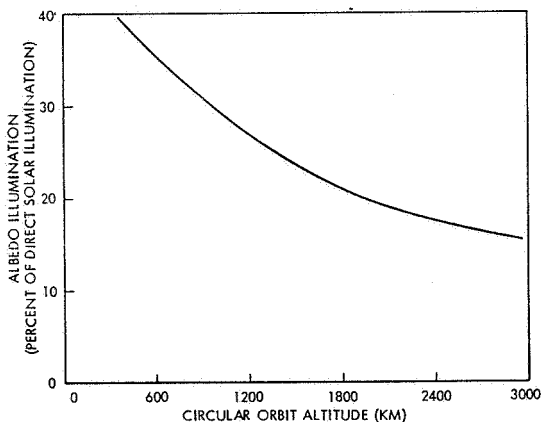


Fig. 2.4-5. Calculated Maximum Contribution of Earth Albedo Illumination to Solar Cell Output as a Function of Altitude for a Uniform Diffuse Reflecting Earth with Albedo Equal to 0.34 (Ref. 2.4-20)

2.5 THE SPACE RADIATION ENVIRONMENT

Radiation may be defined as the emission and propagation of energy through either space or a material medium. The space radiation environment is composed of cosmic rays, electromagnetic radiation, Van Allen belt radiation, auroral particles, and solar flare particles.

The data given in this section is approximate and intended for general information only. If more precise design data is required, the latest revision of Ref. 2.5-1 should be consulted.

2.5.1 Definition of Radiation Terms

Radiation Types

Radiation types may be generally classified as either electromagnetic (zero rest mass) or particulate (finite rest mass). Electromagnetic radiation includes ultraviolet light, X-rays, and gamma rays. Particulate radiation consists of electrons, protons, neutrons, alpha particles, and others. The more frequently encountered radiation types are defined as follows:

Alpha Particle (α)	A positively charged particle identical to all properties of the nucleus of a helium atom, consisting of two protons and two neutrons.
Beta Particle (β)	A negatively or positively charged electron emitted from a nucleus with an energy range of approximately 1 MeV.
Electromagnetic Radiation	Radiation having wavelengths from approximately 10^{-7} to 10^{-11} cm.
Photon	The generic term for the particular aspects of electromagnetic radiation. Photons of nuclear origin are called X-rays. Photons have wave-like properties, but occur as discrete energy quanta. The energy of a photon is inversely proportional to its wavelength.
Bremsstrahlung	The secondary radiation induced by high energy electrons which are deflected by another charged particle such as a nucleus. The bremsstrahlung photons are X-rays having energies near that of high energy electrons, but which are more penetrating than the electrons themselves.
Cosmic Rays	High energy particles or electromagnetic radiation originating in interstellar space.

Electron (e) An elementary particle of rest mass $m = 9.109 \times 10^{-31}$ kg and a charge of 1.602×10^{-19} coulomb; its charge may be positive or negative. A negative electron is called a negatron, but the term electron is often used. A positive electron is called a positron. Negative electrons occurring in space are designated by e^{-} .

Gamma Rays (γ) Electromagnetic radiation having wavelengths from approximately 10^{-8} to 10^{-11} cm. Gamma rays are highly penetrating, and are emitted by a nucleus in its transition from a higher to a lower energy state.

Proton (p^{+}) A positively charged particle of mass number 1 (having a mass of 1.672×10^{-27} kg) and a charge equal in magnitude to the electron (i.e., 1.602×10^{-19} coulombs). It is the nucleus of a hydrogen atom.

X-Ray Electromagnetic radiation having wavelengths of approximately 10^{-8} cm. X-rays are highly penetrating and are usually formed by bombarding a metallic target in a high vacuum with a particle. X-rays are also called roentgen rays

Radiation Energy

Radiation energy terms are defined as follows:

eV (electron volt)	A unit of energy equivalent to 1.6×10^{-19} joule.
keV	10^3 electron volts
MeV	10^6 electron volts
BeV	Billion electron volts (no longer to be used since "billion" means 10^9 in the USA but 10^{12} in other countries; the correct form is GeV).
GeV	10^9 electron volts
Hard and Soft	Designations for approximate energies. Hard X-rays have energies greater than several keV and have great penetration, while soft X-rays have lower energies and are less penetrating.

Radiation Flux

Radiation flux terms are defined as follows:

Flux Flux defines the number of particles, photons, or energy passing through a given area in a specified time, usually given in particles·cm⁻²·s⁻¹ or photons·cm⁻²·s⁻¹. Flux may also be specified in terms of the number of particles per unit time passing through an area on the surface of a sphere enclosed by a solid angle. The units are particles·cm⁻²·s⁻¹·sr⁻¹ where a steradian (sr) is defined as the solid angle which encloses a surface on a sphere equal in area to the radius of the sphere squared.

Fluence (Integrated Flux) The total particles·cm⁻² in any given time period.

Omnidirectional Flux The number of particles of a particular type that would transverse a test sphere of 1 cm² cross-sectional area in 1 second (particles·cm⁻²·s⁻¹).

Unidirectional Flux The flux arriving at a test sphere per unit solid angle from any particular direction having units of particles·cm⁻²·s⁻¹·sr⁻¹. If the incident radiation is isotropic, the unidirectional flux equals the omnidirectional flux divided by 4π (there are 4π steradians in a sphere). The conversion of omnidirectional into unidirectional flux in conjunction with solar cell damage calculations is more complex, however, and is discussed in Ref. 2.5-1.

Radiation Dose

Radiation dosage can be expressed either in terms of the exposure dose, which is a measure of the radiation field to which a material is exposed, or in terms of the absorbed dose, which is a measure of the energy absorbed by the radiated material.

Absorbed dose units:

Joule/gram The energy expressed in joules absorbed by a gram of the irradiated material.

Rad An absorbed dose defined as 1 x 10⁻⁵ joules (100 ergs) of radiation energy of any type absorbed per gram of any irradiated material.

Exposure dose units:

Roentgen (R) An exposure dose defined as the quantity of X- and gamma-radiation which will produce one electrostatic unit of electrical charge (3.335 x 10⁻¹⁰ coulombs) in the mass of dry

air contained in 1 cm³ at standard conditions of temperature and pressure (0.001293 gram). This amount of energy gives an absorbed dose of 87.7 x 10⁻⁷ joules of energy per gram of air.

Joules/gram carbon, joules/gram (C)

An indirect measure of a gamma radiation field based on an absorbed dose using carbon as a standard. One roentgen, R, of gamma rays is equivalent to approximately 87.7 x 10⁻⁷ joules/gram carbon.

Dose Rate

The rate of energy delivered or absorbed, e.g., R/month, R/year, rad/day.

Damage Equivalent Radiation Dose in Solar Cells

For convenient calculation of solar cell performance degradation in a corpuscular radiation test environment and simplified laboratory radiation test methods, the concept of "normally incident damage equivalent 1-MeV fluence" was evolved. Particulate radiation damage to solar cells is dependent on the energy and type of the particle. Conversion into "1-MeV fluence" utilizes so-called "equivalent damage coefficients," as discussed in Ref. 2.5-1. The unit of equivalent fluence is 1-MeV electrons per cm², or in brief "e/cm²" for a specified time period, usually either 1 year or end-of-mission.

Space Radiation Zones

The space radiation environment is characterized by the earth radiation zone (Van Allen belts), the auroral zone, and the interplanetary zone. Types of radiation found in space include electrons, protons, cosmic rays, and electromagnetic radiation, consisting of ultraviolet rays, X-rays, and gamma rays.

Geomagnetic Coordinates

Normally, it is convenient to plot the radiation intensity in the earth's radiation zone in geomagnetic rather than geographic coordinates. The origin of these coordinate systems coincide, but the geomagnetic axis is tilted by 11.5 degrees with respect to the axis of rotation of the earth.

The Earth Radiation Zone

The earth radiation zone (Ref. 2.5-2) is characterized by magnetically-trapped electrons and protons. This zone, often referred to as the Van Allen belts, is made up of two concentric belts, the inner belt and the outer belt. The inner belt extends from approximately 300 to 6400 km, with the intensity reaching a maximum at 2900 to 3200 km above the geomagnetic equator. The inner belt is sometimes referred to as the hard belt, and contains high energy protons of energies to 700 MeV, with electrons in the 20 keV to 1 MeV range. The outer belt extends from about 13,000 to 59,000 km where the region of high intensity is at 16,000 to 24,000 km and up. This belt, called the soft belt, consists primarily of electrons from 20 keV to 5 MeV and some protons over 60 MeV.

The Auroral Zone

The auroral zone is located between approximately 60 and 65 degrees geomagnetic latitude. The auroral

displays are produced by low energy (less than 200 keV) electrons entering the atmosphere. Protons may also be present. The auroral particles are easily stopped and, consequently, do not present a serious radiation problem.

The Interplanetary Zone

Radiation in interplanetary space consists of an energetic cosmic flux and pulses of radiation associated with solar flares. The largest flares, consisting of high energy protons, are extremely rare. The smallest flares occur as often as eight times per day. In addition to these sources of interplanetary radiation, there also exists a continuous ejection of low energy particles, primarily protons and electrons from the sun, known as the solar wind. The distribution of the solar wind particles is assumed to obey the inverse-square law with the sun acting as a point source.

Cosmic rays of galactic origin consist of protons (~93 percent) and alpha particles (~7 percent) along with smaller amounts of heavier elements. The energy of the protons is in the range of 5×10^8 eV to 2×10^{10} eV. Although energies are quite high, the free space flux of particles is 2.5 particles \cdot cm $^{-2}$ \cdot s $^{-1}$. Since this flux is small, radiation damage due to cosmic rays usually needs to be considered only on very long space flights.

2.5.2 Geomagnetically Trapped Electrons*

Electrons in the earth's radiation belts are trapped by the geomagnetic field. Inasmuch as the geomagnetic field is continually varying during day-night cycles and due to solar activity, the flux density and energy spectrum at a given point in space also varies continually. Time-averaged values of flux have been prepared and are known as "Trapped Radiation Belt Models." The most recently updated models for electrons are as follows:

Model Designation	Radiation Zone	Energy Range (MeV)	Reference
AE4	Outer Belt	>0.04	2.5-3
			2.5-4
			2.5-5
AE5	Inner Belt	>0.04	2.5-5 2.5-6 2.5-7

2.5.3 Geomagnetically Trapped Protons*

Similarly to electrons, protons are also trapped by the geomagnetic field. The most recently updated, time-averaged models for trapped protons are as follows:

Model Designation	Radiation Zone	Energy Range (MeV)	Reference
AP1	Inner Belt	30 - 50	2.5-8
AP5	Outer Belts	<4	2.5-9
AP6	Inner Belt	4 - 30	2.5-10
AP7	Inner Belt	>50	2.4-11

* For a more detailed discussion of this subject, see Ref. 2.5-2. The importance of this environment to solar cell arrays is discussed in Section 2.5-8.

2.5.4 Solar Flare Protons

Solar flares are eruptions of the sun that are associated with optical phenomena (called "sun spots") and with the emission of energetic particles (the emissions of importance to solar cell arrays are mainly proton and alpha particles). The frequency with which sun spots occur increases to a maximum and decreases again during approximately 11-year long "solar cycles." The duration of "solar maximum" is approximately 7 years. The solar cycles of current interest are defined as follows (Refs. 2.5-2 and 2.5-12):

Solar Cycle No.	Period of Cycle	Duration of Maximum Activity
19	1953 - 1964	1955 - 1961
20	1964 - 1975	1965 - 1972
21	1975 - 1986	1977 - 1983

Sun spot cycles have been observed and recorded for more than 200 years but emitted energetic particles have been observed only since approximately 1954 during the nineteenth and twentieth solar cycles. The following conclusions have been drawn:

- There exists insufficient statistical correlation between the occurrence of solar flare events that affect the electrical performance of solar cells and the occurrence of sun spots to accurately predict the magnitude and time of solar cell array performance degradation due to solar flare events.
- The solar cell degradation that occurs as a consequence of solar flares is essentially due to solar flare protons.
- Most of the solar flare protons that damage solar cells occur in one (or a few) anomalously large flares that seem to occur during a time span of 3 to 4 years centered around the middle of the solar maximum activity.

These findings suggest that reasonable predictions of solar cell damage due to solar flares can be made only over reasonably long periods (at least 1 year). Many solar flare proton models have been developed; these are treated in summary form in Refs. 2.5-1 and 2.5-12.

2.5.5 Radiation at Synchronous Altitude

In terms of contributing to total solar cell damage, the radiation environments at synchronous altitude rank as follows for most longer missions during periods of maximum solar activity:

- 1) Solar flare protons on station
- 2) Trapped electrons on station
- 3) Trapped electrons and protons during transfer orbits.

During periods of low solar activity (see Section 2.5.4), the solar cell damage due to solar flare protons moves from first place to third.

The total radiation environment causes two radiation components to enter the solar cell: one through the coverglass (front) and one through the substrate (back).

Solar Flare Protons

Solar flare proton measurements were made only during the last two solar cycles (see Section 2.5.4) and only in the energy range from 10 to 100 MeV. The observed data was compiled by Ref. 2.5-13 and is shown in Figure 2.5-1. The observed data has been extrapolated to energies lower than 10 MeV and forms the basis for predicting the flux for the next (twenty-first) solar cycle.

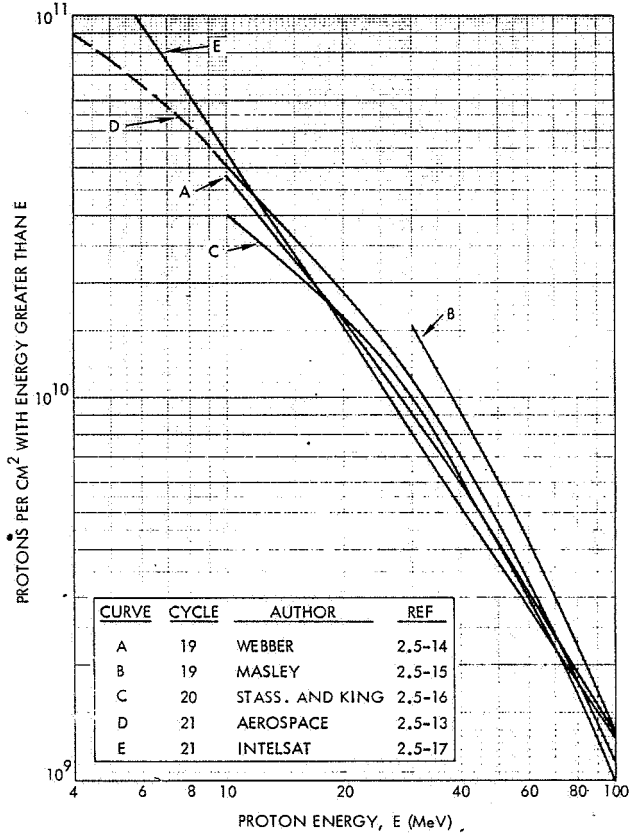


Figure 2.5-1. Integral Solar Flare Proton Fluxes for Three Solar Cycles

Two solar proton flux models for the twenty-first solar cycle that have found widespread acceptance in satellite systems specifications, denoted here as the "Aerospace" and "Intelsat V" models, are shown in Figure 2.5-1 also. The "Aerospace" Model (Ref. 2.5-13) applies an arbitrary safety factor of 1.5 to the average of the flux observed during the nineteenth and twentieth cycle (actually to the average of the two nineteenth-cycle curves and the twentieth-cycle curve according to Refs. 2.5-14, 2.5-15 and 2.5-16 in Figure 2.5-1) whereas the "Intelsat V" model is a straight-line (on Figure 2.5-1) approximation to the higher flux observed during the nineteenth cycle. The "Intelsat V" model can be represented analytically as follows (Ref. 2.5-17):

0.01 ≤ E ≤ 1.0 MeV:

$$\Phi_p(>E) = 6.5 \times 10^{15} \exp(-9.0 E)$$

1.0 ≤ E MeV:

$$\Phi_p(>E) = 1.5 \times 10^{12} E^{-1.53}$$

where Φ_p is in $p \cdot cm^{-2}$ and E is in MeV.

The two different models described above yield somewhat different damage-equivalent 1 MeV fluence values; however, the total impact on predicted end-of-life solar cell array power output is generally less than a few percent (depending upon specific array design parameters and the number of years in orbit).

Most of the total proton flux during the past two solar cycles has occurred during one (or a few) anomalously large solar proton events. The number of these events is too small to warrant a meaningful statistical analysis for predicting the time of occurrence of anomalously large events. Table 2.5-1 shows all of the larger proton events observed during the twentieth solar cycle grouped by year. According to this table, the annual relative solar flare proton flux was approximately:

1966-1971 5 percent per year
 1972 70 percent per year

Therefore, a small degradation due to ordinary flare protons should be allowed for during the entire active solar period, even if no anomalously large flare events occur in some years.

Table 2.5-1. Major Solar Flare Proton Events During Twentieth Cycle (Based on data from Ref. 2.5-16)

Year	Flux for E > 10 MeV (10 ⁷ p · cm ⁻²)	Percentage of Total 7-year Flux	
		Annual	Cumulative
1966	4 160	5.0	5.0
1967	75 66 3		
1968	41 9 26 110 28	6.5	15.9
1969	6 4 150 87		
1970	3 10 6 8 26 10	1.9	25.3
1971	150 3 38		
1972	7 2250	68.9	100
	3280	100.0	-

Solar Flare Alpha Particles

The alpha particle flux is typically neglected. Ref. 2.5-17 specifies the alpha particle integral fluence to be taken as 5 percent of the solar flare proton spectrum shown above.

Trapped Electrons on Station

The trapped electron environment is defined by the AE4 Model (Ref. 2.5-3, 2.5-4 and 2.5-5) which, for synchronous altitude, can be approximated closely by the following set of equations for the integral electron spectrum (Ref. 2.5-17):

$$E \leq 0.3:$$

$$\log_{10} \phi_e(>E) = -3.0 E + 7.7$$

$$0.3 \leq E \leq 3.5:$$

$$\log_{10} \phi_e(>E) = -1.25 E + 7.2$$

where ϕ_e is in $e \cdot \text{cm}^{-2} \cdot \text{s}^{-1}$ and E is in MeV.

The AE4 model supersedes the earlier AE3 model (Ref. 2.5-18). Compared with the AE4 model, the AE3 model showed a slightly higher electron flux at energies below 0.7 MeV and lower flux above 0.8 MeV. For most solar cell array designs, the damage equivalent 1-MeV fluence calculated from the two models is somewhat different, but the impact on predicted end-of-life power output is generally less than a few percent (depending upon time in orbit and specific array design parameters).

Trapped Electrons and Protons in Transfer Orbits

The material presented in Sections 2.5.2 and 2.5.3, respectively, applies for the transfer orbits also.

2.5.6 Interplanetary Radiation

The particulate radiation of importance to solar cell arrays in interplanetary space is usually due to solar flare protons only. Solar flare proton events are described in Section 2.5.4. Because solar flare proton clouds emanating from the sun enlarge upon their departure from the sun, the proton flux density within the cloud decreases with distance from the sun. It is generally, but not universally, assumed that a solar cell array penetrating such a cloud will be exposed to a flux that is proportional to between D^{-2} and D^{-3} , where D is the array-sun distance (Ref. 2.5-12).

2.5.7 Radiation Zones of the Planets

This section is reserved for future expansion of this handbook.

2.5.8 Effects of Radiation on Solar Cell Arrays

The effects of radiation on solar cells, solar cell covers, and other array materials is discussed in the following paragraphs. Details on radiation effects are given in Ref. 2.5-1.

Effects on Solar Cells

Solar cells in orbit are "damaged" (i.e., their energy conversion efficiency is permanently reduced) mainly due to irradiation with electrons and protons. In lower earth orbits both geomagnetically trapped electrons and protons may be of significance, while at higher altitudes (such as at or near synchronous

altitude) during periods of high solar activity solar flare protons may add significantly to the total cell-damaging fluence. The radiation environments are responsible for solar cell degradation both during transfer orbits and on-station orbits.

The radiation particles of significance to solar damage have approximately the following energy ranges when they impinge on the solar cell covers:

- Electrons - 0.2 to 1 MeV
- Protons - 4 to 40 MeV.

The actual radiation environments seen by the solar cells differ from the naturally existing environment because of the following:

- The energy-flux spectra of the natural radiation environments are modified by the solar cell radiation shields
- Cells receive radiation both through the front shield (coverglass) and the back shield (substrate), i.e., the radiation environment seen by the solar cells is in part design related.

Solar cell radiation "damage" does not constitute a mechanical damage, but rather a nearly permanent degradation of the cell's energy conversion efficiency capability, as discussed in Section 3.3.

The effects of the earth's radiation on solar cell power output can be estimated as follows:

- Determine the damage equivalent 1-MeV fluence for trapped electrons from Figures 2.5-2 and 2.5-3.
- Determine the damage equivalent 1-MeV fluence for trapped protons from Figures 2.5-4 and 2.5-5.
- Sum the fluence components found in the two preceding steps and determine the cell's output degradation from appropriate degradation curves given in Section 3.3.

A distinctly different and separate damage mechanism from the so-called "bulk" damage mechanism discussed above may occur due to low energy protons (having energies in the order of hundreds of keV) impinging on small solar cell areas that are not adequately protected by glass, adhesive, or metallization. This so-called low-energy proton damage may be severe; it is discussed further in Sections 3.3.3 and 8.3.6.

Effects on Solar Cell Covers

Solar cell covers are discolored (darkened) by particulate radiation, thereby absorbing some of the sunlight. This increased light absorption reduces solar cell output by two mechanisms:

- Loss in illumination of the cell
- Increased array operating temperature and hence a decrease in cell efficiency.

The loss in illumination and, hence, power output due to earth's charged particle radiation can be estimated for circular orbits by first using the environmental data (converted into deposited energy in fused silica) shown in Figures 2.5-4 and 2.5-5 and then consulting the cover transmission loss data given in Section 4.9.

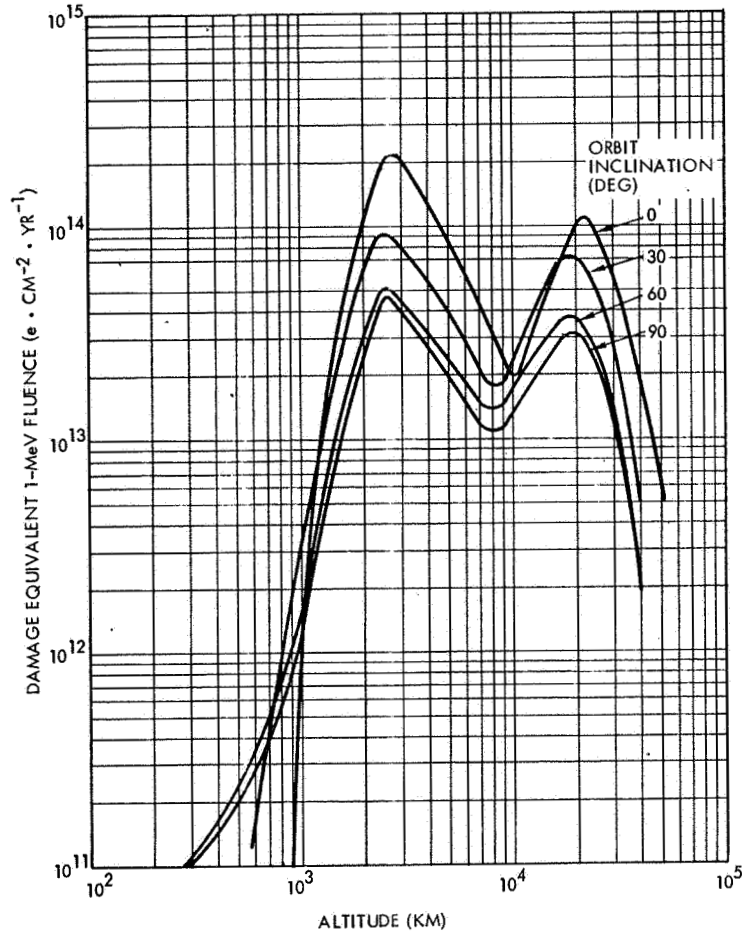


Fig. 2.5-2. Damage Equivalent 1-MeV Fluence in Circular Earth Orbits due to Trapped Electrons for I_{sc} and P_{mp} of Silicon Cells Protected by 0.15-mm Thick Fused Silica Covers and Infinitely Thick Back Shields (per Ref. 2.5-1)

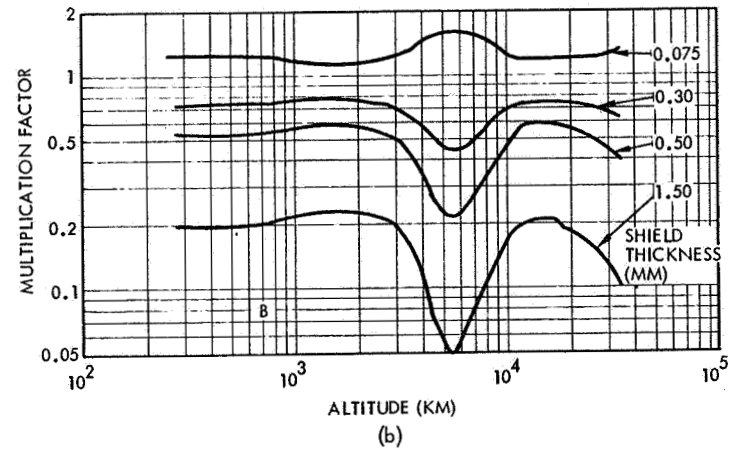
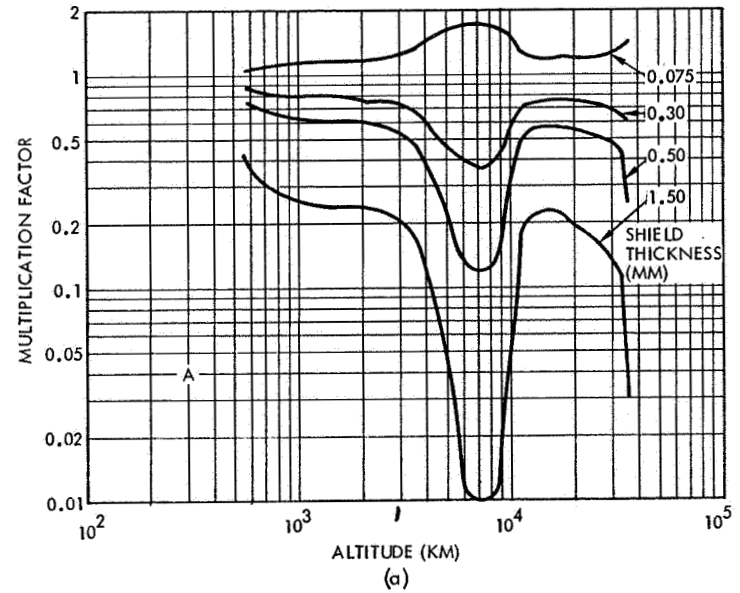


Fig. 2.5-3. Multiplication Factors for Damage Equivalent 1-MeV Fluence Shown in Figure 2.5-2 for Four Different Cover Thicknesses for (a) 0-Degree Inclined Orbits and (b) 90-Degree Inclined Orbits (per Ref. 2.5-1)

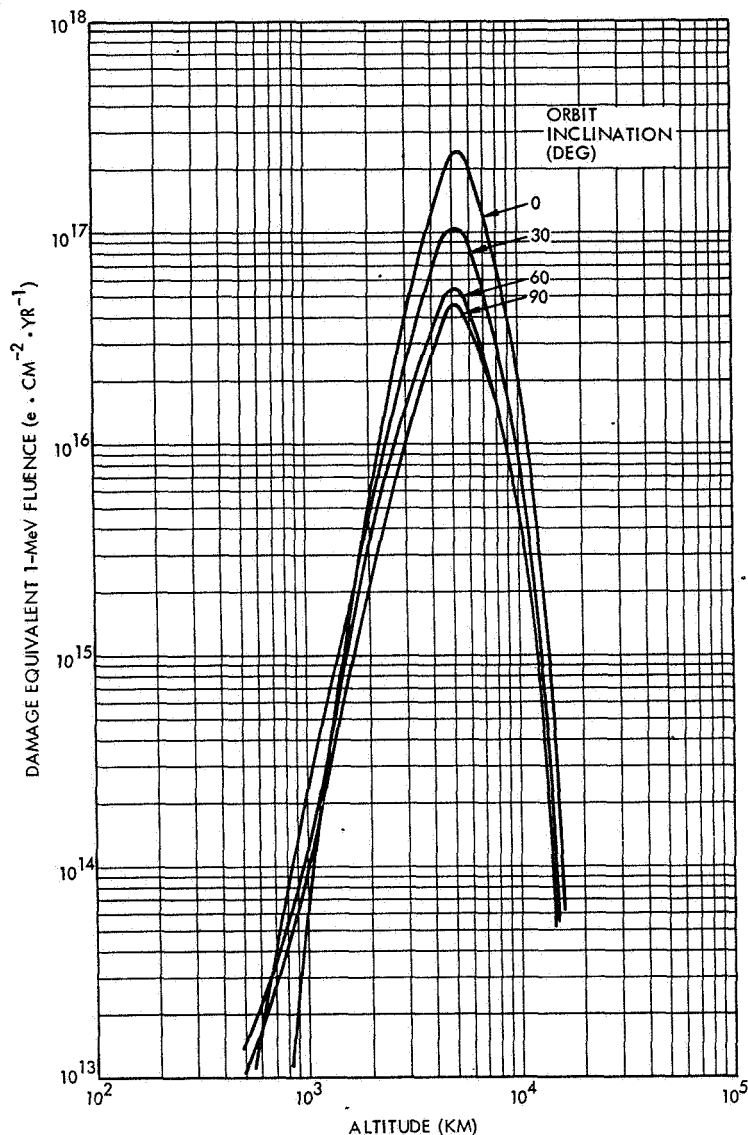


Fig. 2.5-4. Damage Equivalent 1-MeV Fluence in Circular Earth Orbits due to Trapped Protons for P_{mp} of Silicon Cells Protected by 0.15-mm Thick Fused Silica Covers and Infinitely Thick Back Shields (per Ref. 2.5-1)

Effects on Other Array Materials

Organic materials, as a class, are the least stable in a radiation field. Radiation damage to organic materials is dependent upon the total energy absorbed and sometimes upon the radiation intensity. Damage is usually not dependent upon the type of radiation but may be dependent on the particle energy. Radiation

damage to polymers may occur because of the removal of a bonded electron leading to bond rupture, free radicals and discoloration. Polymers may be degraded by a loss in mechanical strength, an increase in vapor pressure and viscosity, and a reduction in molecular weight.

It is important to note that test data from radiation exposure in the presence of air and in a vacuum environment indicates that radiation damage is reduced considerably in vacuum. This is explained by the fact that the presence of an oxidizer in the environment causes oxidation of ionized polymers which results in greater alteration of the molecular structure than in a chemically inert (vacuum) environment. Inert atmospheres available in the laboratory, having an oxygen content as high as 1 part per million may be insufficiently pure for such tests. Vacuum of less than 10^{-6} torr (1.3×10^{-4} N · m⁻²) is usually mandatory.

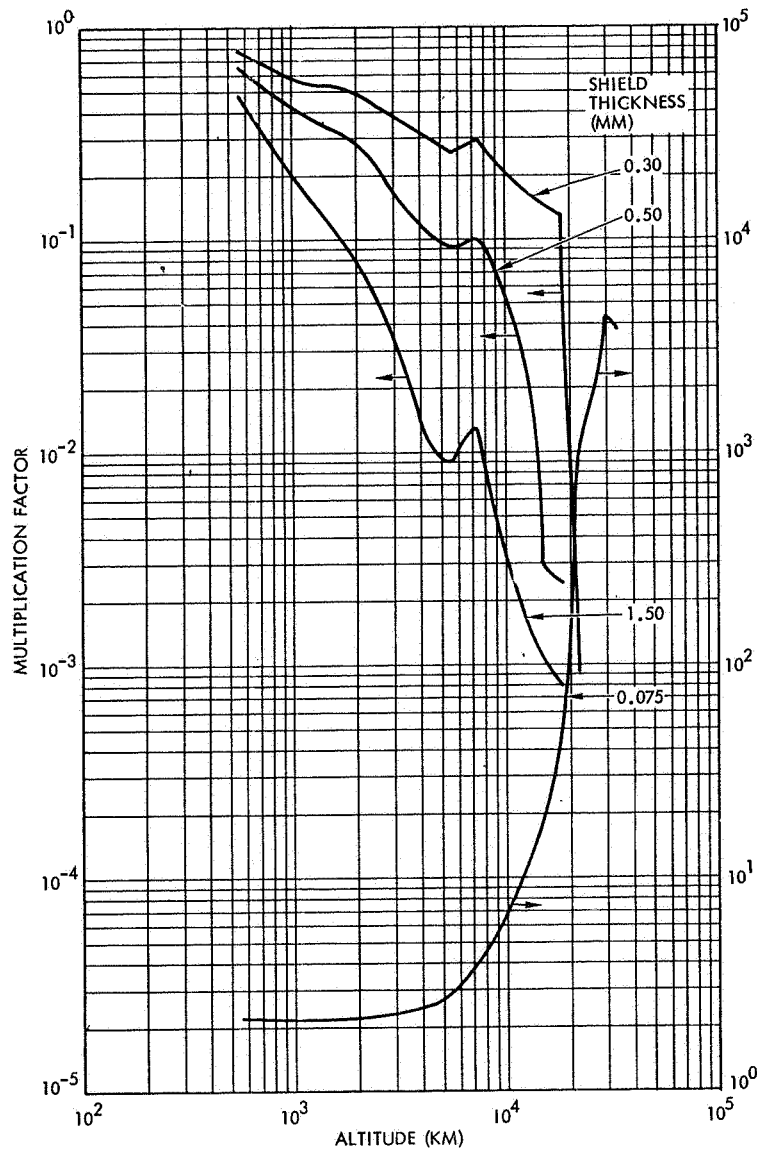
Solar cell array materials and components (other than solar cells and covers) of special interest to radiation damage studies (in regard to both mechanical and electrical characteristics) are the following:

- Electrical insulation on wires, terminals, connectors, and between the solar cells and a metallic substrate
- Adhesives, both exposed and lightly shielded
- Blocking diodes, shadow bypass diodes, Zener diodes, and temperature transducers.

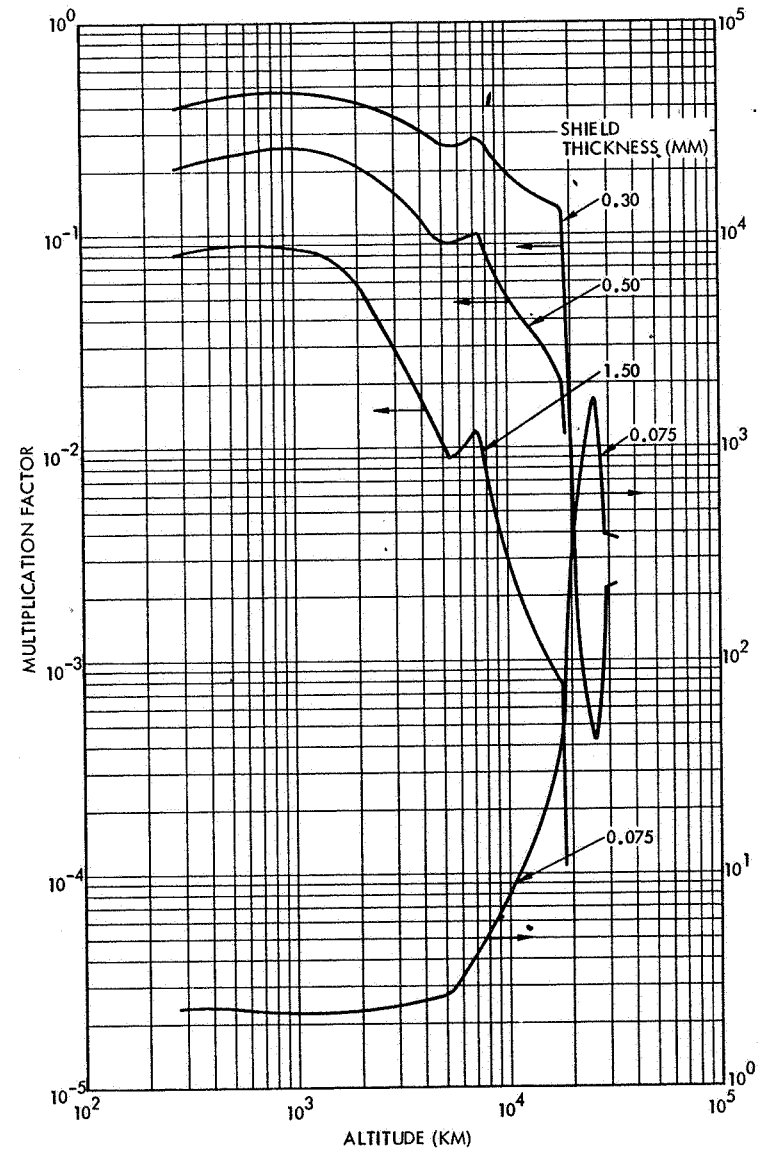
It should be noted that the corpuscular radiation, even that from solar flares, travels in spiral orbits along geomagnetic flux lines and thereby becomes an "omnidirectional" flux which also impinges on the array backside.

2.5.9 Particulate and Ultraviolet Radiation Combined

In most practical satellite orbits, corpuscular and ultraviolet radiation exists simultaneously. Divergent views exist regarding the effect of such combined radiation on solar cell assemblies. One view, supported by ground testing is that ultraviolet exposure bleaches some of the darkening induced by corpuscular radiation. The other view, supported by comparing ground test data with orbital data, holds that the simultaneous combined exposure causes greater darkening than each exposure alone. However, the data of the very few ground tests which have been performed is in question, orbital data analysis is not very accurate, and the darkening mechanism is not fully understood at this time.



(a)



(b)

Figure 2.5-5. Multiplication Factors for Damage Equivalent 1-MeV Fluence Shown in Figure 2.5-4 for Four Different Cover Thicknesses for (a) 0-Degree Inclined Orbits and (b) 90-Degree Inclined Orbits (per Ref. 2.5-1)

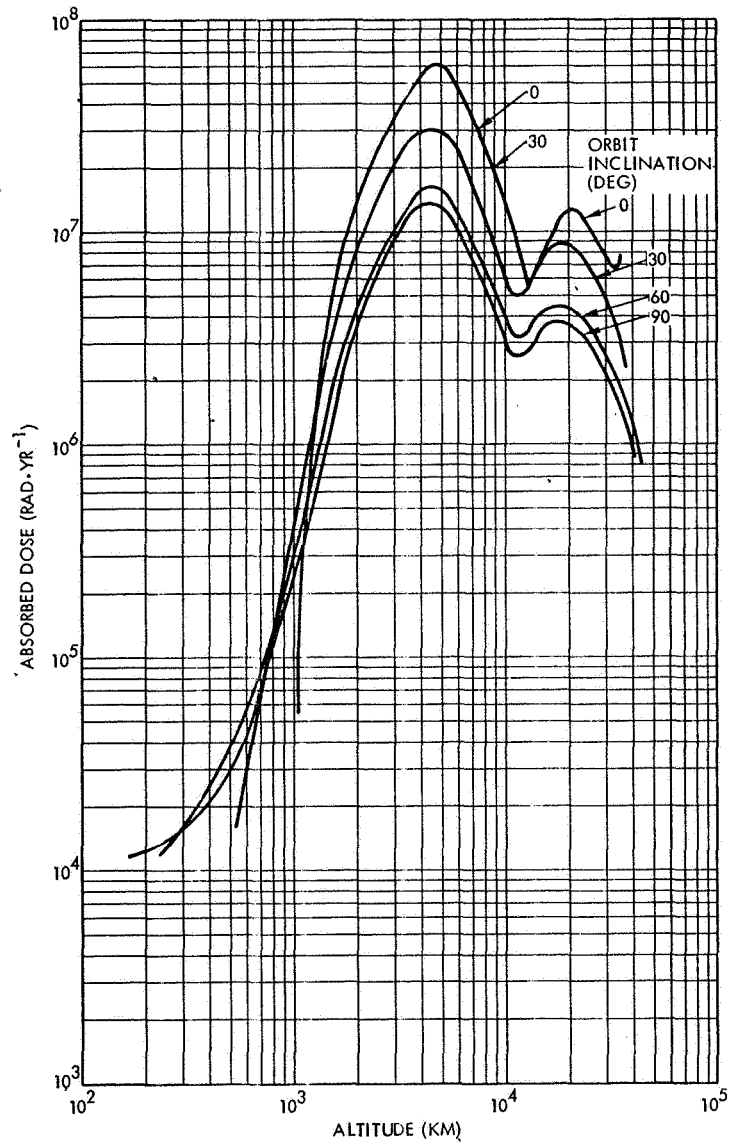


Fig. 2.5-6. Average Absorbed Dose in 0.15-mm Thick Covers in Circular Earth Orbits due to Trapped Electrons

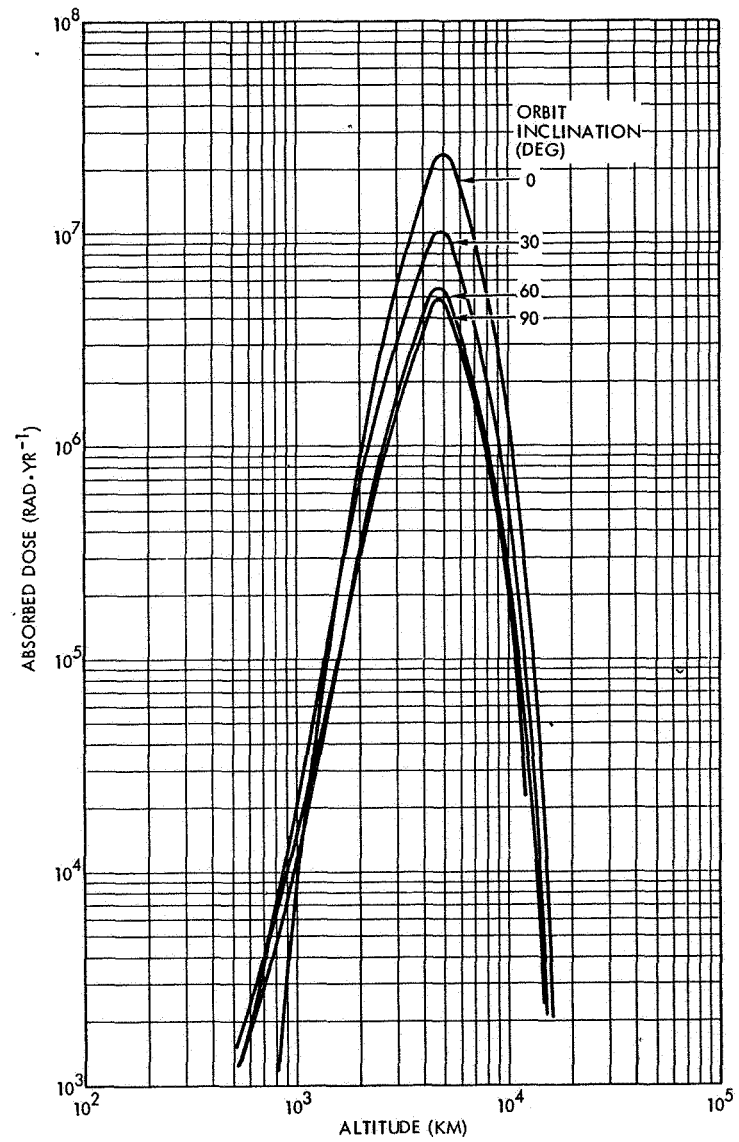


Fig. 2.5-7. Average Absorbed Dose in 0.15-mm Thick Covers in Circular Earth Orbits due to Trapped Protons

2.6 ORBITAL EFFECTS

Solar cell array performance capability and performance degradation depend upon the orbit characteristics and the array/spacecraft attitude, i. e., the orientation relative to the solar vector. The important orbital effects on solar cell arrays are as follows:

- Duration and frequency of solar eclipses, causing
 - a) Temporary interruptions in array power output
 - b) Cyclical temperature variations and attendant mechanical stresses that may, in time, lead to mechanical and electrical performance degradation
- Variable angular relationships between the solar illumination and the array surfaces which affect array power output
- Cumulative damage to the solar cells due to charged particles orbiting the earth.

The angle-of-illumination and solar eclipse duration are discussed in this section. Radiation damage is treated in Section 2.5. The analytical aspects of orbital mechanics as well as orbital terminology are given in Section 9.10.

2.6.1 Spacecraft Motion in Orbit

During unpowered space flight, the center of mass of a satellite moves in an orbit that is generally elliptic, parabolic or hyperbolic. Interplanetary probes describe ellipses of which the sun occupies one focus. Natural planetary satellite orbits are elliptical. Artificial satellite orbits are also elliptical but, in many cases, are of such dimensions as to be considered circular. Ellipses may have eccentricities ranging from zero (for circular orbits) to any value less than unity; orbits with eccentricities of unity are parabolas and those with eccentricities greater than unity are hyperbolas.

All spacecraft orbits are disturbed by forces that may arise from gravitational and electromagnetic fields, solar wind pressure or aerodynamic drag. The perturbing forces are counteracted by the spacecraft attitude control system; however, frequently the solar cell array is designed to aid the attitude control system. The most common array design consideration in this respect is the minimization of the external electromagnetic field (dipole moment) produced by the electrical current flow in the array circuits (see Section 8.10).

2.6.2 Solar Eclipses — Power Loss and Temperature Cycling

Whenever the view from the sun to the spacecraft is obstructed by a planet or one of its satellites, the spacecraft is said to be in an eclipse. If the sun is completely obscured by an object (as viewed from the

spacecraft), the satellite finds itself in the umbra, or full shadow, of the object. If the sun is only partially obscured, the satellite is in the penumbra. When a spacecraft is in a penumbra shadow, the solar illumination is reduced by approximately the same percentage as the area of the solar disk (as it appears from the spacecraft) is obscured. The number of eclipses experienced over the lifespan of a spacecraft depends mainly upon the orbit altitude and eccentricity, being highest for circular orbits at the lowest practical altitudes. Figure 2.6-1 illustrates the relationship between the number of eclipses and the flight altitude for circular orbits.

Not all eclipses of a spacecraft in a given orbit are of the same duration. Variations are produced by the motion of the planet around the sun resulting in changes to the angular relationship between the earth-sun line and the orbit plane. Fractional sun time of circular orbits is illustrated in Figure 2.6-2. Subtraction of the fractional sun time from unity gives the fractional eclipse time. Figure 2.6-3 shows the eclipse duration in real time. The temperature variations due to eclipses of varying duration can be determined from the data given in Section 9.6.

2.6.3 Solar Cell Array Orientation

The power output capability of a solar cell array is significantly affected by its orientation to the sun. This orientation is determined by mission-imposed requirements for attitude control and maneuverability, by the capability of the attitude control subsystem and by the physical configuration of the solar array and the spacecraft body. The interaction of mission requirements and spacecraft design characteristics is illustrated in Table 2.6-1, which also contains examples of typical earth-orbiting spacecraft and descriptions of solar array orientation.

Solar cell arrays may be fixed relative to the spacecraft coordinate system or oriented toward the sun. Fixed arrays may be spacecraft body-mounted (approximating cylindrical, spherical, or tetrahedral shapes), or in the form of deployed panels, or both. Oriented arrays are generally composed of flat panels that are driven and controlled in one or more axes. The array drive systems are designed to track the sun and are often capable of off-pointing part or all of the array to reduce excess power.

Table 2.6-1 does not describe all of the possible array-spacecraft configurations. Some possible configurations are limited to special applications because of constraints on field-of-view or power capability. For example, beside orienting the principal axis of a spin-stabilized spacecraft perpendicular to the orbit plane, it is also possible to point the axis toward the earth or to fix it in inertial space. However, earth-pointing spin-stabilized spacecraft with cylindrical solar cell arrays usually require auxiliary solar panels to compensate for reduced power at satellite high noon (i. e., when the solar vector is parallel to the satellite spin axis).

Two-axis control of a flat panel is required to maintain its pointing directly to the sun. A solar cell array attitude control system such as that contained in the flexible rolled-up solar array (FRUSA) system (see Chapter 6) provides this control. Most other oriented solar cell arrays are, however, controlled in only one axis with second axis control provided, if it is required, by rotation of the entire spacecraft. Table 2.6-1 shows spacecraft axis orientation for selected examples and, in each case, identifies the axis that is used for array control. It is seen from the table that various options exist for reducing the impact of spacecraft orientation on power output. For example, a yaw rotation performed twice per orbit permits substitution of a flexible harness for a set of sliprings. Canting the panels with respect to the array drive axis reduces

the effect of seasonal changes of the angle between the sun vector and the orbit plane. In the case of a geosynchronous equatorial orbit, the canting of the oriented panels by 11.7 degrees, coupled with seasonal yaw axis rotations, can provide an array power increase of approximately 4 percent after 1 year over an array configuration that otherwise experiences the total effect of the 23.4-degree inclination of the ecliptic plane.

Section 9.10 contains an analytic treatment of orbital mechanics and spacecraft configuration orientation analysis at a level of detail sufficient for the detailed calculation of the insolation intercepted by solar array surfaces.

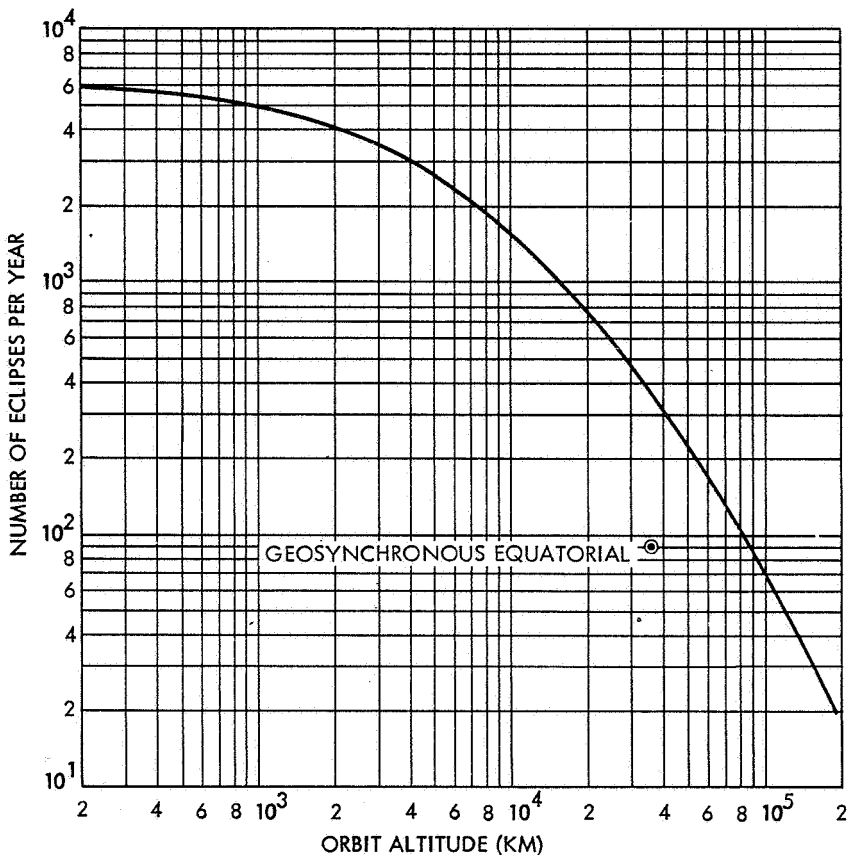


Figure 2.6-1. Maximum Number of Annual Satellite Eclipses in Circular Earth Orbits

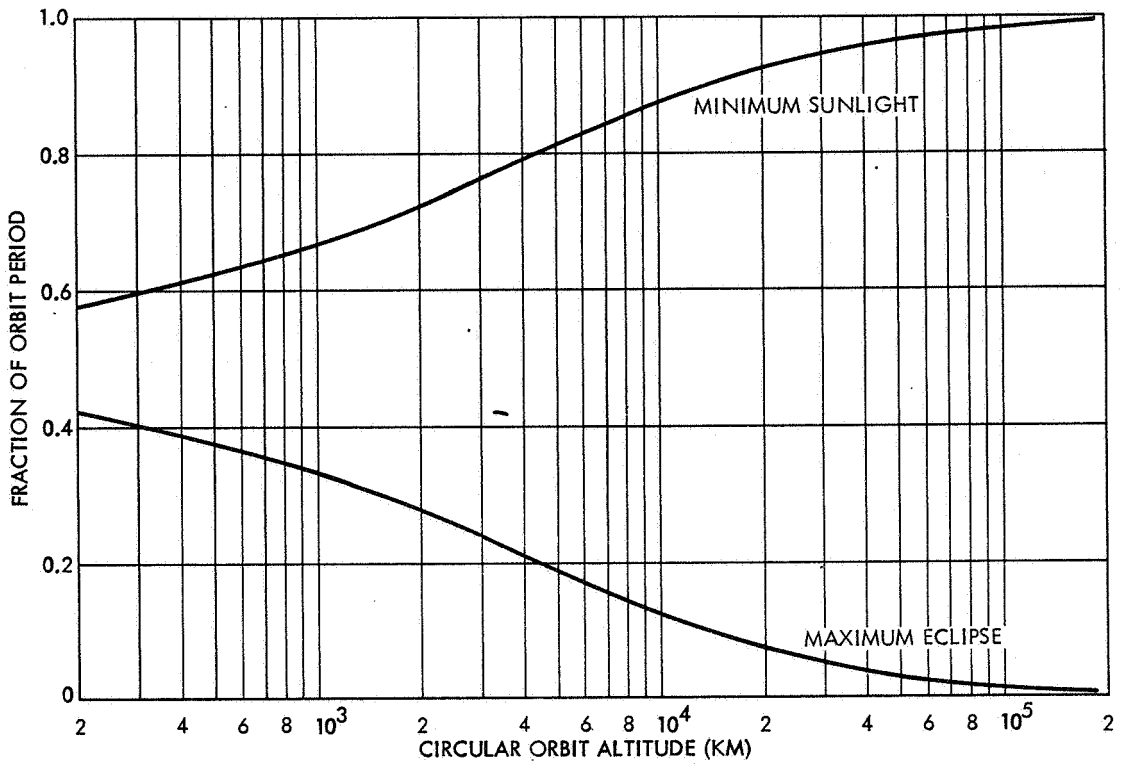


Figure 2.6-2. Fractional Sun Time of Circular Earth Orbits

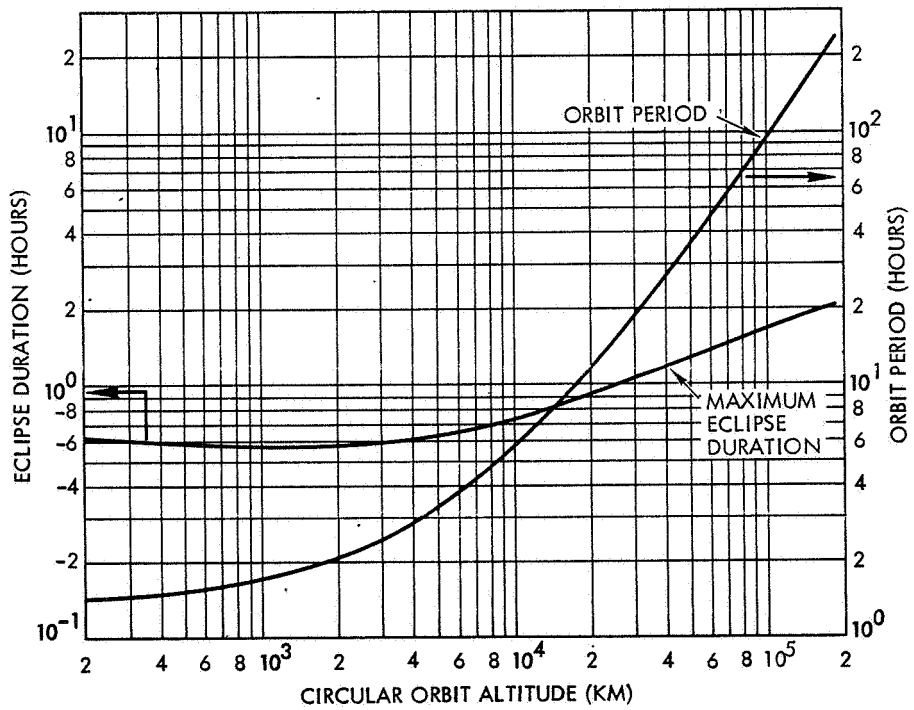


Figure 2.6-3. Orbit Period and Eclipse Duration of Circular Earth Orbits

Table 2.6-1. Examples of Solar Array Orientation

Solar Array Configuration	Method of Spacecraft Attitude Control	Spacecraft Axis Orientation			Selected Examples			
		Roll	Pitch	Yaw	Orbit Inclination (deg)	Insolation Angle to Solar Array (deg)	Spacecraft	Comments
Body-mounted fixed cylinder	Spin-stabilized	Direction of flight	Spin axis	Toward earth	0	±23.4	Intelsat IV	Geosynchronous altitude
					102	30 to 60 (reference pitch axis)	Tiros	Sun-synchronous orbit
Deployed fixed orthogonal panels	Gravity-gradient	(See comments)	(See comments)	Toward earth	125	(See comment)	NTS-1	Variable insolation depending upon panel angle with respect to yaw axis, yaw angle, position in orbit and season
Deployed partially oriented (one-axis) panels	Reaction wheel	Array drive axis	Toward earth	Toward earth	90	0	POGO	180-degree yaw maneuver required twice per orbit; no array drive sliprings
Deployed oriented (one-axis) panels	Reaction wheel	Direction of flight	Array drive axis	Toward earth	0	±23.4	FLTSATCOM	Geosynchronous attitude; insolation angle does not include other pointing requirements
		Toward sun	Array drive axis	Toward earth	32	0	OAO	Star pointing obtained by rotation about pitch axis
		Direction of flight	Array drive axis	Toward earth	99	±6	ERTS-1	Sun-synchronous orbit; panels canted 33 degrees to pitch axis
Deployed oriented (two-axis) panels	Reaction wheel	Array drive axis	Array drive axis	Toward earth	Any	0	FRUSA	Array system provides two-axis control independent of spacecraft attitude control

REFERENCES (CHAPTER 2)

- 2.1-1 U.S. Standard Atmosphere, 1962, U.S. Committee on Extension of Standard Atmosphere, Washington, D. C., Government Printing Office, December 1962.
- 2.1-2 NASA TMX-53865, "Natural Environment Criteria for the NASA Space Station Program (Second Edition)," D.K. Weidner, Editor; Marshall Space Flight Center, August 1970.
- 2.1.3 W. Luft, C. C. McCraven and L. A. Aroian, "Temperature and Humidity Effects on Silicon Solar Cells," Conference Record of the 7th Photovoltaic Specialists Conference, 1968.
- 2.1.4 A. G. Pickett and M. M. Lemcoe, Handbook of Design Data on Elastomeric Materials Used in Aerospace Systems, Southwest Research Institute, San Antonio, Texas, ASD-TR-61-234, January 1962.
- 2.1-5 "Solar Cell Contact Development," Contract NAS5-11595, Applied Sciences Division, Litton Systems, Inc.
- 2.1-6 W. H. Becker and S. R. Pollack, "The Formation and Degradation of Ti-Ag and Ti-Pd-Ag Solar Cell Contacts," Conference Record of the 8th IEEE Photovoltaic Specialists Conference, 1970.
- 2.1-7 C. J. Bishop, "The Fundamental Mechanism of Humidity Degradation in Silver-Titanium Contacts," Conference Record of the 8th IEEE Photovoltaic Specialists Conference, 1970.
- 2.1-8 H. Fischer and R. Gereth, "New Aspects for the Choice of Contact Materials for Silicon Solar Cells," Conference Record of the 7th Photovoltaic Specialists Conference, 1968.
- 2.1-9 M. Stern and H. Wissenberg, "The Electrochemical Behavior and Passivation of Titanium," Journal of the Electrochemical Society, 106, 755, 1959.
- 2.1-10 P. Berman and R. K. Yasui, "Effects of Storage Temperatures on Silicon Solar Cell Contacts," Technical Report 32-1541, Jet Propulsion Laboratories, October 1971.
- 2.1-11 R. K. Yasui and P. A. Berman, "Effects of High-Temperature, High-Humidity Environment on Silicon Solar Cell Contacts," Technical Report 32-1520, Jet Propulsion Laboratories, February 1971.
- 2.2-1 J. B. Kendrick, "TRW Space Data," Third Edition, TRW Systems Group, TRW Inc., 1967.
- 2.3-1 J. B. Kendrick, "TRW Space Data," Third Edition, TRW Systems Group, TRW Inc., 1967.
- 2.3-2 Handbook of Astronautical Engineering, H. H. Koelle, ed., McGraw-Hill Book Co., New York, 1961.
- 2.3-3 R. V. Burry, "Final Report, Space Transfer Phase Propulsion System Study (Vol. 4, Appendices)," Report R-3923, Rocketdyne Division, North American Aviation, Inc., Canoga Park, California. NASA Contract NAS7-88, February 1963.
- 2.3-4 D. K. Weidner, "Natural Environment Criteria for the NASA Space Station Program (Second Edition)," NASA TM X-53865, George C. Marshall Space Flight Center, Alabama, August 1970.
- 2.3-5 "Vacuum Alters Materials," U. S. Army Ordnance, Frankford Arsenal, Philadelphia, Information Materials Engineering, July 1959.
- 2.3-6 H. M. Preston and N. E. Wahl, "Influence of Ultraviolet and Vacuum Environments on Structural Plastics," Institute of Environmental Sciences, 1960 Proceedings, Los Angeles, April 1960.
- 2.3-7 First Symposium, Surface Effects on Spacecraft Materials, F. J. Clauss, ed., J. Wiley and Sons, Inc., New York, 1960. (Palo Alto, California, May 1959).
- 2.3-8 R. W. Fredericks and D. E. Kendall, "Geomagnetic Substorm Charging Effects on Defense Satellite Communication System - Phase II," Presented at Air Force Weapons Laboratory's Command, TRW Systems, July 1973.
- 2.3-9 S. E. DeForest, "Spacecraft Charging at Synchronous Orbit," Journal of Geophysical Research, 77, 651, 1972.
- 2.3-10 R. T. Naumann, "The Near Earth Meteoroid Environment," NASA TN-D-3717, November 1966.
- 2.3-11 F. A. Wade, "Martian Environmental Effects on Solar Cells and Solar Cell Cover Glasses," Report No. 3101, Jet Propulsion Laboratory Contract No. 952582, Texas Tech University, August 1971.
- 2.3-12 J. A. Fager, "Effects of Hypervelocity Impact on Protected Solar Cells," AIAA No. 65-289, July 1965.

- 2.3-13 K.D. Smith, "The Solar Cells and Their Mounting," Bell Systems Technical Journal, July 1963.
- 2.3-14 "Behavior of Materials in Space Environment," American Rocket Society Meeting, 9-15 October 1961.
- 2.3-15 R. W. Rostron, "The Space Radiation Environment at Synchronous Altitude and Its Effects on Communications Satellites," AIAA Paper No. 70-481, presented at AIAA 3rd Communications Satellite Systems Conference, Los Angeles, 1970.
- 2.3-16 J. Moses, E. Miller, J. Miller, and L. Zoller, "Contamination of Optical Surfaces by Solid Rocket Exhausts," NASA TN-P&VE-P-67-2, May 1967.
- 2.3-17 B. A. Sodek and C. Y. Chow, "Reaction Control System Rocket Engine Space Plume Flow Fields," Brown Engineering Report RL-SSL-039, April 1968.
- 2.3-18 N. Borson, "Rocket Plumes as Contamination Sources," Optical Contamination in Space Symposium, Aspen, Colorado, August 1969.
- 2.3-19 G. M. Arnett, "Lunar Excursion Module RCS Engine Vacuum Chamber Contamination Study," NASA TM X-53859, July 1969.
- 2.3-20 P. J. Martinkovic, "Bipropellant Attitude Control Rocket (ACR) Plume Effects on Solar Cells, Optics and Thermal Paint," AFRPL-TR-70-87, Air Force Rocket Propulsion Laboratory, Directorate of Laboratories, Air Force Systems Command, United States Air Force, Edwards, California.
- 2.3-21 R. O. Rantanen and J. P. Thornton, "Deposited Contaminants Effects on Solar Array Power Loss," Conference Records of the Tenth IEEE Photovoltaic Specialists Conference, Palo Alto, California, 1973.
- 2.3-22 "MSFC Skylab Mission Report - Saturn Workshop," NASA TM X-64814, Skylab Program Office, George C. Marshall Space Flight Center, October 1974.
- 2.4-1 J. B. Kendrick, "TRW Space Data," Third Edition, TRW Systems Group, TRW Inc., 1967.
- 2.4-2 F. C. Johnson, Journal of Meteorology, Vol. 11, No. 6, December 1954.
- 2.4-3 NASA Space Vehicle Design Criteria (Environment), Solar Electromagnetic Radiation, NASA SP-8005, May 1971.
- 2.4-4 The American Ephemeris and Nautical Almanac, Anon., U.S. Nautical Almanac Office, U.S. Government Printing Office, Washington, D. C., current annual edition.
- 2.4-5 C. W. Allen, Astrophysical Quantities, The Athlone Press, University of London, 1964.
- 2.4-6 ASTM E 490-73a "Standard, Solar Constant and Air Mass Zero Solar Spectral Irradiance Tables."
- 2.4-7 Based on previously unpublished work by H. Rauschenbach.
- 2.4-8 Deterioration of Materials, Causes and Preventive Techniques, G. A. Greathouse and C. J. Wessel, eds., New York, Reinhold, 1954.
- 2.4-9 J. A. Stevenson and J. C. Grafton, "Radiation Heat Transfer Analysis for Space Vehicles," Technical Report 61-119 (Part I), ASD, December 1961.
- 2.4-10 J. Jensen, et al., Design Guide to Orbital Flight, McGraw-Hill, New York, 1962.
- 2.4-11 C. G. Goetzl and J. B. Singletary, Space Materials Handbook, 1962.
- 2.4-12 J. P. Millard and C. B. Neel, "Albedo and Earth Radiation Deduced from Emissivity Sensors on the First Orbiting Solar Observatory," AIAA Paper No. 64-317, 1964.
- 2.4-13 D. Christensen, "Engine Operating Problems in Space: The Space Environment," CR-294, NASA, 1965.
- 2.4-14 "Earth Albedo and Emitted Radiation (NASA Space Vehicle Design Criteria)," SP-8067, NASA, 1971.
- 2.4-15 A. J. Dennison, "Illumination of a Space Vehicle Surface due to Sunlight Reflected from Earth," ARS Journal, April 1962.
- 2.4-16 F. G. Cunningham, "Earth Reflected Solar Radiation Input to Spherical Satellites," ARS Journal, July 1962.
- 2.4-17 P. Hrycak, "Effects of Secondary Radiation on an Orbiting Satellite," ARS Journal, August 1962.
- 2.4-18 E. Levin, "Reflected Radiation Received by an Earth Satellite," ARS Journal, September 1962.
- 2.4-19 F. G. Cunningham, "Earth Albedo Input to Flat Plates," AIAA Journal, June 1963.
- 2.4-20 W. E. Allen, "Design and Analysis of Solar Cell Array Configurations for Vertically Stabilized Satellites in Near-Earth Orbits," Technical Memorandum TG-1066, The John Hopkins University Applied Physics Laboratory, August 1969.
- 2.5-1 J. R. Carter, et al., The Solar Cell Radiation Handbook, Report No. 21945-6001-RU-00, TRW Systems, prepared under JPL Contract No. 953362 and NAS 7-100, June 1973.
- 2.5-2 NASA SP-8116, "The Earth's Trapped Radiation Belts," March 1975.
- 2.5-3 G. W. Singley and J. I. Vette, "The AE-4 Model of the Outer Radiation Zone Electron Environment," NSSDC 72-06, NASA GSFC National Space Science Data Center, August 1972.
- 2.5-4 G. W. Singley and J. I. Vette, "A Model Environment for Outer Zone Electrons," NSSDC 72-13, NASA GSFC National Space Science Data Center, December 1972.

- 2.5-5 M. J. Teague and J. I. Vette, "A Model of the Trapped Electron Population for Solar Minimum," NSSDC 74-03, NASA GSFC, April 1974.
- 2.5-6 M. J. Teague and J. I. Vette, "The Inner Zone Electron Model AE-5," NSSDC 72-10, NASA GSFC National Space Science Data Center, November 1972.
- 2.5-7 M. J. Teague and J. I. Vette, "The Use of the Inner Zone Electron Model AE-5 and Associated Computer Programs," NSSDC 72-11, NASA GSFC National Space Science Data Center, November 1972.
- 2.5-8 J. I. Vette, "Models of the Trapped Radiation Environment," Vol. I: "Inner Zone Protons and Electrons," NASA SP-3024, 1966.
- 2.5-9 J. H. King, "Models of the Trapped Radiation Environment," Vol. IV: "Low Energy Protons," NASA SP-3024, 1967.
- 2.5-10 J. P. Lavine and J. I. Vette, "Models of the Trapped Radiation Environment," Vol. V: "Inner Belt Protons," NASA SP-3024, 1969.
- 2.5-11 J. P. Lavine and J. I. Vette, "Models of the Trapped Radiation Environment," Vol. IV: "Inner Belt Protons," NASA SP-3024, 1970.
- 2.5-12 NASA SP-8118, "Interplanetary Charged Particle Models (1974)," March 1975.
- 2.5-13 Private communication with R. G. Pruett of The Aerospace Corporation, El Segundo, California, December 1975.
- 2.5-14 W. R. Webber, "An Evaluation of the Radiation Hazard due to Solar Particle Events," Report No. D2-90469, The Boeing Company, December 1963.
- 2.5-15 A. J. Masley and A. D. Goedeke, "Complete Dose Analysis of the November 12, 1960, Solar Cosmic Ray Event," Life Sciences and Space Research, North Holland Publishing Co., Amsterdam, 1963.
- 2.5-16 E. G. Stassinopoulos and J. I. King, "An Empirical Model of Energetic Solar Proton Fluxes with Applications to Earth Orbiting Spacecraft," Document No. X-601-72-489, GSFC, December 1972.
- 2.5-17 "Intelsat V, Request for Proposals and Alternatives," Comsat BG-8-23E, W/3/74, 28 March 1974.
- 2.5-18 J. I. Vette, A. B. Lucero and J. A. Wright, "Models of the Trapped Radiation Environment," Vol. III: "Electrons at Synchronous Altitudes," NASA SP-3024, 1967.

NASA SPACE VEHICLE DESIGN
CRITERIA MONOGRAPHS*

Environment

SP-8005	Solar Electromagnetic Radiation, revised May 1971
SP-8010	Models of Mars' Atmosphere (1974), revised December 1974
SP-8011	Models of Venus Atmosphere (1972), revised September 1972
SP-8013	Meteoroid Environment Model—1969 (Near Earth to Lunar Surface), March 1969
SP-8017	Magnetic Fields — Earth and Extra-terrestrial, March 1969
SP-8020	Surface Models of Mars (1975), revised September 1975
SP-8021	Models of Earth's Atmosphere (90 to 2500 km), revised March 1973
SP-8023	Lunar Surface Models, May 1969
SP-8037	Assessment and Control of Spacecraft Magnetic Fields, September 1970
SP-8038	Meteoroid Environment Model — 1970 (Interplanetary and Planetary), October 1970
SP-8049	The Earth's Ionosphere, March 1971
SP-8067	Earth Albedo and Emitted Radiation, July 1971
SP-8069	The Planet Jupiter (1970), December 1971
SP-8084	Surface Atmospheric Extremes (Launch and Transportation Areas), revised June 1974
SP-8085	The Planet Mercury (1971), March 1972
SP-8091	The Planet Saturn (1970), June 1972
SP-8092	Assessment and Control of Spacecraft Electromagnetic Interference, June 1972
SP-8103	The Planets Uranus, Neptune, and Pluto (1971), November 1972
SP-8105	Spacecraft Thermal Control, May 1973
SP-8111	Assessment and Control of Electro-static Charges, May 1974
SP-8116	The Earth's Trapped Radiation Belts, March 1975
SP-8117	Gravity Fields of the Solar System, April 1975
SP-8118	Interplanetary Charged Particle Models (1974), March 1975

Structures

SP-9011	Buffeting During Atmospheric Ascent, revised November 1970
SP-8002	Flight-Loads Measurements During Launch and Exit, revised June 1972
SP-8006	Local Steady Aerodynamic Loads During Launch and Exit, May 1965
SP-8012	Natural Vibration Modal Analysis, September 1968
SP-8014	Entry Thermal Protection, August 1968
SP-8022	Staging Loads, February 1969
SP-8029	Aerodynamic and Rocket-Exhaust Heating During Launch and Ascent, May 1969
SP-8042	Meteoroid Damage Assessment, May 1970
SP-8043	Design-Development Testing, May 1970
SP-8044	Qualification Testing, May 1970
SP-8045	Acceptance Testing, April 1970
SP-8050	Structural Vibration Prediction, June 1970
SP-8053	Nuclear and Space Radiation Effects on Materials, June 1970
SP-8054	Space Radiation Protection, June 1970
SP-8060	Compartment Venting, November 1970
SP-8072	Acoustic Loads Generated by the Propulsion System, June 1971
SP-8077	Transportation and Handling Loads, September 1971
SP-8079	Structural Interaction with Control Systems, November 1971
SP-8099	Combining Ascent Loads, May 1972

Guidance and Control

SP-8016	Effects of Structural Flexibility on Spacecraft Control Systems, April 1969
SP-8018	Spacecraft Magnetic Torques, March 1969
SP-8024	Spacecraft Gravitational Torques, May 1969
SP-8027	Spacecraft Radiation Torques, October 1969
SP-8034	Spacecraft Mass Expulsion Torques, December 1969
SP-8036	Effects of Structural Flexibility on Launch Vehicle Control Systems, February 1970

* These documents are available from the National Information Service, Springfield, Virginia 22161.

SP-8047 Spacecraft Sun Sensors, June 1970
SP-8058 Spacecraft Aerodynamic Torques,
 January 1971
SP-8065 Tubular Spacecraft Booms (Extendi-
 ble, Reel Stored), February 1971

SP-8074 Spacecraft Solar Cell Arrays, May
 1971
SP-8098 Effects of Structural Flexibility on
 Entry Vehicle Control Systems, June
 1972

CHAPTER 3
SOLAR CELLS

CONTENTS

		Page			Page
3.1	Solar Cell Types	3.1-1			
	3.1.1 Classification of Solar Cells	3.1-1		3.6.3 Irreversible Changes	3.6-3
	3.1.2 General Design Features	3.1-2		3.6.4 Low Temperature, Low-Intensity Operation	3.6-4
	3.1.3 The Fabrication Process	3.1-2	3.7	Reverse-Biased Solar Cells	3.7-1
	3.1.4 Semiconductor Materials and Their Properties	3.1-3		3.7.1 Cause for Reverse Bias	3.7-1
	3.1.5 Effects of Base Resistivity	3.1-3		3.7.2 Silicon Solar Cell Reverse Characteristics	3.7-1
	3.1.6 Drift Field Solar Cells	3.1-4		3.7.3 Effects of Reverse Bias on Silicon Solar Cells	3.7-1
	3.1.7 Lithium-Doped Silicon Solar Cells	3.1-4			
3.2	Electrical Characteristics	3.2-1	3.8	Mechanical Characteristics	3.8-1
	3.2.1 Cell Polarity and Bias Polarity	3.2-1		3.8.1 Cell Sizes	3.8-1
	3.2.2 Current-Voltage Characteristics	3.2-1		3.8.2 Cell Thicknesses	3.8-1
	3.2.3 Series Resistance	3.2-2		3.8.3 Size/Thickness/Cost Tradeoffs	3.8-1
	3.2.4 Shunt Resistance	3.2-2		3.8.4 Active Area	3.8-1
	3.2.5 Energy Conversion Efficiency	3.2-2	3.9	Contacts	3.9-1
	3.2.6 Ultimate Energy Conversion Efficiency	3.2-3		3.9.1 Contact Configurations	3.9-1
	3.2.7 Curve Factor	3.2-3		3.9.2 Contact Metallization	3.9-1
	3.2.8 Fill Factor	3.2-3		3.9.3 Solder Coverage	3.9-1
3.3	Effects of Corpuscular Radiation	3.3-1		3.9.4 Contact Integrity	3.9-1
	3.3.1 Solar Cell Damage	3.3-1		3.9.5 Effects of Temperature on Contact Integrity	3.9-3
	3.3.2 Damage Equivalent 1-MeV Fluence	3.3-1		3.9.6 Contact Surface Roughness	3.9-3
	3.3.3 Low Energy Proton Damage	3.3-2	3.10	Optical Characteristics	3.10-1
	3.3.4 Radiation Damage Annealing	3.3-2		3.10.1 Front Surface Finish	3.10-1
	3.3.5 Photon Effects	3.3-3		3.10.2 Antireflective Coatings	3.10-1
3.4	Effects of Cell Thickness	3.4-1		3.10.3 Spectral Response Defined	3.10-1
3.5	Effects of Illumination	3.5-1		3.10.4 Spectral Response of Solar Cells	3.10-2
	3.5.1 Changes in Intensity at Constant Cell Temperature	3.5-1	3.11	Theoretical Solar Cell Models	3.11-1
	3.5.2 Effects of Series Resistance	3.5-1		3.11.1 DC Model Theory	3.11-1
	3.5.3 High-Intensity, High-Temperature Operation	3.5-1		3.11.2 AC Model Theory	3.11-4
3.6	Effects of Temperature	3.6-1	3.12	Recent Developments and Future Trends	3.12-1
	3.6.1 Reversible Changes in Output	3.6-1		References (Chapter 3)	3. R-1
	3.6.2 Temperature Coefficients	3.6-1			

TABLES

3.9-1	Factors Influencing Contact Pull Strength	3.9-3
-------	---	-------

3.1-1	Portion of a Planar, Single-Crystal, N-on-P Silicon Solar Cell	3.1-3	3.5-3	Comparison of Current-Voltage Characteristics for Conventional 5-grid and High-Intensity 13-grid Cells at 2 Temperatures at $2.8 \text{ W} \cdot \text{cm}^{-2}$ (Solar Constants) Illumination Intensity	3.5-2
3.1-2	Crossover Fluence of Conventional 0.25-mm Thick Solar Cells with SiO Coating	3.1-3	3.6-1	Average Temperature Coefficient for I_{sc} , I_{mp} and P_{mp} from T to 28°C Normalized to Conditions at 28°C	3.6-3
3.1-3	Effects of Varying Base Resistivity on Power Output	3.1-4	3.6-2	Average Temperature Coefficients for V_{mp} and V_{oc} from T to 28°C	3.6-3
3.2-1	Solar Cell Electrical Output Characteristics; (a) I-V Curve, and (b) P-V Curve	3.2-1	3.6-3	Variation of Series Resistance with Temperature	3.6-3
3.2-2	Effect of Series Resistance on I-V Curve Shape of 2 x 2 cm Solar Cell	3.2-2	3.6-4	Variation of Curvature Factor, K, and Power Change, ΔP_m , with Temperature	3.6-3
3.2-3	Effect of Shunt Resistance on I-V Curve Shape of 2 x 2 cm Solar Cell	3.2-3	3.6-5	Typical Low Temperature, Low Intensity Solar Cell Output Characteristics	3.6-4
3.3-1	Typical Variations of Solar Cell Current-Voltage Characteristics with Temperature Before (Solid Lines) and After (Dashed Lines) Irradiation	3.3-2	3.8-1	Solar Cell Sizes	3.8-1
3.3-2	Solar Cell Current Loss Function Curve	3.3-2	3.9-1	Some Solar Cell Contact Configurations	3.9-2
3.3-3	Photon and Thermal Induced Changes of Solar Cell Power Output After Particle Irradiation	3.3-3	3.9-2	Contact Pull Strength of Solder-Coated Titanium-Silver Contact n-on-p Solar Cells as a Function of Temperature	3.9-3
3.4-1	Maximum Power Density Per Unit Active Cell Area Versus Cell Thickness for 1-3 ohm-cm and 7-10 ohm-cm N/P Silicon Cells. At One Solar Constant AMO Illumination Intensity, 28°C , Pre-Irradiation	3.4-1	3.10-1	Idealized Spectral Response Curves of a Glassed Silicon Solar Cell for (a) Constant Number of Photons Per Unit Wavelength Input and (b) Constant Energy Per Unit Wavelength Input	3.10-2
3.4-2	Effects of Thickness and Fluence on Conventional Solar Cell Performance	3.4-1	3.10-2	Relationships Between Wavelength, Wave Number, and Photon Energy	3.10-2
3.5-1	Typical I-V Curves of a 1 x 2 cm Solar Cell at Three Different Illumination Levels	3.5-1	3.10-3	Changes in the Spectral Response Characteristics	3.10-3
3.5-2	Current-Voltage Characteristics for 5-Grid, 10 ohm-cm Silicon Cell at Temperatures from 30° to 150°C	3.5-2	3.11-1	Schematic Diagrams of the Properties of Solar Cell p-n Junctions	3.11-2
			3.11-2	Ideal Solar Cell Model	3.11-4

CHAPTER 3

SOLAR CELLS

A solar cell is a two-terminal, solid-state semiconductor device which converts solar energy into electrical energy by utilizing the photovoltaic effect.

Solar cells are the major building blocks of solar arrays. Cells are electrically connected in parallel and series in sufficient quantity to produce the desired electrical output under specified operating conditions.

Some material related to the discussion of solar cells is found in other sections as follows:

The Solar Constant
Charged Particle Radiation
Antireflective Coatings
Angle-of-Incidence Effects
Solar Cell Specifications

Solar Cell Performance Data

Volume I
Section 2.4
Section 2.5
Section 4.3
Section 4.8
Sections 10.8
and 10.9

Volume II
Chapter 3

3.1 SOLAR CELL TYPES

The only solar cell type currently in use for space applications is of planar geometry and is made from single-crystal silicon. A variety of mechanical sizes and electrical characteristics are available. Essentially all solar cells for space programs are procured to particular specifications which differ slightly from program to program and from one procuring organization to another. The basic characteristics common to all such solar cells are described in this section.

3.1.1 Classification of Solar Cells

Solar cells may be classified into different device families and cell types according to certain technological characteristics or according to some practical aspects. Technological classification is usually related to peculiar solar cell designs, materials, and fabrication processes as follows:

- General design features
- Semiconductor material
- Semiconductor material properties
- Base (bulk) resistivity
- Cell polarity
- Drift fields
- Junction depth (spectral response)
- Front surface preparation
- Antireflective coating.

Each of these families of devices may, with small variations of certain process steps, yield solar cells that can be further classified according to the following characteristics:

- Efficiency (power output)
- Size
- Thickness
- Contact type and configuration
- Number of gridlines of front contact (series resistance)
- Contact metals
- Contact metal coatings.

Classification of solar cells according to practical aspects is often related to usage or to certain aspects relating to their development. Typical classes of cells (all are of n-on-p polarity) are as follows, listed in order of increasing power output (Ref. 3.1-1):

- Conventional Solar Cells

Also called "standard" solar cells, these cells utilize pre-1972 fabrication technology and are characterized by the following:

Starting Material: Crucible-grown p-type silicon, either nominal 2 ohm·cm (range 1-3 ohm·cm) or nominal 10 ohm·cm (ranges 6-15, 6-14, 7-14, or 7-15 ohm·cm).

Junction Depth: Held between 0.3 and 0.5 μ m which corresponds to a sheet resistance of between 35 and 55 ohms per square.

Contact Configuration: Ohmic collector bar between 0.9 and 1.25 mm in width, three gridlines/cm, lines are 0.15 to 0.20 mm in width.

Antireflection Coating: Always silicon monoxide (SiO_x).

Cell Thickness: Ranges from 0.20 mm nominal to 0.35 mm nominal, usually ± 0.05 mm.

Cover: Cut-on filter typically around or above 400 nm.

These cells have been produced for space programs in great quantities from 1964 on and are neither "standardized" in design or performance, nor are they related to "standard solar cells" discussed in Section 11.3 in conjunction with the calibration of the solar light intensity.

- Hybrid Solar Cells

These cells are also known as intermediate, shallow, junction, blue, violet, K6-A (Hughes Aircraft Designation), high efficiency, or Comsat cells. However, there is some controversy over whether or not the Comsat cell has a back surface field. A subdivision into Hybrid A and Hybrid B cells is based on power output only. Hybrid cells do not contain electrostatic fields of the type which characterizes "field" cells described below.

Power Output: For a given resistivity and thickness this cell develops from 3 to 12 percent more power than a "conventional" cell.

Starting Material: Same as conventional cell.

Junction Depth: Ranges from 0.10 to 0.25 μ m. The diffusion processing is the same as that for conventional cells; however, either time and/or diffusion temperature is reduced.

Contact Configuration: In most cases an ohmic bar is still used; however there are some versions that have contact pads

connected by narrow bars. Generally the ohmic bar is now quite narrow, of the order 0.5 mm. The number of gridlines is increased; this cell type can have from 5 to 12 gridlines/cm, depending on the average junction depth called out for the cell. The gridlines are much narrower, ranging from 0.05 to 0.08 mm in width. Standard vacuum deposition techniques are used for contact application. The grids are never solder-coated, because of their size; therefore the contact system requires the use of titanium-palladium-silver. If the cell has soldered contacts, the back contact may not contain palladium, since it is not necessary. The Comsat cell, as made by Comsat, uses a chromium-silver contact system instead of Ti-Pd-Ag.

Antireflection Coating: Tantalum pentoxide (Ta_2O_5) is always used on this cell type.

Cell Thickness: Same as conventional cell.

Cover: Fused silica with a cut-on filter at approximately 350 nm or ceria-doped microsheet which has a natural cut-on at this wavelength.

• Field Cells

These cells are also known as p^+ , BSF (back surface field), Helios (Spectrolab designation), or K6-B (Hughes Aircraft designation) cells. These cells are of the drift field type. The electrostatic drift field is built into the base region immediately adjacent to the back contact.

Power Output: At 0.20 and 0.25 mm, output is 5 to 8 percent higher than hybrid cells. Above 0.25 mm, output is 4 to 6 percent higher than hybrid. Much of the gain in power output comes from the significant increase in open circuit voltage developed by the field. Values of V_{oc} for 10 and 20 ohm-cm material are equivalent to that of nominal 2 ohm-cm silicon.

Starting Material: Same as conventional cell with one major exception; resistivity range is nominal 10 ohm-cm or nominal 20 ohm-cm (range 15 to 45 ohm-cm).

Junction Depth: Ranges from 0.15 to 0.25 μm .

Contact Configuration: Same as hybrid cell.

Antireflection Coating: Same as for hybrid cell.

Cell Thickness: Same as conventional cell, but greatest advantage is for 0.20 mm thickness.

Cover: Same as for hybrid cell.

• Black Solar Cells

These cells are also known as CNR (Comsat nonreflecting), "velvet" (NASA-Lewis designation), textured, sculptured (Hughes Aircraft designation), or nonreflecting cells.

These cells comprise the newest family of high-efficiency solar cells that is characterized by a "rough" front surface in contrast to all other solar cells, which have a "smooth" or polished front surface. The rough front surface is produced by an etching process that produces small "pyramids." This pyramidal, "sculptured," or "textured" surface exhibits a low reflectance, i. e., it "looks black."

Power Output: When produced as black hybrid cells, approximately 5 to 7 percent greater; as field type, approximately 4 to 6 percent greater than hybrid cells.

Starting Material: Depends upon whether it is a hybrid or field version. The crystal orientation must be $\langle 100 \rangle$ to achieve the pyramidal surface.

Junction Depth: Same as either hybrid or field cell.

Contact Configuration: Same as hybrid or field cell.

Antireflection Coating: Ta_2O_5

Cell Thickness: Same as conventional cell.

Cover: Same as for hybrid cell.

3.1.2 General Design Features

General design features describe such devices as:

- Planar p-n junction cells
- Vertical multijunction cells
- Schottky barrier cells
- Heterojunction cells
- Grating solar cells.

The only solar cell used for space applications (both past and current usage) is the single-crystal, silicon, planar, p-n junction type cell. Other cell types are under development, and their future space application is being studied. Further details on the various developmental cell types are given in Section 1.2 (History of Solar Cells and Covers).

3.1.3 The Fabrication Process

Modern n-on-p solar cells (Figure 3.1-1) are fabricated by first growing single-crystal p-type silicon ingots, and cutting and slicing them into thin wafers. An n-type impurity is then diffused at high temperature into the wafer surfaces, thereby forming a diode junction less than 1 μm from the surface. The diffused layer is subsequently removed from all but one large surface which then is referred to as the cell's active, or light sensitive, area. Next, metallic contacts are applied to both the diffused n-layer and to the p-base layer. In a final step an antireflective coating is deposited over the active area. Some cell contacts are also coated with soft solder.

On some cell types (known as " p^+ " and "back field" cells) a p^+ -region is diffused into the p-base region near the p-contact during an intermediate fabrication step.

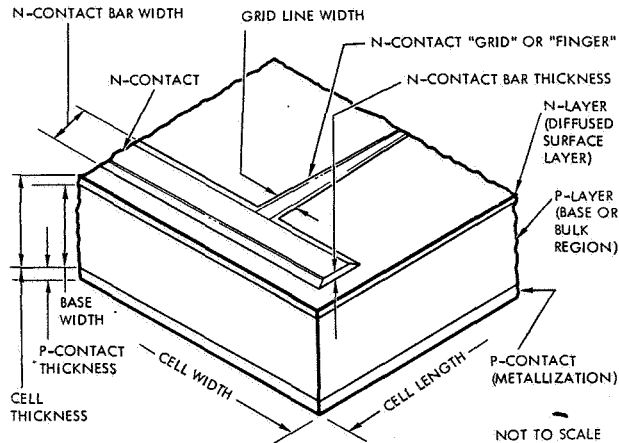


Fig. 3.1-1. Portion of a Planar, Single-Crystal, N-on-P Silicon Solar Cell

3.1.4 Semiconductor Materials and Their Properties

The only material of current interest for space application is silicon. For a number of reasons, gallium-arsenide would theoretically be a slightly better choice than silicon for space-type solar cells; however, the technology of producing and refining high quality material is much more advanced for the abundant silicon than it is for the rare gallium used for gallium arsenide cells. For this and other reasons, silicon solar cells currently perform significantly better than gallium-arsenide cells.

Semiconductor material properties that may significantly influence both the solar cell output and its rate of degradation due to charged-particle radiation include the following:

- Crystallinity (single or polycrystal material)
- Dislocation density
- Impurity types and concentrations (including both impurities that do and that do not affect the electrical resistivity).

As an example, solar cells made from crucible-grown silicon exhibit different electrical characteristics from cells made from zone-refined silicon of the same base resistivity and made by the same cell fabrication process.

As another example, solar cells made from large-diameter crucible-grown silicon ingots have exhibited a slightly different susceptibility to charged particle radiation than cells made by identical processes from small diameter ingots. The difference in cell characteristics apparently arise from small thermodynamic and metallurgical differences that occur in the crystal-growing process as a consequence of changing the crystal diameter.

Semiconductor electrical properties are, in general, altered permanently by heat treatments and processing at elevated temperature. Some electrical changes take place only at temperatures above 800° to 1100°C. Other electrical changes, especially those that are caused by migration (or diffusion) of metal into the silicon, may occur at temperatures as low as 500°C. Permanent electrical and mechanical changes

may occur also at interfaces between the contact metals and the semiconductor material at temperatures above 150°C.

Significance to Array Designer

Since the semiconductor material properties (and therefore, the solar cell performance characteristics) are subject to change due to changes in the cell manufacturing process, it is important to define, control, and maintain a given process once a statistically significant sample of cells (see Section 1.1 of Volume II) has been tested and characterized electrically. Some solar cell specifications require such process definition by utilizing a "Process Identification Document" (see Section 10.9).

3.1.5 Effects of Base Resistivity

Choice of the solar cell material base resistivity affects both the pre-irradiation energy conversion efficiency and the cell radiation resistance of conventional silicon cells. An increase in the base resistivity lowers the efficiency while it increases the radiation resistance. A consequence of this cell behavior is that for low fluence missions, low base resistivity (1 to 3 ohm·cm) cells provide the largest output; while for high fluence missions, high base resistivity (7 to 14 ohm·cm) cells provide the highest output.

At the crossover fluence (Figure 3.1-2), both 2- and 10-ohm·cm cells have the same power output (cell area and thickness being assumed to be the same). The crossover point generally falls within a fluence range between 1×10^{14} and 1×10^{16} e·cm⁻² of 1-MeV energy and depends heavily on the initial output (efficiency) of the cells being compared.

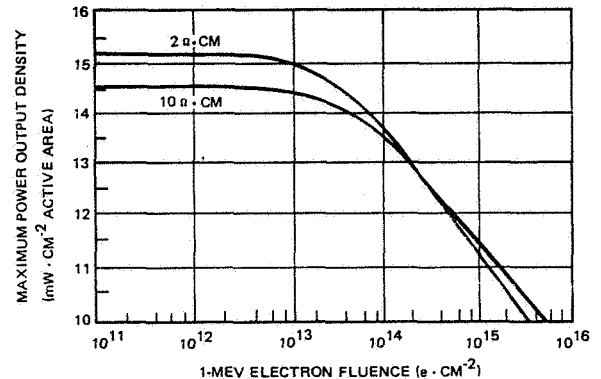
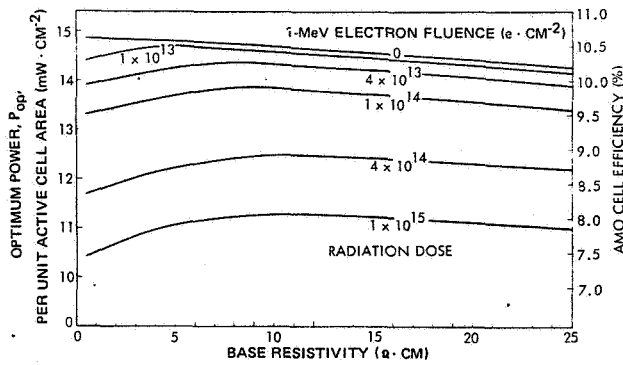


Fig. 3.1-2. Crossover Fluence of Conventional, 0.25-mm Thick Solar Cells with SiO Coating (Ref. 3.1-2)

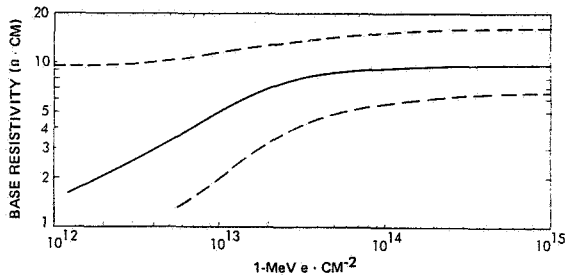
An optimum base resistivity can be defined at which the absolute cell output is greatest after a given radiation dose. Figure 3.1-3 shows that absolute power output after irradiation is a mild function of base resistivity. Therefore, optimizing base resistivity is of little engineering significance, and rather broad tolerances of the base resistivity are permissible. Typical tolerance ranges in the past were:

Nominal	Range
1 or 2 ohm·cm	1 to 3 ohm·cm
10 ohm·cm	7 to 14 ohm·cm

From Ref. 3.1-3. Reprinted with permission of the IEEE.



(a) OPTIMUM POWER OUTPUT VERSUS BASE RESISTIVITY FOR DIFFERENT FLUENCES



(b) OPTIMUM BASE RESISTIVITY VERSUS 1-MeV ELECTRON FLUENCE (SOLID LINE SHOWS OPTIMUM BASE RESISTIVITY. DASHED LINES SHOW RESISTIVITY FOR 1 PERCENT LOWER P_{op} THAN OBTAINED WITH OPTIMUM BASE RESISTIVITY)

Fig. 3.1-3. Effects of Varying Base Resistivity on Power Output (Ref. 3.1-3)

3.1.6 Drift Field Solar Cells

Drift field solar cells are also known as back contact field cells, back surface field cells, and p^+ cells. A drift field, in general, is an electrostatic field built into a solar cell during an additional diffusion process step that introduces an impurity gradient in the cell. The purpose of such impurity gradient is to more efficiently collect light-generated minority carriers (Refs. 3.1-4 and -5).

Currently available drift field cells have an impurity gradient near their back (or p) contact. This drift field, or back contact field, is created by a p^+ region between the p-base region and the p-contact

metallization. The p^+ region acts as a reflector for minority carriers (i. e., electrons in the p region) so that the cell, especially a thin cell, appears to exhibit a longer minority carrier diffusion length and, therefore, the cell's I_{sc} is increased. In addition, cells with p^+ regions show also increased V_{oc} and V_{mp} output.

Apparently, the back contact field is also subject to charged particle radiation damage. Currently available high-efficiency solar cells with p^+ fields show a severe "collapse" of their I-V curves at high fluences, so that for certain applications these cells may offer no advantage at the end of the mission life over lower efficiency cells without drift fields. Nevertheless, drift field cells are currently being utilized in conjunction with thick coverslides for moderately severe radiation environments.

The performance of currently available drift field cells is given in Chapter 3 of Volume II.

3.1.7 Lithium-Doped Silicon Solar Cells

Lithium-doped silicon solar cells constitute a class of developmental devices that exhibit a relatively high charged particle radiation hardness. This radiation hardness is achieved by the addition of lithium to the n-base silicon of p-on-n cells. The lithium causes an apparent annealing of radiation-induced damage and effects a recovery of cell output after irradiation. The recovery effect is particularly noticeable when the radiation consists of protons or other heavy particles.

For lithium-doped p-on-n cells to produce a greater end-of-life power output (efficiency) than conventional n-p cells of 10 ohm-cm base resistivity (see definition in Section 3.1.1), the following conditions must be satisfied (Ref. 3.1-6):

- The cell operating temperature in space must be at least 20°C for oxygen-lean silicon and 60°C for oxygen-rich silicon for the annealing rate to be of significance when the radiation dose rate is as found in geosynchronous orbit.
- The lithium concentration must be controlled during the cell fabrication process and adjusted for a specific end-of-mission fluence.

The recently developed families of high efficiency solar cells (Section 3.1.1) appear to have pushed the need for further development of lithium-doped silicon cells into the background. Further details on the development of lithium-doped cells are given in Section 1.2.

3.2 ELECTRICAL CHARACTERISTICS

Electrically, solar cells are two-terminal devices. Illumination of solar cells causes a voltage to appear across their terminals which is capable of delivering electrical current, power, and energy to an externally connected load circuit.

3.2.1 Cell Polarity and Bias Polarity

Cell polarity and bias polarity of solar cells are defined as follows:

- The polarity of the output voltage of an illuminated solar cell is such that the p-contact becomes positive and the n-contact becomes negative.
- An illuminated solar cell connected to a load and delivering power is said to operate in its "forward" mode.
- A solar cell, illuminated or not, is said to be biased in its "forward" direction by an external source when the positive terminal of the source is connected to the cell's p-contact and the negative terminal is connected to the n-contact.
- A solar cell, illuminated or not, is said to be biased "in reverse" by an external source when the positive terminal of the source is connected to the cell's n-contact and the negative terminal is connected to the p-contact.

3.2.2 Current-Voltage Characteristics

Current-voltage characteristics, or in brief I-V curves, describe the solar cell electrical terminal characteristics most completely. The term "I-V curve" has become customary even though the term should be "V-I curve," if one takes the term "X-Y coordinate system" as a reference. A solar cell I-V curve illustrated in Figure 3.2-1a passes through three significant points:

- I_{sc} , short-circuit current (cell terminal voltage is zero)
- P_{mp} , maximum power output point, also known as the optimum power output point, P_{op}
- V_{oc} , open-circuit voltage (cell terminal current is zero)

The maximum power point, P_{mp} , corresponds to the maximum conversion efficiency, η_{max} . This point is located where the rectangle having the largest area can be drawn inside the I-V curve. The I-V curve is tangent to a constant-power curve, also called an "iso-efficiency" curve at the P_{mp} point. At the P_{mp} point $dP/dV = 0$ (Figure 3.2-1b). From a set of several constant-efficiency curves drawn on the I-V curve plot, the actual cell operating efficiency can be determined when the cell is operated off the maximum power point (i. e., when the terminal voltage $V \neq V_{mp}$).

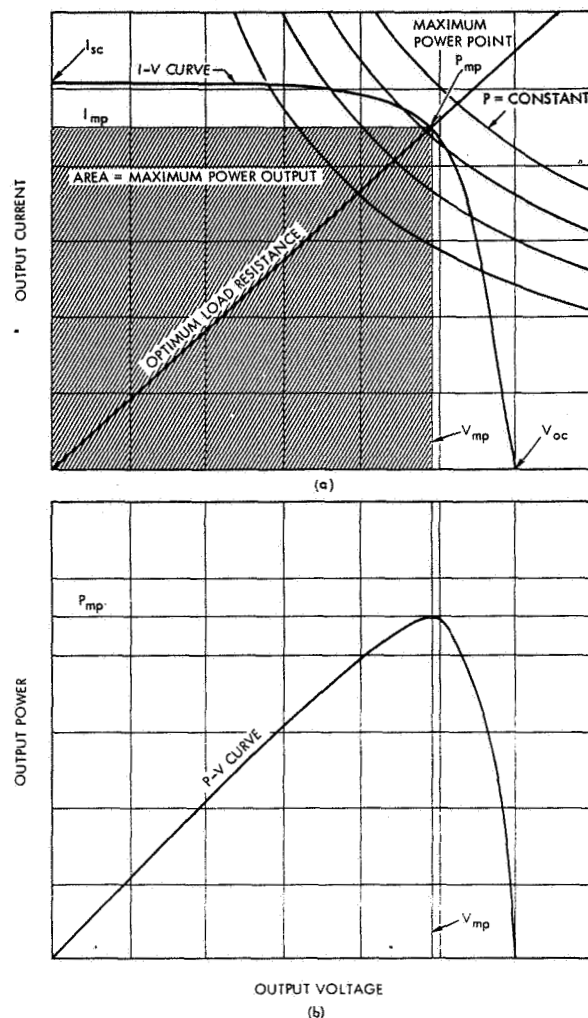


Fig. 3.2-1. Solar Cell Electrical Output Characteristics; (a) I-V Curve, and (b) P-V Curve

Corresponding to P_{mp} there is a "maximum-(or optimum-)power" current, I_{mp} , and "maximum-power" voltage, V_{mp} . A straight line drawn from the origin through P_{mp} (Figure 3.2-1a) represents the optimum load resistance, R_{Lopt} , for this cell. The slope of this line is $1/R_{Lopt} = I_{mp}/V_{mp}$.

Frequently, the values for P_{mp} , V_{mp} , and I_{mp} are to be determined from experimentally obtained I-V curves. As seen from Figure 3.2-1a, the point of tangency of the I-V curve and a constant-power curve is not sharply defined; as an aid to more closely defining the P_{mp} point, a "P-V curve, as shown in Figure 3.2-1b, can be constructed. P-V curves can be plotted during the solar cell test when I-V curves are taken

(a signal multiplier is required as described in Chapter 11 in connection with solar cell testing) or they can be computer-generated from I-V curve data.

The I-V curve shown in Figure 3.2-1a is only the first-quadrant portion of the entire I-V curve. In general, the I-V curve extends from the second quadrant through the first quadrant into the fourth quadrant, as discussed in greater detail in Sections 9.1 and 9.2.

Sometimes the I-V curve is shown rotated such that I is plotted on the abscissa and V on the ordinate. Such presentation is logical and correct except it is not conventional in the sense that according to the solar cell theoretical model, output current is the dependent variable which usually is plotted on the ordinate. (Actually, the nomenclature "I-V" curve is reversed.)

Sometimes the photovoltaic portion of the I-V curve is shown "upside down" in the fourth quadrant. This presentation originated during the 1950's when rectifier diode curve tracing equipment was used to study solar cells. Such equipment displays the dark diode or solar cell forward I-V curve on an oscilloscope screen in the first quadrant and illumination of the junction shifts the curve "downward" along the negative current axis into the fourth quadrant. As shown in Section 9.1 such representation, while logically self-consistent, is inconsistent with modern circuit analysis techniques and leads to unnecessary conceptual difficulties, such as negative power output.

Another reason (but an incorrect one) for showing the output current as negative arises from the solution of the so-called "continuity equation" (see Section 3.11) which assigns a negative sign to the cell current. This calculated cell current is an internal cell current which must flow in a certain direction to maintain the conservation of electrical charges. According to modern circuit theory (see Sections 9.1 and 9.2), when this internal cell current flows in an outside circuit, the "sign" of it reverses and it flows identically to the conventional current from a higher to a lower potential.

3.2.3 Series Resistance

The series resistance, R_s , of a solar cell is an idealization of internal dissipative electrical losses which can be deduced to occur in the cell by observing its terminal behavior (Ref. 3.2-1). Cell series resistance represents in lumped fashion all distributed resistance elements in the semiconductor, its ohmic contacts and the semiconductor/contact interfaces. The largest contribution arises from the resistance of the diffused layer. Since R_s is a lumped quantity, it varies with practically every parameter such as cell I-V characteristics, illumination level, temperature (see Section 3.6.2), and radiation damage. Nevertheless, its use in engineering design and analysis is expedient and eminently practical (for measurement techniques see Section 11.2).

Small variations of R_s can have a profound impact on the energy conversion efficiency of the cell (Figure 3.2-2). Such variations are usually caused by the manufacturing process but changes in R_s may also be caused by environmental exposure such as heavy-particle radiation damage, temperature cycling, and humidity. (See also Section 3.5.2.)

3.2.4 Shunt Resistance

A portion of the electrical energy generated inside the solar cell is lost through internal cell leakage. Several such leakage paths have been identified:

- Through the cell p-n junction (recombination current)

- Along the outer cell edges (surface leakage)
- Through n-contact metalization shunting the junction at microscopic flaws (such as surface scratches).

These leakage paths are neither uniformly distributed across the cell area nor uniform from one cell to the next. In general, they are nonlinear, unstable, and not reproducible during testing (Ref. 3.2-2). The effects of all leakage paths are conceptually united for array design engineering in the so-called shunt resistance, R_{SH} (see Section 9.2).

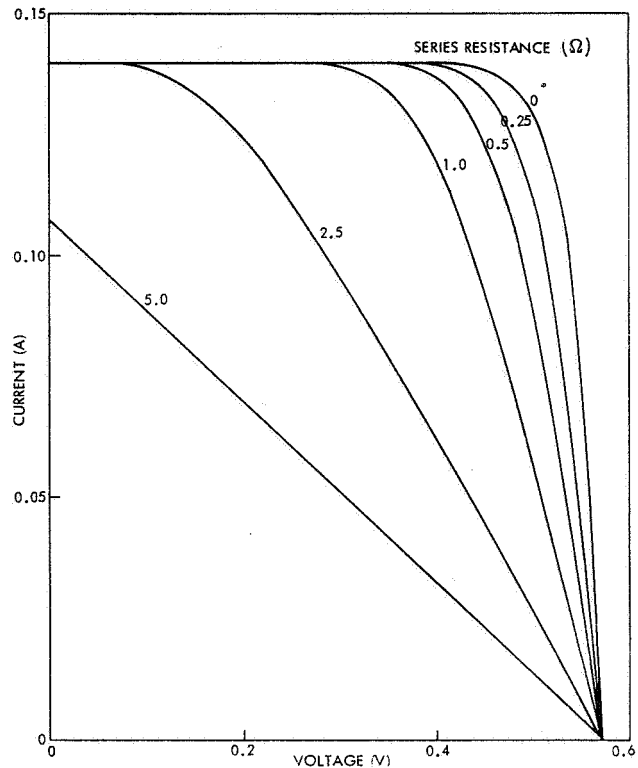


Fig. 3.2-2. Effect of Series Resistance on I-V Curve Shape of 2 x 2 cm Solar Cell (Illustrative Example)

The typical range of shunt resistance for 1 by 2 cm to 2 by 6 cm cells is from 10^3 to 10^5 ohm. Shunt resistance is not controlled during the manufacturing process except that at times it may be monitored for production process control purposes (see also Section 3.7). The effects of shunt resistance for array design purposes are usually negligible for operation near one solar constant (Figure 3.2-3), but become significant at lower light levels.

3.2.5 Energy Conversion Efficiency

Efficiency, η , of a solar cell is defined as

$$\eta = P_{out}/P_{in} = P_{out}/p_{in} \cdot A_c$$

where P_{out} is the electrical power output of the cell, P_{in} is the energy input to the cell, p_{in} is the solar illumination level per unit area or the value of the solar constant (see Section 2.4), and A_c is the active solar cell area upon which the solar energy is incident.

A cell operates at its maximum efficiency, η_{max} , when its ultimate power output capability is utilized by an optimized load at a particular illumination intensity and cell operating temperature. The cell's operating efficiency, η_{op} , is the efficiency at which the cell is actually being utilized. For example, solar cell arrays are frequently designed such that $\eta_{op} = \eta_{max}$ at the end of mission life after the initial maximum solar cell efficiency, η_{max} , has degraded due to environmental exposures to η_{max} . If the load power requirement throughout mission life remains constant, the actual operating efficiency at beginning of life is equal to the end-of-life operating efficiency (i. e., $\eta_{op} = \eta_{max}$) notwithstanding the fact that η_{max} may be considerably greater than η_{op} and may be degrading severely during mission life.

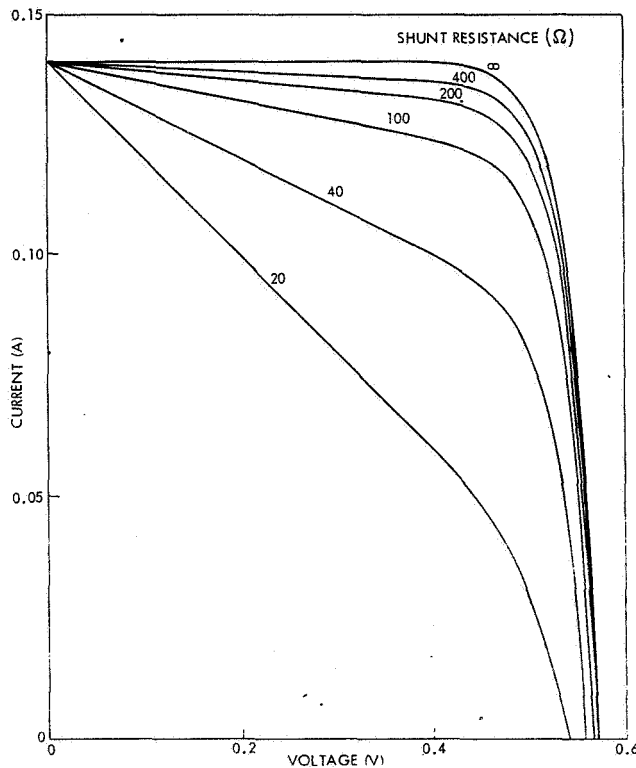


Fig. 3.2-3. Effect of Shunt Resistance on I-V Curve Shape of 2 x 2 cm Solar Cell (Illustrative Example)

The maximum solar cell energy conversion efficiency depends mainly upon the following:

- Solar cell internal construction, dimensions, active area, specific material properties, photovoltaic junction characteristics, anti-reflective coating, surface texture, and contact and grid configuration.
- Illumination level
- Operating temperature
- Particulate irradiation damage
- Temperature cycling and other environmental exposure history.

3.2.6 Ultimate Energy Conversion Efficiency

Occasionally the "ultimate" or "theoretically possible" energy conversion efficiency has been calculated. Such calculations are not purely theoretical, however, in that they consider actually measured solar cell material properties and junction characteristics. The main purpose of such calculations is to establish a reference against which the current state of the art can be compared and to define directions for further research.

Current production type silicon solar cells have initial (i. e., unirradiated) efficiencies of between 10 and 13 percent. Theoretical predictions now estimate that efficiencies of 22 percent should be achievable (Ref. 3.2-3).

The major loss mechanisms which presently prevent solar cells from reaching higher efficiencies are related to technological limitations in the silicon material refining and solar cell fabrication processes (Ref. 3.2-4).

3.2.7 Curve Factor

The "curve factor" is used in theoretical work associated purely with the exponential junction characteristics and deviations therefrom observed in actual solar cells. The curve factor modifies the ideal junction characteristics and appears as the "A" factor in the theoretical model as defined in Section 9.2.

3.2.8 Fill Factor

The "fill factor" is a term that is used to quantitatively describe the "squareness" or "sharpness" of the I-V curve. The "squarer" such a curve is, the greater the maximum power output, P_{mp} , may be for a given I_{sc} and V_{oc} . For example, "squareness" is reduced (i. e., the I-V curve "softens") as the internal cell series resistance, R_s , is increased. Many other cell parameters also affect the fill factor. The fill factor (FF) is defined as

$$FF = \frac{V_{mp} I_{mp}}{V_{oc} I_{sc}} = \frac{P_{mp}}{V_{oc} I_{sc}}$$

and is always less than unity. The fill factor is a practical quantity to use when one wishes to compare different solar cells under the same conditions as is required in manufacturing process control. Its use, however, may be misleading or even erroneous when one wishes to determine changes in the cell I-V curve shape due to environmental degradation, for instance. It can be shown that when the solar cell operating temperature or illumination intensity is varied over a range in which the I-V curve shape does not change the calculated value of the fill factor will change.

Illustrative Example

Let a solar cell be measured at two different temperatures. Let the measured cell parameters at the first temperature be unprimed, and those at the second, higher temperature be primed. For simplicity, let only the cell output voltage change by ΔV (i. e., $I'_{sc} = I_{sc}$, $I'_{mp} = I_{mp}$, $V'_{oc} = V_{oc} + \Delta V$, and $V'_{mp} = V_{mp} + \Delta V$). The fill factor at the second temperature, then is

$$FF' = \left(\frac{V_{mp} + \Delta V}{V_{oc} + \Delta V} \right) \cdot \frac{V_{oc}}{V_{mp}} \cdot FF$$

$$FF' = 0.978 FF$$

even though the curve shape has not changed.

For a hypothetical cell having $V_{mp} = 0.45$, $V_{oc} = 0.55$ V,
 $\Delta V = -0.05$ V,

The "fill factor" includes the alterations of the I-V curve shape which are caused by the "curve factor."

3.3 EFFECTS OF CORPUSCULAR RADIATION

3.3.1 Solar Cell Damage

Irradiation of solar cells with electrons, protons, neutrons, and other particles causes permanent mechanical damage at the atomic level within the solar cell. This damage has a drastic, deleterious impact on almost all solar cell parameters. Degradation is found in:

- Short-circuit current output
- Open-circuit voltage output
- Maximum power output
- Energy conversion efficiency
- Spectral response (at the long wavelengths).

Changes in other parameters are found to affect:

- Temperature coefficients
- Series resistance
- I-V curve shape.

The magnitude of the I-V curve degradation with radiation, in general, depends upon the following:

- Solar cell wafer thickness and presence or absence of electric drift fields in the cell
- Solar cell minority carrier lifetime (initial and after irradiation)
- Solar cell base resistivity and silicon material parameters (initial)
- Particle type (mass and charge)
- Particle kinetic energy (usually expressed in units of electron-volts)
- Cell temperature (while being irradiated)
- Cell temperature/time profile during which damage annealing may take place
- Previous exposure to radiation (accumulated fluence or damage)
- Illumination level during or after irradiation (photon-induced damage).

Generally, protons and neutrons cause greater degradation in the cell power and voltage output capabilities than electrons. Details of the physics of the degradation mechanism and other aspects of radiation effects are treated in the Solar Cell Radiation Handbook (Ref. 3.3-1).

Radiation Resistance

Also known as radiation tolerance or hardness, radiation resistance is a term frequently used in radiation studies of semiconductors. Most frequently these terms denote a value of particle fluence at which a device parameter has degraded to a specific fraction (usually 75 percent) of its original value. This fluence is also known as the critical fluence. These terms are of little interest to solar cell array designers because the relative degradation (or lack thereof) is not important. Rather, the absolute values of the solar cell performance parameters, after the cell has received a specific value of particle fluence, are important.

3.3.2 Damage Equivalent 1-MeV Fluence

For analytical and test convenience, the concept of "damage-equivalent, normally-incident (DENI), monoenergetic, 1-MeV fluence," or, in brief, "1-MeV fluence," has been developed.

Damage Coefficients

The actual damage produced in solar cells by electrons of various energies is related to the damage produced by 1-MeV electrons by the so-called "damage coefficients for electrons." Similarly, the damage produced by protons of various energies is related to the damage produced by 10-MeV protons by the "damage coefficients for protons." The damage produced by 10-MeV protons is, in turn, related to the damage produced by 1-MeV electrons by a single damage conversion factor. One 10-MeV proton does approximately the same damage as 3000 1-MeV electrons (numbers ranging from 2000 to 7000 have been used).

Electron Damage

Electrons damage solar cells such that a single value of equivalent 1-MeV fluence can be used to describe the degradation of cell currents and voltages.

Typical solar cell I-V curves before and after exposure to a heavy dose (approximately $10^{15} \text{ e} \cdot \text{cm}^{-2}$) of 1-MeV electrons are illustrated in Figure 3.3-1. This figure illustrates an increase in the temperature coefficient for I_{sc} and no change in the temperature coefficients for V_{oc} and V_{mp} .

Proton Damage

Protons (and other heavy particles) damage solar cells such that two different values of equivalent 1-MeV fluence must be used; one value is used to describe the degradation of cell currents and another value is used to describe the degradation of cell voltages.

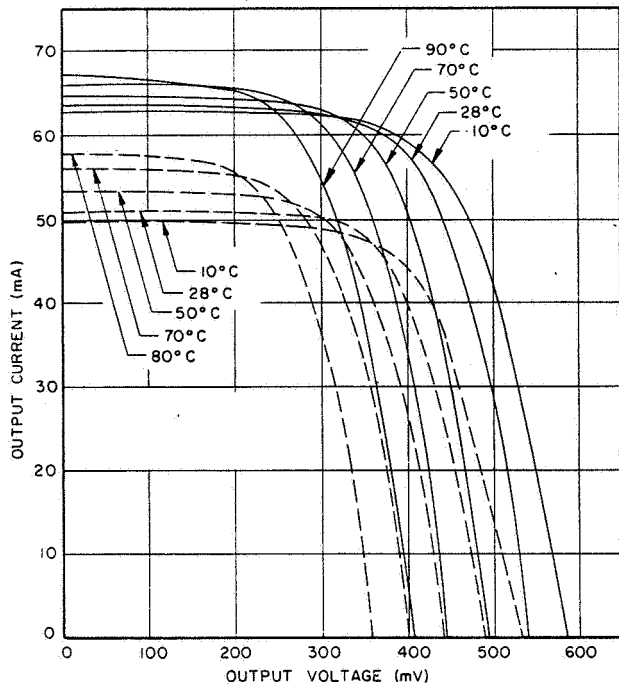


Fig. 3.3-1. Typical Variations of Solar Cell Current-Voltage Characteristics with Temperature Before (Solid Lines) and After (Dashed Lines) Irradiation (Illustrative Example)

3.3.3 Low Energy Proton Damage

Low energy proton damage is defined in this handbook as being restricted to that damage mechanism which causes shunting of the p-n junction; thereby the low energy proton damage mechanism can be treated separately from and becomes independent of minority carrier lifetime considerations. Low energy proton damage can occur in one of two ways:

- From medium or higher energy protons having sufficient energy to just penetrate the solar cell covers or contact metallizations
- From lower energy protons incident directly on the solar cells in small gap areas that are not protected by the solar cell covers or contacts.

The number of protons that can be expected to penetrate solar cell covers are usually of no significance in most orbits except in those which are in the radiation belts. However, the number of low energy protons that can potentially damage solar cells directly are available in great abundance not only in the radiation belts, but also above them and at synchronous altitude. The proton energy levels of concern are in the 100 to 500 keV range when incident on the silicon front surface, and up to approximately 5 MeV when incident on the front of coverglasses.

Protons which come to rest (i.e. lose all their energy) near the solar cell p-n junction introduce shunt paths across the junction. These shunts cause the cell output to degrade significantly more than the ratio of the damaged cell area to the total cell area may indicate. The shunt defect induced by low energy protons has a diode-like current-voltage characteristic which leads to a relatively small loss in I_{sc} and to progressively larger losses toward P_{mp} and V_{oc} . This is indicated by the "loss function" of Figure 3.3-2.

3.3-2

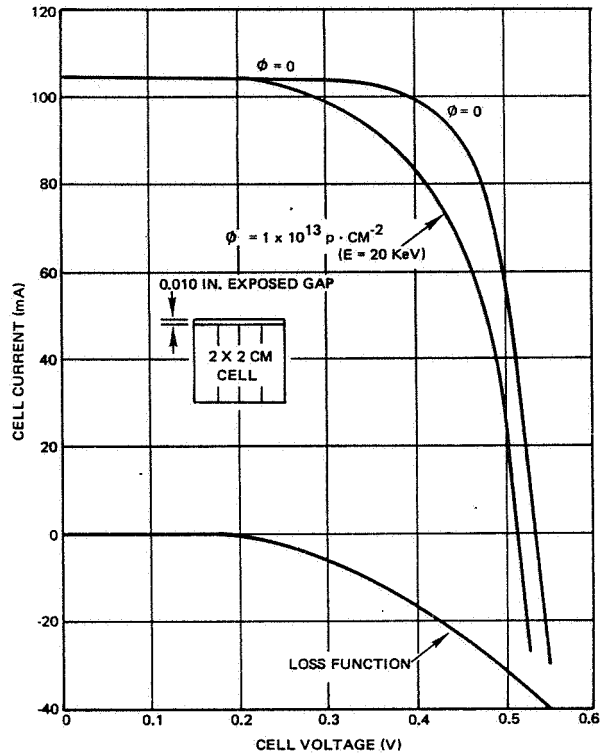


Fig. 3.3-2. Solar Cell Current Loss Function Curve (from Ref. 3.3-2)

The low energy proton damage mechanism was discovered on several satellites in synchronous orbit, and was verified by extensive ground testing. Excessive orbital degradation due to low energy proton damage had been as large as approximately 20 percent (Ref. 3.3-2).

The results of numerous investigations with regard to low energy proton damage in geosynchronous orbit can be summarized for design purposes as follows:

- Even small unprotected areas (in the order of 1 percent) can lead to excessive output degradation (in the order of 10 percent at P_{mp})
- Small unprotected strips of cell area parallel to the n-contact collector bar are several times more damaging than unprotected strips away from the n-contact.
- The entire active cell area not covered by metallic contacts should be protected by the coverglass.

(For design implementation of full cell coverage by covers see Section 8.3.)

3.3.4 Radiation Damage Annealing

In general, the crystalline damage and associated electrical degradation sustained by a solar cell during exposure to corpuscular radiation is not totally stable. Two phenomena have been observed on irradiated cells: damage annealing and further degradation during exposure to sunlight (the latter phenomenon is discussed in Section 3.3.5).

Damage annealing occurs only at temperatures above approximately 20°C, and tends to be more significant for proton and neutron irradiated cells than

for electron irradiated cells. The observed magnitude in recovery of the solar cell power output after 1 MeV electron irradiation ranges from zero to a few percent (typically less than 5 percent). Higher annealing temperatures (up to approximately 100°C) accelerate the annealing process, but do not appear to change the amount of possible recovery.

Damage annealing was found to occur only in solar cells made from crucible-grown silicon, the typical process used in the USA for producing solar cell material (Refs. 3.3-3 and 3.3-4).

Analysis of orbital flight data (Section 11.13) has verified that a part of the solar cell output lost due to solar flare proton events is regained after some time.

3.3.5 Photon Effects

Solar cells that have sustained electrical degradation during irradiation with electrons may either degrade further or recover during subsequent long-term illumination (photon irradiation). A further electrical degradation can be expected in all solar cells fabricated from float-zone refined silicon that was typically used in Europe during the 1960's and early 1970's. The discovery of the photon degradation mechanism is credited to Crabb (Ref. 3.3-3); he found the following photon degradation after 1-MeV electron irradiation:

- After $6 \times 10^{13} \text{ e} \cdot \text{cm}^{-2}$ - 3.7 percent I_{sc} degradation
- After $2.2 \times 10^{15} \text{ e} \cdot \text{cm}^{-2}$ - 8.5 percent I_{sc} degradation

Comparative, controlled experiments by Fischer and Pschunder (Ref. 3.3-4) verified the photon degradation process in float-zone silicon cells and found a damage annealing process in crucible-grown silicon cells. Furthermore, these experiments identified both reversible and irreversible instability problems in both unirradiated and irradiated solar cells which may have an impact on the ultimate solar cell calibration accuracy than can be achieved. The conclusions from Ref. 3.3-4 are:

- Light (photon) induced degradation occurs in 1 ohm·cm, crucible grown n-on-p silicon cells after 12 hours at one solar constant (before particle irradiation) as follows:

I_{sc} degradation - 1.8 percent

V_{oc} degradation - 1.3 percent

P_{mp} degradation - 3.2 percent

- Because the 1 ohm·cm, crucible-grown silicon cells are unstable, they should not be used as standard solar cells.
- The light (photon) induced degradation in the output of 1 ohm·cm and 10 ohm·cm float-zone silicon and of 10 ohm·cm crucible-grown silicon cells (before particle irradiation) is typically less than 1 percent.
- The photon degradation causes a loss in both the minority carrier lifetime and the cell's red response. This leads to the conclusion that lifetime is not a constant material property as heretofore assumed, but rather depends strongly on thermal and light exposure history of the material.
- Photon irradiation immediately after 1-MeV electron irradiation to a fluence of $1 \times 10^{15} \text{ e} \cdot \text{cm}^{-2}$ resulted in the further degradation of 10 ohm·cm float-zone and 1 ohm·cm crucible grown silicon cells, but led to recovery of the 10 ohm·cm crucible-grown and 1 ohm·cm float-zone silicon cells (see Figure 3.3-3).

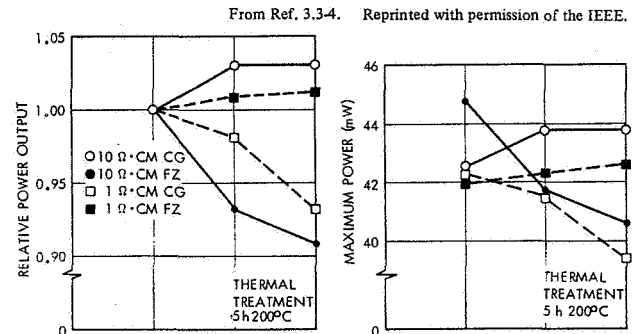


Fig. 3.3-3. Photon and Thermal Induced Changes of Solar Cell Power Output After Particle Irradiation (10^{15} 1-MeV Electrons per cm^2 , Followed by 160 Hours of One Solar Constant AMO Illumination, per Ref. 3.3-4)

3.4 EFFECTS OF CELL THICKNESS

A significant contribution to the total weight of a solar cell array is made by the solar cells (see Section 8.2). Therefore, attempts to reduce the array weight frequently focus on reducing the solar cell thickness. A reduction of cell thickness will result in a reduction of cell output (i. e., efficiency) when the cell thickness approaches or becomes less than the mean minority carrier diffusion length.

The reduction in output is mainly due to a curtailment of the cell's red response (see Section 3.10.4).

A reduction in cell output has been observed whenever unirradiated cells with ohmic back contacts become thinner than approximately 0.4 mm (0.016 inch), as shown in Figure 3.4-1. The effect of reduced cell

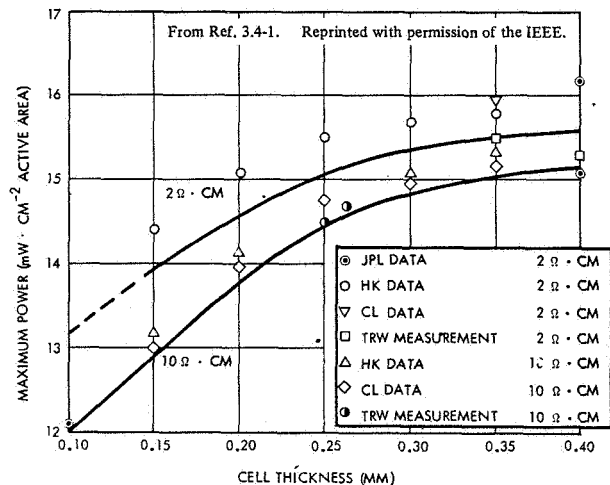


Fig. 3.4-1. Maximum Power Density Per Unit Active Cell Area Versus Cell Thickness for 1-3 ohm-cm and 7-10 ohm-cm N/P Silicon Cells. At One Solar Constant AMO Illumination Intensity, 28°C, Pre-Irradiation (based on data from Refs. 3.4-1 and 3.4-3)

thickness is diminished or eliminated by introducing an electric field in the cell base near the back contact (see Section 3.1.6).

Charged particle irradiation of solar cells decreases their minority carrier lifetime. Hence, the cell thickness at which the effect on power output becomes noticeable moves toward lower values of cell thickness with increasing radiation dosage, as shown in Figure 3.4-2, for cells with ohmic back contacts. Currently available cells with back contact fields tend to degrade with radiation as rapidly as cells with ohmic back contacts; however, after they have received a 1-MeV dose of approximately 10^{15} e. cm⁻², they tend to degrade more rapidly (see Section 3.3 of Volume II).

A comprehensive experimental study of the effects of reduced cell thickness on solar cell characteristics, performed in 1965 through 1967 (Refs. 3.4-1 and 3.4-2), still provides most of the thin cell engineering data in use today. This data is shown in detail in Section 3.4 of Volume II.

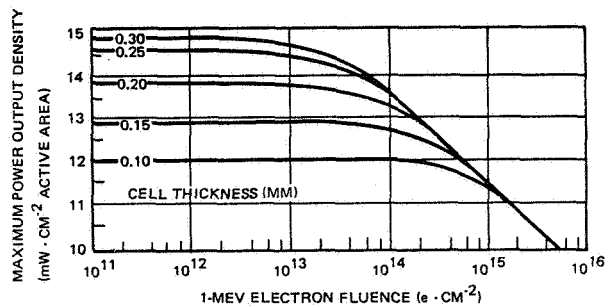


Fig. 3.4-2. Effects of Thickness and Fluence on Conventional Solar Cell Performance (Ref. 3.4-3)

3.5 EFFECTS OF ILLUMINATION

The solar cell illumination intensity depends upon the following:

- Angle of incidence (including array geometry and orientation)
- Solar distance
- Solar energy concentration (mirrors, etc.)
- Transmission losses in coverslides and other optical elements in front of the solar cell
- Solar eclipses
- Shadowing.

3.5.1 Changes in Intensity at Constant Cell Temperature

Changing the illumination intensity incident on the solar cells (keeping everything else constant, such as the cell's temperature and the illumination's spectral distribution) changes the cell's output characteristics, as shown in Figure 3.5-1. Each point on the cell's I-V curve translates very nearly along the cell's series resistance (R_S) line, so that the I-V curve shifts toward lower current and toward higher voltage values with decreasing intensity (Ref. 3.5-1). Even though a lowering of the intensity causes a shift toward higher voltages, the open-circuit voltage actually decreases.

For most solar cell types that were designed to operate at approximately one solar constant intensity, the I-V curve shape is essentially invariant with intensity over the range from approximately 0.5 to 2 solar constants. The cell's I_{SC} is practically proportional to the intensity, V_{OC} changes logarithmically, and R_S is very nearly constant. The greater the intensity deviation from the cell's design intensity becomes, the greater will be the cell's I-V curve shape change (Figure 3.5-2).

3.5.2 Effects of Series Resistance

An interesting phenomenon (applicable to spinning arrays, for example) that results from reduced illumination (less than one solar constant) is that cells having higher series resistance (i.e., "poorer" cells) show a greater absolute power output than cells having lower series resistance (i.e., "better" cells with "sharper" I-V curves). The reason for this is that cells are normally "graded" (i.e., their performance is measured for flight acceptance) at one solar constant intensity, while at the lower, operating intensity the I-V curve shifts toward higher voltages. Since the magnitude of this voltage shift is directly proportional to the magnitude of the series resistance, cells with higher series resistance cells will exhibit a greater voltage gain than cells with lower series resistance.

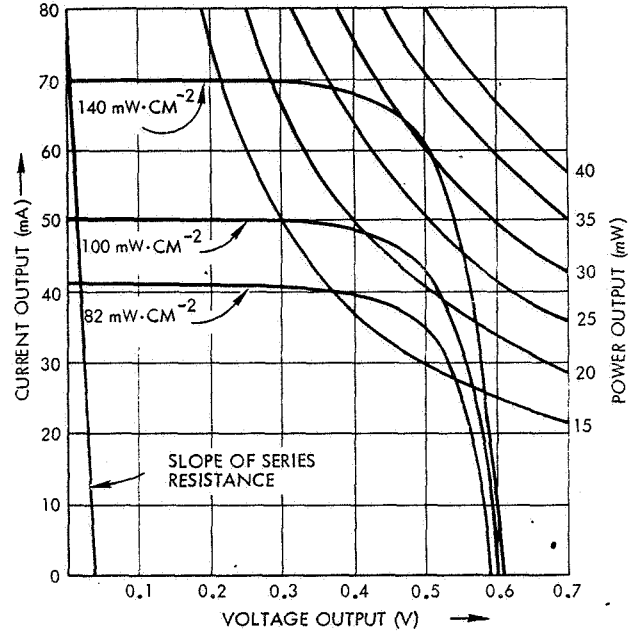
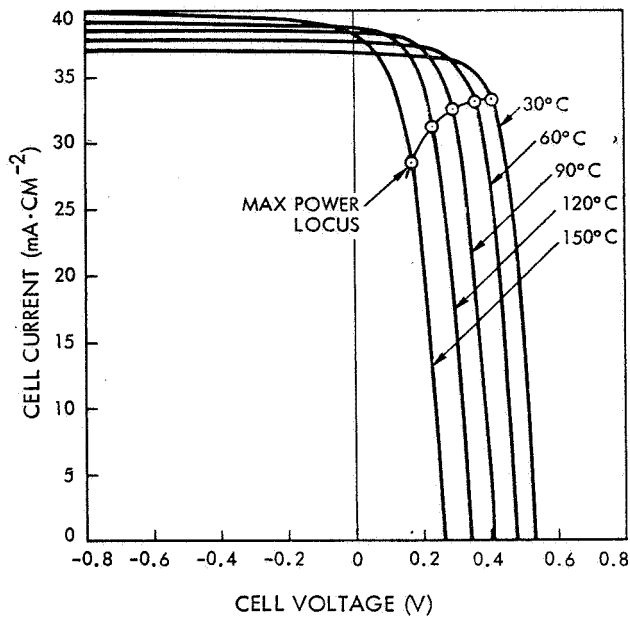


Fig. 3.5-1. Typical I-V Curves of a 1 x 2 cm Solar Cell at Three Different Illumination Levels (Constant Spectral Distribution and Temperature, Illustrative Example)

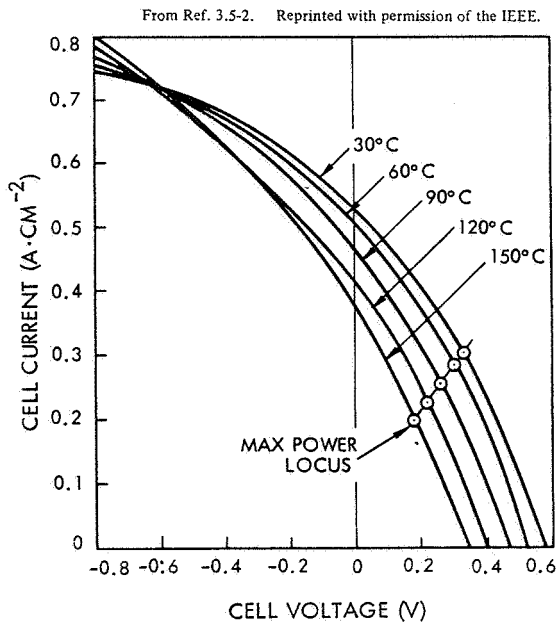
3.5.3 High-Intensity, High-Temperature Operation

Conventional solar cells are efficiency-optimized for operation at near one solar constant and 30°C. Such cells perform poorly at very high illumination levels and even worse at the accompanying higher operating temperatures (Figure 3.5-2). High-intensity, high-temperature operation is of interest both for solar probes ("inbound" missions) and for solar energy concentrators. For example, the solar intensity at Mercury is 6.67 solar constants, and potentially practical solar concentration ratios of up to 3:1 have been studied for space use, and ratios exceeding 200:1 for terrestrial use. Such high-intensity operation requires special solar cell design.

The major electrical loss in the solar cell, especially at higher intensities is in the diffused layer resistance. Therefore, high-intensity solar cells have dense gridline patterns. Experimental 1 by 2 cm cells evaluated had 13 gridlines for operation between 0.5 to 20 solar constants, and 30 gridlines for operation up to 800 solar constants. The typical differences between the I-V curves of conventional (5 gridlines) and "high intensity" (13 gridlines) solar cells available in the mid 1960's are shown in Figure 3.5-3.



(a) AT ONE SOLAR CONSTANT INTENSITY



(b) AT 20 SOLAR CONSTANT INTENSITY

Fig. 3.5-2. Current-Voltage Characteristics for 5-Grid, 10 ohm-cm Silicon Cell at Temperatures from 30° to 150°C (Illustrative Example, Ref. 3.5-2)

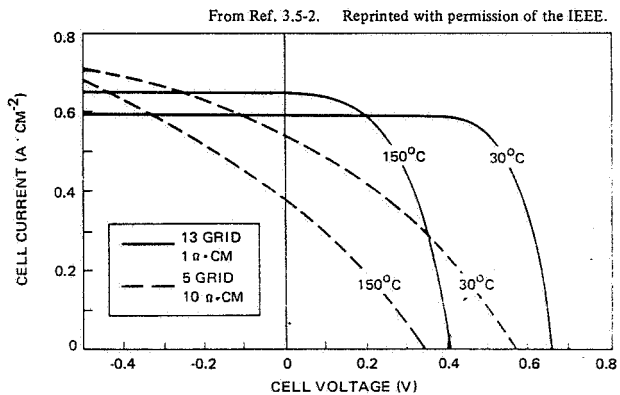


Fig. 3.5-3. Comparison of Current-Voltage Characteristics for Conventional 5-grid and High-Intensity 13-grid Cells at 2 Temperatures at $2.8 \text{ W} \cdot \text{cm}^{-2}$ (Solar Constants) Illumination Intensity (Illustrative Example, Ref. 3.5-2)

The reduction of the resistance of the diffused layer can be accomplished in several ways: Refs. 3.5-3 and 3.5-4 report optimization of the gridline width and grid spacings (i.e., gridline density), while Ref. 3.5-5 reports the use of highly doped and deep-diffused light-sensitive layers.

High intensity solar cell experiments using both p-on-n and n-on-p silicon solar cells were reported by Ref. 3.5-6. Further cell optimization work on solar cell types intended for solar concentrator applications for up to two solar constants was reported by Refs. 3.5-7 and 3.5-8 and by Ref. 3.5-9 for up to four solar constants, and by Ref. 3.5-10 for up to approximately 400 solar constants. The effects of base resistivity and junction depth on the operation of silicon cells for up to 10 solar constants were reported by Refs. 3.5.11, 3.5.12 and 3.5.13. Test results from several cell types at intensities of up to seven solar constants were reported by Ref. 3.5.14.

Comparisons of the high-intensity, high temperature performance of space-type silicon cells with experimental gallium arsenide cells were made by Refs. 3.5.11 and 3.5.15. Temperature control in space of solar cells operated at high intensity was treated by Ref. 3.1.16.

A capability of silicon solar cells to withstand high temperature has also arisen from heat sterilization requirements of interplanetary probes. Silicon cells with solder-covered, electroless nickel-plated contacts have successfully passed heat sterilization requirements of 145°C for 36 hours in an ambient atmosphere (Ref. 3.5.17).

3.6 EFFECTS OF TEMPERATURE

3.6.1 Reversible Changes in Output

A change in cell temperature causes three changes in the cell I-V curve:

- A scaling of the I-V curve along the current axis
- A translation (shifting) of the I-V curve along the voltage axis
- A change in the I-V curve shape affecting the "roundness" of the "knee" region of the I-V curve.

An increase in the cell operating temperature causes a slight increase in the cell short-circuit current and a significant decrease in cell voltage. The increase in short-circuit current is a function of illumination level. Its value, typically less than 0.1%/°C, depends upon the spectral distribution of the illuminating light (filtered sunlight) and the spectral response of the solar cells (i. e., the cell thickness, junction depth, antireflective coating, and state of radiation damage of the cell).

Scaling of the I-V curve along the current axis essentially corresponds to a change in the cell's energy conversion efficiency which, in turn, is due to a change in the cell's collection efficiency with temperature (see Sections 3.10.3 and 3.10.4). Scaling of the I-V curve consists of multiplication of the value of the output current at each point on the I-V curve by a constant; for an increase in temperature, this constant is greater than unity and for a decrease in temperature it is less than unity.

The change in voltage with temperature is due to a change in the diode conduction characteristics. With increasing temperatures the entire I-V curve translates toward lower voltages at a rate of approximately 2.2 to 2.3 mV.°C⁻¹. This voltage temperature coefficient is nearly the same for all nonirradiated, thick base width solar cells (for V_{oc} and for V_{mp}), as well as for general rectifier diodes. Variations in the voltage temperature coefficients are frequently indicative of changes in the cell material properties, junction or contact characteristics, and leakage properties.

The voltage temperature coefficient is mildly, if at all, affected by radiation damage, but appears to be affected by cell thickness. At higher temperatures (above 80° to 100°C) and at lower temperatures (below approximately -80° to -100°C), the voltage temperature coefficients become anomalous on many flight type cells. The low-temperature anomaly is, in part, caused by nonohmic contacts on the silicon wafer and is, therefore, related to manufacturing process control. Cells with well-behaved temperature coefficients over very large ranges could be manufactured, however, if the need for them arises (an economic penalty would have to be paid for them).

With increasing temperature the "knee" region of the I-V curve tends to become more "rounded." This "knee softening" can be accommodated analytically by either using separate temperature coefficients for I_{sc} , I_{mp} , V_{mp} , and V_{oc} , or by defining a temperature coefficient for R_s , or by defining a separate "curve rounding" factor. Differences between the temperature coefficients of V_{oc} and V_{mp} are usually indicative of changes in the I-V curve shape with temperature. Changes in the I-V curves with temperature are shown in Figures 3.5-2 and 3.5-3 of the previous section.

With increasing temperature the cell's reverse saturation current increases in the same way the reverse current of conventional diodes increases. However, this increase in true reverse current is usually not observable because it is masked by the much larger solar cell leakage currents. Cell leakage currents do not have a well-defined temperature dependence (see Section 3.7). In the avalanche breakdown region, solar cells (like Zener diodes) show decreasing breakdown voltages with increasing temperatures.

3.6.2 Temperature Coefficients

Many different temperature coefficients have been defined, usually in response to some specific analytical problem or in conjunction with some specific computer algorithm. The most straightforward definitions of the short-circuit current coefficient, β_I , and the open circuit voltage coefficient, β_V (at constant intensity), are

$$\beta_L = \frac{dI_{sc}}{dT} \quad \text{and} \quad \beta_V = \frac{dV_{oc}}{dT}$$

However, these definitions are not very useful in that both β_I and β_V are linear over a relatively small range of temperature only. Therefore, the most frequently used temperature coefficients are defined as

$$\beta_I = \frac{I_{sc}(T_i) - I_{sc}(T_o)}{T_i - T_o} \quad \text{and} \quad \beta_V = \frac{V_{oc}(T) - V_{oc}(T_o)}{T - T_o}$$

where T is the temperature at which the cell output is sought and T_o is the reference temperature (usually 28°C). Both of these coefficients change with temperature and β_I also changes with intensity. Therefore, a better (for small intensity changes only) and also frequently used definition is

$$\beta_I' = \frac{I_{sc}(T)}{I_{sc}(T_o)(T - T_o)}$$

The units of this normalized temperature coefficient are "°C⁻¹" or "%·°C⁻¹."

Illustrative Example

A hypothetical solar cell has the following characteristics:

<u>At $T_o = 25^\circ\text{C}$</u>	<u>At $T = 125^\circ\text{C}$</u>
$I_{sc} = 0.14\text{A}$	$I_{sc} = 0.15\text{A}$
$V_{oc} = 0.5\text{V}$	$V_{oc} = 0.3\text{V}$

Then the latter three temperature coefficients are:

$$\beta_I = \frac{0.15 - 0.14}{125 - 25} = 1 \times 10^{-4} \text{ A}/^\circ\text{C}$$

$$\beta_V = \frac{0.3 - 0.5}{125 - 25} = -2 \times 10^{-3} \text{ V}/^\circ\text{C}$$

$$\beta_I' = \frac{0.15}{0.14(125 - 25)} = 1.1 \times 10^{-2} \text{ }^\circ\text{C}^{-1}$$

$$= 1.1 \text{ } \%/^\circ\text{C}$$

For planetary missions where large temperature variations are accompanied by large intensity changes, the above temperature coefficients are not sufficiently accurate. Therefore, one of the following three approaches may be used:

- More comprehensively defined temperature coefficients
- Direct interpolation of solar cell test data
- Mathematical modelling of cell behavior as a function of cell temperature and intensity, without recourse to temperature coefficients.

Comprehensive Temperature Coefficients

The current-voltage characteristic is transformed from a reference condition of temperature and intensity (T_o, H_o) to a new temperature and intensity (T_i, H_i) using the following equations. For short-circuit, I_{sc} , and open-circuit voltage, V_{oc} , Ref. 3.6-1 has shown that:

$$I_{sc}(T_i, H_i) = I_{sc}(T_o, H_o) \left(\frac{H_i}{H_o} \right) + \bar{\alpha}_{H_i} (T_i - T_o)$$

$$V_{oc}(T_i, H_i) = V_{oc}(T_o, H_o) + \bar{\beta}_{H_i} (T_i - T_o) - \Delta I_{sc} R_s$$

$$\Delta I_{sc} = I_{sc}(T_i, H_i) - I_{sc}(T_o, H_o)$$

or

$$\Delta I_{sc} = I_{sc}(T_o, H_o) \left(\frac{H_i}{H_o} - 1 \right) + \bar{\alpha}_{H_i} (T_i - T_o)$$

From these equations Ref. 3.6-2 has developed expressions for any voltage (V) and current (I) along the I-V curve:

$$I(T_i, H_i) = I(T_o, H_o) \left(\frac{H_i}{H_o} \right) + \bar{\alpha}_{H_i} (T_i - T_o)$$

$$\Delta I = I(T_i, H_i) - I(T_o, H_o)$$

$$= I(T_o, H_o) \left(\frac{H_i}{H_o} - 1 \right) + \bar{\alpha}_{H_i} (T_i - T_o)$$

$$V(T_i, H_i) = V(T_o, H_o) + \bar{\beta}_{H_i} (T_i - T_o) - \Delta I_{sc} R_s$$

$$- K_{H_i} I(T_i, H_i) (T_i - T_o)$$

where

$\bar{\alpha}_{H_i}$ = average short-circuit current temperature coefficient from T_o to T_i at intensity H_i

$\bar{\beta}_{H_i}$ = average open-circuit voltage temperature coefficient from T_o to T_i at intensity H_i

R_s = internal cell series resistance

K_{H_i} = average curvature correction factor from T_o to T_i at intensity H_i (this factor is strictly a "geometric" correction factor to change the I-V curve shape, and has nothing to do with the curve factor of Section 3.2.7 or the fill factor of Section 3.2.8)

$$\Delta P_m = P_m(T_i, H_i) - P_m(T_o, H_o)$$

$$K_{H_i} = -\Delta P_m / \left[I_m^2(T_i, H_i) (T_i - T_o) \right]$$

where

$P_m(T_o, H_o)$ = maximum power at reference condition T_o, H_o

$P_m(T_i, H_i)$ = maximum power for translated current-voltage characteristics from T_i, H_i to T_o, H_o

I_m = current at maximum power, T_i, H_i

The value of K is positive for a softening of curvature (increasing radius of curvature) with increasing temperature. The product $K_{H_i} I(T_i, H_i)$ is the voltage change per unit temperature change resulting from changes in the I-V curve shape. Knowing K, the change in power output, ΔP_m associated with the change in the I-V curve shape can be calculated from the last equation.

Test Data Example

Ref. 3.6-2 reports test results from 49 N/P, SiO-coated silicon solar cells, 2 ohm·cm base resistivity 8-cm² size, 0.35 mm (0.014 inch) thick, glassed with 150 μm (0.006 inch), thick microsheet covers with 410 nm ultraviolet reflective and MgF₂ anti-reflective coatings. These cells were manufactured by Centralab during 1970 for the Skylab Orbital Workshop solar cell array. These data were measured over the temperature range of -110° to +110°C using a Spectrosun solar simulator. These data were analyzed and are shown in Figures 3.6-1 through 3.6-4.

Modelling Without Temperature Coefficients

Ref. 3.6-3 has developed an approach for intensity/temperature ranges from 0.036 solar constant and -160°C cell temperature up to six solar

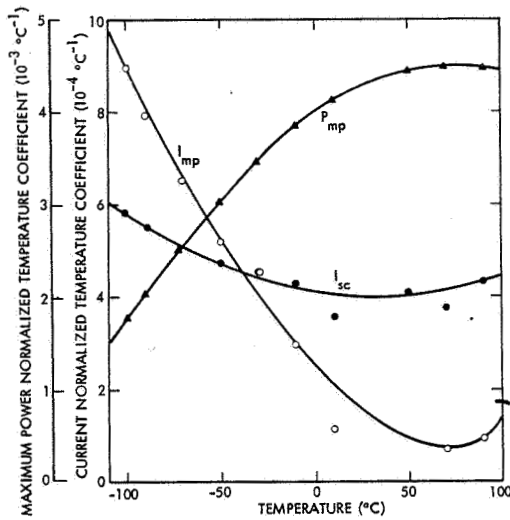


Fig. 3.6-1. Average Temperature Coefficient for I_{sc} , I_{mp} and P_{mp} from T to 28°C Normalized to Conditions at 28°C

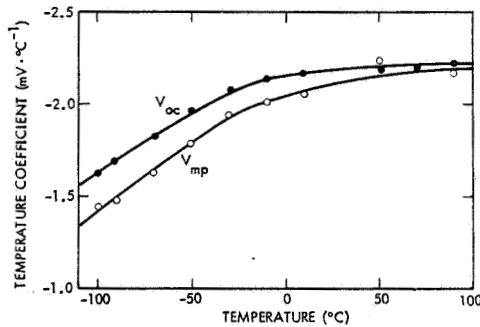


Fig. 3.6-2. Average Temperature Coefficients for V_{mp} and V_{oc} from T to 28°C

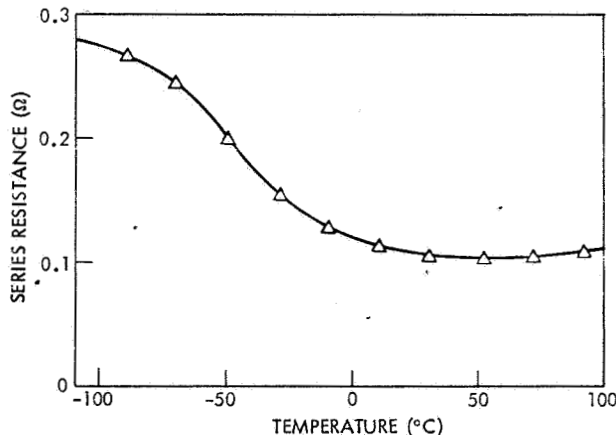


Fig. 3.6-3. Variation of Series Resistance with Temperature

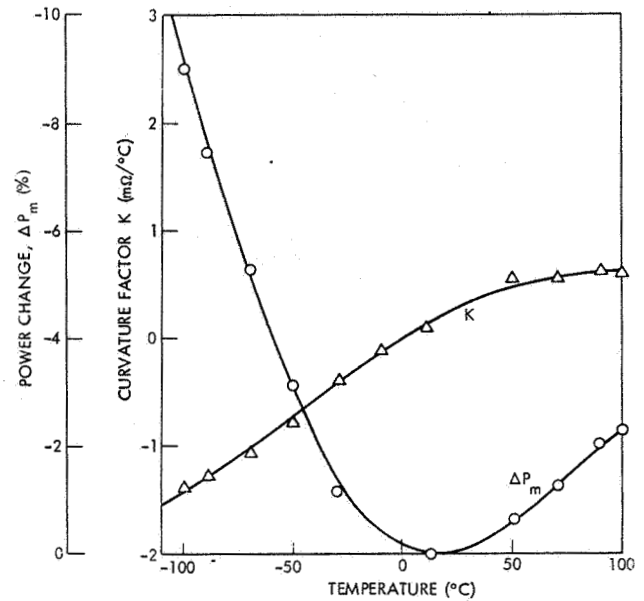


Fig. 3.6-4. Variation of Curvature Factor, K , and Power Change, ΔP_m , with Temperature

constants and 160°C cell temperature. According to this method, I_{sc} and V_{oc} are expressed by fifth-order polynomials which have been curve-fitted to the experimental data. The functions which describe the cell parameters as functions of temperature, T , and solar intensity, H , are

$$I_{sc}(T, H) = C(T)H$$

where

$$C(T) = c_0 + c_1 T + c_2 T^2 + c_3 T^3 + c_4 T^4 + c_5 T^5$$

and similarly for voltage

$$V_{oc}(T, H) = A(T) + B(T) \log_{10} H$$

where

$$A(T) = a_0 + a_1 T + a_2 T^2 + a_3 T^3 + a_4 T^4 + a_5 T^5$$

and

$$B(T) = b_0 + b_1 T + b_2 T^2 + b_3 T^3 + b_4 T^4 + b_5 T^5$$

The numerical values for all of the coefficients a_i , b_i , and c_i were determined with computerized curve-fitting techniques from the experimental data.

3.6.3 Irreversible Changes

At Elevated Temperatures

Exposure of solar cells to elevated temperature may, under certain conditions, lead to permanent electrical and mechanical damage including the following:

- Solution of silver from the cell contacts in solder at temperatures above the solder melting point (see Section 7.1.5), resulting potentially in a reduction of contact pull strength and in electrical output degradation.
- Corrosion of unprotected, nonpassivated Ti-Ag contact solar cells when in the presence of very high humidity for extended periods of time (see Section 2.1) resulting potentially in a reduction of contact pull strength and electrical output degradation.

At Low Temperatures

Exposure of solar cells to low temperature may cause mechanical failures (such as silicon spalling) that are induced by thermomechanical stress (see detailed discussion in Sections 9.7 and 9.8). Failures of solar cells, assembled into an array, may occur when the following conditions exist:

- Temperatures below approximately -100°C .
- Thick solder coatings on cells (generally in excess of 25 to 50 μm).
- Thick layers of adhesive having a relatively large mismatch of coefficient of linear expansion relative to those of silicon and glass (see Chapter 7 and Section 9.7).
- Coverslide and cell-to-substrate adhesives having relatively high glass transition temperatures (see Section 7.11 of Volume II).

3.6.4 Low Temperature, Low-Intensity Operation

Conventional solar cells perform inadequately at low solar intensity and low temperature as would be encountered, for example, during a Jupiter mission (as low as 0.03 solar constant and -120° to -170°C).

This inadequate solar cell performance is due to the fact that only some cells behave as they are predicted to behave while other cells exhibit one or more of the following anomalies (Figure 3.6-5):

- A "rectifying contact" (Schottky barrier)
- A low shunt resistance
- A "double slope" or "double break" I-V curve.

All three of these anomalies are related to the design, construction and fabrication technology of conventional solar cells. Attempts to screen from conventional cells those cells which would operate satisfactorily at low intensity, low temperature conditions have not been successful (Ref. 3.6-4). Therefore, if solar cells were to be used for such missions effectively, special solar cells would need to be developed and fabricated with the appropriate controls (for details see Ref. 3.6-5).

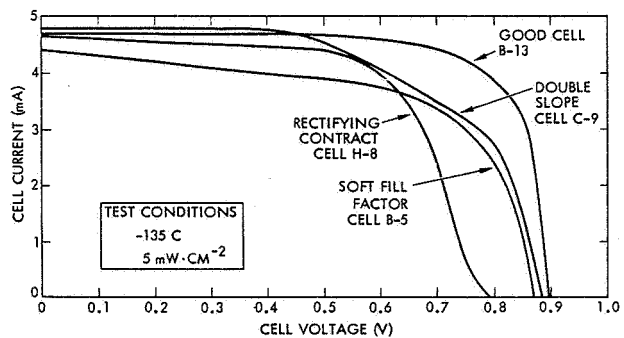


Fig. 3.6-5. Typical Low Temperature, Low Intensity Solar Cell Output Characteristics (Ref. 3.6-5)

3.7 REVERSE-BIASED SOLAR CELLS

3.7.1 Cause for Reverse Bias

A solar cell within an array of cells may become reverse biased when it fractures, becomes shadowed, or degrades more rapidly than other solar cells in the same electrical circuit. A necessary condition for a cell to become reverse biased is that a current must flow (in the normal forward direction) through a solar cell array circuit and that a cell (or parallel-connected group of cells) in that circuit limits the current flow. A reverse bias (defined in Section 3.2.1) then develops across the current-limiting cell (or group of cells), as described in Section 9.1.6.

The magnitude of the reverse voltage increases when the available driving voltage and driving current increase and when the limit-current passed by the cell (or group of cells) decreases. Typical conditions which increase the potentially occurring reverse biasing of solar cells are as follows:

- High-voltage solar cell arrays (i. e., relatively large numbers of solar cells connected in series).
- Array loading at or near short-circuit current (the voltage available for reverse bias is limited by the difference between the solar cell circuit open-circuit voltage and the array load voltage, as described in Section 9.1.6).
- Array loading at normal bus voltage when the array temperature is abnormally low (such as after exit from an eclipse).

3.7.2 Silicon Solar Cell Reverse Characteristics

When compared with other silicon p-n junction devices, such as rectifiers, silicon solar cells generally exhibit large reverse leakage currents per unit junction area even at relatively low voltages. Under test, the reverse current-voltage characteristics are frequently unstable and not repeatable for reverse voltages exceeding about 5 volts (Ref. 3.7-1).

The solar cell reverse characteristics are typically not controlled during the cell manufacturing process except that they are occasionally monitored for certain process control activities. The design of contemporary silicon solar cells is such that the exposed p-n junction area around the perimeter of the cell is totally unprotected and subject to surface contamination, ion migration, moisture accumulation, and other surface effects. The close proximity of the metallic n-contact to the junction adds another source for potential contamination.

The solar cell reverse characteristics are symbolically represented by the cell's shunt resistance as discussed in Section 3.2.4.

3.7.3 Effects of Reverse Bias on Silicon Solar Cells

Reverse-biased solar cells may be subject to the following:

- Rapid and excessive heating
- Slight, permanent power output loss
- Permanent short-circuit failure.

Cell Heating

The rate at which reverse-biased solar cells heat up, as well as the upper temperature limits they may attain, depends primarily upon the magnitude of the reverse voltage, current flow, thermal mass, and lateral thermal conductivity of the array. Solder melting temperatures can be reached in a few minutes on 30-volt arrays, for example, under certain conditions (see Section 9.1.6).

Cell Output Loss

A slight amount of cell power output (less than 1 percent) may be lost permanently as a result of subjecting solar cells to reverse voltages exceeding 15 volts for some period of time (12 minutes), according to Ref. 3.7-1.

Permanent Short-Circuit Failure

Some silicon solar cells may permanently short when exposed to a combination of high temperature, high reverse bias, and high power dissipation. Test results (Ref. 3.7-1) of conventional n-p, 2-ohm-cm cells of 2 by 4 cm size and 0.36-mm thickness, believed to be applicable to all currently available planar silicon solar cell types, have shown that all of the following stress conditions must exist simultaneously for cells to fail:

- Cell reverse bias greater than 20 volts
- Cell current greater than 0.2 ampere
- Cell dissipation greater than 4 watts
- Cell temperature above -120°C
- Stress conditions to prevail for some length of time (at 125°C cell temperature, 50 percent of all failed cells failed after 1-minute exposure).

3.8 MECHANICAL CHARACTERISTICS

3.8.1 Cell Sizes

Older Sizes: 2 x 0.5 cm
2 x 1 cm
1 x 2 cm

Current Sizes: 2 x 2 cm
2 x 4 cm
2 x 6 cm

Sizes up to 4 x 10 cm have been made experimentally. Smaller quantities of 1 x 1 cm, 2 x 3 cm, and 3 x 3 cm also have been produced; 2 x 6 cm is the largest currently practical size. Frequently, "nominally" 2 x 4 cm and 2 x 6 cm size cells are actually cut to 2 x 4.1 and 2 x 6.2 cm size. This "oversizing" in the long direction (i. e., electrically in the parallel direction) permits the direct use of either a larger number of smaller cells or a smaller number of larger cells connected in parallel for a particular solar cell layout drawing without having to change the drawing. The "oversized" 2 x 6.2 cm cell, for example, has the same "width" as three 2 x 2 cm cells plus two intercell gaps. The electrical output of "oversized" cells either may be equivalent to the output of the number of 2 x 2 cm cells which they can replace, or it may be greater (usually at a higher cost) by the ratio of the increased active cell area (typically 2 to 4 percent greater).

The relative solar cell sizes are illustrated in Figure 3.8-1.

3.8.2 Cell Thicknesses

Older Thicknesses: 0.50 mm (0.020 inch)
0.36 mm (0.014 inch)

Recent Thicknesses: 0.30 mm (0.012 inch)
0.25 mm (0.010 inch)
0.20 mm (0.008 inch)

Thicknesses down to 0.08 mm (0.003 inch) have been made experimentally; 0.20 mm thick cells are the thinnest currently practical cells, 0.25 mm thick cells have been used in quantities exceeding 0.5 million units.

3.8.3 Size/Thickness/Cost Tradeoffs

Increasing the size of solar cells provides an advantage to the array assembler in that the latter has to handle fewer parts for the same power level array. The solar cell manufacturer also saves some mechanical cutting time, but has a greater attrition during cell fabrication. The ultimate size of a cell which can be fabricated depends upon the largest diameter and greatest length of a silicon ingot which can be grown and cut into wafers with the equipment on hand.

The solar cell array designer will have increasing difficulties both with thermal expansion mismatches between the larger cells and the substrate, and with developing satisfactory cell interconnector systems (see Section 5.3).

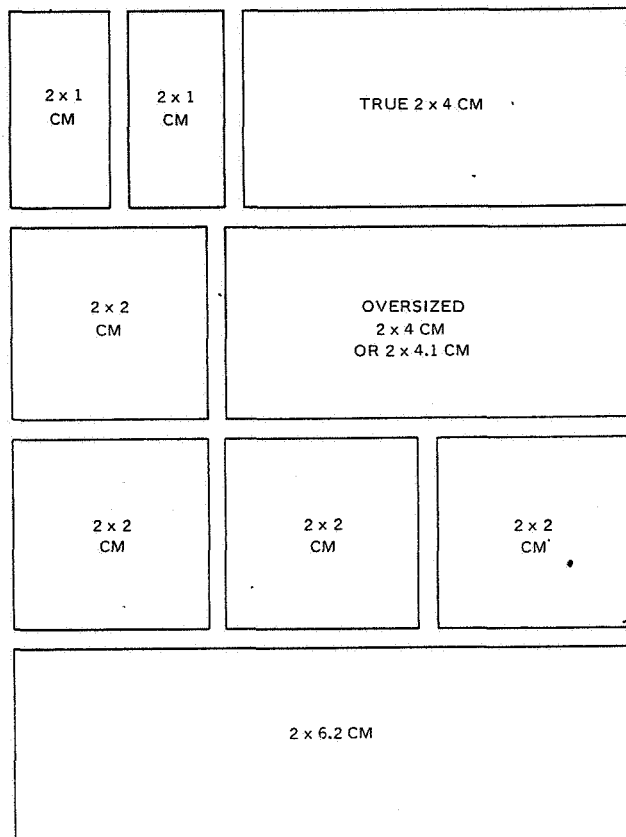


Fig. 3.8-1. Solar Cell Sizes (Relative)

Breakage and, therefore, unit cost generally increases as cell thickness is reduced and the cell size is increased. However, proper handling techniques can most likely be developed to handle very thin or very large solar cells.

Large area cells tend to bow due to internal stresses. During array assembly this bowing can cause difficulties in controlling the uniformity and thickness of both the coverslide adhesive and the cell-to-substrate adhesive. Bowing of cells is one of the reasons that 2 x 6 cm cells are currently the largest practical cells.

3.8.4 Active Area

The solar cell's active area, A_c , is the light-sensitive area of a solar cell which is always smaller than the junction area of a planar cell. Some of the junction area, by necessity, is covered with electrical contacts and so-called "gridlines" or "fingers" which aid in the electrical power collection from the illuminated active cell areas. The quoted efficiency of solar cells is not a unique number in that sometimes it is calculated based on the total overall cell area (4cm^2

for a 2 x 2 cm cell), while at other times it is based on only the net active, non-contact-bearing solar cell front area (3.7 cm² for a 2 x 2 cm cell). In most cases, however, it is based on the so-called "active" area including the gridlines but excluding the n-contact bar (3.8 cm² for a 2 x 2 cm cell). To avoid such ambiguity, solar cell output should be quoted in terms of actual output power at a given cell temperature, light intensity and spectrum, such as "50 mW at 28°C, one solar constant, AMO (Air Mass Zero)," for example.

The output of solar cells changes as both the active and the total area is changed. The parameters I_{sc} , P_{mp} , and I_{mp} (see definitions in Section 3.2.2) increase very nearly proportionately with an increase in active area, while V_{mp} and V_{oc} remain very nearly constant. Small deviations from true proportionality occur because the active solar cell area is in practice shunted by two electrical paths: a nonilluminated forward-biased diode path under the cell contact areas on the front (active) side, and a leakage path through the shunt resistance.

3.9 CONTACTS

3.9.1 Contact Configurations

Ohmic Contacts

The purpose of the metallic contacts on the semiconductor elements of solar cells is to facilitate:

- The collection of carriers (electrons and holes, see Section 3.11.1)
- Attachment of conductors for electrical cell interconnections.

To minimize internal electrical losses in the cell, the electrical resistance of the cell contacts should be low, the electrical resistance of the semiconductor-to-contact interface should be low, and the semiconductor-to-contact interface should not form a junction (known as a Schottky barrier; defined in Section 1.2). Contacts that are free of Schottky barriers have the same linear current-voltage characteristics in either direction of current flow, i. e., they are "purely ohmic." On some cells, Schottky barriers become noticeable only at low temperatures (see Section 3.6.4).

The term "ohmic contact" or simply "ohmic" is frequently used to describe the upper contact bar (but not the gridlines) of "gridded" solar cells. Sometimes, but less frequently, the back contact is also referred to as an "ohmic." In this usage connotation, there exists no relationship to the electrical properties discussed above.

Solar cell contact geometries differ from type to type and from one cell manufacturer to another. Each contact type provides advantages and disadvantages during the array assembly. Full-area contacts extend to the cell edge, while "picture frame" contacts are slightly smaller than the cell area and expose active cell area all around the contact bar. Wrap-around contact cells have both the p- and n-contacts on their back sides to maximize the active cell area and ease assembly. Fig. 3.9-1 shows some typical contact configurations.

3.9.2 Contact Metallization

The contacts currently in use on silicon solar cells are deposited titanium/silver layers. The titanium, deposited first on the well-cleaned silicon surface, is typically 0.1 μm thick. The following silver layer is typically 3 to 5 μm thick.

Titanium/silver contacts are sensitive to humidity (see Section 2.1.6) and require protection therefrom. Humidity protection can be obtained by a thin, typically 20 to 50 nm thick palladium interlayer between the silver and the titanium. This palladium layer has been found to passivate the contacts and gridlines. A thin, soft solder coating of at least 2 μm thickness also protects the contacts and gridlines from humidity. Solar cell antireflective coatings such as SiO_x do not provide significant protection from humidity.

3.9.3 Solder Coverage

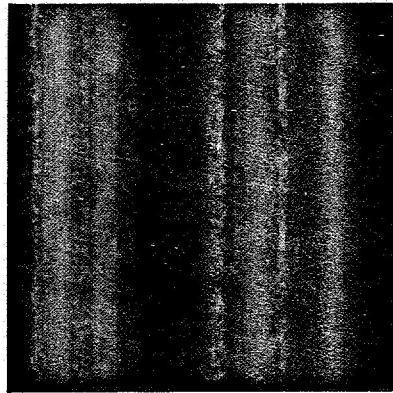
Cell contacts are delivered either solder free or solder covered. Solder covered contacts may be "dipped" or "pressed." Dipped solder is typically 75- μm thick on the average. It forms a meniscus when molten and freezes with the solder thickness peaking at about 150 μm . Machine or hand pressing of the solder-covered contacts at temperatures above solder melting squeezes out solder. Different solder thicknesses can be obtained, but thickness control is difficult. A cleanup process to remove solder flash may also be required. (Solder thickness control may be required for low temperature operation, low energy proton protection, and assembly convenience.)

3.9.4 Contact Integrity

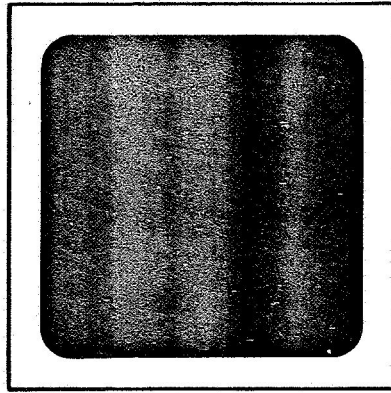
Contact strength is defined as the capability of metallizations (i. e., contacts) to adhere to the silicon solar cell wafer. The purpose of these metallic contacts is two-fold: (a) to establish permanent, low electrical loss interfaces between metallic circuit conductors and the semiconducting silicon, and (b) to provide convenient areas to which solar cell interconnectors can be attached.

High mechanical contact strength is not necessarily synonymous with good electrical properties of the contact, but, in most cases, tests of contact strengths permit assessment of potential solar cell problems which, in turn, can negatively influence the solar cell array assembly processes and the array performance in space. For this reason, solar cell contact pull-strength tests have become one of the most important tests (next to electrical output testing) for monitoring and assuring adequate solar cell and array quality.

Contact strength is measured in two ways: (a) during the cell manufacturing cycle, vacuum-deposited metallizations are tape-peel tested, and (b) after the cell manufacture has been completed, pull-strength tests are performed. For pull-strength testing, wires or ribbons are soldered or welded to the cell contacts and a force is applied to separate the wires or ribbons from the cell. The direction of application of this pull force relative to the cell surface ranges from 0 degrees (shear loading) to 90 degrees (peel loading for thin wires and ribbons, or tensile loading for thick wires and ribbons). A 45-degree pull test is believed to cause the most realistic mixture of shear and peel loading of soldered joints, simulating actual stresses of interconnectors on solar cells in orbit. At any rate, a good correlation between the actual stresses on the cell contacts when assembled in a solar cell array and the stresses imposed by pull test methods has not been reported, and actual pull-strength requirements have not been established. The practice has been to maximize the solar cell contact strength during the solar cell manufacturing process and, for array assembly quality assurance purposes, to establish certain minimum strength requirements using specific test methods and procedures. These test methods usually have meaning only in the context for which they were established. As a consequence of this, most pull test data are presented in the literature

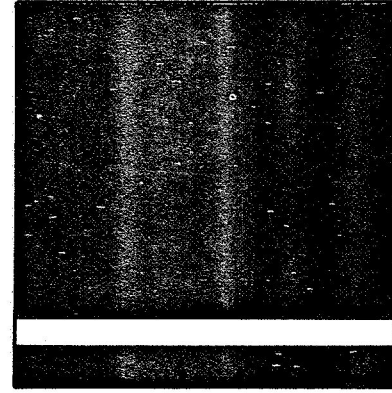


FULL CONTACT



PICTURE FRAME CONTACT

BACK
(P)

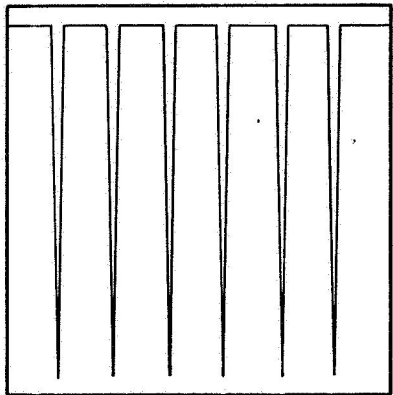


P-CONTACT

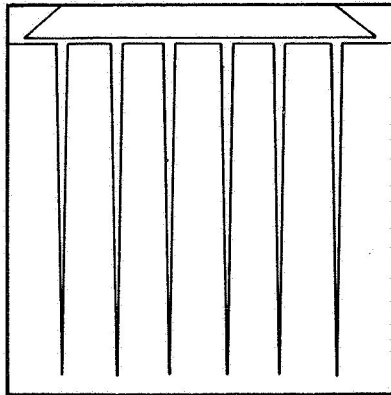
ETCHED STRIP
SEPARATING
P AND N

WRAPAROUND
N-CONTACT

N-LAYER GRIDLINES
WRAP AROUND CELL
EDGE TO N-CONTACT
ON BACK SIDE

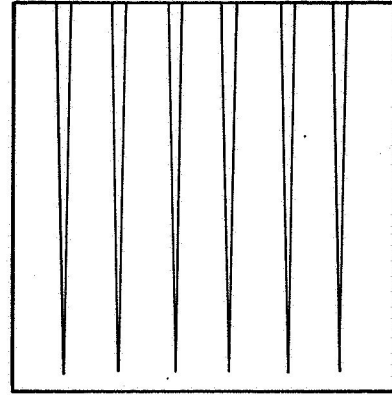


BAR CONTACT



CORNER DART CONTACT

FRONT
(N)



(a) FRONT-BACK CONTACTS

(b) WRAPAROUND CONTACT

Fig. 3.9-1. Some Solar Cell Contact Configurations

in units of force rather than force per unit area, and the size of the bond area is usually not stated. This is justifiable because in most practical tests a reasonably uniform contact loading cannot be achieved. The factors which can affect the contact pull strength are presented in Table 3.9-1.

Table 3.9-1. Factors Influencing Contact Pull Strength

Soldered Joints	Welded Joints
Solder joint area	Weld nugget area
Solder thickness on contact	Metallization thickness on contact weld nugget area
Solder fillet cross section	Ribbon thickness, ductility, and stiffness
Wire or ribbon thickness and stiffness	Ribbon surface roughness and plating thickness
Angle and rate of pull force	Angle and rate of pull force
	Surface roughness of silicon wafer underneath weld area

The true contact strength of solderless welded joints is very difficult to measure in that even small bending moments applied by the interconnector to the typically very small weld nugget in many cases causes the tensile strength of the silicon to be exceeded and the silicon to spall. For this reason, shear loading of the contacts leads to a more realistic contact integrity assessment.

3.9.5 Effects of Temperature on Contact Integrity

The contact pull test strength varies with temperature. This phenomenon is of interest because most solar cell arrays operate at temperatures other than room temperature, and the stresses and material properties under actual operating conditions may be quite different from those observed in near room-temperature pull strength testing. It was found that the 90-degree pull strength is greatest between 0° and -100°C and falls off rapidly below -100°C and above 0°C (Figure 3.9-2). The falloff at higher temperatures is expected due to a reduction in the strength of solder. The falloff at lower temperatures is also expected, but is due to an increase in the strength of solder and associated prestressing of the silicon. This thermally induced prestress reduces the silicon's capability to support external tensile loads and leads predominantly to silicon spalling during pull testing.

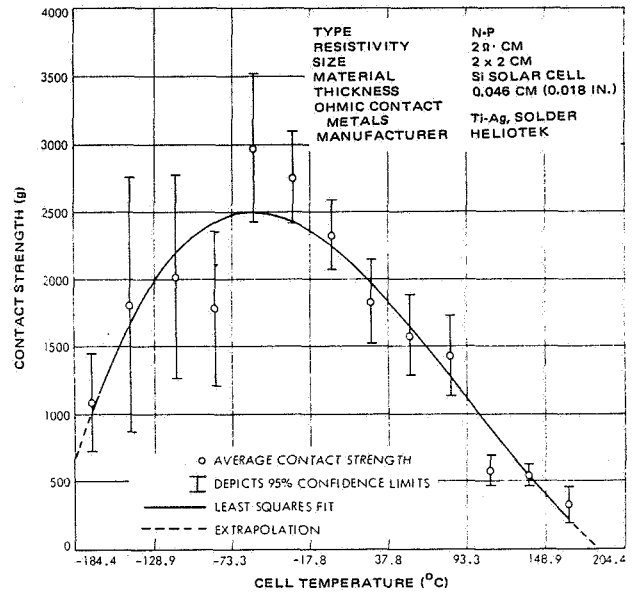
3.9.6 Contact Surface Roughness

Certain solderless solar cell interconnector bonding operations require a certain smoothness of the contact metallization, the underlying silicon surface, the interconnector material, and the interconnector plating (if a plating is used). The degree of the required smoothness depends upon the following (not in order of importance):

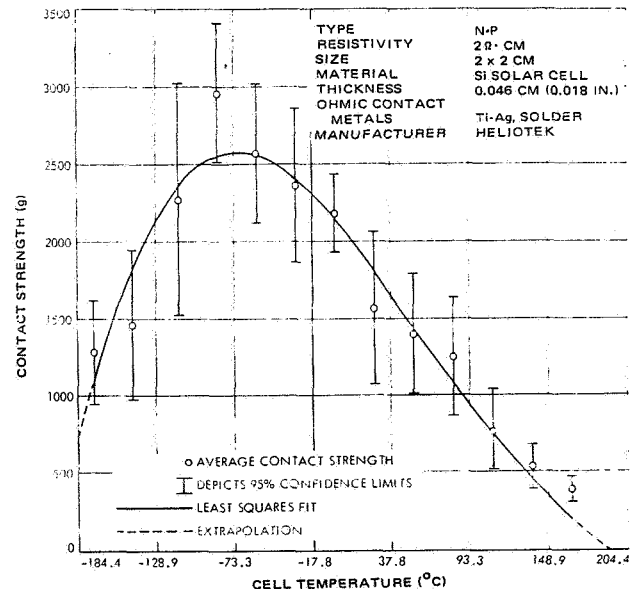
- Stiffness of cell interconnector
- "Footprint" area of bonding tool

- Bonding method
- Bonding schedule (bonding parameters)
- Amount of soft metal available to fill crevices in the parts to be bonded.

Various solderless interconnector bonding techniques are discussed in Section 10.4.2; however, the surface finish currently believed to be required for parallel-gap resistance welding of Ti-Ag and Ti-Pd-Ag contacts is 0.4 μm rms or better (see Section 10.4.2).



(a) N-CONTACT STRENGTH (90-DEGREE PULL)



(b) P-CONTACT STRENGTH (90-DEGREE PULL)

Fig. 3.9-2. Contact Pull Strength of Solder-Coated Titanium-Silver Contact n-on-p Solar Cells as a Function of Temperature (Ref. 3.9-1)

3.10 OPTICAL CHARACTERISTICS

The optical and thermo-optical characteristics of solar cells in an array are determined in part by the cells and in part by the coverslide. Since many of the optical characteristics of glassed solar cells are not readily separable into independent cover and cell characteristics, the detailed discussion of these interdependent characteristics is given in Section 4.3. Only those cell characteristics that are independent of the coverslide are discussed in the following sections.

3.10.1 Front Surface Finish

Solar cells come with different front (light-sensitive) surface finishes. Some surface finishes are related to certain solar cell design requirements of high-efficiency cells, while others are related only to specific solar cell processing steps. Typical front surface finishes are as follows:

- Polished—mirror-like finish, high reflectance
- Mat—smooth finish, medium reflectance
- Rough—special etching process produces a textured, serrated surface of very low reflectance

The magnitude of the visually observed front surface reflectance, however, is not necessarily directly related to relatively high cell output (see Section 4.3) because the surface finish (being related to mechanical defects of the crystal lattice) also influences both the cell's energy conversion efficiency and the cell's series resistance (diffused layer sheath resistance). Rough surface cells are a relatively new family of high efficiency cells. These cells are discussed further in Sections 1.2 and 3.1.1.

Effects of Rough Surfaces

The front surface reflectance does generally affect the solar absorptance (see Section 7.13 for definition) and thereby the cell operating temperature in space. High-efficiency "black" and "textured" surface cells tend to operate at slightly higher equilibrium temperatures in space than the more polished cells do, and thereby may lose some of the efficiency gain that these cells show when compared to other cells at the same (test) temperature.

3.10.2 Antireflective Coatings

The purpose of antireflective coatings on the front, active surface of solar cells is to minimize reflection losses at the interface between the coverslide adhesive and the silicon wafer (see Section 4.3).

Antireflective coatings are typically oxides that are vapor-deposited or sputtered onto the silicon cells. Since these coatings are usually hard and dielectric, their deposition over metallic contact areas should be prevented where solar cell interconnectors are to be welded or soldered. Control of antireflective coatings is typically achieved via a mechanical drawing attached to the solar cell specification (Section 10.9).

Antireflective coatings are generally too porous to protect Ti-Ag contacts from corroding in high-humidity, high-temperature environments (see also Section 2.1.6).

3.10.3 Spectral Response Defined

Solar cell spectral response curves appear in various forms in the literature. The cell output may be shown relative to:

- The energy falling onto the cell (constant energy input versus wavelength)
- The number of photons incident on the cell (constant number of photons versus wavelength).

The cell output may be shown as a function of

- Wavelength (λ)
- Light frequency (f or $\omega = 2\pi f$)
- Wave number ($N = \lambda^{-1}$ or $2\pi \cdot \lambda^{-1}$)
- Photon energy

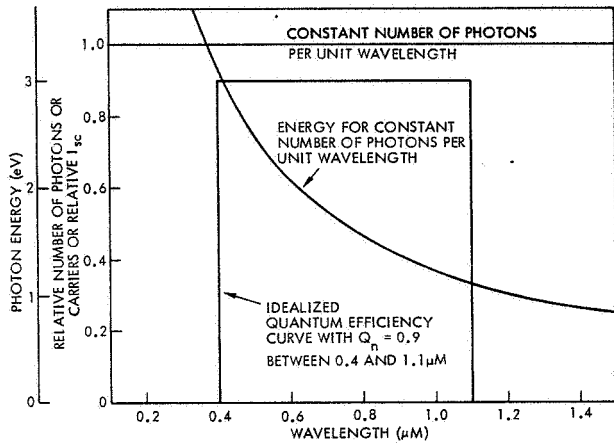
The spectral response curve of interest to array design engineers is the cell output relative to constant energy input at all wavelengths. The cell output measured in an experimental setup is typically the I_{sc} , while the energy input is measured with a radiometer-type of instrument. Radiometers (such as thermocouples or thermopiles) measure the product of the incident number of photons per unit time and per unit area, and the energy of the incident photons. The solar cell I_{sc} output (in amperes) represents the number of minority carriers per unit time collected from the cell area.

A spectral response curve relative to constant numbers of incident photons for all wavelengths is of special interest in solar cell device development. Such spectral response curves are frequently called quantum efficiency or collection efficiency curves. The nomenclature used by different authors is not uniform; however, the tendency is as follows:

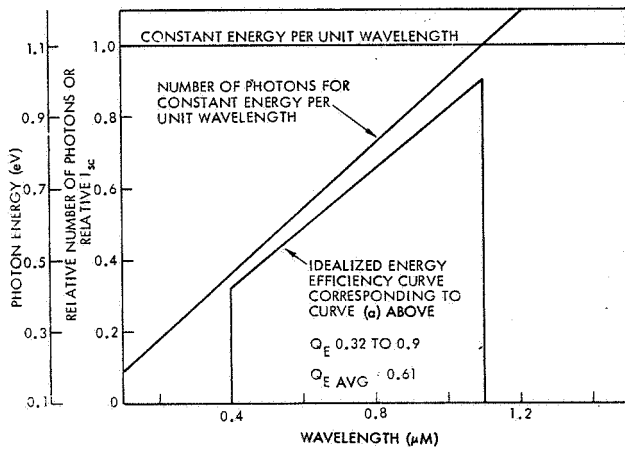
- Quantum efficiency denotes the number of electron-hole pairs or minority carriers created per photon (having an energy greater than 1.1 eV for silicon cells) incident on the cell or per photon absorbed in the silicon.
- Collection efficiency denotes the number of minority carriers collected by the junction per photon incident on the cell, or per photon absorbed in the silicon, or per photon absorbed in a specified region in the cell.

The conversion of constant-number-of-photon spectral response curves into constant-energy curves is illustrated in Figure 3.10-1. This figure shows highly idealized spectral response curves of a silicon cell covered with a filter having 0.4 μm cut-on wavelength. To convert the curve of Figure 3.10-1A into

that of Figure 3.10-1B, the value of the cell output at each wavelength is simply divided by the photon energy corresponding to that wavelength. Thereafter, the newly obtained curve is scaled to some convenient vertical scale (usually the peak of the response curve is normalized to 100 percent). Figure 3.10-2 can be used to find the relationship between photon energy, wavelength, and wave number. The relationship between wavelength and light frequency is given in Section 2.4.3.



(a)

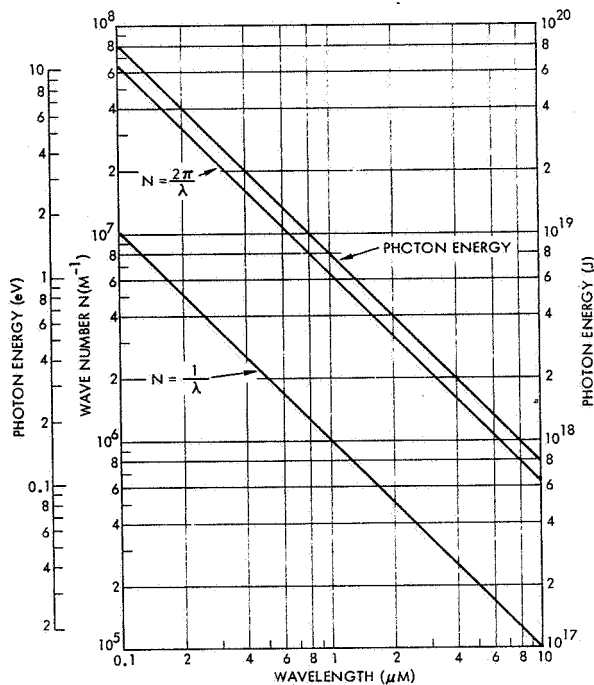


(b)

Fig. 3.10-1. Idealized Spectral Response Curves of a Glassed Silicon Solar Cell (Cut-on Wavelength 0.4 μm ; Energy Gap 1.1 eV Corresponding to 1.1 μm Wavelength) for (a) Constant Number of Photons Per Unit Wavelength Input and (b) Constant Energy Per Unit Wavelength Input

3.10.4 Spectral Response of Solar Cells

The sensitivity of single-crystal planar junction silicon solar cells ranges from approximately 0.3 to 1.2 μm . In general, solar cell spectral response characteristics depend heavily on solar cell design, construction, material properties, and optical coatings. Solar cells for space use are practically never used without any filters or covers which further modify the cell response. The solar cell spectral response changes with both temperature and radiation



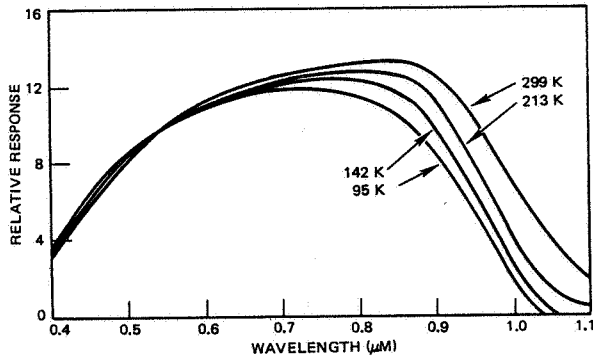
Applicable unit conversion factors are:		
Multiply	by	to obtain
J (joules)	6.25×10^{18}	eV (electron volts)
eV	1.6×10^{-19}	J
μm	10,000	\AA (Angstrom units)

Fig. 3.10-2. Relationships Between Wavelength, Wave Number, and Photon Energy

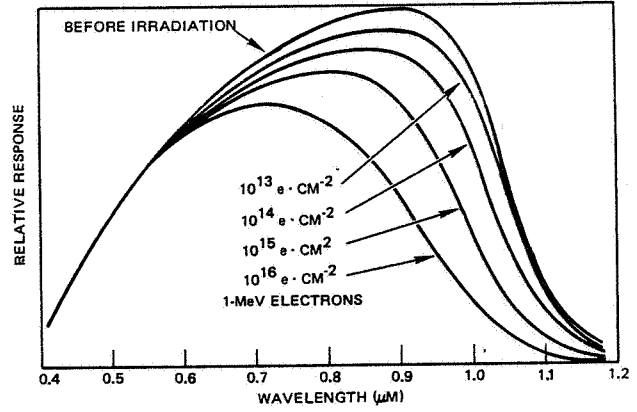
damage. With increasing temperature, the red response increases while the blue response remains approximately constant. This increase in red response is due to both a shift in the "absorption edge" of the silicon around 1.1 μm toward longer wavelengths (below 1.0 μm wavelength the silicon is absorbent and above 1.2 μm the silicon is transparent) and an increase in the minority carrier lifetime. The increase in red response results in the observed increase in I_{sc} with increasing temperature (Figure 3.10-3a).

Corpuscular radiation degrades the red response of cells (Figure 3.10-3b). The extent of degradation depends upon the particle species and energy. This phenomenon is related to the defect centers introduced into the crystal lattice by the radiation, which, in turn, lowers the mean diffusion length of the minority carriers. As a consequence of this, the electron-hole pairs created by "red light" photons further away from the junction than the diffusion length are no longer collected.

Similarly, red response is lost when the cell base width (i.e., cell thickness) is made equal to or smaller than the mean diffusion length (Figure 3.10-3c). However, after appreciable corpuscular radiation damage when the degraded diffusion length is less than the base width, thick and thin cells have the same output (everything else being constant).

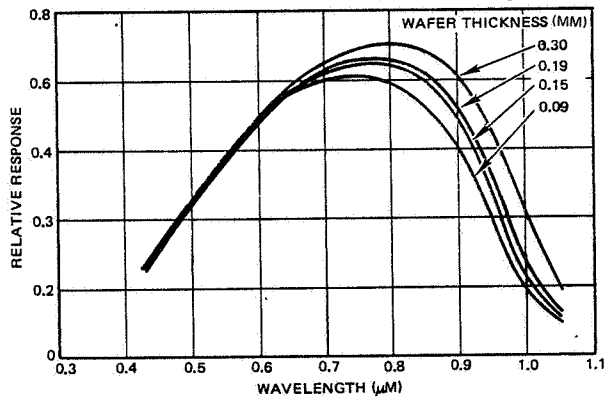


(a) CHANGES WITH TEMPERATURE (BASED ON REF. 3.10-1)



(b) CHANGES WITH PARTICULATE RADIATION (BASED ON REF 3.10-2)

From Ref. 3.10-3. Reprinted with permission of the American Society of Mechanical Engineers.



(c) CHANGES WITH CELL THICKNESS (BASED ON REF. 3.10-3)

Figure 3.10-3. Changes in the Spectral Response Characteristics (Illustrative Examples)

3.11 THEORETICAL SOLAR CELL MODELS

Theoretical models of the solar cell are derived from solid-state physics theory. Such derivations are lengthy and result in models which are especially useful for the solar cell researcher (see Refs. 3.11-1 through 3.11-3). Since practicing solar cell array engineers are usually not so much interested in solid state theory but want to know "how a solar cell works," the essential elements of the derivation of a solar cell mathematical model and the associated semiconductor terminology are illustrated below.

In Section 9.2, the theoretical solar cell model is expanded into several practical models which form the basis for computerized solar cell array performance prediction methods.

3.11.1 DC Model Theory

The starting point for the derivation of the solar cell model is an idealized, nonilluminated piece of semiconductor material containing a p-n junction as depicted schematically in Figure 3.11-1a. For a silicon solar cell both the p-side and the n-side consisted originally of so-called intrinsic silicon, a Group IV element in the periodic chart of elements which has four electrons in its outer shell. During the silicon crystal growing process the p-material was created by adding a relatively small quantity of a Group III element such as boron to the melt. The addition of the Group III element to the melt is called "doping" with an "acceptor" or "p-type" impurity. The atoms of a Group III impurity locate themselves by substitution into the regular arrangement of silicon atoms within the crystal "lattice" structure. The Group III atoms have three electrons in their outer shell, thus they need one more electron to share with the four valence electrons for silicon. Therefore, they behave electrically as immobile negative acceptor ions which capture (accept) originally free electrons, i.e., they have produced "holes" somewhere else in the lattice.

The n-side (Figure 3.11-1a) was created during the "junction formation" or "diffusion" process. During this process slices of p-type silicon material (solar cell wafers) were exposed at elevated temperatures to an environment containing a Group V element such as phosphorous. These Group V atoms, called "donor" or "n-type" impurities, diffuse into the surface and substitute themselves into the silicon lattice and, because of their higher concentration, "overdope" the already present p-type impurity. Because Group V atoms possess five electrons in their outer shell, they "donate" an electron and thereby become immobile positive donor ions after their electrons are lost.

The changeover from p-type to n-type material occurs in the less than 1- μ m thick "transition" region or "transition zone." The "p-n junction," an idealized electrical concept which does not directly represent the physical change from p-type to n-type material, actually is located somewhere in the volume (cross-sectional area in Figure 3-11-1a) enclosing the transition region.

At temperatures above 0 K thermal agitation of the atomic lattice structure generates mobile (i.e., "free") electrons and holes in both the p-type and n-type material. These free electrons and holes move through the material in random fashion. Due to the effects of doping with impurities, the concentration of free holes in the p-material, p_p , is much greater than the concentration in the n-material, p_n , and the concentration of free electrons in the n-material, n_n , is much greater than in the p-material, n_p (Figure 3.11-1b). Consequently, the holes in the p-material and the electrons in the n-material are called "majority carriers" and the holes in the n-material and the electrons in the p-material are called "minority carriers." The operation of p-n junction diodes and solar cells depends upon the behavior of the minority carriers; hence, such devices are "minority carrier devices."

Because there is an excess of "carriers" (i.e., holes or electrons) on either side of the transition region (Figure 3.11-1b), there exists a hole density gradient, dp/dx , across the transition region which tends to cause holes to "diffuse" from the p-region into the n-region. Similarly, an electron density gradient, dn/dx , tends to diffuse electrons from the n-material into the p-region. The "diffusion currents" (actually current densities) J_p and J_n , for holes and electrons respectively, are of the magnitude

$$J_p = -eD_p \frac{dp}{dx} \text{ and } J_n = eD_n \frac{dn}{dx} \text{ A/m}^2$$

where e is the electronic charge and D_p and D_n are the diffusion constants (material properties) for holes, p , and electrons, n , respectively. (The minus sign indicates flow to the left in Figure 3.11-1.)

The actual concentration of holes in the n-material, as well as the concentration of electrons in the p-material decreases with increasing distance from the transition region, as shown in Figure 3.11-1c due to a "recombination" process consisting of "electrons falling into holes." The time period between the instant of "injection" of a carrier into a type of material where it is a minority carrier and the instant it recombines with a majority carrier is called the "minority carrier lifetime"; the distance it travels between injection and recombination is called its "diffusion length." Lifetime, τ , and diffusion length, L , are related by

$$L_p = \sqrt{D_p \tau_p} \text{ and } L_n = \sqrt{D_n \tau_n}$$

where D_p and D_n are the diffusion constants for the holes and electrons, respectively.

In solar cells the important process is to "inject" minority carriers by utilizing the energy of incident photons (sunlight) to "create electron-hole pairs" and to "collect" the minority carriers. The number of

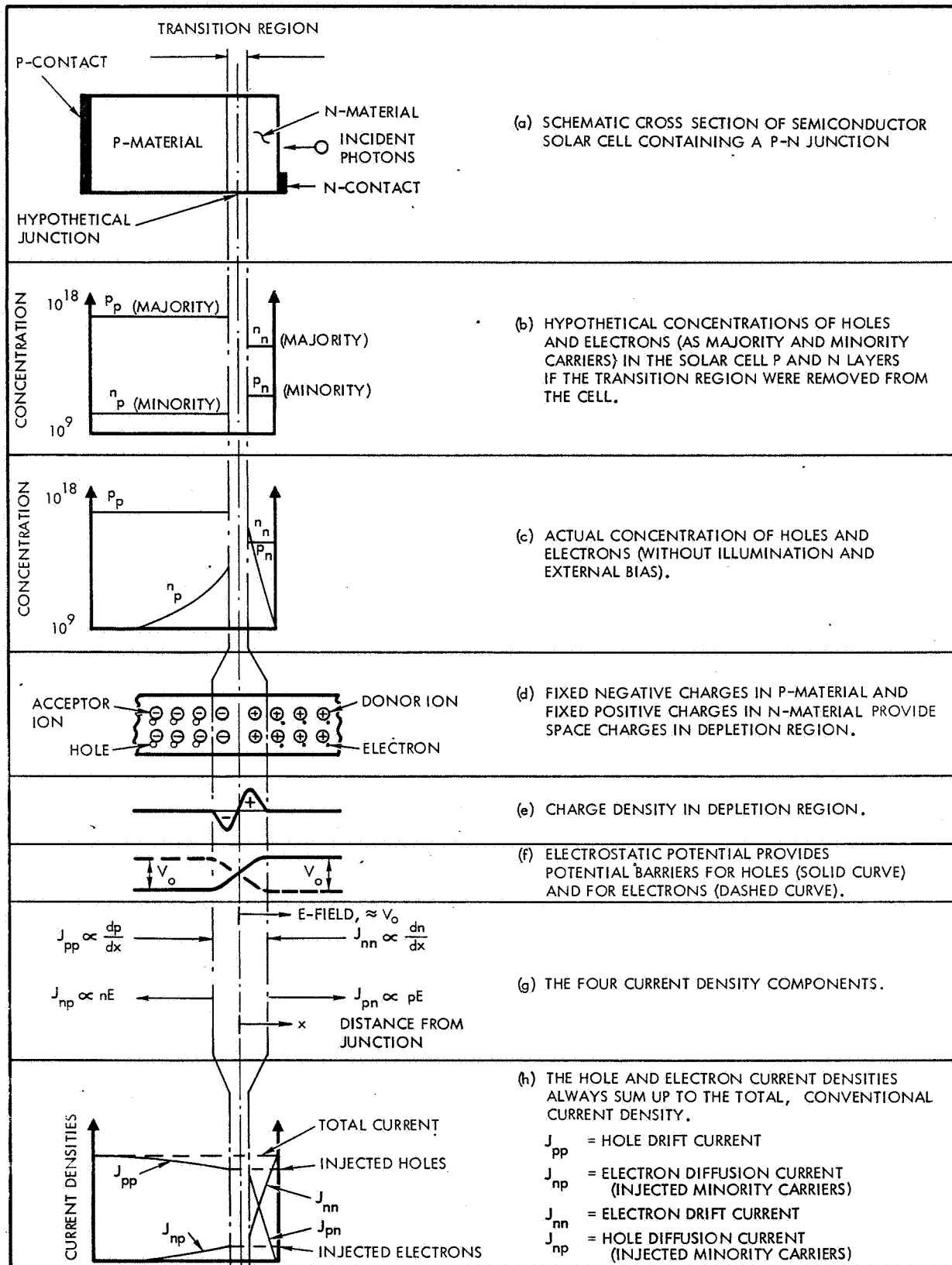


Fig. 3.11-1. Schematic Diagrams of the Properties of Solar Cell p-n Junctions

incident photons per unit area and time (i. e., the light intensity) is referred to as the "injection level,"

As a result of the diffusion currents across the transition region, the high concentration of free electrons coming from the n-region provides great opportunity for recombination with holes associated with the acceptor atoms in the p-material. Conversely, the holes coming from the p-material recombine with electrons in the n-material. As a consequence of this recombination process in the transition "space," the donor and acceptor ions are "depleted" of free electrons and holes. Hence, the transition region is also called the "space charge" region or the "depletion" region (Figure 3.11-1d). The electric "charges" of the immobile ions in the depletion region provide an electrostatic potential which opposes the diffusion currents. This electrostatic potential, V_o , called the "potential barrier," in turn causes holes to "drift" from the n-material to the p-material and electrons in the opposite direction (Figure 3.11-1f). This is to be expected because a piece of matter in equilibrium with its environment must have charge neutrality. The "drift current" (in opposite direction to the diffusion current) for electrons (n) and holes (p), respectively, is

$$J_n = ne\mu_n V_o \quad \text{and} \quad J_p = pe\mu_p V_o$$

where μ is the "mobility" of electrons and holes, respectively. The mobilities are material constants and are related to the diffusion constants by the Einstein equation

$$\frac{D_p}{\mu_p} = \frac{D_n}{\mu_n} = \frac{kT}{e}$$

where k is Boltzmann's gas constant, T is the absolute temperature and e is the electronic charge.

The dynamic equilibrium of diffusion and drift of holes and electrons at any time, t , and at any distance, x , from the hypothetical p-n junction must satisfy the principle of conservation of charge (Figure 3.11-1g). This principle is expressed by the "equation of conservation of charge" or the "continuity equation" as follows for holes in the n-region (a similar equation can be written for electrons in the p-material)

$$\frac{\partial p_n(x)}{\partial t} = \frac{p_n(x) - p_{no}}{\tau_p} + D_p \frac{\partial^2 p_n(x)}{\partial x^2} - \mu_p \frac{\partial \{p_n(x)V_o\}}{\partial x}$$

This equation states that the increase in minority carrier hole concentration in the n-material due to all processes at a distance x with time t (the left term of the equation) equals the externally injected hole concentration (due to bias or exposure to light) in addition to the thermal equilibrium concentration, p_{no} , (the first term on the right-hand side) plus the contributions from the diffusion and drift currents (the second and third term on the right-hand side, respectively).

The solution of the continuity equation (nonilluminated case) requires two boundary conditions. One boundary condition is that the injected hole concentration decreases away from the junction of $p_n(x) \rightarrow 0$ as $x \rightarrow \infty$. For the other boundary condition it can be shown that the hole concentration $p_n(0)$ at the junction (i. e.,

at $x = 0$) depends upon the thermal equilibrium (minority carrier) hole concentration p_{no} and the externally applied voltage, V , by the relationship

$$p_n(0) = p_{no} \exp \frac{eV}{kT}$$

This equation and a similar one for electrons are the key equations in rectifier theory. Using both of the above boundary conditions in the solution of the continuity equation and applying the fact that the total, conventional current through the device must be constant at any distance x , the diode equation (dc case) results.

$$J = J_o \left(\exp \frac{eV}{kT} - 1 \right)$$

where the saturation current density is given by

$$J_o = \frac{eD_p p_{no}}{L_p} + \frac{eD_n n_{po}}{L_n}$$

It can also be shown that the temperature dependence of the saturation current is

$$J_o(T) = eA_o \left(\frac{D_p}{N_d L_p} + \frac{D_n}{N_a L_n} \right) T^3 \exp \left(\frac{-eV_g}{kT} \right)$$

where N_a and N_d are the acceptor and donor concentration, respectively, and V_g and A_o are material constants.

For the case of an illuminated p-n junction (i. e., a solar cell), solution of the continuity equation leads to an additional term in the diode equation which represents the "light-injected" minority carrier concentrations (i. e., holes in the n-material and electrons in the p-material). These light-generated minority carriers, or these "carrier productions" by the solar cell give rise to the "light-generated" current, I_L (or current density J_L), which is available for flowing in an external electric circuit. The complete solar cell equation is then as follows (per unit area)

$$J = J_L - J_o \left(\exp \frac{eV}{kT} - 1 \right)$$

For this theoretically derived equation an equivalent idealized electrical circuit may be synthesized as shown in Figure 3.11-2. The current source produces a current of magnitude J_L equal to the "injection level" (i. e., light intensity) while the cell I-V (or J-V) curve shape is defined by (a) the value of J_L and (b) by the current J_D flowing internally across the cell's ideal semiconductor junction at a particular cell absolute temperature, T , and terminal voltage, V .

In the continuity equation the quantity $p_n(0)$ (i. e., $p_n(x)$ for $x = 0$), represents the concentration of holes in the n-material due to either an external forward bias or due to minority carrier holes injected into the bulk of the n-material by incident photons. As soon as an external forward bias is applied or photons are incident causing, in turn, the p-n junction to become forward biased, the internal electric field (Figure 3.11-1d) causes holes to drift from the p-side to the

n-side. While crossing the junction the hole drift current becomes an injected hole current in the n-material. Similarly, the electron drift current in the n-material becomes an injected electron current in the p-material. At any distance, x , the sum of the hole and electron currents equals the total current density, J (Figure 3.11-1h).

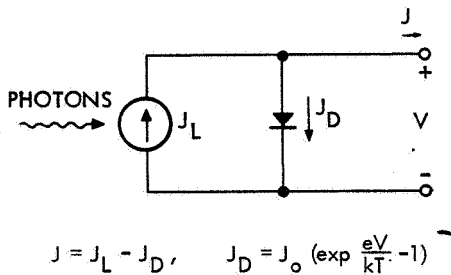


Fig. 3.11-2. Ideal Solar Cell Model

As the holes approach the junction (J_{pp} in Figure 3.11-1h), some of them recombine with the injected electrons (J_{np}), thereby lowering the total current density, J . Solar cell manufacturers, in an attempt to maximize the cell output, J , expend significant amounts of effort to reduce such recombination. Long diffusion length, L , and long lifetime, τ , aid in reducing recombination losses. On the other hand, charged-particle irradiation produces crystal defects which reduce the effective diffusion length and lifetime. Effective diffusion length in unirradiated cells is also reduced when the cell base width (cell thickness) is

made equal to or smaller than the mean diffusion length. This is actually the case for modern silicon cells thinner than approximately $350 \mu\text{m}$ and explains the reduction in short-circuit current output when cell thickness is reduced.

3.11.2 AC Model Theory

The solution of the continuity equation which resulted in the dc diode equation, as shown in Section 3.11.1, is actually complex for the general case and contains both a dc and an ac part (Ref. 3.11-4). The ac part is of the form

$$J = (G_p + iS_p) v \exp(i\omega t)$$

where $(G_p + iS_p) = A_p$, the complex admittance for holes diffusing into the n-layer. The real part, G_p , is the conductance while the imaginary part iS_p is the susceptance. The voltage, v , is the magnitude of the sinusoidal signal at the cell terminal superimposed on the dc terminal voltage, V , and $\exp(i\omega t) = (\cos \omega t + i \sin \omega t)$, and ω is the circular frequency.

The numerical value of A_p at low frequencies indicates a conductance paralleled by a capacitance. At higher frequencies both the conductance and the susceptance increase, approximately one-half an order of magnitude for each order of magnitude increase in frequency.

Such solar cell behavior has been verified experimentally, even though the numerical results turned out quite different. Also, at higher frequencies inductive components not predicted theoretically come into play. Practical ac models are presented in Section 9.2.5.

3.12 RECENT DEVELOPMENTS AND FUTURE TRENDS

In recent years, solar cell energy conversion efficiencies have increased. The increases in efficiency were due to the following:

- A redefinition of the solar constant in 1971 from 139.6 to 135.3 $\text{mW}\cdot\text{cm}^{-2}$, resulting in an apparent increase in cell efficiency of 3.2 percent (for example, from $\eta = 10.00\%$ $\eta = 10.32\%$).
- A general change in the solar test temperature from 28° to 25°C, resulting in an apparent increase in cell efficiency of approximately 1.5 percent at beginning of life and of 2.2 percent after irradiation with 1-MeV electrons to a fluence of $1 \times 10^{16} \text{ e}\cdot\text{cm}^{-2}$.
- Improvements in the solar cell construction, resulting in a 10 to 20 percent increase in cell efficiency over conventional cells.

The following improvements in the solar cell construction have resulted in higher cell conversion efficiency:

- Shallower junctions (0.1 to 0.2 μm instead of 0.3 to 0.4 μm in conventional cells), resulting in an enhanced cell blue response.
- A larger number of gridlines to reduce the cell internal series resistance.
- Thinner gridlines and smaller contact areas to increase the active cell area.
- In some cell types the addition of a p^+ back field in the cell base region to aid in the

collection of minority carriers from the base region (the usefulness of back fields for cells subject to high charged particle fluences is currently being debated) however, see Section 3.1.6).

- A change from SiO antireflective coatings on conventional cells to Ta_2O_5 , having lower absorption and a more favorable index of refraction than SiO (see Section 4.3).
- In some cell types a change from the conventional base resistivity of 7-14 $\text{ohm}\cdot\text{cm}$ to 2 $\text{ohm}\cdot\text{cm}$ for high charged particle fluence applications (the photon degradation of these cells has not been evaluated yet; see Section 3.3.5).

The development of the high-efficiency cells that have become available recently and described in Section 3.1.1 has not been completed. Almost daily, process developments and solar cell designs are being advanced that push the state of the art toward higher efficiency, lower cost, and more radiation-resistant solar cells. For the next few years, the development of new solar cell types, as well as the refinement of the currently existing cell types, can be expected to continue. Major sources of information concerning space-type solar cells include the following:

- Solar cell manufacturers
- The Photovoltaic Specialists Conferences, sponsored by the IEEE and held at approximately 18-month intervals
- The Intersociety Energy Conversion Engineering Conferences held annually.

REFERENCES (CHAPTER 3)

- 3.1-1 Provided through the courtesy of J. Scott-Monck, Spectrolab, Inc.
- 3.1-2 Based on previously unpublished data measured by TRW during 1968. (Solar cells were SiO-coated, 2 x 2 cm, unglassed, 2 ohm-cm from Heliotek, 10 ohm-cm from Centralab.)
- 3.1-3 W. Luft and H. Rauschenbach, "Effects of Base Resistivity on the Characteristics of N-on-P Silicon Solar Cells," 6th IEEE Photovoltaic Specialists Conference Records, Vol. III, March 1967.
- 3.1-4 M. Wolf, "Drift Fields in Photovoltaic Solar Energy Converter Cells," Proceedings of the IEEE, Vol. 51, No. 5, May 1963.
- 3.1-5 I. Mandelkorn et al., "Design, Fabrication and Characteristics of New Types of Back Surface Field Cells," TMX 71486, NASA 1973.
- 3.1-6 P.A. Berman, "Summary Results of JPL Lithium-Doped Solar Cell Development Program," Conference Records of the 9th IEEE Photovoltaic Specialists Conference, May 1972.
- 3.2-1 M. Wolf and H. Rauschenbach, "Series Resistance Effects on Solar Cell Measurements," Advanced Energy Conversion, Vol. 3, Pergamon Press, 1963, pp. 455-479.
- 3.2-2 H. S. Rauschenbach and E. E. Maiden, "Breakdown Phenomena in Reverse Biased Silicon Solar Cells," Conference Records of 9th IEEE Photovoltaic Specialists Conference, May 1972.
- 3.2-3 M. Wolf, "A New Look at Silicon Solar Cell Performance," Energy Conversion II, 1971, pp. 63-73.
- 3.2-4 M. Wolf, "Potential Improvements in Efficiency and Cost of Solar Cells," Conference Records of the 10th IEEE Photovoltaic Specialists Conference, November 1973.
- 3.3-1 J.R. Carter, Jr. and H. Y. Tada, The Solar Cell Radiation Handbook, TRW Systems Group, for the Jet Propulsion Laboratory, June 1973.
- 3.3-2 "ATS Power Subsystem Radiation Effects Study, Phase I/Final Report," Report No. SSD 80089R, Hughes Aircraft Company, February 1968.
- 3.3-3 R. L. Crabb, "Photon Induced Degradation of Electron Irradiated Silicon Solar Cells," Records of the 9th IEEE Photovoltaic Specialists Conference, 1972.
- 3.3-4 H. Fischer and W. Pschunder, "Investigation of Photon and Thermal Induced Changes in Silicon Solar Cells," Records of the 10th IEEE Photovoltaic Specialists Conference, 1973.
- 3.4-1 E. L. Ralph, "Performance of Very Thin Silicon Solar Cells," Proceedings of the 6th Photovoltaic Specialists Conference, March 1967.
- 3.4-2 J.H. Martin, R.L. Statler, and E. L. Ralph, "Radiation Damage to Thin Silicon Solar Cells," Intersociety Energy Conversion Engineering Conference, Miami Beach, Florida, August 13-17, 1967.
- 3.4-3 Based on previously unpublished data measured by TRW during 1968, (Solar cells were SiO-coated, 2 x 2 cm, unglassed, 2 ohm-cm from Heliotek, 10 ohm-cm from Centralab.)
- 3.5-1 M. Wolf and H. Rauschenbach, "Series Resistance Effects on Solar Cell Measurements," Advanced Energy Conversion, Vol 3., Pergamon Press, 1963, pp. 455-479.
- 3.5-2 W. Luft, "Silicon Solar Cell Performance at High Intensities," IEEE Transactions on Aerospace and Electronics, Vol. AES-6, No. 6, November 1970.
- 3.5-3 M. Wolf, "Limitations and Possibilities for Improvements of Photovoltaic Solar Energy Converters, Part 1: Considerations for Earth's Surface Operation," Proceedings of the IRE, Vol. 48, July 1960, pp. 1246.
- 3.5-4 M.F. Lamorte, "Internal Power Dissipation in Gallium Arsenide Solar Cells," Advanced Energy Conversion, Vol. 3, 1963, pp. 551-563.
- 3.5-5 Joseph J. Wysocki, "The Effect of Series Resistance on Photovoltaic Solar Energy Conversion," RCA Review, March 1961, pp. 57-70.
- 3.5-6 P. Schoffer and C. Pfeiffer, "Performance of Photovoltaic Cells at High Radiation Levels," Transactions of the ASME, July 1963.
- 3.5-7 E. L. Ralph and P. Berman, "Silicon Cells for Use in Concentrated Solar Energy," Proceedings 17th Annual Power Sources Conference, May 1963.
- 3.5-8 P. Berman and E. L. Ralph, "Improved Solar Cells for Use in Concentrated Sunlight," Proceedings 18th Annual Power Sources Conference, May 1964.

- 3.5-9 Phillip A. Johnston, "Laboratory Experiments on the Performance of Silicon Solar Cells at High Solar Intensities and Temperatures," TN D-2733, NASA, March 1965.
- 3.5-10 Peter Schoffer, "High Power Density Solar Photovoltaic Conversion," Proceedings 18th Annual Power Sources Conference, May 1964.
- 3.5-11 Jacob D. Broder, Harold E. Kautz, Joseph Mandelkorn, Lawrence Schwartz, and Robert P. Ulman, "Solar-Cell Performance at High Temperatures," TND-2529, NASA, December 1964.
- 3.5-12 "Silicon Solar Cells for Near-Sun Missions," Electro-Optical Systems, Inc., California, 1965.
- 3.5-13 J. F. Foster, A.C. Wilbur, D.C. Briggs, and S. Friedlander, "Silicon Solar Cells for Near-Sun Missions," 6th Photovoltaic Specialists Conference, Vol. I, March 1967.
- 3.5-14 D. C. Brigg, "Experimental Study of Solar Cell Performance at High Solar Intensities," Philco-Fold Corporation, California, November 1967.
- 3.5-15 John V. Foster, James R. Swain, Seymour H. Winkler and Ferdinand R. Schwarz, "A Comparison of Gallium Arsenide and Silicon Solar Cells for a Solar Mission," Proceedings of the 5th Photovoltaic Specialists Conference, October 1965.
- 3.5-16 Sidney Gross, "Discussion of Power Systems for Solar Probes - Solar Photovoltaic Concepts," Intersociety Energy Conversion Engineering Conference, Los Angeles, September 1966.
- 3.5-17 JPL Spacecraft Program Summary, Report No. 37-28, Vol. 3, November 1965.
- 3.6-1 J.D. Sandstrom, "A Method for Predicting Solar Cell Current-Voltage Curve Characteristics as a Function of Incident Solar Intensity and Cell Temperature," Records of the 6th Photovoltaic Specialists Conference, IEEE, Cocoa Beach, Florida, March 1967.
- 3.6-2 J. Bruno, "Sunlight Checkout Test for SAS," Final Report, Volumes I, II and III, Report No. MCR-71-320, Martin-Marietta Corporation, March 1972.
- 3.6-3 R.E. Patterson and R.K. Yasui, "Parametric Performance Characteristics and Treatment of Temperature Coefficients of Silicon Solar Cells for Space Applications," NASA TM 32-1582, Jet Propulsion Laboratory, May 1973.
- 3.6-4 W. Luft, "Silicon Solar Cells at Low Temperature," IEEE Transactions on Aerospace and Electronic Systems, Vol. AES-7, No. 2, March 1971.
- 3.6-5 A. R. Kirkpatrick, "Silicon Solar Cell Development and Radiation Effects Study for Low Temperature and Low Illumination Intensity Operation," Report N72-26033, NASA CR 114429, Ion Physics Corporation, Burlington, Massachusetts, January 1972.
- 3.7-1 H.S. Rauschenbach and E.E. Maiden, "Breakdown Phenomena in Reverse Biased Silicon Solar Cells," Conference Records of 9th IEEE Photovoltaic Specialists Conference, May 1972.
- 3.9-1 R.K. Yasui and P.A. Berman, "Solar Cell Contact Pull Strength as a Function of Pull Test Temperature," NASA TR 32-1563, Jet Propulsion Laboratory, Pasadena, California
- 3.10-1 H.W. Brandhorst, Jr., and R.E. Hart, Jr., "Spectral Responses of Silicon Solar Cells at Low Temperature," TMX 52870, NASA, 1970.
- 3.10-2 W. Luft, "Effects of Electron Irradiation on N-on-P Silicon Solar Cells," Advanced Energy Conversion, Vol. 5, Pergamon Press, 1965, pp. 21-41.
- 3.10-3 J.H. Martin et al., "Radiation Damage to Thin Silicon Solar Cells," Intersociety Energy Conversion Engineering Conference, Miami Beach, Florida, August 1967.
- 3.11-1 M.B. Prince, "Silicon Solar Energy Converters," Journal of Applied Physics, Vol. 26, pp. 534 to 540, 1955.
- 3.11-2 M. Wolf and H. Rauschenbach, "Series Resistance Effects on Solar Cell Measurements," Advanced Energy Conversion, Vol. 3, Pergamon Press, pp. 455-479, 1963.
- 3.11-3 M. Wolf, "Potential Improvements in Efficiency and Cost of Solar Cells," Conference Records of the 10th IEEE Photovoltaic Specialists Conference, November 1973.
- 3.11-4 W. Shockley, Holes and Electrons in Semiconductors, Van Nostrand, New York, 1950.

CHAPTER 4

SOLAR CELL FILTERS AND COVERS

CONTENTS

	Page		Page
4.1 Construction and Terminology	4.1-1	4.5.3 Reactive Sputtering	4.5-1
4.1.1 Classification of Covers	4.1-1	4.5.4 Electron-Beam Deposition	4.5-1
4.2 The Cover/Space Interface	4.2-1	4.5.5 High Vacuum Sputtering	4.5-2
4.2.1 Optical Design Considerations	4.2-1	4.5.6 Radio-Frequency Sputtering	4.5-2
4.2.2 Practical Considerations	4.2-2	4.5.7 Electrostatic Bonding	4.5-2
4.2.3 Thermal Control	4.2-2	4.6 Integral Organic Covers	4.6-1
4.3 The Cell/Cover Interface	4.3-1	4.6.1 Spray-on Coatings	4.6-1
4.3.1 Optical Design Considerations	4.3-1	4.6.2 Heat-Laminated Covers	4.6-1
4.3.2 Practical Considerations	4.3-1	4.7 Conductive Coatings	4.7-1
4.3.3 Effects of Cell Glassing	4.3-1	4.7.1 Characteristics of Conductive Coatings	4.7-1
4.4 Discrete Inorganic Covers	4.4-1	4.7.2 Design Requirements	4.7-1
4.4.1 General Design Features	4.4-1	4.7.3 Design Experience	4.7-1
4.4.2 Cover Filters	4.4-1	4.8 Angle-of-Incidence Effects	4.8-1
4.4.3 Cover Materials	4.4-2	4.8.1 Effects of Nonnormal Incidence	4.8-1
4.4.4 Mechanical Characteristics	4.4-3	4.8.2 First-Surface Reflectance	4.8-1
4.4.5 Brittleness	4.4-3	4.8.3 Changes in Internal Reflections and Transmission	4.8-1
4.4.6 Cover Adhesive	4.4-4	4.8.4 Design Considerations for Cylindrical Arrays	4.8-1
4.5 Integral Inorganic Covers	4.5-1	4.8.5 Radiation Effects	4.8-2
4.5.1 Fused Glass	4.5-1	References (Chapter 4)	4. R-1
4.5.2 Thermal Decomposition	4.5-1		

TABLES

4.2-1 Indices of Refraction and First-Surface Reflection Losses at Normal Incidence from Several Solar Cell Cover Materials	4.2-1	4.3-2 Typical Measured Solar Cell Output Changes Due to Installation of Covers	4.3-2
4.3-1 Indices of Refraction and Reflection Losses at Interfaces between Two Optical Media	4.3-1	4.4-1 Inorganic Solar Cell Coverslide Materials	4.4-2
		4.6-1 Change in Solar Cell Output Expressed as a Ratio of Covered to Uncovered Cell I_{sc} due to Heat-Sealing of FEP-Teflon Covers	4.6-1

FIGURES

4.2-1 Light Beam Incident on Interface of Two Different Optical Media	4.2-1	4.4-4 Solar Cell Cover Orientation Markings	4.4-3
4.4-1 Illustration of Nomenclature for Blue-Reflecting Solar Cell Covers	4.4-1	4.6-1 Transmission Degradation of 125 μm Thick FEP-Teflon due to Ultraviolet Irradiation	4.6-1
4.4-2 Illustration of Nomenclature for Blue-Red-Reflecting Solar Cell Covers	4.4-2	4.8-1 First-Surface Reflection for Fused Silica and Effective Intensity That Would Reach the Cell in the Absence of Additional Reflection and Absorption Losses Versus Angle of Incidence	4.8-1
4.4-3 Change of Transmission Characteristics of Blue-Reflecting Filter Due to Installation on SiO_2 -coated 2 ohm-cm Silicon Solar Cell	4.4-2		

CHAPTER 4

SOLAR CELL FILTERS AND COVERS

The "optical interface" between the cell and sunlight constitutes an "optical system" having the following components (in the order of penetration by the sunlight):

- Antireflective layer on the cover (if used)
- Cover bulk material
- Ultraviolet-reflective layer on the cover (used only when the cover bulk material transmits ultraviolet radiation)
- Cover adhesive (if used)
- Antireflective layer on the active solar cell surface
- Solar cell bulk material.

Some material related to the discussion of solar cell covers is found in other chapters and sections as follows:

- Historical developments -- Section 1. 2
- Cover material properties -- Chapter 7, Volumes I and II
- Cover adhesive properties -- Chapter 7, Volumes I and II
- Charged particle radiation -- Section 2. 5
- Ultraviolet radiation -- Section 2. 4
- Cover specifications -- Sections 10. 8 and 10. 10
- Cover sizing for low-energy proton protection -- Sections 3. 3. 7 and 8. 3. 5.

4.1 CONSTRUCTION AND TERMINOLOGY

4.1.1 Classification of Covers

Solar cell covers may be classified according to the following:

- a) Substrate (or bulk) material
 - Inorganic
 - Organic
- b) Method of Attachment to Solar Cell
 - Discrete (adhesive-mounted)
 - Integral
- c) Type of Optical Filter
 - Filterless
 - Reflecting
 - Absorbing
- d) Special Features
 - Conductive Coatings
 - Partial mirrors

The classification of covers by substrate material is associated primarily with the cover's resistance to darkening under ultraviolet and corpuscular radiation. In general, more radiation resistant materials are also higher in cost than lower radiation resistant materials. Inorganic covers tend to exhibit much higher radiation resistance than organic covers.

Practically all solar cell covers used for space programs (not counting flight experiments) have been of the inorganic, discrete type. With few exceptions, these covers have been adhesive-mounted to the solar cells.

Most solar cell covers used for space programs carried first-surface magnesium-fluoride anti-reflective coatings and second-surface ultraviolet reflective filters. Since about 1971 the use of absorbing ultraviolet filters (ceria-doped glasses) has been spreading.

Special solar cell covers such as those using conductive coatings and others have been used successfully but only occasionally to satisfy specific mission requirements.

4.2 THE COVER/SPACE INTERFACE

4.2.1 Optical Design Considerations

When normally incident light is traversing the interface between two optical media having different indices of refraction, a portion of the light, r , is reflected and the remainder, τ , is transmitted into the next medium. The reflected portion of the incident light is given by the reflectance

$$r = \frac{(n_2 - n_1)^2}{(n_2 + n_1)^2} \quad (4.2-1)$$

where n is the index of refraction of an optical medium, subscript 1 refers to the medium from which the light is approaching the interface, and subscript 2 refers to the medium into which the light is entering. For the special case of solar cell covers in space, the index of refraction of space is $n_1 = 1$ and that of the cover, n_2 , is a material property, as given in Table 4.2-1 for several materials. This table also gives the corresponding values of r according to Eq. 4.2-1; r indicates the portion of light lost and not available for conversion into electrical energy by the solar cell.

Table 4.2-1. Indices of Refraction and First-Surface Reflection Losses at Normal Incidence from Several Solar Cell Cover Materials

Material	Wavelength λ (μm)	Index of Refraction n	Reflectance r (%)	Reference No.
Empty space	0 to ∞	1	0	-
Fused silica (Corning 7940)	0.5 to 0.7	1.46	3.5	4.2-3
	1.0	1.45	3.4	4.2-3
Microsheet (Corning 0211)	-	1.531	4.4	4.2-3
Ceria-doped microsheet	-	1.537	4.5	4.2-4
FEP-Teflon	-	1.341 to 1.347	2.2	4.2-5
R63-489 adhesive	-	1.43	3.1	4.2-6
	-	1.41	-	4.2-1
SiO	0.4 to 1.1	1.8 to 2.0	9.6	4.2-1
TiO _x	-	2.2	14.0	4.2-7
Silicon	0.5	4.1	37.0	4.2-8
	1.0	3.5	31.0	4.2-8
Sapphire	0.4 to 1.1	1.71	6.7	4.2-1
Natural Quartz	0.4 to 1.1	1.53 to 1.57	4.7	4.2-1
Mg F ₂	0.4 to 1.1	1.37 to 1.39	2.6	4.2-1
Ta ₂ O ₅	0.4 to 1.1	2.15	13.3	4.2-9

Note: r - reflected fraction of light without antireflective coating per Eq. 4.2-1.

For nonnormal angles of incidence, i.e., when the incident beams make an angle ϕ_1 with the normal to the cell covers (see Figure 4.2-1), r is given by "Fresnel's formula"

$$r = \frac{1}{2} \frac{\tan^2(\phi_1 - \phi_2)}{\tan^2(\phi_1 + \phi_2)} + \frac{1}{2} \frac{\sin^2(\phi_1 - \phi_2)}{\sin^2(\phi_1 + \phi_2)} \quad (4.2-2)$$

where the angle of the refracted beam with the normal, ϕ_2 , is related to ϕ_1 by "Snell's law"

$$n_1 \sin \phi_1 = n_2 \sin \phi_2 \quad (4.2-3)$$

The reflectance, r , according to Eq. 4.2-2, increases with increasing angles of incidence, ϕ_1 (for normal incidence $\phi_1 = \phi_2 = 0$), and is one of the reasons for the deviation of the solar cell output from the "cosine law" discussed in Section 4.8.

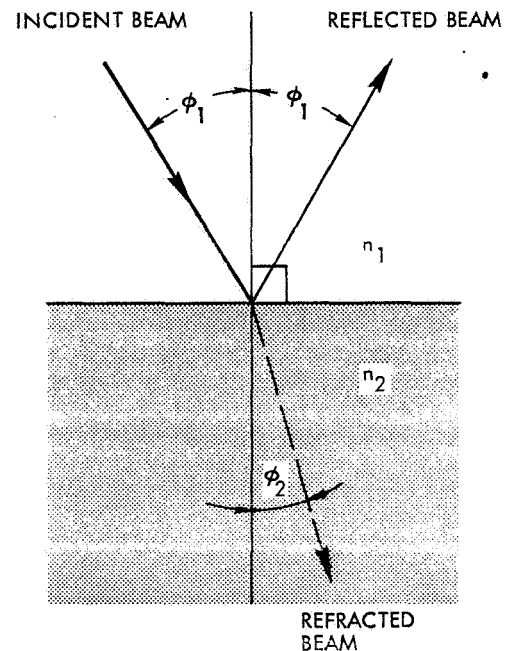


Fig. 4.2-1. Light Beam Incident on Interface of Two Different Optical Media

To minimize reflection losses at the front surface, so-called antireflection or antireflective coatings have been developed. Such coatings are typically very thin and are made of vacuum-deposited magnesium fluoride, MgF. Such antireflective coatings are one or several quarter-wavelengths thick (typically at the solar cell peak spectral response under sunlight illumination, viz., approximately $0.6 \mu\text{m}$ wavelength). In addition to their natural index of refraction, they utilize

optical interference phenomena to provide an "effective" index of refraction, n_e . Minimum reflection losses occur (at a single wavelength) when

$$n_e^2 = n_1 \cdot n_2 \quad (4.2-4)$$

Replacement of a single quarter-wavelength layer by two or more such layers, each having a slightly different effective index of refraction, causes the minimum reflectance wavelength to broaden into a wavelength band. In actuality, it is impossible to fabricate homogeneous quarter-wavelength layers so that a broadening of the minimum reflectance band occurs naturally.

The theoretical aspects of refraction and reflection are treated in most of the more comprehensive books on physics or optics; their application to solar cell covers is developed in detail in Refs. 4.2-1 and 4.2-2.

4.2.2 Practical Considerations

Antireflective coatings on the outer, or front, surface of solar cell covers are subject to the following significant environmental exposures:

- Cleaning with solvents and non-abrasive cleaning aids (cotton or paper products)
- Long-term exposure to humidity or humidity at elevated temperature
- Ultraviolet radiation
- Charged-particle and other corpuscular radiation

Antireflective coatings must be resistant to these environmental exposures. The only coating which

meets these requirements and therefore has been used and is still being used today is magnesium fluoride, MgF_2 .

4.2.3 Thermal Control

The equilibrium temperature of a solar cell array in space depends upon (among others) the solar absorptance and the hemispherical emittance of the covered solar cells (a lower cell temperature results in higher cell efficiency). The solar absorptance is determined primarily by the solar cell front surface and secondarily by the cut-on wavelength of the cover filter. The emittance is primarily determined by the far-infrared (long wavelength) properties of the cover bulk material. Thermo-optical properties are given in Sections 7.13 and 7.14. The analytical aspects of thermal control are discussed in Section 9.6.

For the thermal control of solar cell arrays intended for solar probes, special provisions must be made to prevent excessively high operating temperatures. Potential solutions to such severe thermal control problems, in regard to solar cell cover selection, include the use of "blue-red" filters and partial mirrors. Blue-red filters (see Section 4.4.2) reflect most of the solar energy into space that cannot be utilized by the solar cell in its range of spectral response. By judiciously designing the width of the transmission wavelength band, the balance between array electrical output and operating temperature can be adjusted.

Partial mirrors may belong to one of two types: a) partially transmitting and partially reflecting, or b) nearly fully reflecting over some areas and nearly fully transmitting over other adjacent areas. The former type is also known as the semi-transparent type, and the latter type is often referred to as a "mosaic", "striped" or as "half-mirrored". Reference 4.2-10 describes the characteristics and performance of such covers in detail.

4.3 THE CELL/COVER INTERFACE

4.3.1 Optical Design Considerations

The cover/cell interface contains two optical transition regions:

- From the cover bulk through the ultraviolet reflective interference filter (if such a filter is used) into the cover adhesive
- From the solar cell antireflective coating into the cell semiconductor material.

The reflection and refraction equations given in Section 4.2 apply also for the cases discussed in this section, except that the antireflective coating on the solar cell also acts as a (multiple) quarter-wavelength thick interference filter. The cover adhesive is typically thicker than 20 μm and, therefore, is classified as "optically thick." (That is, interference phenomena are not induced by it.)

- The primary objective of the optical design of the cover/cell interface is to minimize losses at the interfaces between optical media having differing indices of refraction and to minimize absorption losses in the wavelength region in which the solar cell is responsive.

A secondary objective is to minimize the solar absorptance and maximize the emittance of the covered cell assembly, thereby minimizing the solar cell operating temperature and maximizing the solar cell efficiency during operation in space.

Minimization of the reflection losses can be achieved by selecting materials having indices of refraction that (according to Eq. 4.2-4, Section 4.2.1) result in minimum reflection losses.

In a practical sense, the indices of refraction of the silicon, adhesive, or coverslides cannot be altered. Instead, antireflective (AR) coatings must be used to provide an optical "impedance match" between the different media in contact with each other in accordance with Eq. 4.2-4. The UV reflective coating on the coverslide also serves as an antireflective coating between the cover and the cover adhesive while another AR coating is applied to the solar cell. The AR coating on the cell also relies partly on optical interference effects and partly on the natural index of refraction of the coating material. The theoretically expected reflection losses, r , from the differences in the indices of refraction only, are given in Table 4.3-1. This table also gives the desired index of refraction, n_e , which, according to Eq. 4.2-4, yields the lowest reflectance.

If a minimum reflection is desired at a specific wavelength of light, the "optical thickness" of the coating must be one-fourth wavelength. The optical thickness is defined as the product of the physical thickness and the index of refraction. Since a single layer antireflection coating typically has constant

Table 4.3-1. Indices of Refraction and Reflection Losses at Interfaces between Two Optical Media

Material Interface	n_1/n_2	r (%)	n_e
Air/silicon	1.0/3.4 to 4.1	33.5	1.94
Fused silica/Adhesive	1.46/1.43	0.01	1.445
Microsheet/Adhesive	1.53/1.43	0.11	1.48

Notes:

r - reflectance without AR coating

n_e - effective index of refraction of an ideal AR coating which would give a minimum reflectance at the interface

reflection properties over a fairly large wavelength range, it is possible to achieve a coating designed for minimum reflection at a specific wavelength (such as about 0.6 μm for space-type solar cells) while good antireflection properties over most of the solar cell response range can be maintained at a given angle of incidence. In general, the coating thickness on cells intended for operation near normal angles of incidence should be greater than that on cells intended for spinning satellites (see Section 4.8.4).

4.3.2 Practical Considerations

The actual surface roughness of most solar cell types is so large that the foregoing equations cannot really be used to calculate the correct thickness of an antireflective layer. Furthermore, in practice it is not possible to deposit homogeneous antireflective layers on solar cells that have a uniform index of refraction.

Small variations in the antireflection layer fabrication process can have effects on the optical properties of the coatings that may result in significant variations in solar cell output. These coating variations frequently go unnoticed when solar cells are tested bare (unglassed) but manifest themselves after the cells have been glassed.

4.3.3 Effects of Cell Glassing

Installation of a cover on a solar cell (commonly called "glassing") decreases or increases the amount of light energy reaching the solar cell. Therefore, the solar cell output parameters change due to glassing as described in Section 3.5 (Effect of Illumination).

The properties and characteristics of antireflective solar cell coatings can be adjusted such that the following parameters are maximized:

- Bare (unglassed) cell output
- Cell output increased due to glassing (or minimizing output loss)
- Glassed cell output.

Obviously, only the last parameter (absolute cell output after glassing) is of significance. With Ta₂O₅ coatings, for example, the coating can be "adjusted" to provide approximately from 0 to 6 percent output gain due to glassing; however, coatings with about 1.5 percent gain yield the highest absolute power output after glassing (using fused

silica covers with 0.35 μm cut-on wavelength and DC 93-500 adhesive).

Typical cover installation losses and gains for various antireflection coatings are shown in Table 4.3-2.

Table 4.3-2. Typical Measured Solar Cell Output Changes Due to Installation of Covers

Solar Cell Characteristics		Cover Characteristics		Adhesive	I _{sc} Output Change (%) ⁽¹⁾		
Type	Antireflection Coating	Material	Cut-on Wavelength (m)		Typical	Minimal	Maximal ⁽²⁾
n/p	SiO	Fused Silica	0.41	R63-489	-2.5	-1	-4
n/p	Ta ₂ O ₅	Fused Silica	0.35	DC 93-500	+1.5	0	+6

Notes: (1) A positive change denotes output increase.

(2) For controlled processes only; for uncontrolled processes the range may be significantly greater toward the low cell output side.

4.4 DISCRETE INORGANIC COVERS

4.4.1 General Design Features

Solar cell covers for use on current space type solar cell arrays are coated, transparent plates of inorganic materials which have approximately the same dimensions as the solar cells. Solar cell covers are also known as coversides, coverslips, or coverglasses. The material from which the plates are made is referred to as the cover substrate material.

Solar cell covers with reflecting filters are typically coated on both sides. The "outer" or exposed side of the cover has a single layer anti-reflective coating which is designed to enhance the transmission of light energy through the cover and into the solar cell.

The other or "inner" side of the cover has an ultraviolet (UV) energy reflective coating. The purpose of this coating is two-fold:

- To protect the adhesive used to bond the covers to the cells from damaging UV radiation. (Some adhesives may not require UV protection; see Section 4.9.)
- To reflect the (short) wavelength region of the solar spectrum which is not converted by the solar cell into electrical energy (i. e., to decrease the solar absorptance of the cover/cell assembly; see Section 4.2.3).

Solar cell covers having absorbing filters are typically coated on one side only. This coating is on the "outer" side of the (mounted) cover and serves as an antireflective filter. The cover bulk material absorbs ultraviolet radiation and thereby protects the cover adhesive.

The equilibrium temperature in space of solar cell arrays having absorbing filter covers tends to be only slightly higher than that of arrays having reflecting filters because the absorbing filters exhibit a higher emissivity (see Section 4.2.3).

4.4.2 Cover Filters

Filters on solar cell covers block certain wavelength bands and transmit others. Cover filters may be of the absorbing or reflecting type. Examples of absorbing filters are the ceria-doped glass filters; they absorb the ultraviolet radiation which may damage the cover adhesive. Examples of reflecting filters are the so-called "blue" and "blue-red" reflecting, multilayer, interference type filters. The reflecting filters are located on

the "inner" surface of the (mounted) solar cell cover to be protected from environmental damage.

Filter Nomenclature

Figures 4.4-1 and 4.4-2 illustrate the nomenclature for the commonly used "blue" reflecting filter and a "blue-red" reflecting filter which was developed for solar probes (Ref. 4.4-2). Additional filter characteristics are given in Section 10.10.

Changes in Transmission Characteristics

The transmission characteristics shown in Figures 4.4-1 and 4.4-2 are obtained when the cover is surrounded on both sides by air or vacuum. However, when the cover is cemented to a cell, its transmission characteristics change because of the change in the index of refraction of the optical media (i. e., cover adhesive) on the light exit side. Such a typical change is illustrated in Figure 4.4-3.

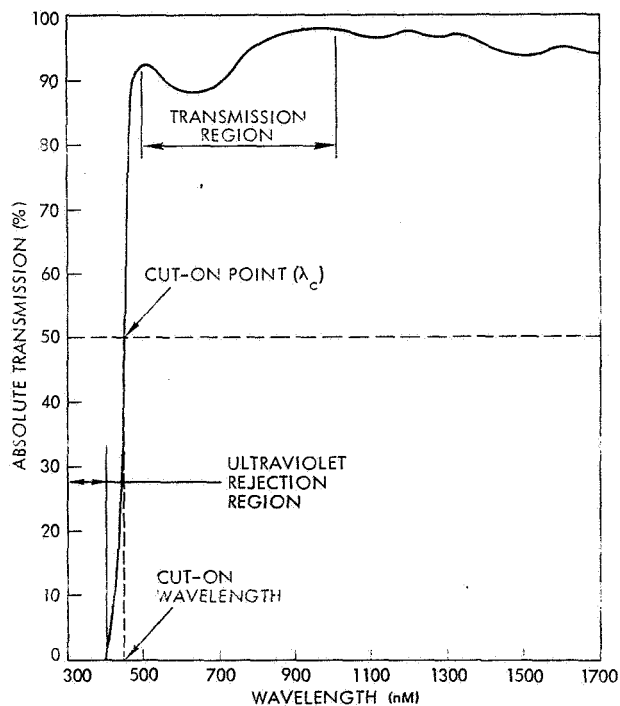


Fig. 4.4-1. Illustration of Nomenclature for Blue-Reflecting Solar Cell Covers (Ref 4.4-1)

4.4.3 Cover Materials

Covers have been fabricated from the materials shown in Table 4.4-1. Industrial grade fused silica has probably been used most widely, in thicknesses ranging from 0.15 mm (0.006 inch) to 1.5 mm (0.060 inch). Microsheet has also been used extensively, but typically only in a 0.15-mm thickness to limit radiation-induced darkening of the light absorption within the microsheet covers.

Table 4.4-1. Inorganic Solar Cell Coverslide Materials

Material	Supplier Code
Fused silica	-
Industrial grade	Corning Glass 7940
UV grade	Corning Glass 7940
Microsheet	Corning Glass 0211
Cerium-doped microsheet	Corning Glass 0212
Ceria-stabilized microsheet	Pilkington Perkin-Elmer
Sapphire	Special Order (Linde)

Synthetic sapphire and fused silica, especially the UV-grades of fused silica, are less susceptible to UV and charged-particle induced darkening than microsheet, but are also more costly.

The resistance of microsheet to radiation-induced darkening can be significantly improved by the addition of a small percentage of cerium to the glass melt prior to extrusion of the microsheet. The resulting cerium-doped microsheet (the cerium exists as an oxide in the glass) possesses two properties of interest to the solar cell array designer:

- A high transmission and a low rate of radiation-induced darkening
- A natural short-wavelength cutoff to protect the cover adhesive from UV damage (without the use of an applied UV reflecting multilayer filter).

Cerium-doped, also called ceria-stabilized, microsheet covers have been available since 1971 and have found increasing uses, especially in solar cell arrays for European space programs.

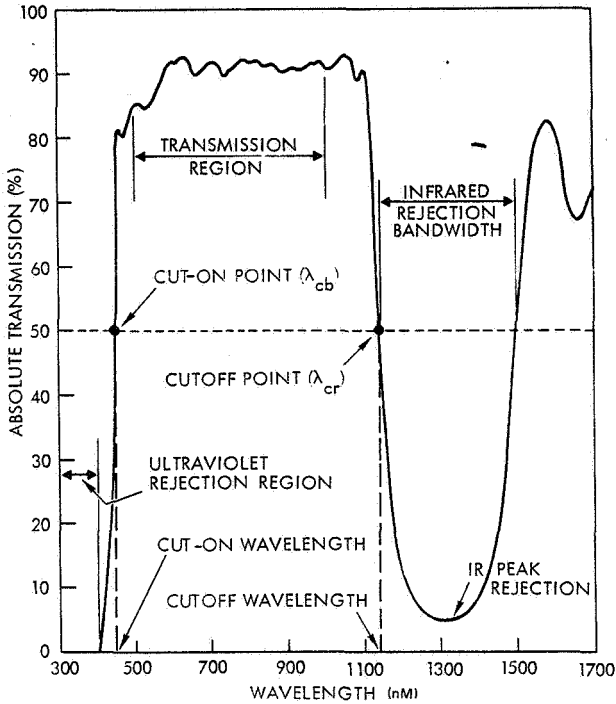
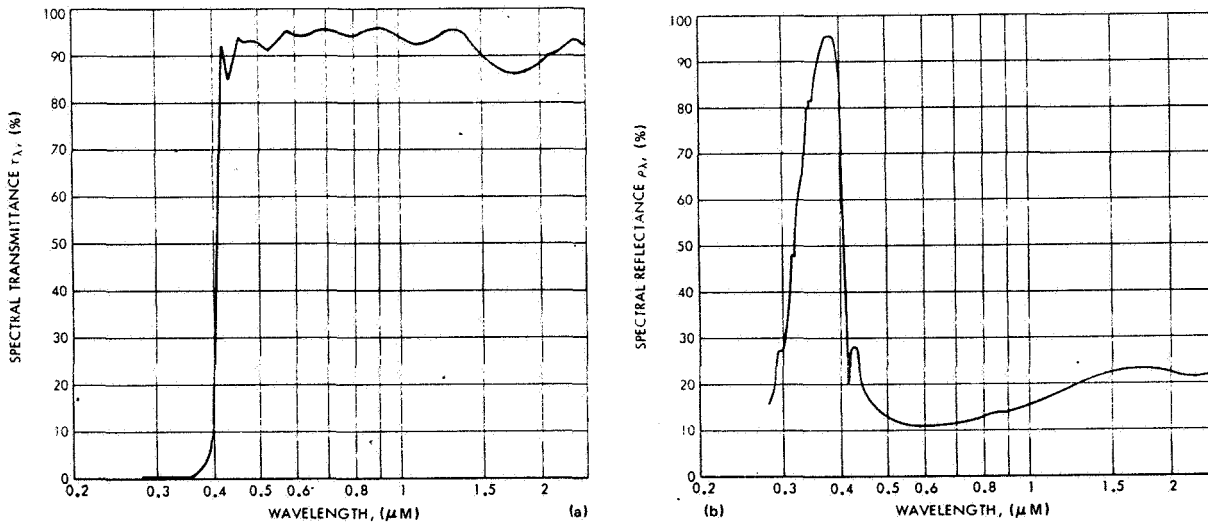


Fig. 4.4-2. Illustration of Nomenclature for Blue-Red-Reflecting Solar Cell Covers (Ref. 4.4-1).



NOTE: CURVE IN (a) IS MEASURED BEFORE, CURVE IN (b) AFTER INSTALLATION. TO CONVERT THE SPECTRAL REFLECTANCE CURVE IN (b) TO A SPECTRAL TRANSMISSION CURVE, SUBTRACT THE VALUE OF THE SPECTRAL REFLECTANCE AT EACH WAVELENGTH FROM 100 PERCENT.

Fig. 4.4-3. Change of Transmission Characteristics of Blue-Reflecting Filter (0.41 μm cut-on) Due to Installation on SiO-coated 2 ohm·cm Silicon Solar Cell (Ref. 4.4-2)

4.4.4 Mechanical Characteristics

Cover Sizes

Discrete solar cell covers are frequently referred to as "undersize", "same-size", or "oversize" covers. These designations describe the cover size relative to the cell size. Prior to 1968, most covers were "undersized" by approximately 50 to 500 μm for assembly tooling reasons. After the discovery of low-energy proton damage during 1967/68 (see Section 3.3.3), oversized solar cell covers began to be utilized for orbits through the radiation belts and at synchronous attitude (see also Section 8.3.5).

"Same-size" covers are somewhat of a misnomer in that in actual practice solar cells and covers, even when fabricated to the same dimensional and tolerance specifications, will not be of exactly the same size, owing to size and angularity variations that occur normally in the cutting and solar cell etching operations. With "same-size" covers low energy proton damage is possible.

For orbits where low-energy protons are absent (in the lower altitude earth orbits, "undersize" or "same-size" covers are acceptable.

"Oversize" covers typically "overhang" the solar cells on 3 or all 4 sides by between 0 and 1 mm (see Section 8.3.5).

Cover Tolerances

Typical cover tolerances are as follows:

Length	$\pm 50 \mu\text{m}$
Width	$\pm 50 \mu\text{m}$
Thickness	± 25 to $\pm 50 \mu\text{m}$
Parallelism of edges	$\pm 50 \mu\text{m}$
Perpendicularity	90 deg ± 30 min.

Non-Functional Defects

Workmanship-type defects are typically permitted as follows:

Edge chips	0.25 mm maximum projecting into the cover	
Corner chips	0.25 to 0.50 mm maximum in any direction	
Bubbles	Cover Thickness (mm)	Maximum Bubble Size (mm)
	Less than 0.18	0.08
	Up to 0.38	0.13
	Up to 0.63	0.25
	Greater than 0.63	0.38

Cell covers can be purchased with different coating orientation markings, as shown in Figure 4.4-4. The markings assure that the ultraviolet reflective coating is down and protected from the space environment, while the different types permit flexibilities in the glass/cell stack design and in assembly process automation.

The light transmitting surfaces of solar cell covers, except for flame-polished microsheet

covers, are typically cut from synthetic crystals and mechanically polished. The cover sides perpendicular to the light transmitting surfaces are rough cut only.

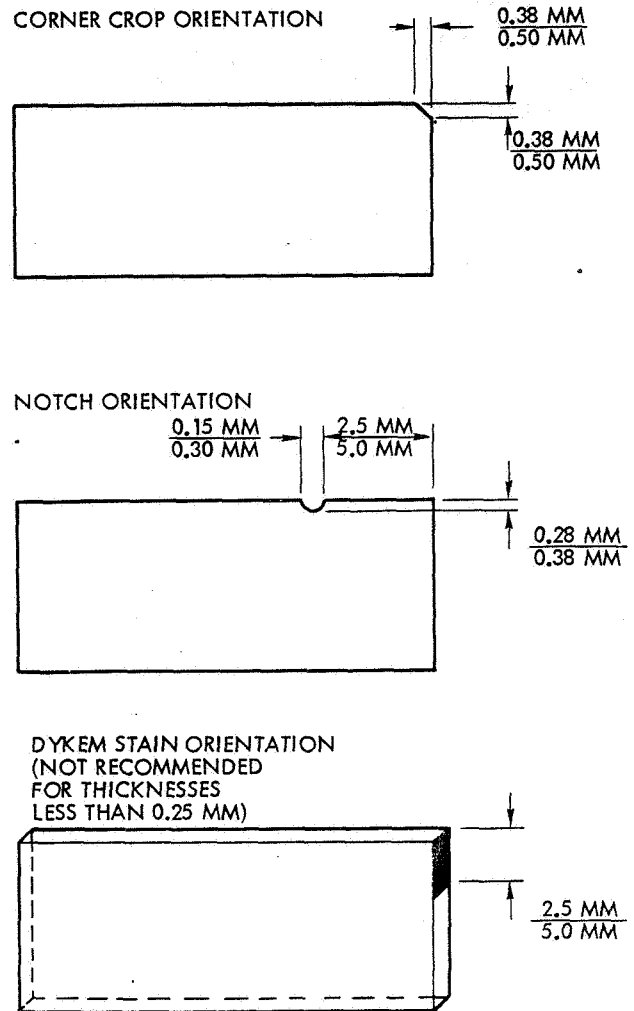


Fig. 4.4-4. Solar Cell Cover Orientation Markings (Shown in the positions in which they are to be bonded to the cells; UV-coating is down.) (Ref. 4.4-1).

4.4.5 Brittleness

A major consideration in selecting a cover-slide material and thickness, both for ease of handling and for thermally induced stresses, is the brittleness of the covers. During the 1960's, it was generally considered that 0.15 mm-thick fused silica covers were more brittle (i. e., cracked more readily) than 0.15-mm thick microsheet covers; whereas during the early 1970's microsheet covers were presumed to be more brittle. The degree of brittleness was usually judged from array assemblers' experience, rather than from measured data. Recently, brittleness problems have been reported by array assemblers using ceria-doped microsheet covers in thicknesses between 0.10 and 0.15 mm; again, no measured data were reported.

Generally, no cover cracking problems occur with any covers thicker than 0.25 mm, except for corner and edge imperfections such as chips and nicks.

4.4.6 Cover Adhesive

Discrete solar cell covers are permanently attached to solar cells using so-called "cover adhesives". Cover adhesives must possess the following characteristics:

- High light transmission in the 0.35 to 1.2 μm wavelength band
- Low degree of darkening from ultraviolet and particulate radiation
- Resistance to thermo-mechanically induced stresses (lack of debonding, crazing, etc.) especially stresses occurring at low temperature and during temperature cycling.

The following adhesives have been used widely:

- | | |
|----------------------------------|------------------|
| • RTV 602
(formerly LTV 602) | General Electric |
| • Silgard 182 | Dow Corning |
| • R63-488
(formerly XR6-3488) | Dow Corning |
| • R63-489
(formerly XR6-3489) | Dow Corning |
| • DC 93500 | Dow Corning |

Primers

To improve the adhesion of the adhesives to the cover or cell, so-called "primers" are occasionally used. For most primers to be effective, their thickness must be relatively small and well-controlled. Many primers tend to darken excessively under ultraviolet radiation.

For most missions the use of a primer is unnecessary and may cause only unnecessary expense in manufacturing and repairing solar cell array assemblies.

4.5 INTEGRAL INORGANIC COVERS

The fabrication of discrete coverslides and their installation over individual solar cells involves many operations and associated costs. Efforts have been made to eliminate some of these operations and thereby reduce the cost of glassed cells by either (a) directly applying a cover to a cell without the use of an adhesive or (b) forming a cover integrally on the cell's active surface.

The primary reasons for applying integral coatings to solar cells and eliminating the adhesive between the cell and the coverglass are as follows:

- The adhesive type system is costly. Present costs for 4-cm² covers vary from \$0.50 to \$3.50, depending on the covers and filters required, plus an additional assembly cost of approximately \$1.00 (Ref. 4.5-1).
- The covers, especially those of thin glass are fragile and this complicates array assembly, particularly with covers thinner than 0.15 mm.
- It removes the requirement for UV rejection filters on the underside of the coverglass, also a cost factor.
- The power-to-weight ratio of cell/coverglass assemblies can be increased for missions which require no more than 0.15 mm-thick filters.

The requirements for and characteristics of integral covers consist of those for discrete covers and additional ones relating to the integral cover fabrication process and to the thermal expansion properties of the cover material. Certain integral cover fabrication processes (i.e., solar cell cover material application processes) can deteriorate the solar cell efficiency and I-V characteristics by mechanisms other than optical effects. Improperly matched cover and cell thermal expansion characteristics will cause severe internal stresses and cause the covered cell to fracture during exposure to low temperature or to temperature cycling.

Numerous efforts have been attempted to develop a successful method of applying the integral glass cover directly to the silicon solar cell. However, as of this writing, success has not been achieved in the sense that fully developed and tested integral covers could be purchased and used for flight hardware with a high degree of confidence of mission success. The following is a partial list of some of these efforts.

4.5.1 Fused Glass

A limited amount of success was achieved with coatings which were applied in glass-slurry form and fused to the cell at a temperature between 850° and 950°C. A major disadvantage of the procedure was that the solar cell diffusion and contact application procedures had to be modified to prevent this high-temperature fusing cycle from drastically degrading the cells (Ref. 4.5-1).

4.5.2 Thermal Decomposition

The thermal decomposition process involves passing of an inert gas, as a carrying vapor, from a deposition agent over heated solar cells. The decomposing vapor deposits a film on the cells. A large number of silanes have been used with deposition temperatures in the range of 400° to 900°C. The major disadvantage of this technique is the relatively high deposition temperature leading to severe cell degradation and the relatively poor film quality for depositions thicker than 1 μm (Ref. 4.5-1).

4.5.3 Reactive Sputtering

SiO₂ films in excess of 25 μm thickness have been deposited on silicon by reactive sputtering. Silicon is used as the cathode in this process and the sputtering operation in an oxygen-rich atmosphere deposits SiO₂ on the substrate (Ref. 4.5-1).

Reactively sputtered SiO₂ can produce a thick film which is exceptionally smooth; however, the sputtering rate must be kept below 0.02 μm per minute and the substrate temperature must be kept above 500°C. Consequently, 21 hours of continuous deposition would be required for producing a good film of 25 μm thickness. At this temperature, however, severe cell degradation occurs. At higher deposition rates or lower substrate temperatures this process produces unsatisfactory films (Ref. 4.5-1).

4.5.4 Electron-Beam Deposition

SiO₂ films in excess of 0.125 mm have been deposited by focused electron beam techniques using quartz as the source material. A major advantage of this technique is the substrate's relatively low temperature during deposition. Normally the substrate temperature may be below 50°C during the deposition to minimize thermal-stress problems. A disadvantage of this technique is the degree of control required to maintain a low evaporation rate in order to keep large particles of quartz from being evaporated. Highly strained films, which readily strip from the silicon are commonly deposited with this technique unless a very low deposition rate (normally less than 0.03 μm per minute) is utilized. Integral covers capable of withstanding typical space thermal cycling environments have not been produced (Ref. 4.5-1).

A similar process, called electron beam evaporation, was used by Ref. 4.5-2 to deposit Corning Glass No. 1720 (an aluminosilicate glass) onto TiO_x-coated silicon solar cells. Integral cover coatings of up to 0.15-mm thickness were produced but only coatings of 0.05-mm thickness had sufficiently low internal stress to withstand limited qualification testing. Cells with 0.05-mm-thick covers exhibited 10 percent efficiency and those with 0.10-mm-thick covers 9 percent. These coatings exhibited relatively low light transmission below 0.5 μm wavelength, but radiation induced darkening was only slight. These covers would not be suitable for blue-sensitive, modern, high-efficiency solar cells.

4.5.5 High Vacuum Sputtering

This technique has reportedly yielded films with excellent optical and mechanical characteristics; however, the rate at which the films are deposited is very low. An average SiO_2 deposition rate is $0.01 \mu\text{m}$ per minute. No flight quality covers have been produced (Ref. 4.5-1).

4.5.6 Radio-Frequency Sputtering

It has been demonstrated that complex thin films, such as certain glasses and Pyrex (Corning 7740), deposited by radio-frequency (RF) sputtering may have physical and chemical properties basically identical with the parent bulk material. The RF sputtering process has the advantage of high deposition rates (greater than $1 \mu\text{m}$ per minute for SiO_2) and low substrate temperatures (less than 200°C). RF deposited integral quartz films of 25- to $50\text{-}\mu\text{m}$ thickness have successfully passed five thermal shock cycles from -196°C to $+100^\circ\text{C}$ with no mechanical or physical deterioration or delamination from the solar cell. Again, acceptable coatings for space applications have not been produced (Ref. 4.5-1).

A more recently developed RF sputtering process of Dow Corning Glass No. 7070 (a borosilicate glass) onto TiO_x -coated silicon solar cells was reported by Ref. 4.5-3. This glass was found to produce relatively low stresses. The light transmission loss in 0.12-mm-thick covers occurred below $0.4 \mu\text{m}$ and fell to 95 percent at $0.35 \mu\text{m}$, making this cover useful for modern, blue-sensitive high-efficiency solar cells. In a thickness of $50 \mu\text{m}$, the sputtered 7070 glass showed a 1 percent broad-band transmission loss after irradiation with 10^{15} electrons per cm^2 of 1-MeV energy.

4.5.7 Electrostatic Bonding

The most recent and most successful method of preparing integrally covered silicon solar cells utilizes an electrostatic field to bond (without adhesive) discrete covers to solar cells (Ref. 4.5-4). The bonding operation, known also as electrostatic field-assisted glass-to-metal sealing technique, is performed at approximately 400°C and requires the presence of a strong electric field for several minutes. The bond is permanent and the bond strength is greater than the ultimate strength of silicon. The cover material, Dow Corning Glass No. 7070 (a borosilicate glass), can be bonded to SiO_x and Ta_2O_5 solar cell coatings. Covers of 0.15- to 3.0-mm thickness have been bonded.

Environmental tests conducted on 0.15- to 0.30-mm-thick covers showed that the radiation-induced darkening of 7070 glass is similar to that of microsheet (Corning Glass No. 0211) and not significantly worse than that of adhesive-mounted (Sylgard 182 with Sylgard Primer) fused silica covers (Corning Glass No. 7940). Ultraviolet radiation was found to almost completely bleach the charged-particle induced darkening of 7070 and 0211 glass. The transmission and transmission degradation data for the above and various other materials are given in Section 7.13.

Alignment of the covers during the bonding operation is critical and subject to the same considerations that apply to adhesive-mounted covers in relation to possible low-energy proton degradation of the solar cell (see Sections 3.3.3 and 8.3.5).

4.6 INTEGRAL ORGANIC COVERS

4.6.1 Spray-on Coatings

During the late 1950's and 1960's considerable effort went into the development of spray-on solar cell coatings. Lockheed announced several such developments but the exact properties and performance of these coatings never became well known.

4.6.2 Heat-Laminated Covers

A more recent development in integral inorganic covers was the invention of FEP-Teflon covers by the NASA Lewis Research Center (Refs. 4.6-1 through 4.6-3). FEP-Teflon, a transparent, colorless plastic film material (see Chapter 7), is heat-sealed at temperatures of approximately 290° to 310°C, while under pressure and without an adhesive directly to the solar cell active surfaces.

The absence of the ultraviolet (UV) reflective coating enhances the blue response of the cell and thereby the overall cell output. The application of FEP-Teflon covers to solar cells that were coated with different AR materials resulted in neither a gain nor a loss in cell output for four of seven materials, as documented in Table 4.6-1 (Ref. 4.6-4). The data obtained by this reference for coatings possessing adequate mechanical integrity

(given in Table 4.6-1) apparently are for nonoptimized AR coating thicknesses. The gain in I_{sc} due to coating bare cells is also given in Table 4.6-1.

The resistance of FEP-Teflon to ultraviolet and corpuscular radiation is significantly less than that for inorganic cover materials. Under exposure to ultraviolet and corpuscular radiation the clear FEP-Teflon becomes yellowish (similar to microsheet, Corning Glass 0211) and brittle (Ref. 4.6-5). The broad-band light transmission as detected by conventional SiO-coated silicon solar cells degrades approximately as shown in Figure 4.6-1. Other investigators have found somewhat less degradation due to ultraviolet irradiation and have subscribed a significant portion of the FEP-Teflon embrittlement to prolonged exposure to temperatures above 60°C (Ref. 4.6-6). Apparently, elevated temperatures cause embrittlement even in the absence of significant doses of ionizing radiation.

Table 4.6-1. Change in Solar Cell Output Expressed as a Ratio of Covered to Uncovered Cell I_{sc} due to Heat-Sealing of FEP-Teflon Covers (Ref. 4.6-4)

Cell Coating	n	I_{sc} (coated)/ I_{sc} (uncoated)	I_{sc} (covered)/ I_{sc} (uncovered)	Relative Covered Cell I_{sc}
SiO	1.9	1.34	1.00	1.34
SiO _x (graded)	1.46- 1.90	1.37	0.95	1.30
SiO ₂	1.46	Not evaluated	Not evaluated	--
MgF ₂	1.4	1.30	0.95	1.24
Si ₃ N ₄	2.1	1.26	1.00	1.26
Al ₂ O ₃	1.5- 1.7	Not given	0.95	--
TiO ₂	2.4- 2.7	1.26	1.00	1.26
Ta ₂ O ₅	2.4	1.31-1.38	1.00	1.31-1.38

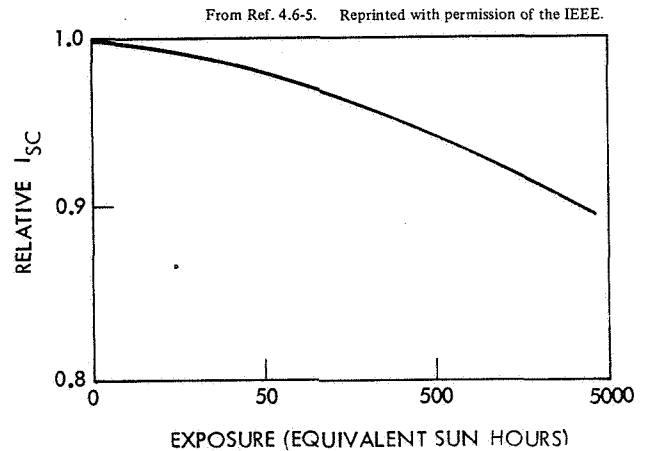


Fig. 4.6-1. Transmission Degradation of 125 μ m Thick FEP-Teflon due to Ultraviolet Irradiation (2 UV Solar Constants in 0.25 to 0.38 μ m Wavelength Band, at 65°C, in Vacuum of 10^{-4} N·m⁻², Measured with SiO-Coated, Conventional Silicon Solar Cell in Simulated AMO Sunlight per Ref. 4.6-5)

4.7 CONDUCTIVE COATINGS

4.7.1 Characteristics of Conductive Coatings

Conductive coatings are thin (about 10 μm thick) transparent, electrically conductive films that are deposited on the outer (first) surface of solar cell covers and other optical elements to achieve equipotential outer surfaces of a spacecraft. Conductive coatings have been used only on a small number of spacecraft, but for certain missions they are essential.

Conductive coatings are metal oxides such as tin oxide or indium oxide. To date, only indium oxide (InO) has been used for space hardware. According to Ref. 4.7-1, neither the chemical composition nor the electrical conduction mechanism of indium oxide is known exactly. The conduction properties of InO are primarily similar to those of a metal and secondarily similar to those of n-type semiconductors having a carrier density of 10^{19} cm^{-3} and a Hall mobility of $100 \text{ cm}^2 \cdot \text{V}^{-1} \cdot \text{s}^{-1}$. The temperature coefficient of electrical resistance is about $5 \times 10^{-4} \text{ }^\circ\text{K}^{-1}$ ($=0.05\% \cdot \text{K}^{-1}$).

4.7.2 Design Requirements

The actually required surface conductivity is strongly mission and design dependent; however, as a general guideline, the resistance from any (external) point on the solar cell array (or the spacecraft) to (spacecraft) ground may not need to be lower than 10^4 ohms and may possibly be higher than 10^6 ohms. The maximum permissible resistance must be calculated based on the maximum permissible voltage (electrostatic potential) gradient on the spacecraft/solar cell array, the maximum plasma-induced current flow, and the potential erosion of the conductive coating by charged particle and ultraviolet radiation that is expected for a particular mission. Depending upon the length of the current path in the conductive coatings of a specific solar cell array design, the actually required surface resistance of the coating, in units of ohms per square, is then calculated. OCLI recommends that the sheet resistance be held to below 10^4 ohms per square (Ref. 4.7-2).

An increase in the electrical conductivity is achieved by an increased thickness of the conductive coating. At the same time, however, the transmittance of the coating decreases. A compromise between electrical conductivity and optical transparency is required. The emittance of the cover also diminishes as the conductive coating thickness is increased.

4.7.3 Design Experience

A number of different solar cell covers and second surface mirrors (used for thermal control), carrying a first-surface conductive coating, have been fabricated, tested and flown. Some of this experience is accounted for in the following.

Solar Cell Substrate Covers for Explorer 31

Fused silica panels (Corning Glass No. 7940) of 250-mm length, 76-mm width and 1.5-mm thickness served in a dual function as solar cell covers and as structural support members for the solar cells (Ref. 4.7-3). The sheet resistance of the transparent conductive layer on the "outer" side was specified to be no greater than 1000 ohms per square. A second, highly conductive, non-transparent coating along the edge of the face of each panel served as current collector and facilitated electrical grounding.

On their "inner" sides the panels carried a blue-reflecting filter with 0.41 μm cut-on wavelength. The overall (blue filter and conductive coating) average transmission characteristics (in air) were specified to be at least 85 percent in the wavelength band between 0.45 μm and 1.10 μm , 85 percent between 0.60 μm and 0.80 μm and 76 percent between 0.50 μm and 0.60 μm . The typically achieved transmittance was about 95 percent between 0.45 μm and 1.10 μm .

Second Surface Mirrors

A number of second surface mirrors, carrying conductive coatings on their first surface, were tested at the Boeing Radiation Effects Laboratory for the combined effects of temperature, ultraviolet radiation and proton radiation expected during a near-sun mission (Ref. 4.7-2). The test conditions were as follows:

Vacuum:	$10^{-5} \text{ N}\cdot\text{m}^{-2}$ or less
Temperature:	$174 \pm 5^\circ\text{C}$
Illumination:	16 solar constants intensity in the 0.25 μm to 0.40 μm wavelength band
Proton Energy:	10 keV
Proton Flux:	$10^{10} \text{ p}\cdot\text{cm}^{-2}\cdot\text{s}^{-1}$
Proton Fluence:	$3 \times 10^{16} \text{ p}\cdot\text{cm}^{-2}$
Test Duration:	13000 equivalent ultraviolet sun hours

The test results were as follows:

Sheet Resistance:	The resistance of parts having an initial value of less than 25,000 ohms per square increased by factors of between 1.5 and 5 for UV only, protons only, or UV and protons combined.
-------------------	--

Solar Absorptance: An increase of less than 0.05 was measured after 812 hours of exposure.

Solar Cell Covers for HELIOS and GEOS

The solar cell covers were discrete, oversized fused silica covers of 0.15-mm thickness, and carried InO conductive and 0.35 μm cut-on wavelength, blue-reflecting coatings. The InO coatings were electrically terminated in pairs of Ti-Pd-Ag contact pads located on two opposite cover edges. The contact pads were sized to 1.05 mm x 1.80 mm x 10 μm . The covers were electrically interconnected in series and connected to spacecraft ground. Cover interconnectors, utilizing silver-plated molybdenum, were parallel-gap resistance welded to the cover contact pads (Refs. 4.7-1 and 4.7-4).

The required sheet resistance for HELIOS (Ref. 4.7-1) was 10^4 ohms per square maximum; actually achieved values were 900 ± 50 ohms. The light transmission loss in the conductive coating caused a 2.5 percent loss in the solar cell I_{sc} output. An additional 1 percent power loss was caused by shadowing of the solar cells by the cover interconnect contact pads. The conductive coating was found to be undegraded after the following exposures:

- 95 percent relative humidity at 20°C for 200 hours
- 95 percent relative humidity for three 24-hour cycles between $\leq 37^\circ\text{C}$ and 52°C with 2 hours dwell at the upper limit
- Ten temperature cycles between -193°C and $+177^\circ\text{C}$ with a rate of change of about 400°C per minute.

4.8 ANGLE-OF-INCIDENCE EFFECTS

4.8.1 Effects of Nonnormal Incidence

When the angle of incidence of the illumination deviates from zero degrees (normal incidence), the power output capability of the solar cells will be reduced. The solar cell short-circuit current will fall off approximately according to the cosine of the angle of incidence while the maximum available power will fall off faster than the cosine indicates. Deviations from the "cosine law" generally are of great significance to the array designer. The deviations may be due to the following which are all angle-of-incidence dependent:

- Optical effects relating to the first-surface reflectance of the cover slide.
- Optical effects relating to apparent changes in the optical thickness of coatings and filters, thereby causing apparent changes in the spectral transmittance and reflectance values.
- Edge effects relating to refraction, scattering and additional light collection by solar cells and covers, especially by thicker covers.
- Shadowing of solar cells by solar cell cover edges, solar cell interconnectors, wires and other relatively small array components.

4.8.2 First-Surface Reflectance

The reflectance at any surface (interface between two optical media having different indices of refraction) is given by Fresnel's formula (Eq. 4.2-2). This formula was evaluated by Ref. 4.8-1 for fused silica covers (without any coatings) and resulted in Figure 4.8-1. This figure shows both the fraction (ratio) of incident light reflected from the cover front surface and that transmitted into the cover. A significant deviation from the "cosine law" at the larger angles is evident. The presence of an antireflective coating on the cover front surface modifies the front surface reflectance, reducing the reflectance at the smaller angles and accentuating the increase in reflectance at the larger angles.

4.8.3 Changes in Internal Reflections and Transmission

Increasing angles of incidence on the solar cell cover front surface also cause varying reflection and transmission losses in the cover, cover adhesive, and solar cell and at the cover/adhesive and adhesive/cell interfaces as follows:

- Antireflective coatings on the solar cells increase their apparent optical thickness.

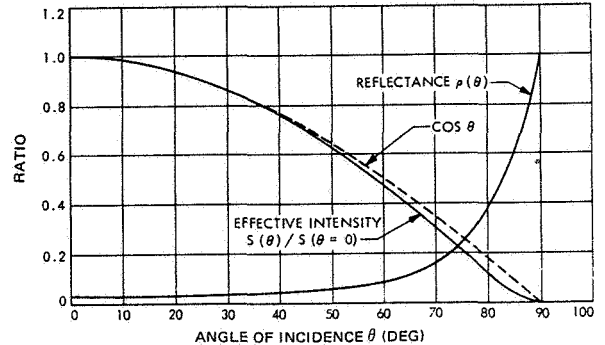


Fig. 4.8-1. First-Surface Reflection for Fused Silica and Effective Intensity That Would Reach the Cell in the Absence of Additional Reflection and Absorption Losses Versus Angle of Incidence (Ref. 4.8-1)

- The apparent spectral response of the solar cell changes (the cell appears to be more deeply diffused).
- Multi-layer blue-reflecting coatings on the covers tend to shift their apparent cut-on wavelengths toward shorter wavelengths.
- Absorbing filters (such as ceria-doped microsheet) increase their apparent thickness and thereby shift the cut-on wavelengths toward longer wavelengths.

4.8.4 Design Considerations for Cylindrical Arrays

On cylindrical solar cell arrays the angle of incidence of the solar illumination on the solar cells ranges always from 90 degrees (grazing incidence) to nearly zero degrees (normal incidence). An "equivalent angle of incidence" can be postulated for a hypothetical flat array that would contain the same number of solar cells as the illuminated side of a cylindrical array and that would produce the same power output (assuming the same cell temperature). For an angle of 90 degrees between the solar vector and the array spin axis the equivalent angle of incidence is around 60 to 70 degrees. The precise equivalent angle depends strongly on all the characteristics discussed elsewhere in Section 4.8; however, the conclusion to be drawn from these effects is that solar cells and covers that were design-optimized for normal angle of incidence illumination may not perform optimally on cylindrical arrays. Ref. 4.8-2 describes one approach to the optimization

of cells and covers for solar cells on spinning arrays. According to this reference, the following highly interdependent parameters should be optimized for an angle-of-incidence of 70 degrees resulting in a considerable power output increase (in excess of 5 percent):

- Solar cell antireflective coating thickness in conjunction with the coating's index of refraction, the cell's spectral response and the cover cut-on wavelength
- Cover antireflective coating thickness
- Intercell spacing (actually the cover-to-cover spacing) in conjunction with the cover size (relative to the cell size) and the cover thickness.

4.8.5 Radiation Effects

Corpuscular and ultraviolet radiation may cause two independent effects that are related to angle-of-incidence phenomena:

- Changes in the spectral response of the solar cell and the spectral transmittance of the cover and cover adhesive
- Excessive cover adhesive degradation due to edge-lighting of the adhesive at shallow angles of incidence.

The effects of radiation on solar cells are described in Section 3.3 and the effects on solar cell covers and adhesive are described in Section 7.13. Excessive adhesive darkening due to edge-lighting is described in Ref. 4.8-2. This reference alleges that anomalously large optical losses observed on many satellites in orbit (see Section 11.13) may be caused by this mechanism.

REFERENCES (CHAPTER 4)

- 4.1-1 "Solar Cell Cover," Product Specification No. 602400, Optical Coating Laboratory, Inc., July 1971.
- 4.2-1 G. Seibert, "Increased Solar Cell Output by Improved Optical Matching, Part I: Theoretical Considerations," ESRO TN-90 (ESTEC), March 1969.
- 4.2-2 G. Seibert, "Increased Solar Cell Output by Improved Optical Matching, Part II: Experimental Results," ESRO TN-91 (ESTEC), April 1969.
- 4.2-3 "Corning Glass Works," Product Data Sheet.
- 4.2-4 "Solar Cell Coverslips," Product Data Sheet, Pilkington Perkin-Elmer.
- 4.2-5 "Teflon-FEP," Technical Information Bulletin, Dupont.
- 4.2-6 "Dow Corning," Product Data Sheet.
- 4.2-7 W. Luft, "Status of TiO_x Antireflective Coating in the U. S.," IEEE Transactions on Aerospace and Electronic Systems, Vol. AES 10, No. 2, March 1974.
- 4.2-8 M. Neuberger and S. J. Welles, "Silicon," Report DS-162 for Air Force Materials Laboratory under Contract F33615-68-C-1225, October 1968.
- 4.2-9 E. L. Ralph, J. Scott-Monck, "Development and Space Qualification of New High-Efficiency Silicon Solar Cells," Records of International Conference, Photovoltaic Power Generation, Hamburg, Germany, September 1974.
- 4.2-10 R. G. Ross, et al., "Measured Performance of Silicon Solar Cell Assemblies Designed for Use at High Solar Intensities," JPL TM 33-473, March 1971.
- 4.4-1 "Solar Cell Cover," Product Specification No. 6024000, Optical Coating Laboratory, Inc., July 1971.
- 4.4-2 R. G. Ross, et al., "Measured Performance of Silicon Solar Cell Assemblies Designed for Use at High Solar Intensities," Technical Memorandum 33-473, Jet Propulsion Laboratory, March 1971.
- 4.5-1 Anon, "Survey and Study for an Improved Solar Cell Module, STOD Task No. 43," JPL Document No. 900-270, August 1969.
- 4.5-2 H. Somberg, et al., "Manufacturing Methods for Silicon Solar Cells with Integral Coverslips," Technical Report AFML-TR-72-81, Air Force Materials Laboratory, Air Force Systems Command, Wright Patterson Air Force Base, Ohio 45433, July 1972.
- 4.5-3 G. Brackley, et al., "Integral Covers for Silicon Solar Cells," Records of the 9th IEEE Photovoltaic Specialists Conference, Silver Springs, Maryland, May 1972.
- 4.5-4 A. R. Kirkpatrick, "Stress Free Application of Glass Covers for Radiation Hardened Solar Cells and Arrays," Technical Report AFAPL-TR-75-54, Air Force Aeropropulsion Laboratory, Air Force Systems Command, Wright Patterson Air Force Base, Ohio, 45433, August 1975.
- 4.6-1 A. F. Forestieri, J. Broder and D. T. Bernatowicz, "Silicon Solar Cell Array Patent Application," NASA Case LEW-11, 069-1 Patent Application No. 83,816, October 1970.
- 4.6-2 A. F. Forestieri and J. Broder, "Improvements in Silicon Solar Cell Cover Glass Assembly and Packaging using FEP-Teflon," NASA TMX-52875, July 1970.
- 4.6-3 S. A. Greenberg, M. McCargo, and W. L. Palmer, "Investigation of FEP-Teflon as a Cover for Silicon Solar Cells," Report No. NASA CR-72970, LMSC-D243070, Lockheed Palo Alto Research Laboratory, August 1971.
- 4.6-4 J. D. Broder and G. A. Mazaris, "The Use of FEP-Teflon in Solar Cell Cover Technology," NASA TM X71485, NASA Lewis Research Center, Cleveland, Ohio.
- 4.6-5 H. S. Rauschenbach, et al., "FEP-Teflon Encapsulated Solar Cell Modules - Further Progress," Conference Records of the Eleventh IEEE Photovoltaic Specialists Conference, Catalog No. 75CH0948-OED, 1975.
- 4.6-6 Private Conversation with A. F. Forestieri, NASA Lewis Research Center, Cleveland, Ohio, 1975.

- 4. 7-1 H. Gochermann, "Vorlaeufiger Schlussbericht, Entwicklung und Qualifikation einer Conductive-Coating-Technik, Vertrags-Nr. RVI 1-07/16/70 Z," Allgemeine Electricitaets-Gesellschaft, AEG-Telefunken, Wedel, Germany, October 1971.
- 4. 7-2 Private communication with I. Sachs, Optical Coatings Laboratory, Inc., Santa Rosa, California, 1975.
- 4. 7-3 "Specification SSE-4-S-74, Fused Silica Panels," The John Hopkins University, Applied Physics Laboratory, Silver Spring, Maryland, July 27, 1974.
- 4. 7-4 G. Pohl and H. Braasch, "The GEOS Solar Generator," Conference Records of the 11th IEEE Photovoltaic Specialists Conference, Catalog No. 75CH0948-OED, 1975.
- 4. 8-1 R. G. Ross, et al., "Measured Performance of Silicon Solar Cell Assemblies Designed for Use at High Solar Intensities," Technical Memorandum 33-473, Jet Propulsion Laboratory, March 1971.
- 4. 8-2 R. W. Objorden, "Solar Cell Optical Design Considerations," Conference Records of the Ninth IEEE Photovoltaic Specialists Conference, Silver Spring, Maryland, May 1972.

CHAPTER 5
ELECTRICAL INTERCONNECTIONS

CONTENTS

	Page		Page
5.1 Terminology	5.1-1	5.3.11 Mechanical Design of Imbedded Interconnectors	5.3-10
5.1.1 Solar Cell Interconnectors	5.1-1	5.3.12 Mechanical Design of Solar Cell Stacks	5.3-11
5.1.2 Module Interconnectors	5.1-1	5.3.13 Electrical Design	5.3-11
5.1.3 String Terminations	5.1-1	5.3.14 Reliability Considerations	5.3-12
5.1.4 U-Turns and Turn-Arounds	5.1-1	5.4 Wiring and Cabling	5.4-1
5.1.5 Connectors	5.1-1	5.4.1 Selection Criteria for Wires and Cables	5.4-1
5.1.6 Terminals	5.1-1	5.4.2 Weight Considerations	5.4-1
5.1.7 Wires and Cables	5.1-1	5.4.3 Design Practices	5.4-2
5.1.8 Blocking Diodes	5.1-1	5.5 Diodes	5.5-1
5.1.9 Shunt Diodes	5.1-1	5.5.1 Blocking Diodes for Energy Conservation	5.5-1
5.1.10 Stress	5.1-1	5.5.2 Blocking Diodes for Fault Isolation	5.5-1
5.2 Interconnector Design Examples	5.2-1	5.5.3 Blocking Diode Characteristics	5.5-1
5.2.1 Solar Cell Interconnector Design Requirements	5.2-1	5.5.4 Blocking Diode Design Requirements	5.5-3
5.2.2 Solar Cell and Interconnector Failure Modes	5.2-1	5.5.5 Blocking Diode Installation Practices	5.5-3
5.2.3 Historical Developments	5.2-2	5.5.6 Shunt Diodes for Minimizing Output Losses	5.5-3
5.2.4 Current State of the Art	5.2-5	5.5.7 Shunt Diodes for Protecting Solar Cells	5.5-4
5.2.5 Soldering Versus Welding	5.2-7	5.5.8 Shunt Diode Characteristics	5.5-4
5.3 The Solar Cell Interconnector Design Problem	5.3-1	5.5.9 Shunt Diode Design Requirements	5.5-5
5.3.1 Thermally Induced Stresses in Joints	5.3-1	5.5.10 Shunt Diode Installation Practices	5.5-5
5.3.2 Stresses in Joints Due to External Forces	5.3-2	5.6 Connectors and Terminals	5.6-1
5.3.3 Stresses in Expansion Loops	5.3-3	5.6.1 Selection of Connectors or Terminals	5.6-1
5.3.4 Stresses in Imbedded Interconnectors	5.3-6	5.6.2 Connector Reliability	5.6-1
5.3.5 Stresses in Solar Cell Stacks	5.3-6	5.6.3 General Design Practices	5.6-1
5.3.6 Design of Interconnector Configurations	5.3-7	5.6.4 Selection of High-Current or Low-Current Terminations	5.6-2
5.3.7 Interconnector Material Selection	5.3-8	References (Chapter 5)	5. R-1
5.3.8 Mechanical Design for Series Loops for Front-back Contact Solar Cells	5.3-9		
5.3.9 Mechanical Design of Series Loops for Wraparound Contact Solar Cells	5.3-9		
5.3.10 Mechanical Design of Parallel-Loops	5.3-10		

TABLES

5.2-1 Temperature Cycling Requirements for Solar Arrays for Various Missions	5.2-1	5.5-1 Illustration of Impact on Power Subsystem Performance when a Single-Point Failure on the Array/Spacecraft Interface Occurs	5.5-2
--	-------	--	-------

FIGURES

5.2-1	Typical Failure Mode Due to Severe Thermal Environments	5.2-2	Body Diagram and Finite Element Representation, B	5.3-3	
5.2-2	Fracture of 50 μm -thick Silver Conductor Imbedded in FEP-Teflon after 100 to 150 thermal cycles between -196 and +100°C	5.2-3	5.3-4	Bimetallic Bus Bar Eliminates Rotational Forces on Solder Joints	5.3-3
5.2-3	Rigid Shingle	5.2-3	5.3-5	Changes in Cell Spacings due to Low Temperature	5.3-4
5.2-4	Early Spectrolab Interconnect Approach	5.2-3	5.3-6	Required Loop Deformation, R, With Points x, y Coincident and Temperature Variable	5.3-5
5.2-5	Solaflex Interconnections Using Type AB-2020 Cells	5.2-3	5.3-7	Loop Deformation Resulting from Different Choices of Substrate Materials, Interconnector Material and Interconnector Attachment Distance	5.3-6
5.2-6	Submodule, 2 x 2 cm Cells by Six Cell Wide	5.2-4	5.3-8	Alternate Cross-Sectional Interconnector Configurations for Front-back Contact Solar Cells	5.3-9
5.2-7	Submodule, 2 x 6 cm Cells by Two Cells Wide	5.2-4	5.3-9	Alternate Cross-Sectional Interconnector Configurations for Wraparound Contact Solar Cells	5.3-10
5.2-8	Two-Part Interconnect Design for Two 2 x 6 cm Cells with Zero Parallel Stress	5.2-4	5.3-10	Definition of Bending Axes	5.3-10
5.2-9	Heliotek Interconnector	5.2-4	5.3-11	Power or Voltage Loss in Cell-to-Cell Copper Interconnector Having N Current Paths Between Cells	5.3-12
5.2-10	Wire-Mesh Interconnectors	5.2-5	5.5-1	Some Possible Blocking Diode Locations and Potential Electrical Failure Areas	5.5-2
5.2-11	Expanded Metal Mesh Interconnector Concept	5.2-5	5.5-2	Illustration of a Near-Short-Circuit Fault Between Adjacent Strings of Solar Cells	5.5-2
5.2-12	Examples of Expanded Metal Mesh Interconnectors	5.2-5	5.5-3	Illustration of the Use of Conventional Rectifier Type Diodes as Shunt Diodes	5.5-4
5.2-13	Interconnect Configuration Varieties	5.2-6	5.5-4	Use of Unencapsulated Rectifier Waivers on the Back Side of Flexible, Overlapping Solar Cell Module	5.5-4
5.2-14	Fatigue Life of Soldered and Welded Solar Cell Interconnecting Systems, Estimated in 1972	5.2-7	5.5-5	Solar Cell Module, Solar Cell With Integral Shunt Diode, and Interconnector Design	5.5-4
5.3-1	Free Body Diagram of Two Bars Made of Different Materials Having Initial Length, L_0 , after a Change in Temperature for (a) Unrestrained Expansion and (b) Restrained Expansion	5.3-1	5.5-6	Electrical Schematic of Integral Diode Circuit	5.5-5
5.3-2	Illustration of Calculated Thermo-mechanical Stress in Silicon Induced by Two Different Interconnector Metals at Three Different Low Temperatures	5.3-2	5.5-7	Integral Diode Forward I-V Characteristics	5.5-5

CHAPTER 5

ELECTRICAL INTERCONNECTIONS

The electrical energy generated by the hundreds or thousands of solar cells on an array must be collected and conducted to the satellite electrical (load) equipment and, usually, to an energy storage battery. Solar cell interconnectors, or interconnects, conduct the electric current from one cell to the next and, at the end of a series string of solar cells, to a terminal or tie point. From these tie points, current conductors (wires) lead to other terminals or tie points, connecting increasing numbers of solar cell strings in parallel. On some arrays the solar panel wire

harness is permanently wired to the array-to-spacecraft bus wiring while on other arrays plug-in type connectors are used. Most arrays utilize blocking or isolation diodes for circuit fault isolation and/or to prevent nonilluminated solar cells from dissipating power.

Typical electrical interconnectors, wires, diodes and connectors that are in use on solar cell arrays are the subject of this chapter. The corresponding material properties and design data are given in Chapter 7.

5.1 TERMINOLOGY

The terminology for solar cell array subassemblies and the various electrical circuit interconnecting elements used by the many workers in this field is quite diverse. The following nomenclature is defined only for the purpose of discussion in this handbook; however, this particular terminology is based on what appears to be the most frequent usage throughout the industry.

5.1.1 Solar Cell Interconnectors

Solar cell interconnectors, also known as "interconnects," are conductive elements that electrically connect individual solar cells in series and/or parallel arrangements. Interconnectors may simply consist of wires, but more typically they consist of metallic mesh or shaped metal ribbons.

5.1.2 Module Interconnectors

Frequently solar cells are pre-assembled (usually for manufacturing convenience) into modules consisting of between 2 and usually less than 100 cells. After installation of the modules on the solar panel or array substrate, the modules are electrically interconnected via module interconnectors (or module interconnects). Module interconnectors may be identical to solar cell interconnectors or may be quite different in design.

5.1.3 String Terminations

An "electrical string" of solar cells, also called a group or a circuit, consists of a number of solar cells connected in parallel and series that provides power output at a bus voltage (there may be several busses on a spacecraft: shunt bus, primary power bus, battery charging bus, etc). At each end of the electrical string the solar cells are connected to a power collecting conductor, called the bus. Bus conductors are typically insulated round conductors, stranded wires, or flat cables.

In general, special interconnector elements are used that provide stress-free, electrically redundant interconnections between the solar cells and the bus. Frequently the string terminations utilize the solar cell interconnectors and provide only the facility to connect the bus conductors.

5.1.4 U-Turns and Turn-Arounds

"Electrical strings" (see String Terminations above) are often physically longer than the solar cell array substrate. In those cases the electrical string must be "turned around" by 90 degrees or in hairpin fashion by 180 degrees so that two "physical strings" come into being. In some cases more than two physical strings may be required to accommodate one electrical string on a substrate.

Interconnectors used for U-turns or turn-arounds may be similar to module interconnectors or string terminations, or they may be required to be of a different design.

5.1.5 Connectors

Connectors are cable termination assemblies designed for quick connecting and disconnecting, usually referred to as "mating" and "demating", respectively. The conductive portions of the connectors are referred to as contacts. Contacts may be "male" or "female." Connectors with female contacts are also called "receptacles" and "sockets." Connectors are available to be fitted to the ends of round cables or flat cables.

5.1.6 Terminals

Terminals are electrical elements, fastened to insulating terminal strips, terminal boards, or "barrier strips," that permit repeated joining and unjoining of two or more wires from different circuits. For space applications, the joints are usually soldered.

5.1.7 Wires and Cables

Wires may be round (circular or cylindrical) or flat (ribbon) conductors that may be used insulated or bare. A number of wires bundled together is called a cable. A number of flat conductors contained within sheet-like insulators is called a "flat-cable" or a printed-circuit cable.

5.1.8 Blocking Diodes

Also called isolation diodes, blocking diodes are rectifier type diodes that are permanently inserted between electrical strings of solar cells and a power bus such that they will conduct electrical current from illuminated solar cells to the bus, but will block current flow from the bus through the solar cell strings when, for whatever reason, the string output voltage is less than the bus voltage.

5.1.9 Shunt Diodes

Also called bypass diodes and shadow diodes, shunt diodes are connected in parallel with solar cells or submodules (groups) of solar cells such that when the solar cells are illuminated the shunt diode is biased in reverse. During periods when some of the solar cells in a string of cells become shadowed, fractured, or fail in an open-circuit mode, the shunt diodes automatically become forward biased and thereby permit power to flow from the remaining illuminated solar cells of the string to the power bus.

5.1.10 Stress

In the context of this chapter, "stress" denotes mechanically and thermomechanically induced forces that are internal to materials. Stress and the associated terminology are defined in detail in Section 9.7 (Thermomechanical Stress Analysis). Additional definitions are given in conjunction with the discussions of specific material properties given in Chapter 7.

5.2 INTERCONNECTOR DESIGN EXAMPLES

5.2.1 Solar Cell Interconnector Design Requirements

The purpose of solar cell interconnectors is to conduct electrical energy from the individual solar cells to the power collection wire harness throughout the defined mission life of the solar cell array. To fulfill this purpose, the interconnectors must meet the following general requirements:

- Physical
 - a) Be manufacturable, handleable and repairable
 - b) For certain lightweight array designs, possess ability to be rolled, folded or bent
 - c) For certain missions, be nonmagnetic
 - d) Protect the solar cell junction from low energy proton damage
 - e) Shield the solar cell from corpuscular radiation as effectively as the solar cell cover
 - f) For certain designs, be lightweight.
- Environmental

Withstand the following:

 - a) Terrestrial environments during fabrication, test, and assembly, according to Section 2.1
 - b) Launch and flight dynamic environments, according to Section 2.2
 - c) Space environment, according to Section 2.3
 - d) Operational temperature ranges, according to Section 2.4.1
 - e) Solar eclipse induced temperature cycling stresses, according to Table 5.2-1 and Section 2.6.2.
- Electrical
 - a) Remain electrically continuous, mainly in the series (current-flow) direction and to a lesser degree in the parallel direction
 - b) Remain attached to the solar cell contact
 - c) Possess adequate electrical conductivity.

5.2.2 Solar Cell and Interconnector Failure Modes

Silicon solar cell arrays for space use are subject to a number of temperature-related, mechanical failure mechanisms, as illustrated on Figure 5.2-1,

Table 5.2-1. Temperature Cycling Requirements for Solar Arrays for Various Missions (Ref. 5.2-1)

Mission	Life (years)	Number of Cycles	Temperature Limits (°C)	
			Low	High
Near-earth orbits; scientific, manned or unmanned	1 to 3	5000 to 50,000	0 to -70	70 to 110
Synchronous earth orbits; communications	1 to 10	100 to 700	-80 to -180	0 to 80
Interplanetary probes				
Inbound	1 to 3	<5	-100	175
Outbound	1 to 3	<5	-190	80
Lunar surface, stationary	1 to 2	<25	-180	130

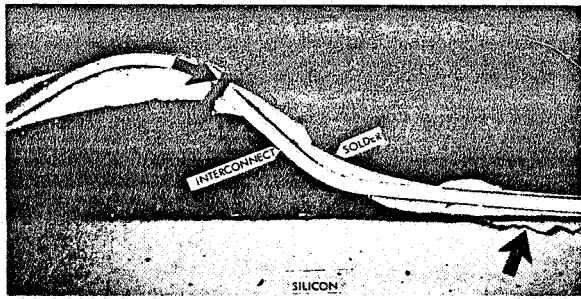
From Ref. 5.2-1. Reprinted with permission of the IEEE.

which, in time, may cause the electrical output from the solar cell array to degrade. Open-circuit failures of soldered joints on the array can be caused by creep at higher temperatures, typically in excess of 100°C, and by silicon fracture at lower temperatures, typically below -100°C. Under less severe upper and lower temperature limits, large numbers of alternating stresses, caused by cyclic temperature variations of solar cell arrays, can lead to fatigue cracking of solar cell interconnectors and interconnector solder joints. Imbedded interconnectors may fail when the strength of the surrounding dielectric material approaches or becomes greater than the strength of the interconnector conductor (see Figure 5.2-2).

Failure Definition

In the ideal case, any component or assembly of components should survive its intended mission without any failure or deterioration. In actuality, however, the properties and characteristics of presently known materials require that the overall design accommodate deterioration and certain types of "failures." In a practical sense, then, a solar cell array "failure" must be defined. A typical definition of "failure" is the degradation of array power output below a certain tolerable limit. In the context of solar cell interconnector and joint fatigue life, the array degradation is assessed (independent of other degradation mechanisms such as charged particle radiation) statistically using joint and loop failure rates established by ground testing. While loop failures are usually clearly observable open-circuit failures, joint failures are usually not well definable for the following reasons:

- Some workers believe that the onset of cracking is a failure.
- Some workers believe that any highly stressed solder joint will crack (Refs. 5.2-3, 5.2-4,



(a) FATIGUE FAILURE OF INTERCONNECTOR LOOP AND SOLDER JOINT

CAUSES:

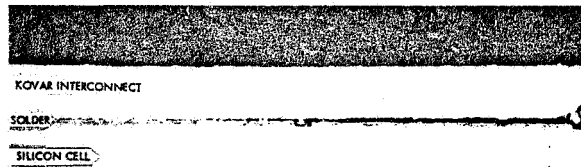
INTERCONNECTOR LOOP RADIUS TOO SMALL AND SOLDER PLATING TOO THICK FOR REQUIRED TEMPERATURE CYCLING RANGE AND NUMBERS OF CYCLES



(b) STRESS AND FATIGUE FAILURES OF SOLDER AND SILICON CELL

CAUSES:

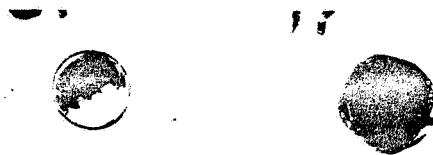
EXCESSIVE SOLDER THICKNESS FOR REQUIRED LOW TEMPERATURE. APPLICABLE BELOW -100°C .



(c) FATIGUE FAILURE OF SOLDER IN SOLDER JOINT

CAUSES:

LIMITATION OF SOLDER MATERIAL PROPERTIES. APPLICABLE ABOVE -100°C .



(d) STRESS FAILURE OF SILICON CELL (SPALLING)

CAUSES:

EXCESSIVE ADHESIVE THICKNESS FOR REQUIRED LOW TEMPERATURE. APPLICABLE BELOW APPROXIMATELY -120°C .

Fig. 5.2-1. Typical Failure Mode Due to Severe Thermal Environments

and 5.2-5; also see Section 5.2-5) so that the onset of cracking is not a realistic criteria.

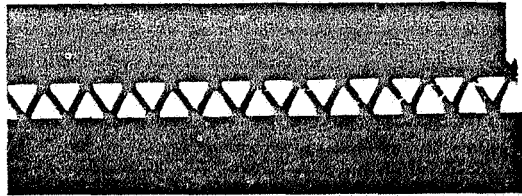
- The relationship between the onset of cracking and propagation of a crack to complete joint fracture during temperature cycling has not been established (Ref. 5.2-6).
- In a functional sense, only a completely fractured joint constitutes mechanical joint failure, but not necessarily an electrical open-circuit failure of that particular joint.
- Joints, when located on the solar cell back side (bottom) contacts, when imbedded in adhesive, or when physically not separable from the cell contact during inspection by probing, cannot positively be identified either as being completely fractured and still making pressure contact, or as being only partially fractured.

The criterion for what constitutes a "failed" joint must, therefore, be defined in the light of reliability and other considerations for each specific design case and project requirement.

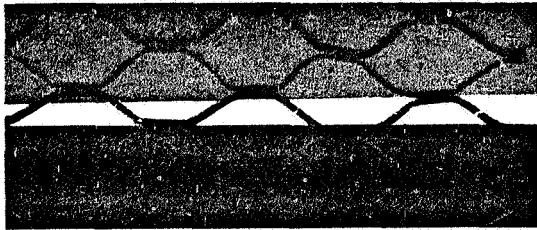
5.2.3 Historical Developments

Until the end of 1960, many solar cell arrays were arrangements of parallel and series-connected modules, each consisting of a small number of cells connected in series, generally about five cells of 1 x 2 cm size. These five-cell modules were assembled by directly soldering the front contact strip of each cell to the bottom contact of the opposite side of the adjacent cell, forming a rigid "shingled" subassembly, as shown in Figure 5.2-3.

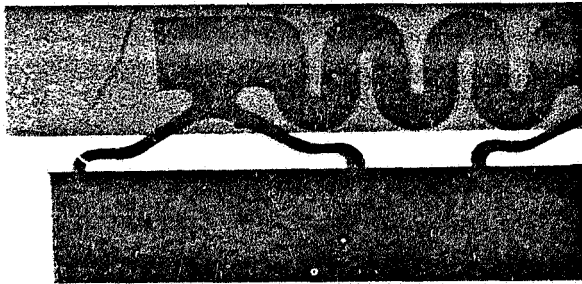
The geometry of such configurations created high stress points, especially at the intercell solder joints. Such assemblies have led to frequent problems, in many cases as the result of repetitive thermal cycling.



a) FINE MESH



b) COARSE MESH



c) SHARED INTERCONNECT CONFIGURATION

Fig. 5.2-2. Fracture of 50 μm -thick Silver Conductor (in-plane expansion loops) Imbedded in FEP-Teflon after 100 to 150 thermal cycles between -196 and $+100^\circ\text{C}$ (Ref. 5.2-2).

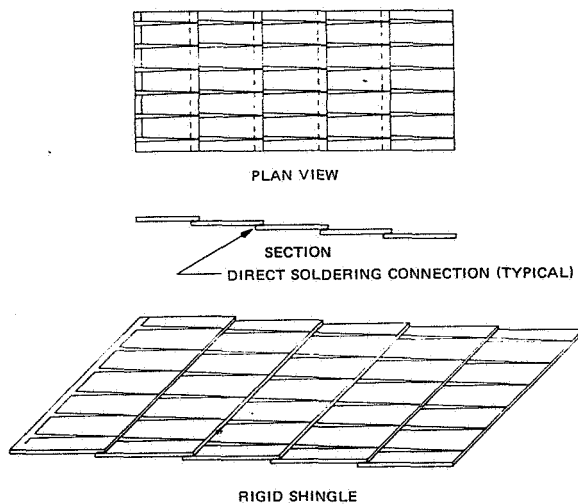


Fig. 5.2-3. Rigid Shingle (Ref. 5.2-7)

The most frequent failure mode was separation of solar cell contact metallization (electroless nickel plating at that time) from the silicon wafer.

The next generation of cell interconnectors consisted of solid or stranded wires that in snake-like fashion connected positive and negative cell contacts. This wire implementation made a first attempt to reduce mechanically or thermally induced stress. A significant improvement in interconnector flexibility was achieved by utilizing formed and shaped metallic "piece parts".

Spectrolab introduced the so-called "Solaflex" system of interconnection at the beginning of 1961. The Solaflex technique is based upon the use of parallel bussed submodules. In this arrangement cells are connected into small parallel groups, using a "tab strip" soldered along the bottom of the cells. The series interconnecting tabs extend out and up from the edge of the bus, and are stress relieved before connection with the next succeeding series group, as shown in Figure 5.2-4* for an early version of the design. Redundancy is achieved by use of the multiple tabs and solder joint connections (Ref. 5.2-8).

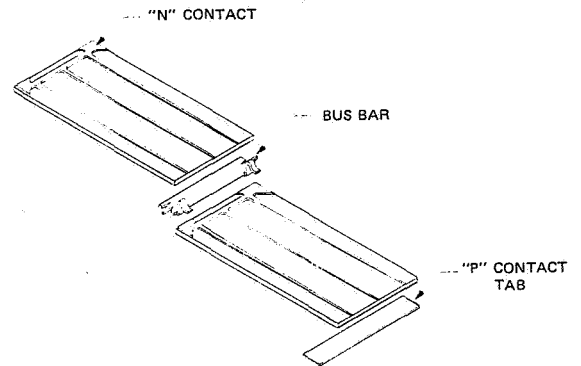


Fig. 5.2-4. Early Spectrolab Interconnect Approach (Ref. 5.2-7)

To further reduce the possibility of interconnection failure, the more recent Solaflex interconnection technique now incorporates a bus bar with extended interconnectors or tabs on the underside of the cell so as to locate the positive and negative connections in close proximity on opposite faces of the cell. An illustration of this extended bus system is shown in Figure 5.2-5.*

Two additional Spectrolab configurations are illustrated in Figures 5.2-6 and 5.2-7. Figure 5.2-6 illustrates 2 X 2 cm cells interconnected as described above, and Figure 5.2-7 illustrates the interconnection of the large area 2 x 6 and 2 x 7.15 cm cells, as used on the Skylab Apollo Telescope Mount solar array. However, as well developed as these designs were, they exhibited performance limitations as mission

*The use of the series-parallel planar arrangement of solar cells described in Figures 5.2-4 and 5.2-5 and developed by Spectrolab, are covered by U.S. Patent No. 3094439, new reissued as Patent No. RE 25,647 assigned to Spectrolab, Division of Textron, Inc., and by additional pending patents.

requirements became more severe and solar cell sizes became larger. Spectrolab and Heliotek, both Divisions of Textron, Inc., developed a two-metal interconnect system for 2 x 6 cm cells by 1968 (Figure 5.2-8). To accommodate deep-temperature cycling of lightweight, low thermal mass solar cell arrays for operation in geosynchronous orbit or interplanetary flight, Heliotek developed the so-called "wraparound interconnector" (Figure 5.2-9).

die-cutting, expansion, rolling flat, and annealing. Copper mesh, made by the same process, has been a close second. Occasionally, mesh interconnectors have been produced by chemical etching.

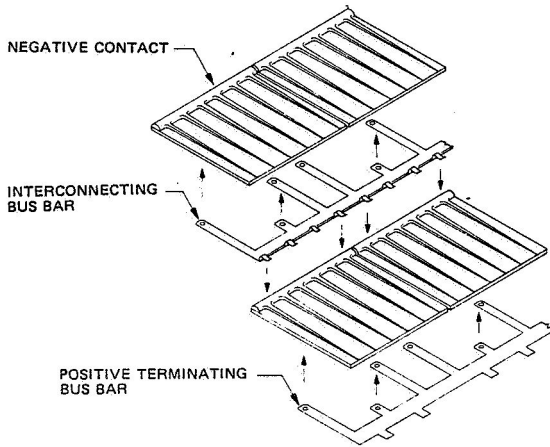


Fig. 5.2-5. Solaflex Interconnections Using Type AB-2020 Cells (Ref. 5.2-7)

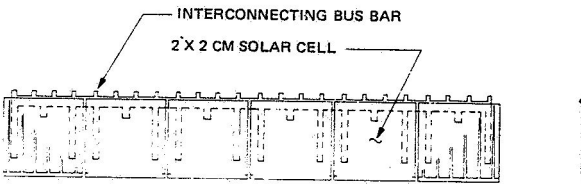


Fig. 5.2-6. Submodule, 2 by 2 cm Cells by Six Cells Wide (Ref. 5.2-7)

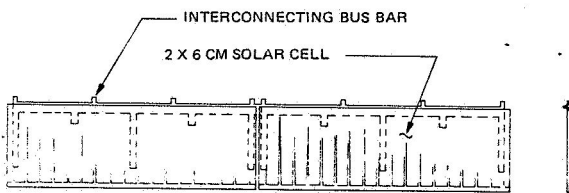


Fig. 5.2-7. Submodule, 2 x 6 cm Cells by Two Cells Wide (Ref. 5.2-7)

A different approach was used by Julius who used a combination of expanded metallic mesh (Figure 5.2-10 on the cell back contacts and wires on the front contacts (Ref. 5.2-9). Thereafter, Haynos (Ref. 5.2-10) eliminated the wire portion of the cell interconnectors and used the expanded metallic mesh to connect cells both in parallel and in series (Fig. 5.2-11). Expanded metallic mesh interconnects have since been used widely in a variety of sizes and materials, mainly because of their low fabrication cost and ease of installation during solar cell module and array fabrication (Figure 5.2-12). The most popular mesh has been from 50 to 125 μm thick soft silver, made by

From Ref. 5.2-3. Reprinted with permission of the IEEE.
SOLDER TO "P" CONTACT
18 PLACES PER CELL -
BACK SURFACE

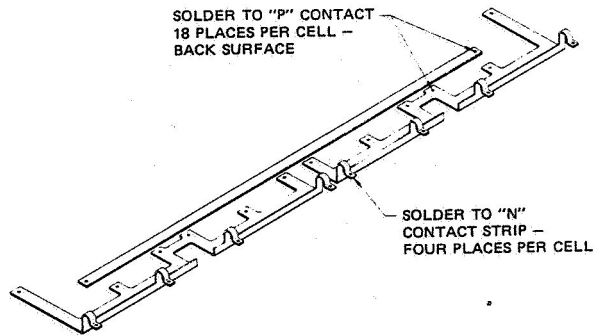
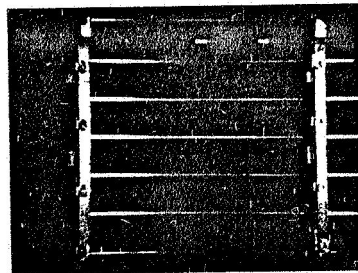
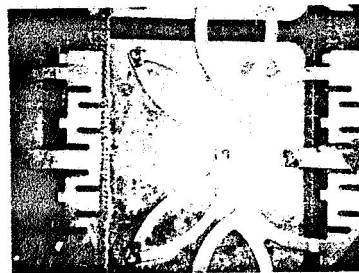


Fig. 5.2-8. Two-Part Interconnect Design for Two 2 x 6 cm Cells with Zero Parallel Stress (Ref. 5.2-3)



(a) FRONT SIDE



(b) REAR SIDE

Fig. 5.2-9. Heliotek Interconnector (Ref. 5.2-11)

The drawback of metallic mesh interconnectors is that the mesh loses its flexibility when it is either imbedded in adhesive or covered with solder. Under such conditions, mesh performs no better than a solid sheet of the same material. Furthermore, the fine metal strands caused handling problems during soldering, and were subject to early fatigue life failure in thermal cycling. To improve the cell interconnecting technique, several workers used formed metal strip interconnectors.

Many other organizations have also developed formed metal-strip type cell interconnectors. These formed metal strips are usually made from copper, beryllium-copper, or Kovar, and occasionally also

from molybdenum. Kovar and molybdenum, having expansion coefficients close to silicon, permit lower operating temperatures and larger numbers of temperature cycles than copper or copper-alloys. Molybdenum would be preferable over Kovar because it is nonmagnetic, however, it is difficult to plate with solderable coatings on a production basis. Some of the interconnector types which have been in use are shown in Figure 5, 2-13.

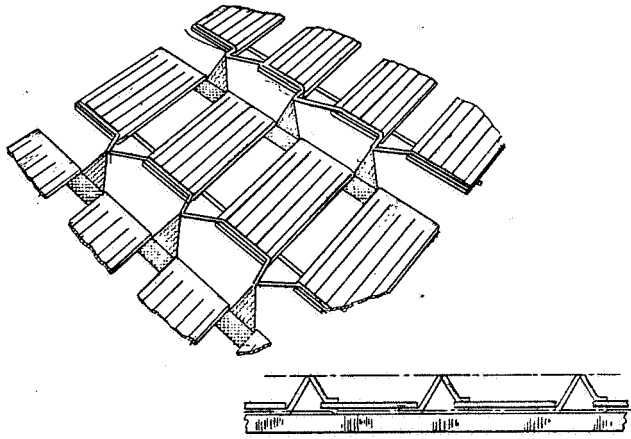


Fig. 5.2-10. Wire-Mesh Interconnectors (Ref. 5, 2-9)

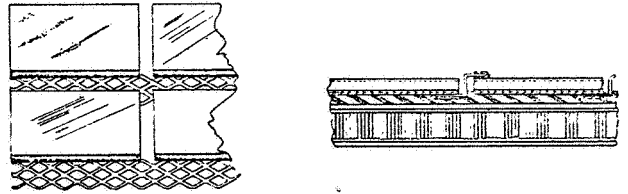
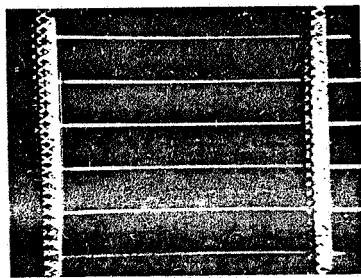


Fig. 5.2-11. Expanded Metal Mesh Interconnector Concept (Ref. 5, 2-10)

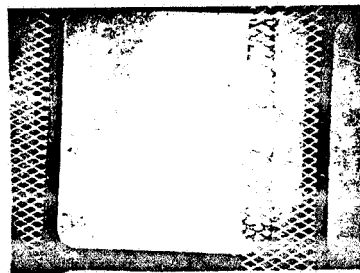
5.2.4 Current State of the Art

While it is probably true that the interconnector designs flown in the past have met their respective mission requirements, the recent trend toward longer mission durations and lighter weight (lower thermal mass) array construction has significantly increased the low-temperature stress and thermal cycling fatigue problems for solar cell interconnectors.

Since these problems have been of considerable interest for years, JPL sponsored a symposium in March 1970 on solar cell interconnector design and analysis that was attended by representatives of cell manufacturers and solar cell users (Ref. 5, 2-13). This symposium revealed that all solar cell stack interconnector designs to that date had been developed by trial-and-error methods. Specific designs had been tested only to demonstrate compliance with

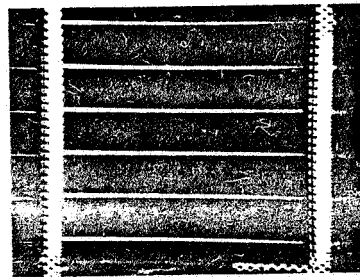


FRONT SIDE

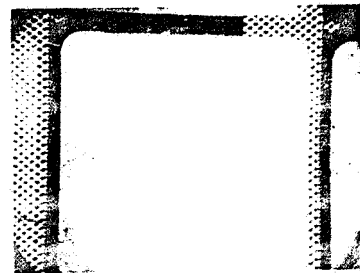


REAR SIDE

(a) GENERAL ELECTRIC INTERCONNECTOR



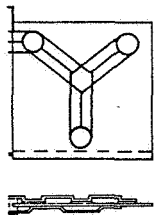
FRONT SIDE



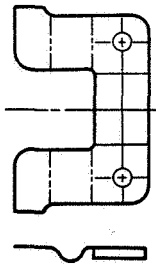
REAR SIDE

(b) BOEING INTERCONNECTOR

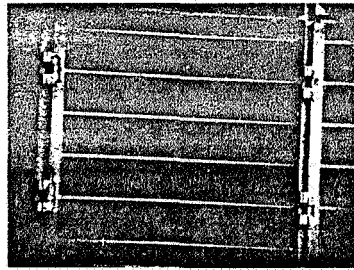
Fig. 5.2-12. Examples of Expanded Metal Mesh Interconnectors (Ref. 5, 2-11)



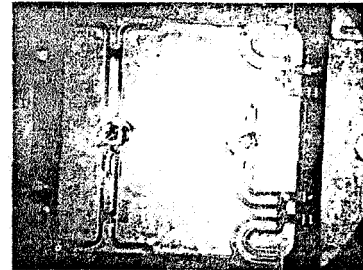
(a) LOCKHEED



(b) TRW

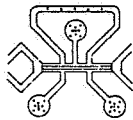


FRONT SIDE



REAR SIDE

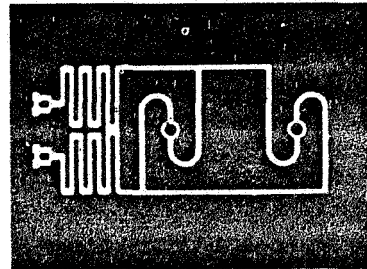
(c) ELECTRO-OPTICAL SYSTEMS



(d) JPL



(e) INDUSTRY-WIDE



(f) RECENT LOCKHEED

Fig. 5. 2-13. Interconnect Configuration Varieties [Refs. 5. 2-7 and 5. 2-11, (b) based on Ref. 5. 2-9]

specific single-point requirements. Design margins or ultimate design capabilities were generally unknown. Analytical procedures for purposely designing a solar cell array mechanically to meet specific requirements or to predict the thermomechanical performance of existing designs for different requirements were lacking.

Since that time, significant progress was made by various industrial and government organizations in systematizing the interconnector design process and developing analytical tools with which internal stress and deformation distributions in the interconnector expansion loops and in solder or weld joints can be studied (see Sections 9. 7 and 9. 8). However, the basic selection of the general interconnector configuration is still a creative exercise for the designer.

Many government agencies and private companies have been very active in the interconnect design area. It can be assumed that every company involved in designing of solar cell assemblies has its own special design(s) which it considers proprietary. All of these designs attempt to provide the ultimate in connecting a number of cells (generally up to five or six) together for a parallel group, and at the same time connect to another identical group in series. All provide a redundancy in electrical connections with some designs actually intended to operate under the conditions of a partial or a complete cell fracture.

The current solar cell interconnector design state of the art is characterized by the following:

- A marked increase in the theoretical understanding and analytical modelling capability of the underlying physical phenomena has occurred only relatively recently.

- Sufficient knowledge of the thermomechanical properties of the materials of interest to solar cell array design and interconnector design, over the temperature range of interest, has been obtained only very recently.
- A unified, systematic, deliberate and comprehensive design approach to the entire solar cell stack and cell interconnecting problem is still emerging.

Interconnector Types

Solar cell interconnectors can be divided into two groups: mesh and formed strips. Mesh is either rolled, expanded metal or etched foil, while formed strips are either die-cut or etched.

The formed strips may have either "coplanar" or "out-of-plane" stress relief loops. Coplanar or "in-plane" loops actually work by out-of-plane warpage of the loop material in the same way as the mesh deforms. Out-of-plane loops of formed strips deform by changing loop size or bend radii and are, therefore, easiest to analyze.

Formed metal strips are usually made from copper, beryllium-copper or Kovar and occasionally also from Invar and molybdenum. Invar, Kovar, and molybdenum, having expansion coefficients close to silicon, permit withstanding lower operating temperatures and larger numbers of temperature cycles than copper or copper alloys. Molybdenum would be preferable over Kovar because it is nonmagnetic; however, it is a difficult material to use (see Section 7. 1).

Expanded metal mesh is made from either copper or silver. Silver mesh, rolled flat after expansion, seems to have been preferred by industry.

5.2.5 Soldering Versus Welding

Interconnectors have been attached to solar cell contacts by a variety of methods. The most frequently used process has been soft soldering with a 60 percent lead, 38 percent tin, and 2 percent silver composition. Recently, soldered joints were found to exhibit a limited temperature cycling fatigue life. Therefore, welded, solderless joints have been developed. These solderless joints promise to possess a longer fatigue life than soldered joints under severe thermal cycling conditions. However, the precise thermal cycling capabilities of soldered and welded joints are presently unknown for the following reasons:

- Factors related to workmanship and process control strongly influence the ultimate life of the joints.

- Analytical procedures by themselves do not permit sufficiently accurate fatigue life predictions to be made.
- An insufficient amount of empirical data exists from which the ultimate life of joints could be ascertained with sufficient confidence.

Figure 5.2-14 illustrates the advance of the ultimate life time of soldered joints to larger and larger values over the years. (Decreasing temperature was plotted upwards in this figure because decreasing temperature corresponds to increasing strain, as discussed in Section 9.8, and permitted correlation of interconnector temperature cycling test data with general fatigue life test data and with fatigue life theory.)

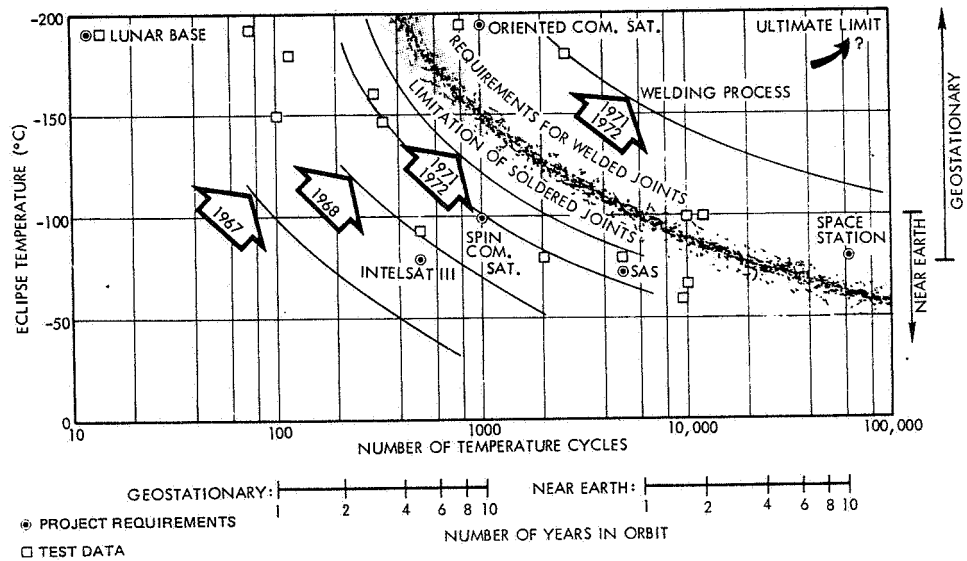


Fig. 5.2-14. Fatigue Life of Soldered and Welded Solar Cell Interconnecting Systems, Estimated in 1972. (The project identifications are of no significance to this presentation.) (Ref. 5.2-11)

HANDBOOK USE

The handbook may be used to clarify specific concepts or to develop a complete solar cell array design. Depending upon the need of the handbook user, the approach to finding the proper discussion most rapidly may vary somewhat from the usual procedure, as described below.

<u>Needed Data</u>	<u>Source to Consult</u>
Material properties data	Detailed Table of Contents - Volume II, Chapter 7
Solar cell data	Detailed Table of Contents - Volume II, Chapter 3
Definitions, clarifications	General Table of Contents - Volume I, or Detailed Table of Contents preceding a specific chapter or Index - Volume I

To start conceptual design work

Section 8.6

To perform detailed array design work

Chapter 8, Detailed Table of Contents

To analyze a design

Chapter 9, Detailed Table of Contents

For the user to familiarize himself with the material in the handbook, first consult the less detailed Table of Contents at the beginning of Volume I and then refer to the more detailed Table of Contents at the beginning of each chapter.

In general, when specific questions are to be answered, the Index located at the end of Volume I will be helpful in locating the appropriate discussions most expeditiously.

5.3 THE SOLAR CELL INTERCONNECTOR DESIGN PROBLEM

The solar cell interconnector design activity essentially comprises the selection of materials and the conceiving of a configuration such that the combination of both reduces stresses in the interconnector/solar cell joints and in the interconnector expansion loops to permissible values. The permissible stress levels vary depending upon specific mission requirements, solar cell array design characteristics and various spacecraft or project oriented tradeoffs.

Stresses of greatest significance to the designer are typically induced in the joints and in the interconnector expansion loops by two separate mechanisms:

- Differences in the coefficients of linear thermal expansion of materials in intimate contact
- By externally applied forces and moments that may arise from any of the following:
 - a) From handling during fabrication and assembly
 - b) In orbit from small but significant dimensional changes in the solar cell layout and interconnector geometry when the array temperature changes.

The total stresses in joints and loops caused by temperature variations and by external forces can be found by superposition of the stresses from the different mechanisms discussed separately in the following sections.

The analytical developments in the following sections are intended to illustrate trends only. More rigorous analytical approaches to stress and fatigue analysis are given in Sections 9.7 and 9.3, respectively.

5.3.1 Thermally Induced Stresses in Joints

For illustration, consider two separate metallic strips made of different materials but having the same length, L_0 , at temperature T_0 . At any other temperature, T , the lengths of the strips will change by

$$\Delta L_1 = L_0 \alpha_1 \Delta T \quad (5.3-1a)$$

$$\Delta L_2 = L_0 \alpha_2 \Delta T \quad (5.3-1b)$$

where $\Delta T = T - T_0$ and α is the average coefficient of linear thermal expansion (see Section 7.11). The subscripts 1 and 2 refer to the first and second strip of material, respectively.

Now let both of these metallic strips be intimately bonded together (like silver plating on a silicon solar cell wafer, for example) so that the strips are no

longer free to expand to their length L_1 or L_2 , respectively. Rather, both strips must expand to a common length, denoted by L_3 (see Figure 5.3-1). The intimate bond can be thought of as producing a tensile force, F_1 on one bar and a compressive force, F_2 , of equal magnitude on the other bar. From the definition of the modulus of elasticity (see Section 7.5) each force produces a change in length, $\Delta L'$, of the bar such that

$$\frac{\Delta L'}{L_0'} = \frac{1}{E} \frac{F}{A} \quad (5.3-2)$$

where L_0' is the initial length when $F = 0$, E is the elastic modulus and A is the cross-sectional area of the bar. Under equilibrium conditions

$$F_1 = -F_2 \quad (5.3-3)$$

$$\Delta L_1 + \Delta L_1' = \Delta L_2 + \Delta L_2' \quad (5.3-4)$$

$$L_0 \alpha_1 \Delta T + \frac{L_0'}{E_1} \cdot \frac{F_1}{A_1} = L_0 \alpha_2 \Delta T - \frac{L_0'}{E_2} \frac{F_2}{A_2} \quad (5.3-5)$$

In general, $L_0 = L_0'$ so that

$$\alpha_1 \Delta T + \frac{1}{E_1} \left(\frac{F_1}{A_1} \right) = \alpha_2 \Delta T - \frac{1}{E_2} \left(\frac{F_2}{A_2} \right) \quad (5.3-6)$$

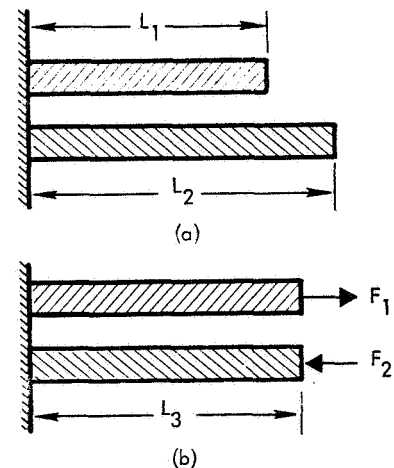


Fig. 5.3-1. Free Body Diagram of Two Bars Made of Different Materials Having Initial Length, L_0 , after a Change in Temperature for (a) Unrestrained Expansion and (b) Restrained Expansion (strips intimately bonded to each other)

and the stress in the first material is

$$\frac{F_1}{A_1} = \frac{E_1 (\alpha_1 - \alpha_2) \Delta T}{1 + (A_1 E_1 / A_2 E_2)} \quad (5.3-7)$$

and the stress in the second material is

$$\frac{F_2}{A_2} = - \left(\frac{A_1}{A_2} \right) \left(\frac{F_1}{A_1} \right) \quad (5.3-8)$$

Let us assume that the first material is a solar cell interconnector and the second material is the silicon wafer of a solar cell and let us, for simplicity in the illustration, neglect the solar cell contact metallization. Also, let us express the area where the stresses occur as

$$A = wd \quad (5.3-9)$$

where w is the width and d the thickness of the materials. Substituting Eq. 5.3-9 into Eqs. 5.3-8 and 5.3-7, combining 5.3-8 with 5.3-7 and cancelling w , the stress in the silicon is

$$\frac{F_2}{A_2} = - \left(\frac{d_1}{d_2} \right) \cdot \left[\frac{E_1 (\alpha_1 - \alpha_2) \Delta T}{1 + \frac{d_1 E_1}{d_2 E_2}} \right] \quad (5.3-10)$$

Eqs. 5.3-7, 5.3-8 and 5.3-10 illustrate the following which are of interest to the interconnector designer:

- The stress in either material is directly proportional to the difference in the thermal expansion coefficients.
- The stress in the silicon decreases as the interconnector thickness decreases ($F_2/A_2 \rightarrow 0$ as $d_1 \rightarrow 0$).
- The stress in the silicon becomes lower when the interconnector stiffness, E_1 , is made lower (also, at high stress levels the actual value of E_1 becomes smaller as the material begins to yield; see Section 7.5).

Eq. 5.3-10 actually cannot be used to predict realistic stresses in the silicon because the stress does not distribute itself uniformly throughout the thickness of the silicon solar cell wafer but rather tends to concentrate in a shallow layer under the metal tab. This stress concentration can be observed as silicon spalling and divoting during temperature cycling. Using such temperature cycling-induced silicon fractures, the stress concentration factors have been determined (Ref. 5.3-1) and applied to the calculation of stresses in the silicon as a function of interconnector thickness for two different interconnector metals and three different values of ΔT . The three-layer model (including solder between the cell and the interconnector) which was used for this analysis is shown in Section 9.7.3. The results of the analysis, shown in Figure 5.3-2, illustrate the reduction in stress in the silicon when the interconnector thickness is reduced and/or when the coefficient of linear thermal expansion (molybdenum) is closer to that of silicon.

From Ref. 5.3-1. Reprinted with permission of the Gordon and Breach, Science Publishers, Ltd.

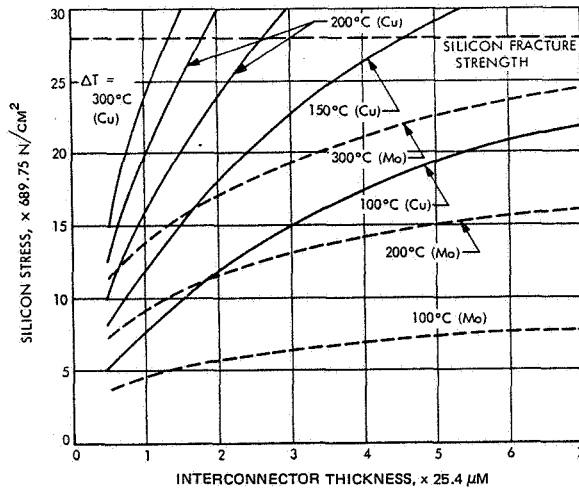


Fig. 5.3-2. Illustration of Calculated Thermo-mechanical Stress in Silicon Induced by Two Different Interconnector Metals at Three Different Low Temperatures ($\Delta T = T_0 - T$) (Ref. 5.3-1)

5.3.2 Stresses in Joints Due to External Forces

Changes in the intercell gap width with temperature cause expansion loops to deform. This deformation, in turn, causes two types of forces to be transmitted to the soldered or welded joints:

- Shear forces, attempting to slide the interconnector attachment areas along the solar cell contacts
- Moments (or torques), attempting to pry the interconnector attachment areas away from the solar cells.

An idealization of an out-of-plane stress relief loop in the series-direction between two typical "flat mounted" solar cells is illustrated in Figure 5.3-3A. When the interconnector loop is removed from both cell contacts, its free-body diagram is as illustrated in Figure 5.3-3B. The shear forces are denoted by P and the prying moments by M .

Stresses Due to Contact Pull and Peel Testing

The strength of soldered, welded, or otherwise bonded joints (bond strength) between solar cell interconnectors and solar cell contacts is evaluated by pull or peel testing (see Section 11.5 for details). The stresses and test failure modes created by such tests are strongly dependent upon the interconnector stiffness and the test method (especially upon the angle of the applied pull force) and may or may not reflect the actual loading of the joints or their response to this loading. The following significant stress conditions may be created by the test:

- Tensile stresses in interconnector, joint, cell contact, and silicon surface
- Shear stresses in joint and cell contact
- Peel stresses in joint and cell contact.

From Ref. 5.3-2. Reprinted with permission of the American Chemical Society.

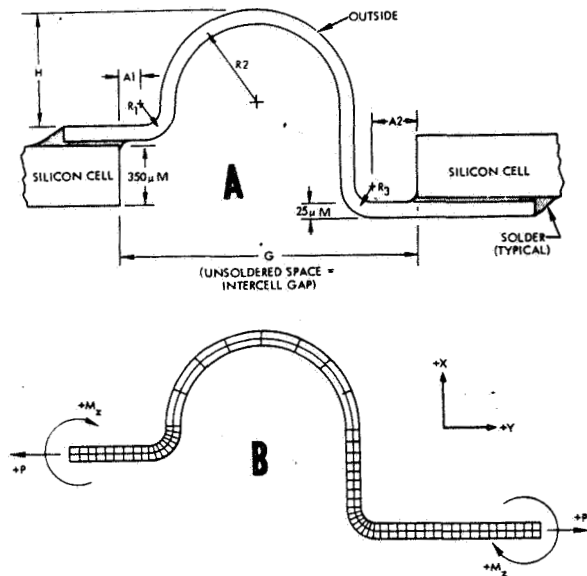


Fig. 5.3-3. Typical Interconnector Loop Model for Soldered Joints, A, and Its Free Body Diagram and Finite Element Representation, B (Ref. 5.3-2)

Origin of Joint Stresses due to Torques (Rotational Forces)

For illustration consider two solar cells that are parallel-connected by a bus bar, as illustrated in Figure 5.3-4. Assume that at room temperature the assembly is stress free (Figure 5.3-4a). Exposure to low temperature will cause all components to contract, each by a different amount. Figure 5.3-4b shows that a bus bar made from copper would contract approximately by the same amount as the aluminum substrate, but considerably more than the silicon solar cells. If the tabs extending from the bus bars are relatively short and stiff, rotational forces on the soldered or welded joints are unavoidable. Figure 5.3-4c illustrates that the use of a low-expansion bus bar (Kovar) would also cause rotational forces, but in a different way.

The ideal design solution to eliminate rotational forces consists of utilizing a "bimetallic" bus bar, as shown in Figure 5.3-4d. Ideally, the parts of the bus bar which are attached to the solar cells have a coefficient of linear thermal expansion identical to that of the solar cells, while the remaining parts have an expansion coefficient identical to that of the substrate. For practical design cases, a combination of Kovar or Invar and copper for the bus bar may be more than adequate for aluminum substrates. Such "bimetallic", or two-part bus bars actually have been implemented (see Ref. 5.3-4).

5.3.3 Stresses in Expansion Loops

Stresses of significance to solar cell interconnector and wire stress relief loops (also called "service loops") include tensile, compressive, shear, and bending stresses. Bending stresses in interconnectors and wires arise from different changes in length of different components on the solar cell array with changes in temperature.

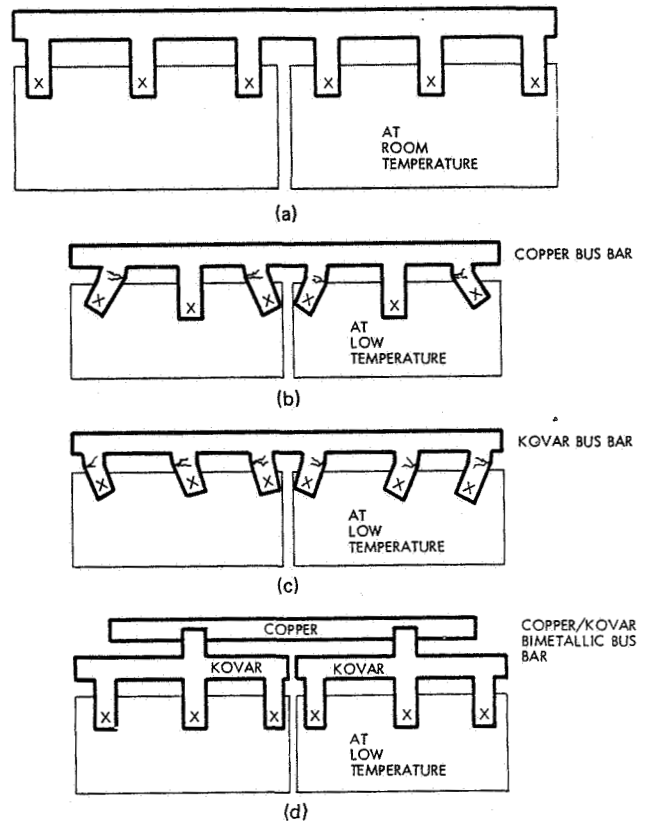


Fig. 5.3-4. Bimetallic Bus Bar Eliminates Rotational Forces on Solder Joints (aluminum substrate) (Ref. 5.3-3)

In unplated interconnectors the internal stresses in the expansion loops are largely due to forces (displacements) applied externally at the ends of the loops. In plated interconnectors additional, internally created stress components arise from differences in the coefficients of linear thermal expansion of the base materials and the platings. The stresses in plated interconnectors, especially in areas where the maximum bending takes place, may readily exceed the yield strength of the plating material and cause cracks to develop in the plating that may propagate into the base material and lead to unsuspected, premature fatigue failure of the expansion loops.

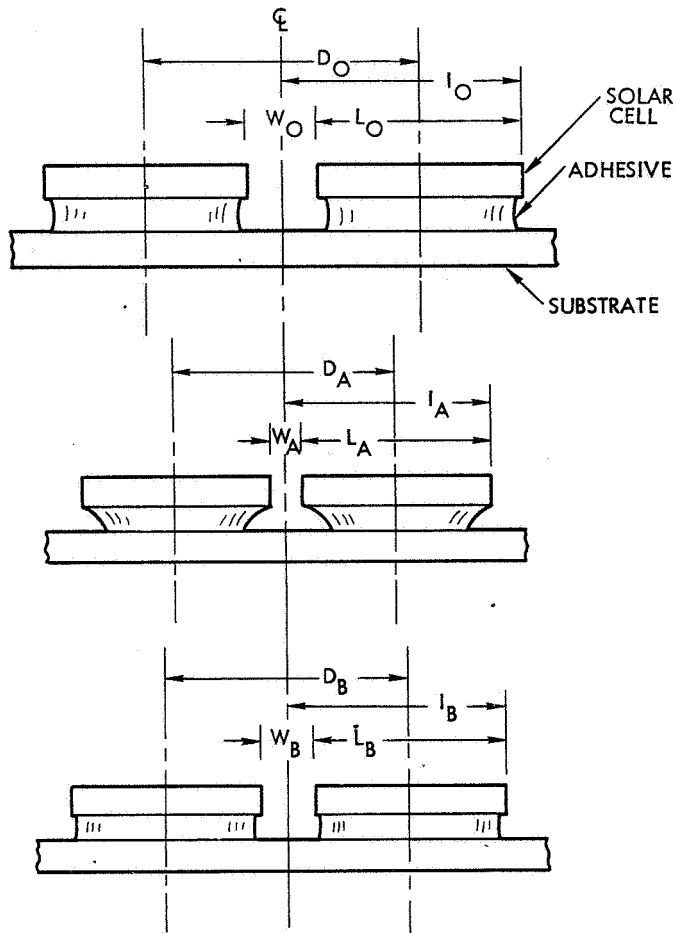
Changes in the Intercell Gap Width

Consider the schematically illustrated cross section of an assembly of two solar cells (without interconnectors) mounted to a substrate, as shown in Figure 5.3-5. The top sketch (Case O) shows the array in equilibrium and stress free at a reference temperature T_0 . The center-to-center distance between solar cells is D_0 , the cell length is L_0 , the intercell gap width is W_0 and cell indexing distance is I_0 . From the geometry of the assembly,

$$W_0 = D_0 - L_0 \quad (5.3-11)$$

and

$$I_0 = L_0 + W_0/2 \quad (5.3-12)$$



CASE O
 ASSEMBLY IS FREE OF STRESS AT EQUILIBRIUM TEMPERATURE T_0 .

CASE A
 ASSEMBLY IS FREE OF STRESS AT LOW TEMPERATURE T_L WHEN ADHESIVE HAS ZERO SHEAR STIFFNESS.

CASE B
 ASSEMBLY IS UNDER HIGHEST STRESS AT LOW TEMPERATURE T_L WHEN ADHESIVE HAS INFINITE SHEAR STIFFNESS

Fig. 5.3-5. Changes in Cell Spacings due to Low Temperature

Now let the temperature of this assembly be lowered to T_L and equilibrium be established again. The assembly may now be either stress-free (Case A) or under stress (Case B), depending upon the stiffness of the cell-to-substrate adhesive.

Case A

In Case A (Figure 5.3-5) the hypothetical zero-stiffness adhesive permitted undisturbed contraction of the solar cells and the substrate in accordance with their respective thermal expansion coefficients due to the decrease in temperature $\Delta T = T_L - T_0$ (ΔT is a negative quantity for this example) so that

$$L_A = L_0(1 + \alpha_c \Delta T) \quad (5.3-13)$$

and

$$D_A = D_0(1 + \alpha_s \Delta T) \quad (5.3-14)$$

where α_c and α_s are the linear thermal expansion coefficients for the cell and the substrate, respectively. Also

$$W_A = D_A - L_A = W_0 + W_0 \alpha_s \Delta T + L_0(\alpha_s - \alpha_c) \Delta T \quad (5.3-15)$$

Since for practical purposes $W_0 \ll L_0$ Eq. 5.3-15 reduces to

$$W_A = W_0 + L_0(\alpha_s - \alpha_c) \Delta T \quad (5.3-16)$$

The change in gap width is

$$\Delta W_A = W_A - W_0 = L_0(\alpha_s - \alpha_c) \Delta T \quad (5.3-17)$$

Similarly

$$I_A = I_0 + I_0 \alpha_s \Delta T \quad (5.3-18)$$

and the change in the indexing distance is

$$\Delta I_A = I_A - I_0 = I_0 \alpha_s \Delta T \quad (5.3-19)$$

Eq. 5.3-17 confirms the intuitive suspicion that the change in the cell gap width, ΔW_A from W_0 to W_A is proportional to the cell length, L_0 , the differential expansion coefficient ($\alpha_s - \alpha_c$) and the temperature excursion, ΔT . Eq. 5.3-19 indicates that the change in the cell indexing distance, ΔI_A , is identical to the change in the substrate length (cell center-to-center distance) $\Delta D_A = D_0 - D_A$.

Practical cases of nearly-zero-stiffness adhesives are found when using RTV adhesives above approximately -100°C or adhesive spot bonds rather than full area bonds placed at the center lines of the solar cells.

Case B

In Case B (Figure 5.3-5) a hypothetically "stiff" adhesive in the shear direction is used between the solar cells and the substrate such that the cell and substrate on either side of the adhesive interface contract or expand at identical rates (assuming further that the elastic modulus of the adhesive is negligibly small). As a consequence of this stiff coupling between cell and substrate, the cells become stressed in compression, and the substrate (over the extent of the bond area) becomes stressed in tension, resulting in a greater amount of contraction of the solar cell length, but in a lesser amount of contraction of the substrate as compared to Case A above. The degree to which the cells and the substrate deform depends upon the ratio of the lateral stiffness of the solar cells to that of the substrate. The lateral stiffness in this example is the product of the elastic modulus times the cross-sectional area (of either the solar cells or the substrate) in the direction parallel to the substrate or cell dimensions D and L in Figure 5.3-5, respectively.

The effect of a stiff coupling between the solar cells and the substrate of Case B is a lesser change in the gap width than was observed in Case A, so that

$$W_B < W_A \quad (5.3-20)$$

and

$$\Delta W_B < \Delta W_A \quad (5.3-21)$$

Practical cases of stiff coupling between solar cells and the substrate arise from the use of certain epoxy type adhesives, thin bond lines and lower temperatures than approximately -120°C .

Loop Deformation

For illustration, consider the interconnector between the two series-connected solar cells in Figure 5.3-6a and the corresponding free-body diagram in Figure 5.3-6b. From this figure it is seen that

$$A + L + R = D + B \quad (5.3-22)$$

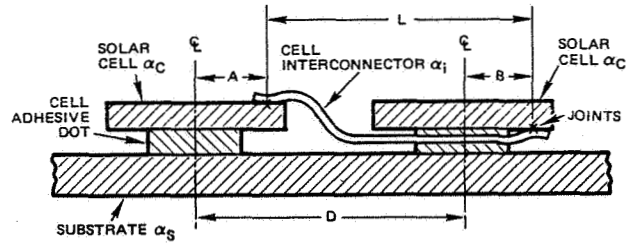
where R is the required deformation of the expansion loop because points x and y are actually coincident and permanently fastened together.

A change in temperature, ΔT , will change all dimensions as follows (after rearranging the terms):

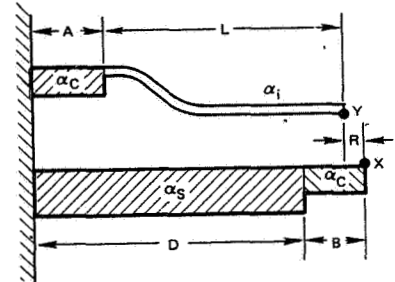
$$\Delta R = D\alpha_s \Delta T + (B - A)\alpha_c \Delta T - L\alpha_i \Delta T \quad (5.3-23)$$

where the α 's are the average coefficients of linear thermal expansion (defined in Section 7.11) and the subscripts s , c and i refer to the substrate, cell, and interconnector, respectively. Rearranging the terms again, we obtain

$$\frac{\Delta R}{\Delta T} = D\alpha_s + (B - A)\alpha_c - L\alpha_i \quad (5.3-24)$$



(a) SCHEMATIC CROSS SECTION



(b) FREE-BODY DIAGRAM

Fig. 5.3-6. Required Loop Deformation, R , With Points x , y Coincident and Temperature Variable

This equation is plotted parametrically in Figure 5.3-7 for a range of values for α_s and α_i covering most practical design cases. The condition where $B = -10$ mm represents the usual interconnector loop designs depicted in Figure 5.3-8(a) and (b) of Section 5.3.8.

If $R = 0$ at $T = T_0$, the interconnector is stress free at T_0 . For the interconnector to remain stress free at any temperature, the condition $\Delta R/\Delta T = 0$ is required for the temperature range between T_0 and T . The conditions under which the interconnector remains stress free are found by setting Eq. 5.3-24 equal to zero so that

$$D\alpha_s + (B - A)\alpha_c = L\alpha_i \quad (5.3-25)$$

Practical solutions to Eq. 5.3-25 show the following:

- If the expansion coefficients of the substrate and interconnector materials are alike ($\alpha_s = \alpha_i$) and if the interconnector is attached to the lower contact directly below the upper contact (distances $B = A$ in Figure 5.3-6), then the interconnector remains stress free ($\Delta R = 0$) at any temperature.
- If α_s and α_i are different, Eq. 5.3-25 can be solved by substituting Eq. 5.3-22 with $R = 0$ to find the interconnector length, L , for which the interconnector remains stress free at any temperature:

$$L = \left(\frac{\alpha_c - \alpha_s}{\alpha_c - \alpha_i} \right) D \quad (5.3-26)$$

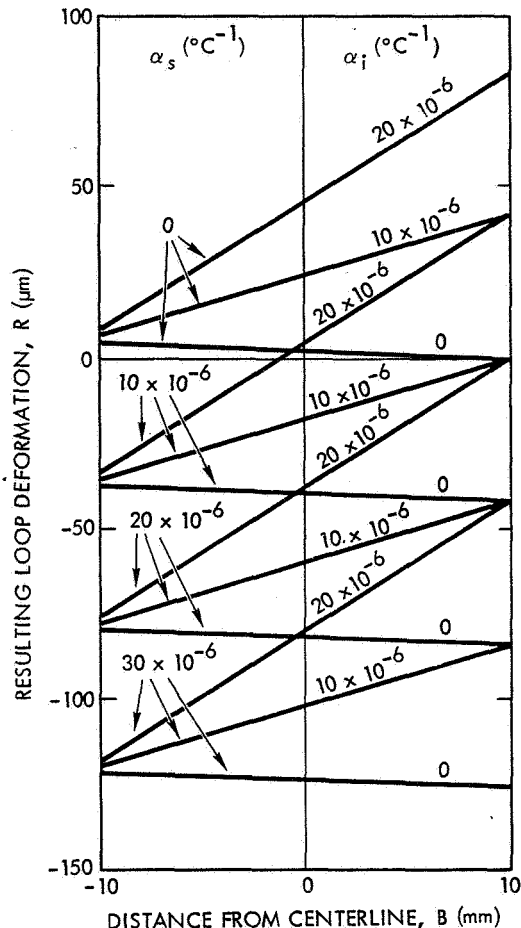


Fig. 5.3-7. Loop Deformation Resulting from Different Choices of Substrate Materials (α_s), Interconnector Material (α_i) and Interconnector Attachment Distance (B) [according to Eq. 5.3-14 for $A = 10$ mm, $D = 21$ mm, $T = -175^\circ\text{C}$ (for actual values of α see Section 7.11)]

In a practical sense, a purely stress-free interconnector design cannot be achieved because the coefficients of linear thermal expansion of different materials are uniquely nonlinear with temperature. Nevertheless, significant stress reductions and fatigue life extensions can be achieved by this method. A so-called "stress-free" interconnector, based on Eq. 5.3-26, was patented (Ref. 5.3-5) and utilized by Ref. 5.3-6.

Simulated Thermal Cycling Testing

Simulated thermal cycling testing of interconnector expansion loops consists of mechanical stretching and compressing of the loops at room temperature by the same amount as the loops would be deformed when the array undergoes thermal cycling. Test results have shown that simulated thermal cycling testing of loops predicts a much longer fatigue life than actual thermal cycling testing predicts (Ref. 5.3-6), thereby verifying that the thermally induced stresses are most significant in assessing interconnector loop fatigue life.

5.3.4 Stresses in Imbedded Interconnectors

Imbedded interconnectors include such elements as conductors in flat cables, conductors bonded to substrates, and solar cell interconnectors encased by adhesive or other dielectric material.

Stresses in imbedded interconnectors of significance include tensile, compressive, shear, and bending stresses. These stresses arise from the differences in the coefficients of linear thermal expansion of the different materials in intimate contact with each other. The stress magnitude increases mainly at lower temperatures where the strength and stiffness of most insulating materials used on solar cell arrays increases significantly. Excessively high stresses can occur particularly at low temperatures where they may cause open-circuit failure of conductors.

The probability of conductor failure increases with a decrease in array temperature and with increases in the insulator/conductor cross-sectional area ratio and the insulator/conductor material strength ratio.

5.3.5 Stresses in Solar Cell Stacks

For the purpose of discussion in this handbook, solar cell stacks are defined as hypothetical mechanical subassemblies that contain the following elements:

- A portion of the substrate
- Cell-to-substrate adhesive
- Solar cell
- Cover-to-cell adhesive
- Solar cell cover
- Solar cell interconnectors attached to the cell contacts.

For extremely low temperature operation (below about -150°C), the stresses in the solder joints, for example, may be affected by stress components arising from the presence of the other elements in the solar cell stack.

Stresses of significance to solar cells, solar cell array substrate, and solar cell covers, independent of additional stress components that may be caused by the solar cell interconnectors, include the following:

- Tensile, compressive bending and peel stresses in the solar cells and in the substrate due to the adhesive coupling between the cells and the substrate.
- Tensile, compressive, shear, torsional and localized bending stresses in the solar cells (in the silicon wafer) in areas where the cell contacts are applied, especially where relatively thick contact metallizations (such as solder) are used and where solar cell interconnectors are attached.
- Tensile, compressive, shear and bending stresses in the silicon wafer that were introduced during the solar cell manufacturing (diffusion) process (see Sections 3.1.3 and 7.6).
- Tensile, compressive, shear and peel stresses in the solar cell, cover adhesive and solar cell covers.

Excessively high stresses, typically at low temperatures, may cause the following:

- Substrate damage (face sheet adhesive bond failures),
- The ultimate strength of the solar cell to be exceeded (silicon spalling)
- Cell-to-substrate adhesive bond separation
- Solar cell covers fracture.

5.3.6 Design of Interconnector Configurations

The design of the interconnector configuration is related to two distinctly different portions of the interconnectors:

- The contact pads that will be attached (by soldering, welding or otherwise) to the solar cell contacts.
- The conductors ("arms" and "legs") between the contact pads (in the parallel and series current-flow direction).

In most designs the thermal expansion loops (out-of-plane or in-plane) are formed by the series and parallel-conductors ("legs" and "arms," respectively).

General Design Practices for Contact Pads

The following should be considered when designing the contact pads of solar cell interconnectors:

- The pad size (area) should be compatible with the available solar cell contact area. On the upper cell contact the pads should be as small as practical to maximize the active solar cell area. Except for small wrap-around contact areas, no such limit exists normally on the lower cell contact.
- The pad size and the pad location on the cell contacts should be compatible with the solar cell cover design and cover installation tolerances.
- The pad size and joint area should be as large as practical for the following reasons:
 - 1) To minimize the stress in the joints due to external forces and torques transmitted by the interconnectors into the joints.
 - 2) To increase the number of thermal cycles required to propagate a fatigue crack through the entire joint area.
- The pad dimensions should be compatible with the tip size of the soldering, welding or bonding equipment to be used, and should permit repair work to be performed by unsoldering or debonding from a defective solar cell and rebonding to a new cell.
- Sharp corners and abrupt changes in dimensions can act as stress risers and, therefore, should be avoided.

Additional Design Practices for Soldered Pads

The designer of solar cell interconnector contact pads that are to be attached by soldering should

consider the following in addition to the general design practices described above:

- During soldering the pad should facilitate the formation of a solder fillet around the pad circumference.
- The practice of using solder reflow inspection holes in the pads is currently controversial. Some workers believe that the existence of such holes lead to earlier joint fatigue failures. However, other workers favor the opposite viewpoint. Therefore, it is suggested that a decision for or against solder reflow inspection holes be based on experimental data obtained for each specific design that is considered for flight use.
- The surface of the pad (or its plating) should promote solder wetting. A precoating of the pad with solder (using electroplating or any other method) is desirable (Ref. 5.3-7).

Additional Design Practices for Welded Pads

The designer of solar cell interconnector contact pads that are to be attached by welding should consider the following in addition to the general design practices described above:

- The pad size and area can conveniently be made much larger than the weld joint area; the high temperature achieved by welding will cause sufficient interconnector material deformation to obtain good joints.
- The surface roughness of the pads should be controlled to permit high-quality welds to be made (see Section 3.9.6).
- The interconnector plating material and thickness should be selected to permit high-strength weld joints to be made (Ref. 5.3-8).

Additional Design Practices for Thermocompression-bonded Pads

The designer of solar cell interconnector contact pads that are to be attached by thermocompression bonding should consider the following in addition to the general design practices described above:

- The bond strength tends to increase with increasing bonding temperature and stylus pressure, requiring precautions to be taken to prevent contact oxidation and cell fracturing (Ref 5.3-9).
- In general, the bond strength between interconnectors and silicon solar cells tends to be higher for the softer and lower melting point materials.
- Cell and interconnector surface finish should be smooth (probably better than 0.1 μm rms) and total material thickness (such as silver platings) in the bond area should be at least 5 μm .
- Since thermocompression bonding occurs at temperatures below the melting point of materials, the pad size must be smaller than the bonding stylus.

Additional Design Practices for Ultrasonically Bonded Pads

The designer of solar cell interconnector contact pads that are to be attached by ultrasonic bonding should consider the following in addition to the general design practices described above:

- Ultrasonic bonding of solar cell interconnectors appears to be most suitable for aluminum interconnectors. Bonding of other metals by ultrasonic methods appears to be more critical than bonding by other methods. Therefore, it is recommended that the design effort for interconnectors that are to be bonded ultrasonically be supported by adequate developmental testing, especially by pull testing before and after temperature cycling (Refs. 5, 3-9 and 5, 3-10).

General Design Practices for Conductors and Expansion Loops

The design of solar cell interconnector conductors ("arms" and "legs" between the contact pads) should consider the following:

- Conductors should be as short as possible to minimize electrical resistance and potential damage in handling and during launch, but they should be sufficiently long to prevent thermal expansion loops from transmitting significant stresses into the soldered or welded joints.
- Conductors should be designed symmetrically about the soldered or welded joints so as to cause no rotating forces to act on the joints (see Section 5.3.2) when the interconnector is loaded in tension or compression (i. e., when adjacent cells during thermal cycling move closer together or farther apart).
- Conductors should be redundant for both reliability and electrical conductivity reasons.
- Conductors should possess adequate strength (material yield strength and cross-sectional area) to withstand fabrication, handling, assembly, and operational forces arising from imbedment (see Section 5.3.11).

Additional Design Considerations for Mesh Interconnectors

The designer of solar cell interconnectors and expansion loops that are made from metal mesh should consider the following:

- Mesh displays excellent flexibility when unrestrained; however, this flexibility depends upon the freedom of a piece of mesh to contract in one direction when elongated into a perpendicular direction. After soldering or welding to solar cells and attaching the cells to a substrate, the flexibility of the mesh is largely lost. Imbedment of the mesh further reduces its flexibility.
- Expanded and flattened mesh may be more flexible than etched or stamped mesh if some of the original warping is retained by the expanded mesh after flattening. (See the discussion of in-plane loop deformation modes in Section 5.3.9).

Additional Design Considerations for Shaped Interconnectors

The designer of solar cell interconnectors and expansion loops that are made from etched or stamped and formed metal piece parts should consider the following:

- Shaped interconnectors can be configured in a limitless variety. Practical limitations exist only for interconnectors that are to be fabricated by stamping (diecutting). By chemical etching almost any configuration can be fabricated with little difference in cost.

5.3.7 Interconnector Material Selection

The selection of a solar cell interconnector material requires making engineering choices and specifying the following:

- Metal and general chemical composition
- Purity
- Temper
- Platings (if any)
- Thickness of base metal and platings
- Surface finish of base metal and platings.

From the many available materials, the following metals and platings have been found most suitable for long life or severe temperature-cycling requirements:

- Copper, annealed, oxygen-free high-conductivity (OFHC), unplated or silver plated
- Silver, annealed, high-fine
- Kovar, annealed, nickel/copper/solder or silver plated
- Invar, annealed, silver plated
- Aluminum, 1100 pure, annealed, unplated or silver plated
- Molybdenum, annealed, silver plated
- Beryllium copper, annealed.

The material selection process is intimately related to the overall interconnector design process through the following material characteristics:

- Thermally induced stresses in the joints are lowered when the coefficient of linear thermal expansion of the interconnector (base material and plating) approaches that of silicon.
- Thermally induced stresses in the joints are lowered when the interconnector is made more "flexible" by:
 - a) Selecting a low modulus of elasticity material
 - b) Selecting a high ductility material
 - c) Utilizing a low-yield strength interface material in the joint area (plating, for example).
- Stresses in the interconnector expansion loops are lowered and loop fatigue life is increased by using a more ductile material.

- The electrical losses and the interconnector weight are reduced by using a higher electrical conductivity material or a thicker high-conductivity plating on low-expansion base metals.

5.3.8 Mechanical Design for Series Loops for Front-back Contact Solar Cells

Series loops are solar cell interconnector thermal expansion loops that bridge intercell gaps in the direction of current flow through strings of illuminated solar cells.

For conventional front-back solar cell contacts, the interconnector must connect the contact on the top of one cell to the contact on the bottom of the next cell. The available alternate interconnector configurations (in cross section) include the following:

- Z-step without loop -- step deforms (Figure 5.3-8a)
- Z-step with loop - step and loop deform (Figure 5.3-8b)
- Loop only (for overlapping cells only) -- loop deforms (Figure 5.3-8c)
- Wraparound interconnector -- loop does not deform; in-plane stress relief loops on bottom of both cells deform in a plane perpendicular to the plane of the paper (Figure 5.3-8d; described in Ref. 5.3-13)
- "Stress-free" interconnector -- loops deform negligibly (Figure 5.3-8e).

The choice of the cross-sectional expansion loop configuration from those shown in Figure 5.3-8 is independent of the plane-view geometry of the interconnectors discussed in Section 5.3.6; however, the dimensions of the expansion loops depend strongly upon the magnitude and frequency of the intercell gap width variation throughout mission life and to some degree on the plane-view geometry. Other significant design considerations include manufacturability and potential interference with the solar cell cover.

Design Practices

The fatigue (flex) life of expansion loop configurations a, b and c in Figure 5.3-8 can be increased as follows:

- Reduce the interconnector thickness
- Increase the expansion loop height
- Increase the distance (and thereby the interconnector length) between attachments to the cells, measured across the intercell gap
- Select a material with inherently greater flex life capability
- Modify the dimension of the interconnector loop in the direction in Figure 5.3-8 which is perpendicular to the plane of the paper such that the maximum bending moment no longer concentrates at a single point on the loop when viewed as shown in Figure 5.3-8.
- Prevent solder from filling (wicking) and stiffening expansion loop radii
- Prevent adhesive overflow from stiffening expansion loops.

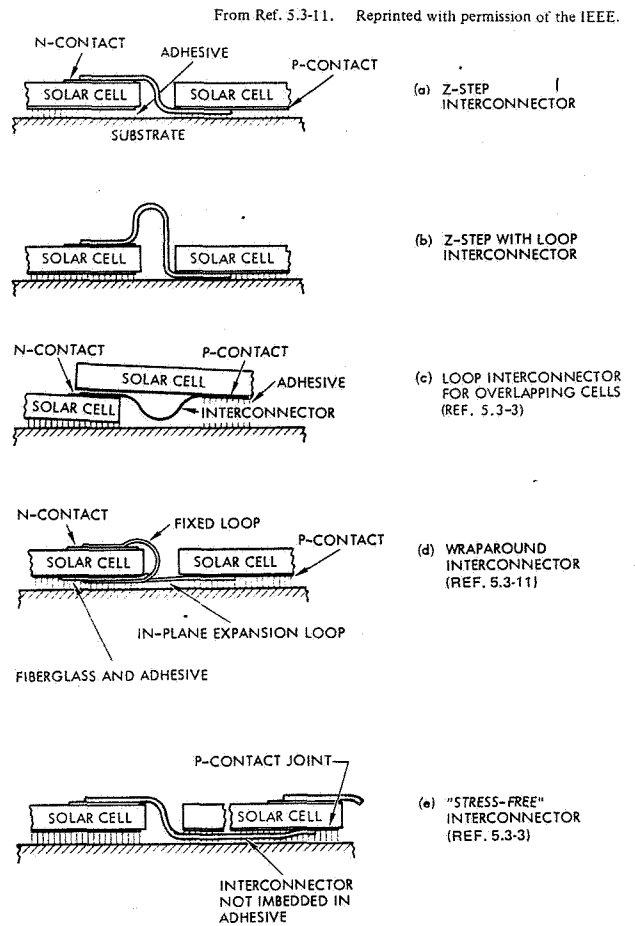


Fig. 5.3-8. Alternate Cross-Sectional Interconnector Configurations for Front-back Contact Solar Cells

The calculations of the expansion loop dimensions of configurations a, b and c in Figure 5.3-8 are described in Section 9.7. Loop configuration d is discussed in Section 5.3.8. The analysis of configuration e is given in Section 5.3.3.

5.3.9 Mechanical Design of Series Loops for Wraparound Contact Solar Cells

Series loops are solar cell interconnector thermal expansion loops that bridge intercell gaps in the direction of current flow through strings of illuminated solar cells.

For wraparound contact solar cells, the solar cell p and n contacts are on the same cell side and in the same plane. The available alternate interconnector configurations (in cross section) include the following:

- Loop - loop deforms (Figure 5.3-9a)
- In-plane -- interconnector deforms in a plane perpendicular to the plane of the paper (Figure 5.3-9b)
- "Stress-free" interconnector -- interconnector deforms negligibly (Figure 5.3-9c).

Loop Configuration a in Figure 5.3-9 is generally impractical because of interference of the loop with the solar cell covers and a relatively large substrate

area requirement which, in turn, leads to a poor packing density. However, if it is to be used, the considerations of Section 5.3.8 apply.

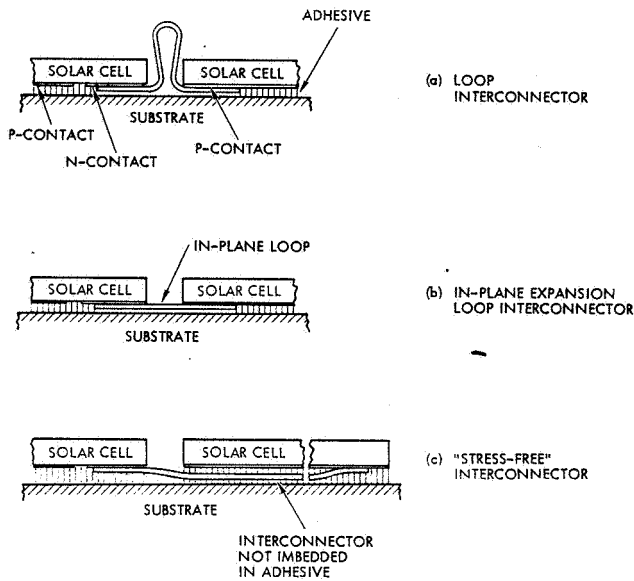


Fig. 5-3-9. Alternate Cross-Sectional Interconnector Configurations for Wraparound Contact Solar Cells

In-Plane Loop Deformation Modes

In-plane expansion loops deform by either one or both of these mechanisms:

- True in-plane bending of portions of the interconnectors in the "hard-to-deform" direction (about the Z-axis shown in Figure 5.3-10)
- Out-of-plane warping of portions of the interconnectors and bending in the "easy-to-deform" direction (the bending in this case is about the X-axis shown in Figure 5.3-10).

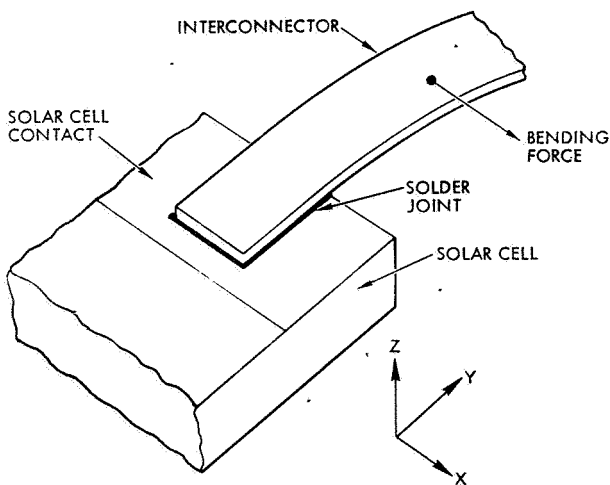


Fig. 5.3-10. Definition of Bending Axes

Design Practices

To assure adequate fatigue life of in-plane expansion loops, the following should be considered:

- The in-plane expansion loops must be able to endure the same deformations as the out-of-plane expansion loops (see Sections 5.3.3 and 5.3.8).
- Rotational forces at the interconnector ends (soldered or welded joints) must be prevented (see Section 5.3.2).
- Interconnectors imbedded in adhesive or other dielectric material are to be treated as discussed in Section 5.3.11.

5.3.10 Mechanical Design of Parallel-Loops

The design of thermal expansion loops in solar cell interconnectors that electrically connect solar cells in parallel is essentially similar to the design of the series loops. The loops may be placed either on the top of solar cells so that they take on the appearance of out-of-plane loops or they may be placed on the cell's underside in which case they are essentially identical to in-plane interconnectors for wrap-around contact solar cells.

5.3.11 Mechanical Design of Imbedded Interconnectors

Interconnectors may be semi-imbedded (glued to a substrate, for example) or fully imbedded (encased by adhesive or any other dielectric material). In either case, the interconnectors (restrained from deforming in their intended manner) can cause the following effects:

- Shear stressing of the soldered or welded joints, leading to premature joint failures.
- Tensile stressing of the interconnector conductors, leading to premature conductor fracture (open-circuit failure, as illustrated in Section 5.2.2).

Design Practices

To assure adequate fatigue life of imbedded in-plane or Z-step expansion loops, the following should be considered:

- Reduce the imbedded, effective interconnector stiffness (caused by the conductor and the surrounding dielectric) by bringing the expansion loops as close to the joints as possible
- Design the expansion loops such that they can locally slice through the dielectric and develop small cavities in which they can more freely deform
- Make the interconnectors significantly stronger than the surrounding dielectric material (strength = yield strength x cross-sectional area; see Section 7.5)
- Shape and size the expansion loops such that high stress concentrations are avoided
- Minimize stresses in the joints, as described in Section 5.3.1.

5.3.12 Mechanical Design of Solar Cell Stacks

The elements of solar cell stacks (defined in Section 5.3.5) are subject to the following design considerations in regard to thermomechanical stresses, especially at low temperatures.

Substrate

The design requirements for the substrate may be influenced by the solar cell stack behavior as follows:

- The substrate's rigidity or flexibility may contribute to stresses in the silicon at the solar cell/substrate interface.
- Insufficiently flat substrate surfaces ("dimples" in thin-facesheet honeycomb panels) may lead to irregular adhesive layer thickness and stress riser effects.
- Insulating layers on conductive substrate facesheets may be debonded from the substrate by excessive forces exerted by the cell-to-substrate adhesive.

Cell-to-Substrate Adhesive

The selection of the specific adhesive and/or the solar cell stack design and/or the cell stack-to-substrate mounting method may be restrained by the following:

- At low temperatures the stress in the adhesive and in the lower surface of the silicon solar cell wafer generally increases with increasing adhesive thickness.
- Adhesive layer thicknesses of less than 25 μm may prohibit proper curing of certain adhesives.
- Below the brittle point (glass transition region) the adhesive may cause additional, significant stress components in soldered or welded joints due to tensile, compressive or shear loading of imbedded interconnectors.

Solar Cells

Solar cells, even at room temperature, are not free of internal stress. The internal stress arises from the following:

- The p and n layers have different atomic densities due to the effects of doping (see Section 3.11).
- The silver contacts (over titanium and palladium, if used) are sintered at elevated temperature and contract at a greater rate than the silicon during cooling.
- Solder coatings contract at a greater rate than the silicon during cooling.
- The strength of solder increases significantly with decreasing temperature.

Cell-to-Cover Adhesive

Thermomechanical stresses may be caused by the cover adhesive in the following: the solar cell, the cover, the adhesive, and the soldered or welded joints between the cell interconnectors and the cell's front

surface contacts. In general, stresses are minimized by minimizing the adhesive layer thickness. However, some adhesives do not cure properly when their thickness is below about 25 μm .

5.3.13 Electrical Design

The interconnector electrical design must be performed in conjunction with the mechanical design because the thermomechanically imposed design requirements tend to be in opposition to the design requirements for good electrical performance: the mechanical requirements favor long, small cross-sectional conductors using low-thermal expansion (high resistivity) materials while the electrical requirements call for short, large cross-sectional conductors having low resistivity.

Design Criteria

The adequacy of the electrical interconnector design is judged on the basis of electrical losses in the interconnector system. Losses may be expressed in terms of voltage drops or power (I^2R) losses. The values of these two losses, when expressed as fractions, are the same.

A convenient expression is "percent cell output loss" because this quantity has approximately the same value when based on single cell or on total array output capability.

Interconnector Material Selection

After an interconnector material is selected for thermomechanical reasons and after the interconnector shape is defined, the interconnector material may have to be plated to achieve the desired electrical conductivity. If the basic interconnector material is a low-expansion alloy (Kovar, Invar, etc.), the electrical conductivity of this material can usually be ignored and only the highly conductive plating (copper, silver, etc.) needs to be considered.

The effect on electrical conductivity due to overplating with solder should be considered with caution because extensive thermal cycling tends to destroy the continuity of smooth solder coatings and causes their electrical resistance to increase (see Section 5.3.2).

Values of the relative resistivity and conductivity of various interconnector and plating materials are given in Section 7.9.

Interconnector Sizing

The total electrical resistance, R , between two series-connected solar cells is

$$R = \rho L / AN$$

where ρ is the resistivity, L is the current path length (between solder joints), A is the cross-sectional area of each interconnector "leg" and N is the number of interconnector "legs" per cell.

For a design criterion which specifies a maximum voltage drop of D ,

$$D = IR = I_p L / AN$$

where I is the nominal cell output current and the other symbols are defined above. Replacing the cross-sectional area, A , with w for width and d for thickness

of a commonly used rectangular cross-sectional area of interconnectors,

$$D = \rho IL / Nwd$$

A graph of D versus w for copper is shown in Figure 5.3-11 for conveniently estimating interconnector electrical performance characteristics.

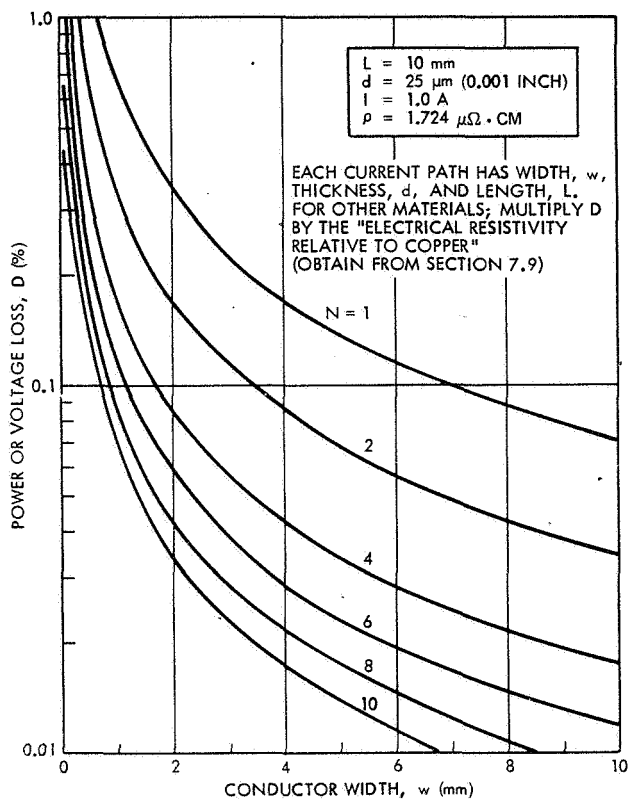


Fig. 5.3-11. Power or Voltage Loss in Cell-to-Cell Copper Interconnector Having N Current Paths Between Cells

Plating Thickness Sizing

A conductor of length, L, resistivity, ρ_o , with rectangular cross section, having width, w, and thickness, d, has a resistance of

$$R_o = \frac{\rho_o L}{wd}$$

A conductive plating of such conductor, having a resistivity ρ_p and a plating thickness, d_p , has a resistance of

$$R_p = \frac{\rho_p L}{2d_p(w + d + 2d_p)}$$

The combined plated conductor resistance is

$$R = \frac{\rho_o \rho_p L}{\rho_p wd + 2d_p \rho_o (w + d + 2d_p)}$$

For high-resistivity, low expansion alloys such as Kovar or Invar, $R_o \gg R_p$ so that the plated conductor resistance can be simplified to $R = R_p$. A further simplification is possible when the plating thickness is much less than the interconnector base material thickness ($d \gg d_p$) so that

$$R \approx \frac{\rho_p L}{2d_p(w + d)}$$

and for multiple cell-to-cell conductors

$$D = \rho IL / Nwd'$$

where $d' = 2(d_p + d_p d/w)$ and N is the number of conducting "legs" in parallel.

For practical interconnector cases ($d_p d/w \gg d_p$) so that approximately

$$d' = 2d_p$$

and

$$D = \rho IL / Nw(2d_p)$$

For $d' = 25 \mu\text{m}$, Figure 5.3-11 can be used for selecting w for a given D, or conversely, for given w and D, select the plating thickness, d_p .

5.3.14 Reliability Considerations

Reliability considerations may influence solar cell interconnector design as follows:

- Determination of the number of redundant solder joints on each cell contact
- Determination of the number of redundant interconnector conductors ("legs") between solar cells
- Collection of output current from portions of (accidentally) fractured solar cells.

Redundancy

If the fraction of failed interconnector conductors or soldered or welded joints at end-of-life is known (from life testing, for example), the required number of joints on the cells and conductors between cells can be calculated by the methods described in Section 9.9. The application of reliability considerations to solar cell interconnector and array design is treated in Section 8.6.

Current Collection from Fractured Solar Cells

The probability of fractured solar cells on arrays is relatively low, however, a fractured cell may adversely affect the power output of an entire string, as discussed in Section 9.3.2. To minimize the

effects of fractured cells, Ref. 5.3-1 recommends the use of redundant joints on the cell and the locating of the interconnector soldering or welding tabs such that when a cell fractures, the largest possible fraction of the cell area remains electrically connected (both p and n sides) to the string of cells.

5.4 WIRING AND CABLING

5.4.1 Selection Criteria for Wires and Cables

The following provides a checklist for the design and/or selection criteria that may apply to wires and cables (both to their conductors and insulators) used on solar cell array exterior surfaces and for connecting solar cell array assemblies to each other and to the spacecraft.

- Environmental Criteria

- a) Vacuum Stability

- Outgassing
 - Embrittlement

- b) Radiation Resistance

- Ultraviolet
 - Charged Particles
 - Plasma

- c) Temperature

- Embrittlement at low temperature
 - "Cut-through" and "cold-flow" (creep) at high temperature
 - Heating due to I^2R -losses
 - Cooling by radiation and conduction

- Physical Criteria

- a) Wire and Cable Type

- Round
 - Flat (printed circuit)
 - Solid
 - Stranded

- b) Use-Related

- Weight
 - Handleability
 - Flexibility (deflection per unit bending force)
 - Flex life
 - Limpness (lack of inherent stiffness)
 - Tensile strength (related to launch environments and wire tie-down design)
 - Color coding
 - Strippability
 - Termination method
 - Conductor coatings (related to solderability)

- Electrical Criteria

- a) Conductor Cross-sectional Area

- Resistance
 - I^2R heating
 - Conductor strength relative to insulator strength over entire temperature range (related to conductor breakage)

- b) Resistance

- Maximum voltage drop (power loss)
 - Array impedance (cable impedance)
 - Redundancy
 - Conductor material choice

- c) Voltage Rating

- Safety Factor (insulation breakdown voltage divided by operating voltage)
 - Insulation deterioration with time in space

- d) Electromagnetic Interference (EMI)

- Cable shielding or twisting
 - Grounding

- e) High-voltage Effects

- Corona (related to insulation breakdown)
 - Insulation life

5.4.2 Weight Considerations

Solar cell array wires and cables conduct the electrical energy from the solar cells to the array (or panel) output connector or output terminal strip. Wires and cables on larger arrays (especially on larger lightweight arrays) may constitute a substantial fraction of the total array weight. On smaller arrays (1 kW and smaller) the minimum wire size is frequently determined by reliability requirements rather than by electrical performance goals. Generally, only on physically larger and higher powered arrays (1 kW and up) do the electrical losses become significant and determine the minimum conductor cross sections. Typical weight tradeoff studies involve such considerations as:

- Number of required parallel-redundant wires
- Length of wire runs
- Insulation requirements
- Insulator and conductor temperature
- Method of connection of electrical strings to primary spacecraft power bus and physical location of isolation diodes (on array or inside spacecraft)
- Maximum permissible voltage drop (may affect the number of solar cells connected in series)
- Heat transfer to and from wire (may affect insulation integrity and resistance of conductor)
- Electromagnetic compatibility and interference criteria.

For an example of bus wiring optimization, considering constant and variable voltage losses from smaller segments of larger arrays, see Ref. 5.4-1.

5.4.3 Design Practices

Minimum wire sizes, redundancy, and insulation voltage ratings are typically mission and project peculiar. Resistance values for various gage conductors are readily available in various standard electrical handbooks and military wire specifications. Insulation properties are readily available from cable manufacturers and specific literature (see the bibliography to this chapter).

Wire routing on solar cell arrays should be performed carefully and follow these guidelines:

- Avoid routing wires over sharp edges; conductive edges may electrically short circuit, while nonconductive edges may "cut through" insulation and potentially also cause wire-to-wire shorts. Ensure that wire insulation has good "cut-through" resistance.
- Provide thermal expansion loops; copper expands and contracts with temperature at a different rate than aluminum, fiberglass-epoxy, Kapton, or other materials.
- Provide sufficient quantity and quality of wire tiedown places (spot bonds, cable clamps, etc.) to prevent wire damage during launch and liftoff (see Section 2.2 for design practices for launch vibration environments).
- Assure that insulating materials are compatible with:
 - a) The ionizing radiation dose expected during mission life
 - b) The temperature range, both operating and nonoperating, that the array will be exposed to considering the rise in wire temperature due to current flow
 - c) Any outgassing requirements.
- When wires are bundled, the inner wires will operate at a higher temperature; wire size should be determined based on proper derating.
- The bend radius of a single wire should be at least several times its outside diameter. The bend radius of a wire bundle should be not less than ten times its outside diameter.
- Current feed and return wires of the same circuits should be twisted.
- Signal wires (from temperature transducers, etc.) should be kept separate and away from power wires as much as practicable.
- Stranded wires possess greater flex life than solid wires.
- Wires or wire bundles passing over flexible interfaces, hinged joints, etc., should be looped around their joints, such that a minimum of wire twisting rather than a large amount of bending occurs when the joint articulates.

5.5 DIODES

On solar cell arrays, two types of diodes may be used:

- Blocking diodes, also known as isolation diodes
- Shunt diodes, also known as shadow diodes or bypass diodes.

In the following subsections blocking and shunt diodes, their characteristics, and their use are described. In principle, both types of diodes are identical. However, in practice, diverse physical size constraints and electrical requirements usually lead to quite unlike parts in appearance and performance. The nomenclature of diodes and their polarity and bias definitions are given in Section 9.1.1.

5.5.1 Blocking Diodes For Energy Conservation

A nonilluminated array behaves as a string of series-connected rectifier diodes connected in their forward conduction mode across the power bus. The amount of current that could be drained by a nonilluminated array or string of cells without isolation diodes depends upon the bus voltage, but typically could range between 0 and 30 percent of the current which the same array or string would produce when fully illuminated (see Section 9.3).

Blocking diodes conserve energy not only when solar cells become nonilluminated, but whenever the solar cell string output capability falls below the bus voltage (more precisely, when the strings V_{oc} fall below the sum of the voltage and the diode forward drops)

The blocking diodes, however, cause a voltage drop that subtracts from the solar cell output voltage and thereby causes an energy loss when the solar cells produce energy. For example, for a typical 30-volt array and an 0.6-volt diode voltage drop, 2 percent of the energy generated by the solar cells is lost in the form of heat in the blocking diodes.

A decision for using or not using blocking diodes can, in part, be based on the tradeoff between energy losses by nonilluminated cells (described in detail in Section 9.3) and energy losses in the blocking diodes. This tradeoff may be affected by the following:

- Percentage of nonilluminated strings of solar cells and fractional time of nonillumination. (For a body-mounted, spinning array, blocking diodes are almost always essential)
- Power level of the array
- Bus voltage variations in relation to the solar cell I-V curve variations in orbit throughout mission life.

5.5.2 Blocking Diodes for Fault Isolation

When properly placed, blocking diodes may prevent serious or even catastrophic power subsystem failures when primary power bus short-circuit faults occur. Such faults can occur in the following places:

- In cables
- In connectors
- At terminals
- Between adjacent strings of solar cells
- Between solar cell circuits and metallic structural elements (such as a metallic substrate).

Faults can be initiated by inadequate design considerations, improper handling, misuse and/or by operational effects. Operational effects include launch and deployment stresses, thermal expansion and contraction, high-temperature creep (punch-through) of insulating materials and micrometeoroid impacts.

Illustrative Example

Four of several possible locations for blocking diodes near a solar cell array/spacecraft interface are illustrated in Figure 5.5-1. The shaded areas in the figure illustrate areas where the susceptibility of wires to damage is relatively high. Table 5.5-1 illustrates the impacts of diode and wire faults on the power subsystem performance capability of a simple, hypothetical system.

A failure mode and effects analysis similar to that described in the Illustrative Example above can and should be performed for each solar cell array design to determine the optimum location of the blocking diodes. Such analysis could also demonstrate the need for blocking diodes in the first place.

Another likely and catastrophic short-circuit failure mode could occur even on nonconductive substrates as illustrated in Figure 5.5-2. At low temperatures (in an eclipse) adjacent solar cell strings could touch each other and cause a primary bus near-short-circuit fault. A similar fault could exist in a single string which is turned in hairpin fashion by 180 degrees such that the positive and negative string ends are adjacent to each other.

5.5.3 Blocking Diode Characteristics

Typical isolation diodes are conventional, high-reliability rectifier diodes with suitable current ratings. Since these diodes are operated in the space

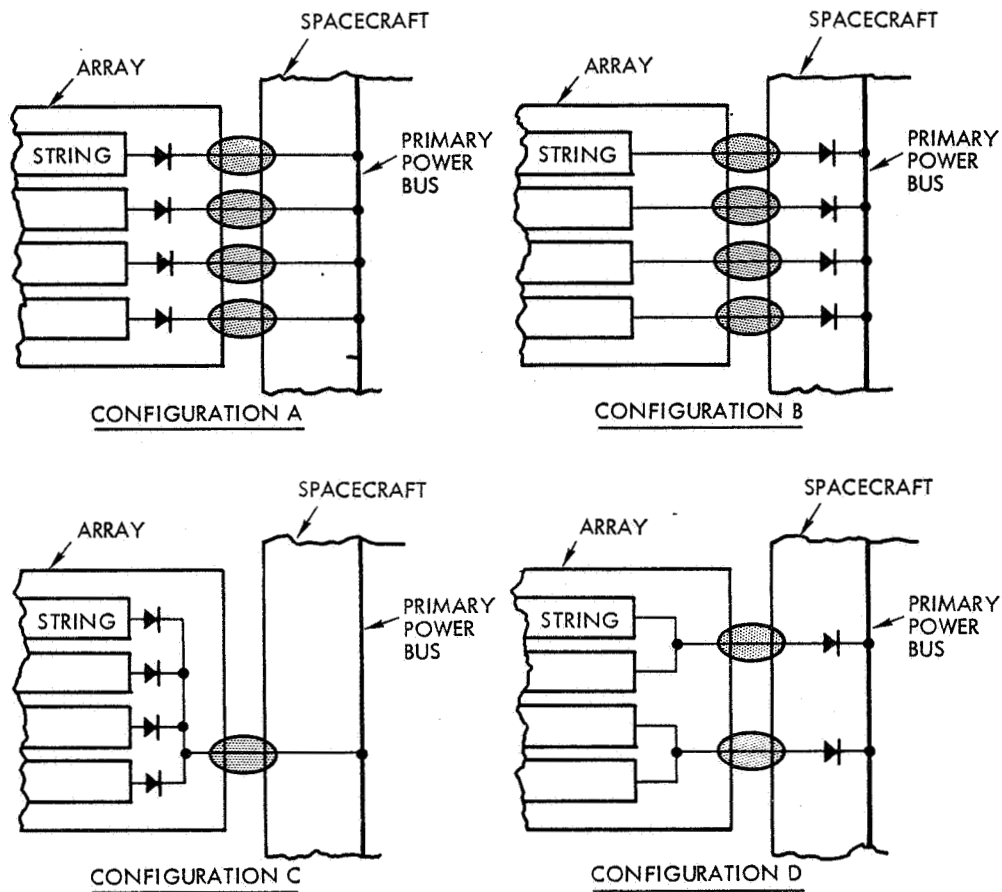


Fig. 5.5-1. Some Possible Blocking Diode Locations and Potential Electrical Failure Areas (shaded).

Table 5.5-1. Illustration of Impact on Power Subsystem Performance, when a Single-Point Failure on the Array/Spacecraft Interface Occurs (Hypothetical solar cell array consists of four strings without redundancy.)

Configuration	Subsystem Power Loss (Percent)			
	Failure of One Diode		Failure of One Wire	
	Short	Open	Short to Ground	Open
A	~0	25	100	25
B	~0	25	25	25
C	~0	100	100	100
D	~0	50	50	50

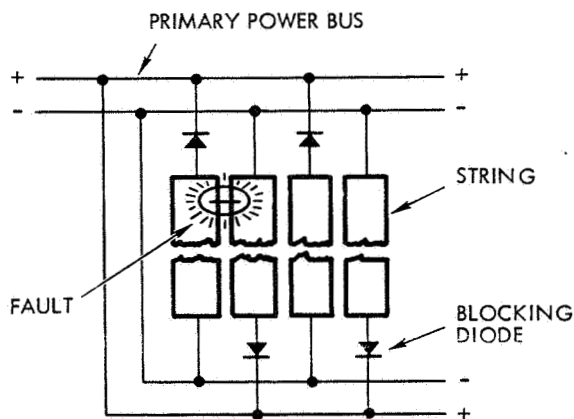


Fig. 5.5-2 Illustration of a Near-Short-Circuit Fault Between Adjacent Strings of Solar Cells (Blocking diodes prevent a catastrophic primary bus failure.)

vacuum environment with a very limited amount of conduction and/or radiation cooling, they must be appropriately derated from their terrestrial current-carrying capability. On the other hand, higher diode operating temperatures result in lower forward voltage drops.

Recently, blocking diodes have been developed that have the physical properties of solar cells and the electrical properties of conventional rectifier diodes. Such blocking diodes are especially useful for flexible solar cell array blankets. According to Ref. 5.5-1, these diodes require coverslides and have the following characteristics (only sample quantities have been produced):

Size (including cover)	10 x 20 x 0.38 mm
Weight	0.258 g max
Forward Voltage Drop (20°C)	0.8 volt max at 0.3 ampere 1.2 volts max at 3.0 amperes
Reverse Leakage Current (20°C)	0.1 mA max at 80 volts 1.0 mW max at 140 volts
Coverslide	Fused silica, Corning Glass 7940 Second surface aluminized
Cover Adhesive	RTV 3144 or R63-489
Thermo-optical Characteristics (glassed)	$\alpha_S = 0.10 \pm 0.01$ $\epsilon_H = 0.81$

Corpuscular radiation damages the junction characteristics of isolation diodes, resulting in lower forward voltage drops and increased reverse leakage current. Normally, however, even a several order of magnitude increase in the reverse leakage current caused by such radiation from microamperes to milli-amperes is inconsequential for most applications.

Some isolation diodes of the axial lead, glass-envelope type are sensitive to light falling approximately perpendicular to the axial direction onto the silicon diode wafer. Illumination of the rectifier diode causes changes in the diode conduction characteristics similar to those caused by illumination of a solar cell (see discussion in Section 3.1). The effects of illuminating a blocking diode are:

- Increased forward voltage drop
- High current flow in the reverse direction (compared to the "dark" reverse leakage), depending on the amount of light incident on the diode junction.

5.5.4 Blocking Diode Design Requirements

Blocking diode specifications may vary depending upon whether the diodes are located on the solar cell array or in the spacecraft interior. However, in general, blocking diodes are selected according to the following criteria:

- Lowest possible forward voltage drop at the nominal current level and at the actual diode operating temperature. Frequently, this current level is the average or peak current at end of life

- Sufficient peak-inverse voltage rating, based on post-irradiation, worst diode temperature, highest bus voltage with superimposed transient voltage spikes and assumed solar cell string short-circuit failure conditions
- Reliability and preferred failure mode. The preferred failure mode should be "open-circuit" so that a desired reliability can be obtained by parallel-redundant diodes. If the preferred failure mode were "short-circuit," series-redundant diodes would be required that would cause an additional diode voltage drop and a corresponding array output power loss
- Capability to withstand temperature cycling throughout mission life without mechanical or electrical failure.

5.5.5 Blocking Diode Installation Practices

Blocking diodes should be mounted and installed considering the following:

- Assure adequate heat dissipation
- Reduce thermally induced stress on the diode leads; diodes and their leads have different coefficients of expansion than circuit boards, terminal strips, or other means of mechanical support
- Provide mechanical stress relief and support to sustain the launch environments (see Section 2.2 for design practices in regard to vibration and other loads).
- Shield the silicon wafer from sunlight.
- Provide means for testing diodes in both the forward conduction and reverse directions after the diodes have been installed.

5.5.6 Shunt Diodes for Minimizing Output Losses

On partially shadowed solar cell arrays the array power output may decrease by a greater amount than what may be deduced from the amount of array area that is shadowed. This mechanism and how shunt diodes can improve the array power output capability is discussed in detail in Section 9.3 (Array Circuit Models).

The power output capability of a fully illuminated array may also be limited by fractured (broken) solar cells. This can occur when parts of the fractured cells become electrically disconnected from their remainders. The effects of fractured cells in an array are similar to those of a partial shadow on the array (see Section 9.3).

Shunt diodes are connected across rows of parallel-connected solar cells (submodules) or across modules (several submodules connected in series) such that the shunt diodes are reverse-biased (see Section 9.1.1 for definition) when all solar cells are fully illuminated. When the current flow through any solar cell submodule becomes limited, it may be due to shadowing or cell fracture. This "affected" submodule automatically becomes reverse-biased (provided that a load is connected to the array) and hence the parallel-connected shunt diode becomes forward-biased and conducts. Thus, the full current can flow in this shunt diode-equipped submodule. However, the voltage output capability of a string of solar cells, containing such

an affected submodule, is reduced by the voltage drop that appears across the shunt diode.

5.5.7 Shunt Diodes for Protecting Solar Cells

Solar cell arrays may be subject to temporary, partial shadowing and the power loss from the shadowed solar cell strings may be of no consequence. There exists, however, the probability that some solar cells may become permanently damaged from such shadowing. The solar cells may become reverse-biased (described in detail in Section 9.3) to such magnitude that permanent cell short-circuit failures may occur (described in Section 3.7).

The maximum reverse bias that can develop across solar cells can be limited by the installation of shunt diodes, as described in Section 5.5.6.

5.5.8 Shunt Diode Characteristics

Essentially three different types of shunt diodes have been used:

- Conventional, packaged rectifier diodes
- Unpackaged diode wafers
- Shunt diodes integral with the solar cells (so-called "integral shunt diodes").

The major criteria in selecting shunt diodes is their physical size and eventual location on the solar cell array. The only practical way for installing shunt diodes is in the immediate vicinity of the solar cells (or submodules) they are to protect.

The use of conventional rectifiers as shunt diodes can severely lower the solar cell packing density (defined in Section 8.9) because the diodes and their leads take up a considerable amount of space (see Figure 5.5-3). On relatively small solar cell panels, or when only few submodules require shunt diode protection, the space (surface area) requirements by conventional rectifiers may be tolerable; however, on relatively large panels with many cells to be protected, their use becomes impractical.

From Ref. 5.5-2. Reprinted with permission of the Gordon and Breach, Science Publishers, Ltd.

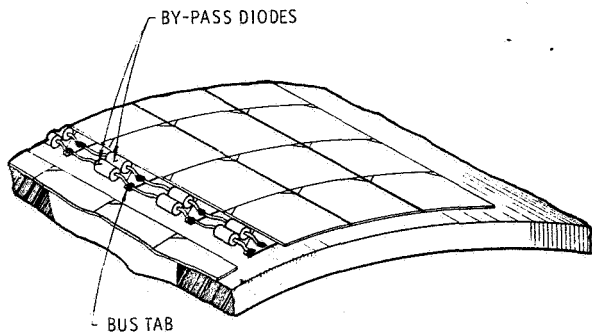


Fig. 5.5-3. Illustration of the Use of Conventional Rectifier Type Diodes as Shunt Diodes (Ref. 5.5-2)

For the protection of large numbers of solar cells on a densely packed array, the best location of shunt diodes is underneath the solar cells. Figure 5.5-4 illustrates one possible approach of using unpackaged rectifier wafers in a flexible, overlapping solar cell module. A redundant pair of diodes protects each

three-cell submodule (2 x 2 cm cells). After installation on the substrate, neither the diodes nor the solar cell interconnector expansion loops were imbedded in adhesive. Both the solar cell interconnectors and the diode leads were made from Kovar ribbons that were plated with copper and solder. The diode wafers were touching the solar cells but they were not attached to the cells. This design was qualified for temperature cycling between -160° and +80°C for 300 cycles. The diodes were made to special order at the time.

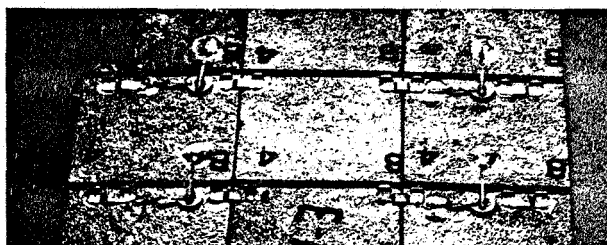


Fig. 5.5-4. Use of Unencapsulated Rectifier Wafers on the Back Side of Flexible, Overlapping Solar Cell Module (Ref. 5.5-3)

A significant improvement in the use of shunt diodes, especially on cells installed "flat" on a substrate (by the "flat laydown" technique) can potentially be achieved when solar cells with integral shunt diodes are used. Figure 5.5-5 illustrates the solar cell and interconnector design. Figure 5.5-6 shows the solar cell interconnector design for use in the conjunction with such solar cells schematically. Figure 5.5-7 indicates relatively high forward voltage drops that would be inadequate for low-voltage arrays (less than 100 volts), but that could be adequate for high-voltage arrays (over 1 kV). Negligible leakage currents were observed with reverse voltages up to 30 volts (Ref. 5.5-2).

From Ref. 5.5-2. Reprinted with permission of the Gordon and Breach, Science Publishers, Ltd.

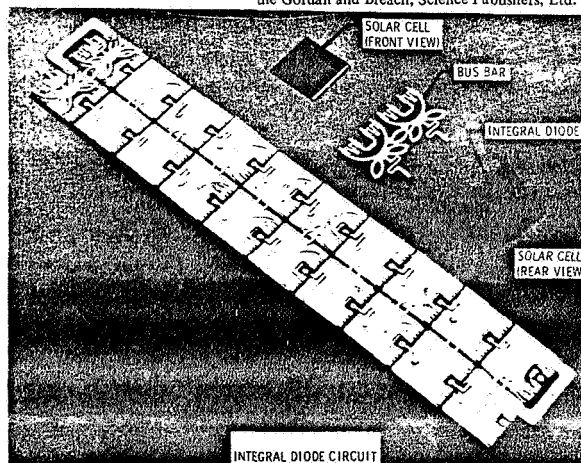


Fig. 5.5-5. Solar Cell Module, Solar Cell With Integral Shunt Diode, and Interconnector Design (Ref. 5.5-2)

Solar cells with integral Schottky-barrier diodes have been reported by Ref. 5.5-4 to have lower forward voltage drops than the diffused diodes of Ref. 5.5-2 exhibit. Schottky-barriers (metal-semiconductor junctions transporting majority carriers) have been fabricated using Ti-Pd-Ag contacts

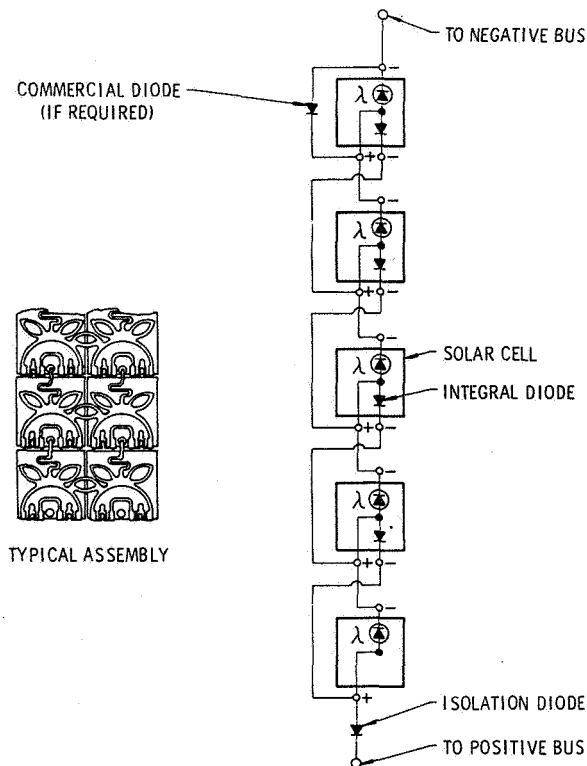


Fig. 5.5-6. Electrical Schematic of Integral Diode Circuit (Ref. 5.5-2)

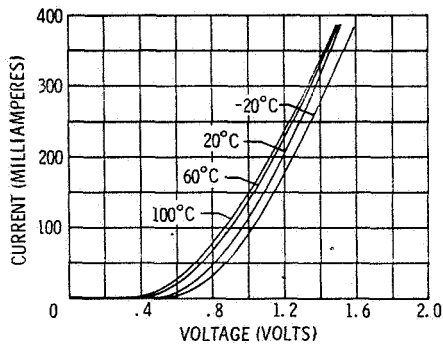


Fig. 5.5-7. Integral Diode Forward I-V Characteristics (Ref. 5.5-2)

that, for the diode to form, were rendered nonohmic by a temperature treatment. These diodes did not require large areas for voltage drops to be low, but rather required long junction periphery. Diode drops of 1.2 volts for 10 ohm-cm cells and 0.8 volts for 1 ohm-cm cells at 0.15 ampere and at room temperature have been reported.

The incorporation of Schottky diodes (as well as diffused diodes) on the cell back sides reduces solar cell power output by several mechanisms (Ref. 5.5-3):

- Increased cell series resistance (in the base region)
- Leakage current through the integral shunt diode
- A photovoltaic current produced by the shunt diode junction and flowing such that it subtracts from the cell output current
- A transistor effect causing a current flow which also subtracts from the cell output current.

For these losses to be small, the solar cells with integral diodes must be designed carefully and their fabrication processes must be controlled very closely.

5.5.9 Shunt Diode Design Requirements

The more significant parameters of shunt diode specifications are as follows:

- Physical size of diode and diode leads that are compatible with the solar cell layout and space available for installation
- Lowest possible forward voltage drop
- Low reverse leakage current relative to cell (or submodule) output current (at 1 volt for protection of single cells or submodules, for example) after irradiation and at the highest diode operating temperature
- Capability to withstand temperature cycling throughout mission life without electrical failure.

5.5.10 Shunt Diode Installation Practices

For conventional packaged rectifier diodes the practices described in Section 5.5.5 apply. For un-packaged wafers and solar cells with integral shunt diodes, the solar cell interconnector design considerations of Section 5.3 apply.

5.6 CONNECTORS AND TERMINALS

5.6.1 Selection of Connectors or Terminals

The decision to use either connectors or terminals on solar cell arrays as well as the selection of the types of connectors or terminals is generally project peculiar. Also, some organizations prefer one type of connector or terminal over another, depending upon what their past failures and successes were with specific connector or terminal designs. Many firms have developed very specific process and assembly procedures and techniques for certain types of connectors which virtually assure their successful flight, even though other organizations may have been less successful with that same type.

For weight reasons and sometimes due to packing density restraints, usually the smallest and lightest connectors or terminals are selected. Manufacturing ease and workmanship considerations also play important roles in connector and terminal selection.

When selecting connectors and terminals, it is usually advantageous to specify a size that has a few more contacts than actually required during an early design stage. Frequently, during the later design stages additional circuits must be accommodated that may or may not be related to the solar cell array layout. If no such additional requirements arise, the unused contacts can always be used in parallel with others to improve the connector reliability.

5.6.2 Connector Reliability

In general, connectors are less reliable than hard-wired connections between terminals. The advantage of connectors, however, is that they permit greater freedom during the post-fabrication test and systems integration checkout phases, especially on more complex spacecraft electrical systems.

Connectors become less reliable with the number of times they are mated and demated because of wearing away (wiping) of usually soft contact metals such as gold. To minimize the deleterious effects due to repeated mating, so-called "connector savers" are used. Connector savers are short male/female adapters of identical types to the flight connectors. The connector savers are mated with the flight connector only once on one side, while all repeated connections for test and checkout purposes are made on the other side. The connector savers are removed after all spacecraft systems have been successfully checked out.

The disadvantage of hardwiring to terminals is that wires may be soldered and unsoldered only a limited number of times, because, during each heating cycle, the possibility of scavenging of terminal plating by the molten solder and weakening of the terminal/insulating material interface exists and usually occurs to some degree.

5.6.3 General Design Practices

The following general design practices are recommended:

- Avoid high-vapor pressure alloys and metallic coatings, such as brass, zinc, and cadmium, because these materials may vaporize and condense on cooler spacecraft surfaces and cause thermal or optical problems. (For sublimation rates of metals in vacuum see Section 2.3.2).
- Select insulating, bonding, and potting materials for low outgassing rates in vacuum, or pre-outgas these materials prior to assembly on the spacecraft. (For outgassing properties of materials see Sections 2.3.2 and 7.16).
- Select insulating, bonding, and potting materials to be compatible with the ultraviolet and charged-particle radiation environment. Charged particles impinge on all sides of the solar cell array from all directions (i. e., are omnidirectional) and may penetrate metallic shields. (For radiation effects on materials see Sections 2.4.3 and 2.5.4).
- Use adequate derating factors for current-carrying capability of contacts (i. e., pins and sockets) and terminals.
- Use adequate voltage ratings of insulators for wires, terminal boards, and terminal blocks. Insulators should not be stressed to levels where corona discharge may start. (Some materials such as Teflon are more subject to damage by corona than others.) Also consider that the arc-over voltage rating decreases significantly for several minutes during ascent of the space vehicle (see Section 2.1).
- Provide adequate wire strain relief at connectors and terminals.

Information concerning current design and performance of connectors and terminals can be found in the following sources:

- EDN Magazine
- Electronic Packaging and Production Magazine
- Electronic Products Magazine
- Evaluation Engineering Magazine

- Handbook of Wiring, Cabling and Interconnecting for Electronics, Charles E. Harper, Editor-in-Chief, McGraw-Hill Book Co., 1972.
- Insulation Magazine
- Machine Design (Magazine), 1975 Reference Issue, Penton Publishing Co., April 1975.
- Packaging Magazine
- Technical bulletins, Hitemp Wires Co.
- Technical papers and product information data sheets issued by Raychem Corporation, Menlo Park, California.

5.6.4 Selection of High-Current or Low-Current Terminations

There are essentially two alternate approaches for conducting solar cell output current across solar panel or array interfaces:

- Many low-current conductors, typically two conductors or two redundant pairs for each electrical string.

- A few high-current conductors (typically two redundant pairs) for each mechanically separable solar panel.

The criterion for the selection of the best alternate approach must be established for each specific design case and must consider at least the following:

- Placement of the blocking diodes (see Section 5.5.)
- Size and flexibility constraints on cables that cross mechanical interfaces (see Section 5.4.)
- Mechanical considerations of interfaces with respect to potential damage (chafing, pinching, cutting, etc.) to cables during handling, assembly, test, launch, deployment and in the space environment
- Reliability estimates of the wires, connectors, blocking diodes solder joints and other elements that may be involved.

REFERENCES (CHAPTER 5)

- 5.2-1 W. Luft, "Solar Cell Interconnector Design," IEEE Transactions on Aerospace and Electronic Systems, vol. AES-7, No. 5, September 1971.
- 5.2-2 "FEP-Teflon Encapsulated Solar Cell Module Development," Final report on work performed by TRW for the NASA Lewis Research Center, Cleveland, Ohio, under Contract NAS 3-16742, to be published late 1976.
- 5.2-3 J.D. Gum et al., "Solar Arrays Utilizing Large Area Silicon Solar Cells," Conference Records of the 7th Photovoltaic Specialists Conference, November 1968.
- 5.2-4 W. Luft and E. Maiden, "Temperature Cycling Effects on Solar Cell Panels," IEEE Transactions on Aerospace and Electronic Systems, vol. AES-5, No. 6, November 1969.
- 5.2-5 "Development of Highly Reliable Soldered Joints for Printed Circuit Boards", Final Report No. 8402A, Westinghouse Defense and Space Center, Aerospace Division, Baltimore, Maryland, August 1968.
- 5.2-6 D. J. Curtin and W. T. Billerbeck, "Advanced Interconnect Systems for Lightweight Solar Arrays," Proceedings of the Section "The Photovoltaic Power and its Application in Space and on Earth," International Congress "The Sun in the Service of Mankind," Paris, France, July 1973.
- 5.2-7 "Survey and Study for an Improved Solar Cell Module," Document No. 900-270, Jet Propulsion Laboratory, August 1969.
- 5.2-8 A. E. Mann, et al., "Solar Cell Array," U.S. Patent No. 3,094,439, June 1963.
- 5.2-9 R. F. Julius, "Solar Cell Array," U.S. Patent No. 3,375,141, March 1968, filed July 1963.
- 5.2-10 J. G. Haynos, "Interconnection of Solar Cells," U.S. Patent No. 3,459,391, August 1969, filed February 1964.
- 5.2-11 From TRW's privately funded and mostly previously unpublished work on solar cell assemblies.
- 5.2-12 W. R. Baron, "Solar Cells with Flexible Overlapping Bifurcated Connector," U.S. Patent No. 3,459,597, TRW, Inc., August, 1969.
- 5.2-13 L. W. Butterworth and R. K. Yasui, "Structural Analysis of Silicon Solar Arrays," NASA Jet Propulsion Laboratory Technical Report No. 32-1528, May 1971.
- 5.3-1 E. L. Ralph and J. Roger, "Silicon Solar Cell Interconnectors for Low Temperature Applications," Proceedings of the International Solar Cell Colloquium, Toulouse, France, 1970.
- 5.3-2 H. S. Rauschenbach and P. S. Gaylard, "Prediction of Fatigue Failures in Solar Arrays," Proceeding of the Seventh Inter-society Energy Conversion Engineering Conference, San Diego, California, September 1972.
- 5.3-3 Various TRW Systems internal previously unpublished reports.
- 5.3-4 J. D. Gum et al. "Solar Arrays Utilizing Large Area Silicon Solar Cells," Conference Records of the 7th IEEE Photovoltaic Specialists Conference, Pasadena, California, November 1968.
- 5.3-5 U.S. Patent No. 3,837,924, "Solar Array," W. R. Baron, TRW Inc., Sept. 24, 1974.
- 5.3-6 W. Luft, "Solar Cell Interconnector Design," IEEE Transactions on Aerospace and Electronic Systems, vol. AES-7, No. 5, September 1971.
- 5.3-7 Anon., "Development of Highly Reliable Soldered Joints for Printed Circuit Boards," Final Report No. 8402A, Westinghouse Defense and Space Center, Aerospace Division, Baltimore, Maryland, August 1968.
- 5.3-8 W. Luft, "Lightweight Welded Solar Cell Modules," Records of the International Conference, Photovoltaic Power Generation, Hamburg, Germany, Sept 1974.
- 5.3-9 H. S. Rauschenbach and A. F. Ratajczak, "FEP-Teflon Covered Solar Cell Array Advancements," Conference Records of the Tenth IEEE 1973 Photovoltaic Specialists Conference, Palo Alto, California.
- 5.3-10 D. R. Lott, "Solar Array Flexible Substrate Design Optimization, Fabrication, Delivery and Test Evaluation Program," Final Report for Contract NAS 8-28432, Lockheed Missiles and Space Company, Inc., Report No. LMSC-D384284, March 1975.
- 5.3.11 E. L. Ralph and R. K. Yasui, "Silicon Solar Cell Lightweight Integrated Array," Conference Records of the 8th IEEE Photovoltaic Specialists Conference, Seattle, Washington, 1970.

- 5.4-1 J. Roger, "Optimal Bus Bars for Rectangular Solar Arrays," Records of the 9th Photovoltaic Specialists Conference, Silver Spring, Maryland, May 1972.
- 5.5-1 E. Levy, Jr., and R. J. McGrath, "Reverse Current Blocking Diodes for Flexible Solar Array Protection," Technical Report AFAPL-TR-75-23, Air Force Aeropropulsion Laboratory, Air Force Systems Command, Wright Patterson Air Force Base, Ohio 45433, April 1975.
- 5.5-2 R. M. Diamond and E. D. Steele, "Solar Arrays with Integral Diodes," Solar Cells, Proceedings of the International Colloquium organized by the European Cooperation Space Environment Committee (ECOSEC), July 1970, Toulouse, France, Gordon and Breach Science Publishers, New York, 1971.
- 5.5-3 W. Luft, "1967 Technology Report on Photovoltaic Conversion," TRW Systems Group, Report No. 99900-6414-5000, December 1967.
- 5.5-4 H. Fischer and W. Pschunder, "Technology and Performance Characteristics of Integral Diode Solar Cells," Proceedings of the Section "The Photovoltaic Power and its Applications in Space and on Earth," International Congress "The Sun in the Service of Mankind," Paris, France, July 1973.

CHAPTER 6

SUBSTRATES AND DEPLOYMENT MECHANISMS

CONTENTS

	Page		Page
6.1 Solar Cell Arrays - An Overview	6.1-1	6.2-11 Very Large Flexible Flat-pack Arrays	6.2-14
6.1.1 Solar Cell Array Types	6.1-1	6.2.12 Lightweight Flexible Flat-pack Arrays	6.2-17
6.1.2 Solar Cell Array Size	6.1-2	6.2.13 FEP-Teflon Encapsulated Solar Cell Modules	6.2-17
6.1.3 Comparative Array Characteristics	6.1-2	6.2.14 Flexible Roll-out Arrays, U.S.	6.2-20
6.2 Substrate Designs	6.2-1	6.2.15 Flexible Roll-out Arrays, European	6.2-20
6.2.1 Strong Honeycomb Sandwich Array	6.2-1	6.3 Deployment Mechanisms	6.3-1
6.2.2 Carbon Fiber Composite Rigid Panels	6.2-1	6.3.1 Deployable Booms	6.3-1
6.2.3 Fiberglass Composite Rigid Panels	6.2-3	6.3.2 Spring/Actuator Systems	6.3-4
6.2.4 Typical Honeycomb Sandwich, Rigid Panels	6.2-4	6.4 Array Orientation Drive and Power Transfer Mechanisms	6.4-1
6.2.5 Flexible Rigid-Frame Panels	6.2-5	6.4.1 Solar Cell Array Drive Systems	6.4-1
6.2.6 Membrane, Rigid-Frame Panels	6.2-8	6.4.2 Power Transfer Assemblies	6.4-1
6.2.7 Woven Tape, Rigid-Frame Panels	6.2-9	6.4.3 Lubrication	6.4-1
6.2.8 Hollowcore, Rigid Panels	6.2-9	6.4.4 FLTSATCOM Design Example	6.4-2
6.2.9 Flexible Flat-pack Arrays	6.2-9	6.4.5 Nimbus II Design Example	6.4-2
6.2.10 Perforated Flexible Flat-pack Arrays	6.2-13	References (Chapter 6)	6. R-1

TABLES

6.3-1 Basic Beam Cross Section Forms	6.3-2	6.3-5 Extendible Structures	6.3-5
6.3-2 Beam and Beam Member Cross Section Variations	6.3-2	6.3-6 Most Favored Boom Types	6.3-9
6.3-3 Extension/Retraction Methods	6.3-3	6.3-7 Blanket/Boom Arrangement in Developmental Arrays or Satellite Programs	6.3-10
6.3-4 Basic Stowage Methods and Variations	6.3-4		

FIGURES

6.1-1 Array Options	6.1-1	6.2-7 Sandwich Substrate Design	6.2-4
6.1-2 Comparative End-of-Life Cell Array Performance	6.1-2	6.2-8 Solar Array Stowed and Extended	6.2-4
6.2-1 Skylab with Two Solar Cell Array Systems	6.2-2	6.2-9 Cross Section of Substrate and Frame	6.2-5
6.2-2 OWS Solar Cell Array Wing Assembly	6.2-2	6.2-10 FLTSATCOM Satellite and Solar Cell Array Configuration	6.2-6
6.2-3 OWS Array Fully Deployed, ATM Array Still Stowed	6.2-2	6.2-11 LRSA Substrate Configuration	6.2-7
6.2-4 Geometry of the ICS Solar Cell Array for OTS	6.2-3	6.2-12 LRSA Panel Frame Geometry	6.2-7
6.2-5 ICS Developmental Solar Cell Array	6.2-3	6.2-13 Frame Cross-Section and Substrate Attachment Design	6.2-8
6.2-6 Development Test Array Developed by Matra	6.2-4	6.2-14 One Wing of ULP by MBB	6.2-8
		6.2-15 Open Weave Substrate	6.2-9

6.2-16	Boeing/JPL Foldout Solar Cell Array	6.2-10	6.2-29	"V" Configuration, Single Boom 110 W/kg Roll-out Solar Cell Array Concept	6.2-19
6.2-17	Electro Optical Systems Hollowcore Folding Solar Cell Array	6.2-11			
6.2-18	CTS Spacecraft and Solar Cell Array	6.2-12	6.2-30	FEP-Teflon Encapsulated Solar Cell Module	6.2-20
6.2-19	CTS Solar Cell Array Blanket	6.2-13	6.2-31	Hughes FRUSA	6.2-21
6.2-20	RAE Lightweight Solar Cell Paddle	6.2-14	6.3-1	Different Arrangements for Deployable Solar Cell Arrays	6.3-9
6.2-21	RAE Substrate Configuration	6.2-15	6.3-2	FLTSATCOM Spring Hinge Configuration	6.3-10
6.2-22	Lockheed Space Station Solar Cell Array	6.2-15	6.3-3	FLTSATCOM Deployment Boom Mechanism	6.3-11
6.2-23	Space Station Substrate Assembly	6.2-15	6.3-4	Matra Holddown System	6.3-12
6.2-24	Space Station Substrate Reinforced Edge Laminate	6.2-16	6.3-5	Matra Deployment Springs and Fittings	6.3-12
6.2-25	Space Station Complete Module Joint	6.2-16	6.3-6	Matra Deployment Mechanisms	6.3-12
6.2-26	Baseline 110 W/kg Solar Cell Array Configuration	6.2-17	6.3-7	Matra Deployment Control Mechanism	6.3-12
6.2-27	110 W/kg Array Substrate Configura- tion	6.2-18	6.4-1	TRW FLTSATCOM SADA	6.4-3
6.2-28	Rear View of Solar Cell Blanket, GE 110 W/kg Design	6.2-19	6.4-2	Nimbus II SADA	6.4-4

CHAPTER 6

SUBSTRATES AND DEPLOYMENT MECHANISMS

Substrates are the structural elements that mechanically support and hold in place the solar cells as well as the electrical solar cell interconnectors and wires. Substrates may be flat or curved, rigid or flexible, and carry solar cells on one side or on both sides.

Dozens of concepts concerning substrates and deployment mechanisms have been proposed and developed to some level over the last 10 years. Some designs are in use on operational satellites; others never got out of the laboratory or off the drawing board. Emphasis will be on those more successful

designs that have been developed and proven feasible or have been derived for power requirements much larger than what is commonly required for today's satellites.

Because the substrate and the deployment mechanism are such an integral part of a solar cell array system, this chapter will present a brief description of the array design along with the substrate and deployment mechanism to provide the designer some insight into how these elements were used and how they affected overall array performance.

6.1 SOLAR CELL ARRAYS – AN OVERVIEW

The actual power required from a satellite solar cell array depends upon the specific mission of the satellite. Over the last several years there has been a marked tendency to require more power. Because of booster limitations (liftoff capacity and payload volume), this trend makes it increasingly important for the designer to select the proper type of solar cell array for the specific satellite application.

The selection of the proper array requires careful consideration of the interfaces between the array and other satellite subsystems. Not only does the specific satellite mission provide constraints on the array, but the selection of a specific type of array can strongly influence the configuration of the satellite as discussed in Section 8.1.

6.1.1 Solar Cell Array Types

Solar cell arrays for satellite application can be divided into two broad categories: body mounted or deployable. While the body-mounted array is relatively straightforward, a deployable array confronts the designer with many options. Figure 6.1-1, taken from Ref. 6.1-1, is one method of depicting the array options. Body-mounted arrays invariably require rigid substrate arrays, since the substrate is an integral part of the satellite body. However, there exists a complexity of substrate designs for the deployable array.

Body-mounted arrays are the simplest types of arrays, and have been employed on many of the earlier and smaller satellites for which the power requirements were small and which were spin stabilized. They suffer from a poor solar cell utilization efficiency and have a definite maximum power output limitation. By taking into account such factors as available shroud volume (which dictates maximum satellite size), spin stabilization moment-of-inertia requirements, and solar cell type, it can be shown that power availability ranges from 50 to 1000 watts. However, for satellites requiring more than 200 watts of power, a deployable array is often chosen, especially if three-axis stabilization is required by payload or mission. The substrates for this class of arrays are typically constructed from sheet/stringer or aluminum sandwich panels. These arrays are, however, of straightforward design, and entail little or no risk or complexity relative to the deployable array designs.

Deployable arrays can, as indicated in Figure 6.1-1, be subdivided into those with the orientation (with respect to the satellite body axes) remaining fixed with time, and those which are articulated with respect to the satellite (through an orientation drive mechanism and/or despun platform) so that they can be oriented to remain pointed toward the sun as the satellite moves in its orbit.

From Ref. 6.1-1. Reprinted with permission of the Centre National d'Etudes Spatiales.

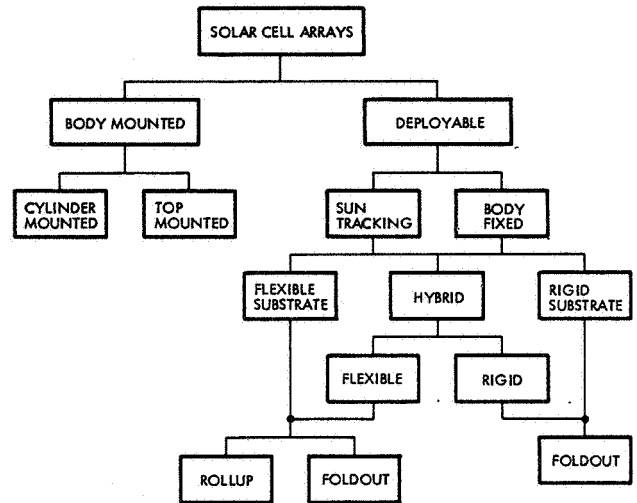


Fig. 6.1-1. Array Options (Ref. 6.1-1)

As illustrated in Figure 6.1-1, the deployable arrays are usually subdivided according to the type of substrate on which the solar cells are mounted. Broadly taken, these can be called "flexible" or "rigid." The distinction between flexible and rigid arrays is related only to the relative physical characteristics of the substrate itself and not to that of the fully deployed array.

Figure 6.1-1 suggested two broad categories for substrates (flexible or rigid); however, this classification may be somewhat artificial when one considers the specific types of substrates that have been developed. Obviously, a thin laminate of Kapton and fiberglass can be classified as flexible and an aluminum facesheet and honeycomb sandwich can be classified as rigid. However, a design that utilizes interwoven strips or a single membrane stretched across a frame to make an integral panel can be classified as both flexible (in terms of the substrate) and rigid or stiff (in terms of the panel).

Rigid arrays have historically been the most common type of deployable array, due both to the relatively simple and reliable construction and to the fact that they can provide some power in their stowed configuration. The mass of the rigid substrate or panel, however, can be significant, particularly for large power arrays. During the 1965 to 1971 time period different approaches were tried in an attempt to reduce the weight of the rigid array (inflatable, rigidizing plastic; beryllium frame; or aluminum

panel electroforming). These solutions, for the most part, proved to be too complex or too expensive for ultimate application. In recent years, however, there has been a resurgence of activity in the development of low-weight, rigid-substrate solar cell arrays. The results of these programs have, for the most part, been quite encouraging such that many near term satellites with power requirements between 1 to 2 kW will be launched with deployable rigid arrays. The major breakthrough has been the use of new materials and processes (composites and laminates).

For the very large power requirements (>10 kW), and as an option in place of the rigid array for the moderate power requirements (1 to 2 kW), the light-weight flexible array has shown promise. Several concepts have been developed over the last 10 years and shown to be a viable design approach. The flexible array, however, as mentioned, cannot provide power when stowed (overcome through use of a hybrid design) and it also suffers from a high incidence of coverglass and solar cell breakage during handling and tests. Its complexity (considering both the rollup and foldout design) is considered to be greater than the rigid deployable array.

6.1.2 Solar Cell Array Size

From the establishment of the satellite power utilization requirements, mission duration, orbit parameters, and solar cell output will come the gross size of the solar cell array. With this gross sizing, the designer can begin the structural design process of considering alternative methods of achieving a satisfactory design to meet the power requirements within the constraints of weight, cost, stowage volume, satellite mission and functional characteristics.

The substrate design, however, will be a factor affecting the sizing of the array because the efficiency of the solar cell is a function of operating temperature and charged particle radiation fluence; the substrate will affect both of these factors. As a general rule, the thinner the substrate, the greater the temperature extremes and the less the radiation protection. This results in lower solar cell output, thus requiring a greater number of cells to provide the required power. Hence, some substrate designs are not as attractive as the first impression indicates because of the negative impact on array size or the requirement to provide additional protective or insulative layers.

6.1.3 Comparative Array Characteristics

A summary table or figure comparing the specific weight and power performance of different array designs may be dangerous and misleading. This is because power, radiation fluence, mission duration, solar cell type, solar cell cover type, temperature, and natural frequency all have an effect on the specific weight and power density characteristics; and the numbers reported in the literature reflect these effects. Commonplace shortcomings in the literature include (a) failure to include all pertinent components in the weight summary and (b) no consideration of space environmental effects on power output is included.

Figure 6.1-2 is a compilation of data presented in Section 6.2 and attempts to present consistent data. Results reflect end-of-life (EOL) power characteristics. The data includes the weight of all pertinent array components including deployment mechanism, stowage container (if any), as well as substrate and electrical stack. Solar array drive mechanisms are not included.

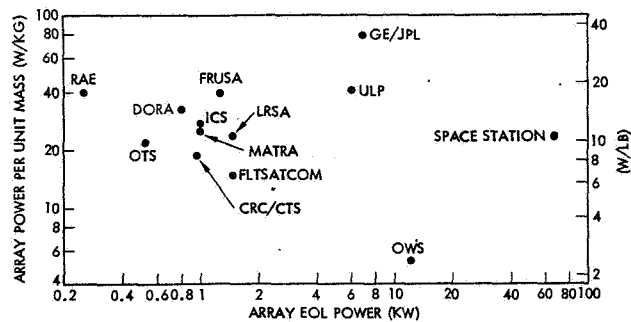


Fig. 6.1-2. Comparative End-of-Life Cell Array Performance (Includes deployment mechanisms but excludes orientation and power transfer mechanisms. The project abbreviations denote array types discussed in Section 6.2.)

6.2 SUBSTRATE DESIGNS

Some of many different types of array substrate designs, that have been flown or developed for specific flight projects or for planned future projects, are discussed and illustrated in this section in the following order:

- Rigid substrates
- Flexible substrates
 - Foldout arrays
 - Rollup arrays

6.2.1 Strong Honeycomb Sandwich Array

The Skylab spacecraft (illustrated in Figure 6.2-1) is a manned vehicle which carries two separate solar cell array systems: the Apollo Telescope Mount (ATM) array and Orbital Workshop (OWS) array. During launch, both arrays are stowed in folded-up positions. The ATM array is stowed coaxially above the OWS and protected by a nose cone. The two wings of the OWS array are stowed on the sides of the OWS and protected during launch by a beam fairing.

Due to the high dynamic forces occurring during launch, the OWS array is relatively strong and, therefore, heavy. The ATS array is of a somewhat lighter-weight design.

The OWS array consists of two wing assemblies, as shown in Figure 6.2-2, each of which contain

- A forward fairing
- A beam fairing
- Three wing sections.

The wing assemblies are permanently attached to the Orbital Workshop (OWS) cylindrical structure through the forward fairing assemblies. Machined, hinged fittings attach the beam fairings to the forward fairing assemblies. During launch they are also attached to the OWS structure by six explosive attachment fittings, distributed along the length of the beam fairings.

After Skylab is inserted into orbit, spring-loaded deployment actuator-dampers release the beam fairings and drive them outward to pivot about their hinges. Following this, 12 panels (10 active and 2 inactive) in each of the six wing sections unfold in the aft direction from the beam fairings until the stabilizer beams retain them in an extended position (see Figure 6.2-3).

Each solar cell panel consists of a 9.7 mm thick aluminum honeycomb substrate approximately 3.31 m long by 0.74 m wide. The facesheets are 0.2 mm aluminum. The solar cells are 0.36 mm thick covered with 0.15 mm microsheet coverglasses. The cells are bonded directly to the aluminum substrate through holes in a 50 μ m thick, insulating Kapton sheet.

The OWS array characteristics, including solar cells at the end of life (less than one year in low altitude earth orbit), are as follows:

Solar Cell Panel

Output (EOL)*	204 watts
Mass per unit area	5.08 kg/m ² (1.04 lb/ft ²)
Power per unit mass	19.2 W/kg (8.7 W/lb)
Mass per unit power	52.1 kg/kW (115 lb/kW)

Total Array Assembly (60 panels)

Output (EOL)*	12.24 kW
Area	126 m ² (1357 ft ²)
Mass	2309 kg (5091 lb)
Mass per unit area	18.3 kg/m ² (3.75 lb/ft ²)
Power per unit mass	5.3 W/kg (2.4 W/lb)
Mass per unit power	189 kg/kW (416 lb/kW)

6.2.2 Carbon Fiber Composite Rigid Panels (Based on Refs. 6.2-1, 6.2-2 and 6.2-3).

Messerschmitt-Bölkow-Blohm (MBB) developed, under contract to ESTEC, a rigid panel, foldup, flat-pack array. The array structure utilizes advanced composites for much of the structure and is thus called the improved composite structure concept (ICS). The concept is now proposed for application to the Orbital Test Satellite (OTS) (see Figure 6.2-4).

Figure 6.2-5 shows the developmental ICS array which consists of three hinged panels and a deployment yoke. The panels and yoke are flat packed against one another and pretensioned against the satellite sidewall at four points with a mechanical spacing of 25 mm between panels to ensure no panel-to-panel contact during the launch phase. The stowed array is designed to have a natural frequency in excess of 25 Hz so as not to result in large amplitude panel deflections. Deployment is through a pulley and cable system.

Each ICS developmental panel is approximately 1.3 x 1.7 m (the OTS array being built consists of two

*Note: The following abbreviations are used throughout this chapter.

BOL = Beginning of Life
EOL = End of Life
EOM = End of Mission

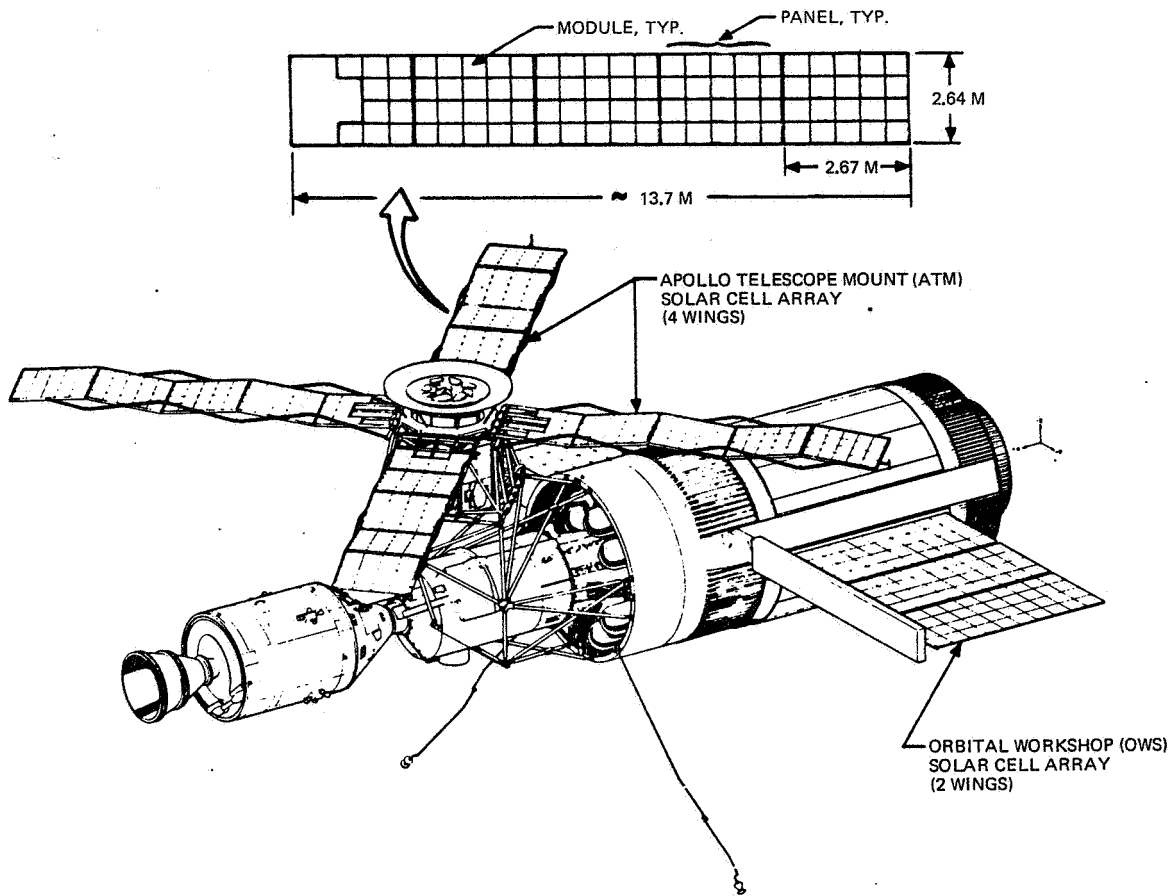


Fig. 6.2-1. Skylab with Two Solar Cell Array Systems
(Courtesy of Marshall Space Flight Center)

From Ref. 6.2-25. Reprinted with permission of the IEEE.

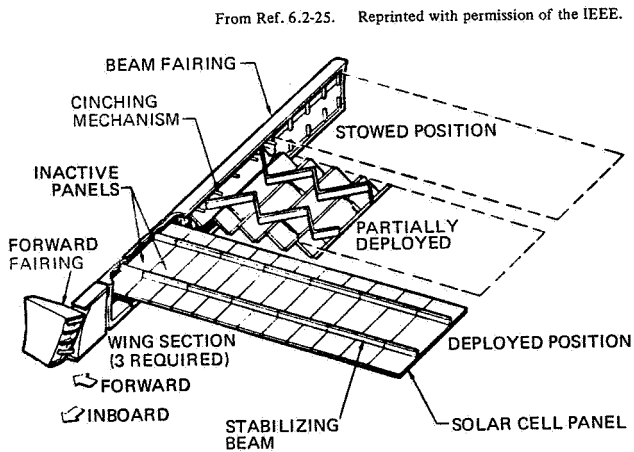


Fig. 6.2-2. OWS Solar Cell Array Wing Assembly (Ref. 6.2-25)

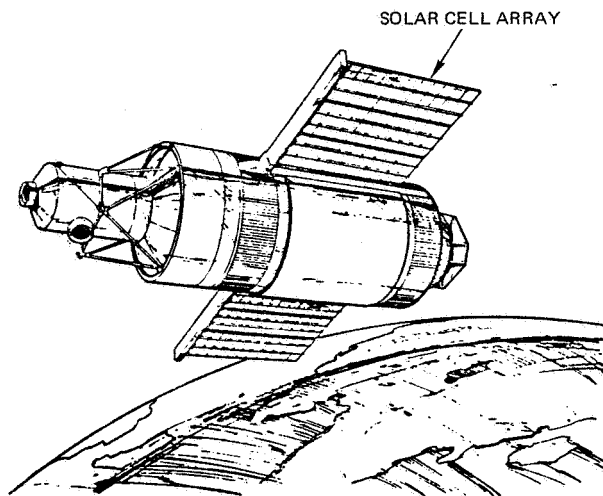


Fig. 6.2-3. OWS Array Fully Deployed, ATM Array Still Stowed (Ref. 6.2-25)

From Ref. 6.2-1. Reprinted with permission of the American Astronautical Society.

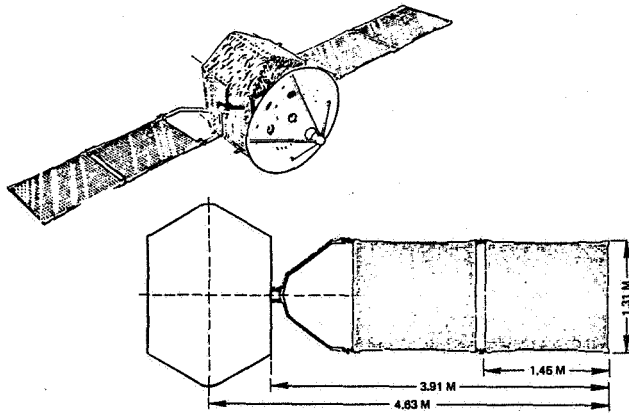


Fig. 6.2-4. Geometry of the ICS Solar Cell Array for OTS (Ref. 6.2-1)

Array mass per unit area (including solar cells and deployment mechanism, but excluding the orientation mechanism) 2.7 kg/m² (0.55 lb/ft²)

Power per unit mass (1 kW EOL) 27.6 W/kg (12.5 W/lb)

Mass per unit power (1 kW EOL) 36.3 kg/kW (80 lb/kW)

OTS Array

Panel mass per unit area 1.12 kg/m² (0.23 lb/ft²)

Array mass per unit area 3.17 kg/m² (0.65 lb/ft²)

Power per unit mass (520 watts EOL) 21.6 W/kg (9.8 W/lb)

Mass per unit power (520 watts EOL) 46.3 kg/kW (102 lb/kW)

6.2.3 Fiberglass Composite Rigid Panels (Based on Refs. 6.2-4 and 6.2-5)

MATRA developed, under contract to CNES and ESTEC, a rigid panel, foldup, flat-pack array. The structure utilizes a combination of composite and metal elements for the array structure. This developmental work was essentially done in competition with the MBB/ICS array design.

Figure 6.2-6 shows the development test model fabricated and tested to demonstrate concept feasibility. The array consists of five hinged panels and a deployment yoke. The panels and yoke are flat-packed against one another and are prestressed against the spacecraft sidewall at six points with a mechanical spacing of 5.1 mm between panels to ensure no panel-to-panel contact during the launch phase. The stowed array panel has a natural frequency of 34 Hz. Deployment is achieved through a pulley and cable system.

The array panel is approximately 1.0 m long by 1.5 m wide. The substrate design is shown in Figure 6.2-7. It consists of a 0.15-mm thick fiberglass epoxy front facesheet, 20-mm thick aluminum honeycomb core and a perforated 0.30-mm back facesheet. Each 12-mm diameter perforation coincides with each cell of the honeycomb structure. Two methods are used to fabricate the sandwich substrate: (a) a prepreg facesheet is used without any additional adhesive layer and (b) the core is edge coated with adhesive using the epoxy in the facesheets. The edges of the substrate are equipped with channel-shaped, 0.1-mm thick aluminum closeout elements to provide additional stiffness and attachment points for the hinge fittings. There are two spring hinge fittings on each hinge line.

For 0.20-mm thick solar cells with 0.10-mm thick covers, the MATRA solar cell array characteristics for an EOL power level of 1 kW are as follows:

Mass per Unit Area

Panel substrate without solar cells 1.12 kg/m² (0.23 lb/ft²)

Panel substrate with deployment mechanism but without solar cells 1.27 kg/m² (0.26 lb/ft²)

Array without orientation mechanism 2.54 kg/m² (0.52 lb/ft²)

From Ref. 6.2-3. Reprinted with permission of the IEEE.

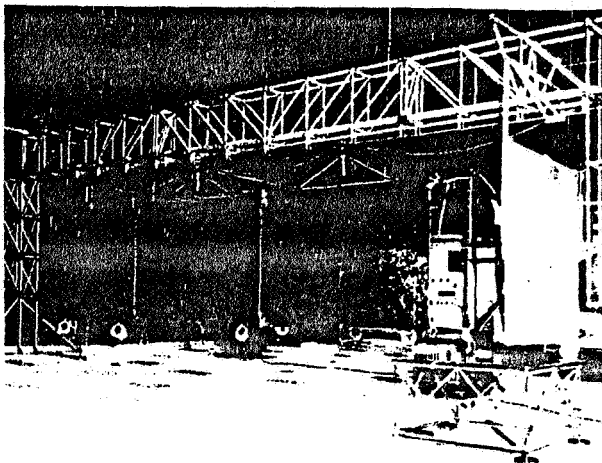


Fig. 6.2-5. ICS Developmental Solar Cell Array (Ref. 6.2-3)

panels 1.3 x 1.5 m). It consists of an aluminum honeycomb core 20-mm thick in a carbon fiber composite frame and covered with two carbon fiber composite facesheets. The facesheets and edge members are constructed from a specially wound, open-weave fiber matrix fabricated on a drum. The edge frame consists of a square, 20-mm tube on two sides, with a channel section on the other two sides. Edge hinge fittings are constructed from short carbon fiber moldings bonded into the channel sections at four locations per panel. The yoke is also a full carbon fiber, rectangular cross section tube fabricated from the same open weave design. The substrate is insulated from the solar cells by a Kapton blanket.

The characteristics of the ICS and the OTS solar cell arrays are as follows:

ICS Array

Panel mass per unit area (structure only) 1.42 kg/m² (0.29 lb/ft²)

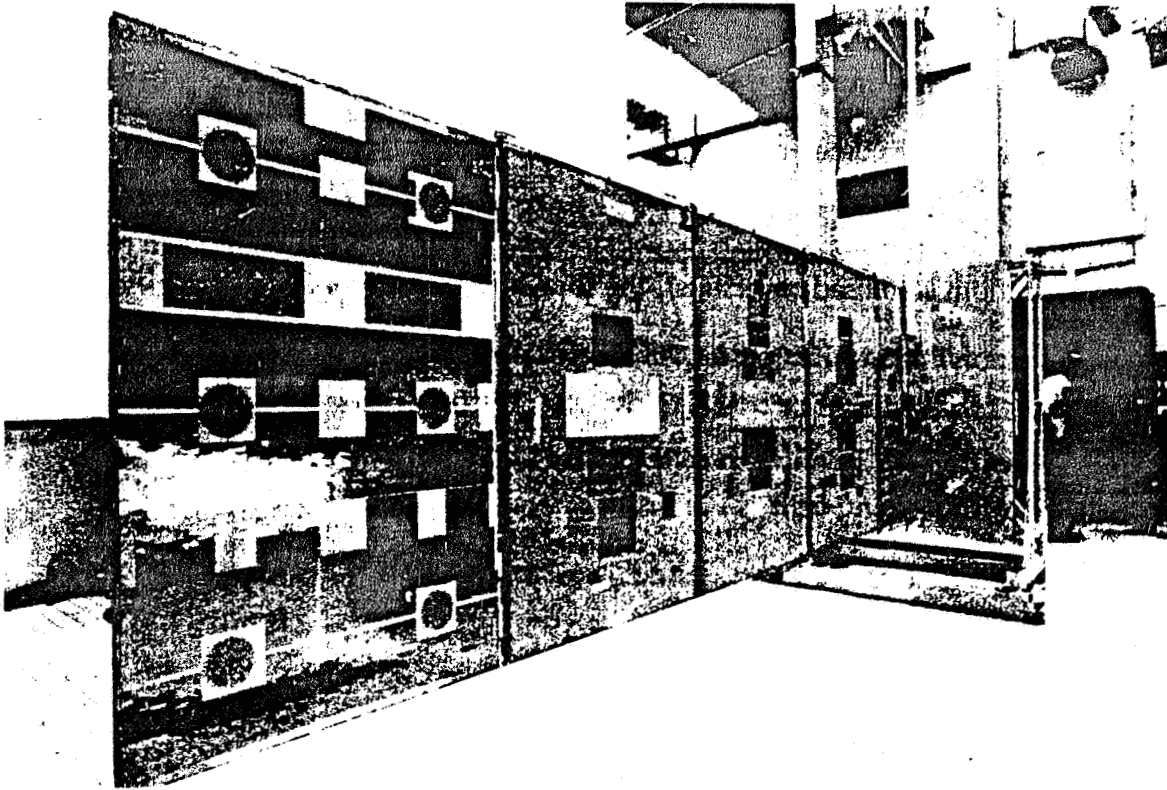


Fig. 6.2-6. Development Test Array Developed by Matra (Ref. 6.2-5)

From Ref. 6.2-5. Reprinted with permission of the Centre National d'Études Spatiales.

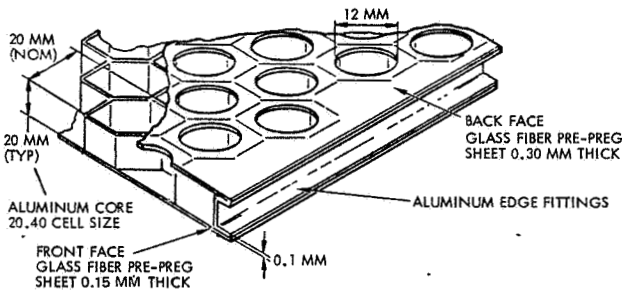


Fig. 6.2-7. Sandwich Substrate Design (Ref. 6.2-5)

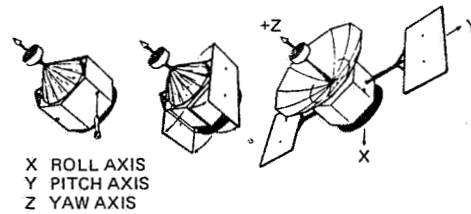


Fig. 6.2-8. Solar Array Stowed and Extended

Specific Performance

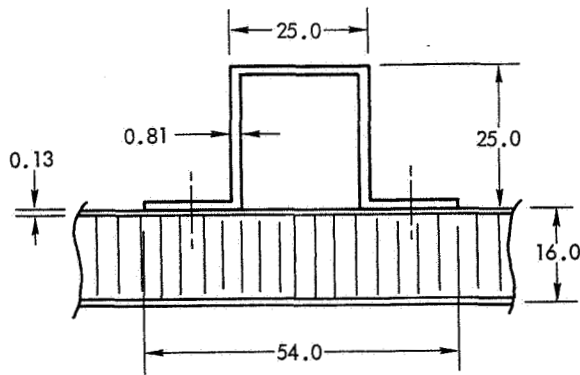
Power per unit mass	25.1 W/kg (11.4 W/lb)
Mass per unit power	39.9 kg/kW (88 lb/kW)

6.2.4 Typical Honeycomb Sandwich, Rigid Panels
(Based on previously unpublished TRW data)

TRW Systems is prime contractor for the Navy's Fleet Satellite Communications System (FLTSATCOM). The solar array system is as shown in Figure 6.2-8, and consists of two paddles on opposite sides of the satellite. The paddles are stowed wrapped around

the spacecraft and deployed as shown. Each paddle consists of three panels of nearly identical configuration; the three panels are attached together by spring hinges. The center panels are connected through deployment booms to the spacecraft. EOL power is 1.47 kW.

A typical panel is 2.82 m long by 1.28 m wide. It consists of a sandwich substrate supported by a frame around the perimeter. Also included as part of the frame is a cross member 1.31 m from the bottom of the panel. Figure 6.2-9 illustrates a typical cross-section of the frame and sandwich substrate. The substrate consists of 0.13-mm aluminum facesheets bonded (with film adhesive) to 16 mm thick aluminum honeycomb core. The gauge of the nominal 25-mm square aluminum hat section frame is 0.81 mm. The frame is mechanically attached to the substrate with



DIMENSIONS IN MM

Fig. 6.2-9. Cross Section of Substrate and Frame

screws/inserts. The deployment boom is a square cross-sectional aluminum element with hinge assemblies that are controlled by a pulley/cable system. The fundamental natural frequencies are 25 Hz stowed and 0.32 Hz deployed. The solar cells used are conventional silicon cells 0.20-mm thick with a 0.15-mm thick coverglasses.

The FLTSATCOM solar cell array characteristics for an EOL power level of 1.47 kW are as follows:

Mass per Unit Area

Substrate only	2.05 kg/m ² (0.42 lb/ft ²)
Array structure without deployment and solar cells	3.3 kg/m ² (0.67 lb/ft ²)
Array structure without deployment boom but with solar cells	4.3 kg/m ² (0.88 lb/ft ²)
Array structure with boom and solar cells	4.7 kg/m ² (0.97 lb/ft ²)

Specific Performance

Power per unit mass (without deployment boom)	16.4 W/kg (7.3 W/lb)
Power per unit mass (with deployment boom)	14.6 W/kg (6.6 W/lb)
Mass per unit power (without boom)	62.6 kg/kW (138.0 lb/kW)
Mass per unit power (with boom)	69.2 kg/kW (152.5 lb/kW)

6.2.5 Flexible Rigid-Frame Panels
(Based on Refs. 6.2-6 and 6.2-7)

Over the last 2 years TRW Systems has been developing a lightweight rigid solar array (LRSA) design for application to a variety of defense and communication satellites. This design contrasts with many of the other rigid array concepts in that a relatively high stiffness and, hence, high fundamental frequency is not considered of prime importance.

The baseline satellite used for comparative development of the experimental solar cell array is FLTSATCOM, a communications satellite using two deployable solar cell wings, each wing comprised of three panels hinged to one another. The stowed and deployed configuration is shown in Figure 6.2-10. The center panels are connected through deployment booms to the spacecraft. In the stowed condition, the six panels are wrapped around the spacecraft. During deployment the three panels on each side first latch up to form a plane and then the two paddles are pivoted around the deployment boom hinge points as the two booms straighten out. Each of the panels is approximately 2.6 m long by 1.3 m wide and EOL power for the array is 1.47 kW. (The LRSA has slightly different dimensions than the array described in Section 6.2.4.)

Structural analyses for solar cell substrates have been historically based on linear, small deflection theory. The substrates were essentially an assemblage of rigid flat and/or curved plates exhibiting good bending stiffness. Many structural analysis computer programs were available that could adequately predict deflections and internal stress distributions providing that the structural response was in the linear, small deflection regime. The classical rigid substrate, structurally tuned to have a fundamental frequency in excess of 35 Hz, was also heavy.

The LRSA concept departs from the historical norm by utilizing a very lightweight and flexible substrate attached to a rigid frame. As the substrate is loaded normal to its surface, it initially deflects as a plate in bending until sufficient curvature permits the applied load to be reacted as in-plane "membrane" loads in the deformed substrate. In order to utilize this membrane concept, the frame to which the substrate is attached must be capable of supplying the required edge restraint to the substrate. The frame must be stiff torsionally and in bending about both axes.

In general, to avoid interaction with the satellite attitude control system, the deployed solar array must have bending frequencies exceeding 1 to 2 Hz. If the solar array frequencies are lower than 1 Hz, then the attitude control system must be designed to filter out oscillation from the nonrigid array. No low frequency restraint was placed on the solar array design in this case. The deployed array frequency response is governed by the deployment booms in this case, not by the array substrate.

Structurally, the solar array must be designed to withstand the acoustic and launcher release loads imposed by the launch vehicle. The deflections of the solar panels during launch were limited to 7 cm. To maintain acceptable deflections during launch vibration and to avoid high amplification from the launcher release loads, first modal frequencies above 9 Hz were desirable. This requirement governs the stiffness design of the solar panels.

The penalty for such low frequency design compared to the more common minimum frequency requirement of 35 Hz is that the boost loads analysis becomes complicated, since the array and the spacecraft bending frequencies are in the same regime. Also, a nonlinear structural analysis program must be used to predict stresses and deflections. Nevertheless, the potential weight savings warrant a detailed analysis, since acceptance of a high minimum frequency would require either heavy substrates or a different stowage method in return for a simplified analytical effort.

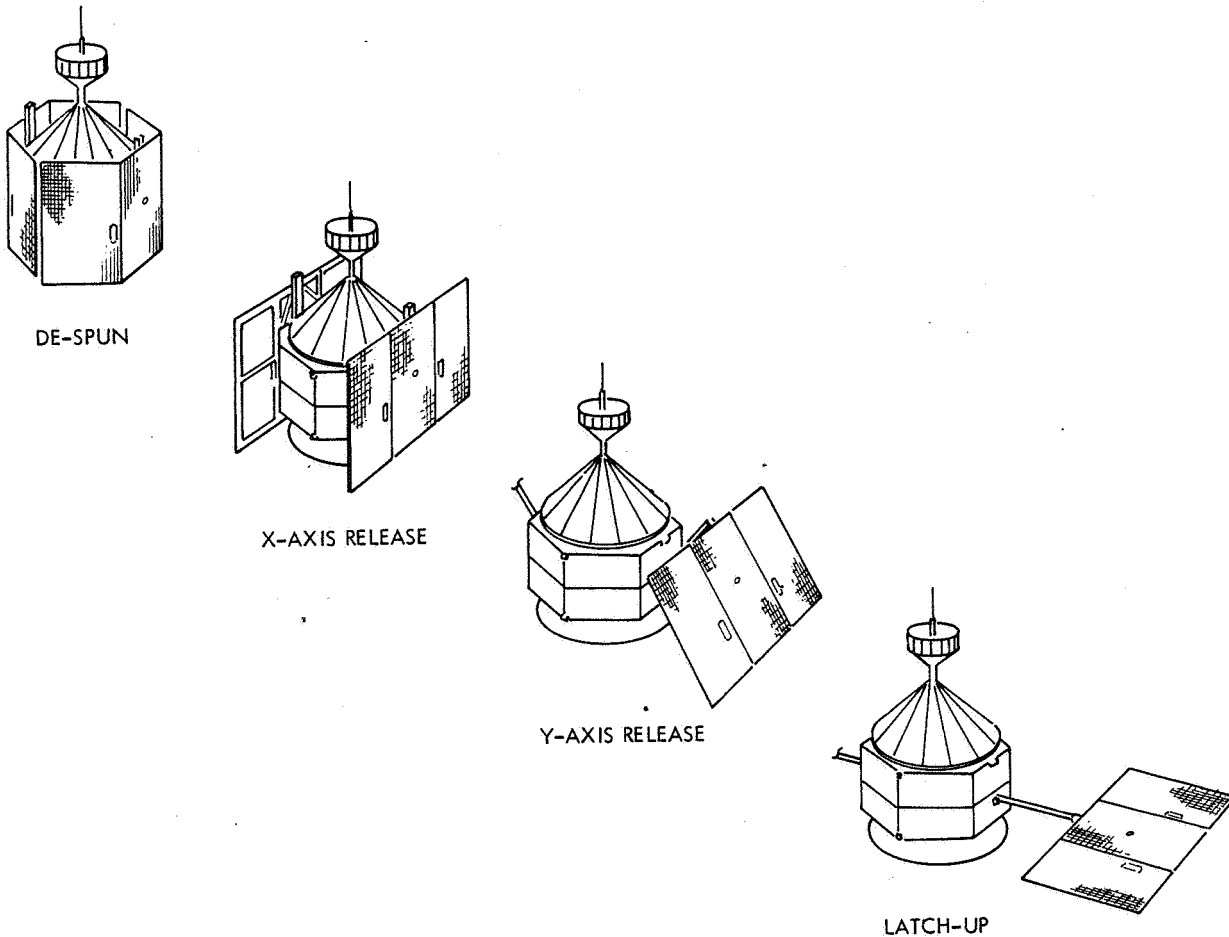


Fig. 6.2-10. FLTSATCOM Satellite and Solar Cell Array Configuration

The LRSA substrate is a sandwich construction of Kapton facesheets bonded to an aluminum honeycomb core (see Figure 6.2-11). The adhesive is applied to the edge of the core only, rather than the usual method of using film type adhesive with its uniform inefficient distribution across the total facesheet surface area in order to save weight. The outer facesheet, which provides a flat surface for solar cell attachment, has a thickness of $50\ \mu\text{m}$ (0.002 in.). The inner facesheet has a thickness of $75\ \mu\text{m}$ (0.003 in.) and has 51 percent of its surface area perforated with randomly spaced circular holes permitting heat in the front facesheet to radiate through the back to space. An additional $75\text{-}\mu\text{m}$ thick layer of perforated Kapton is bonded to the inner facesheet in the area where the substrate attaches to the frame to locally increase the inner facesheet intercell buckling allowable. The honeycomb core is 1 cm (0.40 in.) thickness 5052 aluminum that has a density of $2.6\ \text{g}/\text{cm}^3$.

The supporting frame is shown in Figure 6.2-12. It consists of tubular members with a 2.5 by 3.8 cm (1.0 x 1.5 in.) rectangular cross section with rounded corners. The frame dimensions for each panel are 2.35 by 1.19 m (8.4 x 4.2 feet) center to center with

one cross member at 1.32 m (4.3 feet) from the bottom member. The frame is constructed from multi-layer graphite-epoxy tape. For the unit fabricated, the substrate was attached to the frame with screws as shown in Figure 6.2-13. However, for a flight configuration, an adhesive bond could be used for additional weight savings.

The solar cells used are the high efficiency violet response cells, 0.20-mm thick, with 0.15-mm thick covers. It should be noted that, because of the relative flexibility of the sandwich substrate alone, the solar cells provide additional bending and membrane stiffness to the substrate.

A LRSA panel was fabricated and subjected to static, acoustic, and sine-vibration tests for evaluation. Mass-simulated solar cells and groups of live solar cells were mounted on the panel to observe their effects. Results indicated that the panel successfully withstood 16 g uniform loading, 145 dB/OA acoustic environment and 1 g sinusoidal vibration from 4 to 100 Hz. Maximum substrate deformation was 3.8 cm and the lowest resonant frequency was 8.2 to 9 Hz.

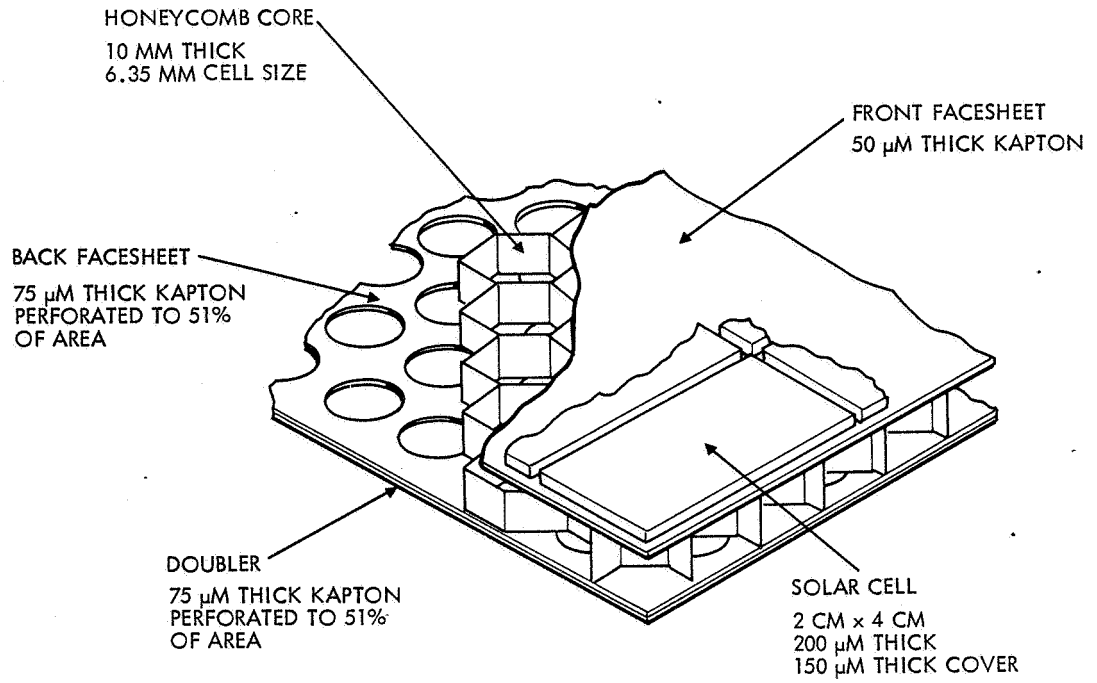


Fig. 6.2-11. LRSA Substrate Configuration

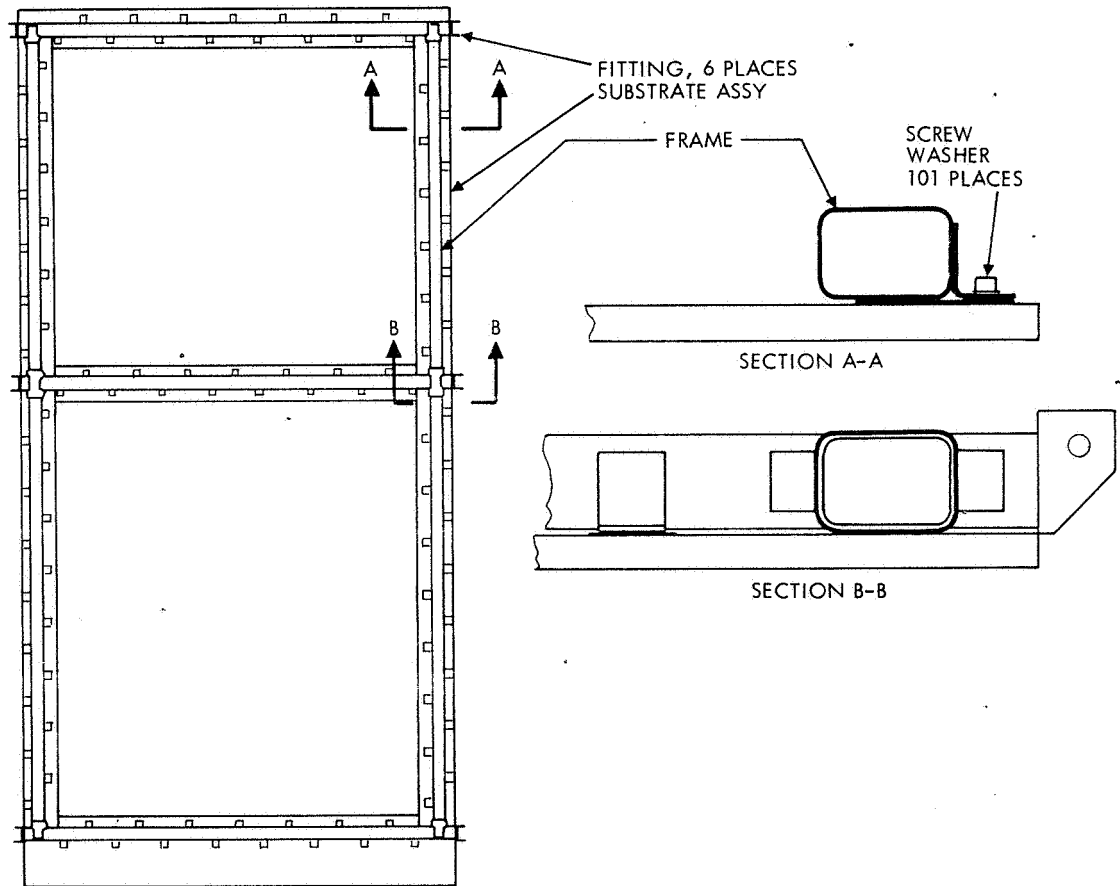


Fig. 6.2-12. LRSA Panel Frame Geometry

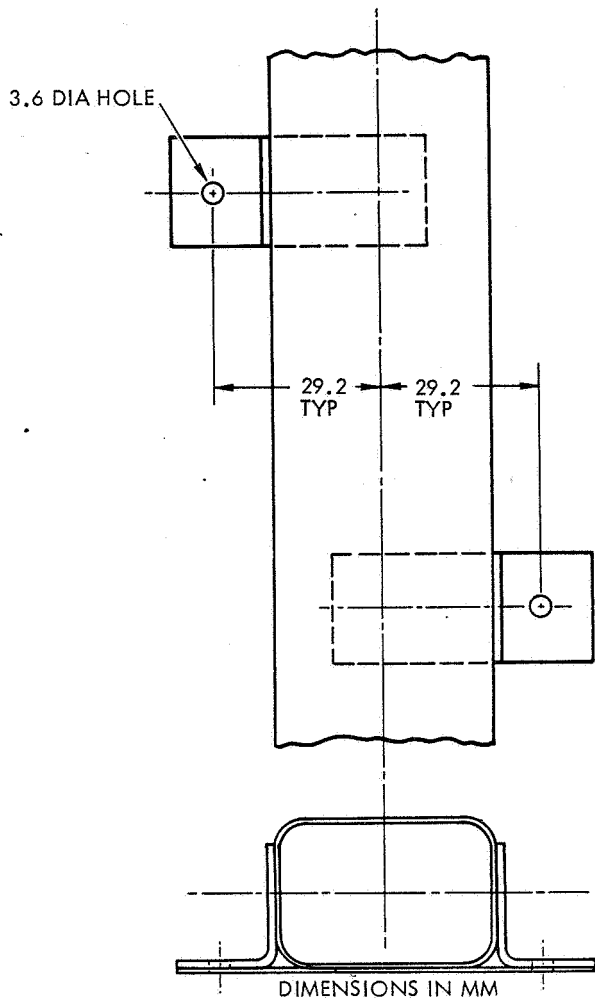


Fig. 6.2-13. Frame Cross-Section and Substrate Attachment Design

The LRSA panel design can be applied to a flat-pack configuration as well as to the wraparound stowage scheme used. The array characteristics are as follows:

Mass per Unit Area

Honeycomb sandwich without frame	0.64 kg/m ² (0.13 lb/ft ²)
Panel structure, including deployment spring hinges between panels, but excluding solar cells and deployment boom	1.7 kg/m ² (0.34 lb/ft ²)
Panel structure as above except with solar cells	2.6 kg/m ² (0.54 lb/ft ²)
Panel structure with solar cells and a carbon fiber deployment boom system	3.1 kg/m ² (0.63 lb/ft ²)

Specific Performance (1.47 kW EOL)

Without deployment boom system; power per unit mass	28.0 W/kg (12.7 W/lb)
With deployment boom system; power per unit mass	24.0 W/kg (10.9 W/lb)
Without deployment boom system; mass per unit power	35.7 kg/kW (78.7 lb/kW)
With deployment boom system; mass per unit power	41.7 kg/kW (92 lb/kW)

6.2.6 Membrane, Rigid-frame Panels
(Based on Refs. 6.2-8 and 6.2-9)

Messerschmitt-Bölkow-Blohm (MBB) has been developing, under a variety of contracts to ESTEC and GFW, several advanced lightweight rigid array concepts. The latest in the evolutionary line is called the ultra lightweight panel (ULP) and is being developed for GFW for application to a German TV broadcast satellite (FRS).

Figure 6.2-14 shows the overall array geometry. It consists of a series of hinged panels and a deployment yoke that flat-pack into a very compact package. The panels and yoke touch each other along their framework and are preloaded against the spacecraft sidewall to preclude relative frame vibrations. No stowage container is used. The stowed array is designed to have a natural frequency ≈25 percent above the spacecraft natural frequency (20 to 30 Hz).

From Ref. 6.2-9. Reprinted with permission of the Deutsche Gesellschaft für Luft und Raumfahrt EV.

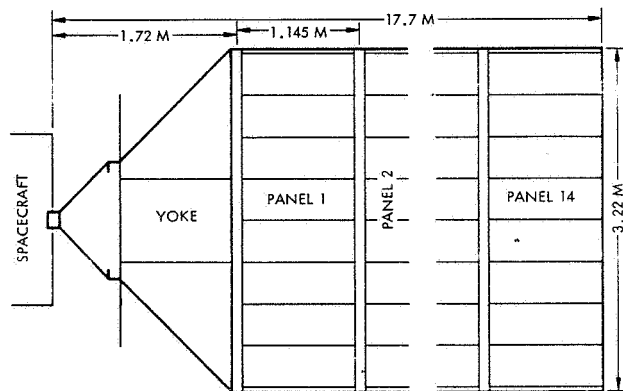


Fig. 6.2-14. One Wing of ULP by MBB (Ref. 6.2-9)

Each panel consists of a rigid, carbon-fiber composite support, rectangular cross-sectional frame, and a pretensioned, flexible substrate composed of 0.25-μm Kapton membrane reinforced with fiberglass. The rectangular panel frame is subdivided by thin, carbon-fiber composite channel cross-sectional rods which clamp the substrate. The Kapton/fiberglass membrane substrate is pretensioned in only one direction, parallel to the 3.22 m long edge of the panel.

The substrate is approximately 0.5-mm thick and the frame height is approximately 25 mm. Each panel has the following characteristics:

Panel without solar cells; mass per unit area	0.703 kg/m ² (0.144 lb/ft ²)
Array with all components; mass per unit area	1.53 kg/m ² (0.313 lb/ft ²)
Power per unit mass (6 kW EOL)	40.8 W/kg (18.5 W/lb)
Mass per unit power (6 kW EOL)	24.5 kg/kW (54 lb/kW)

6.2.7 Woven Tape, Rigid-frame Panels (Based on Refs. 6.2-10 and 6.2-11)

Boeing, under contract to JPL in the late 1960's, and TRW, under contract to INTELSAT in 1974, investigated the potential of an open weave or tape concept for a lightweight substrate design. Figure 6.2-15 illustrates the basic concept.

The substrate consists of fiberglass reinforced Kapton strips. The cells are connected directly to the substrate through spot adhesive. The back surface can be painted (epoxy) for both thermal control and low proton energy protection.

This design concept has the following advantages, as compared to a continuous, full substrate:

- An open substrate design facilitates greatly repair procedures.
- The emittance of the epoxy paint is greater than FEP Teflon or Kapton substrates.
- Wraparound contact cells can be used because of the easy access to the weld joints.

The substrate is attached to a support frame. In the Boeing design (Figure 6.2-16) the substrate is sandwiched between beryllium frames to form an integral panel. These panels can then be hinged together to form an array. Results from the Boeing study indicated the following weight characteristics:

Substrate only	0.894 kg/m ² (0.183 lb/ft ²)
Panel, without cells (102 m ² ; 1100 ft ²)	2.4 kg/m ² (0.49 lb/ft ²)

6.2.8 Hollowcore, Rigid Panels (Based on Ref. 6.2-12)

Electro-Optical Systems developed, under contract to NASA, a rigid substrate concept shown in Figure 6.2-17. This design employs an electroformed biconvex aluminum hollowcore substrate. The biconvex shape provides added stiffness to the very thin two-membrane concept. To form a panel, the substrate is supported in a frame (in this case a beryllium tubular frame).

The hollowcore substrate mass, without the tubular frame, is 1.43 kg for the 2.02-m² panel. With the frame and with 0.10-mm thick solar cells, carrying a 25- μ m thick integral cover and a 25- μ m thick Kapton insulating sheet between the solar cells and the substrate, the panel mass is 2.33 kg. Additional mass allocations must be made for hinges and other stowage and deployment mechanisms. The panel mass per unit area is as follows:

Without frame and cells	0.713 kg/m ² (0.146 lb/ft ²)
With frame and cells	1.15 kg/m ² (0.236 lb/ft ²)

6.2.9 Flexible Flat-pack Arrays (Based on Refs. 6.2-13, 6.2-14 and 6.2-15)

Under subcontract to the Canadian Communications Research Center, AEG-Telefunken is fabricating the solar array system for the Communications Technology Satellite (CTS) (see Figure 6.2-18).

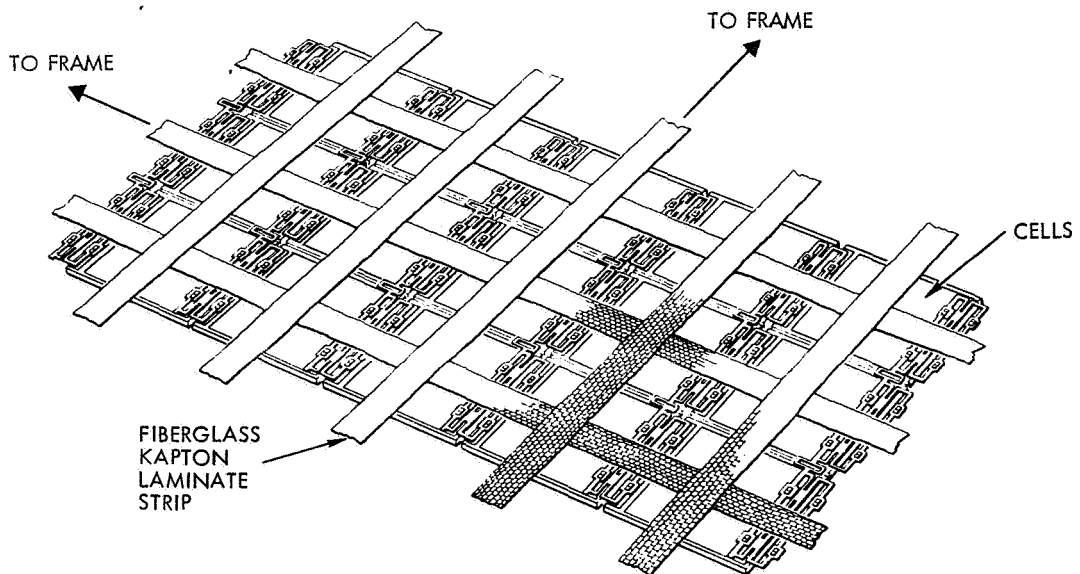


Fig. 6.2-15. Open Weave Substrate (backside shown) (Ref. 6.2-10)

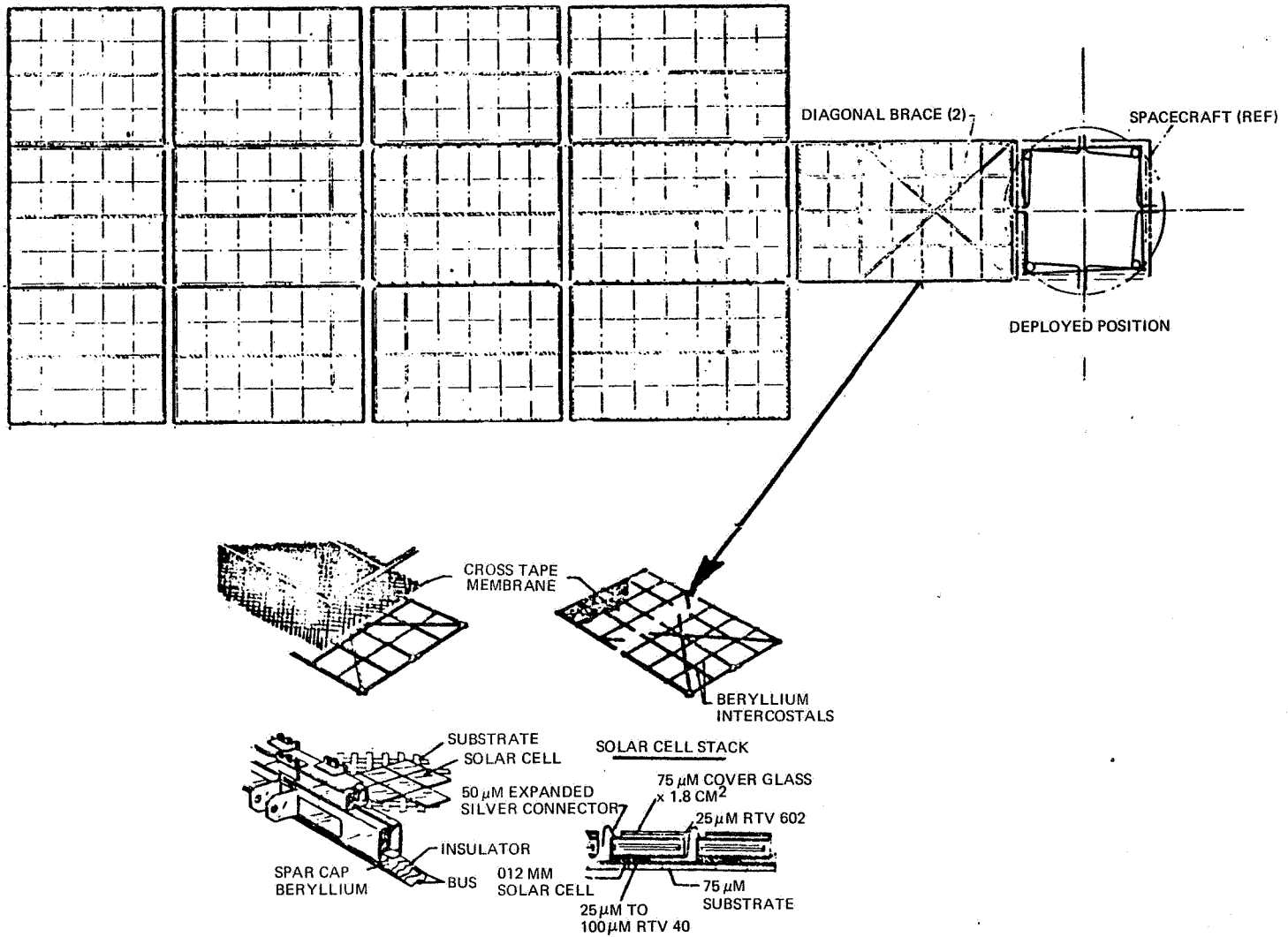


Fig. 6.2-16. Boeing/JPL Foldout Solar Cell Array (Ref. 6.2-11)

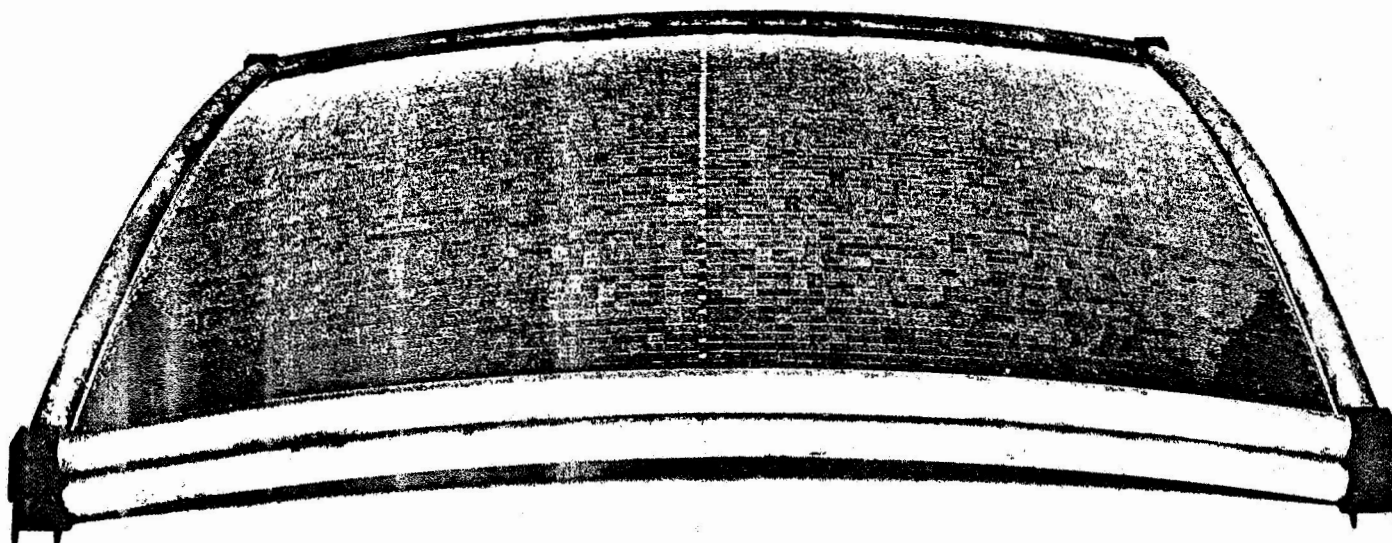


Fig. 6.2-17. Electro Optical Systems Hollowcore Folding Solar Cell Array
(Phase II demonstration panel) (Ref. 6.2-12)

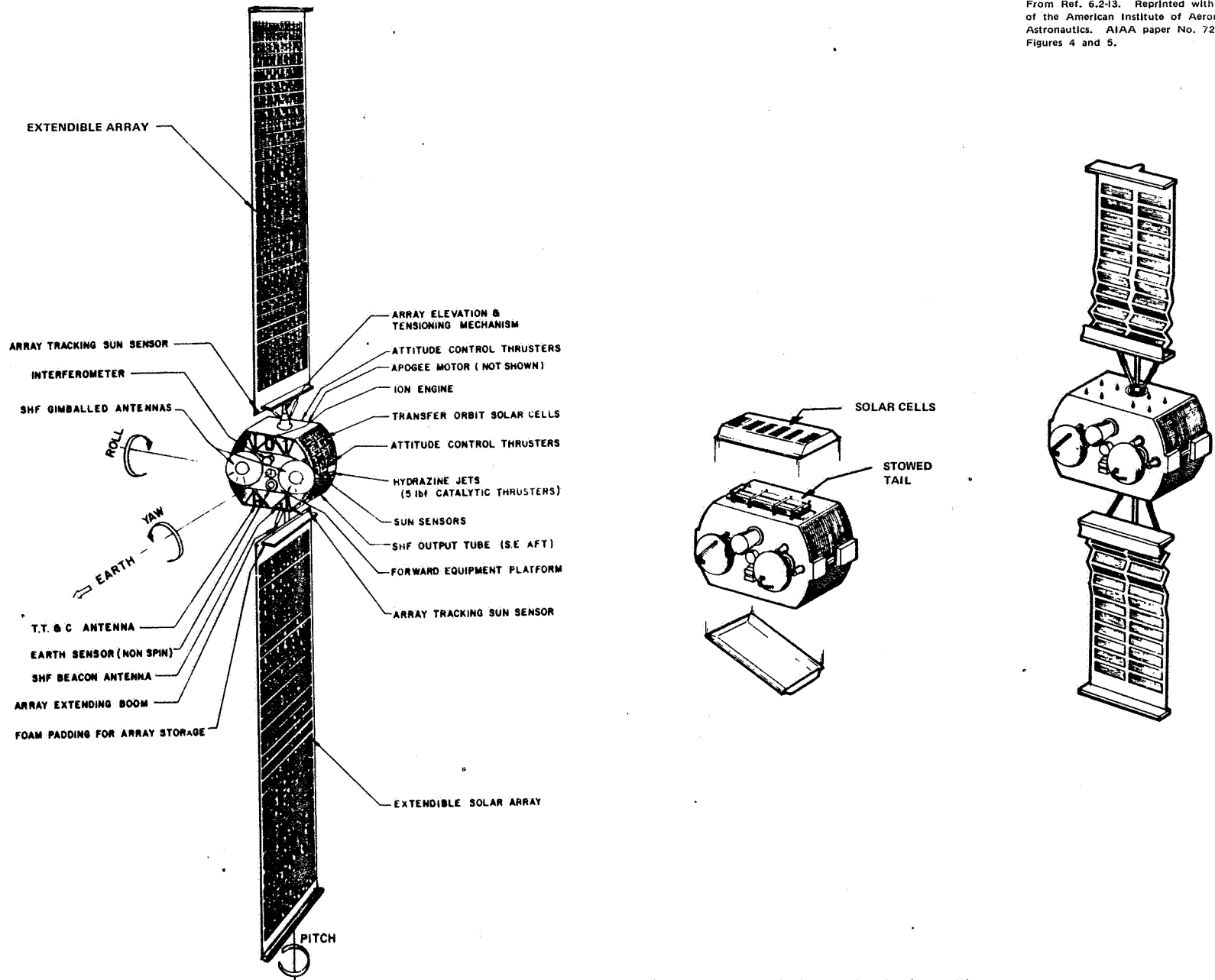


Fig. 6.2-18. CTS Spacecraft and Solar Cell Array (Ref. 6.2-13)

Each wing consists of a flexible blanket 6.52 m long by 1.3 m wide. Each wing consists of 30 foldable panels, 26 of which are solar cell covered (see Figure 6.2-19). The array is designed to stow accordion fashion between two honeycomb sandwich panels. Polyurethane foam interleaf material is inserted between folds to protect the solar cells and interconnects. The packaged array is stowed within a jettisonable cover on which are solar cells to provide power during transfer orbit. Deployment is achieved with a motorized, single element, 0.18-mm thick stainless steel, 35-mm diameter BISTEM boom located behind and on the shadowed side of the blanket. The boom is extended to produce a 27-N tension on the blanket.

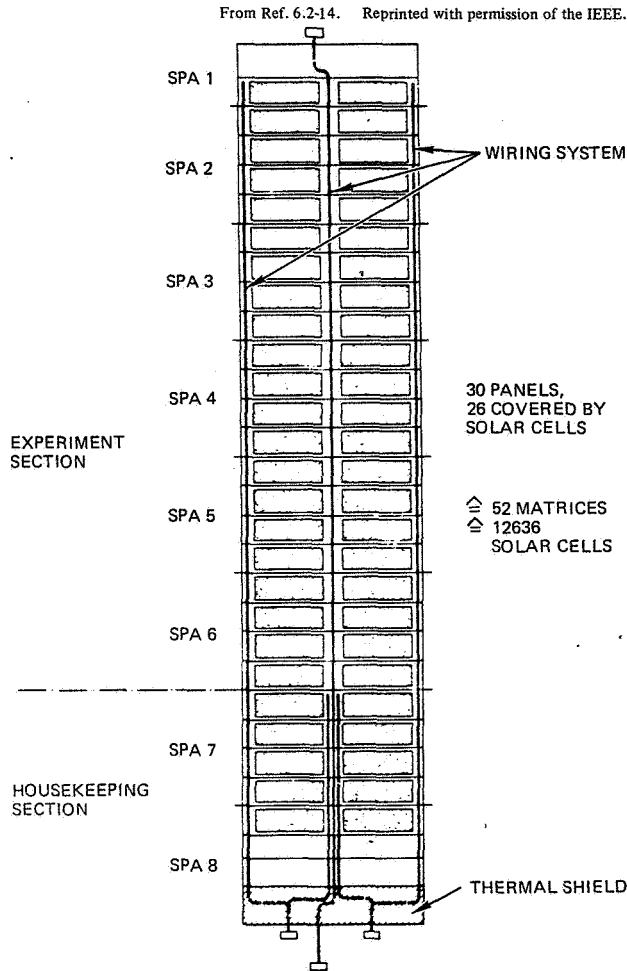


Fig. 6.2-19. CTS Solar Cell Array Blanket (Ref. 6.2-14)

The blanket consists of a laminate of 25- μ m Kapton and 36- μ m fiberglass. The total thickness of the composite is 66 μ m, accounting for the polyester adhesive layer. The blanket is cut into 4 panel assemblies. At both ends of each assembly are attached piano type hinges for mechanical interconnection of adjacent panels. Intermediate folds are achieved by creasing the substrate. Solar cells are bonded directly to the substrate. The solar cell stack consists of 0.2-mm thick cells with 0.1-mm thick microsheet covers.

The CRC/CTS solar cell array characteristics for a power level of 0.95 kW at EOL (2 years) are as follows:

Mass per Unit Area

Substrate without solar cells	0.88 kg/m ² (0.18 lb/ft ²)
Total array, without orientation drive and without jettisonable container	2.5 kg/m ² (0.52 lb/ft ²)
Total array as above except with jettisonable container	3 kg/m ² (0.6 lb/ft ²)

Array Power per Unit Mass

Solar cells with substrate only	64.6 W/kg (29.3 W/lb)
Total array without orientation drive and without jettisonable container	22 W/kg (9.9 W/lb)
Total array as above except with jettisonable container	19 W/kg (8.6 W/lb)

Mass per Unit Power

Solar cells with substrate only	15.5 kg/kW (34.1 lb/kW)
Total array without orientation drive and without jettisonable container	45.4 kg/kW (100 lb/kW)
Total array as above except with jettisonable container	52.6 kg/kW (116 lb/kW)

6.2.10 Perforated Flexible Flat-pack Arrays (Based on Refs. 6.2-16, 6.2-17 and 6.2-18)

Over the last several years, the Royal Aircraft Establishment (RAE) has been involved with the development of a flat-pack, deployable, flexible substrate solar cell array which is deployed by telescoping tubes. The design principles were space demonstrated on a small version of the larger development array on the British X4 meteorological satellite (EOL power \approx 64 watts).

Figure 6.2-20 shows the solar array paddle configuration. The array blanket, 4.21 m long by 0.90 m wide, is supported and divided into subpanels by aluminum honeycomb cross-members extending from an aluminum telescopic mast. For launch, the panels fold between cell patches into a honeycomb stowage compartment and are interleaved with sheets of corrugated 25- μ m Kapton, which remain behind in the compartment when the paddle is deployed. The solar cell array is deployed pneumatically through a six-section aluminum telescopic mast, using nitrogen gas at 0.33 MN/m² (48 psi). When fully deployed, each section is mechanically latched, tensioning the panels to about 9 N, and the gas is allowed to leak away.

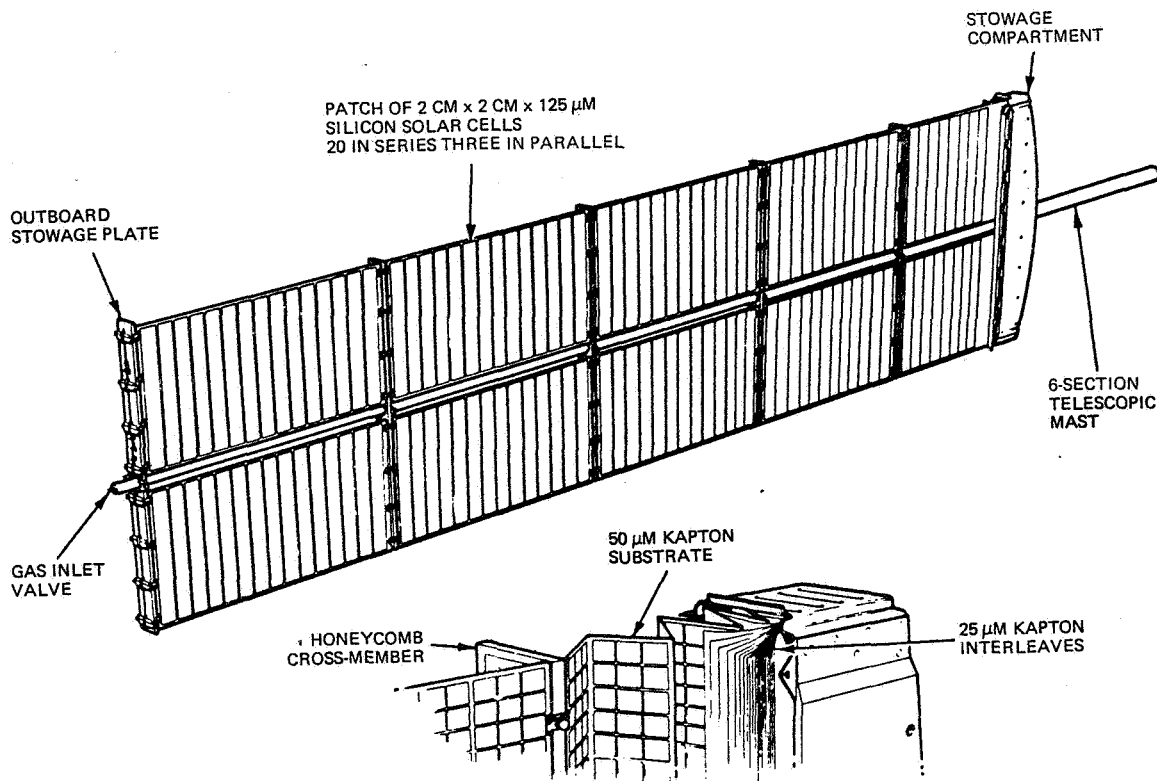


Fig. 6.2-20. RAE Lightweight Solar Cell Paddle (Ref. 6.2-26)

The substrate is as shown in Figure 6.2-21. It consists of a perforated 50- μ m thick Kapton sheet. The windows in the Kapton were actually triangular as opposed to the circular shape shown, exposing 54 percent of the cell area. Interconnectors were 25- μ m silver plated molybdenum. The cells are interconnected and mounted on the substrate by a solder through cementless technique. The back side of the array is finished with a high emittance coating. Solar cells are Ferranti 125- μ m thick, wraparound contact cells, covered with 0.1-mm thick, Pilkington Perkin-Elmer ceria stabilized glass.

The RAE solar cell array characteristics for an EOL power level of 250 watts are as follows:

Mass per Unit Area

Substrate with solar cell interconnectors, solder and paint, but without solar cells	0.13 kg/m ² (0.026 lb/ft ²)
Substrate with solar cells	0.63 kg/m ² (0.13 lb/ft ²)
Paddle with stowage structure	1.7 kg/m ² (0.34 lb/ft ²)

Power per Unit Mass

Substrate with cells only	101 W/kg (46 W/lb)
Entire system	40 W/kg (18 W/lb)

Mass per Unit Power

Substrate with cells only	10 kg/kW (22 lb/kW)
Entire system	25 kg/kW (55 lb/kW)

6.2.11 Very Large Flexible Flat-pack Arrays
(Based on Ref. 6.2-19)

Lockheed is developing under NASA contract a solar array system for a manned space station. This development has been on-going since 1970. Figure 6.2-22 shows an artist concept of the 929 m² solar array design. This array would be almost an order of magnitude larger than anything flown to date. The solar array can be classified as a flexible substrate, flatpack, foldout design. Each wing consists of 10 strip assemblies deployed through use of a single articulated lattice boom (Astromast). Each of these strips is stowed by folding it on itself, in flatpack fashion, within a container mounted on the side of the space station.

The substrate consists of the following materials and material thicknesses in cross-section, starting with the top surface: 25- μ m Kapton, 12- μ m FEP Teflon, 25- μ m of copper interconnect, 12- μ m FEP Teflon and 25- μ m Kapton. Figure 6.2-23 shows the substrate, with the cells and coverglass. This substrate configuration is laminated into modules approximately 0.6 x 1.8 m. At the edges, each module substrate is reinforced with fiberglass webs (see Figure 6.2-24). Modules are attached to one another through a locking bar/aluminum joint bar as shown in Figure 6.2-25.

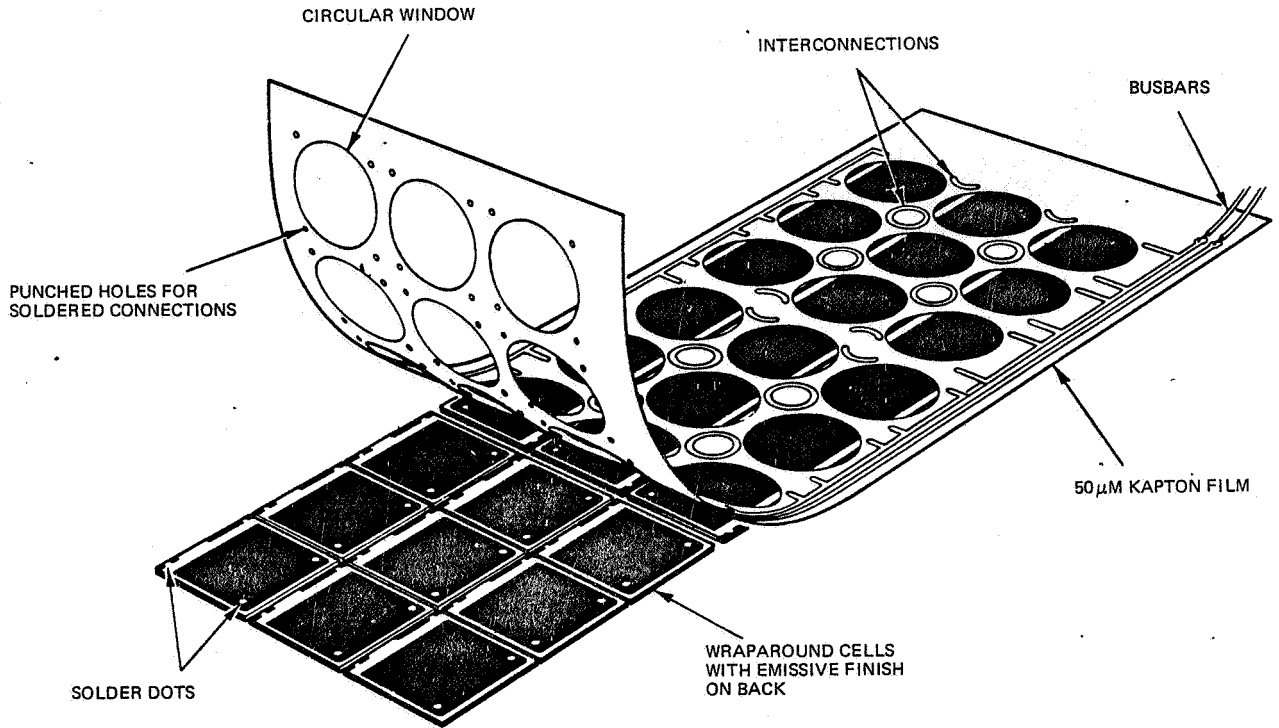


Fig. 6.2-21. RAE Substrate Configuration (Ref. 6.2-26)

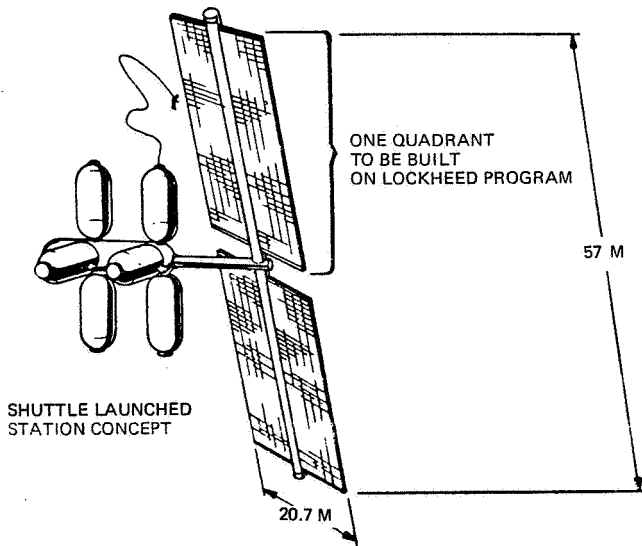


Fig. 6.2-22. Lockheed Space Station Solar Cell Array (Ref. 6.2-19)

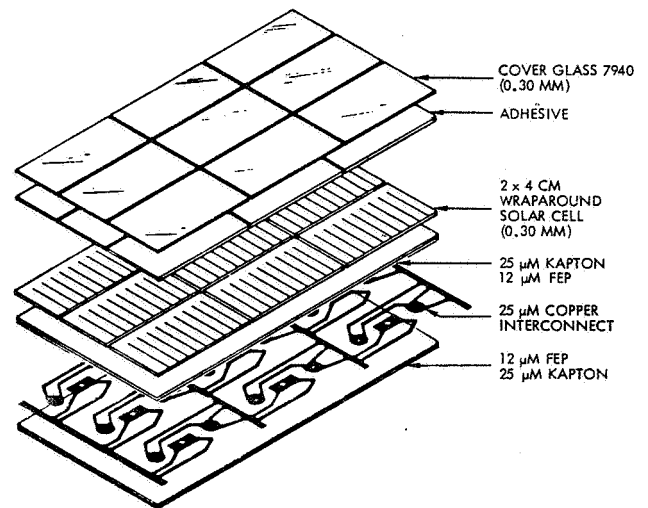


Fig. 6.2-23. Space Station Substrate Assembly (Exploded View) (Ref. 6.2-19)

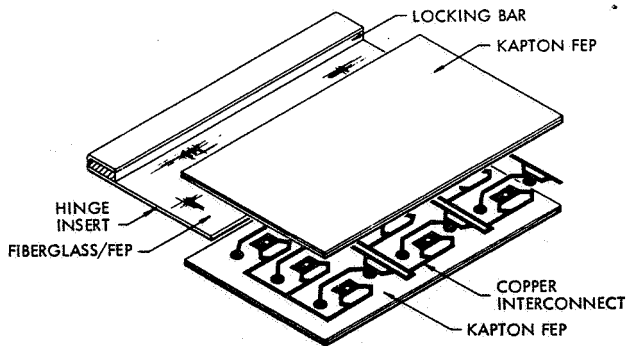


Fig. 6.2-24. Space Station Substrate Reinforced Edge Laminate (Ref. 6.2-19)

The characteristics of each space station module are as follows:

Mass, substrate only	0.16 kg
Mass, total module	1.69 kg
Area	1.04 m ²
Substrate only; mass per unit area	0.16 kg/m ² (0.032 lb/ft ²)
Total module; mass per unit area	1.86 kg/m ² (0.38 lb/ft ²)

The characteristics of each "strip" (an assembly of 42 modules) are as follows:

Mass, solar cell stacks only	56.31 kg
Mass, total strip	81.48 kg
Area	43.7 m ²
Mass per unit area	1.86 kg/m ² (0.38 lb/ft ²)

The projected characteristics of the total space station array for an EOL power level of 66 kW are as follows:

Mass without ODAPT	2683 kg
Mass with ODAPT	4044 kg
Mass, ODAPT only	1361 kg
Mass per unit area without ODAPT	3.1 kg/m ² (0.63 lb/ft ²)
Power per unit mass without ODAPT	24 W/kg (11 W/lb)
Mass per unit power without ODAPT	41 kg/kW (90 lb/kW)

The ODAPT is the orientation drive and power transfer mechanism.

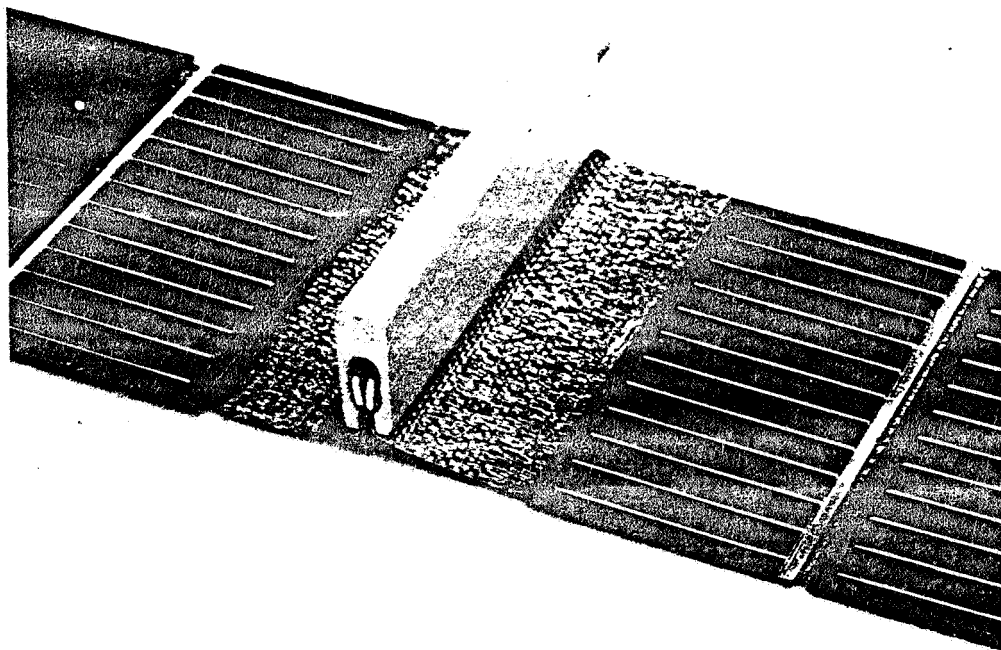


Fig. 6.2-25. Space Station Complete Module Joint (Ref. 6.2-19)

6.2.12 Lightweight Flexible Flat-pack Arrays
(Based on Ref. 6.2-20)

The General Electric Company, under JPL sub-contract, performed a design feasibility study for NASA. The objective of the study was to assess the feasibility of a 10 kW BOL, 110 W/kg (50 W/lb) solar array for application to a variety of interplanetary, synchronous and manned space station missions.

The concept developed consists of a single deployable mast (Astromast) which supports two flexible solar cell blankets (18.6 m long by 2.8 m wide per blanket) (see Figure 6.2-26). The 10 kW BOL power is generated through 125- μ m thick Ferranti cells, bottom wraparound configuration, protected with a 38- μ m integrally deposited coverglass. The flexible solar cell blankets are stowed for launch by folding into a flatpack package which is retained in compression within a stowage container. Interlayer cushions of Kapton are used to protect the cells when stowed. When deployed the Astromast exerts 27 N of tension on both blankets.

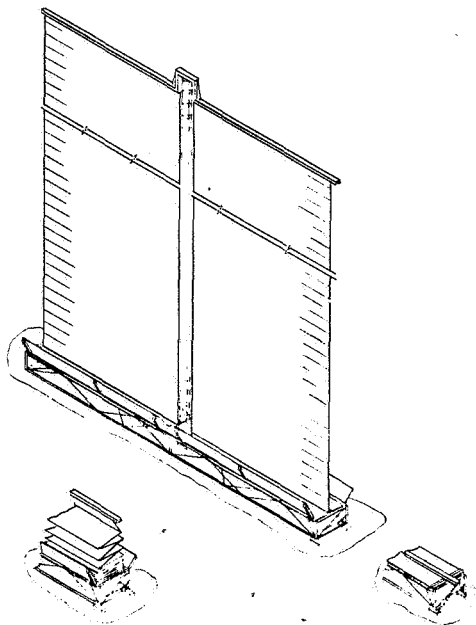


Fig. 6.2-26. Baseline 110 W/kg Solar Cell Array Configuration (Ref. 6.2-20)

The substrate design is similar to the RAE configuration in construction. Each solar cell blanket consists of an interconnection of 30 identical strips, as shown in Figure 6.2-27. The substrate is a 50- μ m perforated Kapton membrane (see Figure 6.2-28). The perforations serve to reduce weight and provide for more effective thermal radiation. The fold hinge between blanket strips consists of FEP Teflon which is heat sealed to the Kapton substrate. The interconnects are 25- μ m silver plated molybdenum. The solar cell backs are coated with a 50- μ m thick emissive finish. The cells are mounted to the substrate by a solder through cementless technique.

The solar cell array characteristics for an EOL power level of 6.9 kW are as follows:

Mass per Unit Area

Substrate with solar cell interconnectors, solder, and paint, but without solar cells	0.11 kg/m ² (0.023 lb/ft ²)
Substrate with solar cells	0.45 kg/m ² (0.093 lb/ft ²)
Array with stowage structure	0.83 kg/m ² (0.17 lb/ft ²)

Power per Unit Mass

Substrate with solar cells only	143 W/kg (65 W/lb)
Entire array system	79 W/kg (36 W/lb)

Mass per Unit Power

Substrate with solar cells only	7.0 kg/kW (15.5 lb/kW)
Entire array system	13 kg/kW (28 lb/kW)

As a side study a "V"-stiffened solar array configuration was conceived as a means of obtaining significant increases in minimum array resonant frequency (see Figure 6.2-29). In this concept storage would be on a drum rather than flatpacked.

6.2.13 FEP-Teflon Encapsulated Solar Cell Modules
(Based on Refs. 6.2-21 and 6.2-22)

TRW is developing under contract to NASA an integral encapsulated solar cell substrate design. The integral assembly consists of cells, covers, substrate and cabling as shown in Figure 6.2-30.

Modules are constructed either from conventional front/back contact solar cells or from wraparound contact solar cells. The 0.2-mm thick, solderless cells are first interconnected into the usual series/parallel-connected matrix of cells. Each matrix is then heat laminated between two sheets of clear FEP Teflon and to a Kapton substrate. The FEP Teflon layer over the active cell area is 125 μ m thick and serves as a shield against charged particles and as a thermal control surface. The lower, or inner FEP layer is 50 μ m thick and serves as an adhesive between the solar cells and the 25- μ m load bearing Kapton substrate sheet. During lamination, the two layers of FEP fuse together to completely encapsulate the cells and interconnectors.

Adjacent modules are mechanically interconnected via 25- μ m Kapton hinge strips which are heat-sealed to the module edges using 50- μ m FEP Teflon as a thermoplastic adhesive. Bus bars are made from silver-plated copper strips secured to the Kapton by pressure sensitive adhesive.

The FEP cover layer replaces both the glass covers with their UV reflective and antireflective coatings, and the cover adhesive used on conventional solar cell arrays. The FEP cover sheet provides integral low energy proton protection, acts as the adhesive to bond cells to the Kapton substrate, and mechanically protects the cells and interconnects.

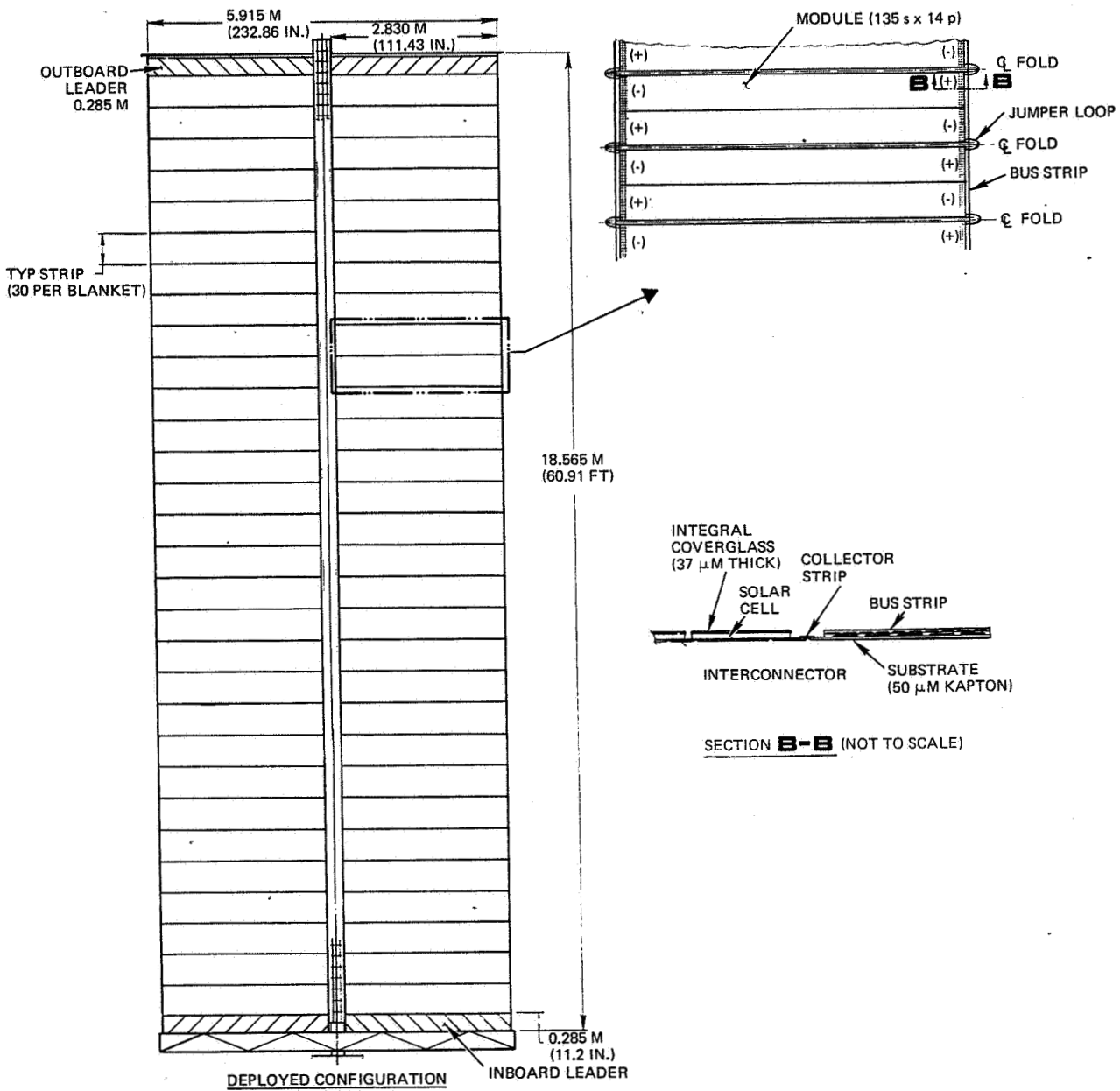


Fig. 6.2-27. 110 W/kg Array Substrate Configuration (Ref. 6.2-20)

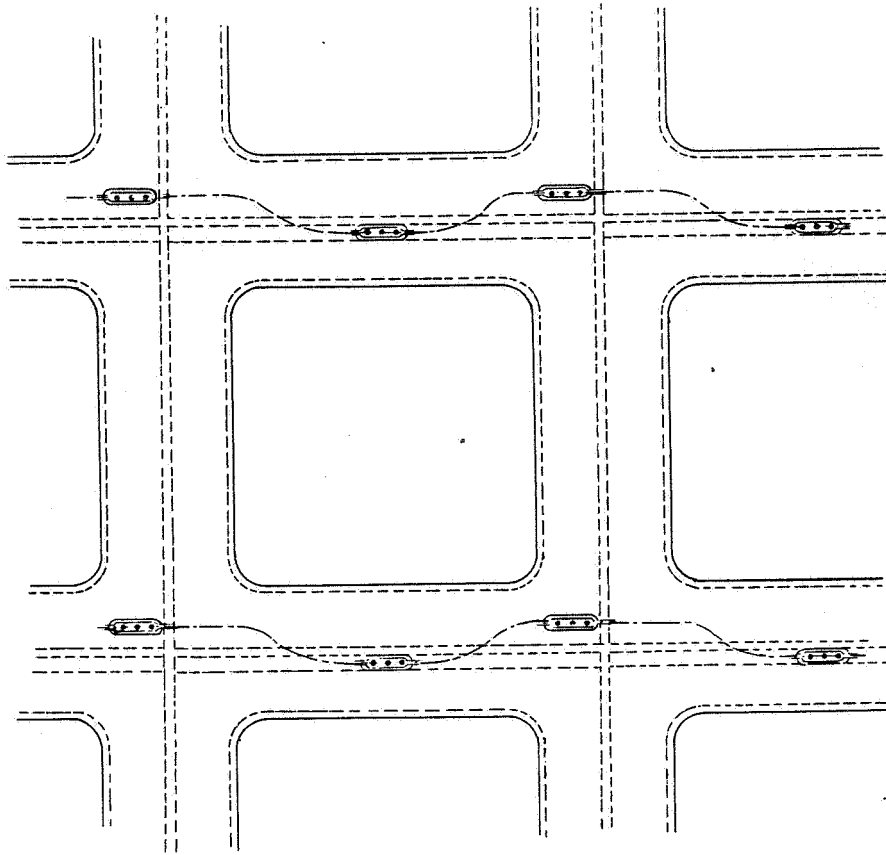


Fig. 6.2-28. Rear View of Solar Cell Blanket, GE 110 W/kg Design (Ref. 6.2-20)

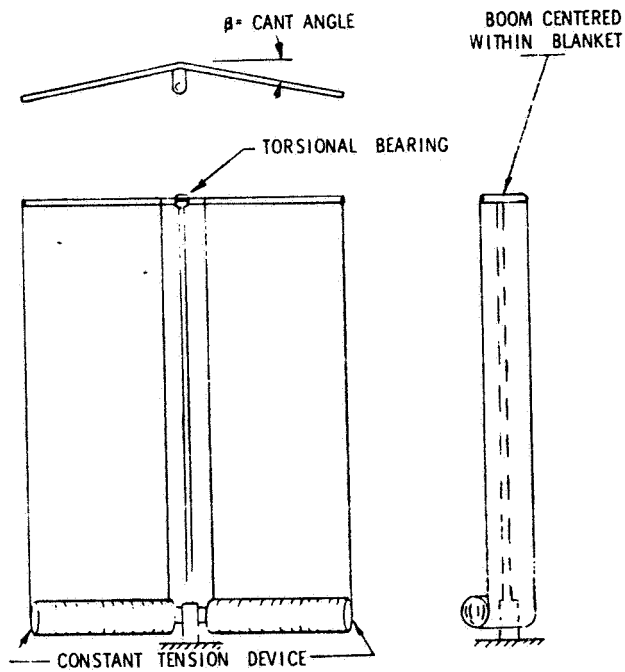


Fig. 6.2-29. "V" Configuration, Single Boom
110 W/kg Roll-out Solar Cell
Array Concept (Ref. 6.2-20)

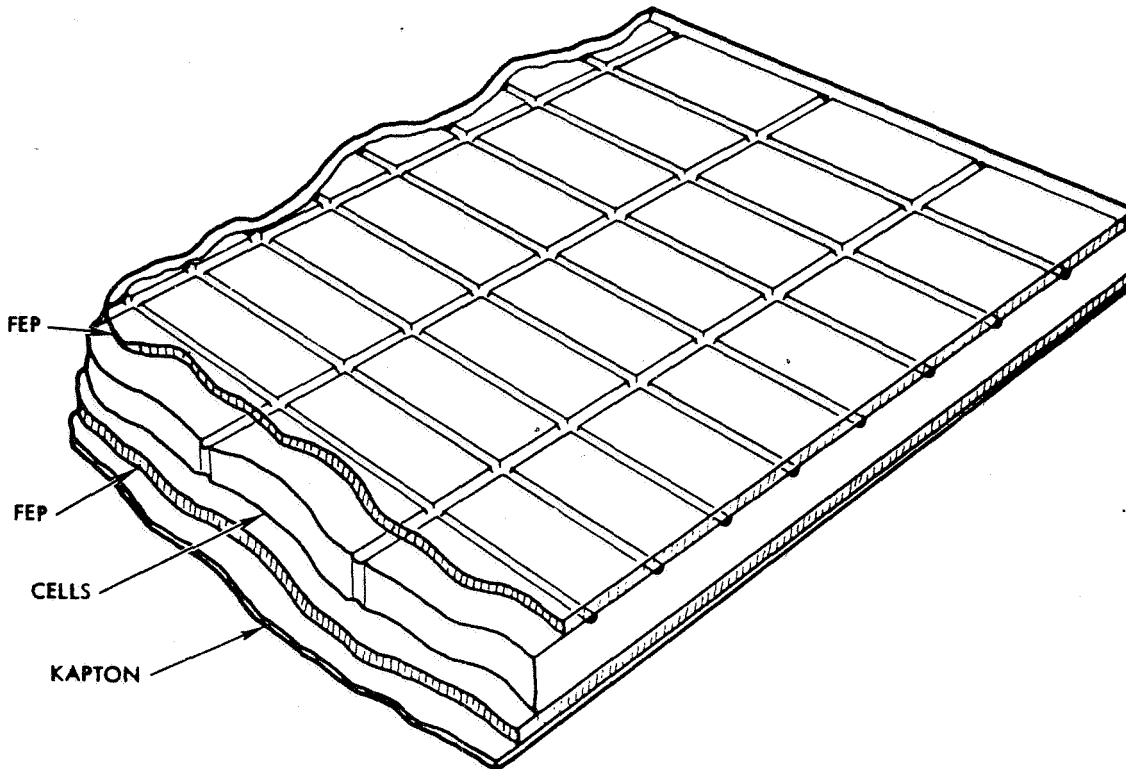


Fig. 6.2-30. FEP-Teflon Encapsulated Solar Cell Module

An entire solar cell array blanket would consist of a number of modules. Such a blanket could be either mounted on a rigid frame, folded up accordion-like with a support frame or rolled up on a drum of at least 8 inches in diameter. In the latter two cases, deployment would be facilitated by a spreader bar/extendible boom arrangement.

Specific density of the integral substrate (including solar cells) is approximately 1.25 kg/m^2 (0.255 lb/ft^2).

6.2.14 Flexible Roll-out Arrays, U.S.
(Based on Ref. 6.2-23)

Hughes Aircraft Corporation, under contract to the Air Force, developed a flexible roll-up solar cell array (FRUSA). The system was launched as a flight experiment in 1971 aboard an Agena spacecraft and performed satisfactorily.

Figure 6.2-31 shows the roll-up array design. The system uses two solar cell blankets 4.9 m long by 1.7 m wide which are rolled up on a single 20-cm diameter drum. An embossed 50- μm thick Kapton cushion protects the solar cells in the launch stowed configuration. During extension, this cushion is rolled up on an auxiliary takeup roller. The blankets are deployed from the common drum by a pair of extendible BISTEM steel booms, 22 mm in diameter and held under a nominal 14-N tension.

The solar cell blankets are continuous laminates of Kapton and fiberglass. Silicon solar cells are 0.18 mm thick covered with a 0.15 mm thick microsheet. Power after 4 months in orbit was 1260 watts.

The solar cell array characteristics are as follows:

Solar cell substrate without solar cells; mass per unit area	0.14 kg/m^2 (0.029 lb/ft^2)
Substrate with solar cells; mass per unit area	0.93 kg/m^2 (0.19 lb/ft^2)
Total system; mass per unit area	2.0 kg/m^2 (0.40 lb/ft^2)
System; power per unit mass	40 W/kg (18 W/lb)
System; mass per unit power	25 kg/kW (55 lb/kW)

6.2.15 Flexible Roll-out Arrays, European
(Based on Ref. 6.2-24)

Under contract to ESTEC and GFW, AEG-Telefunken developed two roll-up solar array systems. ROSA stands for rollout solar array (single blanket) and DORA stands for double blanket rollout array. Both concepts are similar to the Hughes FRUSA, in that a flexible membrane is deployed from a drum using extendible BISTEM booms. Development units were fabricated and tested to establish concept feasibility.

The blanket substrates for both units are 5.0 m long by 1.0 m wide. They are constructed from a laminate of 25- μm Kapton, 36- μm fiberglass, and 5- μm adhesive for a total thickness of 66 μm . The blanket is rolled up on a 15-cm diameter drum. Cushioning is

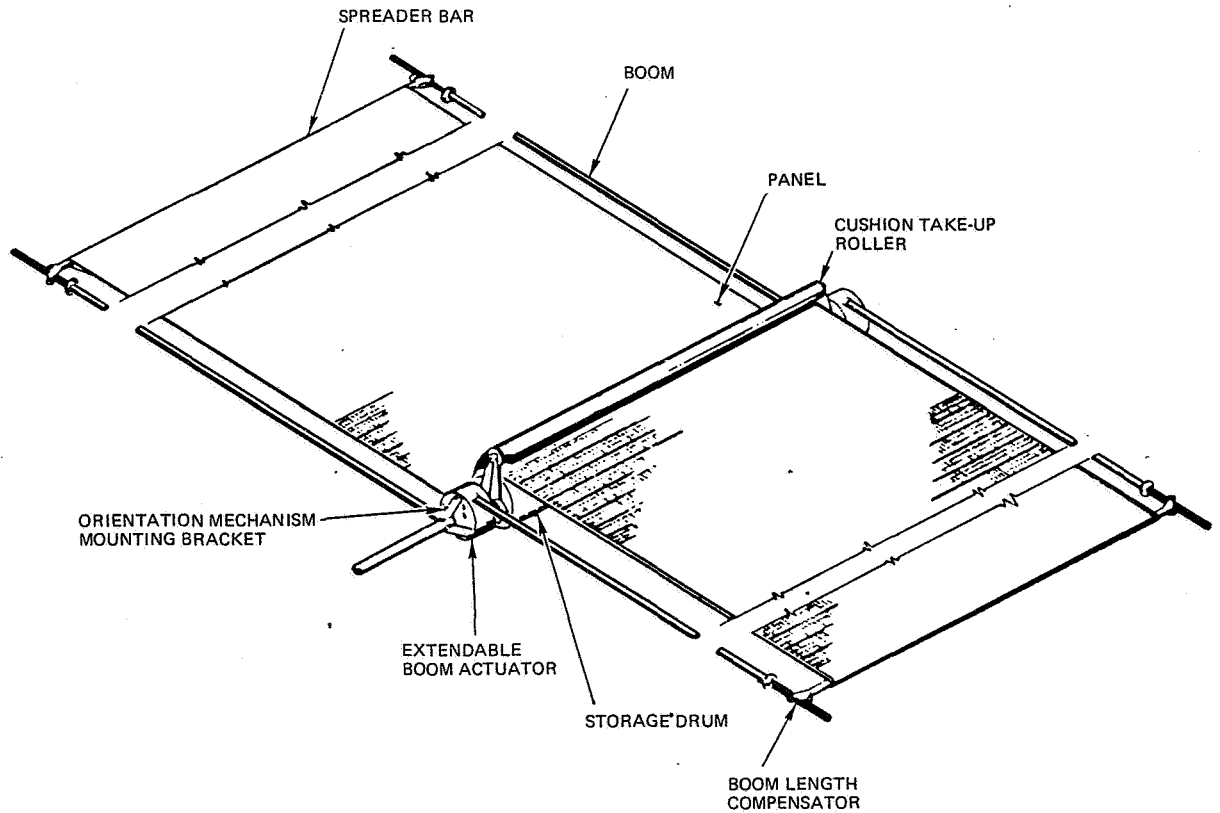


Fig. 6.2-31. Hughes FRUSA (Ref. 6.2-23)

provided during stowage by a 2- μm thick polyurethane foam layer, which stows on a separate drum as each blanket is deployed. Deployment of each blanket is achieved by two stainless steel, 22-mm diameter BISTEM units. Each blanket is pretensioned to 32 N. Mass-simulated solar cells and covers (360 μm total thickness) are bonded directly to the blankets.

For a power level of 0.8 kW, the DORA system has the following characteristics:

Substrate only; mass per unit area	0.083 kg/m ² (0.017 lb/ft ²)
Entire system; mass per unit area	2.4 kg/m ² (0.5 lb/ft ²)

Power per unit mass	33 W/kg (15 W/lb)
Mass per unit power	30 kg/kW (67 lb/kW)

The DORA characteristics were extrapolated by Ref. 6.2-24 to a 3.5 kW array. For such a power level, each array blanket would be approximately 11 m long by 2 m wide. For a combined solar cell and cover thickness of 0.30 mm, the array characteristics would be as follows:

System mass per unit area	1.7 kg/m ² (0.35 lb/ft ²)
Power per unit mass	45.4 W/kg (20.6 W/lb)
Mass per unit power	22.0 kg/kW (48.5 lb/kW)

6.3 DEPLOYMENT MECHANISMS

For other than the body-mounted solar arrays, some mechanical system is required to deploy the array structure from its stowed position after the launch phase of a mission. Depending upon the type of deployable array design, deployment can be achieved (a) through the use of a pulley/cable/spring actuator system or (b) through the use of an extendible boom.

6.3.1 Deployable Booms

The central mechanical component of any packaged flexible solar array system is the deployment boom which erects and/or retracts the flexible substrate. Because it comprises a sizeable portion of the total system weight, careful attention to selection and design of the proper approach is important.

An extensive summary of deployable boom technology is contained in Ref. 6.3-1. While that reference is only current to 1972, the numerous concepts identified are still representative of what is available today. The principle effort over the last few years in boom technology has been in the use of newer, more efficient materials, rather than the development of revolutionary new concepts. Thus, much of the descriptive material presented in this subsection will be drawn from that reference.

The desirable features of a deployable boom are as follows:

- Low weight
- Small package size
- Reliable performance
- Sufficient bending and torsional stiffness
- Good bending strength
- Low thermally induced response
- Good positioning accuracy.

An actuator normally does not possess all these features simultaneously. Most often a compromise has to be made in order to choose a design.

Basic Structural Forms

Table 6.3-1 shows the basic common forms of beams and beam members in use. Each member has advantages, and the selection of one over another involves tradeoff by weight, strength, cost, availability and fabricability.

Table 6.3-2 shows beams and beam member cross sectional variations. The form variations are generally the result of a functional consideration and not purely structural (i. e., the thin tubular form results from the requirement that the member be flattened for stowage).

Most solid or tubular beams become inefficient as load carrying members when the length approaches 15 m. A substitute for the solid form is the truss structure. Truss-configured beams are the most efficient structures in terms of stiffness and weight for large dimensional applications.

Stowage/Deployment Techniques

Table 6.3-3 illustrates the basic stowage methods and their variations. Folding is the method most used for stowing beams and beam members. It is mechanically the simplest and most versatile stowage method. Folding is used as a basic method for stowing beams with hinges and without hinges (i. e., inflatable, lenticular tubes, curved tapes). Combined folding methods can be used to form multiple beam element booms.

Rolling beams on drums is a popular technique. The beam occupies little volume when stowed in relation to its extended size. It can be used for stowing beams of a variety of cross sections. The technique stresses the material so that the beam thickness is such that the yield strain is not exceeded; this limits the beam strength. Coiling can be considered a variation of rolling.

Telescoping beams for stowage is also a relatively common method. Their stowage efficiency ratio of stowed to extended height is relatively low; however this can be improved by combining folding with telescoping.

Table 6.3-4 shows the extension/retraction prime movers, that when combined with the beam section and stowage technique, creates a mechanism that can be used to operate the erection of the solar array. The prime movers can be interchanged depending on the design constraints.

Element Types

Table 6.3-5 presents a brief description of 20 unique linear element extendible structures that incorporate combinations of the basic structural forms. Stowage techniques and deployment techniques were given in the previous tables.

While several boom types have been designed and developed as indicated, only a few have been used in actual developmental or operational solar array systems. Table 6.3-6 identifies those designs along with the specific solar array design or satellite program. The preferred designs include:

- Extendible reel stored (Type 16, Table 6.3-5)
- Articulated or coiled lattice mast (Type 8/9, Table 6.3-5)
- Telescoping cylinders (Type 2, Table 6.3-5)

Table 6.3-1. Basic Beam Cross Section Forms (Ref. 6.3-1)

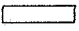


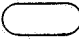
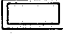


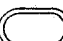
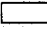


STRUCTURE	FORM	STRUCTURAL CHARACTERISTICS	COMMENTS
SOLID		GOOD TENSION MEMBER, MOMENT OF INERTIA CHANGES IN ORTHOGONAL DIRECTIONS	ECONOMICAL MATERIAL SECTION, FLAT SURFACES FACILITATE FABRICATION OF TRUSS STRUCTURES
		FAT SECTION SUITABLE FOR HIGH SHEAR LOADS	PRIMARYLY USED IN MECHANISMS; HOWEVER, USEFUL FOR SHORT BEAMS OR STRUTS
		FAT SECTION SUITABLE FOR HIGH SHEAR LOADS, CONSTANT MOMENT OF INERTIA	ECONOMICAL MAT'L SECTION, BEAM END FITTINGS FABRICATED WITH SIMPLE DRILLED HOLES
		MOMENT OF INERTIA CHANGES IN ORTHOGONAL DIRECTIONS	USUALLY A FORGED SHAPE; USED EXTENSIVELY AS A SIMPLE BEAM
TUBES		TORSIONALLY GOOD, PROVIDES DIFFERENT MOMENT OF INERTIA IN ORTHOGONAL AXIS	WIDELY USED IN ANTENNA STRUCTURES WHERE IN WAVEGUIDE SERVES ITS NORMAL MICROWAVE FUNCTION AS WELL AS STRUCTURAL SUPPORT
		TORSIONALLY GOOD, PROVIDES EQUAL MOMENT OF INERTIA IN ORTHOGONAL AXIS	USED IN STRUCTURES WHERE FLAT SURFACES FOR MOUNTING OR FABRICATION ARE DESIRED
		TORSIONALLY STIFFEST WEIGHT FORM AVAILABLE, CONSTANT MOMENT OF INERTIA	ECONOMICAL, WIDELY USED FORM COMMERCIALY AVAILABLE IN A BROAD SELECTION OF MATERIALS AND ALLOYS
		TORSIONALLY GOOD, PROVIDES DIFFERENT MOMENT OF INERTIA IN ORTHOGONAL AXIS	USUALLY PRODUCED IN FABRICATION SHOP BY FLATTENING A ROUND TUBE
TRUSS BEAMS		TORSIONALLY GOOD, PROVIDES DIFFERENT MOMENT OF INERTIA IN ORTHOGONAL AXIS	COMMONLY USED IN BRIDGE TRUSSES OR ANY TRUSS WITH UNSYMMETRICAL LOADING
		TORSIONALLY GOOD, PROVIDES EQUAL MOMENT OF INERTIA IN ORTHOGONAL AXIS	COMMONLY USED WHERE LOADS ARE SYMMETRICAL SUCH AS RADIO TOWERS
		TORSIONALLY GOOD, MOMENT OF INERTIA MAY BE VARIED IN ANY OF THREE DIRECTIONS	GENERALLY USED FOR SYMMETRICAL LOADS, HOWEVER, CAN BE MADE ASYMMETRICAL FOR SPECIAL CONDITIONS

Table 6.3-2. Beam and Beam Member Cross Section Variations (Ref. 6.3-1)

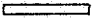




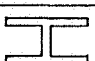
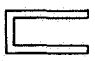
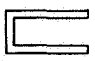
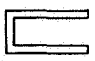



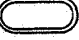




BEAM FORM	VARIATION	COMMENTS
 OPEN SECTIONS		LOW OUT-OF-PLANE STIFFNESS LIMITS THIS TO LOW BENDING AND TORSIONAL LOAD APPLICATIONS.
		LOW TORSIONAL STIFFNESS, HIGH DYNAMIC DAMPING, EVEN WHEN MADE TO OVERLAP. WIDELY USED AS SMALL DIAMETER, LONG MEMBERS FOR ELECTROMAGNETIC ANTENNA. SEVERE THERMAL BENDING PROBLEMS.
		BROAD RANGE OF SIZES AND MATERIALS AVAILABLE. SUITABLE FOR STIFFENERS OR COMPONENT PARTS OF A BUILT-UP BEAM OR COLUMN.
		SIMILAR TO ABOVE WITH SLIGHTLY IMPROVED BENDING STRENGTH.
		WIDELY USED AS STRUCTURAL BEAMS. IDEAL FOR HIGH BENDING LOADS ABOUT THE MAJOR PRINCIPAL AXIS
 		AS ABOVE EXCEPT HIGHER FLANGE BUCKLING HAZARD. SHEAR CENTER NOT COINCIDENT WITH C.G.
		
 ROUND TUBE	 	APPROACHES THE STRUCTURAL CHARACTERISTICS OF A THIN WALLED TUBE. EXACT MECHANICAL PROPERTIES DEPEND UPON INDIVIDUAL DESIGN. USUALLY <6 IN DIA AND WITH APPROX 250:1 DIAMETER TO THICKNESS RATIO. CRITICAL REVIEW OR APPLICATIONS ARE REQUIRED TO MINIMIZE THERMAL BENDING PROBLEMS.
 FLATTENED TUBE	 	USUALLY IN THIN WALLED SECTIONS. BENDING LOAD CAPACITY VARIES WITH LATERAL CURVATURES. TEST DATA LIMITED, ANALYSIS METHOD NOT DEVELOPED FOR BEAM WITH SEALED EDGES. CENTER PIECE HELPS STABILIZE SHAPE, HENCE INCREASES STRENGTH AND STIFFNESS. HOWEVER INCREASED DRUM WEIGHT SHOULD BE STUDIED IN A TRADE-OFF.
 TUBULAR DELTA		USUALLY IN THIN WALLED SECTIONS AND LIMITED IN SIZE TO 6 INCHES PER SIDE.

Table 6.3-3. Extension/Retraction Methods (Ref. 6.3-1)

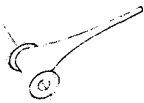
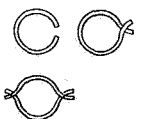
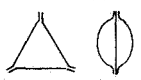


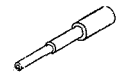
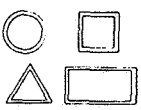
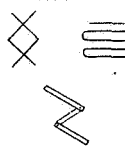
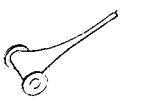

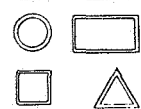
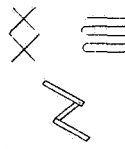
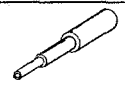

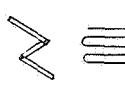
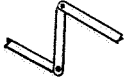
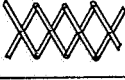
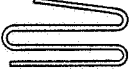
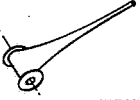

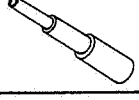
PRIME MOVER	STOWAGE METHOD	BEAM SECTION FORM	CHARACTERISTICS
ELECTRIC MOTOR	 REEL STORED		REMOTE ACTUATION, CAPABLE OF MULTIPLE EXTENSIONS AND RETRACTIONS. SOME MODELS INCORPORATE TWO STORAGE REELS THAT ARE INTERCONNECTED AND DRIVEN BY A COMMON MOTOR.
			REMOTE ACTUATION, CAPABLE OF MULTIPLE EXTENSIONS AND RETRACTIONS. USES THREE STORAGE REELS INTERCONNECTED AND DRIVEN BY A COMMON MOTOR.
			REMOTE ACTUATION, CAPABLE OF MULTIPLE EXTENSIONS AND RETRACTIONS. A SINGLE STORAGE REEL IS DRIVEN BY THE MOTOR..
			WIRE TRUSS IS FOLDED AND ROLLED UP ON A SINGLE, MOTOR DRIVEN REEL.
	 TELESCOPING		REMOTE EXTENSION MAY BE ACCOMPLISHED BY MOTOR DRIVEN WINCH ACTION OR A MOTOR DRIVEN HYDRAULIC SYSTEM. BEAM SECTIONS MAY BE SOLID OR TRUSS.
 FOLDING	VARIOUS	REMOTE EXTENSION MAY BE ACCOMPLISHED BY MOTOR DRIVEN WINCH ACTION OR BY A MOTOR DRIVEN SCREW JACK (USUALLY IN CONJUNCTION WITH MECHANICAL SPRINGS).	
MECHANICAL SPRINGS	 REEL STORED	SAME BEAM SECTION USED AS ELECT. MOTOR CONFIG	SPRING MOTOR POWERS EXTENSION ONLY, MANUAL RETRACTION REWINDS MOTOR.
	 TELESCOPING		SPRINGS OR SPRING MOTOR POWERS EXTENSION ONLY, REQUIRES MANUAL RETRACTION. GENERALLY USED WITH A DAMPER TO CONTROL EXTENSION DYNAMICS.
	 FOLDING	VARIOUS	SPRINGS AT EACH JOINT EXTEND STRUCTURE. MANUAL RETRACTION REQD. MAY BE USED IN CONJUNCTION WITH AN ELECTRICAL MOTOR THAT WILL ASSIST IN EXTENSION AND CONTROL EXTENSION DYNAMICS.
PNEUMATIC (STORED GAS)	 TELESCOPING		SLIDING SEALS MAKE TELESCOPIC MAST GAS TIGHT, GAS PRESSURE EXTENDS CYLINDERS. MANUAL RETRACTION REQD.
	 FOLDING	VARIOUS	SEALED TUBES INFLATED WITH GAS PRESSURE, MANUAL RETRACTION REQD. PNEUMATIC ACTUATORS MAY BE EMPLOYED TO ERECT HINGED JOINTS, AGAIN MUST BE RETRACTED MANUALLY.

Table 6.3-4. Basic Stowage Methods and Variations (Ref. 6.3-1)

METHOD	VARIATIONS	CHARACTERISTICS	COMMENTS
FOLDED		STOWS BY DISPLACEMENT ONLY, STOW VOLUME IS APPROX. EQUAL TO EXTENDED VOLUME.	SIMPLE, EFFECTIVE, AND WIDELY USED, LIGHT WEIGHT FOR MORE HEAVILY LOADED SYSTEMS.
		STOWS VERY COMPACTLY, REQUIRES LATCHES TO DEVELOP RIGIDITY. EXCELLENT DEPLOYMENT DEVICE	MULTIPLE HINGE JOINTS REQUIRE PRUDENT DESIGN TO MINIMIZE LOOSENESS. USUALLY SPRING LOADED AGAINST A DAMPER MECHANISM.
		STOWAGE CAPABILITY DEPENDS UPON THE MATERIAL ALLOWABLE STRESS AND THICKNESS. INFLATABLES USING METAL FOILS STOW VERY COMPACTLY	NO JOINTS OR LATCHES REQUIRED TO PROVIDE A RIGID STRUCTURE. COLUMN STRENGTH IS LIMITED BY MATERIAL THICKNESS, STOWED CONFIGURATION, AND ALLOWABLE STRESS. NO REMOTE RETRACTION.
ROLLED		BEAM IS WRAPPED AROUND A REEL AND ITSELF. REQUIRES A SECTION OF THE BEAM REMAIN EXTENDED BUT STOWS COMPACTLY. CAN BE SELF EXTENDING BUT USUALLY MOTOR DRIVEN	USUALLY CAPABLE OF MANY EXTENSIONS AND RETRACTIONS WITHOUT DEGRADING PERFORMANCE, DEVELOPS FULL STRENGTH AT PARTIAL EXTENSION. COLUMN STRENGTH IS LIMITED BY MAT'L THICKNESS STOW CONFIG. & STRESS
		USUALLY SELF EXTENDING BY STORED SPRING ENERGY, ALTHOUGH SOME MOTOR DRIVEN MODELS HAVE BEEN USED	CAPABLE OF MANY EXTENSIONS OR RETRACTIONS WITHOUT DEGRADING PERFORMANCE. COLUMN STRENGTH IS VERY LIMITED.
TELESCOPED		STOWED VOLUME FROM 20 TO 50 PERCENT OF EXTENDED VOLUME. DESIGNS READILY ADAPT TO DEVELOP ALL USABLE STRENGTH ON INDIVIDUAL MEMBERS	SIMPLE, FEW PARTS, MAKE DESIGN VERY RELIABLE. MAY BE TRUSSES, TUBES OR COMBINATIONS OF THE TWO

- Folding beam solid cross section (Type 3, Table 6.3-5)
- Lazy tongs (Type 4, Table 6.3-5)
- Simple pantograph (version of Type 5, Table 6.3-5).

Of those identified above, the Bistem (Type 16) is used with great frequency on moderate-sized deployable, flexible substrate arrays. For very large arrays, the Astromast (Type 8 or 9) is preferred because of its structural efficiency.

Blanket/Boom Arrangements

Regardless of the blanket stowage method (i.e., rollup and flat-pack), either two booms or a single boom can be used as illustrated in Figure 6.3-1. The single boom should be near the center line of the blanket whereas in the two-boom scheme, the booms should be near either edge of the blanket. A two-boom scheme provides a greater torsional rigidity than the single-boom design. A single-boom scheme can be obtained in two ways — one with an offset boom and the other with a split blanket. In the offset design, the blanket is one piece and the boom is offset from the blanket plane. In the case of the split design, the blanket is split in two halves and the boom is placed in the plane of the blanket in between the two halves. A split configuration requires a longer blanket (and boom) than the offset configuration for an array width to obtain an equal blanket area. Table 6.3-7 summarizes blanket/boom arrangements for some developmental array programs and satellite programs.

6.3.2 Spring/Actuator Systems

Unlike the multitude of concepts and configurations associated with deployment booms discussed in Section 6.3.1, spring/actuator systems are fairly standard. Components include

- Torsion or compression springs at the hinge lines
- Dampers
- Closed-loop cable system to kinematically constrain and couple the deployment between panels
- Latch-up system.

The following subsections provide a brief description of spring/actuator systems for a few operational arrays.

FLTSATCOM Array

This solar array structure was described in Section 6.2.4. The array consists of two deployable wings attached to the spacecraft through a hinged beam. Each wing consists of three panels. In the launch configuration, the six panels are folded around the six sides of the spacecraft. Pyrotechnic devices are used to secure the panels during the launch. Hinge fittings are incorporated at three locations for each panel.

Table 6.3-5. Extendible Structures (Ref. 6.3-1)



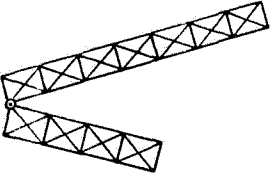

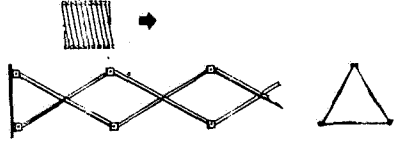
NO. & NAME OF EXTENSIBLE STRUCTURE	ILLUSTRATION	DESCRIPTION & OPERATION OF STRUCTURE & MECHANISM (RETRACTION CAPABILITIES)	GENERAL DESIGN COMMENTS
1 TELESCOPING TRIANGULAR TRUSS		<p>CONCENTRIC TRIANGULAR TRUSS SECTIONS SUPPORTED BY ROLLERS. SECTIONS ARE EXTENDED AND LATCH IN THE FULL EXTENDED POSITION. CAN BE UNLATCHED AND RETRACTED</p>	<p>TRIANGULAR SHAPE PROVIDES EXCELLENT STIFFNESS-TO-WEIGHT CHARACTERISTICS. MEMBERS MAY BE SIZED-UP ACCORDING TO LOAD REQUIREMENTS AND PACKAGING ENVELOPE. VERY SIMPLE DESIGN ANALYSIS. AN EXTREMELY EFFICIENT BEAM IF THREE OR LESS TELESCOPIC SECTIONS ARE USED. LOOSENESS IN THE JOINTS WILL YIELD A NON-LINEAR SYSTEM AND MUST BE AVOIDED OR MINIMIZED. AN IDEAL BEAM FOR THERMAL BENDING WHEN USED WITH A CONSTANT SUN ANGLE, AS EXPOSURE TO SUNLIGHT CAN BE NEARLY EQUAL ON ALL LONGITUDINAL MEMBERS. UNEVEN SIDE HEATING COULD PRODUCE DEFORMATION AND RESULT IN RETRACTION PROBLEMS.</p>
2 TELESCOPING CYLINDERS		<p>CONCENTRIC SOLID TUBES IN GRADUATED DIAMETERS. SECTIONS ARE EXTENDED AND LATCH IN THE FULL EXTENDED POSITION. CAN BE UNLATCHED AND RETRACTED</p>	<p>COLUMN LOADED THIN WALL TUBES ARE BEST USED FOR INTERMEDIATE LENGTH BEAMS (LESS THAN 50 FT.). INCREASES IN LENGTH REQUIRE AN INCREASE IN TUBE DIAMETER TO MAINTAIN A MINIMUM SLENDERNESS RATIO. SIMULTANEOUSLY THE TUBE WALL THICKNESS MUST BE INCREASED TO MAINTAIN A LOW R/T RATIO TO AVOID LOCAL BUCKLING. CONSIDERABLE OVERLAP IS REQUIRED TO AVOID ROTATIONAL LOOSENESS. NONUNIFORM TEMPERATURES WILL CAUSE BENDING. CROSS-SECTION WILL NOT REMAIN CIRCULAR AND MUST BE ANALYZED FOR BINDING DURING RETRACTION. THERMAL CONTROL SURFACE MUST WITHSTAND SLIDING ABRASION DURING EXTENSION AND RETRACTION.</p>
3 FOLDING BEAM		<p>SECTIONS MAY BE TRUSS, TUBULAR, OR SOLID; HINGES ON EITHER END AND LATCHES AT FULL EXTENSION. USUALLY DEPLOYED BY A TENSION CABLE SYSTEM WITH PULLEYS AT EACH JOINT. CAN BE UNLATCHED AND RETRACTED.</p>	<p>CHARACTERISTICS ARE THOSE OF THE BASIC SECTION SELECTED; MAY BE VERY EFFICIENT, DEPENDING UPON THE DETAIL DESIGN. LOOSENESS IN THE JOINTS WILL RESULT IN A DYNAMICALLY NON-LINEAR SYSTEM AND MUST BE MINIMIZED. THERMAL BINDING IS UNLIKELY. ALL OTHER THINGS EQUAL, THIS BEAM GENERALLY REQUIRES MORE STORAGE SPACE THAN A TELESCOPING BEAM.</p>
4 LAZY TONG		<p>STRUCTURAL PANELS HINGED TOGETHER AND STABILIZED ATTACHMENT TO HINGED BEAMS AT THE EDGES. THE HINGED BEAMS ARE SOMEWHAT LONGER FROM PIVOT TO PIVOT THAN THE STRUCTURAL PANELS. THE PANELS ALIGN TO ACCEPT COLUMN LOADS. MAY BE LATCHED AT FULL EXTENSION, USUALLY NOT RETRACTABLE ONCE LATCHED. USUALLY SPRING-LOADED; MAY HAVE SCREW JACK ASSISTANCE. COULD USE A TENSION CABLE SYSTEM AS IN NO. 3 BUT THE NUMBER OF JOINTS IS USUALLY HIGH.</p>	<p>VERY COMPACT STOWAGE. THIS BEAM IS AN EFFECTIVE DEPLOYMENT DEVICE. PROPER LOCKING OF PANELS IS REQUIRED TO CHANGE THE DEVICE INTO A STRUCTURE. THE LARGE NUMBER OF JOINTS WILL PROBABLY LEAD TO A NON-LINEAR STRUCTURE, WHICH MAKES MEANINGFUL DYNAMIC ANALYSIS DIFFICULT.</p>
5 TRI AXIS PANTOGRAPH		<p>THREE LAZY TONGS TIED AT THE NODES WITH U-SHAPED CLIPS. MAY BE LATCHED AT FULL EXTENSION. AS IN NO. 4, MOSTLY USED AS A SPRING-LOADED, NON-RETRACTING DEVICE INVOLVING ONLY LIGHT COLUMN LOADS. MAY USE A SCREW JACK ASSIST WHICH WILL CONTROL DEPLOYMENT.</p>	<p>THIS IS A GOOD DEPLOYMENT DEVICE BUT A VERY POOR STRUCTURE, INHERENTLY NON-LINEAR WITH LOW LATERAL AND TORSIONAL STIFFNESS. COLUMN STRENGTH IS LIMITED BY THE EXTENSION MECHANISM; OR EVEN IF LATCHED IN THE EXTENDED POSITION, ALL OF THE STRUCTURAL MEMBERS ARE LOADED IN BENDING. THERMAL BENDING WILL BE SMALL IF BEAM SELF SHADING IS HELD TO A LOW VALUE. VERY COMPACT STOWAGE.</p>

Table 6.3-5. Extendible Structures (Continued)

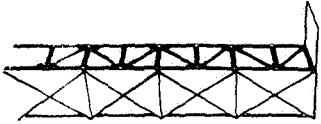
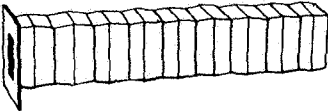
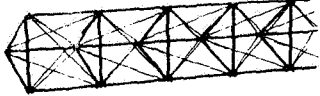
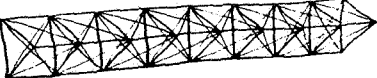

NO. & NAME OF EXTENDIBLE STRUCTURE	ILLUSTRATION	DESCRIPTION & OPERATION OF STRUCTURE & MECHANISM (RETRACTION CAPABILITIES)	GENERAL DESIGN COMMENTS
6 EXTENSIBLE TRUSS		TWO LAZY TONGS CONNECTED WITH PANELS TO PRODUCE A RECTANGULAR TRUSS BEAM WHEN EXTENDED; PANELS ALIGN TO ACCEPT COLUMN LOADS. MAY BE LATCHED AT FULL EXTENSION; USUALLY NOT RETRACTABLE ONCE LATCHED. MAY USE A SCREW JACK ASSIST WHICH WILL CONTROL DEPLOYMENT.	VERY COMPACT STOWAGE. PRUDENT LATCH DESIGN WILL MAKE THIS A REASONABLY STIFF STRUCTURE. HOWEVER IT WILL INHERIT SOME LESS DESIRABLE STRUCTURAL QUALITIES SUCH AS NON-LINEARITY AND LOW TORSIONAL STIFFNESS. LATCHES MAKE RETRACTION MORE DIFFICULT, LESS RELIABLE. SELF SHADING MAY PRODUCE EXCESSIVE THERMAL BENDING AND MAY INDUCE BINDING IF RETRACTION IS ATTEMPTED. BEAM IS NOT RIGID UNLESS FULLY EXTENDED.
7 BOX BELLOWS (JACK-IN-THE-BOX)		FLAT RECTANGULAR PANELS JOINED LONGITUDINALLY BY HINGES, INCORPORATING TORSION SPRINGS AND SUPPORTED BY FLANGES. HINGES OPEN INWARD AND OUTWARD ON ALTERNATE PANELS. MAY BE LATCHED AT FULL EXTENSION, USUALLY NOT RETRACTABLE.	VERY COMPACT STOWAGE. BASIC DESIGN PROVIDES GOOD TORSIONAL STIFFNESS. HOWEVER, THE HIGH L/B (SLENDERNESS RATIO) AND THE LOW B/T (LOCAL STIFFNESS) REQUIREMENT MAKE THIS STRUCTURE VERY INEFFICIENT FOR LONG BEAMS. HOLES, AT LEAST ON THE SUN SIDE, ARE PROBABLY REQUIRED TO MINIMIZE TEMPERATURE DIFFERENCES. EFFECT OF NONUNIFORM TEMPERATURES ON ABILITY TO REFOLD WOULD HAVE TO BE EVALUATED. BEAM IS NOT RIGID UNLESS FULLY EXTENDED.
8 ASTROMAST ARTICULATED LATTICE		TRIANGULAR SECTIONS ARE RIGID; THE LONGITUDINAL LINKS PIVOT AT EACH BAY. FOLDING IS ACHIEVED BY LOOSENING ONE TENSION MEMBER (WIRE ROPE) IN EACH BAY; THE TENSION MEMBERS ARE LOCKED AS EACH BAY IS EXTENDED. RETRACTABLE.	COMPACT STOWAGE. THIS BEAM CAN BE MADE AS EFFICIENT AS THE BASIC TRIANGULAR TRUSS, WITH HIGH STIFFNESS TO WEIGHT RATIO. BEAM IS AT FULL STRENGTH AT ALL TIMES DURING DEPLOYMENT. REMOTE (AUTOMATIC) DEPLOYMENT MAY BE MORE COMPLICATED THAN REQUIRED FOR OTHER DEPLOYABLE STRUCTURES. UNIFORM SOLAR ILLUMINATION IS BEST ACHIEVED IN A TRIANGULAR OPEN TRUSS BEAM.
9 ASTROMAST COILABLE LATTICE		FIBERGLASS CONSTRUCTION WITH WIRE ROPE TENSION MEMBERS. LONGITUDINAL SECTIONS ARE CONTINUOUS; THE TRIANGULAR BAY SECTIONS ARE RIGID AND PIVOTED ON THE LONGITUDINAL MEMBERS. RETRACTABLE. FIBERGLASS BATTENS (SIDES OF TRIANGULAR SECTION) ARE BUCKLED TO BEGIN COILING OPERATION.	COMPACT STOWAGE, LINEAR SYSTEM, HIGH STIFFNESS TO MASS RATIO. BEAM IS AT FULL STRENGTH AT ALL TIMES DURING DEPLOYMENT. HOWEVER, THIS BEAM IS LIMITED TO LOW LOAD APPLICATIONS. AS THE LOAD INCREASES, THE REQUIRED DIAMETER OF THE LONGERON INCREASES AND QUICKLY BECOMES TOO STIFF TO COIL IN A REASONABLE STORAGE AREA. LOW TEMPERATURE BENDING CHARACTERISTICS MAY BE A PROBLEM. THE LOW THERMAL CONDUCTIVITY OF FIBERGLASS WILL ACCENTUATE TEMPERATURE NON-UNIFORMITY. PLASTIC WILL REQUIRE A PROTECTIVE THERMAL COATING TO RESIST U.V. DAMAGE, ETC.
10 TRI EXTENDER LMSC		*TRIANGULAR BOOM, PANTOGRAPH LINKS CONNECT THE LONGITUDINAL MEMBERS. EACH LONGITUDINAL MEMBER HAS A LENTICULAR SECTION BETWEEN THE LAZY TONG NODES SIMILAR TO EXT. STRUCTURE NO. 12. THE LENTICULAR SECTIONS ARE FLATTENED THEN BUCKLED ALTERNATELY INWARD/OUTWARD TO STOW. NOT RETRACTABLE.	COMPACT STOWAGE, LINEAR SYSTEM. AN EXCELLENT STIFFNESS TO MASS RATIO IS ACHIEVED WITHOUT THE COMPLICATION OF LATCHES. THE LONGERONS BEND TO STOW BUT THE SECTION TO BE BENT IS FIRST FLATTENED WHICH LOWERS THE STRESSES SIGNIFICANTLY. HOWEVER, THE BENDING WILL LIMIT THE COLUMN LOADING SOMEWHAT. BROAD LENTICULAR SECTIONS MAY CAUSE MORE SELF SHADING THAN CIRCULAR SECTIONS. THE BEAM IS NOT RIGID UNLESS FULLY EXTENDED. NO REASONABLE RETRACTION SYSTEM HAS BEEN PROPOSED FOR THIS BEAM.

Table 6.3-5. Extendible Structures (Continued)

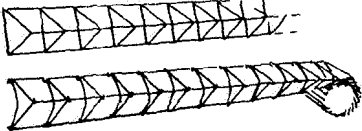
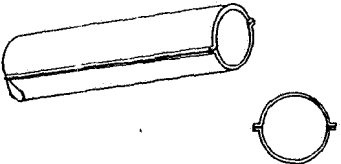
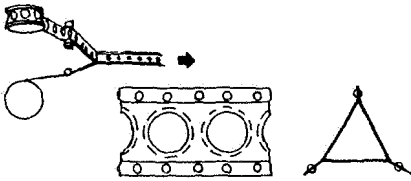
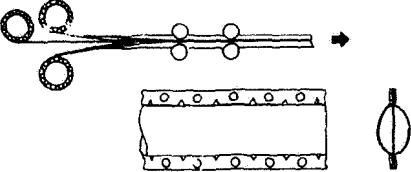
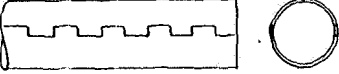
NO. & NAME OF EXTENDIBLE STRUCTURE	ILLUSTRATION	DESCRIPTION & OPERATION OF STRUCTURE & MECHANISM (RETRACTION CAPABILITIES)	GENERAL DESIGN COMMENTS
11 TRIANGULAR WIRE		<p>SOLID SPRING WIRE CONSTRUCTION. TRIANGULAR SECTIONS WELDED TO LONGERONS. ONE LEG OF THE TRIANGULAR SECTION IS MADE TO FLEX (OR HINGED) SO THAT THE REMAINING 2 SIDES CAN BE BROUGHT TOGETHER. THE FOLDED BEAM CAN THEN BE ROLLED UP ON A REEL. REEL ROTATED BY ELECT. MOTOR & GEAR TRAIN, RETRACTION ACCOMPLISHED BY REVERSING MOTOR. IF RETRACTION IS NOT REQD, SPRING FORCE (OR MOTOR) MAY BE USED FOR EXTENSION.</p>	<p>REQUIRES DIAGONAL MEMBERS TO ACHIEVE REASONABLE TORSIONAL STIFFNESS. BENDING STRESSES IN LONGERONS DURING STOWAGE WILL LIMIT THEIR SIZE AND CONSEQUENT COLUMN LOADING CAPACITY. ANY THERMAL CONTROL SURFACES MUST RESIST ROLLING ABRASION AND FLEXING; HOWEVER, THIS IS AN EXCELLENT DESIGN TO MINIMIZE THERMAL DEFLECTIONS. MINIMUM DEPLOYMENT/RETRACTION PROBLEMS ARE ANTICIPATED. LINEAR DYNAMIC SYSTEM, FULL-BEAM STRENGTH COULD BE DEVELOPED AS THE BEAM EXTENDS. VERY COMPACT STOWAGE.</p>
12 LENTICULAR WELDED BEAM		<p>TWO PIECES OF SPRING TAPES ARE PRE-FORMED TO APPROXIMATE A HAT SECTION. THE TWO TAPES ARE WELDED TOGETHER AT THE FLANGES. THE SECTION IS FLATTENED AND ROLLED UP ON A REEL FOR STOWAGE OR CAN BE LOCALLY FLATTENED AND BENT IN A FIRE HOSE FOLD. THE MOTOR DRIVEN REEL WOULD BE RETRACTABLE; THE FIRE HOSE FOLD WOULD NOT BE RETRACTABLE.</p>	<p>LINEAR DYNAMIC SYSTEM, VERY COMPACT STOWAGE. BEAM DEVELOPS FULL STRENGTH AS IT IS DEPLOYED. THIS BEAM IS GOOD FOR MEDIUM LENGTH APPLICATIONS (LESS THAN 50 FT). AS LENGTH INCREASES THE BEAM BECOMES INEFFICIENT FOR COLUMN LOADS. THE MOMENT OF INERTIA OF THE BEAM SECTION MAY BE INCREASED IN ONE DIRECTION WITH VERY LITTLE EFFECT ON STOWAGE VOLUME OR STRESSES. WELDED JOINTS SIMPLIFY THERMAL ANALYSIS. HOLE PATTERN PROBABLY REQUIRED. THERMAL COSTINGS MUST WITHSTAND ROLLING ABRASION. THIS AND SIMILAR BEAMS COULD HAVE A THERMAL COMPENSATING CURVE BUILT IN.</p>
13 TRIBEAM (LMSC)		<p>BEAM COMPOSED OF 3 SPRING TAPES WITH EDGE FLANGES CONTAINING VELCRO TAPE AND SNAP FASTENERS. TAPES ROLL-UP ON REELS ARRANGED ABOUT THE BEAM CENTERLINE. REELS ARE INTERCONNECTED & ROTATED BY ELECT. MOTOR & GEAR TRAIN, RETRACTION ACCOMPLISHED BY REVERSING MOTOR.</p>	<p>HIGH DYNAMIC DAMPING, FAIRLY COMPACT STOWAGE. FOR MEDIUM LENGTH THIS IS A GOOD SELECTION. AS THE LENGTH APPROACHES 50 FT THE TRIBEAM BECOMES INEFFICIENT FOR SIGNIFICANT COLUMN LOADS. REQUIRES HOLES TO MINIMIZE THERMAL DEFLECTION. INSIDE AND OUTSIDE REQUIRE ROLLING ABRASION RESISTANT THERMAL COATINGS. POOR THERMAL CONDUCTION THROUGH THE VELCRO TAPES SHOULD CAUSE NO MAJOR PROBLEMS, IF ADEQUATE HOLE PATTERN IS USED, ESPECIALLY WHEN USED WITH A CONSTANT SUN ANGLE.</p>
14 INSTARECT (SANDERS)		<p>3 PIECE BEAM, TWO OUTER PRE-FORMED SPRING TAPES ARE FLATTENED & ROLLED-UP ON REELS. THE CENTER (FLAT) SPRING TAPE WITH EDGE INDEX HOLES & SLOTS IS ALSO STORED ON A REEL. THE EDGES OF THE 3 TAPES INTERLOCK AS THE BEAM EXTENDS. REELS ARE INTERCONNECTED & ROTATED BY AN ELECT. MOTOR & GEAR TRAIN. RETRACTION ACCOMPLISHED BY REVERSING MOTOR.</p>	<p>LINEAR DYNAMIC SYSTEM, FAIRLY COMPACT STOWAGE. AGAIN A MEDIUM-LENGTH BEAM CANDIDATE. HIGH R/T RATIOS IN THE CURVED SHEETS AND HIGH B/T RATIO ON FLAT SHEET LIMIT THE COLUMN LOAD CAPACITY. NOT LIKELY EFFICIENT IN LENGTHS GREATER THAN 50 FT. THE BEAM MOMENT OF INERTIA CAN BE INCREASED IN ONE DIRECTION WITH LITTLE EFFECT ON STOWAGE VOLUME OR STRESSES. SUBJECT TO LARGE THERMAL DEFLECTIONS IF CENTER IS SOLID. TEMPERATURE GRADIENTS DIFFICULT TO PREDICT BECAUSE OF UNCERTAINTY IN EDGE CONTACTS AND COMPLEX INNER STRUCTURE. HOLES MAY BE REQUIRED IN ALL THREE TAPES.</p>
15 INTERLOCKING EXTENDIBLE REEL STORED		<p>2 PIECES OF PRE-FORMED SPRING TAPES ARE FLATTENED & ROLLED-UP ON REELS. THE EDGES OF THE TAPES INTERLOCK AS THE BEAM EXTENDS. REELS ARE INTERCONNECTED & ROTATED BY AN ELECT. MOTOR & GEAR TRAIN. RETRACTION ACCOMPLISHED BY REVERSING MOTOR.</p>	<p>LINEAR DYNAMIC SYSTEM, VERY COMPACT STOWAGE. THIS BEAM (CONSIDERED AS A SOLID TUBE) IS GOOD FOR SHORT TO MEDIUM LENGTH APPLICATIONS (LESS THAN 50 FT). AS LENGTH INCREASES THE BEAM BECOMES INEFFICIENT FOR COLUMN LOADS. TEMPERATURE PREDICTION UNCERTAINTY IS INCREASED IF THE SUN DOES NOT SHINE SYMMETRICALLY ON THE INTERLOCKING LINE. HOLE PATTERN MAY BE REQUIRED TO OBTAIN REASONABLE THERMAL DEFLECTIONS. ROLL ABRASION RESISTANT THERMAL COATINGS ARE REQUIRED.</p>

Table 6.3-5. Extendible Structures (Continued)

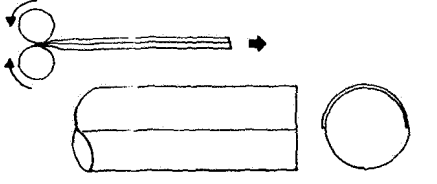
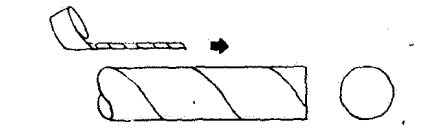

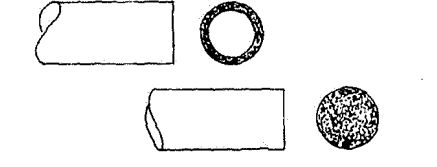
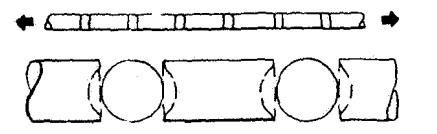
NO. & NAME OF EXTENDIBLE STRUCTURE	ILLUSTRATION	DESCRIPTION & OPERATION OF STRUCTURE & MECHANISM (RETRACTION CAPABILITIES)	GENERAL DESIGN COMMENTS
16 EXTENDIBLE REEL STORED		<p>PRE-FORMED SPRING TAPE (OR TAPES) ARE FLATTENED AND ROLLED UP ON A REEL FOR STOWAGE. THESE ARE THE SIMPLEST OF THE REEL STORED BEAMS. THE REEL IS ROTATED BY AN ELECT. MOTOR & GEAR TRAIN. RETRACTION IS ACCOMPLISHED BY REVERSING MOTOR.</p>	<p>LINEAR DYNAMIC SYSTEM, VERY COMPACT STOWAGE, LOW TORSIONAL STIFFNESS. AS ABOVE, INEFFICIENT IN LONGER LENGTHS. TEMPERATURE PREDICTION IS MORE DIFFICULT BECAUSE THE JOINT THERMAL CONDUCTANCE IS UNLIKELY TO BE REPEATABLE. HOLE PATTERN MAY BE REQUIRED TO OBTAIN REASONABLE THERMAL DEFLECTIONS. ROLL ABRASION RESISTANT THERMAL COATINGS REQUIRED.</p>
17 SPRING HELIX		<p>TUBE IS FORMED BY A HELICALLY PRE-STRESSED SPRING TAPE WHOSE OVERLAPPING COILS FORM A RIGID TUBE WHEN EXTENDED. MAY BE SELF-EXTENDING OR MOTOR DRIVEN. THE MOTOR DRIVE CONTROLS DEPLOYMENT SPEED AND PERMITS REMOTE RETRACTION.</p>	<p>VERY COMPACT STOWAGE, VERY LOW AXIAL AND TORSIONAL STIFFNESS. COLUMN LOAD CAPACITY, LATERAL AND TORSIONAL STIFFNESS DEPEND ON FRICTIONAL FORCES EXISTING BETWEEN OVERLAPPING LAYERS. NO RELIABLE METHOD OF ANALYSIS HAS BEEN ESTABLISHED. STIFFNESS WILL BE DERIVED MAINLY BY TESTS. ROLL ABRASION-RESISTANT THERMAL COATINGS REQUIRED. MATERIAL CONTINUITY AND THE RESULTING SPIRAL THERMAL CONDUCTANCE PROBABLY RESULTS IN LOWER THERMAL DEFLECTIONS THAN A NON CONTINUOUS TUBE SECTION.</p>
18 INFLATABLES		<p>GAS TIGHT TUBES (MYLAR, FOIL, MYLAR) ARE FLATTENED AND FOLDED FOR STORAGE. AN EXTERNAL GAS SUPPLY INFLATES AND ERECTS (AND REMOVES THE WRINKLES) THE TUBES. THE ALUM. FOIL SANDWICHED IN MYLAR THEN IS A THIN-WALLED TUBE AND LENDS ITSELF TO ANALYSIS. GAS PRESSURE IS RELIEVED WHEN THE SYSTEM REACHES EQUILIBRIUM. MAY BE USED AS A MULTIPLE-TUBE SYSTEM STIFFENED BY SPACERS AND GUY WIRES. ARE USUALLY NOT RETRACTABLE.</p>	<p>HIGH DAMPING; PROBABLY A NON-LINEAR SYSTEM; VERY COMPACT STOWAGE. STRENGTH AND STIFFNESS VARY GREATLY AS THE STRUCTURE IS FOLDED MORE OR LESS, I.E., THE WRINKLED CONDITION OF THE FOIL. EMPIRICAL RESOLUTION MUST BE USED TO ESTABLISH FOLDING TECHNIQUES AND LIMITS. MYLAR DEGRADES WHEN EXPOSED TO U.V., SO A PROTECTIVE COATING MUST BE USED. LARGE FRONT-TO-BACK TEMP. GRADIENTS ARE LIKELY, PARTICULARLY IF MULTIPLE TUBE SYSTEM IS USED. ADHESION OF THERMAL CONTROL SURFACE TO THE MYLAR MAY BE DIFFICULT TO ACHIEVE.</p>
19 RIGIDIZED INFLATABLES		<p>TWO SYSTEMS ARE SHOWN: (A) A SOLID CORE OF RIGID FOAM IS FORMED INSIDE A FABRIC FORM WHILE RESTRAINED BY A DIE. THE PRESSURE OF THE FOAM FEEDS IN THE FABRIC FORM AS THE RIGID FOAM IS FORCED OUT THE OPPOSITE END; (B) PRE-TREATED GELATINE-GLASS FIBER LAMINATED TUBES MADE FLEXIBLE WITH A SOFTENING AGENT. THE TUBES ARE GAS-INFLATED IN SPACE AND THE SOFTENING AGENT EVAPORATES, LEAVING THE TUBES STIFF. COMPLETE RIGIDITY IS ACHIEVED IN 10 TO 20 HOURS. IS NOT RETRACTABLE.</p>	<p>HIGH DAMPING, LINEAR SYSTEM, CONVENIENT STOWAGE SYSTEM. FOAM MATERIALS HAVE A VERY LOW YOUNG'S MODULUS. TO MAKE UP THAT DEFICIENCY, A LARGE AMOUNT OF FOAM MUST BE PROVIDED, THEREIN DEFEATING THE ADVANTAGE OF USING A LOW DENSITY MATERIAL. LARGE FRONT-TO-BACK THERMAL GRADIENTS ARE LIKELY. THERMAL CONTROL SURFACE APPLICATION MAY BE A PROBLEM.</p>
20 FLEXIBLE TETHER		<p>CYLINDRICAL SECTIONS WITH SPHERICAL SEATS ON EACH END, ALTERNATE WITH BALLS, ENTIRE ASSEMBLY HAS CENTER HOLE TO ACCEPT FLEXIBLE TENSION MEMBER. THE TENSION MEMBER IS FIXED TO ONE END; TENSION REACTED AGAINST THE OPPOSITE END CAUSES THE LOOSE PARTS TO ALIGN AND FORM A STRAIGHT COLUMN (THE SHORTEST LENGTH OF CABLE).</p>	<p>POOR STORAGE CHARACTERISTICS (THE STOWED VOLUME IS EQUAL TO THE EXTENDED VOLUME). THE TETHER REQUIRES THE CONCENTRATION OF MASS TO BE NEAR THE CENTER OF THE BEAM, RESULTING IN A POOR STRUCTURE FOR STIFFNESS. THERMAL DEFLECTIONS ARE DEPENDENT UPON MATERIAL AND THICKNESS OF STRUCTURE.</p>

Table 6.3-6. Most Favored Boom Types

Boom Type	Solar Array/ Satellite Program	Array Type	Notes
Extendible reel storage	● CRC/CTS	Foldout flexible	Bistern
	● Hughes/FRUSA	Rollup flexible	
	● AEG/ROSA	Rollup flexible	
	● AEG/DORA	Rollup flexible	
	● GE/JPL 30 W/LB	Rollup flexible	
Articulated lattice mast	● LMSC Space Station	Foldout flexible	Astromast
	● GE/JPL 50 W/LB	Foldout flexible	
Telescoping cylinder	● RAE	Foldout flexible	-
	● X4 Satellite	Foldout flexible	
Folding beam	● Skylab, Orbital Workshop	Foldout rigid	-
Lazy tongs	● Skylab, Apollo Telescope Mount	Foldout rigid	-
Pantograph	● SNLAS	Foldout flexible	-

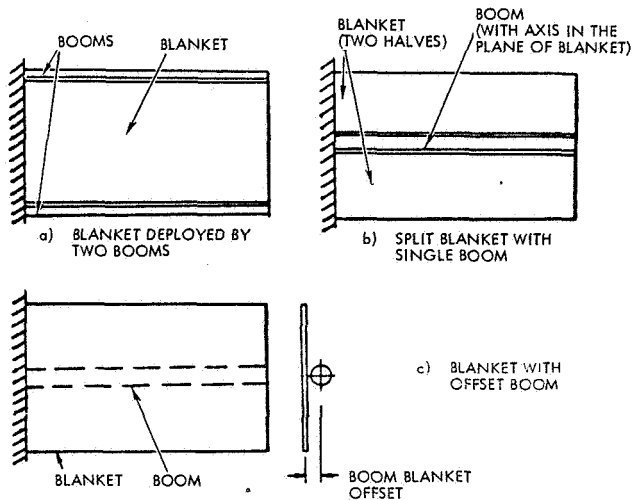


Fig. 6.3-1. Different Arrangements for Deployable Solar Cell Arrays

The array deployment sequence is composed of two discrete events. (See Figure 6.2-8 from Section 6.2.4.) Outer panel release is accomplished by actuation of four sets of redundant bolt cutters. Deployment springs at each panel hinge actuate the outer

panels to deploy 60 degrees to form a plane with the center panel of each wing. Spring latches are incorporated at the hinges to provide structural latch-up of the panels (see Figure 6.3-2). When the outer panels are latched, the two wings are released to deploy by actuator compression springs incorporated at boom hinges located at both ends of the boom (one at the base of the array wing, the other at the solar cell array drive/spacecraft sidewall interface) (see Figure 6.3-3). The boom and array panels of each wing are kinematically constrained to deploy symmetrically through the use of a constraint cable/pulley mechanism that goes along the length of the boom.

Matra Array

This solar cell array design was described in Section 6.2.3. The array consists of four rigid substrate panels and a yoke that are flat-packed and prestressed against the spacecraft wall by a spring-loaded rod (see Figure 6.3-4).

There are two hinges on each hinge line. These hinges carry the pulley of the deployment linkage constraint mechanism. Also located along the hinge edge of the panels (but separate from the hinges) are two torsion spring fittings as shown in Figures 6.3-5 and 6.3-6. Upon activation of the array holddown system, the panels deploy outward through the stored energy in the spring fittings.

The deployment is controlled through the use of a direct linkage between the relative motions of each hinge line, thus reducing the deployment to a 1 degree-of-freedom process (see Figures 6.3-6 and 6.3-7). The linkage system, comprised of pulley and belt, is attached along alternate sides of adjacent panels. A spring with a tension adjuster is included in the linkage system to compensate for thermal expansion effects.

ICS and ULP Arrays

The flat-pack arrays are similar in configuration to the Matra array (see Section 6.2.2 and 6.2.6). The deployment mechanisms are also similar.

The deployment energy is provided by small spiral springs located at each hinge (spring is integral with the hinge). The deployment is force controlled by a closed cable loop system to provide directional control and redundancy. The cable loop system prevents backlash of the interhinged panels and collision with the spacecraft. This forced control reduces the complex multiple panel array to a 1 degree-of-freedom system. Upon full deployment, the panels would latch up through a leaf spring/cam arrangement at each hinge location. No damping devices are required because the final latch-up shock could be absorbed by the array structure.

Table 6.3-7. Blanket/Boom Arrangement in Developmental Arrays or Satellite Programs

Program	Blanket Type	Boom Type (no. per wing)	Blanket/Boom Arrangement
CRC/CTS	Foldout	Bistem (1)	Single/Offset
Hughes/FRUSA	Rollout	Bistem (2)	Single/In-plane
AEG/ROSA	Rollout	Bistem (2)	Single/In-plane
AEG/DORA	Rollout	Bistem (2)	Single/In-plane
GE/JPL 30 W/LB	Rollout	Bistem (1)	Split/In-plane
LMSC/Space Station	Foldout	Astromast (1)	Split/In-plane
GE/JPL 50 W/LB	Foldout	Astromast (1)	Split/In-plane
RAE	Foldout	Telescoping (1)	Split/In-plane
X4 Satellite	Foldout	Telescoping (1)	Split/In-plane
Skylab ATM	Foldout	Lazy Tong (2)	Single/In-plane
Skylab OWS	Foldout	Folding Beam (2)	Single/Offset
SNIAS	Foldout	Pantograph (1)	Single/Offset

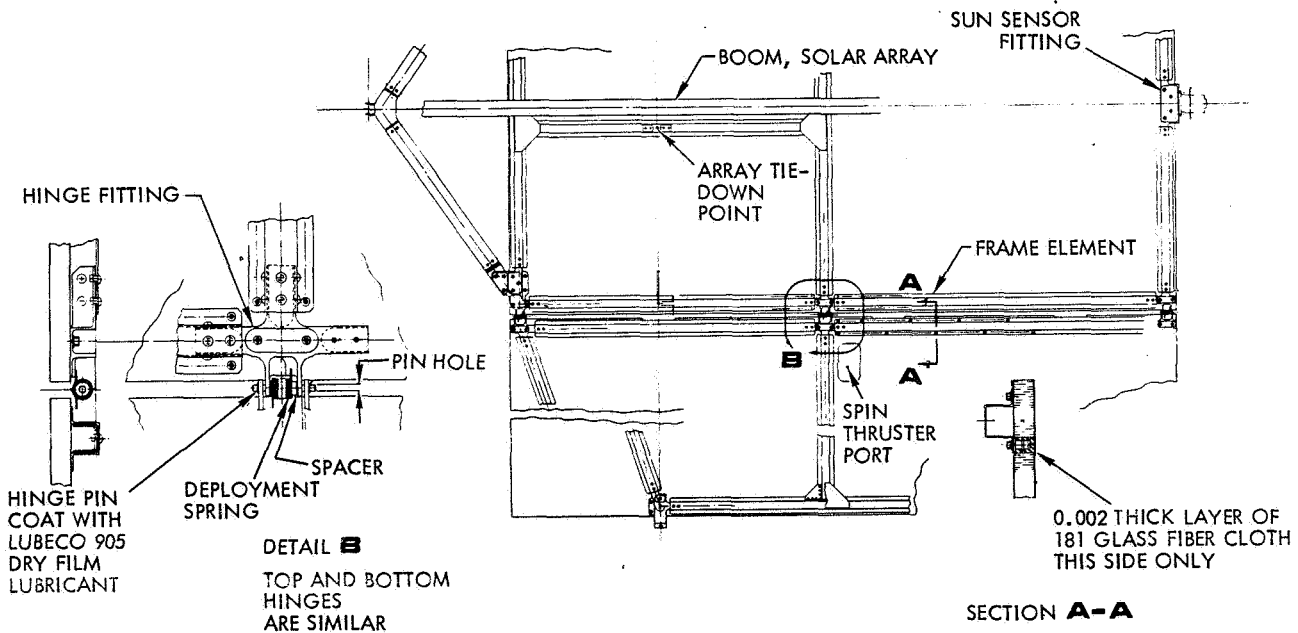


Fig. 6.3-2. FLTSATCOM Spring Hinge Configuration

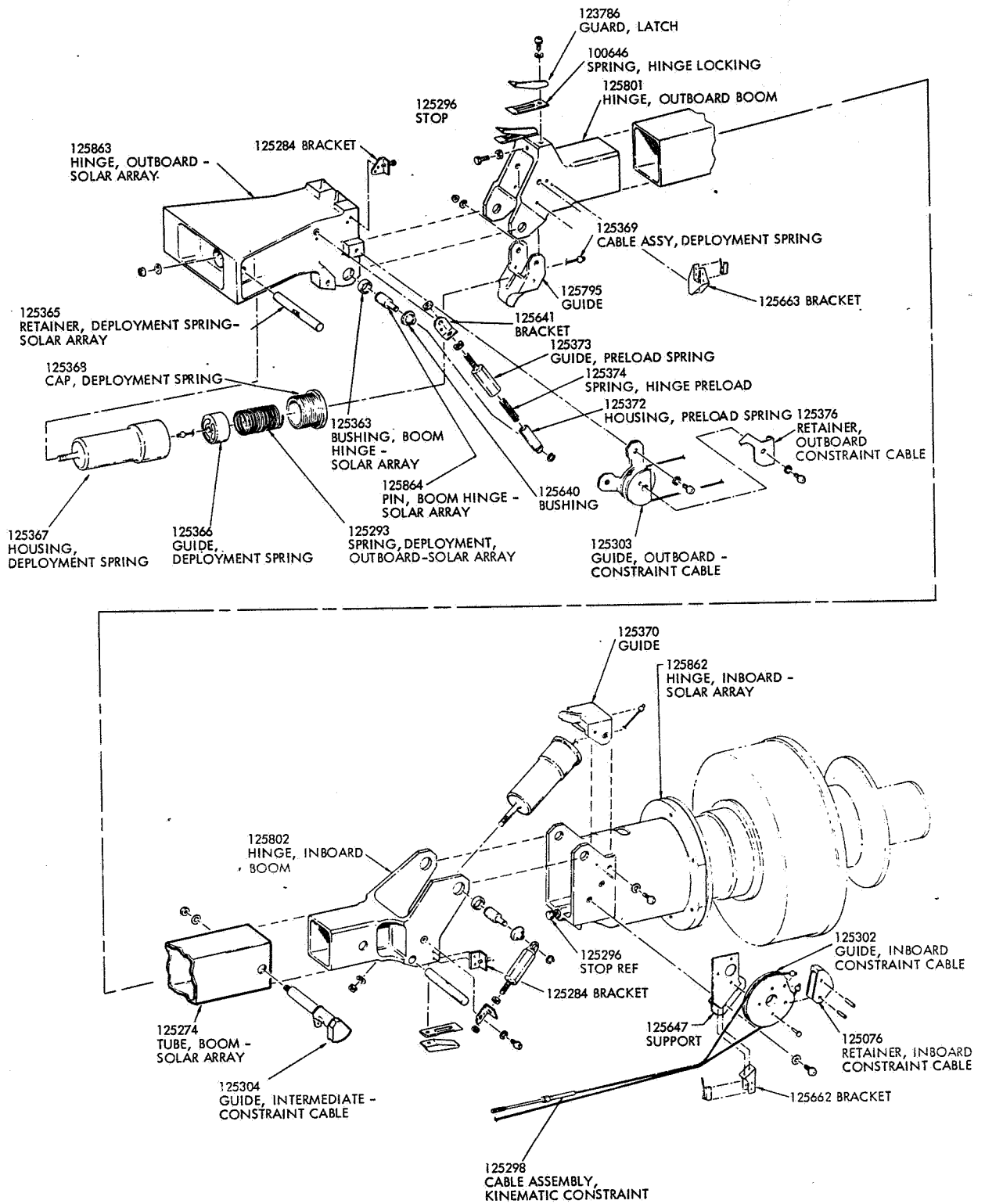


Fig. 6.3-3. FLTSATCOM Deployment Boom Mechanism

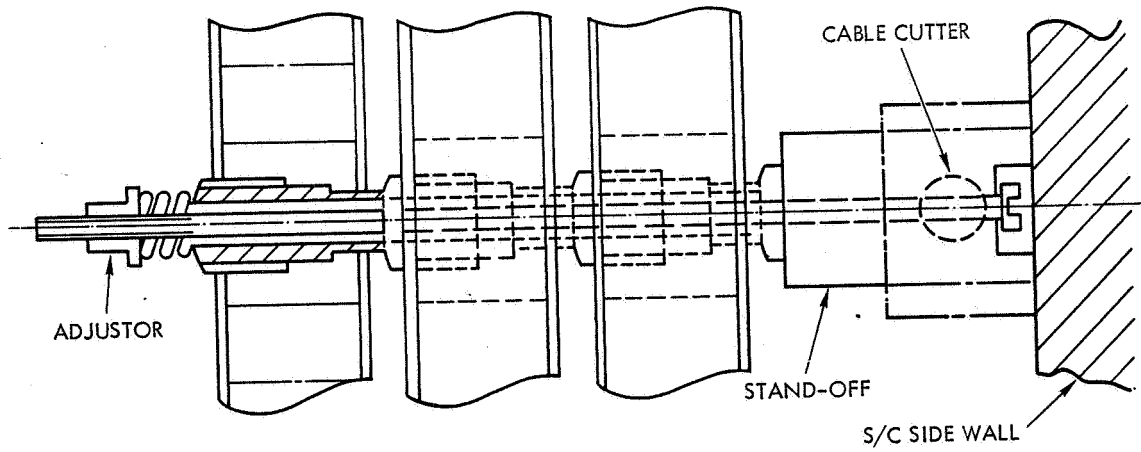


Fig. 6.3-4. Matra Holddown System (Ref. 6.3-2)

From Ref. 6.3-2. Reprinted with permission of the Centre National d'Etudes Spatiales.

From Ref. 6.3-2. Reprinted with permission of the Centre National d'Etudes Spatiales.

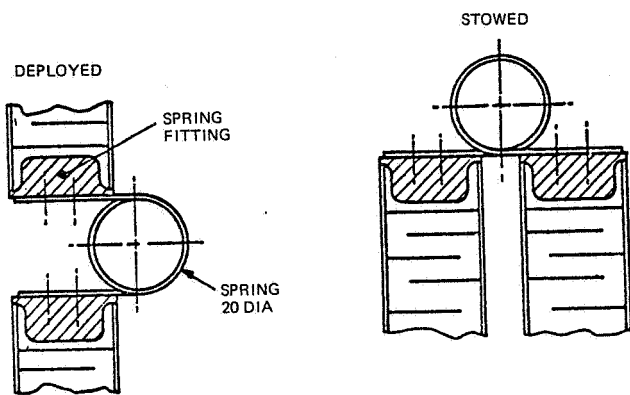


Fig. 6.3-5. Matra Deployment Springs and Fittings (Ref. 6.3-2)

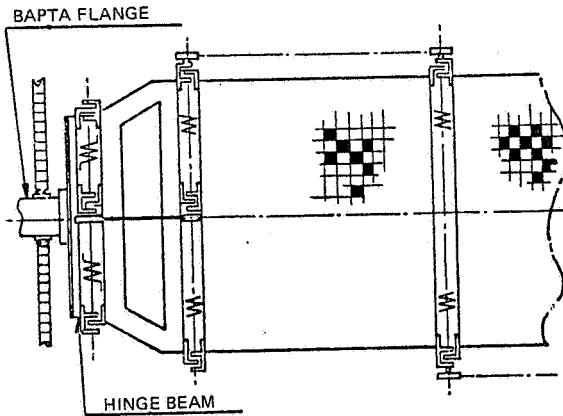


Fig. 6.3-6. Matra Deployment Mechanisms (Ref. 6.3-2)

From Ref. 6.3-2. Reprinted with permission of the Centre National d'Etudes Spatiales.

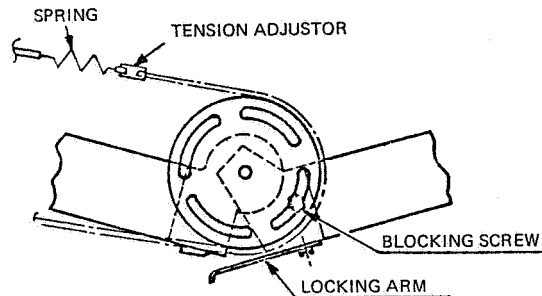
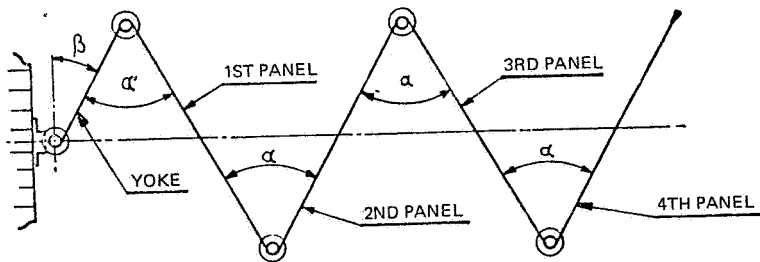


Fig. 6.3-7. Matra Deployment Control Mechanism (Ref. 6.3-2)

6.4 ARRAY ORIENTATION DRIVE AND POWER TRANSFER MECHANISMS

As indicated in Section 6.1, deployable arrays can be classified as "body fixed" and "suntracking". To achieve the suntracking capability, an electro-mechanical subsystem is required (1) to continuously keep the solar array properly oriented with the sun vector and (2) to transfer the electrical power generated by the arrays to the satellite power conditioning subsystem. Thus, it is comprised of two distinct components that are integral with one another - a motorized drive system and an electrical power transfer system. As a structural system it must also provide the following functions:

- Provide the mechanical interface and structural support for the solar arrays
- Provide structural support and housing for the various components (bearings, slip rings, gears, motor, etc.)

A solar cell array drive assembly is also known as a SADA. An orientation drive and power transfer mechanism is known as an ODAPT. ODAPT/SADA's have been designed with and without a sun sensor as part of the control loop. In the former, a signal from the sun sensor causes the drive system to be activated. In the latter design, once the array is initially locked onto the sun, the rotation is controlled by a clock/stepper motor arrangement which rotates the array automatically a finite increment over a finite time interval.

The LMSC Space Station reports (Refs. 6.4-1 and 6.4-2) include a comprehensive review of ODAPT/SADA's. Any solar cell array designer seeking information about alternative choices for the many subsystems is recommended to these references for detailed historical data.

6.4.1 Solar Cell Array Drive Systems

A drive system is defined as a unit having a motor to supply rotational power, slip rings or power transfer cables for taking electrical power across the rotating joint, and several sets of bearings to maintain proper alignment of the various mechanical parts.

A variety of drive systems have been employed in existing satellite designs. Most systems are between 5 and 15 cm in diameter and are designed in such a way that the satellite structure is wrapped around the drive system. Approximately 50 percent of the systems developed provide full rotation, while the remaining provide limited rotation from zero to 360 degrees.

Most of the motors used have been brushless motors, either ac servo, dc stepper, or dc torque. Brush motors have also been used (i. e., OSO and TACSAT). Motors for other programs drive through gears which produce overall gear ratios for their respective drive systems ranging from 1:1 to 10⁶:1.

Either deep groove radial and/or preloaded angular contact ball bearings have been the preferred choice for bearings. Roller bearings usually require more torque to drive than ball bearings because they make line contact. Roller bearings are also more susceptible to skewing loads caused by built-in misalignments which increase the torque losses and reduce bearing life. Most ball bearings are constructed from 440C stainless steel rings and balls. In most of the previously flown satellites lubrication is self-contained within the bearings.

6.4.2 Power Transfer Assemblies

The design of the power transfer system and the selection of materials will be influenced by the current/voltage ratio used by the satellite. Dielectric properties of the electrical insulation will be more important for the high voltage system, but the high current system will require heavier conductors and larger contacts (and more power will be consumed in overcoming the greater frictional drag). Electrical heating due to contact resistance in brushes and conductors will result in power loss and cause brushes to run hotter. The higher operating temperature in the brushes will affect the choice of lubricant.

Almost all satellites that require continuous rotation arrays use slip rings, while flex cables are used where limited rotation is acceptable. Other devices considered include rotary transformers, rolling contacts, liquid metal slip rings. A variety of slip ring configurations have been used including:

- V-groove ring with wire brushes
- U-groove ring with wire brushes
- Drum ring with wire brushes
- Drum ring with button brushes
- Disc ring with button brushes

The ring is silver or gold plated copper or other suitable base material. Button-type brushes are made from a composite material containing silver, copper, and graphite with a suitable lubricant such as molybdenum disulfide (MoS₂). Wire brushes are made from some precious metal. Factors critical in brush design include current density, temperature and acceptable wear rates.

6.4.3 Lubrication

Lubrication is required in two areas: (a) for bearings, gears and other mechanical devices; and (b) for electrical brushes and contacts. The absence of oxygen and water vapor requires that lubricants be specifically incorporated into brush compositions to prevent rapid brush wear; and the hard vacuum of space limits the selection of bearing and gear lubricants to low volatility oils and greases and to solid films and self-lubricating solids.

GE Versilube and BBRC Vac Kote oils and greases have been widely used in satellite bearing designs. Solid films have been successfully used when limited to slow speed or intermittently-operated mechanisms. Oil lubricants must be provided with reservoirs for application to long term vacuum. The purpose is to maintain the atmosphere of oil molecules in the vicinity of the parts so that the net loss of lubricant to space vacuum is from the reservoirs rather than from the impregnated materials. Oil-type lubricants mean potential contamination problems due to evaporation and thus more complex sealing designs must be employed with them rather than with solid lubricants.

In terms of solid lubricants, molybdenum disulfide (MoS_2) or niobium diselenide (NbSe_2) are used. The latter has the advantage of also being a good conductor. Graphite, normally used in atmospheric applications, loses its lubricating qualities in a space vacuum. Evaporation loss from solid lubricants is negligible and therefore no reservoir system is required.

6.4.4 FLTSATCOM Design Example (Based on previously unpublished TRW data)

Figure 6.4-1 shows the layout design of the Solar Array Drive Assembly (SADA). The assembly consists of two identical drive units which are connected in tandem for redundant operation. Each drive unit consists of a 1.8 degree per step stepper motor (4-phase, permanent magnet, inductor-type) which is coupled to the input of a harmonic drive reducer. The harmonic drive ratio is 100:1 which results in an output step size of 0.018 degree per step. The motor will be operated by sequential energization of one phase at a time and at normal speed the excitation has a pulse width of 100 milliseconds, which occurs every 4.32 seconds. The drive unit on the spacecraft side is the primary drive. Its housing is mounted to the spacecraft and is nonrotating. The housing of the secondary drive is the output member and rotates with respect to the primary drive housing, whether driven by the primary or secondary motor.

In normal operation the primary drive is used and its harmonic drive is used in the conventional manner, i. e., wave generator input, circular spline stationary, and flexspline output. The primary drive flexspline output drives into the flexspline of the secondary drive via a connecting shaft. In effect, the secondary drive is backdriven by the primary drive, but the rotating interface between the shaft (flexspline) and housing (circular spline) of the secondary drive is held against rotation by the detent torque of the motor. Thus, in normal operation, the secondary drive is carried on the output shaft of the primary drive and revolves as a unit.

When the secondary drive operates, its harmonic drive is used with the wave generator as the input, the flexspline stationary, and the circular spline as the output. The flexspline is held stationary by the detent holding capability of the primary drive. Thus, in secondary drive operation, its shaft (flexspline), the connecting shaft, and the primary drive shaft (flexspline) are held stationary with the primary drive housing, and only the housing of the secondary drive rotates.

The drive unit shaft is supported in the housing with a duplex pair of ball bearings at one end and a single radial bearing at the other end. The duplex pair is clamped axially in the housing and on the shaft while the radial bearing is unconstrained axially in the housing to accommodate axial thermal expansion. The duplex pair is in back-to-back arrangement for

maximum moment rigidity. The shafts and housings are made from titanium alloy to minimize the differential expansion between them and the steel bearings (440C), so that changes in internal fitup due to temperature excursion and subsequent internal loads in the bearings and friction torques will be minimized.

Other structural parts, specifically the cylindrical enclosure for the slip ring assembly in the middle of the drive, are made of 2024 aluminum alloy. The external surface of the SADA is painted black for high thermal emissive property.

Rolling and sliding parts of the electromechanical parts will be lubricated with NPT-4. Lubricant loss through the running gap of the slip ring enclosure will be replenished from Nylasint reservoirs impregnated with NPT-4 oil. These are mounted in several locations throughout the assembly. The internal surfaces of the assembly will be lightly coated with NPT-4 during the assembly process to provide an additional source of lubricant. Also, all the bearings, the main support bearings and those within the rotating components, have phenolic laminate retainers which are vacuum impregnated with NPT-4 oil.

A disk type of slip ring assembly is mounted between the rotating interface of the two drive housings. The brush block assembly is mounted on the primary drive housing, and the slip ring disk is on the secondary drive housing. The slip ring assembly contains 36 signal rings (18 on each face of the disk) and two power rings (one on each face) which are equivalent to four power rings, each capable of carrying 30 amperes. All circuits have redundant brushes. The signal circuits consist of precious metal wire brushes riding in V-groove rings. The base material of the rings is copper which is nickel plated followed by a thin layer of hard gold.

Two single-turn potentiometers are mounted on the stationary side of the slip ring enclosure. Anti-backlash gears on the potentiometer shafts are geared off the slip ring shaft with a 1:1 ratio. The potentiometers contain a conductive plastic resistive element, which is lightly coated with NPT-4 lubrication.

The SADA weighs 6.8 kg and is capable of transferring approximately 1.1 kW (BOL) of power from the solar cell array to the power conditioning unit.

6.4.5 Nimbus II Design Example (Based on data provided by JPL)

The Nimbus II SADA is shown in Figure 6.4-2. The assembly consists of a motor gearhead unit, a potentiometer unit, and a subassembly unit containing a clutch, output shaft, and gearing. The motor of the motor gearhead unit is a Size 11, two-phase AC Servo motor; it drives a 12000:1 spur gear train in the gearhead section. All bearings and gear meshes of the motor gearhead are lubricated at assembly with G-300 silicone grease. A nylasint reservoir in the motor cover is impregnated at assembly with F50 silicone oil. The output gear of the motor-gearhead drives a 7:1 spur gear reduction train in the housing subassembly unit and connected to the output shaft. A ball-detent face clutch is provided in this gear train to protect the motor gearhead from injury by back-driving from the shaft end. All parts in this subassembly are lubricated with G-300 silicone grease and a nylasint reservoir is impregnated with F50 silicone oil. The potentiometer unit is mounted to the housing subassembly and contains four wire-wound potentiometer cups. It is driven by a 1:1 gear train from the output shaft independent of the clutch. The potentiometer bearings are

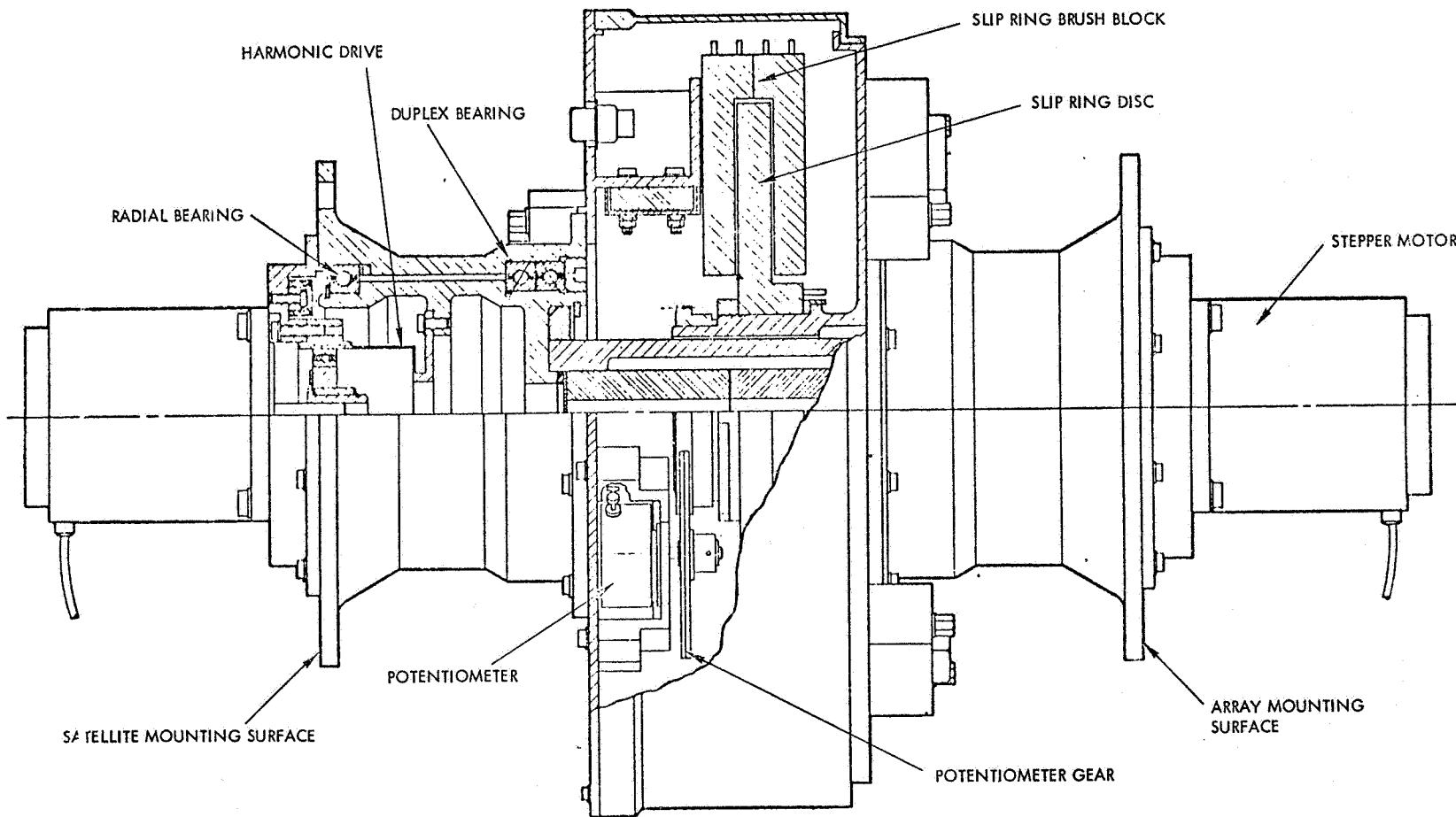


Fig. 6.4-1. TRW FLTSATCOM SADA

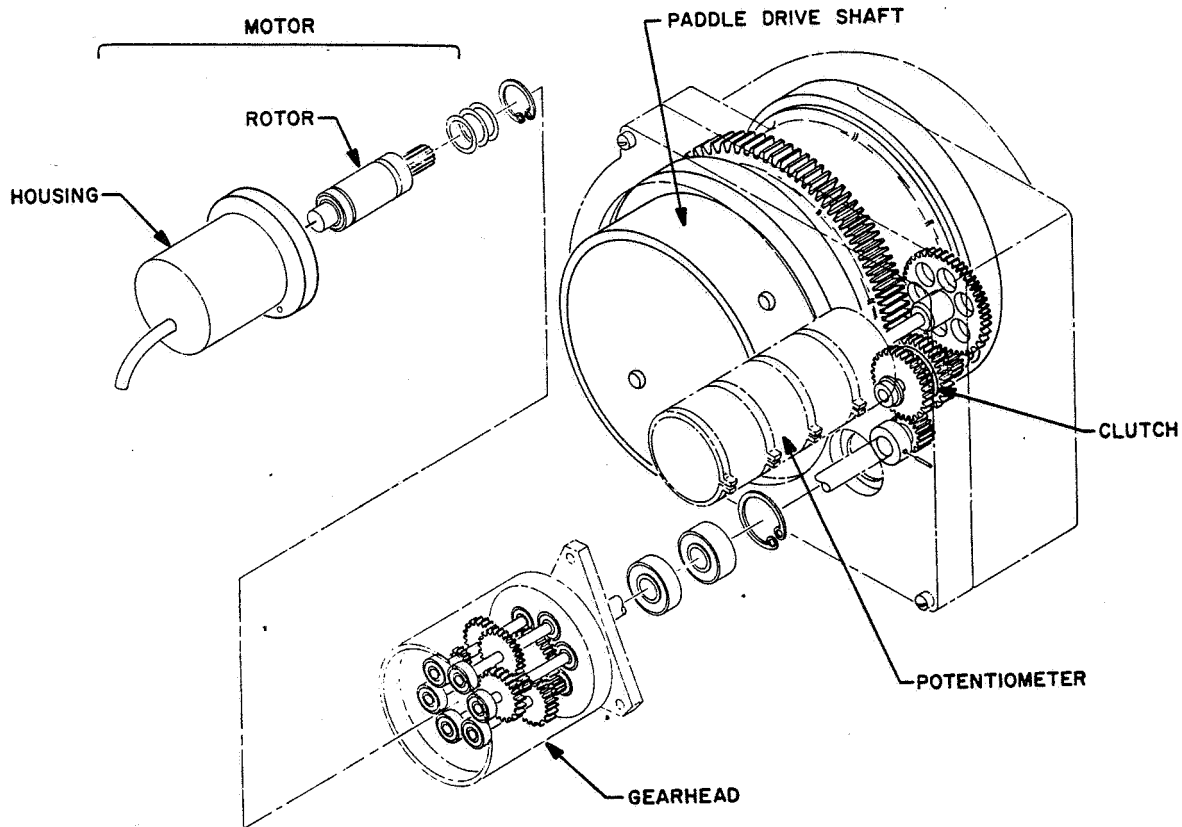


Fig. 6.4-2. Nimbus II SADA

lubricated with G-300 grease; the wiper and windings are unlubricated noble metals. Design data of the SADA are tabulated below:

Motor	2 ϕ , 26 vac, 400 Hz, Size 11 servo motor; nominal maximum speed 4500 rpm.
Gearhead	12, 121:1 gear ratio, seven passes, straight spur gearing.
Clutch	Ball-detent face-type clutch; four stacked Belleville-Washer type springs loading the ball-detent faces. Clutch slip torque 123 cm·N (175 in·oz), nominal.
Housing Gearing	All spur gears, 2.33:1 gear ratio before clutch, 3:1 gear ratio after clutch.

Assembly	84,847:1 overall gear ratio. Nominal output torque 367 cm·N (520 in·oz). Normal anticipated required torque less than 64 cm·N (90 in·oz).
Lubrication	General Electric G-300 silicone grease in gears and bearings. Nylasint reservoirs impregnated with F50 oil.
Bearings	R2, R3, R4 sizes; 440C stainless steel balls and races, ribbon retainers.
Weight	2.3 kg, approximately.

REFERENCES (CHAPTER 6)

- 6.1-1 E. Ashford and H. Lechte, "Satellite System Considerations in Selection of Solar Array Generators," Proceeding, Photovoltaic Power and Its Application in Space and on Earth, Paris, 1973.
- 6.2-1 D. E. Koelle, "Advanced Lightweight Rigid Solar Arrays Based on Carbon Fiber Technology," XXV Congress of the IAF, Amsterdam, 1974.
- 6.2-2 G. J. LaRoche, "Basic Solar Panel Techniques at MBB and Their Application," Proceedings of the 10th IEEE Photovoltaic Conference, Palo Alto, California, 1973.
- 6.2-3 R. L. Crabb and L. Schneider, "Development of an Advanced Lightweight Rigid Solar Array," Proceedings of the 10th IEEE Photovoltaic Conference, Palo Alto, California, 1973.
- 6.2-4 W. Palz, "Results and Future Prospects of Photovoltaic Power Development in France," Proceedings of the Photovoltaic Power and Its Application in Space and on Earth, Paris, France, 1973.
- 6.2-5 H. Larsson, "Problems of Development and Test of Large Lightweight Solar Arrays," Proceedings of the Photovoltaic Power and Its Application on Space and on Earth, Paris, France, 1973.
- 6.2-6 W. Luft, et al., "Light Rigid Solar Array Development," Presented at the 11th IEEE Photovoltaic Specialists Conference, Arizona, 1975.
- 6.2-7 D. A. Corbett, et al., "Lightweight Rigid Solar Array Structural Considerations," Presented at the 11th IEEE Photovoltaic Specialists Conference, Arizona, 1975.
- 6.2-8 D. E. Koelle, "Advanced Lightweight Rigid Solar Arrays Based on Carbon Fiber Technology," XXV Congress of the IAF, Amsterdam, 1974.
- 6.2-9 H. Bassewitz, et al., "Requirements and Design of an Ultra Lightweight Solar Array (ULP)," Proceedings, Photovoltaic Power Generation Conference, Hamburg, Germany, 1974.
- 6.2-10 W. Luft, "Lightweight Welded Solar Cell Modules," Proceedings, Photovoltaic Power Generation Conference, Hamburg, Germany, 1974.
- 6.2-11 J. A. Carlson, "Development of Lightweight Panels," NASA CR 66832.
- 6.2-12 "Phase II, Large Area Solar Array," Boeing Final Report D2-113355-7, 1968.
- 6.2-13 C. A. Franklin and E. H. Davison, "A High Powered Communications Technology Satellite for the 12 and 14 GHz Bands," AIAA Fourth Communications Satellite Systems Conference, Washington, D. C., 1972.
- 6.2-14 R. Buhs, "Layout and Technology of the CTS Solar Array Blanket," Proceedings of the 10th IEEE Photovoltaic Specialists Conference, Palo Alto, California, 1973.
- 6.2-15 S. S. Sachdev, et al., "The CTS Deployable Solar Array Subsystem," Proceedings, Photovoltaic Power Generation Conference, Hamburg, Germany, 1974.
- 6.2-16 F. C. Treble, "The RAE Lightweight Solar Array," Proceedings, The Photovoltaic Power and Its Application in Space and on Earth Congress, Paris, France, 1973.
- 6.2-17 F. C. Treble, "Status Report on RAE Advanced Solar Array Development," Proceedings of the 9th IEEE Photovoltaic Specialists Conference, Maryland, 1972.
- 6.2-18 B. Collins, "Power Generation for the X4 Spacecraft," Proceedings of the Photovoltaic Power Generation Conference, Hamburg, Germany, 1974.
- 6.2-19 Second Topical Report, "Space Station Solar Array Technology Evaluation Program," LMSC-A99S719, 1971.
- 6.2-20 "Feasibility Study of a 110 Watt/Kg Lightweight Solar Array System," Final Report No. 73SD4256, General Electric, May 1973.
- 6.2-21 H. S. Rauschenbach, et al., "FEP-Teflon Encapsulated Solar Cell Modules," Proceedings of the 11th IEEE Photovoltaic Specialists Conference, Phoenix, Arizona, 1975.
- 6.2-22 H. S. Rauschenbach, et al., "FEP Teflon Covered Solar Cells Array Advancements," Proceedings of the 10th IEEE Photovoltaic Specialists Conference, Palo Alto, California, 1973.

- 6.2-23 G. Wolff, "The Flight of the FRUSA,"
Proceedings of the 9th IEEE Photovoltaic
Specialists Conference, Maryland, 1972.
- 6.2-24 S. Karius, "Roll-Out Solar Arrays for High
Power Applications," The Photovoltaic Power
and Its Applications in Space and Earth
Congress, Paris, France, 1973.
- 6.2-25 N. B. North and D. F. Baker, "Solar Array
System for the Skylab Orbital Workshop,"
Conference Records of the 9th IEEE Photo-
voltaic Specialists Conference, 1972.
- 6.2-26 F. C. Treble, "Progress in Advanced Solar
Array Development," Conference Records
of the 8th IEEE Photovoltaic Specialists
Conference, 1970.
- 6.3-1 "Evaluation of Space Station Solar Array
Technology," First Topical Report No.
A981486, LMSC 1970 and 1972.
- 6.3-2 H. Larsson, "Problems of Development and
Test of Large Lightweight Solar Arrays,"
Proceedings of the Photovoltaic Power and
Its Application on Space and on Earth, Paris,
France, 1973.
- 6.4-1 Second Topical Report, "Space Station Solar
Array Technology Evaluation Program,"
LMSC-A99S719, 1971.
- 6.4-2 "Evaluation of Space Station Solar Array
Technology," First Topical Report No.
A981486, LMSC 1970 and 1972.

CHAPTER 7
MATERIAL PROPERTIES

CONTENTS

	<u>Page</u>		<u>Page</u>
7.1 General Characteristics of Some Specific Metals	7.1-1	7.9 Electrical Properties of Conductors	7.9-1
7.1.1 Aluminum	7.1-1	7.9.1 Definitions	7.9-1
7.1.2 Beryllium-Copper	7.1-1	7.9.2 Relative Electrical Properties	7.9-1
7.1.3 Copper	7.1-1		
7.1.4 Invar	7.1-1	7.10 Electrical Properties of Dielectrics	7.10-1
7.1.5 Kovar	7.1-2	7.10.1 Definitions	7.10-1
7.1.6 Molybdenum	7.1-3	7.10.2 Properties of Significance in Space	7.10-1
7.1.7 Silver	7.1-3		
7.1.8 Solder	7.1-4		
7.2 General Characteristics of Some Specific Nonmetals	7.2-1	7.11 Thermal Expansion Properties	7.11-1
7.2.1 Adhesives and Sealants	7.2-1	7.11.1 Definitions	7.11-1
7.2.2 Conductive Adhesives	7.2-1	7.11.2 Instantaneous Coefficients of Linear Expansion	7.11-1
7.2.3 Kapton	7.2-2	7.11.3 Average Coefficient of Linear Expansion	7.11-2
7.2.4 FEP-Teflon	7.2-2	7.11.4 Normalized Thermal Expansion	7.11-2
7.2.5 Fused Silica	7.2-2	7.11.5 Conversion of Temperature Coefficients	7.11-2
7.2.6 Microsheet	7.2-3	7.11.6 Relative Thermal Expansion	7.11-2
7.2.7 Ceria-Doped Microsheet	7.2-3		
7.3 Mass, Density and Weight	7.3-1	7.12 Specific Heat and Heat Conductance	7.12-1
7.3.1 Definitions	7.3-1	7.12.1 Definitions	7.12-1
7.3.2 Relative Density	7.3-1	7.12.2 Relative Thermal Conductivity	7.12-1
7.4 Centroids, Moments of Inertia and Radii of Gyration	7.4-1		
7.4.1 Definitions	7.4-1	7.13 Transmission, Reflection and Absorption of Light	7.13-1
7.5 Elastic Modulus, Poisson's Ratio and Ultimate Strength of Metals	7.5-1	7.13.1 Definitions	7.13-1
7.5.1 Definitions	7.5-1	7.14 Emission and Absorption of Heat	7.14-1
7.5.2 Relative Material Properties	7.5-2	7.14.1 Definitions	7.14-1
7.6 Elastic Modulus, Poisson's Ratio and Ultimate Strength of Silicon and Glass	7.6-1	7.15 Magnetic Properties	7.15-1
7.6.1 Definitions	7.6-1	7.15.1 Definitions	7.15-1
7.6.2 Test Data	7.6-1	7.15.2 Magnetic Materials on Solar Cell Arrays	7.15-1
7.7 Elastic Modulus, Poisson's Ratio and Ultimate Strength of Other Nonmetals	7.7-1	7.16 Outgassing and Weight Loss	7.16-1
7.7.1 Definitions	7.7-1	7.16.1 Definitions	7.16-1
7.8 Elongation and Reduction in Area	7.8-1	7.16.2 Test Methods	7.16-1
7.8.1 Definitions	7.8-1	References	7.R-1

TABLES

7.2-1	Types of Code 7940 Fused Silica	7.2-3	7.12-1	Constants θ and a for Low-Temperature Heat Capacities	7.12-1
-------	---------------------------------	-------	--------	--	--------

FIGURES

7.1-1	Typical Contraction Curves Representing a Heat Which Transformed at -120°C and Another Heat That Showed No Transformation at -196°C	7.1-2	7.6-1	Flexural Strength of Silicon Solar Cells and Coverglass	7.6-1
7.1-2	Solubility of Silver in Tin-Lead Solders at Various Temperatures	7.1-4	7.7-1	Typical Stress-Strain Diagram for Elastomers	7.7-1
7.3-1	Density of Metals Relative to Copper	7.3-1	7.8-1	Tensile Test Specimens	7.8-1
7.5-1	Diagram of Stress, σ , and Strain, ϵ , Due to Applied Force, F	7.5-1	7.9-1	Electrical Resistivity of Metals Relative to Copper	7.9-2
7.5-2	Typical Stress-Strain Diagram for Ductile Metals	7.5-1	7.9-2	Electrical Conductivity of Metals Relative to Copper	7.9-3
7.5-3	Typical Stress-Strain Diagram for Brittle Metals, Silicon, and Glass	7.5-1	7.10-1	Equivalent Circuit of a Dielectric	7.10-1
7.5-4	Modulus of Elasticity of Metals in Tension Relative to Copper	7.5-2	7.11-1	Illustration of Three Different Linear Thermal Expansion Parameters	7.11-1
7.5-5	Specific Stiffness of Metals Relative to Copper (soft annealed)	7.5-3	7.11-2	Coefficient of Thermal Expansion of Metals Relative to Silicon	7.11-3
7.5-6	Specific Strength of Metals Relative to Copper	7.5-3	7.12-1	Thermal Conductivity of Metals Relative to Silver	7.12-2
			7.15-1	Illustration of Hysteresis Loops on B-H Diagram for Magnetically "Hard" and Magnetically "Soft" Materials	7.15-1

CHAPTER 7

MATERIAL PROPERTIES

The material properties included in this handbook are of significance to several different aspects of solar cell array design:

- Material selection
- Determination of the array mass properties
Mass (weight) and moment of inertia
- Electrical design
Conductivity and dielectric strength
- Thermal design
Equilibrium temperatures and eclipse temperature profiles
- Mechanical design and stress analysis
Thermal expansion, stress and fatigue life.

A general discussion of material properties is given in this chapter; the detailed data is presented in

Chapter 7 of Volume II. Certain specific characteristics and properties of materials and components when not included in this chapter or in Chapter 7 of Volume II, may be found in the following chapters of either Volume I or Volume II:

In Chapter 2: Environmental Effects on Materials and Components

In Chapter 3: Characteristics of Solar Cells

In Chapter 4: Characteristics of Solar Cell Filters and Covers

In Chapter 5: Characteristics of Solar Cell Interconnectors, Wires and Blocking Diodes

In Chapter 6: Data on Structural Elements (Substrates) and Deployment Mechanisms

7.1 GENERAL CHARACTERISTICS OF SOME SPECIFIC METALS

The following materials are used for or are of interest to the designers of solar cell interconnectors and other circuit conductors:

- Aluminum
- Beryllium-copper
- Copper
- Invar
- Kovar
- Molybdenum
- Silver
- Solder

Some of the characteristics of these materials are described in the following paragraphs; their properties are given in Volume II.

7.1.1 Aluminum

Many different commercial grades of aluminum are available. However, only the industrially pure form, designated by A1100 with temper 0 (fully annealed) has been used for solar cell interconnectors.

A1100 is a soft, highly ductile material that can be readily worked by most commercially available processes. It can be plated with silver or other metals to facilitate joining. A1100 can be welded and ultrasonically joined.

7.1.2 Beryllium-Copper (Based on Ref. 7.1-1)

Beryllium-copper is an alloy that consists mainly of copper and usually of less than 3 percent cobalt, less than 2 percent nickel and less than 1 percent beryllium. It is commercially available in several tempers, ranging from soft annealed to hard, and as a high-conductivity grade. Its most frequent application is for electric current carrying springs. It has occasionally been used as a solar cell interconnector material, presumably because it exhibits a higher ultimate strength than pure copper.

Beryllium-copper can be worked readily by conventional processes and can easily be plated. It can be soft soldered and welded. Annealing is not recommended to be performed outside the mill but hardening heat treatments are possible.

Beryllium-copper has been reported to be notch sensitive. Therefore, caution for the use of this material for solar cell interconnector expansion loops appears to be indicated.

7.1.3 Copper

Many different commercial grades of copper are available. However, per Ref. 7.1-2, it has been found that for solar cell interconnectors only oxygen-free, high-conductivity (OFHC) copper is an acceptable material.

The lack of oxygen in OFHC copper retards the formation of fatigue cracks in bending while the absence of other impurities increases the material's ductility and electrical conductivity.

OFHC copper is a soft, highly ductile material that can be readily worked and plated by most commercially available processes. It is easily solderable and weldable.

7.1.4 Invar (Based on Refs. 7.1-3 and 7.1-4)

Invar is a nickel-iron alloy with low thermal expansion properties. Of all the nickel-iron alloys, those with 36.0 percent nickel content exhibit the lowest thermal expansion for solar cell array applications. Two of such alloys are marketed under the following names by the respective organizations:

- Invar "36" - Carpenter Technology Corporation, Carpenter Steel Division, Reading, Pennsylvania
- Unispan 36 - Universal-Cyclops Specialty Steel Division, Cyclops Corporation

Chemical Composition

Typical, by percent weight:

Nickel	36.0
Manganese	0.35
Silicon	0.12-0.30
Aluminum	0.1
Carbon	0.04-0.12
Phosphorous	0.015
Iron	Balance

Workability

Invar can be cold and hot worked. For mild forming and blanking, a Rockwell hardness of B-90 is recommended. For sharper bending and deep drawing, a Rockwell hardness of B-75 is recommended.

Annealing

Cold work stresses can be relieved by heating to temperatures above 540°C for 5 minutes followed by air cooling. Higher annealing temperatures result in lower hardness; a 650°C anneal results in a Rockwell hardness of B-87 to B-88 while a 1040°C anneal results in a Rockwell hardness of B-66 to B-68.

Welding

Parts must be free of oxides, oil, and sulfur-containing substances before and during welding.

Thermal Expansion

The heat treatment of Invar affects its thermal expansion characteristics. The following heat treatments have been reported to yield the lowest thermal expansivity (per Refs. 7.1-4 and 7.1-5):

- Heat to 760°C to 840°C (830°C typical) and water (or oil) quench
- Then stabilize low thermal expansivity as follows:
Heat to 315°C for 1 hour and air cool
- Then relieve quench-induced stresses and stabilize dimensions as follows:
Heat to 95°C for 48 hours and air cool.

The heating should be done in an inert or, better, a reducing atmosphere which must be free of sulfur. The carbon content of the Invar should not exceed 0.15 percent to achieve the lowest thermal expansion properties.

7.1.5 Kovar (Based on Ref. 7.1-6)

Kovar is an alloy that was especially developed for making glass-to-metal seals. Because its low thermal expansion coefficient very nearly matches that of silicon, Kovar is of interest as a solar cell interconnector material. Kovar is a registered trademark of the Westinghouse Electric Corporation.

Chemical Composition

<u>Element</u>	<u>Percent by Weight, Typical</u>
Nickel	29
Cobalt	17
Manganese	0.45
Silicon	0.10
Carbon	0.02
Iron	Balance

Thermal Expansion

After annealing in hydrogen for 1 hour at 900°C and 15 minutes at 1100°C, the average linear coefficient of expansion is typically quoted for a "gamma" crystalline structure. Like all other iron-nickel-cobalt alloys, Kovar is subject to a phase transformation at some temperature below -78.5°C. During the phase transformation, a part or all of the gamma crystalline structure changes permanently to an alpha structure which has a considerably larger thermal rate of expansion than the gamma structure.

Actual Temperature of Transformation

The temperature of -78.5°C has been selected for convenience, since this is the temperature resulting from an excess of dry ice in acetone. Production testing by Kovar manufacturers or processors does not involve determination of the actual temperature of transformation of each heat.

Tests of a large number of production heats, however, have indicated that the actual temperature of transformation is considerably below -78.5°C. On

a special test of 14 production heats, actual determination of transformation temperatures was as follows:

- Six heats showed no transformation at -269°C
- Five heats showed partial transformation at -196°C
- Three heats showed partial transformation at -120°C.

For solar cell interconnector production requirements, special lots of Kovar can be obtained by selection to ensure meeting lower transformation points than meeting the standard guaranteed value of -78.5°C.

Contraction at Low Temperatures

Figure 7.1-1 shows the contraction of one particular heat of Kovar which partially transformed at -120°C (Curve A) and the contraction of another particular heat which showed no transformation at -196°C (Curve B).

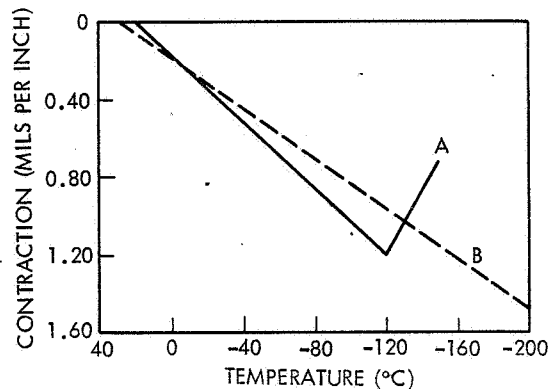


Fig. 7.1-1. Typical Contraction Curves Representing a Heat Which Transformed at -120°C (Curve A) and Another Heat That Showed No Transformation at -196°C (Curve B)

Machining

Standard machining practices can be used with Kovar, however, relatively slow cutting speeds and high-speed steel or tungsten carbide tools are recommended. Recommended coolants are conventional compositions except that they should be sulphur-free.

Forming

The forming properties of Kovar are similar to those of mild steels. Kovar may be deep-drawn, however, the following precautions are recommended:

- Tooling should be designed to prevent over-stressing the metal.
 - a) Keep holddown pressures to a minimum to ensure metal flow from the outside rather than stretching.

- b) Open-end eyelets should be cupped with a closed end before final piercing.
 - c) On the initial draw, punch radius should be a minimum of four times material thickness. Reduce successively on redraws.
 - d) On the initial draw tools, the difference between die and punch diameter should be three times the thickness of the material.
 - e) Radius on final draw should be not less than material thickness. Sharper radii should be made by a subsequent coining operation.
- Scratches and tool marks should be minimized.
 - a) On large parts, all defects must be removable by light polishing with 180-grit aluminum oxide abrasive cloth.
 - b) Surface defects of small parts must be removable by a nominal amount of tumbling.

Design of Formed Parts

- Inside radii at the corners should be not less than the thickness of the metal to avoid the expense of coining sharper radii.
- To prolong tool life, allow as great a tolerance on all dimensions as will satisfy the requirements of the assembly-and-function of the part.
- For economy and prompt delivery, specify standard stock thickness of metal whenever possible.

Annealing

Recommended procedure for relief of stress and work hardening of Kovar parts is as follows:

- Wash and degrease parts.
- Anneal in atmosphere-controlled furnace (atmosphere may be wet or dry hydrogen, dissociated ammonia, cracked gas, or similar neutral atmosphere).
- Annealing temperature is not critical, but high temperatures and long time periods promote large grain growth. Complete stress relief is obtained in the range of 700°C (1292°F) to 1100°C (2012°F) held for a minimum of 15 minutes after the parts have attained the temperature of the hot zone, and then placed in the cooling zone before exposure to air. A typical schedule follows:
 - a. Hold at 870°C (1600°F) for 20 minutes.
 - b. Place in cooling zone for one-half hour or until the parts are at less than 175°C (350°F) before removal to the air.

The foregoing intermediate annealing procedure is distinct from heat treatment for cleaning, strain relief, and degassing just prior to glass sealing. The latter should be done in a wet hydrogen atmosphere for a longer period, such as 1000°C for 30 minutes.

Corrosion Resistance

Kovar oxidizes readily and similarly to soft steels. Adequate protection from humidity is, therefore, required.

Plating

Kovar may be solder-plated directly by dipping. Typically, however, the Kovar surface is "passivated" by a thin nickel strike, followed by a copper or silver plating to enhance the electrical conductivity and finally by a solder plating.

7.1.6 Molybdenum (Based on Ref. 7.1-7)

While primarily developed for high-strength, high-temperature applications, its low coefficient of thermal expansion makes molybdenum desirable for solar cell interconnectors. Pure molybdenum, also known as "moly," is brittle at and below room temperature and above 1000°C. Special alloys are available to reduce brittleness over a specific temperature range. Moly exhibits directional properties that call for consideration during bending operations. Smaller bend radii than twice the material thickness are not practical, even at elevated temperature. For shearing or stamping, blanking quality moly should be specified to prevent excessive lamination (spalling).

Experience with moly solar cell interconnectors gained by several organizations showed that the material should have been produced by an arc-cast process. Plating of moly has been a problem for years, but now several organizations offer reliable moly plating, usually by vacuum deposition of a Ti or Pd passivation coating followed by a silver layer. Humidity and peel tests have been found necessary to verify control of the plating process quality.

Moly can be obtained from the General Electric Company, Sylvania, and Metallwerk Plansee, Austria (U.S. distributor: Schwartzkopf Development Corporation, Holliston, Massachusetts).

7.1.7 Silver (Based on Ref. 7.1-8)

For use on solar cell arrays, "fine silver" (the commercially pure form of silver) is usually specified. Of all the metals, fine silver has the highest electrical and thermal conductivities. Its ductility and malleability are second only to those of gold. The "softness" of fine silver, especially in the form of thin, narrow ribbons or thin wires, often presents a major problem in manufacturing.

Fine silver is available in finenesses ranging from 999.0 to 999.99. (It is customary to express purity of silver in parts per thousand and concentration of impurities in percent.)

Workability

Fine silver can be hot or cold worked. It work-hardens at a lower rate than most metals; however, its low strength usually limits the degree of cold work that can be done in one operation.

Weldability

The absorption of oxygen in the silver undergoing processing at elevated temperatures leads to embrittlement of the material or the weld joints. The silver should be deoxidized before welding and shielded during welding by inert or reducing (hydrogen) atmospheres.

Silver does not oxidize in air, but tarnishes rapidly if sulfur is present in the atmosphere. Silver tarnish removers are commercially available and are recommended to be used prior to welding of silver.

7.1.8 Solder

For soldering to silver or silver-plated parts (such as the common Ti/Ag solar cell contacts), SN62 solder (62 percent Sn, 36 percent Pb, 2 percent Ag) is typically used. The silver content prevents an excessive amount of silver being scavenged from the cell contacts and dissolved in the solder. The solubility of silver as a function of solder alloy temperature is illustrated in Figure 7.1-2.

For soldering to gold or gold-plated parts, the scavenging of gold by the solder is reduced by adding indium to the solder.

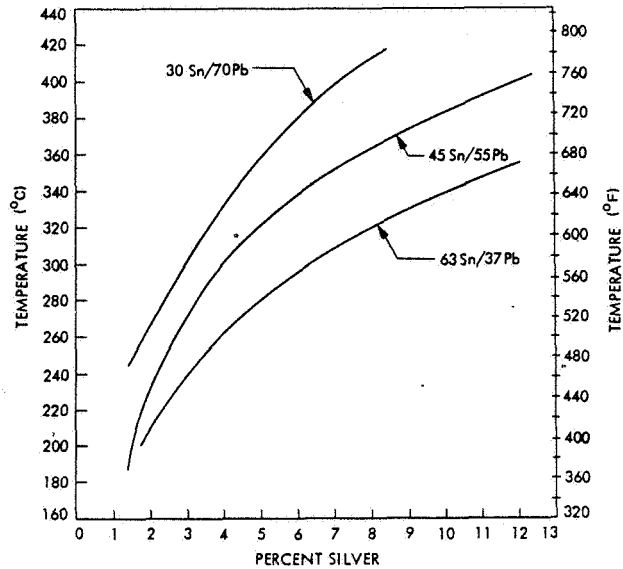


Fig. 7.1-2. Solubility of Silver in Tin-Lead Solders at Various Temperatures (Ref. 7.1-9)

7.2 GENERAL CHARACTERISTICS OF SOME SPECIFIC NONMETALS

The major classes of nonmetallic materials used on solar cell arrays are as follows:

- Silicon (solar cells) and glasses (solar cell covers)
- Adhesives
- Plastic Films

The material properties of these materials are discussed in the following subsections. Some properties of silicon solar cells are also discussed in Chapter 3 and those of solar cell covers in Chapter 4.

7.2.1 Adhesives and Sealants

Two major adhesive systems are required for solar cell arrays. One system is used to attach the solar cells to the structure (substrate); the second is used to bond the solar cell coverglasses to the cells. The requirements for attaching the solar cells to the structure vary with the various arrays under consideration, but in general must have the following properties:

- High thermal conductivity
- Low outgassing in the vacuum environment
- Thermophysical and mechanical properties that are compatible with those of the solar cells and their support structure
- Repairability during the fabrication phase
- Adequate strength to resist vibration and thermally induced stress.

The adhesive for bonding the coverglasses to the solar cells must be transparent to electromagnetic radiation in the wavelengths from approximately 0.35 to 1.1 μm and not degrade appreciably under ultraviolet and particulate irradiation.

Additional adhesive systems are required for bonding insulating sheets to metallic substrates, bonding wires and miscellaneous mechanical and electrical parts and connectors to the substrate, and for potting connectors.

The term "adhesive system" is typically used to describe, or at least imply that an "adhesive" is more than just a simple product. "Adhesive systems" usually are comprised of the following:

- Surface preparations (cleaning, scrubbing, degreasing, etc.) of the components to be bonded
- Application and curing of a primer, if used, on a specified humidity/temperature/time schedule
- Measuring, mixing and de-airing of multi-compound adhesives and control of shelf life

- Application and bonding within specified time limits to prevent skin-over
- Curing of the adhesive on a specified humidity/temperature/time schedule
- Cleanup, bake-out, pre-outgassing, etc., as and if required.

All adhesives, including the nonsolvent types, produce volatile byproducts upon curing. These byproducts of adhesives currently used on solar cell arrays may be either of an acidic or of an alcoholic type. The acidic byproducts may combine with moisture from the ambient air and form acids that can, under severe conditions, corrode solar cell contacts. The susceptibility of a particular solar cell and array design to a potential corrosion mechanism should be determined by test.

For each specific adhesive, the manufacturer's recommendations should be followed closely and their data sheets should be consulted.

Epoxy-Polyamide Adhesives

During the 1960's, several polymeric systems were considered. Most systems exhibited little energy absorbing capability. Epoxy-polyamide adhesives have been used on earlier solar cell arrays, such as on the IMP spacecraft and on the Mariner 1964 solar panels. Their performance in space has apparently been satisfactory.

Silicone Rubber Adhesives

Two generic types of RTV silicone rubbers, the methyl-phenyl silicones and the dimethyl silicones, have found use in bonding applications for solar cells. The methyl-phenyls have superior low-temperature properties, although the dimethyls have been more widely used in past space flights by JPL. In a test program seven candidate silicone rubber adhesives of these two types were evaluated. Two dimethyl silicones (RTV-41 and RTV-602) are adhesives used for solar cell array applications by JPL, whereas the remaining methyl-phenyl materials are used by others. The test results are shown in Sections 7.5 through 7.8 and 7.11 of Volume II.

7.2.2 Conductive Adhesives

Conductive adhesives have the following potential applications on solar cell arrays:

- Attachment of solar cells to power pickup circuitry, especially during array repair
- Interconnections between grounding straps and metallic surfaces and of flat conductors, in addition to mechanical fasteners.

Even though conductive adhesives have not been fully investigated for use in space and have not been

used widely, they are a potentially attractive and, on a small scale, a necessary means of making reliable electrical interconnections for such applications as bolted-together, high-current bus bars, RF ground straps, and flat conductor interfaces between dissimilar metals. In these applications the adhesive serves mainly as a conductive medium while an additional structural element (bolt, rivet, etc.) provides the mechanical strength.

Because of the specialized nature of conductive adhesives and their applications in solar cell arrays, no generally applicable data was found for inclusion in this handbook.

7.2.3 Kapton (Based on Ref. 7.2-1)

Kapton is a registered trademark of the DuPont Company for its flame resistant, transparent, gold colored polyimide film. Kapton does not melt but chars and decomposes above 800°C. There is no known solvent for the film.

Kapton is marketed by DuPont as Kapton "Type H" film; when combined with heat-sealable FEP-fluorocarbon resin ("Teflon"), Kapton film is called "Type HF." The Type H film is available in the following thicknesses and widths:

Nominal Thickness		Maximum Width	
inches	μm	inches	cm
0.0005	12.5	18	45.7
0.001	25	28	71.1
0.002	50	28	71.1
0.003	75	34	86.4
0.005	125	34	86.4

Kapton retains its physical properties and dimensional stability over a wide range of temperatures. Relative to other organic films, Kapton has a very high cut-through resistance and creep strength at elevated temperatures. Kapton has a relatively high resistance to tearing but, once a tear has started, it propagates easily under only a slight load. The FEP layer on Type HF film resists such tear propagation. Kapton has also excellent creasing and repeated foldability characteristics.

Workability

Kapton can readily be sheared, die-cut, laminated, metallized, punched, formed, and adhesive coated. Three-dimensional configurations can be fabricated only with difficulty by "heat forming" (i.e., creep at elevated temperature under high loading). When used as a wire insulator, it must be wrapped around the conductor and held in place with an adhesive or FEP-Teflon.

7.2.4 FEP-Teflon (Based on Ref. 7.2-2)

Teflon is a registered trademark of the DuPont Company for its fluorocarbon resins. FEP-Teflon is a nonflammable, transparent, colorless, thermoplastic, fluorocarbon film. FEP is abbreviated from fluorinated ethylene propylene. In contrast to FEP-Teflon, TFE-Teflon is of a milky-white color.

FEP-Teflon is inert to all known chemicals and solvents except for fluorine, compounds containing fluorine, and molten alkali metals. FEP-Teflon exhibits anti-stick properties and a low coefficient of

friction. It has good impact and tearing resistance and is continuously usable up to 200°C. It melts at 260°C to 280°C.

FEP-Teflon films are available in three types:

- Type A - heat seals to itself and to other materials (adhesives will usually not stick to its surfaces)
- Type B - one surface modified to permit its use in laminations using any of many commercially available adhesives
- Type C20 - both sides modified to accept adhesives.

FEP-Teflon film is available in the following thicknesses and widths:

Thickness		Width	
inches	μm	inches	cm
0.0005	12.5	30	76.2
0.001	25	48	121.9
0.002	50	48	121.9
0.005	125	48	121.9
0.010	250	48	121.9
0.020	500	48	121.9

Because of its heat-sealing capability, dielectric properties, optical qualities and chemical stability, FEP-Teflon has found extensive use on spacecraft exteriors and in electronic equipment. The mechanical strength and dimensional stability of FEP-Teflon is significantly improved when it is laminated to Kapton film.

Workability

FEP-Teflon can readily be cut, sheared, punched, metallized, folded, formed, and adhesive coated (Types B and C20 only, see above) and laminated. One of its attractive properties for space applications is that it can be heat-sealed directly to a variety of materials including Kapton, metals, silicon and glass, without the use of an adhesive or primer, except that a silane (siloxane) adhesion promoter may be required in certain applications.

7.2.5 Fused Silica (Based on Refs. 7.2-3 and 7.2-4)

Fused silica, also called fused quartz, for solar cell array applications is a synthetic, colorless and highly transparent silicon dioxide glass. In contrast to natural quartz, fused silica is nearly (industrial grade) or completely (ultraviolet-grade) free of impurities that result in transmission-impairing color centers during ultraviolet or charged particle radiation. Like other glasses, fused silica is a supercooled liquid, exhibiting a softening at elevated temperatures (above 1000°C) rather than a well-defined melting point. Due to its low coefficient of thermal expansion, it can endure severe thermal shock without shattering.

Workability

Fused silica must be cut with diamond saws and polished. The material is brittle but can withstand severe thermal shock treatments.

Chemical Durability

Fused silica has excellent resistance to ordinary weathering. It also has the typically high resistance of silica to attack by nearly all chemical reagents. Rapid attack occurs only on exposure to hydrofluoric acid or concentrated alkaline solutions, the rate of attack being increased at elevated temperatures.

When exposed to weathering (corrosion by atmospheric gases, i. e., CO₂, H₂O), fused silica shows virtually no clouding of the surface or electrical surface leakage.

The following are examples of the chemical durability of Code 7940 fused silica:

Reactant	Reaction Time (hours)	Temperature (°C)	Surface Erosion (μm)
Water	24	100	0.012
5% HCl	24	95	0.025
5% NaOH	24	95	12

Availability

Three types of Code 7940 fused silica available from Corning Glass Works are given in Table 7.2-1.

7.2.6 Microsheet (Based on Ref. 7.2-5)

Microsheet is thin, optical-quality glass sheet with a flame-polished surface finish. It is made in several thickness ranges from 50 to 610 μm. Microsheet is cut to size with diamond saws.

Availability

Microsheet is available in cut rectangles, squares, circles, and in standard stock sheets, which measure about 13 x 14 inches.

Stock Code Sheet	Gage No.	Thickness Range	
		(in.)	(μm)
583538	00	0.0020 - 0.0033	50 - 84
583539	0	0.0033 - 0.0051	84 - 130
583540	1	0.0051 - 0.0063	130 - 160
583541	1-1/2	0.0063 - 0.0075	160 - 190
583542	2	0.0075 - 0.0098	190 - 250
583543	3	0.0098 - 0.0138	250 - 350
583544	4	0.0180 - 0.0240	350 - 610

7.2.7 Ceria-doped Microsheet

The addition of a small percentage of cerium oxide to some glasses has been found to prevent the formation of color centers in these glasses during exposure to ultraviolet and charged-particle radiation. Solar cell covers made from cerium stabilized microsheet became commercially available in Great Britain in 1971 and later in the U.S.

Ceria-doped microsheet, in 0.1-mm thickness, exhibits a natural, sharp cut-on wavelength at approximately 0.35 μm (about 0.36 μm for 0.3 mm thickness) and thereby does not require the application of a blue-reflecting coating.

The cost of ceria-doped microsheet is reportedly lower than the cost of either microsheet or fused silica covers with blue-reflecting coatings.

Table 7.2-1. Types of Code 7940 Fused Silica

Maximum Dimension— Diameter or Diagonal (in.)	Striae Grade in Direction of View per Spec JAN-G-174	Maximum No. Seeds/ cu in	Maximum Average No. of Seeds/ cu in	Maximum Mean Diameter of Seeds (in.)	Maximum % Projected Area/in Light Path	Anneal nm/cm Path Difference
Industrial Grade						
Up to 18	D	50	10.00	0.080	0.120	20
18 to 36	D	100	18.00	0.250	0.250	20
36 to 60	D	100	18.00	0.500	0.350	20
Optical Grade						
Up to 10	A	4	0.40	0.020	0.005	10
10 to 14	A	4	0.40	0.030	0.005	10
14 to 18	A	4	0.40	0.040	0.005	10
18 to 36	A	25	3.00	0.080	0.036	10
36 to 60	A	100	10.00	0.150	0.120	10
Ultraviolet Grade						
Up to 18 x 4 thick	Same internal quality as optical grade with guaranteed minimum transmission at 185 nm in 10 mm thickness as follows:					
			<u>Internal</u>	<u>External</u>		
			70%	63%		

7.3 MASS, DENSITY AND WEIGHT

7.3.1 Definitions

Mass is the physical measure of the inertial property of a body. Mass offers a resistance to a force that intends to change the velocity of a body. At small speeds of the body relative to the speed of light, mass is effectively invariant throughout the universe. At higher speeds, the mass, m , depends upon the speed of the body relative to an observer as follows:

$$m = m_0 \left[1 - (v^2/c^2) \right]^{-1/2}$$

where m_0 is the value of the mass at rest, v is the body's speed, and c is the speed of light. Particles moving with speeds such that $m \neq m_0$ are also called "relativistic" particles. The unit of mass is the kilogram (kg).

Density is defined as mass per unit volume for both homogeneous and nonhomogeneous bodies. Density is expressed either in g/cm^3 or in kg/m^3 , or in unitless ratio to the density of pure water at 4°C .

The unitless form of density is also known as "specific density" or as "specific gravity."

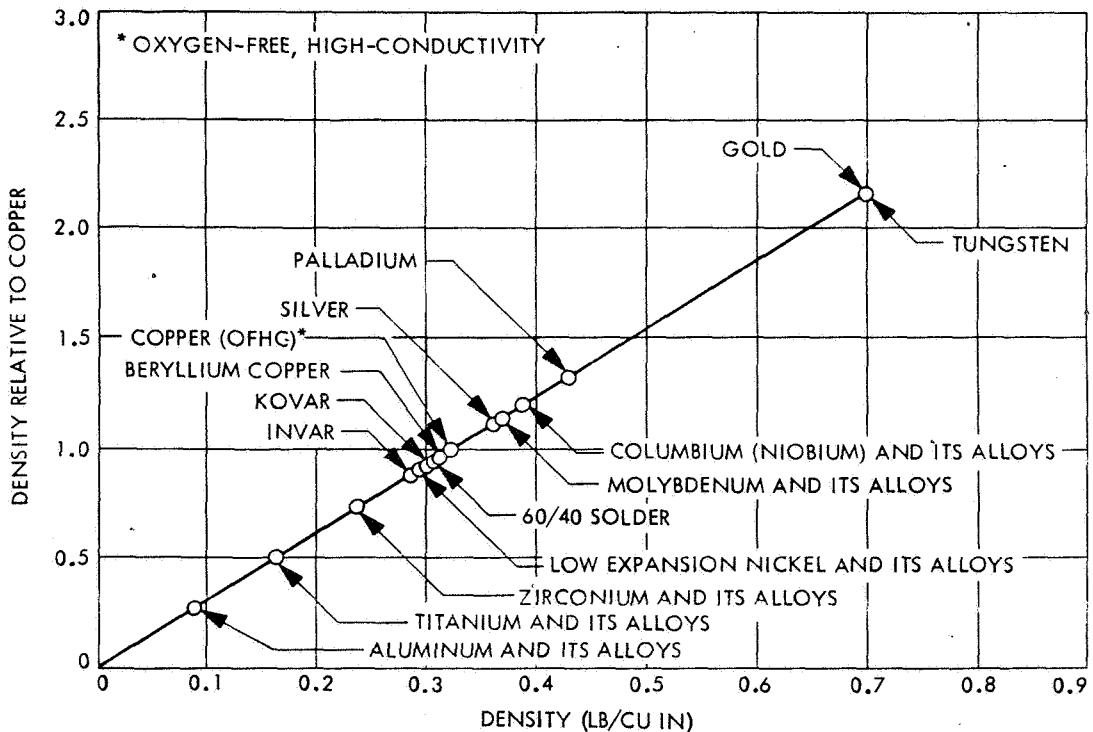
Weight is the force exerted on a body of mass, m , by the gravitational force of the earth or another large body. Weight, w , of a body with mass, m , is defined as:

$$w = mg$$

where g is the acceleration of gravity. On earth the value of g changes with distance from its center (altitude) and with geographic latitude. The unit of weight is the same as that of force and is the newton (N). The gravitational acceleration at the earth's mean sea level is 9.80665 m/s^2 . For example, 1 liter = $1 \text{ dm}^3 = 1 \times 10^{-3} \text{ m}^3$ of water has a mass of approximately 1 kg and, at sea level, weighs 9.8 N.

7.3.2 Relative Density

Typical density values for several metals relative to the density of copper are shown in Figure 7.3-1. The densities for various solar cell array materials are given in Volume II, Section 7.3.



UNIT CONVERSION: MULTIPLY LB/CU IN BY 27.68 TO OBTAIN $\text{G} \cdot \text{CM}^{-3}$

Fig. 7.3-1. Density of Metals Relative to Copper (Ref. 7.3-1)

7.4 CENTROIDS, MOMENTS OF INERTIA AND RADII OF GYRATION

7.4.1 Definitions

The centroid is the center of an area or of a volume. For an area located in an x-y plane the coordinates of the centroid are given by

$$\bar{x} = \frac{1}{A} \int x dA \quad \text{and} \quad \bar{y} = \frac{1}{A} \int y dA$$

where integrals are taken over the entire area, A. If a system of parallel forces is applied to a body from any direction, their resultant will always pass through the centroid. In the special case where the gravitational field acting on a body is uniform over the entire body, the center of gravity coincides with the centroid. In general, the centroid of a body is the center of mass of this body. The coordinates of the centroid of a body located in an x-y-z orthogonal coordinate system can be found from:

$$\bar{x} = \frac{\sum m_i x_i}{\sum m_i} \quad \bar{y} = \frac{\sum m_i y_i}{\sum m_i} \quad \bar{z} = \frac{\sum m_i z_i}{\sum m_i}$$

where m_i are the masses of each of the i elements of the body and x_i , y_i , and z_i are the respective coordinates of each of the i elements.

The moment of inertia of a body is a measure of the body's rotational inertia about some specific axis. The moment of inertia of a body or system of bodies is defined as

$$I = \int r^2 dm$$

where r is the distance of each mass element, dm , from the axis of rotation and the integral is taken over the entire mass of the body or system of bodies. The moment of inertia, I , is related to the net torque, τ , on the body about the same axis by the angular acceleration, α :

$$\tau = I\alpha$$

The radius of gyration, k , relates the moment of inertia, I , of a real body with total mass, M , about an axis to a hypothetical point mass, M , at a distance, k , from the same axis such that

$$k = (I/M)^{1/2}$$

7.5 ELASTIC MODULUS, POISSON'S RATIO AND ULTIMATE STRENGTH OF METALS

7.5.1 Definitions

An external force applied to a body that is restrained from moving tends to deform that body. The resultant internal force in the body that opposes the external force, F , is called stress, σ . Any deformation of the body that takes place as a result of the external force is called strain, ϵ . Both stress and strain may be tensile, compressive, or in shear (see Figure 7.5-1).

Stress and strain are experimentally related to the stress-strain diagram (Figure 7.5-2). Hooke's law states that strain is proportional to stress within the elastic range or up to the proportional limit. The proportionality constant for axial (compressive or tensile) stress is called Young's modulus, or elastic modulus, or the modulus of elasticity, E ; for shear stress the proportionality constant is the shear modulus, G . The yield strength is the unit stress (above the elastic limit) at which a small, specified permanent deformation occurs (unit stress is the stress per unit area). The highest point on the stress-strain curve is called the ultimate strength. Permanent or plastic deformation is associated with most materials; exceptions are brittle materials such as glass, fused silica, silicon, and molybdenum. Such brittle materials exhibit stress-strain diagrams, as shown in Figure 7.5-3.

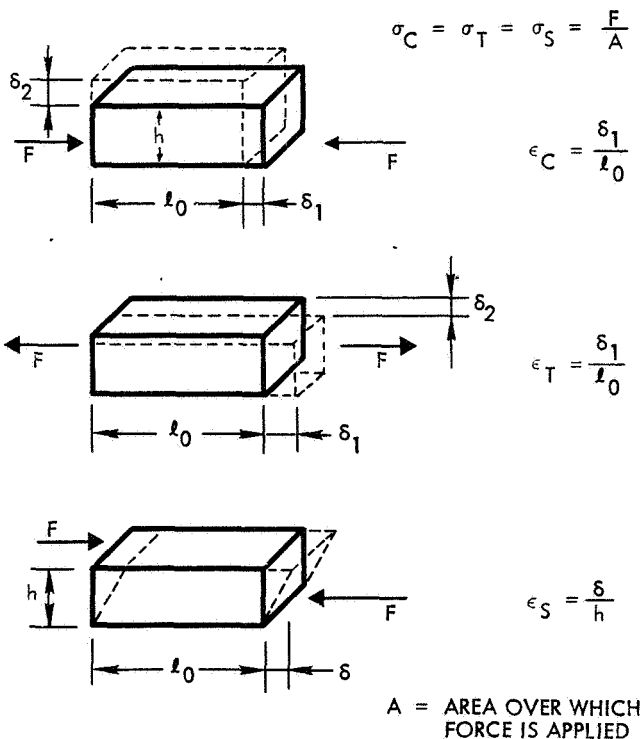


Fig. 7.5-1. Diagram of Stress, σ , and Strain, ϵ , Due to Applied Force, F

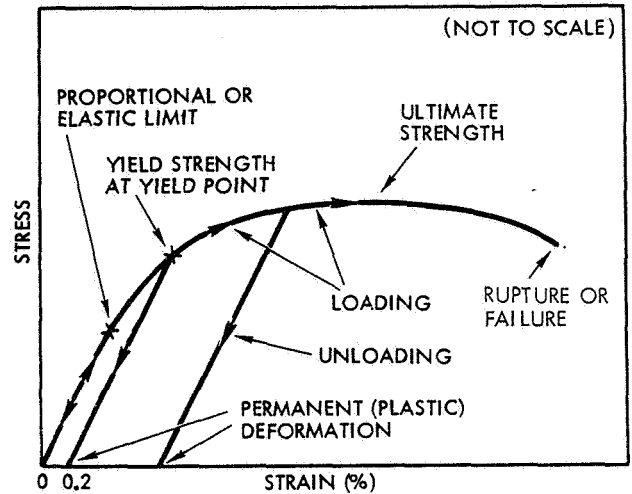


Fig. 7.5-2. Typical Stress-Strain Diagram for Ductile Metals

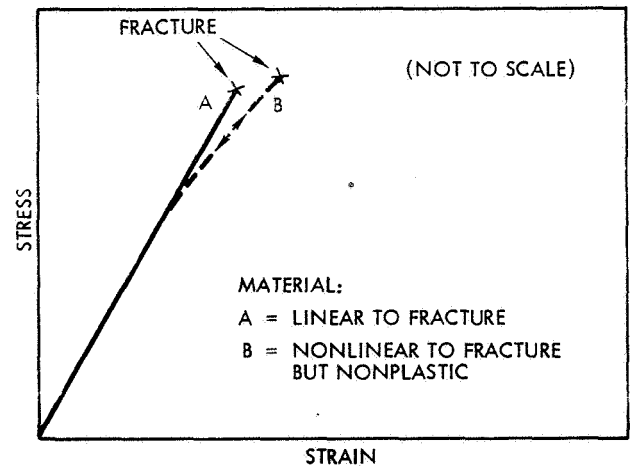


Fig. 7.5-3. Typical Stress-Strain Diagram for Brittle Metals, Silicon, and Glass

Materials capable of sustaining large deformations without failure are said to be plastic, or to exhibit plasticity. Plasticity under tensile loading is referred to as ductility and under compressive loading as malleability.

A body that is deforming under an external force applied in a given direction will also deform in a direction perpendicular to the direction of the force.

Within the elastic range, Poisson's ratio, ν , provides a measure of the body's resistance to lateral deformation, called stiffness:

$$\nu = \frac{\delta_2/h}{\delta_1/l_0} = \frac{1}{2} - \frac{E}{6K} = \frac{E}{2G} - 1$$

where δ_1 and δ_2 are defined in Figure 7.5-1 and K is the bulk modulus, as defined below. The elastic modulus is

$$E = \frac{\sigma}{\epsilon} = \frac{F/A}{\delta_1/l_0} = 2G(1 + \nu)$$

where σ and ϵ are defined in Figure 7.5-1 for tensile or compressive loads. The shear modulus is

$$G = \frac{F/A}{\delta/l_0} = \frac{F l_0}{\delta A} = \frac{E}{2(1 + \nu)}$$

and the bulk modulus, K , relates the change in volume, ΔV , of a body with volume, V , under hydrostatic pressure, F/A , as follows:

$$K = -\frac{F/A}{\Delta V/V} = \frac{E}{3(1 - 2\nu)}$$

The foregoing undefined symbols, illustrated by Figure 7.5-1, are:

A = cross-sectional area to which a force is applied

F = forces, externally applied

l_0 = initial length

δ = deflections (subscripts are defined in Figure 7.5-1)

The term "stiffness" is used to indicate the inherent resistance of a material (or a structural element) to deform or deflect by an amount, δ , under the influence of an externally applied force, F . The stiffness, k , of a material is similar to the stiffness of a spring,

$$k = F/\delta$$

and is related to the elastic modulus E (or shear modulus G) as follows:

$$k = EI \quad \text{in bending}$$

$$k = EA \quad \text{in axial loading}$$

$$k = GA \quad \text{in shear loading}$$

where A is the area as defined above and I is the moment of inertia of the beam under bending stress.

7.5.2 Relative Material Properties

Comparisons of three different material properties of various materials are given in Figures 7.5-4 through 7.5-6 (Ref. 7.5-1).

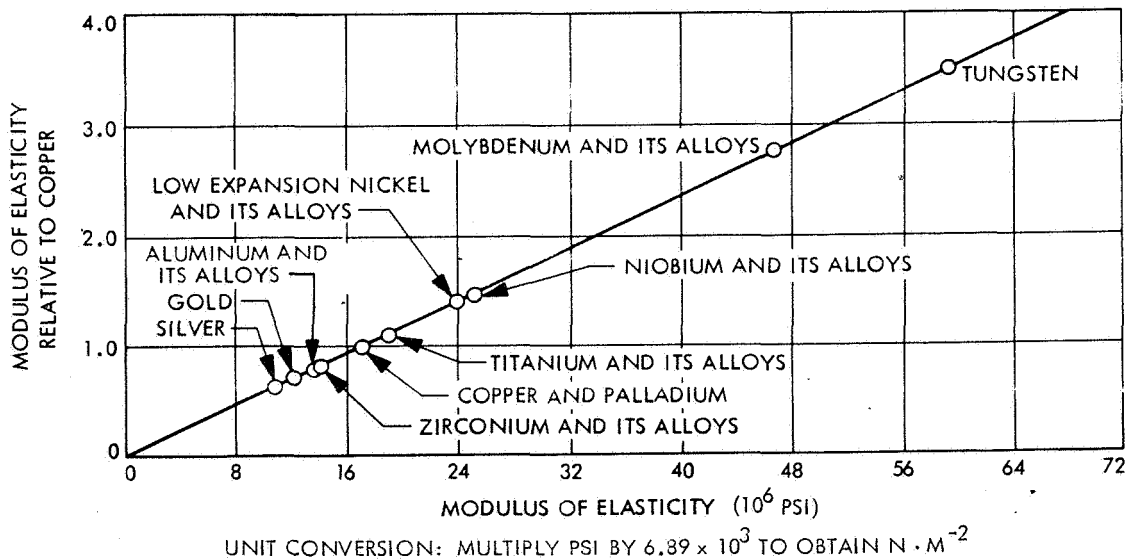


Fig. 7.5-4. Modulus of Elasticity of Metals in Tension Relative to Copper

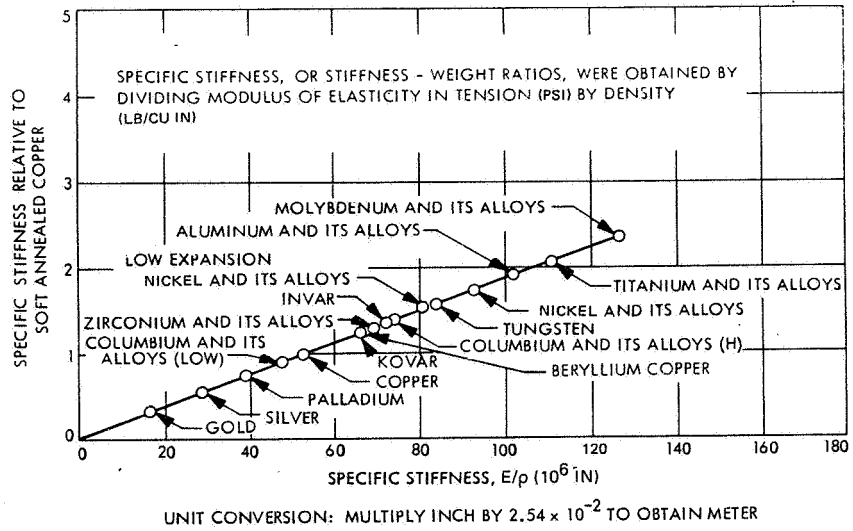


Fig. 7.5-5. Specific Stiffness of Metals Relative to Copper (soft annealed)

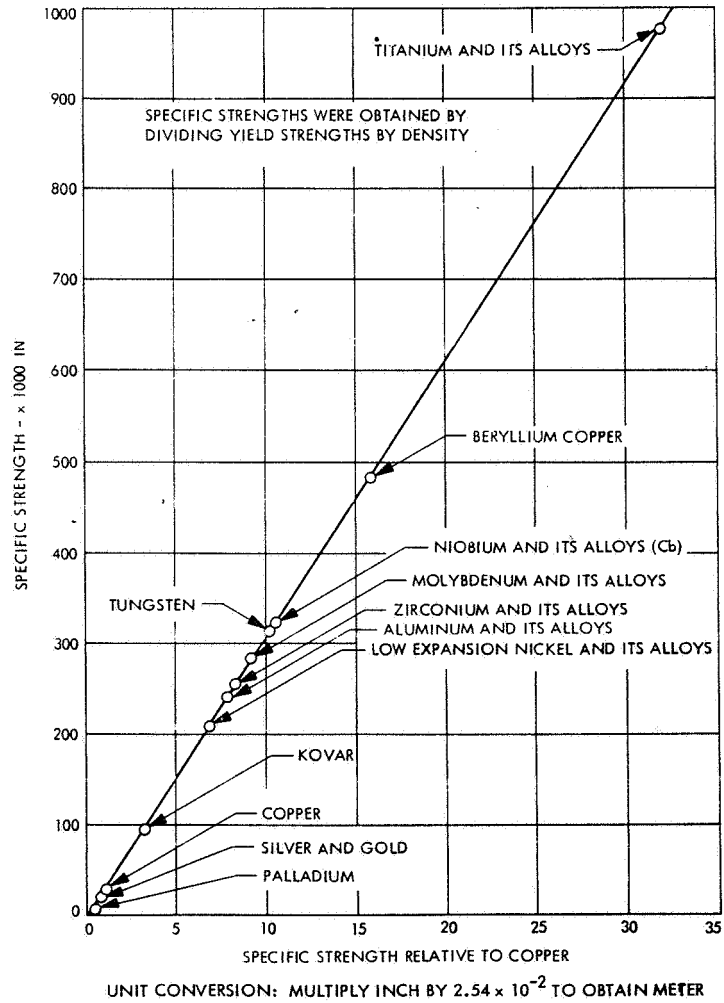


Fig. 7.5-6. Specific Strength of Metals Relative to Copper

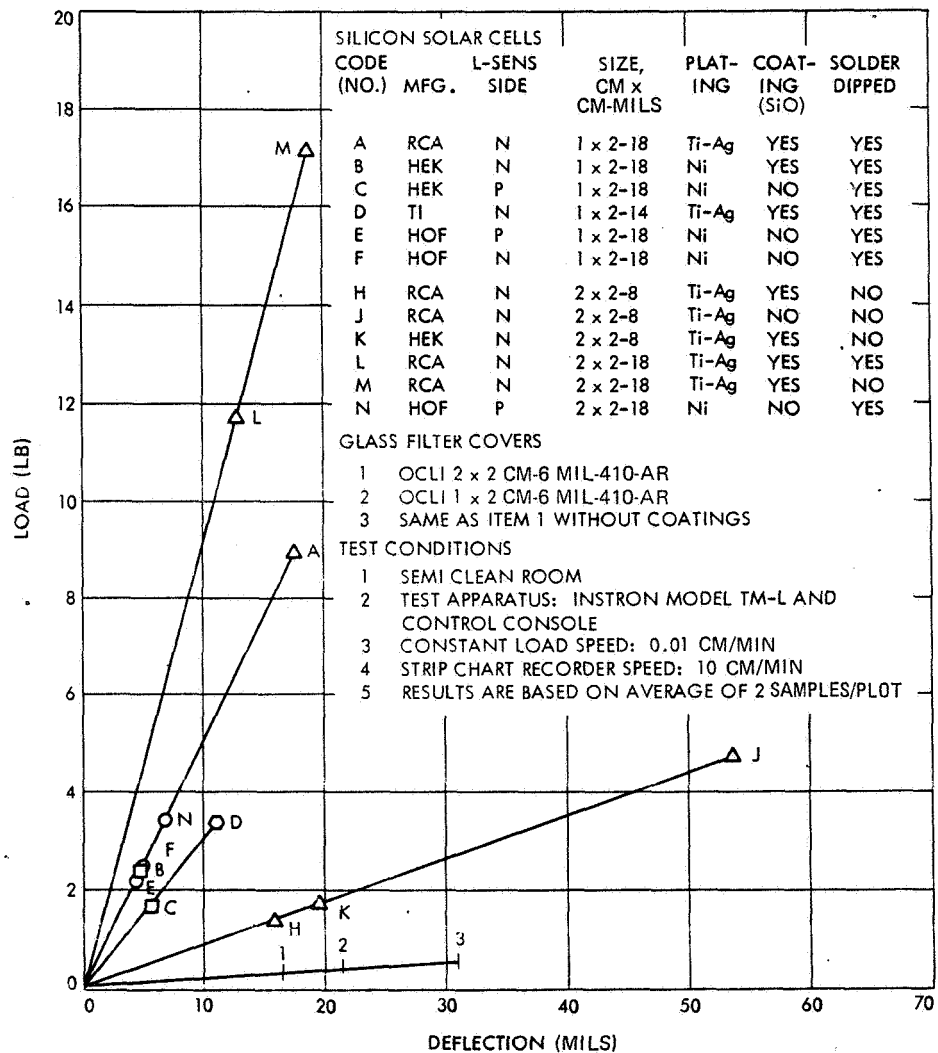
7.6 ELASTIC MODULUS, POISSON'S RATIO AND ULTIMATE STRENGTH OF SILICON AND GLASS

7.6.1 Definitions

The definitions of these terms are identical to those given in Section 7.5, except that the stress-strain curve terminates approximately at the yield point as shown in Figure 7.5-2. For engineering purposes, silicon and glass do not deform plastically, but rather fail abruptly by brittle fracture (see Figure 7.5-3).

7.6.2 Test Data

A comparison of the flexural strength of several different groups of silicon solar cells and coverglasses is shown in Figure 7.6-1. The flexural strength indicates the magnitude of the applied load required to cause failure in bending.



UNIT CONVERSION: MULTIPLY LB BY 4.45 TO OBTAIN N
MULTIPLY MILS BY 2.54×10^{-2} TO OBTAIN MM

Fig. 7.6-1. Flexural Strength of Silicon Solar Cells and Coverglass (Ref. 7.6-1)

7.7 ELASTIC MODULUS, POISSON'S RATIO AND ULTIMATE STRENGTH OF OTHER NONMETALS

7.7.1 Definitions

The definitions of these terms are identical to those given in Section 7.5, except that nonmetals may, depending upon their temperature, behave like elastomers, metals, or glasses. The stress-strain characteristics of metals were described in Section 7.5 and those of glasses in Section 7.6. The stress-strain characteristics of elastomers are different from those of metals and glasses in that they can sustain relatively large plastic deformation without taking a permanent set. Figure 7.7-1 illustrates a typical elastomer stress-strain characteristic that shows complete recovery of a large strain. The rate of recovery may be relatively slow for some materials, taking from minutes to hours.

Elastomers include such materials as room temperature vulcanizing (RTV) rubbers, silicone adhesives and sealants, and similar rubber-like organics and plastics.

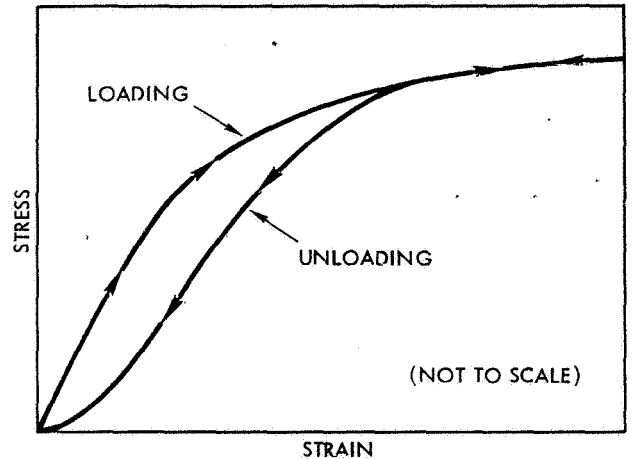


Fig. 7.7-1. Typical Stress-Strain Diagram for Elastomers

7.8 ELONGATION AND REDUCTION IN AREA

7.8.1 Definitions

Elongation and reduction in area are indicators of the ductility of a material. Both of these parameters are determined by tensile testing specimens of initial length, L_0 , and cross-sectional area, A_0 , until rupture occurs. Both parts of the fractured specimens are fitted together again and the final length, L_f , and minimum cross-sectional area in the necked-down region, A_f , are measured (see Figure 7.8-1). Elongation, EL , and reduction in area, RA , are calculated by

$$EL = (L_f - L_0)(100\%)/L_0$$

$$RA = (A_0 - A_f)(100\%)/A_0$$

Typically, the initial length $L_0 = 2.0$ inches (5.08 cm).

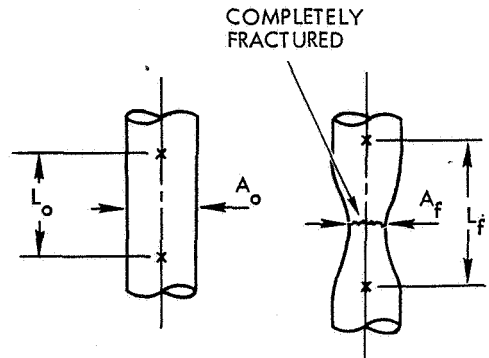


Fig. 7.8-1. Tensile Test Specimens

7.9 ELECTRICAL PROPERTIES OF CONDUCTORS

7.9.1 Definitions

The absolute volume resistivity, ρ , is a material-peculiar proportionality constant which permits the calculation of the resistance, R , of a piece of conductor with cross-sectional area, A , and length, L , such that

$$R = \rho L/A$$

The units of ρ are ohm \cdot m, but typically are given in $\mu\text{ohm} \cdot \text{cm}$ or ohm \cdot circular-mils/foot. Unit conversion factors are given in Section 7.1 of Volume II.

The temperature coefficient, α , of resistivity gives the ratio of the change in resistivity due to a change in temperature in degrees centigrade relative to the resistivity at 20°C. The resistance, R , at any temperature, T (°C), relative to the resistance R_0 measured at some reference temperature, T_0 , is

$$R = R_0 \left[1 + \alpha(T - T_0) \right]$$

For example, the resistance of an aluminum conductor of 1 meter length and 1 mm² cross-sectional

area at 20°C is $R_{20} = 28.3$ milliohms. At 120°C the same conductor exhibits an approximate increase in resistance by $\alpha(T - T_0) = 0.35$ (or 35 percent) for a total resistance of $R_{120} = 28.3 (1 + 0.35) = 38.2$ milliohms.

The conductivity, γ , is the inverse of the resistivity, ρ , of a conductor

$$\gamma = 1/\rho$$

The recommended units of conductivity are ohm⁻¹ \cdot m⁻¹; the use of "mho/m" is discouraged.

7.9.2 Relative Electrical Properties

Relative resistivity indicates the relative resistance of an otherwise identical conductor to that of one made from annealed copper at the same temperature. Typical values are given in Figure 7.9-1.

Values of conductivity relative to copper are given in Figure 7.9-2.

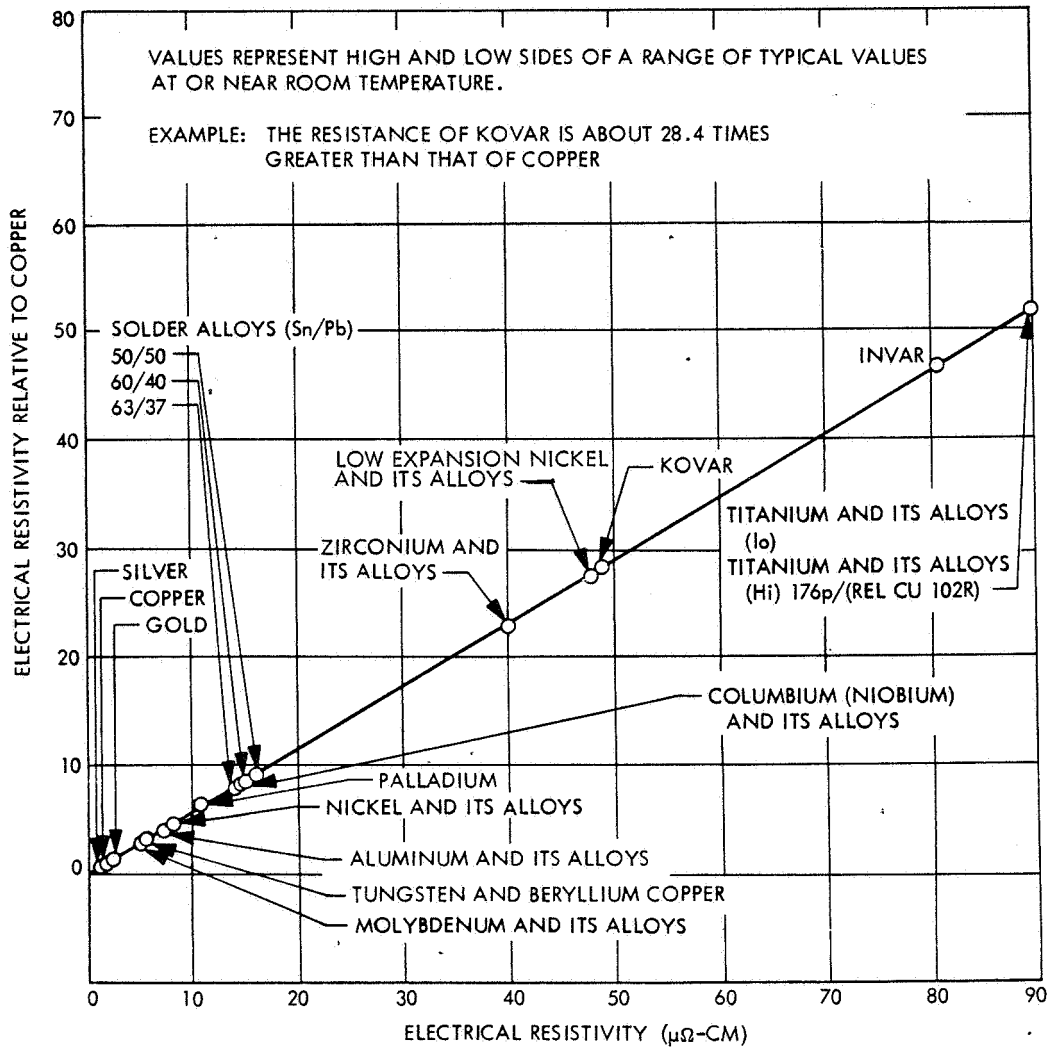


Fig. 7.9-1. Electrical Resistivity of Metals Relative to Copper (Ref. 7.9-1)

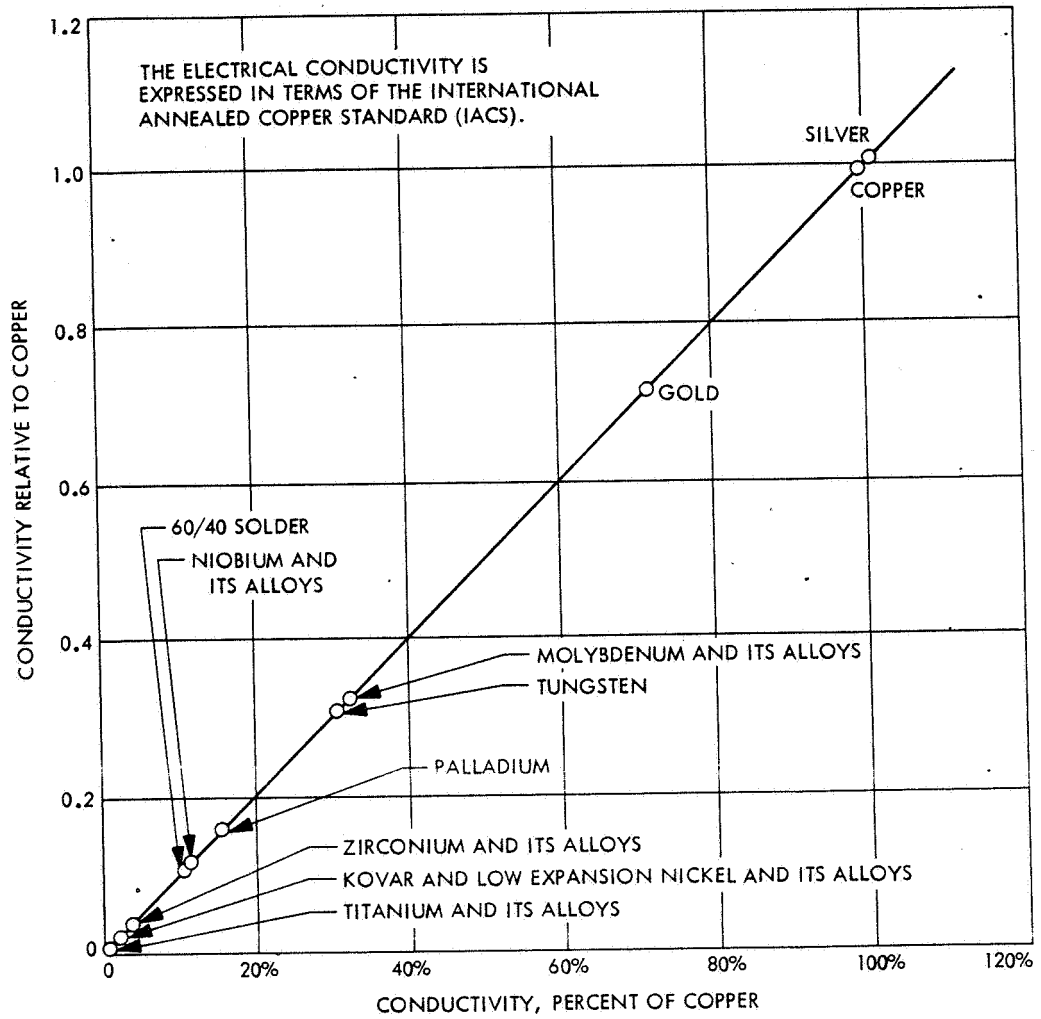


Fig. 7.9-2. Electrical Conductivity of Metals Relative to Copper (Ref. 7.9-1)

7.10 ELECTRICAL PROPERTIES OF DIELECTRICS

7.10.1 Definitions

Dielectric materials are electrical insulators. Aside from wire insulation, the main application of dielectric sheets on solar cell arrays is to electrically insulate the solar cell rear contacts from metallic substrates. The primary electrical properties of dielectrics that are of interest to the array designer are the voltage breakdown characteristics of and the electrical current leakage through the dielectric material. The equivalent circuit of a dielectric of unit area is shown in Figure 7.10-1; both resistances, as well as the capacitance, are highly nonlinear.

The leakage resistance is expressed as

$$R_L = \rho t/A$$

where ρ is the volume resistivity (see Section 7.9) of the dielectric, t is the sheet thickness, and A is the area of the dielectric covered with solar cells and other noninsulated conductors.

In general, all dielectrics possess leakage paths under ambient terrestrial conditions. This leakage is due to imperfections in the material ("pin holes") and due to moisture absorption by the dielectric. In addition to these two mechanisms, ionic conduction may contribute to leakage. Ionic conduction is caused by mobile ions that may be present in the dielectric material. The concentration of mobile ions typically is greater in the softer resins than in harder resins and tends to increase with increasing water absorption in the dielectric and with increasing temperature.

The dielectric strength of an insulating material is defined as the ratio of its breakdown voltage to its thickness, also known as the maximum potential gradient that the material can withstand. In general, the dielectric strength (volts per unit thickness) increases with decreasing film thickness, and decreases with increasing time during which the electrical stress is applied. The effect of time under stress is significantly greater for applied ac voltages than for dc voltages.

7.10.2 Properties of Significance in Space

In the space environment, leakage currents and voltage breakdown phenomena that may have caused testing problems in the terrestrial environment will largely disappear; however, vacuum-outgassing and radiation-induced phenomena tend to deteriorate the dielectric with increasing time. Solar cell arrays that move in and out of plasma clouds (see Section 2.3.3) may require their dielectric film thickness to be sized based on ac rather than dc voltage ratings.

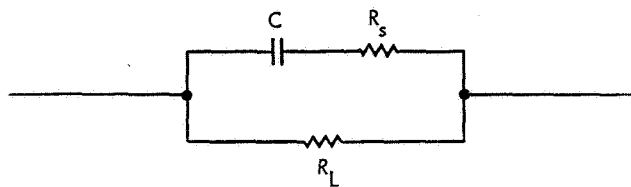


Fig. 7.10-1. Equivalent Circuit of a Dielectric

7.11 THERMAL EXPANSION PROPERTIES

7.11.1 Definitions

Physical bodies change their size with temperature. If they increase their size with increasing temperature, as they generally do, they exhibit a "positive" temperature coefficient. For a given change in temperature, a hole in a body changes its size by precisely the same amount as would a hypothetical body, made of the same material, which could be fitted precisely into the hole.

Coefficients of Linear Thermal Expansion

The coefficient of linear (as contrasted by with area or volume) thermal expansion is defined such that

$$L_{T_2} = L_{T_1} [1 + \alpha(T_2 - T_1)] \quad (7.11-1)$$

where L is the length of a piece of material and T is the temperature. Solving for α

$$\alpha = \frac{L_{T_2} - L_{T_1}}{L_{T_2}(T_2 - T_1)} \quad (7.11-2)$$

The α in Eq. 7.11-1 has been interpreted in the literature to express the following quantities:

- Instantaneous coefficients of expansion (α)
- Average coefficients of expansion ($\bar{\alpha}$)
- Normalized thermal expansion ($\Delta L/L$).

The normalized thermal expansion is not a coefficient even though occasionally, but erroneously, called a coefficient in the literature. The three different meanings of Eq. 7.11-2 are illustrated in Figure 7.11-1 and defined below.

7.11.2 Instantaneous Coefficients of Linear Expansion

The instantaneous coefficient, α , is determined experimentally by measuring a change in length, ΔL , of a specimen for a given change in temperature, ΔT . To make the data universally useful, the change in length is normalized by dividing by L_0 , the initial specimen length at room temperature, T_0 . For the instantaneous coefficient, Eq. 7.11-2 becomes, for the i -th increment:

$$\begin{aligned} \alpha_i \text{ (from } T_i \text{ to } T_{i+1}) &= \frac{1}{L_0} \frac{(L_{i+1} - L_i)}{(T_{i+1} - T_i)} \\ &= \frac{1}{L_0} \frac{L_i}{T_i} \end{aligned} \quad (7.11-3)$$

where the ΔT 's are relatively closely spaced intervals. The data points (α_i, T_i) are entered in a graph of α versus T and interconnected by a smooth curve (Figure 7.11-1a). The value of α at a given T gives the instantaneous coefficient of expansion. In order to use the instantaneous coefficient in computations, it must be converted into an "average" coefficient, as defined below.

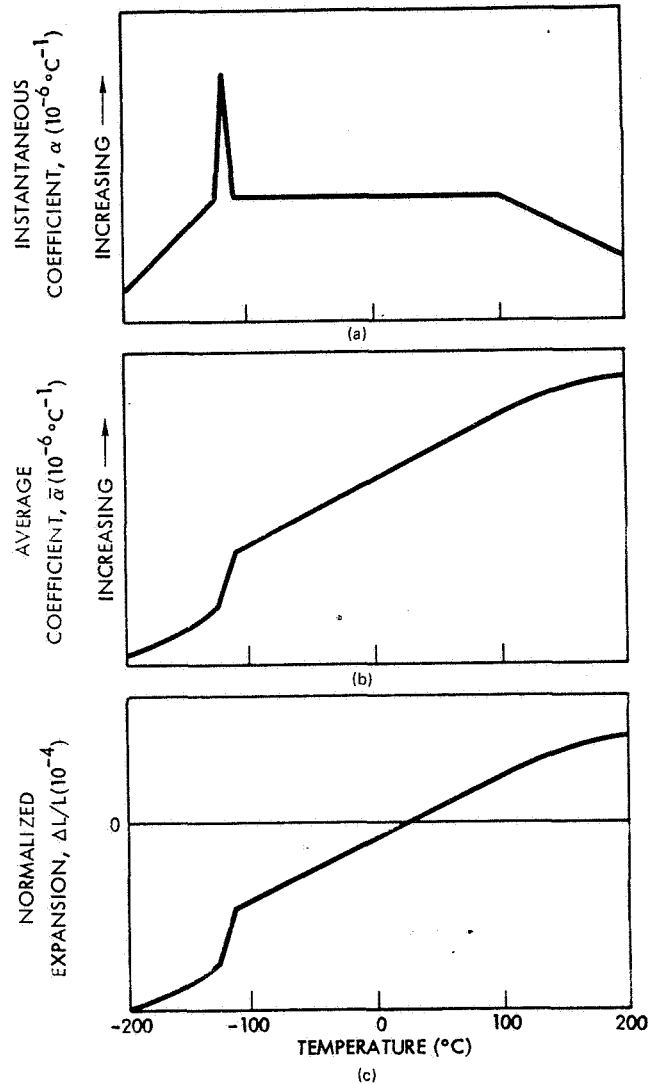


Fig. 7.11-1. Illustration of Three Different Linear Thermal Expansion Parameters (Idealized Silicone Characteristics)

7.11.3 Average Coefficient of Linear Expansion

The average, or mean, coefficient of expansion is defined by

$$\bar{\alpha} = \frac{1}{L_0} \frac{(L_j - L_0)}{(T_j - T_0)} \quad (7.11-4)$$

and is accurate only for the specific T_j 's measured (see Figure 7.11-1b). The value of $\bar{\alpha}$ at any given T_j gives the average coefficient of expansion when the temperature changes from T_0 to T_j .

The temperature coefficients typically given in the literature are based on the average change in length from $T_0 = 0^\circ\text{C}$ or $T_0 = 20^\circ\text{C}$ to a given T . Hence, they are called average coefficients and are denoted by $\bar{\alpha}$. To calculate the change in length, ΔL , of an object due to an increase in temperature from T_1 to T_2 , Eq. 7.11-1 is applied twice (with a change of subscripts as indicated below) such that

$$\begin{aligned} \Delta L &= L_{T_2} - L_{T_1} = L_{T_0} \left[1 + \bar{\alpha}_2 (T_2 - T_0) \right] \\ &\quad - L_{T_0} \left[1 + \bar{\alpha}_1 (T_1 - T_0) \right] \end{aligned}$$

where the subscripts of $\bar{\alpha}$ indicate that they are applicable only for the specific temperature range $T_2 - T_0$ or $T_1 - T_0$, respectively.

7.11.4 Normalized Thermal Expansion

Since the temperature coefficients defined by Eq. 7.11-2 are cumbersome to use in engineering, the normalized thermal expansion, $\Delta L/L$, is frequently given as a function of temperature. The quantity $\Delta L/L$ is occasionally, but erroneously, labeled expansion coefficient. On a $\Delta L/L$ -vs- T curve, $\Delta L/L = 0$ at room temperature. The slope of the $\Delta L/L$ -vs- T curve is the temperature coefficient α of Eq. 7.11-2 as the quantity $(L_{T_2} - L_{T_1})$ approaches zero.

The normalized thermal expansion is also known as unit expansion.

7.11.5 Conversion of Temperature Coefficients

The instantaneous coefficient is converted into the average coefficient by integration:

$$\bar{\alpha}_{(T_0 \text{ to } T_j)} = \int_{T_0}^{T_j} \alpha dT$$

where $\alpha = \alpha(T)$, as given by Eq. 7.11-3 or by a graph like Figure 7.11-1a.

The average coefficient is converted into the instantaneous coefficient by differentiation at each T taken from a graph like Figure 7.11-1(b):

$$\alpha = \frac{d\bar{\alpha}}{dT}$$

The general changes in the curve shapes due to integration or differentiation can be verified by reference to Section 9.1.3.

The average coefficient is converted into the normalized expansion Figure 7.11-1(c) by multiplication:

$$\frac{\Delta L}{L} = \bar{\alpha}(T - T_0)$$

where each $\bar{\alpha}$ and corresponding $(T - T_0)$ is taken from a graph like Figure 7.11-1(b).

Units and Unit Conversion

The correct units of the instantaneous and average coefficients are " $^\circ\text{C}^{-1}$ " or " $^\circ\text{F}^{-1}$ " or " $^\circ\text{K}^{-1}$." Typically, the units are stated in the literature as "inch/inch/ $^\circ\text{F}$ " or "cm/cm. $^\circ\text{C}$." Inasmuch as inch/inch cancel each other, the values of

$$\frac{\text{inch}}{\text{inch} \cdot ^\circ\text{C}} = \frac{\text{cm}}{\text{cm} \cdot ^\circ\text{C}}$$

The only change in the value of the coefficients occurs when the change is due to a different temperature unit:

Multiply	by	to obtain
$^\circ\text{F}^{-1}$	1.8	$^\circ\text{C}^{-1}$
$^\circ\text{C}^{-1}$	1.0	$^\circ\text{K}^{-1}$
$^\circ\text{C}^{-1}$	1/1.8	$^\circ\text{F}^{-1}$

7.11.6 Relative Thermal Expansion

The average coefficients of thermal expansion of several metals relative to that of silicon is illustrated in Figure 7.11-2.

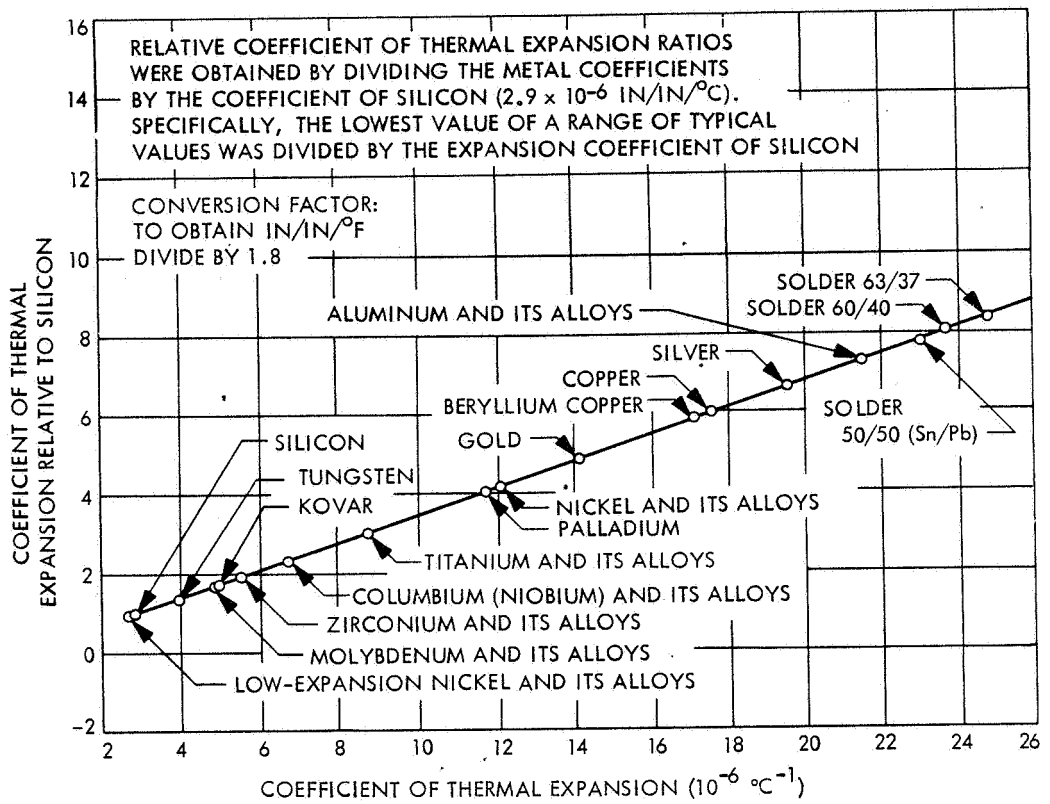


Fig. 7.11-2. Coefficient of Thermal Expansion of Metals Relative to Silicon (Ref. 7.11-1)

7.12 SPECIFIC HEAT AND HEAT CONDUCTANCE

7.12.1 Definitions

The heat capacity at constant pressure is defined as

$$c_p = \frac{dQ}{dT} \quad (7.12-1)$$

where dQ is the increase in stored heat energy in a substance due to an increase in absolute temperature, dT .

The specific heat capacity of a substance is the heat capacity per unit mass. Of special interest to solar cell array design is the heat capacity of crystalline solids, such as metals and semiconductors. From the thermodynamic theory of such solids,

$$c_p = \frac{9\alpha^2 VT}{k} + c_v \quad (7.12-2)$$

where

α = the coefficient of thermal expansion

V = the volume

T = the absolute temperature

k = the compressibility

c_v = the heat capacity at constant volume.

It has been found that experimental data for c_v of many metals can be fitted to

$$c_v = 464.4 \left(\frac{T}{\theta} \right)^3 + aT \quad (7.12-3)$$

where c_v is in units of calories per mole per degree Kelvin. The values of θ and "a" are given for some metals in Table 7.12-1. Eq. 7.12-3 reflects the thermodynamic behavior of metals as follows: the $(T/\theta)^3$ term is the main contributor to the heat capacity at higher temperatures due to crystal lattice vibrations, while at very low temperatures the "aT" term, due to free electrons, is the principal contributor. According to Eq. 7.12-2, c_v and c_p go to zero as

T goes to zero. Eq. 7.12-2 can be used to estimate values of c_p versus temperature when no experimental data are available.

The thermal mass of an object is defined by the product $c_p m$, where m is the total mass of that object.

The thermal conductivity or heat conductivity, k , of a substance is a measure of the transfer of a quantity of heat, Q , during a time interval, t , through a substance of thickness, d , and cross-sectional area, A , due to a temperature difference, ΔT , across the thickness, such that

$$Q = k \frac{\Delta T \cdot A \cdot t}{d}$$

Hence k is a proportionality constant which depends upon the specific material. Metals have the highest heat conductivities of all known materials and silver has the highest heat conductivity of all metals.

7.12.2 Relative Thermal Conductivity

The heat conductivities of some other metals relative to the heat conductivity of silver are given in Figure 7.12-1.

Table 7.12-1. Constants θ and a for Low-Temperature Heat Capacities [Units are chosen so that $c_v = 464.4(T/\theta)^3 + aT$ is in calories per mole per degree Kelvin]

Metal	θ	$a \times 10^4$
Al	419	3.48
Ag	229	1.54
Cu	335	1.78
Pt	233	16.07
Pb	90	7.15
Mg	410	42.1
Sn	185	4.0

From Ref. 7.12.1. Used with permission of McGraw-Hill Book Co.

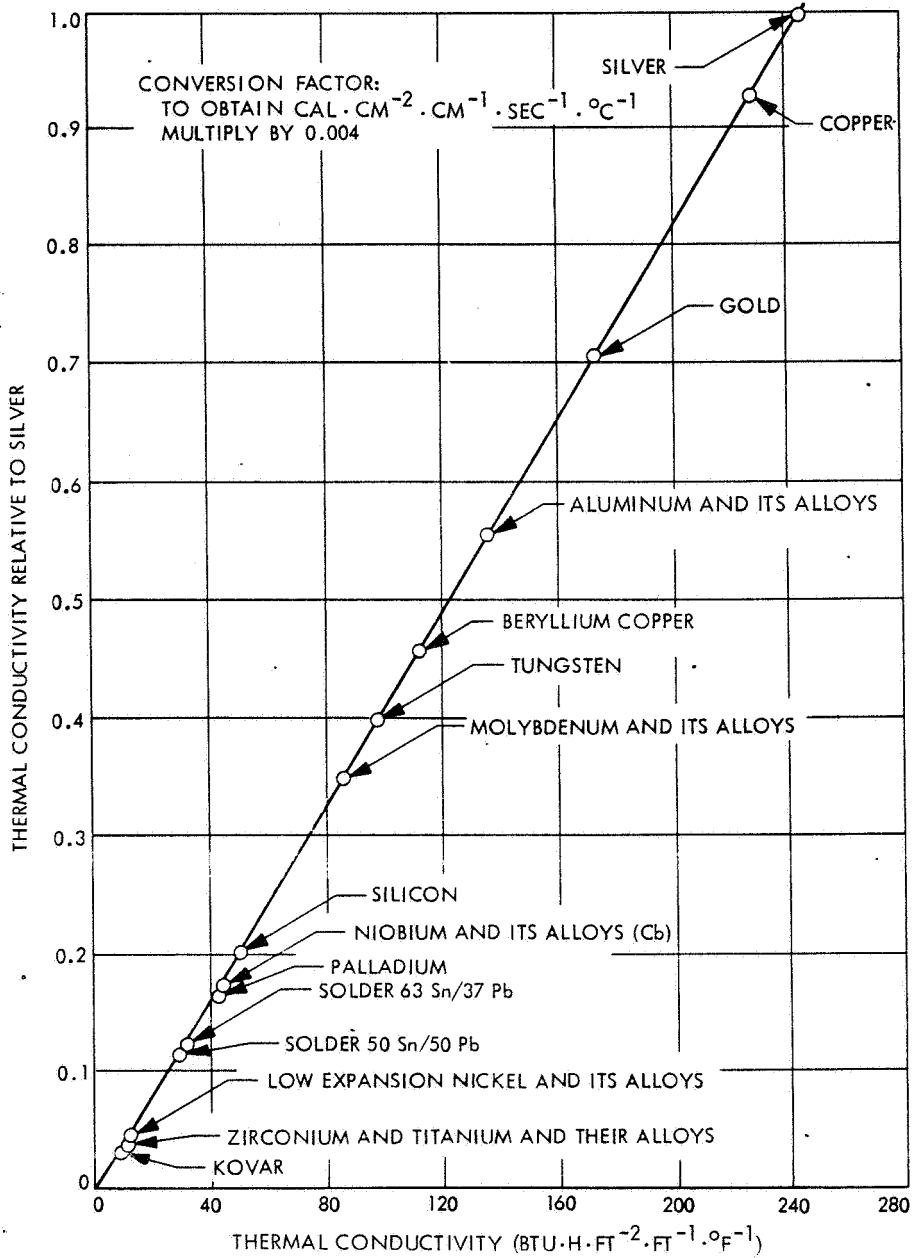


Fig. 7.12-1. Thermal Conductivity of Metals Relative to Silver (Ref. 7.12-2)
(For additional unit conversion factors see Section 7.1
of Volume II.)

7.13 TRANSMISSION, REFLECTION AND ABSORPTION OF LIGHT

7.13.1 Definitions (Based on Ref. 7.13-1)

The radiant solar energy flux (sunlight) incident on the solar cell array front surface is partly reflected from that surface, partly absorbed by it and partly transmitted into deeper layers of the array (through the solar cell covers into the solar cells).

When the incident flux is reflected from a smooth, polished surface, the reflected beam is referred to as specular reflection. Reflections from rough surfaces are termed diffuse. The ratio of the reflected radiant flux to the incident radiant flux is the reflectance. The same ratio for a specific wavelength of the flux is the spectral reflectance. The ratio of the reflected radiant flux to the radiant flux incident upon a specific surface is called the reflectivity of that surface. In practice, the terms reflectance and reflectivity are used interchangeably.

The ratio of the transmitted radiant flux (at some distance measured from the front surface of the transmitting media) to the flux that entered the media is called the transmittance or internal transmittance. Frequently, the front-surface reflectance is not subtracted from the transmittance. Transmission of flux may be specular or diffuse; in the latter case it is called scattered. The ratio of the transmitted to the entered flux at a specific wavelength is termed spectral transmittance. Transmittance at normal incidence through a flat plate is defined as transmissivity or percent transmission. In practice, the terms transmittance and transmissivity are used interchangeably.

Electrical transmittance is sometimes used to denote changes in the cover transmittance as determined by solar cell short-circuit current output.

The ratio of the absorbed radiant flux to the incident flux is called the absorptance. The same ratio at a specific wavelength is the spectral absorptance. In practice, the terms absorptance and absorptivity are used interchangeably. The common logarithm (base 10) of the absorptance is termed the absorbance (or spectral absorbance, respectively). The absorptance in a homogeneous media increases with thickness according to

$$I = I_0 e^{-at}$$

where I is the flux density at a distance, t , from the front surface at which the density of the entered flux is I_0 . The constant $e = 2.718\dots$ and " a " is the absorption coefficient (" a " is a function of wavelength). The wavelength at which the absorptance changes abruptly (in silicon at about $1.2 \mu\text{m}$) is referred to as the absorption edge.

The absorptance, α , reflectance, ρ , and transmittance, τ , are related such that at any point in a material under thermodynamic equilibrium and at any wavelength or any wavelength band

$$\alpha + \rho + \tau = 1$$

7.14 EMISSION AND ABSORPTION OF HEAT

7.14.1 Definitions

The radiant flux emitted per unit area by a body or by a source is called the emittance. The emittance per unit wavelength band is termed spectral emittance, and when integrated over all wavelengths, total emittance. The radiant flux emitted into all directions (especially from a diffusing or rough surface) per unit area is referred to as hemispherical emittance. The radiant flux emitted per unit area, Q_R , is related to the absolute temperature, T , by Stefan's law:

$$Q_R = \epsilon \sigma T^4$$

where ϵ is the emissivity (defined below) and σ is the Stefan-Boltzmann constant (see Section 7.2, Volume II).

The emissivity is the ratio of the radiant flux emitted by a surface ("gray body") to the flux emitted by a perfect or ideal (so-called "black body") radiator. The emissivity may be total or spectral. Most of the heat rejected from a solar cell array operating at approximately 300°K (27°C) is emitted in the wavelength range between 2 and 20 μm .

Of particular interest to solar cell array designers is the "alpha-over-epsilon ratio," α/ϵ , where α is the solar absorptance and ϵ the hemispherical emittance. The solar absorptance is defined as the spectral absorptance (see Section 7.13.1) integrated over the solar spectrum (see Section 2.4.2).

7.15 MAGNETIC PROPERTIES

7.15.1 Definitions*

All metallic alloys containing iron, nickel, and cobalt such as Kovar or Invar are "magnetic." A "magnetic" material is a loosely defined term which indicates that such a material becomes measurably (in an engineering sense) magnetic when it is subjected to an external magnetizing force. This magnetizing force may result from a current-carrying electric conductor. The degree to which a material becomes "magnetic" in response to a given magnetizing force is expressed by the material's magnetic susceptibility, χ .

For magnetic design work, the quantity of permeability, μ , is generally used to relate the magnetic flux density, B , created in a piece of magnetic material which is subjected to an externally applied magnetizing force, H , such that

$$B = \mu H$$

The permeability, μ , (and similarly χ) varies with the applied magnetization, H , up to its saturation value, μ_m . The value of μ also changes with temperature, decreasing with increasing temperature up to the Curie temperature, or Curie "point." Above the Curie temperature, materials essentially lose their magnetic properties.

The magnetic susceptibility, χ , is related to the permeability, μ , such that

$$\mu = \mu_0 + \chi$$

where μ_0 is the permeability of empty space. In vacuum, $\chi = 0$, $\mu = \mu_0$. Values of μ can be obtained by determining the slope of a magnetization curve on a B-H diagram, as shown in Figure 7.15-1. This figure displays the resulting flux density, B , of the magnetism that is induced in a material by an external magnetizing force, H , when the magnetizing force alternates cyclically and is at least as great as to cause the induced magnetism (magnetic induction) to saturate in the positive and negative directions. If the magnetizing force, H , were returned to and left at zero after having magnetically saturated the material to B_s , the material would retain some magnetism, as denoted by the retentivity, B_{rs} .

The magnetizing force required to reduce induced magnetism to zero ($B = 0$) is referred to as the coercive force, H_{cs} . Magnetically "hard" materials, used for permanent magnets, exhibit relatively large values of H_{cs} . Magnetically "soft" materials, used for transformer cores and similar applications, exhibit relatively small values of H_{cs} .

The area enclosed by the hysteresis loop is proportional to the energy required to remagnetize the material in the opposite direction. This energy is dissipated in the form of heat in the material.

7.15.2 Magnetic Materials on Solar Cell Arrays

The two magnetic materials of current interest in solar cell interconnector design are Kovar and Invar. Both of these materials are said to be magnetically "soft" because they retain relatively little permanent magnetism after having been magnetized to saturation in a strong magnetic field.

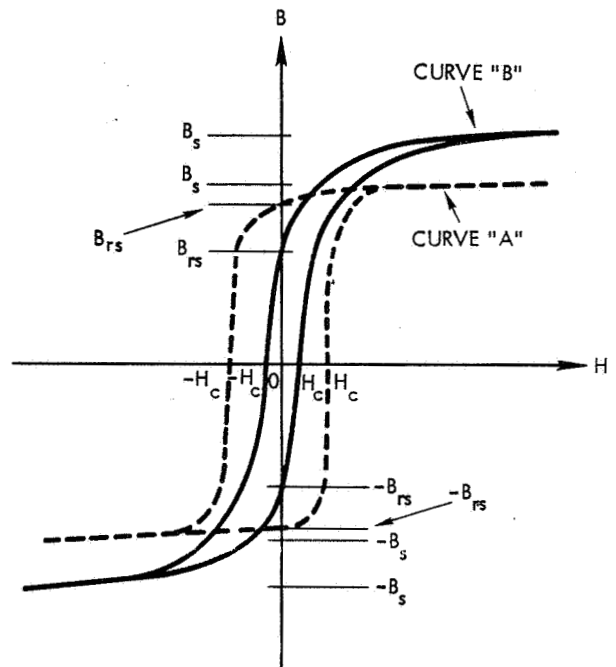


Fig. 7.15-1. Illustration of Hysteresis Loops on B-H Diagram for Magnetically "Hard" (Curve A) and Magnetically "Soft" Materials (Curve B)

*Based on Refs. 7.15-1 and 7.15-2.

7.16 OUTGASSING AND WEIGHT LOSS

7.16.1 Definitions

Organic materials in the space vacuum environment lose volatile components adsorbed on, absorbed in, or otherwise contained in these materials. The rate of outgassing and the total quantity of material outgassed depends upon the mobility of the outgassing substances through the material, the outgassing path lengths, the material temperature, and the time during which outgassing takes place. The total mass of material outgassed is measured by the "weight loss."

Outgassing characteristics of materials are of interest to spacecraft and solar cell array designers because outgassed products may condense on colder surfaces such as solar cell coverglasses and thermal control coatings and, after being irradiated with charged particles and ultraviolet radiation, severely alter the optical and thermophysical properties of these surfaces. Hence, the use of certain high-outgassing materials may be restricted for some spacecraft and array designs, or vacuum-bake procedures prior to launch may have to be implemented.

7.16.2 Test Methods

The currently most acceptable outgassing test method is the Stanford Research Institute (SRI) method. This method was developed under NASA-JPL sponsorship and consists of the following equipment and test procedures (Ref. 7.16-1):

- Preconditioning of the test samples (of about 0.1 to 0.3 gram mass) for 24 hours in ambient air having 50 percent relative humidity

- Weighing of the test samples and collector plates (see below)
- Placement of the test samples into cavities in a copper bar such that all volatiles must escape through an exit port (a 6.3-mm diameter hole) in a copper cover which is placed over each cavity, and placement of a chromium-plated collector plate in direct line of sight of the exit port at a distance of 12.5 mm from the exit port
- Evacuation of the test apparatus and heating of the copper bar with test specimens to 125°C for 24 hours while maintaining the collector plates at 25°C
- Reweighing of the test samples and determining the percentage of the total mass loss (TML)
- Reweighing of the collector plates and determining the percentage of the mass of the collected volatile condensable materials (CVCM) based on the initial mass of the samples.

The test results obtained by this (and any other) method depend to a large degree upon the mix ratios of two-part adhesives and their curing cycles.

REFERENCES (CHAPTER 7)

- | | | | |
|-------|--|--|--|
| 7.1-1 | Data Sheet, "Brush High Conductivity Beryllium Copper Strip," The Brush Beryllium Company, Cleveland, Ohio, July 1963. | 7.2-1 | "DuPont Kapton Polyimide Film," Technical Information Bulletin H-1. |
| 7.1-2 | D. R. Lott, "Solar Array Flexible Substrate Design Optimization, Fabrication, Delivery, and Test Evaluation Program," Final Report, NAS 8-28432, Report No. LMSC-D384284, Lockheed Missiles and Space Co., Inc., March 1975. | 7.2-2 | "DuPont Teflon FEP Fluorocarbon Film," Technical Information Bulletin T-1C. |
| 7.1-3 | "Selection, Engineering and Fabrication of CarTech Alloys for Electronics, Magnetics and Electrical Applications," product and applications brochure published by Carpenter Technology Corporation, Reading, Pennsylvania, 1965. | 7.2-3 | Corning Glass Works Product Information Sheet on Fused Silica Code 7940. |
| 7.1-4 | "Unispan 36, Low Thermal Expansion Alloy," product and applications brochure published by Universal-Cyclops Specialty Steel Division, Cyclops Corporation, 1968. | 7.2-4 | E. U. Condon and H. Odishaw, <u>Handbook of Physics</u> , 2nd Edition, McGraw-Hill, 1967. |
| 7.1-5 | B. S. Lement, C. S. Roberts, and B. L. Averbach, "Determination of Small Thermal Expansion Coefficients by a Micrometric Diletometer Method," <u>The Review of Scientific Instruments</u> , Vol. 22, No. 3, 1951. | 7.2-5 | Corning Glass Works Product Information Sheet IC-31, July 1961. |
| 7.1-6 | Westinghouse Technical Data Bulletin No. 52-460, Westinghouse Electric Corporation, Materials Manufacturing Division: Metals Plant, Blairsville, Pennsylvania 15717, March 1965. | 7.3-1
7.5-1
7.6-1
7.9-1
7.11-1 | } R. K. Yasui, "Summary of Work Accomplished in the Area of Photovoltaic's Supporting Development," JPL Document 320-31601-2-3420. |
| 7.1-7 | "How to Make Out with Moly," Schwartzkopf Development Corporation, Holliston, Massachusetts, Brochure and Guide to the Use of Molybdenum. | 7.12-1 | E. U. Condon and H. Odishaw, <u>Handbook of Physics</u> , McGraw-Hill, 1958. |
| 7.1-8 | "Alloy Digest," published by Engineering Alloys Digest, Inc., Upper Montclair, New Jersey, June 1971. | 7.12-2 | R. K. Yasui, "Summary of Work Accomplished in the Area of Photovoltaic's Supporting Development," JPL Document 320-31601-2-3420. |
| 7.1-9 | R. A. Marzek, "Survey and Study for an Improved Solar Cell Module, Document 900-270, Jet Propulsion Laboratory, August 1969 | 7.13-1 | E. C. Condon and H. Odishaw, <u>Handbook of Physics</u> , 2nd Edition, McGraw-Hill, 1967. |
| | | 7.15-1 | D. G. Fink, <u>Standard Handbook for Electrical Engineers</u> , 10th Edition, McGraw-Hill, 1969. |
| | | 7.15-2 | "Cartech Alloys for Electronic, Magnetic and Electrical Applications," Product Information published by Carpenter Technology Corporation, Reading, Pennsylvania, 1965. |
| | | 7.16-1 | W. A. Campbell et al., "Outgassing Data for Spacecraft Materials," NASA TN D-8008, Goddard Space Flight Center, 1975. |

CHAPTER 8
DESIGN SYNTHESIS AND OPTIMIZATION

CONTENTS

	Page		Page
8.1 Development of Design Requirements and Criteria	8.1-1	8.5 Thermal Design	8.5-1
8.1.1 Definitions	8.1-1	8.5.1 Temperature Control	8.5-1
8.1.2 Design Requirements and Criteria	8.1-1	8.5.2 High-temperature Control	8.5-2
8.1.3 Mission Impact on Array Design	8.1-1	8.5.3 Design Sensitivity	8.5-2
8.1.4 Design Interfaces	8.1-4	8.6 Conceptual Array Design	
8.1.5 Documentation	8.1-6	8.6.1 Array Sizing	8.6-1
8.1.6 Realistic Requirements	8.1-6	8.6.2 Configuration Selection	8.6-3
8.1.7 Realistic Criteria	8.1-6	8.7 Electrical Design	8.7-1
8.1.8 Policy Constraints	8.1-7	8.7.1 Series Connection of Solar Cells	8.7-1
8.2 Design and Optimization	8.2-1	8.7.2 Parallel Connection of Solar Cells	8.7-1
8.2.1 The Design Process	8.2-1	8.7.3 Solar Cell Array Layout	8.7-2
8.2.2 The Optimization Process	8.2-2	8.7.4 Interconnectors and Wiring	8.7-2
8.2.3 Optimization Criteria	8.2-2	8.7.5 Hot-Spot Design Considerations	8.7-4
8.2.4 Design Review	8.2-2	8.7.6 Designing for Reliability	8.7-4
8.3 Radiation Shielding Design	8.3-1	8.8 High-voltage Arrays	8.8-1
8.3.1 The Environment	8.3-1	8.8.1 Requirements	8.8-1
8.3.2 Determination of Shielding Thickness	8.3-1	8.8.2 Design Practices	8.8-1
8.3.3 Shielding by the Solar Cell	8.3-2	8.9 Electrostatic Shielding Design	8.9-1
8.3.4 Balancing Front- and Back Side Shielding	8.3-3	8.9.1 Requirements	8.9-1
8.3.5 Absorbed Dose in Cover	8.3-3	8.9.2 Design Practices	8.9-1
8.3.6 Shielding against Low-energy Protons	8.3-3	8.10 Magnetic Design	8.10-1
8.4 Optical Design	8.4-1	8.10.1 Magnetic Forces	8.10-1
8.4.1 Ultraviolet Filter Cut-on Wavelength	8.4-1	8.10.2 Magnetic Cleanliness	8.10-1
8.4.2 Solar Cell Antireflecting Coatings	8.4-2	8.10.3 Magnetic Dipole Moment	8.10-1
8.4.3 Non-normal Incidence Effects	8.4-2	8.10.4 Design Practices	8.10-2
		References	8. R-1

TABLES

8.1-1 Electrical and Optical Design Requirements Derived from Natural and Induced Environments and from Interface Constraints	8.1-2	8.3-1 Variations in Fused Silica Shielding Thickness with Actual Thickness	8.3-2
8.1-2 Physical and Thermal Design Requirements Derived from Natural and Induced Environments and from Interface Constraints	8.1-3	8.3-2 Variation in Shielding Thickness with Material	8.3-2
8.1-3 Design Criteria	8.1-4	8.3-3 Solar Cell Base Thickness Shielding Effectiveness for Particulate Irradiation Incident on the Cell Back Side	8.3-3
8.1-4 Primary Design Considerations for Certain Classes of Space Missions	8.1-5	8.5-1 Heat Capacitances of Different Metals	8.5-2
8.1-5 Mission Parameters of Significance to Arrays in Radiation Environments	8.1-5	8.5-2 Flat Solar Panel Temperature Variation as a Function of Orbit Altitude	8.5-4
8.1-6 Solar Cell Array Design Interfaces	8.1-6	8.6-1. Packing Densities for 2 x 2 cm and 2 x 4 cm Solar Cells	8.6-2
8.2-1 Typical Assignment of Design Activities	8.2-1	8.6-2 Relative Area of Faceted Cylinders	8.6-5

FIGURES

8.3-1	Typical Solar Cell Shielding	8.3-1	8.6-1	Comparative Output of Five Different Array Configurations as a Function of Sun Angle	8.6-3
8.3-2	Description of Alternate Approaches	8.3-2			
8.3-3	Cell Stack of Approach I, Example	8.3-3	8.6-2	Aspect Ratios of Paddle Mounted Arrays, Shadowing Effects Ignored	8.6-4
8.3-4	Design for Approaches II and III, Example	8.3-4			
8.3-5	Adhesive Fillets in Approach III	8.3-4	8.6-3	Aspect Ratios of Conical Solar Arrays	8.6-4
8.4-1	Relative Output as Function of Wavelength of Covered Solar Cells in Sunlight	8.4-1	8.7-1	Solar Cell Array Layout Dimensions	8.7-3
8.5-1	Solar Cell Array Temperature as a Function of Solar Distance	8.5-3	8.10-1	A Circular Loop Carrying a Current, I , with a Point, $P(r, \theta)$, off the Axis of Symmetry	8.10-1

CHAPTER 8

DESIGN SYNTHESIS AND OPTIMIZATION

Design synthesis is the process by which a new design is evolved. The evolution of the design is comprised partly of making judicious selections from known materials, components and assembly processes, and partly of making new, often unique, contributions to the state of the art. That part of the design process that deals with selections is mostly a result of tradeoff studies and already constitutes some form of design optimization. However, contributions to the state of the art are mostly of a creative, inventive nature.

This chapter was written not only to provide the designer with some fundamental concepts that permit him to conduct his own tradeoff studies, but also to

provide some stimulus for evolving currently unknown, future approaches.

The first step in the solar cell array design synthesis process is to define the requirements and criteria which the finished product is to meet. A significant portion of the design requirements are derived in Section 8.1 from the anticipated array environment (discussed in Chapter 2). The next step is to select from the available parts, materials, and components (discussed in Chapters 3 through 7) those which most likely will meet the array design objectives. The process of selecting and assembling the appropriate array building blocks and estimating their performance when integrated into an entire array is the subject of the remaining sections of this chapter.

8.1 DEVELOPMENT OF DESIGN REQUIREMENTS AND CRITERIA

8.1.1 Definitions

Design criteria and requirements are concrete technical statements according to which the design will ultimately be analyzed, tested, and evaluated. Typically, requirements are derived from natural or induced environments and from interface constraints, while criteria are based on value systems that are intended to relate to success or failure. Design requirements are the basic elements which delineate the designers task. Requirements come from several different sources: the natural environment (vacuum, radiation, etc.), the induced environment (temperature, vibration, etc.), and from interfaces (power, weight, reliability, etc.). Not all of the "original" requirements are directly useful to the designer. For example, to withstand a 60-minute solar eclipse time may be a "real" requirement but this must be translated for the array designer and test engineer into "x" numbers of temperature cycles between $-y^{\circ}$ and $+z^{\circ}$ C. Furthermore, what "withstand" means in terms of measurable or inspectable pass/fail criteria must be defined. The process of translating, or converting, the "real" requirements into "design" requirements and design criteria is the subject of this section.

8.1.2 Design Requirements and Criteria

Essentially all solar cell array design requirements are performance related. They may be classified into two large groups:

- Performance requirements which affect the electrical design (including solar cell and cover selection) and the array electrical performance under stipulated operating conditions
- Design and construction requirements which affect the array mechanical design and performance.

Typically the requirements sections of solar cell array specifications are divided into two such groups. Optical and thermal design requirements do not fit well into any of these two categories and perhaps, therefore, are occasionally missed. In this handbook, the optical design aspects (mainly transmission) are arbitrarily grouped with the mechanical requirements. Tables 8.1-1 and 8.1-2 provide check lists for the more significant design requirements as they may appear for a large spacecraft project with many diversified payloads, while Table 8.1-3 gives a list of typical design criteria.

Design criteria may clearly, potentially, or not at all affect array performance. Therefore, such criteria, both in their development and in their justification, will always be surrounded by controversy. Nevertheless, they must be established and they are as "real" as any other requirements in terms of their impact on parts procurement, fabrication and rework cost, quality assurance buy-off, and delivery dates. Typical examples of the more frequently encountered design criteria are discussed in Table 8.1-3.

8.1.3 Mission Impact on Array Design

The overall mission plan typically provides a major set of design requirements and design constraints for the solar cell array design, as discussed in the following.

• Satellite Orientation

Non-oriented, tumbling satellites require solar cells on essentially all surface areas so that the solar cell array power output level remains reasonably constant for all angles of satellite orientation. If a body-mounted array cannot provide sufficient power, a paddle configuration may be used.

Earth-pointing orbiters require either body-mounted arrays or flat, sun-oriented arrays. Frequently, semiorientation is used where the angle of incidence varies somewhat throughout the year and normal incidence occurs only twice a year, if at all.

Inertially stabilized satellites and probes, using earth-pointing antennas, may have either body-mounted, paddle wheel, fixed flat panel, or sun-oriented flat panel solar cell arrays. Most synchronous orbit communication satellites launched prior to 1976 were spin stabilized and carried cylindrical solar cell arrays. Many newer types of synchronous orbit communication satellites designed for launches during the late 1970's and 1980's are of the three-axis stabilized type and will use full or semisun orientation of their solar cell arrays.

Interplanetary probes may be of the spin-stabilized or three-axis stabilized type. Spin stabilized probes can use either body-mounted or paddle arrays, while three-axis stabilized probes can use either (deployable) fixed flat arrays or fully (or semioriented) flat arrays.

• Orbital Parameters

The orbital parameters determine the solar cell damaging charged particle radiation flux and the thermal cycling stress on the array assembly. Next to the array configuration and orientation, both of these parameters constitute the most significant design considerations for the array. Table 8.1-4 provides the details for the most significant environments for various classes of missions.

Additional mission parameters of significance to solar cell arrays for which radiation is a primary consideration are related to the mission profile, also called the mission time line, as indicated in Table 8.1-5.

Table 8.1-1. Electrical and Optical Design Requirements Derived from Natural and Induced Environments and from Interface Constraints

Variable	Source	Conversion Method	Design Requirement
Power Output Power Level Power Profile Voltage Level Voltage Profile	Power system load and energy balance analysis (9.0), * distribution losses, battery charge/discharge voltage analysis, load equipment voltage range	Used directly to specify design requirements	Power and voltage levels through one orbit and throughout life
Illumination Intensity Configuration Orientation Shadowing Solar Distance Solar Constant	Mission analysis, spacecraft and array configuration	Configuration and orientation determine illumination level (2.6, 8.7); shadowing determines fraction of array inoperative (9.3); solar distance and solar constant determine illumination level (2.4)	Illumination variables define the operating conditions for which the array power output design requirements are specified
Particulate Radiation Trapped Electrons Trapped Protons Solar Flare Protons Low Energy Protons Other Man-made }	Natural environment (2.5) Usually customer-specified	All radiation components, except low energy protons, are converted into solar cell damage-equivalent 1-MeV electron fluence and into ionizing dose for cover and adhesive transmission degradation (2.5, 3.3). Low energy proton damage is assessed separately (3.3)	Damage equivalent 1-MeV fluences for various front and back shield thicknesses and masses. Ionizing doses (rads) for cell covers, cover adhesive, and other exposed materials. Both require oversizing of array
Ultraviolet Radiation	Natural environment (2.4)	Cover adhesive, and other material degradation test results are used directly (2.4, 8.4, 11.8, 11.13). UV intensity is adjusted for illumination intensity variables (see above)	Light transmission degradation requires oversizing of array
Meteoroids	Natural environment (2.3)	Engineering estimates (2.3)	Usually not considered
Deposits	Contamination, due to outgassing of spacecraft materials, or due to rocket expulsions (2.3)	Test results and/or engineering estimates based on observed spacecraft anomalies	Program peculiar, causes typically 0 to 2 percent power loss, sometimes applied only locally. May restrict use of strongly outgassing materials
Lifetime Useful Life Wearout Life End of Life	Mission analysis	Used directly in the assessment of time, fluence, and dose dependent degradation mechanisms	Defines a condition for which the array power output design requirement is specified
Reliability	Overall system reliability assessment and allocation to array. Given for a specified time after launch	Used directly to determine required circuit redundancy and array oversizing, based on failure rates and failure effects	Defines a condition for which the array power output design requirement is specified
Distribution Losses Interconnectors Wiring and Cabling Blocking Diodes	Peculiar to design of power system, distribution system, and solar cell array	Used directly in array sizing, either in form of series resistance or voltage drop	Defines a condition for which the array power output design requirement is specified
Electrical Grounding Radio Interference Space Plasma	Electromagnetic compatibility analysis	Engineering judgments based on analysis, test data, and experience	Grounding straps, metallic substrates, electrical RF impedance

* Numbers in parentheses refer to applicable handbook sections.

Table 8.1-2. Physical and Thermal Design Requirements Derived from Natural and Induced Environments and from Interface Constraints

Variable	Source	Conversion Method	Design Requirement
<p>Temperature</p> <p>Operating Eclipse exit On-station Transfer orbit</p> <p>Nonoperating Launch Acquisition Eclipse minimum</p>	<p>Determined partially by illumination intensity variables and partially by design (2.4, 8.7, 9.6).*</p>	<p>Used directly as follows:</p> <p><u>Operating</u>: Affects power output analysis.</p> <p><u>Nonoperating</u>: Eclipse minimum temperature, together with on-station operating high temperature, determines array fatigue life (9.8). For thermal analysis see 9.6. For temperature cycling test results see 11.11.</p>	<p>Operating temperature defines a condition for which the array power output design requirement is specified. May in turn require specifications of α, ϵ. Temperature cycling requirement must be met by cover/adhesive/cell/adhesive/substrate assembly, cell interconnectors, and solder (weld) joints, diodes, and other materials. Extreme high or low temperature may limit material selection.</p>
<p>Pressure Altitude</p>	<p>Rate of ascent analysis based on booster thrust and satellite weight (2.1).</p>	<p>Depressurization rate analysis, high voltage analysis and tests.</p>	<p>Array substrate venting (honeycomb, box beams, etc.) and electrical insulation (arcing at low pressure).</p>
<p>Humidity</p>	<p>Handling and storage requirements imposed by customer.</p>	<p>Engineering estimates based on test data.</p>	<p>May require use of humidity resistant solar cells or may require controlled humidity protection of solar cells and array.</p>
<p>Launch Environment</p> <p>Acceleration Mechanical Shock Vibration Acoustic Field</p>	<p>Structural dynamic analyses. Results depend upon launch vehicle and specific satellite/array design.</p>	<p>Engineering judgment based on test data.</p>	<p>Affects mainly array structure. May limit freedom in solar cell stack mounting, interconnector design, wire and cable routing and bonding, and layout (damping pads).</p>
<p>Mass</p> <p>Weight Center of Mass Moment of Gyration Stiffness</p>	<p>System analyses of mass properties, attitude control, interactions, stability, etc.</p>	<p>Analysis and allocation of requirements.</p>	<p>Affects mainly array structure. For array designer, specifies maximum weight. May also limit mass distribution on array.</p>
<p>Magnetic</p> <p>Magnetic Moment Magnetic Cleanliness</p>	<p>Attitude control and experiment interfaces.</p>	<p>Engineering estimates based on magnetic analysis and tests.</p>	<p>May limit freedom of string layout, require back wiring or preclude use of magnetic materials (example: Kovar interconnectors)</p>
<p>Miscellaneous</p> <p>Transducers Temperature Other</p> <p>Test Points Output Dark I-V</p> <p>Handling Storage Transportability Repairability Transient Overvoltage Schematic Diagram Insulation Resistance Voltage Breakdown</p> <p>Identification and Marking</p>	<p>Various overall system or subsystem analyses and interface requirements.</p>	<p>Used directly or are based on engineering judgment.</p>	<p>Usually imposed in response to specific requests from interfacing subsystems or operational procedures.</p>

*Numbers in parentheses refer to applicable handbook sections.

Table 8.1-3. Design Criteria

Criteria	Category ^a
1. Design-Related	
Potential Failure Modes and Effects	F
Circuit Fault Isolation	F
Redundancy	F
Design Margin	F
Electrical	F
Mechanical	F
Thermal	F
Electrical Layout	F
Defects Induced by Environmental Testing	D
Cell and Cover Cracking	D
Interconnect and Wire Breakage	D
Bond Separations	D
Testability (test points, connectors, etc.)	D
Handleability (handling fixtures, protective covers, etc.)	D
Protrusions (snagging clothing)	D
Packing Density	D
Repairability	D
Manufacturability (parts size, complexity, etc.)	D
Insulation Resistance and Voltage Breakdown	F
2. Workmanship (see Section 11.4 for details)	
Solder Fillets	D
Welding Electrode Imprints	D
Wire Wrapping on Terminals	D
Coverglass Positioning over Solar Cell	D
Wire Routing and Lead Dressing	D
Wire Bonding to Substrate (size, shape, etc.)	D
Cell Interconnector Deformations	D
Material and Parts Discolorations	D
Adhesive in Cell-to-Cell Gaps	D
3. Imperfections	
Coverglass Edge and Corner Chips	D
Cracked Covers	D
Solar Cell Edge and Corner Chips	D
Cracked Solar Cells	D
Thermal Control Coating Scratches	D
Pinholes in Cover or Cell Filter Coatings	C
Cell Interconnector Deformations and Discoloration	D
4. Cleanliness	
Solder Flux Residue on Parts	D
Solder Flux Residue on Coverglass	D
Adhesive on Coverglass	D
Dust and Dirt on Coverglass	D
Finger Prints on Coverglass	D
Finger Prints on Thermal Control Paint	D

^aF = Functional
D = Decisionable (i.e., either functional or cosmetic, depending upon specific conditions)
C = Cosmetic

• Power Level

The general end-of-mission power level to be provided by the array determines the general array concept. Body-mounted arrays for today's commonly used launch vehicles are limited to less than 1 kW output. Array designs that must provide power levels in excess of what can be provided by a body-mounted array must be of a deployable nature. Power levels between approximately 0.5 and 2 kW can be handled with relatively simple deployable arrays; for higher power levels the complexity of the mechanical array design increases with increasing array size.

• Mission Duration

For missions during which considerable charged particle doses are encountered or during which the array is subjected to a very large number of severe thermal cycles, the mission duration (design life) becomes a significant design criteria. The 1976 state of the art indicated approximately the following design life limitations that can be achieved with high confidence:

- Geosynchronous Orbits - 7 years
- Near-Earth Orbits - 2 years
- Radiation Belt Orbits - 2 years

Mission durations of significantly less length than these indicated limitations permit greater latitude in material choices, design practices and hardware production methods. However, mission durations of equal or greater length than stated above require more careful control of materials and stringent control of design practices and production processes.

8.1.4 Design Interfaces

The successful solar cell array designer is a successful worker of interfaces. Table 8.1-5 provides a check list of the typical interfaces which may be required and which may impose design requirements or constraints on the array. Some of the more significant interfaces are discussed below.

Substrate Interface

The substrate should provide a surface that accommodates good adhesive bonding of the cell and a support that prevents deleterious flexure of the cells. The material and design should also be selected with consideration for desired structural properties and the total weight penalty to the spacecraft. Consideration should be given to the nature and bonding of the dielectric insulating layer with respect to stability and integrity, as dictated by mission requirements.

The substrate supporting the interconnected solar cells is frequently of aluminum- or fiberglass-faced honeycomb. Attention should be given to matching the thermal expansion coefficient of the substrate and the silicon solar cells. Materials such as fiberglass, and some plastics used as facing for a honeycomb substrate, have the advantage of thermal expansion properties compatible with those of silicon and usually eliminate the need for additional electrical insulation.

Table 8.1-4. Primary Design Considerations for Certain Classes of Space Missions

Mission Class	Altitude of Heliocentric Distance	Trapped Charged Particles	Solar Flare Protons	Low Energy Protons	Ultra-violet Radiation	High Temperature	Low Temperature	Temperature Cycling
Geosynchronous Orbits	38.5×10^3 km	X	X	X	X		X	X
Earth Orbits through Radiation Belts	$10^3 - 10^5$ km	X	X	X	X			X
Near-Earth Orbits	$\leq 10^3$ km				X			X
Inbound Probes, Interplanetary	< 1 AU		X	X	X	X		
Outbound Probes, Interplanetary	> 1 AU						X	

Table 8.1-5. Mission Parameters of Significance to Arrays in Radiation Environments

Mission Phase	Effect on Array
Parking Orbit Altitude and Length of Time	When altitude greater than about 3×10^2 km, radiation damage is incurred
Transfer Orbit Altitude and Length of Time	Above 3×10^2 km altitude, radiation damage is incurred
Launch Date	Solar flare proton flux damage
Mission Duration	Accumulated solar cell damage

- Spacecraft attitude control and, where applicable, array orientation requirements, capabilities, and method of operation (including efflux from thrusters).

Launch Vehicle Constraints

The launch vehicle for the mission which the array will power must be taken into account because of constraints it imposes with respect to:

- Total weight limitation for the array
- Dimensional limitations on the launch configuration of the array
- The characteristics of the vibration, thermal, acoustical, and gravitational stresses that will be imposed on the array during launch and separation from the launch vehicle.

Spacecraft Design Constraints

The interface conditions between the solar cell array and other elements of the spacecraft systems should be specified, where possible, by interface definition documentation. It should be demonstrated that both the array and the spacecraft elements with which it interfaces will perform satisfactorily when the specified conditions are met.

It should be demonstrated that the performance of the array will not be adversely affected by the presence or the operation of other spacecraft systems. Factors to be considered include:

- Electrical interfaces with spacecraft electronics and power conditioning equipment
- Shadowing of the array by booms, antennas, or other parts of the spacecraft or the array
- Mechanical interfaces, including stability, rigidity, relative motions, deployment, alignment, and access
- Radiation interfaces with radioactive devices (nuclear power or calibration sources)

If an extendible paddle or oriented array is required, provision must be made for folding or otherwise reducing the array to fit the inside dimensions of a launch vehicle nose cone during launch and for extending the array once it is in space. Depending on the match between the body of the spacecraft and the envelope size, this design requirement may lead to stringent limitations on permissible solar cell array area.

The launch vehicle characteristics also establish a maximum for the weight of the spacecraft for a given trajectory or orbit. Depending on the weight budget for the spacecraft, there may be a stringent constraint on the allowable solar cell array weight. Weight optimization studies dealing with alternate materials for all elements of the array, thickness of coverslides, and total number of cells should be performed if such a condition exists.

Launch typically introduces a severe level of vibrational, thermal, acoustics, and gravitational stresses. Each launch vehicle provides its own peculiar combination of stresses. Testing is recommended to ensure that the launch environment does not reduce solar array performance to an unacceptable level. Likewise, testing is recommended to ensure that the maneuvers up to the achievement of a stable

Table 8.1-6. Solar Cell Array Design Interfaces

Interfacing Design Activity	Nature of Data
Spacecraft	Configuration and size, orientation to sun, shadows and reflections, solar distance
Mechanical	Substrate Size and geometry String layout Unavailable areas and cutouts Weight Methods of Mounting and Deployment
Thermal	Array Temperature Operating Eclipse low temperature Post-launch high temperature During-launch heating Thermophysical Cell operating efficiency Absorptance, emittance Thermal control coatings Deposits (outgassing)
Electrical	Array Output Power levels and profiles Minimum, mean, maximum Beginning/end of life Maximum lower voltage Power quality (ripple, etc.) Bus impedance Interconnections Cabling connectors Circuit arrangement Transducers (temperature sensors, etc.) Wiring and blocking diode losses Fault Isolation and Prevention Blocking diodes Redundancy Electromagnetic Compatibility (EMC) Grounding and bonding Spacecraft charging protection Twisting and shielding of wires Arcing
Management	Cost Development Time Risk
Magnetic	Attitude Control Cancellation of magnetic moments Experiments Nonmagnetic materials
Ground Handling and Test	Provisions for mounting Protective covers and containers Permanent or temporary handling facilities Test points or connectors

orbit (including stage separation and spacecraft antenna and array deployment) do not unduly impair solar array performance.

8.1.5 Documentation

The development of design requirements and criteria is one of the most important aspects of the design process. During the early phases of a design not many numerical design requirements are defined and few, if any, design criteria are available. Therefore, the process of converting the real or natural requirements into design and test requirements is an ongoing process which may well fall within the responsibility of the designer. However, this conversion should be well documented and subjected to review.

During a design review in the latter stages of the design process, the analytical and test results obtained are compared with the "specified" design requirements in a so-called "capability versus requirements" analysis.

8.1.6 Realistic Requirements

Realistic design requirements are those which (a) are indeed necessary to be met by the solar cell array to assure spacecraft mission success as defined in a top-level specification, and (b) which can actually be met within the current or to-be-developed state of the art. Any requirements which call for performance in excess of that needed for mission success are not realistic, no matter how desirable they may be. Mission success is defined here as meeting specified mission objectives, based on predicted performance, under specified operational conditions, including assumed failure modes, probability, reliability, and design margin considerations. Excessive requirements are defined here as unrealistic because they may cause the expenditure of resources for which there is no justification.

Realistic design requirements may also include some requirements which exist but which are neither specified nor known to the design team. It is incumbent on each individual designer to search for such potentially hidden requirements and bring them out in the open for further consideration, especially when mission success could potentially be impaired.

8.1.7 Realistic Criteria

After the array design has been completed to some level (conceptual, preliminary, final, etc.), it must be evaluated against some criteria to permit it to be judged a "good," "adequate," or "inadequate" design. The development and definition of these criteria, then, are equally as important as the design requirements.

Some of the design criteria are clearly derived from design requirements; others are established, frequently arbitrarily, by procuring organizations, specification writers, quality assurance organizations, company standard practices and policies, and frequently by the solar cell array designer himself. The assessment of whether or not design criteria are realistic, that is, whether they assure, impair, or are inconsequential to mission success, is usually much more difficult than is the assessment of design requirements. However, their potential impact on array flight performance, or fabrication cost and schedule may be just as severe or wasteful as in the case of unnecessary design requirements.

8.1.8 Policy Constraints

Certain design practices are constrained by various policies. Applicable policies may be issued by the following organizations:

- Procuring organizations (the customer)
- Project office
- Company.

Typical examples of such policies include the following:

- Military specifications and similar documents for certain materials, components and processes
- Project approved parts lists

- Company quality assurance manuals and workmanship standards
- Company drafting room manuals
- Company electrical and mechanical design manuals
- Company and project oriented procurement policies
- Company and project design review policies.

The designers responsibility is to adhere to such applicable policies and, in case of conflict between specified requirements and restraining policy, bring such conflict to the attention of the appropriate management for proper resolution.

8.2 DESIGN AND OPTIMIZATION

Designing a solar cell array comprises the making of detailed plans according to which the solar cell array will ultimately be fabricated and tested. The adequacy of the design is verified throughout and after the design phase by analysis, test and comparison (similarity) to previously flown hardware. The design process typically requires reiterative selection and arrangement of components and materials and design analysis.

Almost always the process of reiterating a design involves some form of design optimization. The purpose of design optimization may be to truly optimize the overall satellite system, or just the solar cell array, with respect to some definite criteria (such as lowest cost or lowest weight), or it may be to achieve a balance between various design objectives. It should be realized that a well optimized satellite system may lead to a highly nonoptimized solar cell array design. Therefore, it is incumbent on the array designer to interface thoroughly and frequently with the overall system designers, as well as other involved subsystem designers, to assure that the results of any array design or redesign activities meet, first of all, the overall satellite system design objectives and, only secondarily, to optimize, in consonance with the overall system, the array design.

8.2.1 The Design Process

The design process itself may be broken down and analyzed according to the following criteria by:

- Design phase (level of design detail)
- Design personnel
- Design specialty.

The analysis of the design process according to design phase is typically as follows:

- Conceptual Design
A new array design for a newly conceived mission is created; tradeoff studies involve concepts rather than precise answers.
- Preliminary Design and Design Optimization

Solar cells and covers are selected and a detailed array design evolves on paper; design optimization and tradeoff studies involve more accurate analyses.

- Final Design and Analysis

The solar cell layout is definitized; all remaining components and materials are selected. The performance of the final design is predicted accurately and its functional adequacy is demonstrated by rigorous analyses and exploratory tests.

- Product Design

Components, materials and fabrication and assembly processes are specified in conjunction with production equipment designs. Production drawings are prepared.

- Design Verification

Test procedures are prepared and the adequacy of the hardware design is demonstrated by formal verification test and confirmed by previous flight experience of similar hardware.

A conceptual, creative solar cell array design phase does not occur on each project: frequently the preliminary design phase involves redesign and adaptation of already designed and qualified hardware to new or redefined spacecraft missions, or cost reduction (value engineering) efforts.

Subdivision of the design process by design personnel considers that typically different personnel (residing in different skill centers of a functional organization) are involved in different design activities as shown in Table 8.2-1.

Table 8.2-1. Typical Assignment of Design Activities

Design Activity	Design Specialists
Definition of design requirements, design criteria and design constraints	Mission planners, system designers and others
Designing the array	Creative design engineers
Analysis and computation	Analysts and mathematicians
Product design	Packaging engineers and draftsmen
Verification testing	Test engineers and technicians
Material, component, and process selection	Materials and process engineers and components engineers
Documentation	Specification and procedure writers
Design review	Senior engineers and analysts with systems experience

Subdivision of the design process according to areas of technological specialty may be as follows:

- Radiation effects
- Optical design
- Thermal design
- Electrical design
- Mechanical design.

The design process is described in this handbook utilizing subdivision according to technology. Sections 8.3 through 8.10 provide the details of the various design activities.

8.2.2 The Optimization Process

Design optimization is a continuously ongoing process which is particularly important during the early (conceptual) design phase of a project. Frequently not recognized as such, design optimization is a direct result of informal design critiques that take place between interfacing design team members. Often, informal design critique leads to significant design improvements (i. e., design optimization).

Design optimization activities may also result from the findings of formal design reviews, customer redirections, improvements made in components and materials by suppliers, and from new research and development efforts undertaken elsewhere.

8.2.3 Optimization Criteria

Solar cell array optimization criteria are almost always dictated by overall spacecraft systems requirements and design constraints. Throughout a complete sequence of spacecraft design phases, the solar cell array designer can expect to be involved in any of the design, test, and documentation activities described in this handbook and be called upon to perform, or at least contribute to, various tradeoff studies. The results of these tradeoffs, usually a number of "point" designs, are then used in a decision-making process which results in the selection of an "optimum" design solution.

Only relatively infrequently are continuously varying design parameters developed and their functional characteristics investigated for points of maxima or minima that would reflect an optimized design in a mathematical sense.

Design optimization criteria of significance to the solar cell array designer may include the following:

- Power output at significant points in orbit (such as at maximum solar distance, worst-case off-pointing, or end-of-life)
- Array mass
- Array size
- Array cost
- Development time and risk factors
- Reliability.

8.2.4 Design Review

Formal design reviews are typically held to examine a design in detail after a given design phase has been completed. Each project has at least one

major, formal design review that is held after completion of the major design activity and prior to fabrication of assembly tooling and flight hardware. When necessary, this major design review may be held in several separate parts to facilitate scheduling of long-lead items (items requiring long ordering or delivery periods).

The purpose of formal design reviews is to have the design critiqued by a relatively large number of senior specialists who understand both the unit (component) aspects of the solar cell array as well as the systems implication. Typical, specific items of the design to be examined are as follows:

- Basic Design Objectives

- Operational mission
- Mission reliability
- Functional modes and characteristics
- Physical characteristics (size, weight, c.g., etc.)
- Power output under various conditions
- Environmental extremes
- Fail safe.

- Design Implementation

- Functional flow (block) diagrams
- Equipment specifications
- Test specifications
- Fail-safe and redundancy provisions
- Assessed reliability (compared to apportionment)
- Drawings, structural and packaging
- Drawings, schematics
- Measurements data
- Parts, materials and processes lists
- Qualification test data.

- Supporting Arguments

- Description of alternate designs
- Tradeoff analyses
- Interface compatibility analyses
- Tolerance accumulation analyses
- Use of preferred parts, materials and processes.

Members of the design review team are instructed to follow a review plan. A typical review plan would include the following guidelines:

- Look for:

- Misunderstandings
- Omissions
- Errors
- Functional inadequacies
- Excessive risk.

- Review for:
 - Use of prior state of the art
 - Soundness of invention
 - Accurate documentation
 - Complete documentation
 - Experimental proof.
- Assess:
 - Variety of alternatives
 - Depth of analysis
 - Logical convergence
 - Decisiveness
 - Cost and value awareness.
- Plan for:
 - Specific items of discussion by the Design Review Committee
 - Specific documented "payoff" from the Design Review Meeting.

The findings of a design review are typically summarized in Design Review Minutes. As a result of the review, three types of important notices may be issued by the design review committee chairperson:

- Action Items - assigned (and "monitored to closeout") when additional work is necessary to resolve critical problems which inhibit approval of the design as presented.
- Agreements - entered into Design Review Minutes to record important concurrences reached that are essential for approval of the design as presented.
- Alerts - entered into Design Review Minutes to communicate the need for extra caution during subsequent design, test, production or operational phases.

8.3 RADIATION SHIELDING DESIGN

Radiation shielding design is concerned with the protection of solar cells from the particulate radiation environment found in space. Since complete protection of the solar cells is not feasible, the typical radiation shielding design activities involves making tradeoffs and finding optimum compromises between at least the following major parameters:

- Solar cell end-of-life power output
- Solar cell array mass (especially as determined by the substrate and solar cell cover masses)
- Solar cell array component and assembly cost.

8.3.1 The Environment

The natural space radiation environment (as described in Sections 2.5.2 through 2.5.7) affects solar cell arrays as discussed in Section 2.5.8. Depending upon the orbit, the space radiation environment may require implementation of two distinctly different radiation shielding design approaches:

- Shielding against radiation penetration of the solar cell cover and the solar cell beyond the cell's junction to minimize the reduction in minority carrier lifetime, as discussed in Sections 3.3.1, 3.3.2 and 3.11.1.

- Shielding against low energy protons that become absorbed at or near the solar cell junction to prevent electrical shunting of the cell, as described in Section 3.3.3.

Shielding design activities concerning penetrating radiation are best performed by first converting the natural environment (Section 2.5) into damage-equivalent 1-MeV fluence, as described in Section 9.11), and then utilizing the 1-MeV fluence, as described in Sections 8.3.2 through 8.3.4.

Shielding design activities concerning low energy protons, discussed in Section 8.3.6 do not require conversion of the natural environment into 1-MeV fluence.

8.3.2 Determination of Shielding Thickness

To a first-order approximation, the shielding effectiveness of a solar cell cover is proportional to the mass density of the shielding material. However, no simple relationship exists for the effect of shield thickness (Figure 8.3-1). Therefore, "shield thickness" is usually expressed in units of

$$(\text{mass density}) \times (\text{shield thickness})$$

or mass per unit area. Convenient conversion tables are given in Tables 8.3-1 and 8.3-2.

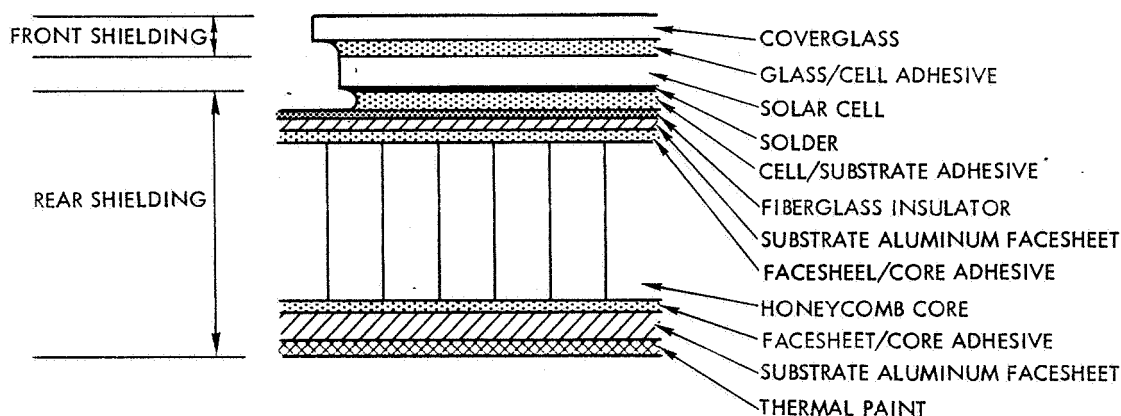


Fig. 8.3-1. Typical Solar Cell Shielding

Table 8.3-1. Variations in Fused Silica Shielding Thickness with Actual Thickness

g/cm ²	1.68E-2	3.35E-2	6.71E-2	1.12E-1	1.68E-1	3.35E-1
g/cm ²	0.0168	0.0335	0.0671	0.112	0.168	0.335
inch	0.003	0.006	0.012	0.020	0.030	0.060
mm	0.075	0.15	0.30	0.50	0.75	1.50

Table 8.3-2. Variation in Shielding Thickness with Material

Material	Density (g/cm ³)	Shielding Thickness per 25 μm (0.001 in.) Thickness (g/cm ²)	Shielding Thickness Relative to Fused Silica
Coverglass - Fused Silica	2.20	5.59E-3	1.00
Coverglass - Microsheet	2.51	6.38E-3	1.14
Glass/Cell Adhesive	1.0 to 1.70	2.54E-3 to 4.32E-3	0.45 to 0.77
Silicon Wafer	2.4	6.1E-3	1.09
Solar Cell Back Solder	7.82	3.38E-3	0.60
Cell/Substrate Adhesive	1.10	2.79E-3	0.5
Fiberglass Insulator	1.87	4.75E-3	0.85
Substrate Al Facesheet	2.82	7.16E-3	1.28
Honeycomb Core	0.026	6.60E-5	0.0118
Thermal Control Paint	1.55	3.94E-3	0.70

The total front and back-side shield thicknesses, d_{sf} and d_{sb} , are calculated by adding the shield thickness (in g/cm²) of all "i" front elements and of all "j" back-side shield thicknesses, respectively:

Front shield thickness

$$d_{sf} = \sum_{i=1}^n d_{si}$$

Back shield thickness

$$d_{sb} = \sum_{j=1}^m d_{sj}$$

For substrate materials not listed in Table 8.3-2 and for composite substrates, the total shield thickness, d_{st} , of a multilayer sandwich structure can be found from

$$d_{st} = \rho_1 t_1 + \rho_2 t_2 + \dots + \rho_n t_n = \sum_{i=1}^n \rho_i t_i \quad (\text{g/cm}^2)$$

where the ρ_i are the material densities in g/cm³ and the t_i are the corresponding thicknesses in cm. All material must cover the same substrate areas; for honeycomb core, use the expanded core density, and for interconnectors, use an average interconnector density per total substrate area considered. (A design example is illustrated in Chapter 12.)

8.3.3 Shielding by the Solar Cell

Radiation incident on the solar cell back-side also reduces the solar cell output. This occurs due to two mechanisms: reduction of the minority carrier lifetime by all particles, and introduction of a mild junction at the cell back contact by protons of certain energies. The exact cell degradation due to back-side irradiation is presently not well established so that it may be safest to assume that back side-irradiation is not shielded at all by the solar cell silicon base layer thickness. For more optimistic assessments the shielding thicknesses of Table 8.3-3 have been used.

For so-called "field" solar cells (described in Section 3.1.1) the back-side radiation damage may be considerably greater than for other, non-field cells. Therefore, detailed design approaches should be based on actual test data of the solar cells contemplated for a specific mission.

Table 8.3-3. Solar Cell Base Thickness Shielding Effectiveness for Particulate Irradiation Incident on the Cell Back Side

Cell Thickness		Shielding Thickness	
(inches)	(mm)	(% of thickness)	(g/cm ²)
0.014	0.35	86	0.0734
0.012	0.30	83	0.0608
0.010	0.25	80	0.0488
0.008	0.20	75	0.0366

8.3.4 Balancing Front- and Back-Side Shielding

For minimum-weight solar cell array designs, it is important to approximately balance the quantities of the 1-MeV fluence components that damage the solar cells from the front (through the cover) and from the back side (through the substrate). A balance of radiation damage is achieved when the shielding thicknesses (see Section 8.3.2) of the solar cell cover and of the substrate are equal.

8.3.5 Absorbed Dose in Cover

Radiation particles entering any material collide with the atoms of that material. In each collision the radiation particles lose some of their energy until they finally come to rest. If the particle's original energy is sufficiently high and the material is a relatively thin plate (such as a solar cell cover), the particle exits from the plate with reduced energy.

Since the radiation particles in space can have energies over a wide range and the particles having lower energies tend to be more numerous (see Section 2.5), the number of particles that come to rest in a solar cell cover (i.e., the absorbed dose) is greatest near the front surface of the cover and diminishes with increasing distance from the front surface. Different particle types are absorbed at different rates, while materials with higher densities absorb more (i.e., exhibit greater absorbed dose values) than those with lower densities. The effect of density on absorption is in accordance with the discussion in Section 8.3.2.

The amount of cover darkening associated with the absorbed dose is at the present time unclear. Therefore, it is suggested that the test data of Section 11.7 and the orbital performance data of Section 11.13 be consulted.

8.3.6 Shielding Against Low Energy Protons

To prevent excessive power degradation due to low energy proton damage, three approaches for completely shielding the active solar cell area are possible: Approach I employs an oversized coverglass which positively protects the entire active cell area; Approach II uses a coverglass overhanging the active solar cell area in one direction only, and one adhesive fillet for protecting a gap between the cover and the contact bar; Approach III uses a cell stack with the cover being flush with two cell sides and adhesive fillets covering each of the two otherwise unprotected gaps. These three approaches are illustrated in Figure 8.3-2 together with the original undersized cover baseline design, identified as Approach IV.

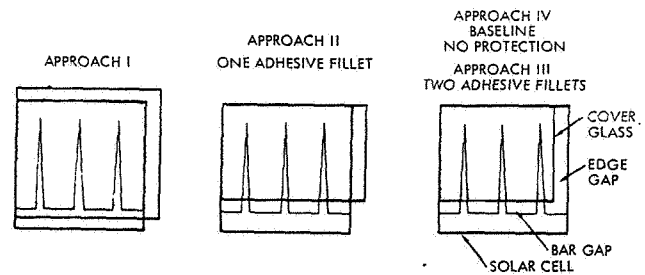


Fig. 8.3-2. Description of Alternate Approaches (Gaps and Glass Overhangs Grossly Exaggerated for Illustration)

Description of Approach I

The desired low energy proton protection is obtained by installing coverglasses on the solar cells so that the entire active cell area, as well as a portion of the n-contact areas, are protected from the proton flux. In one version of this approach the cover is installed with one edge indexed 1.00 ± 0.05 mm off the outer cell edge which runs along the N-contact strip, as shown in Figure 8.3-3. In another version of this approach, a slightly larger cover than shown in Figure 8.3-3 also overhangs the left-hand cell edge.

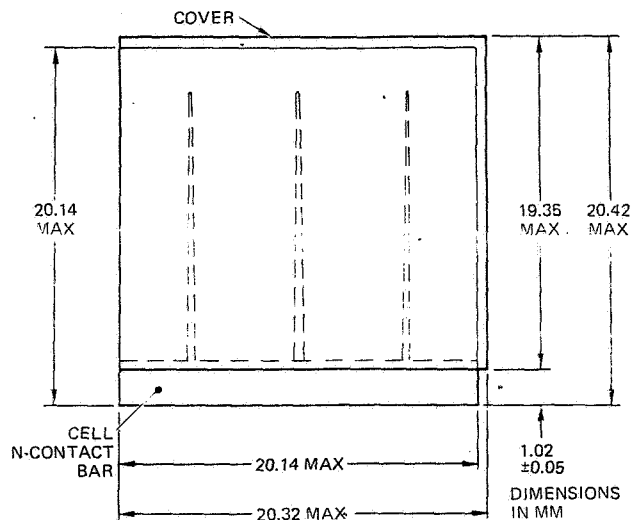


Fig. 8.3-3. Cell Stack of Approach I, Example

The assembled cell stack always exhibits overhanging coverglass on at least two sides. For perfectly square-cut cells and covers, this overhang may range from 0.02 to 0.5 mm in the worst case, and is estimated to fall within 0.1 to 0.2 mm most of the time. This minimum overhang is required because cells may have as much as 0.15 mm run-out (covers 0.10 mm) due to nonsquare cutting. However, due to the center indexing in the glassing operation, only one-half of this total 0.25 mm run-out will probably cause cover overhang. The chipping problem of the overhanging glass may be minimized by allowing an adhesive fillet to form under the glass overhanging the cell.

Description of Approach II

The following alternate approach to the desired low energy proton protection was considered (shown in Figure 8.3-4):

- Covers are smaller than the active cell area in one dimension, and overhang the cell area in another dimension.
- An adhesive bead is applied over the active cell area gap between the n-contact collector bar and the edge of the coverglass.

Description of Approach III

The following alternate approach to the desired low energy proton protection was considered:

- Covers are smaller than the active cell area.
- An adhesive bead is applied over the active cell area between the n-contact collector and the edge of the coverglass.
- A natural adhesive fillet is allowed to form along the outer cell edge normal to the collector bar.

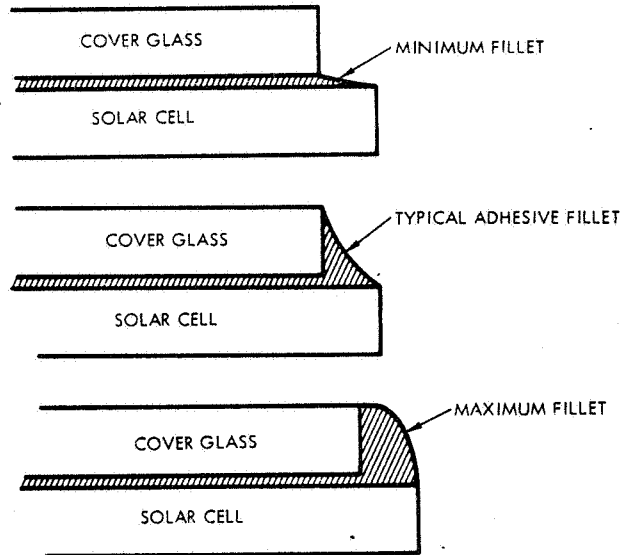


Fig. 8.3-5. Adhesive Fillets in Approach III

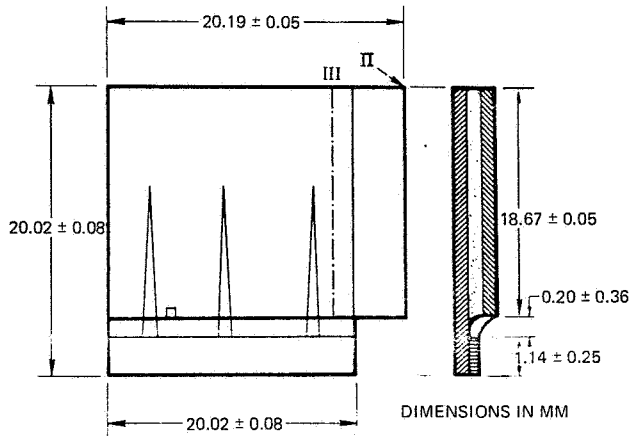


Fig. 8.3-4. Design for Approaches II and III, Example

Installation of and Requirements for Adhesive Fillets

After glassing and soldering the cells, an adhesive bead is applied across the unprotected active area strip between the n-contact bar and the cell cover edge. The width of this strip is nominally 0.20 mm and may vary to 0.6 mm in extreme cases. The outside strip will be protected by an adhesive fillet, as shown in Figure 8.3-5. Care should be taken not to overclean this edge fillet which forms somewhat naturally. A maximum fillet (as shown in the figure) is desirable.

Suitable materials for coating uncovered active solar cell areas must be compatible with other materials and adhesive systems already in use on the solar panels. For example, R63-489 was considered an excellent candidate material initially because it was used on earlier solar cell panels for bonding cover-glasses. It has to be eliminated, however, when it is to be applied to an otherwise completely assembled panel because it will not cure properly in the presence of RTV-511 which is used for bonding modules to the substrates. It may be used, of course, if it is applied to the cells at an earlier assembly level.

Materials selected have to withstand temperatures ranging from approximately +100°C to -140°C, proton and electron bombardment over the entire energy range, and ultraviolet radiation. The materials must adhere to silicon solar cells (with anti-reflective coating), adhere to cured cover adhesive, and possess adequate adhesive and cohesive strength to withstand vibration and centrifugal forces of the spacecraft; they must meet these requirements after exposure to the space environment for prolonged periods of time. It is highly desirable that the materials selected do not reduce electrical output and are capable of maintaining adequate transmission characteristics after being subjected to ultraviolet and particulate radiation over the life of the spacecraft.

In addition to the above requirements, the material must be capable of being applied economically and in a controlled manner. That is to say, it has to be flowed into areas a few thousandths of an inch wide, but must be prevented from flowing under modules or between cells to such an extent that panel weight becomes excessive or the temperature expansion gaps between adjacent cells or the solar cell interconnector expansion loops become filled.

Adhesive and flexible epoxy fillets for low energy proton protection have been used successfully by several solar cell array manufacturers, generally as a "retrofit" to already existing designs. As an example for the Intelsat III array, a final process was adopted using Dow Corning RTV-3140 protective coating with 0.1 percent by weight of Calcofluor White fluorescent material added. The process required that the material be applied with an air-actuated resin dispenser (hypodermic syringe) and that visual examinations be made by Manufacturing and Quality Assurance personnel in a darkened room under ultraviolet light. (The flight performance of the Intelsat III array is shown in Section 11.13.)

Most modern array designs now use fully overhanging covers because of lower in-orbit degradation and lower assembly and inspection cost than can be achieved with the adhesive bead approach.

In practice, the cut-on wavelength for conventional cells is not set to λ_3 or λ_4 but rather to λ_5 . The reason for this is that the solar energy in the wavelength range below λ_5 causes more cell heating and associated cell output power loss than could have been obtained from a cell with the cut-on set to λ_4 . A similar argument applies also to blue-sensitive cells except that the cut-on wavelength must be moved toward much shorter wavelengths in order to keep the cell output losses to a minimum. However, as the cut-on wavelength is moved toward shorter wavelengths, the degree of darkening of the cover adhesive may increase, thereby setting a practical lower limit on the cut-on wavelength. Increased darkening results in less light transmission to the cell and increased light absorption, and hence in higher cell operating temperatures.

Practical cut-on wavelengths have been 425 nm for earlier conventional cells, 400 nm for more recent conventional cells, and 350 nm for modern high-efficiency and blue-sensitive cells (for definitions of solar cell types see Section 3.1.1). Data on adhesive darkening as a function of cut-on wavelength has not been published (see Section 11.13 for orbital data).

8.4.2 Solar Cell Antireflecting Coatings

Different solar cell antireflective coating types and their effects on cell output due to installation of covers are discussed in detail in Section 4.3.

8.4.3 Non-normal Incidence Effects

Non-normal angles of incidence of the sunlight on the solar cells occur always on spinning arrays and

when flat solar cell arrays are "off-pointed" (when the outward normal to the array surface is not pointing directly at the sun).

The effects of non-normal sunlight incidence may include the following, depending somewhat upon specific designs:

- Apparent changes in the optical thicknesses of antireflecting coatings and reflecting and absorbing blue filters, and hence changes in the spectral transmission and reflection characteristics
- Apparent changes in the spectral response of solar cells (less blue response with increased off-pointing)
- Increased cover adhesive darkening due to the sunlight striking the adhesive layer on the side of the cell stack and the adhesive (the entire adhesive area will be nearly uniformly illuminated because the adhesive layer will act as a "light pipe")
- Edge effects due to illumination of the edges of thicker covers, in conjunction with the cell-to-cell spacings on the array (Ref. 8.4-1).

Off-pointing effects are discussed further in Section 4.8 (Angle-of-Incidence Effects). In practice, these effects are usually negligible for flat arrays that are off-pointing by no more than about 30 degrees. For spinning body-mounted or paddle-wheel arrays, however, the non-normal incidence effects may account for several percent (as high as in the order of 5 percent) of power loss when not properly considered.

8.5 THERMAL DESIGN

Solar cell array thermal design activities are concerned with the following effects:

- Solar cell operating temperature control
- Eclipse exit temperature control
- Thermal control surface design (glass, reflecting filters, paints, cooling fins, etc.)
- High-temperature operation
- Thermal gradients in structural elements
- Local high temperatures (hot spots).

The thermal design of a solar cell array is usually carried out by thermodynamics and heat transfer specialists in conjunction with the overall satellite system thermal design activity. This section provides guidelines for both the array designer and the thermal specialist to work together effectively, and for the array designer to make simplified analyses independent of the thermal specialist.

8.5.1 Temperature Control

The objectives of solar cell array temperature control are to:

- Minimize the solar cell operating temperature during periods of illumination, thereby maximizing the energy conversion efficiency capability of the solar cells
- Maximize the solar cell nonoperating temperature during periods of severe off-pointing or nonillumination (during eclipses) thereby minimizing low-temperature stresses and eventual fatigue failures of solar cells interconnectors.

From the discussion of the solar cell array temperature in space in Sections 9.6.4 and 9.6.5, the steady-state operating temperature is given by

$$T_{op} = \left[\frac{(\bar{\alpha}_s - F_p \eta_{op}) A_F}{(\bar{\epsilon}_{HF} A_F + \epsilon_{HB} A_B)} \frac{S \cos \Gamma}{\sigma} \right]^{1/4} \quad (8.5-1)$$

and the transient eclipse temperature as a function of eclipse time, t_e , is given by

$$T_e(t_e) = T_{op} \left[1 + \frac{3(\bar{\epsilon}_{HF} A_F + \epsilon_{HB} A_B) T_{op}^3}{\bar{m} \bar{c}_p} t_e \right]^{-1/3} \quad (8.5-2)$$

where the symbols (defined in the sections indicated) represent:

$\bar{\alpha}_s$ = average solar cell solar absorptance (Section 9.6.1)

F_p = solar cell packing factor (Section 9.6.1)
 η_{op} = solar cell operating efficiency (Section 3.2.5)
 A_F = array total front side area
 A_B = array total back side area
 $\bar{\epsilon}_{HF}$ = average hemispherical emittance of the array front side (Section 9.6.1)
 ϵ_{HB} = hemispherical emittance of the array back side (Section 9.6.1)
 S = value of the solar constant (Section 2.4.2)
 σ = Stefan Boltzmann's constant (Section 7.2 of Vol. II)
 $\bar{m} \bar{c}_p$ = array thermal mass (Section 9.6.5)
 Γ = angle of incidence of the sunlight on the solar cells (Section 9.4.4)

Common to both of the above equations are the emissivity of the array's front and back sides and the emitting areas. From this it follows that a lowering of the operating temperature through enhanced heat emission causes an undesirable lowering of the eclipse exit temperature. Therefore, the best approach is first to lower the array's average solar absorptance (increasing the solar cell efficiency), and second to improve the heat emission.

A low eclipse exit temperature can be raised by increasing the thermal mass of the array by either increasing the total mass of the array, or by substituting materials having higher specific heat capacitances. The metal beryllium has been used for this purpose because it can absorb about twice as much heat per unit mass as aluminum can absorb (see Table 8.5-1).

Decreasing $\bar{\alpha}_s$

The average effective solar absorptance (defined in Section 9.6.1) of the array can be lowered by any one or combination of the following:

- Using spectrally selective reflecting filters rather than absorbing filters to reflect all sunlight that cannot be converted into electrical energy (see Section 4.4.2)
- Minimizing cover and cover adhesive darkening at end-of-mission (see Sections 2.8.5 and 4.8.5)
- Covering all array areas not covered by solar cell active areas with highly sunlight-reflective materials (see Section 7.14 of Vol. II)
- Maximizing the end-of-mission solar cell energy conversion operating efficiency (defined in Section 3.2.5).

Table 8.5-1. Heat Capacitances of Different Metals (Ref. 8.5-1)

Material	Density, $\frac{m}{(g/cm^3)}$	Specific Heat, $\frac{C_p}{(J \cdot kg^{-1} \cdot ^\circ K^{-1})}$	Thermal Mass, $\frac{m \cdot C_p}{(J \cdot cm^{-3} \cdot ^\circ K)}$	Required Mass for Equal Heat Storage $(g \cdot J^{-1} \cdot ^\circ K)$
Beryllium	1.85	1920	3.55	0.52
Aluminum	2.70	920	2.48	1.1
Steel	8.0	500	4.00	2.0
Copper	8.9	380	3.38	2.6

Decreasing A_α

A decrease in the absorbing area, A_α , reduces the operating temperature without significantly affecting the eclipse exit temperature. A decrease in the area can be achieved by the following:

- Array off-pointing, reducing A_α by the cosine of the angle of incidence (see Section 9.4.4)
- Covering all nonsolar cell areas with highly reflective materials.

Increasing $\bar{\epsilon}$

The average, effective emittance (defined in Section 9.6.1) of the array can be increased by any one or combination of the following:

- Increasing the emittance of the solar cell covers (for example, ceria-stabilized micro-sheet has a higher emittance than fused silica, but also a higher absorptance)
- Covering all array areas not covered by solar cell active areas with highly emitting (but also reflecting) materials (such as white thermal control paint)
- Covering the array back sides with highly emitting materials.

8.5.2 High-Temperature Control

High-temperature problems are typically encountered on spacecraft that approach the sun or the inner planets (see Section 2.3.1). Reduction of the solar cell operating temperature is, therefore, paramount, and, since it is typically achieved by increasing the emitting areas, the subsequently encountered low-temperature problems may have to be tolerated. Solar cell operating temperatures can be reduced by any one or combination of the following:

- Off-pointing—non-normal angles of incidence reduce solar heating proportional to the cosine of the angle of incidence
- Mosaic array—highly reflecting and emitting thermal control elements are interspersed with the solar cells to decrease both $\bar{\alpha}$ and A_α and increase both $\bar{\epsilon}$ and A_ϵ
- Partially reflective covers—a portion of the area of each solar cell cover carries a highly reflective coating, thereby reducing both $\bar{\alpha}$ and A_α while keeping $\bar{\epsilon}_{HF}$ and A_ϵ constant

- Semitransparent covers—the solar cell covers carry a partially reflecting, partially transmitting coating applied uniformly over the cover areas, thereby reducing $\bar{\alpha}$ without affecting $\bar{\epsilon}_{HF}$
- Cooling fins—flat or curved solar cell panels carry radiating fins, thereby increasing the emitting area on the array back side
- Nonflat array geometry—solar panels having conical or other shapes exhibit greater effective emitting areas than absorbing areas
- Spinning array configurations—the emitting array is approximately π times as great as the absorbing area.

Thermal control of solar cell arrays for sunprobes is described (among others) by Ref. 8.5-2 for approaches utilizing various types of reflecting filters on solar cell covers.

8.5.3 Design Sensitivity

The sensitivity of the solar cell array temperature to changes in any of the parameters that affect the cell temperature can be studied by differentiation of Eq. 8.5-1 or 8.5-2 with respect to the parameter that is of interest. If the differentiated equation is divided by the original equation, the result permits evaluation of the fractional change in absolute temperature.

Illustrative Example No. 1

Q: What is the change in operating temperature due to a change in the solar absorptance, $\bar{\alpha}_S$, from 1.00 to 0.95?

A: Eq. 8.5-1 can be restated as

$$T^4 = k(\bar{\alpha}_S - F_p \eta_{op}) \tag{8.5-3}$$

where k is a constant representing all other symbols in Eq. 8.5-1 (k is of no further interest). Differentiating Eq. 8.5-3, we obtain

$$4T^3 \partial T = k(\partial \bar{\alpha}_S) \tag{8.5-4}$$

Dividing Eq. 8.5-4 by Eq. 8.5-3 and rearranging terms:

$$\frac{\partial T}{T} = \frac{\partial \bar{\alpha}_S}{4(\bar{\alpha}_S - F_p \eta_{op})}$$

Substituting numbers, assuming $F_p \cdot \eta_{op} = 0.1$, and letting $\partial T = \Delta T$ and $\partial \bar{\alpha}_S = \Delta \bar{\alpha}_S = \bar{\alpha}_{S2} - \bar{\alpha}_{S1}$, we obtain

$$\frac{\Delta T}{T} = \frac{0.95 - 1.00}{4(0.95 - 0.1)} = \frac{-0.05}{4 \times 0.85} = -0.0147$$

For an operating temperature of 300°K (23°C), $\Delta T = -0.0147 \times 300 = -4.4^\circ\text{K}$. For an operating temperature of 330°K (53°C), $\Delta T = -0.0147 \times 330 = -4.9^\circ\text{K}$. Hence, a lowering of $\bar{\alpha}_S$ from 1.00 to 0.95 reduces the array temperature by approximately 5°K or 5°C.

Illustrative Example No. 2

Q: What is the change in the operating temperature due to a change in the front side emittance, $\bar{\epsilon}_{HF}$?

A: Restating Eq. 8.5-1 as

$$T^4 = k'(\bar{\epsilon}_{HF} A_F + \epsilon_{HB} A_B)^{-1} \quad (8.5-5)$$

and differentiating with respect to $\bar{\epsilon}_{HF}$ yields

$$4T^3 \partial T = - \frac{k' A_F \partial \bar{\epsilon}_{HF}}{(\bar{\epsilon}_{HF} A_F + \epsilon_{HB} A_B)^2} \quad (8.5-6)$$

Dividing Eq. 8.5-6 by Eq. 8.5-5 and letting the partial differentials become increments results in

$$\frac{\Delta T}{T} = - \frac{A_F \Delta \bar{\epsilon}_{HF}}{4(\bar{\epsilon}_{HF} A_F + \epsilon_{HB} A_B)} \quad (8.5-7)$$

Illustrative Example No. 3

Q: What is the change in eclipse exit temperature due to a change in $\bar{m} \bar{c}_p$ by 10 percent?

A: Restating Eq. 8.5-2 as

$$\left(\frac{T_e}{T_{op}}\right)^{-3} = 1 + 3(\bar{\epsilon}_{HF} A_F + \epsilon_{HB} A_B) T_{op}^3 t_e (\bar{m} \bar{c}_p)^{-1} \quad (8.5-8)$$

and differentiating Eq. 8.5-8 with respect to $\bar{m} \bar{c}_p$ yields

$$-\frac{3}{T_{op}^{-3}} T_e^{-4} \partial T_e = -3(\bar{\epsilon}_{HF} A_F + \epsilon_{HB} A_B) T_{op}^3 t_e (\bar{m} \bar{c}_p)^{-2} \partial (\bar{m} \bar{c}_p) \quad (8.5-9)$$

Dividing Eq. 8.5-9 by Eq. 8.5-8 and letting the partial differentials become increments results in

$$\frac{\Delta T_e}{T_e} = \left\{ \frac{(\bar{m} \bar{c}_p)}{(\bar{\epsilon}_{HF} A_F + \epsilon_{HB} A_B) T_{op}^3 t_e} \right\}^{-1} \Delta (\bar{m} \bar{c}_p) \quad (8.5-10)$$

For most cases the operating temperature, T_{op} , is between 100°K and 400°K so that the term in Eq. 8.5-10 containing T_{op} is small compared to "3" so that Eq. 8.5-10 can be simplified to

$$\frac{\Delta T_e}{T_e} = \frac{1}{3} \frac{\Delta (\bar{m} \bar{c}_p)}{\bar{m} \bar{c}_p} \quad (8.5-11)$$

For a 10 percent change in $\bar{m} \bar{c}_p$, $\Delta (\bar{m} \bar{c}_p) / (\bar{m} \bar{c}_p) = 0.10$ and $\Delta T_e / T_e = 0.10/3 = 0.0333$. For an original eclipse exit temperature of 100°K (-173°C), ΔT_e would be $100 \times 0.0333 = 3.3^\circ\text{K}$ or °C. An increase in $\bar{m} \bar{c}_p$ results in an increase in T_e ; for the example T_e increases from 100°K to 103.3°K (from -173°C to -169.7°C).

Figure 8.5-1 shows the variation of steady-state solar array temperature as a function of solar distance for selected values of α/ϵ . Table 8.5-2 shows the temperature variation of a sun-oriented flat array as altitude is increased from 370 km to geosynchronous altitude. (The orbit normal is assumed to be displaced 90 degrees from the solar vector.)

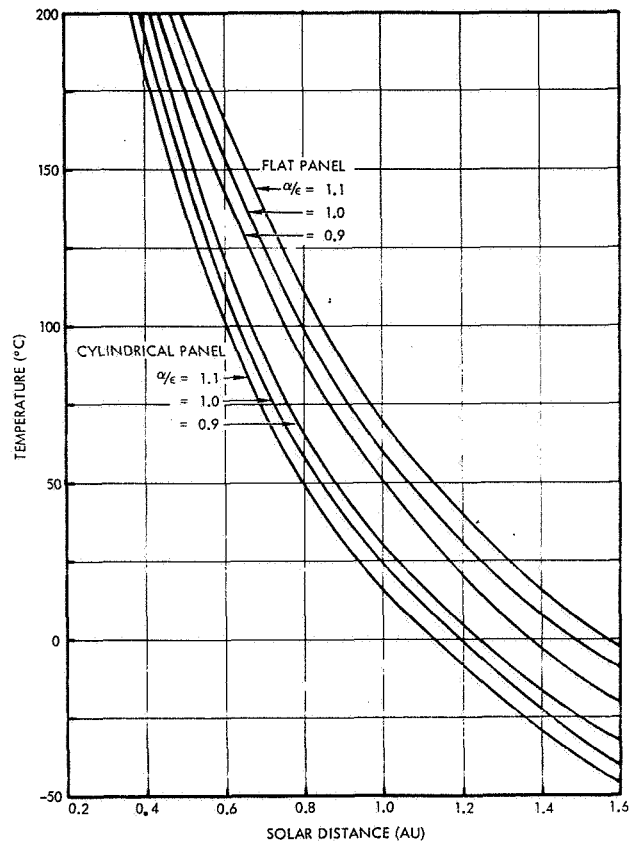


Fig. 8.5-1. Solar Cell Array Temperature as a Function of Solar Distance (Flat panel and spin axes are perpendicular to sunlight; cylindrical arrays are spinning.)

Table 8.5-2. Flat Solar Panel Temperature Variation as a Function of Orbit Altitude

Circular Orbit Altitude (km)	Solar Panel Steady-State Temperature (°C)
370	67
740	65
1,110	64
1,850	62
7,410	57
14,820	55
22,240	54
35,880	53

8.6 CONCEPTUAL ARRAY DESIGN

At the beginning of a conceptual design phase, a solar cell array design is typically nothing more than an appropriately labelled rectangle on a system's block diagram. Typically, very few spacecraft design details and solar cell array design requirements, if any at all, are available.

In order to trigger the evolution of a quantitative design concept and to start a (frequently long) chain of tradeoff studies and design reiterations, a minimal number of array design parameters must at first be assumed without proper justification. This section provides sufficient information to start a conceptual design activity.

8.6.1 Array Sizing

Array sizing is an analytical process by which the physical and electrical properties are established that describe a solar cell array which meets a specific performance (output) requirement at some critical mission time (usually at end-of-mission). The objective of array sizing during a conceptual design phase is to establish the required number of solar cells, array area, and array mass.

The array sizing process is typically carried out for a number of different candidate combinations of solar cells, covers, and substrates and is repeated during subsequent design phases to develop greater design details. Such detailed array sizing, including the determination of the number of solar cells connected in series and in parallel, is discussed in Sections 8.7.1 through 8.7.3.

Sizing Procedure

Step (a) Select one (or more) candidate combination(s) of array components intended for the design-to-emerge as follows:

Solar cell -- from Chapter 3

Solar cell covers -- from Chapter 4

Substrates -- from Chapter 6

Step (b) For each candidate configuration of Step (a) determine for the end-of-mission (or for any other mission-critical event) the glassed, degraded, maximum power output, P_C , of a single solar cell from

$$P_C = P_o \cdot S' \cdot F_{RAD} \cdot F_{T_{op}} \cdot F_M \cdot F_{SH} \cdot F_{BD} \cdot F_{CONF} \quad (8.6-1)$$

where

P_o = initial, unglassed and undegraded solar cell output at normal incidence at one solar constant AM0 intensity, and at a reference temperature (25° or 28°C) obtained from Chapter 3 of Volume II.

S' = effective solar intensity, including the effects of cover transmission degradation, solar distance and non-normal incidence as defined in Section 9.4.5.

F_{RAD} = solar cell radiation degradation factor defined by either one of the following:

- $F_{RAD} = 1 - PD/100$

where PD = percent orbital solar cell degradation according to Section 11.13.2.

- $F_{RAD} = P_{mp\phi} / P_{mpo}$

where P_{mp} = cell maximum power output. The additional subscripts ϕ and o refer to the end-of-mission 1-MeV fluence, ϕ , and the initial, zero-fluence condition, respectively. Both are obtained from test data (Chapter 3, Vol. II). The 1-MeV fluence, ϕ , is obtained according to the procedure described in Section 9.11.

$F_{T_{op}}$ = operating temperature degradation factor defined by

$$F_{T_{op}} = P_{mpT_{op}} / P_{mpo}$$

where the additional subscripts T_{op} and o refer to the operating temperature and reference temperature, respectively. $P_{mpT_{op}}$ is computed according to Section 9.4.8 while T_{op} is estimated according to Section 9.6.4. If appropriate values of F_p and n_{op} , required in Section 9.6.4, are not yet defined, one can assume as a first cut $F_p = 0.9$ and $n_{op} = 0.05$ for long-life high-radiation or higher-temperature orbits and $n_{op} = 0.1$ for low radiation or lower-temperature orbits.

F_M = miscellaneous assembly and degradation factors identified and discussed in Section 9.4.1 and not covered specifically in Eq. 8.6-1. For most array design cases F_M will range from 0.95 to 1.00.

F_{SH} = shadowing factor, as defined in Section 9.5. For unshadowed arrays $F_{SH} = 1.00$.

F_{BD} = blocking diode and wiring loss factor, prorated for a single cell and defined by

$$F_{BD} = 1 - \frac{V_D + V_W}{V_B + V_D + V_W} \quad (8.6-2)$$

where

V_D = diode voltage drop

V_W = voltage drop of the wiring between the array and the load spacecraft

V_B = array bus voltage at the spacecraft load

If the blocking diodes and wiring losses are not yet defined ($V_D + V_W$) = 1.4 V is a good first-cut approximation for single silicon diodes on arrays below 1 kW size, and ($V_D + V_W$) = 2.8 V for higher power levels.

F_{CONF} = configuration factor, also known as aspect ratio, as given in Section 8.6.2. (For flat-plate arrays, $F_{CONF} = 1$. For cylindrical, spinning arrays, $F_{CONF} = 1/\pi$.)

Step (c) Determine solar cell array characteristics as follows:

Number of Solar Cells:

$$N = P_A / P_C \quad (8.6-3)$$

where

P_A = required power output

P_C = single-cell output from Eq. 8.6-1.

Substrate area:

$$A_s = A_c N / F_p \quad (8.6-4)$$

where the packing factor F_p is defined below and A_c is the overall solar cell area.

Substrate mass:

$$M = mA_s \quad (8.6-5)$$

where m is the mass per unit area (kg/m^2) from Section 6.2.

Packing Factor

The packing factor is defined as a unitless ratio given by

$$F_p = \frac{N \cdot A_c}{A_s} \quad (8.6-6)$$

where

N = total number of solar cells on a given solar cell panel or array

A_c = overall area of a solar cell

A_s = substrate area

Different definitions for A_s are being used depending upon how A_s is to be used in computations. A_s may define the following substrate areas or portions thereof:

Areas under the solar cell modules and strings only

All so-called "available" areas onto which solar cell circuits, including cabling, may be mounted

The substrate gross area with the exception of areas reserved for hinges and similar elements and with the exception of cutouts (larger openings) in the substrate

The entire gross, overall areas without regard to solar cell circuit placement and unavailable areas.

Frequently, the applicable literature does not provide any indications as to which definition was used by the author.

Practical packing factors, using the first definition above, range around 0.85 to 0.92. Packing factors of 0.95 and greater are very difficult to achieve with flat solar cell laydown designs (defined in Section 5.2). Conical and trapezoidal solar cell panels may exhibit packing factors as low as 0.5 to 0.6.

Packing Density

The packing density indicates the number of the solar cells of a given size which can be fitted into a given substrate area. The packing density, N' , is related to the packing factor (Eq. 8.6-6) as follows:

$$N' = \frac{A_s F_p}{A_c} \quad (8.6-7)$$

Table 8.6-1 provides some examples of different packing densities.

Table 8.6-1. Packing Densities for 2 x 2 cm and 2 x 4 cm Solar Cells

F_p	Number of Cells per ft ²		Number of Cells per m ²	
	2 x 2 cm	2 x 4 cm	2 x 2 cm	2 x 4 cm
0.8	186	93	2000	1000
0.9	208	104	2250	1125
1.0	232	116	2500	1250

8.6.2 Configuration Selection

The evolution of the solar cell array configuration is strongly dependent upon the evolution of the overall spacecraft design and is primarily in response to the following interface considerations:

- Payload and communication equipment directional pointing requirements
- The range of the angles of incidence of the sunlight falling onto the spacecraft and onto the solar cell array throughout mission life
- The change in the array-to-sun distance during mission life
- The required power level and power profile of the array
- Size, volume and mass constraints imposed by the launch vehicle and the overall spacecraft design.

Different solar cell array configurations are illustrated in Section 1.1. For conceptual design studies, use of the projected solar cell areas of the array as discussed in this section usually provides sufficient analytical accuracy.

Configuration Tradeoffs

For more refined configuration studies actual solar cell array I-V characteristics should be used rather than the projected areas. One commonly used method is to assume a hypothetical array of 100 cells in parallel by 100 cells in series and to compute the array output by the method described in Section 9.4 for a number of different geometries and estimated operating temperature. The deviations of actual array power output curves from the projected area curves may be substantial.

Different geometric shapes may be added to the array to achieve a desired power profile (power output as a function of the sun angle θ in Figures 8.6-1 and 8.6-2).

Figure 8.6-1 shows the comparative power output of a number of different array configurations, as a function of angle of incidence. This figure will help to select the most desirable array configuration, or combination of configurations, to obtain any desired power profile as function of sun angle. Figure 8.6-2 permits the optimization of paddle angles while Figure 8.6-3 permits the optimization of cone angles. The relationships between a circular array and approximation of a circular array by a series of flat facets is illustrated in Table 8.6.2.

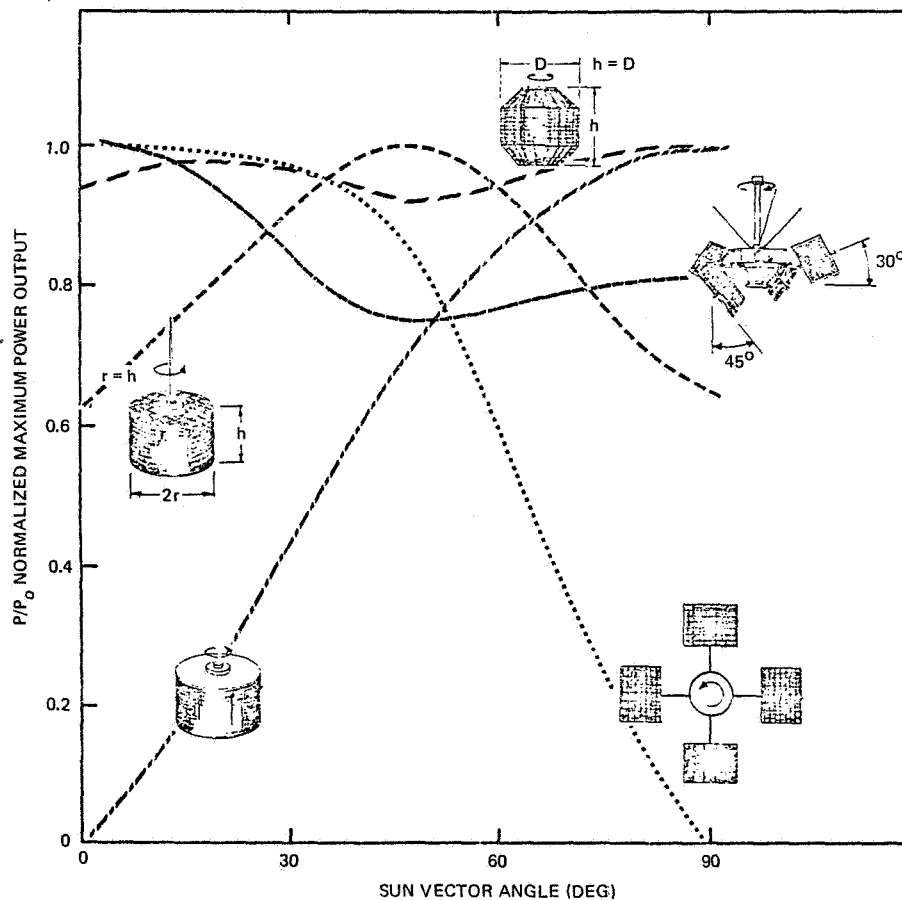


Fig. 8.6-1. Comparative Output of Five Different Array Configurations as a Function of Sun Angle (i. e., the angle between the solar vector and the satellite spin axis)

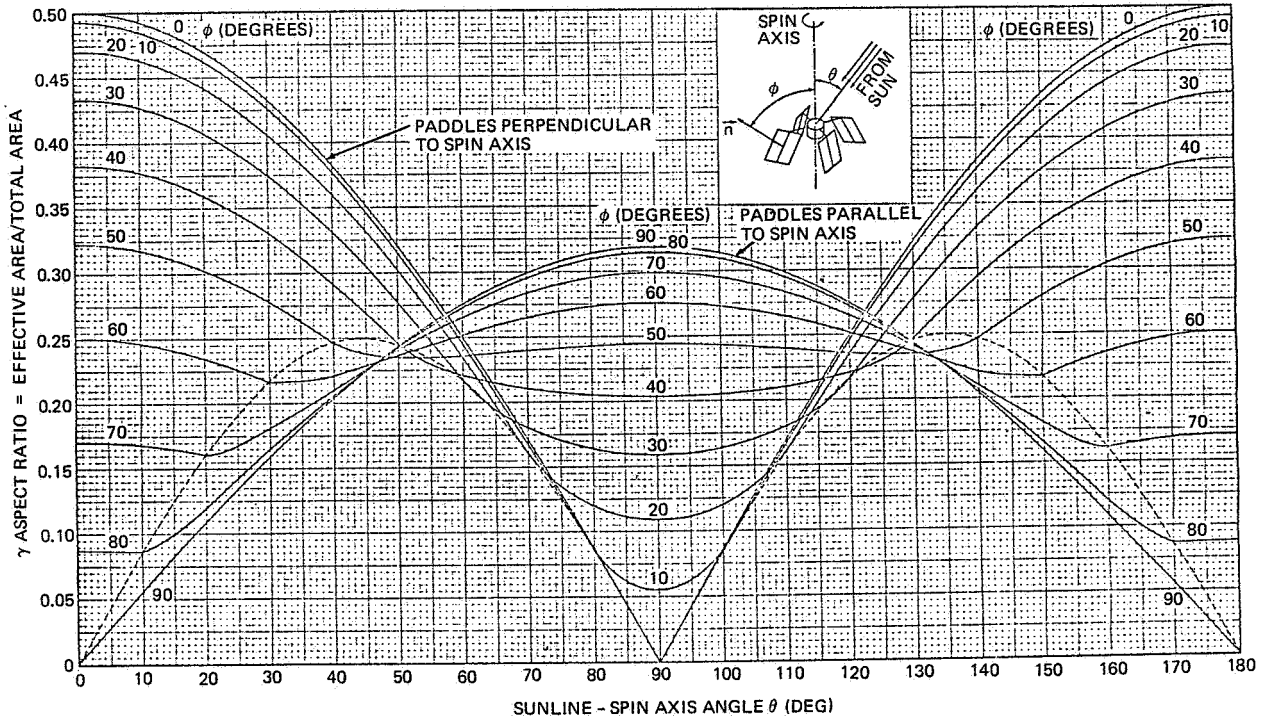


Fig. 8.6-2. Aspect Ratios of Paddle Mounted Arrays, Shadowing Effects Ignored (Ref. 8.6-1)

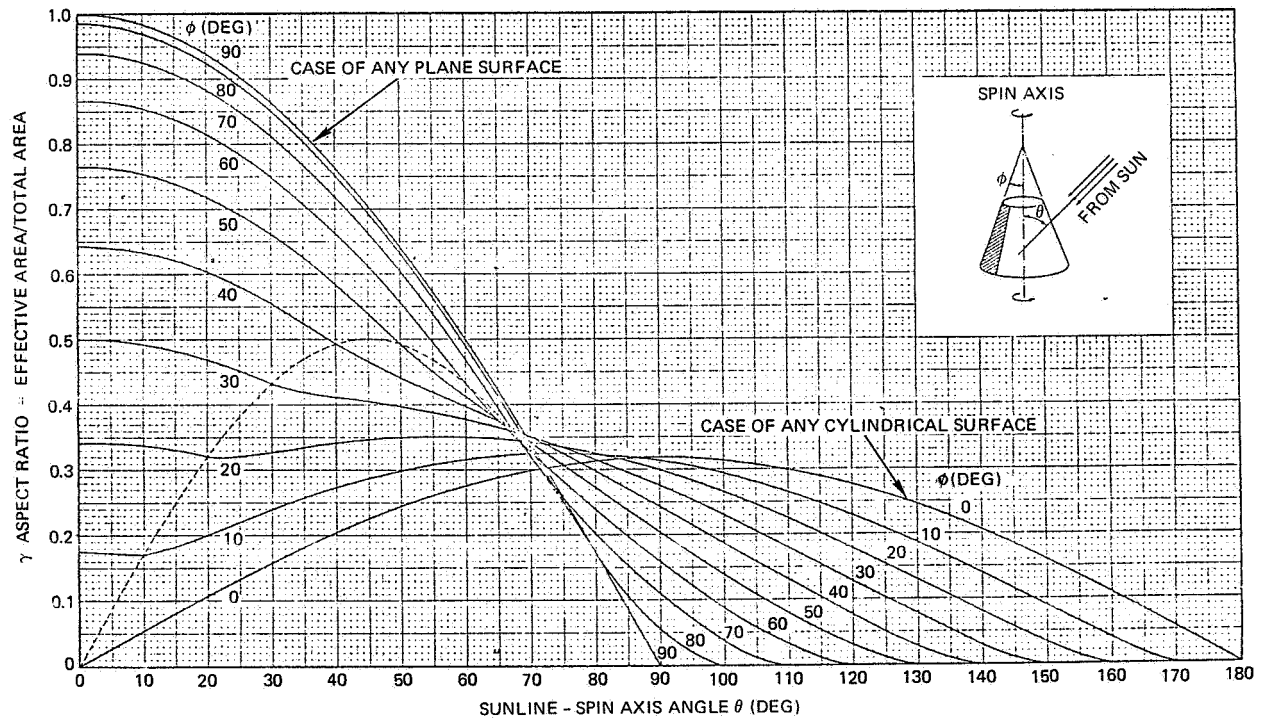


Fig. 8.6.3. Aspect Ratios of Conical Solar Arrays (Ref. 8.6-1)

Table 8.6-2. Relative Area of Faceted Cylinders

Number of Facets n	Relative Area, A _R
∞ (cylinder)	1.000
4	0.637
6	0.827
8	0.900
10	0.936
12	0.955
16	0.974
20	0.984
24	0.988

$A_R = A_n / A_\infty = \infty$ and
 $A_n = \frac{1}{2} n r^2 \sin(2\pi/n)$
 where A_n is the area of a polygon of n sides inscribed in a circle of radius r.

8.7 ELECTRICAL DESIGN

The electrical design activities described in this section are of a more detailed nature and presuppose the existence of a conceptual design as developed in Section 8.6. Electrical design activities include the following:

- Determination of the accurate number of solar cells to be connected into series/parallel circuits
- Layout (placement) of the solar cells and solar cell circuits on the substrate
- Wiring of the solar cell circuits with considerations given to electromagnetic and electrostatic design requirements.

8.7.1 Series Connection of Solar Cells

A sufficient number of solar cells must be electrically connected in series to provide the bus voltage plus any voltage drops in the blocking diodes and in the wiring. The required number of cells in series, N_S , is found from

$$N_S = \frac{V_B + V_D + V_W}{V_{mp}} \quad (8.7-1)$$

where

V_B = spacecraft load or battery bus voltage

V_D = array blocking diode forward voltage drop

V_W = total wiring voltage drop between the solar cells and the spacecraft load or the battery (in both the hot and return lines)

V_{mp} = solar cell end-of-mission (or other mission critical event) degraded output voltage at the cell's maximum-power point and under operating temperature and intensity. (For a detailed discussion of solar cell performance and degradation see Sections 3.2 through 3.6)

The value of V_B is usually project-peculiar. Values for V_D are given in Section 5.5 and/or applicable manufacturer's data sheets. Values for V_W are frequently project-peculiar; however, Section 8.7.4 provides a procedure for selecting V_W for a minimum-weight array-plus-bus wiring design. Values for V_{mp} can be determined from the following procedure: for each of the solar cell and cell cover types selected in Section 8.6 (or for the types for which a design already exists), determine for the end-of-mission (or for any other mission-critical event) the glassed, degraded, maximum-power voltage of a single cell from

$$V_{mp} = V_{mp\phi} + \Delta V_{S'} + \beta_{VP}(T_{op} - T_o) \quad (8.7-2)$$

where

$V_{mp\phi}$ = glassed solar cell maximum power output voltage at the reference temperature T_o after irradiation with 1-MeV electrons to a level of $\phi \text{ e} \cdot \text{cm}^{-2}$

$\Delta V_{S'}$ = change in the maximum power voltage due to a change in the light intensity from S to S' , as described in Section 9.4.5. The corresponding voltage change is determined from the solar cell data in Chapter 3 of Vol. II, or from Section 9.4.7.

β_{VP} = temperature coefficient for the maximum power voltage, as defined in Section 3.6.2

T_{op} = solar cell operating temperature obtained from Section 8.5.3 or from Section 9.6.4

T_o = solar cell standard test temperature (25°C or 28°C)

8.7.2 Parallel Connection of Solar Cells

Let a group of N_S solar cells, all connected in series (as discussed in Section 8.7.1), be defined as a "series string," or simply as a "string" of cells. The total solar cell array consists of N_p strings that are connected in parallel and, together, provide the required load current. N_p is found from

$$N_p = \frac{I_L}{I_{mpav}} \quad (8.7-3)$$

where I_{mpav} is the average maximum-power point current output of all N_p cells in parallel after glassing and degradation, at the operating temperature, T_{op} , and under reduced illumination conditions due to cover darkening and non-normal incidence. To compute I_{mpav} , proceed as follows:

$$I_{mpav} = \frac{\sum_{i=1}^n I_{mpi}}{n} \quad (8.7-4)$$

where

$$I_{mpi} = I_{mp} \cdot (S')_i \cdot [1 + \beta'_{Ip}(T_{op} - T_o)] \cdot F_m \cdot (F_{SH})_i \quad (8.7-5)$$

and

$I_{mp\phi}$ = glassed (but with undegraded transmission) solar cell maximum-power point output current at the reference temperature T_o after irradiation with 1-MeV electrons to a level of $\phi \text{ e} \cdot \text{cm}^{-2}$.

S_i' = effective solar intensity for the i -th parallel-connected string of cells, including the effects of cover transmission degradation, solar distance and non-normal incidence, as defined in Section 9.4.5. S_i' is in units of "solar constants." For a flat panel array, all S_i' are the same and the subscript i may be dropped.

β_{ip}' = temperature coefficient for I_{mp} , as defined in Section 3.6.2, expressed in units of " $^{\circ}\text{C}^{-1}$."

T_{op} = solar cell operating temperature obtained from Section 8.5.3 or from Section 9.6.4.

T_o = solar cell standard test temperature (25°C or 28°C).

F_m = miscellaneous solar cell assembly and degradation factors identified and discussed in Section 9.4.1 and not specifically covered in Eq. 8.7-5. For most array designs F_m will range from 0.95 to 1.00.

F_{SHi} = the shadowing factor for the i -th parallel-connected string of solar cells as described in Section 9.3.2. For unshadowed strings $F_{SH} = 1.00$.

Parallel-Circuits

As a minimum, all series strings of cells are parallel-connected at their ends. However, it has been common practice to parallel-connect groups of cells at the cell level into strings that have 2, 3, 4, or more cells connected in parallel.

The purpose of such parallel connection is to achieve higher array reliability by providing a parallel current path in case of a cell open-circuit failure due to cell fracturing, contact lifting, or interconnect failures.

In case of an open-circuit failure, adjacent parallel-connected solar cells can share a part or all of the current flow that is blocked by an open-circuited solar cell. The amount of current which can be carried by the unfailed cells depends upon the difference between the cell's operating current level before the failure occurred and the sum of the short-circuit currents of the parallel-connected unfailed cells after failure. If that current difference is less than the current which was originally carried by the cell which failed, the unfailed cells will be driven into reverse bias, as described in Section 9.1.6. Reverse-biased solar cells can, in turn, be caused to fail by excessive reverse bias voltage or by excessive power dissipation and subsequent overheating, as discussed in Section 3.7.

If reverse biasing of solar cells can occur on a particular design, the design practices given in Section 8.7.5 should be considered.

8.7.3 Solar Cell Array Layout

The purpose of the electrical design array layout activity is to:

- Subdivide the array electrically into series strings of parallel-connected solar cells

- Arrange these strings on the available substrate area to achieve the highest possible power output per unit area
- Provide for electrical conductors from the solar cell circuits to the solar panel or array terminals
- Provide for blocking (isolation) and shadowing (bypass) diodes, if required.

Dimensional Analysis

The minimum gap sizes between adjacent cells are determined by:

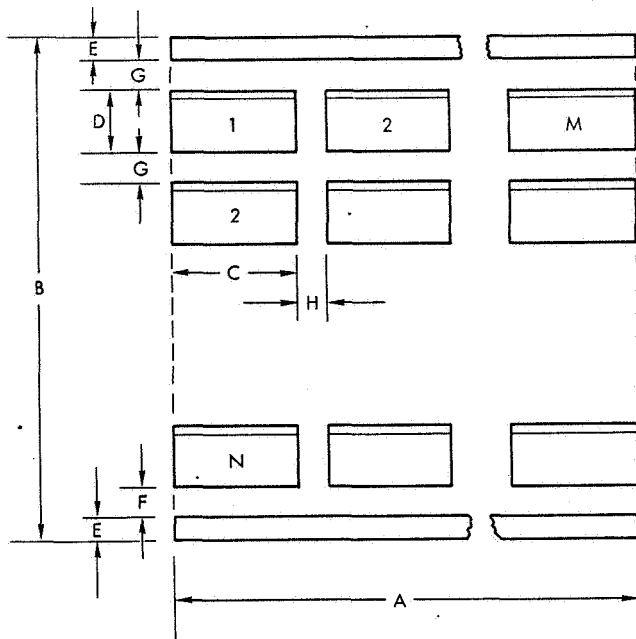
- Solar cell/cover assembly dimensions
- Thermal expansion coefficients of substrate
- Glass transition temperature of cell-to-substrate adhesive and bond area (see Section 5.3)
- Lowest possible temperature excursion
- Tolerances on the assembly process (such as noncentered cell-to-substrate adhesive pads)
- Interconnector expansion loop size
- Manufacturing tooling tolerances and manufacturing process limitations
- Voltage differentials between adjacent solar cells.

Minimum practical gaps are 0.1 mm between adjacent cells in the parallel-connected group of cells, 0.5 mm between cells in the (electrical) series directions and 0.5 to 1.0 mm between adjacent electrical strings. This gap size refers to the cell-to-cell gap width when undersized or "same" size covers are used, and to cover-to-cover gaps when oversized covers are used. Using the definitions given in Figure 8.7-1, the required area for a group or string can be calculated.

8.7.4 Interconnectors and Wiring

The electrical output from the solar cells is collected by solar cell interconnectors and is transmitted by cables, wires, or flat conductors to the terminals of a solar cell panel or solar cell assembly, as discussed in Chapter 5. The terminal board or connector mates with a connector or "pig tail" from the spacecraft bus. The various types of electrical circuit components for solar cell arrays, as well as appropriate design practices, are all described in detail in Chapter 5. Electrical conductor sizing is described in the following paragraphs.

Weight limitations for most spacecraft usually do not permit electrical conductors to be sized for near-zero power losses. Instead, the permissible power loss is determined by a tradeoff between the weight due to increased conductor size and the weight due to increased array size (Ref. 8.7-1). For arrays having power levels in the order of 1 kW, total power losses in the spacecraft primary bus wiring in the order of 1 percent are common, ranging from about 0.5 to 3 percent for different designs.



$$A = MC + (M - 1)H$$

$$B = ND + NG + F + 2E$$

DIMENSION

- C = SOLAR CELL WIDTH - PARALLEL
- H = CELL GAP - PARALLEL
- D = CELL LENGTH - SERIES
- G = CELL GAP - SERIES
- E = END CONTACT BAR WIDTH
- F = END CONTACT/CELL GAP

NOTE: DIMENSIONS C AND D MUST BE BASED ON THE MAXIMUM CAVITY SIZE OF GLASSED CELLS.

Fig. 8.7-1. Solar Cell Array Layout Dimensions

Conductor/Array Mass Tradeoff

Consider the solar cell array terminals to be separated from the load terminals by the distance L. The total resistance of a pair of conductors between the array and the load is

$$R_2 = 2\rho L/A$$

and their total mass (neglecting the insulation) is

$$m_c = 2LAd$$

where

- ρ = electrical conductivity of conductors
- A = cross-sectional area of conductors
- d = density of conductors

Let the required load power be P_L and the power losses in the conductor be P_R . The array must, therefore, be sized to provide $P_L + P_R$.

Let the array mass corresponding to P_L be m_L and the array mass corresponding to P_R be m_R . Then the sum-total of the masses of the array and the conductors is

$$M = m_L + m_R + m_c$$

However,

$$m_R = m_L P_R / P_L$$

and

$$P_R = I_L^2 R_2 = I_L^2 \rho L / A$$

and

$$P_L = V_L \cdot I_L$$

where

V_L = load voltage

I_L = load current.

Therefore

$$M = m_L + \frac{2m_L I_L \rho L}{A V_L} + 2LAd$$

Differentiating M with respect to A and setting the result equal to zero permits the minimum M to be found for which the cross-sectional area, denoted by A_m , is given by

$$A_m^2 = m_L I_L \rho / V_L d$$

The value for A_m can then be used to calculate the P_R for which M results in a minimum (lowest weight) configuration.

Illustrative Example

Consider a solar cell array having to supply 1 kW of load power output at a terminal pair which is 10 meters distant from the array. Let the bus voltage be 50 volts and let the array be an aluminum honeycomb panel substrate covered with 0.20 mm thick solar cells and 0.15 mm thick covers.

From Section 6.2.4 the array mass is approximately $m_L = 60$ kg. From above, $I_L = 1000 \text{ W} / 50 \text{ V} = 20 \text{ A}$. For copper conductors $\rho = 1.72 \times 10^{-6} \text{ ohm} \cdot \text{cm}$ (from Section 7.9 of Vol. II) and $d = 8.89 \text{ g} \cdot \text{cm}^{-3}$ (from Section 7.3 of Vol. II). Substituting these values into the last equation, $A_m = 0.068 \text{ cm}^2$. The corresponding total conductor resistance is $R_2 = 2\rho L/A = 50 \text{ m}\Omega$ and the losses are $I^2 R_2 = 20$ watts or 2 percent.

Aluminum vs. Copper Conductors

The resistance of a single conductor is given by

$$R = \rho L / A$$

and its mass by

$$M = ALd = \rho d L^2 / R$$

where

ρ = electrical resistivity of conductor

L = conductor length

d = conductor density.

Let the mass of an aluminum conductor be denoted by M_a and that of a copper conductor by M_c . The mass ratio of two, for the same resistance, R, and length L, is

$$\frac{M_a}{M_c} = \frac{\rho_a d_a}{\rho_c d_c}$$

The subscripts a and c refer to aluminum and copper, respectively. For

$$\rho_a / \rho_c = 1.64 \text{ (Section 7.9.2)}$$

and

$$d_a = 2.70 \text{ and } d_c = 8.89 \text{ g.cm}^{-3} \text{ (Section 7.3)}$$

$$M_a / M_c = 0.50$$

Hence, aluminum conductors weigh one-half of copper conductors for the same power loss and conductor length.

8.7.5 Hot-Spot Design Considerations

The so-called "hot-spot" phenomenon due to reverse-biasing of solar cells (as described in Section 9.1.6) may lead to solar cell failures and associated solar cell array power losses, as described in Section 3.7.

The magnitude of the hot-spot problem, if it exists at all for a given design, depends upon both the electrical and the thermal solar cell array designs. Potentially damaging reverse voltages can occur only if the difference between the load voltage and the solar cell string open-circuit voltage is sufficiently high. Potentially damaging heating of reverse-biased solar cells can occur only if the heat dissipation in the cell or cells is of sufficient duration and of sufficient magnitude relative to the quantity of heat conducted and radiated away from the cell or cells.

If a given design is suspected to be subject to a hot-spot problem, it should be analyzed according to Section 9.1.6. Sections 9.1.5, 9.6.3, and 9.6.4 permit the solar cell temperatures to be estimated.

If an analysis shows that a real or a potential hot-spot problem exists, the following design changes should be considered to reduce the magnitude of the reverse voltage and/or heat dissipation:

- Eliminate operational short-circuiting of an array or array section (i. e., let shunt regulators shunt the array to the load voltage rather than to near short-circuit).
- Reduce the number of solar cells connected in series, or install shunt diodes across each parallel-group of cells. For example, the splitting up of the array into two equal-sized, series-connected arrays, tied together by a common bus connected to a shunt regulator, effectively reduces the number of cells in series by one-half.
- Use single cell series strings rather than parallel-connected groups of cells in the series strings (strings are defined in Section 8.7.2).
- Increase the number of cells connected in parallel (at the cell level) until unfailed cells can carry just a little more current than a failed (open-circuited) cell originally carried. (This typically requires about 10 cells in parallel.)
- Increase the lateral heat conduction and/or heat dissipation from solar cells and the substrate.

8.7.6 Designing for Reliability

Array design for reliability involves two aspects:

- Oversizing of the array by one or more series-strings of cells (defined in Section 8.7.2) to compensate for potential string failures that may occur during a mission due to statistically estimated failure rates of solar cells, interconnectors, soldered or welded joints, connectors, etc.
- Providing redundant current paths through soldered or welded joints, interconnectors, wires, connectors, etc.

Failure rates and effects and reliability analyses are treated in Section 9.9.

8.8 HIGH-VOLTAGE ARRAYS

8.8.1 Requirements

High-voltage solar cell arrays, attractive for direct operation of ion-thrust engines, have been studied for voltage ranges between 2 and 16 kV. High-voltage effects become increasingly pronounced as the array voltage increases above 100 volts and as the available array output current level decreases correspondingly (assuming a fixed power output array).

Specific high-voltage effects encountered during space flight include the following:

- Leakage currents of significant magnitude can be carried by the space plasma surrounding the array (see Section 2.3.3), thereby shunting a significant portion of the solar cell array output.
- High-voltage stress and corona can deteriorate or destroy insulating materials (see Section 7.10).

8.8.2 Design Practices

Design practices presently envisioned to be required for successful high-voltage array operation include the following:

- Complete insulation of the high-voltage array solar cell circuits, including solar cells, interconnectors and joints, from the surrounding plasma
- Minimization or complete avoidance of pinholes and voids in the insulating layers
- Provisions for shunt diodes to both increase the array reliability and to minimize hot-spot (reverse biasing) effects, as described in Sections 5.5.5 through 5.5.10 and in Section 9.1.6.

Additional information concerning the design of high-voltage solar cell arrays is given in Refs. 8.8-1 and 8.8-2.

8.9 ELECTROSTATIC SHIELDING DESIGN

8.9.1 Requirements

Certain satellite experiments require that the plasma in which a satellite moves does not become disturbed in the vicinity of the satellite. An electrically neutral satellite can be designed approximately when the entire satellite, including its solar cell array, is made "equipotential." This can be achieved with conductive coatings placed over all nongrounded and dielectric surfaces, connected to spacecraft ground. A typical requirement for a maximum potential difference of 0.5 volt between any two points on the satellite can most likely be achieved by sizing the conductive coatings for a maximum resistance of 10^5 ohms to ground. Typically pinholes and voids up to 5 mm in diameter and expansion gaps up to 2 mm in width and of any length are permissible.

8.9.2 Design Practices

Conductive coatings over the solar cell array must reach over all solar cells, contact bars, and wiring. Two different approaches have been used:

- Solar cells are mounted to a transparent "superstrate" which not only carries on its outer surface the conductive coating, but also serves as the mechanical holding device for the solar cells within an array frame structure (Explorer 31)
- Solar cells mounted to a conventional substrate are covered with individual cover-glasses each of which carries a conductive coating and coating terminal pads. The individual covers are then interconnected by welding ribbons to the terminals similarly as solar cells are interconnected (Helios).

Additional design requirements to achieve an electrostatically clean solar cell array are:

- Minimize the voltage level of any circuit element (i. e., use low bus voltage, ground the center of the array, etc.)

- Cancel electromagnetic fields by back wiring and counter-flow of currents (Section 8.10)
- Shield all wiring and circuits electrostatically.

Candidate materials for conductive coatings are indium oxide (In_2O_3) (used on Explorer 31 and GEOS), beryllium oxide (BeO) and tin oxide (SnO_2). Contact reinforcements could be silver, gold or other metals compatible with both the conductive coating and an assembly process. Special considerations to be given to the design and fabrication process control of conductive coatings are the following:

- The conductive coating must adhere to the substrate over the entire environmental range of exposure (ultraviolet and charged particle irradiation, temperature cycling) without subliming, cracking, or being eroded away.
- Light transmission to the solar cells should be maximized.
- The long wavelength emittance should be maximized and the solar absorptance minimized (an $\alpha = 0.93$ was achieved on Explorer 31 for a coating conductivity of 1 to 3×10^3 ohms per square.
- Metallic contact areas on the outer surface should be minimized because metals generally have low emittance and can cause significant increases in array operating temperature.

Currently only indium oxide has been qualification tested and used on space flight programs. Additional information concerning electrostatic shielding is given in Refs. 8.9-1 and 8.9-2.

8.10 MAGNETIC DESIGN

8.10.1 Magnetic Forces

An illuminated solar cell array is composed of a network of current loops which, when moved through the earth's natural magnetic field, will produce a force which will perturb the attitude of the satellite unless it is compensated for by the satellite's attitude control system (Ref. 8.10-1).

As orbit altitude increases, the strength of the earth's magnetic field decreases. At geosynchronous altitude the solar radiation torque is the dominant effect and, from the viewpoint of attitude control, the minimization of solar array dipole moments is of less importance. For the case of the typical geostationary communications satellite, magnetic torque requirements are usually specified only for flat, oriented arrays (Ref. 8.10-2).

8.10.2 Magnetic Cleanliness

Occasionally satellites contain instruments that are sensitive to locally-generated magnetic fields. In particular, interplanetary probes are usually equipped with magnetometers for the measurement of weak natural fields throughout the journey. It is, therefore, essential that solar arrays for this type of satellite be designed in a manner which ensures that their magnetic fields are maintained below the threshold level of the measurement system.

8.10.3 Magnetic Dipole Moment

In regions of space where it is defined, the scalar magnetic potential satisfies Laplace's equation

$$\nabla^2 V_m = 0, \quad (8.10-1)$$

where

∇^2 = divergence of the gradient (or the Laplacian operator),

V_m = scalar magnetic potential

and where the current density $\vec{J} = 0$.* Referring to Figure 8.10-1, the magnetic induction \vec{B} at an arbitrary point P off of the axis of a circular current loop can be calculated using Eq. 8.10-1. The results for $r \geq a$, expressed in terms of spherical polar coordinates, are:

$$V_m = \frac{\mu_0 I}{2} \left[\frac{a^2 \cos \theta}{2 r^2} - \frac{3a^4}{16 r^4} (5 \cos^3 \theta - 3 \cos \theta) + \dots \right], \quad (8.10-2)$$

* A vector is identified with a bar.

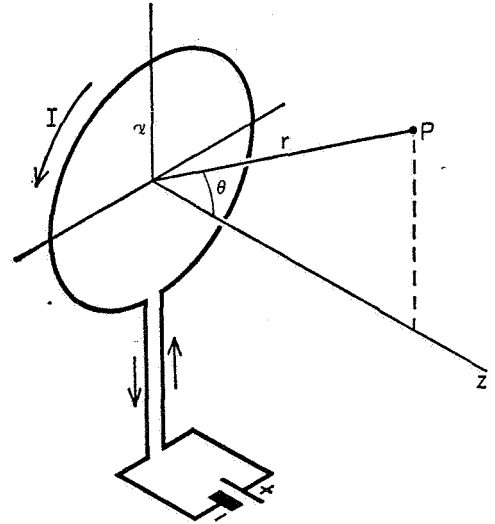


Fig. 8.10-1. A circular Loop Carrying a Current, I, with a Point, P (r, θ), off the Axis of Symmetry

$$\left. \begin{aligned} B_r &= -\frac{\partial V_m}{\partial r}, \\ B_\theta &= \frac{1}{r} \frac{\partial V_m}{\partial \theta}, \text{ and} \\ B_\phi &= 0 \text{ because of symmetry about the } z\text{-axis.} \end{aligned} \right\} (8.10-3)$$

If

$$\frac{a^2}{r^2} \ll 1$$

all but the first term in the series for V_m may be neglected to obtain

$$V_m = \frac{\mu_0 I}{4\pi} \frac{\pi a^2 \cos \theta}{r^2} \quad (8.10-4)$$

where μ_0 is the permeability of vacuum. The term $(\pi a^2 \cos \theta)/r^2$ is the solid angle subtended by the circuit at a remote point P(r, θ).

Let

$$\vec{m} = I \vec{S} \quad (8.10-5)$$

where

\vec{m} = dipole moment of the current loop,

\vec{S} = a vector whose magnitude is equal to the area of the loop.

Since \vec{m} is perpendicular to the loop in a direction determined by the right-hand rule, by substitution

$$V_m = \frac{\mu_0}{4\pi} \frac{\vec{m} \cdot \vec{r}_1}{r^2} \quad (8.10-6)$$

where \vec{r}_1 is a vector along the z-axis whose magnitude is $r \cos\theta$.

A more general expression for \vec{m} can be written for the case of nonplanar, noncircular loops of a conductor with differential volume $d\tau$ and current density \vec{J} . However for the purpose of ordinary design, Eqs. 8.10-6 and 8.10-3 are sufficient. The vector \vec{B} is called the magnetic induction. It is expressed in webers/m² — the weber being a volt-second. Conversion factors between frequently-used magnetic units are given in Section 7.1 of Vol. II.

8.10.4 Design Practices

A magnetically-clean solar panel or array can be obtained by:

- Utilizing backwiring techniques to obtain dipole moment cancellation within a single circuit (Ref. 8.10-3).
- Arranging solar cell circuits of identical layout dimensions in a manner which utilizes symmetrical or mirror properties of the array configuration to provide dipole moment cancellation.
- Reducing or eliminating the use of materials which may become magnetized.

In the case of a) the backwiring can be either one or more insulated wires or a sheet or mesh-type conductor laminated within the cell stack. For example, Ref. 8.10-3 considers in detail the magnetic field characteristics of various round-conductor configurations used as backwiring on large-area high-power solar arrays. The reference recommends that:

- Backwiring for the solar cells of a string (series-parallel circuit) be balanced. Offset backwiring should not be utilized. Injection and collection of solar cell currents for each string should be central and not offset.
- Multiple backwiring should be used for the various strings, both inboard and outboard. Three-wire backwire systems with spacing arranged to produce a "quadrupole null" is recommended.

- Bus bars collecting the string currents for a blanket or panel should be balanced.
- An engineering failure mode analysis should be made for failure modes consisting of one or more open-circuited backwires.

Reference 8.10-4 contains formulas which define the field near twisted leads which carry equal and opposite direct currents. It is shown that, under certain conditions, twisting of wires may strengthen rather than weaken the field.

For the case of solid sheet or foil conductors it may be possible to obtain an unequal current distribution within the conductor even though the injection and collection configuration is adequate. Ref. 8.10-5 describes both current and temperature gradients in thin sheet conductors resulting from a longitudinal component of the Hall effect. (The effect is most pronounced with conductors of high resistivity such as are used for sheet heaters.)

The use of sheet-type backwiring will affect the thermal conductance of the cell stack.

In the case of b) the symmetric or mirror properties inherent in the solar array configuration can be utilized to not only reduce the contaminant magnetic field but also to assist in the selection of the location of sensitive instruments. Ref. 8.10-6 contains a detailed description of this procedure.

Finally, in the case of c), the use of materials which may become magnetized should be avoided in design situations which require extreme cleanliness. However, under normal circumstances the use of Kovar as a solar cell interconnect material may be entirely reasonable. For example, NASA-GSFC evaluated Kovar as a candidate interconnector material for the ATS-6 satellite solar array. The proposed application consisted of approximately 1.4 kg of the material distributed over a total area of 20 m² in 8000 separate connections. The ATS-6 solar panels are each 2.44 m long and are located at their nearest point about 6.40 m from a magnetometer. The results of the evaluation performed by the GSFC Magnetic Test Facility were:

- Comparison with similar configurations indicated that the maximum field at the magnetometer would be a few tenths of a gamma if the Kovar were magnetized to a fairly high level (e.g. 300 gamma at at 0.46m).
- There would be little likelihood of the Kovar becoming magnetized. Spacecraft demagnetization ("deperm") would eliminate magnetization.
- The Kovar would not distort the earth's magnetic field in the immediate vicinity of the magnetometer.

Although Kovar was approved for this application, the material was not selected for the final design for other unrelated reasons.

REFERENCES (CHAPTER 8)

- 8.4-1 R.W. Opjorden, "Solar Cell Optical Design Considerations," Conference Record of the 9th IEEE Photovoltaic Specialists Conference, Silver Spring, Maryland, May 1972.
- 8.5-1 "Beryllium in Aero/Space Structures," The Brush Beryllium Company, Cleveland, Ohio.
- 8.5-2 R.G. Ross, et al., "Measured Performance of Silicon Solar Cell Assemblies designed for use at High Solar Intensities," TM 33-473, Jet Propulsion Laboratory, March 1971.
- 8.6-1 Saint-Jean, NASA TN D-1904, 1963.
- 8.7-1 J. Roger, "Optimal Bus Bars for Rectangular Solar Arrays," Conference Records of the 9th IEEE Photovoltaic Specialists Conference, 1972.
- 8.8-1 E. Levy, Jr., et al., "High Voltage Solar Cell Power Generating System," Conference Records of the 10th IEEE Photovoltaic Specialists Conference, 1973.
- 8.8-2 K.L. Kennerud, "High Voltage Solar Array Operation in the Ionosphere," Conference Records of the 8th IEEE Photovoltaic Specialists Conference, 1970.
- 8.9-1 A. Atzei and J. Capart, "Evaluation and Reduction of the Electromagnetic Fields Associated with a Solar Array," Conference Records of the 9th IEEE Photovoltaic Specialists Conference, 1972.
- 8.9-2 H.W. Boller, et al., "Solar Cells and Generator Technology for the Helios Sun Probe," Conference Records of the 9th IEEE Photovoltaic Specialists Conference, 1972.
- 8.10-1 W.M. Robbins, Jr., "Electromagnetic Forces on Space Structures," NASA CR-476, May 1966.
- 8.10-2 L.E. Wiggins, "Relative Magnitudes of the Space-Environment Torques on a Satellite," AIAA Journal, Vol 2, No. 4, April 1964.
- 8.10-3 J.M. Sellen, Jr., "Backwire and Busbar Placement for Magnetic Cleanliness on Large Area Solar Arrays," Report No. 12738-6007-R0-00, TRW Systems Group, June 1969 (part of Ref. 8.10-7).
- 8.10-4 A.Y. Alksne, "Magnetic Fields Near Twisted Wires," IEEE Transactions on Space Electronics and Telemetry, December 1964.
- 8.10-5 J.D. Tarasuk et al., "Temperature and Current Distribution in an Electrically Heated Wide Metallic Foil," Eleventh Annual Meeting of the Society of Engineering Science, November 11-13, 1974, Duke University, Durham, N.C.
- 8.10-6 J.M. Sellen, Jr. and H.S. Ogawa, "Contaminant Magnetic Fields from Large Area Solar Arrays," Report No. 12738-6006-R0-00, TRW Systems Group June 1969 (part of Ref. 8.10-7).
- 8.10-7 R.K. Cole et al., "Study of Electric Propulsion Spacecraft Plasmas and Field Interactions," Report No. 12738-6016-R0-00, TRW Systems Group, prepared under NASA Contract NAS 7-100 for the Jet Propulsion Laboratory, California Institute of Technology, July 1970.

CHAPTER 9
DESIGN ANALYSIS

CONTENTS

	Page		Page
9.1 Circuit Analysis	9.1-1	9.6.5 Estimating Eclipse Exit Temperatures	9.6-3
9.1.1 Components and Conventions	9.1-1	9.6.6 Electrical-Heat Transfer Analogy	9.6-4
9.1.2 Circuit Theory	9.1-2	9.6.7 Body-Mounted Cylindrical Arrays	9.6-5
9.1.3 Driving Forces and Network Responses	9.1-5	9.6.8 Panel and Paddle Arrays	9.6-7
9.1.4 Operating Points	9.1-5	9.6.9 Computer Programs	9.6-8
9.1.5 Power Relationships	9.1-5	9.7 Thermomechanical Stress Analysis	9.7-1
9.1.6 Reverse-biased Solar Cells	9.1-10	9.7.1 Mechanical Behavior of Materials	9.7-1
9.2 Practical Solar Cell Models	9.2-1	9.7.2 Stresses in Rigid Bonded Layers	9.7-4
9.2.1 Limitations of Basic Model	9.2-1	9.7.3 Stresses in Flexible Bonded Layers	9.7-7
9.2.2 Improved Physical Models	9.2-1	9.7.4 Stresses in Interconnector Expansion Loops	9.7-9
9.2.3 Analytical Models for Computer Work	9.2-2	9.7.5 Effects of External Forces and Moments on Soldered and Welded Joints	9.7-10
9.2.4 Nonanalytical Models	9.2-6	9.8 Fatigue and Wearout Analysis	9.8-1
9.2.5 Selecting the Proper Model	9.2-7	9.8.1 Stress Versus Fatigue Analysis	9.8-1
9.2.6 Practical AC Models	9.2-8	9.8.2 Stress and Strain Loading	9.8-1
9.3 Array Circuit Models	9.3-1	9.8.3 Fatigue of Materials	9.8-2
9.3.1 Illuminated Arrays	9.3-1	9.8.4 Application to Solar Cell Arrays	9.8-3
9.3.2 Partially Shadowed Arrays	9.3-2	9.9 Reliability Analysis	9.9-1
9.3.3 Nonilluminated Arrays	9.3-8	9.9.1 Definitions	9.9-1
9.4 Array Electrical Performance Prediction	9.4-1	9.9.2 Failure Modes and Effects	9.9-1
9.4.1 Analytical Approach	9.4-1	9.9.3 Failure Rates	9.9-2
9.4.2 Sequence for Shifting I-V Curves	9.4-1	9.9.4 Reliability Models	9.9-2
9.4.3 Gathering of Input Data	9.4-1	9.10 Orbital Mechanics	9.10-1
9.4.4 Angle of Incidence	9.4-4	9.10.1 Definitions	9.10-1
9.4.5 Effective Solar Intensity	9.4-4	9.10.2 Simplified Orbit Theory	9.10-2
9.4.6 Glassed Solar Cell I-V Curve	9.4-5	9.10.3 Altitude in Elliptic Orbit	9.10-3
9.4.7 Solar Cell I-V Curve at Changed Intensity	9.4-6	9.10.4 Location in Space	9.10-4
9.4.8 Solar Cell I-V Curve at Operating Temperature	9.4-6	9.10.5 Illumination of the Orbit Plane	9.10-5
9.4.9 Degraded Solar Cell I-V Curve	9.4-6	9.10.6 The Sun Angle	9.19-6
9.4.10 Array I-V Curve	9.4-6	9.10.7 Solar Eclipses	9.10-7
9.5 Shadow Analysis	9.5-1	9.11 1-MeV Fluence Analysis	9.11-1
9.5.1 Definitions	9.5-1	9.11.1 General Procedure	9.11-1
9.5.2 Development of Shadow Patterns	9.5-1	9.11.2 Analysis Inputs	9.11-1
9.5.3 Application to Solar Cell Arrays	9.5-3	9.11.3 Circular Earth Orbits	9.11-2
9.6 Thermal Analysis	9.6-1	9.11.4 Elliptic Earth and Transfer Orbits	9.11-2
9.6.1 Definitions	9.6-1	9.11.5 Interplanetary Trajectories	9.11-3
9.6.2 Heat Transfer by Radiation	9.6-2	References	9. R-1
9.6.3 Heat Transfer by Conduction	9.6-3		
9.6.4 Estimating Operating Temperatures	9.6-3		

TABLES

9.1-1	Current-Voltage Relationships of Circuit Elements	9.1-3	9.6-2	Incident Heating of a Rotating Cylinder in a Synchronous Equatorial Orbit During Equinox	9.6-7
9.1-2	Combination of Elements	9.1-4			
9.1-3	Voltage and Current Dividers	9.1-4	9.10-1	Calculated Values of the Sun Central Angle	9.10-6
9.1-4	Basic Waveforms	9.1-6			
9.2-1	Approximate Low-Frequency AC Parameters for Conventional 2x2 cm Silicon Solar Cells	9.2-9	9.10-2	Solar Cell Array Degrees-of-Freedom	9.10-6
9.6-1	Analogous Quantities	9.6-5	9.11-1	Tabulation of 1-MeV Fluence Components	9.11-1

FIGURES

9.1-1	Simple Battery Circuit	9.1-1	9.2-8	The Transformations an I-V Curve Experiences as a Function of Solar Intensity and Cell Temperature	9.2-8
9.1-2	Forward Biased p-n Junction Device	9.1-1			
9.1-3	Solar Cell I-V Curve Presentations	9.1-2	9.2-9	Solar Cell Small-Signal AC Model	9.2-9
9.1-4	Equivalent Sources	9.1-4	9.2-10	Solar Cell Impedance	9.2-10
9.1-5	Two-loop Circuit with Current Directions and Voltage Polarities Arbitrarily Assigned	9.1-4	9.2-11	Phase Angles for Impedances of Fig. 9.2-10	9.2-10
9.1-6	Typical Networks and Their Responses to Various Non-Sinusoidal Driving Sources	9.1-7	9.2-12	Average Solar Cell I-V Curve	9.2-11
9.1-7	Two Possible Operating Points, Q_1 and Q_2	9.1-8	9.2-13	Range of Incremental Solar Cell Diode Resistances for Solar Cells of Fig. 9.2-12	9.2-11
9.1-8	Combining Load Characteristics	9.1-8	9.2-14	Nimbus-B Solar Cell Array Output Impedance Versus Frequency	9.2-11
9.1-9	Simple Power System	9.1-8	9.3-1	Solar Cell Subgroup Configuration	9.3-1
9.1-10	Solar Cell Array, Storage Battery, and Load Connected in Parallel	9.1-9	9.3-2	Effects of Illumination and Shadowing on the Current-Voltage Relationships of a Solar Cell and a Submodule with Two Cells in Parallel	9.3-2
9.1-11	Energy Balance Model	9.1-9			
9.1-12	Measurement of P_E	9.1-9	9.3-3	Current-Voltage Characteristics of Two Unequal Solar Cells Connected in Series	9.3-4
9.1-13	Solar Cell and Load Model	9.1-9			
9.1-14	Relationships Between Solar Cell Bias Voltage and Power Dissipation	9.1-10	9.3-4	I-V Curves of a Partially Shadowed String Without Shunt Diodes	9.3-5
9.1-15	General Block Diagram of Solar Cell Array Power Subsystem	9.1-10	9.3-5	I-V Curves of the Partially Shadowed String of Figure 9.3-4 with Shunt Diodes	9.3-6
9.1-16	Module Design and Model	9.1-10	9.3-6	Partially Shadowed String Characteristics for Illustrated Shadow Pattern	9.3-7
9.1-17	Current-Voltage Characteristics of Conventional Design at 77°C	9.1-11	9.3-7	Accurate and Approximate I-V Curves of the Partially Shadowed String of Figure 9.3-6	9.3-7
9.1-18	Graphical Solution for the Two Designs at 77°C	9.1-12	9.4-1	Solar Cell Array Electrical Performance Prediction	9.4-2
9.2-1	Equivalent Circuit and I-V Curve of Solar Cell Defined by Equation 9.2-1	9.2-1	9.4-2	Solar Array Geometry for Paddle-Wheel Solar Array Configurations	9.4-4
9.2-2	Distributed Solar Cell Model and Simplification to Second-Order Lumped Parameter Model	9.2-2	9.4-3	Solar Cell Array Geometry for Flat or Body-Mounted Solar Panels	9.4-4
9.2-3	Solar Cell I-V Curve	9.2-4	9.4-4	Solar Cell Array Geometry for Flat Solar Cell Panels	9.4-5
9.2-4	Solar Cell I-V Characteristics as a Function of Temperature	9.2-5	9.5-1	Shadow Geometry	9.5-2
9.2-5	Solar Cell I-V Characteristics as a Function of Intensity	9.2-6	9.5-2	Dimensionless Representation of Normalized Umbra Width, u/d , and Penumbra Width, p/d , as a Function of Normalized Distance to Shadow Casting Object, s/d	9.5-2
9.2-6	Error Introduced by the Approximate Eq. 9.2-15 at the Maximum Power Point Compared to Provided Input Data as a Function of Illumination Intensity and Cell Temperature	9.2-7			
9.2-7	Error Introduced by Assumption of Constant Curve Shape	9.2-7			

9.5-3	Further Shadow Geometry to Show Relation of Distance, s , to Apparent Solar Diameter, $2R$, and Object Width, d	9.5-2	9.7-11	Basic Model of Three Laminated Layers	9.7-7
9.5-4	Normalized Object Half-Width, $d/2R$, Versus Normalized Shadow Plane Distance from Object, s/d	9.5-3	9.7-12	Axial and Shear Stress Distribution in a Bonded Joint for Different Values of the Stiffness Parameters βL	9.7-8
9.5-5	View from Shadow Area Towards Sun for $s < B$, Starting from Sun-Object Centerline and Moving Towards Edge of Penumbra	9.5-3	9.7-13	Variation of the Relative Edge Displacement of a Bonded Joint with the Stiffness Parameter βL	9.7-8
9.5-6	View from Shadow Area Towards Sun for $s > B$, Starting from Sun-Object Centerline and Moving Towards Edge of Penumbra	9.5-4	9.7-14	Simplified Interconnector Model	9.7-9
9.5-7	Normalized Illumination Intensity as a Function of Normalized Location Within the Shadow, m/R , with the Normalized Distance, s/b , as a Parameter	9.5-4	9.7-15	Variation of Nondimensional Force Coefficient f with Geometric Ratios h and s	9.7-10
9.5-8	Average Light Intensity, \bar{I} , in a Shadow from a Long Object Parallel to the Shadow Plane as a Function of Normalized Distance, s/B	9.5-5	9.7-16	Variation of Nondimensional Moment Coefficients m_{1L} and m_{2R} with Geometric Ratios h and s	9.7-10
9.5-9	Example of Shadow Across a Solar Cell Module Consisting of Series-Parallel Connected Cells	9.5-5	9.7-17	Illustration of Interface Shear Stress Distribution in an Interconnector/Solar Cell Joint ($m = t_1/t_2 \ll 1$) for the Three Loading Conditions	9.7-11
9.5-10	Normalized Segment Area, S/R^2 , as a Function of Normalized Segment Height, h/R	9.5-6	9.8-1	Comparison of Mechanical and Thermal Loading with Plasticity	9.8-2
9.6-1	Heat Exchange by Radiation Between Two Small Black Surface Elements	9.6-3	9.8-2	Fatigue Life of Silver as a Function of Effective Strain Range	9.8-3
9.6-2	Typical Cylindrical Solar Cell Array	9.6-6	9.8-3	Fatigue Life of Solder Predicted by Method of Universal Slopes	9.8-3
9.6-3	Typical Flat Solar Cell Arrays	9.6-8	9.8-4	Comparison of Shear Stresses for Various Interconnector Materials	9.8-4
9.6-4	Thermal Network for Solar Cell Panel	9.6-8	9.8-5	Comparison of Effective Plastic Strains for Various Interconnector Materials	9.8-4
9.7-1	Bar Loaded Axially in Tension	9.7-1	9.8-6	Computed Fatigue Lives for Various Interconnector Materials Superimposed on Experimental Data of Ref. 9.8-12	9.8-4
9.7-2	Characteristic Material Stress-Strain Curves	9.7-2	9.9-1	Solar Cell Array Power Loss Due to Random Cell Open-Circuit Failures or Cell Fractures	9.9-3
9.7-3	Strain Hardening Characteristics	9.7-3	9.9-2	Required Number of Interconnectors Per Solar Cell to Meet Specific String Reliabilities When the End-of-Life Percentage of Open Joints is Known	9.9-3
9.7-4	Three-Dimensional Stresses on an Infinitesimal Cube of Material Subjected to an Arbitrary External Load	9.7-3	9.9-3	Reliability Models for System Mission Probability of Success, P_S	9.9-4
9.7-5	Two-Strip Model	9.7-4	9.10-1	Reliability for Angular Momentum	9.10-2
9.7-6	Force and Moment Equilibrium Between Interior Stresses and Edge Shear and Normal Stresses	9.7-6	9.10-2	Geometry of the Ellipse	9.10-3
9.7-7	Influence of Variation in Half-Length/Thickness Ratio on Shear Stress at Interface	9.7-6	9.10-3	Geocentric Equatorial Coordinate System	9.10-4
9.7-8	Influence of Variation in Half-Length/Thickness Ratio on Normal Stress at Interface	9.7-6	9.10-4	Definition of Geometry for Determination of Sun Angle, θ , Between Sun Line and Array Central Axis	9.10-6
9.7-9	Longitudinal Stress in Strip at Various Distances from End of Strip	9.7-6	9.10-5	Percent Sun Time as a Function of Altitude and Sun Angle for Circular Orbits	9.10-7
9.7-10	Thermal Stresses in Solder Layer on Silicon	9.7-7	9.11-1	Solar Cell DENI 1-MeV Fluence After Penetration of a Fused Silicon Cover of Given Thickness	9.11-2

CHAPTER 9

DESIGN ANALYSIS

A substantial portion of the solar cell array design process consists of analyzing or predicting with computational procedures the performance of solar cell arrays. Performance is defined here in a larger sense to encompass both the array's power output capability and its ability to successfully withstand the environmentally induced thermal, mechanical, and electrical stresses during its terrestrial and space life span.

The analytical areas covered in this handbook include photovoltaic output prediction, shadowing and "hot spot" analyses, thermal (temperature) and

thermomechanical stress and fatigue analyses, and reliability models.

For most of the analytical processes employed in solar cell array design work, extensive computer programs are in existence and are being utilized by the aerospace industry. The general features of these programs are described in this chapter.

Occasionally the need arises to perform analyses "by hand" rather than by the use of a computer. To facilitate such computations, simplified procedures are given.

9.1 CIRCUIT ANALYSIS

In this section the solar cell polarity definition and circuit analysis principles are reviewed. Models and analogs are given which permit "hot-spot" and simplified temperature analyses to be performed. This section provides a basis for all following sections in this chapter.

9.1.1 Components and Conventions

Consider a circuit containing an electrochemical battery (Figure 9.1-1). By long-established convention, the current flow is from the positive battery terminal through the external circuit to the negative battery terminal, and then inside the battery from the negative to the positive battery terminal. Current always flows from a higher (more positive) potential to a lower (more negative) potential. A voltmeter connected to the battery with its positive lead attached to the positive battery terminal will provide a positive ("right") reading. An ammeter connected into the circuit with its positive terminal to the positive battery terminal will also provide a positive ("right") reading ("plus" of an ammeter always connects to the higher voltage point).

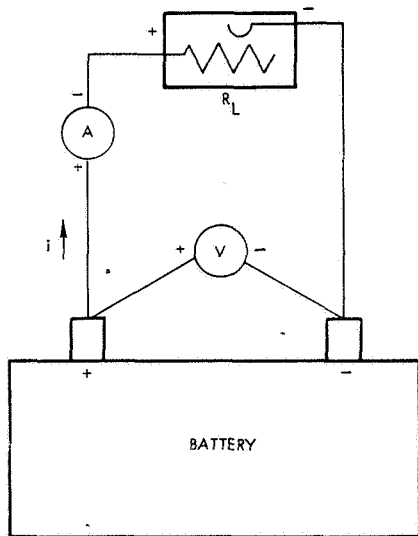


Fig. 9.1-1. Simple Battery Circuit

The flow of electrons is exactly opposite to that of the (conventional) current. For instance, the current flows "into" the anode (or plate) of a vacuum tube and comes "out of" the cathode (filament) but the electrons are emitted by (come out of) the cathode and propagate to the anode.

A semiconductor diode is forward biased when the (conventional) current flows through it in the direction of the arrow of the printed-on diode symbol. This happens when the positive side of a voltage source is

connected to the diode p-layer and the negative side to the n-layer. Hence, the diode symbol arrow points from p to n or from the anode to the cathode (Figure 9.1-2).

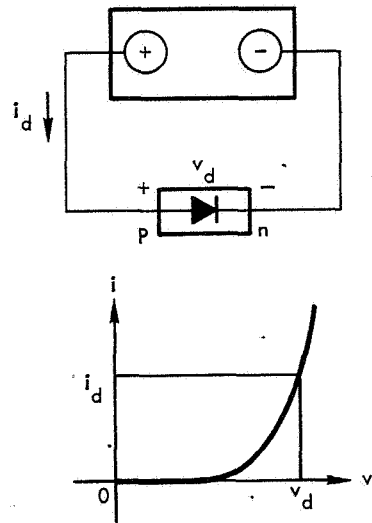


Fig. 9.1-2. Forward Biased p-n Junction Device

The diode symbol printed on a zener diode is in the same direction and has the same physical meaning as that of the ordinary (rectifier) diode except that in use zener diodes are "reverse" biased (i. e., positive voltage is connected to the n-layer).

A nonilluminated solar cell is forward biased like a diode, namely by connecting the positive terminal of a bias supply to the cell p-contact. An illuminated solar cell develops a "forward" output, i. e., its p-contact is the positive voltage terminal. When the negative terminal of an overpowering external bias supply is connected to a cell p-contact, the cell becomes reverse biased regardless of the illumination level.

Solar cell and array I-V characteristics are typically shown in the first quadrant of the voltage (abscissa)-current (ordinate) coordinate system (Figure 9.1-3b). This presentation is consistent with the theoretical solar cell model in which current is a function of voltage. It is equally consistent with electrical measurement techniques where positive voltage, current, and power output are obtained from the cell working into a positive conductance load. Some earlier presentations of the I-V curve in the fourth quadrant of the same coordinate system led to negative current, positive voltage, and hence confusingly, to negative power output from the cell into a negative conductance load (Figure 9.1-3a).

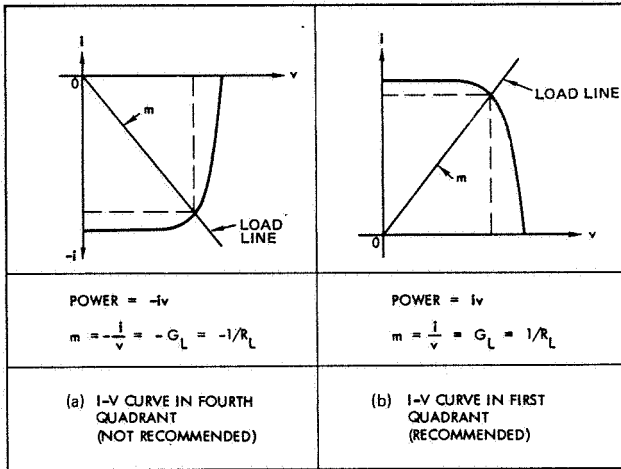


Fig. 9.1-3. Solar Cell I-V Curve Presentations

9.1.2 Circuit Theory

Circuit theory is concerned with the macroscopic analysis of electrical circuits and devices at their terminals. Circuit analysis is based on the principle of conservation of energy and the validity of all physical and chemical laws. Real circuits and devices are modeled by a selection of, or combination of, the two active elements (sources) and the three passive elements shown in Table 9.1-1. All conductors are ideal (i.e., without resistance or impedance). The five circuit elements in Table 9.1-1 are abstractions which have no physical meaning in terms of their I-V characteristics as given in this table. Similarly, real components are never "pure" elements and are never linear over all ranges of voltages and current. Because of the nonlinear behavior of real components, it is usually necessary to develop different circuit models to describe the actual hardware as truthfully as possible for the specific case to be analyzed. Specific models of the same physical circuit that may be considered, are dc (direct current), low frequency, high frequency, and small signal and large signal analyses.

Network Simplifications

Networks can frequently be simplified by combining parallel or series connected elements into single elements, according to Table 9.1-2. Complex ladder networks may be simplified by step-by-step combinations of series and parallel elements. Sometimes circuits may be simplified by looking for equipotential junctions and connecting them with conductors. Table 9.1-3 lists voltage and current dividers helpful for circuit simplification. Networks may often be simplified by using one of the three theorems below.

Thevenin's theorem: Any active terminal pair a-b composed of combinations of active and passive elements can, with respect to these terminals, be represented as an ideal voltage source $V_o(t)$ in series with an operational element (impedance, etc.) $Z_s(p)$ between terminals a-b. The voltage $V_o(t)$ is the open-circuit voltage of the terminals a-b (i.e., no external elements connected to them). The impedance function $Z_s(p)$ is the (driving point) impedance function measured at the terminals a-b when all internal ideal voltage sources are shorted and all internal ideal current sources are opened (i.e., all sources set to zero).

The letter p denotes the operational form of the time derivative. For dc analysis, $Z_s(p)$ is simply R.

Norton's theorem makes the same statement for a network in terms of its short-circuit current and driving point admittance for an equivalent current source in parallel with that admittance.

The conversion of voltage sources into current sources and vice versa is as follows (see Figure 9.1-4):

Any ideal voltage source, $V_o(t)$, in series with an impedance, Z_o , is equivalent to an ideal current source, $I_o(t)$, in parallel with an impedance, Z, such that $Z_o = Z$ and $V_o = ZI_o$.

It should be noted that a voltage source must always be connected to a series element and a current source to a parallel element if infinite currents and voltages are to be prevented.

Network Equations

Any network may be analyzed by writing either node equations or loop equations for the circuit under consideration and solving those for the desired quantity. These network equations are based on Kirchhoff's laws which are as follows:

Kirchhoff's current law states that the algebraic sum of all currents leaving or entering any junction (node) at any time is zero. His voltage law states that the algebraic sum of all branch voltages around any closed loop at any time is zero.

Example of Analysis by Loop Equations

Consider the circuit of Figure 9.1-5. It has four branches and three nodes.

As a first step, we arbitrarily assign branch currents and node voltages to the circuit. Their direction and polarity will always come out right; i.e., when a value comes out positive, it is as initially assumed. If it comes out negative, it is opposite to that initially assumed. Also, we assign the (also arbitrary) artificial loop currents i_a and i_b .

We now apply Kirchhoff's voltage law and write the loop equations

$$-V_0 + i_1 R_1 + i_2 R_2 = 0$$

$$-i_2 R_2 + i_3 R_3 + i_4 R_4 = 0$$

We can reduce the number of unknowns from 3 to 2 by noting that $i_a = i_1$ and $i_3 = i_4 = i_b$ and make the equations solvable

$$-V_0 + i_a R_1 + (i_a - i_b) R_2 = 0$$

$$-(i_a - i_b) R_2 + i_b R_3 + i_b R_4 = 0$$

Table 9.1-1. Current-Voltage Relationships of Circuit Elements

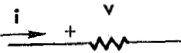
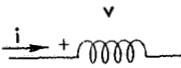
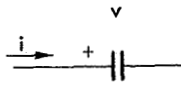
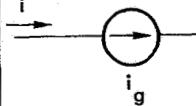
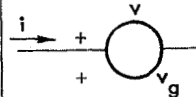
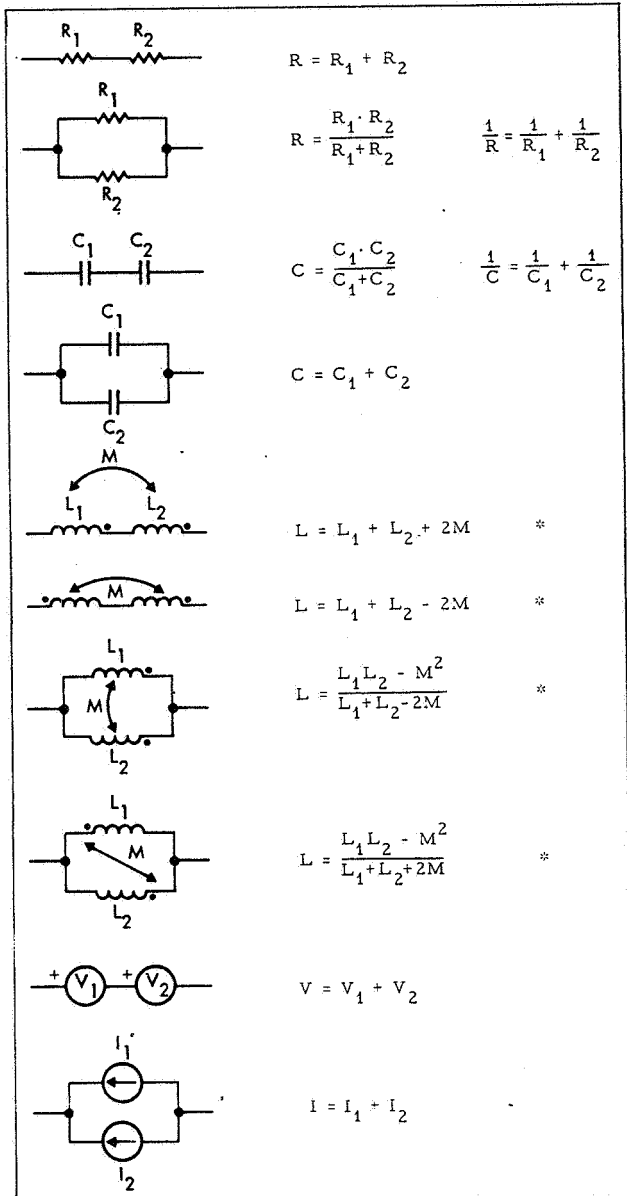
Element	Parameter	Unit	Symbol	Current-Voltage Equation	Relationships
Resistor	Resistance R	Ohms		$v = Ri$	Power $P_R = Ri^2 = Gv^2$
	Conductance G	Ohms ⁻¹		$i = Gv$	
Inductor	Inductance L	Henrys		$v = L \frac{di}{dt}$	$v = \frac{d\lambda}{dt}, \lambda = Li$
	Inverse Inductance Γ	Henrys ⁻¹		$i = \frac{1}{L} \int_0^t v(t)dt + i(0)$	Stored energy $W_L = \frac{1}{2} Li^2 = \frac{1}{2} i\lambda = \frac{1}{2L} \lambda^2$
Capacitor	Capacitance C	Farads		$i = C \frac{dv}{dt}$	Stored energy $W_C = \frac{1}{2} Cv^2 = \frac{1}{2} qv = \frac{1}{2C} q^2$
	Inverse Capacitance D	Farads ⁻¹		$v = \frac{1}{C} \int_0^t i(t)dt + v(0)$	$i = \frac{dq}{dt}, q = Cv$
Current Source	Current	Amperes		$i = i_g$	
Voltage Source	Voltage	Volts		$v = v_g$	

Table 9.1-2. Combination of Elements



*Equations apply also for $M = 0$.

Table 9.1-3. Voltage and Current Dividers

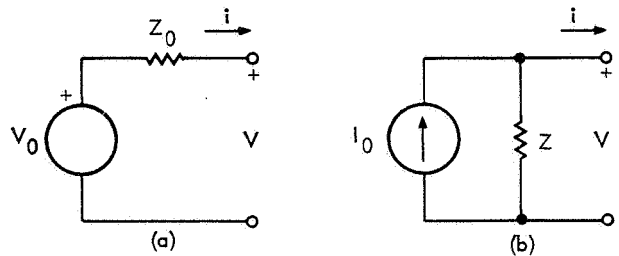
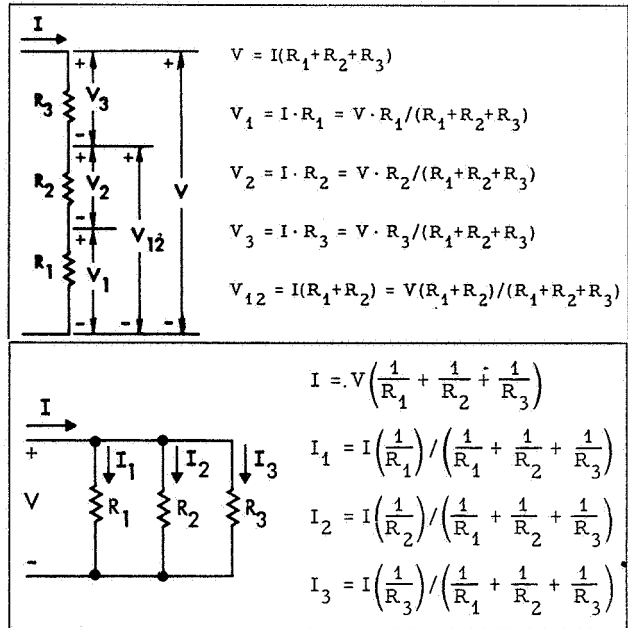


Fig. 9.1-4. Equivalent Sources. (Sources (a) and (b) are equivalent sources if $Z_0 = Z$ and $V_0 = ZI_0$.)

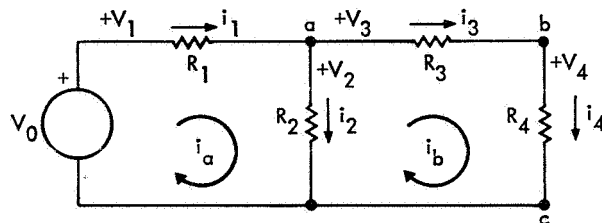


Fig. 9.1-5. Two-loop Circuit with Current Directions and Voltage Polarities Arbitrarily Assigned

Example of Analysis by Node Equations

Using Kirchoff's current law, we see in Figure 9.1-5 that at nodes a, b, and c

$$-i_1 + i_2 + i_3 = 0$$

$$-i_3 + i_4 = 0$$

$$+i_1 - i_2 - i_4 = 0$$

We also note that $V_1 = V_0 - V_2$ and $V_3 = V_2 - V_4$, so that

$$-\frac{V_1}{R_1} + \frac{V_2}{R_2} + \frac{V_3}{R_3} = 0$$

$$-\frac{V_3}{R_3} + \frac{V_4}{R_4} = 0$$

This pair of equations can be written as

$$-(V_0 - V_2)G_1 + V_2G_2 + (V_2 - V_4)G_3 = 0$$

$$-(V_2 - V_4)G_3 + V_4G_4 = 0$$

which can again be solved. Simultaneous equations in several unknowns are usually solved by the method of substitution, or by determinants, or by modern, high-level language computer codes.

If the foregoing circuit had contained capacitances and/or inductances, the analysis would have been similar, except that the I-V relationships of Table 9.1-1 would have been used. For convenience, the operational forms $p \equiv d/dt$ and $1/p \equiv \int dt$ are frequently used.

9.1.3 Driving Forces and Network Responses

In general, the purpose of a network analysis is to determine the response of the network under consideration to a particular driving force (voltage or current source) if the network is predominantly passive, and to determine the performance of the network under a variety of load conditions if the network is predominantly active (the solar cell array or energy storage battery, for instance). Analysis of a given real system may require the formulation and solution of more than one set of network equations representing the same system.

Waveforms and Circuit Elements

The response of a network depends significantly on the waveform of the driving source. The interest in the response of a network is usually connected with time, except for the steady-state, dc case. Of special interest in array analysis are driving sources having basic waveforms and mathematical descriptions, as shown in Table 9.1-4. One of the non-sinusoidal waveforms can be obtained from the other by integration or differentiation. Comparison with Table 9.1-1 shows that a step current, $i_0U(t)$, applied to a capacitor produces a slowly rising voltage response in this capacitor

$$v_c(t) = \frac{1}{C} \int_0^t i_c(t) dt + v_c(0); i_c(t) = i_0U(t); t > 0$$

$$\therefore v_c(t) = \frac{1}{C} i_0t + v_c(0)$$

The capacitance can, therefore, be utilized to integrate a current waveform and, conversely, differentiate a voltage waveform. An inductance differentiates a current and integrates a voltage waveform.

The responses of a number of basic networks of interest in solar cell array analysis to some driving sources of interest are shown in Figure 9.1-6.

9.1.4 Operating Points

Operating points (also known as quiescent points) are formed by the intersections of the I-V characteristics of two or more elements connected in series or parallel. Typically, the operating point is determined by a dc analysis, and further interest exists to examine the circuit's small signal ac response.

For a resistively loaded solar cell the operating point is defined by the intersection of the load line and the cell's I-V curve (Figure 9.1-3).

Frequently, an array is loaded by a combination of resistive and constant-power loads (Figure 9.1-7). If the load requirement is less than the array capability, two intersections exist and the power system operation may be unstable, flipping back and forth between the two operating points. The combination of loads is obtained by summing the load currents at constant voltages, as illustrated in Figure 9.1-8.

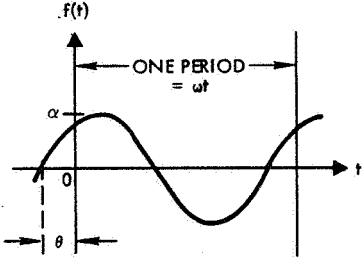
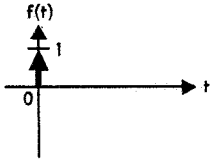
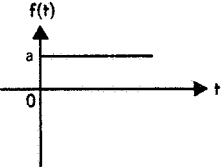
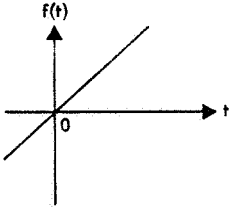
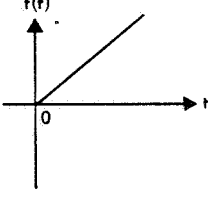
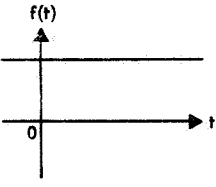
The operating point of the simple power system of Figure 9.1-9 frequently is to be determined. The three components — array, battery, and load — are all connected in parallel, so that V is common to all of them. First it is necessary to assign a direction to the positive current flow. Either charging or discharging may be associated with "positive" current flow; it depends only on the viewpoint. For convenience, let us (arbitrarily) define "positive" current as coming out of the positive battery terminal. Since by Kirchoff's law $I_L = I_A + I_B$, the bus voltage V must adjust itself. There is only one solution for this case and if it has been found, all branch currents and voltages are known. The graphical solution of a simple power subsystem problem is illustrated in Figure 9.1-10. In the case of the battery being charged (left graph of Figure 9.1-10), the available array current, I_A , is greater than the load current, I_L , and the magnitude of the battery charging currents is $|I_B| = I_A - I_L$. In the case of the battery being discharged (right graph of Figure 9.1-10), the available array current, I_A , is less than the required load current, I_L , requiring a current from the battery of magnitude $|I_B| = I_L - I_A$.

9.1.5 Power Relationships

Power Characteristics of Sources

Power or energy sources in electric circuit analysis are hypothetical circuit elements which do not reflect physical sources. By definition, any ideal voltage source can supply an infinite amount of current, power, and energy while an ideal current source can supply an infinite voltage, power, and energy. As

Table 9.1-4. Basic Waveforms

Function	Equation	Description
	$f(t) = \alpha \sin(\omega t + \theta)$ $\omega = 2\pi f$	Sinusoidal Function
	$f(t) = \delta(t)$ $\delta(t) = \frac{d}{dt} U(t)$ $\int_{0^-}^{0^+} \delta(t) dt = 1$	Impulse Function
	$f(t) = aU(t)$ $U(t) = \int_0^t \delta(t) dt$	Step Function
	$f(t) = at$	Rising Function
	$f(t) = atU(t)$	Ramp Function
	$f(t) = a$	DC

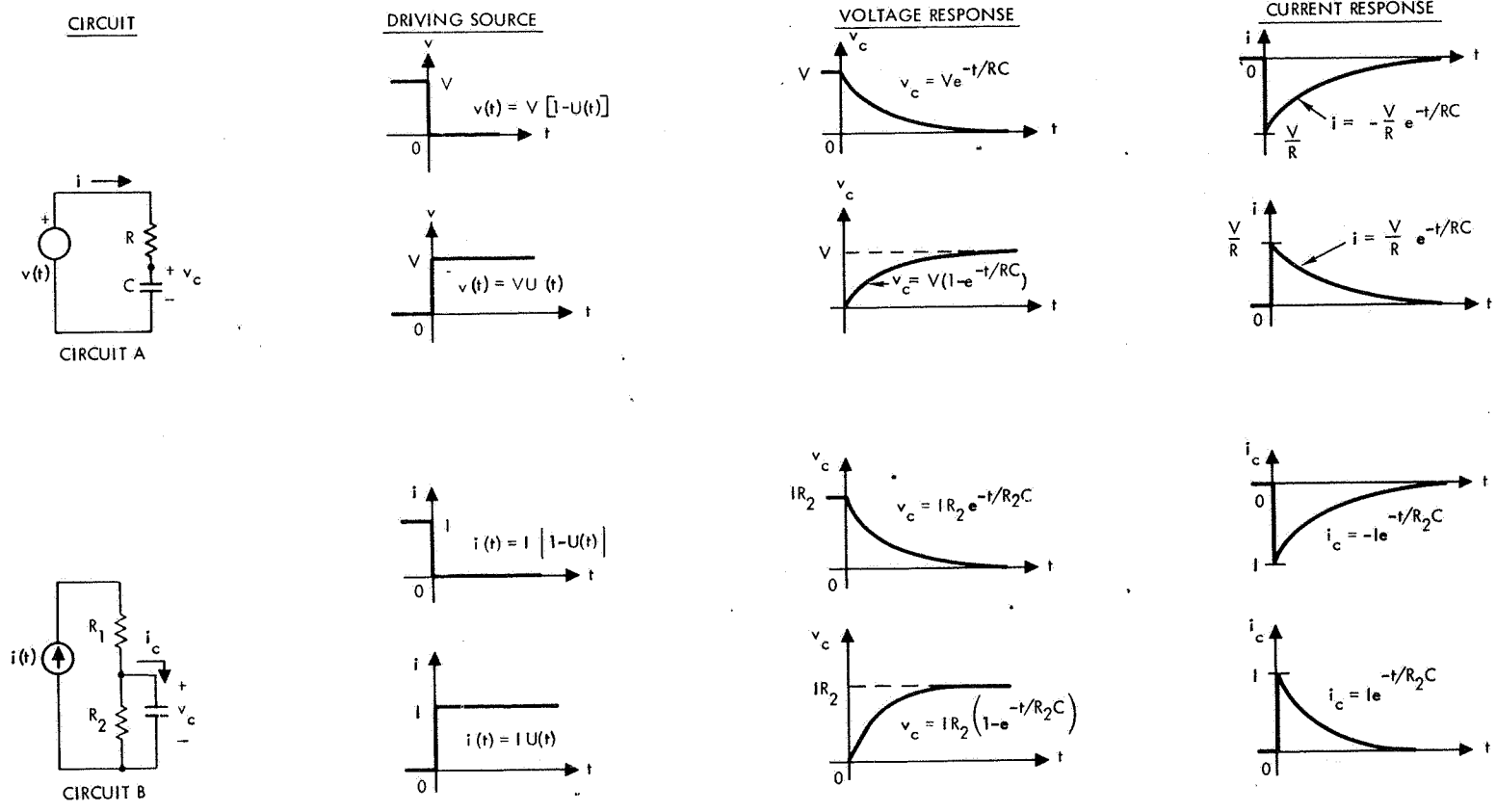


Fig. 9.1-6. Typical Networks and Their Responses to Various Non-Sinusoidal Driving Sources

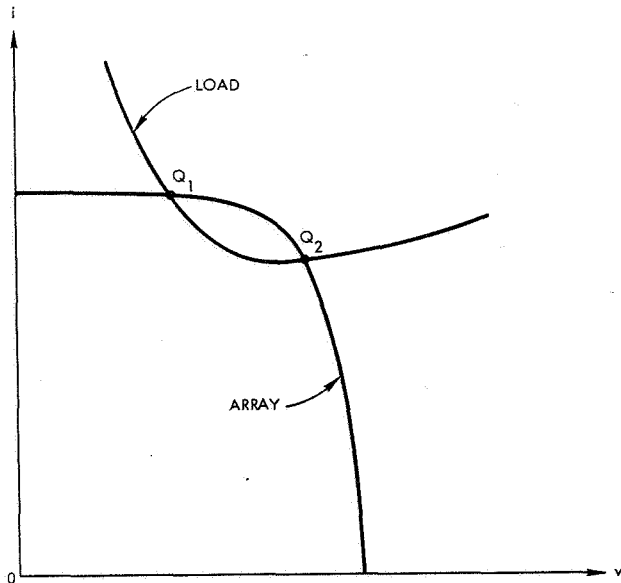


Fig. 9.1-7. Two Possible Operating Points, Q₁ and Q₂

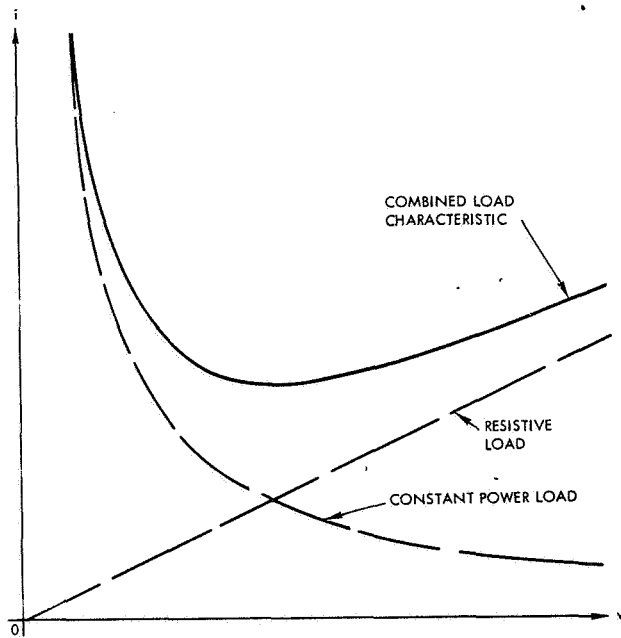


Fig. 9.1-8. Combining Load Characteristics

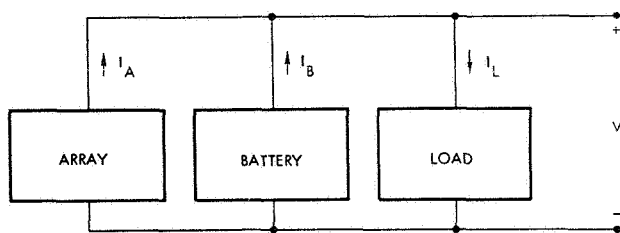


Fig. 9.1-9. Simple Power System

a corollary to this, both sources can be a sink of any amount of power or energy. The power or energy which such sources supply or accept (absorb) is defined by their terminal voltages and currents, and is totally independent of the amount of power dissipated in the resistance or conductance associated with the voltage or current sources, respectively.

The concept of power dissipation in ideal sources, as real as it may be, is frequently questioned. Correctly speaking, one should rather speak of power "absorption." The question is, then, where the absorbed power goes because the principle of conservation of energy applies. The answer will be provided by writing and solving an energy balance equation. In the special case of a reverse-biased solar cell, all of the energy goes into heating of the cell, as shown in the next discussion.

Power Dissipation in Reverse-Biased Solar Cells

The total energy input which contributes to heating of a reverse-biased solar cell consists of both the solar radiation input and the full electrical energy input as measured by the product of cell terminal current and terminal voltage. This conclusion can be derived independently either from energy balance or from electrical circuit considerations.

Energy Balance Considerations

In the steady state and in space, the solar cell temperature, T (absolute), is determined by the energy flow balance (or power balance) equation derived from Figure 9.1-11, as follows:

$$P_R = P_S - P_E \quad (9.1-1)$$

and from Stefan-Boltzmann's law

$$P_R = \epsilon \sigma T^4 \quad (9.1-2)$$

where ϵ is the emissivity and σ is Boltzmann's constant.

The solar input, P_S , and the electrical output from the cell, P_E , are independent variables. The radiant heat energy outflow from the cell, P_R , is the resulting or dependent variable. P_E depends on the load but is limited to $\eta_{max} P_S$ if the load is passive (η_{max} is the maximum solar cell efficiency at the actual operating conditions and as defined in Section 3.2.5). If the load contains an energy source, P_E may take on large negative values, indicating heat dissipation in the cell.

If the cell operates in its normal power output mode, the wattmeter in Figure 9.1-12 measures the cell output. If the cell becomes reverse-biased, V (in Figure 9.1-12) and, therefore, P_E become negative, i.e., power flows into the cell. From Equation (9.1-1) above,

$$P_R = P_S - (-P_E) = P_S + P_E \quad (9.1-3)$$

which confirms that, as far as the cell is concerned it "sees" both the solar input, P_S , and the electrical input, $P_E = V \cdot I$, as read on the wattmeter or on independent voltage and current meters. The product $V \cdot I$ in the dc steady state always gives the correct dissipation.

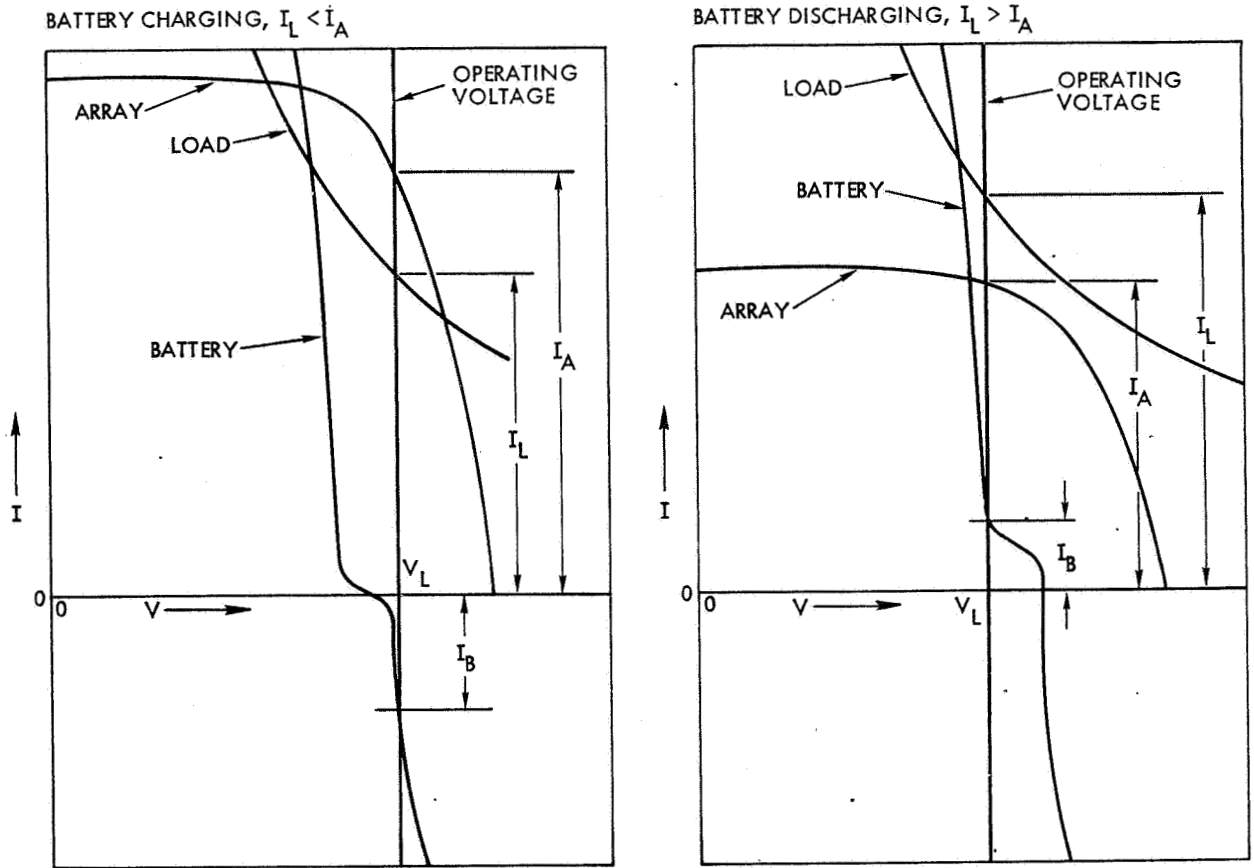


Fig. 9.1-10. Solar Cell Array, Storage Battery, and Load Connected in Parallel (Condition $\Sigma I = 0$ must be satisfied in all cases)

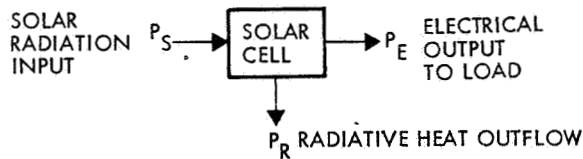


Fig. 9.1-11. Energy Balance Model

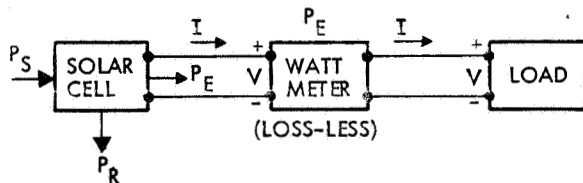


Fig. 9.1-12. Measurement of P_E

Electrical Circuit Considerations

For positive solar cell output voltages according to the convention of Figure 9.1-13, the cell current and power output varies as shown to the right of the current axes in Figures 9.1-14a and 9.1-14b. Figure 9.1-14c illustrates that when the cell operates at its maximum power point the amount of power available for cell heating, P_R , is at a minimum.

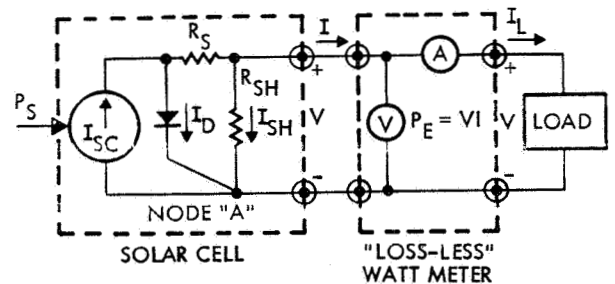


Fig. 9.1-13. Solar Cell and Load Model (see text for limitations of this model)

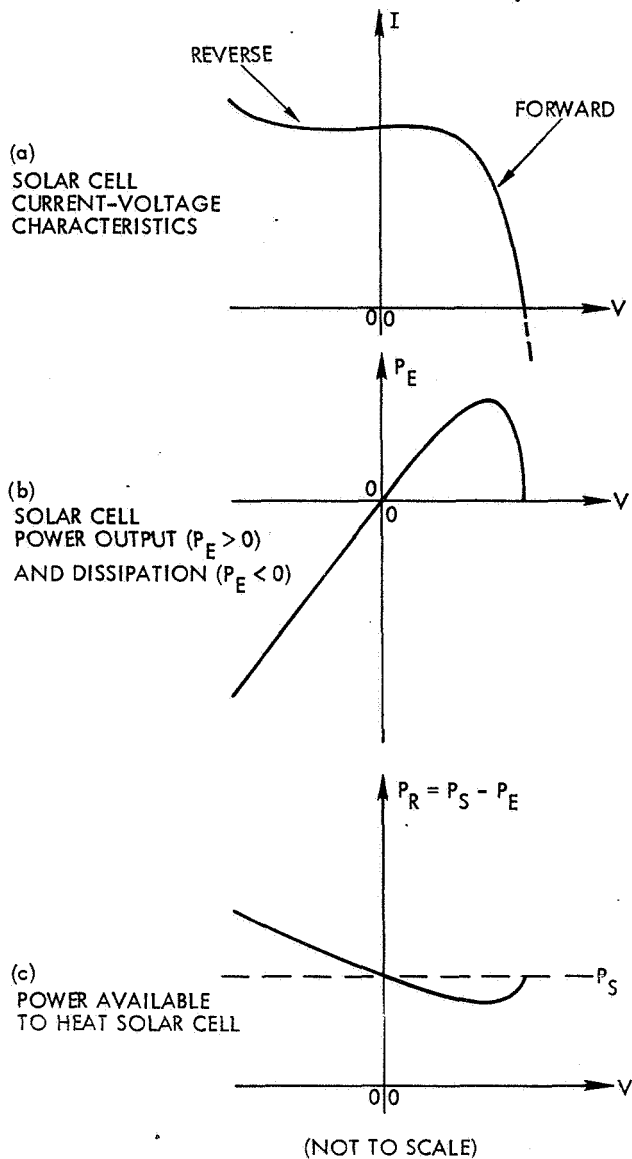


Fig. 9.1-14. Relationships Between Solar Cell Bias Voltage and Power Dissipation

For negative cell voltages, i.e., reverse bias (achieved with a generator within the load), the power output from the cell is negative according to the convention of Figure 9.1-13, which means that the power is dissipated within the cell. This is consistent with Figure 9.1-13 and Figure 9.1-14a). Figure 9.1-14c) shows the increase in P_R for increasing reverse bias.

It is also evident from Figure 9.1-13 that if the polarity of V reverses, all current greater than I_L , i.e., $I - I_L$, must flow through R_{SH} because the diode blocks the current flow. Again the dissipation in the cell is independently determined by P_S and P_E , and $P_R = P_S - P_E$. In the fully shadowed case $P_S = 0$ and $P_R = P_E$. Hence, in the fully shadowed case the curve of $P_R(V)$, Figure 9.1-14c) exists only to the left of the origin.

9.1.6 Reverse-Biased Solar Cells

This section describes the circuit analysis aspects of the so-called "hot spot" problem and the analytical methods of solution. In general, the solar cell array is electrically subdivided into a number of solar cell "modules" (also called "strings") which are connected through blocking diodes to the main array bus. The bus voltage, V_B , is held relatively constant by some kind of regulator independently of the solar cell array output capability. The nomenclature is defined in Figure 9.1-15. A single submodule containing an "affected" cell (i.e., a failed-open or shadowed cell) may be isolated from the remainder of the string, as illustrated in Figure 9.1-16.

The reverse voltages on, and the power dissipations in the cells connected in parallel with the affected cell are obtained by writing suitable loop and node equations and solving them. The node equations for current and the loop equations for voltage, taken in the direction of current I_1 are as follows:

$$\text{At node A: } I_A - I_U = 0$$

$$\text{At node B: } I_U - I_1 = 0$$

$$\text{Loop } I_1: \quad V_A + V_U - V_B = 0$$

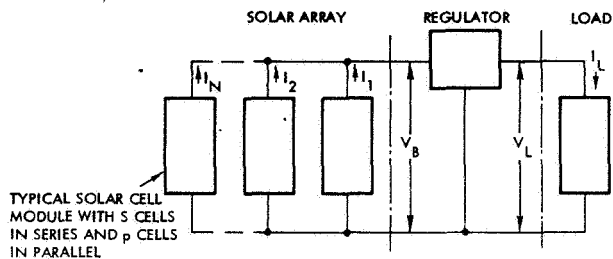


Fig. 9.1-15. General Block Diagram of Solar Cell Array Power Subsystem

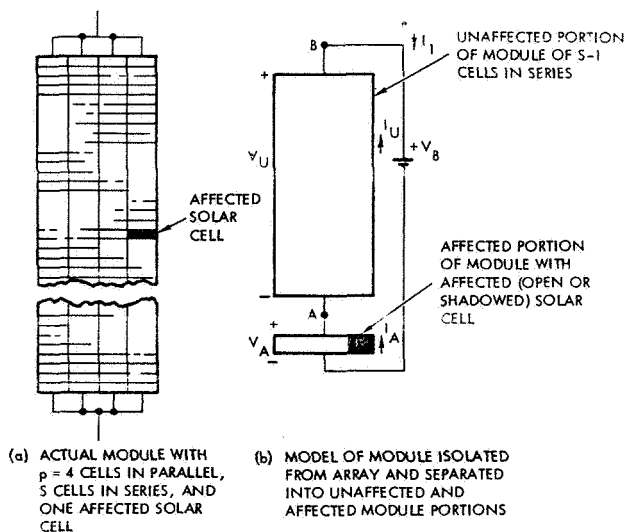


Fig. 9.1-16. Module Design and Model

These nonlinear equations, existing in the first and second quadrant of the I-V coordinate system, must now be solved simultaneously. This can be accomplished with numerical (computerized) or graphical methods. The latter is illustrated here.

First, the current-voltage (I-V) characteristics of the three circuit elements of Figure 9.1-16 are constructed, based on actual solar cell test data. For example, Figure 9.1-17 shows these combined I-V curves for two variations of a particular design, namely, two and four cells in parallel by 154 cells in series. Also shown for each case are two different reverse leakage values; one is based on a very low leakage current (at any voltage) while the other cell is based on a very high leakage current which had been measured on a sample of cells. The method for constructing I-V curves of partially shadowed (or open) solar cell circuits is based on Section 9.3.

The graphical solutions of Equations (9.1-1) through (9.1-3) are effected with reference to Figure 9.1-17 as follows. From Equations (9.1-1) and (9.1-2) it is obvious that the current in all circuit

elements is the same, i. e., $I_A = I_U = I_I$. The objective is now to find that current for which Equation (9.1-3) is satisfied, that is, for which $V_A = V_U - V_B$ (note that V_A is a negative quantity and the signs are consistent). The graphical solution can be simplified by plotting $I_U(V_U - V_B)$ instead of $I_U(V_U)$ and inverting the sign of V_A . This is shown in Figure 9.1-18. The intersections of the curves readily provide the operating points Q_1 through Q_4 .

In Figure 9.1-18 only four operating points are shown. In practice, however, things are more complicated. For the design with two cells in parallel ($p = 2$), the not-failed or unshadowed cell in an affected submodule may be biased at any point between Q_1 and Q_2 , provided, of course, that its reverse characteristics lies within that range. For the design with four cells in parallel ($p = 4$), the affected submodule may be biased between Q_3 and Q_4 ; however, the dissipation in each of the three unaffected cells is one-third of that indicated by Q_3 and Q_4 only if all three cells have the same (i. e., perfectly matched) reverse characteristics. If the reverse characteristics are mismatched, one cell may dissipate a greater amount than is the case when the dissipation is equally shared by the cells.

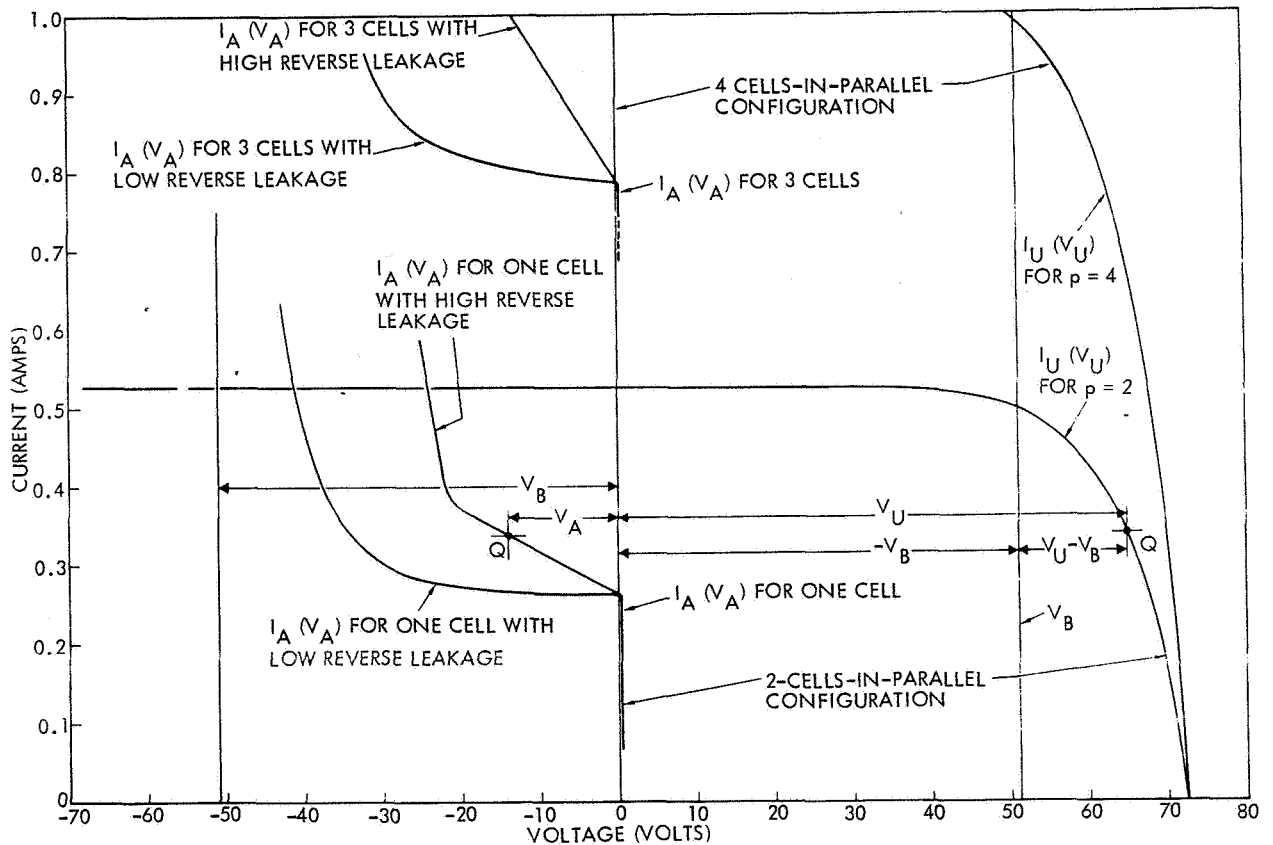


Fig. 9.1-17. Current-Voltage Characteristics of Conventional Design at 77°C

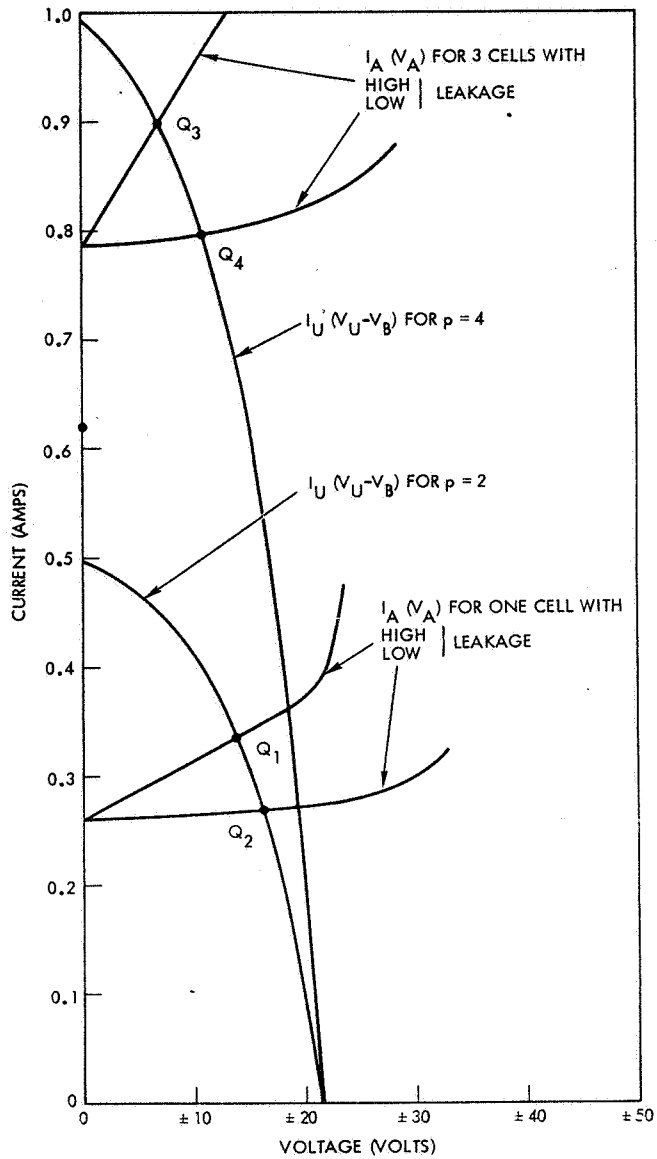


Fig. 9.1-18. Graphical Solution for the Two Designs at 77°C

9.2 PRACTICAL SOLAR CELL MODELS

9.2.1 Limitation of Basic Model

The basic solar cell equation derived from solid-state physics theory was shown in Section 3.2. This equation, however, does not represent the actual solar cell I-V characteristics with sufficient accuracy to be useful for engineering analysis. Observations of the solar cell terminal characteristics under a variety of test conditions have led to the inclusion of three additional parameters— A , R_S , and R_{SH} —in the solar cell equation, as follows:

$$I = I_L - I_o \left[\exp \left[\frac{e(V + I \cdot R_S)}{kT} \right] - 1 \right] - \frac{V}{R_{SH}} \quad (9.2-1)$$

where the symbols are defined as follows:

A = an arbitrary curve-fitting constant between 1 and 5

R_S = cell's series resistance (see Figure 9.2-1)

R_{SH} = shunt resistance (see Figure 9.2-1)

I = cell's output current

I_L = light-generated current

I_o = diode saturation current

e = electronic charge

V = cell's terminal voltage

k = Boltzmann's constant

T = absolute temperature

The solar cell model in Figure 9.2-1 has been used widely for solar cell and array analysis (Ref. 9.2-1); however, it still exhibits some minor but occasionally objectionable deviations from actual solar cell characteristics. One of the reasons for such deviations is the difficulty in accurately measuring the cell series resistance (see Section 11.2). Therefore, more detailed cell models have been developed, as discussed in the following. No single model exists at this time which accurately represents all currently available solar cells over all ranges of temperature, illumination intensity, and radiation damage.

The term " $(V + I \cdot R_S)$ " in Eq. 9.2-1 is sometimes shown as " $(V - I \cdot R_S)$." This term represents the diode voltage, V_D , inside the solar cell. The magnitude of this diode voltage is greater than the cell terminal voltage, V , when power is delivered by the cell to an external load. If the flow of positive current for the cell model is defined (arbitrarily) as in Figure 9.2-1, then $V_D = (V + I \cdot R_S)$. On the other hand, if the positive current flow would be defined

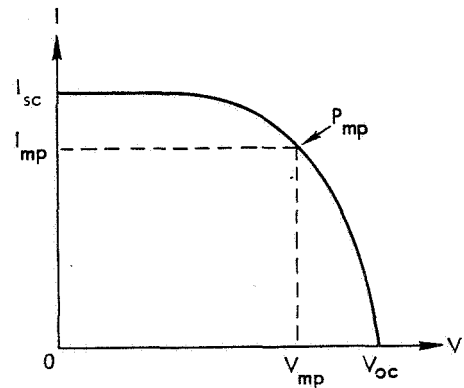
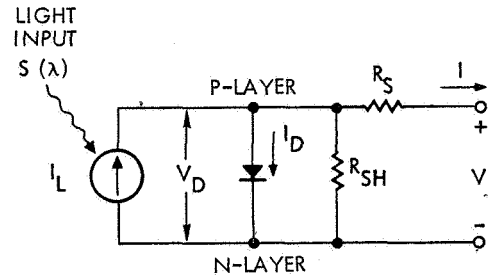


Fig. 9.2-1. Equivalent Circuit (Top) and I-V Curve (Bottom) of Solar Cell Defined by Equation 9.2-1

opposite to that shown in Figure 9.2-1, the sign would reverse so that $V_D = (V - I \cdot R_S)$ would become the correct form (see also Section 9.1 for conventions).

9.2.2 Improved Physical Models

Physical models are primarily of interest to the solar cell device engineer in that they can aid him in deepening his understanding of the energy conversion mechanism and in improving the operating efficiency of the solar cells. To the array designer, physical models are of interest only to the extent that they allow him to develop analytical tools with which he can accurately predict array performance over a wide range of operating conditions.

Inasmuch as in a planar solar cell the p-n junction, series resistance and other cell parameters are distributed over a relatively large area, individual circuit element representations by so-called "lumped parameter" models are expected to lead to errors. In an actual cell, voltage gradients and varying current densities are found throughout the device. As a first

step of improvement, a "second order" lumped parameter model was developed (Figure 9.2-2d). The values of the equivalent circuit components were determined from actual solar cell measurements of earlier p-on-n cells which exhibited double-diode characteristics (Ref. 9.2-2). Recently, modern n-on-p cells were also found to have two distinctly different, dominant p-n junction characteristics which are related to minority carrier diffusion and recombination effects (Ref. 9.2-3).

- The parameters I_o , A , and R_S are very difficult to measure over all ranges of interest.
- Even if all these parameters were known to a statistically significant degree, they would not yield sufficiently accurate computer-generated I-V curves as required for array analysis.

From Ref. 9.2-2. Reprinted with permission of the Pergamon Press, Inc.

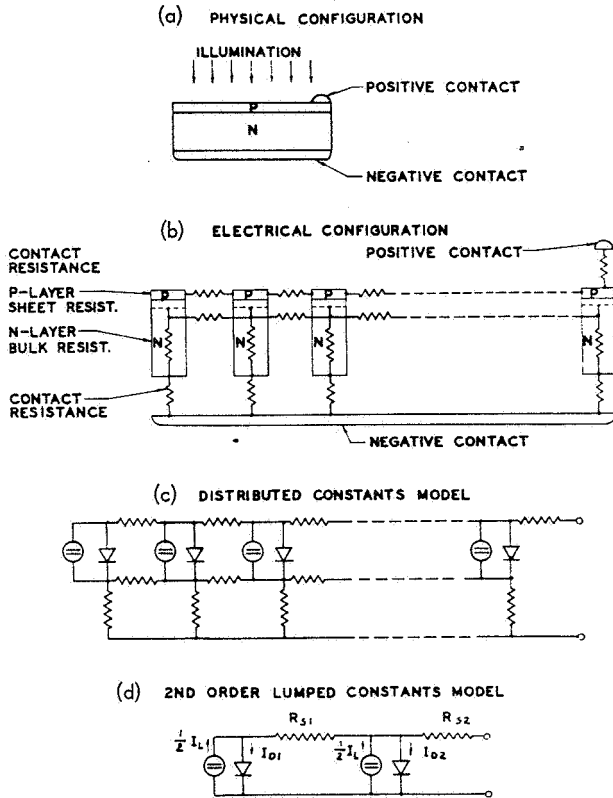


Fig. 9.2-2. Distributed Solar Cell Model and Simplification to Second-Order Lumped Parameter Model (Illustrated for p-on-n Cells, from Ref. 9.2-2)

A fully distributed parameter solar cell model was evaluated using transmission line theory (Ref. 9.2-4), while a detailed distributed series resistance model was developed specifically for grid-line optimization work (Ref. 9.2-5). However, these two models are of no significance to the array designer.

None of the physical models lend themselves in a practical way to solar cell or array performance analysis. The reasons for this are three-fold:

- Essentially all of the solar cell parameters (in Eq. 9.2-1 or Figure 9.2-1) vary with any one or any combination of temperature, illumination intensity, and radiation damage.

9.2.3 Analytical Models for Computer Work

Analytical expressions of the solar cell I-V curve shape generally are derived from the solar cell model, Eq. 9.2-1. This equation is altered such that the computer can derive its own curve-fitting constants from the experimental solar cell test data input. Three typical models are shown below.

"General Electric" Model*

This solar cell mathematical model is based on Eq. 9.2-1 which defines the relationship between current and voltage of the device. Eq. 9.2-1 is rewritten as follows:

$$I = I_L - I_o \left\{ \exp [k_o (V + R_S I)] - 1 \right\} - V/R_{SH} \quad (9.2-2)$$

where

I = current through the load

I_L = photovoltaic current across the junction

R_S = series resistance

R_{SH} = shunt resistance

$k_o = e/AkT$ = coefficient of the exponential

k = Boltzmann's constant

T = absolute temperature, °K

e = electronic charge, 1.6×10^{-19} coulombs

A = a curve fitting constant

I_o = reverse saturation current of the ideal diode characteristic

The solar cell is thus represented as a light-activated constant-current generator in parallel with an ideal diode with correction terms for series and shunt resistance.

Next, Eq. 9.2-2 is solved for V :

$$V = R_{SH} \left(I_L - I - I_o \left\{ \exp [k_o (V + R_S I)] - 1 \right\} \right) \quad (9.2-3)$$

* A portion of this material is quoted from Ref. 9.2-6.

Now defining and introducing the parameters

$$v = \frac{V}{V_{oc}} \quad i = \frac{I}{I_{sc}} \quad i_o = \frac{I_o}{I_{sc}} \quad i_L = \frac{I_L}{I_{sc}}$$

$$r_p = \frac{R_{SH} I_{sc}}{V_{oc}} \quad r_s = \frac{R_S I_{sc}}{V_{oc}} \quad \alpha = k_o V_{oc}$$

in Eq. 9.2-3 (with V_{oc} , I_{sc} and R_{SH} as defined in Sections 3.2.2 and 3.2.4) gives

$$v = r_p \left(i_L - i - i_o \left\{ \exp[\alpha(v + r_s i)] - 1 \right\} \right)$$

$$i = i_L - \frac{v}{r_p} - i_o \left\{ \exp[\alpha(v + r_s i)] - 1 \right\}$$

Now since $i = 0$ when $v = 1$, and $v = 0$ when $i = 1$, one obtains the following two equations:

$$1 = r_p [i_L + i_o - i_o \exp(\alpha)]$$

$$1 = i_L + i_o - i_o \exp(\alpha r_s)$$

Hence, only three parameters need be independently chosen. For reasons of convenience, r_s , r_p and α were chosen as independent with i_L and i_o determined by

$$i_o = \frac{r_p - 1}{r_p} \left[\frac{1}{\exp(\alpha) - \exp(\alpha r_s)} \right]$$

$$i_L = 1 + i_o \left[\exp(\alpha r_s) - 1 \right]$$

Consequently, only three points on the normalized I-V characteristic are sufficient to determine the three parameters r_s , r_p , and α . From these three parameters and measured values of I_{sc} and V_{oc} , one can derive a complete mathematical model based on Eq. 9.2-2. These five parameters are temperature dependent and must be determined from empirical data. A computer program exists which calculates the I-V characteristic of a solar cell array based on the above model. Temperature-dependent parameters have been generated for a number of solar cell types.

"Hughes" Model*

The starting point is Eq. 9.2-1. To simplify the mathematical development, it is convenient to neglect the V/R_{SH} term and to redefine Eq. 9.2-1 through a change in variables. Let $K_1 V_{oc} = AkT/e$, $K_2 I_{sc} = I_o$, and $I_L = I_{sc}$, as follows:

$$I = I_{sc} - I_{sc} K_2 \left[\exp\left(\frac{V + IR_S}{K_1 V_{oc}}\right) - 1 \right] \quad (9.2-4)$$

* A portion of this material is quoted directly from Ref. 9.2-7.

With reference to Figure 9.2-1 and Eq. 9.2-4, an expression for cell output power P can be written as

$$P = IV = VI_{sc} \left\{ 1 - K_2 \left[\exp\left(\frac{V + IR_S}{K_1 V_{oc}}\right) - 1 \right] \right\} \quad (9.2-5)$$

At the cell maximum power point, $V = V_{mp}$, $I = I_{mp}$, and

$$\frac{dP}{dV} = 0$$

$$\frac{dP}{dV} = I_{sc} \left\{ 1 - K_2 \left[\exp\left(\frac{V_{mp} + I_{mp} R_S}{K_1 V_{oc}}\right) - 1 \right] \right\}$$

$$- K_2 I_{sc} V_{mp} \left[\exp\left(\frac{V_{mp} + I_{mp} R_S}{K_1 V_{oc}}\right) \right] \frac{1}{K_1 V_{oc}} \left(1 + R_S \frac{dI}{dV} \right) \quad (9.2-6)$$

But from Eq. 9.2-4,

$$\frac{dI}{dV} = \frac{-\frac{K_2 I_{sc}}{K_1 V_{oc}} \exp\left(\frac{V + IR_S}{K_1 V_{oc}}\right)}{1 + \frac{R_S K_2 I_{sc}}{K_1 V_{oc}} \exp\left(\frac{V + IR_S}{K_1 V_{oc}}\right)} \quad (9.2-7)$$

Evaluating Eq. 9.2-7 at the maximum power point, substituting the result into Eq. 9.2-6 and dividing by I_{sc} , we have

$$0 = K_2 + 1 - K_2 \exp\left(\frac{V_{mp} + I_{mp} R_S}{K_1 V_{oc}}\right)$$

$$- \frac{V_{mp} K_2}{K_1} \left[\frac{1}{V_{oc} \exp\left(\frac{V_{mp} + I_{mp} R_S}{K_1 V_{oc}}\right) + \frac{R_S K_2 I_{sc}}{K_1}} \right] \quad (9.2-8)$$

Now, under open-circuit conditions when $I = 0$ and $V = V_{oc}$, Eq. 9.2-4 can be solved for K_1 :

$$K_1 = \left[\ln\left(\frac{1}{K_2} + 1\right) \right]^{-1} \quad (9.2-9)$$

By substituting Eq. 9.2-9 into Eq. 9.2-8, noting that $\exp(A \ln B) = B^A$, we have

$$0 = K_2 + 1 - K_2 \left(\frac{1}{K_2} + 1\right)^{\left[\frac{V_{mp} + I_{mp} R_S}{V_{oc}}\right]}$$

$$- \frac{V_{mp} K_2 \ln\left(\frac{1}{K_2} + 1\right)}{\left[V_{oc} \left(\frac{1}{K_2} + 1\right)^{\left[\frac{V_{mp} + I_{mp} R_S}{V_{oc}}\right]} + R_S K_2 I_{sc} \ln\left(\frac{1}{K_2} + 1\right)\right]} \quad (9.2-10)$$

However, by substituting Eq. 9.2-9 into Eq. 9.2-4, we find

$$R_S = \frac{V_{oc} \left\{ \frac{\ln \left[\frac{1 + K_2 - (I_{mp}/I_{sc})}{K_2} \right]}{\ln \left[\frac{1}{K_2} + 1 \right]} \right\} - V_{mp}}{I_{mp}} \quad (9.2-11)$$

$$\frac{V_{mp} + I_{mp} R_S}{V_{oc}} = \frac{\ln \left(\frac{1}{K_2} + 1 - \frac{I_{mp}}{K_2 I_{sc}} \right)}{\ln \left(\frac{1}{K_2} + 1 \right)} \quad (9.2-12)$$

Substituting Eq. 9.2-12 into Eq. 9.2-10 results in an equation for K_2 as a function of I_{sc} , I_{mp} , V_{mp} , and V_{oc}

$$0 = \frac{I_{mp}}{I_{sc}} \cdot \frac{\left(\frac{V_{mp}}{V_{oc}} \right) \ln \left(\frac{1}{K_2} + 1 \right)}{\left[\frac{1}{1 + K_2 - (I_{mp}/I_{sc})} \right] \frac{I_{sc}}{I_{mp}} \left[\frac{V_{mp}}{V_{oc}} \ln \left(\frac{1}{K_2} + 1 \right) - \ln \left(\frac{1}{K_2} + 1 - \frac{I_{mp}}{K_2 I_{sc}} \right) \right]} \quad (9.2-13)$$

Eq. 9.2-13 cannot be solved in closed form for K_2 but a numerical solution can be obtained in a conventional manner. Eq. 9.2-13 has more than one root and care must be taken to select the proper K_2 value which usually corresponds to the smallest absolute value of R_S . Eqs. 9.2-9 and 9.2-11 define R_S and K_1 as functions of K_2 . The final model is formed by substituting the numerical values of K_1 , K_2 , and R_S from Eqs. 9.2-9, 9.2-11 and 9.2-13, respectively, into Eq. 9.2-4 which defines the cell I-V curve. The required inputs to fully define the model are the four common cell parameters I_{sc} , I_{mp} , V_{mp} , and V_{oc} . The translation of these quantities with temperature, illumination intensity and radiation dose follows the same procedures discussed above and below.

The model represented by Eq. 9.2-4 is valid only for the "forward bias" operating region of the solar cell. As shown in Figure 9.2-3, an avalanche breakdown occurs for "reverse bias" potentials in the -30 to -40 V range. This region of the solar cell I-V characteristic is not controlled by the cell manufacturers, and typically a considerable variation will be found in the breakdown voltage. Eq. 9.2-14 is proposed as a general cell model for both operating regions. For a typical cell, $V_b = 30$ V and $B = 15$.

$$I = I_{sc} \left\{ 1 - K_2 \left[\exp \left(\frac{V + IR_S}{K_1 V_{oc}} \right) - 1 \right] + K_2 \exp \left(\frac{-V - V_b}{BK_1 V_{oc}} \right) \right\} \quad (9.2-14)$$

The avalanche breakdown effect is of importance in high voltage array design.

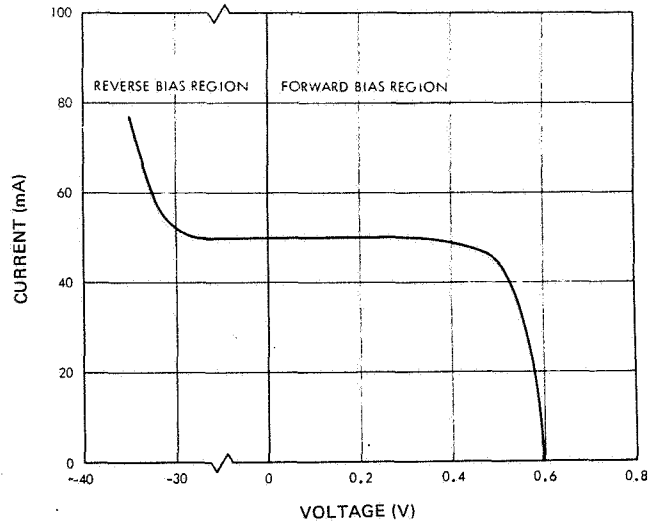


Fig. 9.2-3. Solar Cell I-V Curve (Ref. 9.2-7)

The accuracy of this model in the "forward bias" operating region has been investigated. A computer routine was developed to determine optimum values of I_{sc} , V_{mp} , I_{mp} , and V_{oc} to match experimental I-V curves. This optimization program used a gradient technique to solve for the set of input parameters which minimized the mean-squared error between the calculated and experimental I-V data points. Data over an environmental range from 10°C to 90°C and for radiation doses between 0 and 10^{15} 1-MeV electrons/cm² were compared.

The curves of Figures 9.2-4 and 9.2-5 are examples which illustrate the results of this accuracy study.

The optimized data, representing the full capability of the model, resulted in a typical rms error of 0.2 percent in either current or voltage. The model predictions based on experimental values of the input parameters realized an accuracy on the order of 2 percent or better over the entire environmental range.

"TRW" Model*

The solar cell I-V curve is also based on Eq. 9.2-1 and is represented by the following equation:

$$I = I_{sc} \left(1 - C_1 \left\{ \exp \left[\frac{V}{(C_2 V_{oc})} \right] - 1 \right\} \right) \quad (9.2-15)$$

where

$$C_1 = \left[1 - \left(\frac{I_{mp}}{I_{sc}} \right) \right] \left\{ \exp \left[\frac{-V_{mp}}{(C_2 V_{oc})} \right] \right\} \quad (9.2-16)$$

and

$$C_2 = \left[\left(\frac{V_{mp}}{V_{oc}} \right) - 1 \right] \left[\ln \left(1 - \frac{I_{mp}}{I_{sc}} \right) \right] \quad (9.2-17)$$

* A portion of this material is quoted from Ref. 9.2-8.

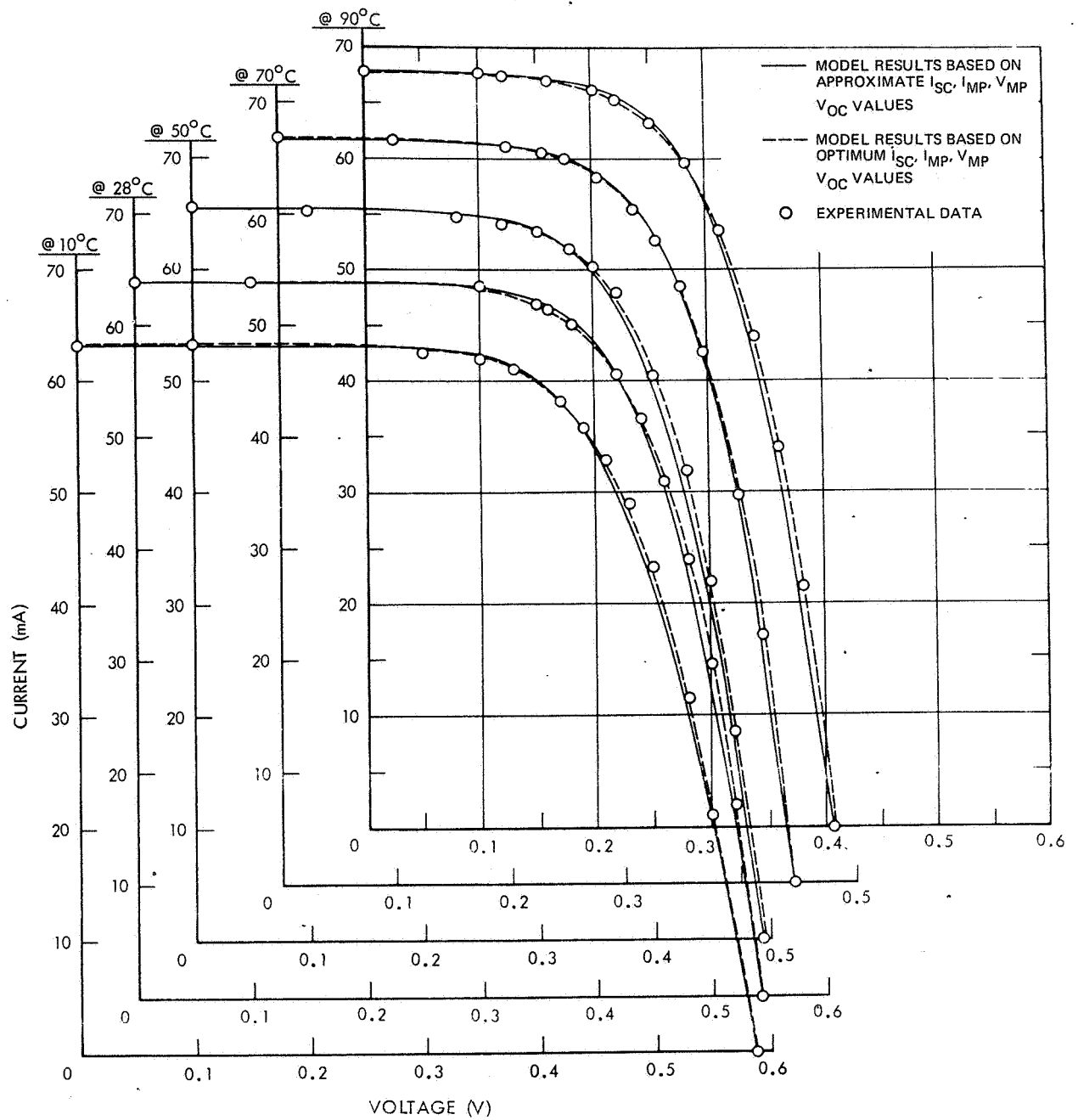


Fig. 9.2-4. Solar Cell I-V Characteristics as a Function of Temperature (Ref. 9.2-7)

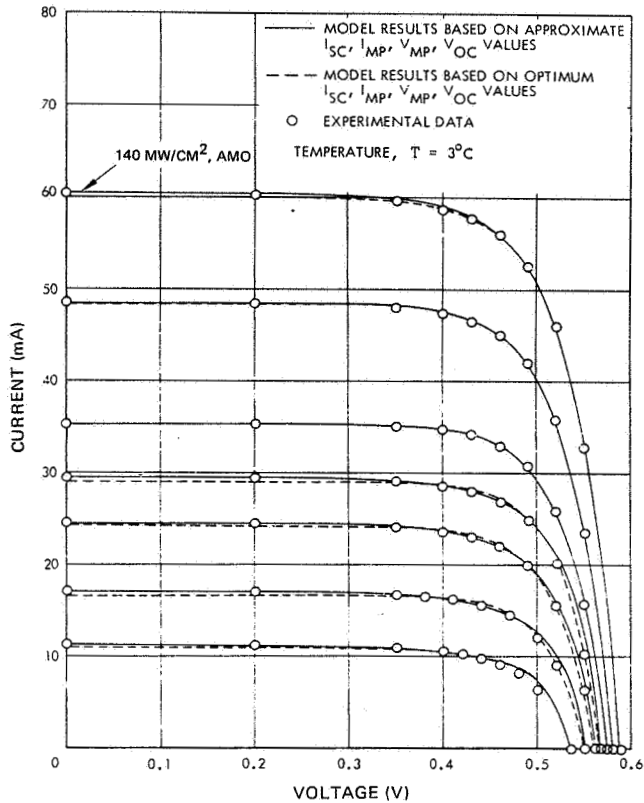


Fig. 9.2-5. Solar Cell I-V Characteristics as a Function of Intensity (Ref. 9.2-7)

Eq. 9.2-15 results in a considerable error at light intensities above two solar constants. Empirical investigation revealed that a better agreement between the calculated and actual characteristics can be obtained at higher intensities with the following equation:

$$I = K_6 - \left[\exp \left(K_4 V^m - K_5 \right) \right] \quad (9.2-18)$$

Expressing the constants again in terms of the three characteristic cell points results in the following equation:

$$I = I_{sc} \left\{ 1 - C_3 \left[\exp \left(C_4 V^m \right) - 1 \right] \right\} \quad (9.2-19)$$

where the constants are defined as follows:

$$m = \left[\ln \left(C_5 / C_6 \right) \right] / \left[\ln \left(V_{mp} / V_{oc} \right) \right] \quad (9.2-20)$$

$$C_4 = C_6 / (V_{oc})^m \quad (9.2-21)$$

$$C_5 = \ln \left\{ \left[I_{sc} (1 + C_3) - I_{mp} \right] / (C_3 I_{sc}) \right\} \quad (9.2-22)$$

$$C_6 = \ln \left[(1 + C_3) / C_3 \right] \quad (9.2-23)$$

The constant C_3 could not be expressed in terms of the three characteristic points, but through trial and error it was found that a value of 0.01175 for C_3 will produce the least errors over the range of illumination and temperature considered. With this value substituted for C_3 , the other constants are reduced to the following:

$$m = \left[\ln(C_5 / 4.46) \right] / \left[\ln(V_{mp} / V_{oc}) \right] \quad (9.2-24)$$

$$C_4 = 4.46 / (V_{oc})^m \quad (9.2-25)$$

$$C_5 = \ln \left[(1.01175 I_{sc} - I_{mp}) / 0.01175 I_{sc} \right] \quad (9.2-26)$$

$$C_6 = 4.46 \quad (9.2-27)$$

The absolute accuracy of the model (according to Eq. 9.2-15) is as follows:

- At an illumination intensity of one solar constant the equation used to generate the cell characteristic introduces an error of less than 0.3 percent at the maximum power point at cell temperatures of 90°C. At 30°C the error is only about 0.03 percent (see Figure 9.2-6).
- The assumption of nonchanging curve shape results in errors which increase with temperature and illumination intensity. Starting with a characteristic defined at one sun and 30°C, the error at one sun and 70°C is 2.0 percent (see Figure 9.2-7). With increasing light intensity the error increases.
- The temperature of body mounted solar cell arrays on spinning spacecraft in earth orbit normally varies in the range from -20°C to +40°C when illuminated. Considering that the illumination intensities varies over the array, the total error introduced by the curve-shifting technique normally ranges from -1.0 to 0 percent. A negative error means that the computer predicts a lower output than is actually expected.

9.2.4 Nonanalytical Models

An analytical expression of the solar cell I-V curve is not required for computer work. Discrete sets of I-V data points representing the otherwise smooth I-V curve may be stored in the computer memory. These sets of points may be translated point-by-point to operating conditions different from those for which test data exists. An example of such a model follows:

JPL Model*

The typical transformations which take place to an I-V curve with changing light level and cell temperature are illustrated in Figure 9.2-8. The transformations are accomplished as a point-by-point translation of a photovoltaic curve characteristic, whose voltage and current coordinates, V_1 and I_1 , respectively, are

* A portion of this material is quoted from Ref. 9.2-9.

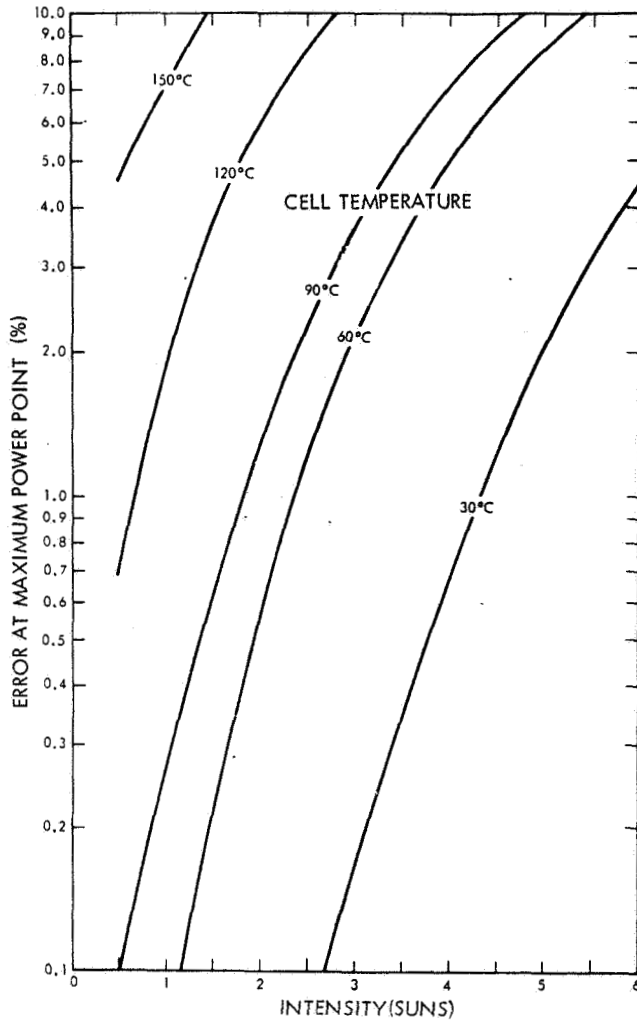


Fig. 9.2-6. Error Introduced by the Approximate Eq. 9.2-15 at the Maximum Power Point Compared to Provided Input Data as a Function of Illumination Intensity and Cell Temperature (Ref. 9.2-8)

known at a reference temperature T_1 , and a reference solar intensity, L_1 . The general equations for extrapolating these reference coordinates to a new cell voltage, V_2 , and cell current, I_2 , at temperature T_2 and solar intensity, L_2 , are of the form:

$$I_2 = I_1 + I_{sc1} \left(\frac{L_2}{L_1} - 1 \right) + \alpha(T_2 - T_1) \quad (9.2-28)$$

$$V_2 = V_1 - \beta(T_2 - T_1) - \Delta I_{sc} R_S - K(T_2 - T_1) I_2 \quad (9.2-29)$$

$$\Delta I = \Delta I_{sc} = I_{sc1} \left(\frac{L_2}{L_1} - 1 \right) + \alpha(T_2 - T_1) \quad (9.2-30)$$

$$P_2 = I_2 V_2 \quad (9.2-31)$$

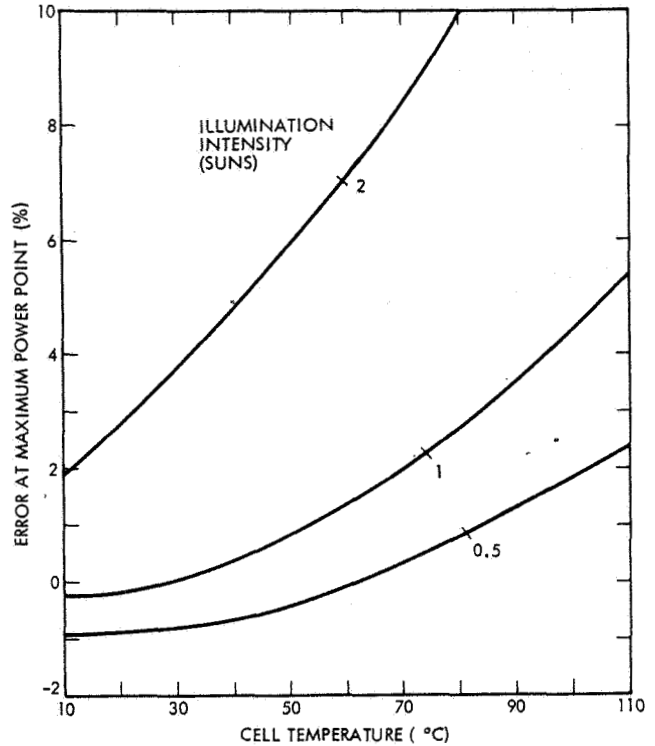


Fig. 9.2-7. Error Introduced by Assumption of Constant Curve Shape (Equation 9.2-15) (Ref. 9.2-8)

where α and β are the temperature coefficients for current and voltage, respectively, and K is a curve shape adjustment factor.

In reference again to Figure 9.2-8, the first transformation is a translation of current proportional to the change in light level and temperature according to Eq. 9.2-28. The second transformation is a translation of voltage accomplished by the second and third terms of Eq. 9.2-29. The last transformation, as noted and seen as the solid line displaced from the dashed curve, is performed by the last term in Eq. 9.2-29.

It was found that it was necessary to treat the temperature coefficients, α and β , and the curve shape adjustment factor, K , as variables with both solar intensity and temperature. All three of these parameters were determined from extensive solar cell test data obtained at discrete levels over the entire range of interest. Since this hybrid empirical-analytical model was developed for interplanetary missions, radiation degradation was not included.

Another widely used program that uses sets of I-V data points is described in Ref. 9.2-10.

9.2.5 Selecting the Proper Model

Any solar cell model used for computerized array analyses must meet the following criteria:

- It must, with sufficient accuracy, simulate I-V curves over the range of interest of temperature, illumination level and radiation damage.

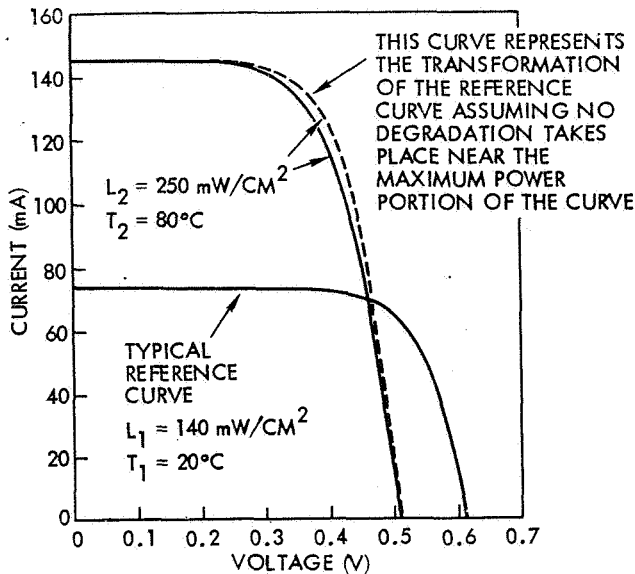


Fig. 9.2-8. The Transformations an I-V Curve Experiences as a Function of Solar Intensity and Cell Temperature

- It must permit, with sufficient accuracy, the manipulation of the I-V curves, as required for predicting the array performance under certain specified array operating conditions.

Both the "range of interest" and the numerical definition of "sufficient accuracy" are mission and program peculiar. The range of interest for specific cases can be estimated from the data in this handbook as follows:

- Temperature and Illumination Range – Section 2.4
- Radiation Damage Range – Section 2.5
- Effects of Environment on Solar Cell I-V Curves – Chapter 3.

A "sufficiently accurate" analysis, in general, is one in which the probable error of the analysis is equal to or less than the design margin. For power output predictions the accuracy of the analysis should be highest at the maximum power point, but may be lower at the I_{sc} and V_{oc} "ends" of the I-V curve. However, for the sizing of power regulating electronic equipment, knowledge of I_{sc} or V_{oc} may be required more accurately than knowledge of P_{mp} . If one solar cell model cannot (with sufficient accuracy) predict the entire I-V curve, separate computer runs may have to be made using slightly different input values to achieve the desired results.

The accuracy of any computerized array analysis is typically highest for those operating conditions for which direct solar cell test data are input into the computer. For these direct input conditions, an accuracy of better than ± 0.1 percent should be expected. For extrapolations toward the extremes of the range of interest, with an absence of test data, the accuracies tend to deteriorate to ± 1 percent or, in extreme cases to ± 10 percent. Inasmuch as the actually occurring inaccuracies are highly computer-program and case dependent, the array analyst should attempt to ascertain the most likely accuracy of his analysis.

9.2.6 Practical AC Models

The theoretical ac model of semiconductor junctions described in Section 3.11.2 has been applied by Ref. 9.2-11 to alloyed and by Ref. 9.2-12 to diffused p-n junction, silicon photo diodes. For small ac signals (compared to the dc bias voltage of the junction) these references have shown that the ac output voltage component, v_{ac} , that is superimposed on the dc output voltage, V_{dc} , is

$$v_{ac} = \frac{qM(1-r)QAF(\alpha, \omega) \cdot \exp(j\omega t)}{Y_{ac} + Y_L}$$

where

q = electronic charge

M = degree of modulation of the input light level

ω = angular frequency of modulation of the input light level ($\omega = 2\pi f$)

r = front surface reflectivity

Q = steady-state illumination level (photons $\cdot \text{cm}^{-2} \cdot \text{s}^{-1}$)

A = illuminated surfaces area

$F(\alpha, \omega)$ = function independent of time

Y_{ac} = internal admittance of the junction

Y_L = admittance of the load

For the frequency range of interest, Y_{ac} is a parallel combination of R_{ac} and C_{ac} such that

$$R_{ac} = (kT/qJ_o A) \exp(-qV_{dc}/kT)$$

and

$$C_{ac} = W(sR_{ac})^{-1}$$

where

k = Boltzmann's constant

T = absolute temperature

J_o = reverse saturation current density

s = surface recombination velocity

and

$$W = (2.46D_n/\omega_o)^{0.5}$$

with

D_n = minority carrier diffusion constant in the p-region of a p-on-n junction

ω_o = cutoff frequency of the junction.

Experimental investigations have shown that for photodiodes operated in the photovoltaic mode, the transition capacitance, C_T , (measured under conditions of zero illumination and zero to reverse bias) and the shunt resistance, R_{SH} , must be included in addition to R_{ac} and C_{ac} . For solar cells, the series resistance R_S must also be included. The small-signal ac equivalent circuit including all terms is shown in Figure 9.2-9.

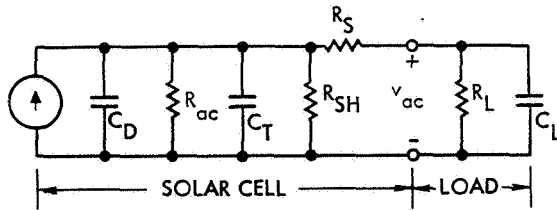


Fig. 9.2-9. Solar Cell Small-Signal AC Model

The capacitance, C_{ac} , is also known as the diffusion capacitance, C_D . The values for C_D , C_T , R_{ac} vary with the incident light level, the cell temperature, the cell operating voltage, and the solar cell material constants and processing parameters. For conventional n-on-p, 2 x 2 cm, 0.25 mm thick, silicon solar cells (defined in Section 3.1.1) of 10 ohm-cm base resistivity produced during the 1967 through 1969 time span, the parameters discussed above were found by Refs. 9.2-13 and 9.2-14 to have the approximate values shown in Table 9.2-1. The values in this table are for frequencies up to approximately 5000 Hz. Above this frequency minority carrier storage effects cause the value of C_D to diminish with increasing frequency until $C_D = 0$ and C_T is the only capacitance remaining at the higher frequencies. The value of C_T depends upon V_{dc} as follows:

$$C_T = K(V_{dc})^{-0.5}$$

where K is a constant for a given solar cell. The experimentally determined impedance and phase angle values for the solar cells discussed above are shown in Figures 9.2-10 and 9.2-11. The impedance, Z , and the phase angle, ϕ , are given by

$$Z = v/i$$

and

$$\cos\phi = Z/R_D$$

respectively, and the capacitances are related by

$$C_D + C_T = \sin\phi/(2\pi fZ)$$

where v and i are the cell small-signal ac voltage and current, respectively, the other symbols are as previously defined, and the incremental diode dc resistance, R_D , is defined as

$$R_D = |dv/di|$$

at any point of the photovoltaic output portion of a photo-diode or solar cell under steady-state illumination. R_D is related to R_{ac} as follows (see Figure 9.2-9):

$$R_D = \frac{R_{ac} \cdot R_{SH}}{R_{ac} + R_{SC}} + R_S$$

The variation of R_D as a function of the cell bias voltage, V_{dc} , for the cell I-V curve illustrated in Figure 9.2-12 is given in Figure 9.2-13. Near short-circuit current R_{ac} becomes very large and R_{SH} dominates the cell impedance. Near open-circuit voltage, R_{ac} becomes small and R_S exerts a large influence on the impedance (compare this with the experimental data in Sections 3.2.3 and 3.2.4).

Table 9.2-1. Approximate Low-Frequency AC Parameters for Conventional 2 x 2 cm Silicon Solar Cells (One Solar Constant AM0 Intensity, 28°C Cell Temperature)

V_{dc} (mV)	R_{ac} (Ω)	R_s (Ω)	R_{SH} (k Ω)	C_D (μF)	C_T (μF)
550	0.2-2	0.1-0.5	5-50	2	0.06
350	1-10	0.1-0.5	5-50	0.2	0.06

Ref. 9.2-15 reports the impedance measured on an entire solar cell array. The array consisted of two parallel-connected panels having a total of 98 cells in series and 112 cells in parallel. The cells (conventional SiO_x -coated, 1 to 3 ohm-cm cells of 20 x 20 x 0.35 mm size) were grouped into 12 strings that were connected through parallel-redundant blocking diodes to the array bus. The array was tested in natural terrestrial sunlight of 104 mW/cm² intensity. The array temperature was 20°C and its output values were as follows: $I_{sc} = 10.55$ amperes, $V_{oc} = 56$ volts, and $V_{mp} = 46$ volts. The ac impedance was measured at $V_{dc} = 35$ volts (a point on the I-V curve that is at 76 percent of V_{mp}) with an ac voltage of $v_{ac} = 5$ volts peak-to-peak. The test results are shown in Figure 9.2-14.

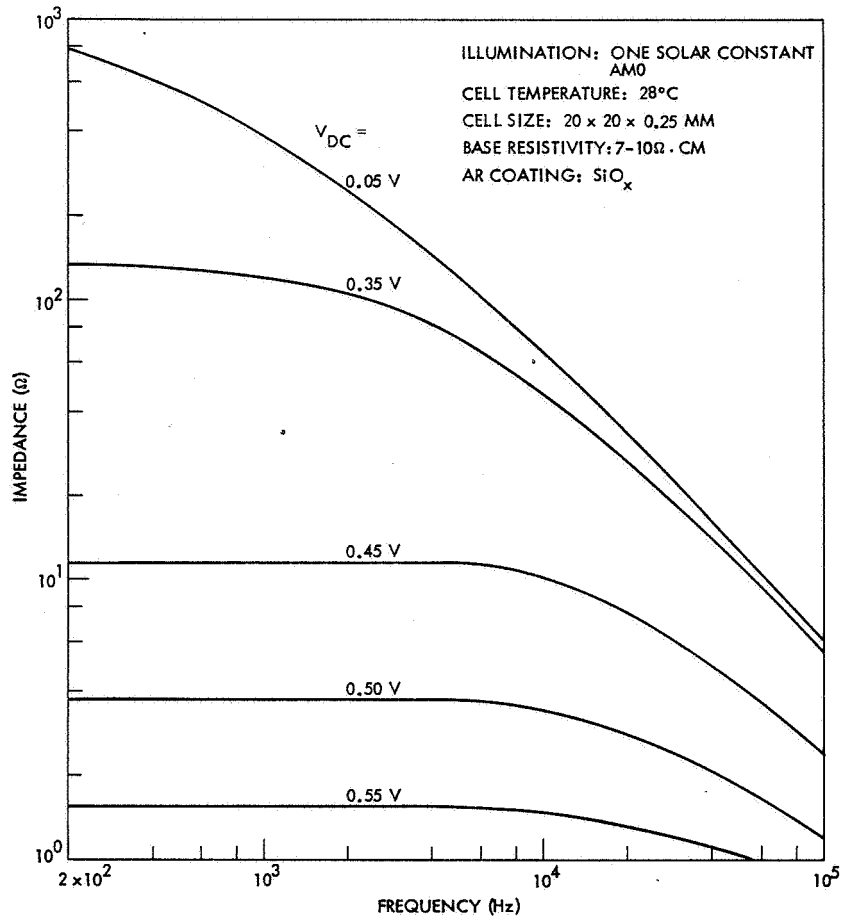


Fig. 9.2-10. Solar Cell Impedance (Ref. 9.2-13)

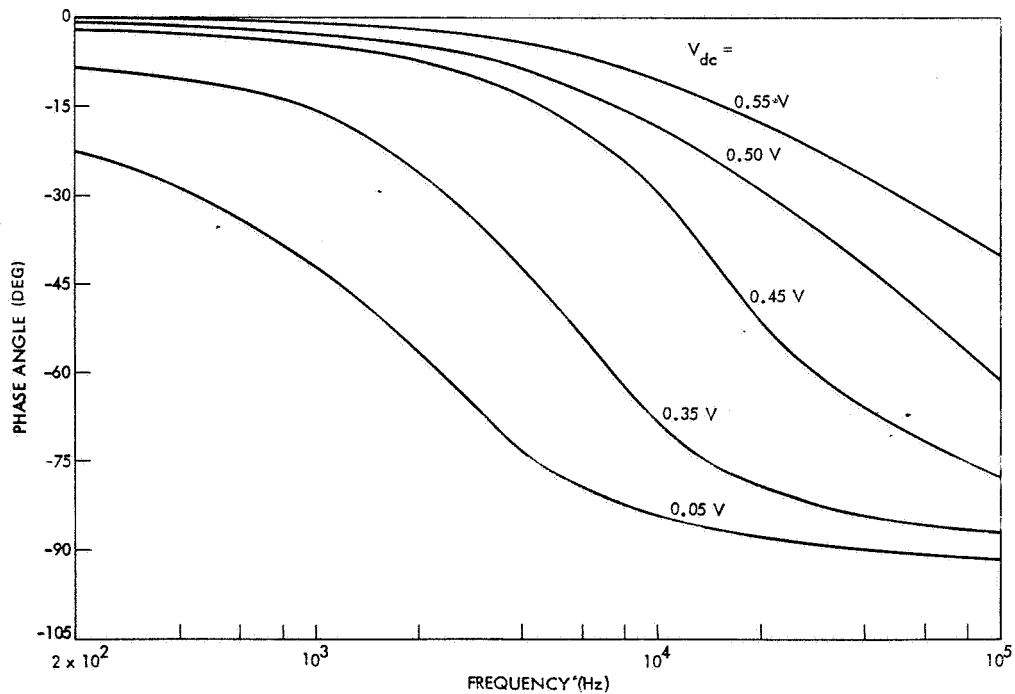


Fig. 9.2-11. Phase Angles for Impedances of Fig. 9.2-10

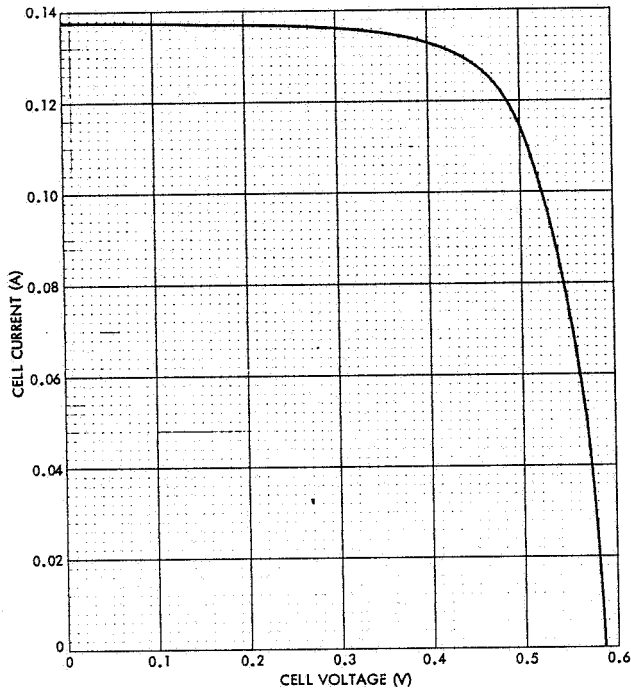


Fig. 9.2-12. Average Solar Cell I-V Curve (11-Cell Sample, Conventional 20 x 20 x 0.2 mm, n-on-p, $10 \Omega \cdot \text{cm}$, One Solar Constant AM0, 28°C)

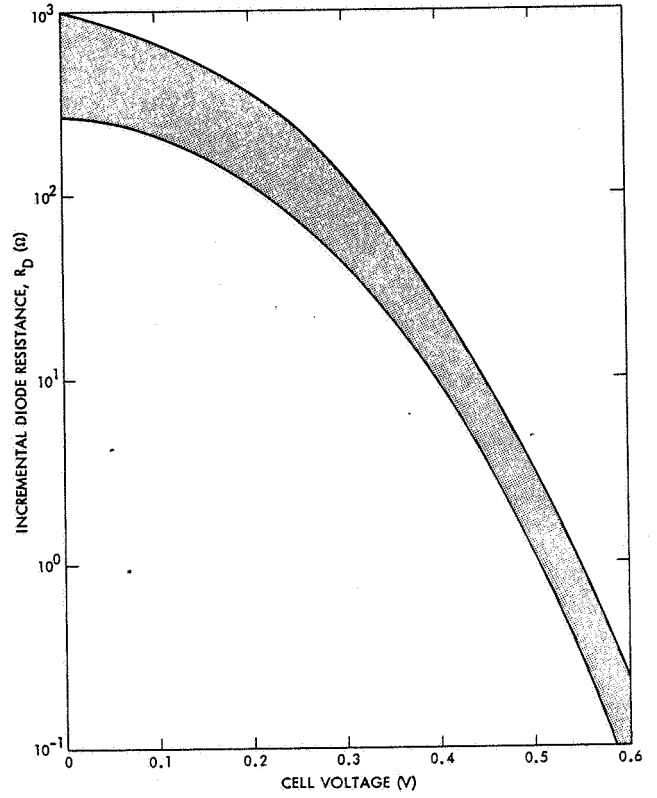


Fig. 9.2-13. Range of Incremental Solar Cell Diode Resistances for Solar Cells of Fig. 9.2-12

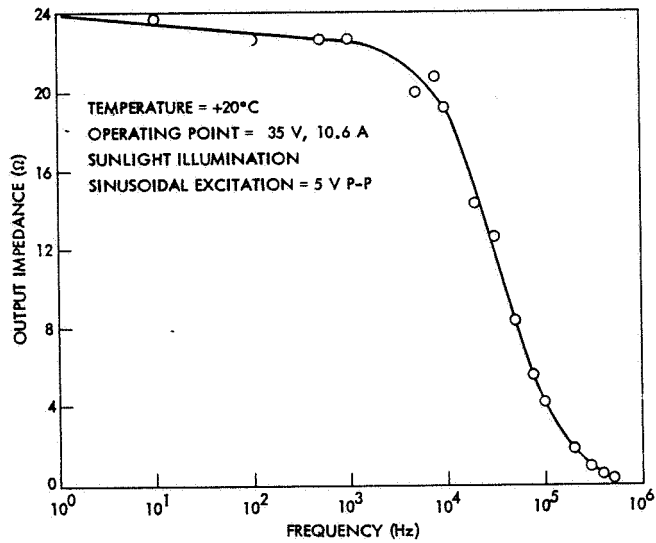


Fig. 9.2-14. Nimbus-B Solar Cell Array Output Impedance Versus Frequency (Ref. 9.2-15)

9.3 ARRAY CIRCUIT MODELS

To be useful for solar cell array analysis, the solar cell models discussed in Section 9.2 must be electrically connected in series-parallel matrices to represent an entire array. Typically, an additional series resistance component representing the solar cell interconnectors and the array wiring, and a voltage drop to account for blocking diode losses are considered. Depending upon the purpose of the array analysis to be performed, different array models may be required. For the assessment of solar cell mismatch losses or for the computation of the output from partially shadowed arrays, much more detailed models are required than for the computation of the output of a uniformly illuminated array that is free of thermal gradients. Array models of increasing complexity are given in the following.

9.3.1 Illuminated Arrays

Simple Array Model*

The solar cell array is divided into a number of parallel subgroups having the general configuration of Figure 9.3-1. The extension of the solar cell model given by Eq. 9.2-4 to represent a matrix of p identical cells in parallel by s cells in series in a uniform environment can be directly defined, as shown in Eq. 9.3-1.

$$I = pI_{sc} \left\{ 1 - K_2 \left[\exp \left(\frac{V + IR_s}{\frac{s}{K_1} + \frac{p}{V_{oc}}} \right) - 1 \right] \right\} \quad (9.3-1)$$

Isolation diodes can be treated as series network elements having the general form of Eq. 9.3-2a:

$$I_d = I_{od} \left\{ \exp \left[\frac{q(V_d - I_d R_{Sd})}{DkT} \right] - 1 \right\} \quad (9.3-2a)$$

where

- I_d = diode current
- I_{od} = diode saturation current
- q = electronic charge
- V_d = diode terminal voltage
- R_{Sd} = diode series resistance
- D = curve-fitting constant
- k = Boltzmann's constant
- T = absolute temperature

For practical array analysis cases, the blocking diode equation can be approximated by the following piecewise linear model:

$$V_d = V_{od} + I_d R_{Sd} \quad (9.3-2b)$$

where V_{od} is the diode threshold voltage (about 0.6 volt for silicon).

Equation 9.3-1 simply "scales" the single cell equation according to the numbers of cells in parallel, p , and in series, s . This model is limited to uniform illumination, no thermal gradients and "identical" solar cell I-V curves. This model leads to errors in that portion of the array I-V curve which lies between the P_{mp} and I_{sc} points. The error arises from the fact that low- I_{sc} solar cells in a series string limit the current flow of the entire string. In an actual array, the I_{sc} values of the individual cells are statistically distributed over a relatively large range. Because of this current-limiting behavior of solar cells, the array I_{sc} is lower than " p " times the average cell I_{sc} . This lowering of the I_{sc} is called a "mismatch" loss and is discussed further in the following subsections.

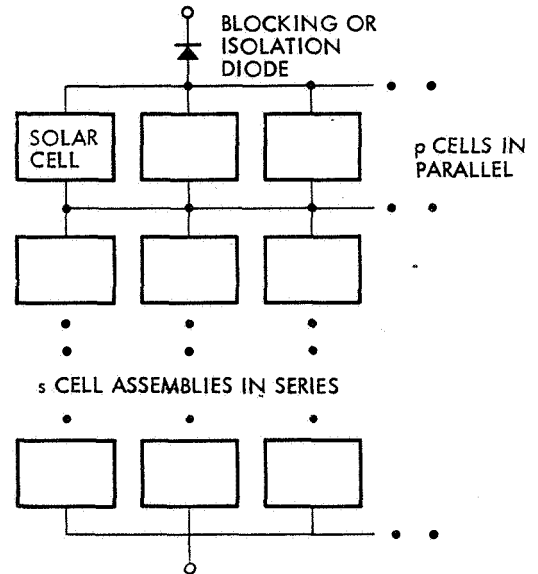


Fig. 9.3-1. Solar Cell Subgroup Configuration

Detailed Array Model*

For the purposes of the following discussion, the solar cell I-V curve is expressed as $I(v)$ to show

* A portion of this material is quoted from Ref. 9.3.1.

* A portion of this material is quoted from Ref. 9.3-2 with the IEEE.

explicitly that I is a function of v . The cell $I(v)$ relationship is either that of Eq. 9.2-1 or was obtained from physical measurements at some standard test conditions. The solar cell is considered a two-port black box with light energy entering one port and current, voltage, and impedance being offered at the other. The equivalent circuit of this black box is of no further interest in this model. The cell's exit port $I(v)$ characteristics are defined by the externally measurable quantities of terminal current, I_c , as a function of terminal voltage, v , at a given light intensity, Q , cell temperature, and state of charged-particle irradiation. Implicit in these output characteristics is the internal cell series resistance, R_S , which causes the familiar voltage translation as Q is varied.

It is assumed that the cell temperature and charged-particle irradiation are held constant for the following. The black box output at some standard conditions (i. e., at light level Q) may be given functionally by

$$\begin{aligned} I_c(v) &= I_L - I_o(v_o) \quad v \geq 0 \\ &= I_L - vG(v) \quad v < 0 \end{aligned} \quad (9.3-3)$$

where I_c is the terminal current, v the terminal voltage, and I_L is a constant current equal to the terminal short-circuit current. $I_o(v_o)$ is a function responsible for the typical solar cell curve shape and corresponds conceptually to the diode conduction current in the simple, lumped-constants solar cell model frequently given by Eq. 9.2-1.

$G(v)$ is a nonlinear conductive element in parallel with the output port terminals which affects the cell characteristics only when v is negative. This element represents the cell reverse characteristics which are important when solar cells are connected into arrays where they are subjected to external bias.

It has been determined experimentally that, at light intensities corresponding to between 0 and 2 solar constants, the solar cell $I(v)$ curve shape is invariant with intensity and translates only along the current and voltage axes. Using this finding, Eq. 9.3-3 may be written for any light intensity different from Q (i. e., at kQ),

$$\begin{aligned} I_c(v) &= kI_L - I_o(v_o - \Delta v) \quad v \geq 0 \\ &= kI_L - vG(v) \quad v < 0 \end{aligned} \quad (9.3-4a)$$

where

$$\Delta v = (1 - k)I_L R_S \quad (9.3-4b)$$

The significance of Eq. 9.3-3 and 9.3-4 is clear in Figure 9.3-2. Curve A in this figure shows a cell curve at intensity Q , while curve B shows the same cell curve at zero intensity, i. e., at $k = 0$. Any point on the A curve of Figure 9.3-2 has shifted along the current axis by the amount of $(1 - k)I_L = I_L$ and along the voltage axis by an amount of $\Delta v = (1 - k)I_L R_S = I_L R_S$. The negative sign in front of Δv is consistent with the observation that the current to be subtracted from the short-circuit current at a given voltage becomes smaller and smaller as the light intensity is reduced to lower and lower values, i. e., the $I(v)$ curve shifts to higher and higher voltages.

From Ref. 9.3-2. Reprinted with permission of the IEEE

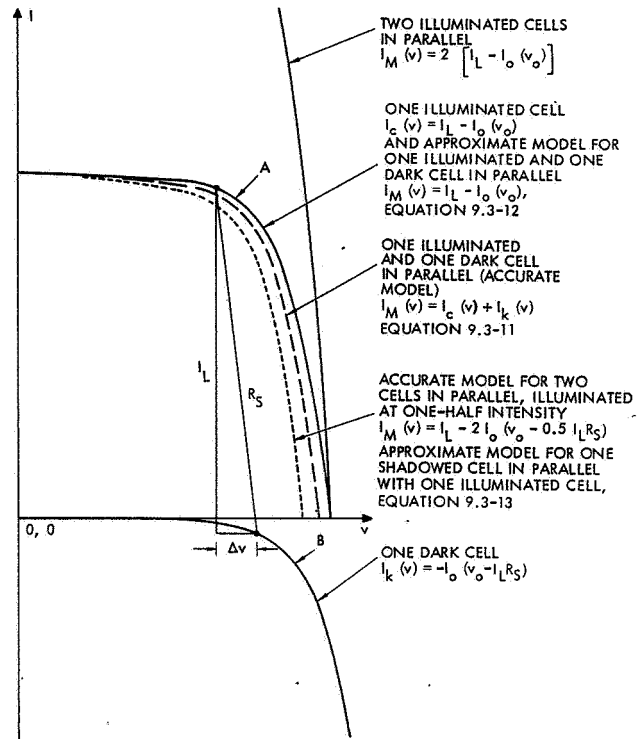


Fig. 9.3-2. Effects of Illumination and Shadowing on the Current-Voltage Relationships of a Solar Cell and a Submodule with Two Cells in Parallel

The intensity modifier, k , may reflect changes in the solar distance, coverglass transmission losses, or angle of incidence effects.

Submodules and Strings

A number of solar cells connected in parallel form a submodule, and a number of submodules in series which provide power directly to the bus is called a string. A submodule composed of p equal cells of Eq. 9.3-4 connected in parallel has characteristics

$$\begin{aligned} I_M(v) &= p \left[kI_L - I_o(v_o - \Delta v) \right] \quad v \geq 0 \\ &= p \left[kI_L - vG(v) \right] \quad v < 0 \end{aligned} \quad (9.3-5a)$$

where

$$\Delta v = (1 - k) I_L R_S \quad (9.3-5b)$$

The first-quadrant portion of the $I(V)$ curve of a string with s submodules in series is obtained by first expressing Eq. 9.3-5 in terms of v and then forming the sum at constant current values of I_s

$$V_s(I_s) = \sum_{i=1}^{i=s} \left[v(I)_i \right]_{I_s} \quad (9.3-6)$$

Eq. 9.3-6 may now be expressed in terms of I and written functionally as

$$I_s(V_s) = p \left[kI_L - I_o(V_s - \Delta V) \right] \quad (9.3-7a)$$

where

$$V_s = sv \text{ and } \Delta V = (1 - k)I_L R_S \quad (9.3-7b)$$

The reverse characteristics of the string $I(V)$ curve are of no importance if isolation diodes connect the string to the bus.

Array

The array consists of all the strings feeding a particular bus system. Its equation is obtained by forming the sum of all string currents at constant voltage values and accounting for the isolation diode drop. If the array voltage, V_A , is forced by an energy storage battery or a number of other power-producing strings, the string voltage, V_s , is also forced so that

$$V_s = V_A + V_D \text{ and } I_s = I_D \quad (9.3-8)$$

where V_D is the isolation diode drop and I_s and I_D the respective string and diode currents.

For an array comprised of m strings, each generally being illuminated at a different intensity, the array current, I_A , is

$$\begin{aligned} I_A(V_A) &= \sum_{j=1}^m \left[I_s(V_A)_j \right] V_A \\ &= p \sum_{j=1}^m \left[k_j I_L - I_o(V_s - V_D - \Delta V)_j \right] V_A \end{aligned} \quad (9.3-9)$$

9.3.2 Partially Shadowed Arrays*

Effects of Shadows on Cells and Submodules

A shadow falling on a portion of a single cell or a submodule will reduce the total output by two mechanisms: (1) by reducing the energy input to the cell, and (2) by increasing internal energy losses in the nonilluminated cell portions. If the energy conversion capability is uniform over the entire active cell area, the short-circuit current will be proportional to the nonshadowed (illuminated) area, regardless of the shape or position of the shadow (at least for up to two solar constants intensity and contemporary solar cells). If the total active cell area is A_t and the illuminated, active portion thereof is A_i , the short-circuit current output of the partially shadowed cell becomes rI_L

where

$$r = \frac{A_i}{A_t} \quad (9.3-10)$$

* Quoted from Ref. 9.3-2 with permission of the IEEE.

Hence, a partial shadow on a cell will have the same effect on I_L as reduced light intensity on a non-shadowed cell. The remainder of the cell $I(v)$ curve will, however, not follow this relationship as will be shown by the examples below.

For illustration, let a submodule at normal incidence consisting of $p = 2$ identical cells in parallel be partially shadowed with $r = 0.5$, and such that one cell is illuminated and the other is dark. From Eq. 9.3-4 the illuminated cell equation with $k = 1$ is $I_c(v) = I_L - I_o(v_o)$, and that of the shadowed or dark cell with $k = 0$ is $I_k(v) = -I_o(v_o - I_L R_S)$. The partially shadowed submodule characteristics are the current sum of these two equations at constant voltage values:

$$\begin{aligned} I_M(v) &= I_c(v) + I_k(v) \\ &= I_L - I_o(v_o) - I_o(v_o - I_L R_S) \end{aligned} \quad (9.3-11)$$

Both the single cell components and their sums are illustrated in Figure 9.3-2.

While Eq. 9.3-11 represents the correct solution to the example given, there are other, approximate solutions available which may solve certain problems more rapidly. These approximations are shown below.

First, assume that the above submodule of two cells in parallel is represented by the illuminated cell only. In this case, the submodule equation is identical to a single cell equation and the losses in the dark cell are neglected:

$$I_c(v) = I_M(v) = I_L - I_o(v_o) \quad (9.3-12)$$

Curve A in Figure 9.3-2 shows that this approximation calculates the power output as too high from this partially shadowed submodule.

Next, assume that the above submodule of two cells in parallel is represented by two equally illuminated cells at one-half of the original intensity. The submodule equation is the sum at constant voltages of two cells of Eq. 9.3-4 with $k = 0.5$

$$I_M(v) = I_L - 2I_o(v_o - 0.5I_L R_S) \quad (9.3-13)$$

This curve, also shown in Figure 9.3-2, is lower than the correct curve.

Before proceeding, Eq. 9.3-11 shall be generalized. If the submodule contains p cells in parallel, and rp of them are illuminated, i. e., $p(1 - r)$ of them are shadowed, then the submodule equation becomes

$$I_M(v) = I_{\text{illum}} + I_{\text{dark}}$$

where

$$I_{\text{illum}} = rp k I_L - rp I_o(v_o - \Delta v_1)$$

where

$$\Delta v_1 = (1 - k)I_L R_S$$

The dark component is

$$I_{\text{dark}} = -(1-r)pI_o(v_o - \Delta v_2)$$

where

$$\Delta v_2 = I_L R_S$$

The dark current component is, of course, independent of the illumination factor k .

Eqs. 9.3-12 and 9.3-13 may be similarly generalized. All three models, shown in Figure 9.3-2, are then expressed as follows:

From Eq. 9.3-11, Accurate Model

$$I_M(v) = rp \left[kI_L - I_o(v_o - \Delta v_1) - \frac{1-r}{r} I_o(v_o - \Delta v_2) \right]$$

$$\Delta v_1 = (1-k)I_L R_S$$

$$\Delta v_2 = (1-r)I_L R_S$$

$$v \geq 0 \quad (9.3-14)$$

From Eq. 9.3-12, Optimistic Approximation

$$I_M(v) = rp \left[kI_L - I_o(v_o - \Delta v) \right]$$

$$\Delta v = (1-k)I_L R_S$$

$$v \geq 0 \quad (9.3-15)$$

From Eq. 9.3-13, Pessimistic Approximation

$$I_M(v) = rp \left[kI_L - \frac{1}{r} I_o(v_o - \Delta v) \right]$$

$$\Delta v = (1-rk)I_L R_S$$

$$v \geq 0 \quad (9.3-16)$$

For all three, Reverse Characteristics

$$I_M(v) = p \left[rkI_L - vG(v) \right] \quad v < 0 \quad \begin{cases} (9.3-14) \\ (9.3-15) \\ (9.3-16) \end{cases}$$

To facilitate writing of Eqs. 9.3-14 through 9.3-16, all three equations for partially shadowed submodules are expressed simply as

$$\begin{aligned} I_M(v) &= I(0) - J(v') \quad v \geq 0 \\ &= I(0) - vG(v) \quad v < 0 \end{aligned} \quad (9.3-17)$$

where $I(0) = rp k I_L$, and $J(v')$ provides the same function for the submodule that $I_o(v_o)$ serves in the cell equation (9.3-3), except that $J(v')$ may represent any of the corresponding terms in Eqs. 9.3-14 through 9.3-16.

In 1961, Luft (Ref. 9.3-3) measured the variation in cell output with the amount of shadowing on some earlier 1 x 2 cm solar cells with 1.5 grid lines per centimeter. He found that the cell open-circuit voltages and the currents near the optimum power point did not correspond to the values which would be expected from light intensity variations, but were mostly lower, depending on the shadow location on the cells. While these variations were relatively significant for single cell measurements, the deviation became less significant when the shadowed cell was part of a larger group of cells (string). In 1966, Treble (Ref. 9.3-4) reported experimental results which showed that the cell I_{SC} is indeed proportional to the nonshadowed cell area and is not affected by shape or position of the shadow. However, he did not report on the variations of other cell parameters as a function of shadowing.

Current-Limiting by Cells or Submodules Connected in Series

In Figure 9.3-3, two cells of unequal output are shown connected in series. The terminal behavior of this cell pair, requiring $I_1 = I_2$, is obtained by summing the cell voltages at constant current values, as illustrated. It is clearly seen that the lower output cell number 1, i.e., a shadowed cell, limits the output from the higher output cell number 2. The amount of the limiting depends, of course, on the reverse characteristics of cell number 1. In order to analyze cells connected in series, the reverse breakdown characteristics must be considered as expressed by the term $G(v)$ in Eq. 9.3-4.

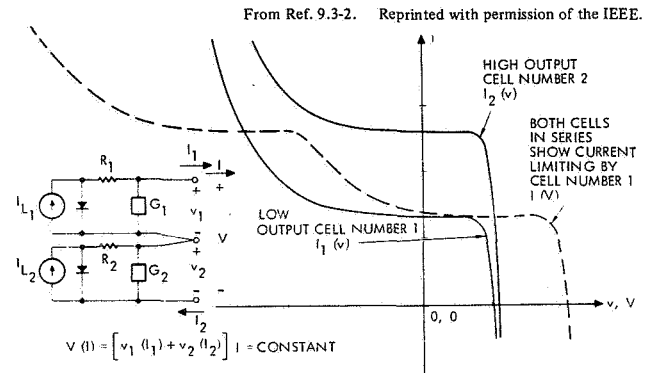


Fig. 9.3-3. Current-Voltage Characteristics of Two Unequal Solar Cells Connected in Series

String Models Without Shunt Diodes

The general current-voltage characteristics of an entire unshadowed solar cell string (Eq. 9.3-7) are nearly identical to the average individual cell characteristics, except for the coordinate scales, some additional series resistance due to cell interconnections, and some minor alterations of the cell $I(V)$ curves due to the string assembly techniques. For simplicity, these effects are understood to be included in the basic cell model and, hence, are omitted in this discussion. The blocking diodes are considered later in the array analysis.

In this section it is assumed that the solar cells have infinite breakdown voltages and zero reverse currents. This assumption is an excellent one as long

as the cell reverse currents remain negligible (compared to the cell output currents) up to voltages in the order of the magnitude of the bus voltage. The model for a partially shadowed submodule with p cells in parallel was shown in Eq. 9.3-17 to be $I_M(v) = I(0) - J(v')$ and the string $I_S(V_S)$ curve was obtained by summing all the s submodule characteristics of that string at constant current values as shown for Eqs. 9.3-6 and 9.3-7 for the nonshadowed case. By substitution

$$I_S(V_S) = I(0) - J(V_S + \Delta V) \quad (9.3-18)$$

Three solutions to Eq. 9.3-18 are outlined for a partially shadowed string consisting of $s = 48$ series-connected submodules of $p = 8$ parallel-connected cells each, illuminated with intensity Q . From the infinite number of possible shadow patterns, three distinct cases of special interest may be isolated:

Case A. The same portions of active cell areas are shadowed in each submodule.

Case B. One submodule is completely shadowed, all others are illuminated.

Case C. Several submodules are shadowed, each by a different amount. The most heavily shadowed submodule is illuminated by the ratio r of Eq. 9.3-10.

The solutions to Eq. 9.3-18 for the cases above, (illustrated in Figure 9.3-4) are as follows:

For Case A. Eq. 9.3-18 is directly applicable since r in this equation is identical to all the r 's in the $s = 48$ submodule equations.

For Case B. According to the assumption of negligible reverse current flow through dark cells, the string output is nearly zero.

For Case C. By the foregoing, the most heavily shadowed submodule limits the string output. Hence, the string output is equal to the sum of $(s - 1) = 47$ fully illuminated submodules plus one partially shadowed submodule, all of the type of Eq. 9.3-17. The graphical solution of this sum is given for submodules according to Eq. 9.3-16 and (for a number of values of r by the dashed curves) in Figure 9.3-4. The solid curves in this figure show experimental data obtained by TRW.

The test results included in Figure 9.3-4 were obtained from a typical string consisting of 1×2 cm size cells with very low breakdown voltages in the order of 2 to 4 V and of 1963-1964 vintage. Very similar results were reported in 1965 by Sullivan (Ref. 9.3-5), who also studied the reverse behavior of several submodules. Based on Sullivan's study of less leaky cells and the characteristics of other, more recently manufactured cells with 20 to 30-V breakdown voltages, the string model of Eq. 9.3-18 without reverse characteristics is indeed a very realistic model leading to much less conservatism in power assessments than may be deduced from Figure 9.3-4.

String Models with Shunt Diodes

From Figures 9.3-3 and 9.3-4 it becomes readily apparent that, if a cell in a series string is shadowed, the amount of current limiting can be reduced, i. e.,

the output increased if cells with low breakdown voltages are used. This thinking has led to the use of shunt, or bypass, diodes connected across shadowed cells or submodules. The addition of these shunt diodes across shadowed submodules produces a very low breakdown voltage artificially. The diodes are connected across the submodules such that the shunt diode goes into forward conduction when the submodule is subjected to reverse bias. A submodule becomes reversed biased when the remainder of the series string containing this submodule tries to force a greater current through this submodule than its short-circuit current permits.

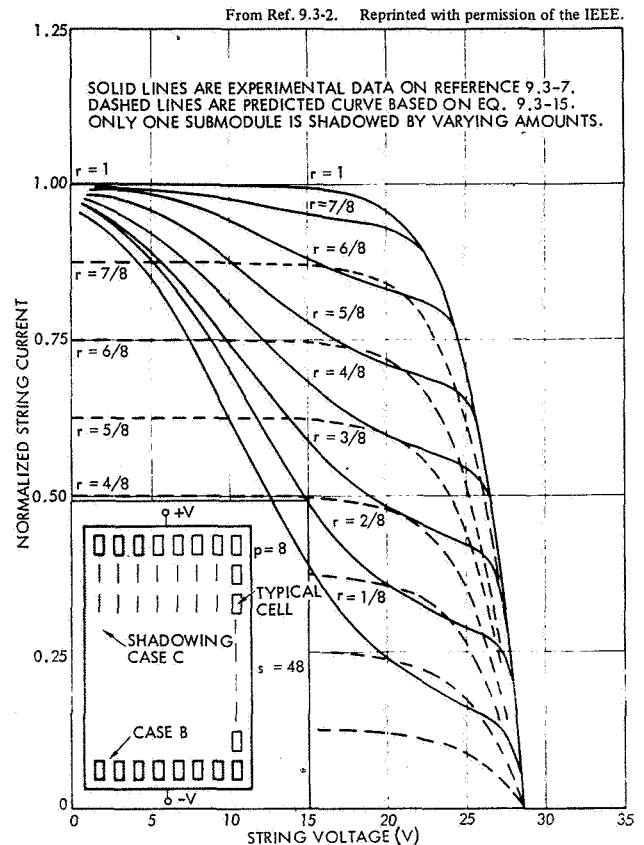


Fig. 9.3-4. I-V Curves of a Partially Shadowed String Without Shunt Diodes

Early work on shunt diode applications was done in 1963 by Baron and Virobik (Refs. 9.3-6 and 9.3-7), who successfully incorporated shunt diodes into the Pioneer Spacecraft solar array. In 1964, Virobik developed an approximate model for solar array analysis utilizing shunt diodes (Ref. 9.3-8). Barton refined this model in 1965 and used it in graphical form for practical array analyses (Ref. 9.3-9). Conn (Ref. 9.3-10) adapted Barton's model in 1966 for the digital computer analyses described by Luft, Barton, and Conn (Ref. 9.3-11).

In the following, a precise string model with shunt diodes is developed as a logical extension of the discussions in the foregoing sections. An approximation is then made which leads to Barton's model. This is accomplished by first substituting the shunt diode characteristics, $I_d(v)$, for $G(v)$ in Eq. 9.3-17, so that the submodule equation with p cells and d shunt diodes in parallel becomes

$$I_M(v) = I(0) - J(v') \quad 0 \leq v$$

$$= I(0) + d I_d(v) \quad v > 0 \quad (9.3-19)$$

where it is implied that the shunt diode forward conduction current flows only when v is negative. The string voltage is obtained similarly as shown earlier by first expressing Eq. 9.3-19 in terms of v , forming the sum

$$V_s(I_s) = \sum_{i=1}^s \left[v(I)_i \right]_I \quad (9.3-20)$$

and expressing it again in terms of I

$$I_s(V_s) = f(I_M, v, p, s, d, r, \dots) \quad (9.3-21)$$

For a partially shadowed string with shunt diodes, the same three shadowing cases studied for a string without shunt diodes are discussed again here.

Case A. Since this case is independent of the reverse characteristics, the results obtained with either Eqs. 9.3-18 or 9.3-21 are identical.

Case B. The string curve is the sum of $(s - 1) = 47$ fully illuminated submodules plus one nonilluminated submodule of Eq. 9.3-19 as illustrated in Figure 9.3-5 for $r = 0$. It will be noted that only the power (and voltage drop) dissipated in the shunt diode is lost.

Figure 9.3-5 also illustrates the resulting summation for eight discrete steps of r , as well as the experimental data obtained by TRW.

Case C. The effect of a general shadow pattern on a string consisting of 20 submodules of seven parallel-connected cells each is illustrated in Figure 9.3-6.

The experimental data substantiate the validity of the model. The somewhat higher experimental current output as compared to the prediction was caused by incomplete shadowing of the cells during the experiment. The theoretical curve of Figure 9.3-6 was obtained by digital computer computations carried out according to Eqs. 9.3-19 through 9.3-21.

In the following, Barton's approximation is described. Inspection of Figures 9.3-5 and 9.3-6 reveals a certain pattern according to which the string $I(V)$ curve shape is altered when cells in a submodule are shadowed. If one submodule is completely shadowed, the $I(V)$ curve will, in general terms, be lowered in voltage by $\Delta V = v + V_d$ where v is the submodule photovoltaic voltage under full illumination and V_d the voltage drop of the shunt diode connected across this now shadowed submodule. If ΔV could be assumed a constant, then a family of curves, each displaced by ΔV to the left of adjacent curves, could be drawn. The highest voltage curve, of course, is the unshadowed output curve, Eq. 9.3-20 and increasing numbers of entire submodules shadowed (shadowing Case B above) would be represented by the lower voltage lines shown in Figure 9.3-7.

Similarly, shadowing of series-connected columns of cells (shadowing Case A above) reduces

the unshadowed string output by $\Delta I = (1 - r)I(0)$ as shown by the current lines in Figure 9.3-7. Any particular shadow pattern on the string can then readily be transformed into the corresponding $I(V)$ curve by the method suggested by and illustrated in Figure 9.3-7. By determining the value for ΔV experimentally, this approximation may become a highly accurate one. To improve the accuracy even more, the sharp corners may be rounded off to approximate the submodule $I(V)$ curve shape knee and the shunt diode knee.

It should be noted that string $I(V)$ curves, as shown in Figures 9.3-4 through 9.3-7, are not shape invariant with intensity or angle of incidence, i. e., all characteristics become $I_s(V_s) = -J(V_s + \Delta V_s)$ with $\Delta V_s = I(0) pR_s$ at zero intensity.

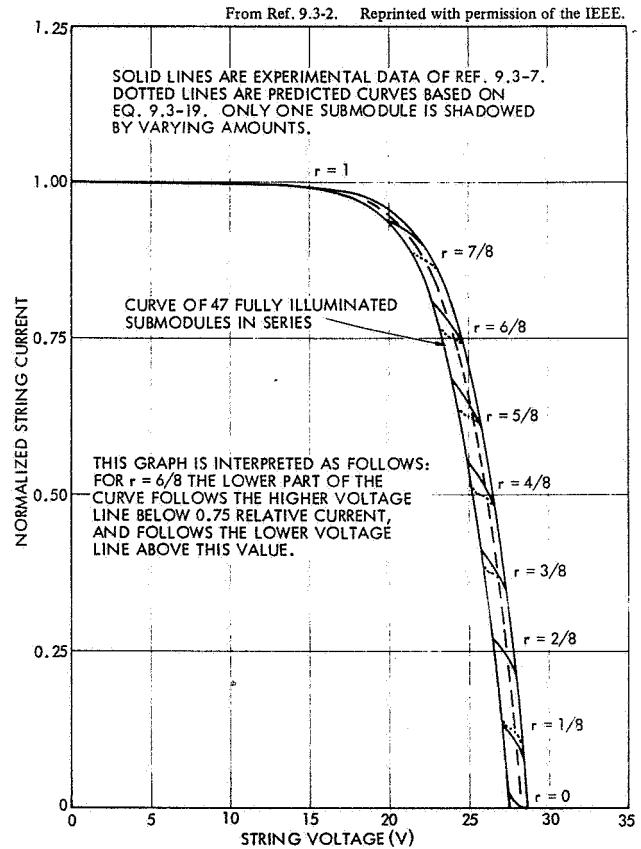


Fig. 9.3-5. I-V Curves of the Partially Shadowed String of Figure 9.3-4 with Shunt Diodes

The Shadowing Factor

The so-called "shadowing factor," F , is defined as the ratio of the output of an entire partially shadowed, arbitrarily sized and shaped solar array to the hypothetical unshadowed output of this same array.

The creation and use of the shadowing factor has been found to be particularly helpful in the analysis of solar arrays with a relatively large number of strings arranged in complicated fashion and subjected to substantial, diverse, and rapidly varying shadow patterns for which the detailed knowledge of the effects discussed earlier would lead to prohibitively large amounts of data to be generated

and processed. While the shadowing factor could be used in the analysis of arrays using shunt diodes, it is developed here only for arrays not using them. Blocking diodes, however, are required.

From Ref. 9.3-2. Reprinted with permission of the IEEE.

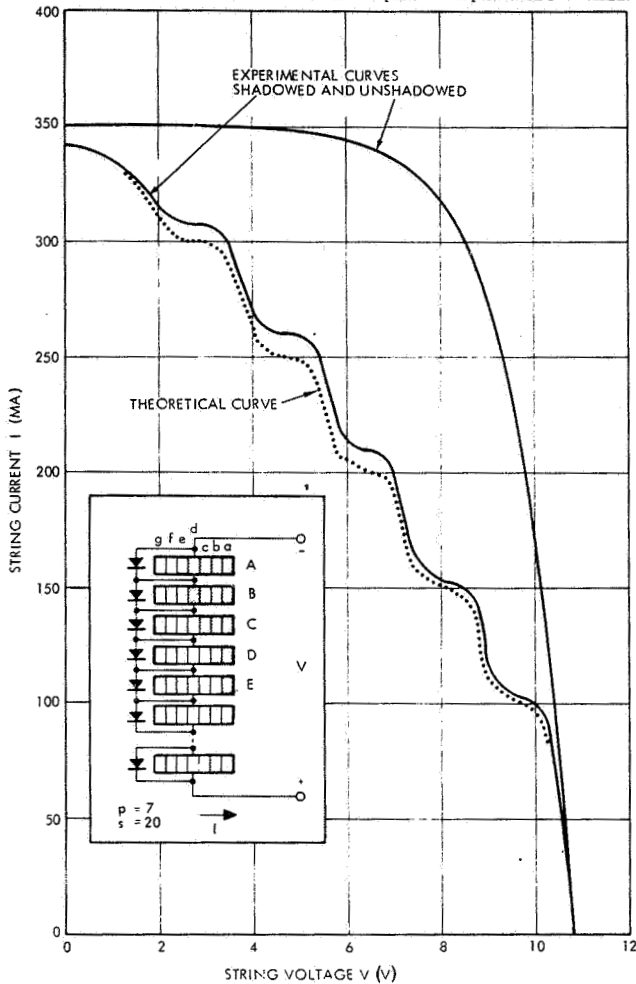


Fig. 9.3-6. Partially Shadowed String Characteristics for Illustrated Shadow Pattern (Shadowing Case C of Figure 9.3-4)

For the following, consider a solar array of a spinning satellite. Define a coordinate system, xyz , such that its origin is located at the center of mass of the arbitrarily shaped satellite. The z -axis coincides with the satellite spin axis, and the center of the sun is always located in the yz -plane. Let the solar array be divided into zones Z , each characterized by its typical zone temperature and zone angle α . Let each zone be divided into flat panels (facets) N , symmetrically distributed and separated by panel angle λ . The first panels of different zones are displaced from the reference panel by an angle X . The solar vector makes an angle θ with the spin axis, and the normal to each panel makes an angle γ with the solar vector. In terms of the given definitions, for each panel of each zone (see illustration in Section 9.4.4):

$$\cos \gamma = \cos \theta \cos \alpha + \sin \theta \sin \alpha \cos [\psi + (N - 1)\lambda + X] \quad (9.3-22)$$

It should be noted that for naturally shaded panels $\cos \gamma$ of Eq. 9.3-22 is negative. Panels with such negative outputs must either be discounted if they connect through blocking diodes to the bus, or they must be considered as loads as discussed earlier in Section 9.1.

The output from a partially shadowed array was given by Eq. 9.3-9. If we define the relationship

$$\begin{aligned} rI(0) \cos \gamma &= 0 & 0 \leq r < 0.5 \\ &= I(0) \cos \gamma & 0.5 \leq r \leq 1 \end{aligned} \quad (9.3-23)$$

for the most heavily shadowed submodule in each string and negligible cell reverse currents, then Eq. 9.3-9 may be restated as

$$I_Z(V_A)_{\theta, \psi} = p \sum_{i=1}^m \rho_i [I(0) \cos \gamma_i - J(V_A)_i] \quad (9.3-24)$$

From Ref. 9.3-2. Reprinted with permission of the IEEE.

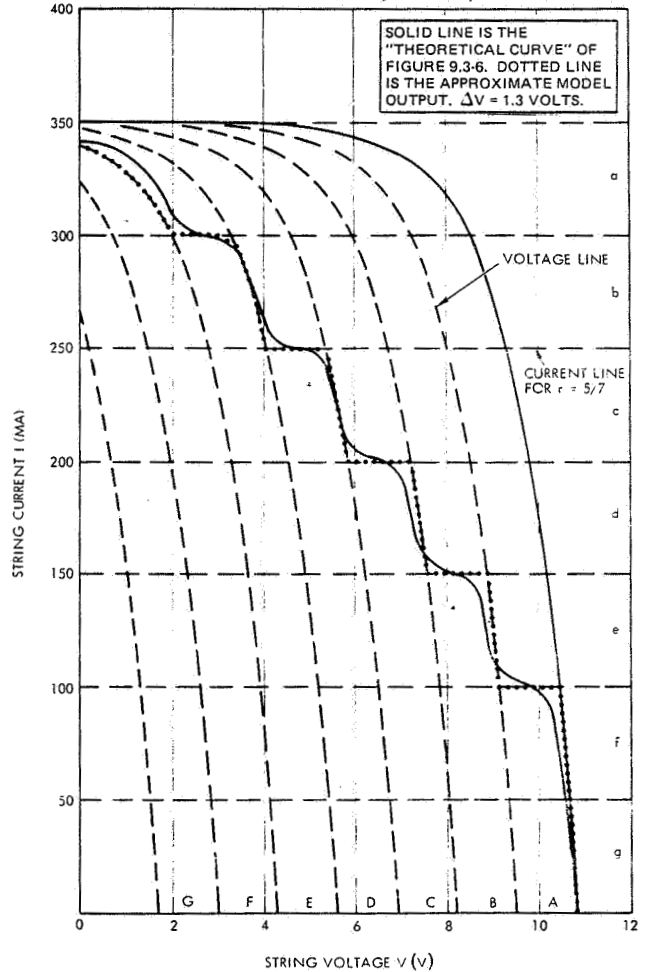


Fig. 9.3-7. Accurate and Approximate I-V Curves of the Partially Shadowed String of Figure 9.3-6

where V_A is still given by Eq. 9.3-9 and ρ_i may be either 0 or 1 depending on whether r in Eq. 9.3-23 is smaller or larger than 0.5. The choice of 0.5 will statistically result in zero error for a large number of strings and random shadow patterns. The unshadowed zone output, $I_{Z0}(V_A)_{\theta, \psi}$, is also given by Eq. 9.3-24, except that all $\rho_i = 1$. The ratio, F , of the partially shadowed zone output to the unshadowed output

$$F(V_A)_{\theta, \psi} = \frac{I_Z(V_A)}{I_{Z0}(V_A)} \Big|_{\theta, \psi}$$

$$= \frac{\sum_{i=1}^m \rho_i [I(0) \cos \gamma_i - J(V_A)_i]}{\sum_{i=1}^m [I(0) \cos \gamma_i - J(V_A)_i]} \quad (9.3-25)$$

indicates the fraction of actually available current. Since, for a given zone, the total as well as this fraction of available current is uniquely determined by the short-circuit currents, Equation 9.3-25 may be restated as

$$F(0)_{\theta, \psi} = \frac{I_Z(0)}{I_{Z0}(0)} = \frac{\sum_{i=1}^m \rho_i \cos \gamma_i}{\sum_{i=1}^m \cos \gamma_i} \quad (9.3-26)$$

where the $I(0)$ terms have cancelled out, and F has been reduced to a geometric projected area relationship. Eq. 9.3-26 may be stated in words as follows: The shadowing factor, F , is the ratio of the actual short-circuit current output to the theoretical output from the total number of strings which would be illuminated in the absence of shadowing.

The instantaneous shadowing factor, F , may be averaged over any range of the spin angle ψ , and/or sun angle θ . Assume that an average shadowing factor, \bar{F} , is to be determined for n values of ψ , all at one θ . Then, from the integral definition of the average

$$\bar{F}_{Z(0)\theta} = \frac{\sum_{i=1}^m \sum_{j=1}^n \rho_{ij} \cos \gamma_{ij}}{\sum_{i=1}^m \sum_{j=1}^n \cos \gamma_{ij}} \quad (9.3-27)$$

Only for special cases, such as when $\Delta\psi = \lambda$, or when n is very large, Eq. 9.3-27 may be written as

$$\bar{F}_{Z(0)\theta} = \frac{\sum_{j=1}^n \sum_{i=1}^m \rho_{ij} \cos \gamma_{ij}}{n \sum_{i=1}^m \cos \gamma_i} \quad (9.3-28)$$

The application of the shadowing factor to array analysis is outlined below. First, the shadowing factors are determined, either according to Eq. 9.3-26 or to Eq. 9.3-27. Next, the shadowing factors are applied for calculating the ratios of the instantaneous or average zone outputs, respectively, to the hypothetical, unshadowed zone output according to Eq. 9.3-7 with $r = 1$:

$$I_Z(V_A)_{\theta, \psi} = pF(0)_{\theta, \psi} \cdot \sum_{i=1}^m [I(0) \cos \gamma_i - J(V_A)_i]_V \quad (9.3-29)$$

$$I_Z(V_A)_{\theta} = p\bar{F}(0)_{\theta}$$

$$\sum_{i=1}^m [I(0) \cos \gamma_i - J(V_A)_i]_V \quad (9.3-30)$$

9.3.3 Nonilluminated Arrays

The I-V curves of nonilluminated (i. e., "dark") solar cell arrays are well represented in the "Simple Array Model" described in Section 9.3.1 except that $I_{sc} = 0$ when the illumination is zero. Temperature gradients and nonuniform solar cell I-V curves do not influence the accuracy of this model for engineering purposes.

Further details of nonilluminated arrays are given in Chapter 11 in connection with "dark forward" testing of solar cell arrays.

9.4 ARRAY ELECTRICAL PERFORMANCE PREDICTION

Electrical performance of a solar cell array is defined here as the electrical power output capability of an array at some specified operating conditions and before or after some specified environmental exposure. Array performance prediction is also known by other terms such as "performance analysis" or "output computation."

The process of electrical performance prediction contains the following elements:

- Determination of the degradation factors related to solar cell array design and assembly.
- Conversion of environmental factors and criteria into array degradation factors.
- Conversion of operational and environmental conditions and criteria into solar cell temperatures.
- Calculation of solar cell array performance capability.

It should be noted that:

- Not all of the input data and design parameters given in this section are applicable for all array designs or all missions.
- For some array designs or missions additional input data may be required and other design parameters may have to be considered.
- The data and information given in this handbook are subject to change as more knowledge about the environment is gained; new solar cells and new array components, materials, and processes are developed; and new test data become available.

9.4.1 Analytical Approach

The general analytical approach followed in this section presupposes the existence of a detailed solar cell array design which is intended for a specific space mission. (The procedures for creating and developing a detailed array design are given in Chapter 8.) The detailed array performance prediction consists of three major activities:

- Gathering of input data
- Performing supporting analyses
- Performing the array output analysis.

Figure 9.4-1 illustrates the general analytical approach and the flow of data between the various analyses. The array output computation is based on the commonly used computerized shifting of I-V curves within an I-V coordinate system to account for environmental and operational effects. The array performance prediction is developed in this section using the

DENI 1-MeV fluence method for determining solar cell degradation, and using orbital data to determine the optical array degradation; however, any other method for determining solar cell and optical (cell cover and cover adhesive) degradation may be substituted for the methods shown here.

The supporting analyses shown in Figure 9.4-1 are discussed in Sections 9.5 through 9.11; the array output analysis is discussed in the following subsections.

9.4.2 Sequence of Shifting I-V Curves

The best method for predicting solar cell and array performance is shifting the cell or array I-V characteristics along their current and voltage coordinates and adjusting the curve shape when required. The proper sequence for such curve shifting is as follows:

- Start with initial, bare cell characteristics obtained under standard test conditions (i.e., 28°C cell temperature, one solar constant intensity, air-mass-zero spectrum).
- Adjust I_{sc} , I_{mp} , and V_{oc} measured under standard test conditions for particulate radiation damage, as expressed for a given damage equivalent 1-MeV fluence.
- Adjust I-V curve for operating solar intensity actually incident on the solar cell through degraded optical elements and at off-point angle. Include cover installation loss or gain. Correct the curve shape, if required.
- Adjust I-V curve for operating temperature. Correct the curve shape, if required.
- Scale up cell characteristics to the array level and include isolation diode and wiring losses, and external series resistance effects.

9.4.3 Gathering of Input Data

In this section the input data listed under "INPUTS" in Figure 9.4-1 is discussed with reference to this figure and in the same sequence as given in this figure from top to bottom.

Solar Cell Cover Factors

The optical transmission factor, F_T , includes all effects that may affect the amount of light reaching the solar cell active surface as follows:

$$F(\theta, \phi_{uv}, \phi_p) = F_{\tau_a}(\phi_{uv}, \phi_p) \cdot F_{\tau_c}(\phi_{uv}, \phi_p) \cdot R_{sc}(\theta, \phi_{uv}, \phi_p) \cdot F_d(t) \quad (9.4-1)$$

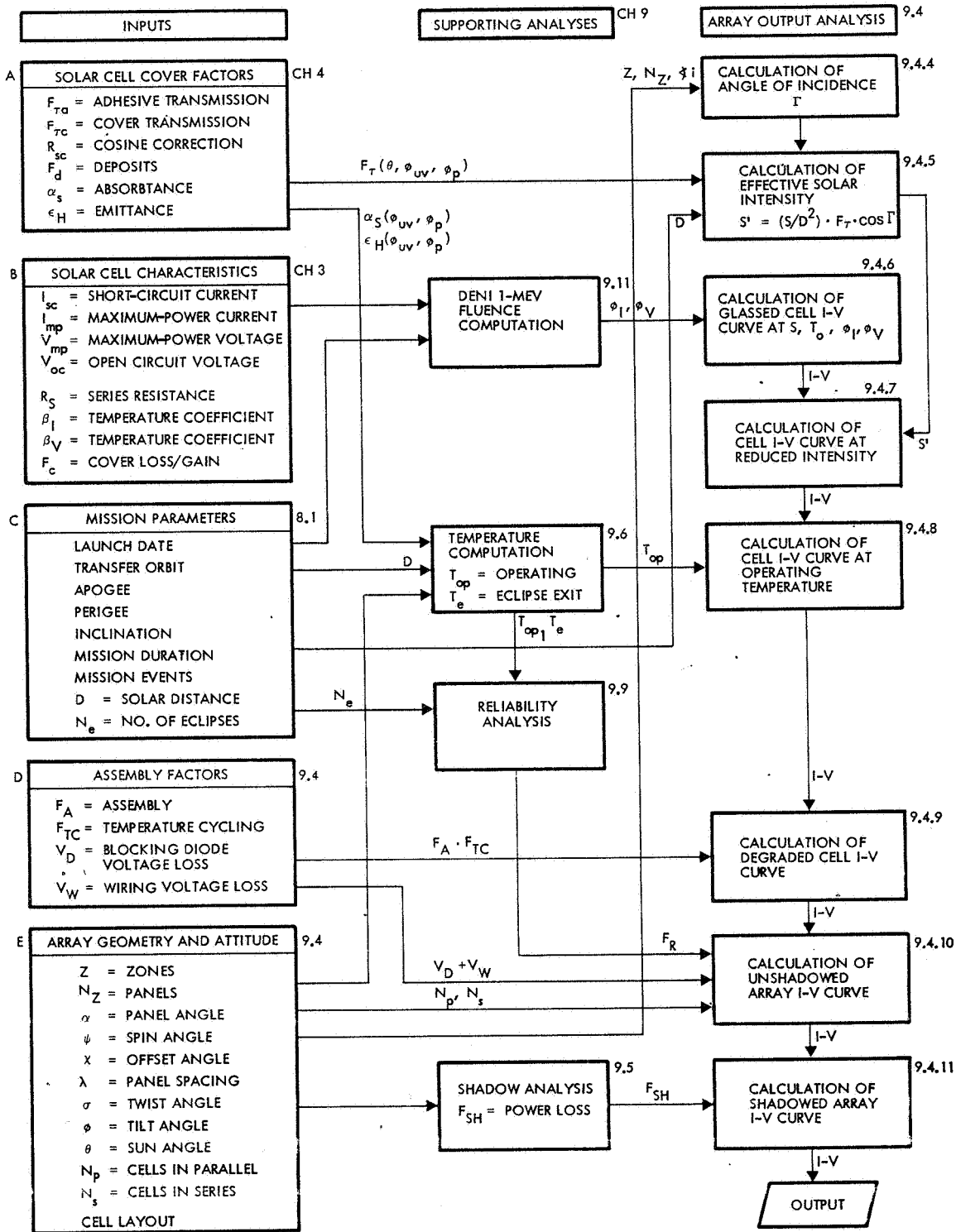


Fig. 9.4-1. Solar Cell Array Electrical Performance Prediction (Numbers to the right of the boxes indicate Handbook chapters and sections where data and analyses are discussed.)

where

$F_{\tau a}$ = adhesive darkening factor, defined as the ratio of the solar cell short-circuit current after adhesive darkening to that before darkening

$F_{\tau c}$ = cover darkening factor, defined as the ratio of the solar cell short-circuit current after darkening to that before darkening

R_{sc} = relative short-circuit current, defined as the ratio of the glassed solar cell short-circuit current actually measured at a given sun off-point angle, θ , to that expected from the cosine of θ (i. e., R_{sc} is the cosine correction factor discussed in Section 4.8)

F_d = light transmission loss factor due to deposits and their darkening with time, defined as the ratio of the solar cell short-circuit current after darkening of the deposits to that before deposits were present (see Section 2.3.5)

$F(\theta, \phi_{uv}, \phi_p, t)$ = indicates that the factor, F , is a function of $\theta, \phi_{uv}, \phi_p, t$

ϕ_{uv} = ultraviolet radiation dose

ϕ_p = particulate radiation dose

t = time in orbit (after launch, or after liftoff, or after orbit insertion).

The radiometric properties, α_S and ϵ_H (defined in Section 7.14) are functions of both ϕ_{uv} and ϕ_p .

Values for the cover factors can be obtained from the following sections of this handbook or from the references given therein.

Factor	Volume I Section	Volume II Section
F_c	4.3.3	
$F_{\tau a}$	11.7, 11.8, 11.9, 11.13	7.13
$F_{\tau c}$	11.7, 11.8, 11.9, 11.13	7.13
R_{sc}	4.8	7.13
α_S	11.6	7.14
ϵ_H	11.6	7.14

Solar Cell Characteristics

The electrical characteristics of the specific solar cells considered for a design may be obtained from the following sources:

- Chapter 3, Volume II, of this handbook
- A test (see Chapter 11)
- The solar cell manufacturer
- The open literature.

The solar cell characteristics required for the analyses described herein are as follows:

- Solar cell I-V curves at standard test conditions (typically 28°C cell temperature, one solar constant intensity and AMO spectrum) before and after irradiation with 1-MeV electrons
- Temperature coefficients for solar cell current (β_I) and voltage (β_V), before and after irradiation with 1-MeV electrons
- Cover installation factor, F_c
- Cell series resistance, R_s .

The cover installation factor, F_c , is defined as

$$F_c = I_{sc}(C)/I_{sc}(U) \quad (9.4-2)$$

where the indices (C) and (U) indicate the "covered" and "uncovered" cell short-circuit current output, I_{sc} . Typically for SiO_x -coated solar cells, F_c is less than unity and for Ta_2O_5 -coated cells, F_c is greater than unity. Values of F_c can be found in Section 4.3.3.

Mission Parameters

The mission parameters listed in Figure 9.4-1 determine or contribute to the following:

- Solar cell radiation dose
- Cover and cover adhesive radiation doses
- Solar cell illumination level
- Solar cell operating temperature
- Solar cell array temperature cycling stress levels.

The launch date is of significance in establishing the solar flare proton environment as discussed in Section 2.5.4.

All mission parameters are peculiar to each specific mission. Mission events include such occasions as planetary encounter, etc. For general information, mission parameters are discussed in the following sections of this handbook:

Mission Parameter	Section
Launch Date and Solar Flares	2.5.4
Transfer Orbits	2.5.5
Apogee, Perigee, Inclination	2.5, 2.6, 9.10
Mission Duration	2.3.7
Mission Events	2.3.1
Solar Distance	2.3.1, 2.4.2
Number of Eclipses	2.6.2

Assembly Factors

Assembly factors reflect a reduction in solar cell array output capability due to unavoidable or deliberately chosen design and assembly process parameters. Assembly factors may be expressed as dimensionless ratios to be applied to output power, current, or voltage, or as incremental series resistances, or as voltage differences. A common practice is to use both ratios and voltage drops as shown in Sections 9.4.5 through 9.4.10.

The values of assembly-related factors may change with time in orbit. For example, blocking diodes, when exposed to particulate radiation, will exhibit lower forward voltage drops but higher reverse leakage currents after irradiation. As another example, solder coatings on solar cell interconnectors may cease to be electrically conductive in the current flow direction after extensive temperature cycling.

The assembly (and assembly degradation) factors may be divided as shown in the following; discussions related to these factors are given in the sections of this handbook as shown:

Parameter	Section
F_A = assembly factor (solar cell power output degradation due to soldering, welding, etc.)	10.4.8
F_{TC} = solar cell array power output degradation due to temperature cycling	11.11.3
V_D = blocking diode voltage losses	2.5.8, 5.5
V_W = interconnector and wiring voltage losses due to resistance and changes in resistance	5.3.13

Array Geometry and Attitude

The spacecraft and solar cell array configuration and the spacecraft attitude (orientation relative to the sun) determine the amount of sunlight intercepted by the solar cells and, hence, the array operating temperature and the solar cell output.

The geometric input parameters are usually obtained from sketches or drawings; their conversion into analytical inputs is shown in Section 9.4.4

9.4.4 Angle of Incidence

For analytical reasons, the solar cell array is centered in a Cartesian coordinate system such that the array's spin axis or axis of symmetry is coincident with one of the axes of the coordinate system (Figures 9.4-2 through 9.4-4).

The array is subdivided into Z zones. Each zone contains only those solar cell panels whose normal unit vector projections on the spin axis are equal.

Each zone is subdivided into N solar cell panels or paddles. Each panel or paddle is angularly displaced from its neighbor by an angle λ . The angle λ is measured in a plane which is perpendicular to the spin axis (i.e., when viewed in the direction of the spin axis) and is always positive.

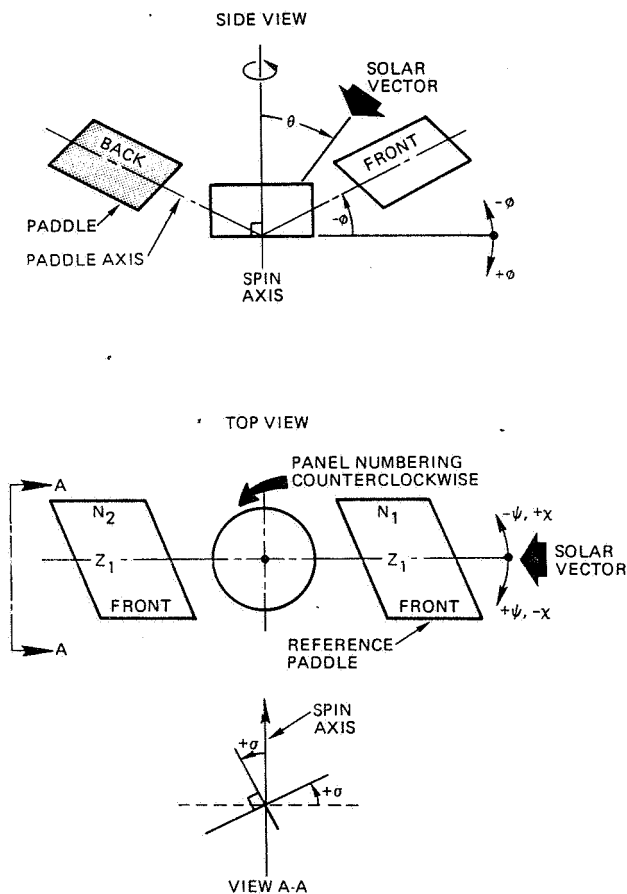


Fig. 9.4-2. Solar Array Geometry for Paddle-Wheel Solar Array Configurations

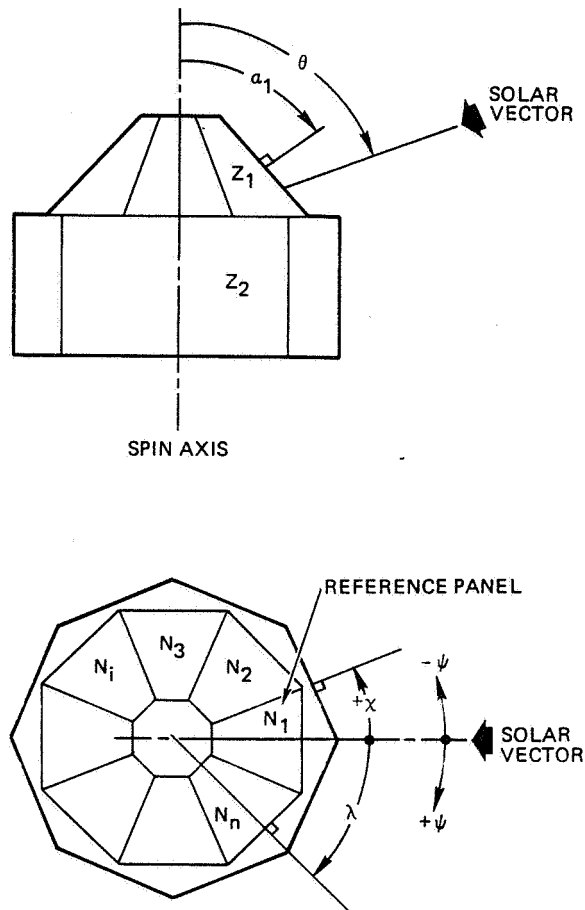


Fig. 9.4-3. Solar Cell Array Geometry for Flat or Body-Mounted Solar Panels

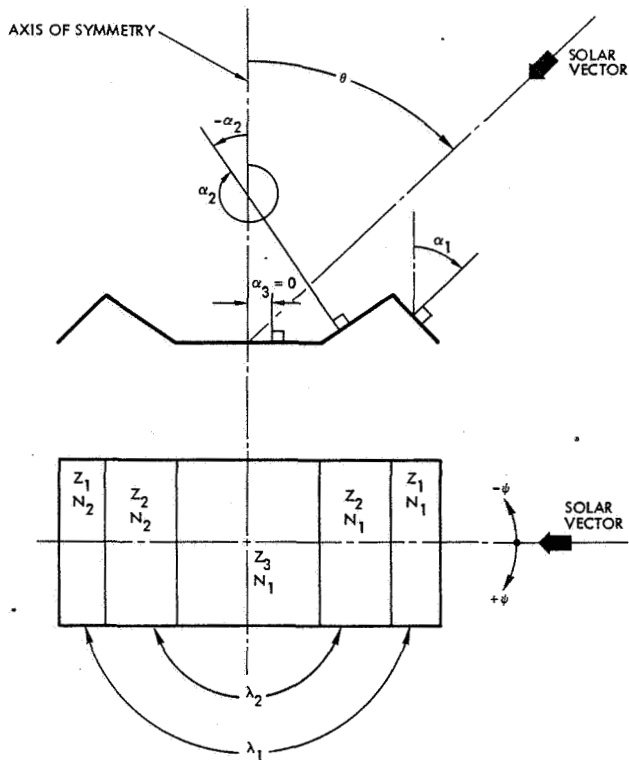


Fig. 9.4-4. Solar Cell Array Geometry for Flat Solar Cell Panels

The normal unit vector of the first panel or paddle in the first zone is (for convenience) placed in a plane defined by that unit vector and the array-sun line (the "solar vector").

The projection (on a plane perpendicular to the spin axis) of the unit vector of the first panel of the second zone makes an angle χ with the projection of the unit vector of the first panel of the first zone. When the projections of both unit vectors are parallel, $\chi = 0$.

The satellite may be spinning in the coordinate system through the spin angle ψ . Initially, $\psi = 0$ for convenience.

For a paddle wheel array configuration, the axis through each paddle in a direction pointing away from the spin axis may be inclined (raised up) from a plane which is perpendicular to the spin axis by an angle ϕ . When a paddle axis is perpendicular to the spin axis, $\phi = 0$.

Each paddle is twisted relative to being plane-parallel to a plane which is perpendicular to the spin axis by an angle, σ . This angle is measured in a counterclockwise direction when viewed along the twist axis in the direction of the spin axis.

For a body-mounted or flat panel array configuration, all normal unit vectors in a given zone make an angle σ with the spin axis.

The angle of incidence, Γ , for each panel or paddle on the array, for a given angle, θ (sun angle), between the array spin axis (spin vector) and the array-sun line (sun vector) can be found from Eqs. 9.4-3 or

9.4-4, respectively. The angles are defined above and in Figures 9.4-2 through 9.4-4.

Paddle-Wheel Configuration

For the i -th panel:

$$\begin{aligned} \cos \Gamma_i &= \sin \sigma \cdot \sin \theta \cdot \sin [\psi + (N_i - 1) \lambda + \chi] \\ &+ \cos \sigma \cdot \sin \phi \cdot \sin \theta \cdot \cos [\psi + (N_i - 1) \lambda + \chi] \\ &+ \cos \sigma \cdot \cos \phi \cdot \cos \theta \end{aligned} \quad (9.4-3)$$

Body-Mounted and Flat Configurations

For the i -th panel:

$$\begin{aligned} \cos \Gamma_i &= \cos \theta \cdot \cos \alpha + \sin \theta \cdot \sin \alpha \cdot \\ &\cos [\psi + (N_i - 1) \lambda + \chi] \end{aligned} \quad (9.4-4)$$

9.4.5 Effective Solar Intensity

The effective solar intensity, S' , is defined as the actual, "effective" light level which is incident upon the active surface of the solar cell and is given by

$$S' = (S/D^2) F_T \cos \Gamma \quad (9.4-5)$$

where the terms are defined and their values obtainable from the sections of this handbook as follows:

<u>Parameter</u>	<u>Section</u>
S = sunlight intensity (in units of solar constants)	2.4.2
D = array-sun distance (in units of AU)	2.4.2, 9.4.3
F_T = solar cell cover factor	9.4.3
Γ = angle of incidence	9.4.4

9.4.6 Glassed Solar Cell I-V Curve

If glassed solar cell data was obtained as input in Section 9.4.3, no further effort is required in this step. If unglassed cell data was obtained, the I-V curves for the unglassed cells are shifted parallel to the current axis until the cell short-circuit current after glassing is

$$I_{scg} = I_{scu} \cdot F_c$$

where I_{scu} is the unglassed short-circuit current of the radiation-damaged cell and F_c is the cover installation factor; both are obtained from Section 9.4.3 under the heading "B. Solar Cell Characteristics." Since F_c typically is within a few percent of unity, the other three solar cell parameters after glassing are

$$I_{mpg} = I_{mpu} + (I_{scg} - I_{scu})$$

$$V_{mpg} = V_{mpu}$$

$$V_{ocg} = V_{ocu}$$

where

I_{mp} = current at maximum power

V_{mp} = voltage at maximum power

V_{oc} = open-circuit voltage

and the additional subscripts "g" and "u" refer to "glassed" and "unglassed" conditions, respectively.

9.4.7 Solar Cell I-V Curve at Changed Intensity

The solar cell I-V curves for a particular radiation damage from Section 9.4.6 are shifted in the I-V coordinate system along the current and voltage axis by amounts ΔI_1 and ΔV_1 given by

$$\Delta I_1 = (S' - S)I_{scg}$$

where

I_{scg} = original cell short-circuit current after glassing before the intensity was changed

S' = effective solar intensity from Section 9.4.5

S = solar intensity (one solar constant) at which the solar cells were originally tested

ΔI_1 is negative and ΔV_1 is positive for reduced intensity (i.e., $S' < S$), leading to a lower short-circuit current, I_{scs} , and a slight shift toward higher voltages even though the actual cell open-circuit voltage will decrease by

$$V_{S'} = k \log (S'/S)$$

where $0.01 \leq k \leq 0.01$, depending upon the cell type. The four solar cell parameters of Section 9.4.6 change as follows due to a change in intensity (indicated by the additional subscript "s"):

$$I_{scs} = I_{scg} + \Delta I_1$$

$$I_{mps} = I_{mpg} + \Delta I_1$$

$$V_{mps} = V_{mpg} + \Delta V_1 + \Delta V_{S'}$$

$$V_{ocs} = V_{ocg} + \Delta V_1 + \Delta V_{S'}$$

9.4.8 Solar Cell I-V Curve at Operating Temperature

The I-V curve obtained in Section 9.4-7 is now adjusted for the actual solar cell operating temperature, T_{op} . The I-V curve shifted in the I-V coordinate system by amounts ΔI_2 and ΔV_2 given by

$$\Delta I_2 = \beta_I I_{sc} (T_{op} - T_o)$$

$$\Delta V_2 = \beta_V (T_{op} - T_o)$$

where

β_I = temperature coefficient (defined in Section 3.6.2) for current in units of " $^{\circ}C^{-1}$ "

β_V = temperature coefficient (defined in Section 3.6.2) for voltage, in units of " $V \cdot ^{\circ}C^{-1}$ "

I_{sc} = the cell I_{sc} before the temperature change

T_o = reference temperature at which the solar cells were initially tested

The values of β_I are usually positive and those of β_V are negative. Therefore, a temperature increase ($T_{op} > T_o$) causes an increase in I_{sc} and a decrease in V_{oc} (see Section 3.6 for details). The four cell parameters of Section 9.4.7 change as follows:

$$I_{scT} = I_{scs} + \Delta I_2$$

$$I_{mpT} = I_{mps} + \Delta I_2$$

$$V_{mpT} = V_{mps} + \Delta V_2$$

$$V_{ocT} = V_{ocs} + \Delta V_2$$

9.4.9 Degraded Solar Cell I-V Curve

The solar cell I-V curve from Section 9.4.8 is now further adjusted for the assembly and temperature cycling degradation factors, F_A and F_{TC} , respectively. The values for F_A and F_{TC} are obtained from Section 9.4.3 under the heading "Assembly Factors."

Both F_A and F_{TC} usually introduce additional series resistance in the solar cell or in an assembly of cells and thereby tend to depress the cell's maximum power output without affecting the I_{sc} and V_{oc} . Therefore, it is desirable to depress both I_{mp} and V_{mp} on the I-V curve by the amounts

$$\Delta I_3 = -(F_A \cdot F_{TC})^{1/2}$$

$$\Delta V_3 = -(F_A \cdot F_{TC})^{1/2}$$

respectively, and letting I_{sc} and V_{oc} remain unchanged. The four cell parameters of Section 9.4.8 will therefore change as follows:

$$I_{scd} = I_{scT}$$

$$I_{mpd} = I_{mpT} + \Delta I_3$$

$$V_{mpd} = V_{mpT} + \Delta V_3$$

$$V_{ocd} = V_{ocT}$$

9.4.10 Array I-V Curve

The unshadowed solar cell array I-V curve is computed from the single cell I-V curves of Section 9.4.9 in the following sequence:

- Multiplication of the single cell current output by the number of solar cells in parallel, N_p , on a given panel or paddle
- Multiplication of the voltage output of the N_p solar cells in parallel by N_s cells in series

- Subtraction of the voltage drops, V_D and V_W , from the panel voltage output (V_D and V_W are obtained from Section 9.4.3 under the heading "Assembly Factors.")
- Summing of all panel and paddle output currents at constant voltages.

The above computations result in an array I-V curve at operating temperature and after environmental degradation. This process of calculation is treated mathematically in Section 9.3.1 and results in the following four array output parameters:

$$I_{sc_A} = I_{scd} N_p$$

$$I_{mp_A} = I_{scd} N_p$$

$$V_{mp_A} = V_{mpd} N_s - (V_D + V_W)$$

$$V_{oc_A} = V_{ocd} N_s - (V_D + V_W)$$

If the solar cell array is partially shadowed, the unshadowed power output must be reduced according to the method described in Section 9.3.2.

The solar cell degradation and array output analysis described above can be performed conveniently by digital computer. Section 9.2.3 describes suitable computer programs for this task.

9.5 SHADOW ANALYSIS

In this section methods are described by which the geometries of the shadows falling on solar cell arrays can be determined. The electrical response of the array to these shadows is discussed in Section 9.3.

9.5.1 Definitions

A shadow is defined as the absence of solar illumination on a solar cell array due to a blocking of the sunlight by a shadow-casting object. For example, an antenna or a boom may cast a shadow on the array at certain angles of illumination (sun angle or spacecraft orientation).

The naturally occurring lack of illumination on the "dark" side of a body-mounted solar cell array (the so-called "eigenshadow") is specifically excluded from the definition of the shadow because the output from these nonilluminated array areas is already computed by the array models of Sections 9.2 and 9.3 to be zero. A second inclusion of the naturally nonilluminated areas in the shadowing factor would lead to erroneous results.

The shadowing factor is a term affecting the electrical performance of the array; it is defined in Section 9.3.2. The shapes of shadows cast on the array are known as shadow patterns. The effect of shadow patterns on the array electrical output depends strongly on the size and location of a shadow on each string of solar cells. Therefore, shadow patterns must be determined in relation to the string layout of solar cells on the array (strings are defined in Section 9.3.1).

9.5.2 Development of Shadow Patterns

The determination of geometrical shadow patterns on the array is discussed in the following paragraphs. Additional techniques of determining shadow patterns may be taken from books on "Descriptive Geometry"; also, computerized or photographic procedures may be employed. The following material is in part quoted from Ref. 9.5-1.

Nomenclature

- A = projected area of shadowing object on a circle with radius R
- α = planar angle subtended by the sun's diameter
- B = length of umbra
- D = diameter of the sun = 0.36×10^6 miles
= 1.4×10^6 km
- d = width or diameter of object causing a shadow
- h = segment height
- I = normalized illumination intensity
- K = relative darkness
- L = distance from the object to sun at 1 AU

- m = distance between center of circle of radius R and center of shadow object of width d
- p = width of the shadow's penumbra
- R = radius of circle subtended by angle α at a distance s
- s = distance from object to surface
- S = shaded segment of luminous circle with radius R
- u = width of the shadow's umbra

Shadow Geometry

Figure 9.5-1 shows the geometry of a shadow cast by a cylindrical rod parallel to a surface (extending perpendicularly through the plane of the paper) onto that surface in the vicinity of earth, where the surface is normal to the object-sun axis. From this figure

$$\alpha_1 = 2 \arctan (D/2L_1)$$

$$\alpha_2 = 2 \arctan [D/2 (L + B)]$$

$$\frac{B_1}{L_1} = \frac{d}{D}, \quad \frac{B}{L} = \frac{d}{D}$$

$$\frac{L}{L_1} = \frac{L_1 + B_1}{L_1} = \frac{D + d}{D}$$

$$\frac{L + B}{L} = \frac{D + d}{D}$$

Since $d \ll D$ we have $L \approx L_1$ and $L + B \approx L$. Therefore

$$\alpha_1 \approx \alpha_2 = 2 \arctan (D/2L) = 9.25 \times 10^{-3} \text{ rad} \quad (9.5-1)$$

$$B \approx B_1 = d/[2 \tan (\alpha/2)] = 108.1 d \quad (9.5-2)$$

Then, the width of the umbra of the shadow becomes

$$u = \frac{d(B - s)}{B} = \frac{108.1 d - s}{108.1} = d - \frac{s}{108.1} \quad (9.5-3)$$

and the width of the penumbra is:

$$p = \frac{d(B + s)}{B} = \frac{108.1 d + s}{108.1} = d + \frac{s}{108.1} \quad (9.5-4)$$

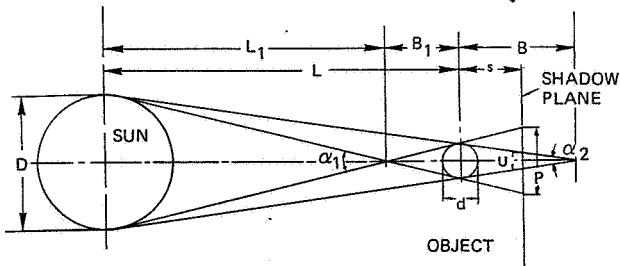


Fig. 9.5-1. Shadow Geometry

Normalized umbra and penumbra widths as a function of normalized distance are shown in Figure 9.5-2.

Intensity Distribution

The light intensity in the umbra is zero. The intensity in the penumbra ranges from unity at the outer edge to zero at the umbra for cases of $s < B$, and from unity to an indeterminate value for cases of $s > B$. The illumination intensity distribution within the shadow, and its average value is a function of the shadow plane location relative to B and of the shape of the shadow-casting object.

The relative darkness at a point in the shadow can be determined by viewing the sun from that point. A portion, A , of the solar disc, appearing to have a radius, R , will be obscured by the object. The relative darkness is $K = A/(\pi R^2)$. The normalized illumination intensity is defined as $I = 1 - K$.

Integrating K over the full shadow area and dividing by the area gives the average darkness \bar{K} . The average normalized illumination intensity within the shadow is $\bar{I} = 1 - \bar{K}$.

Cylinder Parallel to Shadow Plane

The case for a shadow resulting from a cylinder or bar parallel to the shadow plane (and perpendicular to the paper), which is normal to the sun-object axis, is analyzed in detail below.

Figure 9.5-3 shows the view angle, β , from distance, s , of the object with width, d , and the corresponding sun diameter, $2R$. By similarity with Eq. 9.5-1, we have

$$\beta = 2 \text{ arc tan } (d/2s) \quad (9.5-5)$$

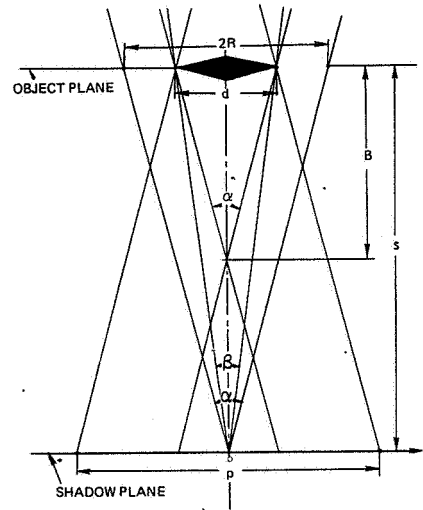


Fig. 9.5-3. Further Shadow Geometry to Show Relation of Distance, s , to Apparent Solar Diameter, $2R$, and Object Width, d

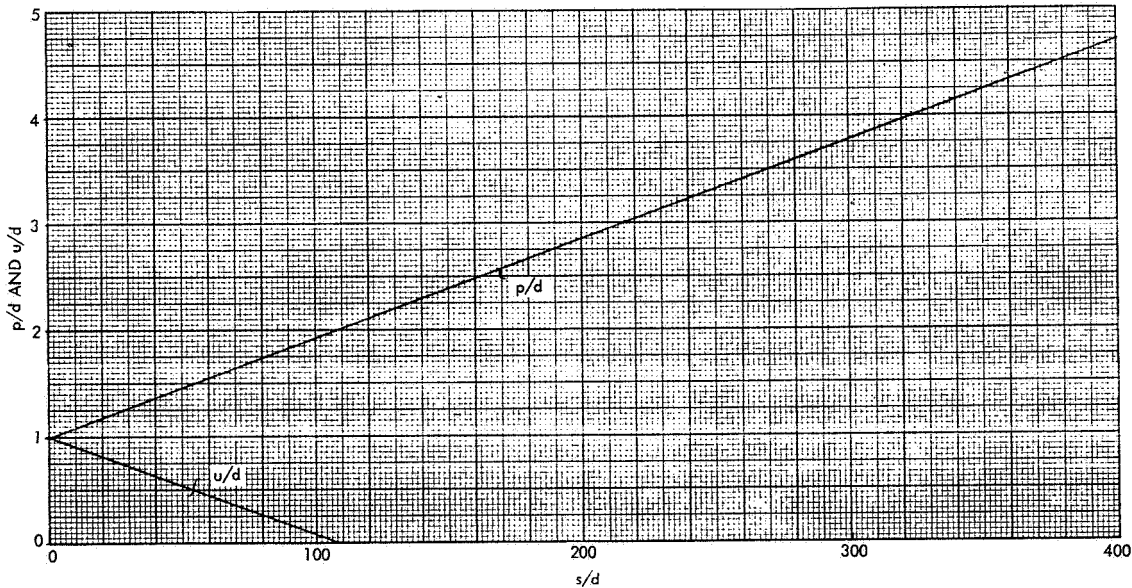


Fig. 9.5-2. Dimensionless Representation of Normalized Umbra Width, u/d , and Penumbra Width, p/d , as a Function Normalized Distance to Shadow Casting Object, s/d

and

$$\alpha = 2 \arctan (R/s) . \quad (9.5-6)$$

Consequently,

$$d/2R = \tan(\beta/2)/\tan(\alpha/2) \quad (9.5-7)$$

and

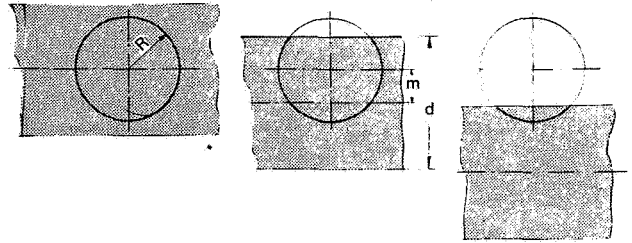
$$d/2R = B/s \quad (9.5-8)$$

At 1 AU we obtain from Eq. 9.5-2

$$d/2R = 108/(s/d) \quad (9.5-9)$$

which is solved graphically in Figure 9.5-4.

Observing the object of width, d , as shown in Figure 9.5-3, from the shadow plane at various locations along the x -axis while moving from $x = 0$ to $x = p/2$ results in images as shown in Figures 9.5-5 and 9.5-6 for the cases of $s < B$ and $s > B$, respectively.



$x = 0$

$0 < x < p/2$

$x < p/2$

Fig. 9.5-5. View from Shadow Area Towards Sun for $s < B$, Starting from Sun-Object Centerline and Moving Towards Edge of Penumbra (refer to text)

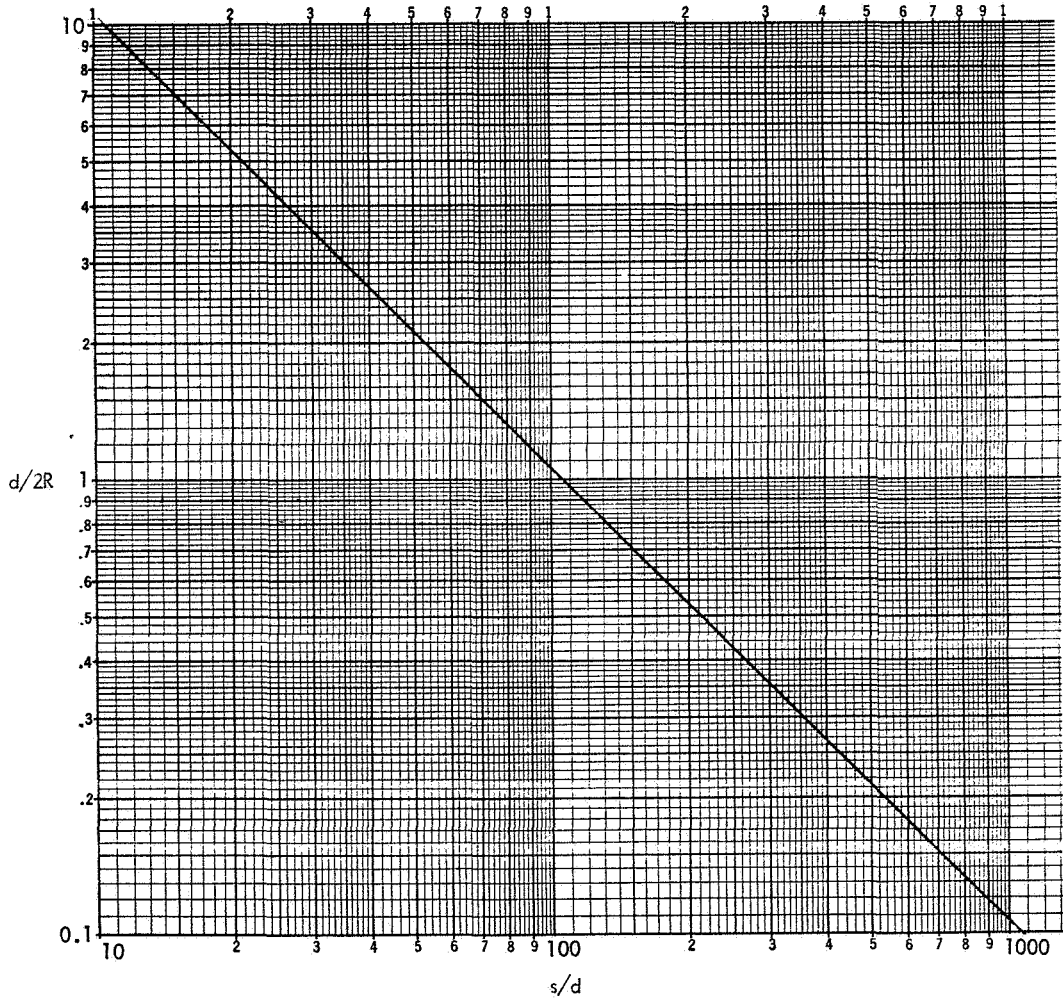


Fig. 9.5-4. Normalized Object Half-Width, $d/2R$, Versus Normalized Shadow Plane Distance from Object, s/d

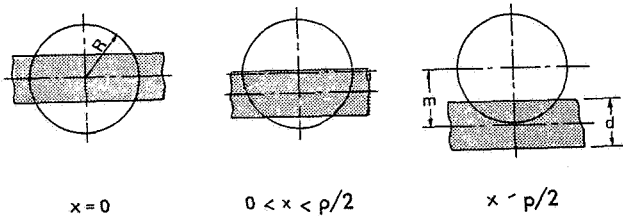


Fig. 9.5-6. View from Shadow Area Towards Sun for $s > B$, Starting from Sun-Object Centerline and Moving Towards Edge of Penumbra (refer to text)

In the case of Figure 9.5-5, the moving point is in the umbra for locations of $x = 0$ to $x = u/2$; $x = u/2$ is reached when $m/R = (r/R) - 1$. While moving from $x = u/2$ to $x = p/2$, the viewing point will be located in the penumbra; $x = p/2$ is reached when $m/R = (r/R) + 1$. By inspection of Figure 9.5-3 it can be seen that

$$u = d - 2R$$

and

$$p = d + 2R$$

For the case of Figure 9.5-6, the moving point is always in the penumbra from $x = 0$ to $x = p/2$.

The normalized illumination intensity as a function of the normalized location in the shadow, m/R , is shown in Figure 9.5-7 with the parameter s/B ranging from 0.5 to 10.

Integrating the area under the curves in Figure 9.5-7 to obtain

$$\bar{I} = \frac{1}{i} \int_0^i I d(m/R)$$

results in the average normalized illumination intensity as a function of s/B shown in Figure 9.5-8.

Multiplying $1 - \bar{I}$ by the normalized shadow width $p/d = 1 + s/B$ (from Eq. 9.5-4), results in a constant

$$(1 - \bar{I}) p/d = 1 \quad (9.5-10)$$

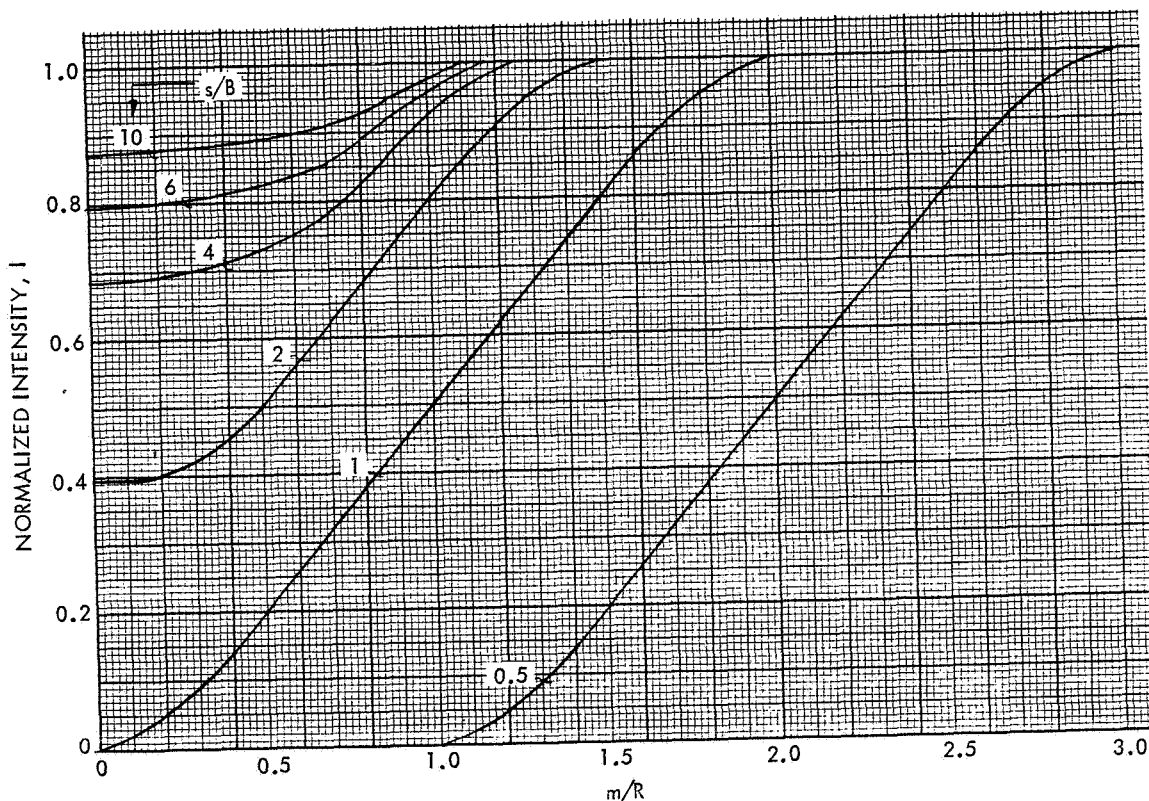


Fig. 9.5-7. Normalized Illumination Intensity as a Function of Normalized Location Within the Shadow, m/R , with the Normalized Distance, s/b , as a Parameter

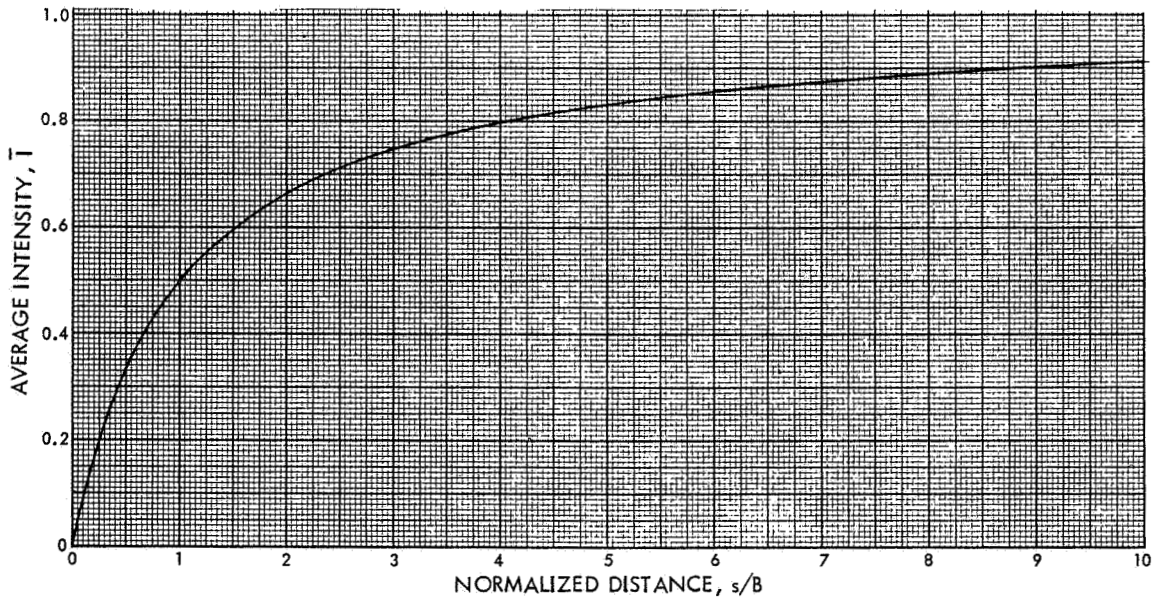


Fig. 9.5-8. Average Light Intensity, \bar{I} , in a Shadow from a Long Object Parallel to the Shadow Plane as a Function of Normalized Distance, s/B

Consequently, the total amount of light intensity loss in any shadow is equivalent to the light intensity loss by an umbra-type shadow which has the same width as the object (for parallel rays of light) and has no penumbra.

9.5.3 Application to Solar Cell Array

For series parallel-connected solar cells subjected to a shadow not exceeding in width the dimension of the parallel connected cells, as shown in Figure 9.5-9, an equivalent total umbra shadow of a width corresponding to a projection of the object can be used to determine the electrical output reduction due to the shadow under consideration.

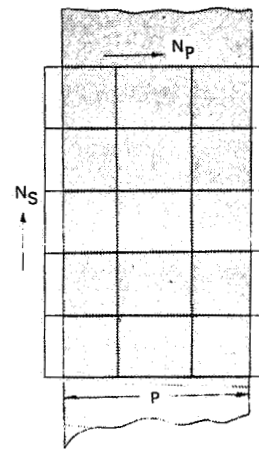


Fig. 9.5-9. Example of Shadow Across a Solar Cell Module Consisting of Series-Parallel Connected Cells

Penumbra Intensity Distribution

In the calculations used to determine the illumination intensity distribution, the segment area of a circle as a function of the segment height must be known. This relationship is shown in Figure 9.5-10.

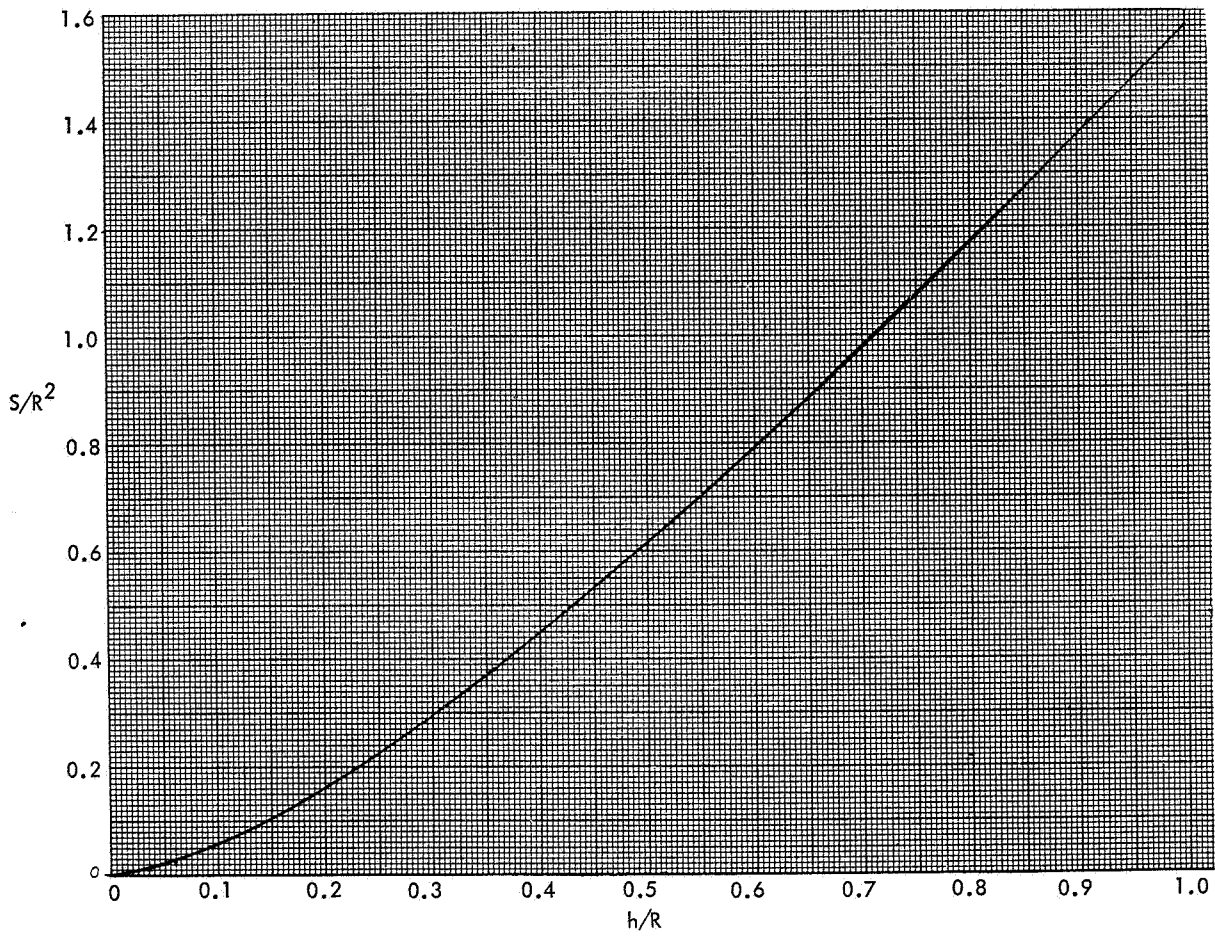


Fig. 9.5-10. Normalized Segment Area, S/R^2 , as a Function of Normalized Segment Height, h/R

9.6 THERMAL ANALYSIS

A thermal analysis of a solar cell array results primarily in predictions of the solar cell operating temperature during periods of illumination and in predictions of the lowest temperatures reached during periods of solar eclipses. Secondary results from a thermal analysis may include solar cell hot spots (defined in Section 9.1.6) and thermal effects on mechanical elements (hinges, etc.). In this section, only the predictions of solar cell operating temperature and array eclipses exit temperature are discussed.

The solar cell operating temperature strongly affects the array output capability and, therefore, must be calculated carefully considering:

- Degraded values of the solar absorptance, α_S , and hemispherical emittance, ϵ_H , of the solar cell stacks and the uncovered substrate front and back sides
- Solar distance (array-sun distance)
- Nonsolar heat inputs to the array
- Array geometry
- Array orientation
- Operating efficiency of the solar cells (not maximum efficiency).

The eclipse exit temperature (together with the number of eclipses) is required to assess the solar cell interconnector fatigue life, solar cell electrical degradation due to temperature cycling, and probabilistic assessments of open-circuit failures of cells, interconnector loops, joints, and blocking diodes (see Reliability Analysis, Section 9.9).

9.6.1 Definitions

The following terminology is commonly used in thermal and heat transfer analyses.

Heat transfer in space occurs by radiation and conduction of heat energy. Conduction occurs only within spacecraft and solar cell array components and materials. Energy exchange by radiation occurs primarily between the spacecraft/solar cell array and the sun, and between the spacecraft/array assembly and space, and secondarily between different elements of the spacecraft/array assembly.

The four material properties of concern in radiation heat transfer are the absorptance or absorptivity, α , the reflectance or reflectivity, ρ , the transmittance or transmissivity, τ , and the emittance or emissivity, ϵ . The material property of concern in heat conduction is the thermal conductivity, k . The material properties of concern in transient thermal analysis are the thermal conductivity, k , the mass, m , and the specific heat capacitance (at constant pressure), c_p . In general, all of these material properties are

functions of temperature, their values tending toward zero as the absolute temperature approaches zero.

The absorptance, α , is the ratio of the energy absorbed by a material to the energy incident on the surface of this material. The spectral absorptance, α_λ , is the absorptance at a specific wavelength, λ . The solar absorptance, α_S , is the spectral absorptance integrated over the solar spectrum

$$\alpha_S = \int_0^{\infty} S(\lambda)\alpha_\lambda d\lambda \quad (9.6-1)$$

where $S(\lambda)$ is the solar spectrum (see Section 2.4.2). For surfaces composed of different materials (such as a solar cell array), an average or mean solar absorptance, $\bar{\alpha}_S$, can be defined such that

$$\bar{\alpha}_S = \frac{\sum_{i=1}^m \alpha_{Si} A_i}{\sum_{i=1}^m A_i} \quad (9.6-2)$$

where

m = number of different surface materials

α_{Si} = solar absorptance of the i -th material

A_i = area of the i -th material having α_{Si} .

An effective solar absorptance, $\bar{\alpha}_{Se}$, which includes the effect of electrical energy flowing from the solar cells and thereby reducing the heating of the cells, can be defined as follows:

$$\bar{\alpha}_{Se} = \bar{\alpha}_S - F_p \eta_{op} \quad (9.6-3)$$

where

F_p = packing factor, defined as the ratio of the total active solar cell area to the total substrate area for which $\bar{\alpha}_{Se}$ is to be determined

η_{op} = solar cell operating efficiency (defined in Section 3.2.5).

The reflectance, ρ , is defined as the ratio of the energy reflected from the surface of a material to the energy incident upon the surface of that material. The spectral reflectance, ρ_λ , is the reflectance at a specific wavelength, λ .

The transmittance, τ , is defined as the ratio of energy inside a transparent material at the exit surface to the energy at the entrance surface (excluding the front surface reflectance). Frequently, the total transmittance, τ_t , is defined as the ratio of the energy emanating from a transparent material to the energy incident on the front surface of that material (including both front surface and back surface reflectance). The spectral transmittance, τ_λ , is the reflectance at a specific wavelength, λ .

The emittance, ϵ , is defined as the ratio of the total emissive power of a (gray) surface to the total emissive power of a black surface at the same temperature. The total emissive power is the total radiant energy emitted (ejected) at a given temperature per unit time and per unit area of a surface. A black surface is the (hypothetical) surface of a (hypothetical) black body having the characteristic of absorbing all radiant energy striking it and reflecting or transmitting none of it (i.e., $\rho = \tau = 0$ and $\alpha = \epsilon = 1$). The monochromatic or spectral emittance, ϵ_λ , is the emittance at a specific wavelength, λ . The directional emittance, ϵ_D , is the emittance measured in a direction vector that makes an angle ϕ to the normal of the surface. The normal emittance, ϵ_N , is the directional emittance measured perpendicular to the emitting surface. The hemispherical emittance, ϵ_H , is the normal emittance integrated over 2π steradians (for experimental relationships between ϵ_N and ϵ_H see Section 11.6.2). For a surface composed of several different materials, an average, or mean, or effective hemispherical emittance, $\bar{\epsilon}_H$, can be defined such that

$$\bar{\epsilon}_H = \frac{\sum_{i=1}^n \epsilon_{Hi} A_i}{\sum_{i=1}^n A_i} \quad (9.6-4)$$

where

- n = number of different surface materials
- ϵ_{Hi} = hemispherical emittance of the i -th material
- A_i = area of the i -th material having ϵ_{Hi} .

Radiant energy incident upon a surface may either be absorbed, reflected, or transmitted. By the principle of conservation of energy, at any instant of time and at a given temperature:

$$\alpha + \rho + \tau = 1 \quad (9.6-5)$$

$$\alpha_\lambda + \rho_\lambda + \tau_\lambda = 1$$

For opaque surfaces $\tau = 0$ so that

$$\alpha + \rho = 1$$

$$\alpha_\lambda + \rho_\lambda = 1 \quad (9.6-6)$$

$$\epsilon = \alpha = 1 - \rho$$

$$\epsilon_\lambda = \alpha_\lambda = 1 - \rho_\lambda$$

The conditions $\epsilon = \alpha$ and $\epsilon_\lambda = \alpha_\lambda$ are defined by Kirchhoff's law which states that at a given temperature the total emissive power for any (gray) surface is equal to its absorptance multiplied by the total emissive power of a black surface at that temperature. However, it should be noted that

$$\alpha_S \neq \epsilon, \quad \alpha_S \neq \epsilon_D, \quad \alpha_S \neq \epsilon_N, \quad \alpha_S \neq \epsilon_H, \quad \bar{\alpha}_S \neq \bar{\epsilon}_H \text{ and } \bar{\alpha}_{Se} \neq \bar{\epsilon}_H$$

The energy, q , emitted by a gray surface is given by Stefan-Boltzmann's law:

$$q = \epsilon \sigma A T^4 \quad (9.6-7)$$

where

- ϵ = emissivity at temperature T
- σ = Stefan-Boltzmann's constant
- A = emitting area
- T = absolute temperature.

The governing physical principle in the solution of any heat transfer problem is the conservation of energy. For any (hypothetical) volume fully enclosed by a (hypothetical) surface:

$$\sum q_{in} + \sum q_{out} + \sum q_{stored} = 0 \quad (9.6-8)$$

where q_{in} and q_{out} are the rates of energy flow per unit time and per unit area through the surface, and q_{stored} is the energy stored inside the volume per unit time (stored energy is discussed in Section 9.6.5 in connection with thermal transients).

9.6.2 Heat Transfer by Radiation

Any surface with area, A , having an average hemispherical emittance, $\bar{\epsilon}_H$, and being at an absolute temperature, T , emits heat energy at a rate given by Eq. 9.6-7. The net rate of energy flow between two different, geometrically neighboring surfaces at different temperatures, T_1 and T_2 , is given by

$$q_{net} = A_1 \mathcal{F}_{12} \sigma (T_1^4 - T_2^4) = A_2 \mathcal{F}_{21} \sigma (T_1^4 - T_2^4) \quad (9.6-9)$$

where \mathcal{F} is a geometric factor (sometimes also known as view factor) defined by

$$\mathcal{F}_{12} = \frac{\text{energy intercepted by } A_2}{\text{energy emitted by } A_1} \quad (9.6-10)$$

$$\mathcal{F}_{21} = \frac{\text{energy intercepted by } A_1}{\text{energy emitted by } A_2}$$

and the subscripts 1 and 2 refer to the first and second surface, respectively. All other symbols are as defined above.

The geometric factor, \mathcal{F} , varies between zero and unity. In practice, \mathcal{F} is determined with an optical instrument consisting of a polished, convex parabolic mirror. The mirror is subdivided into graduations that are calibrated in fractions of F where $F = \mathcal{F}$ when $\epsilon = 1$. That is, \mathcal{F} includes effects of emissivity while F is a purely geometric factor. Alternately, F may be computed (for $\epsilon = 1$) from

$$F_{12} = \frac{1}{A_1} \frac{1}{\pi} \int_{A_1} \int_{A_2} \frac{\cos \theta_1 \cos \theta_2}{s^2} dA_1 dA_2 \quad (9.6-11)$$

where the symbols are defined in Figure 9.6-1.

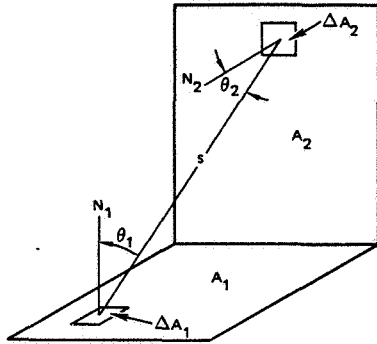


Fig. 9.6-1. Heat Exchange by Radiation Between Two Small Black Surface Elements

9.6.3 Heat Transfer by Conduction

The rate of energy, $q = dQ/dt$, flowing in a thermally conducting medium due to a temperature gradient dT/dx across this medium is given by

$$q = -kA \frac{dT}{dx} \quad (9.6-12)$$

where

- k = thermal conductivity
- A = cross-sectional area of conducting medium

and the minus sign indicates positive heat flow in the positive x -direction in response to a negative temperature gradient, dT/dx (i. e., decreasing temperature with increasing x).

If the conducting medium is homogeneous and is of constant cross-sectional area,

$$\frac{dT}{dx} = \frac{T_H - T_L}{s} \quad (9.6-13)$$

where T_H and T_L are the high and low temperatures, respectively, separated by distance s .

For heat flow through a sandwich of different materials, the same quantity of heat, q , flows through each layer of the sandwich and results in temperature gradients, $\Delta T/\Delta d$, across each layer of thickness d , whose magnitudes are inversely proportional to the thermal conductivity of the layers.

9.6.4 Estimating Operating Temperatures

Solar cell operating temperatures may be estimated by making the following assumptions:

- The temperature gradient throughout the solar cell stack and the substrate thickness is zero (i. e., the array is isothermal).
- There are no thermal interactions between the solar cell array and other structural elements or heat sources of the spacecraft.
- The earth radiation and albedo energy inputs to the array are negligible.

For this simplified case the heat balance equation per unit area is:

$$q_{in} - q_{electrical} = q_{out} \quad (9.6-14)$$

$$\bar{\alpha}_{Se} S \cos \Gamma = (\bar{\epsilon}_{HF} + \epsilon_{HB}) \sigma T^4 \quad (9.6-15)$$

where

$\bar{\alpha}_{Se}$ = effective solar absorptance per Eq. 9.6-3

S = value of the solar constant (Section 2.4.2)

Γ = the angle between the solar cell array normal and the array-sun line (see Section 9.4.4)

$\bar{\epsilon}_{HF}$ = effective hemispherical front side emittance per Eq. 9.6-4

ϵ_{HB} = hemispherical back side emittance

σ = Stefan-Boltzmann constant (Section 7.2, Vol. II)

T = absolute temperature.

Eq. 9.6-15 reduces to the following with the solar cell operating temperature, T_{op} , replacing T :

$$T_{op} = \left(\frac{\bar{\alpha}_{Se} S \cos \Gamma}{\bar{\epsilon}_{HF} + \epsilon_{HB} \sigma} \right)^{1/4} \quad (9.6-16)$$

9.6.5 Estimating Eclipse Exit Temperatures

Solar cell array eclipse exit temperatures may be estimated by making the following assumptions:

- The temperature gradient throughout the solar cell stack and the substrate thickness is zero (i. e., the array is isothermal).
- There are no thermal interactions between the solar cell array and other structural elements or heat sources of the spacecraft.
- The emitting array surface areas on the front and back side are equal.
- The earth radiation and albedo energy inputs to the array are negligible.
- The eclipse is an instantaneous absence of solar illumination (i. e., no penumbra shadow).

For this simplified case the heat balance equation per unit area is:

$$q_{out} + q_{stored} = 0 \quad (9.6-17)$$

$$(\bar{\epsilon}_{HF} + \epsilon_{HB})\sigma T^4 + (\bar{m} \bar{c}_p) \frac{dT}{dt} = 0 \quad (9.6-18)$$

Eq. 9.6-18 can be restated as

$$aT^4 = -b \frac{dT}{dt} \quad (9.6-19)$$

where

$$a = (\bar{\epsilon}_{HF} + \epsilon_{HB})\sigma \quad \text{and} \quad b = (\bar{m} \bar{c}_p) \quad (9.6-20)$$

and the equivalent thermal mass, $\bar{m} \bar{c}_p$, is defined as

$$\bar{m} \bar{c}_p = \sum_{i=1}^n m_i c_{pi} \quad (9.6-21)$$

where m_i is the i -th mass (per unit array area) and c_{pi} is the i -th specific heat capacitance of the n different materials found in that unit area of array. The other symbols are defined in Section 9.6.1.

Eq. 9.6-19 can be restated as

$$-\frac{a}{b} \int_0^{t_e} dt = \int_{T_{op}}^{T_e} T^{-4} dT \quad (9.6-22)$$

where the limits of integration for time, t , are from the start of the eclipse ($t_e = 0$) to t_e , and the limits for temperature, T , are from the operating temperature, T_{op} , to the eclipse temperature, T_e , which is reached at time t_e . The operating temperature, T_{op} , is the array or solar cell temperature according to Eq. 9.6-16 just prior to entering the eclipse. When t_e is equal to the eclipse duration, T_e is the eclipse exit temperature.

Integrating both sides of Eq. 9.6-22 gives

$$-\frac{a}{b} t_e = -\frac{1}{3} (T_e^{-3} - T_{op}^{-3})$$

or

$$T_e(t_e) = T_{op} \left(1 + \frac{3a}{b} T_{op}^3 t_e \right)^{-1/3} \quad (9.6-23)$$

Substituting Eq. 9.6-20 back into Eq. 9.6-23 gives

$$T_e(t_e) = T_{op} \left(1 + \frac{3(\bar{\epsilon}_{HF} + \epsilon_{HB})\sigma T_{op}^3}{\bar{m} \bar{c}_p} t_e \right)^{-1/3} \quad (9.6-24)$$

For most practical cases, the emittance, ϵ , and specific heat capacitance, c_p , are functions of

temperature. As a first order approximation, both ϵ and c_p may be assumed to be linear functions of absolute temperature; i. e., $\epsilon_T = ET$ and $c_{pT} = CT$. Inclusion of ϵ_T and c_{pT} in Eq. 9.6-17 leads to the following three cases. Their applicability should be judged from the value of the expected T_{op} and the decrease of ϵ and c_p with decreasing temperature as shown in Sections 7.12 and 7.14 of Volume II.

Emittance Being a Function of Temperature

The heat balance equation becomes

$$(E_F + E_B)\sigma T^5 + (\bar{m} \bar{c}_p) \frac{dT}{dt} = 0 \quad (9.6-25)$$

which has the solution

$$T_e(t_e) = T_{op} \left(1 + \frac{4(E_F + E_B)\sigma T_{op}^4}{\bar{m} \bar{c}_p} t_e \right)^{-1/4} \quad (9.6-26)$$

Specific Heat Capacitance Being a Function of Temperature

The heat balance equation becomes

$$(\bar{\epsilon}_{HF} + \epsilon_{HB})\sigma T^3 + C\bar{m} \frac{dT}{dt} = 0 \quad (9.6-27)$$

which has the solution

$$T_e(t_e) = T_{op} \left(1 + \frac{2(\bar{\epsilon}_{HF} + \epsilon_{HB})\sigma T_{op}^2}{C\bar{m}} t_e \right)^{-1/2} \quad (9.6-28)$$

Both Emittance and Specific Heat Capacitance Being Functions of Temperature

This case is identical to that of Eq. 9.6-24 where both emittance and specific heat capacitance are invariant with temperature. Hence, for most applications Eq. 9.6-24 can be expected to yield the most realistic eclipse temperatures. (The different results obtained from Eqs. 9.6-24, 9.6-26, and 9.6-28 are illustrated in Chapter 12.)

9.6.6 Electrical-Heat Transfer Analogy

The flow of heat in a thermal field is phenomenologically identical to the flow of electric current in an electric field. Therefore, electrical networks can be used in the analysis of heat transfer problems. Electrical characteristics that are analogous to thermal characteristics are shown in Table 9.6-1. Solutions to electrical network problems are discussed in Section 9.1.

The requirements for an electrical network to analogously represent a thermal heat flow problem are:

- The governing electrical and thermal differential equations or integro-differential equations must be similar.

- The boundary conditions used for solving the equations must be similar.

The electrical analogs for the elements of significance to solar cell array thermal analysis are as shown below; their use is illustrated in Sections 9.6.7 and 9.6.8, and in Chapter 12.

Table 9.6-1. Analogous Quantities

Electrical		Thermal	
Parameter	Unit	Parameter	Unit
Charge, Q	coulomb	Heat energy, Q	watt second
Current, I	ampere	Heat flow rate, q	watt
Potential, V	volt	Temperature, T	kelvin
Resistance, R	ohm	Resistance*	kelvin/watt
Conductivity, k	per (ohm meter)	Conductivity, k	watt/(meter·°K)
Capacitance, C	coulomb/volt	Heat capacitance, mc _p	watt·sec/°K

*Note: See discussion in text.

Conductive Heat Transfer

For a steady-state heat flow, q_{1-2} , from point "1" to point "2" in a homogeneous bar of constant cross-sectional area, A; and length, L, between the two points is

$$q_{1-2} = \frac{kA}{L} (T_1 - T_2) \quad (9.6-29)$$

where

k = thermal conductivity

T₁ = higher temperature

T₂ = lower temperature.

The electrical analog is

$$I_{1-2} = \frac{1}{R_c} (V_1 - V_2) \quad (9.6-30)$$

where

I = current flow from point "1" to point "2"

R_c = resistance

V₁ = higher potential

V₂ = lower potential.

Radiative Heating

For a radiation heat flow, q_s , striking the solar array from a radiation source, the amount of energy flowing into the array is

$$q_{in} = q_s (1 - \rho) \quad (9.6-31)$$

where ρ is the reflectivity (see Section 9.6.1).

The electrical analog is a current source of strength

$$I_{in} = I_s (1 - \rho) \quad (9.6-32)$$

where ρ is still the reflectivity.

Radiative Cooling

For radiation emitted from a surface, the heat flow for steady-state and transient conditions is given by Eqs. 9.6-17 and 9.6-18. The corresponding solution is given by Eq. 9.6-24. The electrical analogs are

$$\frac{1}{R_r} V^4 + C \frac{dV}{dt} = 0 \quad (9.6-33)$$

and

$$V_e(t_e) = V_{op} \left(1 + \frac{3V_{op}^3}{R_r C} t_e \right)^{-1/3} \quad (9.6-34)$$

where the subscripts are as defined for Eq. 9.6-24.

9.6.7 Body-Mounted Cylindrical Arrays

A typical body-mounted cylindrical solar array is shown in Figure 9.6-2a. This configuration requires that the spacecraft be in a spinning mode in order to expose all portions of the array to the sun. For current typical array masses of about 5 kg/m² (1 lb/ft²) or less, uniform temperatures (no cyclic variations due to spinning) result at the rotational speeds of about 1 r/min and higher (typically in excess of 30 r/min used in actual orbiting spacecraft of this type). This fact considerably simplifies the calculations of absorbed solar energy, albedo, and planetary radiation.

Considering the substrate (typically fiberglass honeycomb) and the solar cells as one homogeneous mass, the energy balance equation for the solar cell array is as follows:

$$\overline{m c}_p \frac{dT}{dt} = \frac{1}{\pi} \bar{\alpha}_e SA \cos \theta + q_{pl} + q_{al} + q_{el} - \sigma \epsilon_H AT^4 \quad (9.6-35)$$

where

$\overline{m c}_p$ = thermal mass defined by Eq. 9.6-21

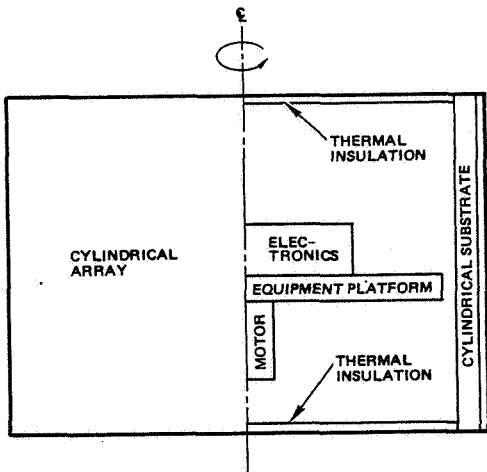
T = absolute temperature

t = time

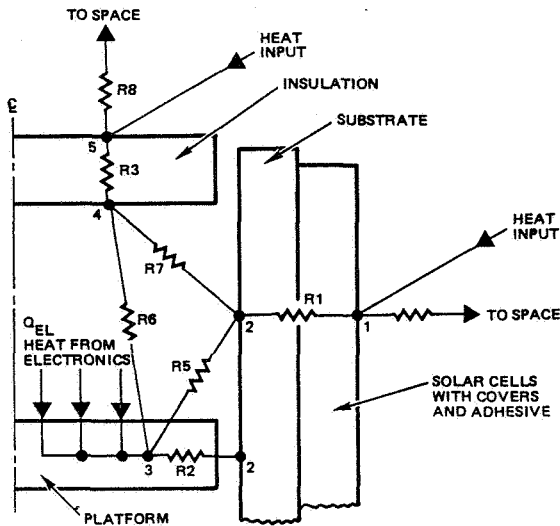
$\bar{\alpha}_e$ = effective solar absorptance (see Eq. 9.6-38)

S = solar constant

A = total surface area



(a) SCHEMATIC OF TYPICAL CYLINDRICAL ARRAY ON SPINNING SATELLITE



(b) THERMAL NETWORK (SIMPLIFIED)

Fig. 9.6-2. Typical Cylindrical Solar Cell Array

- θ = angle between sun vector and the normal to the spin axis
- q_{pl} = planetary radiation
- q_{al} = albedo
- q_{el} = electrical energy radiated from load equipment through the array to space
- σ = Stefan-Boltzmann's constant
- $\bar{\epsilon}_H$ = effective hemispherical emittance defined by Eq. 9.6-4

In this equation the solar constant (due to eclipses), angle θ , and any of the heat flows, q , may be functions of time, t , while the specific heat, c_p , and emittance, ϵ , are functions of temperature. However, unless extreme accuracy is desired constant values of c_p and ϵ may be used for most practical applications. Likewise, the solar absorptance is angle-of-incidence dependent and decreases sharply for solar angles-of-incidence greater than 70 degrees (see Section 2.4.5). Also the effective absorptance is a function of the solar cell operating conversion efficiency, as defined in Section 9.6.1.

Another effective solar absorptance per unit area, denoted by $\bar{\alpha}_e$, can be derived from the following considerations: for normal sun and negligible planetary radiation and albedo:

$$\text{Energy In} = \alpha_c A_c S + (1 - A_c)S \quad (9.6-36)$$

$$\text{Energy Out} = \epsilon_c A_c \sigma T^4 + (1 - A_c)\sigma T^4 + \eta_{op} SA_c \quad (9.6-37)$$

where

α_c = solar cell solar absorptance

A_c = solar cell area

$1 - A_c$ = area of voids between cells with solar absorptance and emittance equal to unity.

ϵ_c = solar cell hemispherical emittance

η_{op} = solar cell operating conversion efficiency (see Section 4.2) ($\eta_{op} SA_c$ = array electrical output)

Noting that for a unit of array area the solar cell area is the same as the packing factor, F_p (defined in Section 9.6.1), the effective absorptance $\bar{\alpha}_e$ can be shown to be as follows (for the gap areas to have $\alpha = \epsilon = 1$):

$$\bar{\alpha}_e = \alpha_c + \frac{1 - F_p(1 + \eta_{op})}{F_p} \quad (9.6-38)$$

The solar cell operating efficiency is mainly a function of the electrical load, as discussed in Section 3.2.5.

The other parameters in Eq. 9.6-35 which merit special consideration are the angle θ , the planetary radiation and the albedo. In general, these parameters will vary as a function of spacecraft position in the orbit or, in other words, as a function of time. It is usual practice to use an orbital heating computer program to calculate these external forms of heating as a function of time for the specific orbits of interest. For high altitude orbits, such as synchronous equatorial orbits, the planetary radiation and albedo are usually negligible and can be disregarded in most cases.

Typical values of synchronous orbital heating to an earth pointing rotating cylindrical spacecraft are shown in Table 9.6-2.

Table 9.6-2. Incident Heating of a Rotating Cylinder in a Synchronous Equatorial Orbit During Equinox

Heat Source	Range of Values During Orbit*
• Solar	0 to 444 W·m ⁻²
• Albedo	0 to 3 W·m ⁻²
• Earth radiation	0.2 W·m ⁻² (essentially constant during orbit)

*Depending upon solar orientation angle.

Eq. 9.6-35 can be simplified when the rate of change of the sun angle θ is small compared to the thermal response of the solar arrays. This occurs, for example, in synchronous equatorial orbits for earth pointing spacecraft with solar arrays sharing less than about 5 kg/m² mass. For such cases Eq. 9.6-35 simplifies to

$$\frac{1}{\pi} \bar{\alpha} SA \cos \theta + q_{e1} = \sigma \epsilon AT^4 \quad (9.6-36)$$

which can be used for hand calculations of cylindrical solar array temperatures at any seasonal angle θ in orbit.

To predict array temperatures with a higher accuracy than Eq. 9.6-36 permits, development of a thermal network of the array is required. It is presumed that a suitable computer program which solves the thermal nodal network equations is available.

A thermal network is developed by dividing the array and its environment into nodes. Each node is assigned an area, weight (mass), and specific heat. All nodes are then interconnected with adjacent nodes and to the surrounding thermal environment, as illustrated in Figure 9.6-2b. From such a network, the appropriate thermal parameters are calculated and input in a specific format for computer solution. The computer solves a system of simultaneous energy balance equations for each node. Both transient and steady-state solutions are possible (see Section 9.6.9).

The format for a typical thermal analyzer computer program is as follows:

Energy Balance on Node 1 (Figure 9.6-2b)

$$\bar{m} \bar{c}_p \frac{\Delta T_1}{\Delta t} = q_{\text{orbital}} - \frac{1}{R_1} (T_1 - T_2) - R_4 (T_1 - T_{\text{space}})$$

The terms not previously defined are as follows:

Δt = calculation time increment specified by the program to provide stability for the finite difference solution of the differential equation

R_1 = conduction resistance defined as x/kA or $1/h_c A_c$ (see Section 9.6.6)

x = heat conduction path length between nodes i, j

k = thermal conductivity of path between nodes i, j

A = conduction area of path between nodes i, j

h_c = contact conductance between surfaces i, j

A_c = contact area between nodes i, j

R_R = radiation resistance defined as:

$$R_R = \epsilon_i \epsilon_j F_{i-j} A_i (T_i + T_j) (T_i^2 + T_j^2)$$

where

$\epsilon_{i,j}$ = emittance nodes i, j

F_{i-j} = view factor node i to j

A_i = radiating area of node i

The approximation $\epsilon_i \epsilon_j F_{i-j}$ is suitable for the high emittance surfaces normally encountered in practice. For low emittance surfaces, a separate computer program should be used to determine the view factor (Section 9.6.1) which accounts for multiple reflections. For the example shown, the orbital heating term (q_{orbital}) would be input as a table representing the timewise variations of the various forms of orbital heating.

For simplicity, the example selected is a case where no circumferential temperature gradient exists in the solar array. Where such gradients are expected, for example due to a high-powered electronic component in close proximity to the array, it is necessary to model the local area as one or more nodes. The nodes are then connected to the surrounding array by the appropriate conduction paths.

9.7.8 Panel and Paddle Arrays

Paddle solar cell arrays consist basically of a flat structural surface (substrate) covered with solar cells. For thermal analyses purposes, paddle arrays are classified as being either one- or two-sided, depending on whether one or both sides are covered with solar cells.

One-sided arrays are maintained nominally normal to the solar vector throughout the orbit, either by a mechanical drive or by the characteristics of the spacecraft attitude control system.

Two-sided paddle arrays may be used when the spacecraft configuration, attitude control, and/or orbital characteristics are such that the solar vector effectively revolves around the paddles and illuminates both sides of the paddles at certain times during the orbit. These arrays are usually fixed relative to the spacecraft. The two types of arrays are schematically illustrated in Figure 9.6-3a and b.

For portions of one-sided paddle arrays which are not in radiation exchange with parts of the spacecraft structure, the following general equation applies:

$$\bar{m} \bar{c}_p \frac{dT}{dt} = \bar{\alpha} SA \cos \Gamma + q_{P1} + q_{A1} - \sigma T^4 (\epsilon_H A + \epsilon_B A_B) \quad (9.6-37)$$

Terms not previously defined are A_B which is the paddle backside surface area (nonilluminated) and $\bar{\epsilon}_B$, the hemispherical emittance of the surface. The term S (solar constant) represents the solar illumination and could either be a constant or a function of time (position in orbit), for example, to account for eclipses and/or shadowing of the array by spacecraft elements such as an antenna. The angle Γ is defined in Section 9.4.4 for various solar cell array configurations.

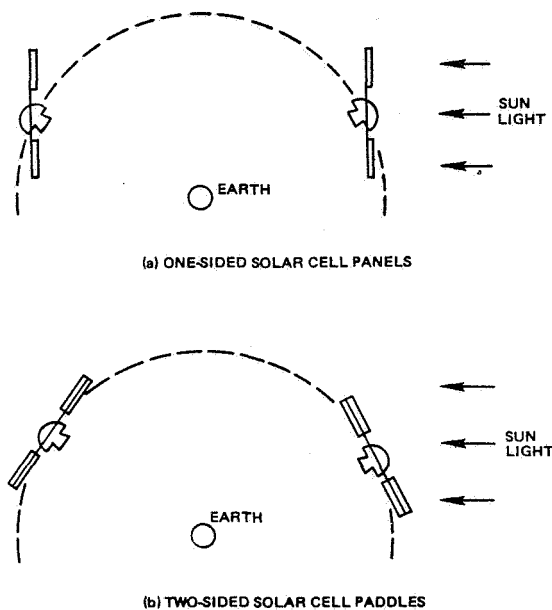


Fig. 9.6-3. Typical Flat Solar Cell Arrays

Assuming continuous solar illumination, no shadowing of the arrays by the spacecraft and negligible planetary radiation and albedo, Eq. 9.6-38 can be used in the following form for preliminary temperature estimates:

$$\sigma T^4 (\bar{\epsilon}_H A + \bar{\epsilon}_B A_B) = \bar{\alpha} S A \cos \Gamma \quad (9.6-38)$$

It is usual practice to make the backside surface a high emitter ($\bar{\epsilon}_B \geq 0.8$), by use of an appropriate thermal control coating in order to reduce the array operating temperature.

To account for radiative heat exchange with adjacent spacecraft surfaces, the last term in Eq. 9.6-37 [$\sigma T^4 (\bar{\epsilon}_H A + \bar{\epsilon}_B A_B)$] is replaced by the following terms:

$$\begin{aligned} & \sigma \epsilon_s F_s A T^4 + \sigma \epsilon_B F_{B-s} A_B T^4 + \sigma \epsilon_1 F_1 A (T^4 - T_1^4) \\ & + \sigma \epsilon_B \epsilon_2 F_{B-2} A_B (T^4 - T_2^4) \end{aligned}$$

where

F_s = view factor of illuminated surface to space

F_{B-s} = view factor of nonilluminated surface to space

ϵ_1 = hemispherical emittance of spacecraft surface 1

F_1 = view factor of solar cells to spacecraft surface 1

T_1 = temperature of spacecraft surface 1

ϵ_2 , } same as above for spacecraft surface 2
 F_{B-2} , } "seen" by the nonilluminated array surface
 A_B

The equation for two-sided paddle arrays is similar to Eq. 9.6-37 except for the following considerations. The backside emittance (ϵ_B) is the same as the front side emittance (ϵ). The angle Γ will be a function of time (or position in the orbit) because the paddle arrays are not mechanically maintained nominally normal to the solar vector.

The procedure and principles for developing a paddle array computer thermal network are the same as discussed in Section 9.6.6. However, unlike the cylindrical arrays which are normally not influenced by the adjacent spacecraft structure or component, portions of the paddle arrays usually will be. To account for this effect, the paddle arrays are usually modelled in sections, as illustrated in Figure 9.6-4.

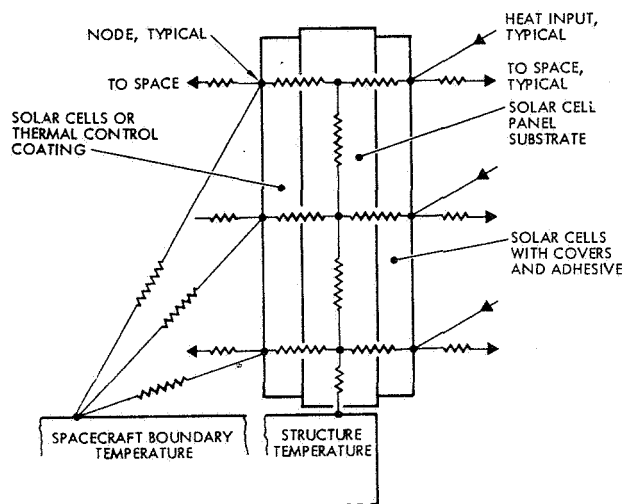


Fig. 9.6-4. Thermal Network for Solar Cell Panel

9.6.9 Computer Programs

The electrical analogs of heat transfer discussed in Section 9.6.6 were "discovered" in the late 1930's, but did not find widespread use until analog computers for solutions of the network equations became available in the early 1950's. During the 1960's the use of digital computers almost completely displaced the use of analog computers. Many digital computer programs have been developed, as illustrated by the following list.

- J.J. Brisbane, "Volume I, Heat Conduction and Stress Analysis of Anisotropic Bodies," Rohm and Haas Co., Redstone Research Laboratories, Huntsville, Alabama, October 1969.

- J. Chateau, "General N-Dimensional Heat Transfer," General Electric Co., Huntsville Operation, July 1966.
- A. L. Edwards, "TRUMP: A Computer Program for Transient and Steady State Temperature Distributions in Multidimensional Systems," UCRL-14754, Rev. I, TID-4500, UC-32, Lawrence Radiation Laboratory, May 1968.
- A. F. Emery and W. W. Carson, "An Evaluation of the Use of the Finite - Element Method in the Computation of Temperature," ASME - Journal of Heat Transfer, pp 136-145, May 1971.
- J. L. Fick, "MLFTHAN-LMSC Thermal Network Analyzer, ZO MLFTHAN," Lockheed Missiles and Space Company, January 1969.
- J. D. Gaski, L. C. Fink, and T. Ishimoto, "Systems Improved Numerical Differencing Analyzer, Users Manual," 11027-6003-R0-00, TRW Systems Group, September 1970.
- J. D. Gaski and D. R. Lewis, "Chrysler Improved Numerical Differencing Analyzer," TN-AP-66-15, Chrysler Corporation Space Division, New Orleans, Louisiana, April 1966.
- L. D. Kovach, "Characteristics and Operation of the Thermal Analyzer," Report No. SM-38577, Douglas Aircraft Co., April 1961.
- H. P. Lee, "Application of Finite - Element Method in the Computation of Temperature with Emphasis on Radiative Exchanges," AIAA 7th Thermophysics Conference, San Antonio, Texas, April 10-12, 1972.
- H. P. Lee and J. B. Mason, "NASTRAN Thermal Analyzer, A General Purpose Finite - Element Heat Transfer Computer Program," NASA Goddard Space Flight Center, 1972.
- D. R. Lewis, J. D. Gaski, and L. R. Thompson, "Chrysler Improved Numerical Differencing Analyzer for 3rd Generation Computers," TN-AP-67-287, Chrysler Corporation Space Division, New Orleans, Louisiana, October 1967.
- P. D. Richardson and Y. M. Shum, "Use of Finite Element Methods in Solution of Transmit Heat Conduction Problems," ASME Paper 69-WA/HT 36, Winter Annual Meeting, Los Angeles, California, November 16-20.
- J. P. Smith, "SINDA User's Manual," 14690-H001-R0-00, TRW Systems Group, April 1971.
- L. W. Spradley, "Finite-Element Thermal Analysis Computer Program," LMSC/HREC D162592, Lockheed Missiles and Space Co., Huntsville, Alabama, October 1970.
- TRW Thermal Analyzer Program (TAP) User's Manual,
 - Part I. Analytical Development, T. Ishimoto, Report No. 66-3331.6-5, April 1966.
 - Part II. Program Description, CDRC Heat Transfer Group, Report No. 3123-23-31, May 1967.
- E. L. Wilson and R. E. Nickell, "Application of the Finite Element Method to Heat Conduction Analysis," Nuclear Engineering and Design, Vol. 4, pp 276-284, 1961.
- F. Yee, "Users Manual, Nonsteady Temperature Analysis of a Two-Dimensional Body by the Finite Element Method," Program E12202, Aerojet Nuclear Systems Company, Sacramento, California, February 1970.

9.7 THERMOMECHANICAL STRESS ANALYSIS

Thermally induced, mechanical stress occurs in most solar cell arrays. Severe stresses typically arise from materials that are in intimate contact but have different coefficients of linear thermal expansion when exposed to high or low temperatures. Typical examples of material combinations leading to high thermally induced stress are:

- Metallic coatings (solder, silver, etc.) on silicon solar cells or on low-expansion metals (Kovar, Invar, molybdenum, etc.)
- Soldered or welded joints between interconnectors and solar cells
- Adhesive bond lines between covers and solar cells, and between solar cells and the substrate.

For many solar cell array applications, the thermally induced mechanical stresses exceed the linear elastic limits of at least several array materials. Thus solar cell array stress analysis, in general, must include both the elastic and the plastic properties of materials as discussed in this section.

Some typical effects of low temperature and temperature cycling on solar cell assemblies are illustrated in Section 5.2.2. The sources of thermomechanically induced stresses in both solar cell interconnectors and in soldered and welded joints, as well as design practices to minimize these stresses, are treated in Section 5.3. The analytical tools to mathematically model the solar cell stack and interconnector systems and to compute thermally induced stresses are presented in the following.

9.7.1 Mechanical Behavior of Materials

Uniaxial Loading

Consider a bar (shown in Figure 9.7-1) of initial cross-sectional area, A_0 , and length, L_0 , which is subjected to axial tensile load, P . The stress, σ , in the bar is equal to the intensity of the loading

$$\sigma_a = \frac{P}{A_0} \quad (9.7-1)$$

where the subscript a denotes that the load is applied axially.

As the load, P , (and thereby the stress, σ) is increased, the length, L , of the bar increases. For small changes in length, this is measured by the axial strain

$$\epsilon_a = \frac{L - L_0}{L_0} = \frac{\Delta L}{L_0} \quad (9.7-2)$$

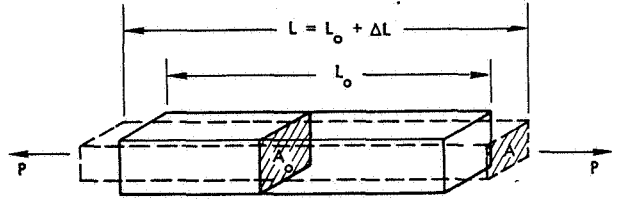


Fig. 9.7-1. Bar Loaded Axially in Tension

For most materials and for relatively small values of strain, the strain is a linear function of the stress. The ratio between the stress and the strain is known as the elastic (or Young's) modulus, E :

$$E = \frac{\sigma_a}{\epsilon_a} \quad (9.7-3)$$

As the bar is stretched axially it contracts in both lateral directions. The ratio of the lateral strain, ϵ_L , to the axial strain, ϵ_a , is known as Poisson's ratio ν (or μ). For a laterally unrestrained bar

$$\nu = -\frac{\epsilon_L}{\epsilon_a} \quad (9.7-4)$$

and the axial strain

$$\epsilon_a = \frac{\sigma_a}{E} \quad (9.7-5)$$

Conversely, if lateral loads are applied to the bar tending to prevent the contraction, the increase in the axial strain is reduced. In particular, if all lateral contraction is prevented, the strain in the axial direction becomes

$$\epsilon_a = \frac{(1 - 2\nu^2)}{E} \sigma_a \quad (9.7-6)$$

As the load on a laterally unrestrained bar is increased, the cross-sectional area, A , of the bar is reduced. Thus, the actual stress or "true" stress, P/A , increases more rapidly than the load, P . The value of the stress computed from Eq. 9.7-1 is designated the "engineering" stress since it is the stress which is used to compute the initial area required for a given load. In the linear elastic region, the difference between the two definitions is inconsequential, but it can be significant in the plastic region, as discussed below.

For larger strains, the concept of the true strain, ϵ' , is used. The true strain equals the sum of the increments of strain, each increment being computed from the current value of length:

$$\epsilon' = \int_0^{\epsilon'} d\epsilon = \int_{L_0}^{L_f} \frac{dL}{L} = \ln \frac{L_f}{L_0} = \ln(1 + \epsilon) \quad (9.7-7)$$

Some materials (Figure 9.7-2a) will fail by rupturing while still on the linear portion of the stress-strain curve. These are designated as linearly elastic and are generally thought of as brittle materials. Typical examples are glass and silicon.

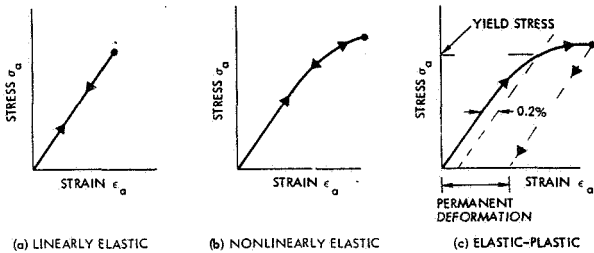


Fig. 9.7-2. Characteristic Material Stress-Strain Curves

Other materials are nonlinearly elastic. After a certain stress level is reached, their stiffness reduces so that stress-strain curves become nonlinear (Figure 9.7-2b). On unloading, these materials essentially retrace their loading curve and regain their initial length. Their performance on successive load cycles is essentially unchanged. Typical examples are some rubbers and elastomers used for bonding.

Most metals are elastic-plastic (Figure 9.7-2c). Above a critical stress, their stress strain curve also becomes nonlinear, but the increase in strain above the linear value, called the plastic strain, is not recoverable. The unloading stress-strain curve is linear and essentially parallel to the initial loading curve. For some metals (annealed low carbon steel) the transition to plasticity is quite sudden, while for others it is more gradual (nickel-chromium stainless steels). Therefore, the stress at which metals become plastic, called the yield stress, is usually defined as the stress at which the deviation of the strain from the linear value equals 0.2 percent. Yielding in materials does not involve rupturing of the molecular bonds, but rather the movement of imperfections or "dislocations" along certain shear planes of the crystal lattice. The total deformation is the summation of these individual shearing deformations. Thus, plastic deformation does not involve any change in volume and the plastic value of Poisson's ratio is 0.5 for all materials.

As the load on the bar is increased past the yield value, the metal continues to deform uniformly along its length; however at some critical load the stretching becomes nonuniform and tends to concentrate in one or more local spots along the length. Due to the accompanying lateral contraction, these local spots of high axial strain have reduced cross-sectional areas called "necks." The maximum value of the engineering stress

(load divided by the initial area) occurs at the load at which necking commences and is defined as the ultimate strength of the material. The corresponding value of the strain is called the uniform elongation. As the stretching of the bar continues further, the true stress (load divided by the minimum area of the neck) will continue to increase and can attain values considerably higher than the ultimate strength.

As necking progresses, the final rupture strength of the bar will be reached. The load at which this occurs may be considerably lower than the maximum load, depending on the necking behavior, but the true stress at failure will be considerably higher than the ultimate stress, as defined above.

The value of the strain at failure is called the elongation. Since the strain after necking is no longer uniform, the elongation is a function of the gage length or distance over which it is measured. Unless specified otherwise, this is usually taken to be 2 inches (51 mm). The shorter the gage length, the higher will be the measured value of the elongation. The maximum local value of the elongation occurs at the center of the necked area and can be determined most conveniently by measuring the reduction in area. Since most of the strain in the necked area is plastic, it can be assumed that the material is strained at constant volume ($\nu = 1/2$). Therefore if A_0 and A are the initial and final cross-sectional areas, respectively,

$$AL = A_0L_0 \quad \text{or} \quad \frac{L}{L_0} = \frac{A_0}{A} \quad (9.7-8)$$

and the true fracture strain

$$\epsilon' = \ln \frac{L}{L_0} = \ln \frac{A_0}{A} = \ln \frac{1}{1 - R} \quad (9.7-9)$$

where $R = (A_0 - A)/A_0$ is defined as the reduction in area. The true fracture strain is often referred to as the ductility, D , and is an important parameter in calculating the low cycle fatigue capability of a material.

When a metal, which has been loaded beyond its yield strength, is reloaded in the same direction, its yield stress will be increased to the value of stress to which it was previously loaded. The metal is then said to be strain hardened (Figure 9.7-3a); if the load cycle is repeated, the metal will remain linearly elastic. However, if the metal is then loaded in the reverse direction (i. e., first tension then compression), for many metals the yield stress will be reduced below its original value (Figure 9.7-3b). This is called the Bauschinger effect. If now the load or strain cycling is continued in the yield region, a new symmetrical stress-strain curve will be developed (Figure 9.7-3c) which may be stronger (higher yield stress) or weaker than the original material values (Ref. 9.7-1).

Biaxial and Triaxial Loading

Consider an infinitesimal cube which is arbitrarily oriented with respect to three reference axes at a point as shown in Figure 9.7-4. On the three parallel pairs of surfaces located at right angles to each other, there are three normal stresses (stresses normal to the surfaces) $\sigma_x, \sigma_y, \sigma_z$ and six shear stresses (stresses parallel to the surfaces, $\tau_{xy}, \tau_{xz}, \tau_{yz}, \tau_{yx},$

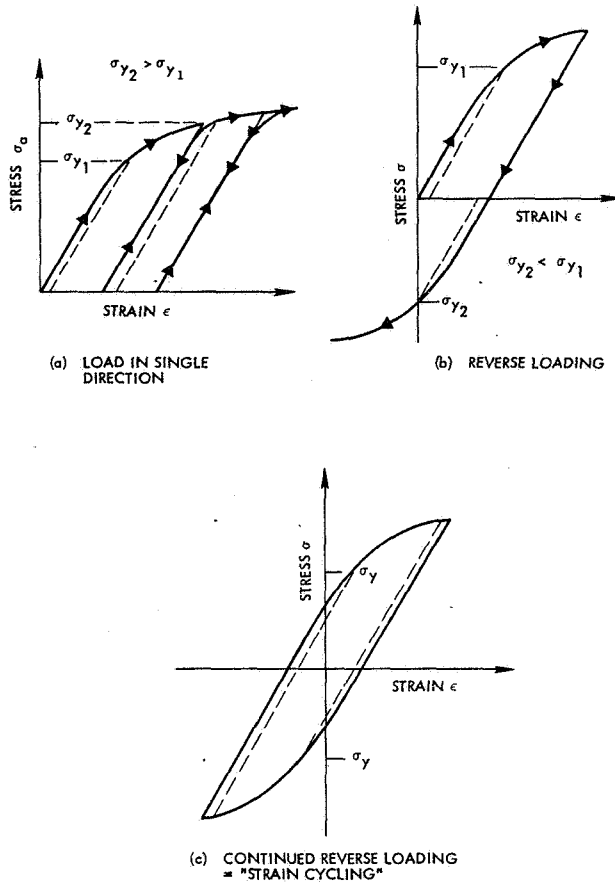


Fig. 9.7-3. Strain Hardening Characteristics

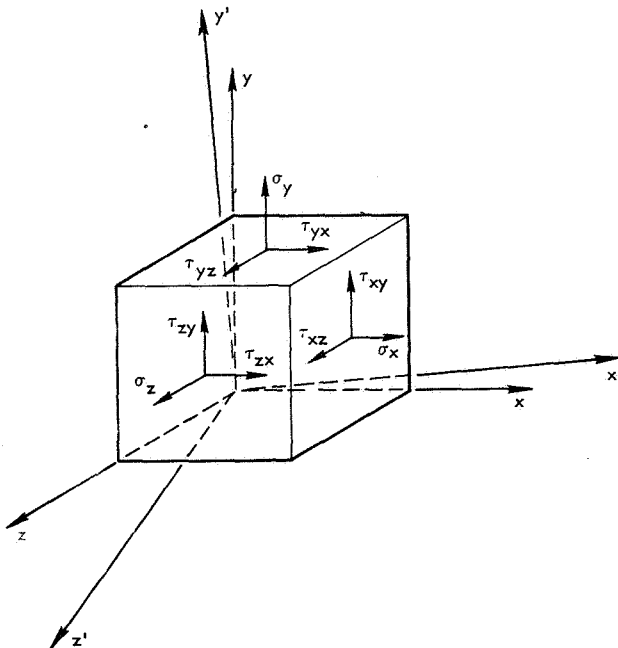


Fig. 9.7-4. Three-Dimensional Stresses on an Infinitesimal Cube of Material Subjected to an Arbitrary External Load

τ_{zx}, τ_{zy} , where the first subscript refers to the outward normal to the surface and the second subscript refers to the direction in which the stress is acting. From the equations of moment equilibrium for the cube it can be shown that $\tau_{xy} = \tau_{yx}$, etc., so that at any point there are six independent stresses. As the cube, initially in the x, y, z coordinate system, is rotated into an x', y', z' coordinate system (both coordinate systems having a common origin), the values of the stresses acting on the cube surfaces change and their variation can be computed by the theory of elasticity (Ref. 9.7-2). According to this theory, there is an orientation of the cube at which all three shear stresses are zero and the normal stresses achieve their maximum values. The three maximum normal stresses are designated as the principal stresses, σ_1, σ_2 , and σ_3 , and the stress state of the center of the elemental volume can be defined in terms of their values and the angular orientations of the principal directions.

The average value of the principal stresses is called the hydrostatic stress

$$p = \frac{1}{3} (\sigma_1 + \sigma_2 + \sigma_3) \quad (9.7-10)$$

and acts as a pressure causing only uniform compression or expansion of the material, but no distortion. The differences between the principal stresses and the hydrostatic stress are called deviatoric stresses

$$\sigma_1 - p, \sigma_2 - p, \sigma_3 - p \quad (9.7-11)$$

and cause distortion of the element. Since yielding of a material is only a function of element distortion, it is a function of the deviatoric stresses. According to the generally accepted Von Mises yield criterion, yielding of a material occurs when the effective stress, defined by

$$\bar{\sigma} = \left(\frac{(\sigma_1 - \sigma_2)^2 + (\sigma_2 - \sigma_3)^2 + (\sigma_3 - \sigma_1)^2}{2} \right)^{1/2} \quad (9.7-12)$$

exceeds the material's uniaxial yield stress. Notice that $\bar{\sigma}$ reduces to the uniaxial value when two of the three principal stresses are zero. Sometimes the Von Mises criterion is referred to as the octahedral shear stress, τ , which differs from the effective stress only by a constant. The distortion energy yield criterion is also equivalent to the Von Mises criterion.

For nonprincipal directions, x, y, z , the equation for the effective stress becomes

$$\bar{\sigma} = \left(\frac{(\sigma_x - \sigma_y)^2 + (\sigma_y - \sigma_z)^2 + (\sigma_z - \sigma_x)^2 + 3(\tau_{xy}^2 + \tau_{yz}^2 + \tau_{zx}^2)}{2} \right)^{1/2} \quad (9.7-13)$$

Since the addition of a hydrostatic pressure, p , has no effect on yielding, the individual stresses in a three dimensional state of stress can be significantly higher than the yield stress.

However, for the commonly assumed two-dimensional state of stress, called plane stress, in

which the stresses in one direction, say z , are always zero, an arbitrary hydrostatic stress cannot be added. As a consequence, the maximum stress value can only be approximately 15 percent greater than the effective stress.

In determining the three dimensional post-yield stress-strain curve, the effective strain $\bar{\epsilon}$ corresponding to the effective stress is defined by

$$\bar{\epsilon} = \left(\frac{(\epsilon_1 - \epsilon_2)^2 + (\epsilon_2 - \epsilon_3)^2 + (\epsilon_3 - \epsilon_1)^2}{2} \right)^{1/2} \quad (9.7-14)$$

where ν has the elastic value for the elastic portion of the strain and $\nu = 1/2$ for the plastic portion. The value of the effective strain also reduces to the uniaxial value when two of the principal strains are zero. Thus, the multiaxial stress-strain curve can be obtained from the results of a uniaxial test up to the strain value at necking, i. e., up to the uniform elongation. Beyond that strain the behavior in uniaxial and multiaxial stress conditions will differ due to the inhibiting of necking in the three-dimensional state of stress.

Until recently the methods of analysis were limited for a nonlinear problem, such as plasticity, so that solutions were available only under simplified conditions or were very approximate. However, with the continuing development and refinement of the finite element numerical solutions, many of these limitations are now being removed and more accurate plastic solutions become possible. However, these new plastic solutions require new, three-dimensional material properties which heretofore have not been investigated in any detail as one-dimensional material properties have.

Linearly elastic or brittle materials generally fail when the maximum normal stress exceeds their ultimate strength. The maximum normal stress, however, may not occur in the directions of the coordinates in which a stress analysis is made; therefore, a calculation of the maximum stress has to be made. For a three-dimensional stress analysis the resulting equations are quite complex, but simplify considerably if a two-dimensional analysis is performed in one of the principal planes. Thus assuming σ_z is a principal stress, the maximum stress in the x - y plane is given by

$$\sigma_{\max} = \frac{\sigma_x + \sigma_y}{2} \pm \sqrt{\left(\frac{\sigma_x - \sigma_y}{2}\right)^2 + \tau_{xy}^2} \quad (9.7-15)$$

Similarly, analysis can be carried out in the x , z , and y , z planes to find both the magnitude and direction of the maximum stress. (For a more complete discussion of this subject see Ref. 9.7-1.)

9.7.2 Stresses in Rigid Bonded Layers

Examples of rigid bonded layers are:

- Metallic contact layers on the silicon solar cells
- Plating layers on solar cell interconnectors
- Interconnector-to-solar cell soldered or welded joints

- Adhesive layers (cover-to-cell and cell-to-substrate) at lower temperatures, typically below -100°C .

To illustrate, consider two long strips of different materials bonded to each other in intimate permanent contact, as shown in Figure 9.7-5. Each material is characterized by its elastic modulus, E , linear coefficient of thermal expansion, α , Poisson's ratio, ν , and thickness, t . As the temperature, T , changes by an amount ΔT from the equilibrium temperature, T_0 , so that $\Delta T = T - T_0$, the two materials tend to expand or contract at different rates. But since they are physically joined together, the changes in length (or strains) in each material must be equal at their interface. If the strips are long compared to their thickness, then away from their edges it can be assumed that the stress conditions across their thickness are uniform. If, in addition, the strips are narrow compared to the length and thickness, the stresses in the lateral (i. e., width) direction can be neglected, and if the strips are restrained from curving (i. e., they remain flat), the strains are

$$\epsilon_1 = \alpha_1 \Delta T + \frac{\sigma_1}{E_1} = \epsilon_2 = \alpha_2 \Delta T + \frac{\sigma_2}{E_2} \quad (9.7-16)$$

where the subscripts 1 and 2 refer to the first and second material, respectively. (This subscript notation is used throughout this section and differs in meaning from that used in Section 9.7.1.)

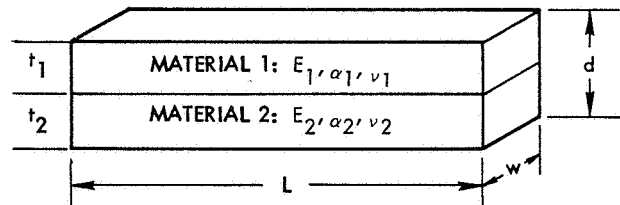


Fig. 9.7-5. Two-Strip Model (Rigid Bond)

Since no net axial load is applied to the two strips, we have the equilibrium equation

$$\sigma_1 t_1 + \sigma_2 t_2 = 0 \quad \text{or} \quad \sigma_2 = -\sigma_1 \frac{t_1}{t_2} \quad (9.7-17)$$

Substituting this expression for σ_2 into Eq. 9.7-16 gives

$$\sigma_1 = -\frac{E_1 \Delta \alpha \Delta T}{1 + mn}, \quad \sigma_2 = \frac{E_2 \Delta \alpha \Delta T}{1 + \frac{1}{mn}} \quad (9.7-18)$$

where

$$\Delta \alpha = |\alpha_1 - \alpha_2|, \quad m = \frac{t_1}{t_2}$$

and

$$n = \frac{E_1}{E_2}$$

For each case, in Eq. 9.7-18 the numerator is the stress in one element which would result if the other element were infinitely rigid, while the denominator gives the reduction in stress due to the actual flexibility of the second element.

For several layers rigidly fastened together, the stress in the i^{th} layer can be shown to be

$$\sigma_i = E_i (\bar{\epsilon} - \alpha_i \Delta T) \quad (9.7-19)$$

where

$$\bar{\epsilon} = \frac{\sum t_i E_i \alpha_i \Delta T}{\sum t_i E_i}$$

is the value of the longitudinal strain.

For the common case in solar cell arrays where the joined layers are not narrow strips but wide plates, the stresses in all directions in the plane of the layers are equal. Therefore, due to the effect of Poisson's ratio the values of E_i in the above equations have to be replaced by their effective values $E_i' = E_i / (1 - \nu)$. Thus for bonded two dimensional layers the thermal stresses can be significantly higher than for one-dimensional strips. In many cases, geometric discontinuities may lead to so-called stress riser effects that may increase the stress in certain, localized areas even more.

Refs. 9.7-3 and 9.7-4 derive the values of stress and curvature, $1/\rho$ (radius ρ), which occur when the layers are allowed to bend. In that case the stresses away from the edges of the layers vary linearly through the thickness with the maximum stresses occurring at the interface between the layers (see Fig. 9.7-6).

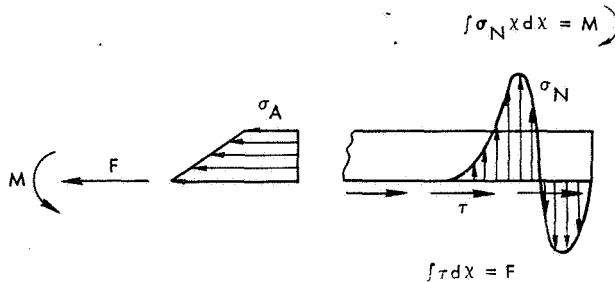


Fig. 9.7-6. Force and Moment Equilibrium Between Interior Stresses (Eq. 9.7-20) and Edge Shear and Normal Stresses

$$\frac{1}{\rho} = \frac{-6 \Delta \alpha \Delta T (1+m)^2}{(t_1 + t_2) [3(1+m)^2 + (1+mn)(m^2 + 1/mn)]} \quad (9.7-20a)$$

$$(\sigma_1)_{\max} = \frac{2}{\rho} \left[\frac{E_1 I_1 + E_2 I_2}{t_1(t_1 + t_2)} + \frac{t_1 E_1}{4} \right] \quad (9.7-20b)$$

For the special case where the two strips have the same elastic modulus and the same thickness, (i. e., $m = n = 1$), the maximum stresses in the two strips are equal to their values without bending as given by Eq. 9.7-18. If, as is the case for solder plating on solar cells, for example, the first layer is much thinner than the second layer (i. e., $m \ll 1$), then Eq. 9.7-20 can be simplified (by neglecting m^2), giving

$$\sigma_1 = \frac{E_1 \Delta \alpha \Delta T}{1 + 4mn} \quad (9.7-21)$$

Comparing Eq. 9.7-21 with Eq. 9.7-18 it is seen that when the effect of curvature is included, the reduction in the stress in layer 1 due to the flexibility of layer 2 is increased by a factor of 4.

The stresses discussed so far exist in portions of the bonded strips which are remote from the edges. However, it is obvious that near the edges additional stresses must exist since the boundary condition at the edges is that the axial stress is zero. The edge problem has been investigated analytically in Ref. 9.7-5 and by a finite element numerical analysis in Ref. 9.7-6. Both analyses are in essential agreement and show that the stresses given by Eq. 9.7-20 persist almost unchanged up to a distance of approximately one total thickness $d = t_1 + t_2$ from the edge. Closer to the edge, normal and shear stresses develop which increase rapidly as the edge is approached. The shear stress balances the axial forces in the members (Figure 9.7-6), that is, the integral of the shear stress equals the axial force in each member and is essentially independent of the values of m and n . The normal, or prying stress balances the bending moments in the layers. Thus, the normal stresses are very sensitive to the values of the thickness and stiffness ratios m and n . For the particular case where $m = 1$, the normal forces are zero. Figures 9.7-7 and 9.7-8 show typical variations of the interface shear and normal forces near the edge of a joint while Figure 9.7-9 shows the variation of the axial stress through the thickness of the layers at various distances near the end. Notice that for the thicker member the axial stress variation through the thickness is quite nonlinear and that the maximum value of the axial stress occurs very near the edge.

Thus, the maximum stresses in the joint occur locally near the ends. If the material is ductile, and if there are only a few load cycles, then these local peak stresses are of little concern since the material will simply yield and relieve the stress. Failure will only occur if the fracture strain capability of the material is exceeded. However, for a brittle material,

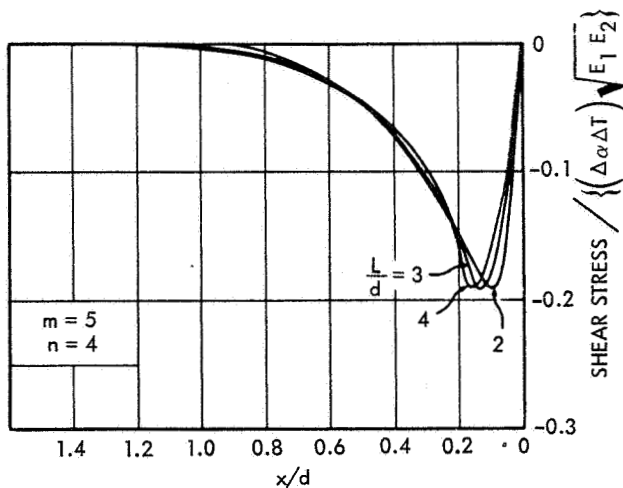


Fig. 9.7-7. Influence of Variation in Half-Length/Thickness Ratio on Shear Stress at Interface (Ref. 9.7-6)

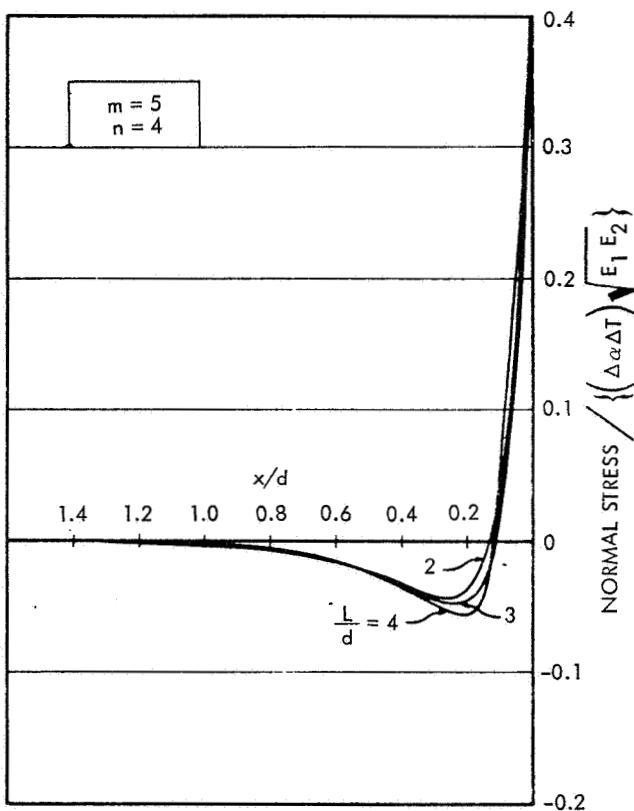


Fig. 9.7-8. Influence of Variation in Half-Length/Thickness Ratio on Normal Stress at Interface (Ref. 9.7-6)

such as silicon, these high stresses can cause failures which involve pulling out small chunks of silicon called divots. If a brittle failure occurs near the edge, it will transfer the undiminished load to the next as yet unfailed section of material so that propagation of the fracture to complete failure ensues. If the load application is repeated many times then failure can

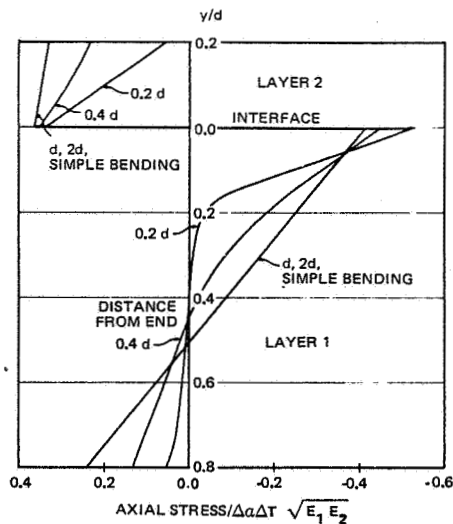


Fig. 9.7-9. Longitudinal Stress in Strip at Various Distances from End of Strip (Ref. 9.7-6)

occur by fatigue at lower stresses than required for failure at the first application of the load. This will be discussed further in Section 9.8.

If the length of the joined strips is less than twice the total thickness, d (such as would be the case for an interconnector joint to a silicon cell), then Ref. 9.7-5 indicates that the axial loads in the layers do not reach the value for a long joint, since the edge effects overlap. However, in this case the cross-sectional stress distribution is not linear, as shown in Figure 9.7-9, and thus the maximum stress in the thicker element could be significantly higher than the stresses computed by Eq. 9.7-20. This was pointed out in Ref. 9.7-7, which noticed experimental silicon failures occurring in joints for which the calculated stresses were less than the strength of the silicon. The experimental results were used to determine a stress concentration factor for this condition.

Illustrative Example

To obtain some numerical insight of typical thermal stresses, assume that a 0.35-mm thick silicon cell with a 25- μm thick layer of solder, initially stress-free at 20°C, is subjected to various temperatures. Actually, since the solder was applied at a higher temperature than 20°C, the solder will be initially under some stress, but this will be ignored for the present. Modifying Eq. 9.7-21 for the biaxial condition, and using subscripts "so" for solder and "si" for silicon:

$$\sigma_{so} = \frac{E_{so} (\alpha_{so} - \alpha_{si}) (T - 20)}{(1 - \nu_{so}) \left(1 + 4 \frac{(1 - \nu_{si}) E_{so} t_{so}}{(1 - \nu_{so}) E_{si} t_{si}} \right)} \quad (9.7-22)$$

Using material property values for 62/36/2 solder and silicon from Chapter 7 of Volume II the solder stresses were computed and are shown in Figure 9.7-10 together with the values of the solder yield stress. Since the stresses in all directions in the plane of the solder are equal, while the stress normal to the surface and the shear stress are zero,

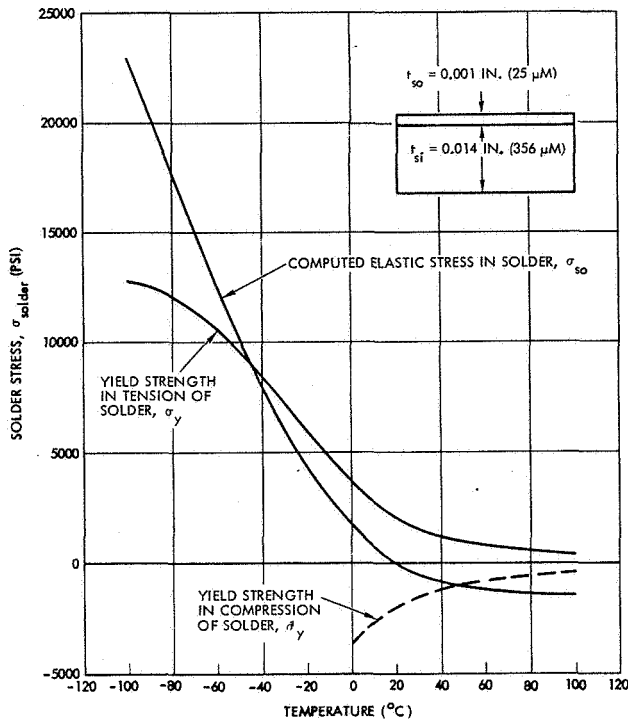


Fig. 9.7-10. Thermal Stresses in Solder Layer on Silicon

$\sigma_1 = \sigma_2 = \sigma_s$, $\sigma_3 = 0$, and the effective stress $\bar{\sigma} = \sigma_s$. Thus the solder yields when σ_s exceeds σ_y . It is seen from Figure 9.7-10 that the solder will yield when subjected to temperatures lower than -45°C or greater than 50°C .

Once the solder yields, Eq. 9.7-22 has to be modified to account for the reduced plastic modulus. This can be obtained from the plastic stress strain curve, but to do this it is necessary to know the effective plastic strain, $\bar{\epsilon}$. The strain in all directions in the plane of the solder equals ϵ_a , while the strain normal to the surface equals

$$\epsilon_n = -\frac{2\nu\epsilon_a}{(1-\nu)} \quad (9.7-23a)$$

$$\epsilon_1 = \epsilon_2 = \epsilon_a, \quad \epsilon_3 = \frac{-2\nu}{1-\nu}\epsilon_a \quad (9.7-23b)$$

and

$$\bar{\epsilon} = \frac{1}{1-\nu}\epsilon_a \quad (9.7-23c)$$

where $\nu \rightarrow 0.5$ for large plastic strains. Thus the effective strain, $\bar{\epsilon}$, is approximately twice the direct strain, ϵ_a , in the plane of the solder. With the decrease in the solder modulus this strain rapidly approaches the strain which would result if the silicon were rigid, i. e., $\Delta\alpha\Delta T$.

9.7.3 Stresses in Flexible Bonded Layers

The previous analysis dealt with the case when the two layers were rigidly fastened together so that there was no relative motion between them at their interface. Another possibility is to bond them with an adhesive layer which is more flexible than either of the two layers and thus allow relative motion between the layers.

Under these conditions it is possible to neglect the axial stiffness of the adhesive layer compared to the other two layers and just consider its shear stiffness. This type of analysis has been developed for the case of load-carrying joints and is developed in Ref. 9.7-8 for the case of thermal stress.

To illustrate, consider the lap joint of length L shown in Figure 9.7-11. This is similar to the previous analyzed joints except for the addition of the third bonding material with thickness, t_3 , and shear modulus, G_3 . The basic equilibrium equations equate the change in axial stress, σ_i , in each of the outer layers to the shear stress, τ , in the bond layer

$$t_1 \frac{d\sigma_1}{dx} + \tau = 0, \quad t_2 \frac{d\sigma_2}{dx} - \tau = 0 \quad (9.7-24)$$

where x is the distance from the center of the joint, the subscripts 1, 2, 3 refer to the respective layers, and

$$\sigma_1 = E_1 \left(\frac{du_1}{dx} - \alpha_1 \Delta T \right)$$

$$\sigma_2 = E_2 \left(\frac{du_2}{dx} - \alpha_2 \Delta T \right) \quad (9.7-25)$$

$$\tau = \frac{G_3}{t_3} (u_2 - u_1)$$

where u_1, u_2 are the displacements in the axial (x) direction in layers 1 and 2, respectively.

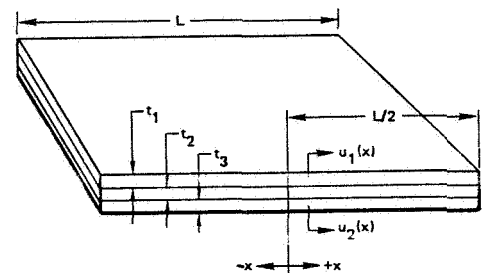


Fig. 9.7-11. Basic Model of Three Laminated Layers

The solution to Eq. 9.7-24 can be obtained in terms of hyperbolic functions, and, after some manipulation can be expressed as

$$\sigma_1 = -\frac{E_1 \Delta \alpha \Delta T}{1 + mn} \left(1 - \frac{\cosh 2\beta x}{\cosh \beta L} \right) \quad (9.7-26a)$$

$$\sigma_2 = -m \sigma_1 \quad (9.7-26b)$$

$$\tau = \frac{2E_1 t_1 \Delta \alpha \Delta T}{L(1 + mn)} \frac{\beta L \sinh 2\beta x}{\cosh \beta L} \quad (9.7-27)$$

$$\Delta u = u_2 - u_1 = \frac{t_3}{G_3} \tau = \frac{1}{2} \Delta \alpha \Delta T L \frac{\sinh 2\beta x}{\beta \cosh \beta L} \quad (9.7-28)$$

$$\Delta u(x = \frac{L}{2}) = \frac{1}{2} \Delta \alpha \Delta T L \frac{\tanh \beta L}{\beta L} \quad (9.7-29)$$

where

$$\beta^2 = \frac{1}{4} \frac{G_3}{t_3} \left(\frac{1}{E_1 t_1} + \frac{1}{E_2 t_2} \right) \quad (9.7-30)$$

βL is a measure of the relative stiffness of the strips and the adhesive.

It is seen that Eq. 9.7-26a for σ_1 is identical to that for the rigidly joined long strips, Eq. 9.7-18, except for the addition of the bracketed term which acts as a correction term, increasing as the edge is approached. These results are plotted in Figures 9.7-12 and 9.7-13. Figure 9.7-12 shows the variation of the axial and

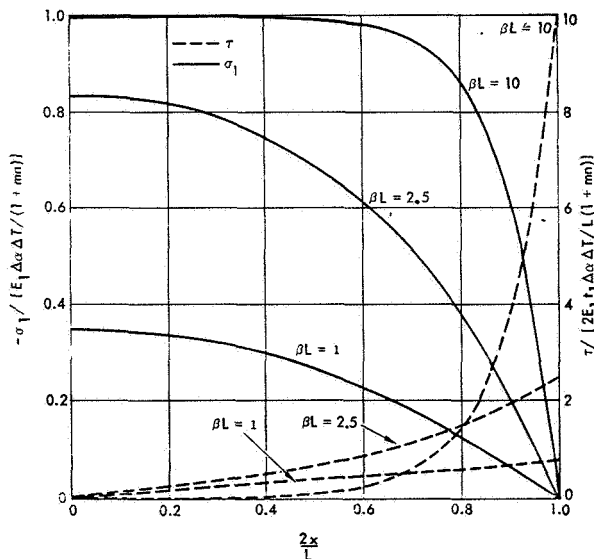


Fig. 9.7-12. Axial and Shear Stress Distribution in a Bonded Joint for Different Values of the Stiffness Parameters βL

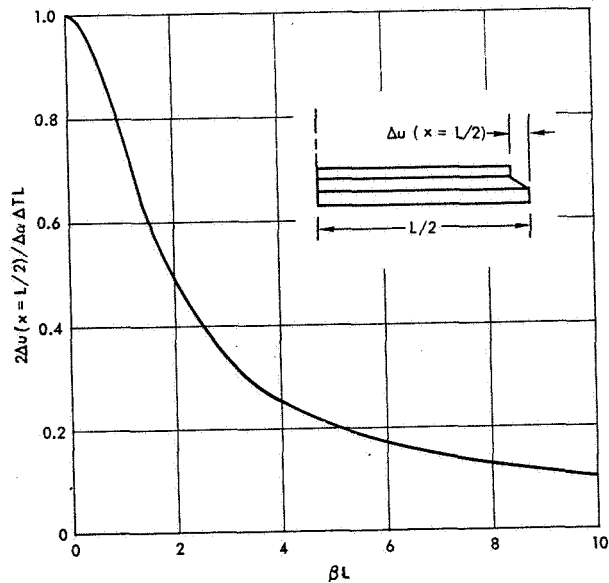


Fig. 9.7-13. Variation of the Relative Edge Displacement of a Bonded Joint with the Stiffness Parameter βL

shear stresses with distance from the edge for three values of the stiffness parameter, βL . For a large value of βL the axial load reaches its limiting value only a short distance from the end of the joint and thereby causes a sharp local peak in the shear stress. This sharp, local stress concentration approximates the previous results for the rigid bond of two strips and is typical of an unyielded solder joint. For low values of βL the axial load increases more slowly and the shear stress varies approximately linearly with distance from the center of the strip. Both the maximum values of the axial stress and shear stress are considerably reduced as the stiffness G/t_2 of the adhesive layer is decreased.

Figure 9.7-13 shows the relative axial displacement $\Delta u(x = L/2)$ between the two strips at their ends. The normalized value is the relative thermal displacement between the two strips without any connection between them. This relative displacement is of interest in determining the displacements required of interconnectors joining successive cells which are bonded to the same substrate.

Illustrative Example

Consider a 10 mil x 0.8 inch square (0.25 mm thick, 2 by 2 cm) silicon cell which is bonded to a 5 mil (0.125 mm) thick aluminum substrate with 4 mils (0.1 mm) of a silicone adhesive having a shear modulus of 500 hsi (3.45 MN/m²); then

$$\beta L = \frac{0.8}{2} \sqrt{\frac{500}{0.004} \frac{1}{10 \times 27 \times 10^3} + \frac{1}{5 \times 10 \times 10^3}} = 0.69$$

Thus the stress distribution approximates the lower curves ($\beta L = 1$) in Figure 9.7-12. However, at temperatures below -100°C , the stiffness of silicone adhesives increases to values as high as 3.45 MN/m^2 (500 ksi). Assuming a value of 0.7 MN/m^2 (100 ksi) for G_3 then

$$\beta L = 9.75$$

so that the stress distribution corresponds to the upper ($\beta L = 10$) curves in Figure 9.7-12. The result of this adhesive stiffening below -100°C is an increase in the axial stress by a factor of 3 for the same value of $\Delta\alpha\Delta T$ and an increase in the shear stress by a factor of 10.

Design Recommendations

From the foregoing analyses the following recommendations can be made:

- Select an adhesive with the lowest possible stiffness (shear modulus) at the required low temperature limit. This is synonymous with selecting an adhesive with the lowest possible glass transition (brittle point) temperature (see Section 7.11).

9.7.4 Stresses in Interconnector Expansion Loops

As illustrated in Section 5.2, a solar cell interconnector expansion loop bridging the gap between adjacent solar cells is deformed during thermal cycling. The magnitude of this deformation, δ , is approximately equal to change in the cell gap width and depends not only upon the value of $\Delta\alpha\Delta T$, but also upon the type of solar cell-to-substrate adhesive.

For illustration, consider the simplified expansion loop of a solar cell interconnector shown in Figure 9.7-14. In general, the interconnector is subjected to the separating force, F , and the moments, M_L and M_R , at the left- and right-hand edges, respectively. It is assumed that the height, D , is fixed by the thickness of the cell and that only the dimensions, H , L and t are available to be changed. In practice the length, L , is limited by the desire to pack the cells as close together as possible and the height, H , is limited by the desire to minimize the projection above the coverslide. Applying strength-of-materials theory, the force and moments can be expressed in terms of the deflection, δ , as follows:

$$F = f \frac{EI\delta}{D^3}, \quad M_L = m_L \frac{EI\delta}{D^2}, \quad M_R = m_R \frac{EI\delta}{D^2} \quad (9.7-31)$$

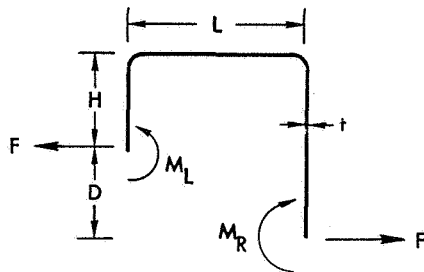


Fig. 9.7-14. Simplified Interconnector Model

where

$$f = \left[-1/6h^3 + 1/3(1 - 1/2h)(1+h)^2 + (1/2 + h + h^2) \frac{h^2 + hs - 1/2}{2h + s + 1} \right]^{1/2} \quad (9.7-32)$$

$$m_L = \frac{h^2 + hs - 1/2}{2h + s + 1} f$$

$$m_R = m_L + f$$

and

$$\alpha = \frac{H}{D}, \quad \beta = \frac{L}{D}$$

The moment, M , at the top of the interconnector is given by

$$M_T = M_L - FH \quad (9.7-33)$$

The values of the nondimensional coefficients f , m_L and m_R are shown in Figures 9.7-15 and 9.7-16 as functions of the shape parameters, h and s . It is seen that both the forces and moments decrease rapidly as h and s are increased, but, for values of h and s greater than 1, the decrease is small. For values of h greater than 0.6 there is negligible change in m_L , but m_R and f continue to decrease as the height ratio h is increased.

For a given interconnector geometry, h , s and D , Eq. 9.7-16 indicates that the force, F , and moments, M_L and M_R , are proportional to the moment of inertia EI of the interconnector cross section, or t^3 for a given material and interconnector width, b . This is in contrast to the case for a simple interconnector without a stress relief loop where the force is proportional to EA , or t for a given material and width (A is the cross-sectional area). Through the use of an interconnector loop of practical dimensions the axial force between solder joints can be reduced by orders of magnitude compared to the value obtained with a straight interconnector. The main problem then becomes the bending stresses in the interconnector and the bending moments applied to the joints.

The maximum stress in the interconnector itself is given by

$$\sigma_m = \frac{F}{A} \pm \frac{Mt}{2I} \quad (9.7-34)$$

where M is the maximum of M_R , M_L , or M_T . For an interconnector made of a single material

$$I = \frac{1}{12} bt^3 \quad (9.7-35)$$

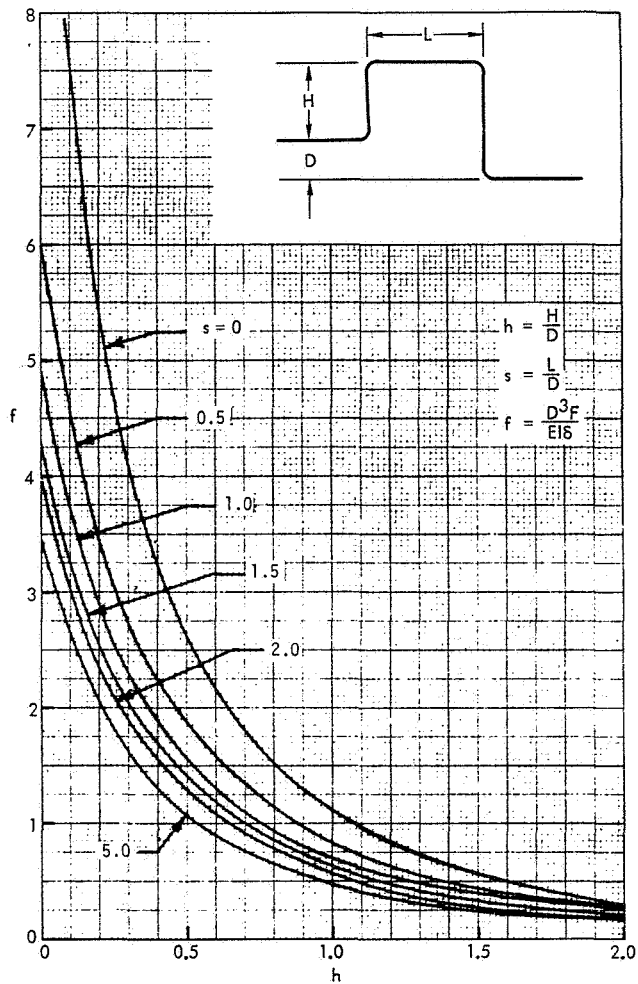


Fig. 9.7-15. Variation of Nondimensional Force Coefficient f with Geometric Ratios h and s

where b is the interconnector width, so that

$$\sigma_m = \left[\frac{1}{12} f \left(\frac{t}{D} \right)^2 + m \left(\frac{t}{D} \right) \right] \frac{E \delta}{D} \quad (9.7-36)$$

Thus, the stress in the interconnector itself due to a given displacement, δ , is also reduced by decreasing the thickness of the interconnector.

If a minimum interconnector cross-sectional area is required for a certain maximum electrical resistance, an improved design interconnector loop, both with respect to the forces and moments applied to the interconnector joint and to stresses in the interconnector itself, can be achieved by reducing the interconnector thickness and increasing its width correspondingly.

9.7.5 Effects of External Forces and Moments On Soldered and Welded Joints

The stress distributions in bonded joints due to external forces and moments are similar to those

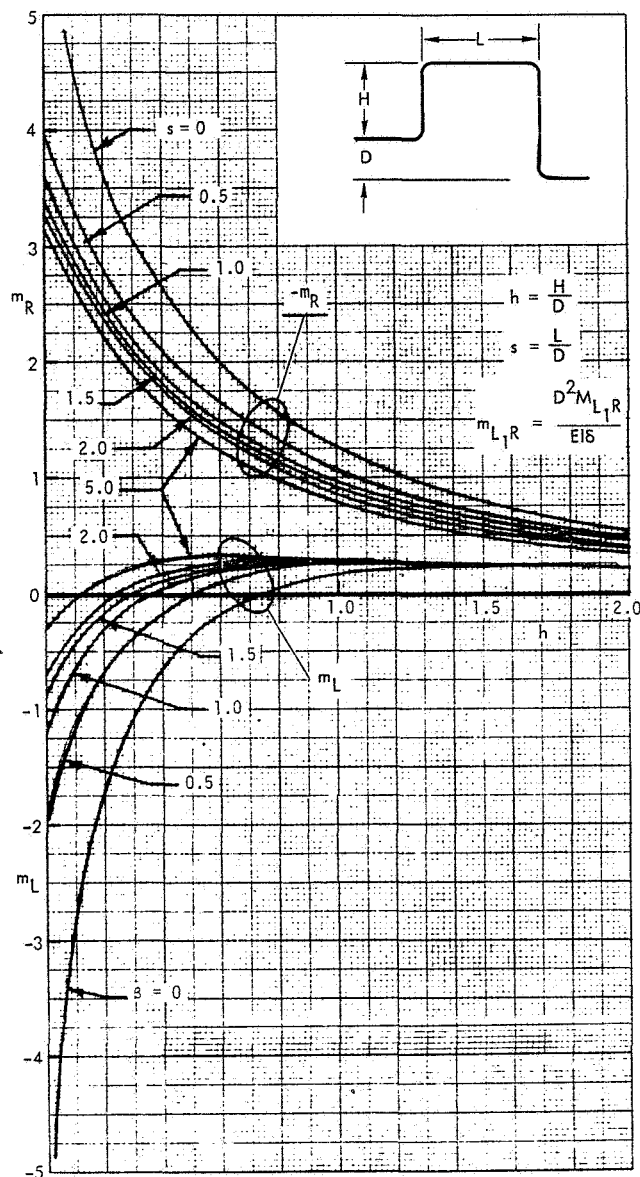


Fig. 9.7-16. Variation of Nondimensional Moment Coefficients m_{1L} and m_{2R} with Geometric Ratios h and s

resulting from thermal stresses, and have been analyzed by methods similar to those presented in Sections 9.7.2 and 9.7.3 (Refs. 9.7-9 through 9.7-11). For small values of the stiffness parameter, βL , the load is transferred gradually from one member to the other and the shear stress distribution is quite uniform. For large values of βL the load is transferred very rapidly at the ends of the joint and the shear stress distributions are sharply peaked. Associated with these peaks in the shear stress distributions are large values of the normal or peeling stress. Figure 9.7-17 shows typical interface shear stress distributions due to axial loads and bending moments for a thickness ratio representative of interconnector/solar cell joints and compares them

Two-Dimensional Modelling

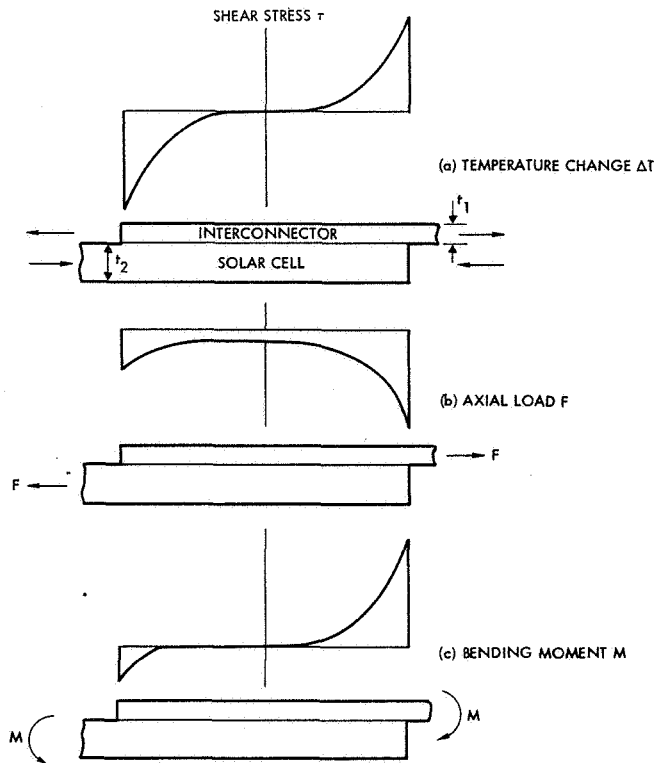


Fig. 9.7-17. Illustration of Interface Shear Stress Distribution in an Interconnector/Solar Cell Joint ($m = t_1/t_2 \ll 1$) for the Three Loading Conditions

with the shear stress distributions resulting from thermal contraction of the interconnectors. For the assumed thickness ratio the maximum shear stress due to a bending moment occurs at the loaded interconnector end while the maximum shear stress due to an axial load occurs at the opposite end. In actual practice this peak will be minimized due to the gradual taper of the solder at that end. Due to the asymmetry of the shear stress distribution the algebraic signs of the applied axial load and moment will influence the stress distributions. For the load directions pictured in Figure 9.7-17, the bending moment adds to the shear stress at the critically loaded end of the interconnector while the axial load subtracts. For the opposite loading directions the reverse stress effects would occur. Since both the thermal stresses and the applied loads are functions of the temperature, their relative directions are unchanged during thermal cycling and are a function only of the configuration. The original magnitude and direction (i. e., sign) depend upon the interconnector configuration, the material choices for the interconnector, cell adhesive and substrate, and the inter-cell gap width.

As discussed previously for ductile materials such as solder, the stress peaks are not of too great a concern for only a few thermal cycles, because the solder will yield and failure will occur only when the fracture strain of the solder is exceeded. The most important effect, however, is in repetitive thermal cycling the stress peaks will initiate cracks and reduce the fatigue life, as discussed in Section 9.8.

Most of the stress conditions discussed above have been treated as two-dimensional when actually they are three-dimensional. In order to treat a three-dimensional problem as two-dimensional, there are three different types of assumptions which are commonly made. The first is the so-called plane stress assumption that the stresses normal to the plane of the section being analyzed are zero. This assumption is applicable when two narrow strips or wires are joined together, but may lead to some error when a narrow strip is joined to a wide strip, such as an interconnector joined to a solar cell.

The second possible assumption is the plane strain or plane deformation assumption according to which the strain normal to the plane of the analyzed section is assumed to be either constant or zero. This is applicable when two very wide strips are joined together. According to the theory of elasticity (Ref. 9.7-2), stresses in the plane being analyzed are identical for both cases under most conditions; however, the stresses in the z direction normal to the plane are different. For plane stress $\sigma_z = 0$, while for plane strain $E_z = 0$ and $\sigma_z = \nu(\sigma_x + \sigma_y)$. Thus, for an elastic analysis, the results appear the same for the two assumptions. However, for a plastic analysis the results can be radically different, since yielding is a function of the effective stress which, according to Eq. 9.7-3, is strongly influenced by the stresses in the z direction. The effect of the z -direction stress decreases the effective stress and, thus, inhibits yielding. As a result the yield areas are more localized and the peak stresses are greatly increased. Thus, a plastic plane strain analysis may predict failure stresses in the brittle silicon cell, whereas a plane stress analysis may not.

The third assumption is that the stress condition is axisymmetric. This gives an exact three-dimensional solution for a weld or solder joint which is circular and located either a long distance or a uniform distance away from the edges of the interconnector or cell. Since many welds or solder joints are approximately round, this is probably the most reasonable assumption for joints subjected to thermal stresses. However, the assumption is less justified when the joint is loaded by external moments or loads.

Three-Dimensional Models

The foregoing three two-dimensional assumptions do not permit accurate assessment of the transfer of a moment or axial load in a wide strip into a single weld or solder joint. Therefore, the desired three-dimensional analyses must be performed using finite element numerical methods. However, adding an additional dimension to the treatment of the problem increases the number of equations to be solved by approximately an order of magnitude. Since the cost of making the calculations varies somewhere between the square and cube of the number of equations, the computing costs can be expected to increase between two and three orders of magnitude for similarly detailed problems. An initial step toward making such a three-dimensional calculation was made by Salama, Powe, and Yasui (Ref. 9.7-12).

Although more detailed three-dimensional analyses appear desirable, there are big gaps in our knowledge of how many of the materials of concern in solar cell design perform under severe cyclic loads. Therefore, it may be more beneficial to conduct a series of carefully controlled tests using fairly simple configurations to gain an understanding of material performance.

9.8 FATIGUE AND WEAROUT ANALYSIS

Failures of materials by fracturing may occur in response to two distinctly different methods of loading (stressing):

- By exceeding the ultimate strength of the material in a single application of the load, the material fails under a static load.
- By cyclically loading a material such that the stress alternates between positive and negative values (viz., tension and compression) but with the peak stress never approaching or exceeding the ultimate strength of the material, the material fails by fatigue.

In general engineering practice, fatigue failures of parts are avoided by designing them such that the stress levels in the parts are sufficiently low (even though there are cases where this is not always possible).

Many solar cell array interconnector design problems, however, cannot be solved by reducing stress levels to values that would result in a very long fatigue life. Rather the design effort must be directed toward extending an *a priori* limited fatigue life to a minimum acceptable number of thermal cycles.

9.8.1 Stress versus Fatigue Analysis

The first step of a fatigue analysis is actually a thermomechanical stress analysis, as described in Section 9.7. The stress analysis is an excellent tool to aid the solar cell array designer in selecting materials and altering configurations until the lowest possible stress in the various array materials for a given temperature cycling range has been found. Ref. 9.8-1 illustrates the use of such static stress analysis to reduce stress levels in critical areas to values that are as low as possible. This reference also shows corresponding temperature cycling test results, confirming the analytical approach.

Ultimate failure of a part by fatigue, however, is not so much related to the stress level, but rather to the material's behavior when it undergoes plastic deformation (viz., when it yields). The capability of a material to withstand alternating plastic deformations is related to the material's microscopic and metallurgical properties that are macroscopically reflected in such terms as ductility, elongation, reduction in area, crack formation, crack propagation, work hardening, work softening, and others.

For many solar cell arrays the cyclically alternating plastic material deformations of solar cell contacts and solar cell/interconnector soldered and welded joints cannot be prevented by design or material selection efforts. A linear-elastic stress analysis will simply indicate that yielding has occurred, while an elastic-plastic stress analysis will indicate the degree to which yielding will take place. The next step, then (since plastic deformation cannot be eliminated), is to

make further design and material selection changes that will prolong either the onset of fatigue cracking or the completion of crack propagation through the interconnectors or interconnector joints. The theoretical investigations of these mechanisms are called fatigue or wearout analyses.

Fatigue failures due to repeated mechanical load cycles are a well-known phenomenon and have been extensively investigated (Refs. 9.8-2, 9.8-3, and 9.8-4). However, there are still many unknown factors and considerable scatter is found in test results. The fatigue life of a part has been found to be proportional to a high power of the stress. Therefore, the approach to obtaining a required fatigue is to increase the amount of material so that the stress is reduced below the level which causes failure. For life requirements in the millions of cycles, maximum working stress levels considerably below the yield strength are required. However, for thermally loaded structures which are subjected to strain rather than stress this approach does not necessarily lead to a solution. As one element of the structure is reinforced it will only cause the load to be transferred to the other elements of the structure. Thus, in many cases where the differential thermal expansions cannot be avoided it may be necessary to live with material yielding and to include its effect in the fatigue analysis.

9.8.2 Stress and Strain Loading

Structural members are said to be loaded by stress (applied force per unit area) or by strain (deformation). An example of stress loading is a coil spring of an automobile suspension system that supports a part of the automobile's weight. An example of strain loading is the thin silver contact layer on a silicon solar cell which is strained (stretched or compressed) by the much stronger and stiffer silicon when the temperature is varied. Strain loading due to changes in temperature is also referred to as thermal loading.

Stress and strain loading is illustrated by the two simplified examples shown in Figure 9.8-1. In Figure 9.8-1a, a bar is stress-loaded by a force. The stress in the bar is unaffected by yielding. In Figure 9.8-1b, the same bar is rigidly clamped at its ends and is subjected to an increase in temperature, ΔT . If the bar were unrestrained, it would increase in length by $\alpha \Delta T L_0$, where α is the thermal coefficient of expansion. The rigid clamping, however, causes a stress, σ , to be developed which would cause a mechanical compression of the unrestrained bar to its restrained length, L_0 . From Eq. 9.7-16, $\sigma/E = -\sigma \Delta T$ or $\sigma = -E\alpha \Delta T$. As the temperature increases to a value where the thermally induced stress exceeds the elastic strength of the bar, the bar begins to yield. This yielding tends to limit the stress in the bar so that failure does not occur even if the computed stress (using an elastic stress analysis) equals or exceeds the bar's ultimate strength.

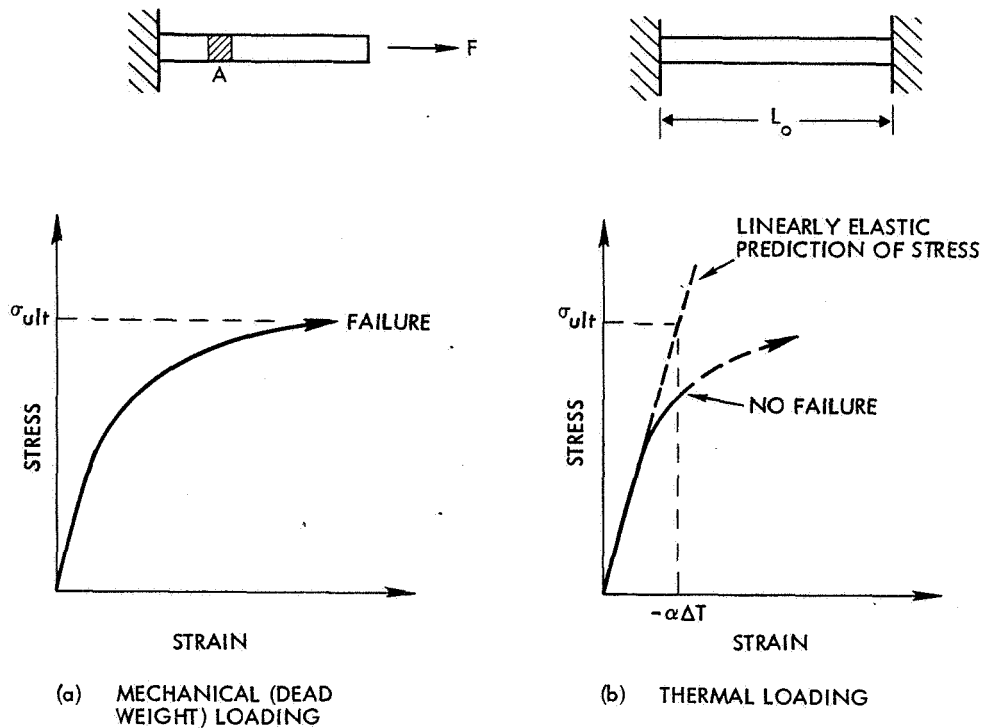


Fig. 9.8-1. Comparison of Mechanical and Thermal Loading with Plasticity

While Figure 9.8-1 illustrates that a member in a mechanically loaded structure is subjected to a given force while a member in a thermally loaded structure is subjected to a given deformation or strain, in actual solar cell and array applications a combination of stress and strain loading exists. Nevertheless, solder coatings, solar cell contacts and solar cell/interconnector joints, even when designed properly, are predominantly loaded by thermally induced strain. Additional stress loading may occur in improperly designed arrays (see Section 5.3).

9.8.3 Fatigue of Materials

In recent years, there have been an increasing number of design cases in which fatigue lives in the thousands rather than the millions of cycles must be accepted and some yielding is required to be endured by the structure. Soldered and welded joints on silicon solar cells operating in geosynchronous orbit are examples where yielding occurs during part of the time. Other cases in which some yielding cannot be avoided are found in heated pressure vessels, nuclear reactor components, and gas turbines. These applications have resulted in a greatly increased emphasis on "low cycle" fatigue or fatigue with relatively large strains and plasticity. For these cases, it has been found that the critical parameter which determines the fatigue life is the strain range, rather than the stress or load range. Thus, as proposed by Manson (Refs. 9.8-5 and 9.8-6), the fatigue life can be expressed implicitly by the empirical formula

$$\Delta\epsilon = D^{0.6} N_f^{-0.6} + 3.5 \frac{\sigma_u}{E} N_f^{-0.12} \quad (9.8-1)$$

where

$\Delta\epsilon$ = total strain range (double amplitude)

N_f = number of cycles to failure

σ_u = material ultimate strength

E = Young's modulus

D = "ductility" or true fracture strain = $\ln 1/(1 - R)$

R = reduction in area.

The first term in the equation represents the contribution of the plastic strain (D being the failure strain for a single cycle) and is the predominant factor for short lives and large strains, while the second term represents the contribution of the elastic strain (σ_u/E being the "elastic" failure strain) and is predominant for large values of N_f . Notice that this equation indicates that a single material may perform differently at the two ends of the fatigue scale. For a good fatigue life at low strain levels, a high value of ultimate strength is required, while for a high fatigue life at large strains a large value of ductility or ultimate plastic strain is required.

Extensive experimental results reported in Ref. 9.8-7 on a wide variety of materials have indicated surprisingly good correlation with this equation. Typical results shown for silver in Figure 9.8-2 indicate that the plastic strain predominates for fatigue

lives of less than 1000 cycles, while the elastic strain predominates for fatigue lives greater than 20,000 cycles with the crossover point occurring at about 10,000 cycles. This is typical of most materials. Thus the plastic strain component predominates for most fatigue lives of interest in solar cell array analysis.

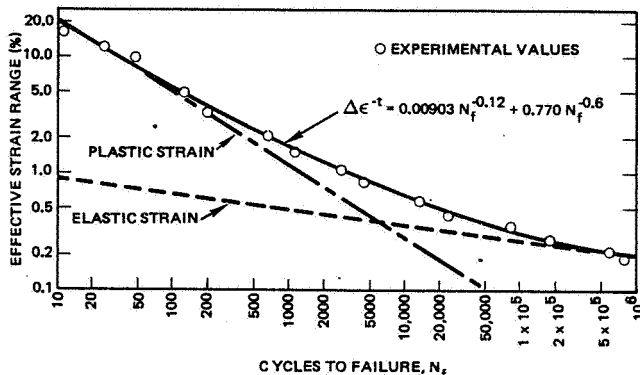


Fig. 9.8-2. Fatigue Life of Silver as a Function of Effective Strain Range (Ref. 9.8-7)

Figure 9.8-3 shows the fatigue of 36/62/2 solder computed in Ref. 9.8-8 for 20°C and -180°C using Eq. 9.8-1. Also shown are room temperature experimental fatigue results obtained in Ref. 9.8-9 for 5Sn/95Pb solder. The room temperature values for solder are essentially identical with the results for silver (Figure 9.8-2). The computed results for the fatigue life at -180°C show a major reduction due to the decreased value of solder ductility at this low temperature. The fatigue life of silver at -180°C would not be similarly affected since its ductility remains unchanged as the temperature is reduced. The reduction of the fatigue life of solder joints cycled to -180°C would not be expected to be as great as shown by the lower curve of Figure 9.8-3 since only a portion of the cycles would occur at that temperature.

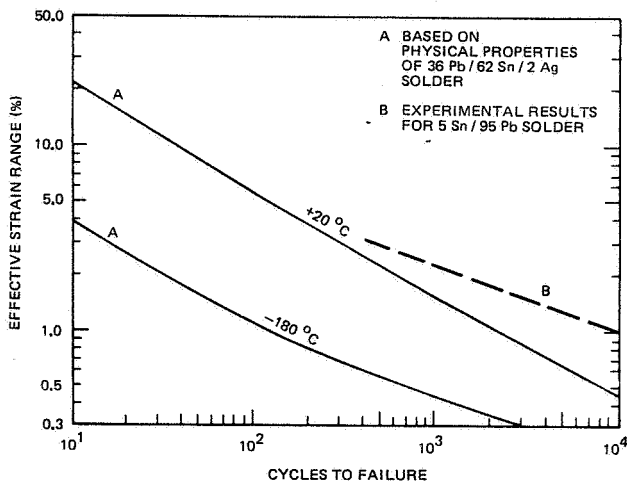


Figure 9.8-3. Fatigue Life of Solder Predicted by Method of Universal Slopes (Mechanically Cycled at Constant Temperature; Curve A per Ref. 9.8-8, Curve B per Ref. 9.8-9)

These experimental results were obtained with uniaxial loading where $\Delta\epsilon$ refers to the strain in the loading direction. For the case of multiaxial loading such as occurs in solder joints, Manson (Ref. 9.8-5) has suggested that, by analogy with the use of effective stresses and strains for plastic stress analyses (see Section 9.7.1), the axial strain range, $\Delta\epsilon$, be replaced by the effective strain range, $\Delta\bar{\epsilon}$:

$$\Delta\bar{\epsilon} = \frac{1}{\sqrt{2(1+\nu)}} \sqrt{(\Delta\epsilon_1 - \Delta\epsilon_2)^2 + (\Delta\epsilon_2 - \Delta\epsilon_3)^2 + (\Delta\epsilon_3 - \Delta\epsilon_1)^2} \quad (9.8-2)$$

where $\Delta\epsilon_i$ are the three principal strains. Several investigations (Refs. 9.8-10 and 9.8-11) have obtained good experimental confirmation of this proposal.

The results discussed above were obtained by mechanically loading the specimens, that is applying external forces to the specimens. This leaves the question as to whether these results are applicable to structures subjected to thermal loading. Manson and Coffin (Refs. 9.8-12 and 9.8-13) attacked this problem and concluded that the mechanically obtained data could be used to compute the fatigue life of a thermally loaded structure when the mechanical properties over the temperature range were similar to those for the mechanical tests. In making this calculation, the computed mechanical strains (strains due to stresses) were used in the calculations. Thermal strains alone do not have an influence on the fatigue life of a chemically stable material.

A second major result of the studies of the low cycle, high strain stress-strain behavior of the material is that the initial stress-strain behavior of the material is modified by strain cycling. It is well known that materials can be strain hardened by loading beyond the yield stress in one direction. However, due to the so-called Bauschinger effect the yield stress for loading in the reverse direction is generally reduced. After continued cycling though, the material develops a symmetrical stress strain behavior which may either be softer or harder than the initial condition. Typically, materials in the hardened condition are softened while materials in the annealed condition are hardened. Thus, it would be expected that solder would be hardened by strain cycling; however, what would happen due to a combination of strain and thermal cycling is unknown. It has been suggested by Manson (Ref. 9.8-5) that strain cycled properties obtained at the mean of the temperature range be used. Thus, for a thermal cycle between +100°C and -180°C, the values at -40°C would be used. Although this is a reasonable assumption for materials whose properties do not vary over the temperature range of interest, it appears questionable for a material like solder whose properties vary quite radically with temperature.

9.8.4 Application to Solar Cell Arrays

Fatigue analyses using the above procedure were made in Ref. 9.8-14 for welded joints between various silver plated interconnector materials and silver contacts on silicon solar cells. The analysis was performed using the SASS III elastic plastic finite element computer program (Ref. 9.8-15) assuming the weld was circular and using the axisymmetric option. The interconnectors were 25 μm thick with 5 μm of silver plating on each side, while the silicon was 254 μm thick with a single side 3 μm thick plating of silver. The results are shown in Figures 9.8-4, 9.8-5 and 9.8-6.

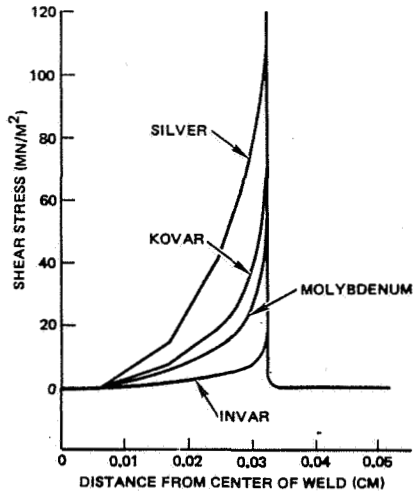


Fig. 9.8-4. Comparison of Shear Stresses for Various Interconnector Materials

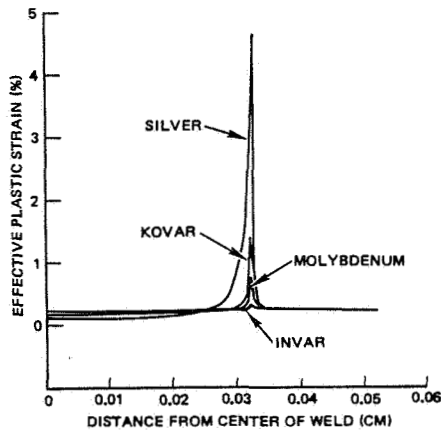


Fig. 9.8-5. Comparison of Effective Plastic Strains for Various Interconnector Materials

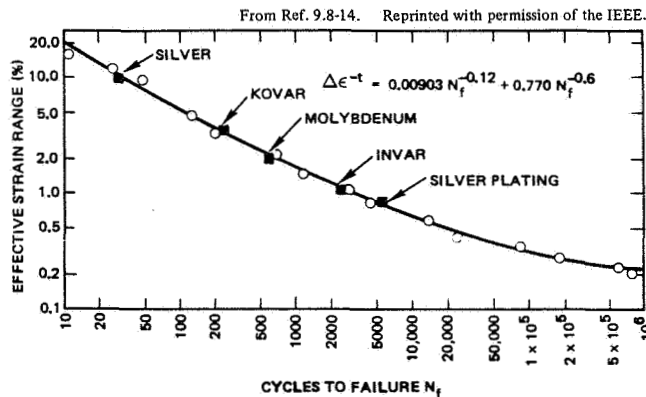


Fig. 9.8-6. Computed Fatigue Lives for Various Interconnector Materials Superimposed on Experimental Data of Ref. 9.8-12 (Ref. 9.8-14)

Figure 9.8-4 shows the variation of the shear stress in the silver across the joint for the various materials for a temperature range of 100° to -196°C. For this temperature range the silver plating on the silicon has yielded so that the effective stiffness of the silver in the joint area is equal to the plastic modulus of the silver rather than to its elastic modulus. This accounts for the fairly wide distribution of the shear stress which would not have resulted from a purely elastic analysis as indicated in Section 9.7-2. Figure 9.8-5 shows the effective plastic strain distribution while Figure 9.8-6 shows the computed values for the fatigue life of the interconnector joints and of the silver plating itself. These results show the considerable fatigue life improvements for Invar and molybdenum interconnectors, compared to silver and to a lesser extent Kovar, which results from the better match between their thermal coefficients of expansion and that of silicon. Silver weld joints are quite sensitive to the thermal match because of the relative thinness of the silver plating compared to the interconnector. Similar results for soldered joints with the same interconnector thickness indicate decreased sensitivity to the interconnector material and more dependence on the solder properties due to the increase in the proportion of solder thickness to the interconnector thickness.

Temperature cycling test results of solar cell array assemblies have shown that the observed fatigue life of soldered and welded joints is significantly greater than the computed fatigue life. There are several reasons for this:

- Failure of fatigue test specimens is typically defined as the onset of cracking, while for solar cell assemblies failure is usually defined as complete joint separation which may cause electrical discontinuity.
- Deposited thin layers of metals may possess different material properties than rolled stock
- The fatigue test results obtained for fatigue test specimens at constant temperature are most likely not directly related to fatigue failures which are induced by large temperature excursions during which the material properties may vary considerably.
- The test atmosphere may have influenced the test results. The empirical fatigue data upon which the analyses was based was obtained by mechanical cycling in a standard atmosphere while solar cell thermal cycling testing was performed in a nitrogen-rich atmosphere. Ref. 9.8-16 and 9.8-17 indicate that the presence of oxygen causes a significant reduction in the fatigue strengths of copper and lead, respectively.

The methods of analyzing the fatigue life of a solar cell array are complex and still need development. However, even without highly accurate results, a fatigue analysis indicates the importance of additional factors beyond those involved in a static analysis, i.e., material yield strength, ductility, cycle strain hardening, or softening, and sensitivity to atmosphere influencing and the resultant readjustment of stresses under cyclic loading. Thereby, fatigue analyses can make a significant contribution to the ultimate performance of the structural design of a solar cell array.

9.9 RELIABILITY ANALYSIS

Solar array reliability analysis is a statistical tool with which one hopes to compute the probability that the array will, after a given length of time in orbit, provide a given amount of electrical output. By 1976, this goal had only partially been reached. Typical reliability analyses as executed today and reported in the literature are concerned with expected and potential random failure mechanisms, wearout phenomena and other, naturally occurring phenomena of a statistical but macroscopic nature which may, in time and when having occurred in certain combinations or frequencies, potentially reduce the available power from the array in excess of the degradation which is predicted due to the reasonably well-known space environment (such as radiation damage, etc.). What has not been included in such reliability analyses are microscopic failure mechanisms and uncertainties in both the environment itself and in the environment-caused degradation of materials and components. Nevertheless, present-day reliability analyses can be excellent tools to aid the array designer to both compare the expected performance of alternate design approaches as well as to determine the weakest link in his chain of design elements.

9.9.1 Definitions

The calculated reliability, R , of a solar cell array is equal to the calculated probability of success, p_s , for the array to produce a given power output at a given time, t , after launch. The power output is that expected after the naturally occurring array output degradation due to charged particle and other environmentally induced mechanisms has taken place. The probability of success is related only to component, material, and joint failures (soldered or welded) including:

- Joint open-circuit failures
- Solar cell short-circuit and open-circuit failures
- Blocking diode short-circuit and open-circuit failures
- Wire cable and connector short-circuit and open-circuit failures.

Each joint or component is assumed to have a certain failure rate, λ , given in units of "number of failures per operating hour" or in units of "bits." A failure rate of "one bit" is defined as 1×10^{-7} failures per solar cell operating hour.

Alternately, the failure rate, λ , may be given in units of "number of failure per temperature cycle" and the time, t , may be given in units of "temperature cycles."

Components and joints are typically assumed to fail in such a fashion that the probability of success, p_s , (i. e., the reliability) of each component or joint is related to the operating time, t , by

$$p_s = R = e^{-\lambda t} \quad (9.9-1)$$

where

e = base of the natural logarithm

λ = failure rate

t = operating time (or number of temperature cycles as appropriate)

The probability of failure, p_f , is given by

$$p_f = 1 - p_s \quad (9.9-2)$$

For two independent failure mechanisms operating on a system or component, the reliability can be expressed as:

$$R = e^{-[\lambda_1 d + \lambda_2 (1-d)]t} \quad (9.9-3)$$

where the terms not yet defined are:

λ_1, λ_2 = two different failure rates

d = duty cycle factor* ($0 \leq d \leq 1$)

As an example, Eq. 9.9-3 would be applicable for cases where one failure rate would apply for temperature-cycling-induced failures while the other failure rate would relate to operating time at the upper equilibrium temperature.

9.9.2 Failure Modes and Effects

Reliability analysis deals essentially with failure modes, failure effects and failure rates. As an illustrative example, consider a small, oriented array consisting solely of two solar cells in parallel by 10 cells in series. Let each group of two paralleled cells be electrically interconnected. Let the only failure mode be solar cell open-circuit failure (cell fracture or contact strip lifting), occurring at some rate. The effect of the first cell failure is a reduction in array output by very nearly one-half (Section 9.3.2). A second cell failure may cause one of two effects, depending upon where this failure occurs. If it occurs in the paralleled cell adjacent to the already failed cell, the array output drops to zero; however, if it

fails anywhere else on the array, no additional output losses occur. It can be seen that if a large number of failure modes, each having its peculiar failure rate, are postulated, failure effects can become quite complex and interrelated. A large number of potential failure modes can indeed be listed and they have actually been observed in ground testing of solar cell arrays. Orbital array performance, however, seems to indicate that the failure rates of these failure mechanisms are typically orders of magnitude lower than observed in ground testing. Practically, therefore, most failures can be lumped into a single "open cell" failure mode with a very low failure rate compared with the failure rates of other components.

The predominant failure mode of solar cell circuits is the open-circuit failure of soldered or welded electrical joints. (Short-circuit failures are rare and are usually the result of correctable manufacturing deficiencies.) The effect of solar cell open-circuit failures may be severe.

For this reason, circuits are generally designed with multiple strings paralleled at the cell level. In physical terms this means that submodules, composed of two or more cells soldered or welded to a common interconnector (usually at the positive contact of n/p silicon cells), are electrically wired in series to form modules. The modules, which may consist of 10 to 20 submodules, are then connected in series to obtain the total required series dimension for the solar cell circuit.

The rationale for this practice is that if electrical connection between any two series cells is lost due to an open-circuit failure, the remaining cells of the affected submodule will each carry a portion of the current of the string containing the open-circuited cell, thereby mitigating the effect of the failure. In general, the power lost due to an open-circuit cell failure decreases as the number of parallel cells in the submodule increases. The capability of the unfailed cells of an affected submodule to carry additional current depends upon the short-circuit currents and the reverse leakage current characteristics of the unfailed cells, and the array voltage available to reverse-bias the unfailed cells. (The capability may also be limited by the ability of the unfailed cells and their electrical connections to dissipate the heat produced when they are reverse-biased as discussed in Section 8.7.2.)

Figure 9.9-1 shows the percentage of solar array power lost as a function of the percentage of cells failed due to random open-circuits for a circuit composed of 10 parallel strings of 42 three-cell submodules in series (1260 cells total). It is seen that even with paralleling at the submodule level, a relatively large power loss results from a relatively small number of open-circuited cells. For example, with 0.08 percent cells failed (one cell) the array power output is reduced by 3.3 percent.

The following assumptions were used in the analysis which produced the results shown in Figure 9.9-1.

- A cell "open" is defined as one which exhibits an infinite impedance which results in a 100 percent cell power loss.
- The first cell failure in any series string (three cells in parallel) produces a 1/3 power output loss from the string. (This is equivalent to a 1/3 current loss at the constant bus voltage.)

- An additional cell failure in the same series string, but not in the same submodule, has no additional effect on power output.
- An additional cell failure in the same series string and in the same submodule produces an additional 1/3 power loss.
- A cell with a power loss less than 100 percent is defined as a cell with a corresponding short-circuit current loss but an unchanged I-V curve shape.
- The general effect of a partial cell failure on power loss is to reduce power by the product of the partial percentage loss and the 1/3 factor.

The analysis consisted of the following steps:

- 1) Each cell was assigned a number from the range of 1 to 1260.
- 2) Using a random number generator, each cell was associated with a failure event.
- 3) As each cell was removed from the circuit the power loss was assessed according to the assumptions stated above.
- 4) Figure 9.9-1 was plotted. Power losses of less than 3.3 percent were obtained by the direct ratio of 3.3 percent power loss per 0.08 percent failures.

Another aspect of reliability concerns the number of soldered or welded connections made to each solar cell. Figure 9.9-2 shows the relationship between the number of connections per cell and the percentage of open joints for cells of a string composed of single cells. From the figure it is clear that, within reasonable bounds, as the reliability goal on the joint failure rate increases, the number of joints per cell must also increase.

Additional examples of solar cell array failure modes and effects are described in Section 5.2.2 of this handbook and by Ref. 9.9-1.

9.9.3 Failure Rates

Solar cell failure rates have not been well established because the failure rates are too low to be measured accurately. The orbital performance of solar cell arrays has indicated that the most likely open-circuit failure rates in orbit are on the order of 1 bit (i. e., one solar cell fails in an open-circuit mode for every 1×10^9 solar cell operating hours).

Temperature cycling ground test data has been used by Ref. 9.9-1 to compute the array reliability. The potential drawback of using ground test data is that such data may represent early-cycle or so-called "burn-in" failure rates that may not be related to wearout failure rates. (For a discussion of burn-in and wearout failure rates, see Ref. 9.9-2.)

9.9.4 Reliability Models

Reliability models are logic block diagrams that represent hardware "systems" in terms of mission success. Let the system, S, be defined by one or more pieces of equipment, or parts, or elements of parts, A, B, C, ... Let the probability of success

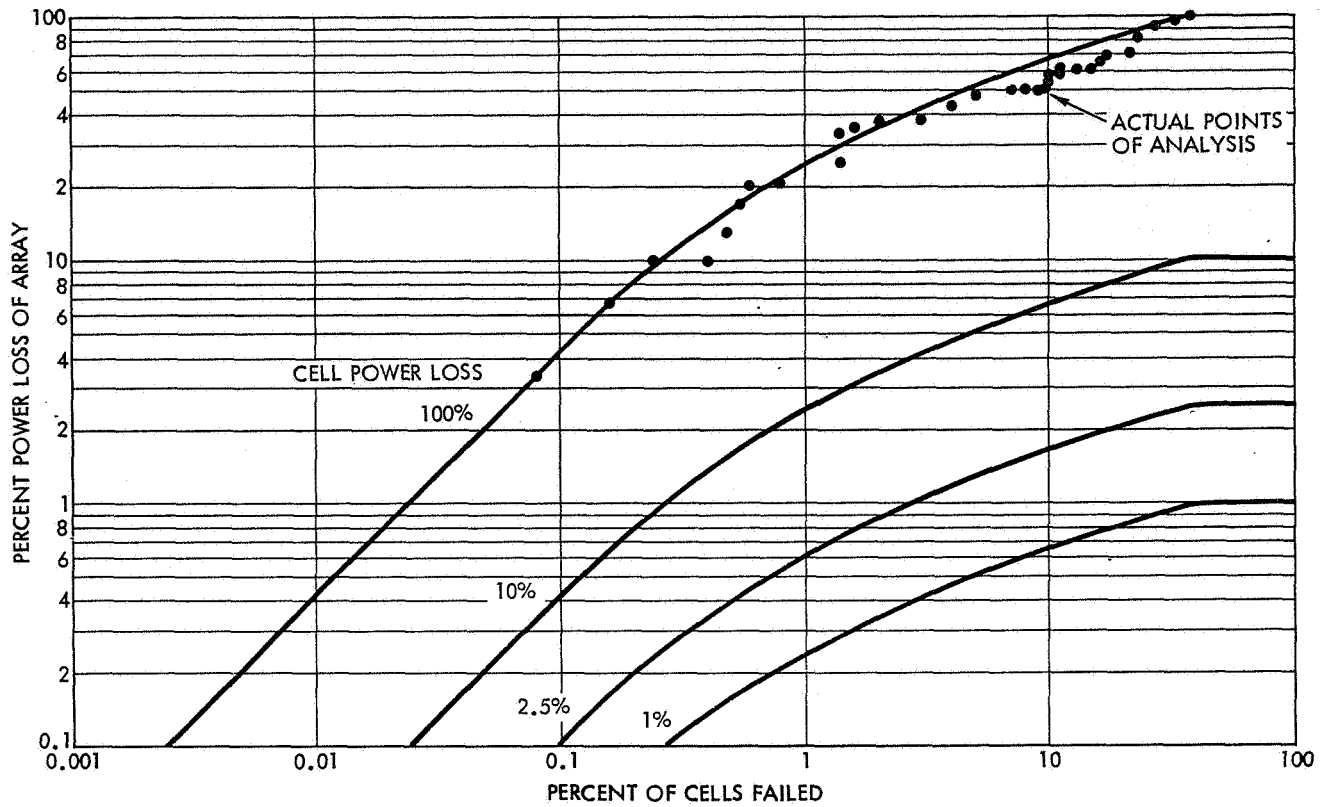


Fig. 9.9-1. Solar Cell Array Power Loss Due to Random Cell Open-Circuit Failures (100% Cell Power Loss) or Cell Fractures (1%, 2.5%, 10% Power Loss) (Illustrative Example)

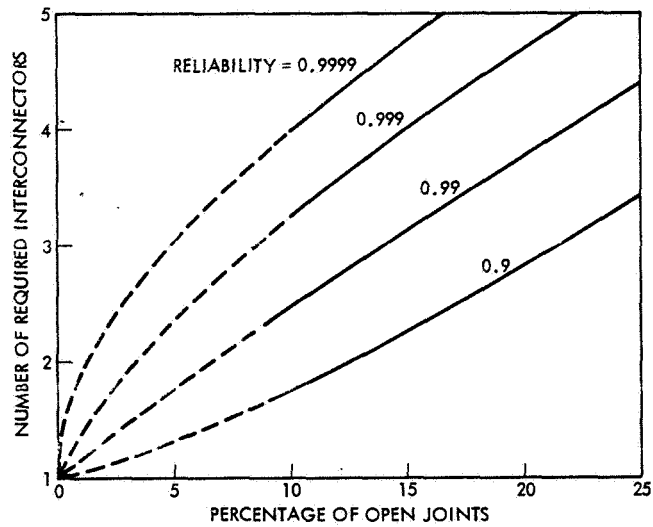


Fig. 9.9-2. Required Number of Interconnectors (Fig. 5.2-13b) Per Solar Cell to Meet Specific String Reliabilities When the End-of-Life Percentage of Open Joints is Known (Illustrative Example)

of the system be defined by P_S and that of the parts by P_A, P_B, P_C, \dots . The system probability of success is as given below for a number of different systems illustrated in Figure 9.9-3 (based on Ref. 9.9-2). The derivation of the so-called survival equations is based on the fact that the system's probability of success depends upon both the probability of mission success with each component operating and the probability of mission success with any component failed. For example, for the second system illustrated in Figure 9.9-3 (two parts in series), the probability of mission success is

$$P_S = P_{SAW} \cdot P_A + P_{SAF} \cdot P_{Af} \quad (9.9-4)$$

where

P_{SAW} = probability of mission success with A working

P_{SAF} = probability of mission success with A failed

P_{Af} = probability of A failing

Since $P_{SAW} = P_B$ and $P_{SAF} = 1 - P_A$, Eq. 9.9-4 becomes

$$P_S = P_B \cdot P_A + 0 \cdot (1 - P_A) = P_A P_B$$

As another example of the derivation of the survival equation, consider the fourth reliability diagram in Figure 9.9-3 (two parts in parallel). The symbols are as defined for Eq. 9.9-4, however, their values are different:

$$P_S = P_{SAW} \cdot P_A + P_{SAF} \cdot P_{Af} \quad (9.4-5)$$

$$= 1 \cdot P_A + P_B (1 - P_A)$$

$$= P_A + P_B - P_A P_B$$

Actual solar cell array models are composed of many detailed reliability diagrams and the survival equations become quite complex. One such analysis is illustrated in detail by Ref. 9.9-1.

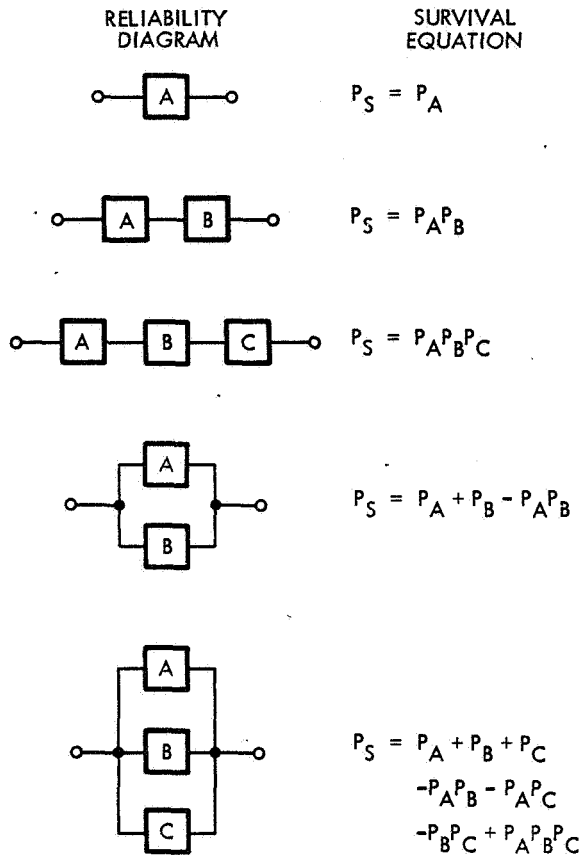


Fig. 9.9-3. Reliability Models for System Mission Probability of Success, P_S

9.10 ORBITAL MECHANICS

Accurate knowledge of orbit and attitude (orientation) is essential to the achievement of proper spacecraft and solar cell array design and performance. However, the prediction and analysis of precise orbital characteristics is complex and lengthy, requiring sophisticated, computerized analytical procedures. Orbital analyses are usually performed by mission analysts and attitude control system designers, and their results are typically available for the solar cell array designer.

This section provides the solar cell array designer with sufficient basic knowledge of orbital mechanics to accomplish the following:

- Permit him to effectively interface with orbital analysts, mission planners, and spacecraft system designers.
- Illustrate the nature and problem of orbital analysis as it affects the design of the solar cell array and its orientation mechanism.
- Furnish the array designer with simplified analytical tools with which he can obtain approximate answers.

9.10.1 Definitions

After launch, a spacecraft may be in powered or unpowered flight, depending upon whether or not a rocket propulsion system accelerates the spacecraft. The flight path of a spacecraft is known as its orbit. Frequently, but not universally, closed-loop flight paths are termed orbits while open-loop flight paths are called trajectories.

Orbital Terminology

When under power, the spacecraft usually is on a spiralling type of path. When unpowered, the flight path can be described (to a first-order approximation) by a conic section. A conic section would describe the flight path accurately if the spacecraft would be subject only to the gravitational forces from the planet or other celestial body, known as the central body, it is intended to orbit or pass. In practice, however, other celestial bodies exert gravitational forces, the sun exerts solar radiation pressure (especially on spacecraft having area-to-mass ratios greater than approximately $2.5 \text{ m}^2/\text{kg}$), and at lower altitudes (below 475 km above the earth, aerodynamic drag exerts forces on spacecraft that perturb a purely conic-section orbit. Spacecraft orbits about the earth are also perturbed by the earth's non-spherical mass distribution and by electromagnetic forces (both due to interactions between the earth's magnetic field with electromagnetic fields produced by current loops on the spacecraft, and due to electrostatic charging of the spacecraft in the space plasma) in addition to the gravitational forces exerted by the sun and the moon.

A spacecraft in an elliptic orbit around a central body reaches its lowest or highest altitude at an apsis (the plural of apsis is apsides). The point nearest the central body is periapsis and the farthest point is apoapsis. A line drawn between periapsis and apoapsis, called the line of apsides, lies in the orbit plane and passes through the center of the central body. The apsides of an earth orbit are called perigee and apogee, those of a solar orbit are called perihelion and aphelion, and those of a lunar orbit are called perilune and apolune.

Time Definitions

The determination of time in a chronometric sense is dependent upon the reference system in which the time is measured. During any one year, the revolutions of the earth about its axis and about the sun is neither uniform nor in a plane called the celestial equator (see Section 9.10.3), so that a true solar day is of variable length. A fictitious mean sun, moving uniformly along the celestial equator, is therefore used for establishing the mean solar time. A true solar year is of the same length as a mean solar year.

The earth is divided into 24 time zones, each being bounded (with local exceptions) by meridians at 15-degree intervals. The conventional time in each zone is the civil time. Astronomers usually use universal time (UT), also known as Greenwich mean solar time.

One complete revolution of the earth, as measured on the celestial sphere (see Section 9.10.4), is defined as one sidereal day or 24 hours of sidereal time. However, since the earth rotates about the sun, one day later the earth must have rotated through a little more than one complete revolution if the day is to be related to sunset and sunrise. Hence, a solar day or 24 hours of apparent solar time, are about four minutes longer than a sidereal day.

The period between successive perihelion passages of the earth is called an anomalous year. Its length is 365.259641 mean solar days. The time required for the earth to complete one revolution about the sun is called one sidereal year. The length of a sidereal year is 365.256360 mean solar days. A tropical year is defined as the period between successive passages of the mean sun through the mean equinox; its length is 365.242198 mean solar days. A more detailed discussion of various time systems and their correlation with ephemeris times is contained in Ref. 9.10-1.

The length of a civil (or Gregorian) calendar year is 365 mean solar days, except for leap years which have 366 days. Leap years are civil years (counted A. D., or anno domini) that are exactly divisible by 4, except when they end in two zeros, unless they are exactly divisible by 400.

9.10.2 Simplified Orbit Theory

Simplified orbit theory is concerned with the description of the orbits of two bodies about each other, without consideration of perturbations of the orbits by the actions of other forces. Perturbations are of significance to satellite mission planners and attitude control system designers, but are usually negligible for solar cell array design work.

Energy and Momentum

After launch, a space vehicle accelerates away from the earth. At some time after launch, the booster or propulsion stage will burn out or will be shut down and the spacecraft will be released from the remaining launch vehicle. After release, the spacecraft will possess kinetic energy, E_k , and potential energy, E_p , given by

$$E = E_k + E_p = mv^2/2 - \mu m/r \quad (9.10-1)$$

where

- m = spacecraft mass
- v = spacecraft velocity
- r = distance between the spacecraft and the center of earth
- $-\mu$ = gravitational parameter. The minus sign is based on the convention that the potential energy of a body is zero if it is at infinity.

The gravitational parameter is defined for the earth by

$$\mu = Gm_e \quad (9.10-2)$$

where

- G = Universal Gravitational constant
- m_e = mass of the earth

In the absence of drag forces or additional propulsion efforts (from the attitude control system, for example), the energy of the spacecraft will be conserved (i. e., will remain constant with time).

The moving spacecraft also possesses momentum which is conserved throughout the spacecraft's life. Linear momentum of a point mass m is defined as mv and angular momentum as $mr^2\omega$ where r is the distance of the point mass from a center and ω is the angular velocity. The tangential velocity of the rotating point mass is ωr , pointing in a direction perpendicular to r . For a satellite in an elliptic orbit about a central body (illustrated in Figure 9.10-1), the angular momentum is given by

$$H = mrv \cos\phi \quad (9.10-3)$$

where

- m = satellite mass
- r = satellite-center of central body distance (see Figure 9.10-1), along the local vertical

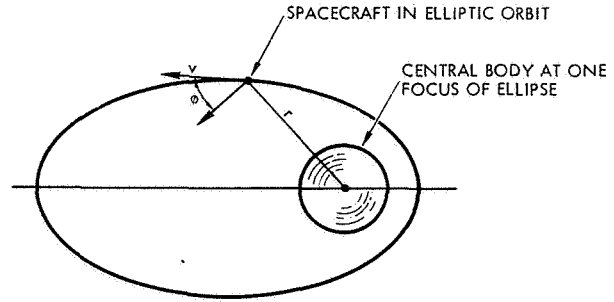


Fig. 9.10-1. Definitions for Angular Momentum

v = tangential satellite velocity (same as in Eq. 9.10-1)

ϕ = angle between the tangential velocity vector (direction of velocity) and the normal to r , also known as the local horizontal.

The spacecraft energy E and angular momentum H will determine the orbit altitude (more correctly the distance r) as a function of time. The orbital relationship is given by Kepler's first law which, when applied to spacecraft, states that spacecraft will describe (closed) circular or elliptic orbits about central bodies if they are permanently associated with them (i. e., when their velocity is lower than the escape velocity for the particular central body, or they will describe (open) parabolic or hyperbolic orbits if they are not permanently associated with them.

Kepler's first law can be stated mathematically by the so-called "vis viva" or "energy" equation:

$$v^2 = \mu \left(\frac{2}{r} - \frac{1}{a} \right) \quad (9.10-4)$$

where

- v = velocity of the spacecraft
- μ = defined by Eq. 9.10-2
- r = as defined previously
- a = semimajor axis as defined in Figure 9.10-2.

For a circular orbit $r = a$ and Eq. 9.10-4 reduces to

$$v_c^2 = \mu/r \quad (9.10-5)$$

where v_c is known as the circular velocity. When the spacecraft possesses the escape velocity, v_e , the orbit becomes a parabola with $a = \infty$:

$$v_e^2 = 2\mu/r \quad (9.10-6)$$

The orbital parameters (illustrated in Figure 9.10-2) are related to spacecraft energy and angular momentum as follows:

$$a = -\mu/2E \quad (9.10-7)$$

$$b^2/a = H^2/\mu \quad (9.10-8)$$

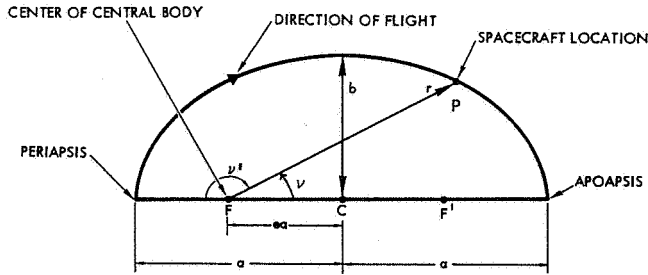


Fig. 9.10-2. Geometry of the Ellipse (One-half of Ellipse Shown for Illustration)

where

- a = semimajor axis
- b = semiminor axis
- μ = defined by Eq. 9.10-2
- E = defined by Eq. 9.10-1
- H = defined by Eq. 9.10-3.

The eccentricity of the ellipse, e , is geometrically related to a and b as follows:

$$e^2 = 1 - b^2/a^2 \quad (9.10-9)$$

Closed Orbits

Satellite orbits follow the same laws as planetary orbits. From the work of Isaac Newton and Johannes Kepler, we know that orbiting satellites describe circular or elliptic orbits in a plane (the orbital plane) about a central body (planet or sun) with the central body being at the center of the circle or at one focus of an ellipse. (Circular orbits are simply a special case of elliptic orbits whose eccentricity equals zero.)

A satellite in an elliptic orbit about a central body describes a path as illustrated in Figure 9.10-2 and given by

$$r = \frac{a(1 - e^2)}{1 - e \cos \nu} \quad (9.10-10a)$$

where all symbols are as defined previously and

ν = angle between apoapsis and P, known as the true anomaly

If the angle is measured from periaapsis, Eq. 9.10-10 becomes

$$r = \frac{a(1 - e^2)}{1 + e \cos \nu} \quad (9.10-10b)$$

(For analytical convenience note that $1 - e^2 = (1 + e)(1 - e)$ and that one of these terms cancels with the denominator if $\nu = 0$ or $\nu = \pi$.)

In this handbook only simple orbits about the earth and the sun are described. For a discussion on interplanetary trajectories see Ref. 9.10-2. For additional discussions of elementary closed orbits see Refs. 9.10-3 and 9.10-4.

Orbit Period

The period of a satellite in an elliptic orbit is measured by the time between successive passes of a characteristic point on the orbit (such as periaapsis). From Newton's formulation of Kepler's third law, the period, T , is related to the semi-major axis by a constant:

$$T^2 = ka^3 \quad (9.10-11)$$

where

$$k = 4\pi^2/\mu \quad (9.10-12)$$

Eq. 9.10-11 shows that the period is independent of the orbit eccentricity.

Open Orbits

Equations for parabolic and hyperbolic orbits are given in Refs. 9.10-5 and 9.10-6. A complete discussion of orbits as conic sections is given in Ref. 9.10-7.

9.10.3 Altitude in Elliptic Orbit

The altitude of a spacecraft (as a function of time) in an elliptic orbit may be of interest to a solar cell array designer for estimating the solar cell radiation damage (described in Section 9.11). Ordinarily, this information would be available from the orbital analyst assigned to the same project. However, in the absence of such data, the array designer may have to perform his own analysis.

The relationship between time and position in orbit is given by Kepler's second law which states that a straight line between the centers of the two bodies orbiting each other (in any closed or open orbit) sweeps out equal areas in the orbital plane in equal intervals of time. Letting the incremental area swept out in incremental time dt be denoted by dA ,

$$\frac{dA}{dt} = \frac{r^2}{2} \frac{d\nu}{dt} = \text{constant} \quad (9.10-13)$$

where r is given by Eq. 9.10-10. The solution of transcendental Eq. 9.10-13 must be obtained by numerical or graphical methods. From the solution, the altitude, h , is found from

$$h = r - R \quad (9.10-14)$$

where r is given by Eq. 9.10-10 and R is the mean radius of the idealized spherical earth.

Analytical Aid

Eq. 9.10-13 can be solved numerically, for example, using the following procedure and a digital computer; the program can be written easily:

- a) Divide the half-ellipse of Figure 9.10-2 into n sectors of equal area, each sector having an area of

$$A_n = \pi ab/2n \quad (9.10-15)$$

- b) Note that the area of each sector is given by

$$A_n = \int_a^b \frac{1}{2} r^2 d\nu \quad (9.10-16)$$

where r is given by Eq. 9.10-10. Utilizing a digital computer, numerically integrate Eq. 9.10-16 by incrementing ν in small steps, starting from $a = 0$ to such a value of b where A_n approximately equals the value of A_n computed by Eq. 9.10-15. Also compute the corresponding values of r and h . Next let $b = a$ and repeat the process until the areas and values of h for all n segments are computed. The values of b thusly determined (while ν is varied from 0 to π radians) are separated by n equal time intervals.

- c) Divide the orbit period T into n equal time intervals and plot h versus successive time intervals, or tabulate the results for further use.

9.10.4 Location in Space

The location of a spacecraft in three-dimensional space requires both the definition of a coordinate system and the description of the spacecraft position within that coordinate system. Hence, six parameters are required to uniquely determine the location of the spacecraft.

One important property of a coordinate system is that it is inertial (i.e., nonrotating in time, but free to translate). For mathematical correctness, heliocentric, geocentric, or other coordinate systems are in use, their choice depending upon the problem to be solved. For orbits about the sun, a heliocentric system is the obviously preferred choice, while for earth orbits a geocentric system is preferred.

The Geocentric Coordinate System

For the purpose of discussion of spacecraft in earth orbits (and in conformance with general practice), let us define a celestial sphere of infinite radius whose center coincides with the center of the earth. All celestial bodies are projected onto the surface of the celestial sphere as they appear in the sky as seen from the earth. A plane of infinite extent through the earth's equator (the equatorial plane) defines the celestial equator on the celestial sphere.

Let the origin of the geocentric coordinate system be located at the center of the immovable, but spinning earth (daily rotation), and let the X and Y-axes lie in the equatorial plane. The Z-axis then is coincident with the earth's spin axis. Also, let the X-axis point toward the first point of Aries, a point on the celestial sphere that originally pointed to, but is now displaced by an angle of about 30 degrees from the constellation Aries. The first point of Aries is now defined by the line of intersection between the earth's equatorial plane with the ecliptic plane, also known as the line of equinoxes or the line of nodes. The resulting coordinate system is shown in Figure 9.10-3.

In the coordinate system defined by Figure 9.10-3, the sun will orbit the earth counter-clockwise in the ecliptic plane and will cross the X-axis at vernal equinox. The angle, ϵ , between the equatorial and ecliptic planes is constant.

A spacecraft in orbit about the earth moves in the orbit plane. The line of intersection between the orbit and equatorial planes is called the line of ascending nodes. The angle subtended by the line of ascending nodes and the X-axis, measured counter-clockwise in Figure 9.10-3, is known as the argument (angle) of the right ascension or, in short, the right ascension, Ω . The angle between the orbital and equatorial planes is the orbit inclination, i_a .

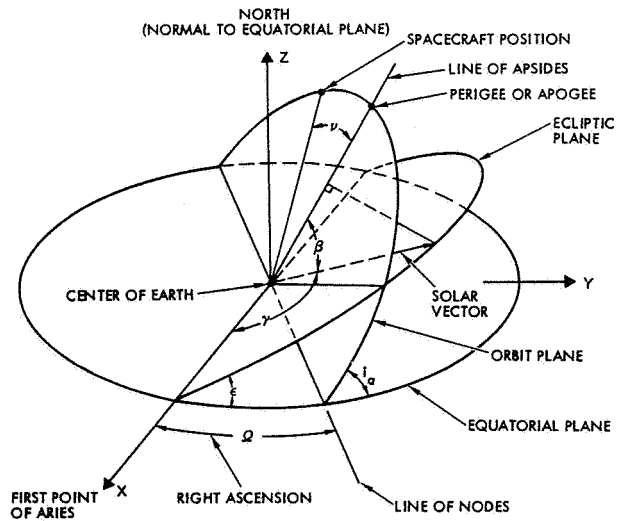


Fig. 9.10-3. Geocentric Equatorial Coordinate System

Of the many different sets of six parameters that can describe the position of a spacecraft in space, the following is a convenient set:

- Orbit inclination, i_a
- Orbit semimajor axis, a
- Orbit eccentricity, e
- Right ascension, Ω
- Epoch time, t_0
- Argument of perigee, ν .

The first and fourth parameters are defined above, and the second and third parameters are defined in Section 9.10.2. The epoch (instant of time) may be any arbitrary point in time, t_0 , from which significant events are counted. Some examples of epoch are: launch date and time, time when passing perigee, or time when passing the ascending node.

The argument of perigee is the angle measured in the orbital plane from perigee to the line from the center of the earth to the spacecraft known as the local vertical. This angle is the same as ν in Figure 9.10-2 and is related to time as shown in Section 9.10.3. A plane perpendicular to the local vertical is known as the local horizontal.

Orbit Inclination

A spacecraft launched from a launch site, located at L degrees latitude, at an azimuth angle of A degrees (i.e., the vehicle's heading measured clockwise from true north) will enter an orbit whose plane is inclined i_a degrees to the equatorial plane such that

$$\cos i_a = \cos L \sin A \quad (9.10-17)$$

For Cape Kennedy $L = 30^\circ\text{N}$ and for Vandenberg $L = 35^\circ\text{N}$, approximately. For range safety reasons, however, not all values of A are permissible, so that some orbit plane inclinations must be obtained by special maneuvers.

The orbit plane inclinations determine the movement of the line of ascending nodes (known as precession) as follows, when the North pole is viewed from the star Polaris:

<u>Inclination (degrees)</u>	<u>Orbit Type</u>	<u>Precession</u>
0	Equatorial	Counter-clockwise
$0 < i_a < 90$	Posigrade	Counter-clockwise
90	Polar	Stationary
$90 < i_a < 180$	Retrograde	Clockwise

9. 10. 5 Illumination of the Orbit Plane

The angle of incidence of the sunlight on the orbit plane is of interest to the conceptual solar cell array designers and constitutes a significant driving function for defining the array's geometric configuration and sun orientation mechanism.

The angle of sunlight incidence on the orbit plane, β , is defined as the geocentric angle between the so-called solar vector (the earth-sun line) and the local vertical (spacecraft-earth center line) in the orbit plane when the spacecraft is closest to the sun (orbit noon).

The angle β is given by

$$\sin\beta = A(B \sin\gamma \cos\Omega - \cos\gamma \sin\Omega) - C \sin\gamma \quad (9. 10-18)$$

where

$$A = \sin i_a$$

$$B = \cos\epsilon$$

$$C = \cos i_a \sin\epsilon$$

γ is defined below

and β is positive when the sun is seen from the earth to lie above (north of) the orbit plane (see Figure 9. 10-3). A more precise equation for β is given in Refs. 9. 10-8 through 9. 10-11.

The orbit plane inclination, i_a , and the ecliptic plane inclination, ϵ , were defined previously. The sun central angle, γ , is measured in the ecliptic plane from the X-axis to the earth-sun line, and is approximately given by Table 9. 10-1. The rate of change of γ due to the earth's rotation about the sun (or the sun's rotation about the earth as defined in Figure 9. 10-2), is denoted by $d\gamma/dt$ and is given approximately by

$$d\gamma/dt = 360/365.24 = 0.98565 \text{ degrees per day} \quad (9. 10-19)$$

If γ is related to a specific angle γ_0 at time t_0 (such as the launch or equinox), γ is given at a later time t by

$$\gamma = \gamma_0 + (t - t_0) \frac{d\gamma}{dt} \quad (9. 10-20)$$

The angle of the right ascension, Ω , decreases with time, mainly due to effects caused by the earth's oblateness. The time rate of change of Ω is given approximately for circular earth orbits by

$$\frac{d\Omega}{dt} = \frac{JR^2 \mu^{1/2} \cos i_a}{(R+h)^{7/2}} \quad (9. 10-21)$$

and for elliptic earth orbits by

$$\frac{d\Omega}{dt} = \frac{JR^2 \mu^{1/2} \cos i_a}{a^{7/2} (1-e^2)^2} \quad (9. 10-22)$$

where

$J = 1.624 \times 10^{-3}$, the dimensionless, general coefficient of gravitational harmonics

$\mu = 3.986 \times 10^5 \text{ km}^3 \text{ s}^{-2}$, the product of the universal gravitational constant and the mass of the earth

and all other symbols are as previously defined.

At time t after the launch (or other epoch) time, t_0 ,

$$\Omega = \Omega_0 + (t - t_0) \frac{d\Omega}{dt} \quad (9. 10-23)$$

When Eqs. 9. 10-21 or 9. 10-22 are expressed with $d\Omega$ a function of dt and the orbital period T per Eq. 9. 10-11 substituted for dt , the resulting angle increment $\Delta\Omega$ gives the regression in degrees longitude between successive orbits. For example, Eq. 9. 10-22 becomes

$$\Delta\Omega = - \frac{2\pi J \cos i_a}{(a/R)^2 (1-e^2)^2} \quad (9. 10-24)$$

Examination of Eq. 9. 10-18 reveals that β varies cyclically at a relatively rapid rate between limits that vary at a slower rate. The rapid rate is due to $d\Omega/dt$ and is of peak-to-peak magnitude $|\beta| = 2|i_a|$. The slower rate is due to $d\gamma/dt$ and determines the variation of the cyclical limit band for β between an upper limit of $(i_a + \epsilon)$ at winter solstice and $(i_a - \epsilon)$ at summer solstice. At the vernal and autumnal equinoxes, the limit band restricts β to the range of $\beta = \pm i_a$.

The largest or smallest values of β for certain values of γ and Ω may be found by differentiating Eq. 9. 10-18 with respect to each of these angles and setting the results equal to zero. The corresponding values of γ and Ω for which β is a maximum (or minimum), denoted by the subscript " β_m ", can be found from

$$\tan\Omega_{\beta m} = -(B \tan\gamma)^{-1} \quad (9. 10-25)$$

$$\tan\gamma_{\beta m} = \frac{C - AB \cos\Omega}{A \sin\Omega} \quad (9. 10-26)$$

Special Cases

Equatorial and sun-synchronous orbits constitute two special cases that illustrate the variation of β during 1 year. For equatorial orbits,

$$i_a = 0 \text{ and}$$

$$\beta = \sin^{-1} (\sin\epsilon \sin\gamma)$$

Table 9.10-1. Calculated Values of the Sun Central Angle

Season (Northern Hemisphere)	Approximate Starting Date	Duration (days)	Approximate Calendar Day, t (day)	Approximate Sun Central Angle, γ (deg)	Solar Declination (deg)
Spring	21 March (Vernal Equinox)	92.77	79.4	0.0	0.0
Summer	21 June (Summer Solstice)	93.50	172.2	88.0	+23.44
Autumn	23 September (Autumnal Equinox)	89.85	265.7	183.4	0.0
Winter	22 December (Winter Solstice)	89.12	355.6	271.0	-23.44
TOTAL		365.24			

The variation of β during 1 year is from $-\epsilon$ to $+\epsilon$ or from -23.44 degrees to $+23.44$ degrees. The variation of β during one orbit is zero. For polar orbits,

$$i_a = 90^\circ \text{ and}$$

$$\beta = \sin^{-1} (\cos \epsilon \sin \gamma \cos \Omega - \cos \gamma \sin \Omega)$$

By selecting a combination of the orbital parameters a and e , one may hope to achieve $d\gamma/dt = d\Omega/dt$ (see Eqs. 9.10-19, 9.10-20, and 9.10-21 for definition). If γ_0 and Ω_0 (Eqs. 9.10-20 and 9.10-23) could be made equal, a sun-synchronous orbit with β varying according to $\beta = \sin^{-1} (0.0413 \sin 2\gamma)$, or between ± 2.3 degrees, would result. In practice, such sun-synchronous orbits can be achieved only for relatively low-altitude circular orbits with inclinations between 92 and 112 degrees and the variation in β being correspondingly larger. Spacecraft in sun-synchronous orbits, also known as constant sunlight orbits, may or may not be subject to eclipses due to the earth's shadow, depending upon the combinations of the orbital parameters.

Table 9.10-2. Solar Cell Array Degrees-of-Freedom

Number of Spacecraft Axes	Number of Array Axes	Array Degrees-of-Freedom	Maximum Range of θ (degrees)
0	0	0	± 180
1	0	1	$\pm \beta$
2	0	2	0 to $\pm \beta$
3	0	3	0
0	1	1	$\pm \beta$
1	1	2	0 to $\pm \beta$
2	1	3	0
0	2	2	0 to $\pm \beta$
1	2	3	0
0	3	3	0

9.10.6 The Sun Angle

The sun angle, θ , was defined in Section 9.4.4 as the angle between the spacecraft-sun line and a central axis (or spin axis) of the solar cell array, measured in a plane defined by the spacecraft-sun line and the spacecraft central axis. Once the sun angle, θ , is known, the angle of illumination (i. e., the angle between the solar vector and the outward normals to the solar cell array surfaces) can be determined by the formulas given in Section 9.4.4.

The sun angle, θ , is determined by the degrees-of-freedom of the solar cell array orientation capability. The degrees-of-freedom are determined by the number of axes about which the array can be rotated as illustrated in Table 9.10-2. Obviously, any three-degree-of-freedom orientation methods can achieve the desired condition of $\theta = 0^\circ$.

To illustrate the relationships between θ and the orbit characteristics, consider the spacecraft with a two-degrees-of-freedom array in Figure 9.10-4. For convenience, let the earth-pointing spacecraft roll axis be coincident with the local vertical, and let the array articulation axis lie in the orbit plane.

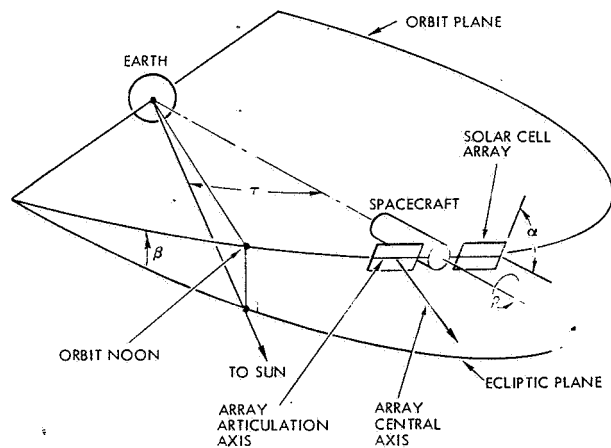


Fig. 9.10-4. Definition of Geometry for Determination of Sun Angle, θ , Between Sun Line and Array Central Axis.

spacecraft location be given by the position angle, τ , measured in the orbit plane in the direction of the spacecraft motion from orbit noon (the point on the orbit path which is closest to the sun). (In the special case illustrated in Figure 9.10-3, orbit noon is coincident with one of the apsides and $\tau = \nu$, where ν is defined by Eq. 9.10-10.) For this spacecraft/array configuration the sun angle is related to the other angles by

$$\cos\theta = (\cos\alpha \cos\rho \sin\beta + \sin\alpha \cos\tau \cos\beta - \cos\alpha \sin\rho \sin\tau \cos\beta) \quad (9.10-27)$$

where

- α = array articulation angle between the array central axis (pointing away from the earth) and the local horizontal
- β = illumination angle of the orbit plane as defined in Section 9.10.5
- ρ = spacecraft roll angle ($\rho = 0$ when the array articulation axis lies in the orbit plane, increasing counter-clockwise when viewed in the direction of the roll axis toward the earth)
- τ = angle from solar noon as described above

Eq. 9.10-27 degenerates into simple expressions for some frequently used array configurations and orientation methods as illustrated in the following. Greater details of the effects of the yaw, pitch, and roll angles in relation to solar cell array orientation are given in Refs. 9.10-4, -10, -11, and -12. Additional discussions of spacecraft and array coordinate systems are given in Refs. 9.10-13 through 9.10-15.

For body-mounted, spinning arrays in equatorial orbits, with the spin axis perpendicular to the orbit plane and pointing northward,

$$\cos\theta = \sin\beta$$

With the spin axis pointing toward the earth along the local vertical,

$$\cos\theta = \cos\beta \cos\tau$$

For oriented, one degree-of-freedom arrays in equatorial orbits, the central axis is pointed into the direction of the sun (but not necessarily directly at the sun) and the tracking mechanism maintains this pointing direction. (Example: the array rotates about an axis through the spacecraft while the spacecraft orientation (pitch, roll, and yaw) is not available to aid in the array orientation.) For this case

$$\theta = \beta$$

9.10.7 Solar Eclipses

Whenever the earth moves into the spacecraft-sun line, the solar illumination of the solar cell array is

interrupted. The length of time of this interruption, known as the solar eclipse (or occultation) time, depends upon the orbit altitude and the β -angle as defined in Figure 9.10-3 (discussed in Section 9.10.5). Defining a fraction of sun time in orbit, f , as

$$f = t_1/T \quad (9.10-28)$$

where t_1 is the time of illumination and T is the orbit period according to Eq. 9.10-11. For circular orbits

$$f = \frac{1}{2} + \frac{1}{\pi} \sin^{-1} \left\{ \frac{[1 - (R/a)^2]^{1/2}}{\cos\beta} \right\} \quad (9.10-29)$$

where R and a are as defined in Sections 9.10.2 and 9.10.3, and β is given by Eq. 9.10-18.

Figure 9.10-5 shows the variation of f (expressed in percent rather than in fractional form) with orbit altitude and β . A detailed method for calculating the fractional sun time for elliptic orbits is given in Ref. 9.10-16.

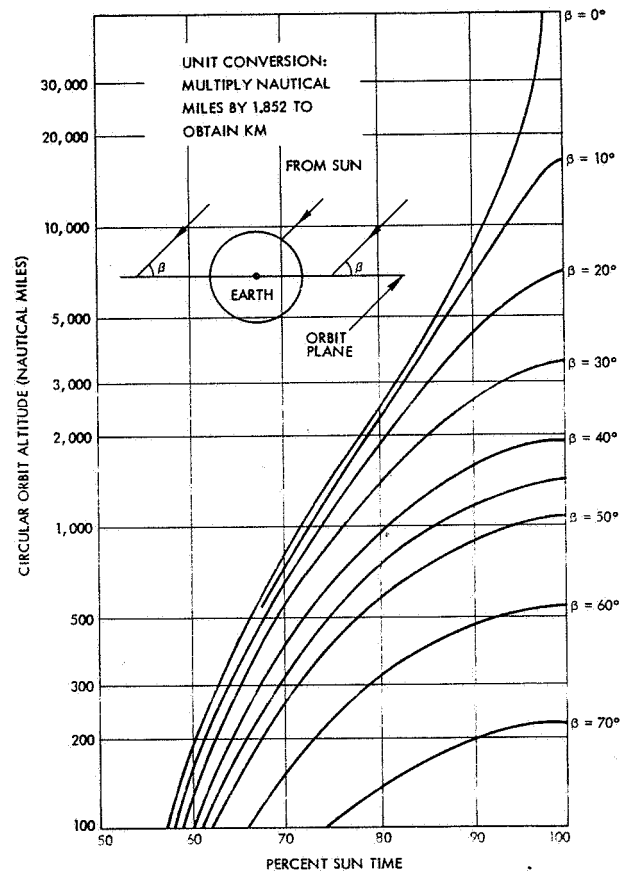


Fig. 9.10-5. Percent Sun Time as a Function of Altitude and Sun Angle for Circular Orbits

9.11 1-MeV FLUENCE DETERMINATION

The radiation environment of significance to solar cell arrays, described in greater detail in Section 2.5 (The Space Radiation Environment), consists of the following:

- Geomagnetically trapped electrons
- Geomagnetically trapped protons
- Solar flare protons
- Solar flare alpha particles
- Man-made hostile radiation environments
- Ultraviolet radiation.

These environments may degrade the array performance during any or all of the following operational conditions:

- Transfer orbits
- Parking orbits
- Operational orbits.

The concept of the 1-MeV fluence and its application to the prediction of solar cell damage in charged particle radiation environments is defined in Section 3.3.2.

This section constitutes a procedure for estimating the approximate solar cell damage equivalent, normally incident (DENI), 1-MeV fluence, abbreviated in the following as "1-MeV fluence."

9.11.1 General Procedure

The 1-MeV fluence must be determined for specific front and back shielding thicknesses because:

- The shielding effectiveness changes with the incident radiation particle type and particle energy
- The mix between different particles as well as their energy distributions change with orbit altitude and orbit inclination.

Different 1-MeV fluence values arise for each shielding thickness from the environment. Table 9.11-1 provides a convenient format for recording and summing of the computed 1-MeV fluence values. For conceptual design work, the determination of the fluence values for P_{mp} and V_{mp} suffices. However, for detailed design work, the same fluence components shown on Table 9.11-1 should also be determined for I_{SC} (see Section 3.3.2 for a discussion of the different 1-MeV fluence values).

The general procedure for estimating the solar cell damage equivalent 1-MeV fluence is as follows:

- Determine the required inputs (Section 9.11-2).

- Determine the 1-MeV fluence components as defined in Table 9.11-1, entering the solar cell from the front side for infinite back side shielding (Sections 9.11.3 through 9.11.5).
- Determine the 1-MeV fluence components entering the solar cell from the back side for infinite front side shielding (Sections 9.11.3 through 9.11.5).
- Enter all 1-MeV fluence components in Table 9.11-1 and sum up.

Table 9.11-1. Tabulation of 1-MeV Fluence Components

ORBIT	PARTICLES	1 - MeV FLUX ($e \cdot cm^{-2} \cdot yr^{-1}$)		1 - MeV FLUENCE ($e \cdot cm^{-2}$)	
		FRONT	BACK	FRONT	BACK
<u>TRANSFER</u>	TRAPPED ELECTRONS				
	TRAPPED PROTONS				
	<u>ORBITS</u> SUBTOTAL				
<u>ON-STATION</u>	TRAPPED ELECTRONS				
	TRAPPED PROTONS				
	FLARE PROTONS				
<u>YEARS</u> SUBTOTAL					
<u>OTHER</u>					
	SUBTOTAL				
TOTAL	SUM VERTICALLY				
GRAND TOTAL	FRONT + BACK	X	X	X	X
<u>SHIELD THICKNESS</u>		NOTES:			
FRONT: _____		1. FOR THE SHIELDING EFFECT BY THE SOLAR CELLS, SEE SECTION 8.3.3.			
BACK: _____		2. FOR COMPUTING SHIELD THICKNESS, REFER TO SECTION 8.3.2.			

Detailed methods for accurately computing the various 1-MeV fluence components are given in the Solar Cell Radiation Handbook, Ref. 9.11-1.

9.11.2 Analysis Inputs

The information required to prepare an estimate of the solar cell-damaging 1-MeV fluence is typically available from the cognizant project office, mission planners or satellite system designers. The minimum information required is as follows:

a) Requirements for All Missions

- Launch date (affects solar flare proton fluence)

- Mission duration (defines end-of-mission, EOM)
- Characteristics of transfer or parking orbits
- Number of transfer or parking orbits
- Design data as shown below in "d."

b) Additional Requirements for Earth Orbits Only

- Apogee (farthest point from earth)
- Perigee (nearest point to earth)
- Inclination (angle between the orbit plane and the earth's equatorial plane).

c) Additional Requirements for Interplanetary Probes Only

- Array-sun distance variation with time after leaving parking orbit.

d) Design Data

An additional required input is the solar cell front and back side shield thicknesses. The method for calculating the equivalent shield thickness is given in Section 8.4.

9.11.3 Circular Earth Orbits

The 1-MeV fluence in circular earth orbits is due to the following charged particles:

Approximate Altitude Range (km)	Radiation Particles
0 to 250	Negligible
250 to 1600	Trapped electrons and protons
1600 to 50,000 (includes synchronous altitude of 35,786)	Trapped electrons and solar flare protons and alpha particles
Above 50,000	Solar flare protons and alpha particles

The value of the 1-MeV fluence for a particular shield thickness due to each of the most significant radiation particle types can be determined from the following:

- For an approximate estimate – from Section 2.5.8
- For an accurate estimate – from the appropriate tables in the Solar Cell Radiation Handbook, Ref. 9.11-1.

Synchronous Orbit

The 1-MeV fluence as a function of front shield thickness (for infinite back shield thickness), shown in Figure 9.11-1, was calculated based on the AE-4 electron model and the "Aerospace solar flare proton model described in Section 2.5.5 (Radiation at Synchronous Altitude). The 1-MeV fluence components for I_{sc} and P_{max} are defined in Section 3.3.2 (Damage Equivalent 1-MeV Fluence).

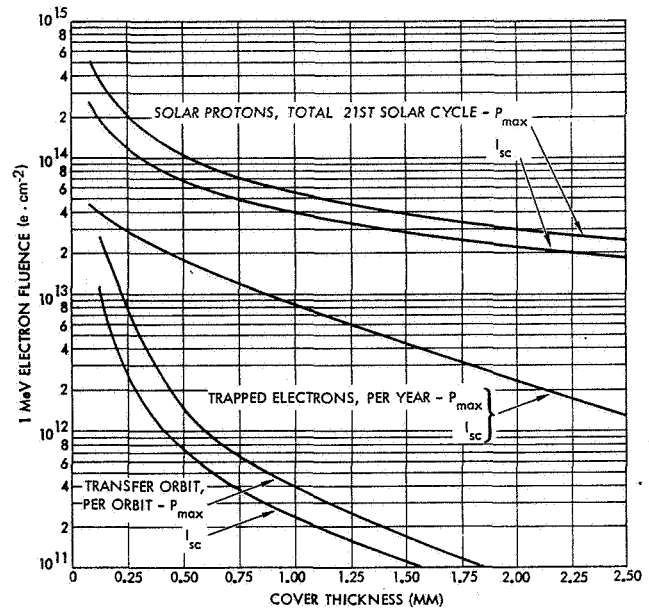


Fig. 9.11-1. Solar Cell DENI 1-MeV Fluence After Penetration of a Fused Silicon Cover of Given Thickness

9.11.4 Elliptic Earth and Transfer Orbits

The total 1-MeV fluence in elliptic and spiral (transfer) orbits, ϕ_T , can be determined from

$$\phi_T = \int_0^T \phi(h) h(t) dt \quad (9.11-1)$$

where

$\phi(h)$ = 1-MeV fluence at altitude h as given approximately in Section 2.5.8 or more accurately in Ref. 9.11-1

$h(t)$ = solar cell array altitude as a function of time, t

T = time at which ϕ_T is sought; typically $T = \text{EOM}$ (end of mission).

Eq. 9.11-1 can be evaluated numerically by using one of the following two procedures:

Graphical Procedure

- a) Prepare a graph of altitude versus time, $h(t)$. The range of t is as follows:

For spiral orbits: from shroud ejection ($t = 0$) to reaching the on-station orbit ($t = T$)

For elliptic orbits: from any point in orbit ($t = 0$) through the same point for one period ($t = T$). (Note: Use Kepler's second law described in Section 9.10.3).

- b) Multiply the h values in the $h(t)$ graph from Step a) with the $\phi(h)$ values for all particles shown in Section 9.11.3 (obtain $\phi(h)$ from Section 2.5.8 or Ref. 9.11-1) to obtain a $\phi(h)h(t)$ graph.
- c) Numerically integrate under the 1-MeV fluence/time graph (either by using a planimeter, or weighing the cut-out curve, or "counting squares"). Enter the resulting data in Table 9.11-1.
- d) Repeat Steps a) through c) for all front shield thicknesses of interest assuming infinite back shielding, and for all back shield thicknesses of interest assuming infinite front shield thickness.

Tabular Procedure

Proceed as described in the graphical procedure above except instead of using a graph, prepare a table of average altitudes, \bar{h} , for constant time intervals, Δt , multiply the \bar{h} values by the $\phi(h)$ values and sum the $\phi(h)\bar{h}(\Delta t)$ tabular entries to obtain ϕ_T .

9.11.5 Interplanetary Trajectories

The 1-MeV fluence in interplanetary space is due to solar flare protons and potentially due to solar flare alpha particles only. The values of the fluence components are given in Section 2.5.6.

REFERENCES (CHAPTER 9)

9. 2-1 J. P. Kirkpatrick, et al., "A Comprehensive Computer Program for Predicting Solar Cell Performance," NASA TM X-2220, Ames Research Center, February 1971.
9. 2-2 M. Wolf and H. Rauschenbach, "Series Resistance Effects on Solar Cell Measurements," Advanced Energy Conversion, Vol. 3, Pergamon Press, 1963.
9. 2-3 R. J. Stirn, "Junction Characteristics of Silicon Solar Cells, Nonilluminated Case," NASA TM 33-557, Jet Propulsion Laboratory, August 1972.
9. 2-4 G. C. Jain and F. M. Stuber, "A Distributed Parameter Model for Solar Cells," Advanced Energy Conversion, Vol. 7, Pergamon Press, 1967.
9. 2-5 R. J. Handy, "Theoretical Analysis of the Series Resistance of a Solar Cell," Solid State Electronics, Pergamon Press, Vol. 10, 1967.
9. 2-6 From notes by N. Sheppard, General Electric Company.
9. 2-7 W. D. Brown, et al., "Computer Simulation of Solar Array Performance," Report No. SSD 70135R, Hughes Aircraft Co.
9. 2-8 W. Luft, J. R. Barton, and A. A. Conn, "Multifaceted Solar Array Performance Determination," TRW Systems Group, Redondo Beach, California, February 1967.
9. 2-9 J. Sandstrom, "A Method for Predicting Solar Cell Current-Voltage Characteristics as a Function of Incident Solar Intensity and Cell Temperature," TR 32-1142, Jet Propulsion Laboratory, July 1967.
9. 2-10 A. F. Obenshain, et al., "The Solar Array Synthesis Computer Program," N69-40246, NASA TM X-63709, X-716-69-390, Goddard Space Flight Center, September 1969.
9. 2-11 D. E. Sawyer and R. H. Rediker, Proceedings of the IRE, 46, 1122 (1958).
9. 2-12 T. E. Hartman, "Transient Photovoltaic Response of Diffused-Junction Silicon Photodiodes," Solid State Electronics, Pergamon Press, Vol. 3, pp. 127-133, 1961.
9. 2-13 D. W. Zerbel, "Fast Response Solar Array Simulator," Final Report for Contract NAS 5-11581, TRW Systems, 1968.
9. 2-14 D. W. Zerbel and D. K. Decker, "AC Impedance of Silicon Solar Cells," Proceedings of the Intersociety Energy Conversion Engineering Conference, Vol. 1, September 1970.
9. 2-15 "Nimbus-B Quarterly Technical Report No. 5, Sept-Nov 1966," Report No. R-3125, Contract NAS 5-9668, RCA Astro Electronic's Division, 1966.
9. 3-1 W. D. Brown, et al., "Computer Simulation of Solar Cell Array Performance," Report No. SSD 701 35 R, Hughes Aircraft Company.
9. 3-2 H. S. Rauschenbach, "Electrical Output of Shadowed Solar Arrays," Conference Record of the Seventh Photovoltaic Specialists Conference, IEEE, November 1968.
9. 3-3 W. Luft, "Partial Shading of Silicon Solar Cell Converter Panels," Conference Paper CP 62-204, AIEE, October 1961.
9. 3-4 F. C. Treble, "Field Tests on UK3 Solar Cell Assemblies," Technical Report No. 66112, Royal Aircraft Establishment, April 1966.
9. 3-5 R. M. Sullivan, "Shadow Effects on a Series-Parallel Array of Solar Cells," Report No. X-636-65-207, NASA/Goddard Space Flight Center, Greenbelt, Maryland.
9. 3-6 Filed patent application now pending by W. R. Baron entitled, "A Method of Reducing the Effects of Cell Shadowing on a Series/Parallel String of Solar Cells, Photovoltaic or Other Incident Energy Conversion Devices," and assigned to TRW, Inc.
9. 3-7 W. R. Baron and P. F. Virobik, "Solar Array Shading and a Method of Reducing the Associated Power Loss," Proceeding of the Fourth Photovoltaic Specialists Conference, Vol. II, PIC-SOL 209/5.1, August 1964.
9. 3-8 P. F. Virobik, "Effect of Shadows on Solar Array Output," Engineering Report No. 9361. -11-E42, TRW Systems Group, December 1964.
9. 3-9 J. R. Barton, "Power Output Analysis of Array Incorporating Shadow Diodes," Engineering Report No. 7062. 6-011, TRW Systems Group, July 1966.
9. 3-10 A. A. Conn, "Computer Computation of Shadow Effects on Solar Cell Arrays," Engineering Report No. 9361.11-E72, TRW Systems Group, December 1966.
9. 3-11 W. Luft, J. Barton, and A. Conn, "Multifaceted Solar Array Performance Determination," presented at 1967 Intersociety Energy Conversion Engineering Conference, Miami Beach, Florida, August 1967.

- 9.5-1 W. Luft, "Analysis of Shadows on Solar Arrays," Engineering Report No. 7442.6-060, TRW Systems Group, January 1968.
- 9.7-1 S. Timoshenko, Theory of Elasticity, McGraw-Hill.
- 9.7-2 B. L. Sandor, Fundamentals of Cyclic Stress and Strain, University of Wisconsin Press, 1972.
- 9.7-3 S. Timoshenko, Analysis of Bi-Metal Thermostats, Journal of the Optical Society of America, Vol. 2, pp. 223-255, September 1925.
- 9.7-4 U. U. Savolainen and R. M. Sears, "Thermostat Metals," Ch. 10; Composite Engineering Laminates, AGH Dietz, ed, MIT Press, 1969.
- 9.7-5 Milton S. Hess, "The End Problem for a Laminated Elastic Strip - II." Differential Expansion Stresses, Journal of Composite Materials, Vol. 3, pp. 630-641, October 1969.
- 9.7-6 A. C. Agerwal and M. W. Hagers, "Differential Expansion in Elastic Laminates," ASCE Journal of the Structural Division, pp. 655-663, April 1973.
- 9.7-7 E. L. Ralph and J. Roger, "Silicon Solar Cell Interconnectors for Low Temperature Applications," Solar Cells, Proceedings of the International Colloquium organized by EOSEC, Toulouse, France, July 1970.
- 9.7-8 L. W. Butterworth and R. K. Yasui, "Structural Analysis of Silicon Solar Arrays," Report No. 32-1528, Jet Propulsion Laboratory, May 1971.
- 9.7-9 J. J. Bikerman, The Science of Adhesive Joints, Academic Press, 1968.
- 9.7-10 L. J. Hart-Smith, "Adhesive-Bonded Lap Joints," NASA CR 112236, Douglas Aircraft Co., McDonnell Douglas Corporation, January 1973.
- 9.7-11 W. J. Renton and J. R. Vinson, "The Analysis and Design of Composite Material Bonded Joints Under Static and Fatigue Loadings," AFOSR-TR-73-1627, Department of Mechanical and Aerospace Engineering, University of Delaware, August 1973.
- 9.7-12 M. A. Salama, R. M. Rowe, and R. K. Yasui, "Thermoelastic Analysis of Solar Cell Arrays and Their Mechanical Properties," TM 33-626, Jet Propulsion Laboratory, September 1973.
- 9.8-1 M. A. Salama, R. M. Rowe, and R. K. Yasui, "Thermoelastic Analysis of Solar Cell Arrays and Their Mechanical Properties," TM 33-626, Jet Propulsion Laboratory, September 1973.
- 9.8-2 H. J. Grover, "Fatigue of Aircraft Structures," NAVAIR 01-1A-13, 1966.
- 9.8-3 P. J. E. Forsyth, "The Physical Basis of Metal Fatigue," American Elsevier, New York, 1969.
- 9.8-4 S. S. Manson, "Fatigue a Complex Subject - Some Simple Approximations," Experimental Mechanics, pp. 193-226, July 1965.
- 9.8-5 S. S. Manson, Thermal Stresses and Low Cycle Fatigue, McGraw-Hill, 1966.
- 9.8-6 L. F. Coffin, "Design Aspects of High Temperature Fatigue with Particular Reference to Thermal Stresses," Transactions ASME, pp. 527-532, April 1956.
- 9.8-7 R. W. Smith, M. A. Hirschberg, and S. S. Manson, "Fatigue of Materials Under Strain Cycling in Low and Intermediate Life Range," TN D-1574, NASA, April 1963.
- 9.8-8 D. J. Curtin and W. U. Billerbeck, Development of Advanced Interconnectors for Solar Cells, Comsat Technical Review, Vol. 4, No. 1, pp. 53-68, 1964.
- 9.8-9 H. S. Rathose, R. C. Yeh, and A. R. Edenfeld, "Fatigue Behavior of Solders Used in Flip-Chip Technology," ASTM Journal of Testing and Evaluation, Vol. 1, pp. 170-178, March 1973.
- 9.8-10 J. L. Mattavi, "Low Cycle Fatigue Behavior Under Biaxial Strain Distribution," ASME Journal of Basic Engineering, pp. 23-31, March 1969.
- 9.8-11 S. Y. Zamrick and J. Goto, "The Use of Octahedral Shear Strain Theory in Biaxial Low Cycle Fatigue," Proceedings of the Int. American Conference on Materials Technology, San Antonio, Texas, Sponsored by Southwest Research Institute, and ASME, pp. 551-562.
- 9.8-12 Manson, S. S., "Behavior of Materials Under Conditions of Thermal Stress," NACA Rep 1170, 1954.
- 9.8-13 Coffin, L. F., Jr., "A Study of the Effects of Cyclic Thermal Stresses on a Ductile Metal," Transactions ASME, Vol. 76, No. 6, pp. 931-950, August 1954.
- 9.8-14 A. Kaplan, "Fatigue Analysis of Solar Cell Welds," Proceedings of the 10th IEEE Photovoltaic Specialists Conference, pp. 281-286, November 1973.
- 9.8-15 J. G. Crose and R. M. Jones, "SAAS III Finite Element Stress Analysis of Axisymmetric and Plane Solids with Different, Orthotropic Temperature Dependent Material Properties in Tension and Compression," SAMSO-TR-71-103, June 1971.
- 9.8-16 N. J. Wadsworth and J. Hutchings, "The Effect of Atmosphere Corrosion on Metal Fatigue," Philosophical Magazine, Vol. 3, pp. 1154-1166, 1964.
- 9.8-17 K. U. Snowdon, "The Effect of Atmosphere on the Fatigue of Lead," ACTA Metallurgica, Vol. 12, pp. 295-303, March 1964.
- 9.R-2

- 9.10-1 F. T. Geyling and H. R. Westerman, Introduction to Orbital Mechanics, Addison-Wesley, Reading, Massachusetts, 1971.
- 9.10-2 H. F. Lesh, "Determination of Interplanetary Trajectories," Technical Memorandum 33-414, Jet Propulsion Laboratory, November 1968.
- 9.10-3 K. A. Ehricke, Spaceflight, Vol. I, "Environment and Celestial Mechanics," Van Nostrand, Princeton, 1960.
- 9.10-4 J. M. A. Danby, Fundamentals of Celestial Mechanics, MacMillan, New York, 1962.
- 9.10-5 R. W. Wolverton, ed., Flight Performance Handbook for Orbital Operations, John Wiley, New York, 1961.
- 9.10-6 J. Jensen, et al., Design Guide to Orbital Flight, McGraw-Hill, New York, 1962.
- 9.10-7 R. M. L. Baker, Jr., et al., An Introduction to Astrodynamics, Academic Press, New York, 1960.
- 9.10-8 The American Ephemeris and Nautical Almanac, Washington, D. C., published annually.
- 9.10-9 L. G. Stoddard, "Eclipse of Artificial Earth Satellites," Astronautic Sciences Review, April-June 1961.
- 9.10-10 W. W. Hough and B. D. Elrod, "Solar Array Performance as a Function of Orbital Parameters and Spacecraft Attitude," Journal of Engineering for Industry, February 1969.
- 9.10-11 W. E. Allen, "Design and Analysis of Solar Cell Array Configurations for Vertically Stabilized Satellites in Near-Earth Orbits," Technical Memorandum TG-1066, The Johns Hopkins University (Applied Physics Laboratory), August 1969.
- 9.10-12 Olsca: Orientation Linkage for a Solar Cell Array, Technical Report AFAPL-TR-68-76, July 1968.
- 9.10-13 A. L. Greensite, Analysis and Design of Space Flight Control Systems, Vol. XII, "Attitude Control in Space," NASA CR-831, August 1967.
- 9.10-14 M. B. Tamburro, et al., Guidance, Flight Mechanics and Trajectory Optimization, Vol. I, "Coordinate Systems and Time Measure," NASA CR-1000, February 1968.
- 9.10-15 L. A. Pipes, Matrix Methods for Engineering, Prentice-Hall, Englewood Cliffs, New Jersey, 1963.
- 9.10-16 F. G. Cunningham, "Calculation of the Eclipse Factor for Elliptical Satellite Orbits," ARS Journal, December 1962.
- 9.11-1 J. R. Carter, Jr. and H. Y. Tada, "Solar Cell Radiation Handbook," TRW Systems Group, Redondo Beach, California (under NASA Contract NAS 7-100), chs 5 and 6, June 1973.

CHAPTER 10
DESIGNING FOR PRODUCTION AND COST

CONTENTS

	Page		Page
10.1 Impact of the Design on Project Costs	10.1-1	10.4.7 Soldering by Inducting Heating	10.4-3
10.1.1 The Final Design: Specifications, Procedures, and Drawings	10.1-1	10.4.8 Parallel-Gap Resistance Welding	10.4-3
10.1.2 The Final Design Review	10.1-1	10.4.9 Thermocompression Joining	10.4-4
10.1.3 Composition of Fabrication Costs	10.1-1	10.4.10 Ultrasonic Joining	10.4-5
10.1.4 Reducing Solar Cell and Cover Costs	10.1-1	10.4.11 Adhesive Bonding Techniques	10.4-5
10.1.5 Tolerances	10.1-2	10.5 Material and Process Specifications	10.5-1
10.1.6 Visual Defects	10.1-2	10.5.1 Typical Requirements for Adhesives	10.5-1
10.2 Specifications	10.2-1	10.5.2 Typical Requirements for Insulating Layers	10.5-1
10.2.1 Intent and Purpose	10.2-1	10.6 Specifying Quality	10.6-1
10.2.2 Types of Specifications	10.2-1	10.6.1 Design-Related Quality	10.6-1
10.2.3 Organization of Specifications	10.2-1	10.6.2 Workmanship	10.6-1
10.2.4 Requirements	10.2-2	10.7 Nondestructive Test (NDT) Methods	10.7-1
10.2.5 Quality Assurance Provisions	10.2-2	10.7.1 Quality Control by NDT	10.7-1
10.2.6 Sampling Plans	10.2-2	10.7.2 Parameters Affecting Weld Quality	10.7-1
10.3 Solar Cell, Cover and Blocking Diode Specifications	10.3-1	10.7.3 Types of NTD Methods	10.7-1
10.3.1 Typical Requirements for Solar Cells	10.3-1	10.7.4 Destructive Tests	10.7-2
10.3.2 Typical Requirements for Solar Cell Covers	10.3-2	10.7.5 Visual Inspection	10.7-2
10.3.3 Typical Requirements for Covered Solar Cells	10.3-2	10.7.6 Infrared Microscope (Augmented Visual)	10.7-2
10.3.4 Typical Requirements for Blocking Diodes	10.3-3	10.7.7 Electrode Setdown	10.7-2
10.4 Assembly Processes	10.4-1	10.7.8 Weld Pulse Monitoring	10.7-2
10.4.1 Metal Joining Techniques	10.4-1	10.7.9 Resistance Measurements	10.7-3
10.4.2 Resistance Soldering	10.4-1	10.7.10 High-Frequency Impedance	10.7-3
10.4.3 Single-point Soldering	10.4-1	10.7.11 Eddy Current	10.7-3
10.4.4 Parallel Gap Soldering	10.4-2	10.7.12 Dark-Forward Voltage Drop	10.7-3
10.4.5 Tunnel Oven Soldering	10.4-2	10.7.13 Infrared Emission	10.7-3
10.4.6 Soldering by Infrared Heating	10.4-2	10.7.14 Infrared Videography	10.7-3
		10.7.15 Acoustic Emission	10.7-3
		10.7.16 Acoustic Signature	10.7-3
		10.7.17 Ultrasonics	10.7-3
		10.7.18 Holography	10.7-4
		10.7.19 Microfocus X-ray	10.7-4
		10.7.20 NDT Inspection Systems	10.7-4
		References	10. R-1

TABLE

10-6.1 Typical Workmanship Inspection Criteria	10.6-2
--	--------

FIGURES

10.4-1	Single-Point Soldering	10.4-1	10.4-5	Parallel-Gap Weld Schedule Development Using 50 μm Thick Silver Interconnects	10.4-4
10.4-2	Parallel Gap Soldering	10.4-2			
10.4-3	Tunnel Oven Temperature-Time Profiles	10.4-3	10.4-6	Parallel-Gap Welding with Excessive Energy on N-Contact Causes Electrical Degradation Which Increases with the Number of Welds Made	10.4-5
10.4-4	Schematic of Focused Radiant Heating System	10.4-3			

CHAPTER 10

DESIGNING FOR PRODUCTION AND COST

The solar cell array designer can significantly influence the development and fabrication cost of solar cell arrays. The influence on cost which is exerted by the array design is often not recognized because it filters into the final design through a number of different, and typically unrelated, documents:

- Parts (solar cell, coverglass, etc.) specifications
- Process and material (adhesives, primers, soldering, etc.) specifications
- Solar cell layout drawings (cell spacing, wire routing, etc.)
- Solar cell interconnector design (defining manufacturing and assembly complexity) and subassembly drawings (tolerances, process control requirements, etc.)
- Workmanship criteria.

Some of the more frequently used production methods and their relationships to the design process and to the overall solar cell array cost picture are highlighted in this chapter.

Solar cell arrays are costly, and if they are of any substantial size, as is the case on most modern spacecraft, they will consume a substantial fraction of the total spacecraft project cost budget. Solar cell array costs, therefore, have been of concern to both project personnel and designers since the beginning of the space program.

Some of the avenues open to the designer for effecting cost reductions are discussed in the following sections. It is estimated that currently arrays are being fabricated at lower costs (based on an average cost per installed solar cell) than they were 10 years ago. Probably it can be said that every reasonable attempt has been made by a large group of diversely skilled individuals over the past 15 years to reduce array cost. It appears, however, that no single patent and no single method has made a major cost impact, but rather, that progress has been made slowly and continually by constantly improving designs, materials, and processes. One area where the cost improvements are visible is in the patent literature. For example, solar cell interconnector patent disclosures (see Chapter 5) praise the virtues of these interconnectors in terms of simplified and lower cost production technology, lower weight, and higher reliability.

10.1 IMPACT OF THE DESIGN ON PROJECT COSTS

10.1.1 The Final Design: Specifications, Procedures, and Drawings

The final design phase for solar cell arrays — like that for most pieces of hardware — concludes with the preparation of a set of specifications (see Section 10.2) and production drawings. From these specifications and drawings, procedures are developed that guide and direct workers and inspectors in the assembly and testing of subassemblies and assemblies.

At least some (or some parts of specifications and drawings) are either prescribed or prepared by a solar cell array designer. Thereby, the designer exercises an influence on the cost of an assembled and tested array. This influence on cost is discussed further in Sections 10.1.3 through 10.1.7.

10.1.2 The Final Design Review

The final design phase culminates in a final design review. The purpose of the review, with respect to costs, is as follows:

- To assure that all pertinent interfaces have been investigated and all interface activities have been completed, as exemplified by:
 - a) Mounting provisions (holes, etc.) of the array substrate
 - b) Connector type and location on the array
 - c) Definitions of areas on the substrate that are not available for solar cell circuits
- To assure that the design is producible, as judged by processing and assembly specialists (manufacturing engineering personnel, etc.).

The general design review process is described further in Section 8.15; specifications are discussed in Sections 10.2, 10.3, and 10.5.

10.1.3 Composition of Fabrication Costs

The solar cell array fabrication costs are very dependent upon specific designs, the quantity and size of solar cells to be assembled, and upon the specific tooling available for assembly. As an overall industry and project average for the 1970 to 1975 time frame, the cost for fabricating solar cell arrays for space use was composed of the following elements:

Material Cost	Approximately 2/3
Assembly Labor	Approximately 1/3

The material cost is primarily due to the solar cells (60 to 80 percent) and secondarily due to cover-glasses and the substrate. Cell interconnectors, wiring, and adhesive are only a small fraction of the cost.

The assembly labor portion of the cost is divided into these three major groupings:

Glassing	Approximately 1/3
Soldering and Subassembly	Approximately 1/3
Cell Installation on Panels and Wiring	Approximately 1/3

10.1.4 Reducing Solar Cell and Cover Costs

The unit cost of solar cells and solar cell covers can be reduced by any one or combination of the following:

- Solar cell and cover design standardization
- Using solar cells having less efficiency than the best state-of-the-art cells
- Using microsheet covers (Corning 0211) instead of fused silica (Corning 7940), even though microsheet exhibits greater optical losses
- Using ceria doped microsheet ultraviolet absorbing covers instead of multilayer reflecting filters on fused silica covers
- Widening the tolerances on the solar cell and cover dimensions
- Permitting a larger degree of so-called "visual" defects.

Since the early days of solar cell use in space, attempts have been made to replace the process of cutting and polishing thin wafers of glass and cementing them to the solar cells with a simpler process. However, none of the coatings directly applied to the solar cells have exhibited adequate mechanical and optical properties for space missions. Solar cell coatings which have been investigated are:

- Vacuum-deposited, thick, inorganic substances
- Sputtered glass
- Glass slurries baked on
- Organic spray-on, cement-on and heat-sealing films.

Development of such coatings, called "integral covers," is still being vigorously pursued. (Additional details are given in Chapter 4.)

10.1.5 Tolerances

The mechanical tolerances of the thickness and the outside dimensions of both the solar cell and the cover should be made no tighter than required by the following:

- Requirements to protect the cell from low energy proton and other radiation damage

- Variations in cell and cover size that can be handled by the assembly tooling
- Closeness to which the array weight must be controlled.

10.1.6 Visual Defects

Visual defects are, in part at least, nonfunctional defects but may, under certain conditions, affect array performance (see Section 8.1). It has been estimated that a 15 percent reduction in solar cell cost could be achieved by relaxing requirements for nicks, chips, discolorations, and similar imperfections (Ref. 10.1-1).

10.2 SPECIFICATIONS

10.2.1 Intent and Purpose

The intent and purpose of any specification is to clearly define what the specified article or process consists of, how it is to function, and how its operation or performance is to be verified. In the case of procurement specifications, the specification forms a part of purchasing agreements and constitutes a legally binding document. In any case, a specification is a key document that, when improperly prepared or carelessly maintained, can lead to undesirable cost impacts and/or schedule delays and, in severe cases, to costly mistakes in design, procurement, fabrication, assembly, or test.

10.2.2 Types of Specifications

The following general types of specifications are typically being used in conjunction with solar cell array design, fabrication, and test activities:

System/Subsystem Specifications

Examples are specifications for an electric power subsystem or a complete deployable solar cell array system, including deployment and stowage hardware.

Equipment Specifications

Examples are specifications for solar cell panels, solar cell arrays or lower-level subassemblies.

Interface Specifications

These documents define those functional or physical characteristics that affect the mating of two or more parts, equipment, subsystems or systems.

Environment Specifications

These specifications establish the environmental (such as temperature, vibration, etc.) requirements for design and the environmental criteria for qualification and acceptance testing.

Test Specifications

Test specifications establish specific test methods and parameters for all levels of tests performed on parts, equipment, subsystems or systems.

Assembly Specifications

These specifications establish all detailed procedures for an assembly process to assure proper functioning of the completed unit. An example is a specification for a glassed solar cell.

Part or Component Specifications

This class of specifications defines the parameters to which a purchased part or component must conform in order to be acceptable to certain procuring authority. The requirements included in such specifications should include all, and only those requirements that are necessary to assure that items purchased to the specification will satisfy the intended performance and reliability level requirements.

Material Specifications

Similar to part or component specifications, material specifications apply to purchased raw or semifabricated materials.

Process Specifications

This class of specifications establishes the acceptable property requirements of processed items and, in addition, may contain detailed requirements for the following elements:

- Materials
- Processes and Inspection Equipment
- Processing or Manufacturing Procedure
- Process Control
- Process Precautions and Special Considerations
- Inspection and Test Procedures.

In many cases, the above specifications are combined into as few specifications as is practical and many requirements are specified on drawings rather than in specifications.

10.2.3 Organization of Specifications

Typical part, component, and equipment specifications (as well as most of the other specifications listed in Section 10.2.2) are divided into the following major sections:

- Section 1. Scope

This section provides a concise abstract of the coverage of the specification.

- Section 2. Applicable Documents

This section lists all specifications, standards, drawings and publications referred to in the text of the specification.

- Section 3. Requirements

This section establishes all and only those requirements that are necessary to assure that the intended purpose, properties or performance are met within prescribed reliability or confidence limits. Requirements should be stated clearly and concisely and free from any vagueness that would require interpretation.

- Section 4. Quality Assurance Provisions

This section defines the complete and detailed provisions that assure a desired quality. There should be a corresponding test or other verification method for each requirement stated in Section 3 of the specification.

- Section 5. Preparation for Delivery

This section covers all aspects of storage, preservation, packing, labelling and marking for shipment.

- Section 6. Notes

This section contains information of a general explanatory nature. It does not contain any statement that could be construed as being contractually binding. Examples of topics are: intended use, applicability of specification, ordering data, definitions and miscellaneous notes.

10.2.4 Requirements

The requirements section of a specification should be subdivided such that each individual requirement is covered in a separate paragraph with a distinctive title. The same requirement should not be specified in two or more separate paragraphs. In general, the individual requirements are grouped as follows:

- Design, Construction and Processing Requirements
- Performance Requirements
- Chemical and Physical Properties
- Dimensional and Weight Requirements
- Color and Finish Requirements.

Each requirement should be stated such that it can be verified by a reproducible method (see Section 10.2.5).

10.2.5 Quality Assurance Provisions

The quality assurance section of a specification is generally subdivided into the following major subsections:

- Qualification
- Acceptance
- Test/Verification Methods.

The qualification and acceptance subsections define all aspects of quality assurance including the following:

- Inspection, test or other verification of raw materials, processes, assemblies, and finished items
- Responsibility for inspection, testing, and verification

- Sampling plans, fail/pass criteria, and dispositions.

The test/verification methods subsection defines the specific methods or procedures that are to be used in verifying compliance with the requirements. For each requirement specified in Section 3 of the specification, there should be a corresponding reproducible verification method in Section 4.

10.2.6 Sampling Plans

There are essentially three different sampling plans in use by solar cell component and array fabricators:

- 100 percent Inspection and Test
- AQL (Acceptable Quality Level) Sampling
- LTPD (Lot Tolerance Percent Defective) Sampling.

The 100 percent inspection and test method is used for solar cell and array output measurements and usually for solar cell array inspection and electrical output testing before and after environmental qualification and acceptance testing.

The AQL or LTPD method (Refs. 10.2-1 and 10.2-2) is usually used for the sampling testing of solar cells and other components. The AQL and LTPD sampling methods are based on different supplier and buyer risks and are related to the type of production as discussed below.

AQL Method

The acceptable quality level (AQL) of a lot submitted for acceptance is a numerical quality index which indicates the nominal percentage of defects (or defects per hundred) specified for a given type of defect of a product.

This method was designed for receiving inspections but is equally useful for process control and final inspections. The probability is high (85 to 99.8 percent) that lots will be accepted when the actual percentage of defects in the lot is equal to the specified AQL. While designed primarily for inspecting continuing series of lots, the AQL method can be used for the inspection of isolated lots.

With the AQL method the producer runs a greater risk that a lot will be rejected than he would with the LTPD method.

LTPD Method

The lot tolerance percent defective (LTPD) level of a lot submitted for acceptance is a numerical quality index which indicates that the consumer will, in one out of ten cases, accept a lot that actually has as many defects as the specified LTPD level indicates.

The LTPD method was designed for continuous production items, such as found in the semiconductor industry, and is not applicable to the inspection of isolated lots.

With the LTPD method a consumer runs a greater risk of accepting defective units than he would with the AQL method. The actual percentage of defects accepted, however, depends upon the following:

- The actual percentage of defects produced
- The probability that defective units are missed in sampling.

10.3 SOLAR CELL, COVER, AND BLOCKING DIODE SPECIFICATIONS

The following sections may be used as check lists for typical specification requirements. Only the major requirements are shown.

10.3.1 Typical Requirements for Solar Cells

The technical content of the requirements section of a typical solar cell specification is as follows (based on Ref. 10.3-1):

- Materials
 - a) Material purity and type
 - b) Base resistivity
 - c) Electrical contact and gridline material
 - 1) Base metal
 - 2) Coating (solder)
 - d) Radiometric properties (solar absorptance)
- Design and Construction
 - a) Uniformity of product and production processes
 - b) Antireflective coating
 - 1) Type (relates to cell output after glassing)
 - 2) Durability
 - 3) Coating defects (permissible void sizes and void counts)
 - c) Location of junction area
 - d) Contact and gridline configuration, dimensions, thickness and defects (voids, pinholes, etc.) and solder thickness, if used
 - e) Silicon surface finish (roughness)
 - 1) Of active surface (textured, polished, etc.)
 - 2) Of contact area (for welded cells only)
 - f) Contact solderability/weldability and contact pull strength
 - g) Chemical compatibility (relates to inhibition of curing of certain adhesives)
- Performance
 - a) Electrical output under specified illumination and cell temperature conditions
 - 1) Output before glassing
 - 2) Output after glassing
 - 3) Output at other than standard test conditions
 - b) High temperature (air or vacuum) exposure
 - c) Storage at temperature and humidity
 - d) Contact integrity after temperature cycling
 - e) Electrical output after temperature cycling
 - f) Electrical output after charged-particle irradiation
- Dimensions and Weight
 - a) Solar cell size, thickness and tolerances
 - b) Maximum weight (typically per hundred cells)
- Color and Finish
 - a) Appearance, color and discolorations
 - b) Mechanical imperfections (nicks, chips, gridline discontinuities)
- Identification of Product
 - a) Marking
 - b) Electrical grading.

The quality assurance provisions of a typical solar cell specification include the following (based on Ref. 10.3-1):

- Responsibility for Inspection Qualification
 - a) Qualification certification and verification
 - b) Qualification sampling for testing
 - c) Qualification tests
 - d) Test dispositions and retest requirements

- Acceptance
 - a) Acceptance certification
 - b) Acceptance sampling for testing
 - c) Acceptance tests
 - d) Test dispositions and retest requirements

- Test Methods
 - a) Visual inspections
 - b) Dimensional measurements
 - c) Contact tape peel tests
 - d) Electrical output and output degradation
 - e) Contact pull testing
 - f) Eraser rub testing after boiling cell in water
 - g) Temperature cycling
 - h) Humidity/temperature exposure
 - i) Weight
 - j) Verification of dimensions
 - k) Miscellaneous, mission-oriented tests (magnetic, vacuum, particle radiation, radiometric, etc.).

10.3.2 Typical Requirements for Solar Cell Covers

The technical content of the requirements section of a typical solar cell cover specification is as follows (based on Refs. 10.3-2 through 10.3-5):

- Materials
 - a) Substrate material type and purity (grade)
 - b) Coating materials and types
- Transmittance Characteristics
 - a) Cut-on wavelength
 - b) Ultraviolet reflection or absorption
 - c) Wideband transmission
 - d) Coating orientation
- Hemispherical Emittance
- Particle Radiation Resistance
- Vacuum
- Storage
- Dimensions
 - a) Size
 - b) Thickness
 - c) Tolerances
- Workmanship
 - a) Surface quality
 - b) Nicks and chips
 - c) Bubbles in glass
 - d) Pinholes, marks, and voids

- Environmental Durability
 - a) Humidity
 - b) Abrasion resistance
 - c) Salt fog
 - d) Adhesive strength (tape peel test)
 - e) Temperature cycling.

The quality assurance provisions of a typical solar cell cover specification include the following (based on Refs. 10.3-2 through 10.3-5):

- Qualification
 - a) Qualification by certification
 - b) Qualification testing
 - c) Test sequence
 - d) Test sample
- Acceptance
 - a) Acceptance tests
 - b) Test sample
 - c) Test failures and disposition
- Test Methods
 - a) Visual inspection
 - b) Dimensional measurements
 - c) Weight
 - d) Coating orientation
 - e) Spectral transmittance
 - f) Humidity/temperature storage
 - g) Temperature cycling
 - h) Salt fog exposure
 - i) Tape peel testing
 - j) Abrasion.

10.3.3 Typical Requirements for Covered Solar Cells

Covered solar cells, also known as glassed solar cells and solar cell stacks, typically must comply with the requirements given in Sections 10.3.1 and 10.3.2 for solar cells and covers, respectively, and the following:

- Dimensions of assembly
 - a) Overall size and tolerances
 - b) Cover location on solar cell and completeness of the cell's junction protection
 - c) Adhesive bond line thickness
- Weight of assembly
- Workmanship
 - a) Adhesive voids, bubbles and tearouts
 - b) Adhesive overflow and cleanup, especially on contact areas
 - c) Nicks, chips, cracks, and imperfections.

The quality assurance provisions typically invoke the applicable inspections and tests first to the un-glassed (bare) solar cells and covers, respectively, and then add the following for covered cell assemblies:

- Qualification
- Acceptance
- Test Methods
 - a) Visual inspections
 - b) Dimensional measurements
 - c) Weight
 - d) Temperature cycling
 - e) Electrical output
 - f) Solar absorptance and hemispherical emittance.

Some requirements may be verified on the assembly level rather than on the component level (such as

temperature cycling), thereby eliminating test duplication and reducing test costs.

The quality assurance provisions typically include testing for the following parameters:

- Forward and reverse characteristics
- Temperature cycling.

10.3.4 Typical Requirements for Blocking Diodes

Blocking diodes for solar cell arrays typically must comply with the following major requirements.

- Forward voltage drop
- Reverse leakage current
- Heat dissipation capability
- Temperature cycling capability.

10.4 ASSEMBLY PROCESSES

10.4.1 Metal Joining Techniques

One of the significant subassembly cost elements is the electrical interconnection of solar cells. With few exceptions cells have been interconnected by soldering the interconnectors to the cells. Solder has typically been of the 36 percent lead, 62 percent tin, 2 percent silver composition. Various methods of soldering have been tried, including soldering irons, parallel-gap resistance soldering, resistance wire machine (peg-tip) soldering, tunnel oven and hot oil bath soldering, and others. Each of these processes has advantages and disadvantages which depend in part on the array design; in part on the production organization, customer preferences, available tooling, previous space qualification status; and many other factors. About the only parameters these processes have in common are (a) that practically all of them have produced hardware which has met the specified mission objectives and (b) most of this hardware was procured on a competitive basis.

For spacecraft being designed and built today and to be built in the future, not all production processes will suffice to produce acceptable hardware, however. Mission requirements have become more severe due to lighter weight array construction and increased mission durations. Therefore, greater attention must now be paid to both the selection and control of production processes. An example of the selection of a new process is parallel-gap resistance welding of solderless solar cells instead of soldering.

Joining Without Solder

While soldering is perhaps the most developed process for joining small electronic components, solder does exhibit some characteristics which limit its use for some solar cell array designs. The limitations of solder are its low strength at elevated temperature, decreasing to zero at approximately 170°C and its relatively short fatigue life (see Chapter 7 and Section 9.8). For solar probes or any other high-temperature solar cell arrays, solder becomes unacceptable. Also, it is now estimated that for 10-year missions in either geosynchronous orbit or in low earth orbits, welded joints may be required for fatigue life reasons (see Section 5.2.5). The heat-sealing of plastic film materials onto solar cells to form "integral" solar cell covers also may require, for processing reasons, welded rather than soldered joints (see Section 4.6.2).

Solderless solar cell interconnector-to-cell joining, or bonding, processes of interest are parallel-gap resistance welding, ultrasonic bonding, thermo-compression bonding, laser welding, electron-beam welding, and similar processes. The first three of these are the simplest processes from a production point of view.

10.4.2 Resistance Soldering*

Resistance soldering (or reflow soldering as it is commonly called) is a microjoining process in which heat is produced by passing an electrical current through either the parts that are to be soldered or through a high resistance soldering tip. The amount of heat produced and the force applied at the soldering tip are controlled by the equipment being used. The solder required at the joint is applied in controlled amounts in the form of solder paste or solder pre-forms or by reflowing the solder on the solar cells or interconnectors. Flux may or may not be used.

The advantages from the use of controlled resistance soldering processes are close control of heat amplitude, heating time, force applied to parts, and amount of solder applied to the joint. There are two basic types of controlled resistance soldering processes:

- Single point, or peg tip
- Parallel gap

10.4.3 Single-Point Soldering*

Single-point controlled resistance soldering is a versatile microjoining process that can be used in a wide variety of "top side" or "one-sided" applications. The process is also used extensively in joining various types of electronic components to printed circuit boards or thin films.

Single-point soldering tips resemble the electrodes used in split-tip resistance welding (Figure 10.4-1). The single-point tip, however, is joined at one end to form a continuous, or "single-point" resistance element.

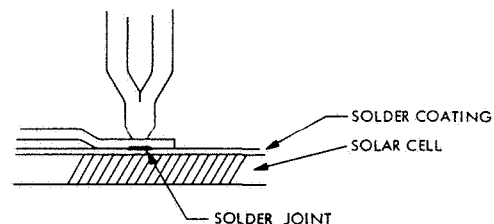


Fig. 10.4-1. Single-point Soldering (Ref. 10.4-3)

* A part of the material in Sections 10.4.2 through 10.4.7 is quoted from Ref. 10.4-1.

The resistance to electrical current of the tip itself produces the heat needed to melt the solder and make the connection. During the electrical energy pulse to the tip, heat is transferred directly to the parts. Since all electrical current passes through the soldering tip, there is no danger of damaging the parts being joined by excessive currents. The electrical resistance of the lead wires, ribbons, or other parts being joined has no effect on the amount of heat produced. However, heat-sink problems can be encountered, depending upon the particular thermal characteristics of the parts involved. Consideration should be given to thermal properties during the design stage of solar cell assemblies.

In the process of making a single-point soldered connection, the soldering tip presses against the parts to be soldered and an electrical energy pulse is passed through the tip for a time duration sufficient to bring the parts and solder alloy to the temperature needed for a reliable solder joint. After the proper temperature has been reached and the energy pulse to the tip has been interrupted, the tip remains in contact with the parts (dwells) long enough for the joint to cool and for the solder to completely solidify.

To improve tip temperature control, tips with attached thermocouples are available. The thermocouples are connected to the controllers which in turn limit the temperature excursion of the tip.

When flux and solder preforms are to be used, it is best to have the flux contained within the preform itself. Flux buildup on parts generally does not interfere with the soldering process. As a general rule, flux shortens soldering time.

When very small sections are being soldered, the force applied at the tip should be low so that the sections are not broken or damaged. The force used need only be sufficient to hold the parts in contact with the solder and base metal. Excessive tip forces can cause penetration through the interconnects; the tip force required usually is proportional to the thickness. Typically, a force of 0.5 N is sufficient for an interconnector thickness of 25 μm whereas 9 to 15 N might be required for a 250 μm thickness.

10.4.4 Parallel Gap Soldering

The parallel gap soldering process is almost identical in principle with parallel gap resistance welding. The heat required for making the solder joint is derived by passing an electrical current pulse from one electrode through the materials being soldered and back to the other electrode. Heat is produced by the resistance of the parts themselves.

Also, in parallel gap soldering, two soldering tips approach the work-piece from one side and contact the interconnect at two points (Figure 10.4-2).

Only one soldered joint, however, is made even though there are two tips. The size of the solder joint depends upon the gap width between tips. The force applied by each tip is the same.

With separately suspended or "loaded" tips the process is well suited for soldering uneven or bent interconnectors. Normally, best soldering results are obtained when both leads and base materials are tinned or have a coating of solder. Solder preforms also can be used between the interconnect and the solar cell.

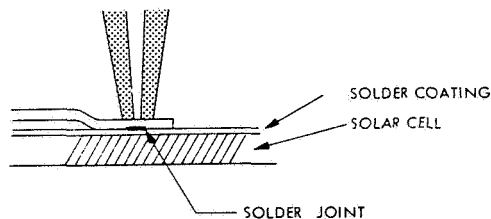


Fig. 10.4-2. Parallel Gap Soldering (Ref. 10.4-3)

Since heat is produced by the resistance of the parts being soldered, the resistivity of the materials must be taken into account. Care must be exercised when flux is used as it may interfere with electrical continuity and the resulting heat produced.

10.4.5 Tunnel Oven Soldering

A tunnel oven is a conveyORIZED soldering system consisting of three process zones: a preheat zone, a hot (or soldering) zone and a cooling zone. The temperature in both the preheat and the hot zones are independently controlled. The conveyor speed is adjustable.

The parts comprising a solar cell submodule are assembled and held together in a holding fixture called a solder boat. The soldering is performed by passing the solder boat through the tunnel oven where it proceeds through the preheat zone, the soldering zone, and then the cooling zone. Since prolonged exposure to high temperature will deteriorate the output of solar cells, it is preferred to subject them to soldering temperatures for a minimum amount of time. By varying both the temperatures in the tunnel oven and the conveyor speed, it is possible to obtain different soldering temperature-time profiles. The variation of the solder boat/submodule temperature with time as the solder boat proceeds through the tunnel oven is shown in Figure 10.4-3. The various curves in Figure 10.4-3 show the effect of varying the temperature in the heat zone of the tunnel oven and the speed of the conveyor through the oven for three modifications of the tunnel oven temperature profile, as used by JPL for the subassembly of solar cells for the Surveyor and Mariner series of spacecraft.

10.4.6 Soldering by Infrared Heating

The energy source used for heating the work-piece is typically a tungsten filament lamp of the quartz-iodine type. The operating temperature of the lamp is 3400°K maximum, and its spectral output ranges approximately from 0.375 to 4.2 μm . The quartz-iodine lamp produces the maximum possible specific energy available in practical types of lamps. Arc and plasma sources produce more power for a given size, but they are more expensive and less flexible in their operation.

To collect the radiation and direct it to the work-piece, mirrors or reflectors are employed. The reflector is shaped such that the energy leaving the source and striking its reflecting surface will be directed to a defined zone, as shown schematically in Figure 10.4-4. The workpiece is placed in the zone where it will absorb maximum radiation and become hot. This zone, often called the focal zone, may be either a spot or a long narrow line. The shape and size of the zone is a function of the shape and size of the source and the reflector.

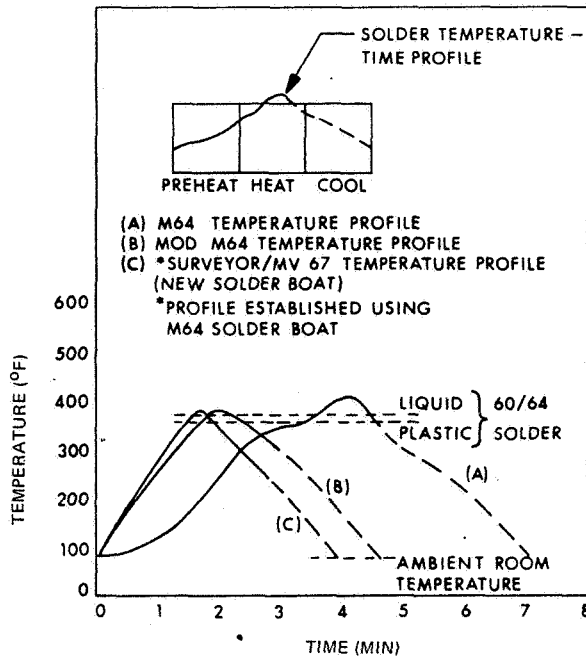


Fig. 10.4-3. Tunnel Oven Temperature-Time Profiles (Ref. 10.4-1)

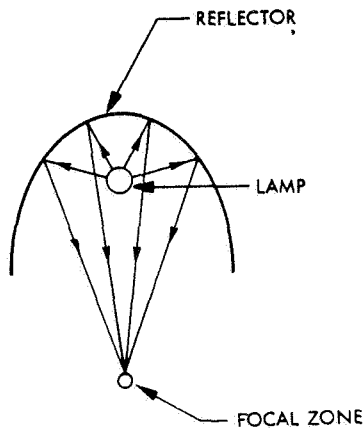


Fig. 10.4-4. Schematic of Focused Radiant Heating System (Ref. 10.4-1)

The rate of heating and the temperature reached by the workpiece depends upon the material it is made from and its surface condition, such as surface roughness and degree of oxidation.

10.4.7 Soldering by Induction Heating

The four characteristics associated with induction heating are:

- Surface heating caused by the immediate secondary current flow on the surface of the workpiece

- Rapid heat transfer to the work surface (this rapid heating is made possible by the fact that the heat is developed directly within the metal, as with all electrical resistance heating, rather than being transmitted through the surface of the metal, as in infrared or furnace-type heating)
- Generation of the energy within the metal without any physical contact between the source of electrical energy and the metal being heated (the medium of energy transmission, the magnetic field, can penetrate any nonmetallic substance placed between the heating coil and the material being heated)
- The size of the workpiece is limited to the size of the radio frequency (RF) heating coil into which the workpiece must be inserted.

10.4.8 Parallel-Gap Resistance Welding

The parallel-gap resistance welding method derives its name from the way it is being performed: a pair of closely spaced, parallel electrodes make contact with the workpiece (solar cell interconnector), an electric current flows through the electrodes and the portion of the workpiece that is underneath and between the two electrodes, and the heat generated in the resistance offered by the workpiece raises the workpiece temperature to or above welding (fusion) temperature. The pressure exerted by the electrodes on the workpiece facilitates making the joint.

It has been argued that the appearance of joints between interconnectors and solar cell contacts in microsection analysis indicates that the joints are not actually welded, but rather are fused, alloyed, thermocompression-bonded or otherwise metallurgically joined. While perhaps of great concern to metallurgists, this handbook will sidestep such arguments as not being overly important to array designers, fabricators, and process controllers and simply state that metallurgically sound (or at times faulty) joints have been made by the parallel-gap resistance welding technique.

Welding Experience

Parallel-gap welding of solar cells was pioneered in Europe since 1968 by AEG-Telefunken. This firm had ceased to produce soldered solar cell arrays at the end of 1971 and has since that time produced only welded arrays. By mid-1975 about 1.2 million welded joints had been made for five flight projects (Ref. 10.4-4). With silver-plated molybdenum interconnectors welded to Ti-Pd-Ag solar cell contacts, solar cell assemblies have been qualified for temperature excursions between -200° and $+200^{\circ}\text{C}$ (Helios) and for temperature cycling for 1100 cycles between -180° and $+80^{\circ}\text{C}$ (International Ultraviolet Explorer; IUE).

Most U. S. solar cell array manufacturers now possess a solar cell welding capability. However, by 1976 only one flight program is said to have used welded joints.

Weldable Materials

The following interconnector materials have been welded to silver solar cell contacts:

- Copper (unplated)
- Pure silver
- Silver-plated copper
- Silver-plated Kovar
- Silver-plated Invar
- Silver-plated molybdenum.

Welding Schedules

Welding schedules must be developed carefully to assure adequate joint quality. In general, the following welding parameters must be considered and controlled:

- Electrode footprint size
- Electrode pressure
- Solar cell heat sinking
- Weld voltage, current and power
- Weld pulse rise, dwell and fall times
- Interconnector stiffness and electrical and thermal conductivity
- Solar cell and interconnector surface roughness and cleanliness.

Inadequate welding parameters may affect the joint strength and/or solar cell electrical performance as follows:

- Inadequate weld power -- low joint strength
- Excessive weld power -- low joint strength
- Excessive weld power -- burned interconnectors
- Excessive weld power -- cell power degradation (see discussion below)
- Excessive weld power -- silicon spalling
- Correct weld power but amplitude too high and dwell time too short -- silicon spalling.

Examples of the development of a weld schedule are given in Refs. 10.4-2 and 10.4-6. Figure 10.4-5 illustrates (for a particular interconnector design) the wide range over which joints having high pull strength can be made. However, not all of the weld schedules produced joints that endured severe thermal cycling testing. The point in Figure 10.4-5 marked "Schedule for Test Specimens" indicates the weld schedule that was chosen for long temperature cycling life. This schedule is a compromise between bond strength and electrical degradation.

Electrical Degradation

Parallel-gap resistance welding on the contact on the diffused side of solar cells (i. e., the n-contact on n-on-p cells) may cause electrical output degradation of the cells. The shallower-diffused and textured-surface solar cell types are more susceptible to this degradation than the deeper-diffused types. The output degradation manifests itself primarily in the maximum power region and is apparently caused by contact metal being driven into the junction area underneath the weld joints, thereby, electrically shunting the solar cell. Ref. 10.4-2 found that by making more weld joints on the

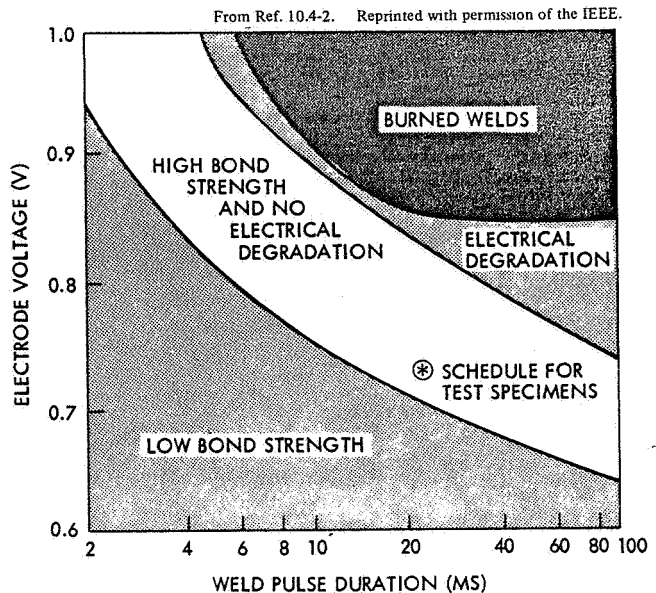


Fig. 10.4-5. Parallel-Gap Weld Schedule Development Using 50 μm Thick Silver Interconnects (Ref. 10.4-2)

same cell the cell output continues to degrade, while breaking the welded tabs from the cell (by pulling silicon divots out of the cell) very nearly restores the original cell power output. This phenomenon, illustrated in Figure 10.4-6, was observed with both silver-plated Kovar and pure silver interconnectors but at different weld voltage levels.

Electrical degradation was not observed after thermocompression joining (at 400°C) and after ultrasonic joining (at room temperature).

10.4.9 Thermocompression Joining

The joining of metals by thermocompression techniques involves forming of a metallurgical bond at elevated temperature and under pressure. The characteristics that differentiate thermocompression joining from welding are that in thermocompression joining:

- The fusion temperature is below the melting or eutectic temperature of each metal or an alloy of the joining metals
- The joining pressure is much greater
- The joining time tends to be longer.

Thermocompression joining is potentially attractive from a mass production point of view in that electrical contact resistances are no longer important, precise electrode positioning is not required and many joints can be made simultaneously.

Thermocompression Joining Experience

Successful thermocompression joining of interconnectors to solar cells has been reported rather sparsely. In general, an increase in the joining temperature and in the joining stylus pressure (electrode force) increases the bond strength. The limiting condition on temperature is rapid oxidation of the cell

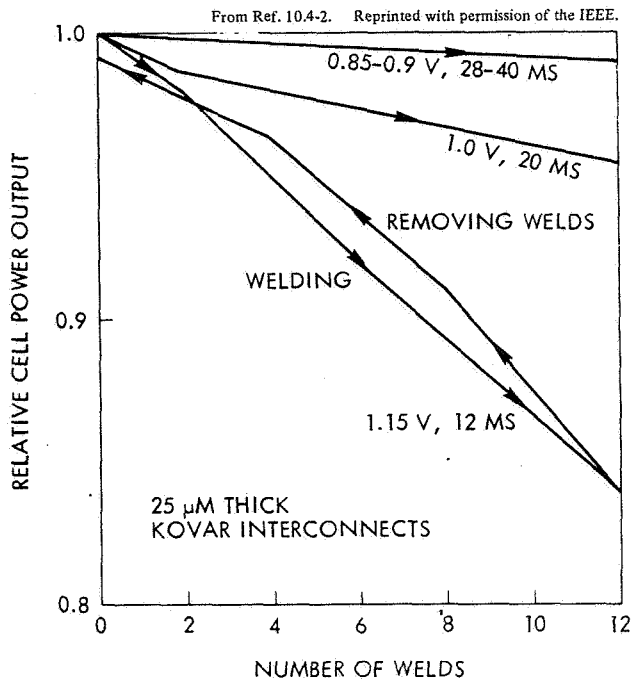


Fig. 10.4-6. Parallel-Gap Welding with Excessive Energy on N-Contact Causes Electrical Degradation Which Increases with the Number of Welds Made (Ref. 10.4-2)

contact and interconnector surfaces when the joining is done in air. The limit on stylus pressure is set by the ultimate strength of silicon.

Solar cell surface roughness and interconnector stiffness apparently play greater roles in thermocompression joining than in parallel-gap welding. Smoother surfaces and more compliant interconnectors, conforming to each other more readily, tend to increase the strength of joints made at a given temperature and under a given pressure.

Joinable Materials

The only solar cell interconnector materials reported as joinable are soft silver or silver plated soft metals. Stiff materials such as Kovar require large joining pressures that tend to fracture the solar cells (Ref. 10.4-2).

Thermocompression Schedules

Thermocompression joints having pull strength values comparable to those made by parallel-gap resistance welding were obtained by Ref. 10.4-2 with both 25 and 50 μm thick pure silver interconnectors. Schedules that resulted in good joints ranged from 9 N for 1200 seconds to 27 N for 1 second at 300°C. Joints made at 400°C exhibited higher pull strength than those made at 300°C. Below 275°C no bonds were obtained.

10.4.10 Ultrasonic Joining

Ultrasonic joining occurs under the influence of elevated temperature, pressure, and high-frequency acoustic vibration. The temperature rise is usually

due to dissipation of the acoustic energy in the joint area; however, supplemental solar cell heating has been employed. For ultrasonic joints to exhibit high strength, the following parameters are critical:

- Acoustic energy coupling into the joint area
- "Grabbing" of the interconnector by the stylus
- Holding of the solar cell immovably without damping
- Acoustic energy level, dwell time and stylus pressure.

The coupling of the acoustic energy into the workpiece is accomplished by a mechanical force/amplitude transformer between the ultrasonic transducer and the bonding stylus, and excitation of the bonding stylus at a location on the stylus such that the least energy input to the joint makes the strongest bond. The proper transformer ratio and stylus excitation location is, in practice, difficult to achieve because different interconnectors and cells offer differing mechanical impedance values to the mechanical/acoustic circuit.

"Grabbing" of the interconnector by the joining stylus depends upon its tip configuration, shape, surface smoothness, and material composition in relation to the interconnector material properties. For a good joint to occur, the stylus normally first bonds itself to the interconnector, then the interconnector joins with the solar cell contact. If the acoustic excitation is continued, the interconnector/cell joint will reach a maximum strength and thereafter will be destroyed again. The stylus typically "sticks" to the interconnector after a maximum-strength joint has been made. In an ideal setup, the stylus/interconnector bond should break at the very moment in which the interconnector/cell joint reaches its maximum strength.

Ultrasonic Joining Experience

Ultrasonic joining of aluminum interconnectors to hundreds of titanium-silver contact solar cells for the Hardened Solar Power System project has been reported by Ref. 10.4-7. Additional experimental work was reported by Refs. 10.4-2 and 10.4-9.

Ultrasonically Joinable Materials

Solar cell interconnector materials that can be joined ultrasonically and exhibit high joint strength include the following:

- Aluminum to aluminum or silver contacts
- Silver to silver contacts

10.4.11 Adhesive Bonding Techniques

One of the most important solar cell array assembly process techniques consists of the bonding together of parts using an adhesive. Examples of adhesive bonding are:

- Substrate fabrication (bonding of honeycomb core to face sheets, solar cell blankets to each other, etc.)
- Bonding of solar cell covers to solar cells
- Bonding of solar cells to the substrate
- Bonding and spot-bonding of electrical conductors to the substrate.

The steps common to all bonding operations include the following:

- Surface preparation and cleaning
- Adhesive preparation (mixing, de-airing, etc.)
- Adhesive application (metering, depositing, etc.)
- Parts locating (clamping, holding, etc.)
- Curing (time, temperature, pressure, humidity)
- Cleanup (removing overflow and flash, trimming, etc.).

Typical adhesive types in use include the following (for details see Chapter 7):

- RTV (room temperature vulcanizing) rubbers, also known as silicone adhesives, sealants, and elastomers
- Epoxies
- Thermo-plastic adhesives
- Thermosetting adhesives.

The appropriate specific bonding techniques are highly dependent upon each specific adhesive. The manufacturers process specifications should be followed closely and carefully (see also Section 10.5).

10.5 MATERIAL AND PROCESS SPECIFICATIONS

10.5.1 Typical Requirements for Adhesives

The following parameters are typically specified in material and process specifications. (The selection of the generic or specific adhesive to be used is up to the designer.)

- Optical quality (for cover adhesive only)
- Surface cleaning and pretreatment requirements
- Mixing ratios (for multi-part adhesives only) and de-airing requirements
- Shelf life
- Pot life
- Skin-over time
- Curing cycle (time, temperature, relative humidity).
- Outgassing (for some projects only)

Quality assurance provisions typically call for the following verification methods:

- Verification that shelf life has not expired
- Preparation and destructive testing of sample coupons to demonstrate that the adhesive cures properly and develops adequate strength.
- Outgassing tests (if required)
- Optical properties measurements (if required)

10.5.2 Typical Requirements for Insulating Layers

The following parameters are usually specified for insulating layers that electrically isolate solar cell circuits from conductive array substrates:

- For adhesive-mounted sheets:
 - a) Maximum sheet size compatible with low temperature and temperature cycling requirements
 - b) Adhesive type, application and curing method
 - c) Surface preparation methods
- For paints:
 - a) Paint type
 - b) Surface preparation
 - c) Application method
 - d) Paint thickness, uniformity and pin hole limitations
 - e) Curing cycle
- For integral coatings (such as hard anodizing):
 - a) Process or treatment details
 - b) Insulating coating thickness
 - c) Post-treatment surface preparation prior to solar cell bonding.

Quality assurance provisions typically call for the following:

- Electrical leakage resistance measurement (wet sponge test)
- Insulation breakdown voltage test
- Mechanical integrity during vacuum-thermal cycling testing.

10.6 SPECIFYING QUALITY

10.6.1 Design-Related Quality

One of the little recognized responsibilities of the designer is his role in relation to product quality. While the designer neither sets basic quality policies of his organization nor directly assures product quality, he determines (more than anybody else in his organization) most of the quality aspects of his product. He does this by selecting and determining the materials and processes to be used, writing or selecting the specifications for these materials and processes, establishing "cosmetic" criteria and dimensional tolerances, and defining required product performance. Thus, the designer, and especially the solar cell array designer, commits his organization to certain quality standards, and to certain production costs. In this sense, drawings, specifications, and procedures are more than plans according to which an array is to be fabricated and tested; they are also the tools by which the designer controls the minimum quality he needs so that his design will meet mission requirements. He, in turn,

must rely on the procurement, production, and quality assurance organizations to implement his design to his ground rules.

10.6.2 Workmanship

Inspectable workmanship criteria can be separated into two groups:

- Functional Criteria – which do or may affect array performance
- Cosmetic Criteria – which do not affect array performance

The dividing line between these two groups generally depends upon an analysis of a specific array design and the specific set of environmental conditions associated with a particular mission. Table 10.6-1 can be used to establish workmanship inspection criteria for each specific case.

Table 10. 6-1. Typical Workmanship Inspection Criteria

Variable	Criteria	Impact
Partially debonded covers and cells, and bubbles and voids in cover adhesive.	Small percentage permissible, depending on power margin, severity of launch environment and temperature cycling extremes in orbit.	Raises cell operating temperature slightly. May cause complete debonding during launch.
Chipped cells and covers	Small percentage permissible for synchronous orbits, larger percentage for low altitude orbits depending upon power margin. No cover defects are permissible for flights through the radiation belts except when power margin is large.	A single cell stack defect may cause degradation of an entire string.
Cover and cell adhesive thickness	Minimum thickness depends mainly on adhesive viscosity and cell flatness. Maximum thickness is limited by low temperature and temperature cycling range and duration.	Temperature cycling test results can establish permissible thickness range.
Overflowed adhesive in cell gaps	Minimum gap width at lowest temperature must be maintained to prevent cells or covers from fracturing.	Temperature cycling test results can establish permissible conditions.
Adhesive or organic material on front surface of cover	Reduction of light input to cell due to excessive darkening. Small areas are inconsequential.	Radiation tests and analysis can establish tolerable conditions.
Broken covers	Cracks which are of such nature that no active cell area can potentially be exposed are purely cosmetic. All other cracks are functional.	Radiation protection and thermal properties are not impaired by certain cracks. If radiation protection is less than complete, degradation of a single cell stack may cause a similar degradation of the entire string of cells.
Broken cells	Cracks are purely cosmetic if a crack has severed both p and n contact areas but each portion of the fractured cell remains electrically connected with adequate redundancy. All other cracks are functional to varying degrees.	Electrical performance is not impaired by certain cracks. However, cracks in silicon can be expected to propagate through contact areas during launch and orbital temperature cycling and may affect electrical performance at that time.

10.7 NONDESTRUCTIVE TEST (NDT) METHODS

10.7.1 Quality Control by NDT

Solar array assembly by welding instead of soldering poses a new set of manufacturing process control and quality assurance problems. While on soldered joints the amount of solder flow and solder filleting is readily inspectable, no such indicators of joint quality are evident in welding. Just as with soldered joints, not all welded joints made are "good" even though apparently the weld schedule, electrodes, and parts surface properties are the same for all welds attempted; therefore, some means of identifying unacceptable welds is needed.

Nondestructive tests (NDT) rely on one or a number of nondestructively measurable or observable attributes which can be correlated to destructively determined weld quality.

10.7.2 Parameters Affecting Weld Quality

Weld quality and quality variability has been found to be influenced by the following (Refs. 10.7-1 through 10.7.11):

- Electrode footprint size
- Electrode spacing
- Electrode dressing (flatness and oxidation)
- Electrode length (for constant-voltage and capacity-discharge welders)
- Electrode pressure
- Conductivity of the interconnector ribbon
- Silver (or other) plating thicknesses on the solar cell contacts and on the interconnectors
- Silicon and interconnector base material surface roughness
- Weld current
- Weld voltage
- Weld joint temperature/time profile
- Welded parts cleanliness and state of oxidation
- Heat-sinking of solar cell.

10.7.3 Types of NDT Methods

The most promising nondestructive test (NDT) methods potentially applicable to the evaluation of solderless joints on solar cells have been selected from the currently known NDT methods by Refs. 10.7-3

through 10.7-5 and others. These NDT methods may be grouped according to the general physical principles they involve or according to the time of their application. The grouping by general physical principle is as follows (the sections in which they are discussed further are also shown):

- Visual inspection -- Sections 10.7.5 and 10.7.6
- Mechanical -- Section 10.7.7
- Electrical -- Sections 10.7.8 through 10.7.11
- Thermal -- Sections 10.7.12 through 10.7.14
- Acoustic -- Sections 10.7.15 through 10.7.17
- Others -- Sections 10.7.18 and 10.7.19.

Inspection systems are discussed in Section 10.7.20. Grouping of the nondestructive test methods according to the time of their application is as follows:

- Pre-joining NDT Methods
 - a) Electrode-to-electrode resistance
 - b) Electrode-to-cell contact resistance
 - c) Interconnector ribbon resistance
 - d) Interconnector-to-electrode resistance
 - e) Interconnector-to-cell contact resistance
- In-Process NDT Methods
 - a) Dark-forward voltage drop of solar cell
 - b) Weld current
 - c) Weld voltage
 - d) Infrared emission
 - e) Acoustic emission
- Post-Joining NDT Methods
 - a) Visual inspection (electrode imprint)
 - b) Resistance
 - c) High-frequency impedance
 - d) Infrared videography
 - e) Holography
 - f) Eddy current
 - g) Microfocus X-ray
 - h) Ultrasonics
 - i) Infrared microscope (augmented visual)
 - j) Acoustic signature.

10.7.4 Destructive Tests

The most significant parameters that define weld joint quality are the joint's capability to withstand:

- Handling and assembly stresses
- Thermal-cycling induced fatigue failures.

The following destructive tests are designed to measure joint quality:

- Contact pull or peel tests
- Temperature cycling testing (life testing).

An additional destructive test method in use is cross-sectioning followed by microscopic inspection (generally known as microcross-sectioning or microsection analysis). However, Ref. 10.7-4 points out that neither contact pull strength nor microsection analysis can positively identify joint quality in terms of its thermal cycling life capability. This view is also held by others and is believed to be applicable to soldered joints as well. A frequently used method (perhaps the most valid one) is to measure the pull strength after the thermal cycling of specimens to end-of-mission conditions. Therefore, it is necessary that the non-destructive test methods are correlated to both contact pull strength and thermal cycling life or post-thermal cycling pull strength.

10.7.5 Visual Inspection

Visual observation of the quality of a solar cell weld joint is restricted to observation of the electrode imprint on the cell interconnector. Typically, 20 to 60 power stereo microscopes are used for inspection. Inspection criteria were developed and employed in the inspection of welded solar cell modules by Refs. 10.7-1 and 10.7-2. These criteria include lower and upper limits on the following.

- Edge definition and depth appearance of the electrode imprint in the upper surface of the interconnector
- Evidence of burned (darkened or discolored) areas of the interconnector, especially between the adjacent electrode footprints.

10.7.6 Infrared Microscope (Augmented Visual)

The "augmented visual" inspection of welded joints utilizes two different approaches:

- Inspection of the weld footprint size and its "visual" appearance (after image conversion to visible light)
- Determination of welding-induced stresses in the silicon (using crossed polarized infrared light filters).

With the infrared inspection techniques, infrared light is being utilized to which silicon is transparent (wavelength greater than $1.2 \mu\text{m}$). The joints are inspected through the silicon wafer, requiring small metal-free silicon surface areas on the wafer side directly opposite the weld joints. The inspection technique with the infrared microscope is similar to direct visual inspection, except that an image converter between the microscope exit and the observing eye converts the infrared light to visible light. Microscope magnification and depth-of-field relationships

are nearly the same as with optical microscopes. One such currently available infrared microscope can be obtained from Research Devices Inc., Berkeley Heights, New Jersey.

10.7.7 Electrode Setdown

A commonly used criteria for judging weld quality in fields other than solar cell arrays is the amount of electrode setdown occurring during the welding operation. Electrode setdown, also known as electrode sinking, occurs as the work piece deforms at elevated temperature under the applied electrode pressure.

The degree of electrode setdown is normally evaluated visually, frequently under a magnifying instrument. When the actual value of electrode displacement is measured during welding, this value is known as dynamic electrode setdown.

For application of this criteria to welded solar cells, see Section 10.7-20.

10.7.8 Weld Pulse Monitoring

A number of investigators have attempted to measure the welding current or voltage pulse shape and correlate it to weld quality.

Typically, on constant voltage welders such as the widely used Hughes Model MCW-550, the current pulse is measured, while on other, common constant current or constant energy (capacitor discharge) machines, the electrode voltage is measured.

The idea behind measuring the pulse shape is that a "good" weld joint offers a certain electrical impedance which, at a certain machine setting, produces a specific weld current or voltage pulse shape. Any variation in this impedance, due to poor ohmic contact either between the interconnector and the solar cell or the welding electrodes and the interconnector, causes a deviation in the weld current or voltage pulse. Detection of this deviation, then, could be used to deduce a lack of weld joint quality.

The results of studies of NDT methods performed by AEG-Telefunken (Wedel, West Germany) with a constant voltage Hughes welder indicated that measuring the welding current was a suitable parameter; however, it did not indicate the energy deposited in the weld joint because during successive welds, the electrode-to-interconnector contact resistance increases due to increasing electrode surface contamination. To aid in the proper measurement of the energy in the weld joint, a set of separate voltage probes were installed adjacent to the weld electrodes and in contact with the cell contacts next to the connector.

Weld Current

Measurement of weld current/time profiles during welding determines a necessary, but not sufficient, condition for achieving adequate weld joint quality. The weld current can be measured by a variety of conventional techniques:

- Voltage drop across a resistance
- Inductive coupling
- Voltage developed across the interconnector ends due to current flow in a portion of the interconnector.

Weld Voltage

The weld voltage may vary (even on so-called constant-voltage welding machines) due to the following:

- Improper value of work piece resistance (too high or too low) across the welding electrode tips
- Electrode wear (shortening) due to frequent dressing
- Welder malfunction (series resistance in switching and other power circuits, low line voltage, high temperature effects during mass production, etc.).

Monitoring of the weld voltage/time profile can detect equipment malfunctions as well as improper welding conditions. Conventional voltage measurement techniques can be used.

10.7.9 Resistance Measurements (dc)

The weld joint quality is determined largely by the temperature/pressure/time profile in the joint volume while the joint is being made. Since for a given welding machine, machine setting, and weld setup the temperature rise depends upon the actual current flow through the work piece and the electrical energy transformed into heat inside the work piece (not at the electrode/work piece interface), control of the electrical resistance is important. The following resistance path measurements have been investigated:

- First electrode - interconnector - second electrode
- One electrode - interconnector - cell contact
- Interconnector end-to-end (inherent conductivity of specific interconnector)
- One electrode - interconnector
- Interconnector - cell contact.

For pre-weld measurements the resistance values should be below a certain maximum value and above a certain minimum value (determined experimentally for a given design and setup). For post-weld measurements the resistance values should be within certain limits or in certain relationships to the pre-weld resistance values.

10.7.10 High-Frequency Impedance

Measurements of the high-frequency impedance of welded joints is expected to indicate the number and size of impurities and nonwelded areas in the joints (Ref. 10.7-5).

10.7.11 Eddy Current

The magnitude of the eddy currents induced in the weld joint areas is expected to be related to impurities and nonwelded areas in the joints (Ref. 10.7-5).

10.7.12 Dark-Forward Voltage Drop

Instantaneous reversible changes in the solar cell dark-forward current-voltage characteristics during the welding cycle can be used as indicators of the temperature reached during welding (Ref. 10.7-4).

The cell may be biased with either a constant-voltage source or a constant-current source; the signal is picked up as a change in cell terminal current or voltage, respectively.

10.7.13 Infrared Emission

The infrared radiation emitted by the weld joint while it is being made can be used to measure the weld joint temperature or temperature/time profile. In practice, problems arise from the following:

- The emissivities of the interconnectors and electrodes are not constant during a production time interval.
- The electrodes, as well as the joint, emit infrared energy.

AEG, as well as the University of Hanover, West Germany, investigated the infrared emission from the weld joint while it was being made. It was found that the variations in emissivity of the interconnectors are quite large so that the infrared radiation received by the large (1 x 2 cm) sensor varied even though the weld joints appeared uniform. Also, the sensor picks up infrared radiation from both the heated joint and the electrode tips. The radiation signals from the electrodes are unwanted signals, and are large in comparison with the signal from the joint itself; therefore, it was desirable to use an optical system with an extremely narrow view angle. No such system could be located which would not interfere with the welding operator.

10.7.14 Infrared Videography

The solar cell is heated uniformly and the joint area is scanned with an infrared detector. Temperature profiles over the solar cell area are displayed on the screen of a cathode ray tube. Unjoined or poorly joined interconnectors are expected to be recorded as being cooler (due to convection cooling) than properly joined interconnectors (Ref. 10.7-5).

10.7.15 Acoustic Emission

Acoustic emission (noise) is caused by the melting, freezing, and stressing of a material. Acoustic emission testing was originally developed for larger objects and was applied by Ref. 10.7-5 to solar cell joints. Acoustic emission melt and cooldown signals were detected with piezoelectric crystals, amplified and displayed on an oscilloscope screen.

Ref. 10.7-5 reports partial success with this method for unglassed solar cells but points out that further development would be required to implement this method on a production basis.

10.7.16 Acoustic Signature

In this method the acoustic transmission and modification of an applied acoustic stimulus by the weld joint is measured (Ref. 10.7-5).

10.7.17 Ultrasonics

The quality of weld joints is expected to influence the reflection of high-frequency ultrasonic waves. It was found that, using an immersion technique and frequencies from 5 to 25 MHz, only nonwelded joints could be discerned (Ref. 10.7-5).

10.7.18 Holography

Holographic techniques are expected to show up imperfections in weld joints. D. R. Lott et al. (Ref. 10.7-5) employed an acoustical immersion technique which used ultrasonic frequencies between 1 and 7 MHz and displayed the resulting signals on a television screen. TRW Systems (Ref. 10.7-6) utilized a laser beam and optical holography; the results were recorded on photographic film. Neither method was able to give an indication of joint quality.

10.7.19 Microfocus X-Ray

In this method, magnified X-ray images of small areas can be obtained. D. R. Lott et al. (Ref. 10.7-5) were unable to obtain definite joint interface displays.

10.7.20 NDT Inspection Systems

Early work on NDT methods indicated that probably there was no single method which would definitely determine joint quality, but that a combination of methods could perhaps do so. Some of these methods are described below.

The NASA Ames Weld Evaluator

The first NDT inspection system believed to come into existence was the NASA Ames Weld Evaluator (Refs. 10.7-7 through 10.7-10). This system was developed specifically for the welding of small ribbons and wires (but not for solar cells) and measures the following parameters:

- Weld pulse voltage across the welding electrodes (see Section 10.7.8)
- Infrared emission (see Section 10.7.13)
- Dynamic electrode setdown (see Section 10.7.7).

The equipment compares each of these three signals with preset lower and upper limits. When any two or all three of the signals are within prescribed limits, the equipment energizes a green "go" light. Otherwise, a red "no-go" light comes on.

During the NDT equipment development and checkout phases, it was found by Sterling that none of the weld parameters alone would be adequate to accept or reject a weld joint, but that the majority voting system was satisfactory. It was also found that different material combinations, as well as different geometries of the welded objects, had a profound effect on the observed parameters.

The NASA Ames Weld Evaluator was evaluated by TRW Systems by welding 25- μ m-thick interconnectors to solderless solar cell contacts. The results of this evaluation showed that (a) the infrared radiation emitted by the electrodes was many times larger than the radiation emitted by the weld joints, and (b) the dynamic electrode setdown (0.2 to 2 μ m, approximately) was below the capability of the setdown sensing circuitry.

Proposal by the British Aircraft Corporation

An NDT system proposed by Ref. 10.7-4 uses the following parameters:

- Resistance between the two welding electrodes prior to welding
- Resistance between one welding electrode and an auxiliary electrode placed on the solar cell contact prior to welding
- Weld current measurements 50 and 100 ms after machine firing.

It was shown experimentally that if the $\pm 2\sigma$ limits are chosen as the pass/fail limits for each of the four parameters above, 92.5 percent of bad welds were found and 5.2 percent of the good welds were rejected.

The Lockheed System

An NDT system discussed by Ref. 10.7-5 uses the following parameters:

- Measurement of resistance between electrodes prior to welding
- Inspection of joints with infrared microscope after welding (see Section 10.7-5).

The AEG-Telefunken Systems

An NDT system that has been operational in a production setting, according to Ref. 10.7-11, utilizes the following parameters:

- Current or voltage pulse versus time display on a storage oscilloscope screen
- Comparison of the maximum weld voltage with preset upper and lower limits
- Analog computation of the time integral of the weld current and comparison with preset upper and lower limits.
- Continuous visual inspection of the welding area with a stereo microscope.

According to Ref. 10.7-11 a new NDT system is being proposed for development that is intended to measure and determine the following:

- Time integral of weld current
- Time integral of weld voltage
- Time integral of weld power
- Electrode pressure
- Electrode setdown
- Resistance prior to welding
- Degree of electrode contamination
- Temperature reached at interconnector in weld area.

REFERENCES (CHAPTER 10)

- 10.1-1 P. A. Iles and K. S. Ling, "How Mechanical Requirements Affect Silicon Solar Cell Costs," ASME Publication 70-Av/SpT-28, Centralab Semiconductor Division, presented at the Space Technology and Heat Transfer Conference, Los Angeles, California, June 21-24, 1970.
- 10.2-1 "Sampling Procedures and Tables for Inspection by Attributes," MIL-STD-105D, Military Standard, U.S. Government Printing Office, Washington, D. C., April 1963.
- 10.2-2 "Semiconductor Devices, General Specification for," MIL-S-19500D, Military Specification, May 1964.
- 10.3-1 "Military Specification, Cells, Solar, Silicon, General Specification for," MIL-C-83443A, May 1975.
- 10.3-2 "Product Specification, Solar Cell Covers," No. 602400, Optical Coating Laboratory, Inc., July 1971.
- 10.3-3 "Product Specification, Solar Cell Cover, Blue Reflecting, on Fused Silica," No. 6024000-01, Optical Coating Laboratory, Inc., July 1971.
- 10.3-4 "Product Specification, Solar Cell Cover, Blue Reflecting on 6 mil Microsheet," No. 6024000-02, Optical Coating Laboratory Inc., July 1971.
- 10.3-5 "Product Specification, Solar Cell Cover, 350 nm Cuton, on Fused Silica," No. 6024000-03, Optical Coating Laboratory, Inc., December 1973.
- 10.4-1 R. A. Marzek, "Survey and Study for an Improved Solar Cell Module, STOD Task No. 43," Document No. 900-270, Jet Propulsion Laboratory, August 1969.
- 10.4-2 H. S. Rauschenbach and A. F. Ratajczak, "FEP-Teflon Covered Solar Cell Array Advancements," Conference Records of the 10th IEEE Photovoltaic Specialists Conference, Palo Alto, California, 1973.
- 10.4-3 R. B. Larson, "Microjoining Processes for Electronic Packaging," Assembly Engineering, (by permission of Hitchcock Publishing Co., Wheaton, Illinois), October 1966.
- 10.4-4 R. Buhs et al., "Welding of Solar Cells in Production Line," Proceedings of the 11th IEEE Photovoltaic Specialists Conference, 1975.
- 10.4-5 H. G. Mesch, "Parallel Gap Welding of Silver-plated Solar Cells," Proceedings of the 10th IEEE Photovoltaic Specialists Conference, 1973.
- 10.4-6 T. C. Eakins, "Results of Solar Cell Welded Interconnection Development," Proceedings of the 7th Intersociety Energy Conversion Engineering Conference, 1972.
- 10.4-7 R. V. Elms, Jr., "Solar Array Welding Development," Proceedings of the 9th Intersociety Energy Conversion Engineering Conference, 1974.
- 10.4-8 D. R. Lott, "Solar Array Flexible Substrate Design Optimization, Fabrication, Delivery and Test Evaluation Program," Final Report LMSC-0384284, Lockheed Missiles and Space Company, Inc., March 1975.
- 10.7-1 H. G. Mesch, "Parallel Gap Welding of Silver-plated Solar Cells," Proceedings of the 10th IEEE Photovoltaic Specialists Conference, 1973.
- 10.7-2 H. S. Rauschenbach and A. F. Ratajczak, "FEP-Teflon Covered Solar Cell Array Advancements," Proceedings of the 10th IEEE Photovoltaic Specialists Conference, 1973.
- 10.7-3 D. R. Lott, "Solar Array Flexible Substrate Design Optimization, Fabrication, Delivery and Test Evaluation Program," Final Report LMSC-D384284, Lockheed Missiles and Space Company, Inc., March 1975.
- 10.7-4 R. M. Jenkins et al., "Non-destructive Testing of Welded Solar Cell Interconnections," Proceedings of the 10th IEEE Photovoltaic Specialists Conference, 1973.
- 10.7-5 D. R. Lott et al., "NDT Evaluation of Solar Cell Weld Joints with Details of Selected Post-bond and Pre-bond Systems," Proceedings of the 11th IEEE Photovoltaic Specialists Conference, 1975.
- 10.7-6 TRW Systems, previously unpublished data.
- 10.7-7 H. F. Sawyer and J. R. Mulkern, "In-Process Non-destructive Microweld Inspection Techniques," presented at MicroElectronic Packaging Conference, Palo Alto, California, November 1968.

- 10.7-8 W. S. Griffiths and H. F. Sawyer, "Non-destructive Weld Inspection Techniques," prepared under Contract NAS2-4166 by W. V. Sterling for NASA Ames Research Center.
- 10.7-9 "Study and Development of Non-destructive Weld Inspection Techniques, Phase I Final Report," NASA CR-73, 207, prepared under Contract NAS2-4166 by W. V. Sterling, Inc., dated March 1968.
- 10.7-10 "Study and Development of Non-destructive Weld Inspection Techniques, Phase II Interim Report," NASA CR-73, 385, prepared under Contract NAS2-4166 by W. V. Sterling, Inc., dated October 1969.
- 10.7-11 R. Buhs et al., "Welding of Solar Cells in Production Line," Proceedings of the 11th IEEE Photovoltaic Specialists Conference, 1975.

CHAPTER 11

EVALUATION AND TEST

CONTENTS

		Page			Page
11.1	The Test Program	11.1-1	11.8	Ultraviolet Irradiation	11.8-1
	11.1.1 Test Objectives	11.1-1		11.8.1 Ultraviolet Test Setups	11.8-1
	11.1.2 Test Types	11.1-1		11.8.2 Far Ultraviolet Test Setups	11.8-1
	11.1.3 Test Plans and Procedures	11.1-2		11.8.3 Test Results	11.8-1
	11.1.4 Test Sequence	11.1-4			
	11.1.5 Data Recording	11.1-4			
11.2	Electrical Performance Measurements	11.2-1	11.9	Combined Environments	11.9-1
	11.2.1 Historical Review	11.2-1		11.9.1 Combined Environments Test Equipment	11.9-1
	11.2.2 Single Cell Measurements	11.2-2		11.9.2 Test Results	11.9-4
	11.2.3 Array Measurements	11.2-5			
	11.2.4 Effects of Lead and Contact Resistance	11.2-5	11.10	Insulation Resistance and Voltage Breakdown	11.10-1
	11.2.5 Solar Simulators	11.2-5			
	11.2.6 Three Types of Solar Cell I-V Curves	11.2-11			
	11.2.7 Measurement of Solar Cell Series Resistance	11.2-11	11.11	Temperature Cycling	11.11-1
11.3	Standard Solar Cells	11.3-1		11.11.1 Test Equipment	11.11-1
	11.3.1 Definitions	11.3-1		11.11.2 Test Results - Mechanical	11.11-1
	11.3.2 The JPL Balloon Flight Program	11.3-1		11.11.3 Test Results - Electrical	11.11-1
11.4	Spectral Distribution and Response	11.4-1	11.12	Dark Forward Testing	11.12-1
11.5	Solar Cell Contact Integrity	11.5-1	11.13	Orbital Flight Data	11.13-1
	11.5.1 Stresses due to Contact Pull Testing	11.5-1		11.13.1 Determination of Array Performance in Space	11.13-1
	11.5.2 Test Procedure	11.5-1		11.13.2 Summary of Solar Cell Array Degradation	11.13-1
	11.5.3 Contact Separation Modes	11.5-2		11.13.3 Nimbus-2	11.13-1
	11.5.4 Test Results	11.5-6		11.13.4 ATS-1	11.13-2
11.6	Thermophysical Properties	11.6-1		11.13.5 Pioneer III, VII and VIII	11.13-6
	11.6.1 Determination of Solar Absorptance	11.6-1		11.13.6 IDSCS (Initial Defense Satellite Communications System)	11.13-6
	11.6.2 Determination of Hemispherical Emittance	11.6-1		11.13.7 OGO	11.13-11
	11.6.3 Measurement of Spectral Reflectance	11.6-2		11.13.8 Intelsat I, II and III	11.13-11
	11.6.4 Measurement of Total Reflectance	11.6-2		11.13.9 LES-6	11.13-12
	11.6.5 Test Results	11.6-2		11.13.10 ATS-5	11.13-13
				11.13.11 ATS-6	11.13-13
				11.13.12 NTS-1 (Timation III)	11.13-13
11.7	Corpuscular Radiation	11.7-1	11.14	Significance of Test Data, Uncertainties and Errors	11.14-1
	11.7.1 Electron Sources	11.7-1		11.14.1 Definitions	11.14-1
	11.7.2 Electron Radiation Test Results	11.7-1		11.14.2 Actual Uncertainties	11.14-2
	11.7.3 Proton Sources	11.7-1		11.14.3 Uncertainties in Inspection	11.14-3
	11.7.4 Proton Radiation Test Results	11.7-2			
	11.7.5 Neutron Sources	11.7-2			
	11.7.6 Neutron Radiation Test Results	11.7-2			
			References		11.R-1

TABLES

11.2-1	Variation in Solar Cell Short-Circuit Current Output with Color Temperature of the Incident Light for Constant Light Intensity as Measured with a Corrected Foot-candle Meter	11.2-3	11.5-1	Contact Pull Test Separation Modes of Ribbons or Wires Soldered to Cell Contacts	11.5-5
11.2-2	Spectrolab Spectrosun Model X-25 Solar Simulator Specifications	11.2-7	11.11-1	Solar Panel Power Loss Due to Temperature Cycling Testing in Air Chambers	11.11-1
11.2-3	TRW Systems LAPSS III Large Area Pulsed Solar Simulator Specifications	11.2-8	11.13-1	Typical Solar Cell Array Degradation in Orbit	11.13-1
11.2-4	Electrical Properties Based on Current Density of 1600 A/cm ²	11.2-11	11.13-2	ATS-1 Solar Cell Characteristics at Various Times in Orbit	11.13-3
11.3-1	Attenuation of Solar Radiation by the Earth's Atmosphere	11.3-2	11.13-3	Satellite Orbits	11.13-9
11.3-2	Repeatability of Standard Solar Cell BFS-17A for 20 Flights over an 8-Year Period	11.3-3	11.13-4	Orbital Parameters and Relative Power Output of Two OGO Solar Cell Arrays	11.13-11
11.3-3	Correlations Between Solar Simulators of Different Organizations	11.3-4	11.13-5	Relative Performance of Eight Intelsat Solar Cell Arrays	11.13-12
			11.14-1	Typical Uncertainties in Predicted Array Performance	11.14-3

FIGURES

11.2-1	Spectral Response of Some Detectors and Spectral Distributions of Some Sources	11.2-4	11.4-1	Spectral Response and Reflectometer Equipment	11.4-1
11.2-2	Schematic Diagram of Solar Cell under Test and Output Measuring Circuit	11.2-4	11.5-1	Definition of Pull Angles	11.5-1
11.2-3	I-V Curves of a Solar Cell at Three Different Light Levels	11.2-4	11.5-2	Solar Cell Ohmic Contact Strength Test Tab	11.5-2
11.2-4	Effect of Lead and Contact Resistance on the Current-Voltage Relationship of a Solar Cell When Using Two-Point Cell Pickoff	11.2-4	11.5-3	Definition of Area for Pull-Test Tab Soldering	11.5-2
11.2-5	4-Point Solar Cell Load Circuit	11.2-5	11.5-4	Solder Joint Acceptance/Rejection Criteria	11.5-2
11.2-6	Back Bias Circuit to Measure True I _{SC} When Large Lead Resistances Are Present	11.2-5	11.5-5	Contact Strength Test Configuration	11.5-3
11.2-7	Spectrosun Model X-25 Optical Schematic	11.2-6	11.5-6	Typical Failure Mode of n Contact, Solder-Coated Titanium-Silver Contacts on n-p Cells, Over a Pull-Test Temperature Range of -112° to 173°C	11.5-3
11.2-8	Spectrosun Model X-25 Spectral Distribution	11.2-6	11.5-7	Typical Failure Mode on n Contact, Solder-Coated Titanium-Silver Contacts on n-p Cells, Over a Pull-Test Temperature Range of -29° to -84°C	11.5-3
11.2-9	Schematic of Flashlamp and Readout Circuit	11.2-9	11.5-8	Typical Failure Mode of n Contact, Solder-Coated Titanium-Silver Contacts on n-p Cells, Over a Pull-Test Temperature Range of -1° to +82°C	11.5-3
11.2-10	Spectral Emission from FX-47A Flash Tube at Two Current Densities Compared with Relative Spectral Emittance of Black Bodies at 7000° and 9400°K	11.2-9	11.5-9	Typical Failure Mode of n Contact, Solder-Coated Titanium-Silver Contacts on n-p Cells, Over a Pull-Test Temperature Range of +110° to +165°C	11.5-4
11.2-11	Comparison of Spectral Output from Xenon Flash Light with the Space Solar Spectrum	11.2-10	11.5-10	Typical Failure Mode of p Contact, Solder-Coated Titanium-Silver Contacts on n-p Cells, Over a Pull-Test Temperature Range of -112° to -173°C	11.5-4
11.3-1	Balloon Flight Configuration	11.3-1			
11.3-2	Comparison of Filtered Xenon Light Source with Space Sunlight	11.3-4			
11.3-3	Comparison of Carbon Arc Light Source with Space Sunlight	11.3-4			

11.5-11	Typical Failure Mode of p Contact, Solder-Coated Titanium-Silver Contacts on n-p Cells, Over a Pull-Test Temperature Range of -1° to +82°C	11.5-4	11.12-5	ATM Panel Dark Forward Terminal Voltage at 25°C for Various Number of Modules in Parallel, Applied Current as a Parameter	11.12-3
11.5-12	Typical Failure Mode of p Contact, Solder-Coated Titanium-Silver Contacts on n-p Cells, Over a Pull-Test Temperature Range of +110° to +165°C	11.5-4	11.13-1	Normalized Current Loss Versus Orbit for Two Solar Cell Experiments	11.13-2
11.6-1	Theoretical and Experimental Values for the Ratio of Hemispherical to Normal Emissivity	11.6-1	11.13-2	A Voltage-Current Family for Unshielded Cell No. 25	11.13-4
11.8-1	Spectral Energy Distribution of Ultraviolet Sources Compared with the Solar Spectrum	11.8-2	11.13-3	Voltage-Current Curves for Cells 15 and 16, with 25 μm Integral Glass (7940) Shields	11.13-4
11.8-2	Relative Photon Energy of Krypton and Xenon FUV Lamps	11.8-3	11.13-4	Voltage-Current Curves for Cell 5, with a 0.15 mm Silica (7940) Shield	11.13-4
11.8-3	Spectral Reflectance for Three Acton Research Corporation FUV Mirror Coatings	11.8-3	11.13-5	Voltage-Current Curves for Cell 20, with a 1.52 mm Silica (7940) Shield	11.13-5
11.9-1	Schematic Drawing of TRW Systems Combined Environment Facility	11.9-1	11.13-6	Maximum Power Versus Time for Several Cells with Various Shields	11.13-5
11.9-2	Sample Holder-Motion Mechanism	11.9-2	11.13-7	Curve Factor, Maximum Power, Open-Circuit Voltage, and Short-Circuit Current Versus Shield Thickness, at 416 Days After Lift-Off	11.13-5
11.9-3	Illustration of Specimen Holder Pickup Technique	11.9-2	11.13-8	Pioneer VI, VII and VIII Solar Arrays	11.13-7
11.9-4	Illustration of One of the Irradiation Patterns Attainable at Sample Holder Plane	11.9-3	11.13-9	Pioneer Solar Array Estimated Nominal Output Characteristic at Bus	11.13-8
11.9-5	Schematic Drawing of Ultraviolet Source Optics	11.9-3	11.13-10	Observed and Projected Cell Short-Circuit Current Degradation	11.13-9
11.12-1	Photovoltaic and Dark Forward Characteristics	11.12-1	11.13-11	Observed, Projected and Calculated Cell Open-Circuit Voltage Degradation	11.13-10
11.12-2	Series Resistance Versus Voltage Obtained Using Illuminated and Dark Curve Methods for Centralab 2x2 cm Cells	11.12-2	11.13-12	Estimated Non-cell Losses and Calculated Cell Short-Circuit Current Loss Projected to 5 Years	11.13-10
11.12-3	Dark I-V Curves at Various Temperatures for an ATM Solar Cell Module	11.12-2	11.13-13	INTELSAT III Solar Cell Array Power Output Variation with Time in Orbit	11.13-12
11.12-4	Dark Forward I-V Curves at 25°C for an ATM Panel with Various Number of Modules in Parallel	11.12-3			

CHAPTER 11

EVALUATION AND TEST

The evaluation phase of a design begins with the crystallization of a test philosophy and the development of a test plan or test specification. Later on in the evaluation phase, detailed test procedures are developed according to which particular test articles are subjected to environmental stress. The resulting test data is analyzed for statistical significance or errors, and forms the basis for accepting or rejecting

the design. The ultimate test of the design, of course, is its performance in orbit.

This chapter provides all of the details which permit test plans to be established, tests to be performed, and the results to be analyzed and compared to existing criteria. Typical general test results are also given.

11.1 THE TEST PROGRAM

11.1.1 Test Objectives

Five basic reasons for testing a device or system are to:

- Provide empirical design data
- Determine functional capabilities
- Evaluate the ability to operate in the required environment
- Determine design limits
- Determine if production units are of the same quality as qualification units

The tests used to make these determinations are called:

- Development tests
- Design verification tests
- Prequalification tests
- Qualification tests
- Preproduction, pilot model, pilot lot tests
- System integration tests
- Production acceptance tests
- Production monitoring tests, quality verification tests
- Reliability tests

The extent of testing is usually a compromise between the testing necessary to assure reliability, and the time, money, and the facilities available to conduct that testing. Most facets of the launch and space environments can be simulated only individually in a relatively simplistic fashion and at comparably high cost. Very few single environments can be simulated simultaneously, such as thermal cycling in vacuum, or ultraviolet and charged particle irradiation in vacuum. Even these combined environments are usually crude replicas of the actual space environment. The most difficult part of testing, however, is the determination of a realistic test level, which on one hand is sufficiently severe to be a true test while on the other hand does not lead to failures which would not occur in actual service. Another important, and often equally difficult, task is the establishment of realistic test pass/fail criteria. A significant part of the determination of pass/fail criteria is the development of reliable inspection methods. For example, great difficulty is encountered in inspecting large solar cell panels for cracked solar cells and cover glasses. Even the best inspectors will not always find all such cracks on panels which contain many thousands of cells and covers during a single inspection. If only one inspection is performed before — and another one is performed after — an environmental exposure, and if during the second inspection a larger number of cracks are found, it cannot be said with any high level of confidence that the additional cracks were caused by the environmental exposure (see Section 11.14.3 for details).

The array designer's job in relation to testing is to interface with both the test engineers and quality assurance engineers in determining test levels, test methods, test procedures, inspection techniques, and pass/fail criteria. It is particularly important for this interfacing to take place when, as is often the case, solar cell array component tests are to be performed as part of the spacecraft test.

11.1.2 Test Types

Development Tests

Development tests are conducted on initial pre-prototype components to check out basic design parameters during the development process. Development tests are used to verify such factors as adhesive bond strength, fatigue life of solar cell interconnectors and solder joints, and solar cell performance before and after environmental exposure. Development tests should verify all requirements necessary to produce a complete set of engineering drawings and/or specifications describing a component capable of meeting its specification requirements. The units used for such tests are usually called breadboard, boiler plate, or engineering models, and are produced specifically for these tests.

The tests should provide data to finalize a new design or to modify an existing design to comply with new requirements. Adjustment, rework, repair, and retest are normal functions of a development test. Specifications should require that all activities, as well as details of all repairs and adjustments, be documented for future correlation with the qualification/production units.

Design Verification Tests

Design verification tests should be conducted on prototype hardware before proceeding to production drawings and actual fabrication of production hardware. Test requirements, toward which the manufacturer must design, should be itemized in the component specification. Design verification tests are planned to prove that a component can meet all of its functional requirements and the most critical of its environmental requirements. Component design verification tests allow system tests to be started with maximum assurance that components can perform their system function prior to performing time-consuming life or reliability tests. Some organizations combine development tests with design verification tests.

Prequalification Tests

Prequalification tests (also called design approval tests, preliminary flight rating tests, flight certification tests, and type approval tests) are conducted on production hardware prior to flight testing to determine whether the article fabricated by production tooling and techniques will perform as capably when fabricated as a prototype. These tests should include

most functional and environmental requirements and some life-cycle tests. The tests should prove that the production hardware can meet all the required parameters for the length of time required by the flight test program. Special stress-to-failure tests are sometimes included as part of prequalification testing. These tests, which can be destructive, are designed to establish margins of safety over minimum design requirements. In some organizations prequalification tests are combined with design verification tests.

Qualification Tests

Qualification tests (also sometimes called design verification tests) are normally formal demonstrations (in contrast to evaluations), usually with the first unit of the production hardware. These are the final test requirements to be met by the component. It is important that qualification test requirements be realistic and not simply be included because it was done before. A primary difference between formal qualification tests and other tests is that the test qualifications are used to demonstrate rather than evaluate the product. Qualification tests verify that the combination of the design, the selected material, and the formal production processes do, in fact, provide equipment with adequate safety margins to perform as required. Safety margins are verified by performing tests at greater than anticipated environmental stresses and at design limit values of selected operational stresses, e.g., static load.

Acceptance Tests

Acceptance tests verify that the production resources are continuing to manufacture units that will operate like the qualification unit and should function successfully in the flight environment. Acceptance test levels and accumulated test time should be controlled so that the test does not significantly subtract from the flight life expectancy.

System Integration Tests

System integration tests are conducted to evaluate the compatibility of the components with system requirements and serve to evaluate and optimize check-out and operating procedures. Although a component may have been correctly designed to fulfill its own functions, its compatibility with related equipment and its performance as part of an integrated system must be demonstrated. Compatibility includes proper interfacing with mating hinges and connectors.

Production Monitoring Tests

Production monitoring tests are conducted at prescribed intervals to subject the product to more intensive or extensive conditions than are encountered in the normal production acceptance test. These tests may be either destructive or nondestructive and are often performed on a sampling basis; their main purpose is to control and monitor production processes, e.g., pull or peel tests of adhesive coupons, peel tests of interconnectors soldered or welded to solar cell contacts and wet-sponge electrical insulation integrity tests.

Reliability Tests

Reliability tests are performed to determine the probability that a component will fulfill its intended function. Components which are cyclic in operation are usually tested for a number of operating cycles until failure, and components which operate continuously are usually tested to determine the mean time

to failure (MTTF) or mean time between failures (MTBF). Continuous life tests may be difficult to simulate, particularly on arrays designed to operate for thousands of solar eclipses in near-earth orbits.

Limit testing, or performance margin testing, determines the margin of safe operation over the specified design conditions. Limit tests are conducted by progressively increasing the severity of a test parameter such as temperature until the component fails. The margin of safe operation over the design conditions is a measure of the component's functional reliability.

11.1.3 Test Plans and Procedures

A distinction is made between test plans and test procedures. The test plan contains general statements regarding a specific program, defining what is to be tested and to what extent. It is normally submitted with a proposal and has the same headings as the test procedure discussed below.

The test procedure is a completely self-contained document which contains all information necessary for the successful performance of a specified test program. The various sections are listed below:

- 1.0 Purpose (including a definition of the test article)
- 2.0 References
- 3.0 Test Schedule (not always required)
- 4.0 Test Conditions and Test Equipment
- 5.0 Requirements and Procedures
- 6.0 Test Witnesses
- 7.0 Test Reports

Typically, in a qualification or acceptance test procedure for a solar cell panel or array assembly, all functional and environmental tests are specified. However, sometimes the complexity of a test requires additional detailed test procedures which pertain only to single tests. Such specific procedures are then called out in the qualification or acceptance test procedure, respectively.

Typical test plans and abbreviated procedures for solar cell arrays are given in the following discussion.

Acoustic Field

Acoustic tests are performed to determine the mechanical and functional integrity of the solar cell array under direct acoustic excitation and acoustically induced mechanical vibration simulating the conditions predicted for liftoff and maximum Q. For such a test the array is typically mounted to a satellite dummy and installed in a reverberant chamber using random noise generators to generate a semireverberant sound field in which the octave band sound pressure levels produced are relatively uniform about the test article. Instrumentation to determine compliance with the specification and the response of the test item consists of several microphones, accelerometers, and strain gages. The specified acoustic test spectrum is established and controlled at a single microphone location. The remaining microphones are used to measure the acoustic levels at positions 90 degrees about the test item to determine spatial distribution and, also, at several locations within the dummy satellite to determine attenuation characteristics. Accelerometers are located on equipment mounting panels, solar panel substrates, and other areas containing components

expected to have large acoustically induced vibration levels. Strain gages are applied to high stress areas, such as adjacent to stringers and reinforcing members, and load carrying members expected to be affected by the acoustically induced vibration.

Temperature (Nonoperating)

The test article is mounted in a temperature chamber and the temperature increased at a specified maximum rate to the specified temperature. Upon stabilization, the temperature is maintained for the required period with the article not operating. The temperature is then decreased and the article removed from the chamber. After visual inspection for damage, the test article is given a performance test.

Temperature-Altitude (Nonoperating)

The test article is mounted in a temperature-altitude or thermal vacuum chamber and subjected to a decrease in pressure equivalent to the specified altitude and a decrease in temperature to the specified temperature. The chamber is maintained at these conditions for the required time with the article not operating. The chamber is returned to ambient conditions and the article removed. The test article is visually inspected for damage and then given a performance test.

Thermal Vacuum Cycling

Solar cell panels are installed in a thermal vacuum chamber with several thermocouples attached to monitor panel temperature during exposure. The specified test temperature is determined from the mean value calculated from the thermocouple outputs. With the panels held at room temperature by radiation, the chamber pressure is reduced to the specified pressure or less. The radiation is removed and the panels are allowed to cool to the specified low temperature. The radiation is then applied to the panels until the specified high temperature is achieved; this condition is maintained for a specified period. The radiation is then removed and the panels are allowed to cool toward the specified low temperature. When the temperature reaches ambient temperature, one exposure cycle is completed. The maximum rate of temperature change is usually specified.

The above temperature changes are repeated for a specified number of cycles. The panels are removed from the chamber after they have stabilized at ambient conditions at the end of the last cycle and are visually inspected for damage or degradation of materials that could impair the mission. The panels are given functional tests as necessary (electrical output, insulation resistance, etc.).

Temperature Cycling (In Lieu of Thermal Vacuum Cycling)

The test article is mounted in the temperature chamber in a manner simulating installation on the spacecraft. Equipment required to operate during this test (as specified in the individual test plan) is turned on at this point and will remain operating for the duration of the test. The test article temperature, monitored by an attached thermocouple, is reduced to the specified low temperature. Upon stabilization, an operational check is made on operating equipments. The test article temperature is then raised to the specified high temperature and stabilized. The operational check is repeated on operating equipments. The temperature is then reduced toward the low temperature and when the test article temperature passes through ambient temperature, one cycle is complete.

A specified number of cycles, as described above, are required for completion of this test. All test articles are inspected at the conclusion of exposure for visible damage and test articles not operated during the exposure are given a performance check.

Sustained Acceleration

The test article is mounted on a centrifuge and accelerated to the required angular velocity to apply the specified acceleration for the specified time interval. Equipment required to operate is operated and continuously monitored during the test. The test article is alternately positioned on the centrifuge to permit application of acceleration along all specified axes in sequence. At the conclusion of exposure, all test articles are given a functional performance test at ambient conditions and an inspection.

Vibration

The test article is mounted on a test fixture in a manner which simulates the spacecraft installation. The test article is subjected to a specified sequence of sinusoidal vibrations or a random vibration (or both) along the specified axes. Test levels and duration are as specified.

Performance parameters, as specified, are continuously monitored during vibration on equipments which are required to be operating by specification in the individual test plan. At the conclusion of the vibration exposure, all articles are visually inspected for damage which could impair performance and then given a functional performance test.

Shock (Mechanical)

The test article is mounted on a shock fixture in the same manner in which it will be installed in the spacecraft. The article is then subjected to a shock pulse in each direction along specified axes to specified test levels.

Equipment required to operate during this test by specification in the individual test plan is monitored continuously. A composite and simultaneous recording is made of the shock pulse, timing marks, calibration line, and selected parameters from the equipment operation. Upon completion of the shock test all test articles are visually inspected for damage that could impair performance and then given a functional performance test.

Humidity (Nonoperating)

The test article is mounted in a humidity test chamber that complies with specified requirements. The temperature and relative humidity in the chamber are then raised from ambient conditions to specified levels over a specified period of time. These conditions will be maintained for a stated minimum time. With the relative humidity held at the specified level, the chamber temperature is reduced to within a specified range over a specified minimum period. This constitutes one cycle.

The humidity test continues for a specified number of cycles. The test article is then removed from the chamber and returned to ambient conditions. Excess moisture may be removed from the article by pouring or by other suitable means. The test article is visually inspected for damage that could impair the mission and given a functional performance test within a maximum specified time interval after removal from the chamber.

During-Test Operating Conditions

It is sometimes of interest to operate equipment while it undergoes an environmental exposure. The purpose of such operation is generally to determine erratic circuit operation and intermittent opens or shorts. Since it is usually impractical to simulate solar illumination during such tests, the following tests are used:

- Dark forward current monitoring
- Blocking diode reverse biasing
- Solar cell circuit-to-substrate resistance monitoring

11.1.4 Test Sequence

The planned tests are specified to ascertain that the deliverable equipment will perform as required by the performance specifications. The general test policy established for a typical project emphasizes component, spacecraft, and satellite testing. The guiding principle is that each essential characteristic and parameter established by the performance specifications be verified at those points in the equipment generation where verification is most readily accomplished and where the probability of future degradation or disruption is at a minimum.

The well-planned sequence of tests is designed to apply environmental stresses approximately in the order in which the equipment will be exposed to stresses after shipment from the factory. The general sequence is defined as temperature storage or cycling, the mechanical stresses during launch, and finally thermal-vacuum or space simulation. Typically, the spacecraft components are all tested separately to verify safety margins in respect to anticipated stresses and the requirements. After the successfully tested components are integrated into a spacecraft, the total spacecraft is tested under selected environmental stresses. Functional performance of the system is verified to be within the specified system limits before, during, and after exposure. Successful operation at the system level within limits serves to verify that adverse accumulation of tolerances has not combined to produce marginal system operations. A similar philosophy is applied to the satellite (spacecraft payload).

An assumption is made that the effects of the various environmental stresses which can occur simultaneously in the real environment are basically independent over the range of anticipated levels. Hence, combinatorial effects of environmental stresses are not considered to be significant from a practical sense, with the exception of temperature and vacuum. This assumption has been borne out adequately by experience with previous spacecraft.

11.1.5 Data Recording

Data Requirements

Environmental and other test equipment and test facilities are typically operated in accordance with standard written procedures which contain explicit instructions on test equipment data items to be monitored and recorded during individual tests. These data items are recorded on test data sheets or copies of the test procedure as appropriate for each test. Environmental test data requirements are as follows:

- Temperature Storage
 - Chamber temperature
 - Time at temperature

- Temperature Altitude
 - Chamber temperature
 - Chamber pressure
 - Time at each temperature and pressure
- Thermal Vacuum
 - Chamber temperature
 - Test article temperature
 - Chamber pressure
 - Time at each temperature and pressure
 - Number of cycles
- Temperature Cycling
 - Chamber temperature
 - Test article temperature
 - Time at each temperature
 - Number of temperature cycles
- Sustained Acceleration
 - Location of center of mass
 - Angular velocity or rpm
 - Resultant acceleration
 - Test article axis
 - Time at acceleration
- Vibration and Acoustic Field
 - Test article axis
 - Exposure time
 - Plot of frequency versus g^2/Hz
- Shock
 - Test article axis
 - Number of shock pulses per axis
 - Response spectra, frequency versus peak g
- Humidity
 - Chamber temperature
 - Chamber relative humidity
 - Time of temperature and humidity
 - Number of cycles

Data Handling and Retention

Data from more formal tests is typically recorded on the appropriate test procedure. These test procedures will, in general, specify characteristics to be verified and will state the test results. Raw test data may be in several forms: strip-chart recordings, digital printouts, polaroid photos of oscilloscope patterns, magnetic tape recordings, still and movie photographs, and computer printouts. Remote data stations will usually be employed during integrated system testing. The complete test procedure and the results from the component tests and such subsystem tests as are applicable should be available for reference during and after the system testing. The measured data should be converted and recorded in a form practical for comparison.

Frequently, Quality Assurance accumulates test data from component and subsystem tests for qualification and flight units, maintains all records, and is responsible for the incorporation of component and subsystem test data into appropriate Test Data Packages.

Test Equipment Calibration

Each instrument and other measuring apparatus upon which the accuracy and precision of test results depend should be calibrated in accordance with established calibration procedures or more frequently where conditions warrant. Calibration records should be maintained. Pretest inspection of instrumentation for evidence of valid calibration labels should be the

responsibility of the test conductor or responsible engineer performing the test. Verification of properly calibrated test equipment for each test setup should then be conducted by Quality Assurance. In the event that a calibration expires during the formal test sequence, the test should be concluded without changing or calibrating the instrument. At the conclusion of each test sequence, any such instrument should be recalibrated and the new calibration data should be included in the test data package.

To ensure instrumentation accuracy, each instrument and measuring device should be calibrated using measurement standards traceable to the National Bureau of Standards. The standard practice of most companies requires the accuracy and resolution of test equipment to be at least ten times greater than the specified tolerance of the element being measured. In some cases, state-of-the-art instrumentation may be used which, of necessity, may have a lower accuracy capability.

11.2 ELECTRICAL PERFORMANCE MEASUREMENTS

11.2.1 Historical Review (Adapted from Refs. 11.2-1 and 11.2-2)

Since the development of the solar cell in the 1950's, solar cell measurement techniques have progressed from an initial volt-ohmmeter test in "fair weather" to high-altitude and space flight experiments, sunlight simulators, accurate spectroradiometric apparatus, and analog and digital data acquisition systems.

Originally, solar cells and solar cell assemblies for use on space vehicles were evaluated in the laboratory by measurement under incandescent illumination. Tungsten lamps with color temperatures of the order of 2700° to 3400°K, compared to the greater than 6000°K effective color temperature of the air-mass-zero sun were used to illuminate the cells. In some cases, but not universally, water filters were used to reduce the infrared spectral content of the incandescent lamps. Because of the necessity of periodically making measurements during solar cell panel fabrication, such equipment was used for in-process measurements at the sacrifice of accuracy and cell matching capability. The change of the water absorption wavelength with temperature, formation of bubbles and algae growth caused such instabilities that most of such filters were abandoned quickly.

The major light source for volume solar cell testing through the mid-1960's was the tungsten lamp. The stability and reliability of tungsten lamps outweighed the disadvantage of the tungsten lamp spectrum being so drastically different from that of sunlight. In the 1950's it was already realized that measurements were not repeatable in tungsten unless the filament voltage, and hence the color temperature of the lamp, was closely controlled and the solar cell temperature was held within close tolerances. The light intensity was adjusted with usually unencapsulated solar cells which were calibrated in natural sunlight against a pyrheliometer, a thermopile specifically designed for measuring solar flux. Solar cells were thus tested under so-called "Standard Tungsten Test Conditions" (unfiltered tungsten light of 2800° ±50°K equivalent to 100 mW/cm² solar radiation at 28°C cell temperature).

This level was set based upon the effect of natural sunlight on solar cells in normal outdoor conditions at an arbitrary intensity level of 100 mW/cm². Thus, "standard" solar cells were taken into natural sunlight and their measured output at any intensity was then extrapolated to 100 mW/cm². The natural sunlight intensity was measured using normal meteorological equipment, particularly a pyrheliometer. Early pyrheliometers were of the 180-degree type but, in an attempt to improve accuracy by eliminating the effects of sky background, these were later replaced with the normal incidence types.

When precision was required, the solar cells were measured in essentially collimated sunlight, and in other cases the sky background was accounted for by applying a correction based upon the ratio of short

circuit currents of a cell measured in uncollimated to that measured in collimated light. Having calibrated several such cells, these "standards" were then taken into the laboratory and used to adjust the intensity of tungsten incandescent illuminators. By adjusting the distance from the lamp or by some optical means, the intensity was changed until the short circuit current of the standard cell reached the same value as that obtained at the 100 mW/cm² natural sunlight condition.

Immediately several problems occurred with this procedure. First of all, natural sunlight conditions at local test sites varied significantly in both intensity and spectral content so that correlation from one day to the next was erratic. To resolve this problem, standard cell calibration began to be performed at Table Mountain, California, then the site of the Smithsonian Institute Solar Observatory, where data on sunlight conditions and spectra had been available for almost 25 years.

Table Mountain is approximately 75 to 100 miles from Los Angeles (depending upon route), accessible to all parts of Los Angeles by good highways, and generally enjoys relatively stable atmospheric conditions. The altitude of the test site is 7516 feet. The mountain is located in the extreme northerly portion of the San Bernardino mountain range immediately adjacent to the Mojave desert. This location, slightly north of Los Angeles and adjacent to the desert, is primarily responsible for the atmospheric conditions, which are generally characterized by relatively clearer skies than found in more southerly locations and lower humidities than are achieved at alternate sites.

Having improved the outdoor illumination condition, attention was next turned to the problem of variation in color temperature of the tungsten sources. Thus, color temperature meters came into use for monitoring the light and the color temperature was corrected by changing lamp voltage.

By thus calibrating solar cells under sunlight conditions which were more nearly reproducible and by maintaining control of the incandescent illumination, it was felt that sufficient accuracy could be achieved to permit adequate extrapolation of outputs to air-mass-zero conditions. However, in 1961 it was discovered that in the attempts to improve solar cell efficiencies the spectral response had been so significantly shifted toward the red as to introduce errors of as much as 15 to 20 percent. Thus, cells and panels made at that time were being measured under sources calibrated against standard cells of different spectral response, such that the cell and panel outputs appeared to be approximately 15 percent more efficient in space than was actually the case. As a result of this problem, considerable attention was focused by industry and government on the test methods.

The first milestone was an industry-wide, long sought-after AIEE-IEEE joint meeting on solar cell standardization in 1959, in which many existing

existing problem areas were defined and others solved. In particular, a standard solar cell encapsulation package with quartz window and liquid temperature control facility was standardized, four-terminal solar cell measurements specified (see Section 11.2.4), and collimation angles for pyrheliometers and solar cells (and minimum atmospheric conditions for calibrating solar cells against the pyrheliometer) defined, among many others. The AIEE shortly afterward established a committee which prepared a specification for measurement of solar cells using simulated solar radiation (Ref. 11.2-3).

The prime source of error in solar cell calibration work at that time was the pyrheliometer. Not only did the actual pyrheliometer calibration seem less accurate than ± 3.5 percent (as had been verified by comparing different units simultaneously in sunlight), but the great difference in spectral response between the pyrheliometer (0.2 to 3.5 μm) on one hand and the solar cell (0.4 to 1.2 μm) on the other caused great errors when solar radiation was measured through atmospheric windows.

Attempts were made in the early 1960's to eliminate the pyrheliometer as much as possible in cell calibration procedures, at least for measurements made in the lower atmosphere. With airplane, balloon and satellite flights, the ultimate in accuracy was hoped to be achievable, but still fell short of the goal. Balloon standards, however, seemed to have the highest calibration accuracy and an increasing number of contracts were written around the "Balloon Standard" as a definitive light intensity standard (see Section 11.3).

During the following years, the development of solar radiation simulators was pursued vigorously, with the hope of finding the ultimate answer to all solar cell measurement problems. Yet spacecraft experiments cast doubt on Johnson's data (Ref. 11.2-4) on the solar constant which had been the "spectral standard" for simulator performance. Spectroradiometric equipment to measure the simulator performance accurately was nonexistent in 1965 and standard solar cells with "space calibrations" to verify simulator performance were not available. Therefore, solar simulators were calibrated by a combination of various methods that were generally trustworthy but lacked a solid backing of "space-calibrated" standard cells or correlation with other valid and "traceable" means.

Small solar simulators covering up to approximately a 5-cm² area and essentially conforming to the AIEE recommendations were constructed. These instruments proved very useful in providing better measurements of individual cells. However, because of limited size, such equipment could not be used for solar cell arrays. The solar cell array manufacturer and spacecraft manager were still unable to properly evaluate the completed arrays by 1965. Although tools were available for examining individual cells, because of the difficulty in correlation between the individual cell testers and the completed arrays, even such small equipment failed to contribute to the solution of the problem, although research programs had benefitted substantially. Thus, the use of Table Mountain for measurement of arrays became increasingly relied upon for final acceptance testing and for evaluation of environmental test performance, whereas for fabrication, incandescent illumination remained the only available source.

With an increasing reliance on Table Mountain, California, for measurements, facilities needed to be prepared. Considerable differences existed between organizations wanting to perform the necessary tests.

Some improvement in this situation was accomplished during 1962 when JPL acquired a test facility on Table Mountain previously operated by the Smithsonian Institute.

On the other hand, technical problems in measurements at Table Mountain occurred frequently. The most significant difficulty related to the availability of suitable weather. To make precise measurements, it was desirable to establish very select atmospheric conditions. Such specifications related to minimum intensity, which could range—depending upon specific programs—from 90 to 100 mW/cm²; horizontal visibility which generally ranged from 5 to 10 miles; and sky radiation (which for various purposes had been specified for as little as 6 to 10 percent of direct sunlight, i. e., approximately 6 to 10 mW/cm²). In some cases measurements were permitted with sky radiations as high as 12 percent. There were almost always limitations on allowable time periods before and after solar noon such that, generally on a good day, only 3 to 4 hours of test time were available.

Particularly when extended poor weather prevailed, there was increasing pressure for alternate test sites. Several such locations were considered and used. Such sites included Palm Springs, Bishop and White Mountain, California; Kitt Peak, Arizona; Sacramento Peak, New Mexico—and on a few occasions, locations in the eastern part of the United States. Unfortunately most of these locations were not so readily accessible and the costs associated with such alternate test sites, particularly for the measurement of large or numerous arrays, were prohibitive.

During the mid-1960's significant progress was made in simulating solar energy in the laboratory. Most of this equipment was not simply directed toward solar cell testing but was also used widely for materials testing, determination of solar absorptivities and thermal balance testing on the subsystems and complete satellite systems. During 1964 the capabilities of such equipment advanced to a point that arrays of solar cells could, in fact, be properly tested. The most widely used solar simulators for solar cell and array testing since the late 1960's are the X25 or X-25L solar simulators developed by Spectrolab Division of Textron Electronics, Inc.

The solar simulators developed in the 1960's, such as the Spectrolab X-25, used high-power, high-pressure xenon arc lamps which operated continuously and illuminated reasonably uniformly an area up to nearly 0.07 m² with a closely matched (when appropriately filtered) air-mass-zero spectrum. A need for illuminating much larger areas and entire arrays, however, continued to exist until the so-called pulsed xenon arc solar simulators became available during the late 1960's. The pulsed solar simulators permit energy densities to be reached in the lamps which can be maintained only for a few milliseconds to prevent lamp destruction. These simulators can thereby provide illumination over an area of 5 meters in diameter at one solar constant intensity.

11.2.2 Single Cell Measurements (adapted from Ref. 11.2-5)

Silicon solar cells are semiconductor devices which convert light energy into electrical energy. Intensity and spectral distribution of the incident light energy, size of illuminated active cell area, and cell temperature are the main factors which determine the electrical output of a solar cell. The cells are tested

for their ability to convert a given amount of light energy into a specified amount of electrical energy.

A typical test setup consists of a light source which allows the beam of maximum intensity to be directed toward the solar cell. The cell is placed at a distance from the lamp with its active surface at a right angle to the optical axis of the light beam. Generally, the greater the distance, the more accurate the measurement. The operating voltage of the lamp is adjusted until its spectral distribution corresponds to a specified value and the intensity is adjusted by varying the distance between the lamp and solar cell.

Measurements in Light from Tungsten Filament Lamps

Solar cells for space use should be measured in simulated air-mass zero (AM0) sunlight (defined in Section 2.4.2). If simulated AM0 sunlight is not available, terrestrial sunlight is the next best choice. Light from tungsten filament lamps is the poorest choice for an illumination source for solar cells because it lacks a sufficient percentage of energy in the short (blue) wavelength portion of the spectrum. The measurements of the output from solar cells intended for space use that are performed in light from tungsten filament lamps are by themselves worthless; an additional cell blue-response measurement must be performed for each cell and the results of the two measurements must be combined and related to cell performance in AM0 sunlight.

If tungsten filament lamps are used, the color temperature of the lamp is controlled. Color temperature is measured with a color temperature meter, which is calibrated against a standard lamp. Most good two-channel color temperature meters will do an adequate job. The most widely used color temperature for measurements and calibration work has been 2800°K. Intensity may be measured with a footcandle meter, having a spectral response closely matched to the spectral response of the human eye (Standard Luminosity Curve, 1924, CIE). Any good footcandle meter may be used if it is either corrected for the standard eye response or calibrated at the color temperature at which the measurement will be performed.

Tungsten lamps used for solar cell measurements are either evacuated or gas-filled. In use are standard types of various manufacturers, ranging from 1-volt 0.2-watt to 125-volt 1000-watt types. The lamps are operated at voltages to produce color temperatures between 1800° and 3400°K and intensities from 1 to 10,000 footcandles. Variations in glass thickness of lamp envelopes have little effect in the wavelength range in which solar cells are responsive.

Excessive blackening of the inside of the lamp changes the spectral output slightly and should be avoided. All lamps with a power consumption of 100 watts or more must be forced-air cooled to prevent early lamp deterioration. While lamps are operated with direct current for critical calibration work, precision-regulated alternating current is used for routine measurements.

The importance of precisely defining the spectral distribution of the tungsten light source is brought out in Table 11.2-1. An explanation for this behavior comes from the different spectral response characteristics of silicon and selenium cells and the different spectral distributions of radiant energy from various light sources. As illustrated in Figure 11.2-1, the corrected footcandle meter is responsive only in the low output region of a tungsten lamp, while the silicon cell is most sensitive near the peak output of the tungsten lamp. A variation in color temperature changes the "blue" to "red" ratio of tungsten and thus

the silicon cell gets a proportionately different amount of energy than the footcandle meter.

Table 11.2-1, together with Figure 11.2-1, also show that various solar cells may put out different amounts of electrical energy with respect to each other when the spectral distribution of the light source is altered. For example, two solar cells may put out a short-circuit current of 20 mA each at 1000 footcandles of 2000°K; but when tested at 1000 footcandles of 2800°K, their output may be 5 and 7 mA, respectively.

Table 11.2-1. Variation in Solar Cell Short-Circuit Current Output with Color Temperature of the Incident Light for Constant Light Intensity as measured with a Corrected Footcandle Meter (Ref. 11.2-5)

Color Temperature* (°K)	Light Intensity† (footcandles)	Relative Solar Cell Output‡ (%)
1800	1000	1182
2000	1000	750
2200	1000	545
2400	1000	432
2600	1000	345
2800	1000	286
3000	1000	241
3200	1000	205
3400	1000	182
6000	1000	100

*1800°K through 3400°K are obtained with tungsten filament lamp; 6000°K is terrestrial sunlight on a cloudless day.

†Corrected footcandle meter spectral response per Figure 11.2-1.

‡Silicon cell spectral response per "average response" in Figure 11.2-1. This is a deep-diffused, conventional solar cell.

Measurements in Simulated Sunlight

Most solar cell measurements are now performed in simulated air-mass-zero sunlight. Nevertheless, differences in the spectral distribution between different simulators and between simulators and natural sunlight do exist and must be considered when accurate measurements are to be performed. Use of a spectrally representative standard solar cell for light level calibration can reduce measurement errors due to spectral mismatch to less than 1 percent.

Figure 11.2-2 shows the equivalent circuit of a solar cell and the basic circuit for measuring the electrical output of the cell. If the load resistor R_L is very small, then the voltage across the cell is also very small and the current through R_L is considered to be the "short-circuit current" or I_{sc} . As R_L is made larger and larger, less current will flow through R_L and more voltage will appear across the cell, until a point is reached where $R_L = \infty$ and $I = 0$. This point is called "open-circuit voltage" or V_{oc} . If all the points of voltage and current of the cell are plotted, a curve similar to Figure 11.2-3 is obtained. This so-called "I-V curve" can be plotted with an X-Y recorder. However, for routine measurements a less costly procedure is employed.

Cells are usually tested at a particular light level for minimum current output into a specified load, or for a minimum current at a fixed cell-voltage, usually 0.43 volt for 10 ohm-cm cells and 0.47 volt for

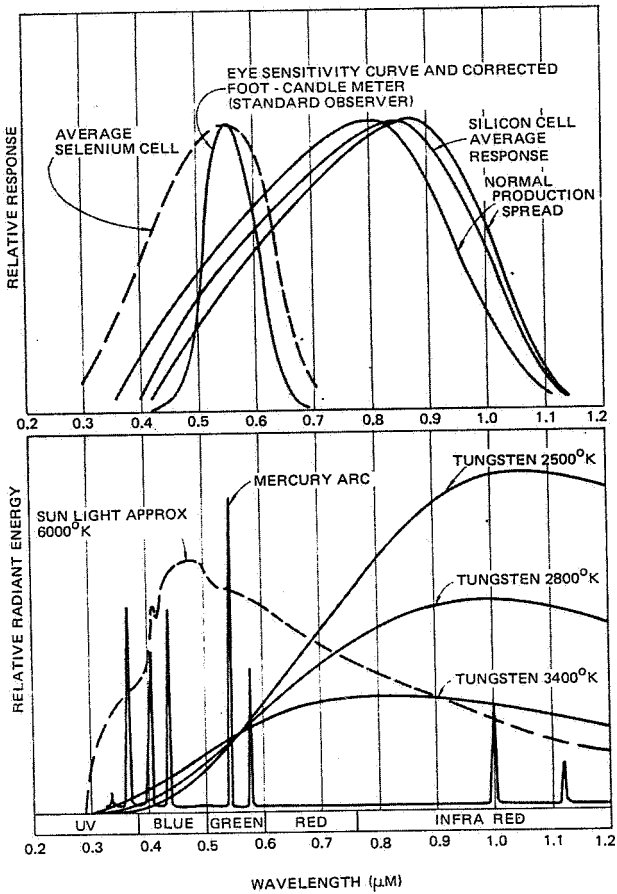


Fig. 11.2-1. Spectral Response of Some Detectors (top) and Spectral Distributions of Some Sources (bottom) (Ref. 12.2-5)

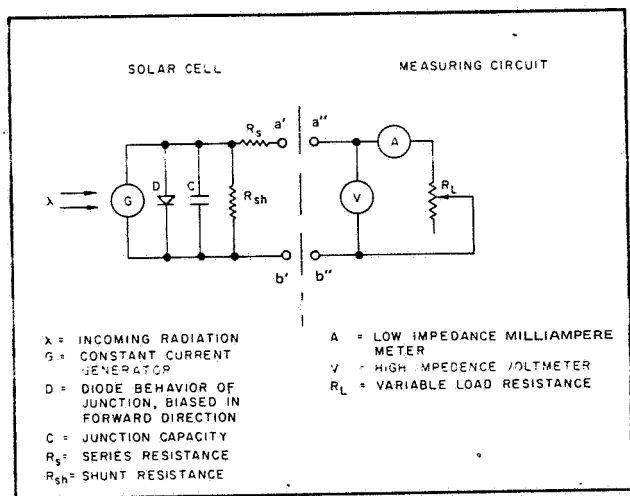


Fig. 11.2-2. Schematic Diagram of Solar Cell under Test (left) and Output Measuring Circuit (right)

1 ohm·cm cells. The load resistance is easily plotted on the graph in Figure 11.2-3: pick any point on the graph, not necessarily on the curve, draw a straight line through the origin and the point, and the line will represent the value for the load according to Ohm's law ($R_L = V/I$) where R_L is in ohms, V in volts, and I in amps. The point where the load line intersects the I-V curve is the operating point of the cell.

The shape and magnitude of the I-V curve depends on the junction characteristics, shunt resistance, and series resistance (D , R_{sh} and R_s , respectively, in Figure 11.2-2), and on the total radiant energy converted into electrical energy, regardless of wavelength composition. For instance, if a certain radiation with a wavelength of 0.4 to 0.7 μm produces a certain I_{sc} , it will also produce a certain I-V curve. Another quantity of radiation between 0.8 and 1.0 μm falling onto the same cell with an intensity that will produce the same I_{sc} as before will also produce the same I-V curve as long as the temperature remains constant. The amount of ripple in the light level, however, may produce different effects in the readout equipment. For example, xenon lamps operated from ac- or unfiltered dc-supplies often produce a depressed knee in the I-V curve as compared to the I-V curve obtained with filtered dc.

Since solar cells have a low impedance at high light levels, current meters in the measuring circuit should also have a very low impedance to prevent measuring errors. For instance, to measure short-circuit current, the internal meter resistance should

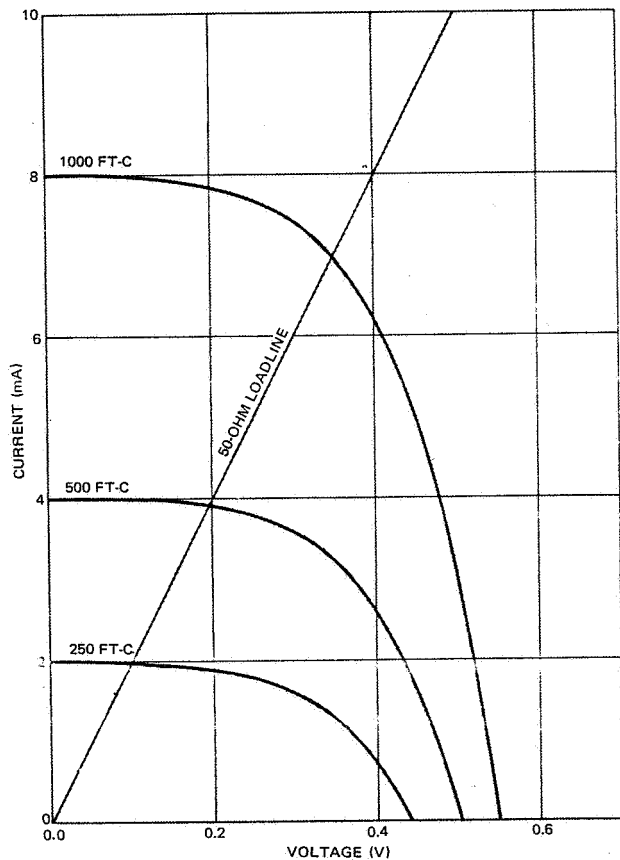


Fig. 11.2-3. I-V Curves of a Solar Cell at Three Different Light Levels (illustrative example)

be 0.1 ohm or less. At low light levels in the cell impedance becomes high and voltage measurements become more difficult. For instance, at 0.01 solar constant the input impedance of a voltmeter should be 10 megohms or more in order to measure open-circuit voltage correctly.

11.2.3 Array Measurements

Array measurements are in principle conducted like single cell measurements. The major differences are that the light source must uniformly cover a larger area and that the readout circuitry must be capable of handling higher power levels.

Most array output measurements in the past were performed in natural, terrestrial sunlight, as discussed in Section 11.2.1. Only recently have solar simulators become available which can illuminate a large area uniformly. These simulators are of the pulsed xenon lamp class, in contrast to the continuously operating "high pressure xenon arc" types, such as used in the Spectrolab X-25, for example. Pulsed lamp operation becomes a necessity because the required continuous power density of a lamp or even a bank of lamps needed to illuminate a modern "average sized" array cannot be achieved physically with the present state of the art. Therefore, solar simulators have been devised in which the lamp is operated at enormous power densities for very short time periods, just long enough to make a measurement. Just as in the case of the continuous simulators, a standard solar cell is used to calibrate the light intensity, usually during each "flash."

11.2.4 Effects of Lead and Contact Resistance

Two important factors that are easily overlooked in cell and array measurements are (a) the resistance in the cable leading from the solar cell to the resistive load and (b) the resistance resulting from poor electrical contact to the cell with metal probes. Both of these may be causing a substantial error in the measurements. Under favorable conditions, these resistances would have negligible effect, but these conditions, especially the contact resistance, cannot always be kept under control. Both of these resistances in effect add series resistance to the cell or the array and depress the "knee" of the I-V curve. For example, in Figure 11.2-2 the measuring circuit is connected with only two wires to the solar cell between point a' and a'', and b' and b'', respectively; these wires and their respective metal probes to the solar cell cause voltage losses, as indicated in Figure 11.2-4 for four different cases. Curve A could result from using a pair of No. 20 copper wires 10 feet in length to connect the cell to the load (0.2 ohm) and at the same time have a slight amount of corrosion on the cell ohmic contact and the metal probes (0.3 ohm). Corrosion-free contacts and probes would still result in a plot resembling Curve B. If the total contact and lead resistance were reduced to 0.005 ohm by using a pair of No. 12 copper wires 3 feet in length, the result would be similar to Curve C, but only if the contacts and probes remained free of any resistance. Curve D is the true cell output for comparison.

The solution to this problem lies in the so-called four-point termination of the cell or array. Figure 11.2-5 shows the circuit used to eliminate the effects of lead and contact resistance. This circuit incorporates the use of two separate pairs of wires leading from four separate probes that make contact with the cell or the array terminals and the current and voltage measuring equipment.

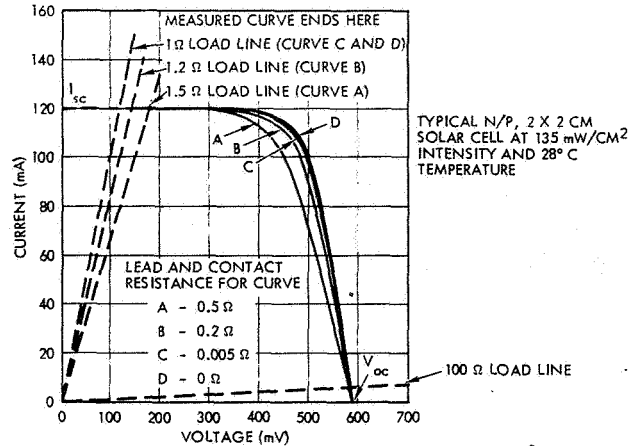


Fig. 11.2-4. Effect of Lead and Contact Resistance on the Current-Voltage Relationship of a Solar Cell When Using Two-Point Cell Pickoff

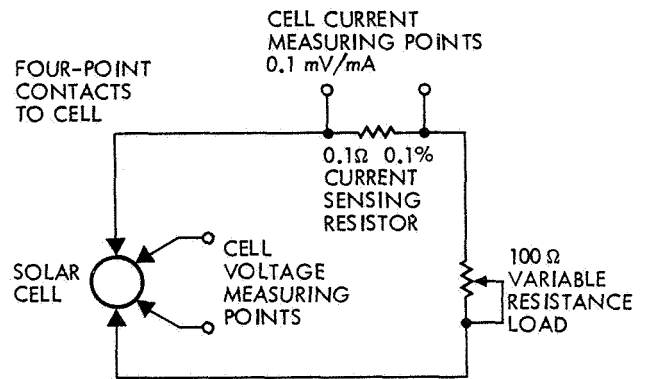


Fig. 11.2-5. 4-Point Solar Cell Load Circuit

The I-V curve resulting from use of two pairs of leads for cell output measurements is the same as Curve D in Figure 11.2-4. The I-V curve is now independent of the circuit resistance with only one exception: a larger value of contact or wiring resistance causes a gap in the curve portion near the short-circuit current. The resistance in the load circuit, however, no longer has an effect upon the shape or accuracy of the solar cell curve. The same holds true for array measurements.

A simple solution to extending the solar cell I-V curve to true short-circuit current or even to negative voltages is the addition of a so-called "back bias," as illustrated in Figure 11.2-6.

11.2.5 Solar Simulators

The solar radiation (or illumination) simulators available today fall into two classes: continuous output and pulsed output. The former type is limited in its use to the testing of relatively small panels. The latter type generally allows accurate testing of large panels and even entire arrays.

The following paragraphs describe examples of instruments of each type which are currently in use and are commercially available.

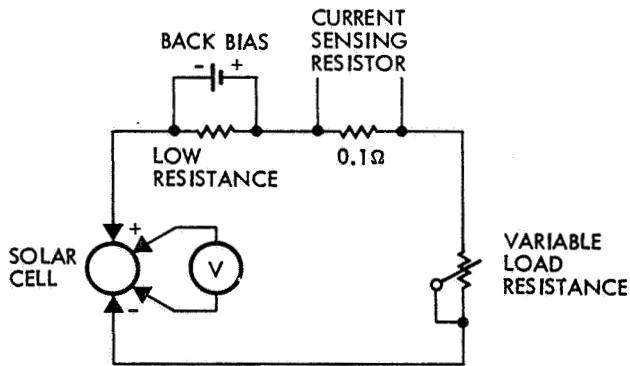


Fig. 11.2-6. Back Bias Circuit to Measure True I_{sc} When Large Load Resistances are Present

Spectrolab Spectrosun Model X-25 Solar Simulator*

A versatile laboratory light source, which uses a 2500-watt xenon lamp, and high quality optics, the Model X-25 solar simulator can be applied to a wide variety of testing applications by the proper selection of externally mounted accessories.

Typical Performance: Beam diameter up to 15 inches; collimation angle to ± 1.2 degrees; filtering to closely match the sun's solar spectrum; intensity of more than one solar constant (140 mW/cm^2). Self-contained in mobile metal cabinet, with beam height electrically adjustable from 1.2 to 1.6 m. Additional specifications are given in Table 11.2-2.

The X-25 optical system, shown in Figure 11.2-7, collects and distributes the radiation from the 2500 watt xenon short-arc lamp to illuminate a projected area with a collimated beam. The heart of the optical system is the specially developed, source collecting mirror mounted with its focus coincident with the arc of the lamp. The optical contour of the collector mirror surface is an aconic section of unique design that optimizes the energy-transfer from the arc of the lamp to the image plane of the projection or collimation system. This special collector directs the maximum amount of energy from the lamp, with correct distribution in the image plane, to provide uniformity of the output beam with minimum filtering corrections. The field/projection lens system magnifies and projects this image either onto a projection plane for illuminating planar targets, or onto the plane of a collimating element, which in turn converts the radiation into a parallel beam. Various options of projected and collimated beams of varying projection distance and/or collimated beam diameters are offered by the various field/projection and collimating lens system accessories. Alternate arrangements and optical systems may be designed to meet special customer requirements, such as larger or smaller beam diameters, or projection distances.

The spectral distribution of the radiation from the Spectrosun Model X-25 solar simulator approximates the sun's emission spectrum (Figure 11.2-8). The basic simulator console is supplied with partial filtering for spectral matching as standard equipment.

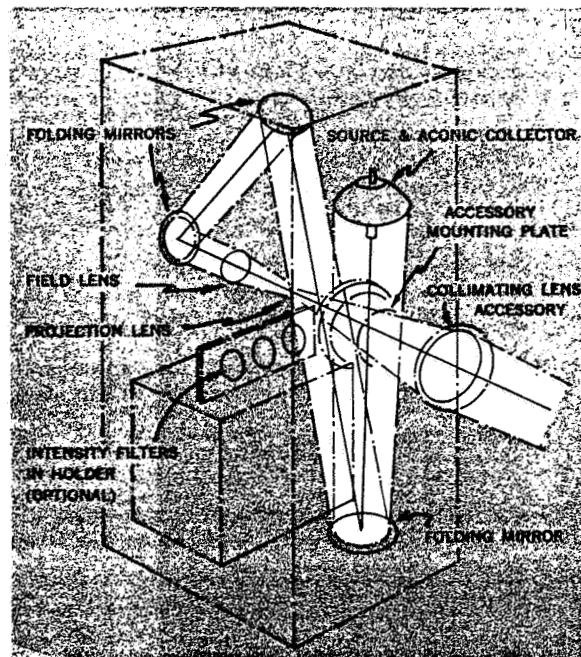


Fig. 11.2-7. Spectrosun Model X-25 Optical Schematic (Ref. 11.2-6)

For users who require a closer match of the simulator output to the sun's zero-air-mass spectrum, a spectral filtering accessory is available. The close filtering is obtained by the application of additional special Spectrolab manufactured interference coatings onto the projection lens.

TRW Systems Large Area Pulsed Solar Simulator Model LAPSS III†

The LAPSS III solar simulator is a complete, portable test set designed for precise output measurements of solar panels and solar arrays. The unit is especially suited for qualification and acceptance testing of production quantities, and has been used by TRW Systems for this purpose successfully for some time. Operating and test costs have been considerably lower than for any other test method previously used. The test set consists of separate power supply and data control consoles and a portable lamp. Specifications for the LAPSS III system are summarized in Table 11.2-3.

The power supply console contains a high voltage, high current dc power supply, pulse forming network, and a lamp igniter circuit. The igniter triggers the lamp upon receipt of a command from the operator. The lamp, a linear xenon flashtube designed for pulsed operation, is mounted in a tripod-supported collimating tube without any optical system.

The data control console houses an electronic load and the data acquisition and correction circuits. The electronic load biases the test specimen to pre-selected points on the unit current-voltage characteristic. Up to ten such points, including short-circuit current and open-circuit voltage, can be programmed.

* Abstracted from Ref. 11.2-6.

† Abstracted from Refs. 11.2-7 and 11.2-8.

Table 11.2-2. Spectrolab Spectrosun Model X-25 Solar Simulator Specifications

Control Panel	Controls include master on-off switch; lamp ignite switch, remote intensity control, beam height control. Monitors include beam intensity, power supply voltage and current and elapsed time indicator. All operating controls and visual monitor displays are functionally arranged on the control panel for ease of operation and immediate and accurate monitoring. Safety interlocks are provided to safeguard against injury to personnel.
Light Source	2500-W xenon short-arc lamp mounted in special strain free adjustable mount designed for positive alignment.
Beam Diameter	Standard basic projection console illuminates more than 30 cm diameter at a distance of 60 cm. Interchangeable projection lens/collimator optics available to provide beam diameters up to 38 cm.
Beam Intensity	1.0 to 1.6 kW/m ² for 30 cm diameter filtered beam (higher for smaller beams) monitored and displayed at control panel, adjustable to within 2 percent. Range can be extended downwards with accessory intensity screen set.
Uniformity of Beam Intensity	Standard ± 10 percent with 2.5 x 2.5 cm monitor; ± 5 percent and ± 2 percent available with uniformity adjusting accessory
Collimation (or projection angle)	Standard basic projection console beam cone angle is ± 14 degrees. Alternate projection cone angles to ± 7 degrees available. Collimated system collimation angles are ± 1.2 degrees for 30-cm diameter and ± 2.4 degrees for 15-cm diameter systems.
Spectral Match	0.25-2.7 μ m high-pressure xenon spectrum as modified by filters and optics. Standard Model X-25 partially filtered. Close filtering available as an accessory.
Optics	Spectrolab-built UV grade lenses, mirrors and aconic collector (patent applied for).
Beam Orientation	Horizontal beam with axis adjustable from 1.2 to 1.6 m from floor.
Power Supply	All solid state, passive servo-controlled output, regulated from 60 to 100 amps, direct current, regulated by light-output sensor controlled from simulator console. (Power supply is built into console.) Power supply is certified by source lamp manufacturer.
Input Power	460 ± 20 V, 3 phase, 6 amps/phase, 60 cycles. No other external power connections required. (230 ± 10 V optional input.) (380 ± 40 V, 3 phase, 50 cycle input on special order.)
Lamp Life	Source lamp rated at 1500 hours, warranted for 1000 hours, when used for at least 20 minutes per ignition.
Ventilation	Internally air cooled; equipped with 15 cm (6 inch) duct outlet.
Size	1.85 m high, 0.62 m wide, 0.66 m deep (basic projection console, less accessory lenses).
Shipping Weight	431 kg (basic console, less accessory lenses).
Accessories	Note: Accessories are mounted external to the main instrument cabinet and should not require realignment of the internal simulator optics. <ul style="list-style-type: none"> • Filter set for close spectral match. • Uniformity adjusting attachment to provide ± 5 percent. • Uniformity adjusting attachment to provide ± 2 percent on special order. <ul style="list-style-type: none"> f/2.0 collimation/projection lens accessory to provide: <ul style="list-style-type: none"> (a) 30-cm diameter beam with ± 1.2-degree collimation angle. (b) 15-cm diameter beam with ± 2.4-degree collimation angle. • Alternate projection lens for: <ul style="list-style-type: none"> (a) Illumination of 30-cm diameter target area at distance of 1.22 m from projection lens. (b) Illumination of 30-cm diameter target area at distance of 1.52 m. • Electrical adjusting mechanism for height adjustment of beam from 1.2 to 1.6 m from floor level. • Intensity adjustment screens (set) for calibrated attenuation of beam intensity. <p>(These specifications are subject to change without notice.)</p>

Table 11.2-3. TRW Systems LAPSS III Large Area Pulsed Solar Simulator Specifications

Specification - Lamp and Power Supply	
Light Source	Linear xenon flashtube with quartz envelope and heavy duty electrodes, mounted without optical systems in collimating tube
Luminous Flux	One solar constant at approximately 9 m from lamp
Flux Uniformity	Typically better than ± 2 percent over 2.1 by 2.1 m area; 9 m from lamp, 2.5 kV power supply voltage, measured with 4 cm ² solar cell (in nonreflective surroundings)
Spectral Match	Unfiltered
Stability	Intensity repeats typically within ± 3 percent; however, data control console corrects intensity variations automatically to within 0.5 percent overall.
Beam Orientation	Horizontal ± 20 degrees
Temperature Rise	Test specimen changes less than 0.008°C per flash of one solar constant intensity
Power Supply	All solid state. Lamp supply voltage adjustable from 1500 to 3000 Vdc (2500 Vdc nominal). Lamp firing interval variable, 10 s at 2500 Vdc.
Input Power	Standard 117 Vac, 60 Hz, 16 A service
Dimensions	Power Supply: 1.85 m high, 0.91 m wide, 1.04 m deep Lamp Housing: 0.43 x 0.43 x 1.17 m Tripod: Adjustable from 0.91 to 1.67 m high above floor
Specification - Data Control Console	
Data Acquisition	Fully automatic upon lamp firing. All solid state.
Voltage Ranges	0-1 Vdc, 0-10 Vdc, 0-100 Vdc
Current Ranges	0-0.1 Adc, 0-1.0 Adc, 0-10 Adc, 0-25 Adc
Temperature Range	Ambient temperature during testing between 10°C and 39°C. Unit corrects output data to 28°C.
Accuracy	Overall test set accuracy and repeatability is typically better than ± 0.5 percent.
Input Power	Standard 117 Vac, 60 Hz, 15 A service
Dimensions	1.60 m high, 0.61 m wide, 0.84 m deep
Equipment Included	Hewlett-Packard, Model 2070A Data Logger X-Y recorder, Mosley, Model 7035A

Upon ignition of the lamp, the light output will rise to a flat-top pulse of approximately one solar constant intensity at 9 meters and 1.7 ms duration. During the central 1-ms interval, gated integrating circuits measure the short-circuit current of a standard solar cell and the test specimen output. The specimen output data is automatically adjusted to one solar constant intensity and 28°C standard test conditions. Both the corrected and uncorrected data may be printed out on a digital printer or plotted in the form of dots with an X-Y recorder.

The duration of the light flash was an important design consideration because of array thermal time constants and the requirement to minimize heating. A flash duration of 2 ms was found to be optimum. The light intensity is maintained constant for a 1-ms interval by means of a five-stage delay line composed of high voltage capacitors and a carefully calculated tapped inductor.

The instrumentation associated with the flashlamp is based on the use of gated integrators, which are

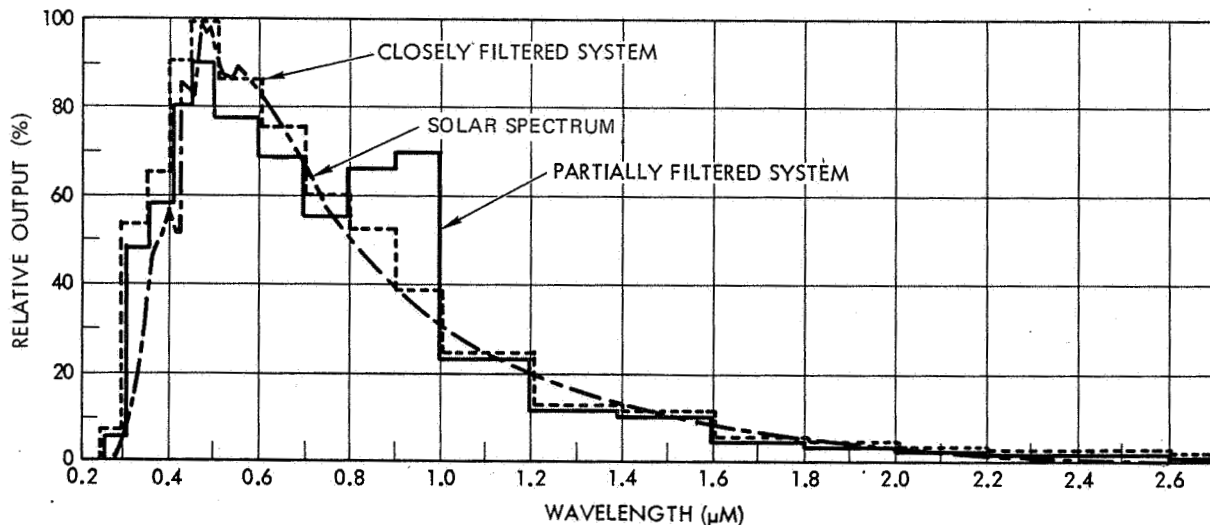


Fig. 11.2-8. Spectrosun Model X-25 Spectral Distribution

activated during the 1-ms constant-intensity interval. Each flash illuminates both the array under test and a standard cell. Variations in the light output from flash to flash are of the order of ± 1 percent, which can be corrected by applying the standard cell reading to each array measurement.

The flashlamp calibrator, in its present form, provides a printed tape output with automatic sequencing to characterize the array I-V curve in a series of six flashes. The first flash determines the short-circuit current, four subsequent flashes establish points around the knee of the curve, and the sixth flash establishes the open-circuit voltage.

The flashlamp has been used to calibrate Intelsat and Pioneer solar arrays. Accuracy and reproducibility are nominally 1 percent without automatic data console correction.

A generalized schematic of the flashlamp system is shown in Figure 11.2-9.

Light Source Characteristics

The effective black-body temperature of xenon flashlamps is a reproducible function of current density in the discharge volume. As shown in Figure 11.2-10, 5300 A/cm^2 corresponds closely to 9400°K and 1700 A/cm^2 is close to 7000°K . Note that the strong xenon emission lines in the red are self-absorbed at increasing current density. This effect eliminates the red content characteristic of xenon lamps operated in the continuous mode. Figure 11.2-11 shows the flashlamp spectrum measured with narrow bandpass filters and compares it to the solar spectrum in space.

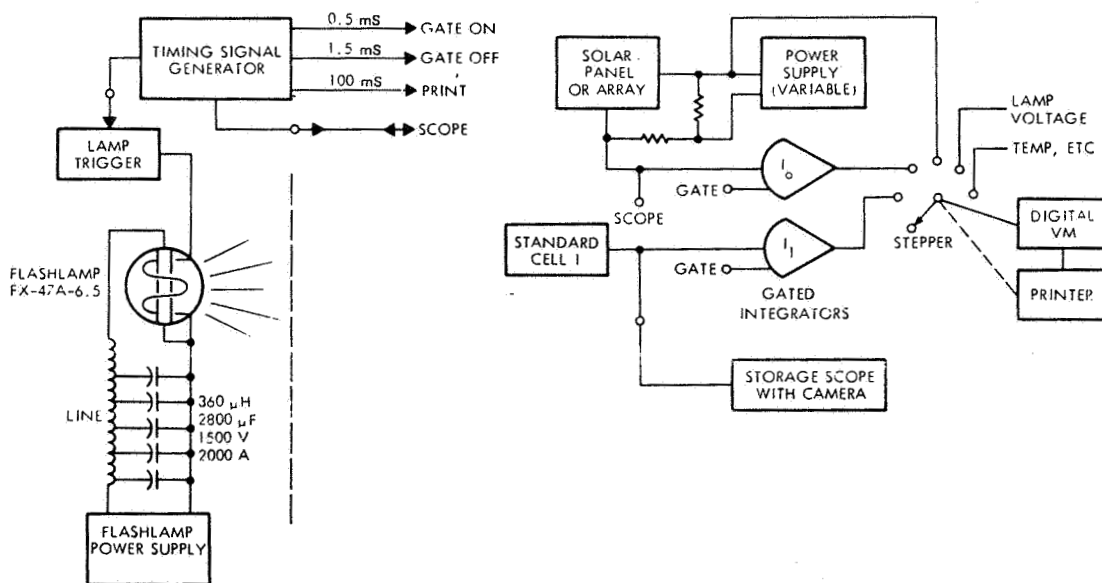


Fig. 11.2-9. Schematic of Flashlamp and Readout Circuit

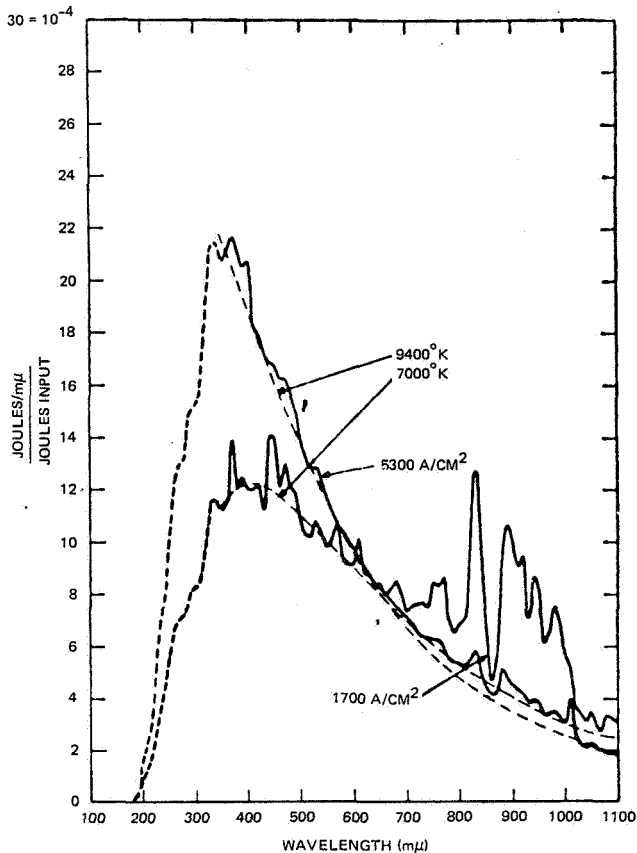


Fig. 11.2-10. Spectral Emission from FX-47A Flash Tube at Two Current Densities Compared with Relative Spectral Emittance of Black Bodies at 7000° and 9400°K (Ref. 11.2-7)

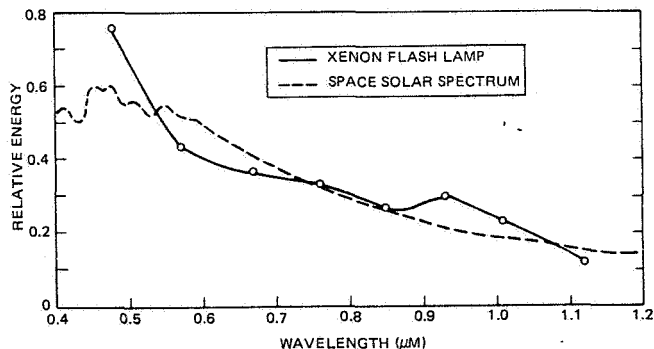


Fig. 11.2-11. Comparison of Spectral Output from Xenon Flash Light with the Space Solar Spectrum

Uniformity of Illumination

The source-to-panel distance is determined by panel size and the acceptable variation of intensity over the panel. For an illuminated circle of radius S ,

$$\Delta M/M \approx S^2/D^2 \quad (11.2-1)$$

where

D = source-panel distance

S = radius of illumination

M = panel illumination

For $\Delta M/M = 0.02$ (a variation of intensity of ± 1 percent), $D/S = 7.07$.

Flashlamp Requirements

The plasma resistivity of linear xenon flashlamps is a function of the current density within the lamp. Similarly, the lamp resistance and lamp current are functions of the current density and lamp geometrical properties. To control color temperature, it is necessary to control current density. When this is done both power and voltage are uniquely determined by the length and bore of the lamp. At high current densities lamp efficiencies of 65 to 75 percent are obtained.

Table 11.2-4 summarizes the electrical properties of three pulsed xenon flashlamps commercially available. They cost under \$100.00 each (1975). The data shown is for a current density of 1600 A/cm² which is the selected design value for the LAPSS III simulator.

The intensity of illumination at a distance, D , from the flashlamp is

$$M = \mu P_e / (4\pi D^2) \quad (11.2-2)$$

where

μ = lamp efficiency

P_e = lamp electrical power

For $M = 1400 \text{ W/m}^2$ (corresponding to sunlight) and for a lamp efficiency of 65 percent,

$$P_e = 2.7(10^4)D^2 \quad (11.2-3)$$

in electrical watts.

Eq. 11.2-1 and 11.2-3 establish the size requirement for the pulsed xenon flashlamp. A lamp size is selected to provide excess power capability. The illumination level can then be adjusted by varying the panel-source distance. Simple reflectors can be used to increase illumination by a factor of 10 or more in special circumstances but at the expense of uniformity.

Light Duration

The time during which the lamp is turned on depends on the peak power required and the rating of the lamp. For the FX-47C-6.5 flashlamp, an upper limit of 4000 W-sec is specified. From Table 11.2-3, a peak power of 1.48 MW is required, leading to a maximum duration (T) of

$$T = 4(10^3)/1.48(10^6) = 2.7(10^{-3}) \text{ seconds}$$

For this design application, a duration of 2000 μs is adequate.

Table 11.2-4. Electrical Properties Based on Current Density of 1600 A/cm²

EGMG Lamp Type	Arc Length, L (cm)	Bore Area, A (cm ²)	Resistance, R (ohms)	Maximum Power P (MW)	Maximum Energy per Flash (joules)
FX-47C-3	7.6	1.32	0.16	0.72	2250
FX-47C-6.5	16.5	1.32	0.35	1.48	4000
FX-47C-12	30.4	1.32	0.65	2.9	9200

Temperature Rise

Assuming that all of the radiant energy is absorbed in a silica or silicon layer 0.25 mm thick, the temperature rise, θ , is given by

$$\theta = MT / (C_p dm) = 7 \times 10^{-3} \text{ }^\circ\text{C} \quad (11.2-3)$$

where

T = flash duration (2ms)

M = illumination (1400 W/m²)

C_p = specific heat of silicon (735 J/kg^oC)

d = density of silicon (2.33 x 10³ kg/m³)

m = cell thickness (0.25 mm)

11.2.6 Three Types of Solar Cell I-V Curves

Solar cell current-voltage characteristics can be obtained by three different methods (Ref. 11.2-9):

(a) Photovoltaic Curve

The cell is fully illuminated and a load resistance across its terminal is varied between 0 and ∞ . The corresponding sets of output current and terminal voltage data points are recorded (continuously or discrete).

(b) Diode Curve

The cell is not illuminated (dark) and an external source forward-biases the cell. As the cell terminal voltage is varied between 0 and approximately 0.6 volt, the corresponding values of input current are recorded.

(c) N-P Junction Characteristics

The cell is illuminated with a variable intensity, invariant spectral distribution source. As the intensity is varied step-wise from 0 to approximately two solar constants, sets of I_{sc} and V_{oc} data points are recorded.

The I-V curves shown previously in Figure 11.2-3 (and practically all other I-V curves shown in this handbook) were obtained with method (a). The nonilluminated cell curves discussed in conjunction with shadowed cell and array performance (Section 9.3) and

with "dark forward" testing (Section 11.12) were obtained by method (b). Method (c) is of interest only in solar cell research.

Neglecting the cell's shunt resistance and using the magnitude of I only (i.e., I = |I|) the three different curves are represented by these solar cell equations:

Method (a):

$$I = I_L - I_o \left\{ \exp \left[\frac{q}{AkT} (V + IR_S) \right] - 1 \right\}$$

Method (b):

$$I = I_o \left\{ \exp \left[\frac{q}{AkT} (V - IR_S) \right] - 1 \right\}$$

Method (c):

$$I_{sc} = I_o \left[\exp \left(\frac{q}{AkT} V_{oc} \right) - 1 \right]$$

where the symbols are defined in Section 9.2.

11.2.7 Measurement of Solar Cell Series Resistance

The determination of the solar cell series resistance by the method described in Ref. 11.2-9 can lead to significant and intolerably high errors in the values of series resistance if the measurement techniques are not tightly controlled. (Series resistance is defined in Section 3.1.) Measurement errors typically arise from these sources:

- Mechanical backlash, friction, inadequate gain, excessive hysteresis, slight miscalibration, or zero-offset in the X-Y recorder used, leading to imprecise I-V curves
- Instabilities in the light levels during the tests, leading to "wavy" and imprecise I-V curves
- Excessive thermal impedance between the solar cell and the heat sink of the test fixture, resulting in distinctly different cell operating temperatures at the different light levels at which I-V curves are plotted.

To eliminate the potential errors caused by the conditions enumerated above, the following procedure has been found to result in very precise values of the cell series resistance R_S :

- Determine the two or more light levels at which series resistance measurements are to be made. These light levels should approximately correspond to those for which precise performance predictions are to be made.
- Determine the temperature difference between the cell test fixture and each cell to be

tested at each light level. If possible, bond cells to a heat sink with solder or adhesive.

- Plot the I-V curves obtained at the different light levels on separate sheets of semitransparent graph paper; then slide the curves over each other until a best match of the I-V curves is obtained. Determine ΔI_{SC} and ΔV_{OC} by the offset of the graph paper rulings.
- Correct ΔI_{SC} and ΔV_{OC} for possible temperature variations and calculate R_S .

11.3 STANDARD SOLAR CELLS*

11.3.1 Definitions

Standard solar cells, calibrated above most of the earth's atmosphere, have been effectively used to aid in the prediction of solar array output in space. The standard cells are mounted in modular form, thereby permitting effective temperature control and providing a means to electrically load the cell and monitor its output. (The modular form also provides protection for the cell during normal handling and from damage which could result from environmental exposure during the calibration flight.)

Standard solar cells are used for two purposes: (a) to determine the absolute value of the solar constant over the spectral response region of solar cells, and (b) to accurately establish the light intensity of solar simulators.

11.3.2 The JPL Balloon Flight Program

Calibration data is obtained for the standard solar cells on high-altitude balloon flights conducted regularly by the Jet Propulsion Laboratory (JPL). The standard solar cell assemblies are mounted on a tracking mechanism which maintains sun orientation. The sun tracker is mounted on the balloon apex, as shown in Figure 11.3-1. The helium-filled balloons are typically launched to reach float altitude 2 hours before solar noon and to remain at that altitude until 2 hours after solar noon. Temperature and electrical data for each standard cell is transmitted to a ground station during the float period. The balloon is commanded to descend by opening a valve and allowing the gas to escape at a controlled rate. The solar cell payload, solar tracker and other reusable equipment are recovered by a ground crew.

After the standard solar cells are returned to JPL, a postflight calibration is performed using a solar simulator to ensure that the cells have not been damaged as a result of earth impact or other handling. If such is the case, the telemetered solar cell data is reduced by a computer program which corrects for intensity and temperature.

Solar cells flown on previous flights have been reflown on several subsequent flights for correlation purposes. One cell in particular, flown over 16 times, has shown a repeatability of within ± 1 percent, thereby indicating that balloon flight standard solar cells not only are rugged and reliable but also that the calibration accuracy obtained exceeds on an absolute basis, the accuracy of all previous solar intensity and solar cell calibration measurement techniques.

The altitude selected for balloon flights from 1970 and on was 36,576 meters (120,000 feet). This higher altitude (24,384 meters previously) was selected to eliminate, as much as possible, the effects of solar energy absorption by the earth's

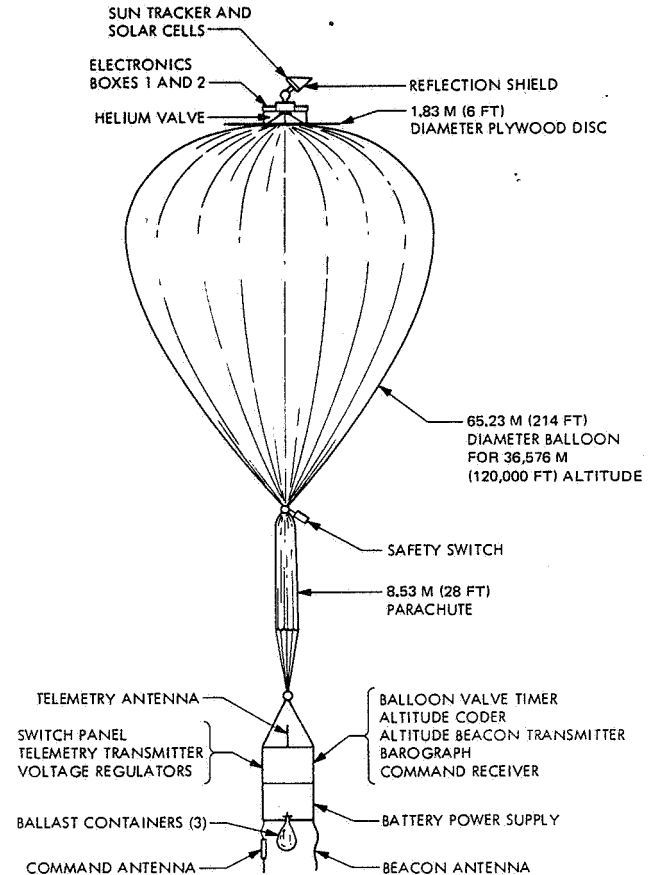


Fig. 11.3-1. Balloon Flight Configuration

atmosphere. Solar cell measurements made on the 1970 flights were to within 0.46 percent of air mass zero as determined by a ratio of the atmospheric pressure at 36,576 meters to that at sea level given in the Air Research and Development Command (ARDC) model atmosphere (Ref. 11.3-2). When the spectral response of a solar cell (0.4 to 1.2 μm) is taken into consideration, the solar irradiation at 36,576 meters is essentially that of space sunlight (Table 11.3-1).

The JPL Balloon Flight System

The main components of the balloon flight system are a helium-filled balloon, a sun tracker, a telemetry system, and a battery power supply, as shown in Figure 11.3-1. The solar cells, which have been assembled into modular form in accordance with JPL Procedure No. EP504443A, are mounted on the face of the sun tracker. Dow Corning No. 340 silicone heat sink compound is applied at the interface of the solar cell module and the sun tracker mounting plate

* Abstracted from Ref. 11.3-1.

Table 11.3-1. Attenuation of Solar Radiation by the Earth's Atmosphere (Ref. 11.3-1)

Pressure, mbar	Altitude			Wavelength Regions								Altitude	IUGG	
	Miles	Thousand feet	Kilometers	0.12 to 0.20 μm	0.20 to 0.29 μm	0.29 to 0.32 μm	0.32 to 0.35 μm	0.35 to 0.55 μm	0.55 to 0.9 μm	0.9 to 2.5 μm	2.5 to 7 μm			7 to 20 μm
0.2	37	200	60	O ₂ Absorbs almost completely	Solar irradiation intensity approximates extra-atmospheric. Attenuation by scattering increases markedly toward shorter wavelengths.								Above 60 km	↑ 110 km
7.5	20	108	33	(0.20 to 0.21 μm Absorption by O ₂) Absorption by O ₃ appreciable	O ₃ absorption not important					Energy small	Energy very small	60 km to 33 km	CHEMOSPHERE	
227	6.8	36	11	No radiation penetrates below about 11 km	O ₃ absorption attenuates more than loss by scattering	O ₃ absorption significantly attenuates radiation	Irradiation diminished mostly by scattering by permanent gases in atmosphere	H ₂ O responsible for major absorption; CO ₂ absorbs slightly at 2 μm . Water vapor (or ice crystals) is found up to about 21.3 km.				Strong O ₃ absorption at 9.6 μm . Strong CO ₂ absorption 12-17 μm	33 km to 11 km	↓ 20 km
795	1.2	6.6	2			Highly variable dust, haze (H ₂ O) (and smoke) responsible for attenuation in regions 0.32 to 0.7 μm		Energy transmitted with small loss down to 2 km	Energy penetrates to sea level only through "windows" at approximately 1.2, 1.6 and 2.2 μm		No significant penetration below 2 km except in "windows" at approximately 3.8 and 4.9 μm	Energy transmitted with moderate loss. Many absorption bands due to atmospheric gases	11 km to 2 km	↓ 11 km
1013				Appreciable penetration through "clear" atmosphere to sea level		Penetration through "clear" atmosphere to sea level about 40%		Dust may rise to more than 4 km				2 km to sea level		TROPOSPHERE
	Sea level			About 7%	About 30%							0 km		↓

to minimize thermal gradients between these surfaces and to ensure the best possible uniform temperature on all solar cells comprising the payload. Wires soldered to the terminals of the solar cell modules electrically connect the solar cells to a 36-position stepping switch.

The sun tracker with the solar cell payload is mounted on the balloon apex. The telemetry system, battery power supply, and several instruments for measuring altitude are suspended beneath the balloon. An electrical cable, incorporated into the balloon during manufacture, connects the top and bottom payloads. A parachute is provided in the event of balloon failure.

The sun tracker is used to position the solar cell payload toward the sun, independent of balloon movements. The tracker is capable of movement in both elevation and azimuth to maintain an "on-sun" condition within ± 2 degrees. A reflection shield attached to the sun tracker prevents unwanted reflected light from reaching the solar cell payload.

The tracker and associated electronics are mounted on standoffs above a plywood disk 1.83 meters (6 feet) in diameter, which, in turn, is bolted to the balloon top end fitting and radio-controlled helium valve. The standoffs provide clearance for the outlet of the helium valve, which is used as an alternate method of controlling balloon descent rate. The plywood disk permits the tracker to "float" atop the helium bubble and minimizes billowing of balloon material around the top payload. The weight of the entire top payload is approximately 25 kg (55 pounds).

During the period that the sun tracker is locked on the sun, solar cell voltages, interspersed with reference voltages and thermistor voltages, are fed into a voltage-controlled oscillator (VCO). The voltages are converted to frequencies and are transmitted to a ground station with a 5-watt FM transmitter modified to operate at an assigned frequency of 217.5 MHz. At the ground station, the data are recorded in digital form on printed paper tape and in analog form on a strip chart recorder. The data are later transferred from the printed tape to punch cards compatible with a JPL computer program.

Accuracy and Repeatability

Accuracy of the balloon flight system has been determined by Zoutendyk (Ref. 11.3-3) to be ± 0.73 percent. Since that time, many small improvements have been made to the solar tracker. This has narrowed the pointing accuracy from ± 4.3 to ± 2.0 degrees. No other significant improvements have been made, but the tracking improvement brings the overall system accuracy to ± 0.49 percent.

Table 11.3-2 lists data gathered on one particular standard solar cell (BFS-17A) over an 8-year period. This cell was used as a reference on nearly every balloon flight and has repeated its mean calibration value in each instance to within 1 percent. From this data, two conclusions can be drawn: (1) That the balloon flight system has maintained excellent stability over the years, and (2) that silicon solar cells are reliable as standards over a long term if properly maintained.

The solar cell standardization program has been a continuing program designed to fill the need for standard solar cells. The use of high-altitude balloons has proven to be feasible, reliable, and an economical method to obtain the needed standards.

Table 11.3-2. Repeatability of Standard Solar Cell BFS-17A for 20 Flights over an 8-Year Period

Flight Date	Output ^a (mA)
9/5/63	60.07
8/3/64	60.43
8/8/64	60.17
7/28/65	59.90
8/9/65	59.90
8/13/65	59.93
7/29/66	60.67
8/4/66	60.25
8/12/66	60.15
8/26/66	60.02
7/14/67	60.06
7/25/67	60.02
8/4/67	59.83
8/10/67	60.02
7/19/68	60.31
7/29/68	60.20
8/26/69	60.37
9/8/69	60.17
7/28/70	60.42
8/5/70	60.32
Mean	60.16 mA
Maximum deviation from mean	0.85%
RMS deviation from mean	0.35%

* Each data point is an average of 20 to 30 data points from each flight. All data are normalized to 1 AU sunlight equivalent and 301°K (28°C) cell temperature.

Balloon Flight Payloads

Payloads for the 1970 balloon flight series were comprised of many types and configurations of solar cell modules (single cells mounted with a load resistor to a heat sink). One of the payloads contained two active cavity radiometers.

The solar cell modules were supplied by six different NASA centers and government agencies. In order to ensure compatibility with the mechanical and electrical requirements of the balloon flight system, all modules were fabricated in accordance with the JPL Procedure for Balloon Flight Solar Cell Modules (Ref. 11.3-4). This procedure delineates physical size, mounting hole dimensions, and load resistor values in addition to material selection and assembly techniques.

The modules were shipped to JPL to permit inspection for workmanship and mechanical tolerances and were then given a pre-flight calibration in the JPL X-25L Spectrolab solar simulator. This calibration serves to correlate the solar simulator data supplied by the various organizations.

In general, correlations between test results obtained in the solar simulators of the different organizations and the JPL solar simulator have held within ± 2.0 percent. However, solar cells other than silicon (e.g., cadmium sulphide), which have different spectral response bandwidths, or silicon solar cells covered with special band-pass filters, have exhibited differences as high as 13.7 percent (Table 11.3-3).

Table 11.3-3. Correlations between Solar Simulators of Different Organizations

Module Number	Cell Type	Manufacturer ¹	Agency	Agency Source	Agency Calib	JPL ² Calib	Deviation from JPL Calib, (%)
GSF-701	N-P	HEK	Goddard	X-25	69.6	70.4	-1.14
GSF-702	N-P	HEK	Goddard	X-25	68.7	69.5	-1.15
GSF-703	N-P	HEK	Goddard	X-25	71.2	72.7	-2.06
GSF-704	N-P	HEK	Goddard	X-25	66.9	67.7	-1.18
GSF-705	N-P	SIE	Goddard	X-25	71.1	71.4	-0.42
GSF-706	N-P	AEG	Goddard	X-25	71.0	71.2	-0.28
LRC-003A	N-P	HEK	Langley	X-25	67.16	67.4	-0.36
LRC-003B	N-P	HEK	Langley	X-25	66.50	66.6	-0.15
LRC-004A	N-P	CRL	Langley	X-25	69.20	69.3	-0.14
LRC-004B	N-P	CRL	Langley	X-25	68.87	68.7	+0.25
IPC-701	N-P	IPC	AFAPL	X-25L	67.0	66.1	+1.36
IPC-703	N-P	IPC	AFAPL	X-25L	66.0	65.5	+0.76
IPC-704	N-P	IPC	AFAPL	X-25L	66.0	65.6	+0.61
MSF-8003	N-P	CRL	Marshall	X-25	59.21	58.0	+2.09
MSF-8004	N-P	CRL	Marshall	X-25	60.97	59.2	+2.99
APL-I ^{***}	N-P	HEK	APL	OCLI-31	88.0	80.5	+9.32
APL-II ^{***}	N-P	HEK	APL	OCLI-31	80.0	82.6	-3.15
APL-III ^{***}	N-P	HEK	APL	OCLI-31	71.6	83.0	-13.73
APL-IV ^{***}	N-P	HEK	APL	OCLI-31	72.9	72.8	+0.14
APL-V ^{***}	N-P	HEK	APL	OCLI-31	81.1	83.5	-2.87

¹HEK = Heliotek, SIE = Siemens Aktiengesellschaft, AEG = AEG-Telefunken, CRL = Centralab, IPC = Ion Physics Corporation.

²JPL calibration using Spectrosun X-25L Solar Simulator, 1-AU sunlight equivalent, 301°K (28°C).

³Set of solar cells each covered with a different band-pass filter.

Differences in test results obtained by various organizations are attributed to the use of different light sources, different standard solar cells used to set the intensity of the light sources, and measurement error. The Jet Propulsion Laboratory employs a filtered xenon light source which closely approximates space sunlight. Most NASA agencies now employ this same type of light source. A comparison of the filtered xenon light source with the NRL space sunlight curve is shown in Figure 11.3-2. Figure 11.3-3 compares the spectral distribution of the carbon arc light source with the NRL space sunlight curve.

In summary, the problems which exist in the correlation of standard solar cells are:

- Solar simulators do not exactly duplicate the sun's spectral distribution.
- There are differences in the spectral distribution among solar simulators. These differences exist due to:
 - (a) Design
 - (b) Degree of spectral filtering
 - (c) Type of lamp
 - (d) Lamp aging
 - (e) Lamp current
 - (f) Condition of optical surfaces
- Solar cells have different spectral responses due to type and diffusion depth.
- Filters placed on a solar cell effectively alter the spectral response.

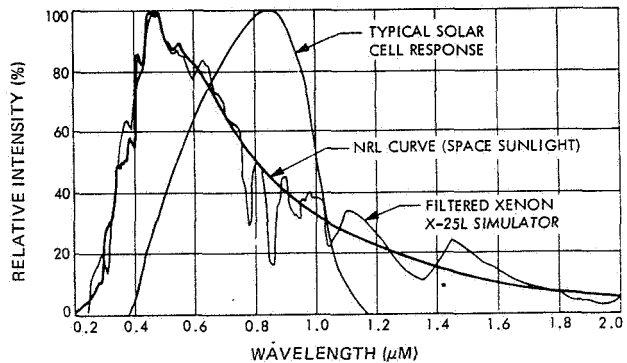


Fig. 11.3-2. Comparison of Filtered Xenon Light Source (X-25L) with Space Sunlight

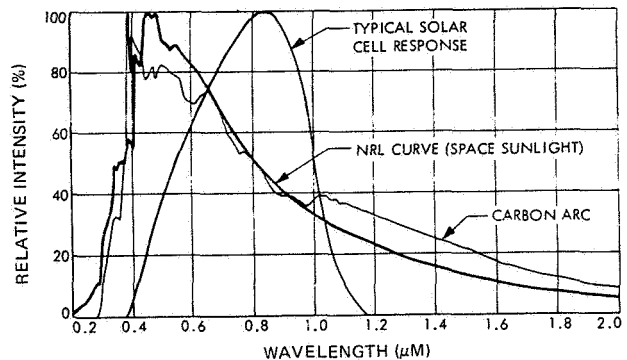


Fig. 11.3-3. Comparison of Carbon Arc Light Source with Space Sunlight

- Inaccuracy of simulator intensity setting
- Instability of simulator intensity setting
- Nonuniformity of the beam pattern

Correlation to space conditions as well as among solar simulators can be achieved to within a ± 2.0 percent tolerance providing that:

- The spectral distribution of the solar simulator closely matches the spectral distribution of the sun.
- A standard solar cell is employed which matches the spectral response of the cell or cells to be measured.
- The optical surfaces of the simulator are kept clean and in good condition.
- Lamp stability and beam uniformity are within the manufacturer's tolerance.
- Means are employed to ensure that the spectral distribution is maintained within established limits.

Data Analysis

Corrections for solar intensity must be made because of the constantly changing earth-sun distance over the course of a year.

For the heliocentric range considered, and for the type of silicon solar cells being tested, it has been shown that the short-circuit current (I_{sc}) of a solar cell at a constant temperature varies directly with solar intensity. It also has been shown that for the heliocentric range considered, the solar intensity varies inversely with the square of the distance from the sun. It follows, therefore, that the short-circuit current of a solar cell at near-earth space conditions varies inversely with the square of the distance from the sun:

$$\frac{I_{sc 2}}{I_{sc 1}} = \frac{1}{D^2}$$

where

$$I_{sc 1} = I_{sc} \text{ at } 1 \text{ AU}$$

$$I_{sc 2} = \text{measured value from balloon flight}$$

$$D = \text{earth-sun distance in astronomical units (AU)}$$

The earth-sun distance (AU) is given for any particular day of a year in regularly published ephemeris tables as the radius vector (Ref. 11.3-5).

It should be noted that the calibration value of a standard solar cell is a function of the mean earth-sun distance and the inverse square law for luminous flux. The balloon flight calibration value of the solar cells does not depend on measured values of the solar intensity.

Corrections for temperature effects on solar cells are made to a standard temperature for ease in data comparison. The temperature of 301.15°K (28°C) came into use since it was an easily obtainable temperature for laboratory measurement of solar cells. To correct the output of a solar cell for temperature effects, the temperature coefficient must be known and is obtained experimentally from laboratory measurements for each cell.

A load resistor is permanently attached to standard cells and loads the solar cells near their short-circuit current points. The load resistor value is usually 1 ohm or less, but can be higher, depending upon the cell size and filter cover used. It is the voltage drop across the load resistor which is actually measured; therefore, the cell output is given in millivolts and the temperature coefficient is in millivolts per Kelvin even though it still relates to the short-circuit current.

Use of Standard Solar Cells

Standard solar cells, calibrated by means of high-altitude balloon flights, are maintained by JPL for flight and advanced development programs. The standards can be used in either of two ways.

- When used with artificial light sources, the standard cell is placed in the light beam and the intensity is adjusted until the output of the standard cell is equivalent to the 1 AU calibrated value or to any desired ratio of the calibrated value. The temperature of the standard cell is held constant at the standard temperature of 301.15°K (28°C). Once the intensity of the artificial light source has been set, test solar cells can be placed in the light beam and their parameters measured.
- When used in terrestrial sunlight, the standard cell is placed in the same field of view as the solar cells or solar array being measured. Provisions should be made to maintain the standard cell at the standard temperature. If this is not practical, then the temperature of the standard must be measured and the output value corrected through application of the temperature coefficient. The output value of the standard solar cell is used to determine the incident solar radiation on the photovoltaic devices under test by direct ratio.

11.4 SPECTRAL DISTRIBUTION AND RESPONSE

The spectral distribution of light sources is measured with the aid of a spectroradiometer. Many different types of spectroradiometers are in use, ranging from relatively simple "filter wheel" devices to sophisticated, continuously recording instruments. In general, very similar or even identical instruments are being utilized for measuring the spectral response of solar cells.

The general problem of measuring the spectral irradiance of sources, including the spectral response of detectors, is treated in Ref. 11.4-1. The electrical, mechanical and optical design considerations applicable

to "filter wheel" spectral radiometers are illustrated in Ref. 11.4-2. Application of a filter wheel to solar cell experiments is illustrated in Ref. 11.4-3.

The use of a filter-wheel spectroradiometer for measuring the reflectance of solar cells covered with antireflective coatings is illustrated in Figure 11.4-1. The band-pass filter indicated in this figure is actually one of 13 filters that cover the wavelength range over which solar cells are responsive. The filters are mounted on a disk ("wheel") and rotated into the optical path as shown.

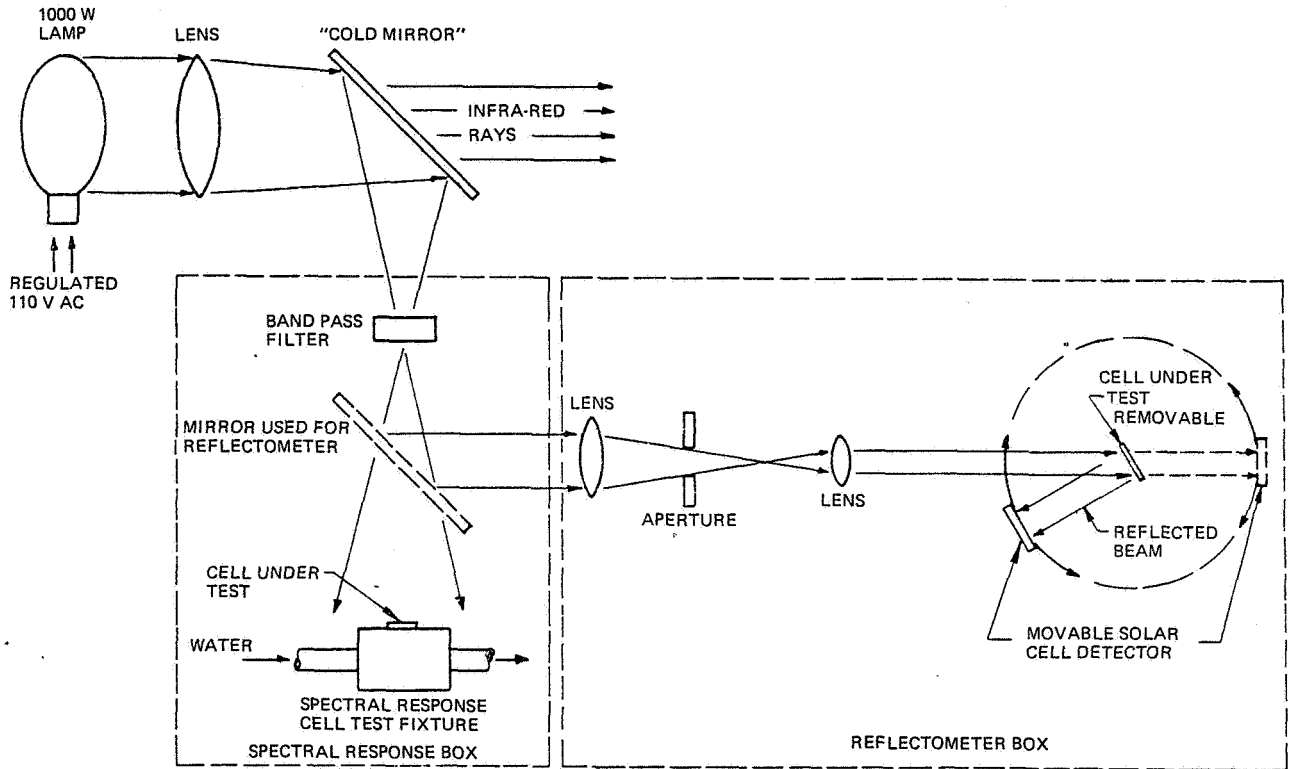


Fig. 11.4-1. Spectral Response and Reflectometer Equipment (Ref. 11.4-4)

11.5 SOLAR CELL CONTACT INTEGRITY*

11.5.1 Stresses Due to Contact Pull Testing

Contact pull testing, also known as peel testing, may be performed for one of two distinctly different purposes:

- To test the adhesion strength of the solar cell contacts to the silicon wafer
- To test the strength of joints made between solar cell interconnectors and the solar cell contacts.

The results obtained from tests for any one of the above purposes, however, are frequently masked by effects related to the other purpose. Certain pull test procedures may even introduce additional parameters that are being evaluated such as the silicon tensile strength in the area below a welded joint or the silicon wafer breaking strength in bending.

Solar cell contact integrity testing is performed by first attaching (soldering, welding, etc.) interconnector ribbons or wires to the solar cell contacts and then pulling or peeling the interconnectors away from the cell contacts.

The pulling of interconnectors off the solar cell contacts can be performed at different angles. Larger-area soldered joints are usually pulled at 90 degrees and smaller-area soldered and welded joints are frequently pulled at 45 degrees. Welded joints on stiff interconnectors (Kovar, etc.) give meaningful results usually only between 0 and 10 degrees. (see Fig. 11.5-1).

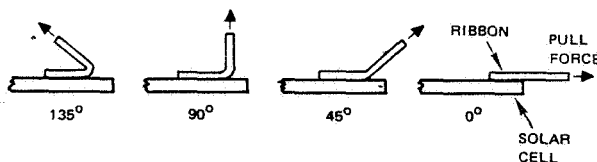


Fig. 11.5-1. Definition of Pull Angles

For designs using relatively small soldered or welded joint areas, the selection of the angle at which the pull force is applied is critical and depends upon the stiffness of the interconnector. In the ideal case, the angle should be selected such that it simulates the actual loading on the joints. The loading expected during orbital temperature cycling can be calculated using conventional methods of stress analysis; however, the most severe stresses may occur during handling in the assembly operations and may not be amenable to analytical prediction. Review of the literature appears to indicate the following:

- The most likely loading (in a practical sense, including handling) is around 45 degrees

- Breaking of an excessive percentage of interconnectors during 0- or 45-degree testing (away from the joint) indicates that 90 degrees may be a better choice
- Excessive silicon divoting, when using stiff interconnectors (Kovar, Invar, etc.), indicates that the pull angle should be reduced.

11.5.2 Test Procedure

In the following, the contact pull test procedure as used by JPL is presented. This procedure is generally valid even though the details of the actual solder joints and soldered ribbons may differ significantly when the procedure is applied by various organizations. The procedure given here is for 90-degree pull tests (the pull force vector being perpendicular to the cell surface); however, other common angles (between the force vector and the cell surface) are 45 and 0 degrees. The 45-degree angle is presumed to load the solder joints in a more realistic fashion by a combination of shear and tension than the 90-degree test. The 0-degree angle is generally used to evaluate welded joints between relatively stiff interconnector materials and solderless contact cells.

The configurations and specifications associated with the contact test tabs are shown in Figure 11.5-2. As noted in this figure, the tabs are fabricated from tin-plated, photo-etched Kovar (iron, nickel, and cobalt alloy), having a thickness of 0.1 mm. Each test tab is bent in a forming fixture at a 90-degree angle before being soldered to the cell. The soldering operation is accomplished semiautomatically by use of a Sippican RS-333 Reflow Soldering System.** A solder preform is added to all nonsolder-coated solar cells, normally having a composition of 62 percent tin, 36 percent lead, and 2 percent silver. When nonsolder-coated cells were to be tested at temperatures above 190°C, however, the preform was fabricated from Alpha solder No. 32, which has a higher tin-to-lead ratio and exhibits a higher melting point than 62-36-2 Sn-Pb-Ag solder preform (which becomes plastic at approximately 165°C). For the solder-coated cells, no preform was used.

The area on the cell contact to which the tabs may be soldered is carefully defined, as shown in Figure 11.5-3, to eliminate extraneous effects and to enhance the uniformity of the pull test results. After soldering, the tab is inspected to ensure its location within the area allowed, as shown in Figure 11.5-3, and to determine that the joint itself is acceptable according to the criteria shown in Figure 11.5-4. The solder joint area, assuming an additional area of about 10 percent for the solder fillet, was calculated to be 3.42 mm. Tab-cell joints that exhibit excessive solder, incomplete solder, or an incomplete solder joint are rejected and not tested. It has been found that many

* Portions of this section are quoted from Ref. 11.5-1.

** Sippican Corporation, Industrial Products Division, Mattapoisett, Massachusetts.

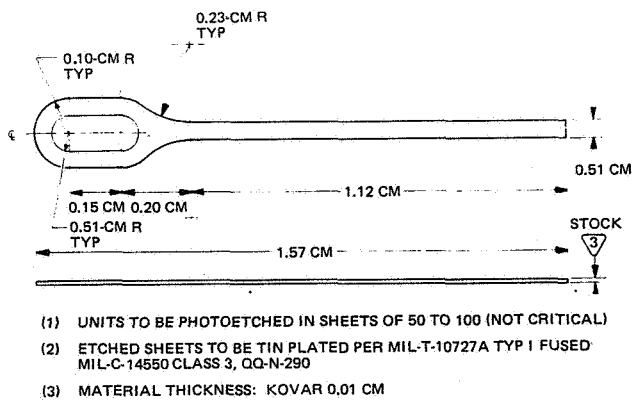


Fig. 11.5-2. Solar Cell Ohmic Contact Strength Test Tab (Ref. 11.5-1)

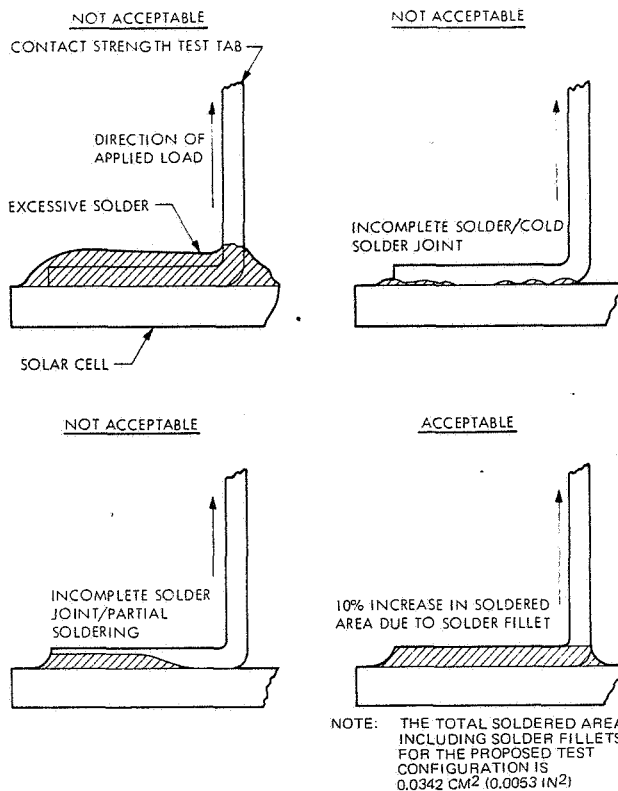


Fig. 11.5-4. Solder Joint Acceptance/Rejection Criteria (Ref. 11.5-1)

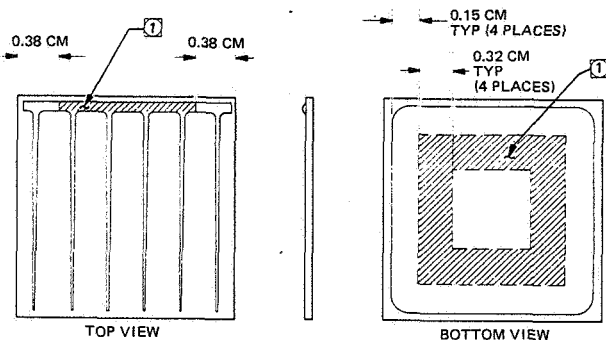


Fig. 11.5-3. Definition of Area for Pull-Test Tab Soldering (Ref. 11.5-1)

apparent inconsistencies in contact pull-strength results are the result of improper tab soldering techniques and that strict adherence to the solder joint inspection criteria defined in Figures 11.5-3 and 11.5-4 are mandatory if meaningful results are to be obtained.

To minimize electrode heating during the soldering reflow operation, the solder time-temperature profile or heat cycle is pulsed twice at a reduced voltage to obtain consistent and uniform soldering. An applied electrode load of 3.3 kg is used, and a total elapsed time of about 4 seconds for each soldering operation is maintained. This operator-independent soldering technique was developed to minimize the effects of variations in the soldering operation. A second major source of anomalous pull-strength test results has been found to result from variations in the soldering technique, and the precise control associated with the technique described has served to greatly minimize such variations.

The contact pull-strength tests are performed with an Instron Universal Material Test Machine* Model TM-1 and a self-contained portable temperature-controlled chamber. A special test fixture is used,

which adapts to cells of varying dimensions so that they can be mounted and properly aligned perpendicular to the direction of the applied load. A copper-constantan thermocouple is mounted between the test specimen and the test fixture so that cell temperature can be monitored and maintained at the desired value. The contacts are pulled at a constant rate of 0.084 ± 0.008 cm/s, which corresponds to 5.04 cm/min, until complete separation occurs. A third major source of anomalous pull strength test results has been found to be associated with variations in the pull rate, and careful control of the pull rate minimizes variations in pull strength. The resultant contact strength is recorded on a strip chart recorder in the form of a stress-strain characteristic curve. After separation, the test specimens are reinspected and analyzed for the interfacial characteristics that led to the separation (e.g., solder failure, contact delamination, broken cells, defective tabs, etc.). A schematic showing the contact strength test configuration is given in Figure 11.5-5. By careful control of the materials, processes, techniques, and inspections involved in performing the contact pull-strength tests, the effects of extraneous variables on the test results are minimized and the validity of the test results greatly enhanced.

11.5.3 Contact Separation Modes

A significant part of contact pull testing is the interpretation of the test results, specifically the classification of contact separation, or "failure" modes. Figures 11.5-6 through 11.5-12 illustrate typical separation modes and Table 11.5-1 classifies them into "failures" or other categories (Ref. 11.5-1).

* Instron Engineering Corporation, Long Beach, California.

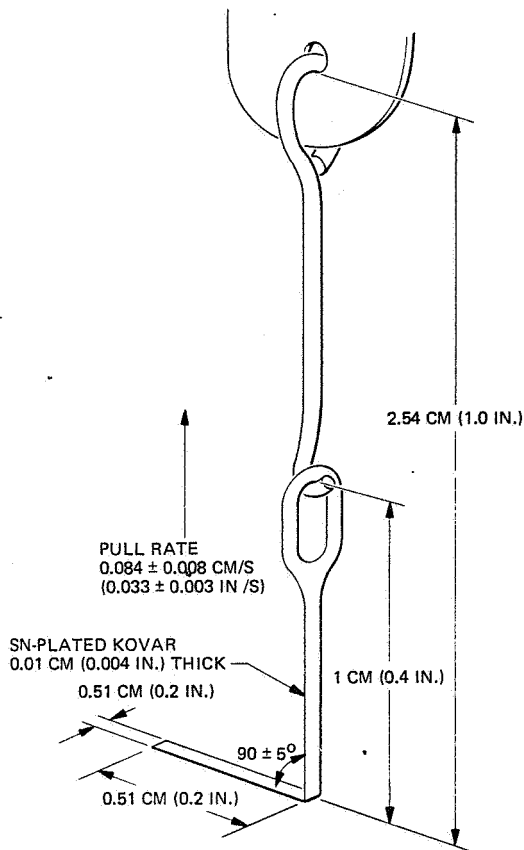


Fig. 11.5-5. Contact Strength Test Configuration
 (Ref. 11.5-1)

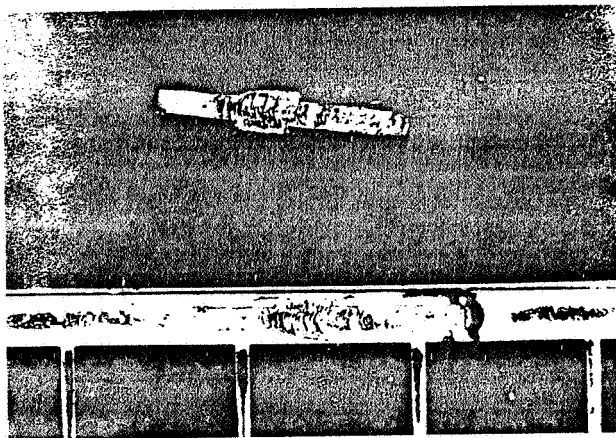


Fig. 11.5-6. Typical Failure Mode of n Contact,
 Solder-Coated Titanium-Silver Con-
 tacts on n-p Cells, Over a Pull-Test
 Temperature Range of -112° to 173°C
 (Ref. 11.5-1)

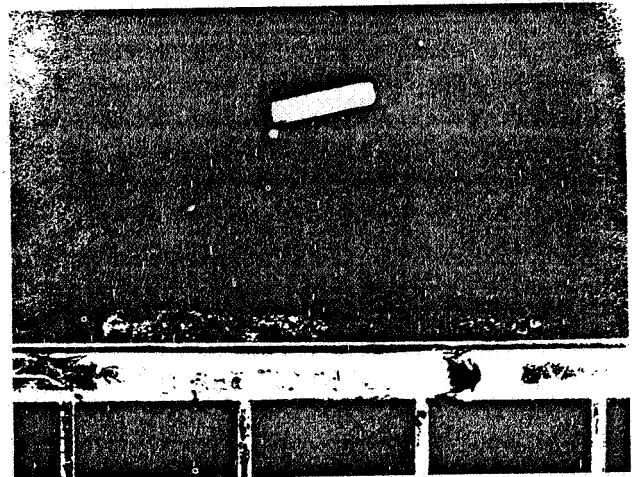


Fig. 11.5-7. Typical Failure Mode of n Contact,
 Solder-Coated Titanium-Silver Con-
 tacts on n-p Cells, Over a Pull-Test
 Temperature range of -29° to -84°C
 (Ref. 11.5-1)

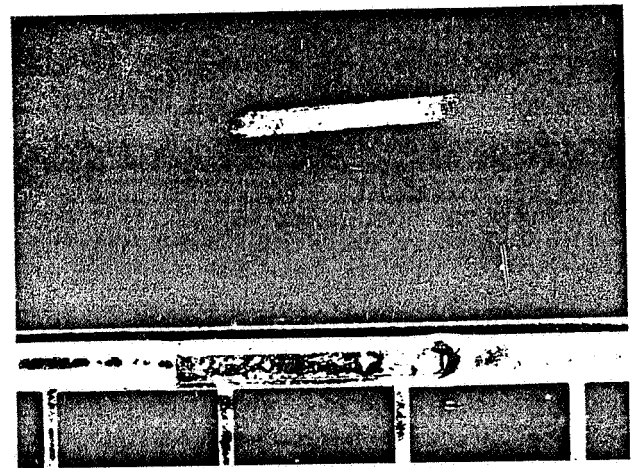


Fig. 11.5-8. Typical Failure Mode of n Contact,
 Solder-Coated Titanium-Silver Con-
 tacts on n-p Cells, Over a Pull-Test
 Temperature Range of -1° to $+82^{\circ}\text{C}$
 (Ref. 11.5-1)

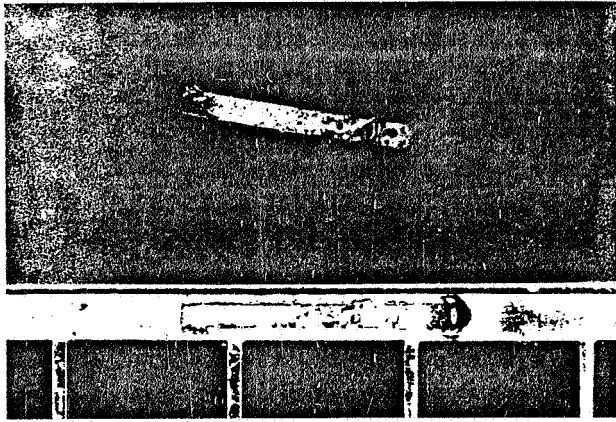


Fig. 11.5-9. Typical Failure Mode of n Contact, Solder-Coated Titanium-Silver Contacts on n-p Cells, Over a Pull-Test Temperature Range of $+110^{\circ}$ to $+165^{\circ}\text{C}$ (Ref. 11.5-1)

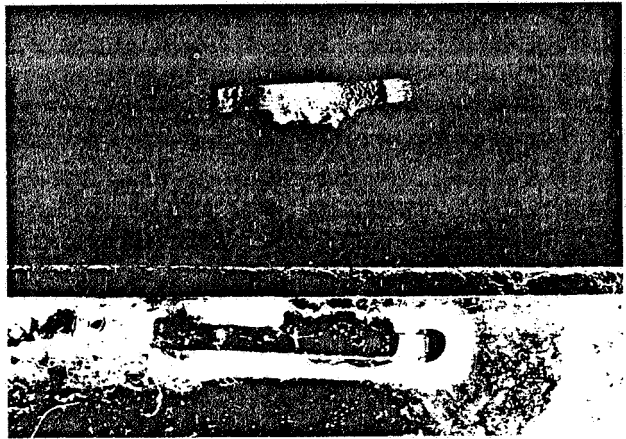


Fig. 11.5-11. Typical Failure Mode of p Contact, Solder-Coated Titanium-Silver Contacts on n-p Cells, Over a Pull-Test Temperature Range of -1° to $+82^{\circ}\text{C}$ (Ref. 11.5-1)

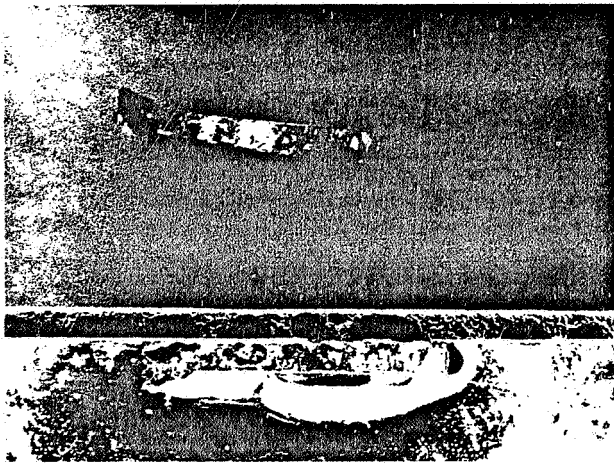


Fig. 11.5-10. Typical Failure Mode of p Contact, Solder-Coated Titanium-Silver Contacts on n-p Cells, Over a Pull-Test Temperature Range of -112° to -173°C (Ref. 11.5-1)

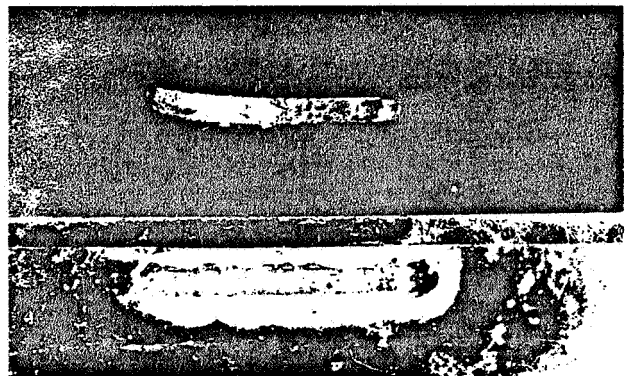


Fig. 11.5-12. Typical Failure Mode of p Contact, Solder-Coated Titanium-Silver Contacts on n-p Cells, Over a Pull-Test Temperature Range of $+110^{\circ}$ to $+165^{\circ}\text{C}$ (Ref. 11.5-1)

Table 11.5-1. Contact Pull Test Separation Modes of Ribbons or Wires (Tabs) Soldered to Cell Contacts

Case	Separation Mode	Interpretation of Separation
1	Tab slipped out of test fixture, broke, tore, or plating or solder coating parted from tab.	Not a cell contact failure. Test result should be discounted and test repeated, if possible on the same cell at a different location on the contact.
2	Solar cell broke near or away from solder joint.	Not a cell contact failure. Test result should be discounted and test repeated, if possible on the same cell at a different location on the contact.
3	Solder joint separated such that some solder and/or contact metal remains on the silicon. Some silicon may be pulled off, now adhering to tab.	Measured pull strength is good indicator of contact strength. Contact adhesion is approximately equal to silicon strength. Generally indicative of good contacts.
4	Silicon spalled and pulled from cell over entire solder joint area.	Contact strength is greater than silicon strength. Generally indicative of disturbed (dislocated) or pre-stressed silicon or presence of micro-cracks.
5	Tab with solder pulled from cell, leaving some or all contact metal on cell.	Either solder did not wet contacts, or contact metallization failed (example: silver pulled off titanium).
6	All metallization pulled from cell under soldered joint.	Typical metal/silicon interface failure. Measured pull strength is indicator of adhesion quality.

At low temperatures the predominant failure mechanisms is silicon fracture, as characterized by massive silicon removal with regular patterns observed in the silicon, corresponding to fracture along crystallographic planes. In this case, removal of silicon does not indicate a desirable contact system. Cells utilizing solder coating appear to be particularly vulnerable to this failure mechanism.

At intermediate temperatures, a combination of failure mechanisms is observed, consisting of silicon fracture, nonstructured silicon removal, delamination of the contact metal or metals from the silicon surface, delamination within the contact metals (to such an extent that contact material remains both on the cell surface and on the pull test tab), and removal of solder.

At the higher temperatures, the predominant failure mechanism is poor solder adherence due to the increased plasticity of the solder and loss of solder strength.

For the electroless nickel-plated contacts on p-n cells, the excessive cell breakage that was also noted was probably due to large stresses occurring in the cell blank as a result of the boron trichloride junction diffusion.

At the low and high temperature extremes, the spread in pull-test results was, in general, smaller than at the intermediate temperatures. This difference occurs because only one failure mechanism predominates at the low and at the high temperatures, namely, silicon fracture and loss of solder adherence, respectively; whereas, many failure modes are operating and competing at the intermediate temperatures.

For solder-coated cells, it is extremely important to control and minimize the solder thicknesses, particularly if the cells are to be exposed to low temperatures.

For solder- and nonsolder-coated cells, particular attention must be paid to controlling the evaporation or plating parameters and the surface condition of the cell prior to evaporation or plating. One must take great pains to minimize surface contaminants by means of cleaning, etching, etc., and to ensure that the cells are not allowed to become recontaminated after the cleaning operations.

At the highest temperatures, where the failure mechanism appeared to be exclusively that of loss of solder tensile strength, performance could be improved only by utilizing a higher temperature melt solder (which may adversely affect the lower temperature characteristics) or by using solderless interconnection techniques, such as welding or bonding.

Particular attention must be given to the materials, processes, and techniques involved in performing pull-strength tests. A careful procedure has been found to greatly increase the reproducibility of the test results and is described in the first part of this section. Some of the major parameters that must be controlled are the area on the cell contacts to which the contact test tabs are attached, the geometry of the test tab, the fabrication of the test tab from material such as Kovar (having a thermal coefficient of expansion approximating that of silicon), the minimization of

variations in soldering technique (eliminating the effects of operator dependency), the proper composition, placement, and geometry of solder preforms if they are used (to prevent such detrimental effects as silver scavenging in titanium-silver contacts), the careful inspection of the soldered pull-test tab and rejection of those that are questionable, and the careful control of the imposed pull rate.

Contact pull-strength tests represent one of the most important tools in evaluating the suitability of the cell for use in space missions. Such a test, however,

is meaningful only to the degree that it does not itself introduce extraneous variables, so that the observed differences, if any, between cell contact systems can be ascribed to differences in either materials or techniques involved in cell manufacturing and not to differences due to variations in the testing techniques.

11.5.4 Test Results

Contact pull test results obtained under various environmental conditions for various solar cell types are given in Refs. 11.5-1 through 11.5-3. A sample of the data of Ref. 11.5-1 is given in Section 3.5.4.

11.6 THERMOPHYSICAL PROPERTIES

Note: For a definition of the terminology used in this section, see Sections 7.13 and 7.14.

11.6.1 Determination of the Solar Absorptance

The solar absorptance of opaque materials (glassed solar cells, etc.) is generally determined in the following manner:

- Measurement of the spectral reflectance, ρ_λ (see Section 11.6.3)
- Calculating the (average) solar reflectance, ρ_S , by integrating over the solar spectrum, S_λ (see Section 2.4.2):

$$\rho_S = \frac{\int_a^b \rho_\lambda S_\lambda d\lambda}{\int_a^b S_\lambda d\lambda}$$

where the limits of integration, a and b , are determined by the wavelength range over which ρ_λ was measured (usually $a = 0.28 \mu\text{m}$ and $b = 2.5 \mu\text{m}$)

- Calculating the solar absorptance, α_S , from

$$\alpha_S = 1 - \rho_S$$

11.6.2 Determination of the Hemispherical Emittance

The hemispherical emittance is generally determined by one of the two methods described below:

Spectral Emittance Method

The spectral emittance method consists of the following steps:

- Measurement of the spectral reflectance, ρ_λ (see Section 11.6.3)
- Calculating the average reflectance, $\bar{\rho}$, by integrating over the Planckian black-body spectral emission spectrum, $P_{T\lambda}$, for a given absolute specimen temperature:

$$\bar{\rho} = \frac{\int_c^d \rho_\lambda P_{T\lambda} d\lambda}{\int_c^d P_{T\lambda} d\lambda}$$

- Calculation of the average normal emittance, $\bar{\epsilon}_N$, from

$$\bar{\epsilon}_N = 1 - \bar{\rho}$$

- Calculation of the average hemispherical emittance, $\bar{\epsilon}_H$, from

$$\bar{\epsilon}_H = \left(\frac{\epsilon}{\epsilon_n} \right) \bar{\epsilon}_N$$

where the ratio ϵ/ϵ_n is a correction factor which is based on experimentally verified electromagnetic theory (Ref. 11.6-1). The values of ϵ/ϵ_n are given in Figure 11.6-1.

From Ref. 11.6-1. Reprinted with permission of the Verein Deutscher Ingenieure-Verlag GmbH.

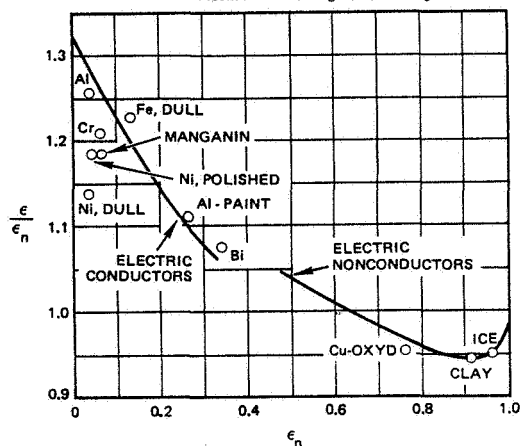


Fig. 11.6-1. Theoretical and Experimental Values for the Ratio of Hemispherical to Normal Emittance (Ref. 11.6-1)

Total Emittance Method

The emittance of a sample can be determined more rapidly by the total emittance method than by the spectral emittance method. The total emittance method steps are as follows:

- Measurement of the total reflectance, $\bar{\rho}$ (see Section 11.6.4)
- Calculation of the total normal emittance, $\bar{\epsilon}_N$, from

$$\bar{\epsilon}_N = 1 - \bar{\rho}$$

- Calculation of the average hemispherical emittance from

$$\bar{\epsilon}_H = \left(\frac{\epsilon}{\epsilon_n} \right) \bar{\epsilon}_N$$

where ϵ/ϵ_n is given in Figure 11.6-1 (see the discussion of ϵ/ϵ_n above).

11.6.3 Measurement of the Spectral Reflectance

Measurement of the spectral reflectance typically utilizes either an integrating sphere or a heated cavity that is attached to a spectrophotometer. The two methods are described below. Each of these methods measures the normal spectral emittance, $\epsilon_{N\lambda}$.

Integrating Sphere Method

The test equipment typically consists of an Edwards-type integrating sphere reflectometer attachment (Ref. 11.6-2) and a Beckman DK2A Spectrophotometer. The adaptation of the Edwards sphere to the Beckman electro-optical system was first made at TRW Systems Group in 1962 to eliminate errors inherent in the standard reflectometer attachment supplied by Beckman Instruments for the DK2A Spectrophotometer. Since 1964, the Edwards Integrating Sphere/DK2A combinations have been marketed by Gier Dunkle Instruments.

The Beckman DK2A is a double-beam ratio-recording spectrophotometer which automatically scans through the wavelength region of interest (from 0.28 to 2.5 microns for glassed solar cells) and records the ratio of the signal from the sample beam and the signal from the reference beam.

The inside surface of the Edwards integrating sphere is coated with Eastman 6080 white paint. This paint is highly reflecting and highly diffusing. Some relatively small openings in the sphere permit the two beams to enter, and lead-sulfide and photomultiplier tube detectors to be mounted. Light sources for the equipment are a hydrogen lamp for the shorter wavelength region and a tungsten filament lamp for the longer wavelengths.

The Edwards sphere also contains a sample holder which places the specimen at the geometric center of the integrating sphere such that none of the energy reflected from the specimen can reach the wall-mounted detector without first being reflected from the sphere wall at least once. This optical design eliminates some large potential errors and permits absolute (in contrast to relative) spectral reflectance measurements to be made.

During operation of the reflectometer, the reference and sample beams are directed into the sphere through a small entrance port. The reference beam is incident on the inside sphere wall but does not pass through the center of the sphere. The sample beam, on the other hand, passes through the center of the sphere and, for the calibration, is incident upon the sphere wall a short distance from the spot where the reference beam is incident. For this premeasurement

calibration, the specimen is retracted slightly from the center of the sphere. The specimen is then translated into the center of the sphere for the actual reflectance measurement. In this geometry, the sample beam is incident upon the specimen, and only that energy which is reflected from the specimen is detected. Let the intensity of the reference beam which is incident upon the sphere wall be denoted by I_R , and let the intensity of the sample beam which is incident upon the specimen be denoted by I_S . The two beam intensities are identical: $I_R = I_S$. The portion of the sample beam which is reflected from the specimen onto the sphere wall is $\rho_\lambda I_S$, where ρ_λ is the spectral reflectance of the specimen. The ratio-recording detector develops a signal which is equal to $\rho_\lambda I_S/I_R = \rho_\lambda$ because $I_S = I_R$. Hence, the instrument provides an absolute measurement of the spectral reflectance, ρ_λ .

Heated Cavity Method

The test equipment and measurement method is in principal similar to that of the integrating sphere method except that, instead of an integrating sphere (at room temperature), a heated cavity is used, and, instead of the sample beam being compared to the reference beam reflected by a highly diffusing and reflecting surface, it is reflected by a platinum foil which is kept by the surrounding heated cavity at 815°C (1500°F).

The test equipment is commercially available from Gier Dunkel Instruments as a Heated Cavity Absolute Reflectometer (Ref. 11.6-3).

11.6.4 Measurement of Total Reflectance

A device for measuring the total reflectance of a sample is described by Ref. 11.6-4. This device has since been refined and the inherent errors given by that reference have been reduced to less than ± 0.02 for most solar cell array materials. The improved device is marketed by Gier Dunkel Instruments as a Model DB-100 Infrared Reflectometer.

11.6.5 Test Results

Some of the more recent test results for thermo-physical properties for solar cell array materials have been reported by Refs. 11.6-5 and 11.6-6.

Additional test data related to radiation damage may be shown or referenced in the following sections of this handbook:

Cover and Cover Adhesive Transmission Degradation

Vol. I Sections 2.4.3, 2.5, 4.8.5, 11.7, 11.8 and 11.9

Vol. II Section 7.13

Thermophysical Properties Degradation

Vol. I Sections 2.4.3, 2.5, 11.7, 11.8 and 11.9

Vol. II Section 7.14

11.7 CORPUSCULAR IRRADIATION

Solar cell radiation damage experiments are performed with electrons, protons, and neutrons. Special equipment is required to generate the particles and increase their speed until the desired particle energy is achieved. Electrons are typically produced by Van de Graaff generators. Low energy protons are produced by equipment similar to the proton source shown in Section 11.9, while high energy protons are generated by cyclotrons. Neutrons are usually obtained as by-products from nuclear reactors.

11.7.1 Electron Sources

As an example of a typical radiation facility, the installation at the Jet Propulsion Laboratory, Pasadena, California, is described in the following paragraphs.

The radiation laboratory at JPL is built around a 3-MeV Dynamitron accelerator manufactured by Radiation Dynamics Inc. This machine produces a useful electron beam in the range of energies between 0.6 and 2.3 MeV at electron beam currents up to 2 mA. This relatively high current capability makes this machine ideal for the irradiation of large areas with high flux rates. The flux rate is adjustable from 1×10^9 e·cm⁻² per second to 1×10^{12} e·cm⁻² per second. The electron beam can be directed (horizontally) down a beam transport system into either one of two experimental areas. Patch panels installed in each area allow the routing of beam monitoring signals to a central data acquisition area near the accelerator control console.

One experimental area is devoted to a semipermanent installation of a vacuum chamber designed for measuring radiation effects in solar cells. An Aerospace Controls Model 302 solar simulator is coupled into the vacuum chamber for producing a beam of light on a 12 x 12 cm test plane. The simulator beam closely approximates solar radiation at one astronomical unit in both intensity and spectrum. All optics are ground from 7940 fused silica for maximum resistance to radiation darkening. A temperature controlled block at the target area can be maintained between -150° and +150°C. Provision is made for the simultaneous irradiation of up to 14 solar cells on this target plane with subsequent *in situ* measurement of their electrical parameters using the solar simulator. A thin aluminum or copper scattering foil is used to diffuse the electron beam uniformly over the target area. A small Faraday cup is mounted in the center of the target area for measuring the electron dose. All areas struck by the beam are water cooled (including the scattering foil). A liquid nitrogen shroud in the chamber is used during solar cell radiations to trap diffusion and fore-pump oil (even though the pumping system is LN₂ trapped), and to cryopump the chamber.

An electromagnet may be used to direct the electron beam into the second experimental room. Here, the beam is brought out into the air through a water cooled titanium foil. Various experimental arrangements may be set up independently of the first area. Irradiations may be done in the open air (an activated charcoal filter is provided for ozone removal), or the beam may be directed into a vacuum chamber through a titanium entrance window.

Electron Energy Spectrum Testing

Most electron radiation testing is performed using a mono-energetic beam of electrons which is incident perpendicularly on the solar cell surface. Ref. 11.7-1 describes a test method by which the JPL facility discussed above was used to generate an electron energy spectrum.

11.7.2 Electron Radiation Test Results

Most solar cell radiation studies are performed with 1-MeV electrons. Typically, the electrons are perpendicularly incident on uncovered (bare) solar cells. The solar cell damage at other electron energies is measured less frequently. Some of the more recent electron radiation test results can be found in Refs. 11.7-1 through 11.7-17. Ref. 11.7-1 gives the results of solar cell irradiation with an electron energy spectrum as found in geosynchronous orbit.

Additional test data related to radiation damage may be shown or referenced in the following sections of this handbook:

Solar Cell Degradation

Vol. I Sections 2.4.3, 2.5, 3.3, 11.8 and 11.9

Vol. II Sections 3.3 and 3.4

Cover and Cover Adhesive Transmission Degradation

Vol. I Sections 2.4.3, 2.5, 4.8.5, 11.8 and 11.9

Vol. II Section 7.13

Thermophysical Properties Degradation

Vol. I Sections 2.4.3, 2.5, 11.8 and 11.9

Vol. II Section 7.14

11.7.3 Proton Sources

A source of low energy protons is described in Section 11.9. Ref. 11.7-18 describes the use of a Tandem Van de Graaff generator for protons in the energy range from 2 to 10 MeV, a Variable Energy

Cyclotron for protons having energies between 10 and 50 MeV, and a Synchro Cyclotron for protons having energies between 50 to 155 MeV.

11.7.4 Proton Radiation Test Results

Some of the more recent solar cell test data obtained with protons is given in Refs. 11.7-13 through 11.7-16, and 11.7-19 through 11.7-28. Test data obtained with low energy protons (see Section 3.3.3) is given in Refs. 11.7-21 through 11.7-28. Ref. 11.7-28 shows solar cell degradation due to low energy protons incident through the substrate on the solar cell back contacts.

Additional test data related to radiation damage may be shown or referenced in the following sections of this handbook:

Solar Cell Degradation

Vol. I Sections 2.4.3, 2.5, 3.3
11.8 and 11.9

Vol. II Sections 3.3 and 3.4

Cover and Cover Adhesive Transmission Degradation

Vol. I Sections 2.4.3, 2.5, 4.8.5,
11.8 and 11.9

Vol. II Section 7.13

Thermophysical Properties Degradation

Vol. I Sections 2.4.3, 2.5,
11.8 and 11.9

Vol. II Section 7.14

11.7.5 Neutron Sources

Ref. 11.7-3 describes the use of a Fast Burst Reactor at the White Sands Missile Range to generate neutrons for solar cell testing.

Additional test data related to radiation damage may be shown or referenced in the following sections of this handbook:

11.7.6 Neutron Radiation Test Results

Some of the more recent solar cell test data obtained with neutrons is given in Refs. 11.7-15, 11.7-17, and 11.7-29.

Solar Cell Degradation

Vol. I Sections 2.4.3, 2.5, 3.3
11.8 and 11.9

Vol. II Sections 3.3 and 3.4

Cover and Cover Adhesive Transmission Degradation

Vol. I Sections 2.4.3, 2.5, 4.8.5,
11.8 and 11.9

Vol. II Section 7.13

Thermophysical Properties Degradation

Vol. I Sections 2.4.3, 2.5, 11.8 and 11.9

Vol. II Section 7.14

11.8 ULTRAVIOLET IRRADIATION

11.8.1 Ultraviolet Test Setups

Ultraviolet test setups differ widely in appearance; however, their common characteristics are a strong source of ultraviolet (UV) radiation and evacuated volumes in which the test samples are contained. One typical UV test system is described below; another system is described in Section 11.9.

One of the UV test systems in use at TRW is available for simulation testing of solar ultraviolet irradiation in a vacuum. This system uses a xenon compact arc lamp and a number of individually pumped sample chambers. In each such *in situ* vacuum test chamber, the sample is in contact with a temperature-controlled (liquid), axially translatable base. The chamber walls consist of UV-transparent quartz tubes. The test samples are maintained in a high vacuum by sputter ion pumps connected to stainless steel tees. All-metal seals are used throughout to maintain ultra high vacuum and to minimize the potential introduction of contaminants. The sample chambers are pumped down to a pressure of less than 10^{-6} torr using molecular sieve sorption pumps and the integral sputter ion pumps on each sample chamber. The construction of the *in situ* chambers permit the sample, while still in a vacuum enclosure, to be placed at the center of an absolute Edwards-type integrating sphere.

A number of individual sample chambers are placed radially around one xenon compact arc lamp located at the center. The chambers are movable along tracks in order to vary the lamp-to-sample distance. Thus, the irradiance on the sample can be set at any value from less than 1 "ultraviolet sun" ($\lambda < 0.4$ microns) to greater than 12 "ultraviolet suns". The lamps used typically range from 2.2 kW to 6.5 kW types. Other sources are available for degradation testing (e.g., the General Electric B-H6 high pressure mercury arc), but the xenon arc source is preferred as a better simulation of the solar spectrum in the ultraviolet region (Figure 11.8-1).

11.8.2 Far Ultraviolet Test Setups

In recent years, the "far ultraviolet" (FUV) region of the solar spectrum (below 200 nm) has been identified

as being most damaging to organic spacecraft materials such as Kapton and Teflon. Radiant energy at these short wavelengths can be obtained from electrodeless "continuum" krypton or xenon lamps. The gas in these lamps is ionized by RF (radio frequency) fields. An RF input power of 120 watts to the xenon lamp produces approximately 7 FUV suns (0.5×10^{14} photons per second) at a distance of approximately 1 meter from the lamp. Typical relative spectra are shown in Figure 11.8-2.

Another type of electrode-less krypton lamp, in use for FUV testing, is a "resonance" lamp. This lamp produces approximately 3×10^{15} photons per second in two single lines: 116.5 and 123.6 nm.

The FUV radiation from the lamps is reflected by special FUV mirror coatings (Figure 11.8-3) and transmitted through magnesium fluoride (MgF_2) windows.

Photodiodes are available for detecting FUV radiation. The National Bureau of Standards provides calibration services in the FUV region between 120 and 254 nm. A typical detector has a rubidium-telluride cathode and a MgF_2 window.

11.8.3 Test Results

Some of the more recent UV test data are reported by Ref. 11.8-6 and in Section 11.9. Additional test data related to radiation damage may be shown or referenced in the following sections of this handbook:

Cover and Cover Adhesive Transmission Degradation

- Vol. I Sections 2.4.3, 2.5, 4.8.5 and 11.7
- Vol. II Section 7.13

Thermophysical Properties Degradation

- Vol. I Sections 2.4.3, 2.5 and 11.7
- Vol. II Section 7.14

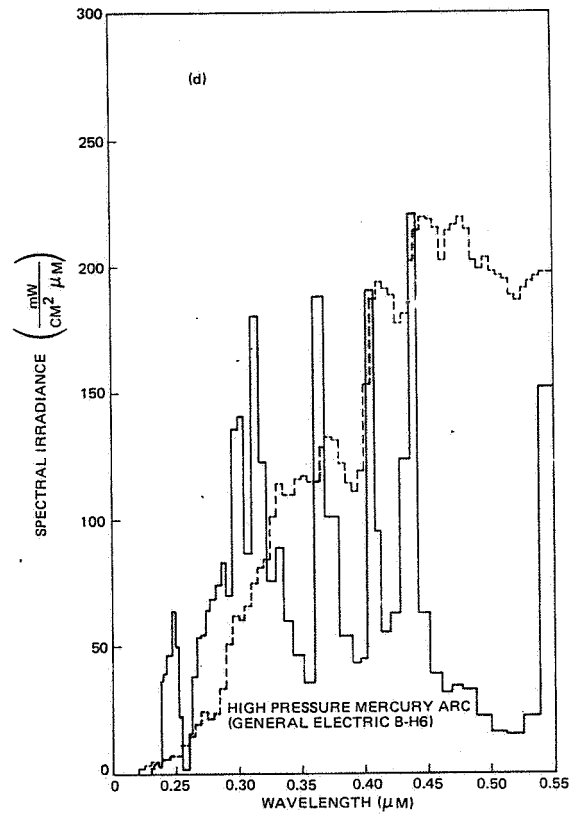
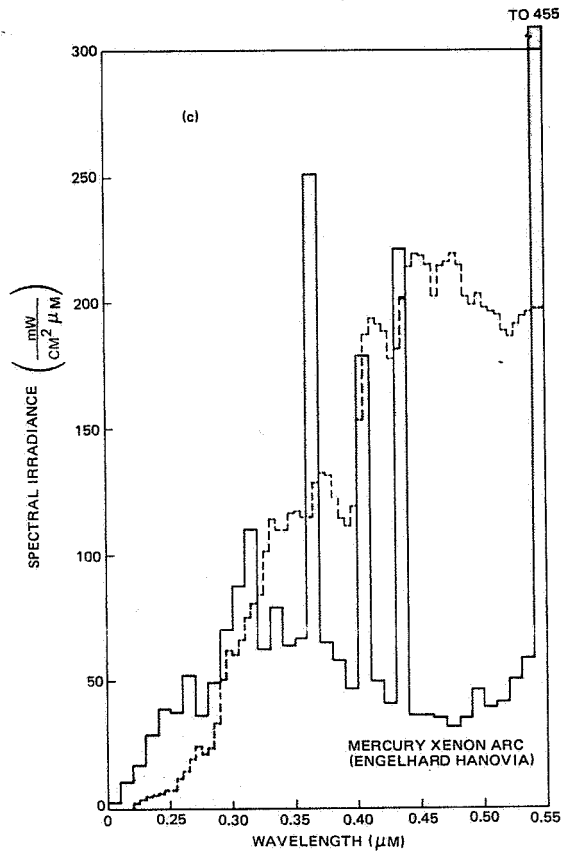
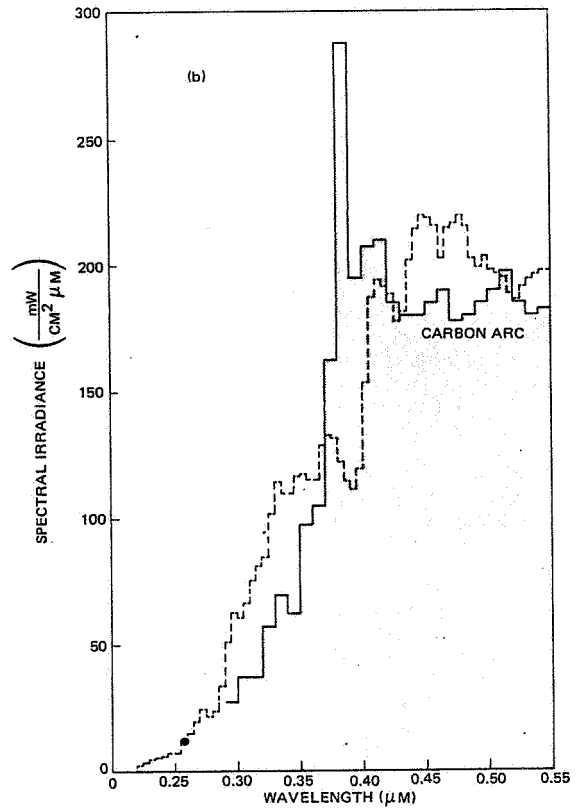
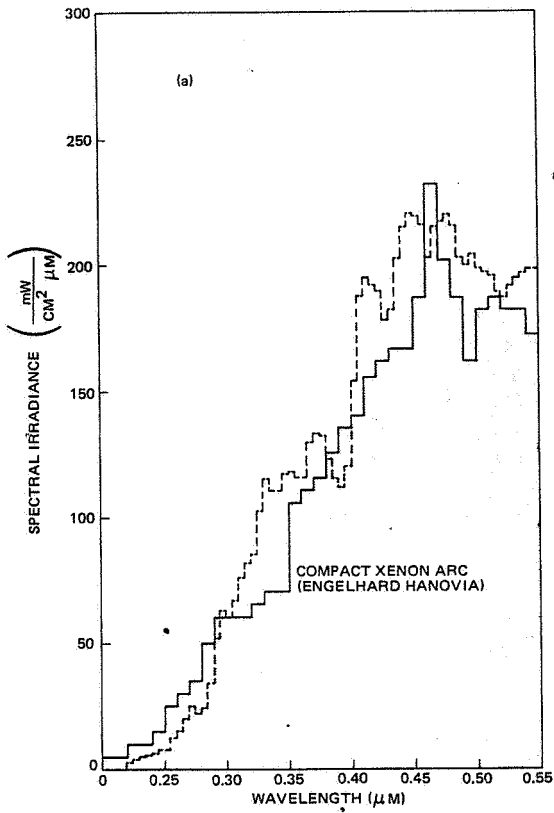


Fig. 11.8-1. Spectral Energy Distribution of Ultraviolet Sources (Solid Lines) Compared with the Solar Spectrum (dashed lines) [(a) and (c) — Ref. 11.8-1, (b) — Ref. 11.8-2, (d) — Ref. 11.8-3]

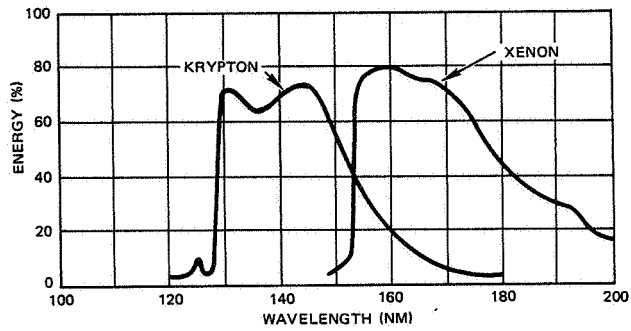


Fig. 11.8-2. Relative Photon Energy of Krypton and Xenon FUV Lamps (Ref. 11.8-4)

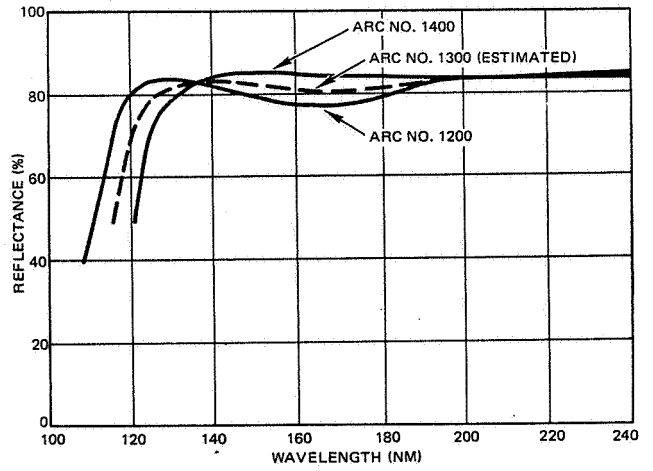


Fig. 11.8-3. Spectral Reflectance for Three Acton Research Corporation (ARC) FUV Mirror Coatings (Ref. 11.8-5)

11.9 COMBINED ENVIRONMENTS

In the actual space environment, ultraviolet and charged particle radiation (electrons and protons), encompassing large variations in energy, are simultaneously incident on solar cell array materials. Inasmuch as synergistic or antis synergistic effects can be expected to occur in materials, the simultaneous exposure of solar cell array materials to various forms of radiation in a vacuum environment is desirable. Such simultaneous exposure is achieved with combined environment test setups. Pre- and post-exposure tests are performed in-situ to prevent chemical changes from occurring in irradiated samples due to the effects of atmospheric oxygen or water vapor.

11.9.1 Combined Environments Test Equipment

As an example of the many different systems of this type that are in existence, one of the facilities in use at TRW is described in the following for illustration (Ref. 11.9-1).

A schematic drawing of the combined environments facility is shown in Figure 11.9-1. Each of the major subsystems will be discussed in the following sections.

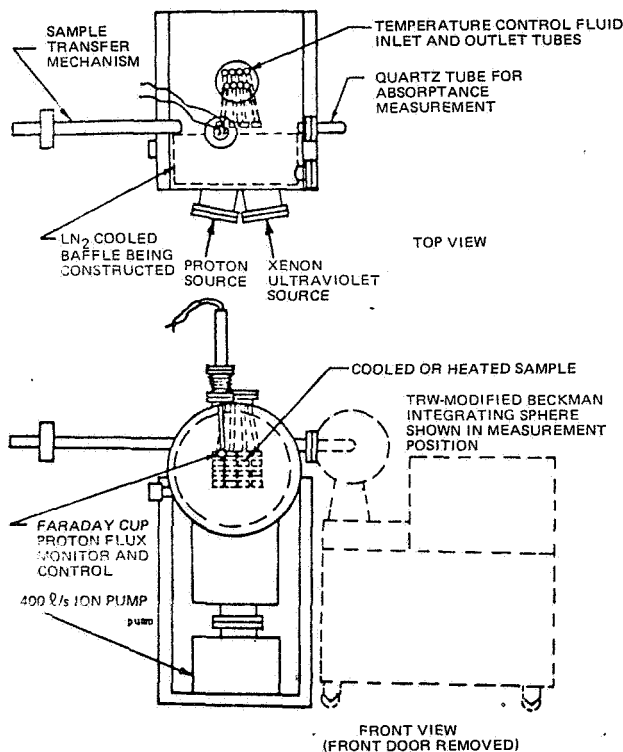


Fig. 11.9-1. Schematic Drawing of TRW Systems Combined Environment Facility (CEF)

Vacuum System

The vacuum chamber is in the form of a horizontally oriented cylinder approximately 18 inches in diameter by 30 inches long with a corresponding test section volume of approximately 125 liters. The chamber materials are:

- Type 304 or 321 stainless steel for the chamber walls and flanges
- Fused silica and glass for the windows
- Crushable copper seals.

No polymeric or other organic surfaces are exposed to the vacuum environment. The ends of the chamber are closed with domed, flanged doors sealed with crushable copper wire rings. A rotatable cantilever end door support mounts on either end of the chamber for end door removal. Numerous flanged ports of various sizes extend from the main chamber to provide access for vacuum pumping, environment components simulation, fluid, mechanical and electrical feedthroughs, viewports, etc.

A 14-inch diameter titanium sublimation pumping (TSP) well extends below the main chamber, and a 400-l/sec ion pump mounts to the bottom of this well. The TSP well has fluid feedthroughs and a copper cold wall for increased pumping speeds. A four-filament titanium sublimator extends through the well wall and provides an estimated extra 1200 l/sec pumping speed to handle peak gas loads during initial pumpdown and sample irradiation.

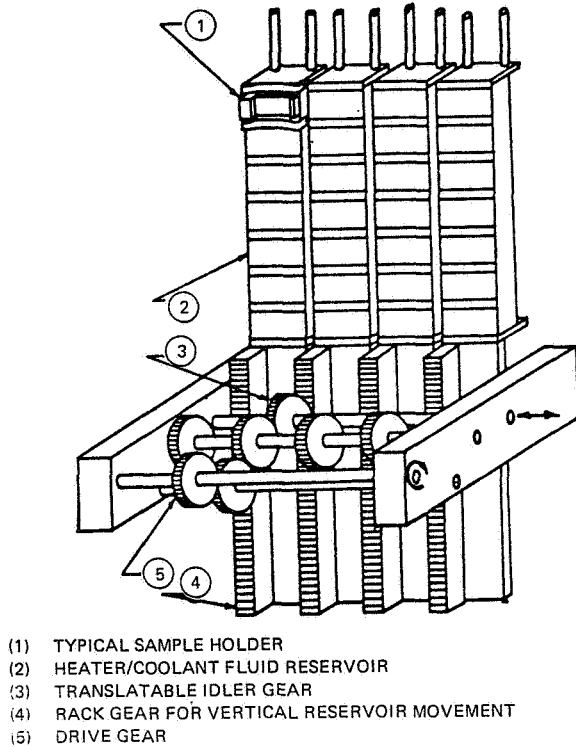
Pumping down to 1 to 10 μ m is accomplished with a portable roughing system consisting of a dry vane mechanical pump and two sorption pumps operated sequentially. During rough pumping, the titanium filaments are outgassed. Upon reaching a pressure between 1 and 10 μ m, the ion pump is started. The TSP is occasionally required to reduce the startup time of the ion pump.

Sample Holder and Transfer Mechanism

The sample holder and transfer system was designed on the basis of the following criteria:

- Sample packaging must be optimized to provide maximum capacity.
- Sample holders must be designed to provide adequate temperature control during exposure
- Sample holders must not place serious limitations on the accuracy of the spectral properties measurements.
- The sample transfer mechanisms must be "clean." The design of the mechanical manipulators to transfer samples in the chamber must be consistent with good ultra-high vacuum practice. Only inorganic or dry film lubricants are to be allowed.

Figure 11.9-2 illustrates the sample holder/transfer system. The system sample capacity, using a 1 x 2 cm rectangular sample size is 28. This sample size was selected for two reasons: this was a commonly-used solar cell/coverglass size, and the sample capacity is much greater for a fixed exposure beam area. Preparation of samples of these dimensions does not present any problems, and the accuracy of spectral measurements is slightly improved using small samples.

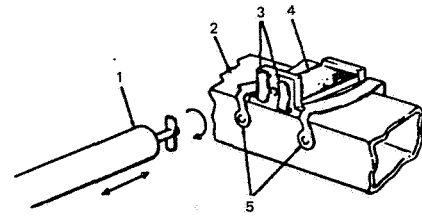


- (1) TYPICAL SAMPLE HOLDER
- (2) HEATER/COOLANT FLUID RESERVOIR
- (3) TRANSLATABLE IDLER GEAR
- (4) RACK GEAR FOR VERTICAL RESERVOIR MOVEMENT
- (5) DRIVE GEAR

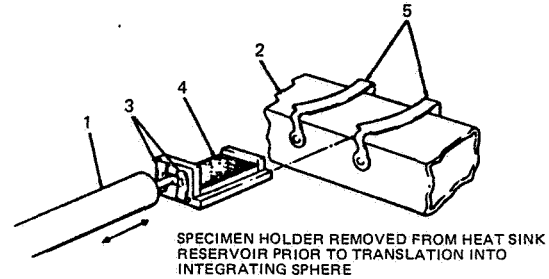
Fig. 11.9-2. Sample Holder-Motion Mechanism

Small individual sample holders (1) are spring mounted on four fluid cooled heat sink trays (2). The trays are vertically translatable using the externally driven spur gear-rack arrangement shown (4). Translation of the idler gear (3) from one rack gear to another allows horizontal movement of individual sample trays using the externally driven gear (5). Any particular sample may thereby be translated to the "pickup" position, removed from the tray (Figure 11.9-3), and translated into the integrating sphere for spectral property measurements.

The operation of removing a particular sample assembly from the heat sink once the sample has been moved to the "pickup" position, consists of (1) inserting the alignment pin on the end of the sample "pickup"/transfer manipulator shaft; (2) rotating the shaft through 90 degrees to engage the "propeller" into the spring clips; and (3) pulling the manipulator back to remove the sample holder from the springs holding it against the coolant tray. Since the transfer manipulator shaft can be rotated after the sample has been removed from the coolant tray, directional reflectance measurements are possible.



SPECIMEN HOLDER IN "PICK-UP" POSITION



SPECIMEN HOLDER REMOVED FROM HEAT SINK RESERVOIR PRIOR TO TRANSLATION INTO INTEGRATING SPHERE

LEGEND:

- (1) SPECIMEN PICK-UP/TRANSFER MANIPULATOR ARM (EXTERNALLY DRIVEN PUSH-PULL ROTARY MOTION FEEDTHROUGH)
- (2) SPECIMEN COOLANT/HEATER RESERVOIR
- (3) BERYLLIUM-COPPER SPRING CLIPS TO LATCH SPECIMEN HOLDER TO MANIPULATOR ARM
- (4) 1 x 2 CM TEST SPECIMEN
- (5) BERYLLIUM-COPPER SPRING CLIPS TO HOLD SPECIMEN HOLDER AGAINST RESERVOIR

Fig. 11.9-3. Illustration of Specimen Holder Pickup Technique

To replace a sample onto the coolant tray, one simply reverses the three steps above.

Figure 11.9-4 illustrates the irradiation pattern which is obtained with the 6-inch diameter ultraviolet beam and 5-inch diameter proton beam with appropriate masks.

Proton Source

The charged particle accelerator consists of three basic components.

- Source - The chamber in which hydrogen is ionized with an RF field and energized with a high potential anode.
- Mass Separator - A section in which the ionized hydrogen is mass separated to provide a near-pure $1H^+$ beam.
- Particle Detector - A Faraday cup particle detector for measuring and monitoring the proton flux.

Source

High purity hydrogen gas (99.999 percent H_2) is bled into the ionizing chamber through a variable leak valve. The ionizing chamber is a Pyrex bulb 6 inches in diameter by 9 inches long, closed on one end and sealed to a high vacuum 6-inch-port flange on the other end. A 10-MHz RF field is set up inside the bulb by passing an RF current through a copper tube coiled around its exterior. A portion of the hydrogen is ionized by this field and is then excited to higher energies by means of a high potential anode ring mounted inside the bulb.

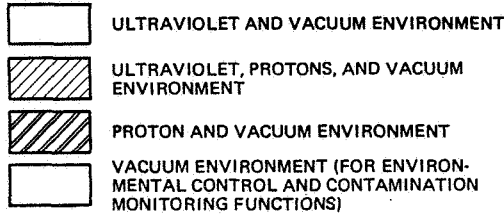
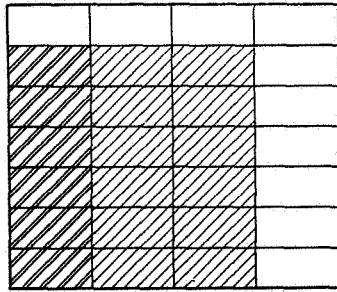


Fig. 11.9-4. Illustration of One of the Irradiation Patterns Attainable at Sample Holder Plane

Mass Separator

Ions are extracted from the plasma and directed towards the target plane through a mass separator to eliminate other ions from the beam. The separator is basically a Bennett tube type RF mass spectrometer which has been enlarged to accept the full 12-cm ion beam and allow protons (H_1^+ ions) to flow undiverted into the test chamber. At the exit end of the mass separator, hot filaments inject thermal electrons into the beam to provide space charge neutralization.

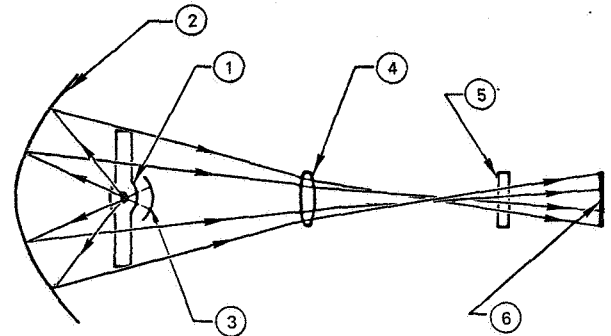
Particle Detector

A Faraday cup particle detector is used to accomplish four operations.

- Map the beam current areal uniformity across the target plane. This is accomplished by attaching the detector to a hermetically-sealed, rotary-push-fill manipulator which, in turn, is mounted on a flanged bellows to permit three degrees of motion.
- Provide a means of determining the beam angular spread. The detector is highly directional and rotatable about an axis parallel to its front face.
- Act as a sensor for beam flux feedback control. The detector is positioned near the edge of the beam during sample irradiation and provides the signal for the beam auto-density controller. The current signal from the Faraday cup is measured with a picoammeter.
- Determine beam energy using retardation techniques.

Ultraviolet Source

A compact arc xenon lamp is used as the ultraviolet source. Focusing optics consisting of a suprasil lens assembly, and first surface collection mirrors are arranged inside a lamp projector housing, as shown in Figure 11.9-5. The lamp is a 3.8 kW xenon lamp and is controllable from approximately 100 mW/cm^2 to 750 mW/cm^2 (below 4000 \AA) at the sample plane. The total irradiance has been measured with a TRW-fabricated electrically compensated, blackened foil radiometer. Filters are used with the radiometer to determine the ultraviolet content of the beam before and after a test.



- (1) 3.8 KW XENON ARC LAMP
- (2) FIRST SURFACE ELLIPSOIDAL PRIMARY MIRROR
- (3) FIRST SURFACE SPHERICAL SECONDARY MIRROR
- (4) FUSED SILICA LENS
- (5) QUARTZ CHAMBER WINDOW
- (6) SAMPLE PLANE

Fig. 11.9-5. Schematic Drawing of Ultraviolet Source Optics

Spectral Reflectance Measurements

Spectral reflectance measurements can be performed on any of the test specimens at any time during the exposure period by removing the desired sample from the heat sink with the sample manipulator and translating it into a fused silica test tube mounted on the wall of the vacuum chamber. A Beckman DK2A spectrophotometer with an integrating sphere of the Edwards, *et al.* (Ref. 11.9-2) type is positioned adjacent to the chamber with the quartz tube protruding into the sphere. This method of measurement has been thoroughly described by Miller, *et al.* (Ref. 11.9-3) and shown to be an accurate technique for materials evaluation work.

System Performance

The Combined Environment Facility has been operated since late 1968. This section will present some of the operational characteristics of the system.

The 400 1/sec ion pump will maintain the system pressure in the 10^{-9} torr range without the simulation sources operating. During proton and ultraviolet exposures, the chamber pressure is maintained in the high 10^{-7} to low 10^{-6} range by using the titanium sublimation pump on an approximately 5-10 minute cycle time (TSP on 90 seconds every 5-10 minutes). This pressure level can be improved by a better sealing method between the hydrogen ionization chamber and the test chamber. Efforts in this area are being pursued by the ion source manufacturer.

The sample holder and transfer mechanism have operated without fault after a thin coating of molybdenum disulfide was burnished on the mating gear parts. Reflectance measurements have also been accomplished on a nominal operational basis. Approximately 1/2 hour is required to transfer a sample to the integrating sphere, make the measurement, and replace the sample in the test chamber.

The proton source has been operated at flux levels from 2×10^8 to 5×10^{10} p/cm² sec. Beam uniformity varies somewhat as a function of beam energy, but is within 15 percent of a nominal center-of-beam value.

Other Features

The following features, not shown above, are part of the total system:

- Low energy electron source
- Particulate beam mass analyzer
- LN₂ cold wall on the main vacuum chamber wall
- Interlock system to automatically shut off certain components in the event that one component ceases to operate properly
- Data acquisition system to continuously monitor and record on X-Y, strip or circular chart recorders the important test parameters such as vacuum level and charged particle and ultraviolet fluxes.

11.9.2 Test Results

Some of the more recent test results obtained with combined environments are described by Refs. 11.9-4 through 11.9-12. Ref. 11.9-13 has analyzed the test results of Refs. 11.9-4 and 11.9-9 through 11.9-11 and has concluded that the optical losses in the solar cell stack vary from approximately 4 to 12 percent for combined ultraviolet and particulate exposures exceeding the dosages that would be expected in 1 year in geosynchronous orbit. Ref. 11.9-13 also found that combined environmental effects cause a greater transmittance loss than exposure to single environments. Ref. 11.9-11 has found that the optical degradation measured on exposed solar cell stacks is greater than measured on individual cover and adhesive samples.

Additional test data related to radiation damage may be shown or referenced in the following sections of this handbook:

Solar Cell Degradation

Vol. I Sections 2.4.3, 2.5, 3.3, 11.7 and 11.8

Vol. II Sections 3.3 and 3.4

Cover and Cover Adhesive Transmission Degradation

Vol. I Sections 2.4.3, 2.5, 4.8.5, 11.7 and 11.8

Vol. II Section 7.13

Thermophysical Properties Degradation

Vol. I Sections 2.4.3, 2.5, 11.7 and 11.8

Vol. II Section 7.14

11.10 INSULATION RESISTANCE AND VOLTAGE BREAKDOWN

The equipment used for the measurement of the leakage resistance and the breakdown voltage of insulating sheets between solar cell circuits and a metallic substrate is of the conventional type and, therefore, is not described herein.

Measurements are best performed by shorting all positive and negative solar cell circuit terminals together, and then measuring the resistance between the solar cell circuits and the substrate. Care should be exercised to prevent solar cell or blocking diode potentials from exceeding safe limits in case a low-resistance path or arc-over suddenly occurs. Solar cells generally are less sensitive to excessive reverse

bias voltages than rectifier diodes because (a) the solar cells have rather large reverse leakage currents at low voltages, and (b) the current flow from insulation resistance measuring equipment is usually limited to a few milliamperes, preventing a large voltage build-up across the solar cells.

Prior to installation of solar cells on a metallic substrate, the insulation quality is frequently determined by a "wet-sponge" test. Experience, however, has shown that for cell-to-substrate voltages below 100 Vdc, pin-holes in the insulating sheet are of no consequence.

11.11 TEMPERATURE CYCLING

11.11.1 Test Equipment

Temperature cycling tests are performed by two basically different methods; in vacuum, and in air. Temperature cycling in vacuum, also known as thermal-vacuum and vacuum-thermal cycling, generally provides good simulation of the space vacuum environment, but a sufficiently fast temperature decay and sufficiently low temperatures, as predicted for deployed solar cell arrays in geosynchronous orbit, are generally not obtainable.

The undesirably low rate of temperature decay is caused by three unavoidable conditions:

- The relatively large thermal mass of structural elements and light sources in the space simulation chamber
- The relatively high heat sink temperature (-196°C for liquid nitrogen cooled walls instead of -273°C for space)
- The relatively inefficient heat transfer by radiation, especially at lower absolute temperatures.

Frequently, liquid nitrogen vapors are introduced directly into the vacuum chamber to accelerate the temperature decay and provide a lower temperature for the array under test. The associated loss in vacuum is temporary and can be minimized by using high-volume vacuum pumps.

Most test problems associated with achieving thermal rates and lower limits that may occur in vacuum-thermal cycling can be avoided when specimens are tested in air or in inert gas atmospheres. Typical air test chambers utilize liquid nitrogen vapor cooling and electric heating in a circulating forced air chamber. The advantages of such circulating air chambers are that

- Almost any desired temperature profile can be achieved.
- Highly accelerated temperature cycling tests may be performed.
- Costs are considerably lower than with vacuum-thermal cycling testing.

The disadvantages of circulating air chambers are three-fold:

- The effects of vacuum are not assessed.
- There is no thermal gradient across the thickness dimension of the array as would be the case of a sun-facing array with its back side radiating to space.
- Chemical and metallurgical effects (such as humidity condensation or oxygen embrittlement) may affect the test results.

To avoid the problems associated with circulating air chambers, special inert gas (dry nitrogen) test chambers have been constructed. The test chamber in use at JPL is of this type; it also simulates the temperature gradient across the test specimens.

11.11.2 Test Results - Mechanical

Temperature cycling mechanical test results include observations of such items as cracking, delaminating and spalling of components, adhesive bonds and metal joints. Some typical solar cell and interconnector failure modes are illustrated in Section 5.2. Some of the more recent mechanical test results are given by Refs. 11.11-1 through 11.11-3.

11.11.3 Test Results - Electrical

Temperature cycling electrical test results typically show solar cell output degradation which usually is due to increased cell and interconnector series resistance. Depending upon the upper and lower temperature limits and the number of temperature cycles incurred, electrical output losses at the maximum point are typically only a few percent but may range from zero to less than 10 percent for "adequate" designs, and in excess of 10 percent for inadequate designs. The judgment of adequacy depends upon the following:

- Loss in electrical conductivity provided by solder or other coatings that become textured and partially or fully nonconductive in the current-flow direction during thermal cycling
- Loss in integrity of the solar cell contacts.

Some recent electrical test results are given in Table 11.11-1.

Table 11.11-1. Solar Panel Power Loss due to Temperature Cycling Testing in Air Chambers

Temperature		No. of Cycles	Power Loss (%)	Reference	Notes
Low (°C)	High (°C)				
-80	100	1500	1.0	11.11-4	(1)
-80	100	4800	3.0	11.11-4	(1)
-140	100	2000	1.2	11.11-4	(1)
-160	60	50-100	1.0-2.0	11.11-3	(2)
-160	75	500	1.1	11.11-4	(1)

Notes: (1) Pressed solder covered solar cells; solder plated Kovar ribbon interconnectors.

(2) Pressed solder covered solar cells; silver mesh interconnectors.

11.12 DARK FORWARD TESTING

The testing of the dark forward solar cell array characteristics has received considerable attention for two reasons: (a) solar simulators which illuminate large areas or volumes sufficiently uniformly so that arrays mounted to spacecraft can be meaningfully tested may not be available, and (b) large articulated, oriented arrays already integrated to a spacecraft and mounted in a stowed condition cannot be readily unfolded for testing. The dark forward test method is the only presently known method which is applicable for these cases.

The dark forward test method consists of the electrical connection of an external dc bias source to the terminals of a nonilluminated solar cell array such that the array becomes forward biased. During the test, the dark forward characteristics of the solar cell "diode" matrix are measured while the bus voltage is varied. Typically, the array current and bias voltage are recorded automatically by electromechanical X-Y plotters.

The forward bias current level is not critical, but best results are obtained when the maximum forward bias current exceeds 50 percent of the short-circuit current which would be obtained under one solar constant illumination.

The accuracy of this test method depends to a large degree upon the accuracy with which the temperature of the array under test can be measured, and upon the temperature uniformity over the entire array which can be achieved. During the test, the forward bias causes a temperature rise of the array under test which, under most practical circumstances, leads to an undesirable error. Therefore, pulsed bias applications (up to 10 seconds dwell time) have been employed.

The dark forward test method was effectively used during the prelaunch checkout phases of the solar cell arrays on Skylab (Ref. 11.12-1). The relationships between the "photovoltaic" output characteristics and the "dark forward" characteristics, are illustrated in Figure 11.12-1. The series resistance of illuminated solar cells (2 x 2 cm, 0.35-mm thick, 2 ohm-cm base resistivity) was found to be a function of both illumination level and cell voltage as shown in Figure 11.12-2. These values of series resistance were used in the computation of the photovoltaic I-V curve based on dark reverse measurements. The method was found to be sensitive to temperature as shown in Figure 11.12-3.

From Ref. 11.12-1. Reprinted with permission of the American Nuclear Society.

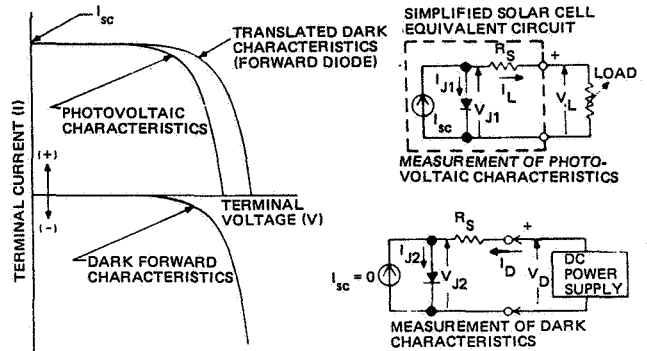


Fig. 11.12-1. Photovoltaic and Dark Forward Characteristics (Ref. 11.12-1)

Panel Checkout Criteria Using the Dark Characteristics*

The checkout criteria proposed for the solar panel involves comparison of the dark I-V characteristics between the initially "calibrated" dark I-V curve and any subsequent dark I-V data obtained. Figure 11.12-4 presents dark I-V curves for various modules in parallel. Figure 11.12-5 is a cross-plot of Figure 11.12-4, showing the relationship between the dark terminal voltage and the number of parallel modules at several currents. These plots indicate that the dark I-V characteristics cannot be used to adequately determine the number of modules connected in the circuit, except for major discrepancies. For instance, in Figure 11.12-5 the change in the dark terminal voltage from 20 to 19 modules is only 0.1 volt, but from 20 to 16 modules, this difference is about 0.7 volt.

The temperature coefficient of the dark terminal voltage at an applied current of 800 mA was found to be about $-0.26 \text{ V}/^\circ\text{C}$. In view of this high sensitivity of voltage to temperature, the temperature of the cells must be accurately determined. For a large solar panel, a problem of thermal gradient across the surface area must also be considered.

* Abstracted from Ref. 11.12-1.

From Ref. 11.12-1. Reprinted with permission of the American Nuclear Society.

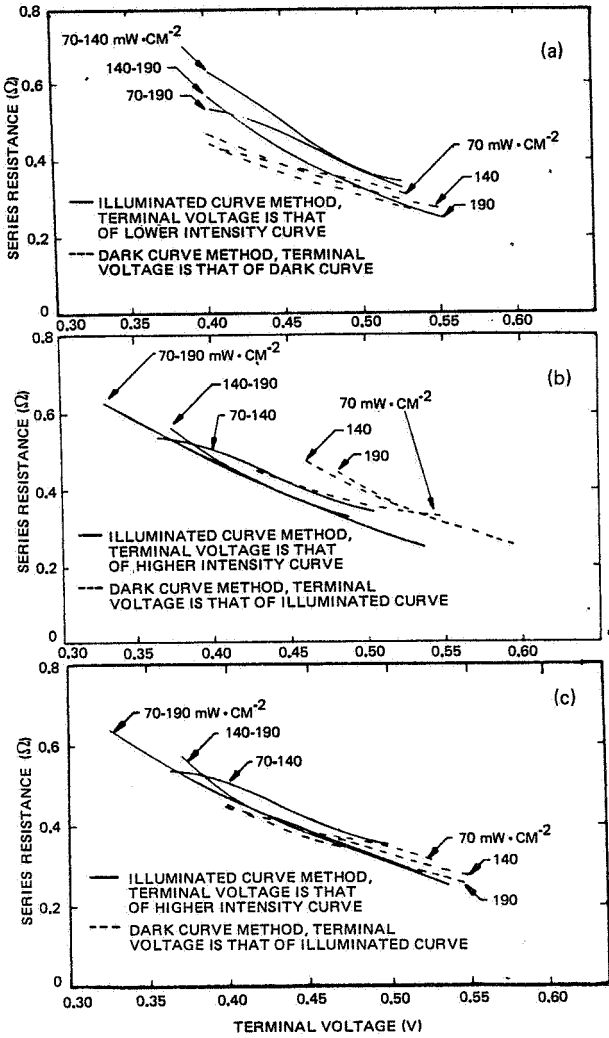


Fig. 11.12-2. Series Resistance Versus Voltage Obtained Using Illuminated and Dark Curve Methods for Centralab 2 x 2 cm Cells (Ref. 11.12-1)

From Ref. 11.12-1. Reprinted with permission of the American Nuclear Society.

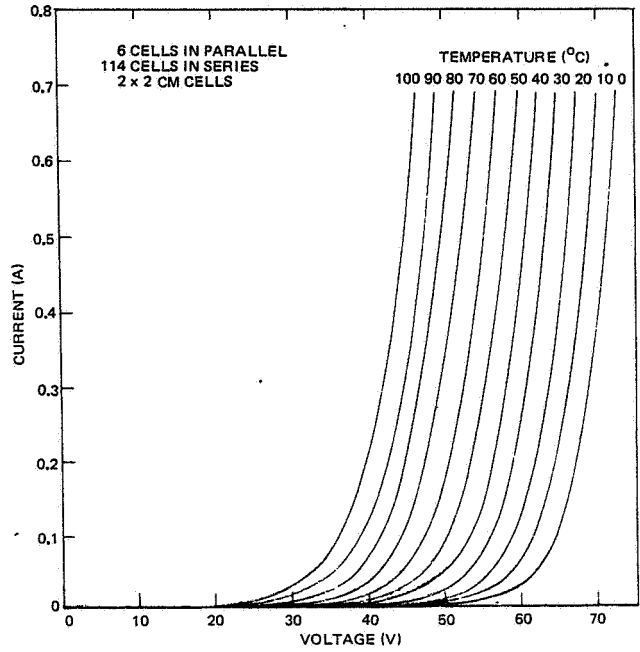


Fig. 11.12-3. Dark I-V Curves at Various Temperatures for an ATM Solar Cell Module (Ref. 11.12-1)

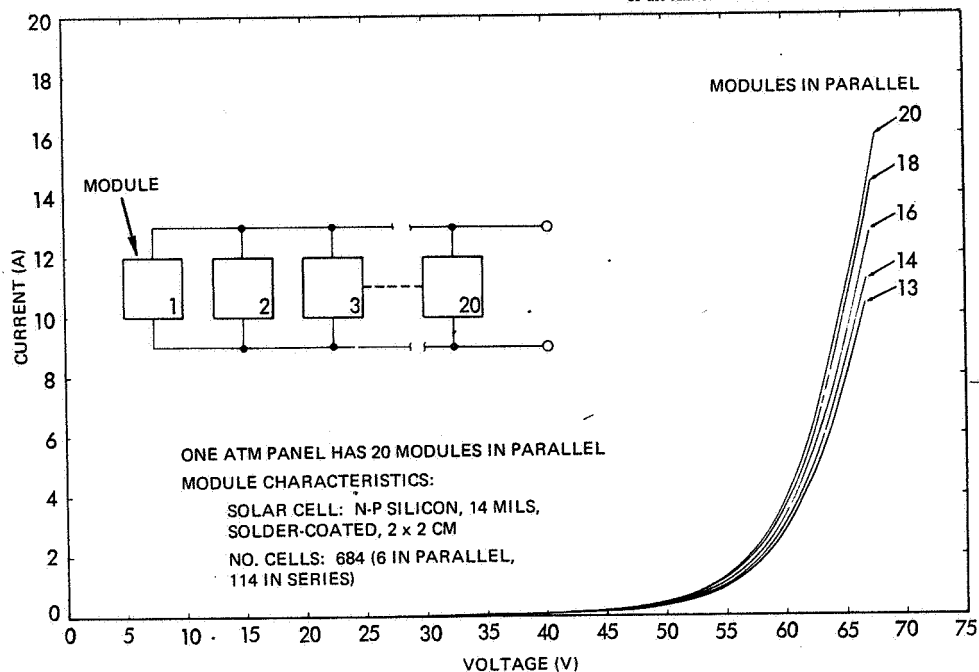


Fig. 11.12-4. Dark Forward I-V Curves at 25°C for an ATM Panel with Various Number of Modules in Parallel (Ref. 11.12-1)

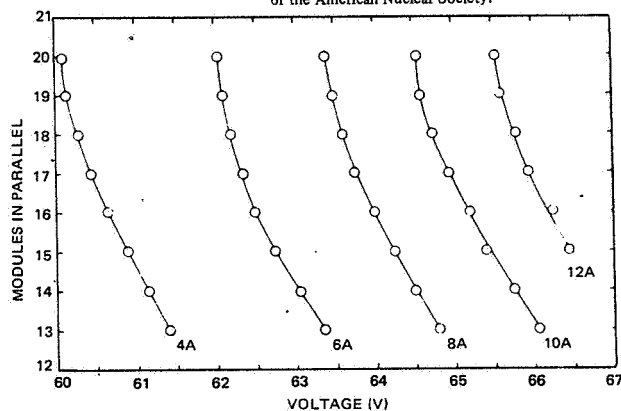


Fig. 11.12-5. ATM Panel Dark Forward Terminal Voltage at 25°C for Various Number of Modules in Parallel, Applied Current as a Parameter (Ref. 11.12-1)

11.13 ORBITAL FLIGHT DATA

11.13.1 Determination of Array Performance in Space

The orbital performance of solar cell arrays can be obtained from two sources:

- Solar cell flight experiments
- Operational satellite array performance

There is generally a considerable lapse of time between solar cell procurement for a given project and completion of orbital data analysis, typically ranging from 3 to 7 years. Adding 2 years for the design and development phase, the solar cell array designer can typically be expected to wait for from 5 to 10 years (conceptual design to array end-of-life) or more before he has full confirmation of the adequacy (or inadequacy) of his design efforts.

11.13.2 Summary of Solar Cell Array Degradation

The orbital performance and degradation of several flight experiments and operational satellites was analyzed by Ref. 11.13-1. This reference found that different solar cell arrays in geosynchronous orbit degrade at significantly different rates that, at the present time, cannot be explained. The typical array degradation characteristics found by Ref. 11.13-1 are shown in Table 11.13-1. The optical (non-cell) losses are relatively large during the first year in orbit and increase very little thereafter. The solar cell radiation damage is relatively small during the first year in orbit but increases significantly thereafter.

Details of the solar cell array construction and performance degradation for the various flight experiments and some operational satellites are given in the following subsections.

11.13.3 Nimbus-2*

The Nimbus-2 spacecraft was launched on May 15, 1966, into a near-circular, 1111 km, high-noon, sun-synchronous orbit. The solar cell radiation experiment on Nimbus-2 consisted of two planar panels, each having 30 series-connected solar cells bonded to an aluminum honeycomb substrate. The cells on one panel were provided with 0.15-mm thick fused silica coverglass bonded to the cells with Furane 15E adhesive. Bonded to the cells of the other panel were 2.54-mm thick fused silica coverglasses, having the same optical filter properties as the 0.15 mm experiment. The radiation experiments received solar illumination at the same incidence angle and for the same period of time as the satellite's solar cell array.

Each solar cell in the experiment was loaded with a 1.46-ohm resistance in order that values of current near the short-circuit point could be monitored. Solar cells for the radiation experiment were obtained from the production line at RCA-Mountaintop as the nominal 1 ohm-cm, n-on-p silicon cells were being manufactured for the Nimbus-2 solar array.

In order to evaluate the degradation of the cell's short-circuit currents; the telemetry values had to be normalized to remove the effect of all factors except solar cell degradation. For each orbit analyzed, the telemetry voltage was obtained during a portion of the orbit not affected by albedo illumination. The value of the telemetry voltage was converted into the average short-circuit current of the 30 cells in each experiment.

*Based on Ref. 11.13-2

Table 11.13-1. Typical Solar Cell Array Degradation in Orbit (after Ref. 11.13-1)

Type of Degradation	Time in Synchronous Equatorial Orbit		Time in 1000 km Circular Polar Orbit	
	1 year	7 years	1 year	7 years
1-MeV Fluence (e·cm ⁻²)*	4.3×10^{13}	3.0×10^{14}	2×10^{14}	1.0×10^{15}
Solar Cell Degradation (%)	.3	15	8	20
Non-Cell Losses (%)	4 - 10	4 - 10	4 - 10	4 - 10
Total Losses (%)	7 - 13	19 - 25	12 - 18	24 - 30

*Note: Calculated values for infinite back shielding thickness

From Ref. 11.13-1. Reprinted with permission of the IEEE.

Figure 11.13-1 shows that for the 0.15-mm experiment the predicted curve agrees reasonably well with the measured curve; a difference of only 1.8 percent separates the two curves at orbit 5200. For the 2.54-mm experiment, the predicted curve does not agree with the measured curve; the predicted curve shows 8.7 percent less degradation than the measured curve at orbit 5200. Since slightly undersized 2.54-mm thick covers were used, this excessive degradation was most likely due to low energy proton damage.

Neither the 0.15-mm nor the 2.54-mm experiments show the expected 3 to 4 percent decrease in current during the first 100 hours of sunlight exposure due to ultraviolet degradation of the coverglass-filter-adhesive solar cell combination. This expected degradation also was not observed with the satellite's solar cell array.

Charged particle damage was not expected to be observed on the experiment until the accumulated 1-MeV flux reached a value of about 10^{13} e \cdot cm $^{-2}$ (about 600 orbits), but a rapid degradation began during the initial orbits, which indicates an effect other than orbital electron and proton damage. The 0.15-mm experiment degradation did not begin until the accumulated 1-MeV flux reached a value at which current was affected. Thus no decrease in current during the first few orbits was observed with both the 0.15-mm experiment and the main solar array, which also has 0.15 mm of coverglass shielding.

11.13.4 ATS-1*

The ATS-1 spacecraft was launched on December 7, 1966. It carried an experiment on solar cell radiation damage. The spacecraft executed one and one-half transfer ellipses (perigee: 185 km; apogee: 42,600 km; period: 15 hours) before entering its final circular, near-synchronous equatorial orbit at 41,190 km altitude. The final station was over the Pacific equator at 157 degrees west longitude. The spacecraft was spin stabilized at about 100 rpm.

Results from 11 of the 30 solar cells will be reported here. These cells were all nominally 1 x 2 cm in size, 0.30 mm thick, silicon, boron-doped, n-on-p and of about 10 ohm-cm base resistivity. It is believed

that these cells were typical of "modern" solar cell technology. There were pairs of cells with 0, 0.025, 0.15, 0.38, 0.76 and 1.52 mm thick shields. The 0.025 mm shields were of an "integral" type (7740 glass powder melted to cover the cells). The other cells bore shields of Corning type 7940 ultraviolet resistant, synthetic fused silica, attached with Dow-Corning type XR-6-3488 adhesive. These shields had blue rejection filters with a 400 mm cutoff to avoid adhesive darkening. Silicon monoxide anti-reflective coatings were also present on the surface of these cells.

Each telemetered solar cell response was corrected for angle-of-incidence, satellite-sun distance of 1 AU, and temperature.

Table 11.13-2 is a numerical summary of the results of this part of the experiment. Important characteristics of the solar cells are given at five different times after liftoff. Columns 5, 6 and 7 show values (averaged over the two cells of a pair) of short-circuit current, open-circuit voltage, and maximum power. Column 8 shows the average value of the "fill factor" (F). This factor is the ratio of the maximum power to the product of short-circuit current and open-circuit voltage. Columns 9, 10, and 11 give the average short-circuit current, open-circuit voltage, and maximum power as percentages of initial values. The latter were those obtained in orbit 0.064 days after liftoff. It is believed that little, if any, damage to these cells had occurred up to this time. All table values were read from voltage-current curves that had been corrected to 24.4°C, one astronomical unit distance, and normal illumination. Quantities in parentheses are uncertain because they were based on extrapolated values for short-circuit current.

Figure 11.13-2 shows the voltage-current characteristics of cell 25 at different times after liftoff. This is a conventional 10 ohm-cm silicon cell with no shield. The maximum power point is indicated on each curve. In some cases part of the curve has been estimated, as shown by a dashed region. The characteristics of cell 26, a similar cell with no shield, were almost identical with those of cell 25 over the great range of radiation damage encountered.

Cells 15 and 16 were those having integral 25 μ m shields. Their averaged curves are shown in Figure 11.13-3, which includes all (corrected) data points. The consistency of the data and the similar degradation of the cells were noted by the experimenter.

* Based on Refs. 11.13-3 and 11.13-4

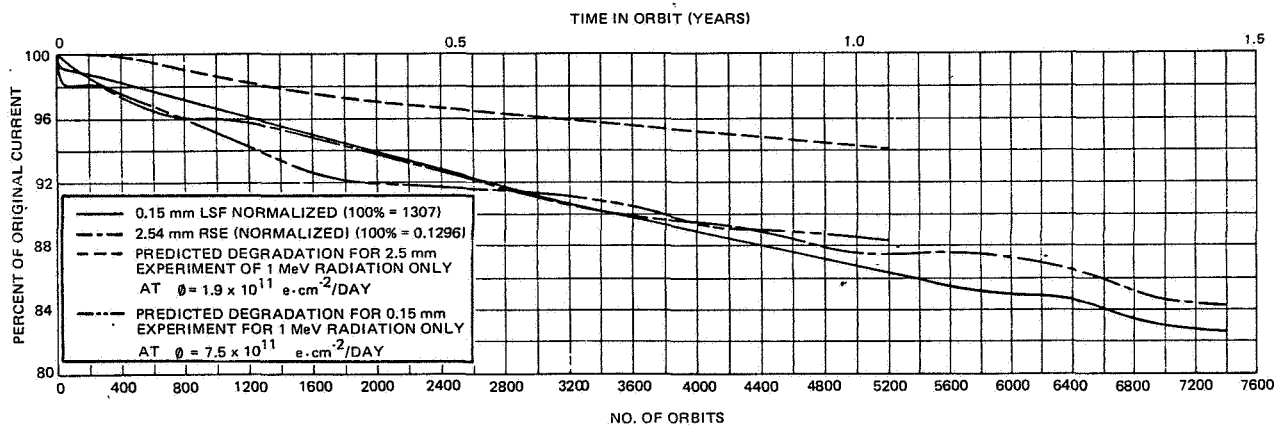


Fig. 11.13-1. Normalized Current Loss Versus Orbit for Two Solar Cell Experiments

Table 11.13-2. ATS-1 Solar Cell Characteristics at Various Times in Orbit (Ref. 11.13-4)

Note: Data normalized to 1.00 AU solar distance, 24.4°C, operating temperature, and perpendicular sunlight incidence.

1	2	3	4	5	6	7	8	9	10	11
Cell No.	Shield Material	Shield Thickness (mm)	Time After Lift-off (days)	I_{sc} (mA)	V_{oc} (mV)	P_M (mW)	Fill Factor	$\frac{I_{sc}}{I_{sc0}}$ (%)	$\frac{V_{oc}}{V_{oc0}}$ (%)	$\frac{P_M}{P_{M0}}$ (%)
25,26	None	0.0	0.064	70.3	548.3	26.7	0.694	100.0	100.0	100.0
		0.0	3.28	61.5	425.8	16.9	0.644	87.6	77.7	63.0
		0.0	20.3	(55.0)	330.6	10.3	(0.566)	(78.3)	60.3	38.5
		0.0	100.7	(44.5)	311.9	6.3	(0.458)	(63.4)	56.9	23.8
		0.0	270.4	(34.5)	305.1	4.0	(0.383)	(49.2)	55.7	15.0
		0.0	416.8	(29.0)	301.6	3.1	(0.349)	(41.4)	55.0	11.4
15,16	7740 Glass	0.025	0.064	62.4	544.0	24.5	0.722	100.0	100.0	100.0
		0.025	3.28	61.6	540.0	24.4	0.735	98.7	99.3	97.6
		0.025	20.3	60.8	538.7	23.8	0.729	97.4	99.0	97.4
		0.025	100.7	59.0	536.8	22.0	0.694	94.5	98.7	89.6
		0.025	270.4	57.2	531.8	21.4	0.702	91.7	97.8	87.4
		0.025	416.8	56.2	528.8	20.8	0.699	90.1	97.2	84.9
5,6	7940 Fused Silica	0.15	0.064	67.9	558.7	27.5	0.724	100.0	100.0	100.0
		0.15	3.28	67.0	560.3	28.1	0.749	98.6	100.3	102.1
		0.15	20.3	65.9	559.5	27.3	0.743	97.0	100.2	97.7
		0.15	100.7	64.9	555.4	26.2	0.727	95.6	99.4	95.5
		0.15	270.4	63.2	552.5	25.6	0.736	93.0	98.9	93.5
		0.15	416.8	62.2	552.4	25.4	0.739	91.7	98.9	92.5
23,24	7940 Fused Silica	0.38	0.064	67.7	560.0	27.1	0.714	100.0	100.0	100.0
		0.38	3.28	67.9	563.0	28.1	0.736	100.4	100.2	103.5
		0.38	20.3	66.4	560.3	26.3	0.707	98.2	99.7	96.9
		0.38	100.7	65.4	557.6	25.9	0.709	96.7	99.3	95.2
		0.38	270.4	63.8	555.6	25.0	0.704	94.4	98.9	91.9
		0.38	416.8	62.7	554.6	24.1	0.692	92.7	98.7	88.7
21,22	7940 Fused Silica	0.76	0.064	69.6	558.8	28.0	0.719	100.0	100.0	100.0
		0.76	3.28	69.1	561.2	28.2	0.729	99.3	100.5	101.1
		0.76	20.3	67.6	555.7	26.9	0.715	97.2	99.5	96.1
		0.76	100.7	66.5	554.1	25.9	0.704	95.6	99.2	92.7
		0.76	270.4	65.6	554.0	25.2	0.695	94.4	99.2	90.3
		0.76	416.8	64.5	551.3	24.3	0.683	92.6	98.7	86.9
20	7940 Fused Silica	1.52	0.064	69.2	563.1	28.4	0.729	100.0	100.0	100.0
		1.52	3.28	68.6	564.0	28.2	0.729	99.1	100.2	99.3
		1.52	20.3	68.2	560.1	27.0	0.707	98.6	99.5	95.1
		1.52	100.7	66.9	557.5	25.4	0.681	96.7	99.0	89.4
		1.52	270.4	66.1	559.4	24.4	0.660	95.5	99.3	85.9
		1.52	416.8	65.0	553.5	23.8	0.660	93.9	98.3	83.5

From Ref. 11.13-4. Reprinted with permission of the IEEE.

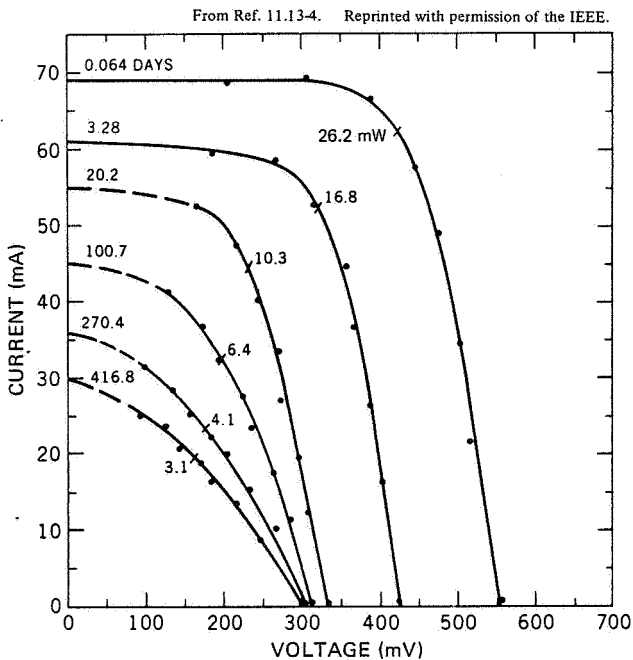


Fig. 11.13-2. A Voltage-Current Family for Unshielded Cell No. 25

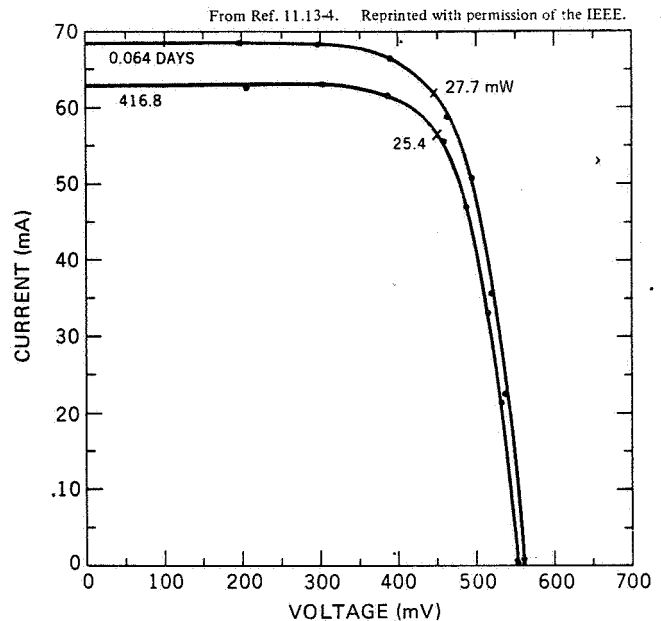


Fig. 11.13-4. Voltage-current Curves for Cell 5, with a 0.15 mm Silica (7940) Shield

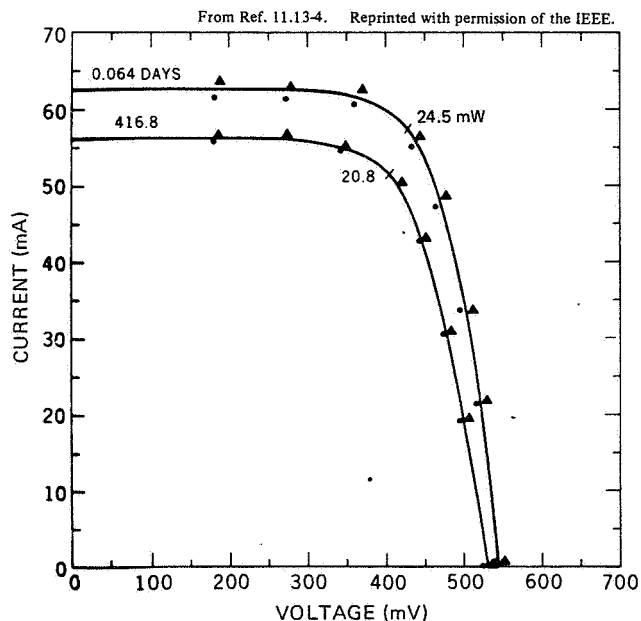


Fig. 11.13-3. Voltage-Current Curves for Cells 15 and 16, with 25 μ m Integral Glass (7940) Shields

In Figure 11.13-4 are shown a pair of curves for cell 5, which bore a 0.15 mm shield. Cell 6 gave very similar results.

Cell 20 (Figure 11.13-5) bore the thickest shield (1.52 mm). Returns from companion cell 19 failed early in the experiment, presumably because of failure in the switching circuitry, which involved 80 micro-miniature relays, their transistor drivers, and address circuitry.

Curves for the 0.38 and 0.76 mm shielded cells are not shown, but were intermediate between those of Figures 11.13-4 and 11.13-5.

The manner in which the maximum power from some of these cells deteriorated with time in orbit is shown in Figure 11.13-6, while Figure 11.13-7 shows the virtue of various thicknesses of shields in protecting several important solar cell properties. The bars on these curves terminate at the data points for the two cells of the pair on which measurements were made.

The data from this experiment supports the following conclusions involving silicon, 10 ohm-cm, n-on-p solar cells with various shields [Corning 7940 fused silica for items d) through g)] as observed over 416 days in synchronous orbit:

- The solar cell degradation was greater than that expected from the particle environment.
- Unprotected solar cells degraded significantly during three passages through the radiation belts during the launch procedure; at 416.8 days after liftoff their maximum power (PM) was 11.4 percent initial value, short-circuit current (I_{SC}) was 42.0 percent, open-circuit voltage (V_{OC}) was 55.0 percent, and curve factor (F) was 0.344.

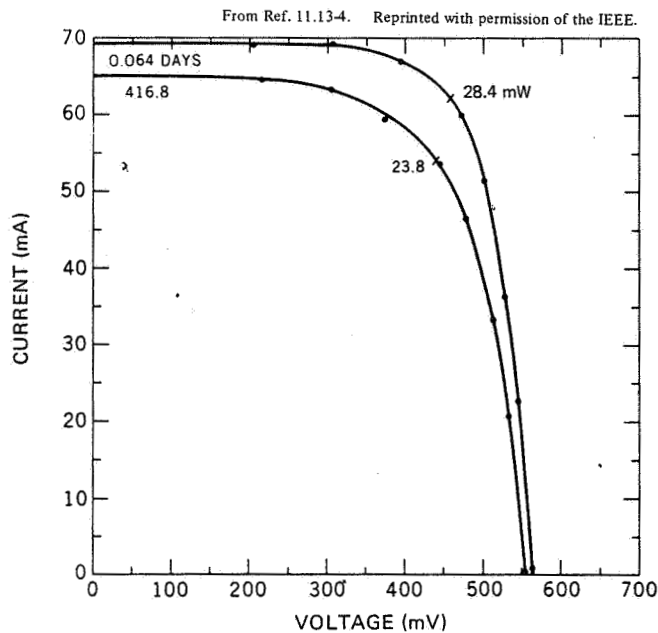


Fig. 11.13-5. Voltage-Current Curves for Cell 20, with a 1.52 mm Silica (7940) Shield

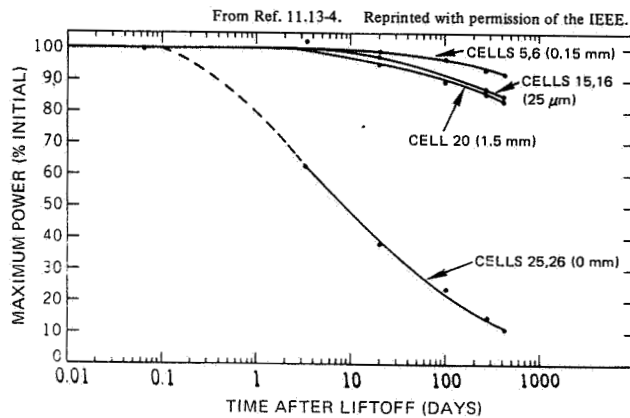


Fig. 11.13-6. Maximum Power Versus Time for Several Cells with Various Shields

- c) For 25 μm (7740 glass) shielded cells $P_M = 84.9$ percent, $I_{SC} = 90.1$ percent, $V_{OC} = 97.2$ percent, $F = 0.699$
- d) For 0.15 mm shielded cells, $P_M = 92.5$ percent, $I_{SC} = 91.7$ percent, $V_{OC} = 98.9$ percent, $F = 0.739$.
- e) For 0.38 mm shielded cells, $P_M = 88.7$ percent, $I_{SC} = 92.7$ percent, $V_{OC} = 98.7$ percent, $F = 0.692$.
- f) For 0.76 mm shielded cells, $P_M = 86.9$ percent, $I_{SC} = 92.6$ percent, $V_{OC} = 98.7$ percent, $F = 0.683$.

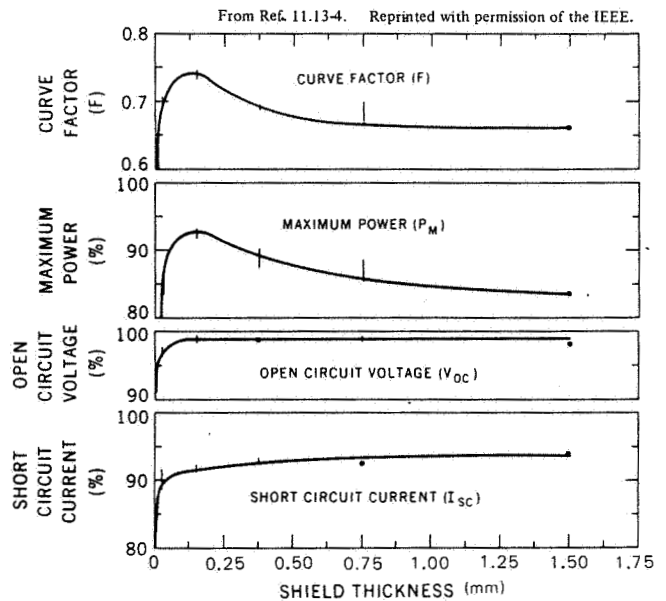


Fig. 11.13-7. Curve Factor (F), Maximum Power (P_M), Open-Circuit Voltage (V_{OC}), and Short-Circuit Current (I_{SC}) Versus Shield Thickness, at 416 Days After Lift-Off

- g) For a 1.52 mm shielded cell, $P_M = 83.5$ percent, $I_{SC} = 93.9$ percent, $V_{OC} = 98.3$ percent, $F = 0.660$.
- h) The degradation in power of the more heavily shielded cells was relatively large compared to degradation in short-circuit current or open-circuit voltage.
- i) The above conclusion points to a damage mechanism (among others) in which series resistance developed within the cell, possibly at the unshielded areas near contacts, by some action not ordinarily considered in radiation damage studies.
- j) Cells bearing 6-mil shields degraded, in power, less than cells bearing either thicker or thinner shields.
- k) Thicker shields were effective in protecting the cells against degradation in short-circuit current.
- l) Short-circuit current was not a valid indicator of solar cell damage under the conditions of this experiment.
- m) To qualitatively account for the shape of the various voltage-current curves it is necessary to postulate various combinations of, (a), illumination decrease; (b), particle radiation damage; and, (c) a mechanism introducing large power losses, in the maximum power region, for heavily shielded cells.

- n) A continued study of solar cell damage both in theory and by laboratory and space experiments is advisable, since questions of both scientific and economic importance have been raised.

11.13.5 Pioneer VI, VII, and VIII*

The array consisted of 10,368 n-on-p silicon solar cells of 1 ohm-cm base resistivity mounted on a cylindrical substrate of 94 cm diameter and 89 cm height. The cells, 1 x 2 cm in size, are covered by 0.15-mm thick microsheet covers with blue-reflective coatings. The covers were attached to the cells after the overlapping type modules were assembled and were then mounted to the substrate. Sufficient excess adhesive provided protection of those active solar cell areas not shielded by coverglass. At 1.0 AU, the array operated at +5°C and produced 80 watts at its maximum power point, and at 1.2 AU it operated at -21°C and produced 60 watts. The array, spinning at 60 rpm, was oriented with its spin axis normal to the ecliptic plane.

The solar cells were connected into 48 strings, each of 54 cells in series by four cells in parallel. Each string was connected to the bus through an isolation diode with approximately 1 volt forward drop. The nominal operating bus voltage of the spacecraft was 31 volts at 1.0 AU. The power subsystem used a storage battery but no voltage regulators.

The experimental data was obtained from on-board telemetry. Bus current, bus voltage and array temperature were measured in succession.

The telemetry resolution introduced resolution errors up to the following magnitudes: voltage, 1.8 percent; voltage error due to temperature error, 1.2 percent; current, 2.4 percent.

These three Pioneer spacecraft are in solar orbits having the following parameters:

	Pioneer VI	Pioneer VII	Pioneer VIII
Perigee (AU)	0.814	1.010	0.992
Apogee (AU)	0.985	1.125	1.089
Inclination (deg)	0.1695	0.097	0.057
Period (days)	311.3	402.9	387.5

Figure 11.13-8 shows the changes in output voltage of three different Pioneer solar arrays launched at different times. This figure indicates that "free space" environments — within the accuracy and resolution of the data — had no measurable effects on the voltage of the Pioneer VI array for 259 days, and on the Pioneer VII array for 15 days. After this time (September 2-4, 1966), a large solar flare, consisting predominantly of protons, was observed (Ref. 11.13-1). The characteristics of the flare were as follows:

- Total integrated flux of 17.2×10^7 protons/cm² of >25 MeV over a 3-day period.
- Two peaks, one on September 3, 1966, the other on September 4, 1966.

Additionally to this solar flare two other major solar events, consisting mostly of electrons, occurred in a period from August 28 through September 10, 1966.

Figure 11.13-8 shows significant voltage degradation commencing immediately following the proton flare of September 2-4, both on the Pioneer VI and VII arrays. It is interesting to note that the flare apparently started a solar cell degradation process which continued for approximately 200 days after the event, then stopped and about 450 days after the flare, converted into an improvement indicative of radiation damage annealing.

Based on the foregoing, it may be concluded (with considerable caution) that a solar flare proton dose of 17.2×10^7 protons/cm² of 25 MeV energy may produce a voltage degradation as high as 4 percent. Figure 11.13-9 shows the array operating points for various orbit conditions.

11.13.6 IDSCS (Initial Defense Satellite Communications System)†

A study of the solar arrays on 19 Air Force IDSCS satellites in near-synchronous (drifting) orbit was performed. The best- and worst-case degradations projected to 5 years, encompassing all cell and noncell (i.e. coverslide system) losses are 12.5 percent and 16.8 percent for short-circuit current and 1.7 and 5.5 percent for open-circuit voltage. Distribution appears Gaussian over these ranges.

Calculated cell degradations, due to residual electrons and flare protons under the 20-mil coverslide shield, indicate that maximum damage regions appear at electron energies near 0.7 MeV and at proton energies near 3 MeV. The ratio of calculated electron to proton cell damage is about 5 to 2.

When these results and calculations are integrated with an understanding of the statistical uncertainties involved and a knowledge of ground cell irradiation data, a number of conclusions follow: noncell losses affecting I_{SC} range from 6 to 12 percent while cell loss, per se, is only about 6 percent (projected to 5 years). Basic V_{OC} loss is about 2 percent but an additional 0 to 3 percent is observed and tentatively credited to low-energy proton damage. The best equivalent fluence for the 5-year projection is 1.2×10^{14} e⁻·cm⁻² of 0.8 MeV energy.

The solar cells were a 1 x 2 cm n-on-p boron doped silicon cell of 1964 vintage with a base resistivity ranging between 7 and 13 ohm-cm. All cells were shielded by 0.51-mm thick fused silica covers applied with Dow Corning XR-6-3489 adhesive. The solar cells were assembled in overlapping (shingled) fashion and excessive cover adhesive was not removed from glassed cell assemblies, thusly providing some low-energy proton protection.

The IDSCS satellite shape is a symmetrical polyhedron consisting of two octahedral truncated pyramids joined by an octagonal cylindrical center section. The height of the satellite body is 79 cm, and the diameter of the circle circumscribing the octagonal cylinder is 91 cm.

*Based on Refs. 11.13-5 and 11.13-6

†Portions of this material are quoted from Refs. 11.13-7 and 11.13-8.

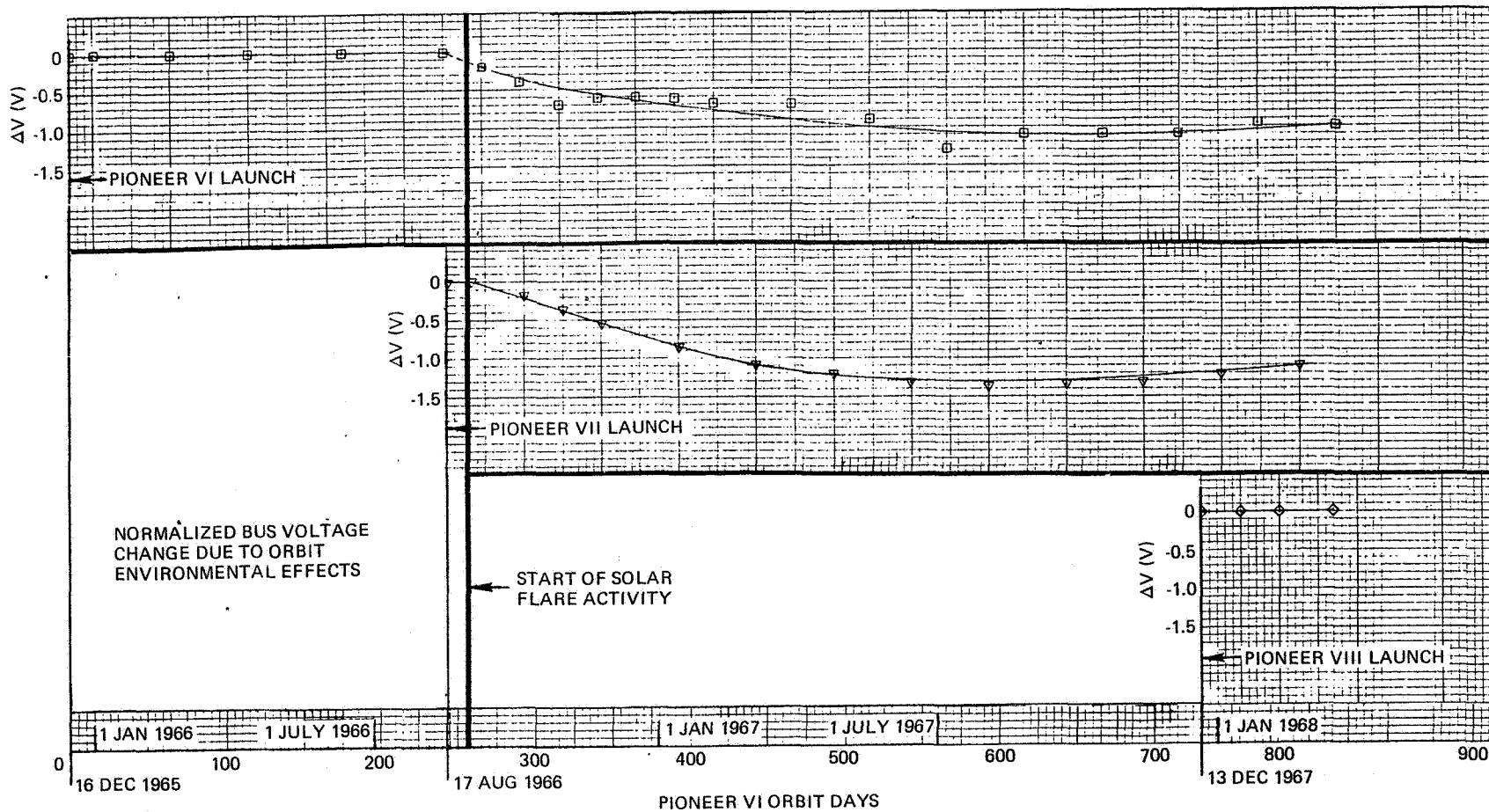


Fig. 11.13-8: Pioneer VI, VII and VIII Solar Arrays

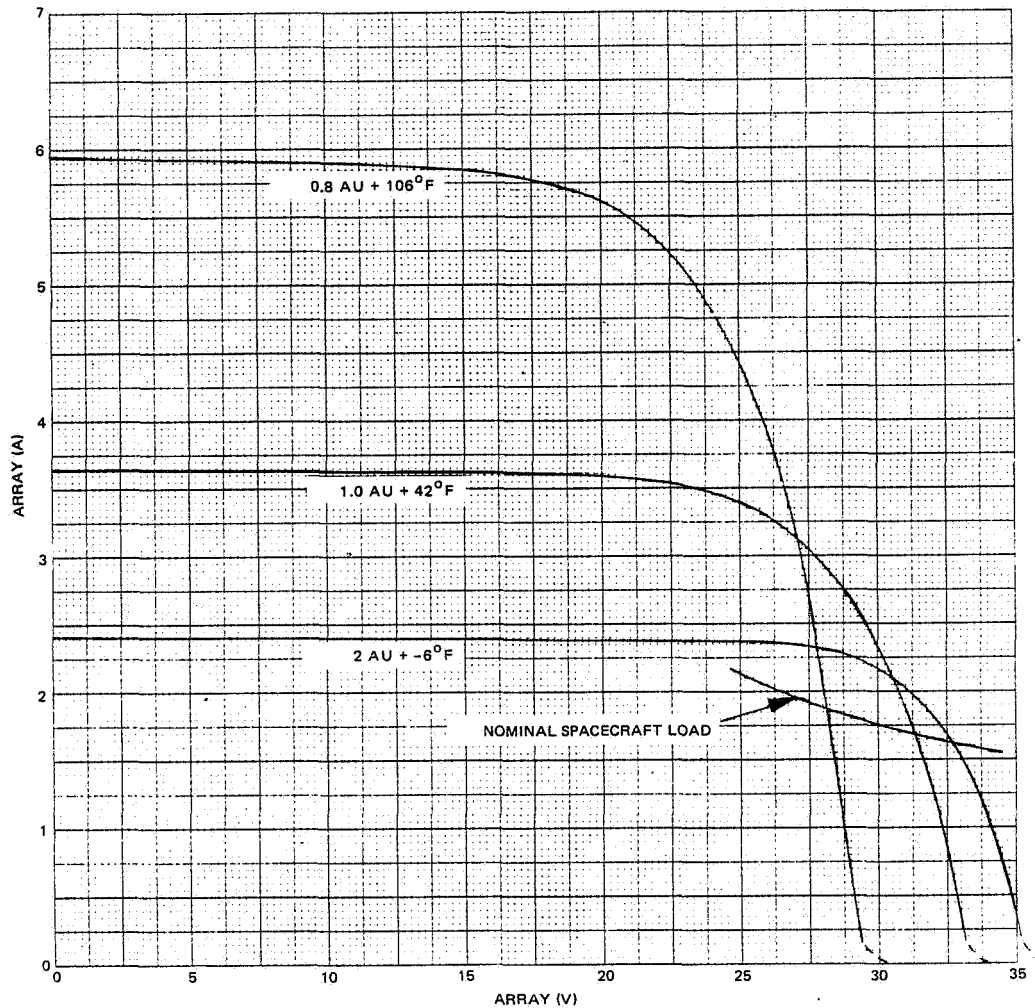


Fig. 11.13-9. Pioneer Solar Array Estimated Nominal Output Characteristic at Bus

Three launches have been considered: The first (7 satellites) on 16 June 1966; the second (8 satellites) on 18 January 1967; and the third (4 satellites) on 1 July 1967.

The nominal orbits for the three launches are given in Table 11.13-3. The individual satellite orbits differed slightly because each had a slightly different initial velocity to ensure separation and eventual distribution around the earth.

Surprisingly large variations were observed in presumably identical satellite solar cell arrays, both as to initial array outputs and to cell degradation rates on-orbit. Initial short-circuit currents and open-circuit voltages show a near Gaussian distribution and span 10.1 and 1.8 percent, respectively. This spread may be attributed to the random solar cell panel selection used in the satellite construction and, in part, to telemetry sensor variations. When all initial parameters are normalized to unity, subsequent degradation levels over 5 years are again

observed to span 5.0 percent for I_{SC} , and 4.0 percent for V_{OC} . Figure 11.13-10 presents the best- and worst-case cell short-circuit current degradation curves, extrapolated to 5 years, for the first two IDSCS payloads (i.e., 15 satellites). All cell and noncell losses are included. The best- and worst-case end points are 0.894 and 0.844. Figure 11.13-11 presents similar open-circuit voltage curves; the best- and worst-case end points are 0.983 and 0.943. Figure 11.13-11 also includes a curve which corresponds to the theoretically calculated V_{OC} degradation, based on the updated radiation environment and best available damage coefficient data. This curve is observed to present an average path between the measured extremes.

Figure 11.13-12 presents the calculated I_{SC} degradation of the cells alone, due to radiation. Comparing this curve with the two extreme curves of Figure 11.13-10, we present the best- and worst-case estimations of noncell (i.e., coverslide assembly) losses projected to 5 years; the curves indicate end points of 0.954 and 0.900.

Table 11.13-3. Satellite Orbits

Orbital Parameter	First Launch 16 June 1966	Second Launch 18 Jan 1967	Third Launch 1 July 1967
Apogee (nmi)	18,606	18,330	18,228
Perigee (nmi)	18,205	18,161	18,191
Eccentricity	0.0092	0.0039	0.00086
Inclination (deg)	0.042	0.41	6.998
Period (min)	1350	1335	1332

Unit Conversion: Multiply nmi by 1.852 to obtain km.

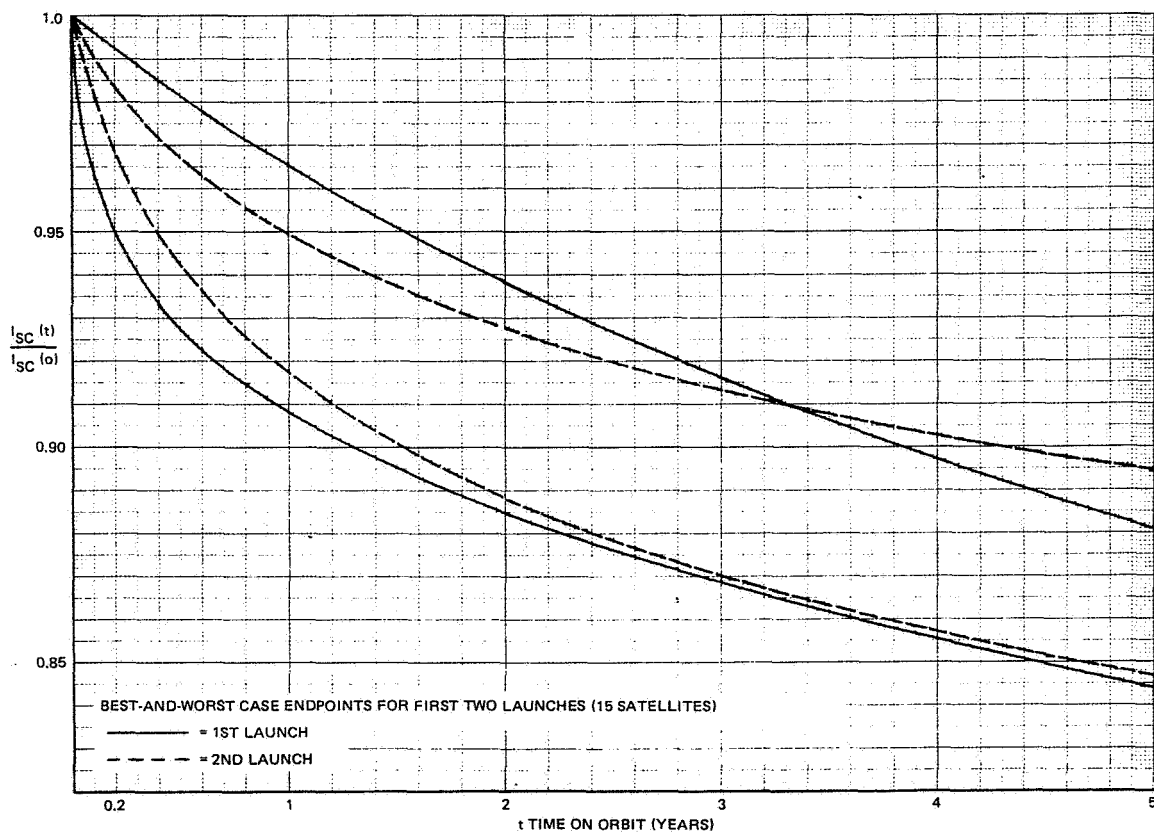


Fig. 11.13-10. Observed and Projected Cell Short-Circuit Current Degradation

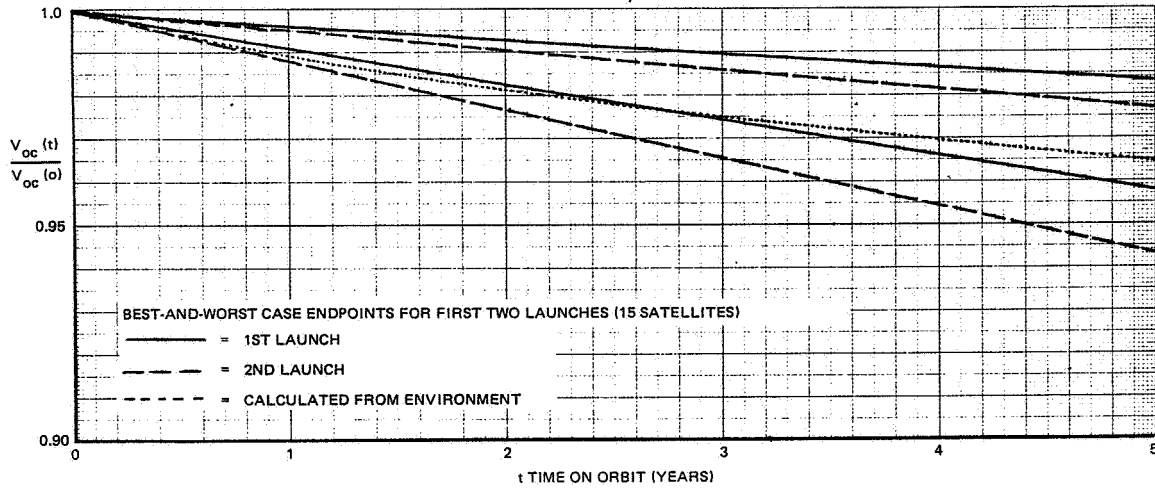


Fig. 11.13-11. Observed, Projected and Calculated Cell Open-Circuit Voltage Degradation

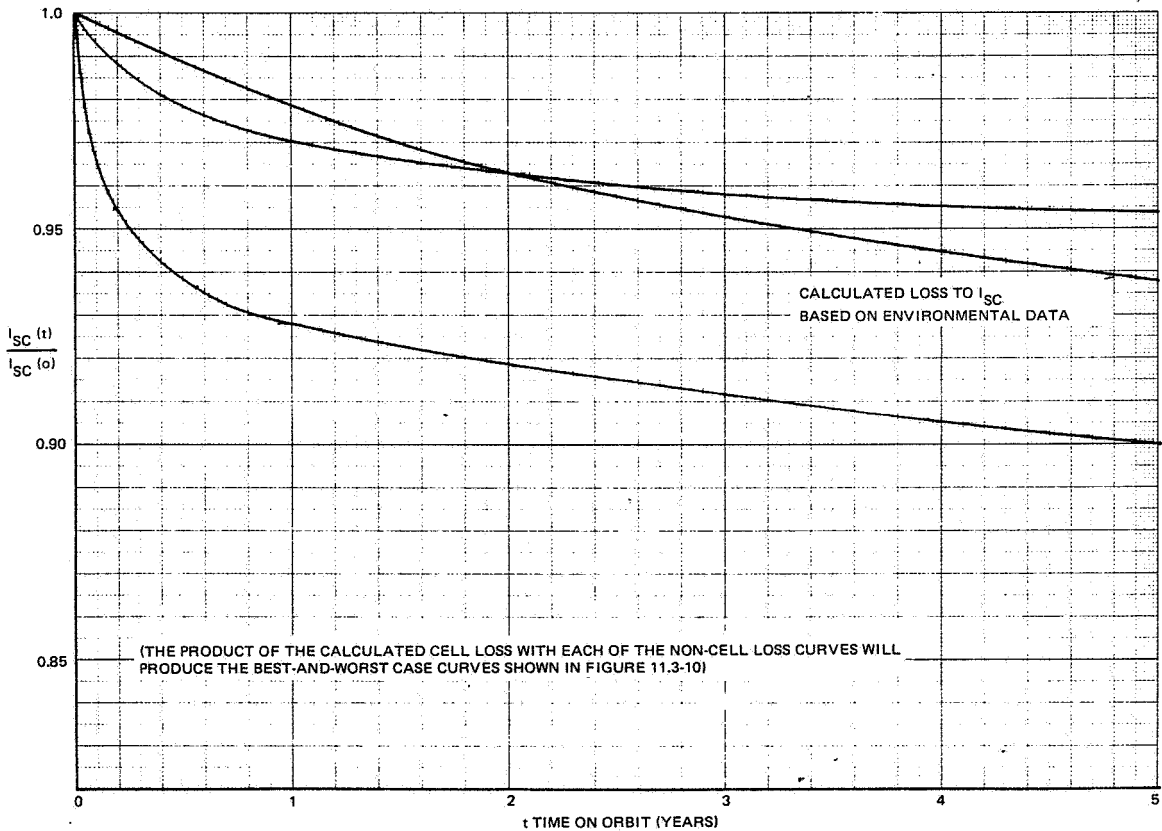


Fig. 11.13-12. Estimated Non-cell Losses and Calculated Cell Short-Circuit Current Loss Projected to 5 Years

11.13.7 OGO (Orbiting Geophysical Observatory)*

Of the six OGO spacecraft that were built, only the last four carried n-on-p solar cells on their arrays. These cells were 2 x 1 cm in size, 0.63-mm thick and covered with 0.15-mm thick microsheet covers. The blue-reflective filters had a 0.435- μ m cut-on wavelength and were bonded with RTV 602 on two arrays for which flight data was obtained. The arrays were flat, one-axis oriented toward the sun. The total number of solar eclipses was less than 100 during their operational periods shown herein. OGO array performance and their respective orbital parameters are shown in Table 11.13-4.

Table 11.13-4. Orbital Parameters and Relative Power Output of Two OGO Solar Cell Arrays

Parameter	OGO-4 (OGO-D)	OGO-5 (OGO-E)
Launch	7-28-67	3-4-68
Inclination	86 degrees	31 degrees (54 degrees in 1971)
Perigee (km)	412 (383 in 1971)	292 (25,985 in 1971)
Apogee (km)	908 (615 in 1971)	146,758 (121,080 in 1971)
Relative Power Output	0.964 after 1.5 years	0.947 after 0.25 years
		0.915 after 0.5 year
		0.84 after 1.0 year
		0.78 after 2.0 years
		0.74 after 3.0 years

11.13.8 Intelsat I, II and III**

The solar cell arrays on the Intelsat I, II and III satellites are of a cylindrical configuration and operate at synchronous altitude. The mechanical characteristics of these arrays are as follows:

- Intelsat I (Early Bird)

Main Array	92 parallel strings of 60 cells in series
Charge Array	Each of two battery charge arrays has four parallel strings

* Based on Ref. 11.13-6

** Based on Refs. 11.13-9 and 11.13-10

Solar Cells	10 x 20 mm, 10 ohm-cm, n-on-p, SiO _x coated; Heliotek, electroless nickel bar contacts, solder dipped; rigid five-cell shingles
Covers	0.30-mm thick Corning 7940 fused silica
Cover Adhesive	General Electric LTV 602
• <u>Intelsat II (F-3)</u>	
Main Array	60 parallel strings; each string has three cells in parallel and 60 cells in series
Charge Array	Each of two battery charge arrays has 14 parallel strings of 60 cells in series
Solar Cells	10 x 20 mm, 10 ohm-cm, n-on-p, SiO _x coated; Heliotek, titanium-silver corner-dart contacts, 25 percent solder dipped, and 75 percent solderless.
Covers	0.30-mm thick Corning 7940 fused silica, not fully protecting the active cell area at the corner-dart contact side
Cover Adhesive	General Electric LTV 602
• <u>Intelsat II (F-4)</u>	
Main Array	34 parallel strings; each string has three cells in parallel and 60 cells in series
Charge Array	Each of two battery charge arrays has 22 parallel strings and 18 cells in series
Solar Cells	20 x 20 mm, 10 ohm-cm, n-on-p, SiO _x coated; Heliotek and Centralab, titanium-silver bar contacts with solder on the N-contacts and zone-soldered P-contacts
Covers	0.30-mm thick Corning 7940 fused silica, leaving unprotected solar cell bar gaps up to 0.4 mm in width
Cover Adhesive:	Dow Corning XR-6-3489

• Intelsat III

Array	80 parallel strings; each string has two cells in parallel and 67 cells in series
Solar Cells	20 x 20 mm, 10 ohm-cm, n-on-p, SiO _x coated; Centralab, titanium-silver bar contacts with solder on the N-contacts and zone-soldered P-contacts
Covers	0.30-mm thick Corning 7940 fused silica, under-sized
Cover Adhesive	Dow Corning XR-6-3489
Low Energy Proton Protection	Dow Corning 3140 Silicone Caulking

According to Ref. 11.13-9, all of the Intelsat I and II arrays degraded at a slightly greater rate than was expected from penetrating charged particle radiation considerations. Low energy proton degradation (see Section 3.3.3) was presumed for Intelsat I and Intelsat II F-3 and F-4 in addition to a possible solar cell contact deterioration on F-4 due to either or both humidity effects on the solderless Ti-Ag contacts and/or thermal stresses on the cell interconnectors (silver mesh) arising from an epoxy cell-to-substrate adhesive.

On F-4, a damage reversal was noted that is similar to that observed in laboratory low-energy proton testing (see Ref. 11.13-11).

No anomalous degradations were observed on the Intelsat III solar cell arrays; their performance is shown in Figure 11.13-13. The arrays provided a greater power output than predicted after 1 year because the actual solar flare proton environment was not as large as assumed for the performance prediction. For comparison, the relative performance of all Intelsat arrays is shown in Table 11.13-5.

11.13.9 LES-6

The sixth Lincoln Laboratory Experimental Satellite (LES-6) was launched into a synchronous orbit on 26 September 1968. Through 1975, I-V characteristics were measured on 30 experimental solar cells including the following types:

- Silicon, n-on-p, SiO_x coated, Corning 7940 covered, manufactured by Texas Instruments.
- Lithium-doped silicon, p-on-n, CeO₂ and SiO coated, Corning 7940 covered, manufactured by Texas Instruments.
- Dendritic and dendritic drift field silicon, n-on-p, Corning 7940 covered, manufactured by Westinghouse.
- Ion implanted silicon, n-on-p, pure quartz covered, manufactured by Ion Physics.
- CdS thin film solar cells, manufactured by Clevite.
- CdTe thin film solar cells, manufactured by General Electric.

From Ref. 11.13-10. Reprinted with permission of the American Chemical Society.

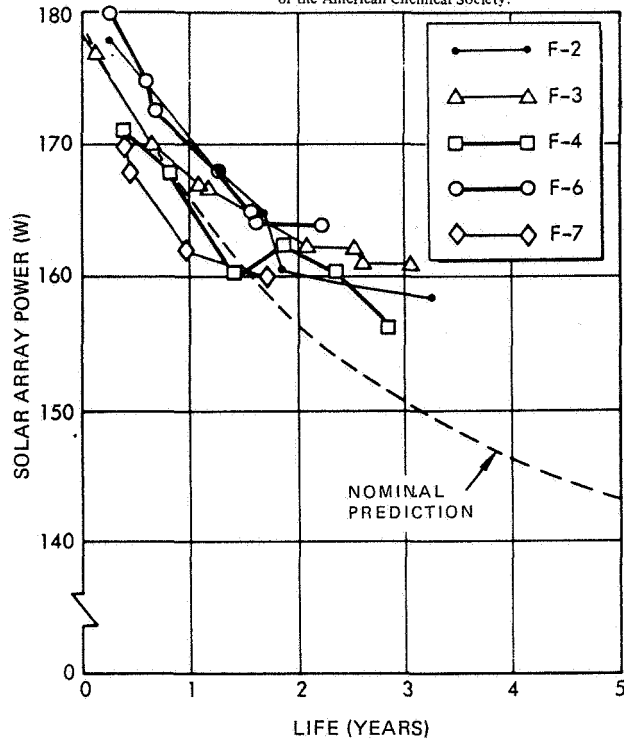


Figure 11.13-13. INTELSAT III Solar Cell Array Power Output Variation with Time in Orbit (Ref. 11.13-10)

None of these solar cells are currently available from these manufacturers and further research and development on these cell types has been in progress for many years. For this reason, none of the flight data is reproduced here. The flight experiment is described in Ref. 11.13-12, while the flight data is contained in Refs. 11.13-13 through 11.13-15. The significant conclusions from this flight experiment are:

- Silicon solar cells that are not fully covered were subject to low energy proton damage of 8 to 12 percent magnitude (see Section 3.3.3). The low energy proton damage effect saturated after 150 to 200 days in orbit.

Table 11.13-5. Relative Performance of Eight Intelsat Solar Cell Arrays

Intelsat Satellite and Flight	After Given Time in Orbit (years)				
	0.35	1	2	3	4
I	0.905	-	0.85	-	0.79
II F-3	-	-	0.82	-	-
II F-4	-	0.87	0.81	-	-
III F-2	-	0.94	0.89	0.88	-
III F-3	-	0.93	0.90	0.89	-
III F-4	-	0.92	0.90	0.86	-
III F-6	-	0.94	0.91	-	-
III F-7	-	0.90	0.89	-	-

- Penetrating radiation damage to solar cells was about 3.5 percent per year for the first 3 years plus 1.75 percent per year for the next 3 years plus an additional 4 to 10 percent initial degradation on coverslide darkening. These initial degradation estimates are based not only on these experiments but also on investigations into ultraviolet and synergistic environmental effects on coverslides according to Ref. 11.13-17.
- Solar flare activity decreased the power output of fairly undegraded 10 ohm·cm cells with 0.15-mm thick covers by 0.85 percent per 10^{10} protons/cm²; power output of similar cells with 0.025-mm thick covers were decreased by 1.4 percent per 10^{10} protons/cm². Subsequent rates of degradation were substantially unaffected by the solar flare event. Presence or absence of small, uncovered active area strips had no noticeable effect on the degradation occurring from a solar flare.
- Damage by protons from a solar flare to lithium-doped p-n cells made from crucible grown material was observed to anneal in orbit within a 4-week period. (Array temperature was nominally 18°C and ranged from 15° to 28°C.)

11.13.10 ATS-5*

The ATS-5 satellite was launched into synchronous orbit on 12 August 1969 and carried a solar cell flight experiment. The experiment consisted of 65 solar cells whose I-V curves could be measured. Some of the cells were mounted on a rigid honeycomb substrate and others on a flexible Kapton/glass cloth film substrate that was exposed to radiation from both sides. The solar cells were mainly production type, conventional silicon cells covered with Corning 7940 fused silica. Cover adhesive was RTV-602.

The satellite failed to achieve its intended gravity stabilized mode and, thereby, reduced the accuracy of the flight data. A large solar flare, 82 days after launch, caused significant solar cell degradation before a baseline output measurement could be made in orbit, causing an additional uncertainty in the orbital data. Failure of an on-board signal processor within the first month in orbit caused one-half of the solar cell data to be lost. For these reasons, the flight data are not reproduced here. However, the following conclusions can be drawn from the experiment:

- Covers of 0.15-mm and 0.30-mm thickness shielded the solar cells as predicted; however, cells with 1.52-mm thick covers degraded by 8 percent for a given 1-MeV fluence where the analysis had predicted only 1 percent degradation. (This finding is similar to that on ATS-1, Section 11.13-4.)
- Solar cells with small unprotected strips of active area are subject to low energy proton damage (see Section 3.3.3).
- Solar cells on the flexible panel degraded no faster than the cells on the rigid panel, showing that radiation incident on the rear surfaces of solar cells may not be a serious problem for two years in synchronous orbit.

* Based on Ref. 11.13-16

11.13.11 ATS-6†

The ATS-6 satellite was launched on 30 May 1974 into synchronous orbit and carried a solar cell flight experiment. I-V curves from 16 different solar cell/cover assembly configurations were obtained from the three-axis stabilized spacecraft. Sixty-five of the solar cells were mounted on a rigid, 6.3-mm thick aluminum honeycomb substrate and 15 of them were mounted on a flexible substrate. The flexible substrate consists of a 25-μm thick fiberglass cloth and a 25-μm thick Kapton sheet and receives space radiation from both sides. The following significant, tentative conclusions can be drawn:

- At the second day after launch, the solar cells exhibited significant deviations from what was expected from their prelaunch testing under a pulsed xenon solar simulator as follows:

I_{sc} -- 1 to 8 percent higher in orbit

V_{oc} -- 0 to 2 percent lower in orbit

P_{mp} -- 2 percent lower to 6 percent higher in orbit

Curve Factor -- softer in all cases in orbit

(The operating temperature in space is between 57° and 87°C; the prelaunch testing was performed at 25°C.)

- The non-cell losses (Corning 7940 fused silica cover and Sylgard 182 adhesive darkening) after 50 days in orbit averaged about 2 percent and may have ranged from 0 to 4 percent for both integral and adhesive-mounted covers.
- The presence or absence of antireflecting and ultraviolet reflecting filter coatings on the Corning 7940 fused silica covers did not seem to affect the optical transmission degradation (but they affected the initial glassed cell output).
- After 247 days (0.68 years) in orbit, the total degradation was:

I_{sc} -- 5.2 to 10.9 percent

V_{oc} -- 0.7 to 1.6 percent

P_{mp} -- 3.8 to 9.1 percent

(The inconsistency that the P_{mp} degradation is less than the combined I_{sc} and V_{oc} degradation is not explained.)

11.13.12 NTS-1 (Timation III)‡

The NTS-1 satellite was launched on 14 July 1974 into a nearly circular orbit having a perigee of 12,193 km, an apogee of 13,606 km, and an inclination of 125.1 degrees. The orbital period is 468.7 minutes. The orbital radiation environment is severe. A solar cell flight experiment carries conventional silicon Centralab and Heliotek cells, Centralab lithium-doped, Comsat violet, and Ferranti float-zone solar cells. Solar cell covers include Corning 7940 fused silica, Pilkington-Perkin Elmer ceria-doped microsheet, and integral Corning 7070 glass. Solar

† Based on Ref. 11.13-18

‡ Based on Ref. 11.13-19

cells are connected into modules consisting mostly of strings of 5, 23, 47, or 48 cells in series. Therefore, the resulting data tends to be dominated by the lowest output or most severely degrading cell in each string. Cell degradation rates were compared to calculated rates based on charged particle damage to the cells only (i.e., the optical losses were not separated out). Ref. 11.13-19 concluded the following from the experiment:

- After 9 days in orbit, the "initial" orbital data indicates the following relative to laboratory measurements with solar simulators:

I_{sc} -- 0 to 14 percent higher in orbit
V_{oc} -- 0 to 3 percent lower in orbit
P_{mp} -- 2 percent lower to 12 percent higher in orbit

- After 261 days (0.72 years) in orbit, the total (optical and cell) degradation relative to the performance on the ninth day ranged from 15 to 25 percent.
- Damage annealing of the lithium-doped cells was observed at cell temperatures of 60°C. No annealing was observed at temperatures of 40°C or less.

11.14 SIGNIFICANCE OF TEST DATA, UNCERTAINTIES AND ERRORS

Any test data, no matter how carefully obtained, is subject to (a) being not absolutely correct (or true), and (b) coming out slightly different in a repeat test. The science of statistics can explain not only why this is to be expected, but also can quantize the amount of variation which can be expected.

11.14.1 Definitions*

For simplicity of illustration, let us measure the short-circuit current (I_{SC}) of a solar cell under an air-mass zero solar simulator. The I_{SC} being measured is called a variable. The recorded I_{SC} value from this test is called data. Assume further that, based on a light intensity measurement using a primary balloon standard solar cell (see Section 11.3), the light intensity was too low by 1 percent. Hence, the data is known to be in error by -1 percent and requires correction. After having corrected the data, the result is then reported in the test report. If this thusly measured solar cell is flown in space, its I_{SC} output will be the true output, denoted here by I_{SC}' . The value of the difference between the measured result of the I_{SC} and true I_{SC}' is the error of this single-sample experiment. However, prior to the space flight, the true I_{SC}' is not known so then we only speculate as to what I_{SC}' might be. We say that the measured result of I_{SC} has associated with it an uncertainty. Since the value of the uncertainty is what one thinks the error might be, uncertainty is based on an estimate or assessment by the experimenter of all the possible errors that might be associated with a specific experiment. The errors can fall into any of these categories:

- Accidental errors; such as a time lag in the solar simulator intensity stability control, or x-y recorder friction.
- Fixed errors; such as deviations in spectral distribution of the solar simulator from that of natural space sunlight.
- Mistakes; such as accidentally using a long-lead two-terminal connection to the solar cell under test instead of a four-terminal connection (see Section 11.2).

Ref. 11.14-1 presents a simple procedure for estimating the uncertainty of single-sample experiments as illustrated above which has been applied to solar cell array measurements by Ref. 11.14-2. Quoting from this reference:

* Adopted from Ref. 11.14-1 and in parts quoted from Ref. 11.14-2.

"An error frequency distribution function can be constructed to describe the errors if a large number of measurements of a variable can be made. Such error frequency functions are often non-Gaussian, but they almost always show that small errors are more likely than big ones, positive and negative errors are about equally probable, and there is no finite upper limit to the possible size of an error. In spite of this, design documents often specify maximum errors or uncertainties. Such numbers should be regarded as highly suspect. It is seldom possible to measure the uncertainty distributions of all the components contributing to the uncertainty of a variable, and another method of describing the uncertainty is required. One method of quoting the best estimate of the value of a variable and the associated measurement error is to give the mean m (arithmetic mean of observed values) and an uncertainty interval w based on specified odds, b . Thus, a variable might be quoted as

$$m \pm w \text{ (b to 1)}$$

which means that the observer is willing to wager odds of b to 1 that the true value lies between $m - w$ and $m + w$. The larger the w , the longer the odds one can safely wager. Expressed another way, this interval of width $2w$ centered on m has a probability of $b/(b+1)$ of containing the true value of the variable.

"Let an observation R be the function of n independent variables

$$R = R(v_1, v_2, \dots, v_n) \quad (11.14-1)$$

If the variables v_i are normally distributed, with uncertainties w_i associated with each v_i , and all w_i have the same odds, then the uncertainty interval w_R for the result having the same odds is given by

$$w_R = \left[\left(\frac{\partial R}{\partial v_1} w_1 \right)^2 + \left(\frac{\partial R}{\partial v_2} w_2 \right)^2 + \dots + \left(\frac{\partial R}{\partial v_n} w_n \right)^2 \right]^{1/2} \quad (11.14-2)$$

This equation gives results that are very nearly correct even when used with uncertainty distribution functions that are grossly nonnormal (e.g., 15 percent error for a triangular distribution).

This is quite a remarkable result in that it holds for distributions which have uncertainty distributions with finite limits such as the triangular distribution. In view of the fact that uncertainty intervals for the variables are not usually known to better than 50 percent, the use of Eq. 11.14-2 is not unreasonable.

"To make use of the uncertainty interval based on odds as discussed by Kline and McClintock, we make use of the statistical confidence limit. Suppose we have a sample population distributed normally, whose true mean μ and true variance σ^2 are somehow known. If we draw a sample of size n at random from this population and calculate a mean \bar{x} from this sample, we can calculate a confidence interval which has a probability $(1 - \alpha)$ of containing the true sample mean. This interval is commonly called a $100(1 - \alpha)$ percent confidence interval. The bounds of the interval are given by

$$\bar{x} \pm Z_{\alpha/2} \left(\frac{\sigma}{\sqrt{n}} \right) \quad (11.14-3)$$

In gambling language, the odds are b to 1 that this interval contains the true mean μ ; b and α are related by $b = (1 - \alpha)/\alpha$. The α used here is a common notation symbol in statistics texts to describe confidence limits and is not to be confused with the α commonly used by photovoltaics engineers in describing the temperature coefficient of solar cell short circuit currents. $Z_{\alpha/2}$ is the value in the standard normal distribution such that the probability of a random deviation greater than $\pm Z_{\alpha/2}$ is α , i. e.

$$\int_{-\infty}^{-Z_{\alpha/2}} f(Z) dZ + \int_{Z_{\alpha/2}}^{\infty} f(Z) dZ = \frac{\alpha}{2} + \frac{\alpha}{2}$$

where

$$f(Z) = \frac{1}{\sqrt{2\pi}} e^{-\frac{Z^2}{2}} \quad \text{and} \quad Z = \frac{x - \mu}{\sigma}$$

"If we are using 95 percent confidence limits, $\alpha = 0.05$ and $Z_{\alpha/2} = 1.96$, and our interval is $\bar{x} \pm 1.96\sigma/\sqrt{n}$. This interval has odds of 19 to 1 for containing the real population mean μ .

"Suppose our samples are drawn from a population just like the one in the example above except that the variance is not known. In this event, which is the usual situation encountered in the real world, we typically estimate the variance with a value s^2 found from a random sample of size n as follows:

$$s^2 = \frac{1}{n-1} \sum_{i=1}^n (x_i - \bar{x})^2$$

or equivalently

$$s^2 = \frac{1}{n(n-1)} \left[n \sum_{i=1}^n x_i^2 - \left(\sum_{i=1}^n x_i \right)^2 \right] \quad (11.14-4)$$

It is most important to note that the factor of 1.96 used in the previous example will no longer insure 95 percent confidence limits. A bigger factor is needed because s^2 is only an approximation for σ^2 . In this case the $100(1 - \alpha)$ percent confidence limits are

$$x \pm \frac{\left(t_{\alpha/2, n-1} \right) s}{\sqrt{n}} \quad (11.14-5)$$

Here, $t_{\alpha/2, n-1}$ is the integral of the Student t distribution (from t to ∞) for $n - 1$ degrees of freedom. This distribution is tabulated in most statistics books. For $n = \infty$, $t_{0.025, \infty} = 1.96$, coinciding with our previous result for known variance, and suggesting that if we could draw an infinite sample size we could compute an accurate s . If we drew a sample of size 5, however, we would have $t_{0.025, 4} = 2.776$ as the multiplier of s/\sqrt{n} .

"One often hears the terms 1σ , 2σ , or 3σ levels or limits used in a rather cavalier fashion in conjunction with engineering data. The implication usually is taken that formula 11.14-3 can be used to set confidence limits. This is rarely the case, however, and Eq. 11.14-5 must be applied."

Further discussion of these points along with examples of their application can be found in Refs. 11.14-2 and 11.14-3.

In most experiments reported in the literature, however, uncertainty is typically taken as being identical to the probable error. The probable error is typically calculated by taking the square root of the sum of squares of the individual errors. The calculated probable errors found in different publications of test results usually differ from each other considerably because some experimenters include more sources of errors than others; the given individual errors due to similar apparatus and equipment are usually quite consistent with each other.

11.14.2 Actual Uncertainties

The total uncertainty (or probable error) for predicting solar cell array performance in space, based on ground testing of array subassemblies (solar panels, modules, or strings) and computer-aided extrapolations to space, is in most cases on the order of a few percent and usually well below 5 percent. Some observed values of uncertainty are shown in Table 11.14-1. The uncertainty increases as the complexity of shadow patterns and the angle of nonnormal incidence of sunlight increases.

Table 11.14-1. Typical Uncertainties in Predicted Array Performance

Project	Uncertainty or Difference from Prediction (%)	Ref.
JPL Statistical Prediction, Mariner	±3.8	11.14-2
General Electric, ERTS-1	2	11.14-3
TRW, Intelsat III	0 to 3	11.14-4
Hughes, Intelsat IV	1 to 2	11.14-5

11.14.3 Uncertainties in Inspection

Many solar cell array design and performance requirements and criteria are verified by inspection. Some examples of such inspections are concerned with the following:

- Cover alignment over solar cells
- Cracked and chipped solar cells and covers
- Adhesive voids and overflow
- Soldered joint quality
- Damaged interconnectors and wires.

Inspectors are inherently not capable of finding all existing defects, even after having received the proper training and orientation. Ref. 11.14-6 gives the following reasons for inspector error:

- Willful errors
 - a) Fraud and collusion
 - b) Falsification for the convenience or to the advantage of the inspector
 - c) Falsification due to management pressure and deadlines.
- Intermediate errors
 - a) Inspector bias (usually affects borderline cases)
 - b) Rounding off (related to readability of meter scales)
 - c) Overzealousness.
- Involuntary errors
 - a) Blunders (usually caused by others rather than the inspector)
 - b) Fatigue
 - c) Human imperfection.

The accuracy, A, of an inspector can be defined (Ref. 11.14-6) by the percentage of defects he can identify correctly:

$$A = \frac{d - k}{d - k + b} \quad (11.14-1)$$

where

- d = number of defects reported
- k = number of nondefective units rejected
- b = number of defects missed

The quantity (d - k) is the true number of defects found by the inspector and (d - k + b) is the true number of defects in the inspection lot.

Illustrative Example

Inspection lot: 10,000 cell stacks mounted to a solar cell panel

Number of cracked covers found: 92

Number of acceptable cracked covers: 2

Number of cracked covers not found: 10

From Eq. 11.14-1, the inspector's accuracy is

$$A = \frac{92 - 2}{92 - 2 + 10} = 90 \text{ percent}$$

In the usual case, the true number of defects, (d - k + b), is unknown because the number of defects missed, b, is unknown. Under the assumption of k = 0, an estimate of the total number of defects, denoted by \hat{N} , can be made from

$$\hat{N} = d/A$$

where d and A are as previously defined.

In the above example,

$$\hat{N} = 92/0.90 = 102$$

and b = 102 - 92 = 10 defects were missed. During a second inspection, either by the same or a different inspector, b₂ = b₁ · A₂ defects would be discovered (under the assumption that the defective covers are marked or recorded). In the above example, if A₂ = 0.90 also, b₂ = 10 × 0.90 = 9 defective cells would be discovered in addition, or 92 + 9 = 101 defectives in both inspections together.

If an environmental exposure had been performed between these two inspections, the additionally discovered nine defective covers would not have been due to the environmental exposure.

In actual industrial settings, inspector accuracies are highly dependent upon the nature of the defects, ease of inspectability, clarity of the definitions of fail/pass criteria, available inspection tools (lighting, etc.), personal comfort or discomfort during inspections, boredom, fatigue, motivation, schedule pressure, general working conditions, time of day (relating to daily alertness and productivity cycles), training and other factors. The actual accuracies for a given number of solar cell panel inspections can, therefore, be expected to be varying both from panel to panel and from one inspection to another inspection of the same panel.

Accuracies of inspectors of solar cell assemblies have not been found in the literature; however, they

can be expected to be similar to the accuracies found in other industries where they range from 50 percent to 100 percent with 80 percent to 90 percent occurring quite frequently.

Recommended Practice

The above discussion suggests the following practices:

- Inspect a solar cell panel prior to an environmental exposure at least twice
- Inspect a solar cell panel at least as many times prior to an environmental exposure as it will be inspected after the exposure.

REFERENCES (CHAPTER 11)

- 11.2-1 H. S. Rauschenbach, "A Discussion of Standard Solar Cells," TRW Internal Report, August 1965.
- 11.2-2 A. E. Mann, "Illumination for Measurements of Output Characteristics of Solar Cell Assemblies," Spectrolab, Div. of Textron Electronics, Inc., 1965.
- 11.2-3 AIEE Solar Simulator Specification.
- 11.2-4 F. S. Johnson, "The Solar Constant," Journal of Meteorology, vol. II, No. 6, pp. 431-439, December 1954.
- 11.2-5 H. S. Rauschenbach, "Understanding Solar Measurements," Hoffman Electronics, Inc., Application Notes, 1959.
- 11.2-6 Data Sheet for Spectrosun Model X-25 Solar Simulator, Spectrolab.
- 11.2-7 G. A. Work, "Pulsed Xenon Solar Simulator Description," TRW Systems Group.
- 11.2-8 "LAPSS-III Solar Simulator," TRW Systems Group Data Sheet.
- 11.2-9 M. Wolf and H. Rauschenbach, Series Resistance Effects on Solar Cell Measurements, Advanced Energy Conversion, vol. 3, Pergamon Press, pp. 455-479, 1963.
- 11.3-1 R. F. Greenwood and R. L. Mueller, "Results of the 1970 Balloon Flight Solar Cell Standardization Program," Technical Report 32-1575, Jet Propulsion Laboratory, December 1972.
- 11.3-2 K. W. Champion and H. L. Pond, "Model Atmospheres," Handbook of Geophysics, ch. 1, p. 10, ed. C. F. Campen, Jr., et al., The Macmillan Co., New York, 1960.
- 11.3-3 J. A. Zoutendyk, "Solar-Cell Power Systems Testing," Technical Report 32-350, Jet Propulsion Laboratory, Pasadena, California, December 1962.
- 11.3-4 R. F. Greenwood, "Solar Cell Modules Balloon Flight Standard, Calibration of," Procedure No. EP50443, Rev. A, Jet Propulsion Laboratory, Pasadena, California, February 1969.
- 11.3-5 The American Ephemeris and Nautical Almanac for the Year 1970, U.S. Government Printing Office, Washington, D. C., 1968.
- 11.4-1 R. Stair et al., "Some Developments in Improved Methods for the Measurement of the Spectral Irradiances of Solar Simulation," NASA CR-201, April 1965.
- 11.4-2 H. K. Gummel and F. W. Smits, "Evaluation of Solar Cells by Means of Spectral Analysis," The Bell System Technical Journal, vol. XLIII, No. 3, May 1964.
- 11.4-3 J. Mandelkorn et al., "Filter-Wheel Solar Simulator," NASA TN D-2562, NASA Lewis Research Center, Cleveland, Ohio, January 1965.
- 11.4-4 E. L. Ralph and M. Wolf, "Effect of Anti-reflection Coatings and Coverglasses on Silicon Solar Cell Performance," Heliotek, Division of Textron Electronics, Inc.
- 11.5-1 R. K. Yasui and P. A. Berman, Solar Cell Contact Pull Strength as a Function of Pull-Test Temperature," Technical Report 32-1563, Jet Propulsion Laboratory, Pasadena, California, August 1972.
- 11.5-2 R. K. Yasui and P. A. Berman, "Effects of High-Temperature, High-Humidity Environment on Silicon Solar Cell Contacts," Technical Report 32-1520, Jet Propulsion Laboratory, Pasadena, California, February 1971.
- 11.5-3 P. A. Berman and R. K. Yasui, "Effects of Storage Temperatures on Silicon Solar Cell Contacts," Technical Report 32-1541, Jet Propulsion Laboratory, Pasadena, California, October 1971.
- 11.6-1 E. R. G. Eckert and R. M. Drake, Jr., Heat and Transfer, 2nd Edition, McGraw-Hill Book Co., Inc., New York, 1959.
- 11.6-2 D. K. Edwards, et al., "Integrating Sphere for Imperfectly Diffuse Samples," Journal of the Optical Society of America, vol. 51, pp. 1279-88, 1961.
- 11.6-3 R. V. Dunkle et al., "Heated Cavity Reflector for Angular Reflectance Measurements," Progress in International Research on Thermodynamics and Transport Properties, American Society of Mechanical Engineers, pp. 541-567, 1962.
- 11.6-4 K. E. Nelson, E. E. Luedke, and J. T. Bevens, "A Device for the Rapid Measurement of Total Emittance," Journal of Spacecraft Rockets, vol. 3, pp. 758-760, 1966.
- 11.6-5 L. B. Fogdall and S. S. Cannaday, "Experimental In Situ Investigation of the Effects of Protons, Ultraviolet Radiation, and Temperature on Thermophysical Properties of Solar Cell Filters and Other Spacecraft Materials," Final Report for Jet Propulsion Laboratory Program HF 525908, February 1971.

- 11.6-6 N. J. Broadway, Radiation Effects Design Handbook, Sec. 2, "Thermal-Control Coatings," N71-32280, Battelle Memorial Institute, Columbus, Ohio, June 1971.
- 11.7-1 L. J. Goldhammer and A. E. Anspaugh, "Electron Spectrum Irradiations of Silicon Solar Cells," Proceedings of the 8th IEEE Photovoltaic Specialists Conference, pp. 201-208, 1970.
- 11.7-2 R. L. Statler, "One MeV Electron Damage in Silicon Solar Cells," Proceedings of the Intersociety Energy Conversion Engineering Conference, pp. 122-127.
- 11.7-3 R. L. Statler and B. J. Faraday, "Annealing of Electron Radiation Damage in Silicon Solar Cells," Action des Rayonnements sur Les Composants a Semiconducteurs, Journees d'Electronique (Toulouse, March 1967), pp. 1-5, 1968.
- 11.7-4 D. J. Curtin and A. Meulenberg, "Statistical Analysis of One MeV Electron Irradiation of Silicon Solar Cells," Proceedings of the 8th IEEE Photovoltaic Specialists Conference, pp. 193-200, 1970.
- 11.7-5 R. L. Crabb, "Photon Induced Degradation of Electron Irradiated Silicon Solar Cells," 9th IEEE Photovoltaic Specialists Conference Recording, pp. 329-330, 1972.
- 11.7-6 L. J. Goldhammer, "Irradiation of Solar Cell Candidates for the ATS-F Solar Cell Flight Experiment," Proceedings of the 9th IEEE Photovoltaic Specialists Conference, 1972.
- 11.7-7 J. Lindmayer and J. Allison, "An Improved Silicon Solar Cell - The Violet Cell," Proceedings of the 9th IEEE Photovoltaic Specialists Conference Recording, pp. 83-84, May 1972.
- 11.7-8 D. J. Curtin and R. W. Cool, "Qualification Testing of Laboratory Produced Violet Solar Cells," 10th IEEE Photovoltaic Specialists Conference Recording, pp. 139-151, 1973.
- 11.7-9 T. J. Faith and A. F. Obenschain, "Temperature, Illumination, and Fluence Dependence of Current and Voltage in Electron Irradiated Solar Cells," 10th IEEE Photovoltaic Specialists Conference Recording, pp. 384-392, 1973.
- 11.7-10 H. Fischer and W. Pschunder, "Investigation of Photon and Thermal Induced Changes in Silicon Solar Cells," Proceedings of the 10th IEEE Photovoltaic Specialists Conference, 1973.
- 11.7-11 W. Luft, "Radiation Effects on High Efficiency Solar Cells," Presented at the International Conference on Evaluation of the Space Environment on Materials, Toulouse, France, June 1974.
- 11.7-12 A. Meulenberg, Jr., J. F. Allison, R. A. Arndt, and J. G. Haynos, "Radiation Damage to the Comsat Non-Reflective Cell," Proceedings of the 11th IEEE Photovoltaic Specialists Conference, 1975.
- 11.7-13 G. A. Haynes and W. E. Ellis, "Effects of 22 MeV Proton and 2.4 MeV Electron Radiation on Boron- and Aluminum-Doped Silicon Solar Cells," NASA Technical Note D-4407, 1968.
- 11.7-14 R. L. Crabb, "Photon Induced Degradation of Electron and Proton Irradiated Silicon Solar Cells," Proceedings of the 10th IEEE Photovoltaic Specialists Conference, 1973.
- 11.7-15 J. Lindmayer and R. A. Arndt, "Effects of Radiation on the Violet Solar Cell," Proceedings of the 10th IEEE Photovoltaic Specialists Conference, 1973.
- 11.7-16 L. J. Goldhammer, "Particulate Irradiations of an Advanced Silicon Solar Cell," Proceedings of the 11th IEEE Photovoltaic Specialists Conference, 1975.
- 11.7-17 W. P. Rahilly, "Electron and Neutron Irradiation of Advanced Silicon Solar Cells," Proceedings of the 11th IEEE Photovoltaic Specialists Conference, 1975.
- 11.7-18 A. Meulenberg, Jr. and F. C. Treble, "Damage in Silicon Solar Cells from 2 to 155 MeV Protons," Proceedings of the 10th IEEE Photovoltaic Specialists Conference, 1973.
- 11.7-19 R. L. Statler, "Radiation Damage in Silicon Solar Cells from 4.6 MeV Proton Bombardment," Report No. 6333, Naval Research Lab, Washington, D. C., 1965.
- 11.7-20 B. E. Anspaugh and J. R. Carter, "Proton Irradiation of Conventional and Lithium Solar Cells: 11-37 MeV," Proceedings of the 10th IEEE Photovoltaic Specialists Conference, 1973.
- 11.7-21 R. G. Downing, "Low Energy Proton Degradation in Silicon Solar Cells," Proceedings of the 5th Photovoltaic Specialists Conference, vol. 2, p. D-7-1, 1965.
- 11.7-22 J. J. Wysocki et al., "Low Energy Proton Bombardment of GaAs and Si Solar Cells," IEEE Transcript of Electron Devices, vol. ED-13, pp. 420-426, 1966.
- 11.7-23 G. J. Brucker et al., "Low Energy Damage in Partially-Shielded Solar Cells," Proceedings of the IEEE (Letters), vol. 54, pp. 798-799, 1966.
- 11.7-24 "ATS Power Subsystem Radiation Effects Study," NAS 5-3823, SSD-80089R, Hughes Aircraft Company, February 1968.
- 11.7-25 "Low-Energy Proton Effects on IDCSP/A Solar Cells," FO4701-68-C-0200 (4135-01)-1, Aerospace Corporation, 1968.
- 11.7-26 E. Stofel and D. Joslin, "Low-Energy Proton Damage to Silicon Solar Cells," IEEE Transcript of Nuclear Science, vol. NS-17, pp. 250-255, 1970.
- 11.7-27 R. L. Statler and D. J. Curtin, "Radiation Damage in Silicon Solar Cells from Low-Energy Protons," IEEE Transcript of Electron Devices, vol. ED-18, pp. 412-417, 1971.

- 11.7-28 E. Stofel and D. Joslin, "Low-Energy Proton Irradiation of Solar Cell Back Contacts," Proceedings of the 8th Photovoltaic Specialists Conference, pp. 209-213, 1970.
- 11.7-29 A. E. Wallis and J. M. Green, "Damage to Recovery Characteristics of Neutron Irradiated Solar Cells," Proceedings of the 10th IEEE Photovoltaic Specialists Conference, 1973.
- 11.8-1 "Hanovia Compact Arc Lamps," Hanovia Lamp Division of Englehard Hanovia, Inc., Newark, New Jersey.
- 11.8-2 TRW Systems, previously unpublished data.
- 11.8-3 "High Brightness Mercury Arc Lamps Capillary Type A-H6 and B-H6 Application Data and Accessory Equipment," GET-1248H, General Electric, Hendersonville, North Carolina.
- 11.8-4 "The Electrodeless Lamp System," Ophthos Instrument Co., Rockville, Maryland.
- 11.8-5 Product Data Sheets, Acton Research Corporation, Acton, Massachusetts.
- 11.8-6 G. S. Goodelle, G. R. Brooks, and J. R. Mosher, "High Vacuum UV Test of Improved Efficiency Solar Cells," Proceedings of the 11th IEEE Photovoltaic Specialists Conference, 1975.
- 11.9-1 G. L. Brown, E. E. Luedke, R. L. Hammel, "Combined Environment Simulation Facility," TRW Systems Group.
- 11.9-2 D. K. Edwards et al., "Integrating Sphere for Imperfectly Diffuse Samples," Journal of the Optical Society of America, vol. 51, pp. 1279-1288, 1961.
- 11.9-3 W. D. Miller and E. E. Luedke, "In Situ Solar Absorptance Measurement, An Absolute Method," Effects of the Space Environment on Materials, vol. 11, Society of Aerospace Material and Process Engineers, 11th National Symposium and Exhibit, St. Louis, pp. 75-84, April 1967.
- 11.9-4 F. J. Campbell, "Status of Solar Cell Cover Material Radiation Damage," Proceedings of the 5th Photovoltaic Specialists Conference, pp. D-2.1-2-14, 1965.
- 11.9-5 L. B. Fogdall and S. S. Cannaday, "Ultraviolet and Electron Radiation Effects on Reflectance and Emittance Properties of Thermal Control Coatings," Final Report AFML-TR-70-156, July 1970.
- 11.9-6 L. B. Fogdall and S. S. Cannaday, "Proton and Electron Effects in Thermal Control Materials," Final Report for NASA-Goddard Contract NAS5-11219, May 1970.
- 11.9-7 L. B. Fogdall, S. S. Cannaday, F. D. Reinke, and B. K. Madaras, "Experimental Study of Effects of Simulated Neutralized Solar Wind on White-Pigment Thermal Control Coatings," NASA CR 73389, Final Report for NASA-Ames Contract NAS2-5343, October 1969.
- 11.9-8 L. B. Fogdall and S. S. Cannaday, "Experimental In Situ Investigation of the Effects of Protons, Ultraviolet Radiation, and Temperature on Thermophysical Properties of Solar Cell Filters and other Spacecraft Materials," Final Report for JPL Program HF 525908, February 1971.
- 11.9-9 L. B. Fogdall and S. S. Cannaday, "Space Radiation Effects of a Simulated Venus-Mercury Flyby on Solar Absorptance and Transmittance Properties of Solar Cells, Cover Glasses, and Adhesives, Presented at the AIAA 6th Thermophysics Conference, AIAA Paper 71-452, 1971.
- 11.9-10 L. B. Fogdall and S. S. Cannaday, "Experimental In Situ Investigation and Temperature on Thermophysical Properties of Solar Cell Filters and Other Spacecraft Materials," Final Report, JPL Program HF 525908, 1971.
- 11.9-11 N. J. Broadway, Radiation Effects Design Handbook, sec. 2, NASA CR-1786, p. 19, 1971.
- 11.9-12 R. A. Arndt, J. Bernard, and R. Reulet, "Effects of Simultaneous Ultraviolet, Electron, and Proton Irradiation of Silicon Solar Cells," Proceedings of the 11th IEEE Photovoltaic Specialists Conference, 1975.
- 11.11-1 B. Gorgens and E. G. Suppa, "Design of the IUE Solar Array," Proceedings of the 11th IEEE Photovoltaic Specialists Conference, 1975.
- 11.11-2 F. C. Trevel et al., "Comparative Deep Thermal Cycling of Solar Cell Panels," Proceedings of the 11th IEEE Photovoltaic Specialists Conference, 1975.
- 11.11-3 A. Smith et al., "Evaluation of Flight Acceptance Thermal Testing for the ATS-6 Solar Array," Proceedings of the 11th IEEE Photovoltaic Specialists Conference, 1975.
- 11.11-4 TRW Systems Group, previously unpublished material.
- 11.12-1 M. S. Imamura and P. Brandtzaeg, Martin Marietta Corporation; and J. L. Miller, NASA Marshall Space Flight Center, "Solar Cell Dark I-V Characteristics and Their Applications," Proceedings of ENERGY 70 Intersociety Energy Conversion Engineering Conference, 1970.
- 11.13-1 D. J. Curtin and R. L. Statler, "Review of Radiation Damage to Silicon Solar Cells," IEEE Transactions on Aerospace and Electronic Systems, vol. AES-11, No. 4, July 1975.
- 11.13-2 Based on data collected and provided by Jet Propulsion Laboratory.
- 11.13-3 R. C. Waddel, "Solar Cell Radiation Damage on Synchronous Satellites ATS-1," Proceedings of the 7th IEEE Photovoltaic Specialists Conference, pp. 195-205, 1968.

- 11.13-4 R. C. Waddel, "Radiation Damage Shielding of Solar Cells on a Synchronous Spacecraft," Proceedings of the 1968 Intersociety Energy Conversion Engineering Conference, vol. 1, pp. 122-137.
- 11.13-5 W. R. Baron, "The Solar Array for the Pioneer Deep Space Probe," TRW Systems, dated January 1967.
- 11.13-6 TRW Systems, previously unpublished data.
- 11.13-7 "Flight Data Analysis of Power Subsystem Degradation at Near Synchronous Altitude," Report No. WDL-TR4223, Philco-Ford Corporation, July 1970.
- 11.13-8 W. T. Picciano et al., "Solar Cell and Coverslide Degradations at Near Synchronous Altitudes," Proceedings of the 8th IEEE Photovoltaic Specialists Conference, pp. 221-225, 1970.
- 11.13-9 D. J. Curtin and J. F. Stockel, "Evaluation of the Performance of Solar Arrays in INTELSAT Spacecraft at Synchronous Altitude," Proceedings of the Intersociety Energy Conversion Engineering Conference, pp. 736-742, 1969.
- 11.13-10 W. H. Wright, "Design and Orbital Performance of the INTELSAT III Power System," Proceedings of the 7th Intersociety Energy Conversion Engineering Conference, 1972.
- 11.13-11 R. L. Statler and D. J. Curtin, "Low Energy Proton Damage in Silicon Solar Cells," Proceedings of the 7th IEEE Photovoltaic Specialists Conference, 1968.
- 11.13-12 F. W. Sarles, Jr., A. G. Stanley, and C. Burrowes, "Solar Cell Calibration Experiments on LES-6," Proceedings of the 7th IEEE Photovoltaic Specialists Conference, 1968.
- 11.13-13 F. W. Sarles, Jr., and A. G. Stanley, "Observed Degradation on the LES-6 Synchronous Solar Cell Experiment," Proceedings of the 8th IEEE Photovoltaic Specialists Conference, 1970.
- 11.13-14 F. W. Sarles, Jr., and A. G. Stanley, "Further Observed Degradation on the LES-6 Synchronous Solar Cell Experiment," Proceedings of the 9th IEEE Photovoltaic Specialists Conference, 1972.
- 11.13-15 F. W. Sarles, Jr., "The LES-6 Solar Cell Experiment After Six Years," Proceedings of the 11th IEEE Photovoltaic Specialists Conference, pp. 199-203, 1975.
- 11.13-16 B. E. Anspaugh, "ATS-5 Solar Cell Experiment After 699 Days in Synchronous Orbit," Proceedings of the 9th IEEE Photovoltaic Specialists Conference, 1972.
- 11.13-17 L. B. Fogdall and S. S. Cannaday, "Experimental In Situ Investigation of the Effects of Protons, Ultraviolet Radiation, and Temperature on Thermophysical Properties of Solar Cell Filters and Other Spacecraft Materials," Boeing Company, Final Report for JPL Program, HF 528908, February 1971.
- 11.13-18 L. J. Goldhammer and J. P. Corrigan, "Early Results of the ATS-6 Solar Cell Flight Experiment," Proceedings of the 11th IEEE Photovoltaic Specialists Conference, pp. 194-198, 1975.
- 11.13-19 R. L. Statler and D. H. Walker, "Solar Cell Experiments on the NTS-1 Satellite," Proceedings of the 11th IEEE Photovoltaic Specialists Conference, pp. 190-193, 1975.
- 11.14-1 S. J. Kline and F. A. McClintock, "Describing Uncertainties in Single-Sample Experiments," Mechanical Engineering, January 1953.
- 11.14-2 B. Anspaugh, "Uncertainties in Predicting Solar Panel Power Output," NASA T. M. 33-673, Jet Propulsion Laboratory, April 1974.
- 11.14-3 A. Kirpich et al., "Flight Performance of the ERTS-1 Spacecraft Power System," Proceedings of 1973 IEEE Power Electronics Specialists Conference.
- 11.14-4 TRW data obtained from COMSAT Corporation.
- 11.14-5 E. Levy, Jr., and F. S. Osugi, "Design and Performance of Intelsat IV Power Subsystem," Proceedings of the 7th Intersociety Energy Conversion Engineering Conference, 1972.
- 11.14-6 J. M. Juran et al., Quality Control Handbook, 2nd Edition, McGraw-Hill Book Company, 1962.

CHAPTER 12
DESIGN EXAMPLE

CONTENTS

	Page		Page
12.1 Conceptual Design	12.1-1	12.2.3 Determining the 1-MeV Fluence	12.2-2
12.1.1 Preliminary Requirements	12.1-1	12.2.4 Number of Cells in Series	12.2-2
12.1.2 First-cut Baseline Concept	12.1-1	12.2.5 Number of Cells in Parallel	12.2-3
12.1.3 Body-mounted Array Alternate	12.1-2	12.2.6 Array Layout	12.2-4
12.1.4 Paddle Array Alternate	12.1-3	12.2.7 Array Area and Mass	12.2-4
12.1.5 Conceptual Design Optimization	12.1-3	12.3 Final Design	12.3-1
12.2 Preliminary Design	12.2-1	12.3.1 Final Design Requirements	12.3-1
12.2.1 Updated Requirements	12.2-1	12.3.2 Design Update	12.3-1
12.2.2 Finding the Shielding Thickness	12.2-1	12.3.3 Operating Temperature Update	12.3-1
		12.3.4 Layout Update	12.3-2
		12.3.5 Array Output Prediction	12.3-2

TABLES

12.2-1(a) Tabulation of 1-MeV Fluence Components for 0.15-mm Covers	12.2-2	12.2-1(b) Tabulation of 1-MeV Fluence Components for 0.30-mm Covers	12.2-2
---	--------	---	--------

CHAPTER 12

DESIGN EXAMPLE

In this chapter the design of a hypothetical solar cell array is described for the purpose of illustrating the following:

- Use of this handbook
- General evolution of an array design that covers all design phases from mission conception to flight acceptance of hardware.

The hypothetical array described herein is actually based on the material from several different spacecraft projects that have been completed successfully at TRW. This material has been generalized, unified, and simplified to permit presentation of the essentials of the design process without becoming involved in project- and company-peculiar constraints and practices.

12.1 CONCEPTUAL DESIGN

The conceptual design phase is concerned with developing a spacecraft/solar cell array concept for an envisioned mission. Frequently, the conceptual design phase, also known as spacecraft definition phase, is carried out as a separate study effort prior to the start of the actual project-related design phase.

12.1.1 Preliminary Requirements

From the project manager, or from the systems or from the subsystems analyst, the following preliminary requirements are presumed to be available:

- Mission—communication equipment to be earth-pointing
- Orbit—geosynchronous equatorial
- Power level—1500 watts at EOM
- End-of-mission (EOM)—5 years
- Bus voltage—30 volts
- Mass constraint—100 kg
- Array configuration—to be determined
- Maximum permissible diameter inside shroud—2.70 meters (108 inches).

12.1.2 First-cut Baseline Concept

For simplicity, let the baseline conceptual array be a fully oriented flat panel. Following the Sizing Procedure in Section 8.6.1*, Step (a), we select a combination of solar cell, cover, and substrate as follows:

- Solar cell—conventional, 0.30 mm (12 mil) thick, 2 x 2 cm size
- Cover—fused silica, 0.15 mm (6 mil) thick
- Substrate—aluminum-faced honeycomb core panel.

The above selection is arbitrary; any other selection could have been made. In any case, other selections will be made at a later time to optimize the design with respect to any of the optimization criteria given in Section 8.2.3 (or others), after the first-cut array baseline concept has been evaluated.

* Unless otherwise stated, all Section and Equation numbers refer to Volume I.

Continuing to follow the Sizing Procedure in Section 8.6.1, in Step (b), we determine the design factors in Eq. 8.6-1 as follows:

P_o — From Figure 3.1-3 in Volume II we find for conventional, glassed cells of 20 x 20 x 0.30 mm size, with 10 ohm · cm base resistivity at 25°C, that $P_{mp} = 58$ mW. The corresponding cell efficiency is

$$\eta = P_{out}/P_{in} = 58/(2 \times 2 \times 135.3) = 0.107$$

or 10.7 percent where the value of the solar constant (135.3 mW/cm²) was obtained from Section 2.4.2.

S' — For Eq. 9.4-5 we find the values of the various parameters as follows:

$$(S/D^2) = S_{ss}/S_{mean} = 130.9/135.3 = 0.967$$

for the lowest illumination level near summer solstice, where the values of the solar constant at summer solstice, S_{ss} , and for the annual mean, S_{mean} , were taken from Section 2.4.2.

$F_T = 1.00 - 0.10 = 0.90$ from Section 11.13, Table 11.3-1 for non-cell (optical) losses.

$\Gamma = 0$ for normal incidence and $\cos \Gamma = 1.00$. Hence from Eq. 9.4-5,

$$S' = 0.967 \times 0.90 \times 1.00 \\ = 0.870 \text{ solar constants}$$

F_{RAD} — using the definition $F_{RAD} = 1 - PD/100$ and obtaining the worst-case percent degradation, PD, from Section 11.13.2, Table 11.13-1 (PD = 15 percent), we obtain

$$F_{RAD} = 1.00 - 0.15 = 0.85$$

$F_{T_{op}}$ — We first estimate the operating temperature, T_{op} from Eq. 9.6-16 in Section 9.6.4 and from Eq. 9.6-3 in Section 9.6.1. According to Section 8.6.1, we assume $F_p = 0.9$, $\eta_{op} = 0.05$ (note that $\eta \neq \eta_{op}$) and $\bar{\alpha}_s = \alpha_s$. From Section 7.14 of Volume II, Table 7.14-1, we find for fused silica covers $\alpha_s = 0.805$. Using Eq. 9.6-3,

$$\bar{\alpha}_{Se} = 0.805 - 0.9 \times 0.05 = 0.76$$

From Section 7.14 of Volume II, Table 7.14-1, we find $\epsilon_{HF} = 0.82$ for glassed cells and from Figures 7.14-5 and 7.14-6 of the same section we estimate $\epsilon_{HB} = 0.85$. Using Eq. 9.6-16, we obtain

$$T_{op} = \left(\frac{0.76}{0.82 \times 0.85} \frac{1353 \times 1.00}{5.67 \times 10^{-8}} \right)^{0.25} = 323^{\circ}\text{K}$$

$$= 50^{\circ}\text{C}$$

We now adjust the 25°C-cell data to 50°C according to Section 9.4.8, using only the voltage shift

$$\Delta v_2 = \beta_V(T_{op} - T_0) = -0.0021(50 - 25)$$

$$= -0.053 \text{ V}$$

The cell power output degrades to

$$P_{mpT_{op}} = P_{mpo} \frac{V_{mpo} + \Delta v_2}{V_{mpo}}$$

$$= 58 \frac{0.430 - 0.053}{0.430} = 50.85 \text{ mW}$$

or

$$P_{mpT_{op}} / P_{mpo} = (V_{mpo} + \Delta v_2) / V_{mpo} = F_{T_{op}}$$

$$F_{T_{op}} = (0.430 - 0.053) / 0.430 = 0.88$$

F_M — We assume arbitrarily a 5 percent design margin for unknown errors and degradation factors, so that $F_M = 0.95$

F_{SH} — We assume no shadows so that $F_{SH} = 1.00$

F_{BD} — We assumed earlier a flat, oriented array. Assuming the use of slip rings in the array orientation linkage, we may want to include the following voltage drops: $V_D = 0.8 \text{ V}$ and $V_W = 1.2 \text{ V}$. For a 30-volt bus, according to Eq. 8.6-2

$$F_{BD} = 1 - \frac{0.8 \times 1.2}{30 \times 0.8 \times 1.2} = 0.94$$

F_{CONF} — for a flat panel, $F_{CONF} = 1.00$.

F_C — Substituting the numerical values calculated above into Eq. 8.6-1, we obtain for the flat, oriented array

$$P_c = 58 \times 0.87 \times 0.85 \times 0.88 \times 0.95 \times 1.00$$

$$\times 0.94 \times 1.00 = 58 \times 0.58 = 33.7 \text{ mW}$$

Continuing with the Sizing Procedure of Section 8.6.1, Step (c), we determine the number of solar cells according to Eq. 8.6-3:

$$N_{flat} = 1500 / 33.7 \times 10^{-3} = 44,510$$

For calculating the substrate area (according to Eq. 8.6-4) we assume a packing factor, $P_c = 0.9$ for the flat array:

$$A_{flat} = 4 \times 10^{-4} \times 44510 / 0.9 = 19.8 \text{ m}^2$$

Now we check the array area for reasonableness. A flat plate array of 19.8 m² could be a square of about 4.5 meters (15 feet) length at each side, or it could be a two-wing array with each wing being nearly 2 m x 5 m (6.6 ft by 16.4 ft) in size. The power per unit area of this array is 1500/19.8 = 75.8 W/m². A comparable array, described in Section 6.2.4, providing 1.47 kW and being comprised of six panels of 2.82 m x 1.28 m in size, has a power per unit area of 1470/21.7 = 67.7 W/m², which is 11 percent lower than our design example. Hence, the flat panel array size of our conceptual design is reasonable.

Continuing with the Sizing Procedure in Section 8.6.1, Step (c), we find m from Section 6.2.4 to be 4.7 kg/m² for an array with 0.20-mm thick solar cells and 0.15-mm thick covers, including the deployment mechanism and central-axis boom.

Since we originally assumed 0.30-mm thick solar cells, we calculate the mass differential to be added to 0.20-mm cells from Section 7.3 of Volume II, Table 7.3-4, as follows:

For 0.10-mm difference in thickness, the mass difference for 2 x 2 cm cells is 0.194 - 0.107 = 0.087 g per cell or 0.087 x 44510 = 3,872 g or approximately 4 kg for the array.

According to Eq. 8.6-5 and adding the 4 kg from above, the array mass is

$$M = 4.7 \times 19.8 + 4 = 97 \text{ kg}$$

This is 3 kg below the preliminary mass limit of 100 kg, so that we conclude from the above analysis that a fully oriented array would most likely meet the specified requirements.

12.1.3 Body-mounted Array Alternate

For an earth-pointing payload, one of two general array configurations is feasible:

- One spacecraft axis points toward the earth, while the articulated, flat panel array points toward the sun (developed in Section 12.1.2).
- The axis of a spinning, body-fixed array coincides with the earth-pointing spacecraft axis, while the array is illuminated at constantly varying angles. The array configuration should be as similar to a spherical shell as possible, or be of the paddle-wheel type. Since the projected area of a sphere is $A_p = r^2\pi$ and the total area is $A_t = 4r^2\pi$,

$$F_{CONF} = A_p / A_t = 0.25$$

$$\text{and } 4A_{flat} = A_{sphere}$$

Returning to the Sizing Procedure of Section 8.6.1 and using the above relationships of the sphere, the number of solar cells is

$$N_{\text{sphere}} = 4N_{\text{flat}} = 178,040$$

Using $F_p = 0.75$, the spherical array area is

$$A_{\text{sphere}} = 4 \times 178040 / 0.75 = 95.0 \text{ m}^2$$

Solving the formula for the area of a sphere for its diameter d_s , we find

$$d_s = (A/\pi)^{0.5} = (95/\pi)^{0.5} = 5.5 \text{ m}$$

This is over twice the permissible array diameter of 2.7 m. Therefore, we synthesize the array, again as a first cut, to be a cylindrical shell of diameter d and height h , with flat solar cell panels having area A_a and A_b , respectively, covering the ends of the cylinder. The projected area of the total array, at any sun angle θ (using the definitions in Section 9.4.4), is

$$A_t = A_a \cos\theta + A_{\text{cyl}} \cos(\theta - \pi/2) + A_b \cos(\theta - \pi) \quad (12.1-1)$$

where the projected area of the cylinder, $A_{\text{cyl}} = dh$, and $A_a = A_b = d^2\pi/4$ with the tacit understanding that A_a or A_b is zero if the cosine of the angle is negative.

Combining symbols and simplifying the angles

$$A_t = \frac{d^2\pi}{4} \cos\theta + dh \sin\theta$$

Since $d_{\text{max}} = 2.7 \text{ m}$, we can write

$$A_t = 5.73 \cos\theta + 2.7 h \sin\theta \text{ m}^2$$

A_t should be about 19.8 m^2 average as θ sweeps from 0 through 360 degrees (or, because of symmetry, from 0 through 90 degrees).

Using the integral definition of the average, dropping the last term in Eq. 12.1-1 (for $0 \leq \theta \leq 90^\circ$) and noting that $\cos(\theta - \pi/2) = \sin\theta$, we find the average total projected area to be

$$\bar{A}_t = \frac{\int_0^{\pi/2} (A_a \cos\theta + dh \sin\theta) d\theta}{\int_0^{\pi/2} d\theta} = 2(A_a + dh)/\pi$$

Solving for h :

$$h = \left(\frac{\bar{A}_t \pi}{2} - A_a \right) / d = \left(\frac{19.8 \times 3.14}{2} - 5.73 \right) / 2.7 = 9.40 \text{ m} = 30.8 \text{ feet}$$

Since it is unlikely that such a long cylindrical array can be properly stabilized about the y -axis by the spacecraft attitude control system, this concept is not feasible.

A mass check is not made at this time because the array could be part of the spacecraft structure and, therefore, could have a greater mass than the allocated 100 kg.

12.1.4 Paddle Array Alternate

From Section 8.6.2; Figure 8.6-2, we find the average aspect ratio for a paddle array to range from approximately 0.20 to 0.35 for $0 \leq \phi \leq 80$ while θ sweeps from 0 to 360 degrees. Therefore, the number of solar cells required is about 3 to 5 times the number of cells required for a flat array. Since the substrates carry solar cells on both sides, the paddle array area is about 1.5 to 2.5 times the area required for a flat array. Recalling that the flat array just met the mass limit, a paddle array mass would be about 1.5 to 2.5 times as great and exceed the 100 kg limit by about 50 to 150 kg. Hence, the paddle array is not a viable alternate for this mission.

12.1.5 Conceptual Design Optimization

The foregoing discussions in Section 12.1.3 and 12.1.4 indicated that the flat panel array configuration was the optimum configuration for the intended mission. Further design optimization efforts that suggest themselves almost naturally are related to the choice of the solar cell type (EOM* efficiency), solar cell thickness (mass) and solar cell cover thickness (affecting both EOM* cell output and array mass).

Since the analysis given in Section 12.1.2 lacks sufficient resolution for such an optimization study, the analyses given in Sections 12.2.2 through 12.2.7 should be utilized instead.

* EOM = end of mission.

12.2 DETAILED DESIGN

A preliminary conceptual design was established in Section 12.1. In this section, greater design details are developed that would permit the preparation of engineering drawings and detailed specifications for parts procurement.

12.2.1 Updated Requirements

Let it be assumed that the overall spacecraft design has been evolved in parallel with the solar cell array design. Due to this activity, some of the requirements will have changed and others will have been added. Let us presume that the following requirements now exist:

- Orbit—geosynchronous equatorial
- Launch dates—1978 and 1983
- Power level—1470 watts EOM
- End-of-mission (EOM)—5 years
- Bus voltage—30 volts
- Mass constraint—100 kg
- Array configuration—flat, one axis sun tracking.
- Maximum envelope—2.7 m in stowed configuration.

12.2.2 Finding the Shielding Thickness

From the array structural designer we find (for example) that the substrate consists of 0.13-mm thick aluminum facesheets bonded to 16-mm thick aluminum honeycomb core (see Section 6.2.4). The solderless solar cells are insulated by a 0.10-mm thick epoxy-filled glass cloth. The substrate back side carries a 43- μ m thick layer of thermal control paint.

The solar cell covers are attached to the cells with a 0.1-mm thick layer of RTV R6-3489. For comparison and for a later design optimization decision, we study both (a) 0.15-mm (6 mil) and (b) 0.30-mm (12 mil) thick fused silica covers.

We determine the shield thicknesses, as described in Section 8.3.2, to be as follows, taking the material property values from the tables in Section 7.3 of Volume II:

Front Shield Thickness

Material	Density ($g \cdot cm^{-3}$)	Actual Thickness (mm)		Fused Silica-Equivalent Shielding Thickness (mm)	
		(a)	(b)	(a)	(b)
Fused silica	2.20	0.15	0.30	0.15	0.30
R6-3489	1.02	0.10	0.10	0.05	0.05
Total				0.20	0.35

Back Shield Thickness

Material	Density ($g \cdot cm^{-3}$)	Actual Thickness (mm)	Fused Silica-Equivalent Shielding Thickness (mm)
Thermal paint	1.55	0.043	0.03
Aluminum facesheet	2.70	0.13	0.16
Core adhesive	1.98	0.07	0.06
Aluminum core	0.026*	16	0.19
Core adhesive	1.98	0.07	0.06
Aluminum facesheet	2.70	0.13	0.16
Epoxy/glass	1.87	0.10	0.08
RTV 118	1.04	0.07	0.03
Total			0.77

* Based on the expanded honeycomb core density per unit area, usually listed in catalogs in units of kg/m^2 (lb/ft^2) for a specific core thickness (height) dimension.

12.2.3 Determining the 1-MeV Fluence

Following the Procedure given in Section 9.11.1, we enter the fused silica equivalent shield thicknesses from Section 12.2.2 in Table 9.11-1, reproduced here as Tables 12.2-1 (a) and 12.2-1 (b) for the two different cover thicknesses, respectively.

Table 12.2-1(a). Tabulation of 1-MeV Fluence Components for 0.15-mm Covers

ORBIT	PARTICLES	1-MeV FLUX $10^{13} \text{ (e} \cdot \text{cm}^{-2} \cdot \text{yr}^{-1})$		1-MeV FLUENCE $10^{13} \text{ (e} \cdot \text{cm}^{-2})$	
		FRONT	BACK	FRONT	BACK
TRANSFER 10.5 ORBITS	TRAPPED ELECTRONS				
	TRAPPED PROTONS				
	SUBTOTAL	1.1*	0.06*	11.6	0.6
ON-STATION 5 YEARS	TRAPPED ELECTRONS	3.1	1.1	15.5	5.5
	TRAPPED PROTONS	-	-	-	-
	FLARE PROTONS			23.0	7.0
	SUBTOTAL			38.5	12.5
OTHER					
	SUBTOTAL				
TOTAL	SUM VERTICALLY			50.1	13.1
GRAND TOTAL	FRONT + BACK			63.2	
SHIELD THICKNESS FRONT: 0.20 mm F. S. BACK: 0.77 mm F. S.		NOTES: 1. FOR THE SHIELDING EFFECT BY THE SOLAR CELLS, SEE SECTION 8.3.3. 2. FOR COMPUTING SHIELD THICKNESS, REFER TO SECTION 8.3.2. *Per Orbit			

Table 12.2-1(b). Tabulation of 1-MeV Fluence Components for 0.30-mm Covers

ORBIT	PARTICLES	1-MeV FLUX $10^{13} \text{ (e} \cdot \text{cm}^{-2} \cdot \text{yr}^{-1})$		1-MeV FLUENCE $10^{13} \text{ (e} \cdot \text{cm}^{-2})$	
		FRONT	BACK	FRONT	BACK
TRANSFER 10.5 ORBITS	TRAPPED ELECTRONS				
	TRAPPED PROTONS				
	SUBTOTAL	0.35*	0.06*	3.7	0.6
ON-STATION 5 YEARS	TRAPPED ELECTRONS	2.3	1.1	11.5	5.5
	TRAPPED PROTONS	-	-	-	-
	FLARE PROTONS			15.0	7.0
	SUBTOTAL			26.5	12.5
OTHER					
	SUBTOTAL				
TOTAL	SUM VERTICALLY			30.2	13.1
GRAND TOTAL	FRONT + BACK			43.3	
SHIELD THICKNESS FRONT: 0.35 mm F. S. BACK: 0.77 mm F. S.		NOTES: 1. FOR THE SHIELDING EFFECT BY THE SOLAR CELLS, SEE SECTION 8.3.3. 2. FOR COMPUTING SHIELD THICKNESS, REFER TO SECTION 8.3.2. *Per Orbit			

Continuing with the procedure given in Section 9.11.3, we find from Figure 9.11-1 the appropriate fluence components for P_{mp} and enter them into Tables 12.2-1 (a) and (b).

12.2.4 Number of Cells in Series

Following the procedure given in Section 8.7.1, we determine first the values of the parameters in Eq. 8.7-1:

$$V_B = 30.0 \text{ volts from Section 12.2.1 (a design constraint imposed by the energy storage battery)}$$

$$V_D = 0.8 \text{ volt at 0.5 ampere at } 50^\circ\text{C from a manufacturer's data sheet}$$

$$V_W = 1.3 \text{ volts, being composed of two voltage drops of 0.15 volt each across a pair of slip rings of the array orientation linkage and 0.5 volt in each wire between the array and the load. This data was obtained from the slip ring assembly specification and a worst-case estimate of 3 percent power loss in the cabling, respectively.}$$

Before the value of V_{mp} can be calculated, we must determine the values of the parameters in Eq. 8.7-2:

$$V_{mp\phi} = 0.400 \text{ V for } \phi = 6.3 \times 10^{14} \text{ 1-MeV e} \cdot \text{cm}^{-2} \text{ (0.15 mm covers)}$$

$$V_{mp\phi} = 0.410 \text{ V for } \phi = 4.3 \times 10^{14} \text{ 1-MeV e} \cdot \text{cm}^{-2} \text{ (0.30 mm covers)}$$

Both $V_{mp\phi}$ values were obtained by interpolating Figures 3.3-2 and 3.3-3 of Section 3.3 in Volume II, while the values of ϕ were taken from Tables 12.2-1(a) and (b).

$\Delta V_{S'}$ is determined according to Section 9.4. First we evaluate Eq. 9.4-5 for both summer solstice and equinox illumination conditions, assuming the same cover transmission degradation factor $F_T = 0.90$ determined in Section 12.1.2. For summer solstice,

$$S' = 0.9675 \times 0.90 \times \cos 23.44 = 0.80$$

where the angle of 23.44 degrees is given by the last equation in Section 9.10.6 (that section describes this specific array concept) and the value of $S/D^2 = 0.9675$ was taken from Section 2.4.2, Table 2.4-1. For equinox $S/D^2 = 1$ and $\cos \Gamma = 1$, so that $S' = 0.90$.

According to Section 9.4.7 with $a = 0.1$,

$$\Delta V_{S'} = 0.1 \log 0.80 = -0.010 \text{ for summer solstice, and}$$

$$\Delta V_{S'} = 0.1 \log 0.90 = -0.005 \text{ for equinox}$$

$$\beta_{Vp} = -2.1 \text{ mV}/^\circ\text{C from Section 3.6.2}$$

$$T_{op} = 50^\circ\text{C from Section 12.1.2 for equinox.}$$

For summer solstice, the solar heating is reduced due to both a greater solar distance and panel mis-orientation. According to Section 9.6.4, Eqs. 9.6-15 and 9.6-16, we can write

$$T_{op} = T_{opo} (S' \cos \Gamma)^{1/4}$$

where T_{op0} is the absolute operating temperature at one solar constant intensity and normal angle-of-incidence. Substituting numbers,

$$T_{op} = 323(0.9675 \times \cos 23.44)^{1/4}$$

$$= 314^{\circ}\text{K} = 41^{\circ}\text{C}.$$

$T_o = 25^{\circ}\text{C}$ from Section 3.3 of Volume II for the cell data selected.

We now evaluate Eq. 8.7-2 for equinox:

$$V_{mp} = 0.400 - 0.005 - 0.0021(50-25)$$

$$= 0.343 \text{ V for } 0.15 \text{ mm covers}$$

and

$$V_{mp} = 0.410 - 0.005 - 0.0021(50 - 25)$$

$$= 0.353 \text{ V for } 0.30 \text{ mm covers}$$

and again for summer solstice:

$$V_{mp} = 0.400 - 0.010 - 0.0021(41 - 25)$$

$$= 0.356 \text{ V for } 0.15 \text{ mm covers}$$

and

$$V_{mp} = 0.410 - 0.010 - 0.0021(41 - 25)$$

$$= 0.366 \text{ V for } 0.30 \text{ mm covers}$$

Since the lowest V_{mp} occurs at equinox, the voltage-sizing of the array must be based on equinox conditions.

Returning now to Section 8.7.1, we evaluate Eq. 8.7-1:

$$N_S = \frac{30.0 + 0.8 + 1.3}{0.343} = 94 \text{ for } 0.15 \text{ mm covers}$$

and

$$N_S = \frac{30.0 + 0.8 + 1.3}{0.353} = 91 \text{ for } 0.30 \text{ mm covers}$$

where N_S is always rounded off to the next higher integer number.

12.2.5 Number of Cells in Parallel

Following the procedure given in Section 8.7.2, we first determine all the parameters of Eq. 8.7-5:

$$I_{mp\phi} = 0.117 \text{ A for } \phi = 6.3 \times 10^{14}$$

$$1\text{-MeV e}\cdot\text{cm}^{-2} \text{ (0.15 mm covers)}$$

$$I_{mp\phi} = 0.119 \text{ A for } \phi = 4.3 \times 10^{14}$$

$$1\text{-MeV e}\cdot\text{cm}^{-2} \text{ (0.30 mm covers)}$$

Both values were obtained by interpolating the P_{mp} graph of Figure 3.3-3 in Section 3.3 of Volume II, resulting in 48 mW and in 50 mW respectively, dividing these numbers by the respective $V_{mp\phi}$ values of Section 12.2.4, and applying an 0.975 glassing loss factor (obtained from Section 4.3.3, Table 4.3-2):

$$\frac{0.048 \times 0.975}{0.400} = 0.117$$

$$\frac{0.050 \times 0.975}{0.410} = 0.119$$

$$\beta_{I_p} = 1 \times 10^{-4} \text{ }^{\circ}\text{C}^{-1} \text{ from Section 3.6.2}$$

$$T_{op} = 50^{\circ}\text{C for equinox}$$

$$T_o = 25^{\circ}\text{C from Section 3.3 of Volume II for the given solar cell data}$$

$$S_i' = S' = 0.90 \text{ for equinox and } S' = 0.80 \text{ for summer solstice, from Section 12.2.4}$$

$$F_m = 0.95, \text{ selected to allow for uncertainties in the design yet to be resolved}$$

$$\overline{F}_{SH} = 0.95 \text{ at equinox and } 0.90 \text{ at summer solstice, estimated from a review of an overall spacecraft drawing and its intended orientation patterns which indicated (for example) approximately 5 or 10 percent, respectively, of the solar cell strings to be shadowed by a solid object. For each of the unshadowed strings (outside of the moving shadow), } \overline{F}_{SH} = 1. \text{ According to Section 9.3.2, Eq. 9.3-28, the average shadowing factor is}$$

$$\overline{F}_{SH} = \frac{\Sigma(\text{Number of Shadowed Strings})}{\text{Total Number of Strings}}$$

We are now ready to evaluate Eq. 8.7-5 (with $I_{mpi} = I_{mp}$) for equinox:

$$I_{mp} = 0.117 [1 + 0.0001(50 - 25)] \times 0.90 \times 0.95$$

$$\times 0.95 = 0.0953 \text{ A for } 0.15\text{-mm covers, and}$$

$$I_{mp} = 0.119 [1 + 0.0001(50 - 25)] \times 0.90 \times 0.95$$

$$\times 0.95 = 0.0969 \text{ A for } 0.30\text{-mm covers.}$$

For summer solstice we have

$$I_{mp} = 0.117 [1 + 0.0001(41 - 25)] \times 0.80 \times 0.95$$

$$\times 0.90 = 0.0802 \text{ A for } 0.15\text{-mm covers, and}$$

$$I_{mp} = 0.119 [1 + 0.0001(41 - 25)] \times 0.80 \times 0.95$$

$$\times 0.90 = 0.0815 \text{ A for } 0.30\text{-mm covers.}$$

Since the lowest P_{mp} occurs at summer solstice, the current-sizing of the array must be based on summer solstice conditions. (The winter solstice conditions are usually more favorable because the solar distance is less than 1 AU, causing a higher array output even though the array temperature also increases.)

We now evaluate Eq. 8.7-3 with $I_{mpav} = I_{mp}$ and $I_L = 1470/30.0 = 49.0\text{A}$ for 0.15-mm thick covers:

$$N_P = \frac{4.90}{0.0802} = 611 \text{ per array}$$

From the spacecraft structural designer we learn (for example) that the array is to consist of six equal-sized panels. For cost reasons, the project manager wishes all six panels to be of identical design and layout. Therefore, N_P must be divisible by 6. The next higher integer that is divisible by 6 is $N_P = 612$, with $N_p = 612/6 = 102$ cells in parallel per panel.

For 0.30-mm thick covers, the corresponding number of cells in parallel is

$$N_p = 606 \text{ per array or } N_p = 101 \text{ per panel.}$$

12.2.6 Array Layout

The number of cells and strings to be accommodated by each of the six substrate panels is as follows (N_S and N_p were determined in Sections 12.2.4 and 12.2.5, respectively):

	For 0.15-mm Covers	For 0.30-mm Covers
N_S	94	91
N_p	102	101
$N_p \cdot N_S$	9588	9191

We now refer to Section 8.7.3 and find that we need to have a solar cell interconnector system design before we can lay out the panel. The procedure given in Section 5.3, with the aid of the procedures given in Sections 5.2, 9.7 and 9.8, permits us to design the interconnectors. Let us assume we have determined the appropriate dimensions for Figure 8.7-1 as follows (whole numbers were chosen for illustration):

- C = 20 mm -- average solar cell width with overhanging cover per Section 8.3.6
- H = 1 mm -- average parallel-direction cell gap
- D = 20 mm -- average solar cell length with overhanging cover per Section 8.3.6
- G = 1 mm -- average series-direction cell gap
- E = 5 mm -- end contact bar width
- F = 1 mm -- average end contact/cell gap

Using the formulas given in Figure 8.7-1, a single string of solar cells with 0.15-mm thick covers has a mechanical length of

$$B = (94 \times 20) + (94 \times 1) + 1 + (2 \times 5) \\ = 1985 \text{ mm}$$

and a width of

$$C + H = 20 + 1 = 21 \text{ mm}$$

Hence, the absolute minimum panel area required for 0.15 mm thick covers is

$$N_p B(C + H) = 102 \times 1.985 \times 0.021 = 4.252 \text{ m}^2$$

A similar analysis for 0.30-mm thick covers shows

$$B = (91 \times 20) + (91 \times 1) + 1 \\ + (2 \times 5) = 1922 \text{ mm}$$

$$C + H = 20 + 1 + 21 \text{ mm}$$

$$N_p B(C + H) = 101 \times 1.922 \times 0.021 \\ = 4.077 \text{ m}^2$$

The difference in panel area is $4.252 - 4.077 = 0.175 \text{ m}^2$, or 1.050 m^2 for the entire array.

We now proceed to fit the solar cell strings onto the substrate area in such a fashion as to maximize the number of solar cells on the available area. Let us assume that we can indeed accomplish this so that we can continue with our design activity. Should we not be able to fit the strings onto the substrate area, we will have to enlarge the substrate area.

12.2.7 Array Area and Mass

Baseline Design

From Section 6.2.4, we find the array substrate mass with 0.20-mm thick cells and 0.15-mm thick covers to be 4.7 kg/m^2 . From Section 12.2.6, the minimum total area, A_t (6 times the panel area, rounded to the next highest tenth), and the corresponding masses, M_t are:

For 0.15 mm Covers	For 0.30 mm Covers
$A_t = 6 \times 4.252 = 25.6 \text{ m}^2$	$A_t' = 6 \times 4.077 = 24.5 \text{ m}^2$
$M_t = 4.7 \times 25.6 = 120 \text{ kg}$	$M_t' = 4.7 \times 24.5 = 115 \text{ kg}$

Mass Differences

From Section 7.3 of Volume II, Table 7.3-4, we calculate a mass difference per cell of 0.087 g between 0.20-mm and 0.30-mm thick 20 x 20 mm silicon solar cells.

From Section 7.3 of Volume II, Table 7.3-5, we calculate a mass difference per cover of 0.145 g between 0.15 and 0.30-mm thick fused silica covers for 20 x 20-mm solar cells.

For the two designs, the array mass differences are as follows:

For	0.15-mm Covers	0.30-mm Covers
Baseline	120 kg	115 kg
Number of Cells, $N = 6N_p N_S$	57528	55146
Cell Mass, 0.087 N/1000	5 kg	5 kg
Cover Mass, 0.145 N/1000	--	8 kg
Total Mass	125 kg	128 kg

Implications

At this point we note that the array design having the thicker covers is about 2 percent heavier but 4 percent smaller than the design with the thinner covers. However, each design exceeds the mass limit of 100 kg. Before redesigning the array, we challenge the given and allocated requirements, especially power output and the array mass. If we cannot get the requirements changed, we must redesign the array and repeat the design process described. Approaches open to us, and their potential impact on array performance, are as follows:

- Use of higher-efficiency solar cells with Ta_2O_5 coatings yielding up to 20 percent power gain at end-of-mission

- Use of thinner solar cells, sacrificing some beginning-of-mission output but usually no end-of-mission output
- Use of a lighter (lower mass) substrate. Note in Section 12.2.2 that the shielding by the substrate is unnecessarily high.

The repeating of the design process will lead to a more and more optimized array, at least with respect to some optimization criteria. In our example, we optimized first for cost (by selecting conventional solar cells), then for mass (by selecting 0.15-mm thick covers). As we optimize further for mass, we will have to pay cost penalties for higher-efficiency solar cells.

12.3 FINAL DESIGN

A detailed design was developed in Section 12.2. It is now necessary to verify by analysis and test that this design does indeed perform as intended. In this final design phase, the analyses are performed to the highest accuracy and the greatest detail possible or practical. While the final design phase typically culminates with the release of production drawings, assembly and test procedures, and design qualification, the discussion in this section will be limited to the major electrical design analyses.

12.3.1 Final Design Requirements

During the course of the design process, many design requirements, design criteria, design constraints, and interfaces will have changed. Also, the accuracy with which these requirements are known will have increased, and permissible deviations (tolerances) will have been established.

For the purpose of illustration, let us assume that the requirements given in Section 12.2.1 have not changed except as follows:

- The array mass limit has been increased from 100 to 135 kg.
- The array size is not to be decreased, but the actual load is only 1400 instead of 1470 watts.
- The array voltage is to be sized to accommodate a positive 5°C error in the prediction of the operating temperature.
- The 4 percent smaller array area due to 0.30-mm thick covers is to be implemented.

12.3.2 Design Update

The array design which comes closest to the updated requirements of Section 12.3.1 is restated here (from Sections 12.2.6 and 12.2.7) for convenience:

- Array: six equal-sized panels
- Panel: $N_G = 91$ cells
 $N_P = 101$ strings
 Mass = 21.3 kg
 Area = 4.077 m² minimum
- Solar Cells: conventional, SiO-coated, 20 x 20 x 0.30 mm
- Covers: 0.30-mm thick fused silica

The number of cells in series must now be increased to meet the 5°C temperature margin requirement. From Section 12.2.4 we obtain the data to re-evaluate Eq. 8.7-2 at 55°C (for 0.30-mm covers):

$$V_{mp} = 0.410 - 0.005 - 0.0021(55-25) \\ = 0.342 \text{ V}$$

From Eq. 8.7-1,

$$N_S = \frac{3.0 + 0.8 + 1.3}{0.342} = 94$$

The 5°C impact on N_P is negligible.

12.3.3 Operating Temperature Update

From Section 12.2.4 we know that the highest operating temperature occurs at equinox. For this condition we now refine the parameters for Eq. 9.6-3 and 9.6-16. The solar cell operating efficiency (see Section 3.2.5) is

$$\eta_{op} = \frac{P_{out}}{P_{in}} = \frac{P_L}{S \times A_c \times N_p \times N_s} \\ = \frac{1400}{0.1353 \times 4 \times 6 \times 101 \times 94} \\ \eta_{op} = 0.045$$

where A_c is the cell area in cm² and the solar constant, S , is in units of W/cm². Note that $\eta_{op} = 0.045$ is very close to our original estimate of 0.05.

The packing factor, F_p , is evaluated from the data of Section 12.3.2 as follows (A_S = substrate area in cm²):

$$F_p = \frac{A_c N_S N_P}{A_S} = \frac{4 \times 94 \times 101}{4.077 \times 10^4} = 0.93$$

which is also very close to our original estimate of 0.90, except that we have not yet provided for substrate area surrounding the solar cell patches. We will need such area for cable routing, fasteners, hinges, etc.

We now estimate $\bar{\alpha}_S$ to increase with time in orbit from the original 0.805 to 0.82 at end of mission, so that Eq. 9.6-3 yields

$$\bar{\alpha}_{Se} = 0.82 - (0.902 \times 0.045) = 0.78$$

Eq. 9.6-16 provides us with the actual operating temperature:

$$T_{op} = \left(\frac{0.78}{0.82 + 0.85} \frac{1353 \times 1}{5.67 \times 10^{-8}} \right)^{0.25}$$

$$= 325^{\circ}\text{K} = 52^{\circ}\text{C}$$

We note that the 5°C design margin was reduced to 3°C . We now have to decide whether to add more cells in series or to be content with a 3°C margin at equinox. At other seasons the temperature margin will be greater. Let us assume that a power subsystem performance analysis has shown that the 3°C margin is sufficient, so that we can proceed with our design activities.

12.3.4 Layout Update

We now accommodate the solar cell strings on the substrates and add additional substrate areas around the solar cells to provide for the location of

the wiring. This additional area should not be counted when the packing factor for a thermal analysis is calculated, but may be counted to evaluate the geometric area packing factor.

After final layout and wire routing, panel drawings are to be prepared and made available for a more accurate determination of the shadowing of solar cell strings (this is not illustrated in this example).

12.3.5 Array Output Prediction and Design Verification

First, the shadowed areas on shadowed solar cell strings must be determined as described in Section 9.5 and an appropriate "shadowing factor" be determined as described in Section 9.3.2.

Thereafter, a detailed computer-aided performance analysis is made according to the procedures given in Section 9.4. The results of some of the supportive analyses called out in Section 9.4 are available in Sections 12.2.2, 12.2.3, 12.3.2, 12.3.3, and 12.3.4.

Next, we compare the results of the array output predictions (array capability) with the design requirements. If this comparison is favorable, the electrical design can be considered complete. Also, if all other (mechanical, thermal, magnetic, etc.) designs have been completed satisfactorily (not illustrated in this example), a prototype or engineering model can be produced and tested to verify by test if our analytical predictions were correct.

INDEX*

A

A—factor, in solar cell equation, 9.2.1
Absorptance
 of heat, 7.14
 of light, 7.13
Acceleration
 in flight, 2.2
 in test, 11.1.3
Acceptance tests, 11.1.2
Acoustic emission, 10.7.15
Acoustic field
 launch, 2.2.5
 testing, 11.1
Acoustic signature, 10.7.16
Active solar cell area, 3.8.4
AC model (see also model)
 array, practical, 9.2.6
 solar cells, theoretical, 3.11.2
Adhesive
 conductive, 7.2.2
 electrical properties, 7.10
 general characteristics, 7.2.1
 mechanical properties, 7.7
 optical characteristics, 4.4.6, 7.13, (7.13)
 outgassing properties, 7.16
 thermal properties, 7.7
 transmission degradation, 7.13
Air mass
 definition of, 2.4.2
 effect on cell output, 2.4.2
Albedo
 definition, 2.4.5
 of planets, 2.3.1
Alpha particles, 2.5.1
Altitude, orbit, 2.6, 9.10.3
AM0—see air mass
AM1—see air mass
Analog circuits, networks, 9.6.6
Angle of incidence
 computing angle of, 9.4.4
 cosine deviation, 4.8
 in orbit, 9.10.6
Annealing
 metals—see specific metal listings
 radiation damage, 3.3.4
Anomaly, true orbital, 9.10.2
Antireflective coatings
 historical development, 1.2
 on solar cells, 4.3, 3.10.2
 on solar cell covers, 4.2
Antireflective filters—see filters
Aphelion
 defined, 9.10.1
 of planets, 2.6
Apoapsis, 9.10.1
Apogee, 9.10.1
AQL—see sampling plans

Arcing
 in air, 2.1.1
 in space, 2.3.3
Area, reduction in, 7.8, (7.8)
Array geometry—see geometry
Array sizing, 8.6.1
Array temperature
 eclipse, 9.6.5
 estimated, 8.5.3
 in space—see temperature
 operating, 9.6.4
AR coatings—see antireflective coatings
Ascending node, 9.10.4
Assembly losses, 9.4.3
Assembly processes—see processes
Assurance—see reliability, quality control
Asteroids, 2.3.1
Astronomical unit, value of, 2.3.1
Atmosphere, 2.1.1
Atmospheric attenuation of sunlight, 2.4.2, 11.3
AU—see astronomical unit

B

Back-wiring, for magnetic field cancellation, 8.10.4
Back surface field, in solar cells, 3.1.1
Balloon standards, 11.3
Base resistivity, 3.1.5
Base width, 3.1.3, 3.4
Bench test—see testing
Beta particles, 2.5.1
Bias, forward, reverse, defined, 9.1.1
Bit rate
 failures—see failure rates
 telemetry, errors due to, 11.13
Bipropellant plume effects, 2.3.5
Black solar cells—see solar cells
Blocking diodes, 5.5
Blue solar cells—see solar cells
Body-mounted arrays,
 described, 1.1, 8.1.3
 output of, 8.6.2
 temperature of, 8.5.3
Bonding—see processes
Bonding, radio-interference, 7.2.2
Breakdown voltage
 of air, 2.1.1
 of dielectrics, 7.10
 testing, 11.10
Bremsstrahlung, 2.5.1
Broken cells—see failures
Broken knee, I-V curve, 3.6.4
Browning—see discoloration
BSF cells—see solar cells
Bulk modulus, 7.5.1
Bulk resistivity—see resistivity

C

Cadmium sulfide solar cells—see solar cells
Calculation, array output, 9.4
Calibration
 equipment, 11.1.5
 frequency of standard solar cells (1.1.7), (1.1.8)
 solar cells, 11.3
 solar simulators, 11.2, 11.3

* All references are to sections. Numbers not in parentheses refer to Volume I; numbers in parentheses refer to Volume II.

Capability vs requirements, 8.1.5
 Cell spacing
 interconnector design related, 5.3.3
 panel layout related, 8.7.3
 Cell—see solar cells
 Center of mass, 7.4, (7.4)
 Centroids, 7.4, (7.4)
 Ceria-doped microsheet, 4.4, 7.2.7
 Characterization, solar cells—see solar cells
 Charged particles, degradation due to—see radiation
 radiation
 Charged particle radiation—see radiation
 Charging, electrostatic, 2.3.3
 Check list
 degradation factors, 9.4.3
 design criteria and requirements, 8.1.2
 interfaces, 8.1.6
 Chemical composition—see specific materials
 Circuit continuity testing, 11.1.3, 11.12
 Circuit elements
 combination of, 9.1.2
 I-V curves of, 9.1.2
 Cleanliness
 electromagnetic—see EMI
 electrostatic, 8.9
 magnetic, 8.10
 physical, 2.1.4, 8.1.2
 CNR solar cells—see solar cells
 Coatings
 conductive, 4.7
 on solar cells, 4.3
 on solar cell covers, 4.2
 on structures, 2.3.2
 thermal control, 7.14, (7.14), 8.5
 Coefficients of thermal expansion—see thermal expansion
 Cold work (see also specific metal listings).
 9.7.1
 Collection efficiency—see efficiency
 Combinations of environments—see environments
 Comets, 2.3.1
 Component procurement, 10.1, 10.2
 Component selection—see selection
 Component weights, (7.3)
 Composition, chemical—see specific materials
 Computer models
 mechanical stress, 9.7.5
 reliability, 9.9.4
 solar cells, 9.2.3, 9.2.4, 9.2.5
 thermal, 9.6.9
 Computer programs—see computer models
 COMSAT solar cells—see solar cells
 Concentrators, 3.5.3
 Condensation, 2.1.2, 2.3.5
 Conductive adhesive, 7.2.2-
 Conductivity
 dielectric, 7.10, (7.10)
 electrical, 7.9, (7.9)
 thermal, 7.12, (7.12)
 of busses, 8.7.4
 of interconnectors, 5.3.13
 Configuration
 effects on output—see geometry
 solar cell arrays, 1.1
 Connectors (also see interconnectors), 5.6
 Constants, table of, (7.2)
 Constant power load, 9.1.4
 Constraints (see also interfaces), 8.1, 8.2
 Construction, solar cell array, 6.1, 6.2
 Contacts
 grids, 3.9.1
 picture frames, 3.9.1
 pull strength tests, 3.9.5, 11.5
 solar cells, 1.2.3, 3.9
 strength, 3.9.5
 Ti-Ag, 2.1.2, 3.9.2
 Contamination
 chemical, 2.1.8
 deposits, 2.3.5
 dust, 2.1.4
 Conventional solar cells—see solar cells
 Convention
 I-V curve, 9.1.1
 solar cell and diode polarity and bias, 9.1.1
 solar cell equation and quadrant, 9.2
 Conversion efficiency—see efficiency
 Conversion factors, (7.1)
 Coordinates
 celestial sphere, 9.10.4
 earth magnetic field, 2.3.8, 2.5.1
 earth radiation fields, 2.5.2
 Coordinate system, spacecraft, array, 9.4.4, 9.10
 Corpuscular radiation—see radiation
 Corrosion
 of Ti-Ag contacts, 2.1.6
 relating to humidity, 2.1.2
 resistance—see specific materials
 Cosine, deviation from, 4.8
 Cosmetic defects—see defects
 Cosmic rays, 2.5.1
 Cost data, 10.1
 Coverglass—see cover
 Coverslides—see cover
 Cover
 adhesive—see adhesive
 cracking, 4.4.5, 10.6
 installation loss/gain factor
 integral, 4.5, 4.6
 protective handling, 2.1.7
 selection, 8.3, 8.4
 solar cell, 4.1
 specifications, 10.3.2
 spectral characteristics, 4.2
 transmission degradation
 due to radiation, 4.8.5
 due to UV, 4.8.4
 Criteria
 design, 8.1
 NASA Monographs, p. 2. R-5
 testing, pass-fail, 11.1.1
 workmanship, 8.1.7, 10.6
 Critical fluence, 3.3.1
 Crossover fluence, 3.1.5
 Current-voltage characteristics—see I-V curve
 Current dividers, 9.1.2
 Current limiting of cells in series—see hot spots
 Current sources, 9.1.2
 Curve factor, 3.2.7, 3.2.8
 Curve shifting, 9.4.2
 Cut-on wavelength, effects of, 8.4.1

D

 Damage-equivalent fluence, 3.3.2, 9.11
 Damage coefficients, 3.3.2
 Damage (see also junction shorting)
 charged particle—see radiation
 electrical, 3.6.3
 physical, 2.1.7
 solar cells—see radiation, humidity, etc.
 UV radiation, 2.4.3
 Darkening—see discoloration
 Dark-forward array characteristics, 9.3.3
 Dark-forward testing 11.12
 Data
 analysis, 11.14
 errors, 11.14, (1.1)
 handling, 11.1.5
 orbital, 11.13
 problems, 11.13.1, (1.2)
 quality of, (1.1)

Data (continued)
 recording, 11.1.5
 reduction, 11.14
 significance of, 11.14
 Date of launch, 2.5.4, 9.4.3
 DB—see decibel
 DC model—see model
 Deceleration, 2.2.2
 Decibel, 2.2.5
 Defects (see also failure)
 functional vs cosmetic, 8.1.2
 temperature cycling-induced, 5.2.2, 11.11
 visual and cosmetic, 10.1.6
 workmanship, 10.6
 Degradation factors, 9.4.3
 Degradation of solar cells in welding, 10.4.8
 Dendrites, 1.2.2
 Deni 1-MeV fluence—see radiation
 Density, 7.3.1, 7.5.1
 atmospheric vs altitude, 2.1.1
 of materials, 7.3, (7.3)
 Deployable arrays, 1.1.2, 6.2
 Deployment mechanism, 6.3, 6.4
 Deposits, 2.3.5
 Depressurization, 2.1.1
 Design constraints (see also interfaces), 8.1.8
 Design criteria—see criteria
 Design factors, 9.4.3
 Design interfaces, 8.1.4
 Design Margin
 Design practices—see specific environmental or design activity
 Design process—see processes
 Design verification tests, 11.1.2
 Development tests, 11.1.2
 Dielectrics, 7.10, (7.10)
 Diffusion
 in solar cell processing, 3.1.3
 of carriers, 3.11.1
 Dimensional analysis
 of cell stack, 8.3.6
 of layout, 8.7.3
 Dimethyl silicone, 7.2.1
 Diodes
 blocking, isolation, 5.1.8, 5.5.1, 5.5.2, 9.3.1
 bypass, shadowing, shunt, 5.1.9, 5.5.6, 5.5.7, 9.3.1, 9.3.2
 characteristics, 5.5.3
 equation convention, 9.2
 failures 5.5.2, 9.9
 installation practices, 5.5.5, 5.5.10
 loss, 9.4
 symbol, polarity, 9.1.1
 testing—see testing
 Discoloration
 of materials, 2.5.8
 of solar cell covers—see radiation effects
 Distribution losses, 9.3, 9.4.3
 Divoting, silicon—see silicon spalling
 Dose dependent degradation—see degradation factors
 Dose
 charged particles—see radiation dose
 UV radiation—see ultraviolet radiation
 Dosimetry, radiation, 11.7
 Double break, in I-V curve, 3.6.4
 Drawings, 10.1.1
 Drift field solar cells—see solar cells
 Ductility, 7.8
 During-test operating conditions, 11.1.3
 Dust, effects of, 2.1.4
 Dynamic impedance, solar cells—see AC model

E

Earth, parameters, 2.3.1
 Eccentricity of orbits, 9.10.2
 Eclipse
 duration in orbit, 2.6.2, 9.10.7
 temperature cycling—see temperature cycling
 temperature in, 9.6.5
 Efficiency
 areal—see packing factor
 calculated, 3.2.5
 changes in, due to solar cell design, 3.1.1
 collection, 3.10.3
 conversion, 3.2.5
 maximum, 3.2.5
 operating, 3.2.5
 optimum, 3.2.5
 ultimate, 3.2.6
 Einstein, unit of, 2.4.3
 Elastic limit, range, 7.5.1
 Elastic modulus—see modulus of elasticity
 Electrical arcing in atmosphere—see breakdown voltage
 Electrical performance models—see power output
 Electrical properties of dielectrics—see dielectrics
 Electrical tests—see testing
 Electromagnetic cleanliness—see EMI
 Electromagnetic radiation, 2.5.1
 Electromagnetic spectrum, 2.4.2, 2.4.3
 Electrons
 in solar cells as carriers, 3.11.1
 in space environment, 2.5.1
 Electron radiation—see radiation
 Electron, 1-MeV equivalence, 3.3.2
 Electrostatic charging, 2.3.3
 Electrostatic cleanliness, 8.9
 Elongation, 7.8, (7.8)
 Emissivity, 7.14, (7.14)
 Emittance, 7.14, (7.14)
 EMI (Electromagnetic interference), 2.3.3, 8.1.2
 Encounter
 meteoroid, 2.3.4
 planetary, 2.3.7
 Energy—see power, solar, etc.
 balance, 9.1.5, 9.6.1
 conversion efficiency—see efficiency
 electrons, protons—see radiation
 solar constant—see solar constant
 Entry, 2.2.2
 Environments, combined, 11.1.4, 11.9
 Environment
 geophysical, 2.1
 launch, 2.2
 micrometeoroids, 2.3.4
 radiation, 2.5
 Environment, space, 2.3
 Epoxy, 7.2.1
 Equilibrium temperature
 body/panel arrays, graph of 8.5.3
 eclipse, estimating of, 9.6.5
 operating, estimating of, 9.6.4
 Equipment
 calibration, 11.1.5
 testing—see testing
 Equipotential array, 8.9
 Equivalent sun hours—see ultraviolet radiation
 Equivalent 1-MeV fluence—see radiation
 Errors
 in inspection, 11.4.3
 of analysis, 11.14
 ESH—see ultraviolet radiation

European arrays, 1.1, 6.1
European solar cells—see solar cells

F

Fabrication processes—see processes
Fabrication process monitoring, 3.1.4, 11.1.2
Facilities—see Chapter 11
Factors—see specific listing
Failure (see also defects)
 definition for temperature cycling, 5.2.2
 definition of, 5.2.2
 effects of on cells in parallel, 8.7.2
 effect on array design, 8.7.6, 9.9.2
 in temperature cycling testing, 11.11
 modes and effects analysis, 5.2.2, 9.9.2
 modes in pull testing of soldered joints, 11.5
 modes in welding, 10.7, 1
 of connectors, 5.6.2
 of interconnectors, 5.2.2
 of solar cells, 8.7.6
 open circuit, 9.9.2
 protection against hot spots, 5.5.7
 protection against short-circuits, 5.5.2
 rates, 9.9.3
Fail-pass criteria in testing, 11.1.1
Far ultraviolet—see ultraviolet radiation
Fatigue
 analysis, 9.8
 failures—see failure
 life, of soldered and welded joints, 5.2.5
FEP Teflon, 7.2.4
Fill factor, 3.2.7, 3.2.8
Filters
 antireflecting, 4.2.1, 4.3.1
 blue-red, 4.4.2
 blue, 4.4.2
 impedance matching, 1.2.4, 4.3.1
 multilayer interference, 1.2.4, 4.2.1, 4.3.1
Filter cut-on wavelength, effects of, 8.4.1
Fingers, contact—see contacts
Finish—see surface finish
First quadrant I-V curve, 9.1.1
Flasher—see solar simulator
Flexible interconnectors, 5.2
Flexible shingles, 5.2
Flow diagram, array power output, 9.4.3
Fluence—see radiation
Flux—see radiation, solar constant, etc.
Footcandle meter, 11.2.2
Forming of metals—see specific materials
Form factor—see curve factor and fill factor
Forward bias, defined, 3.1.2, 9.1.1
Forward characteristics of solar cells, 3.1.2
Fourth quadrant I-V curve, 9.1.1
Four-point probe contacts, 11.2.4
Fracture (see also failure)
 brittle, 5.3.1, 7.5.1
 ductile, 7.5.1
Frequency vs wavelength
 of light, 2.4.3
 spectral response, 3.10.3
Fused silica, 4.4, 7.2.5, (4.2)
FUV—see ultraviolet radiation

G

G-units, forces—see acceleration
Gamma rays, 2.5.1
Gaps between cells—see cell spacing
Gas pressure
 atmosphere, 2.1.1
 in structural components, 2.1.1
 space, 2.3.2

Geomagnetic field, 2.3.8
Geometry
 Coordinate system, spacecraft, array, 9.4.1
 effects of on output, 8.6.2
Geophysical environment—see specific listings
Glassing loss/gain, 4.3.3
Glassing process—see processes
Glass transition, adhesive, (7.11)
Glass, mechanical properties, 7.6 (7.6)
Gravitational constant, 2.2.2, 2.3.6
Gravity
 gradient, 2.3.6
 of planets, 2.3.1
 vs altitude, 2.3.6
 zero, 2.3.6
Grid lines, fingers—see contacts

H

Handling of test data, 11.1.5, 11.14, (1.11), (1.2)
Hardness—see radiation resistance
Hard vacuum—see vacuum
Heat capacitance, 7.12, (7.12)
Heat conductivity, 7.12, (7.12)
Heat transfer by conduction, 7.12, 9.6.3
Heat transfer by radiation, 9.6.2
Heat, specific, 7.12, (7.12)
Hemispherical emittance, 7.14, (7.14), 9.6.1
High efficiency solar cells, 3.1.1, 3.2.6
High intensity effects, 3.5.3
High intensity solar cells, 3.5.3
High temperature effects, 3.6.1, 3.6.3
High vacuum—see vacuum
High voltage arrays, 8.8
Historical background
 cells and covers, 1.2
 design process, 1.3
 interconnector design, 5.2.3
 solar cell arrays, 1.1
 solar cell testing 11.2.1
 solar simulators, 11.2.1
 spacecraft launches, 1.1.1
Hi-pot test—see breakdown voltage
Hot spots
 cause of, 3.7.1
 cell heating, 9.1.5, 9.6
 circuit analysis, 9.1.6
 current limiting by cells, 9.3.1
 damage to solar cells, 8.7.3
 definition of, 9.1.6
 design considerations, 8.7.5
 minimizing effect of, 8.7.5, 9.1.6
 number of cells in parallel, 8.7.2
 number of cells in series, 8.7.1
 power dissipation in cell, 9.1.5
 substrate effect on, 8.7.5
Human engineering, 1.3.5
Humidity
 effects of on cell contacts, 2.1.6
 environment, 2.1.2
 test procedure, 11.1.3
Hybrid solar cells—see solar cells

I

I-V curve
 dark forward, 9.3.3, 11.12
 dark reverse, 3.7.2
 definition of, 3.2.2
 of circuit elements, 9.1.2
 photovoltaic output, 3.2.2, 11.2.2
 p-n junction, different types, 11.2.6
 quadrants, 9.1.1

I-V curve (continued)
 quadrant presentation in, 3.2.2
 reverse, 3.2.2, 3.7.2
 shifting of, 9.4.2
 I_{mp} , I_{op} , I_{sc} , defined, 3.2.2
 Ideal sources, in circuit analysis
 Illumination
 effects on cell output, 3.5
 instabilities in cell, due to, 3.3.5
 level of sun—see solar constant
 Impedance, solar cell, array—see AC model
 Imperfections, 8.1.2
 Inclination
 orbits of planets, 2.3.1
 orbits of satellites, 9.10.4
 Index of refraction
 matching of, 4.2.1
 table of values, 4.3.1
 Induction heating, 10.4.7
 Inertia, moment of, 7.4, (7.4)
 Infrared heating, soldering, 10.4.6
 Infrared
 affecting cell output, 11.2.2
 emission in welding, 10.7.13
 light sources, 10.4.6, 11.2.2
 microscope, 10.7.6
 scanning, 10.7.14
 solar cell response, 3.10.4
 Input data for array analysis, 9.4.3
 Insolation—see solar constant
 Inspection
 criteria, 8.1.2
 of joints, 10.7.5
 uncertainties in, 11.14
 visual defects, 10.1.6
 Instabilities
 of cell output, 3.3.5
 of cell reverse characteristics, 3.7
 of power system, 9.1.4
 Instrumentation—see testing
 Insulation testing, 11.10
 Insulators, cell-to-substrate, 6.2
 Integral solar cell covers—see covers
 Intensity
 correction with standard solar cells, 11.3
 of acoustic field—see acoustic field
 of radiation—see radiation
 of sunlight—see solar constant
 Interactions, plasma, 2.3.2
 Intercell spacing—see cell spacing
 Interconnectors
 design of, 5.3
 electrical resistance of, 5.3.13
 fatigue life of, 9.8
 soldering vs welding, 5.2.5
 Interconnects—see interconnectors
 Interfaces, check list, 8.1.4
 Interference filters—see filters
 Interplanetary trajectory, 9.10.1, 9.10.2, 9.11.5
 Invar, 7.1.4
 In-situ testing, 11.8, 11.9
 Ionizing radiation—see radiation

J

Johnson's solar spectrum, 9.4.2
 Jointing—see processes
 Junction characteristics—see I-V curves
 Junction depth, 3.1.1, 3.10.4
 Junction shorting
 by low energy protons, 3.3.3
 by reverse bias, 3.7.3
 in welding, 10.4.8
 Junction, p-on-n, n-on-p, 3.11.1

K

K6-A, K6-B solar cells—see solar cells
 Kapton, 7.2.3
 Kirchhoff's law
 in circuit analysis, 9.1.2
 in thermal analysis, 9.6.1
 Kovar, 7.1.2
 Krypton lamps, 11.8.2

L

Ladder networks, 9.1.2
 Lamps—see specific listings
 Large area arrays, 6.2.11
 Launch date, 2.5.3, 9.4.3
 Launch vehicle
 constraints, 2.2, 8.1
 environments, 2.2
 Launch, loads due to, 2.2
 Leakage resistance, 7.10
 Life test—see testing
 Life time
 minority carriers, 3.11.1
 instabilities in, 3.3.5
 of missions, 2.3.7
 wearout—see fatigue
 Lightweight array, 6.2
 Light level—see solar constant
 Light level, reduction in, 9.4.3
 Limit testing, 11.1.2
 Lithium-doped solar cells, 1.2.3, 3.1.7
 Load resistance, 9.1.1
 Load, solar cell array, 9.1.4
 Logic, computer program, 9.2.3
 Loop equations, 9.1.2
 Loss factors—see degradation factors
 Loss function (low energy protons), 3.3.3
 Loss in temperature cycling, 9.4.3, 11.11
 Low cost arrays—see cost data
 Low cost processes—see processes
 Low energy proton damage
 mechanism, 3.3.3
 prevention of, 8.3.5
 Low intensity effects, 3.6.4
 Low temperature effects
 on materials, 2.4.1
 on solar cell output, 3.6.4
 LTPD—see sampling plans
 Lubricants, 2.3.2, 6.4.3

M

Machining of materials—see specific materials
 Magnetic cleanliness, 8.10
 Magnetic materials, 7.15
 Magnetic moment cancellation, 8.10.4
 Magnetic properties, 7.15
 Magnetic torques, fields, 2.3.8, 8.10.1
 Malleability, 7.5.1
 Manufacturing procedures, 10.4, 10.5
 Mass loss—see outgassing
 Mass properties—see mass, moment of inertia, etc.
 Mass
 definition and units, 7.3
 of arrays, 6.2
 table of, for components, (7.3)
 thermal, 7.12
 Material properties—see specific properties or materials listing
 Material selection—see selection
 Maximum power point, 3.3.2
 Measurement
 balloon calibration, 11.3
 errors in, 11.2.7, (1.1)

Measurements (continued)
of series resistance, 11.2.7
techniques reviewed, 11.2.1, 11.2.2
with four-point contacts, 11.2.4
with solar simulators, 11.2.5
Mechanical design terminology—see also
Chapter 7, 9.7.1

Metals—see specific listings
Metal joining—see processes
Meteoroid damage, 2.3.4
Meteoroid environment, 2.3.4
Methyl-phenyl silicone; 7.2.1
Micrometeoroids, 2.3.4
Micrometeoroid damage, 2.3.4
Microsheet, 4.4, 7.2.6, (4.3)
ceria doped, 4.4, 7.2.7, (4.4)
Minority carriers, 3.11.1
Minority carrier lifetime—see lifetime
Mismatch losses, 9.3.1
Misorientation—see angle of incidence
Mission duration, 2.3.7

Model
array
array, dark, 9.3.3
array, illuminated, 9.3.1
array, partially shadowed, 9.3.2
array, shadowed—see shadowing
reliability, 9.9.4
solar cell, practical, 9.2
solar cell, theoretical, 3.11.1
structural—see stress
thermal—see temperature
thermoelastic—see stress or fatigue

Modules
descriptions of, 5.2
design, 5.2
fabrication, 10.4, 10.5

Modulus of elasticity
of metals, 7.5, (7.5)
of nonmetals, 7.7, (7.7)
of silicon and glass, 7.6, (7.6)
relative to copper, 7.5.1

Molybdenum, 7.1.4
Moment of inertia, 7.4, (7.4)
Multilayer interference filters—see filters

N

N-on-p junction—see junction, I-V curve,
polarity, etc.
NDT—see nondestructive testing
Networks—see also circuits
analogs, 9.6.6
response, 9.1.3
simplifications, 9.1.2
thermal, equivalent, 9.6.6
Node equations, 9.1.2
Nondestructive testing (NDT), 10.7
Norton's theorem, 9.1.2
Number of cells in parallel, 8.7.2
Number of cells in series (see also hot spots), 8.7.1

O

Occultation—see eclipse
Ohmic contacts—see contacts
Omnidirectional radiation, 2.5.4
Open-circuit voltage, 3.2.2
Operating conditions during test, 11.1.3
Operating points, 9.1.4, 11.2.2
Optical design, 8.4
Optimization of design, 8.2.2, 8.2.3
Optimum power point—see power output
Orbital characteristics of planets, 2.3.1

Orbital dynamics, 9.10
Orbital eclipse—see eclipse
Orbital inclination—see inclination
Orbital life time—see life time
Orbital mechanics, 9.10
Orbital performance—see power, fatigue,
failures, etc.
Orbital period, 2.3.7, 9.10.2
Orbital temperature—see temperature
Orbit
geosynchronous, 2.5.5
transfer, 9.11.4
Orientation error—see angle of incidence
Orientation mechanism, 6.4
Outdoor testing, 11.2.1
Outgassing
data for adhesives, (7.16)
effects of on materials, 2.3.2
mechanism, 2.3.2
recondensation of, 2.3.5
test methods, 7.16
Output loss in temperature cycling, 9.4.1, 11.11
Oversized coverslides, 8.3.6
Oversizing, array 9.4.3

P

P-on-n junction—see junction
Pmp, Pop, defined, 3.2.2
Packing density, 8.6.1
Packing factor, 8.6.1
Paddle arrays, angle of illumination, 9.4.4
Palladium passivated contact cells, 3.9, 11.5
Palladium, (7.5)
Paralleled cells, 8.7.2
Parallel-gap soldering, 10.4.4
Parallel-gap welding, 10.4.8
Parking orbit, 9.11.2
Particle radiation—see radiation
Pass-fail criteria in testing, 11.1.1
Peel tests, contacts, 11.5.1
Peg-tip soldering, 10.4.3
Performance
analysis—see chapter 9 table of contents
characterization, solar cells, 3.1
models—see power output
prediction—see power output
solar cell array (see also spec. parameters), 6.1
Periapsis, 9.10.1
Perigee, 9.10.1
Perihelion, 9.10.1
Photons in solar cells, 3.10.3, 3.11.1
Photon-induced damage to solar cells, 3.3.5
Photon energy, 2.4.2, 2.4.3
Physical characteristics—see also specific listings
cell interconnectors, 5.2
materials, (7.3)
planets, 2.3.1
solar cells, 3.8, 3.9
solar cell arrays, 6.2
solar cell covers, 4.1
Physical constants, (7.2)
PID—see process identification document
Planetary encounter—see encounter
Planetoids, 2.3.1
Planets, 2.3.1, 2.4.2
Plasma interactions with spacecraft, 2.3.3
Plasma, 2.3.3
Plastics, effects of space on—see specific environ.
Plastic range, 9.7.1
Plastic solar cell covers—see covers
Plating—see processes

Poisson's ratio
 defined, 7.5.1
 of metals, 7.1, (7.5)
 of non-metals, 7.2, (7.7)
 of silicon and glass, 7.2, (7.6)

Polarity
 conventions, 9.1.1
 diodes, solar cells, 9.1.1

Power density, acoustic field, 2.2.5

Power dissipation, 9.1.5

Power output vs voltage (P-V curve), 3.2.2

Power output
 analysis, 9.4
 curve shifting, 9.4.2
 estimate, 8.6.1
 input factors, 9.4.3
 maximum, 3.2.2
 optimum, 3.2.2
 prediction, 9.4
 under reverse bias, 9.1.5

Power quality, 8.6.2

Power requirements—see requirements

Power sources, ideal, 9.1.5

Power system analysis, 9.1.4

Pressure, radiation, 2.4.4

Prequalification tests, 11.1.2

Probability
 of micrometeoroid hits, 2.3.4
 of test errors, 11.14, (1.1)

Probable error, 11.14.1

Probe
 four-point, 11.2.4
 spacecraft, 1.1

Procedures, manufacturing, 10.4, 10.5

Processes
 adhesive bonding, 10.4.11
 assembly, 10.4
 bonding schedules, 10.4
 computational—see specific listing
 design, 1.3
 glassing, 10.3.3
 plating—see kovar, molybdenum, etc.
 solar cell fabrication, 3.1.4
 soldering, 10.4.2 thru 10.4.7
 thermocompression joining, 10.4.9
 ultrasonic joining, 10.4.10
 welding, 10.4.8

Process control, welding, 10.7.2, 10.7.3

Process identification document, 3.1.4

Process monitoring, 11.1.2, 3.1.4

Procurement
 of covers, 10.3
 of solar cells, 10.3
 specifications, 10.2

Production monitoring tests, 11.1.2

Program logic, power output analysis, 9.4

Propellant plume effects, 2.3.5

Protons, 2.5.1
 damage, 2.5.5, 3.3.1
 low energy, 3.3.3
 solar flare, 2.5.3
 trapped, 2.5.2

Pull tests, contacts, 11.5

Pulsed solar simulators—see solar simulator

Pyrheliometer, 11.2.1

Q

Qualification
 specification, 10.2.5
 testing, 11.1.2

Quality control
 problems in, 11.14
 required by design, 10.6.1
 specified, 10.2, 10.5
 unnecessary, 8.1.6, 8.1.7, 10.1
 workmanship, 8.1, 10.6.1

Quality of data, (1.1)
 Quartz iodine lamps, 10.4.6
 Quartz—see fused silica
 Quiescent point, 9.1.4

R

Radiation dose
 in cell, 8.3.3, 9.11
 in cover adhesive, 8.3.5, 9.11
 in cover, 8.3.5, 9.11
 in orbit, 8.3.1, 9.11
 in transfer orbit, 9.11

Radiation effects
 on covers, 2.5.8, 11.13.1, 11.9
 on materials, 2.5.8
 on plastics, 2.5.8, 2.5.9
 on solar cells, 2.5.8, 11.13

Radiation hardness, of solar cells, 3.3.1

Radiation (see also electrons, protons, UV, etc.)
 charged particle, 2.5
 damage annealing, 3.3.4
 DENI 1-MeV fluence, 3.3.2, 9.11
 ionizing, 2.5.8
 omnidirectional, 2.5.4
 pressure, 2.4.4
 resistance, 3.3.1
 shielding (front, rear), 8.3
 testing, 11.7
 tolerance, 3.3.1
 1 MeV damage equivalent fluence, 3.3.2, 9.11

Radiometric properties, 7.14

Radius of gyration, 7.4, (7.4)

Random cell failures—see failure

Reduction in area, 7.8, (7.8)

Reflectance
 bare cell, 4.3
 covered cell, 4.2
 thermophysical, 7.13, (7.13)

Refraction, 4.2.1, 4.3.1

Reliability
 analysis, 9.9
 design considerations, 8.7.6
 effect on array sizing, 9.4.3
 of inspection—see inspection
 tests, 11.1.2

Requirements vs capabilities, 8.1.5

Requirements
 check list, 8.1.2
 development of, 8.1
 in specification, 10.2, 10.5
 structural, 6.2
 temperature cycling, 5.3.1

Resistance soldering, 10.4.2

Resistance testing—see testing

Resistivity
 base, solar cells, 3.1.5
 bulk, semiconductor, 3.1.4
 effects of cell output, 3.1.5
 effects on radiation resistance, 3.1.5
 electrical, 7.9, 7.10, (7.9), (7.10)

Reverse bias, 9.1.1, 9.1.6

Reverse characteristics of solar cells, 3.7

Reentry, 2.2.2

Ripple—see power quality

Rollup arrays, 6.2

Roughness, surface—see surface finish

RTV, 7.2, 7.7, (7.7)

Rubber, silicone - see silicone

S

Sample size, 11.14, (1.1)

Sampling plans, 10.2.6

Sapphire, 4.4

Satellites
 man-made, history of, 1.1
 of planets, 2.3.1

Scavenging of silver, gold by solder, 7.1.8
Schottky Barrier, 1.2
Sculptured solar cells—see solar cells
Sealants—see adhesives
Seasonal variation of sunlight—see solar constant
Selection
 criteria, 8.1, 8.2
 of adhesive, 8.3, 8.4
 of array geometry, 8.6.2
 of covers, 8.3, 8.4
 of interconnectors, 5.3, 87.4
 of solar cells, 8.3, 8.6
 of substrate, 8.6
Sequence of curve shifting, 9.4.2
Sequence of tests, 11.1.4
Series-connected cells, current limiting, 8.7.1, 9.3.1
Series resistance
 definition of, 3.2.3
 distributed, lumped models, 9.2.1
 effects of on array output, 3.7
 effects of, 3.5.2
 measurement of, 11.2.7
Shadowed arrays, 9.3.2
Shadowing
 determination of patterns, 9.5
 effect on output, 9.3.2, 9.4
 hot spots, 9.1.5
Shadow diodes—see shunt diodes
Shadow factors, 9.3.2
Shape of array—see configuration or geometry
Shear modulus, 7.5.1, (7.5)
Shielding thickness, radiation, 8.3
Shock testing—see testing
Short-circuit current, definition, 3.2.2
Short-circuit testing—see testing
Shunt diodes
 analytical model, 9.3.1
 description, 5.5.9
 installation practices, 5.5.10
 minimizing losses, 5.5.6
 protecting cells, 5.5.7
Shunt resistance, 3.2.4, 3.7.2
Sigma limits, 11.14, (1.1)
Silicone, 7.2, 7.7, (7.2)
Silicon
 mechanical properties, 3.1.4, 7.6, (7.6)
 spalling and divoting in processing, 10.4.8
 spalling and divoting in testing, 3.6.3, 5.2.2, 11.11
Silver-titanium contacts—see contacts
Silver, 7.1.1
Single-point soldering, 10.3
Sizes, solar cells, 3.8.1
Size constraints—see interfaces
Skylab, 1.1, 6.2.1
Smoothness, surface—see surface finish
Solar absorptance, 7.14, (7.14)
Solar battery—see solar cell array
Solar cells
 AC impedance—see AC model
 adhesive—see adhesive
 array
 construction, 6.1, 6.2
 typical, 1.1, 6.1
 back field, 1.2, 3.1.1
 base region, 3.1.3, 3.4
 black, 1.2, 3.1.1
 blue, 1.2, 3.1.1
 cadmium sulfide, 1.2
 calibration, 11.2, 11.3
 characteristics—see I-V curve
 coatings—see coatings
 cover installation factor, 4.3.1
 degradation, charged particles, 3.3
 description, 3.1
 drift field, 3.1.6
 efficiency—see inefficiency
 equation convention, 9.2.1
 failures, 8.7.6, 9.9.2, 9.9.3
 glassing—see processes
 high efficiency, 3.1.1
 high intensity, 3.5.3
 interconnectors—see interconnectors
 in series (see hot spots also), 8.7.1
 I-V curve—see I-V curve
 K6-A, K6-B, (3.1.1), (3.3.1)
 lithium doped, 3.1.7
 low intensity, 3.6.4
 low temperature, 3.6.4
 mismatch, 9.3.1
 mismatch, 9.3.1
 model
 computerized, 9.2.3, 9.2.5
 derived, theoretical, 3.11.1
 nonanalytical, 9.2.4
 physical, 9.2.1
 modules—see modules
 new developments, 3.12, (3.12)
 performance characterization, 9.4.1
 performance data, (3.0)
 polarity, 3.2.1, 9.1.1
 radiation resistant, 3.3.1
 selection, 8.3
 sizes, 3.8.1
 stack design, 8.3.6
 standards—see standard solar cells
 temperature coefficients—see temperature coefficients
 testing, calibration—see calibration
 textured, 3.1.1
 theory, 3.11
 thickness, 3.8.2
 thin film, 1.2.2
 thin, 3.4, (3.4)
 vertical multijunction, 1.2.2
 violet, 3.1.1
Solar cell-to-cell gaps, 8.7.2
Solar cell-to-substrate adhesive—see adhesives
Solar constant, 2.4.2
Solar distance
 effect on output, 9.4.7
 effect on solar constant, 2.4.2
 of planets, 2.4.2
Solar flares, protons, 2.5.4
Solar intensity—see solar constant
Solar irradiance—see solar constant
Solar noon
 on earth, 11.2.1, 11.3
 orbital, 9.10.6
Solar orbits, 9.10
Solar plasma—see plasma
Solar pressure, 2.4.4
Solar radiation—see solar constant
Solar simulator
 description, 11.2.5
 development, 11.2.1
 spectral match, 11.3
Solar spectrum, 2.4.2
Solar system, 2.3.1
Solar ultraviolet—see ultraviolet radiation
Soldering - see processes
Solderless contact solar cells—see contacts
Solder, 7.1.5
Solder, contacts—see contacts
Solder, joint failures—see failures
Solder, properties of—see specific listings
Solder, scavenging of silver, gold, 7.1.5
Solder, solubility of silver in, 7.1, 5
Solvents, 2.1.8, 2.3.2
Sources, ideal, 9.1.2
Spacecraft charging, 2.3.3
Spacecraft, typical, 1.1
Space environment—see specific listings

- space simulation, 11.1
- space vacuum—see vacuum
- spalling silicon—see silicon, spalling
- specifications
 - arrays, 10.2.2
 - assembly, 10.2, 10.5
 - diodes, 10.3.4
 - glassed cells, 10.3.3
 - purpose of, 10.2.1
 - solar cells, 10.3.1
 - solar cell covers, 10.3.2
 - test, 11.1
- Specific heat, 7.12, (7.12)
- Specific stiffness, 7.5.1
- Specific strength, 7.5.1
- Specific weight—see density
- Spectral distribution
 - solar simulator, 11.2.5
 - sunlight, 2.4.2
- Spectral response
 - defined, 3.10.3
 - of solar cells, 3.10.4
- Spectrum, electromagnetic, 2.4.2
- Spinning spacecraft
 - description, 1.1
 - performance, 8.6.2
 - temperature, 8.5.3, 9.6.7
- Spin-stabilized spacecraft, orbital characteristics, 2.6, 9.10
- Spray on solar cell covers—see covers
- Sputnik, 1.1
- Stability
 - of power system, 9.1.4
 - of solar cells, 3.3.5
- Stabilization, three axis, 1.1, 9.10.6
- Stack, solar cell, design, 8.3.6
- Standardization
 - of design, 1.4
 - of solar cell calibration, 11.3
 - of solar cell testing, 11.2.1
- Standard solar cells
 - of conventional design, 3.1.1
 - defined, 11.3
 - instabilities in, 3.3.5
 - use of, (1.1)
- Statistical analysis, 11.14, (1.1)
- Statistical sampling—see sampling plans
- Stiffness, 7.5.1
- Stiffness, specific, 7.5.1
- Storage battery, 9.1.4
- Storage—see humidity
- Stowage volume constraints—see interfaces
- Strain range, 9.8.3
- Strain, 7.5.1, 9.7.1
- Strength, specific, 7.5.1
- Stress-strain diagrams
 - for metals, 7.5.1
 - for nonmetals, 7.7
 - for silicon and glass, 7.5.1
- Stress analysis, 9.7
- Structural analysis—see stress analysis
- Structural design terminology, 9.7.1
- Sublimation, 2.3.2
- Substorms, magnetic, 2.3.3
- Substrates, 6.2
- Sunlight
 - in space—see solar constant
 - testing, 11.2.1
 - through atmosphere, 11.3
- Sun, physical description, 2.3.1, 2.4.2
- Superstrates, 4.7, 8.9
- Surface finish
 - coverglasses, 4.1
 - interconnectors, 3.9.6
 - solar cell active area, 3.10.1
 - solar cell contacts, 3.9.6
- Surface leakage, solar cells, 3.7

- Surface roughness—see surface finish
- Synergistic effects, 11.1.4, 11.9
- System integration tests (see also testing), 11.1.2

T

- Table mountain testing (see also testing), 11.2.1
- Techniques, testing—see measurement techniques
- Teflon-encapsulated arrays, 6.2.13
- Teflon, 7.2.4
- Temperature/humidity effects, 2.1.2
- Temperature coefficients
 - electrical resistance, 7.9, (7.9)
 - linear expansion, 7.11
 - solar cells, 3.6.2
- Temperature cycling
 - electrical losses, 9.4.1, 11.11.3
 - failures—see failures
 - requirements, 5.3.1
 - test methods, 11.1.3, 11.11.1
 - test results, 11.11.2, 11.11.3
- Temperature vs altitude, 2.1.1
- Temperature
 - analysis, 9.6
 - control in solar cell testing, 11.2.2, 11.2.7
 - correction, 11.3
 - eclipse exit, calculation, 9.6.5
 - effects of on materials, 2.4.1
 - effects of on solar cells, 3.6
 - equilibrium—see temperature, operating
 - estimate in space, 8.5.3
 - gradients, effect on output—see mismatch losses in space, 2.4.1
 - of transportation—see kovar
 - operating
 - operating, calculation, 9.6.4
 - operating, estimates, 8.5.3
 - tests—see testing
- Terminals, electrical, 5.6
- Terrestrial environments—see specific listings
- Testing
 - acceptance, 11.1.2
 - acoustic, 11.1.3
 - breakdown voltage, 11.10
 - combined environments, 11.9
 - dark forward, 11.12
 - dielectrics, 11.10
 - diodes, 11.12
 - electrical, 11.2
 - environmental (see also specific listings), 11.1
 - history, solar cells, 11.2.1
 - in-situ, 11.8, 11.9
 - in natural sunlight, 11.2.1
 - life, 11.1.2
 - non-destructive (NDT), 10.7
 - qualification, 11.1.2
 - radiation, 11.7
 - reliability, 11.1
 - reverse characteristics, 3.7.2
 - series resistance, 11.2.7
 - shock, 11.1.3
 - short-circuit current, 11.2.4
 - solar cells and arrays, 11.2
 - solar cell contact pull and peel, 10.7.4, 11.5
 - spectral response and distribution, 11.4
 - standard solar cells—see calibration
 - temperature, 11.1.3
 - thermal vacuum, 11.11
 - ultraviolet, 11.8
 - vibration, 11.1.3
- Test criteria, 11.1.1
- Test criteria, objectives, 11.1.1
- Test data recording, 11.1.5
- Test equipment calibration, 11.1.5
- Test equipment—see specific listings under testing
- Test errors, solar cells, arrays, 11.2.7, 11.14, (1.1)
- Test level, determination of, 11.1.1

Test plans and procedures, 11.1.3
 Test purpose, 11.1.1
 Test requirements, 11.1.2
 Test results—see specific listings under testing
 Test sequence, 11.1.4
 Test specifications, 10.2, 11.1.4, 11.1.5
 Test techniques—see measurement techniques
 Test types, 11.1.2
 Textured solar cells—see solar cells
 Theory, solar cell operation, 3.11.1
 Thermal analysis, 9.6
 Thermal conduction, 7.12, 9.6.3, (7.12)
 Thermal cycling—see temperature cycling
 Thermal design sensitivity, 8.5.3
 Thermal design, 8.5
 Thermal expansion, 5.3, 7.11, (7.11)
 Thermal mass, 7.12
 Thermal properties—see specific listings
 Thermal radiation, 9.6.2
 Thermal vacuum testing, 11.1.3
 Thermal (see also temperature)
 Thermocompression bonding—see processes
 Thermo-optical properties—see specific listings
 Thevenin's theorem, 9.1.2
 Thickness, solar cells—see solar cells
 Thin-film solar cells—see solar cells
 Thin solar cells—see solar cells
 Time-dependent degradation, 9.4.3
 Time
 effects of, 2.3.7
 for mission life, 2.3.7
 Titanium-silver contacts—see contacts
 Tolerances
 dimensional, of cells, 3.8
 dimensional, of covers, 4.1
 in design, 8.3.6, 10.1.5
 Tolerance, radiation—see radiation
 Tradeoff studies—see optimization of design
 Trajectory—see orbit
 Transfer orbit—see orbit
 Transformation temperature—see kovar
 Transient response, 9.1.3
 Transit time, 2.3.7
 Transmission degradation—see radiation effects
 Transmittance, 7.13, (7.13)
 Trapped electrons and protons, 2.5.2
 True anomaly, 9.10.2
 Tungsten lamps, 11.2.2
 Tunnel oven soldering, 10.4.5

U

Ultimate conversion efficiency—see efficiency
 Ultimate strength
 defined, 7.5.1
 of metals, 7.1, (7.5)
 of non-metals, 7.2, (7.7)
 of silicon and glass, 7.2, (7.6)
 Ultrasonic bonding—see processes
 Ultraviolet radiation
 dose, 2.4.3
 effects of on adhesives, 2.4.3, 11.8
 effects of on covers, 2.4.3
 effects of on materials, 2.4.3, 11.8
 equivalent sun hours, 2.4.3
 of sun, 2.4.3
 far (FUV), 11.8.2
 Uncertainties
 in measurements, 11.14
 in solar constant, 2.4.2
 statistical, 11.14, (1.1)
 Unit conversion factors, (7.1)
 UV—see ultraviolet radiation

V

V_{mp}, V_{oc}, V_{op}, defined, 3.2.2
 Vacuum
 space, test, effects of, 2.3.2
 thermal cycling testing—see testing
 Vanguard, 1.1
 Van allen belts, 1.1, 2.5.2
 Variance, 11.14.1
 Variation in solar constant—see solar constant
 Velvet solar cell—see solar cells
 Venting of substrates, 2.1.1
 Verification of design by test, 11.1.2
 Vertical multijunction solar cells—see solar cells
 Vibration testing—see testing
 Vibration
 crystal lattice, 3.11.1
 during launch, 2.2.4
 Violet solar cells—see solar cells
 Visual inspection, 10.7.2, 11.1.1
 VMJ solar cells—see solar cells
 Voltage-current characteristic—see I-V curve
 Voltage breakdown of air, 2.1.1
 Voltage breakdown test of dielectrics, 11.10
 Voltage dividers, 9.1.2
 Voltage sources, 9.1.2
 Volume, stowage, constraints—see interfaces

W

Waveforms, electrical, 9.1.3
 Wavelength of light, 2.4.2, 2.4.3
 Wave number, 3.10.3
 Wearout—see fatigue
 Weight and mass, 7.3.1, (7.3)
 Weight constraints—see interfaces
 Weight loss—see outgassing
 Weld degradation of solar cells, 10.4.8
 Weld joint failures—see failures
 Weldability—see processes and specific materials
 Welding—see processes
 Welding of solar cells, 10.4.8
 Welding process control, 10.7
 Wires, 5.4
 Wiring losses
 design optimization, 8.7.4
 in array analysis, 9.4.3
 in solar cell testing, 11.2.4
 mass related, 5.4
 Wiring, 5.4
 back, 8.10.4
 Workability—see specific materials
 Workmanship criteria, 10.6
 Workmanship, 8.1.2
 Work hardening (see also specific metal listings),
 9.7.1
 Wraparound contact solar cells—see solar cells
 or contacts

X

X-rays, 2.5.1
 Xenon lamps (also see solar simulator), 11.2.1
 Xenon, pulsed solar simulator—see solar simulator

Y

Yellowing—see discoloration
 Yield strength
 definition of, 7.1, 7.2
 of metals, 7.5, (7.5)
 of non-metals, 7.7, (7.7)
 Young's modulus—see modulus of elasticity

Z

Zero gravity, 2.3.6

1. Report No. 43-38, Vols. I and II		2. Government Accession No.		3. Recipient's Catalog No.	
4. Title and Subtitle SOLAR CELL ARRAY DESIGN HANDBOOK				5. Report Date October 1976	
				6. Performing Organization Code	
7. Author(s) R. H. Josephs				8. Performing Organization Report No.	
9. Performing Organization Name and Address JET PROPULSION LABORATORY California Institute of Technology 4800 Oak Grove Drive Pasadena, California 91103				10. Work Unit No.	
				11. Contract or Grant No. NAS 7-100	
12. Sponsoring Agency Name and Address NATIONAL AERONAUTICS AND SPACE ADMINISTRATION Washington, D.C. 20546				13. Type of Report and Period Covered Special Publication	
				14. Sponsoring Agency Code	
15. Supplementary Notes					
16. Abstract The Solar Cell Array Design Handbook is written at a practicing engineering level and provides a comprehensive compilation of explanatory notes, design practices, analytical models, solar cell characteristics, and material properties data of interest to personnel engaged in solar cell array performance specification, hardware design, analysis, fabrication and test. Twelve handbook chapters discuss the following: historical developments, the environment and its effects, solar cells, solar cell filters and covers, solar cell and other electrical interconnections, blocking and shunt diodes, substrates and deployment mechanisms, material properties, design synthesis and optimization, design analysis, procurement, production and cost aspects, evaluation and test, orbital performance, and illustrative design examples. A comprehensive index permits rapid locating of desired topics. The handbook consists of two volumes: Volume I is of an expository nature while Volume II contains detailed design data in an appendix-like fashion. Volume II includes solar cell performance data, applicable unit conversion factors and physical constants, and mechanical, electrical, thermal, optical, magnetic, and outgassing material properties. Extensive references are provided.					
17. Key Words (Selected by Author(s)) Spacecraft Design, Testing and Performance Spacecraft Propulsion and Power Engineering (General) Space Sciences (General)			18. Distribution Statement Unclassified -- Unlimited		
19. Security Classif. (of this report) Unclassified		20. Security Classif. (of this page) Unclassified		21. No. of Pages 490 (Vol. I) 241 (Vol. II)	22. Price